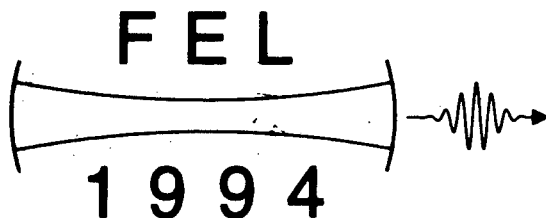


# FREE ELECTRON LASERS

Proceedings of the Sixteenth International  
Free Electron Laser Conference  
Stanford, CA, USA, August 22-26, 1994

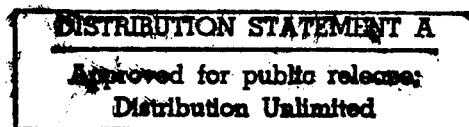
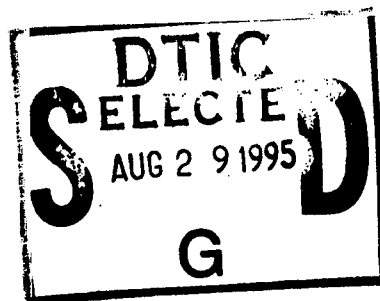


Editors

**T.I. SMITH**

**H.A. SCHWETTMAN**

**R.L. SWENT**



**NORTH-HOLLAND**

19950825 068

# FREE ELECTRON LASERS



**DISTRIBUTION STATEMENT A**  
**Approved for public release;**  
**Distribution Unlimited**

**DTIC QUALITY INSPECTED 5**



# FREE ELECTRON LASERS

Proceedings of the Sixteenth International  
Free Electron Laser Conference  
Stanford, CA, USA, August 22-26, 1994

*Editors*

T.I. SMITH

H.A. SCHWETTMAN

R.L. SWENT

*W.W. Hansen Experimental Physics Laboratory,  
Stanford University, Stanford, CA, USA*

|                                      |   |
|--------------------------------------|---|
| Accession For                        |   |
| NTIS                                 | CRA&I <input checked="" type="checkbox"/> |
| DTIC                                 | TAB <input type="checkbox"/>              |
| Unannounced <input type="checkbox"/> |   |
| Justification _____                  |   |
| By _____                             |   |
| Distribution /                       |   |
| Availability Codes                   |   |
| Dist                                 | Avail and/or<br>Special                   |
| A-1                                  |   |



1995

NORTH-HOLLAND



© 1995 Elsevier Science B.V. All rights reserved.

No part of this publication may be reproduced, stored in a retrieval system or transmitted in any form or by any means, electronic, mechanical, photocopying, recording or otherwise, without the written permission of the Publisher, Elsevier Science B.V., Copyright & Permissions Department, P.O. Box 521, 1000 AM Amsterdam, The Netherlands.

Special regulations for readers in the U.S.A. – This publication has been registered with the Copyright Clearance Center, Inc. (CCC), 222 Rosewood Drive, Danvers, MA 01923, USA. Information can be obtained from the CCC about conditions under which photocopies of parts of this publication may be made in the USA. All other copyright questions, including photocopying outside of the USA, should be referred to the Publisher.

No responsibility is assumed by the Publisher for any injury and/or damage to persons or property as a matter of products liability, negligence or otherwise, or from any use or operation of any methods, products, instructions or ideas contained in the materials herein. Although all advertising material is expected to conform to ethical standards, inclusion in this publication does not constitute a guarantee or endorsement of the quality or value of such product or of the claims made of it by its manufacturer.

⊗ The paper used in this publication meets the requirements of ANSI/NISO 239.48-1992 (Permanence of Paper).

Reprint from

NUCLEAR INSTRUMENTS AND METHODS IN PHYSICS RESEARCH

Section A: Accelerators, Spectrometers, Detectors and Associated Equipment, Vol. 358, Nos. 1–3

The Manuscript of the Proceedings was received by the Publisher: mid-October/mid-December 1994

## Preface

The Sixteenth International Free Electron Laser Conference was held August 22–26, 1994 at Stanford University, Stanford, CA. The conference was organized by the Stanford Picosecond Free Electron Laser Center which is located in the W.W. Hansen Experimental Physics Laboratory and was attended by 230 registered participants from 15 different countries. Scientific contributions to the conference included 48 invited oral presentations and 179 poster presentations.

These Proceedings contain the manuscripts of 190 contributions to the Conference. The number of contributions presented and published attests to the continuing vigor of the field, and a perusal of the Table of Contents will verify the diversity of interests within the field. Following recent precedent, the papers were divided into two categories. The first category contains 144 regular scientific papers which have been subjected to a strict peer review process. The second category contains 46 extended synopses, subjected to minimal review. Some of the contributions were submitted as extended synopses, while others were published as such upon the recommendation of the referees. Those contributions published as extended synopses can generally be characterized as papers describing the status of ongoing or proposed projects, or as summaries of research in progress. To satisfy the page limitation imposed by the publisher, the regular scientific papers were limited to four journal pages and the extended synopses to just two pages.

In addition to the Conference articles, this volume contains two Tables of Operating and Proposed FELs, along with explanatory text. These tables are located just before the author index. One of the tables, compiled by H.P. Freund and V.L. Granatstein, is devoted to long wavelength FELs. The other, compiled by W.B. Colson, addresses short wavelength FELs. It is hoped that these tables will be updated annually and will become a regular part of the proceedings of future Conferences.

With the rapid growth of User activities at FEL facilities in Europe and the United States, 1994 was an appropriate time to organize an FEL Users Workshop. To ensure full participation of the FEL community, while still recognizing the independent interests of the Users, this first FEL Users Workshop was held on the Stanford University campus immediately following the FEL Conference. There were 116 registered participants at the Workshop and 75 scientific contributions. The contributions described experiments, either completed or in progress, using the unique capabilities of FELs. Based on the success of this first Workshop, plans are under way to hold the 2nd and 3rd FEL Users Workshops in conjunction with FEL '95 and FEL '96.

The much anticipated report of the National Research Council, "Free Electron Lasers and Other Advanced Sources of Light", was released August 26, the final day of the FEL Conference. Professor H. Donald Levy who chaired the NRC committee, which was charged with reviewing the scientific research opportunities of FELs, summarized the findings and recommendations at the final session of the Conference. The report, modestly supportive of short wavelength FEL development and specifically supportive of a national far-IR FEL facility, may have a significant impact on funding opportunities for FEL facilities and research in the US. It may also have an indirect impact on the programs of other nations. Copies of the report are available from the Board on Chemical Sciences and Technology, National Research Council, 2101 Constitution Ave., N.W., Washington, DC 21418.

The Editors gratefully acknowledge the financial support of the US Office of Naval Research, the W.W. Hansen Experimental Physics Laboratory, the Stanford Physics Department, and the Office of

the Dean of Research at Stanford University. In addition, we thank Elsevier Science B.V. for their continuing part in the support of the Free Electron Laser Prize. Finally, the Editors would like to acknowledge the important role played by Jeanette Bakker of Elsevier Science B.V. and express their appreciation for her expert assistance, understanding, and patience in the publication of this record of the Sixteenth International FEL Conference.

Todd I. Smith  
H. Alan Schwettman  
Richard L. Swent  
*Guest Editors*

#### Breakdown of the participants by country

|               |    |                          |     |
|---------------|----|--------------------------|-----|
| Belarus       | 1  | Korea                    | 4   |
| P.R. of China | 4  | Russia                   | 13  |
| France        | 13 | Switzerland              | 1   |
| Germany       | 6  | Netherlands              | 16  |
| India         | 1  | United Kingdom           | 5   |
| Israel        | 4  | United States of America | 113 |
| Italy         | 8  | Ukraine                  | 1   |
| Japan         | 40 |                          |     |

#### Breakdown of the published manuscripts by country

|               |    |                          |    |
|---------------|----|--------------------------|----|
| Belarus       | 3  | Korea                    | 4  |
| P.R. of China | 4  | Russia                   | 25 |
| France        | 11 | Netherlands              | 13 |
| Germany       | 4  | United Kingdom           | 2  |
| India         | 1  | United States of America | 78 |
| Israel        | 8  | Ukraine                  | 2  |
| Italy         | 7  |                          |    |
| Japan         | 28 |                          |    |



## Dr. Alberto Renieri and Dr. Giuseppe Dattoli win the 1994 International Free-Electron Laser Prize

The International Free-Electron Laser Prize, awarded annually at the Free-Electron Laser Conference, recognizes outstanding and pioneering contributions in the field of free-electron lasers. At the 16th International Free-Electron Laser Conference, which took place at Stanford University, the 1994 Prize was awarded to Dr. Alberto Renieri and Dr. Giuseppe Dattoli of the ENEA, Frascati, Italy, for their incisive contributions to the theory of free-electron lasers and their leadership role in the FEL and accelerator community.

Alberto Renieri has been involved in research on particle accelerators, colliding beams, and quantum optics since 1969. Dr. Renieri presented one of the earliest classical explanations of the FEL mechanism soon after the first Stanford FEL experiments in the 1970s. He derived an expression for the maximum coherent radiation power in a storage-ring FEL. This well known result is now known as the "Renieri limit". This important result was obtained by noting that the growth in the energy spread on an electron beam that is recycled many times through an undulator is eventually balanced by synchrotron radiation damping. Dr. Renieri has been Director of the ENEA Applied Physics Division since 1993.

Giuseppe Dattoli started his career in high energy physics, working on the electromagnetic properties of charmed particles. He has been involved in quantum optics and FEL research since 1977, working on a broad range of problems, from pulse propagation dynamics to the design of FELs. Dr. Dattoli and Dr. Renieri developed the supermode theory of mode evolution in the FEL oscillator, and used it to describe short pulse effects in RF driven FELs. Dr. Dattoli has used a quantum mechanical analysis to provide a fundamental picture of the FEL interaction from basic principles. Many researchers have found Dr. Dattoli's empirical formulae describing FEL gain to be an important guide in the design of new experiments. Dr. Dattoli is presently the Head of the ENEA Frascati Theory Division.

Dr. Renieri and Dr. Dattoli have made many outstanding contributions to FEL science and technology. We wish them continued success in their endeavors.

Phillip Sprangle  
*Chairman FEL-Prize Committee*

### Host Institutions

Stanford Picosecond Free Electron Laser Center  
W.W. Hansen Experimental Physics Laboratory  
Stanford University, Stanford, CA 94305, USA

### Conference Chairman

T.I. Smith, Stanford University

### International Executive Committee

T.I. Smith, Stanford, USA (*chair*)  
W. van Amersfoort, Nieuwegein, NL  
I. Ben-Zvi, Brookhaven, USA  
W.B. Colson, Monterey, USA  
L.R. Elias, Orlando, USA  
H. Genz, Darmstadt, Germany  
A. Gover, Ramat-Aviv, Israel  
S. Joly, Bruyères-le-Châtel, France  
J.M.J. Madey, Durham, USA  
K. Mima, Osaka, Japan

G. Neil, Newport News, USA  
B. Newnam, Los Alamos, USA  
J.M. Ortega, Orsay, France  
M. Poole, Warrington, UK  
A. Renieri, Frascati, Italy  
C. Roberson, Arlington, USA  
P. Sprangle, Washington, DC, USA  
Y. Tian-Lu, Beijing, China  
N.A. Vinokurov, Novosibirsk, Russia  
C. Yamanaka, Osaka, Japan

### International Program Committee

H.A. Schwettman, Stanford, USA (*chair*)  
S.V. Benson, Newport News, USA  
R. Bonifacio, Milano, Italy  
H.P. Freund, Washington, DC, USA  
G.P. Gallerano, Frascati, Italy  
D. Iracane, Bruyères-le-Châtel, France  
D.A. Jaroszynski, Orsay, France  
E. Jerby, Tel-Aviv, Israel  
K.-J. Kim, Berkeley, USA  
A.N. Lebedev, Moscow, Russia

V.N. Litvinenko, Durham, USA  
D. Oepts, Nieuwegein, The Netherlands  
R. Prazeres, Orsay, France  
G. Ramian, Santa Barbara, USA  
P.J.M. van der Slot, Enschede, The Netherlands  
C.M. Tang, Washington, DC, USA  
W.J. Witteman, Enschede, The Netherlands  
Jialin Xie, Beijing, China  
T. Yamazaki, Tsukuba, Japan  
L.H. Yu, Brookhaven, NY, USA

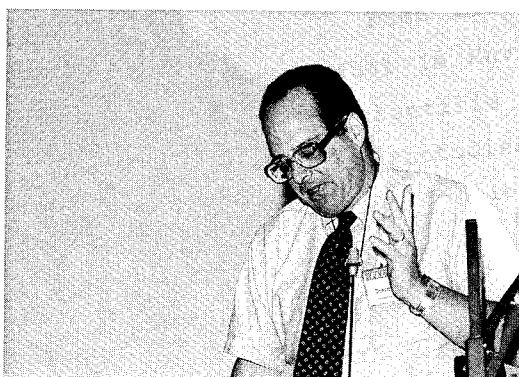
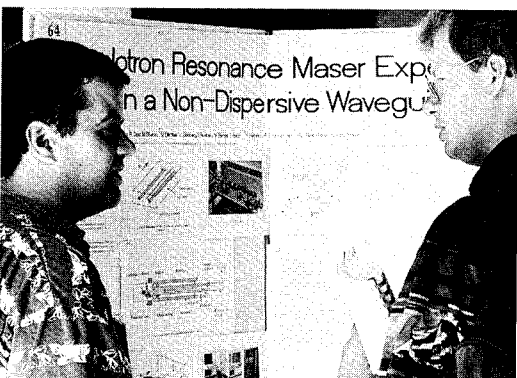
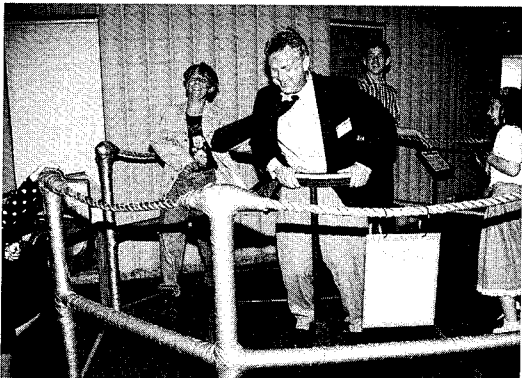
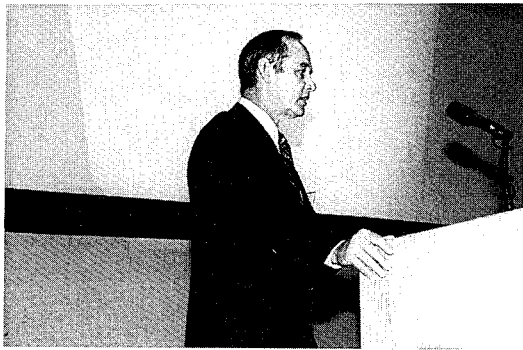
### Local Committee Chairman

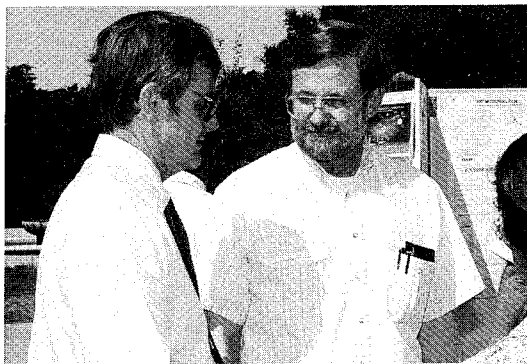
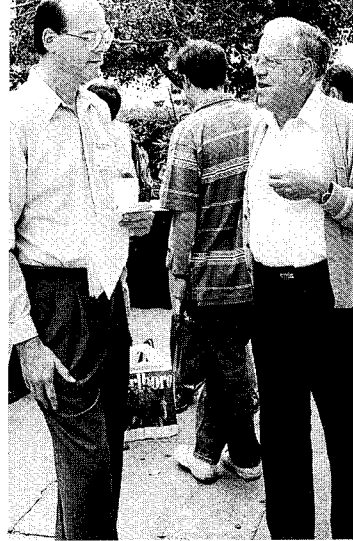
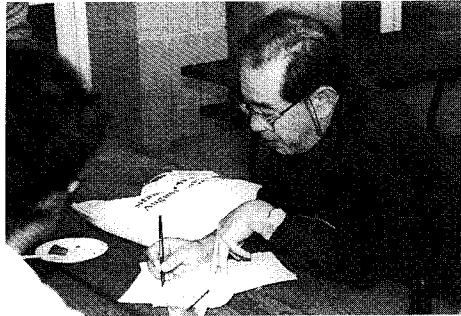
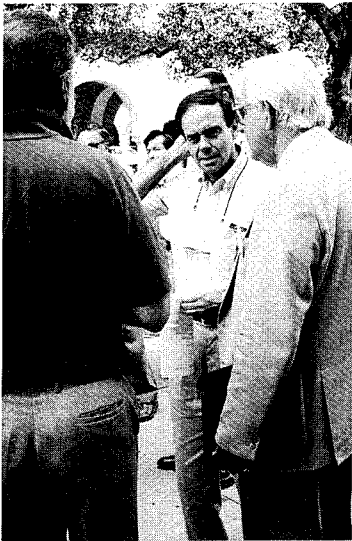
R.L. Swent, Stanford University

### FEL Prize Sub-Committee

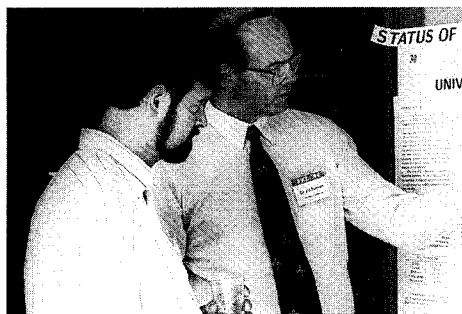
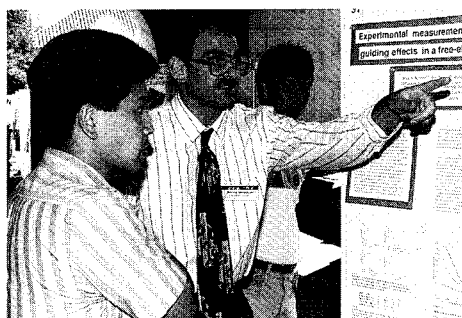
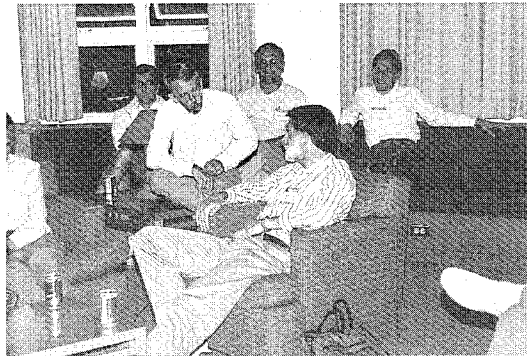
P. Sprangle, Washington DC, USA (*chair*)  
W.B. Colson, Monterey, USA  
L.R. Elias, Orlando, USA

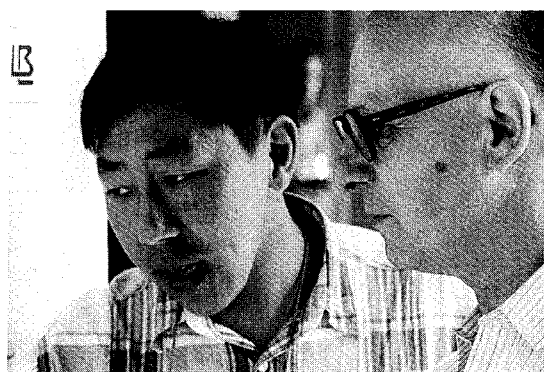
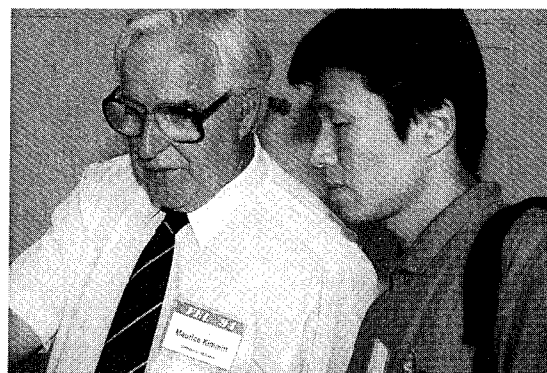
R.M. Phillips, Stanford, USA  
T.I. Smith, Stanford, USA  
N.A. Vinokurov, Novosibirsk, Russia

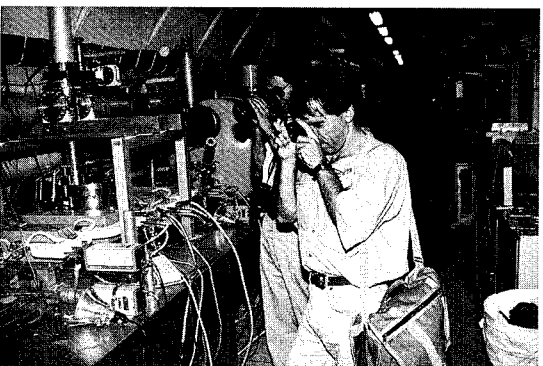
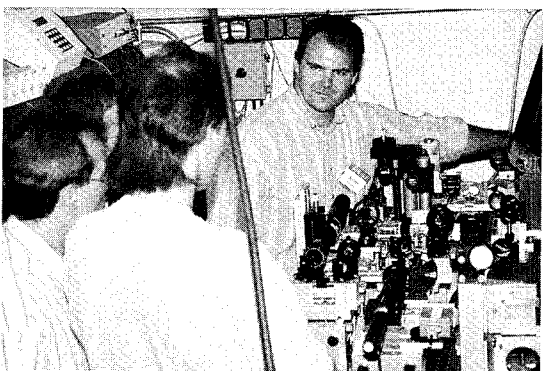
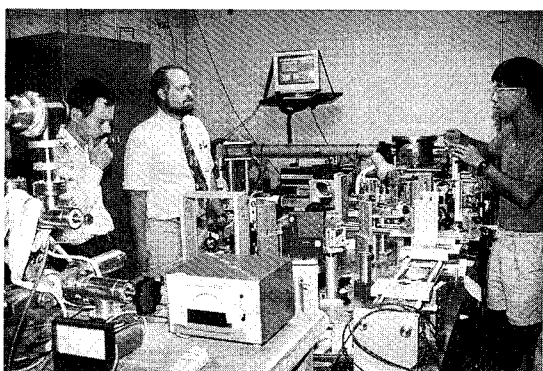
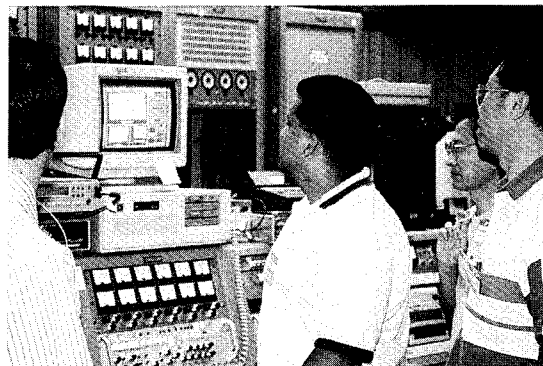
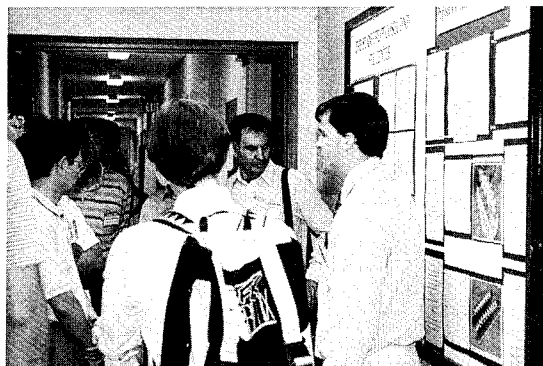














|   |     |
|---|-----|
| Experimental mode analysis of the circular free electron laser<br>T. Mizuno, T. Ootuki, T. Ohshima and H. Saito . . . . .   | 131 |
| Concept of a submillimeter wavelength CARM<br>V.L. Bratman, G.G. Denisov, M.M. Ofitserov, M.I. Petelin and S.V. Samsonov . . . . .  | 135 |
| Theory of the free-electron laser based upon a coaxial hybrid wiggler<br>H.P. Freund, R.H. Jackson, D.E. Pershing and J.M. Taccetti . . . . .   | 139 |
| Cyclotron resonance maser experiment in a non-dispersive waveguide<br>A. Shahadi, E. Jerby, M. Korol, R. Drori, M. Sheinin, V. Dikhtiar, V. Grinberg, I. Ruvinsky, M. Bensal, T. Harhel, Y. Baron, A. Fruchtman, V.L. Granatstein and G. Bekefi . . . . . | 143 |
| Green function analysis of a Raman FEL<br>G. Shvets and J.S. Wurtele . . . . .  | 147 |
| Free-electron maser oscillator experiment in the UHF regime<br>R. Drori, E. Jerby and A. Shahadi . . . . .  | 151 |

## Section V. High power

|  |     |
|--|-----|
| A 130–260 GHz, 1 MW free electron maser for fusion<br>W.H. Urbanus, W.A. Bongers, G. van Dijk, C.A.J. van der Geer, J.P. van Ieperen, A. van der Linden, P. Manintveld, A.B. Sterk, A.V. Tulupov, A.G.A. Verhoeven, M.J. van der Wiel, V.L. Bratman, G.G. Denisov, A.A. Varfolomeev, S.N. Ivanchenkov, A.S. Khlebnikov, M. Catellino, A. Salop and M. Caplan . . . . . | 155 |
| CEBAF UV/IR FEL subsystem testing and validation program<br>G.R. Neil, S.V. Benson, H.F. Dylla and H. Liu . . . . .  | 159 |
| Design study of a G-band FEL amplifier for application to cyclotron resonant heating in magnetic fusion reactors<br>H.P. Freund, M.E. Read, R.H. Jackson, D.E. Pershing and J.M. Taccetti . . . . .  | 163 |
| Time-dependent multi-dimensional simulation studies of the electron output scheme for high power FELs<br>S.J. Hahn, W.M. Fawley, K.-J. Kim and J.A. Edighoffer . . . . .   | 167 |
| Chaotic particle deceleration and FEL efficiency enhancement with an incoherent pump wave or a stochastic undulator<br>Ya.L. Bogomolov, N.S. Ginzburg and E.R. Golubyatnikova . . . . .  | 171 |
| Predicted operating conditions for maintaining mode purity in the 1 MW 200 GHz FOM free electron maser<br>M. Caplan, T. Antonsen, B. Levush, A. Tulupov and W. Urbanus . . . . .   | 174 |
| Spectral dynamics of the FEM<br>P.J. Eecen, A.V. Tulupov and T.J. Schep . . . . .  | 178 |
| Competition of longitudinal modes and the scenario of single-mode regime build-up for the FOM-Fusion-FEM project<br>V.L. Bratman and A.V. Savilov . . . . .  | 182 |
| Electrostatic-accelerator FELs for power beaming<br>I. Kimel and L.R. Elias . . . . .  | 186 |
| Super-power free electron lasers with two-dimensional distributed feedback<br>N.S. Ginzburg, N.Yu. Peskov, A.S. Sergeev, A.V. Arzhannikov and S.L. Sinitsky . . . . .  | 189 |
| Design and performance calculations for a $K_\alpha$ -band CHI wiggler ubitron amplifier<br>J.M. Taccetti, R.H. Jackson, H.P. Freund, D.E. Pershing, M. Blank and V.L. Granatstein . . . . .   | 193 |
| Beam transport through undulators designed for high power FEMs<br>A.A. Varfolomeev and A.V. Smirnov . . . . .  | 197 |
| High power operation of a wiggler-focused sheet beam free electron laser amplifier<br>S. Cheng and W.W. Destler . . . . .  | 200 |
| Free-ion lasers with radiative ion cooling<br>E.G. Bessonov . . . . .  | 204 |



## Section VI. FEL experiments

|  |     |
|--|-----|
| Time-resolved study of sideband generation and transition to chaos on an infrared FEL<br>W.P. Leemans, M.E. Conde, R. Govil, B. van der Geer, M. de Loos, H.A. Schwettman, T.I. Smith<br>and R.L. Swent . . . . .  | 208 |
| Sub-picosecond laser pulse generation on the CLIO FEL<br>R. Prazeres, J.M. Berset, F. Glotin, D. Jaroszynski and J.M. Ortega . . . . .   | 212 |
| Sub-picosecond FEL micropulse length and electron bunch measurements<br>E.R. Crosson, K.W. Berryman, T.I. Smith, R.L. Swent, H.C. Lihn and H. Wiedemann . . . . .  | 216 |
| Observation and characterization of frequency-chirped optical pulses on the Mark III free-electron laser<br>E.B. Szarmes, A.D. Madden and J.M.J. Madey . . . . .   | 220 |
| Two-colour operation of the free-electron laser using a step-tapered undulator<br>D.A. Jaroszynski, R. Prazeres, F. Glotin and J.M. Ortega . . . . .   | 224 |
| Free-electron laser operation and self-amplified spontaneous emission using a step-tapered undulator<br>D.A. Jaroszynski, R. Prazeres, F. Glotin, J.M. Ortega, D. Oepts, A.F.G. van der Meer, G. Knippels<br>and P.W. van Amersfoort . . . . .   | 228 |
| Electron energy spectral measurements in the large-slipage regime<br>W.A. Gillespie, A.M. MacLeod, P.F. Martin, G.M.H. Knippels, A.F.G. van der Meer, E.H. Haselhoff<br>and P.W. van Amersfoort . . . . .  | 232 |
| Experimental measurement of short pulse guiding effects in a free-electron laser<br>B.A. Richman, B. McVey and J.M.J. Madey . . . . .  | 236 |
| High efficiency results at 23 $\mu\text{m}$ on the ELSA FEL and operation with the MONA wiggler<br>Ph. Guimbal, D. Iracane, S. Joly, P. Balleyguier, A. Binet, J.P. Blèsès, J. DiCrescenzo, V. Fontenay,<br>P. Fourdin, G. Haouat, J.G. Marmouget, Y. Pranal, F. Sabary, S. Striby and D. Touati . . . . . | 240 |
| Free-electron laser oscillation with a multibunch electron beam of the 38 MeV L-band linear accelerator<br>at ISIR<br>S. Okuda, Y. Honda, N. Kimura, J. Ohkuma, T. Yamamoto, S. Suemine, T. Okada, S. Ishida, T.<br>Yamamoto, S. Takeda, K. Tsumori and T. Hori . . . . .                                  | 244 |
| Single-bunch and multibunch electron beam generation for FEL experiments with the 38 MeV L-band<br>linear accelerator at ISIR<br>S. Okuda, Y. Honda, N. Kimura, J. Ohkuma, T. Yamamoto, S. Suemine, T. Okada, S. Takeda, K.<br>Tsumori and T. Hori . . . . .   | 248 |
| Wavelength shifting in the Stanford FEL<br>A. Marzali, T.I. Smith and H.A. Schwettman . . . . .  | 252 |
| The saturation of the Beijing FEL<br>J. Xie, J. Zhuang, Y. Huang, Y. Li, S. Lin, R. Ying, Y. Zhong, L. Zhang, G. Wu, Y. Zhang, C. Chao,<br>L. Li, E. Fu, J. Su, Y. Wang and G. Wang . . . . .  | 256 |

## Section VII. FEL technology

|  |     |
|--|-----|
| FEL cavity length measurement with an external laser<br>K.W. Berryman, P. Haar and B.A. Richman . . . . .  | 260 |
| Phase space tomography of relativistic electron beams<br>C.B. McKee, P.G. O'Shea and J.M.J. Madey . . . . .  | 264 |
| Temporal characterization of the Stanford mid-IR FEL micropulses by "FROG"<br>B.A. Richman, K.W. DeLong and R. Trebino . . . . .   | 268 |
| Photocathodes for free electron lasers<br>S.H. Kong, J. Kinross-Wright, D.C. Nguyen and R.L. Sheffield . . . . .   | 272 |
| Fabrication and characterization of cesium telluride photocathodes: A promising electron source for the<br>Los Alamos Advanced FEL<br>S.H. Kong, D.C. Nguyen, R.L. Sheffield and B.A. Sherwood . . . . . | 276 |

|   |     |
|---|-----|
| Photoemission studies on LaB <sub>6</sub> and pure metals using a nanosecond KrF excimer laser<br>M.-q. Qian, M.-r. Yang, Q. Pan, K.-s. Hu, R.-p. Deng, J.-j. Shi, Z.-c. Tao, J.-b. Cheng, Q.-j. Ran and<br>Z.-l. Lin . . . . . | 280 |
| Performance of cesium telluride photocathodes as an electron source for the Los Alamos Advanced FEL<br>S.H. Kong, J. Kinross-Wright, D.C. Nguyen, R.L. Sheffield and M.E. Weber . . . . .                                       | 284 |
| On the use of CsK <sub>2</sub> Sb photocathodes in RF linacs<br>B.M. van Oerle and G.J. Ernst . . . . .   | 287 |
| Laser cooling of an electron beam by the coherent scattering of a strong laser beam<br>T. Taguchi and K. Mima . . . . .   | 291 |
| Visualization of spatial profiles of spectra and intensities in FEL simulations<br>K. Yoshikawa, T. Shinzato, Y. Yamamoto, M. Ohnishi and T. Yamazaki . . . . .   | 295 |
| FEL center user diagnostics and control<br>K.W. Berryman, B.A. Richman, H.A. Schwettman, T.I. Smith and R.L. Swent . . . . .  | 300 |
| The influence of hole-coupling on the transverse structure of intra-cavity light pulses<br>G.H.C. van Werkhoven, B. Faatz and T.J. Schep . . . . .  | 304 |
| Influence of the radial mode structure on the losses in the FELIX hole-coupled resonators<br>G.M.H. Knippels, G.H.C. van Werkhoven, E.H. Haselhoff, B. Faatz, D. Oepts and P.W.<br>van Amersfoort . . . . .                     | 308 |
| Hole coupling experiments on the Mark III FEL<br>G.A. Barnett, S.V. Benson, J.M.J. Madey and E.B. Szarmes . . . . .   | 311 |
| Maximization of FEL gain for a hole-coupled resonator<br>Y.C. Huang, R.H. Pantell, J.F. Schmerge and J. Feinstein . . . . .   | 315 |
| Pulse stacking in the SCA/FEL external cavity<br>P. Haar, H.A. Schwettman and T.I. Smith . . . . .  | 319 |
| Resonator design and characterization for the Israeli tandem electrostatic FEL project<br>I.M. Yakover, Y. Pinhasi and A. Gover . . . . .   | 323 |
| Low-cost electron-gun pulser for table-top maser experiments<br>V. Grinberg, E. Jerby and A. Shahadi . . . . .  | 327 |
| First operation and perspectives of the superconducting linac LISA<br>M. Castellano, M. Ferrario, M. Minestrini, P. Patteri, F. Tazzioli, F. Cevenini and L. Catani . . . . .   | 331 |

### Section VIII. Storage ring FELs

|  |     |
|--|-----|
| Giant laser pulses in the Duke storage ring UV FEL<br>V.N. Litvinenko, B. Burnham, J.M.J. Madey and Y. Wu . . . . .  | 334 |
| Theory of the longitudinal dynamics of a storage ring FEL<br>G. Dattoli, L. Giannessi and A. Renieri . . . . .   | 338 |
| Dynamic behavior of the Super-ACO FEL micropulse<br>T. Hara, M.E. Couprie, A. Delboulbé, D. Garzella, L. Nahon and M. Billardon . . . . .  | 341 |
| mm-wave isochronous FEL and hard X-ray inverse Compton source at the Duke storage ring<br>V.N. Litvinenko, Y. Wu, B. Burnham, G. Barnett and J.M.J. Madey . . . . .  | 345 |
| Expected performance of the mm-wave isochronous FEL at the Duke storage ring<br>V.N. Litvinenko, Y. Wu, B. Burnham and J.M.J. Madey . . . . .  | 349 |
| Lasing in the ultraviolet region with the NIJI-IV storage-ring free-electron laser<br>T. Yamazaki, K. Yamada, N. Sei, H. Ohgaki, S. Sugiyama, T. Mikado, R. Suzuki, T. Noguchi, M.<br>Chiwaki, T. Ohdaira, M. Kawai, M. Yokoyama, S. Hamada and A. Iwata . . . . . | 353 |
| Expected performance of FELINA, the Dutch VUV-FEL in Amsterdam<br>R.J. Bakker, R. Maas, G. Luijckx, V.N. Litvinenko, B. Faatz and P.W. van Amersfoort . . . . .  | 358 |
| The barrel shaped resonator for the photon storage ring<br>A.I. Kleev, A.B. Manenkov and H. Yamada . . . . .   | 362 |

|  |     |
|--|-----|
| Observation of micro-macro temporal structure and saturation mechanism on the UVSOR free electron laser  |     |
| H. Hama, J. Yamazaki, T. Kinoshita, K. Kimura and G. Isoyama   | 365 |
| Dynamics of the Duke storage ring UV FEL   |     |
| V.N. Litvinenko, B. Burnham, J.M.J. Madey and Y. Wu  | 369 |
| A longitudinal feedback for the Super-ACO free electron laser stability in the UV  |     |
| M.E. Couprie, D. Garzella, T. Hara, J.H. Codarbox and M. Billardon   | 374 |
| Effects of an optical klystron on the electron beam of the storage ring NIJI-IV for free-electron lasers   |     |
| M. Yokoyama, N. Sei, M. Kawai, K. Yamada, S. Hamada, S. Sugiyama, H. Ohgaki, T. Mikado, T. Noguchi, R. Suzuki, M. Chiwaki and T. Yamazaki  | 378 |
| Optical cavities for UV free electron lasers   |     |
| M.E. Couprie, D. Garzella and M. Billardon   | 382 |
| Mirror degradation and heating in storage ring FELs  |     |
| D. Garzella, M.E. Couprie, T. Hara, L. Nahon, M. Brazuna, A. Delboulbé and M. Billardon  | 387 |
| Degradation and restoration of dielectric-coated cavity mirrors in the NIJI-IV FEL   |     |
| K. Yamada, T. Yamazaki, N. Sei, T. Shimizu, R. Suzuki, T. Ohdaira, M. Kawai, M. Yokoyama, S. Hamada, K. Saeki, E. Nishimura, T. Mikado, T. Noguchi, S. Sugiyama, M. Chiwaki, H. Ohgaki and T. Tomimasu | 392 |

## Section IX. Wigglers and undulators

|   |     |
|---|-----|
| Magnetic field full test of two-section KIAE-4 undulator  |     |
| A.A. Varfolomeev, Yu.P. Bouzouloukov, S.N. Ivanchenkov, A.S. Khlebnikov, N.S. Osmanov, S.V. Tolmachev, W.H. Urbanus and M.J. van der Wiel                                       | 396 |
| Development of a modified wiggler for higher harmonic lasing of a free-electron laser   |     |
| M. Asakawa, N. Inoue, K. Mima, S. Nakai, K. Imasaki, M. Fujita, J. Chen, C. Yamanaka, N. Nakao, T. Agari, T. Asakuma, A. Moon, N. Ohigashi, T. Minamiguchi and Y. Tsunawaki     | 399 |
| Performance of the undulator for JAERI FEL project  |     |
| R. Nagai, H. Kobayashi, S. Sasaki, M. Sawamura, M. Sugimoto, R. Kato, N. Kikuzawa, M. Ohkubo, E. Minehara, T. Ikehata and H. Mase   | 403 |
| Development of a short-period hybrid wiggler  |     |
| F. Inoue, N. Ikeda, K. Okubo, M. Takahashi and T. Yamanaka  | 407 |
| Magnetic field measurements of the harmonic generation FEL superconducting undulator at BNL-NSLS  |     |
| L. Solomon, W.S. Graves and I. Lehrman  | 411 |
| End fields in the harmonic generation superconducting FEL at BNL-NSLS   |     |
| W.S. Graves, L. Solomon and I. Lehrman  | 414 |
| Betatron oscillations, undulator acceptance and beam conditioning ( $\beta_{\parallel}(r) = \text{const.}$ ) taking space charge effects into account                           |     |
| V.A. Papadichev   | 418 |
| Electron trajectories in a helical wiggler with a uniform axial guide field: a comparison of numerical results with results obtained using an approximate but analytical method |     |
| J.T. Donohue, Ph. Gouard and J.L. Rullier   | 422 |
| Focusing properties of an undulator with anharmonic magnetic fields   |     |
| A.A. Varfolomeev and A.H. Hairtdinov  | 426 |
| Fourier analysis for the rapid calculation of distorted undulator orbits and their correction   |     |
| V.A. Papadichev   | 429 |

## Section X. Theory, conjecture, and speculation

|  |     |
|--|-----|
| On the possibility of the construction of plasma undulators        |     |
| V. Bazylev, V. Goloviznin, M.M. Pitatelev, A. Tulupov and T. Schep | 433 |
| Free electron lasers with static and dynamic plasma wigglers       |     |
| N.I. Karbushev   | 437 |



|   |     |
|---|-----|
| Ultra-short pulse free electron laser oscillators<br>J. Blau, R.K. Wong and W.B. Colson . . . . .   | 441 |
| Stimulated radiation from an electron beam traversing an inhomogeneous electromagnetic wave<br>A.V. Koltsov and A.V. Serov . . . . .  | 444 |
| Self-oscillations and chaos of free-electron laser oscillators with space charge effects<br>E.H. Park, J.K. Lee and T.H. Chung . . . . .  | 448 |
| Features of operation of a FEL with reversed guide field<br>A.A. Silivra and I.A. Goncharov . . . . .   | 452 |
| A proposal for the generation of ultra-short X-ray pulses<br>A.A. Zholents and M.S. Zolotarev . . . . .   | 455 |
| High power self-similar radiation pulse in a free electron laser<br>T.B. Zhang and T.C. Marshall . . . . .  | 459 |
| 3D simulations on output power fluctuation in a short bunch rf-linac FEL<br>Y. Sentoku, H. Furukawa, K. Mima, T. Taguchi, S. Kuruma, H. Yasuda, C. Yamanaka and S. Nakai .                  | 463 |
| Higher harmonic generation in a FEL with an axisymmetric undulator of the induction type<br>N.I. Karbushev, V.D. Sazhin and P.V. Mironov . . . . .  | 467 |
| Nonlinear evolution of the equilibrium electron orbits in a helical wiggler with a positive axial guide magnetic field at magnetoresonance<br>J. Yu and W.A. Gillespie . . . . .            | 471 |
| Free gas bubbles acoustic laser<br>S.T. Zavtrak . . . . .   | 473 |
| Modeling of space charge dominated performance of the CEBAF FEL injector<br>H. Liu, J. Benesch, S. Benson, J. Bisognano, D. Douglas, G. Neil, D. Neuffer, C. Sinclair and B. Yunn . . . . . | 475 |
| Nonlinear wave processes during the propagation of a high-current electron beam in an ion-beam undulator<br>Yu.Ya. Golub and N.E. Rozanov . . . . .   | 479 |
| FEL gain calculation for imperfectly matched electron beams<br>R.L. Swent and K.W. Berryman . . . . .   | 482 |
| Non-linear macroscopic equations for pulse evolution in a high-gain Compton FEL<br>G.H.C. van Werkhoven and T.J. Schep . . . . .  | 485 |
| Computationally efficient spectral analysis of an FEL oscillator using a Green function analysis<br>S. Ishii, G. Shvets and J.S. Wurtele . . . . .  | 489 |
| Formation of distributed feedback in an FEL under multi-wave diffraction<br>V.G. Baryshevsky, K.G. Batrakov and I.Ya. Dubovskaya . . . . .  | 493 |
| A re-examination of scaling laws in the traveling wave interaction<br>H.P. Freund . . . . .   | 497 |
| Theoretical investigation of a waveguide application in a FEL with large $\mu_c$<br>V.I. Zhulin . . . . .   | 501 |
| The interaction between low- and high-frequency waves in a waveguide free-electron laser amplifier<br>W.J. Golightly and S.K. Ride . . . . .  | 504 |
| Visible surface quasi-Cherenkov FEL<br>V.G. Baryshevsky, K.G. Batrakov, I.Ya. Dubovskaya and S. Sytova . . . . .  | 508 |
| Optimization of the free electron laser interaction via electron bunch trapping<br>A.A. Silivra, E.D. Belyavskiy and I.A. Goncharov . . . . .   | 512 |
| 1-D free-electron laser model without the slowly-varying approximation<br>C.-B. Kim, Y.-W. Uhm and J.-K. Lee . . . . .  | 516 |
| A computer model of the energy-current loss instabilities in a recirculating accelerator system<br>J.A. Edighoffer and K.-J. Kim . . . . .  | 519 |

|  |     |
|--|-----|
| POP experiments of the photon–e-beam interaction in the supercavity<br>M. Fujita, T. Asakuma, J. Chen, K. Imasaki, C. Yamanaka, M. Asakawa, N. Inoue, K. Mima, S. Nakai, T. Agari, N. Nakao, A. Moon, N. Ohigashi, T. Minamiguchi and Y. Tsunawaki . . . . . | 524 |
| Problems of autobunching and phase stability for the TBA-driver: calculations and design for a modeling experiment<br>G.G. Denisov, V.L. Bratman, A.K. Krasnykh, E.A. Perelstein, A.V. Savirov, A.S. Sergeev and A.P. Sumbaev . . . . .                      | 528 |

## Section XI. State of FELs, challenges and requirements

|  |     |
|--|-----|
| Status of free electron lasers in 1994<br>W.B. Colson . . . . .  | 532 |
| Materials science in the far-IR with electrostatic based FELs<br>S.J. Allen, K. Craig, B. Galdrikian, J.N. Heyman, J.P. Kaminski, J.S. Scott, M.S. Sherwin, K. Unterrainer, M. Wanke, K. Campman, P.F. Hopkins, A.C. Gossard, D.H. Chow, M. Lui and T.K. Liu . . . . . | 536 |
| Vibrational dynamics in condensed matter probed with linac based FELs<br>A. Tokmakoff, A. Kowk, R. Urhdal, D.A. Zimdars and M.D. Fayer . . . . .   | 540 |
| Scientific opportunities for FEL amplifier based VUV and X-ray research<br>E.D. Johnson . . . . .  | 544 |

## Part II. Extended synopses

|   |        |
|---|--------|
| 1-D simulation model of an FEL with a plasma background<br>T.H. Chung and J.K. Lee . . . . .  | ABS 3  |
| Status of the Grumman Compact Infrared FEL<br>I.S. Lehrman, J. Krishnaswamy, R.A. Hartley, R. Bohanick and M.F. Reusch . . . . .  | ABS 5  |
| The Israeli tandem electrostatic accelerator FEL – status report<br>A. Arensburg, M. Cohen, M. Draznin, A. Eichenbaum, A. Gover, Y. Pinhasi, V. Shternghartz, I.M. Yakover, J. Sokolovsky, B. Mandelbaum, A. Rosenberg, J. Shiloh, G. Hasak, L.A. Levin, O. Shahal, M. Shapira and V. Granatstein . . . . . | ABS 7  |
| Application of a mm-wave free electron laser to the study of high- $T_c$ superconductors<br>E. Giovenale, V. Boffa, P. Dore, A. Doria, G.P. Gallerano, M.F. Kimmitt, R. Trippetti and I. Spassovsky . . . . .   | ABS 9  |
| Commissioning the FELI linac and IR-FEL facilities<br>T. Tomimasu, Y. Morii, E. Ohshita, S. Abe, S. Nishihara, A. Koga, Y. Miyauchi, A. Zakou, E. Nishimura, K. Saeki, A. Kobayashi, M. Yasumoto, E. Tongu and A. Nagai . . . . .   | ABS 11 |
| Status of the Stuttgart Raman free-electron laser project<br>G. Renz and G. Spindler . . . . .  | ABS 13 |
| The optical resonator for the FELICITA I experiment<br>D. Nölle, A. Geisler, M. Ridder, C. Schellnock, T. Schmidt, S. Tammen and K. Wille . . . . .   | ABS 14 |
| Magnetic measurements of the electromagnetic undulator for the FELICITA I experiment<br>M. Ridder, A. Geisler, D. Nölle, T. Schmidt and S. Suermann . . . . .   | ABS 16 |
| Enhanced harmonic generation from a focussing two-period undulator<br>A.V. Tulupov . . . . .  | ABS 18 |
| Improved electron beam transport and diagnosis system for the Darmstadt IR-FEL<br>H. Genz, H.-D. Gräf, R. Hahn, D.A. Jaroszynski, H. Loos, A. Richter, M. Reichenbach, V. Schlott, M. Thomas, J. Töpper, T. Wesp and M. Wiencken . . . . .  | ABS 20 |
| Upgrade of the ENEA compact FEL in the sub-mm region<br>E. Giovenale, F. Ciocci, A. Doria, G.P. Gallerano, M.F. Kimmitt, G. Messina, P. Raimondi, A. Renieri and I. Spassovsky . . . . .  | ABS 22 |
| Design of a far infrared FEL with an electromagnetic wiggler<br>V.L. Granatstein, A.W. Fliflet, W.M. Manheimer and A. Gover . . . . .   | ABS 24 |

|   |        |
|---|--------|
| Frequency response to an electron energy shift<br>R.K. Wong and W.B. Colson . . . . .   | ABS 26 |
| Slicing single micropulses at FELIX<br>E.H. Haselhoff, G.M.H. Knippels and P.W. van Amersfoort . . . . .  | ABS 28 |
| Status of the JAERI free electron laser facility driven by a superconducting rf linac<br>E.J. Minehara, R. Nagai, M. Sawamura, M. Takao, M. Sugimoto, S. Sasaki, M. Ohkubo, N. Kikuzawa, J. Sasabe, Y. Suzuki, Y. Kawarasaki and N. Shikazono . . . . . | ABS 30 |
| Characterization of the mid-IR FEL at Stanford<br>B.A. Richman, E.R. Crosson, R.L. Swent, H.A. Schwettman and T.I. Smith . . . . .  | ABS 32 |
| High gradient linac for compact FELs<br>P. Raimondi and G. Messina . . . . .  | ABS 34 |
| Numerical simulation studies of the design and performance of the AFEL for high average power operation<br>J.C. Goldstein, H. Takeda and D.C. Nguyen . . . . .  | ABS 36 |
| Design of the pseudospark discharge for a Raman FEL<br>M.C. Wang, J. Zhu, Z. Wang, J.K. Lee and T.H. Chung . . . . .  | ABS 38 |
| Demonstration of micropulse energy enhancement with the SCA/FEL external cavity system<br>P. Haar, H.A. Schwettman and T.I. Smith . . . . .   | ABS 40 |
| A new inductive acceleration structure with multiple electrodes for an FEL<br>S. Kawasaki, H. Ishizuka, A. Watanabe, Y. Yamashita, A. Tokuti, S. Nakajima, J. Kishiro, K. Takayama and M. Shiho . . . . .   | ABS 42 |
| Simulations of the Stanford FIREFLY 1 kW free electron laser<br>D.W. Small, R.K. Wong, J. Blau and W.B. Colson . . . . .  | ABS 44 |
| Improved wire deflection method for magnetic field measurements in long undulators<br>A.A. Varfolomeev, A.S. Khlebnikov, N.S. Osmanov and S.V. Tolmachev . . . . .  | ABS 46 |
| Conceptual design of a compact Compton backscatter X-ray source tunable from 3 to 33 keV<br>D.C. Nguyen, S.M. Gierman, W. Vernon and R.L. Sheffield . . . . .   | ABS 48 |
| Three dimensional simulation of an FEL amplifier with an axial field<br>A. Srivastava, L.M. Bali, T.P. Pandya, P. Jha and R.K. Shukla . . . . .   | ABS 50 |
| Wiggler-free FEL with an intense helical beam<br>K.H. Yeom, J.K. Lee and T.H. Chung . . . . .   | ABS 52 |
| Carbon fiber electron injector for free-electron maser experiments<br>M. Korol, E. Jerby, S. Eckhouse, M. Bensal and A. Shahadi . . . . .   | ABS 54 |
| Optical cavity and transport system for FELI<br>K. Saeki, E. Nishimura, A. Kobayashi, S. Abe, A. Zako, M. Yasumoto and T. Tomimasu . . . . .  | ABS 56 |
| Wavelength and power stability measurements of the Stanford SCA/FEL<br>B. van der Geer, M.J. de Loos, M.E. Conde and W.P. Leemans . . . . .   | ABS 59 |
| The effects of high gain in an FEL optical klystron<br>E. Kelsey, J. Blau, D.D. Quick, R.K. Wong and W.B. Colson . . . . .  | ABS 61 |
| Formation and diagnostics of electron beams for micro-FELs<br>H. Ishizuka, S. Musyoki, K. Sakamoto, A. Watanabe, M. Shiho and S. Kawasaki . . . . .   | ABS 63 |
| A comparison between two kinds of chromatic coherent light sources<br>W. Ding, X. Shu and X. Du . . . . .   | ABS 65 |
| An FEL design code running on Mathcad <sup>TM</sup><br>D.C. Nguyen, S.M. Gierman and P.G. O'Shea . . . . .  | ABS 67 |
| The ultra-relativistic FEL near the threshold of stimulated emission<br>V.V. Ognivenko and V.I. Kurilko . . . . .   | ABS 69 |
| Simple theory of simultaneous harmonics operation of an FEL<br>B.A. Richman . . . . .   | ABS 71 |

|  |        |
|--|--------|
| RF systems for JAERI FEL linac<br>M. Sawamura, E.J. Minehara, R. Nagai, M. Sugimoto, M. Takao, R. Kato, N. Kikuzawa and<br>M. Ohkubo . . . . .   | ABS 73 |
| The UCLA high gain infrared FEL<br>G. Travish, M. Hogan, C. Pellegrini and J. Rosenzweig . . . . .   | ABS 75 |
| Performance of the optical cavity control system for the JAERI FEL project<br>R. Kato, M. Sugimoto, R. Nagai, M. Sawamura, M. Takao, N. Kikuzawa, M. Ohkubo, E.J.<br>Minehara and Y. Suzuki . . . . .                              | ABS 77 |
| A new method of equalizing $\beta_{\parallel}$ (conditioning) in an electron beam propagating in a longitudinal<br>magnetic field<br>V.A. Papadichev . . . . .   | ABS 79 |
| Power requirements for high-average power FELs<br>R.A. Lyon and W.B. Colson . . . . .  | ABS 81 |
| Operator supports for the JAERI FEL<br>M. Sugimoto, R. Nagai, R. Kato, M. Sawamura, M. Takao, N. Kikuzawa, M. Ohkubo and E.J.<br>Minehara . . . . .  | ABS 83 |
| The "TEUFEL" undulator<br>J.W.J. Verschuur, G.J. Ernst and W.J. Witteman . . . . .   | ABS 85 |
| Low-level RF control for the AFEL<br>C.D. Ziomek, J.M. Kinross-Wright and J.G. Plato . . . . .   | ABS 87 |
| Electron beam diagnostics for an FEL using optical transition radiation<br>E. Nishimura, K. Saeki, T. Tomimasu, T. Sakai, S. Okuda and J. Ohkuma . . . . .   | ABS 89 |
| Development of the quasi non-destructive electron beam diagnostic method and the measurement<br>of beam emittance<br>T. Sakai, T. Yamamoto, S. Okuda, J. Ohkuma, E. Nishimura, K. Saeki, A. Kobayashi and T.<br>Tomimasu . . . . . | ABS 91 |
| A flexible far-infrared FEL user facility<br>K.W. Berryman and T.I. Smith . . . . .  | ABS 93 |

### Part III. Tables of operating and proposed FELs

|  |     |
|--|-----|
| Long wavelength free electron lasers in 1994<br>H.P. Freund and V.L. Granatstein . . . . . | 551 |
| Short wavelength free electron lasers in 1994<br>W.B. Colson . . . . .                     | 555 |
| Author index . . . . .   | 559 |

# Advanced technologies for a compact rf linac FEL <sup>☆</sup>

D.C. Nguyen

*Los Alamos National Laboratory, Los Alamos, NM 87545, USA*

## Abstract

Advanced technologies such as photoinjectors, short-period microwigglers, and harmonic lasing enable free-electron-laser operation in the infrared with a low-energy ( $\sim 10$  MeV) electron beam and thus potentially reduce the size and cost of FELs. The next-generation, rf-linac FEL will fit in a small laboratory and produce high-power, picosecond infrared.

## 1. Introduction

FELs traditionally have been large, complex, and costly devices. The size of an FEL is principally determined by its electron beam energy which, for optical wavelengths, is tens to hundreds of MeV. Large accelerators are needed to produce the high-energy beams which in turn generate radiations that require shielding. Reducing the beam energy is thus important in keeping the FEL size and cost down. Building infrared FELs with beam energies less than 10 MeV requires using a millimeter-period wiggler or lasing at harmonic frequencies. Matching such a low-energy beam requires a low emittance. Also, because the small-signal gain is typically low for microwigglers and harmonic lasing, the beam must have a small energy spread and a high peak current.

In the past 10 years, advances in photoinjector technology have produced the beam quality needed for microwiggler and harmonic FEL operation [1]. Since its first use in 1988 [2], the photoinjector has become the electron source for many FELs [3–5]. The high-brightness beam in turn spurs further development of millimeter-period wigglers and harmonic lasing. In this paper, I will review these enabling technologies. The goal here is to compare these advanced approaches for designing the next-generation, compact FELs that produce picosecond IR pulses. Because in-depth reviews of the rf guns and wiggler technologies already exist [6,7], I will mention only a few representative examples of these technologies.

## 2. Advanced technologies

### 2.1. Photoinjector

The photoinjector was developed at Los Alamos in 1986 [1]. It produces picosecond electron pulses with a small energy spread ( $\sim 0.2\%$ ) and a peak current up to 300 A [3]. Emittance compensation with an axial solenoidal field yields normalized beam emittance as low as  $1 \pi$ -mm-mrad for a 100-A peak current [5]. The low-emittance beam can be bunched in a chicane to produce peak currents up to 1 kA with minimal emittance growth. Development of L-band and S-band photoinjectors is active at Los Alamos [5] and at Brookhaven National Laboratory [8].

The major issues with photoinjectors are the photocathode and the drive laser. Multi-alkali photocathodes offer high quantum efficiencies (QE), but they are not as rugged as the low-QE ( $< 0.1\%$ ) metal photocathodes. To have appreciable lifetime, the multi-alkali cathodes need a high-vacuum environment, typically  $10^{-9}$  Torr or better. Metal photocathodes, on the other hand, require a high-power ultraviolet drive laser. Recently,  $\text{Cs}_2\text{Te}$  has been shown to be rugged while offering a QE of a few percent [9]. The drive laser must be very stable: temporal jitter less than 0.5 ps, amplitude stability better than 1%, and spatial jitters less than 100  $\mu\text{m}$  at the photocathode are required. Using the photoinjector increases the FEL cost and complexity, which must be weighed against its benefits.

### 2.2. Short-period microwigglers

Short-period wigglers of various designs have been studied and built. Permanent magnet microwigglers are fairly compact and require no power supply. For periods shorter than 1 cm, the magnet gap is typically less than one-third the wiggler period [10]. The small gap increases

<sup>☆</sup> Work supported by LANL Laboratory Directed Research and Development and performed under the auspices of the U.S. Department of Energy.

optical vignetting and requires tight fabrication tolerance to minimize field errors.

Electromagnet wigglers potentially offer very high magnetic fields with millimeter periods. Ben-Zvi et al. at Brookhaven National Laboratory fabricated and tested an 8.8-mm-period superconducting wiggler [11]. At Los Alamos, Warren built and tested a 3-mm-period slotted-tube microwiggler in which a current flowing in wiggly paths produced a strong transverse field [12]. Researchers at the Lebedev Institute and Warren at Los Alamos also built helical wigglers [13]. The helical wigglers produce a higher gain compared with their plane-polarized counterpart, and they emit circularly polarized light. Unfortunately, they do not support harmonic lasing.

Pantell and coworkers came up with a new design for a short-period wiggler that uses a staggered array of iron pole pieces immersed in a longitudinal solenoidal field [14]. The transverse field component is created by redistributing the longitudinal field. Varfolomeev of the Kurchatov Institute showed that the transverse field component could be enhanced by interlacing the iron pole pieces with permanent magnets [15]. This novel scheme produced a 4.5-mm-period wiggler whose magnetic field reached 7.9 kG at a 1.5-mm gap.

### 2.3. Harmonic lasing

First demonstrated with thermionic guns at Stanford and at Los Alamos in 1989 [16,17], harmonic lasing promises short-wavelength output from a relatively low beam energy. Using a 46-MeV beam, O'Shea and coworkers achieved lasing on the third harmonic at 370 nm [18]. The harmonic small-signal gain strongly depends on the wiggler dimensionless parameter  $a_w$ . To produce adequate gain in the harmonics  $a_w$  must be sufficiently high. Warren points out that the small-signal gains peak at different  $a_w$  for the various harmonics [19]. A complication with harmonic lasing is the need to discriminate against the unwanted harmonics. One way to select against the unwanted harmonics is to use an intracavity frequency-dependent loss element [18].

For a fixed wavelength  $\lambda$ , harmonic lasing can reduce the required beam energy or increase the required wiggler period  $\lambda_w$ . Working with a longer  $\lambda_w$  increases  $a_w$ , which is necessary for harmonic gain, but the large  $a_w$  diminishes the short-wavelength advantage of harmonic lasing. The resonant wavelength for the  $n$ th harmonic is given by

$$\lambda = \frac{\lambda_w}{2n\gamma^2} (1 + a_w^2), \quad (1)$$

where  $\gamma$  is the beam relativistic factor. The matching condition dictates

$$\lambda \geq \pi \varepsilon_n^* / (\beta \gamma), \quad (2)$$

where  $\beta = v/c$  is nearly 1 and  $\varepsilon_n^*$  is the normalized 90% emittance. Equating (1) and (2) and using  $\varepsilon_n^* = 4\varepsilon_n$ ,

where  $\varepsilon_n$  is the normalized rms emittance, we have

$$\lambda_w \geq 8\pi n \gamma \varepsilon_n / (1 + a_w^2). \quad (3)$$

Note that both reducing the wiggler period and increasing  $n$  require a lower emittance. For submillimeter periods such as in an electromagnetic wiggler, one must use a low beam energy to keep the required  $\varepsilon_n$  from being too small.

The small-signal gain equation for harmonic lasing, modified by Dattoli's gain reduction for finite emittance and energy spread [20], is given by

$$g_{ss}(n, \varepsilon_n, \sigma_E) = n [JJ(n, \xi)]^2 \left( \frac{N_w}{\gamma} \right)^3 2a_w^2 \pi^2 \frac{j_e \lambda_w^2}{I_A} FF \left( \frac{A_e}{A_0} \right) f_{\max} \left/ \left\{ \left[ 1 + \left( \frac{8nN_w a_w \varepsilon_n}{(1 + a_w^2) \lambda_w} \right)^2 \right] \left[ 1 + 1.7(4nN_w \sigma_E)^2 \right] \right\} \right., \quad (4)$$

where  $\sigma_E$  is the rms energy spread;  $JJ(n, \xi)$  is the difference in Bessel functions defined as

$$JJ(n, \xi) = J_{(n-1)/2}(n\xi) - J_{(n+1)/2}(n\xi);$$

$\xi$  is  $a_w^2/2(1 + a_w^2)$ ;  $N_w$  is the number of wiggler periods;  $j_e$  is the beam current density;  $I_A$  is the Alfvén current;  $FF(A_e/A_0)$  is the filling factor; and  $f_{\max}$  is equal to 0.54 at the peak of the gain curve.

The saturation intensity – defined as the intensity at which the gain is one-half the small-signal gain – for lasing at the  $n$ th harmonic is given by

$$I_s = \frac{1}{8\pi} \left( \frac{\gamma}{N_w} \right)^4 \frac{mc^3}{r_0 (nJJ(n, \xi) \lambda_w a_w)^2}, \quad (5)$$

where  $m$  is the electron mass;  $c$  is the speed of light; and  $r_0$  is the classical electron radius.

Suppose we wish to generate 5  $\mu\text{m}$  with a 10-MeV electron beam. Using a photoinjector, we could generate 2 nC in 10 ps ( $I_{\text{peak}} = 200$  A) with a nominal rms emittance of 5  $\pi$ -mm-mrad and an energy spread of 0.25%. Table 1 lists four possible options of lasing at various harmonics: fundamental with a 4-mm-period wiggler, third harmonic

Table 1  
Comparison of microwiggler and harmonic lasing

| $\lambda_w$<br>(mm) | $N_w$ | $n$ | $B_{\text{peak}}$<br>(T) | $a_w$ | $g_{ss}$<br>(%) | $I_{\text{sat}}$<br>(GW/<br>cm <sup>3</sup> ) | $E_{\text{micro}}$<br>( $\mu\text{J}$ ) |
|---------------------|-------|-----|--------------------------|-------|-----------------|---|---|
| 4                   | 25    | 1   | 0.58                     | 0.15  | 18              | 43  | 102                                     |
| 8.8                 | 11.4  | 3   | 1.1                      | 0.64  | 14              | 36  | 60                                      |
| 11.2                | 10    | 5   | 1.24                     | 0.91  | 12              | 27  | 37                                      |
| 13                  | 7.7   | 7   | 1.3                      | 1.12  | 11              | 21  | 25                                      |

with an 8.8-mm-period wiggler, fifth harmonic with a 11.2-mm-period wiggler, and seventh harmonic with a 13-mm-period wiggler. All four wigglers are of the Halbach type with permanent magnets whose remanent field is 1.05 T and whose gap is fixed at 1.5 mm. The wiggler lengths are kept constant at 10 cm and a 2% resonator round-trip loss and optimum outcoupling is assumed for all cases. Note that the small-signal gains gradually go down as we go to higher harmonics because  $a_w$  is not optimized. The biggest penalty of harmonic lasing is the rapid reduction in micropulse energy at saturation. This is true even if the harmonic gains are as high as the fundamental gain.

### 3. Present status and future prospects

At present, two compact rf-linac FELs are in operation and three others are under construction. The Advanced FEL at Los Alamos has operated at 4–6  $\mu\text{m}$  since 1993 [21]. It reliably generates 100–200 mJ in 10- $\mu\text{s}$  macropulses. The ENEA FEL has operated in the millimeter range and is being upgraded for submillimeter operation [22]. Grumman is constructing a 14-MeV, IR FEL at Princeton [23]. The Institute for Laser Engineering in Japan is using a photoinjector and a 6.6-mm-period wiggler to build a 10- $\mu\text{m}$  FEL [24]. At Stanford, Pantell and coworkers are developing a far-IR FEL with a 4-MeV rf gun and a staggered-array wiggler [25]. Fig. 1 depicts the

operating wavelength and beam energy ranges of the above FELs. The UV-lasing experiment at Los Alamos is also shown for comparison [18]. The two lines correspond to the resonance conditions, assuming  $a_w = 0$ , for wiggler periods of 1 cm – the shortest wiggler period ever used in an FEL – and 5 cm. The region between these two lines is where most FELs operate. Note that millimeter-period wigglers and harmonic lasing allow operation below this region.

I expect the photoinjectors will become smaller and easier to operate in the near future. Progress in microwiggler design and fabrication could deliver a short-period ( $\sim 3\text{-mm}$ ), high-field wiggler. Further efforts in miniaturizing the linac, the klystron and its modulator, however, will be needed before we see an rf-linac FEL that fits in a small room and costs less than \$1 million. These compact FELs will probably operate in spectral regions where no conventional tunable lasers with appreciable power exist. One such region is the 3–100  $\mu\text{m}$  range, where a vast number of molecular vibrations occur. Many of these vibrational resonances can be used for detecting and mapping atmospheric constituents (e.g. LIDAR), in multiphoton molecular dissociation for isotope separation and photochemical processing, and in the study of condensed-phase dynamics. A compact FEL operating at 3–10  $\mu\text{m}$  would find use in laser surgery. In near-field microscopy, an rf-linac FEL could deliver a substantial power through the

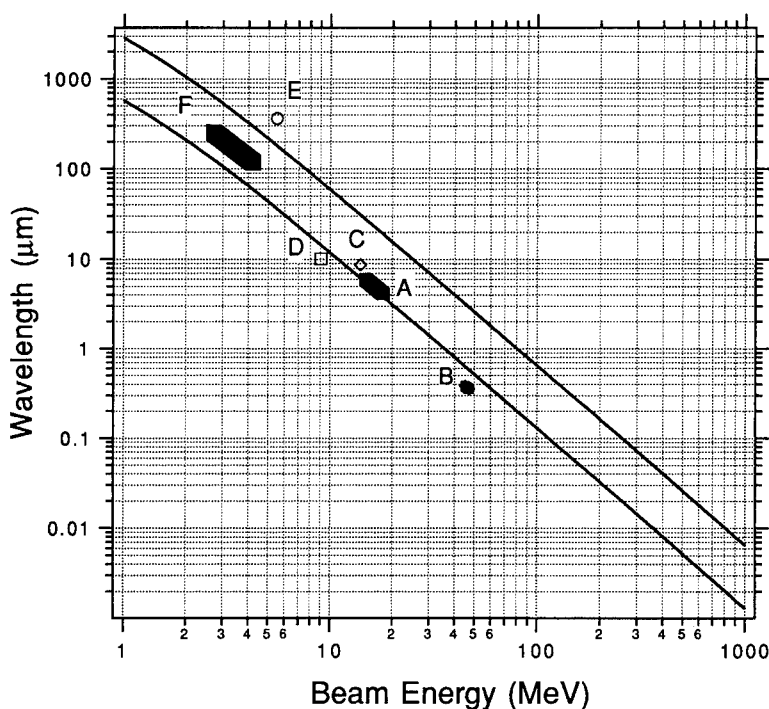


Fig. 1. Plot of FEL wavelength versus energy; the two lines correspond to 1-cm and 5-cm wiggler periods. A: AFEL actual operation; B: APEX UV operation; C: Grumman-Princeton CIR-FEL projected operation; D: ILT projected microwiggler operation; E: ENEA projected submillimeter operation; and F: Stanford projected far-IR FEL operation.

submicron aperture of a microprobe. This capability would be useful for spectrally resolved imaging.

### Acknowledgements

The author is grateful to R.W. Warren, S.M. Gierman, J. Kinross-Wright and R.L. Sheffield for helpful discussion.

### References

- [1] J.S. Fraser and R.L. Sheffield, IEEE J. Quantum Electron. QE-23 (1987) 1489.
- [2] M. Curtin et al., Nucl. Instr. and Meth. A 296 (1990) 127.
- [3] P.G. O'Shea et al., Nucl. Instr. and Meth. A 318 (1992) 52.
- [4] S. Joly et al., Nucl. Instr. and Meth. A 331 (1993) 199.
- [5] R.L. Sheffield et al., Nucl. Instr. and Meth. A 341 (1994) 371.
- [6] C. Travier, Nucl. Instr. and Meth. A 304 (1991) 285.
- [7] R.L. Sheffield et al., LA-UR 89-2851, Los Alamos National Laboratory.
- [8] K. Batchelor et al., Nucl. Instr. and Meth. A 318 (1992) 372.
- [9] S. Kong et al., these Proceedings (16th Int. Free Electron Laser Conf., Stanford, CA, USA, 1994) Nucl. Instr. and Meth. A 358 (1995) 284.
- [10] K. Halbach, Nucl. Instr. and Meth. 187 (1981) 109.
- [11] I. Ben-Zvi et al., Nucl. Instr. and Meth. A 318 (1992) 781.
- [12] R. Warren, Nucl. Instr. and Meth. A 318 (1992) 789.
- [13] V.A. Papadichev and O.A. Smith, Nucl. Instr. and Meth. A 318 (1992) 803.
- [14] A.H. Ho et al., J. Quantum Electron. QE-27 (1991) 2650.
- [15] A.A. Varfolomeev et al., Nucl. Instr. and Meth. A 318 (1992) 809.
- [16] S.V. Benson and J.M.J. Madey, Phys. Rev. A 39 (1989).
- [17] R.W. Warren et al., Nucl. Instr. and Meth. A 296 (1990) 84.
- [18] P.G. O'Shea et al., Nucl. Instr. and Meth. A 341 (1994) 7.
- [19] R.W. Warren, Nucl. Instr. and Meth. A 296 (1990) 512.
- [20] G. Dattoli et al., J. Quantum Electron. QE-20 (1984) 1003.
- [21] D.C. Nguyen et al., Nucl. Instr. and Meth. A 341 (1994) 29.
- [22] E. Giovenale et al., these Proceedings (16th Int. Free Electron Laser Conf., Stanford, CA, USA, 1994) Nucl. Instr. and Meth. A 358 (1995) ABS 22.
- [23] I.S. Lehrman et al., Nucl. Instr. and Meth. A 341 (1994) ABS 31.
- [24] M. Asakawa et al., these Proceedings (16th Int. Free Electron Laser Conf., Stanford, CA, USA, 1994) Nucl. Instr. and Meth. A 358 (1995) 399.
- [25] J. Lewellen et al., *ibid.*, p. 24.





ELSEVIER

## Free electron micro-lasers

C.M. Tang <sup>a,\*</sup>, M. Goldstein <sup>b</sup>, T.A. Swyden <sup>c</sup>, J.E. Walsh <sup>b</sup><sup>a</sup> *Plasma Physics Division, Naval Research Laboratory, Washington, DC 20375-5346, USA*<sup>b</sup> *Dartmouth College, Hanover, NH 03755, USA*<sup>c</sup> *FM Technologies, Inc., Fairfax, VA 22032, USA*

### Abstract

The electron optical properties of microscopic gated field emitter arrays (FEA) are an ideal match to the electron beam requirements of free electron micro-lasers. Projected performance characteristics of the beam generators based on the FEA principle are reviewed and results from recent experiments with a single micro-beam filament are summarized. The latter are shown to support the claim that free electron micro-lasers based on either the Cherenkov or the Smith–Purcell interaction mechanism are a practical possibility.

### 1. Introduction

Spectroscopic and other commercial applications of lasers typically require systems with low to moderate power, compact size and inexpensive cost. Various free-electron laser mechanisms, particularly Smith–Purcell or Cherenkov devices, driven by micro-electron beams [1–5] are interesting in those contexts. A potential source for the beam is the gated field-emitter array, which has high current density and low emittance. In Section 2, we present computer simulations of a simple method of producing collimated sheet beams from gated field-emitters using planar lens fabricated along with the field emitters on the same substrate. The good beam quality of these gated field-emitters imply that tunable infrared oscillators in the IR from tens to hundreds of  $\mu\text{m}$  are feasible. In a series of proof of principle experiments spontaneous emission from a Smith–Purcell device has been obtained. Scaling of the radiation wavelength (288–803  $\mu\text{m}$ ) and the total emitted intensity are in accord with theory.

### 2. Field-emitter technology and beam collimation

The generation of short wavelength radiation in a compact size requires good beam collimation and small beam dimensions, i.e., good emittance. Large growth rates for coherent radiation require high current density, i.e., high beam brightness. A compact electron source with the

required properties is the gated field-emitter array (FEA). Electrons beams from FEAs can be cw or pulsed. Since FEAs comes in a wide variety of configurations, only a few examples will be given below.

Experimental results pertinent to the FEL is summarized. For emitter tips with large radii of curvature, currents up to 200  $\mu\text{A}$  for single tip have been reported by SRI [6] and even higher currents have been measured in  $10^{-6}$  Torr of hydrogen by Philips Research Laboratory [7]. Field-emitter arrays with submicron gate opening diameters and sharp tips have been fabricated by SRI [6] and MIT/Lincoln Laboratory [8]. SRI utilized focused ion beams to fabricated arrays with gate opening diameters of 0.3  $\mu\text{m}$ , and tip-to-tip separation of 0.5  $\mu\text{m}$ . These tips emitted on average 3  $\mu\text{A}$  per tip at a gate voltage of 45 V. Lincoln Laboratory utilized holographic methods to fabricate FEAs with gate opening diameters of 0.16  $\mu\text{m}$  and tip-to-tip separation of 0.32  $\mu\text{m}$ . They measured on average 1.0  $\mu\text{A}$  per tip at a gate voltage around 30–35 V [9]. Refinements in FEA processing are continuing to improve the current per tip, lower gate voltages for electron emission, increase current density, improve lifetime, etc.

The emittance associated with each cone-emitter is small because electron emission occurs only from their tip which has a radius of curvature typically much less than 100 Å. Using EGUN2 [10] to estimate the RMS normalized emittance associated with emitters, we find values typically on the order of a few  $10^{-4}$   $\pi\text{-mm-mrad}$ . A simulation example will be given below.

Despite the low emittance, electron emission patterns from FEA tips have large angular spreads. It is, however, possible to apply focusing lenses to collimate the beams. There are various approaches to beam focusing, but we will limit discussions to two types of electrostatic lens: the

\* Corresponding author. Present address: National Institute of Standards and Technology, Gaithersburg, MD 20899, USA, tel. +1 301 975 4272, fax +1 301 975 3038.

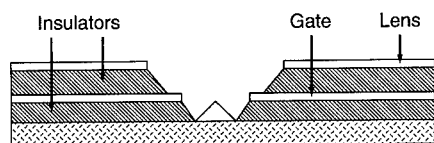


Fig. 1. Schematic of field emitter with thin lens electrode overlapping the gate electrode.

thin overlapping lens and a planar lens for gated cone emitters.

A schematic of a generic thin overlapping lens is shown in Fig. 1. For the thin lens to be effective, the lens opening has to be self-aligned with the gate opening, and the distance of the lens from the gate should be much less than the gate opening diameter. Computer simulations indicate the lens voltage will be comparable to tip voltage for best collimation [11–13]. The overlapping thin lens, however, is difficult to fabricate. Recently, a self-aligned thin lens and gate geometry was successfully made [14] and beam focusing was demonstrated experimentally. The experimental results agree qualitatively with the computer simulations. A potential disadvantage of the thin lens is an experimentally observed reduction in the output current with increased focusing, because of a lowering of the field at the emitter tip due to the proximity of the low lens voltage and possibly because of charging of the insulator between the gate and the lens.

In contrast, the coplanar lens and nearly coplanar lens [15–22], shown in Figs. 2a and 2b, respectively, are very simple to fabricate. For the planar lens to be effective, the lens electrodes must extend over a wide lateral area around the gate electrode. Focusing occurs in a substantial region above the gate surface, providing beam collimation for an effectively larger percentage of the outer beam electrons. Since the lens electrode is now some distance from the tip, the field reduction at the tip by the lens is not expected to be significant. Planar lenses have previously been used for

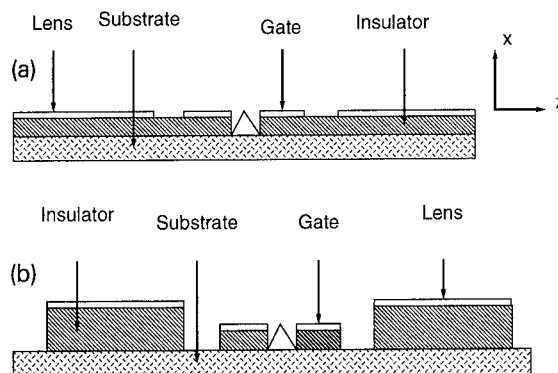


Fig. 2. Schematics of field emitters with planar lens concepts where (a) the lens electrode is coplanar with the gate electrode and (b) the lens electrode is nearly coplanar with the gate electrode.

thermionic cathodes. For field-emitters, the integration of the lens with the emitters on the same substrate simplified alignment and implementation. Planar lens focusing for FEAs has been demonstrated experimentally [18–20].

A self-consistent EGUN2 simulation of a gated field-emitter with a planar lens is shown in Fig. 3. RMS normalized emittance is calculated by EGUN2 to be  $2.1 \times 10^{-4} \pi\text{-mm-mrad}$  in the cylindrical geometry. The emittance would vary somewhat with slightly different sets of parameters, but is expected to remain around the same order of magnitude. We will demonstrate beam collimation for the following example: gate voltage  $V_g = 20$  V, gate opening diameter of  $0.16 \mu\text{m}$ , emitter tip radius of  $50 \text{ \AA}$ , emitter cone half angle of  $30^\circ$ , and emitter current of  $1.0 \mu\text{A}$  in an accelerating gradient of  $10 \text{ V}/\mu\text{m}$ . First, these parameters are simulated with the gate extended to infinity without lenses. Electrons are emitted within a half cone angle of  $65^\circ$  at the emitter tip, propagating outward to the anode like a fan. The emitted current density decreases as

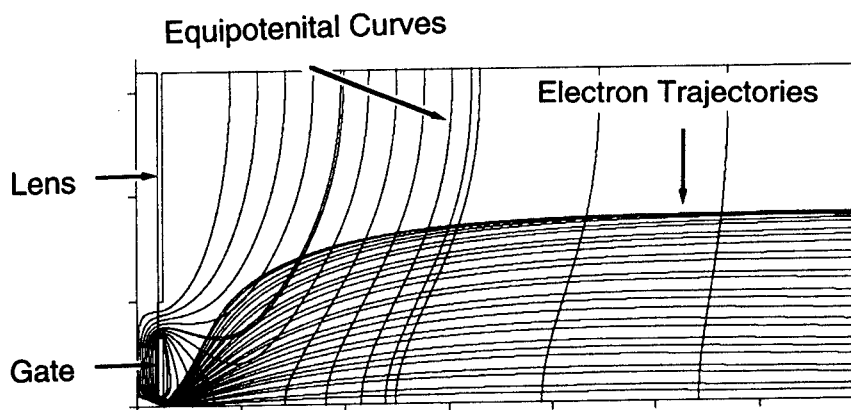


Fig. 3. Equipotential curves and electron trajectories of a cone emitter simulated by EGUN2 in cylindrical geometry with planar focusing lens.

the initial emission angle increases. When the focusing lens of Fig. 2a is added using an outer gate diameter of  $1.0\ \mu\text{m}$ , a gap between the gate and lens electrodes of  $0.25\ \mu\text{m}$ , all the electron trajectories emitted from the half cone angle of  $65^\circ$  at the tip are collimated, as shown in Fig. 3, for a lens voltage of  $V_L = -4\ \text{V}$  and an accelerating field of  $10\ \text{V}/\mu\text{m}$ . For the purpose of simulation, the anode, at  $46\ \text{V}$ , is taken to be the right-hand border of Fig. 3 located  $5\ \mu\text{m}$  from the gate and lens electrodes. The electron beam radius at  $10\ \text{keV}$  is about  $3\ \mu\text{m}$ , calculated by continuing the electron trajectories in uniform accelerating field of  $10\ \text{V}/\mu\text{m}$ .

Next, we show that integrated planar lenses may provide a simple method of producing collimated sheet beams from field-emitters. We consider FEAs with small gate diameters densely packed along a line yielding a current of  $10\ \mu\text{A}/\mu\text{m}$  at a gate voltage of  $50\ \text{V}$ . The emitters and substrate are at ground. We assume a linear gate electrode  $1\ \mu\text{m}$  wide separated on either side from the planar lens by a  $0.5\ \mu\text{m}$  gap. (Fabrication of a  $1\ \mu\text{m}$  gate width using current ion beam systems is difficult, but there is no inherent problems in making self-aligned  $1\ \mu\text{m}$  wide gates with submicron gate diameters.) Lacking a three-dimensional simulation capability for field-emitters, emission from the tip of the cone emitter into a linear geometry that is not rotationally symmetric, cannot be modeled exactly. The following EGUN2 simulations assumed electron emission in the  $(x, z)$  plane from a point source, with emission angles restricted to  $\pm 50^\circ$  and each electron trajectory spaced  $5^\circ$  apart.

For an accelerating field of  $5.0\ \text{V}/\mu\text{m}$ , we show beam collimation by a planar lens at  $-15\ \text{V}$  in Fig. 4. For the simulation, the right-hand edge of the figure is the anode located  $22.5\ \mu\text{m}$  from the emitter wafer. Electrons initially emitted within  $\pm 25^\circ$  are confined in a narrow beam, while the outer rays can be eliminated by aperture. At very low current when space charge is negligible, the collimated beam spot sizes is about  $10\ \mu\text{m}$  at  $40\ \text{keV}$  without any additional focusing. For high current densities such as  $10\ \mu\text{A}/\mu\text{m}$ , when space charge becomes important, it may

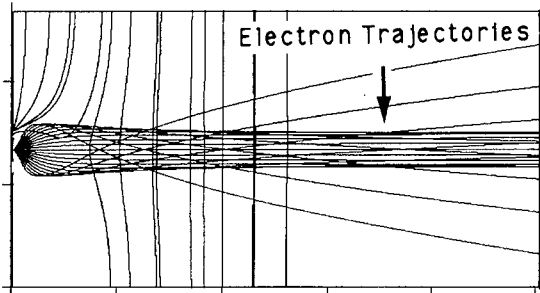


Fig. 4. Equipotential curves and electron trajectories showing beam collimation with planar lens for gate width of  $1\ \mu\text{m}$  and gate voltage of  $50\ \text{V}$  with the planar lens at  $-15\ \text{V}$  and an accelerating field of  $5\ \text{V}/\mu\text{m}$ .

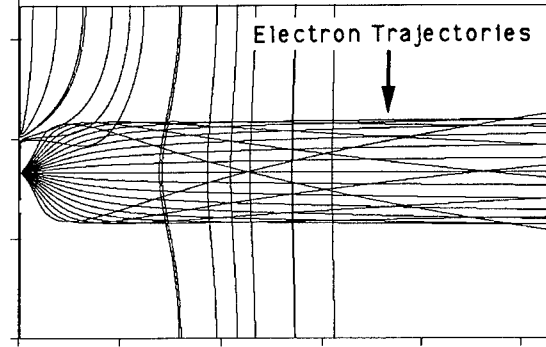


Fig. 5. Equipotential curves and electron trajectories showing beam collimation with planar lens for gate width of  $4\ \mu\text{m}$  and gate voltage of  $100\ \text{V}$  with the planar lens at  $-35\ \text{V}$  and an accelerating field of  $5\ \text{V}/\mu\text{m}$ .

be better not to focus the beam so tightly at low voltage. Additional focusing may be needed for space charge dominated beams.

Wider gate strips allow larger gate diameters that can be fabricated using a wide variety of available methods. Larger gate diameters require higher gate voltages for emission. In the next example, we assume a gate voltage of  $100\ \text{V}$ , with the emitter and the substrate at ground, and a gate electrode  $4\ \mu\text{m}$  wide separated on either side from the planar lens by a  $1.0\ \mu\text{m}$  gap. Again, we assume an averaged line current greater than  $10\ \mu\text{A}/\mu\text{m}$ . As before, EGUN2 simulated electron emission in the  $(x, z)$  plane from a point source with emission angles restricted to  $\pm 50^\circ$  and each electron trajectory separated by  $5^\circ$ . For the simulation, the right-hand edge of the Fig. 5 is the anode, located at  $40\ \mu\text{m}$  from the emitter wafer. We show beam collimation by a planar lens at  $-35\ \text{V}$  in an accelerating field of  $5.0\ \text{V}/\mu\text{m}$ .

The normalized RMS emittance of field-emitters that can now be fabricated was obtained by EGUN2 simulation to be in the range of few  $10^{-4}$  to  $10^{-3}\ \pi\ \text{mm-mrad}$ . All the simulations in Figs. 3–5 show that collimated beams can be obtained in a compact geometry appropriate for free electron micro-laser for various geometries and gate voltages.

### 3. Smith–Purcell experiments with a micro-electron-beam

The beam of the type described in Section 2 might be used to generate radiation from a diffraction grating. When an electron beam is passed over the surface of a metal grating Smith–Purcell radiation is emitted [23]. If the beam travels perpendicular to grooves of spacing,  $D$ , the wavelength spectrum is

$$\lambda = \frac{D}{|m|} \left( \frac{1}{\beta} - \sin(\theta_m) \right),$$

where  $\beta \equiv v_b/c$  is the electron velocity divided by the speed of light. The angle,  $\theta_m$ , is measured between the grating normal and the propagating direction of a wave with spectral order  $m = -1, -2, -3, \dots$ . In order to couple effectively the beam must be located a distance ( $d$ ) from the surface which obeys the constraint,  $d \leq \lambda\beta\gamma/2\pi$ , where  $\gamma \equiv (1 - \beta^2)^{-1/2}$ .

At Dartmouth College, experiments have generated Smith–Purcell radiation [1] with wavelengths ranging from 288 to 803  $\mu\text{m}$ . A 168  $\mu\text{m}$  period diffraction grating generated  $(4.7 \pm 0.94) \times 10^{-9}$  W/sr at 443  $\mu\text{m}$  in a 38  $\mu\text{m}$  bandwidth. The emitting surface area was  $2.4 \times 10^{-8}$   $\text{m}^2$ . Thus, a basic radiance of approximately 0.20 W/(sr  $\text{m}^2$ ) was produced.

A scanning electron microscope was used as an electron beam source in these experiments. The beam typically had a radius that varied from 3 to 30  $\mu\text{m}$ , carried a 50  $\mu\text{A}$  current, and had an energy of 30–40 kV and with a normalized emittance of  $\epsilon_n \approx 10^{-2}$   $\pi\text{-mm-mrad}$ . The beam in these experiments was formed by a tungsten cathode, focused with magnetic lenses and scraped with platinum apertures. The general beam parameters were inferior to what could be generated with an FEA. A linear array could be used in a number of feedback geometries to form an oscillator.

#### 4. Summary

Good agreement between theory and experiment for Smith–Purcell radiation was observed for micro-gratings with beam from electron microscope [1]. Electron beams from FEAs have demonstrated high current density and are predicted to have small emittances. Good beam collimation would be possible. A planar lens, simple to fabricate and easy to implement, may provide useful collimated beams. When the small emittance of the field emitters is confirmed experimentally for sheet beams, compact, tunable oscillators in the infrared with gratings may be possible down to tens of  $\mu\text{m}$  in wavelength.

#### Acknowledgements

Work supported by the Defense Sciences Office of Advanced Research Projects Agency, ONR and the ARO contract DAAL03-91G-0189.

#### References

- [1] M. Goldstein, Ph.D. Thesis, Dartmouth College (1994).
- [2] K. Mima, et al., Nucl. Instr. and Meth. A 331 (1993) 550.
- [3] T. Taguchi and K. Mima, Nucl. Instr. and Meth. A 331 (1993) 597.
- [4] K. Mima et al., Nucl. Instr. and Meth. A 341 (1994) ABS 103.
- [5] T. Taguchi and K. Mima, Nucl. Instr. and Meth. A 341 (1994) 322.
- [6] C.A. Spindt, private communications.
- [7] G.N.A. van Veen, private communications.
- [8] C.O. Bozler et al., J. Vac. Sci. Technol. B 12 (1994) 629.
- [9] M. Hollis, private communications.
- [10] W.B. Herrmannsfeldt, EGUN – An Electron Optics and Gun Design Program, SLAC Report 331 (1988).
- [11] C.M. Tang, A.C. Ting and T.A. Swyden, Nucl. Instr. and Meth. A 318 (1992) 353.
- [12] W.B. Herrmannsfeldt, R. Becker, I. Brodie, A. Rosengreen and C.A. Spindt, Nucl. Instr. and Meth. A 298 (1990) 39.
- [13] R.M. Mobley and J.E. Boers, IEEE Trans. Electron Devices ED-38 (1991) 2383.
- [14] J. Itoh, K. Morikawa, Y. Tohma and S. Kanemaru, Revue Le Vide, les Couches Minces, Suppl. No.271 (Mars–Avril 1994) p. 25.
- [15] C.A. Spindt, Automatically Focusing Field Emission Electrode, U.S. patent 4,874,981 (1989).
- [16] T. Leroux and C. Py, Système permettant de maîtriser la forme d'un faisceau de particules chargées, French patent 92403558.7 (1992).
- [17] W.D. Kesling and C.E. Hunt, J. Vac. Sci. Technol. B 11 (1993) 518.
- [18] C.M. Tang, T.A. Swyden, A.C. Ting, X.F. Liu, L. Yadon, C.T. Sune and G.W. Jones, Technical Digest of the 1993 IEEE Int. Electronics Devices Meeting, Washington, DC, 5–8 Dec. 1993, p. 761.
- [19] C.M. Tang, T.A. Swyden and A.C. Ting, Revue Le Vide, les Couches Minces, Suppl. No. 271 (Mars–Avril 1994) p. 346.
- [20] C.M. Tang, T.A. Swyden and A.C. Ting, JVST, to be published.
- [21] C.E. Holland and C.A. Spindt, Revue Le Vide, les Couches Minces, Suppl. No. 271 (Mars–Avril 1994) p. 377.
- [22] W.D. Kesling and C.E. Hunt, Revue Le Vide, les Couches Minces, Suppl. No. 271 (Mars–Avril 1994) p. 135.
- [23] S.J. Smith and E.M. Purcell, Phys. Rev. 92 (1953) 1069.



ELSEVIER

## A superlattice as an undulator

Yu.A. Malov<sup>\*</sup>, D.F. Zaretsky

*Russian Research Center "Kurchatov Institute", Moscow, 123182, Russian Federation*

### Abstract

The scattering length of ballistic electrons in a semiconductor may be as large as  $2-3 \times 10^{-5}$  cm [M. Heiblum et al., Phys. Rev. Lett. 55 (1985) 2200]. This means that a semiconductor superlattice (SL) with a period of 200 Å may contain more than ten periods and its length is still smaller than the above value.

The motion and photon emission of electrons in a superlattice may be described as in an undulator. Therefore, there is a close analogy between ballistic electrons in a superlattice and electrons in a free electron laser (FEL).

Touching upon this analogy the intensity of photon emission in the IR region and the gain are calculated. It is shown that the amplification can be significant, reaching tens of %.

To obtain IR radiation with variable frequency we propose to use a SL where the currents are injected and passed through without collisions with phonons. As the mean free path for collisions is about  $2 \times 10^{-5}$  cm, the length of the SL has to be smaller than this. We restrict our consideration to a SL of the GaAs/GaAsAl type. Other types may work also, for example, InGaAs/AlGaAs. The injection of carriers in the case of GaAs/GaAlAs SL may be performed as suggested in Ref. [1]. The injection system consists of a heavily doped GaAs layer (thickness 2000 Å, carrier density  $n \approx 10^{18}$  cm<sup>-3</sup>) and a barrier of AlGaAs (thickness 100 Å, undoped). Between the emitter and the SL a potential  $V_E$  is applied. The device is displayed in Fig. 1.

With the help of the potential  $V_E$ , the barrier is lowered and carriers from the emitter are able to pass ballistically through the SL.

In the device displayed two effects may be observed:

1) Spontaneous emission of IR photons by the carriers due to their interaction with the SL periodic potential. Carriers with a kinetic energy larger than the potential amplitude  $U_0$  of the SL begin to oscillate in the direction of their motion. Therefore the photons emitted are directed mainly perpendicular to the axis of the SL.

Let us consider a beam of electrons injected along the SL axis  $x$ . The SL potential is chosen in the form  $U(x) = U_0 \cos qx$ , where  $q$  is the SL wave vector. Then the

spectral intensity of dipole radiation by one electron has following form

$$\frac{d^2\eta}{d\Omega d\omega} = \frac{e^2 v^2}{64c^3} \sin^2\theta \left( \frac{eU_0}{E} \right)^2 \frac{\sin^2 u}{u^2} \epsilon_0 n^2, \quad (1)$$

where  $v$  is the velocity of the ballistic electron,  $E = m^* v^2/2$ ,  $u = n((\omega - qv)/\omega)\pi$ ,  $\theta$  is the angle between  $x$  and the radiation direction,  $\epsilon_0$  is the dielectric constant of the SL, and  $(\sin^2 u)/u^2$  is a diffraction factor.

Relationship (1) has a maximum when  $u$  approaches zero. By this is meant that the frequency of spontaneously emitted photons by ballistic electrons in the SL may be obtained from the expression

$$\omega = qv. \quad (2)$$

As the value of the velocity depends on the injection potential, variation of this potential leads to a variation of  $\omega$ .

Using Eq. (1) we can obtain the total intensity  $\eta$  emitted by the electron:

$$\eta \approx \frac{\pi}{3} \frac{e^2}{\hbar c} \omega \left( \frac{v}{c} \right)^2 \left( \frac{eU_0}{E} \right)^2 \frac{\epsilon_0}{16}. \quad (3)$$

In reality the number of electrons,  $N$ , which may emit photons in the SL depends on the current density  $j_0$  and the SL parameters

$$N = \frac{j_0 S l_0}{ev}. \quad (4)$$

$S$  is the cross-section of the SL, and  $l_0$  its length. The total intensity of emission from an electron beam is equal to

$$I = \eta N = \frac{j_0 S l_0}{ev} \frac{e^2}{\hbar c} \omega \left( \frac{v}{c} \right)^2 \left( \frac{eU_0}{E} \right)^2. \quad (5)$$

<sup>\*</sup> Corresponding author. Fax +7 095 194 1994.

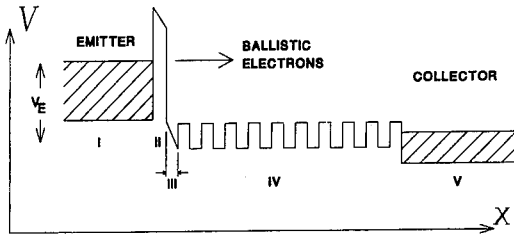


Fig. 1. Superlattice device potential vs. position. Region I is doped GaAs. Region II is undoped AlGaAs. Region III is undoped GaAs. Region IV (the superlattice) is undoped GaAs/AlGaAs. Region V is doped GaAs.

The value of  $I$  may be estimated for some reasonably chosen parameters of the SL and the injected electron current [1] ( $S \sim 10^{-2} \text{ cm}^2$ ,  $j_0 \approx 10^2 \text{ A/cm}^2$ ,  $l_0 \approx 2 \times 10^{-5} \text{ cm}$ ,  $v = 10^8 \text{ cm/s}$ ,  $d = 2\pi/q \approx 200 \text{ \AA}$ ,  $\omega = 3 \times 10^{14} \text{ s}^{-1}$  ( $\hbar\omega \approx 0.2 \text{ eV}$ ),  $eU_0/E \sim 1$ ,  $\epsilon_0 \approx 12.5$ ) leading to  $I \approx 10^{14} \text{ photons/s} = 7 \times 10^{-6} \text{ W}$ .

2) Gain measured in the direction perpendicular to the axis of the SL. (The same direction is the direction of spontaneous radiation.) Now we will estimate the gain. The Hamiltonian describing the motion of an electron of energy  $E$  in the field

$$\epsilon = \epsilon_1 \cos(\omega t - kz) \quad (6)$$

may be written in the form

$$\hat{H} = \hat{U}(x) + \hat{H}' + \hat{H}_0, \quad (7)$$

where  $\hat{H}_0$  is the kinetic energy operator and  $\hat{H}'$  is the electron-wave interaction operator  $H' = -(e\epsilon\lambda/(m^*c))\hat{p}$ , where  $\lambda$  is the wavelength of the electromagnetic field.

The electromagnetic wave (6) is polarized along the SL axis and propagates in a perpendicular direction to the SL axis.

Without the electromagnetic wave, the motion of an electron in the quasiclassical approximation may be written in the form

$$\psi_0 \approx \exp\left(\frac{i}{\hbar} \int_0^x (p^2 - 2m^*eU_0 \cos qx')^{1/2} dx' - \frac{iEt}{\hbar}\right), \quad (8)$$

where  $p$  is the electron momentum,  $E > eU_0$ .

In the presence of the wave an electron may emit or absorb a light quantum. Therefore in a first approximation the wave function will be of the form

$$\psi = \psi_0 + a_1(x)\psi_1 \exp(ikz - i\omega t) + a_{-1}(x)\psi_{-1} \exp(-ikz + i\omega t). \quad (9)$$

Here  $\psi_1$  and  $\psi_{-1}$  follow from the expression for  $\psi_0$  by replacing the initial momentum by  $p_1$  or  $p_{-1}$ , respectively, with  $p_{\pm 1} = (p^2 \pm 2m^*\hbar\omega)^{1/2}$ .  $a_{\pm 1}$  are the amplitudes of absorption and stimulated emission, respectively

( $a_{\pm 1} \ll 1$ ). Using perturbation theory we may obtain the amplitudes in the form

$$a_{\pm 1} = \mp \frac{e\epsilon_0}{4\hbar\omega} \frac{eU_0}{E} \exp\left(\frac{i}{\hbar} (p - p_{\pm 1} \pm q) \frac{x}{2}\right) \times \frac{\sin\left((p - p_{\pm 1} \pm q) \frac{x}{2}\right)}{p - p_{\pm 1} \pm q}. \quad (10)$$

The amplitudes have maximum values if the condition  $p_{\pm 1} - p = \pm q$  is fulfilled. Within the limit  $E \gg \hbar\omega$  this condition can be written as

$$\frac{\omega}{v} = q \pm \frac{p}{8\hbar} \left(\frac{\hbar\omega}{E}\right)^2. \quad (11)$$

This is consistent with Eq. (2) because

$$\frac{p}{8\hbar} \left(\frac{\hbar\omega}{E}\right)^2 \ll q.$$

Using the expression for the perturbed wave function (9), the gain may be calculated. The gain is proportional to the difference between the emission and absorption probabilities  $W_0 = W_e - W_a$ . In our case we have:

$$W_e = |a_{-1}|^2, \quad W_a = |a_{+1}|^2. \quad (12)$$

As a result the gain is

$$G = 8\pi \frac{j_0}{e} W_0 \frac{\hbar\omega}{c\epsilon_1^2} \sqrt{\epsilon_0}. \quad (13)$$

If  $\Delta E/E < 1/(\pi n)$ , where  $n$  is the number of the SL periods, and  $\Delta E$  is the energy spread of the injected electrons, then [2]

$$G = \frac{\pi}{16} \frac{j_0}{e} r_0 \frac{l_0 t^2 c^2}{\lambda v} \left(\frac{eU_0}{E}\right)^2 \times \frac{d}{du} \left(\frac{\sin^2 u}{u^2}\right) \sqrt{\epsilon_0}, \quad (14)$$

where  $r_0$  is the classical radius of the electron, and  $t$  is the interaction time.

The value of  $t$  is determined by the time for light to cross in the direction perpendicular to the SL axis:  $t = l_{\perp} \sqrt{\epsilon_0}/c$ . Estimating the gain per pass using the same SL parameters and current density as before, we obtain  $G = 0.1\%$ .

To increase the gain up to a reasonable value ( $\approx 10\%$ ) the current density has to be increased to  $10^4 \text{ A/cm}^2$ . This current density seems feasible in a pulsed regime.

If  $\Delta E/E > 1/(\pi n)$ , the expression for  $G$  has the following form:

$$G = \pi^2 \frac{j_0}{e} r_0 t \lambda (eU_0)^2 \frac{df}{dE} \Big|_{E=E_0} \sqrt{\epsilon_0}, \quad (15)$$

where  $f$  is the distribution function of the electron beam, and  $E_0 = m^*\omega^2/(2q^2)$ . If we take  $df/dE \sim 1/(\Delta E)^2$ ,  $U_0/\Delta E \sim 10$ , and  $j_0 = 10^4 \text{ A/cm}^2$ , then  $G \approx 10\%$ .

In conclusion two remarks can be made:

- 1) The frequency of the light amplified may be easily changed by variation of the carrier velocity.
- 2) The gain may be increased if several SL are combined in the direction of light propagation. In this case carrier injection has to be made simultaneously, in all SLs.

#### **References**

- [1] M. Heiblum, M.I. Nathan, D.C. Thomas and C.M. Knoedler, *Phys. Rev. Lett.* 55 (1985) 2200.
- [2] Yu.A. Malov and D.F. Zaretsky, *Phys. Lett. A.* 139 (1989) 347.

## Compact high-brightness radiation sources

J. Chen <sup>a,\*</sup>, K. Imasaki <sup>a</sup>, M. Fujita <sup>a</sup>, M. Asakawa <sup>b</sup>, T. Asakuma <sup>b</sup>, S. Nakai <sup>b</sup>,  
C. Yamanaka <sup>a</sup>

<sup>a</sup> *ILT, Yamadaoka 2-6, Suita, Osaka 565, Japan*

<sup>b</sup> *ILE, Osaka University, Yamadaoka 2-6, Suita, Osaka 565, Japan*

### Abstract

The feasibility of compact radiation sources using photon storage technology is discussed. Compact high-brightness radiation sources with photon energies from keV to more than 10 MeV can be realized by this method. These compact radiation sources will meet the requirements of applications in lithography, angiography, fission product annihilation, intense positron source and so on.

### 1. Introduction

Various concepts to enhance the interaction efficiency of Compton scattering radiation have been studied to obtain high flux and high energy monochromatic photons. But the technical limitations on accelerators for producing a high intensity electron beam and on lasers for making a high intensity photon beam had prevented us from achieving the desired enhancement [1–3]. Recent developments in accelerator and FEL/laser technologies opened a new way toward this goal. Great enhancement of Compton scattering radiation can be achieved using a photon storage cavity and a high-brightness accelerator, thus making monochromatic-bright-compact radiation sources with the energy range from soft X-ray to  $\gamma$ -ray possible [4]. In this paper, the basic principles, the status of investigation and future prospects of this technology will be discussed.

### 2. Principle

Compton scattering is a well known phenomenon. Its total interaction cross section  $\sigma_T$  can be estimated from the equation  $\sigma_T = 8\pi r_0^2/3$ , where  $r_0 (= 6.55 \times 10^{-29} \text{ m}^2)$  is the classical electron radius. This equation indicates that the elastic interaction between photon and electron is very small. Recent progress in making high reflectivity mirrors however, offers a possibility to enhance the Compton scattered photon flux by using photon storage. Development of

the photon storage technology was motivated by interest in gravitational wave observation [5]. Fig. 1 shows a schematic picture of the photon storage cavity. The essential points are the mirror reflectivity and the stability of the photon storage cavity.

The reflectivity of the mirror  $R$  can be enhanced to more than 99.999% (5N) by existing optical coating technology. The photon density enhancement inside the cavity can be estimated as  $F = (1 - R)^{-1}$  under perfect conditions. Using 5N mirrors  $F$  will be  $1 \times 10^5$ . In practice, there are certain limitations on cavity/laser stabilities, mode matching, diffraction loss and mirror degradation, so that the upper value of  $F$  we can obtain is only  $10^3$  to  $10^4$ . Even this value is large enough that spontaneous Compton scattering radiation can be used in practical applications. The Compton radiation wavelength can be estimated as  $\lambda = \lambda_0/4\gamma^2$ , where  $\lambda_0$  is the injected photon wavelength. Thus high energy monochromatic photons can be obtained using a low energy accelerator which means it is feasible to build a compact radiation source with high brightness and high photon energy.

This scheme can also be considered as a kind of laser wiggler with the advantage of a large number of interaction periods due to the short wavelength of the laser. For example, there are  $10^4$  interaction periods for an interaction length of 1 cm and a 1  $\mu\text{m}$  laser. High power is required to achieve a large enough  $K$  value. Recent high power laser technology enables us to obtain  $K$  values as high as 1.0 instantaneously, but it is impossible to keep or to repeat the interaction at a high rate due to technical limitations arising from thermal problems. The photon storage technology, however, is expected to overcome this limitation and achieve high average photon intensity.

\* Corresponding author. Tel. +81 6 8798732, fax +81 6 8774799, e-mail jzc@ile.osaka-u.ac.jp.



### 3. Status of investigation

The technical and physical issues, including stability of the cavity and laser, diffraction loss, mode pattern, refractive index of the electron beam and photon-scattering loss inside the cavity, are crucial for the concept of the supercavity X-ray source. Cavity stabilization required for photon storage by a supercavity can be achieved by development of support and temperature control systems of high accuracy. The availability of sub-atomic level piezoelectric transducers and super high-reflectivity mirrors, already make it possible to scan and lock the pump laser frequency with a resolution of 1 kHz to match the spectral transmission range of a photon storage supercavity.

Because the total mirror losses (transmission plus scatter and absorption) can be as small as  $1 \times 10^{-4}$  in a supercavity, diffraction losses for finite-dimension reflectors is anticipated to be significant. The distribution of possible transverse optical modes decreases the luminosity of the photon–electron collision. We have finished a simulation of photon storage in a practical supercavity pumped by a circular symmetric Gaussian beam. The Fox–Li technique has been used to calculate numerically the field distribution, the diffraction losses, and the round-trip phase shift of  $TEM_{0n}$  modes. We pointed out the limitation of the Fox–Li approximate iterative method for treating our ultra-low loss and large Fresnel number optical cavity. A concept of effective Fresnel number is put forward along with a discussion of the convergence of solutions of the iterative equations. The effects of the refractive index of the e-beam and the photon-scattering loss inside the cavity are much smaller than the cavity diffraction loss and so can be neglected.

Our purpose is to estimate transverse optical modes and diffraction losses inside a supercavity when it is excited by a frequency-stabilized cw single mode laser. We chose an effective Fresnel number  $N = 5$  and excitation by a uniform plane wave. After  $5 \times 10^4$  round-trips, the stored laser field distribution is shown in Fig. 2. Assuming

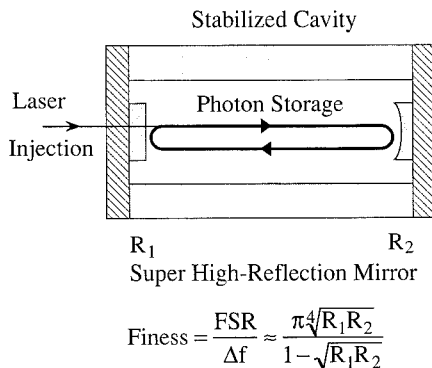


Fig. 1. Schematic picture of photon storage in a cavity with high reflective mirrors.

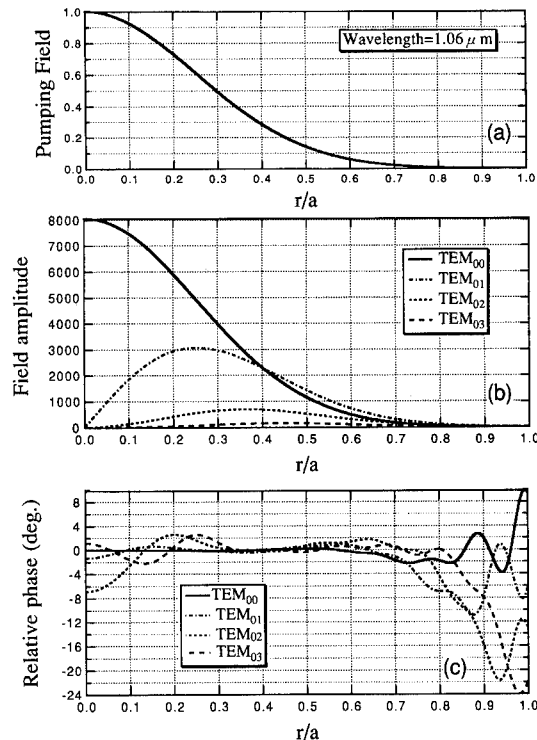


Fig. 2. Pumping laser field, and cavity's saturation field and phase distributions for three lowest modes after  $5 \times 10^4$  round trips under the condition of perfect coupling between the pumping single-mode laser and the supercavity of  $R = 99.99\%$ ,  $g_1 = 1.0$ ,  $g_2 = 0.8$ ,  $N = 5$ .

perfect phase coupling from one round-trip to another, we obtain the peak amplitude of the  $TEM_{00}$  mode equal to 8055. This means the stored laser intensity is 6488 times the original one, if the fraction of the power transmitted at the interface is assumed to be 0.01%, corresponding to a four-nine supercavity. The power fraction throughout the supercavity is therefore 64.88% of the ideal. However, the measured power through value is only 35% which could be due to losses on the interfaces, uncoupling of the wave fronts, or tolerance of the actual mirror reflectance. We are able to determine that higher order transverse modes are unimportant. We find the differences of phase shift per round trip between the lowest three modes are large which means that the fundamental mode can be selected by tuning the pumping laser. From Fig. 2c, we further see that the distributions of relative phases of high order modes change across the optical surface. It is therefore impossible to get a pumping field with the phase front perfectly coupling with phase fronts of the high order modes. For the  $TEM_{00}$  mode, the phase front around the radial axis is smooth so it can accumulate a large fraction of the pumping power. It is possible only for the  $TEM_{00}$  mode to couple with both transverse and longitudinal modes in the main part of the fundamental field distribution when  $r \leq$

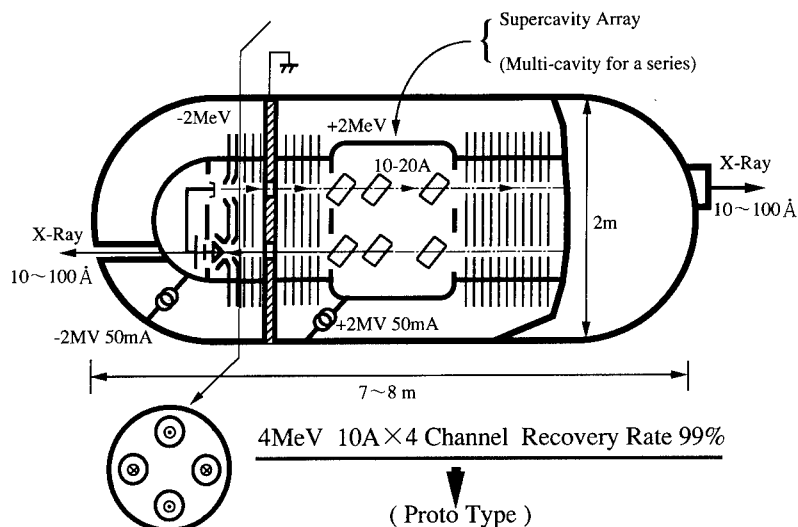


Fig. 3. Typical system for soft X-ray generation.

0.6a. The Fox-Li type code described above can also be used to optimize the practical supercavity design with respect to mirror diameter, spacing, and curvature. It is also proposed to upgrade it to include the FEL transfer function for photon storage by a supercavity FEL oscillator.

Preliminary photon storage experiments were started at ILT/ILE Osaka University using 3N and 4N mirrors. The laser used for these experiments was a monolithic non-planar ring type LD pumped Nd:YAG laser with a narrow bandwidth. The photons were stored with stability and long life inside the cavity in the agreement with our predication. An interaction experiment using the stored CW laser beam and the low energy CW e-beam extracted from an electrostatic electron gun is now under way. Details of this POP experiment are reported elsewhere in this conference.

#### 4. Prospects and applications

Based on this method compact high-brightness radiation sources of several kinds can be constructed. Here we shall classify them into three categories: soft X-ray, hard X-ray and  $\gamma$ -ray, corresponding to three typical systems.

The system to generate soft X-rays of 100 eV to 1 keV will consist of a cw/quasi-cw solid-state laser driven supercavity and a synchronized electrostatic accelerator with e-beam energy recovery. Lithography will be an appropriate application for the high average brightness radiation output from this system. A schematic picture is shown in Fig. 3. The average brightness will reach to  $10^{18}$  photons/(s mm<sup>2</sup> mrad<sup>2</sup> 0.1% bw) with a 4N supercavity. In this system, the use of multipass e-beams and multi-supercavities can increase the total brightness by a factor of 10 compared to that of a single cavity. The advantage of this

system is its compactness. As a result, lower processing cost with high throughput of LSI micro processing can be expected. The processing cost may be one third of the cost of the conventional synchrotron source using a compact storage ring.

The system to generate hard X-rays of 10 to 100 keV will be composed of an RF-linac synchronized with an FEL oscillator or an intense laser-driven cavity. The nearly monochromatic energy spectrum attainable makes this source suitable for angiography [6]. A schematic of the system with an intense laser driven cavity is shown in Fig. 4. The photon cost effectiveness of this method is due to its use of a lower e-beam energy ( $\sim 40$  MeV) and a table-top laser.

The system to generate  $\gamma$ -rays of 1 to more than 10 MeV will be composed of a storage ring with an FEL oscillator or an intense laser driven cavity. A schematic of the system is shown in Fig. 5. The unique feature here is the energy range which might be accessible using a short period laser wiggler and a storage ring. It will open some new and important applications such as intense positron

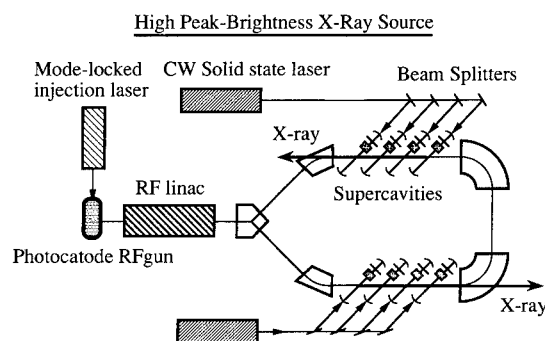
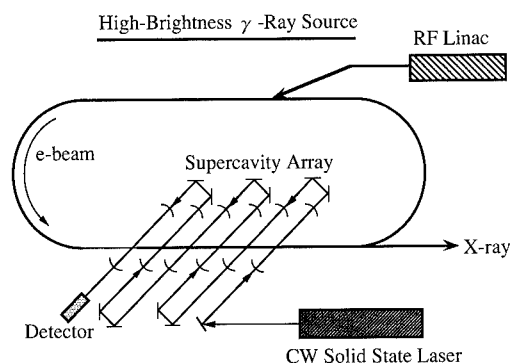


Fig. 4. Typical system for hard X-ray generation.

Fig. 5. Typical system for  $\gamma$ -ray generation.

sources, annihilation of fission products with a life longer than  $10^5$  years and so on. The positron yield will be more than that achieved using a large storage ring and a long wiggler with intense magnetic field [7]. The energy required to annihilate long lived fission products may be comparable to that for muon catalyzed fusion and less than that required for neutron spallation [8]. Additionally by this technology, significant laser cooling may be expected anal-

ogous to synchrotron radiation cooling. Photon ( $\gamma$ -ray)–photon (intense laser) collision at the next linear collider might also be possible.

## 5. Future prospects

The key to this technology is to store large numbers of photons and interact them with the e-beam efficiently. The radiation flux and brightness depend on the e-beam density and the stored photon density and synchronization. These issues will limit the attainable brightness. Fig. 6 indicates the upper limit of brightness as a function of photon energy. The limits are determined by the technologies of damage threshold, reflectivity of optics, stability of the cavity and by FEL or solid state laser properties and high-brightness e-beam properties. The important parameter for the radiation brightness is  $P_0(1-R)^{-1}F_d n_p n_c$ . Here,  $P_0$  is the injected laser power,  $F_d$  is the duty factor,  $R$  is the reflectivity, and  $n_p$  and  $n_c$  are pass number per accelerator and cavity number per pass, respectively. The radiation brightness may reach more than  $10^{25}$  photons/(s mm<sup>2</sup> mrad<sup>2</sup> 0.1% bw). These values exceed that of the middle size synchrotron radiation sources.

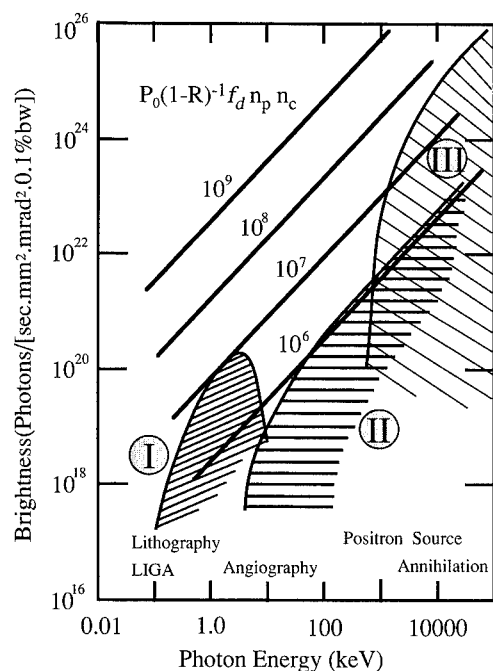


Fig. 6. Brightness limitations of radiation from the interaction of an e-beam with the photon beam stored inside a supercavity. Regions I, II and III correspond to typical systems of Figs. 3, 4 and 5, respectively.

## 6. Summary

Compact radiation sources using photon storage enhance the interaction by  $10^4$  compared to conventional Compton backscattering sources. Typical systems composed of various lasers and accelerators are described. The brightness attained might exceed  $10^{18}$  photons/(s mm<sup>2</sup> mrad<sup>2</sup> 0.1% bw) which already compares with that of middle size storage ring synchrotron sources. The radiation range from soft X-ray to  $\gamma$ -ray can be obtained by this kind of compact system. The parameters required for applications to lithography, angiography, annihilation of long lived fission products intense positron sources and so on can be achieved in the future.

## References

- [1] A. Hasegawa et al., Appl. Phys. 29 (1986) 267.
- [2] A.U. Luccio, USA Pat. No. 4598415 (1986).
- [3] P. Sprangle et al., Appl. Phys. 72 (1992) 5032.
- [4] J. Chen et al., Nucl. Instr. and Meth. A 341 (1994) 346.
- [5] G. Remp et al., Opt. Lett. 17 (1992) 363; N. Uehara et al., Laser Res. 21 (1993) 590, in Japanese.
- [6] E. Rubenstein et al., SPIE 314 (1981) 42.
- [7] P.L. Csonka, Nucl. Instr. and Meth. A 345 (1994) 1.
- [8] Private communication from Nomura, PNC and K. Kase PNC TN 8100-92-011 in Japanese.



ELSEVIER

## A path towards a compact, CW FEL using superconducting rf accelerator technology <sup>☆</sup>

J. Edighoffer <sup>a,\*</sup>, K.-J. Kim <sup>a</sup>, M. Xie <sup>a</sup>, F. Dylla <sup>b</sup>, R. Sheffield <sup>c</sup>, S. Chattopadhyay <sup>a</sup>

<sup>a</sup> Lawrence Berkeley Laboratory, Berkeley, California 94720, USA

<sup>b</sup> Continuous Electron Beam Accelerator Facility, Newport News, VA, USA

<sup>c</sup> Los Alamos National Laboratory, Los Alamos, NM, USA

### Abstract

Recently, several compact FELs have been built based on pulsed linacs and RF photocathode guns. There is now an exciting opportunity to extend the capability of the technique to CW operation by incorporating the recent development in superconducting electron accelerators. The higher average power possible with CW operation will enhance the utility and the versatility of the compact FELs for fundamental research as well as for industrial application. Our vision of an eventual compact high power FEL is one that is targeted to have a foot print of  $1 \times 6$  m<sup>2</sup>. It would consist of a CW RF superconducting photocathode gun closely coupled to a superconducting accelerator cavity, all in a single cryostat, producing a 6–15 MeV beam. The helium refrigerator will be built into the compact dewar as is currently being done for the JAERI FEL in Japan. The FEL output will consist of 10–100  $\mu$ J pulses at 10–70 MHz repetition rate with average power greater than 1 kW. The FEL performance will be optimized in the wavelength range between 10 and 50  $\mu$ m, which is a difficult region for conventional laser techniques. Longer wavelengths can be generated via Cherenkov FEL, and X-rays can be produced via Thomson scattering.

### 1. Introduction

There is an exciting possibility to extend the compact photocathode work of Los Alamos [1] and others to high power CW operation by combining this development with that of the maturing RF superconducting technology [2,3]. Superconducting RF systems can now be designed to operate at about 10 MV/m with significant increases likely in the next few years.

At LBL, we are proposing an R & D program to merge these technologies into a compact CW high power FEL system suitable for university and industrial environments. Fig. 1 shows our vision of what this might look like. It is estimated to occupy a  $1 \times 6$  m footprint. The RF photocathode gun and accelerator would be housed in a single compact cryostat with a self-contained He refrigerator as being done by JAERI [4]. There would be an emittance compensation lens between cavities.

Such a system will be able to generate coherent radiation from several mm to roughly 20  $\mu$ m, and using Compton scattering will produce 100 fs incoherent X-ray pulses. Such a system would provide CW optical beams of 100 W to 1 kW with ps pulse structure in the mm and IR regions.

### 2. Approach

The first step in this program would be to test the electron beam dynamics of a normal conductor copper RF gun designed around the superconducting cavity limits on gradient ( $< 10$  MV/m), using a typical superconducting cavity shape, and restricting focusing coil placement to what would be the non-superconducting beam pipe regions. Fig. 2 shows the layout. The rf photocathode would be a  $3\frac{1}{2}$  cell CEBAF shaped cavity with a Los Alamos type photocathode insertion and processing station. There would then be an emittance compensation coil and a quarter CEBAF cryomodule followed by beam diagnostics. This would allow complete beam dynamics testing at full energy.

Room temperature CW RF is limited to significantly lower gradient and smaller apertures because of the high

<sup>☆</sup> This work was supported by the Director, Office of Energy Research, Office of Basic Energy Sciences, Materials Sciences Division, of the U.S. Department of Energy under Contract No. DE-AC03-76SF00098.

\* Corresponding author.

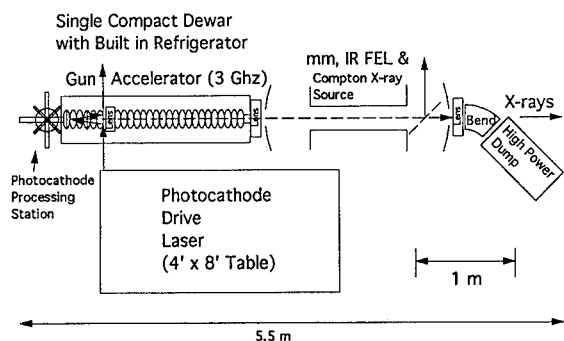


Fig. 1. Our vision of a compact mm, IR and X-ray source combining RF photocathode and CW RF superconducting technologies.

wall losses. Very low frequency 2–6 MV/m room temperature CW structures are possible but are not compact or cost effective. The proposed SELENE room temperature FEL system is designed to operate at about 1 MV/m [5].

The beam would be accelerated to full energy by using a modified CEBAF quarter cryomodule, consisting of two 5-cell 1500 MHz cavities, giving a maximum acceleration of 10 MV [2]. These modifications are being developed at CEBAF and consist of piping the HOM heat load out of the helium bath to the 50 K shield and upgrading the RF input coupler and RF drive to provide 30 kW of input power. The parameters of this mockup system have been modeled using PARMELA which gives the energy spread, bunch length, bunch charge and emittance shown in Table 1. The calculated performance is much better than what is needed in the mm and IR region of the spectrum.

The recent introduction of  $\text{Cs}_2\text{Te}$  photocathode material is very promising and may be well suited to the superconducting cavity. It has high quantum yield, which is particularly desirable for a CW drive laser. Also, cesium is a well bonded part of the crystal structure, making cesium migration to the superconducting surface less likely than in

Table 1

Mockup system operating parameters. CW superconducting operation would be CW at macropulse parameters

|                               | Low charge, high rep rate option | High charge, low rep rate option |
|-------------------------------|----------------------------------|----------------------------------|
| Microbunch charge             | 70 pC                            | 280 pC                           |
| Microbunch length             | 5 ps                             | 5 ps                             |
| Microbunch rep rate           | 76 MHz                           | 19 MHz                           |
| Normalized RMS emittance      | 4 mm-mrad                        | 7 mm-mrad                        |
| Energy spread (FWHM)          | 0.35%                            | 0.2%                             |
| Maximum energy                | 13 MeV                           | 13 MeV                           |
| Macropulse length             | 100 $\mu\text{s}$                | 100 $\mu\text{s}$                |
| Macropulse rep rate           | 10 Hz                            | 10 Hz                            |
| Average macropulse beam power | 69 kW                            | 69 kW                            |
| Average FEL power (0.2%)      | 140 W                            | 140 W                            |
| Wavelength coverage           | IR, mm                           | IR, mm                           |

most other cesiated cathodes. Finally, it can be applied as a thin film on niobium to reduce the problem of heat loss within the cathode material, which if it becomes too large ( $\sim 10 \text{ W/cm}^2$ ) will quench the superconducting material around the cathode. There is also some conjecture that a very thin layer ( $\sim 20 \text{ nm}$ ) will allow Cooper pairs from the superconductor to penetrate to the surface, in effect making the cathode superconducting. The mounting of the photocathode within the superconducting cavity requires some very careful design work.

Successful implementation of the superconducting CW photocathode mockup in copper could be immediately followed by a niobium version that would prove the cathode capability with superconducting rf with known beam dynamics, where the issues mentioned above could be investigated. Then, the addition of beam transport, a wiggler and optics would provide a cw high power FEL. Recirculation and energy recovery could eventually extend this approach to visible and UV CW operation, or high powers.

The merging of the pulsed RF photocathode compact FEL technology with CW RF superconducting structures looks like a promising route to achieving a compact CW high power FEL source covering mm to X-rays.

## References

- [1] D.C. Nguyen, these Proceedings (16th Int. Free Electron Laser Conf., Stanford, CA, USA, 1994) Nucl. Instr. and Meth. A 358 (1995) 3.
- [2] J. Benesch et al., Design of a high power UV FEL for industrial processing, presented at this Conference (16th Int. Free Electron Laser Conf., Stanford, CA, USA, 1994).
- [3] R.M. Sundelin, Proc. 6th Workshop on RF Superconductivity, Oct. 4–8, 1993, CEBAF.
- [4] E.J. Minchira et al., Ref. [1], p. ABS 30.
- [5] H. Bennet et al., Nucl. Instr. and Meth. A 341 (1994) 124.

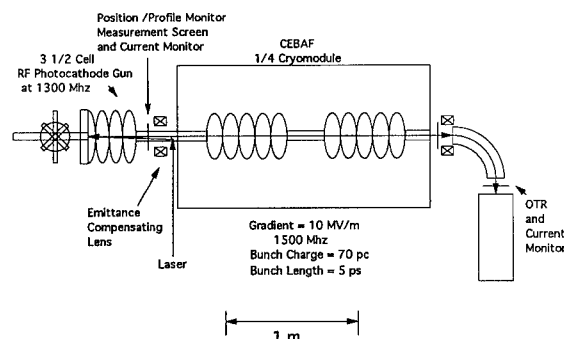


Fig. 2. Layout of superconducting RF photocathode beam dynamics mockup configuration.

# A compact, bright and tunable CW source of soft X-rays

I. Kimel, L.R. Elias \*

*Center for Research and Education in Optics and Lasers (CREOL) and University of Central Florida, Orlando, FL 32826, USA*

## Abstract

A bright, CW, tunable source of soft X-rays is proposed. The X-rays are obtained from the Compton backscattering of intense infrared laser radiation from a high quality electron beam. The incident infrared radiation is the intracavity beam in a high power Nd:YLF laser. This radiation is scattered from a relativistic electron beam generated by electrostatic accelerators. Such an X-ray source would constitute a low cost compact alternative to the more traditional synchrotron rings.

Narrow bandwidth X-ray radiation can be obtained with the use of proper aperturing without the necessity of monochromators. Analytic expressions of the frequency spectrum of the radiation through a certain aperture, are given. These expressions are valid for small undulator parameter and large number of periods.

## 1. Introduction

By their very nature, FELs and related systems are bigger and more costly than conventional lasers. However, efforts can be made to design more compact and lower cost systems. That has been our driving philosophy for some time. To reach shorter wavelength we have tried to resort to the concept of the two-stage FEL [1]. At present we are building a far-infrared FEL with a very short period static undulator [2]. Continuing with that program, we are presenting in this paper the design of a compact X-ray system.

Exploiting the low energy spread and low beam emittance obtained from electrostatic accelerators, we are proposing to generate soft X-rays with appreciable brightness by Compton backscattering of an intense laser light from a high quality DC electron beam. The electron beam produced by a thermionic gun will be accelerated up to 5.7 MeV by an electrostatic accelerator.

Instead of a static undulator, as in synchrotron radiation facilities, our system will employ intense radiation from a Nd<sup>3+</sup> doped YLF<sub>4</sub> laser. At any fixed angle, the radiation obtained from Compton backscattering will be extremely narrowband since the effective number of undulator periods  $N$ , is very large. Then, the usual  $10^{-3}$  fractional bandwidth can be obtained with a proper small aperture, instead of having to use inefficient monochromators as in synchrotron facilities. Analytic expressions of the total frequency spectrum as a function of the aperture size valid for large  $N$ , are also given in the paper.

## 2. X-ray source

Generation of X-rays with synchrotrons or conventional FELs require considerable investment in space and capital equipment. Here, we propose the development of a relatively low cost, compact source of tunable X-ray radiation based on Compton back-scattering of intense CW infrared laser radiation from a relativistic, DC electron beam of moderate kinetic energy ( $E = 5.7$  MeV).

The radiation stored inside a very high-Q cavity YLF laser will serve as an intense (CW) source of photons for the Compton scattering process. Because of very small intracavity YLF laser losses, we expect that the demands for external flash-lamp power will be reasonable ( $P < 3$  kW).

We presently have a 1.7 MV electrostatic accelerator. In order to increase the electron energy up to a maximum of 5.7 MeV, we intend to purchase a second 4 MV accelerator. The existing 1.7 MV negative terminal electrostatic accelerator can be considered as an injector for the second 4 MV positive terminal accelerator.

The 1.7 MV accelerator contains in its terminal the electron gun and the electron collector. After the electrons (generated by the gun) exit the 1.7 MV accelerator they enter the 4 MV accelerator. This is schematically represented in Fig. 1. At the 4 MV accelerator, the electrons are further accelerated through the acceleration tube and arrive at the positive terminal with an energy of 5.7 MeV. At this terminal, the electrons interact with the intense  $1.0 \mu\text{m}$  intracavity YLF laser radiation, and emit the desired soft X-ray radiation by Compton backscattering.

After interacting with the radiation, the electrons are decelerated through the tube DT1 and exit the 4 MV accelerator. Then, they enter the 1.7 accelerator where they

\* Corresponding author. Tel. +1 407 658 6800, fax +1 407 658 6890, e-mail elias@fel.

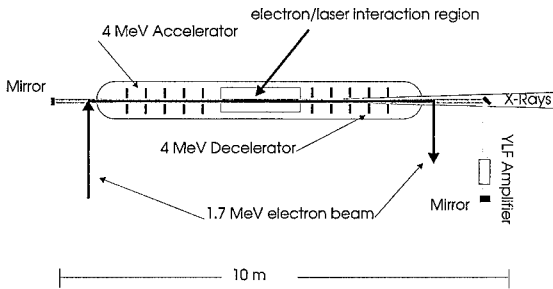


Fig. 1. Tunable X-ray source layout. Both acceleration and deceleration of the electron beam take place in two stages, at the 1.7 MV and 4 MV electrostatic accelerators. One arm of the YLF laser resonator traverses the length of the 4 MV accelerator.

are further decelerated in the tube DT2, after which they are recovered at the collector C. A very high collection efficiency is expected since the energy spread introduced by the interaction is very low. We conclude this section by listing in Table 1 the main parameters of the electron beam.

### 3. Electromagnetic wave undulator

Although YAG lasers constitute one of the most common sources of high power (multi-kilowatt) radiation used in industrial applications, we propose to use a somewhat different solid state gain material known as YLF (Nd:YLF<sub>4</sub>) for some technical reasons. Since only a fraction of the cavity power is extracted from these lasers, the intracavity power can be quite high (i.e., tens of kilowatts). The main operating parameters of the YLF laser are shown in Table 2.

### 4. Radiation spectrum of single electron emission

Alferov et al. [3,4] first derived the energy distribution an electron radiates when traversing an  $N$  period undulator. This energy distribution is a function of  $N$  and the undulator parameter

$$K = \frac{eB_0 \lambda_0}{2\pi mc^2}. \quad (1)$$

Table 1  
Electron beam parameters

|                                     |             |
|-------------------------------------|-------------|
| Maximum electron beam energy        | 5.7 MeV     |
| Maximum DC electron beam current    | 0.3 A       |
| Beam radius over interaction region | 0.3 mm      |
| Transverse emittance                | 0.1 mm mrad |
| Energy homogeneity                  | $10^{-6}$   |

Table 2

Design characteristics of YLF laser

|                                       |                                   |
|---------------------------------------|-----------------------------------|
| Laser wavelength                      | 1.05 $\mu\text{m}$                |
| Transverse laser mode                 | TEM <sub>00</sub>                 |
| Intracavity power                     | 100 kW                            |
| Rayleigh length                       | 0.28 m                            |
| Beam waist                            | 0.3 mm                            |
| Average mode area                     | 0.57 mm <sup>2</sup>              |
| Cavity losses                         | 0.5%                              |
| Cavity length                         | 10 m                              |
| Beam radius at mirror                 | 5.26 mm                           |
| Mode area at mirror                   | 0.87 cm <sup>2</sup>              |
| Power density at mirror               | 115 kW/cm <sup>2</sup>            |
| Flash-lamp power (20% efficiency)     | 2.5 kW                            |
| Effective laser-beam emittance        | 0.3 mm mrad                       |
| Power density over interaction region | $1.73 \times 10^7 \text{ W/cm}^2$ |
| Effective undulator parameter         | $7 \times 10^{-6}$                |

When  $K$  is very small the photon flux per unit frequency and angle radiated by one electron, is given by

$$\frac{d^2 F_1(\omega, \theta, \phi)}{d\omega d\Omega} = \frac{\alpha(\gamma N)^2}{\omega} S(\omega/\omega_f, \theta) A(K, \theta, \phi), \quad (2)$$

where  $\alpha = e^2/(2\epsilon_0 hc)$  is the fine structure constant,  $\omega_f$  is the fundamental frequency

$$\omega_f = \frac{4\pi\beta c\gamma^2}{\lambda_0(1 + K^2/2)}, \quad (3)$$

and

$$S(\omega/\omega_f, \theta) = \left\{ \frac{\sin \pi N \left[ \frac{\omega}{\omega_f} (1 + \gamma^2 \theta^2) - 1 \right]}{\pi N \left[ \frac{\omega}{\omega_f} (1 + \gamma^2 \theta^2) - 1 \right]} \right\}^2, \quad (4)$$

$$A(K, \theta, \phi) = \frac{K^2}{(1 + \gamma^2 \theta^2)^2} \left[ 1 - \frac{4(\gamma \theta)^2 \cos^2 \phi}{(1 + \gamma^2 \theta^2)} \right]. \quad (5)$$

After integrating in  $\phi$  and using  $\xi = 1 + (\gamma \theta)^2$  Eq. (2) yields

$$\frac{dF_1(\omega, \theta)}{d\omega} = \frac{\alpha N^2 K^2}{2\omega} \int_1^{1+(\gamma \theta_0)^2} d\xi \frac{1 + (\xi - 1)^2}{\xi^4} \times \left\{ \frac{\sin \pi N \left[ \frac{\omega}{\omega_f} \xi - 1 \right]}{\pi N \left[ \frac{\omega}{\omega_f} \xi - 1 \right]} \right\}^2. \quad (6)$$

Since  $N$  is very large it is convenient to obtain the leading term in an expansion in  $(1/N)$ . The integral of the leading term yields the photon flux per unit frequency interval

inside a half-angle  $\theta_0$ . This flux, when generated from a perfect electron beam of current  $I$ , is given by

$$\begin{aligned} \frac{dF_{PB}(\omega)}{d\omega} = & \frac{\pi\alpha NK^2(I/e)}{\omega_f} \left( 1 - \frac{2\omega}{\omega_f} + \frac{2\omega^2}{\omega_f^2} \right) \\ & \times \left\{ \frac{\sin^2 \pi N \left[ \frac{\omega}{\omega_f} (1 + \gamma^2 \theta_0^2) - 1 \right]}{\pi N \left[ \frac{\omega}{\omega_f} (1 + \gamma^2 \theta_0^2) - 1 \right]} \right. \\ & - \frac{\sin^2 \pi N \left[ \frac{\omega}{\omega_f} - 1 \right]}{\pi N \left[ \frac{\omega}{\omega_f} - 1 \right]} \\ & + Si \left[ 2\pi N \left( \frac{\omega}{\omega_f} (1 + \gamma^2 \theta_0^2) - 1 \right) \right] \\ & \left. - Si \left[ 2\pi N \left( \frac{\omega}{\omega_f} - 1 \right) \right] \right\}. \end{aligned} \quad (7)$$

As far as we know this is a new result.

The radiation spectrum for the system proposed in this paper is shown in Fig. 2. The dashed line in that figure, represents radiation from a perfect electron beam as given by Eq. (7) for  $N = 2 \times 10^6$  and  $(\gamma\theta_0)^2 = 10^{-3}$  so as to yield 0.1% fractional bandwidth. The solid line in Fig. 2 is the spectrum corrected for inhomogeneous broadening, which will be discussed in the next section. Similarly, Fig. 3 shows the curves for  $(\gamma\theta_0)^2 = 10^{-4}$ , or 0.01% fractional bandwidth.

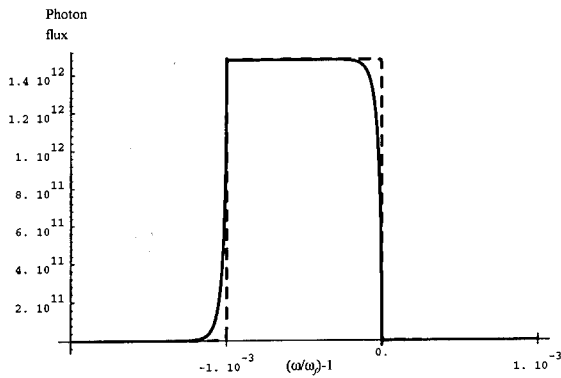


Fig. 2. Expected spectrum from the system proposed in this paper for  $N = 2 \times 10^6$  and  $(\gamma\theta_0)^2 = 10^{-3}$ . The dashed line (almost top hat), obtained from Eq. (7) would be the spectrum for a perfect electron beam (zero emittance, energy spread, etc.). The solid line shows the spectrum containing corrections due to emittance in accordance with Eq. (11).

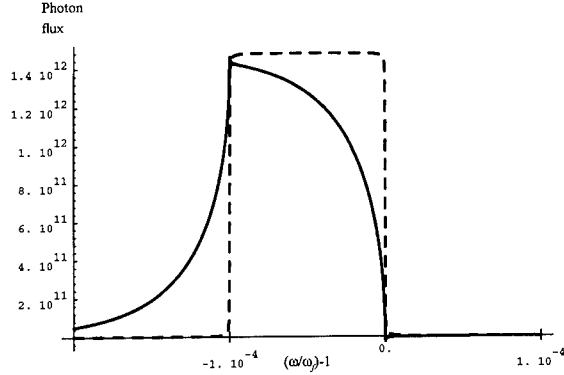


Fig. 3. Like Fig. 2 except that now instead of 0.1%, the fractional bandwidth is 0.01%. Now the corrections due to emittance are more severe.

The number of periods  $N = 2 \times 10^6$  corresponds to an interaction length of  $L = N/(2\lambda) = 1$  m. This is close enough to the optimum length  $= 2\sqrt{3}$  times the Rayleigh length  $= 0.94$  m.

An integration of Eq. (7) over frequencies yields the total photon flux inside a cone of half-angle  $\theta_0$  as

$$F(\omega) = \pi\alpha NK^2(I/e)\gamma^2\theta_0^2. \quad (8)$$

In the case of a wave “undulator” of power  $P$  and mode area  $M_a$  we have

$$K^2 = \frac{e^2\mu_0\lambda_0^2(P/M_a)}{2\pi^2m^2c^3}. \quad (9)$$

## 5. Inhomogeneous broadening

In the last section we worked out the spectrum and total photon flux, first for a single electron and then for a perfect electron beam. In order to treat the case of a more realistic electron beam with energy spread and emittance, we first introduce new variables  $\eta_\gamma$  and  $\eta_\epsilon$ . These are related to the energy spread and emittance by

$$\langle \eta_\gamma^2 \rangle = \overline{(\delta\gamma/\gamma)^2} = \sigma_\gamma^2, \quad \langle \eta_\epsilon^2 \rangle = \epsilon_n^2. \quad (10)$$

In our case, the spectrum of the radiation emitted within a cone of half-angle  $\theta_0$  (corrected for inhomogeneous broadening) can be shown [5] to be

$$\begin{aligned} \frac{dF(\omega)}{d(\omega/\omega_f)} = & \pi\alpha NK^2(I/e) \sqrt{\frac{2}{\pi}} \int_0^\infty dt e^{-t^2/2} \\ & \times \left( \rho^2 + \left[ 1 - \rho \left( 1 + (\epsilon_n/r_e)^2 t^2 \right) \right] \right) \end{aligned}$$



$$\begin{aligned}
& \times \left\{ \frac{\sin^2 \pi N \left[ \rho \left( \xi_0 + \left( \frac{\epsilon_n}{r_e} \right)^2 t^2 \right) - 1 \right]}{\pi N \left[ \rho \left( \xi_0 + \left( \frac{\epsilon_n}{r_e} \right)^2 t^2 \right) - 1 \right]} \right. \\
& - \frac{\sin^2 \pi N \left[ \rho \left( 1 + \left( \frac{\epsilon_n}{r_e} \right)^2 t^2 \right) - 1 \right]}{\pi N \left[ \rho \left( 1 + \left( \frac{\epsilon_n}{r_e} \right)^2 t^2 \right) - 1 \right]} \\
& + Si \left( \pi N \left[ \rho \left( \xi_0 + \left( \frac{\epsilon_n}{r_e} \right)^2 t^2 \right) - 1 \right] \right) \\
& \left. - Si \left( \pi N \left[ \rho \left( 1 + \left( \frac{\epsilon_n}{r_e} \right)^2 t^2 \right) - 1 \right] \right) \right\}, \quad (11)
\end{aligned}$$

where  $\rho = \omega/\omega_f$ . Only the emittance correction is shown since the energy spread correction is much smaller in our system for which  $(\epsilon_n/r_e)^2 = 2.3 \times 10^{-5}$  and  $\sigma_\gamma^2 = 0.35 \times 10^{-7}$ .

For the parameters of the system being proposed here,  $N = 2 \times 10^6$  and  $(\gamma\theta)^2 = 10^{-3}$ , the inhomogeneously broadened spectrum as given by Eq. (11) is shown as the solid line in Fig. 3 (as compared to the dashed line for a perfect electron beam). Since  $2\sigma_\gamma (\epsilon_n/r_e)^2 \ll (\gamma\theta)^2$  the total photon flux through a half-angle  $\theta_0$  given by Eq. (8) is still approximately valid.

A measure of the transverse space coherence of a source is given by its brightness. Up to constants, it is essentially given by the total photon flux (8) divided by the effective (or combined) emittance  $\epsilon_c$  squared (as defined in Ref. [4]). In our case the brightness is

$$B = \frac{\pi \alpha N K^2 (I/e) \gamma^2 \theta_0^2}{(2\pi \epsilon_c)^2}. \quad (12)$$

Fig. 4 compares the brightness of several X-ray sources including the one proposed in this paper, whose range is shown as the grey strip. As indicated in the figure, the brightness of the proposed source is considerably larger (three orders of magnitude) than the X-ray continuum and one or two orders of magnitude greater than single line X-ray tubes. Compared to synchrotron sources, the proposed source brightness is only one hundred times smaller

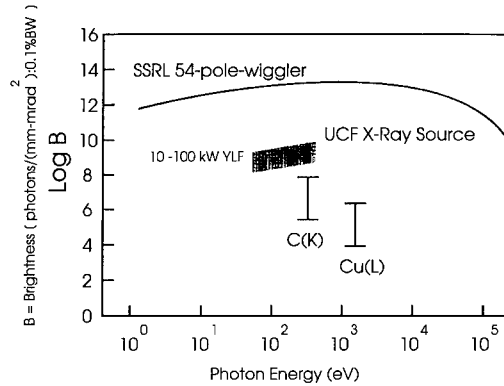


Fig. 4. Comparison of brightness from different X-ray sources. The range of brightness expected from the source proposed in this paper, is shown as the grey strip.

than that expected from the 54-pole Stanford Synchrotron Radiation Laboratory (SSRL) undulator. One has to remember however, that to obtain 0.1% bandwidth, synchrotron facilities must use frequency dispersive components, such as monochromators. On the other hand, the frequency transmission bandwidth of the proposed source will be selected using a physical aperture (i.e., the aperture of the accelerator tube) that by its nature transmits 100% of the flux. That is, all the predicted photon flux shown in the figure will reach the user.

#### Acknowledgements

We gratefully acknowledge the assistance of Prof. M. Bass and personnel of Schwatz Electro Optics Co. in the design of the YLF laser.

#### References

- [1] I. Kimel, L.R. Elias and G. Ramian, Nucl. Instr. and Meth. A 250 (1986) 320.
- [2] L.R. Elias, I. Kimel, D. Larson, D. Anderson, M. Tecimer and Z. Zhifu, Nucl. Instr. and Meth. A 304 (1991) 219.
- [3] D.F. Alferov, Yu.A. Bashmakov and E.G. Bessonov, Sov. Phys. Tech. Phys. 18 (1974) 1336.
- [4] Of the many papers on synchrotron radiation published after Ref. [3] let us only mention, for lack of space, K.J. Kim, in: X-Ray Data Booklet, ed. D. Vaughan (Lawrence Berkeley Lab., 1986).
- [5] I. Kimel and L.R. Elias, paper in preparation.



ELSEVIER

## Preliminary emission characteristic measurements for a \$300k FIR FEL

J.W. Lewellen<sup>\*</sup>, J.F. Schmerge, Y.C. Huang, J. Feinstein, R.H. Pantell

308 McCullough, Stanford University, Stanford, CA 94305, USA

### Abstract

If the free-electron laser is to move from the category of “national facility” to the designation of a “laboratory instrument” it must meet several conditions, including a reduction in cost. For the far infrared, an FEL can be constructed for a component cost of approximately \$300 000 including the accelerator. Such a device has been assembled, using a  $1\frac{1}{2}$  cell RF cavity gun for the accelerator and a staggered-array wiggler consisting of permeable pole pieces in the field of a superconducting solenoid. Spontaneous emission measurements have been performed, and laser gain has been observed. Measurements have been in good agreement with theory.

### 1. Introduction

Characteristics commonly associated with free-electron lasers are large size, high cost, complex designs, high-energy electron beams and manpower-intensive operation. All of these characteristics are acceptable for an instrument built on the scale of a national laboratory, but they preclude the acquisition of such an instrument by a single department or researcher. If the FEL is to enter into widespread use, it must undergo drastic reductions in all of the areas mentioned above, without sacrificing the high peak power, tunability, and other characteristics which make it desirable as a research tool.

A compact, low-cost FEL operating in the 80  $\mu\text{m}$  to 300  $\mu\text{m}$  range may be constructed using an RF gun as the electron accelerator, and a solenoid-derived staggered-array wiggler. Such a device has been built at Stanford University, and coherent spontaneous emission and laser gain have been observed.

### 2. Experimental apparatus

The Stanford far infrared FEL is a solenoid-derived staggered-array wiggler with integral planar waveguide, which has been described in the literature [1–4]. An important feature of this wiggler is that it provides a strong wiggler field for a short wiggler period  $\lambda_w$ . This allows the use of a lower-energy electron beam, thereby reducing

the cost of the accelerator. The wiggler is 1 m long, with wiggler period  $\lambda_w = 1$  cm, a 2 mm waveguide gap and a variable wiggler parameter  $a_w$ . The wiggler field is produced by the interaction of the staggered array of permeable pole pieces with a solenoidal magnetic field, generated by a 1 m long superconducting solenoid with a 50 cm uniform region. The effective length of the wiggler is therefore 50 cm, and the rms value of the wiggler parameter can be varied from 0 to 0.75 by adjusting the solenoid field. The value of  $a_w$  increases relatively uniformly with solenoid field, up to a solenoid field of approximately 7 kG (see Fig. 1). Increasing the solenoid field further does not increase  $a_w$ , but does increase the effective length of the wiggler, as pole pieces outside the 50 cm uniform region are driven into saturation.

The resonator cavity consists of a cylindrical downstream mirror, with a radius of curvature of approximately 1 m in the non-waveguide dimension and planar in the waveguided dimension. The upstream mirror is also cylindrical, with a radius of curvature of approximately 1 m, and with a 2 mm  $\times$  2 mm square hole in the center. This hole provides both a means of coupling power out of the resonator cavity as well as a means for allowing the electron beam to enter the cavity. Both mirrors were constructed from solid copper, and electrically isolated to allow them to be used as Faraday cups. The downstream mirror also serves as the beam dump. It should be noted that no degradation of the downstream mirror reflectivity, surface damage, or adverse thermal effects have been observed as a result of using the mirror as a beam dump. Cavity losses are calculated to be approximately 20%, which is primarily attributable by loss through the hole in the upstream mirror [5].

<sup>\*</sup> Corresponding author. Tel. +1 415 723 3190, fax +1 415 723 4659, e-mail fangs@leland.stanford.edu.

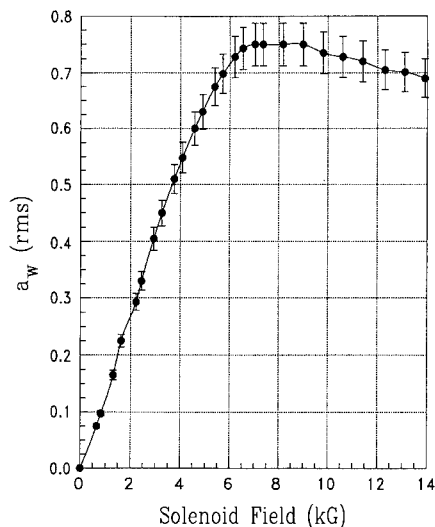


Fig. 1. A plot of measured rms wiggler parameter  $a_w$  vs. longitudinal solenoid field is shown. Error bars are  $\pm 5\%$ . Measurements were made with the pulsed wire technique. The wiggler field itself is uniform to  $\pm 0.5\%$  over the length of the uniform region.

The electron beam is provided by an 8 cm long,  $1\frac{1}{2}$  cell RF gun with thermionic cathode, resonant at 2856 MHz, which has been characterized as reported in the literature [4]. Electron beam kinetic energies of up to 4.5 MeV are attainable, with a normalized emittance  $\epsilon_n = 7\pi$  mm mrad and 6 A micropulse currents in 1% energy spread. Micropulse duration is approximately 10 ps, and macropulse duration is 0.3  $\mu$ s. Energy filtering is performed via two bending magnets and a variable-width slit located in the plane of the bend. Dispersion is controlled by a horizontally focusing quadrupole immediately following the energy filter slits [1].

Since the wiggler incorporates a waveguide, there are two resonant frequencies due to the waveguide dispersion characteristics. For this particular FEL, the long wavelength is on the order of 2.7 mm, and the short wavelength ranges between 80  $\mu$ m and 300  $\mu$ m, depending upon electron beam energy and  $a_w$  [6].

Finally, two detectors were used to perform the spontaneous emission measurements. One, a magnetically tuned InSb detector from QMC Instruments, is sensitive between 140  $\mu$ m and 200  $\mu$ m, and at wavelength greater than approximately 500  $\mu$ m. The other detector is a Ge:Ga detector, sensitive between approximately 120  $\mu$ m and 30  $\mu$ m. Both detectors are operated at liquid-helium temperature.

### 3. Measurements and results

Measurements of the spontaneous emission characteristics of the Stanford FIR-FEL have been performed at

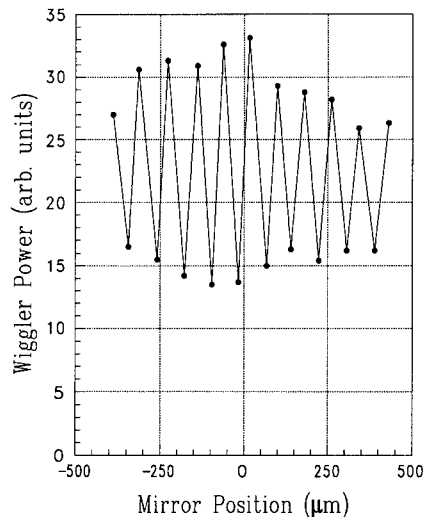


Fig. 2. A plot of measured length enhancement of coherent spontaneous emission is shown. Electron beam kinetic energy  $E_k = 3.2$  MeV, and wiggler parameter  $a_w = 0.75$  rms.

several different beam energies and values of  $a_w$ . The spontaneous emission was found to have a high coherent content, as observed by noting the interference pattern produced by changing the optical cavity length (see Fig. 2). Such interference occurs only when the light generated by one electron bunch overlaps with the light from another electron bunch, where the separation between peaks in the interference pattern is one-half the wavelength. Plots of theoretical and measured wavelengths vs. kinetic energy

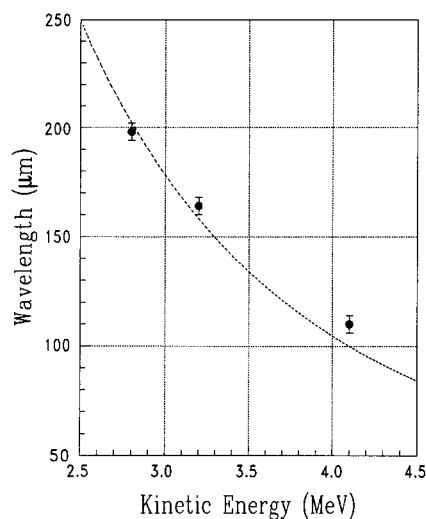


Fig. 3. A plot of measured spontaneous emission wavelength vs. kinetic energy of the electron beam is shown, along with the theoretical curve for wavelength as a function of kinetic energy. In all cases, the wiggler parameter  $a_w = 0.75$  rms and the solenoid field = 7 kG.

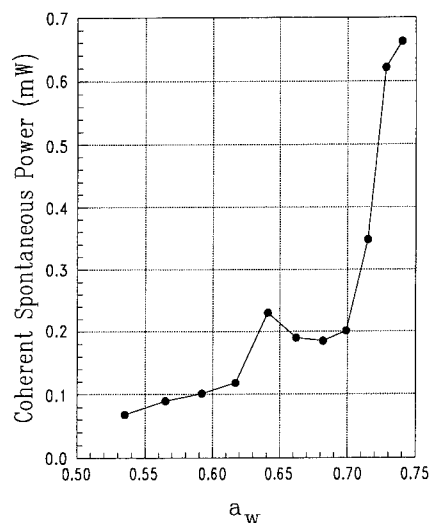


Fig. 4. A plot of measured coherent spontaneous emission power vs. wiggler parameter  $a_w$  (rms) is shown. Power output has been maximized for each point plotted. Electron beam kinetic energy  $E_k = 3.2$  MeV, peak (micropulse) current = 0.8 A and wavelength  $\lambda \approx 160$   $\mu\text{m}$ . Measurements were taken with a detuned cavity, such that there was no overlap between successive optical pulses.

are shown in Fig. 3, and the measured wavelengths are seen to agree reasonably well with those predicted by theory.

The magnitude of coherent spontaneous emission power radiated as a function of  $a_w$  is strongly dependent upon fine structure in the micropulse current. The shape of the curve, however, is relatively insensitive to the fine structure [6]. A plot of measured spontaneous emission power as a function of  $a_w$  is shown in Fig. 4. The shape of the curve agrees reasonably well with theory, but the power is several orders of magnitude higher than what would be expected from a simple half-cosine current pulse (see analysis in Ref. [6]). This may be explained by a different micropulse shape and duration than the ones assumed in the theory.

Finally, laser gain has been observed. The radiation in the laser gain regime is an order of magnitude higher in power than that observed from the coherent spontaneous emission, and the power tunes through a smooth peak as

the cavity length is changed over a distance that is small compared to the dimension of the electron beam pulse.

#### 4. Conclusions

The Stanford FIR-FEL has demonstrated that a far-infrared free-electron laser may be constructed for a component cost of approximately \$300k. The observation of laser gain has demonstrated that such a device, using a solenoid-derived staggered-array wiggler and 8 cm accelerator, is a viable, compact and inexpensive means of producing far-infrared coherent laser radiation. Future plans include reducing cavity losses, saturating laser power, increasing the macropulse duration and installation of an intracavity interferometer to reduce linewidth.

#### Acknowledgements

The authors would like to thank Gian Piero Gallerano for many helpful discussions and insightful observations; Ken Berryman, Todd Smith and Maurice Kimmitt for the use of the Ge:Ga detector, amplifier and optics, along with several thought-provoking conversations; and Helmut Wiedemann, for thoughtful comments and encouragement.

#### References

- [1] Y.C. Huang, J.F. Schmerge, J. Harris, G.P. Gallerano, R.H. Pantell and J. Feinstein, Nucl. Instr. and Meth. A 318 (1992) 765.
- [2] Y.C. Huang, H.C. Wang, R.H. Pantell, J. Feinstein and J. Harris, Nucl. Instr. and Meth. A 341 (1994) 431.
- [3] Y.C. Huang, H.C. Wang, R.H. Pantell, J. Feinstein and J.W. Lewellen, IEEE J. Quantum Electron. QE-30 (5) (1994) 1289.
- [4] Y.C. Huang, H. Wang, R.H. Pantell, J. Harris, J.F. Schmerge and J.W. Lewellen, Design and characterization of a compact, far-infrared free-electron laser, to be published in IEEE J. Quantum Electron.
- [5] Y.C. Huang, R.H. Pantell, J.F. Schmerge and J. Feinstein, these Proceedings (16th Int. Free Electron Laser Conf., Stanford, CA, USA, 1994) Nucl. Instr. and Meth. A 358 (1995) 315.
- [6] A. Doria, R. Bartolini, J. Feinstein, G.P. Gallerano and R.H. Pantell, IEEE J. Quantum Electron. QE-29 (5) (1993) 1428.



ELSEVIER

## Recent progress of the compact AFEL at Los Alamos <sup>☆</sup>

D.C. Nguyen <sup>\*</sup>, S.M. Gierman, J.C. Goldstein, J.M. Kinross-Wright, S.H. Kong, J.G. Plato,  
S.J. Russell, R.L. Sheffield, F.E. Sigler, B.A. Sherwood, M.E. Weber, C. Ziomek

*Los Alamos National Laboratory, Los Alamos, NM 87545, USA*

### Abstract

The Advanced Free Electron Laser (AFEL) is a compact, infrared, rf-linac FEL that uses a high-brightness photoinjector and a short-period permanent-magnet wiggler. Lasing at saturation with and without sidebands was achieved over the 4–6  $\mu\text{m}$  region with a nominally 15-MeV electron beam energy and a 1-cm-period, 24-period wiggler. Sideband-free FEL operation was optimized with respect to outcoupling by tuning off the reflectivity curve of the multilayer dielectric mirrors. Sideband operation was achieved using copper mirrors with a 1.1% outcoupling hole. The measured macropulse energy with  $\sim 1300$  micropulses was approximately 50 mJ per 1 nC of beam, corresponding to an output efficiency of 0.25% and a maximum extraction efficiency of 1.4%.

### 1. Introduction

Since 1988, a number of photoinjector-driven FELs have been built and a few others are under construction [1–5]. Although much has been learned about the photoinjector characteristics [6–8], there remain many opportunities in the application of a high-current, low-emittance beam to free-electron lasers. For example, the use of a low-emittance electron beam with a relatively low energy should allow operation at short wavelengths by lasing at harmonic frequencies. This concept was demonstrated in 1993 [9] when O'Shea et al. generated 370-nm UV with a 41-MeV electron beam. A second possibility with the low-emittance beam is the use of a short-period microwiggler to reduce the beam energy requirement, and thus the size and cost of an FEL. A third possibility is to use the high peak currents available from the photoinjector to drive a wiggler with very few periods but with enough gain to lase reliably at saturation. The resulting FEL efficiency which is typically less than  $1/2N_w$ , where  $N_w$  is the number of periods, can be on the order of a few percent if  $N_w$  is a small number. The latter two possibilities were recently realized on the compact Advanced FEL at Los Alamos. Since 1993, the AFEL has lased reliably at 4–6  $\mu\text{m}$  with a 1-cm-period wiggler and a nominal beam energy of 15 MeV. The wiggler with only 24 periods is the shortest wiggler ever used in an FEL. Using such a short

wiggler requires a high peak current to achieve adequate gain and a low-loss resonator to reach saturation reliably. The AFEL photoinjector routinely generates peak currents of  $\sim 100$  A or higher. We predicted a small-signal gain of  $\sim 23\%$  for a 100-A, 5- $\pi$ -mm-mrad electron beam. By varying the outcoupling, we expected to achieve optimum FEL performance. With 15 MeV and 1% extraction efficiency at saturation, the AFEL should be able to extract 150  $\mu\text{J}$  per nC in each micropulse. We present recent experimental results on the Advanced FEL at different outcoupling and compare them with predictions. We show the presence of sidebands and their impact on the FEL performance.

### 2. System descriptions

Details of the AFEL design are described elsewhere [10]. The AFEL present operating parameters are summarized in Table 1. Since the initial lasing experiments, we have made the following changes to the system:

1) *Photoinjector/linac*: We have switched from  $\text{CsK}_2\text{Sb}$  to the more rugged and high-quantum-efficiency  $\text{Cs}_2\text{Te}$  photocathodes. The latter typically have a quantum efficiency greater than 10% at 263 nm and a 1/e lifetime more than 100 hours of operation. A single  $\text{Cs}_2\text{Te}$  cathode can be used for several weeks before replacement. Details on  $\text{Cs}_2\text{Te}$  performance are described in these proceedings [11]. The linac had exhibited multipactoring that negatively impacted its performance during the initial lasing experiments. After washing and reconditioning the linac, we have not observed further multipactoring.

2) *Rf station*: A feed-forward/feed-back system has been implemented on the rf station to correct for both

<sup>☆</sup> Work supported by LANL Laboratory Directed Research and Development and performed under the auspices of the U.S. Department of Energy.

<sup>\*</sup> Corresponding author.

Table 1  
Present AFEL operating parameters

|                                      |                       |                  |
|--------------------------------------|-----------------------|------------------|
| Accelerator and rf                   |                       |                  |
| Frequency                            | 1300 MHz              |                  |
| Number of accelerating cells         | 10 + 1/2 cells        |                  |
| Accelerating gradient (first cell)   | 19 MV/m               |                  |
| Accelerating gradient (others)       | 16 MV/m               |                  |
| Beam energy                          | 15 MeV                |                  |
| Macropulse length                    | 20 $\mu$ s            |                  |
| Amplitude stability                  | $\pm 0.3\%$           |                  |
| Phase stability                      | $\pm 0.5^\circ$       |                  |
| Electron Beam                        |                       |                  |
| Micropulse charge                    | $Q$                   | 1.7 nC           |
| Micropulse width                     | $\tau$                | 17 ps            |
| Peak current                         | $I_{\text{peak}}$     | 100 A            |
| Micropulse frequency                 | $f$                   | 108 MHz          |
| Beam energy                          | $E$                   | 14–17 MeV        |
| Normalized emittance (rms)           | $\varepsilon_n$       | 5 $\pi$ -mm-mrad |
| Energy spread                        | $\Delta\gamma/\gamma$ | 0.25%            |
| Pulse-to-pulse energy fluctuation    |                       | $\pm 0.3\%$      |
| Wiggler (untapered)                  |                       |                  |
| Period                               | $\lambda_w$           | 1 cm             |
| Length                               | $L_w$                 | 24 cm            |
| Gap                                  | $2H$                  | 3 mm             |
| Peak magnetic field                  | $B_w$                 | 0.404 T          |
| Wiggler parameter (rms)              | $a_w$                 | 0.266            |
| Resonator                            |                       |                  |
| Resonator length                     | $L$                   | 1.3836 m         |
| Mirror radius of curvature           | $R$                   | 0.7 m            |
| Rayleigh range                       | $z_R$                 | 13 cm            |
| Wavelength range                     | $\lambda$             | 4–6 $\mu$ m      |
| Outcoupling (ZnSe/ThF <sub>4</sub> ) | $\Gamma$              | 1–6% (variable)  |
| Outcoupling (hole-coupling)          | $\Gamma$              | 1.1%             |
| FEL Performance                      |                       |                  |
| Energy per macropulse                | $E_{\text{macro}}$    | 100 mJ           |
| Macropulse length                    | $t_{\text{macro}}$    | 11 $\mu$ s       |
| Power during macropulse              | $P_{\text{macro}}$    | 9 kW             |
| Macropulse repetition rate           | $f_{\text{macro}}$    | 10 pps           |
| Energy per micropulse                | $E_{\text{micro}}$    | 80 $\mu$ J       |
| Micropulse length                    | $t_{\text{micro}}$    | 19 ps            |
| Micropulse peak power                | $P_{\text{micro}}$    | 4 MW             |
| Micropulse repetition rate           | $f_{\text{micro}}$    | 108 MHz          |
| Extraction efficiency                | $\eta$                | 1.4%             |

systematic and random fluctuations in the amplitude and phase of the cavity accelerating field. It employs an analog feed-back loop as well as an adaptive digital feed-forward correction loop. The feed-back loop corrects for random fluctuations in beam loading and klystron beam voltage levels. The feed-forward loop corrects repetitive errors such as ripples in the klystron voltage caused by the pulse forming network and beam loading transients in the linac cavity. With the existing klystron station, the low-level rf can achieve a field amplitude stability of  $\pm 0.3\%$  and a

phase stability of  $\pm 0.5^\circ$  against large parameter excursions at beam current of 1–2 nC/micropulse.

3) *Optical diagnostics*: A sensitive HgCdTe detector is used to measure the spontaneous emission, or with suitable attenuation, the buildup of spontaneous emission into oscillation. A Molelectron P500 pyroelectric detector with sub-nanosecond response time is used to measure the macropulse length and ring-down. The macropulse energy is measured with either a Molelectron J50 or a Gentec ED-200 pyroelectric energy detector right after the FEL beam exits the CaF<sub>2</sub> window. All energy measurements are quoted after correction for the  $\sim 8\%$  Fresnel reflection loss from the CaF<sub>2</sub> window. The FEL spectral characteristics are measured with an Optical Engineering spectrum analyzer equipped with a 75-grooves/mm grating and a Molelectron pyroelectric array.

### 3. Recent results

#### 3.1. Lasing at saturation

To avoid transients that occurred in the first few microseconds of the rf pulse, the electron beam was turned on during the last 15  $\mu$ s of the rf pulse when the cavity field amplitude and phase were sufficiently flat (Figs. 1a and 1b). The first few microseconds of the current pulse were ramped because the drive laser Pockel cell was opened gradually to avoid ringing. It took another 2–4  $\mu$ s for the FEL to reach saturation, giving a saturated FEL macropulse of  $\sim 11 \mu$ s in duration (Fig. 1c). At 108.33 MHz, there are approximately 1300 micropulses in each macropulse.

#### 3.2. Optimum outcoupling

The optics for this experiment consisted of a copper mirror as a total reflector and a ZnSe/ThF<sub>4</sub> multilayer dielectric (MLD) outcoupler. The copper total reflector had

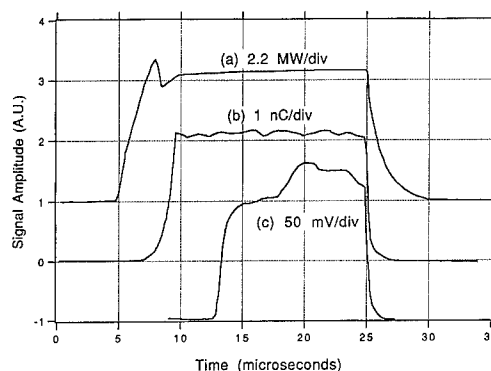


Fig. 1. (a) Rf macropulse with feed-forward/feed-back control; (b) electron beam current; and (c) pyroelectric detector signal.

a reflectivity of 99% and thus introduced a round-trip loss of 1%. The MLD coatings had a reflectivity of 99.0% at 4.5–5.5  $\mu\text{m}$ . Its transmission of 1% provided the out-coupling. By tuning the FEL wavelength to the long wavelength edge of the reflectivity curve, we could increase the outcoupling of the MLD mirror. The measured total cavity loss and outcoupling are plotted versus wavelength in Fig. 2. The difference between the two remains relatively constant at 3–4% and is attributed to the combined loss due to mirror absorption and vignetting optical. Beyond 6  $\mu\text{m}$ , the MLD reflectivity curve dropped sharply with increasing wavelength and small wavelength fluctuations caused large variations in outcoupling, resulting in very unstable lasing. Furthermore, atmospheric water absorption at 6–7  $\mu\text{m}$  significantly reduced the FEL energy incident on the energy meter and prevented accurate pulse energy measurements.

Streak camera measurements of the electron pulses at 15 MeV and 3-mm beam radius on the photocathode yielded an approximately linear relationship between the electron pulsewidth and charge,  $\tau_{\text{fwhm}} = 5.63 \text{ ps} + (6.46 \text{ ps/nC})Q$ . The beam current thus followed a function that asymptotically approached 155 A. Since the peak current was relatively constant at  $\sim 100 \text{ A}$  over the range 1–1.7 nC, the small-signal gain should be relatively constant. For comparison, the observed macropulse energies in different measurements were normalized to the micropulse charge.

In Fig. 3 the predicted and observed macropulse energies per nanocoulomb of beam are plotted vs. wavelength. In spite of a trend of increasing output energy with increasing wavelength, the measured energies do not follow predictions. The best performance was at 6% outcoupling where the observed macropulse energy was 54 mJ/nC, corresponding to a micropulse energy of 42  $\mu\text{J/nC}$  at 15 MeV. From these numbers and a resonator efficiency of 66.7%, we estimated an output efficiency of 0.28% and an

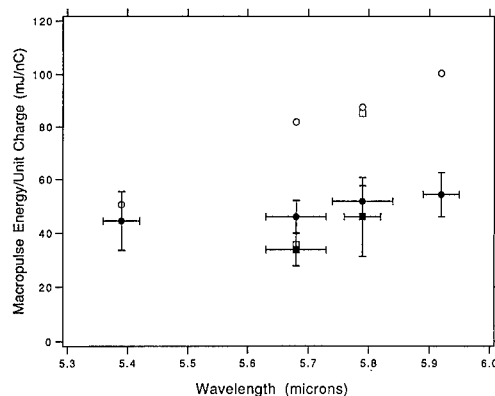


Fig. 3. Predicted (open) and observed (solid) macropulse energy as functions of wavelength. The squares represent a slightly different gain or resonator loss.

extraction efficiency of 0.42%. At output energies less than 40 mJ/macropulse, there are good agreements between measurements and predictions. As the output energies increase, the discrepancies between predictions and measurements also increase, independent of wavelength (Fig. 3). This behavior can be explained by a nonlinear absorption that was observed previously in ZnSe optics at 10  $\mu\text{m}$  [12]. The nonlinear absorption seemed to occur in the ZnSe substrate and had a threshold fluence of about 0.1 J/cm<sup>2</sup>. This and optical damage at high intracavity power severely limit the utility of MLD mirrors for high power FELs.

### 3.3. Sideband generation

We achieved sideband operation with the AFEL by reducing the outcoupling to obtain a larger gain-to-loss ratio. Sidebands were most reliably observed with copper mirrors. The outcoupling mirror had a 0.5 mm diameter hole that gave an approximate outcoupling of 1.1% at 5.6

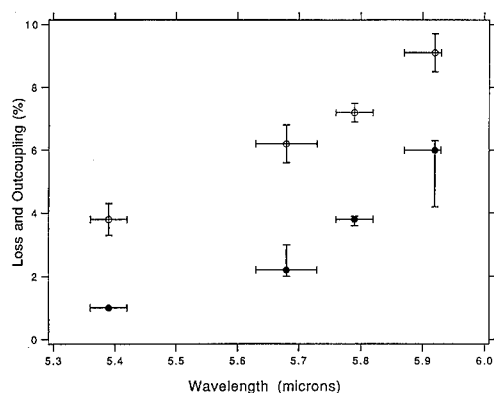


Fig. 2. Multilayer dielectric mirror output coupling (solid) and total resonator loss (open) are plotted versus wavelength.

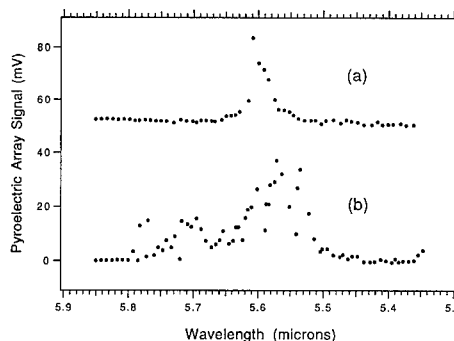


Fig. 4. AFEL spectral characteristics (a) without sidebands and (b) with sidebands.

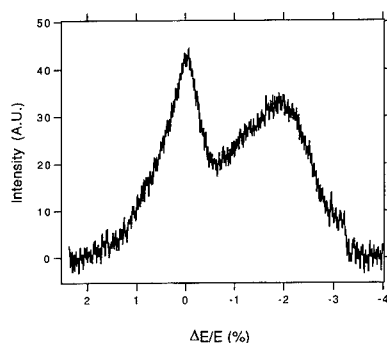


Fig. 5. Electron energy spectrum with lasing. The decelerated electrons form a well-defined distribution peaked at 2% fractional energy loss.

$\mu\text{m}$ . At negative resonator length detuning, the AFEL output exhibited a narrow spectrum (Fig. 4a). As the resonator length was increased, so did the output power until the resonator length reached what we called zero detuning, at which point the AFEL power became unstable and exhibited large excursions in amplitude. Concomitantly, its spectrum became chaotic and displayed significant broadening, mostly to the long wavelength side (Fig. 4b). The highest macropulse energy observed with sidebands was 103 mJ for a micropulse charge of 2 nC. Thus, the normalized macropulse energy was about 50 mJ/nC for an 11- $\mu\text{s}$  macropulse. From these values, we estimated a micropulse energy of 38  $\mu\text{J}/\text{nC}$ . At 15.3 MeV, this corresponds to an output extraction efficiency at saturation of 0.25%. Combined with an outcoupling of 1.1% and a total resonator loss of 6%, the efficiency at saturation is 1.4%.

With strong lasing, the electron energy spectrum exhibited a well-defined distribution shifted down in energy from the injected electron energy (Fig. 5). From the shift in centroid, we measured an extraction efficiency, integrated over the macropulse, of 1%. This value is in reasonable agreement with the efficiency estimated from the measured macropulse energy.

#### 4. Conclusion

The AFEL has lased at saturation over the 4–6  $\mu\text{m}$  spectral region. By tuning off the reflectivity curve of the MLD mirrors, we observed improved performance up to an outcoupling of 6%. The best performance without sideband gave a macropulse energy of  $\sim 55$  mJ/nC corresponding to an output efficiency of 0.28%. Anomalous nonlinear absorption in ZnSe was suspected to cause the low observed efficiency. Beyond 6% (at 6  $\mu\text{m}$  or longer for this set of MLD mirrors), the output became too

unstable to make reliable measurements. By reducing the resonator loss and using copper mirrors, we also observed sidebands. The measured output and extraction efficiencies with sidebands are 0.25% and 1.4%, respectively. In spite of a higher extraction efficiency, it did not give the highest output efficiency due to a lower resonator efficiency – ratio of outcoupling to total loss. At a micropulse charge of 2 nC, the AFEL routinely produces 100 mJ of infrared light in a nominal 11- $\mu\text{s}$  macropulse. Thus, its average power during the macropulse is about 9 kW. With a macropulse repetition rate of 10 pps, the true average power is about 1 W. Since there are approximately 1300 micropulses per macropulse, we estimate a micropulse energy of  $\sim 80$   $\mu\text{J}$  over 19-ps FWHM, yielding a peak power of about 4 MW. The AFEL spectral linewidth without sideband is about 0.5% (0.03  $\mu\text{m}$  FWHM). However, the rf amplitude fluctuated  $\pm 0.3\%$  – a result of both running the klystron near saturation and fluctuations in beam current. Consequently, the AFEL wavelength fluctuated about  $\pm 0.6\%$  from shot to shot.

In the future, we will implement a new rf system with improved amplitude and phase stability. We will also increase the AFEL average power by means of a higher macropulse repetition rate and a more efficient tapered wiggler. Alternatively, the untapered wiggler can be shortened to have only a few periods. This will increase the  $1/2N_w$  extraction efficiency. We will then need to increase the small-signal gain by increasing either  $a_w$  or the electron current or both. The peak current can be increased by bunching the electron beam with a chicane right before the wiggler.

#### References

- [1] M. Curtin et al., Nucl. Instr. and Meth. A 296 (1990) 127.
- [2] P.G. O'Shea et al., Nucl. Instr. and Meth. A 318 (1992) 52.
- [3] S. Joly et al., Nucl. Instr. and Meth. A 331 (1993) 199.
- [4] D.C. Nguyen et al., Nucl. Instr. and Meth. A 341 (1994) 29.
- [5] I.S. Lehrman et al., Nucl. Instr. and Meth. A 341 (1994) ABS 31.
- [6] B.E. Carlsten and R.L. Sheffield, Proc. Linear Accelerator Conf., Williamsburg, VA, 1988, p. 365.
- [7] C. Travier, Nucl. Instr. and Meth. A 304 (1991) 285 and references therein.
- [8] R.L. Sheffield et al., Nucl. Instr. and Meth. A 318 (1992) 282.
- [9] P.G. O'Shea et al., Nucl. Instr. and Meth. A 341 (1994) 7.
- [10] K.C.D. Chan et al., Nucl. Instr. and Meth. A 318 (1992) 148.
- [11] S. Kong et al., these Proceedings (16th Int. Free Electron Laser Conf., Stanford, CA, USA, 1994) Nucl. Instr. and Meth. A 358 (1995) 284.
- [12] J.E. Sollid et al., Proc. LASER'88, Lake Tahoe, CA, (1988), LA-UR 89-560.





ELSEVIER

# UV/X-ray free electron lasers through high-gain single pass amplifiers: basic principles and key issues <sup>☆</sup>

Kwang-Je Kim <sup>\*</sup>

*Lawrence Berkeley Laboratory, Berkeley, California 94720, USA*

## Abstract

We review the basic principles of the high gain free electron laser amplifier for generation of intense, tunable radiation at wavelengths shorter than 1000 Å. Two schemes are discussed: For wavelengths between 1000 and 100 Å, high gain harmonic generation and amplification of a coherent input radiation can be used. For X-ray wavelengths as short as a few Å, self-amplified spontaneous emission is the only known free electron laser scheme. We also present a brief introduction to key issues in realizing these schemes, which will be discussed in detail in other papers in these proceedings.

## 1. Introduction

At present the only practical, tunable radiation source in the wavelength region shorter than 1000 Å are synchrotron radiation devices. High gain free electron lasers (FELs) will be able to provide intense, tunable, coherent radiation in this wavelength region with brightness several orders of magnitudes higher than that from synchrotron radiation.

The current short wavelength record for FELs is 2400 Å achieved at Novosibirsk [1]. Given sufficiently bright electron beams, the high-gain FEL amplifier in a single pass configuration can extend FEL operation to arbitrarily short wavelengths by eliminating the need for high-reflectivity normal-incidence mirrors. Two schemes are envisioned: With a very bright electron beam in a long undulator, the single pass gain may be so high that the noise signal present in the beam is amplified to intense coherent radiation. This is called the self-amplified-spontaneous-emission (SASE) scheme [2], and is the basis of the Linear Coherent Light Source (LCLS) proposal at SLAC to generate coherent radiation for wavelengths as short as 1.5 Å [3]. Another scheme applicable for wavelengths between 1000 and 100 Å is based on the harmonic generation mechanism in a high-gain FEL starting from available coherent input radiation [4,5]. The scheme, called the

high-gain harmonic generation (HGHG) is the basis of the DUV proposal at BNL [6]. The production of high brightness electron beams necessary for these proposals became feasible with the development of the laser driven RF photocathode gun [7].

The purpose of this paper is to describe the basic physics of SASE and HGHG schemes, and to provide an introduction to various issues in realizing them. Detailed discussion of these issues are contained in five papers in these proceedings [8–12].

## 2. Basic Physics

### 2.1. High-gain FEL

The interaction of the electromagnetic field of the radiation beam with electrons in an undulator induces a modulation of the electron density. The density modulation leads to a higher radiation intensity, and the higher intensity in turn causes stronger density modulation. Thus, it is expected that the density modulation as well as the radiation intensity will under certain circumstances grow exponentially as  $\exp(z/L_G)$ , where  $L_G$  is known as the (power) gain length. The basic scaling of a high gain FEL amplifier is determined by the dimensionless parameter [2]

$$\rho = \left( \frac{e^2 Z_0 n K^2 [JJ]}{32 \gamma^3 m c^2 k_u^2} \right)^{1/3}, \quad (1)$$

where  $e$  is the electron charge,  $Z_0 = 377 \Omega$ ,  $n$  is the electron density,  $m$  is the electron mass,  $c$  is the speed of light,  $\gamma$  is the electron energy in units of  $mc^2$ ,  $k_u = 2\pi/\lambda_u$ ,  $\lambda_u$  is the period length of undulator magnet,  $K =$

<sup>☆</sup> This work is supported by the Director, Office of Energy Research, Office of High Energy Physics, High Energy Physics Division, of the U. S. Department of Energy under Contract No. DE-AC03-76SF00098.

<sup>\*</sup> Tel. +1 510 486 7224, fax +1 510 486 7981, e-mail kwangje@lbl.gov.

$eB_0/(k_u mc)$ ,  $B_0$  is the peak magnetic field of the undulator, and  $[JJ]$  is the usual factor involving Bessel function in the case of a planar undulator. The power gain length in the exponential growth regime is proportional to  $k_u/\rho$ . Also the gain bandwidth and the efficiency at saturation are both given approximately by  $\rho$ .

In a 1-D model with vanishing energy spread, the gain length is given by  $L_G^{1-D} = 1/(2\sqrt{3} k_u \rho)$ . Including the 3-D diffraction effect [13,14] and the electron betatron motion [15–19] the gain will be reduced. However, the reduction is small if

$$2k\epsilon_x \leq 1, \quad (2)$$

$$L_G^{1-D}/L_R \leq 1, \quad (3)$$

$$\sigma_\gamma/\gamma < \rho. \quad (4)$$

Here  $k = \omega/c = 2\pi/\lambda$  is the radiation wave number,  $\epsilon_x$  is the rms electron beam emittance (considered the same in the  $x$  and  $y$  plane), and  $L_R$  is the Raleigh length given by  $L_R = 2k\langle x^2 \rangle = 2k\epsilon_x \beta$ , where  $\beta$  is the value of the betatron function and  $\sigma_\gamma$  the rms energy spread. Inequality (2) is the requirement that the area of electron beam phase space be smaller than that of the radiation beam. Inequality (3) is the statement that diffraction is not important in one gain length. Inequality (4) is the statement that the gain bandwidth of high gain FEL is about  $\rho$ .

As an example consider the case of a 10 Å FEL. The emittance in view of Eq. (2) should be about  $10^{-10}$  m rad. Assuming that the relative energy spread is a few times  $10^{-4}$ , it is necessary from Eq. (4) that the value of  $\rho$  be about  $10^{-3}$ . Inserting suitable values for other parameters, it can be shown from Eq. (1) that the required current is a few kA. Thus the electron beam requirements are very stringent.

## 2.2. High Gain Harmonic Generation (HGHG)

The schematic diagram for HGHG is shown in Fig. 1: A coherent UV input is provided by passing the output of a conventional laser through a nonlinear crystal. The FEL device consists of two undulators; the first undulator is resonant with the wavelength of the coherent input and induces modulation in the electron beam energy. The energy modulation becomes density modulation with Fourier components in the input wavelength as well as in higher harmonics. The second undulator is resonant with a higher harmonic, for example, the third harmonic. Thus there is an exponential growth of the radiation at the third harmonic of the input wave length [4]. The efficiency of

the scheme is increased by a dispersive section between two undulators and a tapered section at the end [5].

The coherence of the HGHG output is high, as it is the same as the input coherent radiation. However, the scheme is not suitable for X-ray generation because a suitable input coherent radiation is not available.

The parameters of the DUV proposal at BNL which is based on the HGHG are listed in Table 1.

## 2.3. Self Amplified Spontaneous Emission (SASE)

As a beam of electrons travels through a long undulator, spontaneous radiation is emitted in the beginning as a collection of randomly distributed wavetrains of length  $N\lambda$ , where  $N$  is the number of the undulator periods seen

Table 1  
Major Parameters for the DUV Project [6]

|  |                          |       |
|--|--------------------------|-------|
| <i>Optical beam</i>  |                          |       |
| Wavelength range   | 3000–750 Å               |       |
| Bandwidth  | $10^{-4}$ or trans. lim. |       |
| Peak power   | $\sim 10^8$ – $10^9$ W   |       |
| Energy per pulse   | 0.3–10 mJ                |       |
| Repetition rate  | 360 Hz                   |       |
| Pulse length range   | 0.2–5 ps                 |       |
| <i>Electron beam</i>   |                          |       |
|  | 100 nm                   | 75 nm |
| Energy (MeV)   | 250                      | 290   |
| Current (A)  | 300                      | 300   |
| Norm. rms emittance<br>(mm mrad)                             | 6                        | 6     |
| FWHM local energy<br>spread (%)                              | 0.1                      | 0.1   |
| FWHM global energy<br>detuning range (%)                     | 0.25                     | 0.2   |
| Pulse length FWHM<br>(ps)                                    | 7                        | 7     |
| <i>Input seed</i>  |                          |       |
| Wavelength (nm)  | 300                      | 300   |
| Power (MW)   | 2.5                      | 3, 4  |
| Bandwidth $\Delta \lambda / \lambda$<br>( $\times 10^{-4}$ ) | 1                        | 1     |
| <i>First wiggler (modulator)</i>                             |                          |       |
| Period (cm)  | 3.9                      | 3.9   |
| Magnetic field (T)   | 0.64                     | 0.77  |
| Length (m)   | 2                        | 2     |
| Betatron wavelength (m)                                      | 16                       | 16    |
| <i>Dispersion section</i>                                    |                          |       |
| Length (m)   | 0.2                      | 0.2   |
| Magnetic field (T)   | 0.32                     | 0.34  |
| Dispersion $d\theta/d\gamma$                                 | 1.1                      | 1.0   |
| <i>Second wiggler (radiator)</i>                             |                          |       |
| Period (cm)  | 2.2                      | 2.2   |
| Magnetic field (T)   | 0.75                     | 0.75  |
| Length total (m)   | 12                       | 12    |
| Length untapered (m)   | 5                        | 6     |

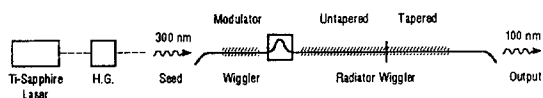


Fig. 1. A schematic illustration of high gain harmonic generation (HGHG) scheme.

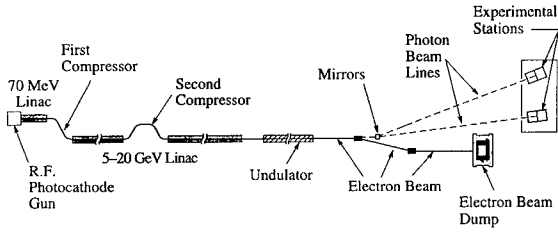


Fig. 2. LCLS schematic overview.

by the beam. The average radiation intensity of the spontaneous radiation is proportional to the total number of electrons, and increases linearly with  $N$ . With an electron beam of sufficiently high intensity and brightness, the electron distribution starts to develop local density modulations with the periodicity of the radiation wavelength, which are randomly distributed over the electron pulse. The radiation intensity then increases exponentially as a function of  $N$ . In this exponential gain regime, the average power spectrum as a function of distance along the undulator,  $z = N\lambda_0$ , is of the form

$$\frac{dP}{d\omega} = e^{z/L_G} S(\omega, z) \left( \frac{dP}{d\omega} \right)_{\text{noise}}, \quad (2)$$

where  $S(\omega, z)$  is a function describing the frequency dependence of the gain, and  $(dP/d\omega)_{\text{noise}}$  is the effective

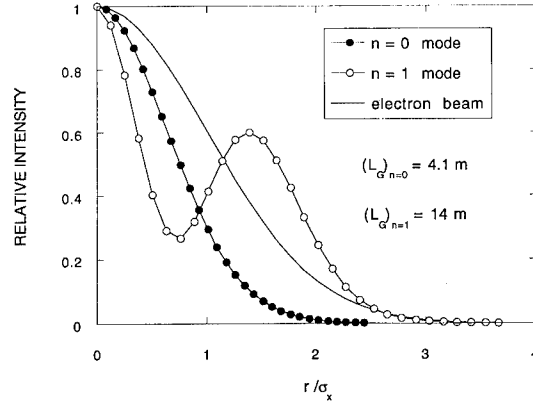


Fig. 4. Mode profiles and growth rate for the higher order transverse modes for the LCLS proposal (figure provided by M. Xie)

input signal due to the beam noise. In a 1-D model, the latter term can be expressed in the following form [15]:

$$\left( \frac{dP}{d\omega} \right)_{\text{noise}} = \frac{\rho E_0}{2\pi}, \quad (3)$$

where  $E_0 = mc^2\gamma_0$  is the energy of a single electron. This power can be interpreted [20] as the spontaneous power emitted in one gain length.

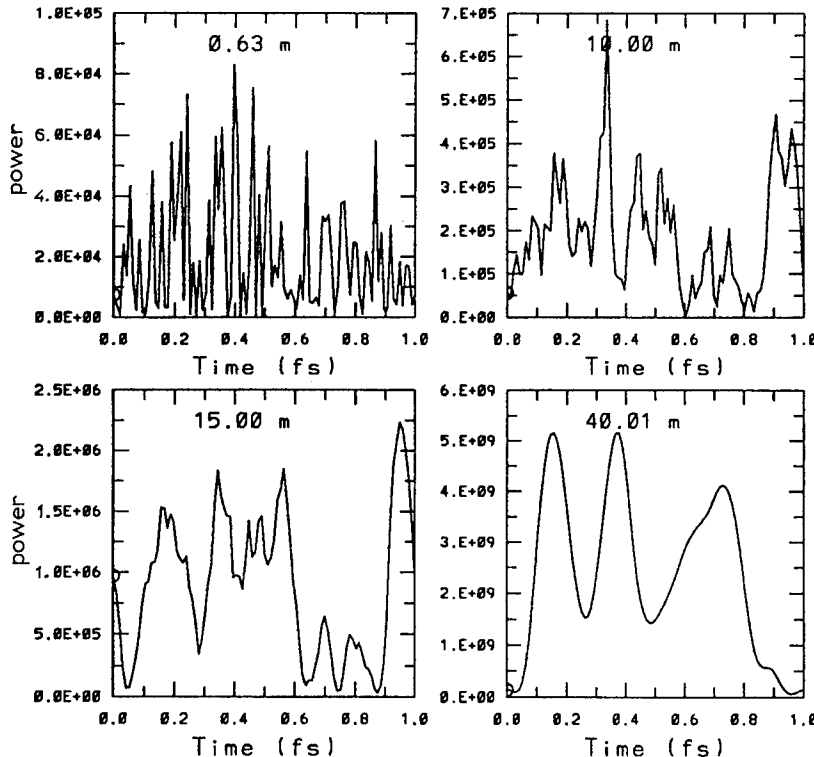


Fig. 3. The result of GINGER simulation for LCLS showing the evolution of SASE temporal profiles (figure provided by W.M. Fawley).

The exponential growth stops, or saturates, when the density modulation becomes near 100%. The electron distribution at saturation is a superposition of local density modulations of period  $\lambda$  and length  $l_c$  (coherence length =  $\lambda/\rho$ ) randomly distributed over the electron pulse [21,22]. The corresponding radiation profile is a collection of randomly distributed wavetrains of length  $l_c$ . Thus the temporal coherence characteristics of SASE are similar to that of spontaneous radiation, the spectral bandwidth being given approximately by  $\lambda/l_c = \rho$ . Assuming the modulation within one coherence length is complete, the radiation intensity from one local density modulation is proportional to the number of electrons in one coherence length squared. Summing up contributions from all local density modulation, one finds that the total radiation power is enhanced compared to that of the undulator radiation by a factor equal to the number of electrons in one coherence length.

SASE is important as the only known scheme to extend FELs to wavelengths as short as a few Å. Fig. 2 is the schematic layout of the LCLS proposal to generate X-rays down to 1.5 Å based on SASE using the SLAC linac [3]. Table 2 gives the major parameters of the LCLS proposal. Fig. 3 shows the result of the GINGER simulation showing the evolution of the SASE temporal profile at different points along the undulator.

The transverse coherence of SASE is determined by the gain competition of higher order transverse modes. When  $2k\epsilon_x \gg 1$ , violating the inequality (2), the gain of the higher order transverse modes is comparable to that of the many transverse modes, i.e., the radiation is transversely incoherent. When the inequality (2) is approximately satisfied, as is the case for the LCLS proposal, the growth of the higher order modes is suppressed [19]. The radiation is then completely coherent transversely. Fig. 4 shows the

mode profiles and growth rates for some of the higher order transverse modes in the case of LCLS proposal.

### 3. Accelerator configurations

The requirements on electron beams for operation of high gain amplifiers are very stringent, as can be seen from the electron beam parameters in Tables 1 and 2. Among various accelerators, linacs are currently the preferred option as the driver for high gain FEL amplifiers for short wavelengths. With the traditional injectors based on thermionic gun and bunchers, the brightness of the linac beams has been usually low due to phase space dilution in the bunching process. However, a new type of injector based on the laser driven RF photocathode gun developed recently at LANL and other laboratories [7] has the capability of producing very high brightness electron beams directly with a beam pulse structure suitable for RF acceleration. The accelerator configurations for the DUV project as well as the LCLS project are both based on a laser driven RF photocathode gun and a linac.

### 4. Key issues

Five papers in these proceedings discuss critical issues in realizing the generation of short wavelength coherent radiation through linac based high gain FEL amplifiers. The first paper deals with the laser driven high brightness photocathode guns [8]. The issues are the quantum efficiency of the photocathode materials, various emittance degradation effects [23] and how to correct them [24], and the drive laser stability. The second paper deals with beam compression and transport [9]. The beams coming out of the photocathode gun need to be further compressed to increase the peak current. In the design of the compressor and the beam transport system through the linac and the long undulator, great care must be exercised to avoid various phase space dilution effects. The third paper deals with undulator construction [10]. The required undulator must have strong magnetic field, many periods especially in the case of SASE, strong focussing field, and tight error tolerance. There are several options for the magnet design; electromagnets, permanent magnets and superconducting magnets. The fourth paper deals with the assessment of simulation codes in their capability to predict the performance of FELs accurately [11]. There are several simulation codes available with different capabilities. It is important to cross check the codes with each other, with theory, and with experiment. The fifth paper deals with the milestone experiments that should be carried out before embarking on the construction of a user facility for an X-ray FEL [12]. It is crucial to test various hardware components, such as the photocathode gun, as well as to carry out integrated experiments at longer wavelengths at 10  $\mu\text{m}$  and at 1000 Å.

Table 2

Possible LCLS parameters for 1.5 Å [3].

Case A: single undulator resonant at 1.5 Å;

Case B: first undulator resonant at 4.5 Å followed by second at 1.5 Å

|                                | Radiation wavelength |                    |                    |
|--------------------------------|----------------------|--------------------|--------------------|
|                                | Case (A)             | Case (B)           |                    |
| $\lambda$ (Å)                  | 1.5                  | 4.5                | 1.5                |
| $\lambda_u$ (cm)               | 2.67                 | 4.0                | 3.0                |
| $B_0$ (T)                      | 1.17                 | 1.14               | 0.98               |
| Undulator type                 | helical              | helical            | helical            |
| Undulator length (m)           | 40                   | 20                 | 20                 |
| $\beta_0$ (m)                  | 7                    | 3.6                | 3.6                |
| Normalized emittance (mm mrad) | 1                    | 1                  | 1                  |
| $E_e$ (GeV)                    | 15                   | 15                 | 15                 |
| Peak current (kA)              | 5                    | 5                  | 5                  |
| Relative energy spread         | $2 \times 10^{-4}$   | $2 \times 10^{-4}$ | $2 \times 10^{-4}$ |
| Bunch length ( $\mu\text{m}$ ) | 40                   | 40                 | 40                 |
| Output power (GW)              | 60                   | 1.4                | 40                 |

## 5. Conclusions and discussions

In this and the five other papers in these proceedings, the basic physics and key issues in generating short wavelength radiation through high gain FEL amplifiers in single pass configuration are examined. These papers show that the high gain FEL amplifier concept based on a linac is within current technological capability, providing exciting scientific opportunities [6,25].

Several alternative options were not included in this discussion; the FEL oscillator technique may also be extended to wavelength shorter than 1000 Å by utilizing grazing incident reflections [26]. A special by-pass of a storage ring is another accelerator option for high gain FELs [27,28]. It may be possible to condition electron beams to ease some of the electron beams to ease some of the electron beam quality requirements [29]. These options are an important part of the total R&D effort towards the generation of short wavelength radiation via the FEL mechanism.

## References

- [1] I.B. Drobyazko et al., Nucl. Instr. and Meth. A 282 (1989) 424.
- [2] R. Bonifacio, C. Pellegrini and L.M. Narducci, Opt. Commun. 50 (1984) 373.
- [3] H. Winick et al., Nucl. Instr. and Meth. A 347 (1994) 199; H.-D. Nuhn et al., short wavelength FELs using the SLAC linac, Proc. EPAC '94, London, England, July 1994.
- [4] R. Bonifacio, L. De Salva Souza, P. Pierini and E.T. Scharlemann, Nucl. Instr. and Meth. A 304 (1991) 224.
- [5] L.-H. Yu, Phys. Rev. A 44 (1991) 5178.
- [6] The Brookhaven National Laboratory DUV Free Electron Laser Conceptual Design Report, Vol. 1 (Jan. 1994, Rel. 1.4).
- [7] R.L. Sheffield, in: Physics of Particle Accelerators, AIP Vol. 184, eds. M. Month and M. Dienes (1989) p. 1500.
- [8] P.G. O'Shea, these Proceedings (16th Int. Free Electron Laser Conf., Stanford, CA, USA, 1994) Nucl. Instr. and Meth. A 358 (1995) 36.
- [9] T.O. Raubenheimer, *ibid.*, p. 40.
- [10] R.D. Schlueter, *ibid.*, p. 44.
- [11] G. Travish, *ibid.*, p. 48.
- [12] I. Ben-Zvi, *ibid.*, p. 52.
- [13] G.T. Moore, Nucl. Instr. and Meth. A 239 (1985) 19.
- [14] E.T. Scharlemann, A.M. Sessler and J.S. Wurtele, Phys. Rev. Lett. 54 (1985) 1925.
- [15] K.-J. Kim, Phys. Rev. Lett. 57 (1986) 1871.
- [16] L.-H. Yu, S. Krinsky and R. Gluckstern, Phys. Rev. Lett. 64 (1990) 3011.
- [17] Y.H. Chin, K.-J. Kim and M. Xie, Phys. Rev. A 46 (1992) 66621.
- [18] L.H. Yu, C.M. Hung, D. Li and S. Krinsky, presented at this Conference (16th Int. Free Electron Laser Conf., Stanford, CA, 1994).
- [19] M. Xie, to be published.
- [20] L.-H. Yu and S. Krinsky, Nucl. Instr. and Meth. A 285 (1989) 119.
- [21] R. Bonifacio, L. De Salvo, P. Pierini, N. Piovella and C. Pellegrini, Phys. Rev. Lett. 73 (1994) 70.
- [22] K.-J. Kim and S.J. Hahn, Ref. [8], p. 93.
- [23] K.-J. Kim, Nucl. Instr. and Meth. A 275 (1989) 201.
- [24] B. Carlsten, Nucl. Instr. and Meth. A 285 (1989) 313.
- [25] Proc. Workshop on Scientific Applications of Coherent X-rays, SLAC/SSRL-0066, Stanford, CA, Feb. 12, 1994.
- [26] B.E. Newnam, NBS Spec. Publ. 746 (1988) 261–269.
- [27] C. Pellegrini, J. Opt. Soc. Amer. B 2 (1985) 259.
- [28] K.-J. Kim et al., Nucl. Instr. and Meth. A 239 (1985) 54; J. Bisognano et al., Part. Accel. 18 (1986) 223; C. Pellegrini, Nucl. Instr. and Meth. A 272 (1988) 364.
- [29] A.M. Sessler, D.H. Whittum and L.-H. Yu, Phys. Rev. Lett. 68 (1992) 309.



ELSEVIER

# High-brightness rf photocathode guns for single pass X-ray free-electron lasers

Patrick G. O'Shea \*

*Free-Electron Laser Laboratory, Department of Physics, Box 90319, Duke University, Durham, NC 27708-0319, USA*

## Abstract

Single-pass X-ray FELs will require very bright, high-current, stable electron beams as drivers. A key element of the accelerator system for such a device is the electron source, which should produce 1 nC bunches with a few hundred amperes peak current and a normalized rms emittance of  $1\pi$  mm mrad. The photocathode rf gun appears to be the only source capable of meeting these requirements. We discuss technological issues associated with beam dynamics, photocathodes, and drive-laser stability. The impact of drive-laser phase stability on buncher performance is discussed in detail.

## 1. Introduction

The invention and refinement of the rf photocathode gun has resulted in a dramatic improvement in electron beam brightness over that delivered by conventional injectors [1]. Rf photocathode guns are now being considered as electron sources for such challenging applications as linear colliders and single-pass X-ray free-electron laser amplifiers. In this paper we consider the electron gun requirements of an FEL operating at X-ray wavelengths from a few tens of Å down to 1.5 Å, and use the proposed Linac Coherent Light Source (LCLS) at SLAC as our system of reference [2]. Existing short wavelength FELs have operated in the oscillator configuration. At wavelengths much shorter than 100 nm however, the reflectivity of resonator optics becomes so low that oscillators are impractical. A self-amplified spontaneous emission FEL avoids the resonator difficulty by operating as a very-high gain amplifier, that reaches saturation in a single pass. As with all FELs, the performance depends critically on the properties of the electron beam.

The final specifications of the LCLS are still in flux, however the following design guidelines provide a basis for discussion in this paper. The rf photocathode gun will generate a 3–10 MeV beam with 1 nC charge in a 2 ps rms bunch and normalized rms emittance of  $1\pi$  mm-mrad and rms energy spread of 0.2%. The beam will be accelerated to 7 GeV and compressed by a factor of 10 to reach a peak current of 2.5 kA. The compression will occur in two stages: a factor of 2 at 100 MeV and a further factor of 5

at 2 GeV. The gain length of the FEL is very sensitive to both the emittance and the peak current of the beam [2]. The transverse emittance required is approximately a factor of 2 better than has been demonstrated in an rf photocathode gun to date. The bunching is very sensitive to the longitudinal phase space of the bunch and hence to timing and amplitude jitter in the rf gun [3]. The stability required is somewhat better than has been demonstrated in operational photoinjectors.

## 2. Transverse emittance

The lower bound on emittance of a 1 nC bunch from a simple photoinjector (using present technology and no emittance compensation) is on the order of  $3\pi$  mm mrad.

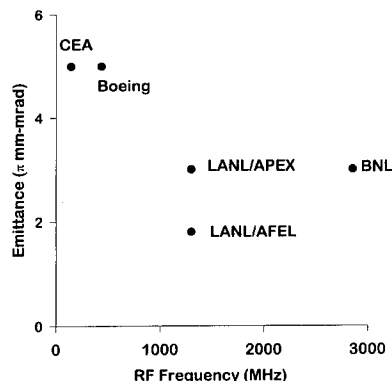


Fig. 1. Measured transverse emittance (normalized, rms) at 1 nC per bunch for representative photoinjectors; emittance compensated: CEA [4], Boeing [5], LANL/APEX [6], LANL/AFEL [7], and uncompensated: BNL [8].

\* Corresponding author. Tel. +1 919 660 2652, fax +1 919 660 2671, e-mail oshea@fel.duke.edu.

Fig. 1 shows the measured performance of some representative photoinjectors [4–8]. The intrinsic emittance of a photocathode source is determined by thermal emittance and is proportional to the product of the source size ( $\sigma_x$ ) and the square root of the effective temperature ( $kT_e$ ):  $\epsilon_T \approx \sigma_x \sqrt{kT_e} \pi$  mm mrad with  $\sigma_x$  in mm, and typically  $kT_e \in [0.2, 0.5]$  eV. The minimum  $\sigma_x$  for a given charge per bunch is determined by the accelerating gradient. For an S-band (2856 MHz) photoinjector operating at 100 MV/m, this limit on  $\sigma_x$  is approximately 1 mm. Therefore the limiting emittance is on the order of  $0.5\pi$  mm mrad. In practice the emittance is increased beyond this value by a number of effects, particularly space-charge forces ( $\epsilon_{sc}$ ) and time varying linear rf fields ( $\epsilon_{rf}$ ) along the bunch. The magnitude of each contribution for a Gaussian beam can be computed using Kim's theory [9]. For the aforementioned conditions and a 10 ps drive-laser pulse width,  $\epsilon_{sc} \approx 3\pi$  mm mrad and  $\epsilon_{rf} \approx 1\pi$  mm mrad. These emittance contributions add in quadrature such that the total emittance is  $\epsilon \approx (\epsilon_T^2 + \epsilon_{sc}^2 + \epsilon_{rf}^2)^{1/2} \approx 3\pi$  mm mrad. The major goal of photoinjector design is to achieve lower emittances either by minimizing the causes of emittance growth or by reversing the growth processes. For most practical cases space-charge induced emittance growth is the major concern.

Two techniques have been advocated for producing 1-nC,  $1\pi$  mm mrad rms emittance beams. The first involves compensating or space charge induced emittance by means of a focusing solenoid (solenoidal emittance compensation) [10]. Solenoidal emittance compensation has been shown to produce beams whose emittance is significantly less than that of a simple photoinjector of similar rf frequency and accelerating gradient [6,11]. Emittance compensation works because most of the space-charge induced emittance growth in a well designed photoinjector occurs without an increase in the entropy of the beam. The space-charge induced distortion is correlated with the position in the bunch and therefore can be removed by applying an appropriate counteracting force before the correlations are diluted by other effects i.e. before the entropy has a chance to grow. The distortion of the phase space may be considered to be a cork-screwing along the bunch that can be unwound by the compensating force. In the simplest case a solenoid is located down stream of the cathode and provides (in conjunction with space charge forces) the appropriate focusing (i.e. compensating) force. The current state of the art for a 1-nC bunch is  $2\pi$  mm mrad in an emittance-compensated L-band injector as indicated in Fig. 1. Recent simulations [12] have shown that  $1\pi$  mm mrad is possible at using emittance compensation in a high-gradient S-band photoinjector. This is an important result as it offers the possibility of achieving significantly smaller emittance than has been demonstrated with the lower gradient L-band guns. In this case of interest here the emittance would grow to about  $3\pi$  mm mrad and then be compensated down to a level of  $1\pi$  mm mrad [13].

The second technique for producing  $1\pi$  mm mrad beams involves producing short, spatially and temporally tailored beams that minimize emittance growth and so do not require post-factum compensation. This latter technique has been evaluated in simulations [14] but has not been demonstrated experimentally at the performance levels required for LCLS. Attempts have been made to tailor the transverse spatial profile of the drive-laser at the Los Alamos APEX facility. These efforts were not successful because of drive-laser instability, and photocathode non uniformity and irreproducibility.

### 3. Jitter sensitivity

As indicated above, the bunching schemes for the LCLS require precise control of the phase-energy correlations in longitudinal phase space. Phase jitter of the drive laser relative to the gun rf fields impact both the phase-energy correlation at the gun and the evolution of correlations in the linac. Current jitter in the gun alters the wakefield induced phase space distortions. Because of phase buffering in the gun, the phase jitter of the beam in the linac is not necessarily equal to the jitter of the drive-laser relative to the rf phase.

To evaluate the sensitivity of the bunching to drive-laser phase jitter we use a simple model which assumes that the correlated energy spread is much greater than the uncorrelated energy spread and  $\delta \gg 1$ , where  $\gamma$  is the electron energy divided by its rest energy. Then we may write the bunching ratio ( $B$ ) i.e. the ratio of the bunch length after ( $\sigma_2$ ) and before bunching ( $\sigma_1$ ) as:

$$B = \frac{\sigma_2}{\sigma_1} \approx \left| 1 - \frac{2\pi f R_{s6}}{c\gamma} \frac{\partial \gamma}{\partial \phi_B} \right| \approx \left| 1 - \frac{2\pi f R_{s6}}{c} \cot \phi_B \right|, \quad (1)$$

where  $f$  is the rf frequency,  $c$  is the velocity of light,  $\phi_B$  is the asymptotic phase of the central particle in the bunch measured in the linac before the buncher and  $R_{s6} = \Delta l / (\Delta p/p)$  is the bunching parameter of the buncher. The sensitivity of  $B$  to injection phase of the drive-laser ( $\phi_0$ ) is:

$$\frac{\partial B}{\partial \phi_0} = \frac{\partial B}{\partial \phi_B} \frac{\partial \phi_B}{\partial \phi_0} = \pm \frac{2\pi f R_{s6}}{c \sin^2 \phi_B} \frac{\partial \phi_B}{\partial \phi_0}, \quad (2)$$

where the positive sign corresponds to under compression and the negative to over compression in the buncher. In general in a multi-section linac  $\phi_B \neq \phi_G$ , the asymptotic phase at the end of the gun. For  $\gamma \gg 1$  at the end of the gun we can write  $\partial \phi_B / \partial \phi_0 \approx \partial \phi_G / \partial \phi_0$  in Eq. (2).

Our concern here is with the sensitivity of  $\phi_G$  to variation in  $\phi_0$ . Travier [15] has shown (using a combination of Kim's theory [9] and simulation) that the asymptotic phase ( $\phi_G$ ) of the central particle in the bunch at the

end of the gun is given in terms of its injection phase ( $\phi_0$ ) at the cathode as:

$$\phi_G = \phi_0 + \frac{1}{2\alpha \sin\left(\phi_0 + \frac{\pi}{6\sqrt{\alpha}}\right)} + \frac{\pi}{15\alpha}, \quad (3)$$

where  $\alpha = eE_0/4\pi fmc$  with  $e$  the electronic charge,  $m$  its mass,  $E_0$  is the peak accelerating electric field. Differentiation of Eq. (1) with respect to  $\phi_0$  gives:

$$\frac{\partial \phi_B}{\partial \phi_0} = \frac{\partial \phi_G}{\partial \phi_0} = 1 - \frac{\cot\left(\phi_0 + \frac{\pi}{6\sqrt{\alpha}}\right)}{2\alpha \sin\left(\phi_0 + \frac{\pi}{6\sqrt{\alpha}}\right)}. \quad (4)$$

Eq. (4) is plotted in Fig. 2 for the case of  $f = 2856$  MHz and  $E_0 = 100$  MV/m, i.e.  $\alpha = 1.63$ . We see that there can be significant buffering of the phase jitter for small  $\phi_0$ . Therefore sensitivity of the bunching ratio to phase jitter can be significantly reduced by running at small  $\phi_0$ .

The asymptotic phase (and hence the bunching ratio) is also sensitive to the accelerating gradient in the gun  $E_0$ . The sensitivity to fluctuations in  $E_0$  is small but may not be negligible. For a nominal value of  $E_0 = 100$  MV/m and  $f = 2856$  MHz,  $\partial \phi_G / \partial E_0$  varies from  $-0.29$  for  $\phi_0 = 10^\circ$  to  $-0.25$  for  $\phi_0 = 60^\circ$ . Fluctuations in gun current will result in changes in  $E_0$  to an extent dependent on the beam loading and cavity  $Q$  of the gun. In contrast to the phase sensitivity, gradient sensitivity is minimized for larger  $\phi_0$ . If we ignore current fluctuations it should be possible to stabilize the accelerating gradient to approximately 0.1%.

The requirement to minimize the transverse emittance generally requires that  $\phi_G \approx \pi/2$  and that  $\phi_0 > 40^\circ$  [9,15]. It is evident from Eq. (3) that sensitivity to jitter may be reduced by having two bunchers one of which over compresses and one of which under compresses so as to cause the jitters to cancel. Simulations [3] with twin bunchers

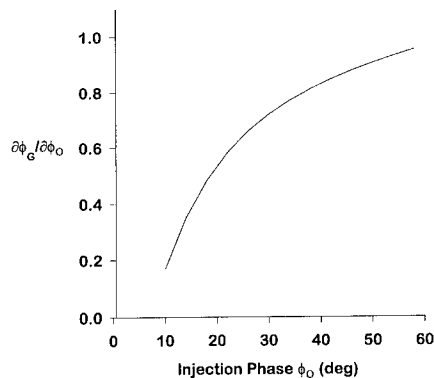


Fig. 2. Sensitivity of asymptotic phase at the end of the gun to drive-laser injection phase variation for  $f = 2856$  MHz and  $E_0 = 100$  MV/m.

Table 1

Characteristics of various photocathodes:  $\eta$  = cathode quantum efficiency in %;  $\lambda_L$  = drive-laser wavelength. The comments in the column labeled "lifetime" are representative of experience in operating photoinjectors

| Material            | $\eta / \lambda_L$ | Lifetime   | Preparation | Ref.    |
|---------------------|--------------------|------------|-------------|---------|
| Cu                  | 0.01/0.26          | very long  | easy        | [17]    |
| Mg                  | 0.06/0.26          | very long  | easy        | [17]    |
| CsK <sub>2</sub> Sb | 5/0.53             | hours-days | difficult   | [5,16]  |
| Cs <sub>2</sub> Te  | 2/0.26             | months     | moderate    | [18,19] |

indicate that the tolerance for phase jitter is  $\pm 0.45^\circ$  ( $\pm 0.5$  ps) and the gun current jitter tolerance is  $\pm 2.2\%$ . The choice of injection phase will depend a compromise between bunching stability (governed by achievable drive-laser stability) and transverse emittance considerations.

#### 4. Photocathodes

In contrast to FEL oscillators, the gun for the LCLS will not have to produce a long train of pulses for initial proof-of principle demonstrations. The LCLS design calls for an average current of 0.14 mA while the current state of the art for rf photocathodes is 32 mA from a CsK<sub>2</sub>Sb cathode driven by a frequency doubled Nd:YLF laser [5]. The initial requirement will be that the cathode produce 1 nC bunches reliably. The CsK<sub>2</sub>Sb cathode lifetime is less than ideal under realistic operating conditions [5,16]. The most promising cathodes are Mg [17] and Cs<sub>2</sub>Te [18,19]. The properties of some cathodes of interest are summarized in Table 1. For single pulse operation the Mg cathode has very good characteristics. However, the Cs<sub>2</sub>Te cathode may prove to be more useful because of the lower drive-laser power required. It is important to have a uniform and reproducible quantum efficiency profile across the cathode. The measured quantum efficiency profile for Cs<sub>2</sub>Te [18] appears to be much more uniform than that reported for CsK<sub>2</sub>Sb [20].

#### 5. Drive lasers

There are two types of mode-locked lasers in common use: fourth harmonic Nd:YAG and Nd:YLF. Recently 3rd harmonic Ti:SAF has been studied for producing very short (sub-picosecond) pulse lengths [21]. When operated under ideal conditions, the phase and amplitude jitter of mode-locked lasers can be very small i.e.  $< 1$  ps and 1% peak to peak respectively. The performance of operating drive lasers has been degraded by some or all of the following conditions: poor temperature control, a non clean-room environment, cavitation in cooling water, and flash-lamp and harmonic crystal aging. The most extensively studied drive-laser has been that of the second-



harmonic Nd:YLF laser at the APEX facility in Los Alamos. The published data for pulse-to-pulse energy stability has been reported to be 1% and 5% peak to peak [22]. Phase jitter with respect to the rf has been reported on the order of 5 ps peak-to-peak over short time scales (seconds) with 10 ps per hour long term drifts [22,23]. Unpublished data [24] from APEX show that phase jitters of 2 ps peak to peak (0.5 to 1 ps rms) and long term drifts of 2 ps were achieved using a phase mixing technique to measure the phase of the drive-laser output relative to the rf together with active feed forward control.

Centroid jitter of the drive-laser spot will result in dipole wakefield modes being excited while mode shape jitter will result in higher-order wakefield modes. Analysis of centroid jitter indicates that a factor of 2 emittance growth is possible in the first six meters of an S-band linac given a 1-nC bunch with a 0.5 mm transverse displacement of a 1-mm drive-laser spot [12]. Simulations for the LCLS indicate that over longer distances emittance growth of 50% is possible with transverse beam displacement of as little as 10  $\mu\text{m}$  [25]. The centroid stability of a 2nd harmonic Nd:YLF drive-laser spot striking the cathode at close to normal incidence has been demonstrated to be approximately 50  $\mu\text{m}$  rms over a few minutes in the APEX photoinjector [22].

The data on drive-laser performance indicate that drive-laser performance will need some improvement for LCLS operation. It should be emphasized that most drive-lasers in operation to date have been one of a kind prototype lasers. The introduction of commercially-produced integrated laser systems along with the use of diode pumped Nd:YLF oscillators and amplifiers offers the possibility of significantly enhanced performance. Preliminary results [26] with such systems indicate sub-picosecond phase stability and less than 50  $\mu\text{m}$  transverse centroid jitter.

## 6. Conclusion

Recent advances in photoinjector technology make it likely that a 1-nC,  $1\pi$  mm mrad beam at a few MeV energy will be produced in the near future.

The performance of photoinjectors has generally been in close agreement with simulations [11]. The main concerns have related to cathode and drive-laser reliability i.e. design performance has been achieved but has been difficult to maintain. Significant improvement beyond this level will be difficult because the thermal emittance of the source is unlikely to be less than  $0.5\pi$  mm mrad. Furthermore, as the emittance decreases the relative sensitivity to

emittance growth during acceleration and transport grows [25].

## Acknowledgements

This paper has benefited from discussions with S. Benson, D. Dowell, J. Early, J. Gallardo, H. Kirk, S. Kong, I. Lehrman, R. Miller, D. Nguyen, D. Palmer, L. Serafini, C. Travier, M. Weber, and A.D. Yermian.

## References

- [1] C. Travier, *Particle Accelerators* 36 (1991) 33.
- [2] H. Winick et al., *Nucl. Instr. and Meth. A* 347 (1994) 199; H.-D. Nuhn, et al., Short Wavelength FELs Using the SLAC Linac, Proc. EPAC'94, London, England (June 1994) SLAC-PUB-6541.
- [3] K.L. Bane, T.O. Raubenheimer and J.T. Seeman, Proc. 1993 Particle Accelerator Conf., Washington, DC (1993) p. 596.
- [4] S. Joly et al., Proc. 1994 European Particle Accelerator Conf., London 1994, to be published.
- [5] D.H. Dowell et al., *Appl. Phys. Lett.* 63 (1993) 2035.
- [6] P.G. O'Shea et al., *Nucl. Instr. and Meth. A* 331 (1993) 62.
- [7] R.L. Sheffield et al., *Nucl. Instr. and Meth. A* 341 (1994) 370.
- [8] K. Batchelor et al., *Nucl. Instr. and Meth. A* 318 (1992) 318.
- [9] K.-J. Kim, *Nucl. Instr. and Meth. A* 275 (1989) 201.
- [10] B.E. Carlsten et al, *J. Quantum Electronics* 27 (1991) 2580.
- [11] I. Ben Zvi, Proc. 1993 Particle Accelerator Conf., Washington, DC (1993) p. 2962.
- [12] J. Gallardo and H. Kirk, to be published.
- [13] D.T. Palmer, personal communication.
- [14] L. Serafini, *Nucl. Instr. and Meth. A* 340 (1994) 40.
- [15] C. Travier, *Nucl. Instr. and Meth. A* 341 (1994) 26.
- [16] P.G. O'Shea et al., *AIP Conf. Proc.* 279 (1993) 743.
- [17] T. Srinivasan-Rao et al., *J. Appl. Phys.* 69 (1991) 3291.
- [18] E. Chevallay et al., *Nucl. Instr. and Meth. A* 340 (1994) 146.
- [19] S.H. Kong, J. Kinross-Wright, D.C. Nguyen and R.L. Sheffield, these Proceedings (16th Int. Free Electron Laser Conf., Stanford, CA, USA, 1994) *Nucl. Instr. and Meth. A* 358 (1995) 272.
- [20] D.W. Feldman et al., *J. Quantum Electron.* 27 (1991) 2636.
- [21] P. Georges et al., Proc. 1993 Particle Accelerator Conf., Washington, DC (1993) p. 3053.
- [22] J.W. Early et al., *Nucl. Instr. and Meth. A* 18 (1992) 381.
- [23] A.H. Lumpkin and J.W. Early, *Nucl. Instr. and Meth. A* 18 (1992) 389.
- [24] J.W. Early, personal communication.
- [25] T.O. Raubenheimer, these Proceedings (16th Int. Free Electron Laser Conf., Stanford, CA, USA, 1994) *Nucl. Instr. and Meth. A* 358 (1995) 40.
- [26] I.S. Lehrman, personal communication.

# Electron beam acceleration and compression for short wavelength FELs

T.O. Raubenheimer \*

*Stanford Linear Accelerator Center, Stanford University, Stanford, CA 94309, USA*

## Abstract

A single pass UV or X-ray FEL will require a low emittance electron beam with high peak current and a beam energy of a few hundred MeV to many GeV. To achieve the necessary peak current and beam energy, the beams must be bunch compressed and accelerated in long transport lines where dispersive and wakefield emittance dilutions are important. In this paper, we will describe the sources and significance of the dilutions during acceleration, bunch compression, and transport through the undulator. In addition, we will discuss sources of jitter as well as possible cancellation techniques.

## 1. Introduction

Recently, a number of single pass UV and X-ray FELs have been proposed [1–4]. These short wavelength FELs impose severe requirements on the electron beam. In this paper, we attempt to survey the issues associated with accelerating and bunch compressing a low emittance beam for a single pass UV or X-ray FEL. Much of this discussion will be based on the parameters for the LCLS, listed in Table 1 [4]. Of the short wavelength single pass FELs presently being discussed, the LCLS has the most severe beam requirements. Although the issues are the same in other designs, the parameters are different and, in general, the tolerances and problems are easier.

In a single pass FEL, the scale of the beam requirements can be determined from the FEL resonance condition, the dimensionless FEL parameter  $\rho$  [5], and the diffraction relation:

$$\lambda_r \sim \frac{\lambda_w}{\gamma^2}, \quad \sigma_{\Delta E/E} \leq \rho, \quad \lambda_r \sim 4\pi \frac{\gamma\epsilon}{\gamma}, \quad (1)$$

where  $\lambda_r$  and  $\lambda_w$  are the radiation wavelength and wiggler period, and  $\sigma_{\Delta E/E}$  and  $\gamma\epsilon$  are the relative energy spread and the normalized transverse emittance; see Ref. [6] for a more detailed discussion of these relations.

Maintaining these three criteria at short wavelengths requires 1) high beam energies, 2) small energy spreads, and 3) small transverse emittances. First, accelerating the beam to high energy is certainly possible, although the accelerators are not inexpensive. Second, from an RF gun,

the energy spread criteria is easily achieved and thus, to maximize the gain in the FEL, the electron beam needs to be compressed. Compression increases both the peak current and, because the longitudinal emittance is conserved, the energy spread. The optimal degree of compression balances the increase in peak current against the increase in the beam energy spread. Finally, the beam emittance needs to be preserved while the beams are accelerated to high energy and compressed. Presently, RF guns are delivering very small emittances, less than 2 mm mrad [7]. It is expected that emittances slightly less than 1 mm mrad will be attained in the near future [8].

In the next sections, we will discuss dilutions of the transverse and longitudinal phase spaces. However, we should first clarify the difference between the “slice” emittance and the projected beam emittance. In these single pass devices, the emittance and energy spread requirements for lasing only need be maintained over a distance  $\lambda_r/\rho$ , sometimes referred to as the cooperation length. This is typically much smaller than the bunch length. For example, in the LCLS, the cooperation length is less than 1  $\mu\text{m}$  while the rms bunch length is roughly 15  $\mu\text{m}$ .

## 2. Transverse phase space

The principal sources of transverse emittance dilution are focusing mismatches and transverse coupling, dispersive and chromatic errors, transverse wakefields and RF deflections, and space charge forces. We will discuss each source briefly. Next, we will describe some emittance correction techniques and finally we will discuss transverse beam jitter. A more detailed discussion of the sources

\* Corresponding author. Tel. +1 415 280 2474, e-mail tor@slac.stanford.edu.

Table 1  
0.45 nm LCLS beam parameters

|                        |                    |
|------------------------|--------------------|
| Energy                 | 15 GeV             |
| Peak current           | 5 kA               |
| $\gamma\epsilon_{x,y}$ | 1 mm mrad          |
| Charge                 | 1 nC               |
| $\sigma_x$             | 15 $\mu\text{m}$   |
| $\sigma_{\Delta E/E}$  | $2 \times 10^{-4}$ |

of emittance dilution and emittance correction techniques can be found in Ref. [9].

Mismatches of the focusing system and transverse emittance (betatron) coupling can lead to an effective emittance increase after the mismatches filament (phase mix). The focusing mismatches arise from errors in the quadrupole placement and strengths while the betatron coupling is primarily introduced by rotation alignment errors of the quadrupoles. With equal  $x$  and  $y$  emittances, the betatron coupling effects are not very significant; the alignment tolerance on the quadrupoles is a few mrad, but, care is needed in the optics design to avoid unwarranted sensitivity to focusing errors. Finally, both of these are multiplicative emittance dilutions and thus the tolerances do not become more severe as the beam emittance is decreased.

Dispersive effects refer to the dependence of the trajectory on energy which arise when the trajectory is deflected and chromatic effects refer to the dependence of the transverse focusing on energy. Because the beam has an energy spread, these effects can lead to emittance dilution. Specifically, dispersive errors arise from injected trajectory errors or misalignments of the beam position monitors (BPMs) which cause the corrected trajectory to be deflected from side-to-side. Chromatic effects arise from limitations of the energy bandwidth of the focusing channel and need to be considered in the optics design.

Both the dispersive and chromatic effects are proportional to the energy deviation or spread. In linacs for FELs, the “uncorrelated” energy spread, i.e. the energy spread of a slice at some position within the bunch, is usually much less than the “correlated” energy deviation which arises from the accelerating RF and the longitudinal wakefields. Thus, the tolerances to limit the emittance dilution of the beam are more severe than the tolerances to limit the dilutions over a cooperation length. Finally, it is possible to use the beam to diagnose the quadrupole and BPM offsets. Presently, beam-based alignment is used in the SLAC linac to align the quadrupoles and BPMs with an rms error of roughly 80  $\mu\text{m}$  [10].

Transverse wakefields arise from offsets of the beam in the accelerating structures. The offsets may result from injected trajectory errors, misalignments of the BPMs, or misalignments of the structures. Wakefield dilutions also occur at beam collimators or in small aperture vacuum chambers. The wakefields deflect the tail of the beam, correlating the transverse phase space with the longitudinal

position within the bunch. RF deflections arise from asymmetries in the input and output couplers on the accelerating structures, structure fabrication errors, and angular orbit errors through the structures. Like transverse wakefields, the RF deflections correlate the transverse phase space with the longitudinal position within the bunch. Finally, both of these dilutions are proportional to the bunch length and can be minimized by compressing the bunch at relatively low energies.

Unfortunately, it can be more difficult to accurately align the accelerating structures than the quadrupoles. As mentioned, quadrupole alignment errors can be accurately determined from the beam deflections, but this is harder with the accelerating structures. One alignment technique with the potential of high resolution is to directly measure the induced dipole modes in the structure.

Space charge forces impose a severe limitation on the transverse emittance and the peak current. There are two regimes that are important: first, forces that arise during straight-line motion, and second, forces that arise in bending magnet systems. In the first case, the force scales linearly with local beam current and inversely with the square of the beam energy ( $1/\gamma^2$ ). The established solution to this problem is to have a relatively low current from the RF gun, accelerate the beam rapidly, and use emittance compensation [11]. The beam can then be compressed to high peak currents at much higher energy where the forces are not as important.

In the second regime, namely in the bending magnets of a bunch compressor, there are space charge forces that do not scale as  $1/\gamma^2$ . Calculations for DC beams [12] and simple geometric arguments would suggest that these forces scale as the square of the beam size divided by the square of the bending radius ( $\sigma_x/\rho$ )<sup>2</sup>. More detailed calculations for bunched beams [13] indicate that the forces scale as ( $\sigma_x/\rho$ )<sup>3/2</sup>. Thus, although the force can be important when compressing low emittance beams, the dilution decreases rapidly with beam radius and usually can be made negligible by properly designing the bunch compressor.

All of the sources described are conservative dilutions: the beam emittance is not actually increased, instead the various degrees of freedom become correlated, leading to an increase in the projected emittance. Because the dilutions are conservative, they can be corrected provided that the correlations have not filamented (phase mixed). Emittance correction of the low energy space charge forces is now a well established technique for RF guns [11]. In the same manner, emittance correction of wakefield and dispersive dilutions is a standard technique in high energy linacs. Presently, emittance correction bumps are used to reduce dilutions in the SLC linac from over 300% to less than 50% [14]. Of course these emittance correction techniques rely on highly accurate diagnostics that can measure the beam centroid and emittance.

Finally, transverse position jitter can arise from variations in the laser spot on the RF gun photocathode, trans-

verse vibration of the quadrupole magnets, or magnet power supply fluctuations. The jitter has three effects: it leads to transverse emittance growth due to wakefields and dispersive effects, it makes tuning of the transverse phase space difficult, and it shifts the position of the beam centroid, causing variations in the FEL output.

The amplification of jitter by the transverse wakefields can be reduced using BNS damping [15] where an energy deviation, correlated with the position within the bunch  $z$ , is used to compensate the effect of the wakefields. In addition, low frequency jitter ( $f \leq f_{\text{rep}}/30$ ) and slow drifts can be reduced with beam-based feedbacks. But, the tolerance on the high frequency jitter is a fraction of the beam size and, as the beam emittance decreases, the tolerances can become severe. Furthermore, it is difficult to eliminate all sources of jitter by design. Additional sources can appear due to subtle hardware failures, necessitating diagnostics to detect and isolate these sources of jitter.

### 3. Longitudinal phase space

At this point, we can discuss the longitudinal phase space. As mentioned, in a short wavelength FEL, the bunch from the RF gun needs to be compressed to achieve maximum gain. The bunch compression is performed by introducing an energy deviation  $\delta$ , correlated with the longitudinal position  $z$  in the bunch, and then passing the bunch through a magnetic system where the path length is energy dependent. When designing the compressions and the transport of the longitudinal phase space, four issues need to be considered: attaining the desired high peak currents, removing any correlated energy deviation which chirps the FEL, making the system insensitive to timing or intensity jitter from the RF gun laser, and transverse phase space issues, i.e. space charge, transverse wakefields, etc. as described in the previous section.

#### 3.1. High peak current

To optimize the gain in a short wavelength FEL, we need very high peak currents. These currents are attained by compressing the bunch length at relatively high energy so that transverse and longitudinal space charge effects are not significant. Ideally, the longitudinal phase space in a bunch compressor is conserved. Unfortunately, the curvature of the RF waveform, the longitudinal space charge forces, and the longitudinal wakefields, introduce  $\delta$ - $z$  correlations that are not linear. Because it is hard to compensate for these nonlinearities in the magnet systems, this dilutes the effective longitudinal emittance and reduces the amount of bunch compression that can be performed. To avoid this, we add large correlations and then only partially compressing the bunch – the residual correlated energy spread is removed later with either the RF or the induced longitudinal wakefields.

When partially compressing the bunch, one can either “under-compress” or “over-compress”. In the former,

the longitudinal phase space is rotated by less than  $90^\circ$ ; in the later, the phase space is rotated past the minimum bunch length. In some instances it can be advantageous to over-compress the bunch [16] however, when the longitudinal emittance is very small, over-compressing exacerbates space charge problems and is not usually applicable for short wavelength FEL drivers.

#### 3.2. Small energy deviation

With high energy short bunches, the primary sources of correlated energy deviation are the longitudinal wakefields and the accelerating RF. The wakefield effects are usually corrected by accelerating the beam ahead of the RF crest. Unfortunately, as the bunches become very short, this technique is no longer effective. For example, in the SLAC linac, with an accelerating gradient of 17 MV/m, the shortest bunch where the RF can be used to compensate for the longitudinal wakefield is roughly 100  $\mu\text{m}$ .

Thus, to achieve very short bunches with small correlated energy spreads one has to either accelerate a longer bunch and then fully compress it at the end of the linac, or, add a large correlated energy deviation, before the bunch is fully compressed, that the longitudinal wakefield removes during the subsequent acceleration. In the LCLS design, we use the later technique since it is difficult to fully compress the bunch.

Finally, the resistive wall wakefield in the undulator will also lead to a correlated energy deviation [17]. For proper operation of the FEL, the induced energy deviation should be much less than the desired bandwidth. For example, if we assume an aluminum undulator vacuum chamber with a 3 mm radius and the LCLS parameters of 1 nC charge, a 15  $\mu\text{m}$  rms bunch length, and a 40 m undulator, we find an induced peak-to-peak energy deviation along the bunch of roughly 20 MeV; this scales inversely with the vacuum chamber radius.

#### 3.3. Longitudinal jitter

When designing the transport and compression sections, we need to consider effects of phase and intensity jitter from the RF gun laser; this is usually a more severe limitation than the RF timing. Both of these effects will change the  $\delta$ - $z$  correlation. In the case of phase jitter, the  $\delta$ - $z$  correlation varies because of the non-linearity of the RF while the variation occurs with intensity jitter because a more intense bunch generates larger wakefields. When the  $\delta$ - $z$  correlation changes, the rotation of the longitudinal phase space changes and the compressed bunch length and peak current vary.

Assuming that the longitudinal emittance is extremely small, we can neglect the uncorrelated energy spread and calculate the dependence of the bunch length on the phase jitter  $\Delta\phi$  after a single compression [18]:

$$\frac{1}{\sigma_z^*} \frac{d\sigma_z}{d\Delta\phi} = \frac{\sigma_{z0}^*}{\sigma_z^*} \left[ \left( \frac{\sigma_z^*}{\sigma_{z0}^*} \pm 1 \right) \cot \phi \right], \quad (2)$$

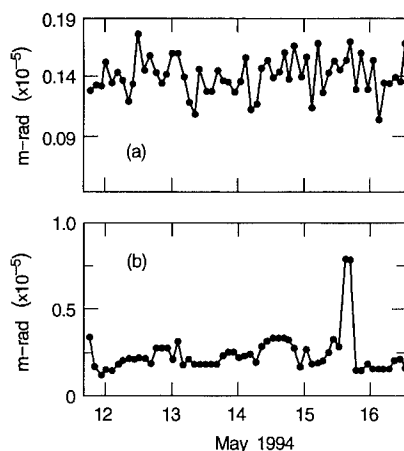


Fig. 1. Vertical emittance at the beginning (a) and end (b) of the SLAC linac during the FFTB experimental program.

where  $\sigma_{z0}^*$  and  $\sigma_z^*$  are the nominal initial and final bunch lengths,  $\phi$  is the nominal RF phase, and the negative sign corresponds to under-compressing while the positive sign is for over-compressing.

At this point, we can perform a similar calculation to include the effect of a second compression and we find two terms in the expression that can be chosen to cancel. For example, if the compression in the LCLS were performed in a single stage, injection phase errors of 60 fs would lead to 10% variation of the peak current. Instead, with two stages, we have an injection phase tolerance of 1 ps for 10% variation of the beam current.

#### 4. Summary

We have attempted to describe the relevant dynamics in the transverse and longitudinal phase spaces during the acceleration and compression of a beam for a short wavelength FEL. We have not touched on the diagnostics or controls requirements which will be exceedingly important for these accelerators. In particular, as the tolerances become tight, one must design the system so that it can be dynamically tuned while the required stability is maintained through fast beam-based feedbacks.

We have not had space to describe the present state of the LCLS design, but the LCLS beam transport has been designed using computer codes, such as PARMELA and those used to design future linear colliders, that have been bench-marked against experimental results. There are some remaining uncertainties with the bunch compression and the SASE physics, but these should be experimentally verified in the next few years [3].

Finally, it is worth noting that many of the emittance preservation requirements for the LCLS are being demonstrated at SLAC routinely. Fig. 1 is a plot of the normalized vertical emittance at the beginning Fig. 1a and end of the 3 km SLAC linac Fig. 1b during a five day run of the Final Focus Test Beam (FFTB) [19]. The beam, with 1 nC of charge, is generated in the SLC damping ring which operates far from the coupling resonance so  $\gamma\epsilon_y \sim 1.5$  mm mrad while  $\gamma\epsilon_x \sim 30$  mm mrad. The bunch is then compressed from an rms bunch length of 6 mm to 500  $\mu$ m at which point it is injected into the SLAC linac and accelerated. The vertical emittance dilution is routinely less than 50%.

#### Acknowledgements

I would like to thank Karl Bane, Franz-Josef Decker, and the members of the LCLS collaboration for many useful discussions and comments. Work supported by the Department of Energy, contract DE-AC03-76SF00515.

#### References

- [1] I. Ben-Zvi et al., Nucl. Instr. and Meth. A 304 (1990) 181.
- [2] L.H. Yu et al., these proceedings (16th Int. Free Electron Laser Conf., Stanford, CA, USA, 1994) Nucl. Instr. and Meth. A 358 (1995) 74.
- [3] I. Ben-Zvi, *ibid.*, p. 52.
- [4] H. Winick et al., Nucl. Instr. and Meth. A 347 (1994) 199; H.-D. Nuhn et al., Proc. 4th Europ. Particle Accelerator Conf., London, England (1994).
- [5] R. Bonifacio, C. Pellegrini and L.M. Narducci, Opt. Commun. 50 (1984) 373.
- [6] K.-J. Kim, Ref. [2], p. 31.
- [7] R.L. Sheffield et al., Nucl. Instr. and Meth. A 341 (1994) 371.
- [8] P. O'Shea, Ref. [2], p. 36.
- [9] T.O. Raubenheimer, Proc. 1993 Particle Accelerator Conf., Washington, DC (1993) p. 11.
- [10] C. Adolphsen et al., Proc. 1989 Particle Accelerator Conf., Chicago, IL (1989) p. 977.
- [11] B.E. Carlsten, Nucl. Instr. and Meth. A 285 (1989) 313.
- [12] E.P. Lee, Particle Accelerators 25 (1990) 241.
- [13] B.E. Carlsten et al., submitted to Phys. Rev. E.
- [14] C. Adolphsen et al., Proc. 1993 Particle Accelerator Conf., Washington, DC (1993) p. 414.
- [15] V. Balakin et al., Proc. 12th Int. Conf. on High Energy Accelerators Fermilab (1983) p. 119.
- [16] F.J. Decker et al., Proc. 17th Int. Linac Conf., Tsukuba, Japan (1994).
- [17] K. Bane, internal SLAC document, SLAC-AP-87 (1991).
- [18] K. Bane et al., Proc. 1993 Particle Accelerator Conf., Washington D.C. (1993) p. 596.
- [19] D. Burke et al., Proc. 4th Europ. Particle Accelerator Conf., London, England (1994).

# Undulators for short wavelength FEL amplifiers ☆

Ross D. Schlueter \*

*Lawrence Berkeley Laboratory, MS 46-161, 1 Cyclotron Road, Berkeley, CA 94720, USA*

## Abstract

Issues critical to the design of undulators for use in short wavelength FEL amplifiers, such as attainable on-axis field strength, device compactness, field quality, required magnetic gap, and strong focusing schemes, are discussed. The relative strength of various undulator technologies, including pure permanent magnet, hybrid, warm electromagnetic, pulsed, and superconducting electromagnetic devices in both helical and planar configurations, are reviewed. Favored design options for proposed short wavelength FELs, such as the Linac Coherent Light Source at SLAC and the DUV Free-Electron Laser at BNL, are presented.

## 1. Introduction

Achieving desired FEL action in SLAC's proposed Linac Coherent Light Source (LCLS) necessitates an undulator with of the order of 1000 periods. The electron beam must be focused over the device length, while the on-axis field strength should provide a desired deflection parameter  $K \approx 2-6$  [1]. In general, a shorter period would result in a shorter undulator length, but a lower attainable  $K$ . Typical focusing required for a 2.7-cm-period device at  $K = 4$  is that of a quadrupole FODO system with 40-cm-long, 50-T/m-gradient quadrupoles separated by 40 cm.

Relative strengths of various undulator technologies in short period linear polarized devices for feasible LCLS gaps of 0.4–0.6 cm are shown in Fig. 1 [2–5]. The LCLS specifications preclude small-period conventional electromagnet devices, since the level of current density required to attain the requisite field strength exceeds the cooling capability. Short-period pure permanent magnet (PM) devices could accommodate superposed external quadrupoles but the large quadrupole bore would preclude the large gradient desired. Canting of PM pieces likewise can produce only weak on-axis gradients [6].

## 2. Short-period pulsed undulators

At Los Alamos, a variety of short period (1–30 mm) pulsed devices have been developed [7,8]. The general aim

there was to push down the period as much as possible, yet still maintain  $K_{rms} \approx 1$ . Performance limits of these devices are: (a) the copper wire temperature at the end of a pulse limits the pulse length, (b) the cooling capability limits the rep-rate, and (c) the tensile strength of the copper wire limits the current. A 2.7-cm-period, 0.86 cm bore bifilar device operating at 5 kA achieved a  $K_{rms} = 1$  for a maximum 100  $\mu$ s pulse length. Maximum rep rates of 1 per minute for solid copper wire and 1 per second for internally cooled copper tubing are achievable. A 0.85-cm-period, 0.8-mm-bore device likewise achieves a  $K_{rms} = 1$ .

## 3. Iron-core superconducting undulator technology

An elegantly-simple, iron-core superconducting undulator technology has been developed at Brookhaven [4]. The design features a superconducting wire wound continuously along the device length around a soft iron mandrel or magnetic yoke which has fins restraining the superconductor while simultaneously serving as poles of the linear undulator. It is capable of providing a tunable, highly-stable, good-quality DC field, with adjustable taperability. Demands on the superconductor are minimal, as the field there is small,  $< 3$  T. The major drawbacks are the presence of the cryogenics and the lack of accessibility to the undulator and ensuing alignment difficulties.

Two devices using this technology have been built at Brookhaven: a 0.88-cm-period, 0.44-cm-gap, 0.6-m-long device with a peak field  $B_0 = 0.47$  T for a 470 nm oscillator experiment and a 1.8-cm-period, 0.80-cm-gap, 1.5-m-long device with a peak field  $B_0 = 0.58$  T for a harmonic generation experiment. Two more such devices are part of Brookhaven's DUV proposal: a 3.9-cm-period, 0.6-cm-gap, 2-m-long modulating undulator with a peak

☆ This work was supported by the Director, Office of Energy Research, Office of Basic Energy Sciences, Material Sciences Division, of the U.S. Department of Energy under Contract No. DEAC03-76SF00098.

\* Tel. +1 510 486 7405, fax +1 510 486 4873.

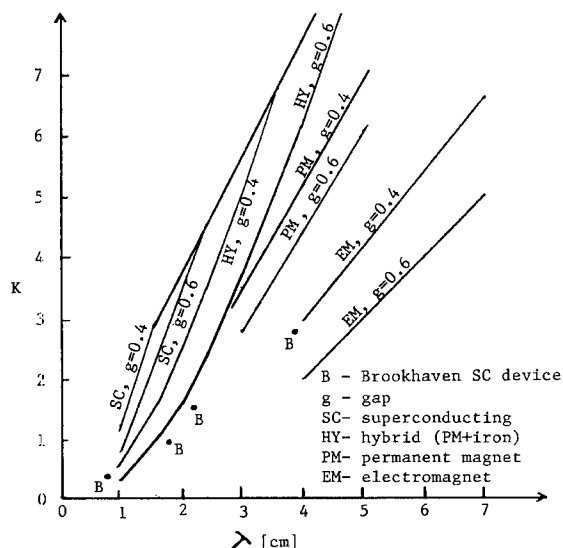


Fig. 1. Relative strength of various undulator technologies in short-period linear-polarized devices for feasible LCLS gaps of 0.4–0.6 cm.

field  $B_0 = 0.77$  and a 2.2-cm-period, 0.6-cm-gap, 7-m-long radiating undulator with a peak field  $B_0 = 0.75$  T. (See the four points labeled “B” on Fig. 1.)

Typically it is the saturation in the pole, rather than the quench limit of the superconductor that limits the attainable field in the regime where this technology outperforms hybrid technology, i.e.,  $0.25 < g/\lambda_w < 0.55$  and  $0.5 \leq \lambda_w \leq 2.5$  cm. This indeed was the case for the Brookhaven

devices. Two modifications that could increase on-axis field in such devices by mitigating pole saturation are [9]: (1) increasing the pole thickness as one moves away from the gap and (2) increasing the pole transverse (i.e.,  $x$ -direction) dimension as one moves away from the gap. Real estate in the  $x$ -direction is inexpensive.

The harmonic generation device and the DUV FEL utilize parabolic pole tips [10] to provide equal plane natural focusing. However, strong focusing in these iron dominated devices is possible, just as is the case with hybrid devices.

For LCLS's larger  $K$ , and thus optimal device period range of 2.7–4.0 cm, the superconducting device performance advantage is increasingly diminished. Incorporating the large gradient into a higher  $K$  device, yet keeping the period, thereby device length, as short as possible is the challenge. Several promising undulator options are being pursued.

#### 4. Strong focusing hybrid undulator

One LCLS possibility is a hybrid device, featuring vanadium permendur poles excited by NdFeB permanent magnets, sections of which have poles that are alternately tilted in the  $+/-$  transverse direction with respect to the midplane and simultaneously wedge-shaped as viewed from above (see Fig. 2). For example, such a device with a 4 cm period, a 0.6 cm gap on-center, a 1.0 cm pole thickness on center, a  $\pm 5.7^\circ$  tilt, and a  $\pm 7.1^\circ$  wedge could provide a 34 T/m gradient and an on-axis field strength of 1.04 T,  $\Rightarrow K = 4$ . Minimum/maximum gap at transverse position

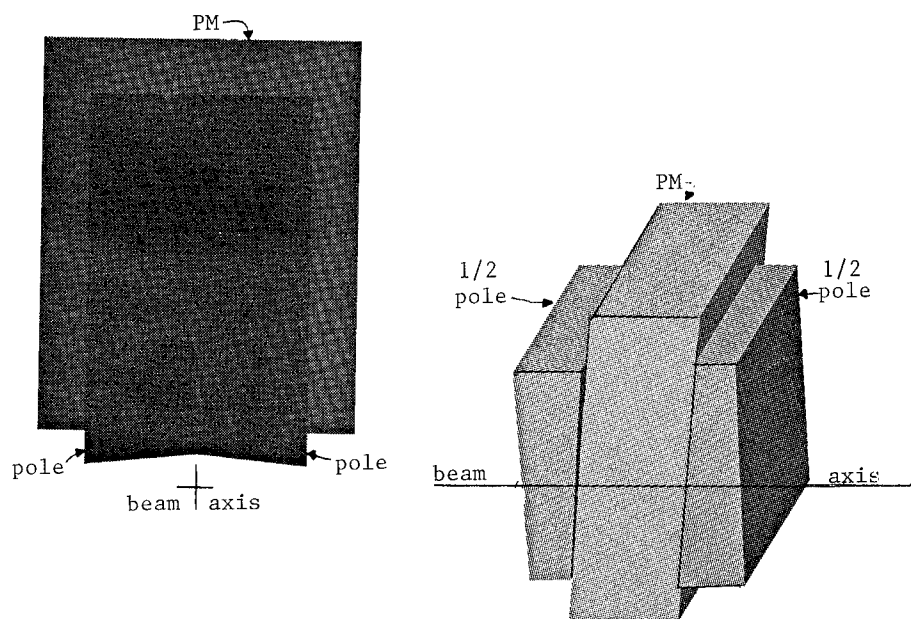


Fig. 2. Half-period of a strong focusing hybrid undulator.

$x = \pm 1$  cm would be 0.40/0.80 cm. The pole thickness at  $x = \pm 1$  cm is  $1.0 \pm 0.25$  cm. The iron pole pieces shape the field, perhaps affording better field quality than is possible with a pure permanent magnet device at this small gap.

#### 4.1. Alternating gradient focusing in a hybrid undulator

The choice of simultaneous pole tilt with respect to the midplane and variable pole thickness follows from a 3-D analysis of the ideal pole shape for the superposition of fields from an undulator and a quadrupole. Let  $(x, y, Z)$  be the horizontal, vertical and axial directions in our ideal strong focusing undulator. Define complex variables  $w \equiv Z + iy$  and  $z \equiv x + iy$ . The desired wiggle field and focusing field are, respectively,

$$B_{\text{wig}}^*(w) = iB_0 \cos(kw), \quad (1)$$

where  $k = 2\pi/\lambda$  and

$$B_{\text{foc}}^*(z) = i2az; \Rightarrow dB_{\text{foc}}/dz = i2a, \quad (2)$$

the gradient. The magnetic scalar potential,  $V$ , where  $\mathbf{B} = -\nabla V$ , in the region is

$$V_{3D} = V_{\text{wig}}(w) + V_{\text{foc}}(z) \\ = (B_0/k) \sinh ky \cos kZ + 2axy. \quad (3)$$

A contour along which  $V$  is constant is an equi-scalar potential surface to which the magnetic field is orthogonal. For our strong focusing undulator, choosing the boundary of the vanadium permendur pole, whose permeability is effectively infinite, to lie along a constant  $V_{\text{wig}} + V_{\text{foc}}$  contour specified by  $V = f(B_0, 2a, \lambda, h)$ , where  $h$  is the half-gap, gives rise to the combination wiggle and focusing fields described above.

Using the hybrid curve in Fig. 1 as a guide, we attempt to attain a desired on-axis field  $B_0 = 1$  T and desired gradient  $2a = 33$  T/m, in a 4-cm-period, 0.6-cm-gap strong focusing undulator. The equi-scalar potential contour along the ideal pole surface passes through the point  $(x, y, Z) = (0, h, 0)$ :

$$V_{3D}(0, h, 0) = (B_0/k) \sinh kh = B_0 h (\sinh kh / kh). \quad (4)$$

Defining  $g \equiv B_0/2a$ , the ideal pole contour (see Fig. 3) is given by

$$1 = \cos kZ \left( \frac{\sinh ky}{\sinh kh} \right) + \left( \frac{y}{h} \right) \left( \frac{x}{g} \right) \left( \frac{kh}{\sinh kh} \right). \quad (5)$$

The complicated three-dimensionally-curved pole shape (Eq. (5)) is approximated by the canted, wedged pole having flat surfaces described at the beginning of this section. This practical design has the desirable feature that the permanent magnet material laced between poles remains a simple cuboid. Of course, our designed pole shape only approximates the curved surface of the ideal pole, and thus harmonics will be present, and  $x$  and  $y$  plane strong focusing are not equivalent locally (though integrated over a wiggle period they are equal in magnitude since in a 3-D structure with coordinates  $(x, y, Z)$ , the integrated field  $B^*(z) \equiv \int_{z_1}^{z_2} B^*(z) dZ$  is analytic with respect to  $z$  if for all  $z$ ,  $B^*(z)|_{z_1} = B^*(z)|_{z_2}$  [11]).

The 3-D TOSCA computer result ( $B_0/2a = 1.04/34.0 = 0.0306$ ) using the canted, wedged, flat surfaced pole achieves very nearly the performance attained in the analytical curved model. Computer runs of analogous designs with poles wedged but not canted and with poles canted but not wedged give gradients of one-third and two-thirds of that when both are employed, assuming the same wiggle

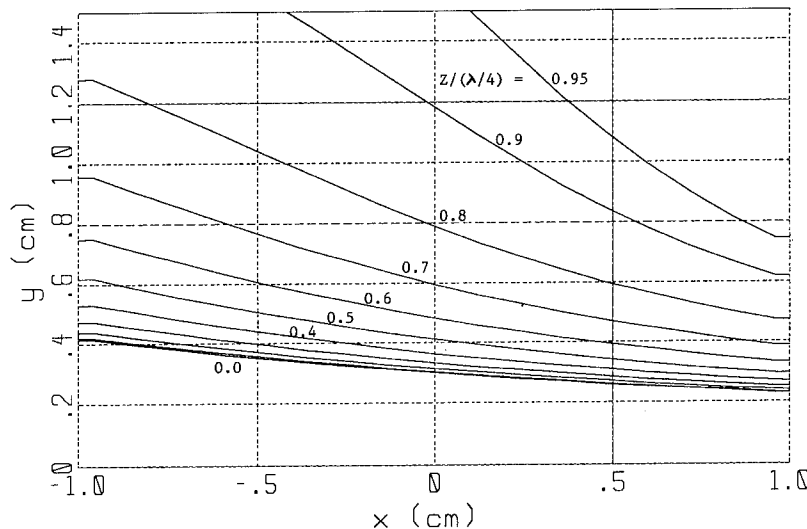


Fig. 3. Ideal pole contour of a strong focusing iron-dominated undulator.



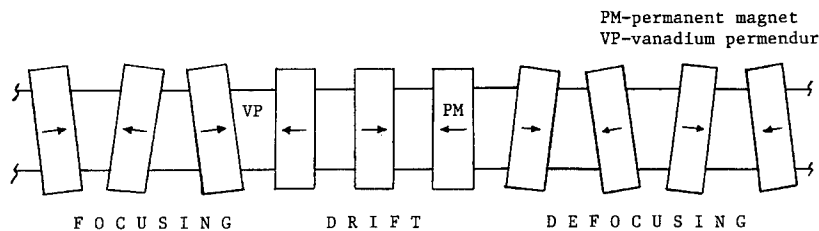


Fig. 4. Focusing, drift, and defocusing sections of a strong focusing hybrid undulator (plan view).

field magnitude in all cases. Thus, for maximum performance and field quality both pole canting and wedging are needed.

Hybrid technology is proven, and the PM sizes for LCLS are small and manageable, with no large forces. Modular construction of a  $\sim 40$  m device is convenient. PM cost for 1000 periods, each consisting of four  $1\text{ cm} \times 3\text{ cm} \times 3\text{ cm}$  arrays at  $\$4/\text{cm}^3$  is only  $\$144\,000$ . Fig. 4 shows the layout over a focusing section, followed by a “drift” section and a defocusing section. The wiggle field is matched throughout the sections.

Regarding ultimate performance limitations and the maximum achievable gradient: if we attempt to increase the gradient by increasing the pole cant and/or wedge, the pole tip will eventually saturate. The  $\mu = \infty$  assumption for the vanadium permendur pole tip is then no longer valid, so the pole contour is no longer an iso-scalar potential surface and the gradient will cease to increase.

It should be noted that a superconducting undulator of the design of the previous section is amenable to the strong focusing produced by pole cants and wedges as described above. The same equations can be used to guide the choice of the magnitudes for a practical, yet effective, optimal pole tip shape. Tradeoffs are the relative ease in tunability, construction and transportability, reliability, radiation resistance, and of course magnetic performance capability.

### 5. Small bore helical superconducting undulator

An alternative LCLS design being considered [12] that offers the additional desirable feature of producing circularly polarized light is a bifilar superconducting undulator. Such a device with a 4-cm period, a 0.5-cm-radius magnetic bore, a 0.7-cm-coil outer radius, with a superconducting wire current density times packing factor of  $\sim 3000\text{ A/mm}^2 \times 0.44$  could produce a rotating on-axis transverse field of  $\sim 1.1\text{ T}$ . A 50 T/m coaxial superconducting quadrupole of the style of the SSC ring quadrupoles positioned just outside of the undulator windings could easily provide the requisite beam focusing.

Alternatively, a device with a 2.7-cm period, a 0.325-cm-radius magnetic bore, a 0.475-cm-coil outer radius,

with a superconducting wire current density of  $\sim 4000\text{ A/mm}^2$  could produce 1.7 T on-axis. As dimensions scale down, the incremental field at the superconductor due to the external quadrupole decreases and thus, fortunately, current density in the superconductor can be higher. With the introduction of superconductors with artificial pinning centers [13],  $J_c$  is markedly increased at these relatively low fields, making these short-period, small-bore devices magnetically attractive.

The multi-laboratory LCLS collaboration is actively pursuing the hybrid and superconducting undulator options and is planning short proof-of-principle prototype devices.

### Acknowledgements

The author thanks Klaus Halbach for guidance and advice in many aspects of undulator theory and design and the other LCLS collaboration members for ideas generated during the evolution of LCLS candidate undulator designs.

### References

- [1] C. Pellegrini et al., Nucl. Instr. and Meth. A 341 (1994) 326.
- [2] K. Halbach, Nucl. Instr. and Meth. 187 (1981) 109.
- [3] K. Halbach, J. Physique C1 44-2 (1983) C1-211.
- [4] I. Ben-Zvi et al., Nucl. Instr. and Meth. A 318 (1992) 781.
- [5] R.D. Schlueter and G.A. Deis, Nucl. Instr. and Meth. A 331 (1993) 711.
- [6] K.E. Robinson and D.C. Quimby, Particle Accelerator Conf., Washington, DC, 1987, p. 428.
- [7] R.W. Warren, Nucl. Instr. and Meth. A 296 (1990) 558.
- [8] R.W. Warren, Nucl. Instr. and Meth. A 304 (1991) 765.
- [9] R.D. Schlueter, in: Synchrotron Radiation Sources – A Primer, ed. H. Winick (World Scientific, River Edge, NJ, 1994).
- [10] E.T. Scharlemann, J. Appl. Phys. 58 (1985) 2154.
- [11] K. Halbach, Lawrence Berkeley Laboratory Report V-8811-1.1-16 (1989).
- [12] S. Caspi, Lawrence Berkeley Laboratory Reports SC-MAG-464, -472, and -474 (1994).
- [13] R.M. Scanlon et al., IEEE Trans. Magn. MAG-30(4) (1994) 1627.

# Performance simulation and parameter optimization for high gain short wavelength FEL amplifiers

G. Travish \*

*UCLA Department of Physics, Los Angeles, CA 90024, USA*

## Abstract

The designers of short wavelength FELs must rely on theoretical and numerical predictions since no experimental data are available for this region. The numerical codes which have been developed, and are being used to design systems at SLAC, BNL, Duke, LBL, CEBAF, LANL and UCLA among others, contain our best theoretical understanding of these systems. This paper analyses the present simulation capabilities for short wavelength designs. We discuss how codes are used to design these new systems, which aspects of our models are well implemented and which are not, methods of verifying the models, comparison with experiment, and finally comments on extrapolating to short wavelengths.

## 1. Overview

Recently, a number of FEL proposals have been put forth in an attempt to provide users with high brilliance radiation at short wavelength (UV and beyond) [1–3]. These new systems propose to operate in wavelength and gain regimes far away from past or present FELs (see Fig. 1). While these new designs offer great promise by using state of the art beam and undulator quality, the performance claims must be carefully examined. Computer simulation being the most powerful tool used to predict the performance of new FELs leads one to investigate our present simulation capabilities.

We discuss in this paper the present computation capabilities for high gain, short wavelength FEL amplifiers. High gain implies many exponential gain lengths of growth of spontaneous emission or an injected signal, while short wavelength is used to indicate “wavelengths shorter than presently achieved” – deep UV and beyond. FEL performance can be modeled with various scaled parameters [4–6]; however, to determine the predictability of simulations we use wavelength as a fundamental parameter.

## 2. How FEL codes are presently used

The complexity and cost (in CPU time) associated with running three dimensional FEL codes along with the large parameter space available to explore, requires the use of

simpler and quicker means for initial design work. Often one begins with one dimensional analytic formulas in order to choose an operating regime. More elaborate models which include diffraction, energy spread, etc. and are easily implemented in spread sheets or mathematics solvers can then be used to perform an initial exploration of a design's sensitivity to parameters (an example is given in Fig. 2) [7]. A promising design can then be studied using three dimensional or multifrequency numerical codes.

An interesting question is whether the above process would be necessary if sufficient computing power were available. An incomplete answer is yes, since changes to the model (code) would still be more easily implemented in the analytic or spread sheet calculations. At present, it is time and CPU intensive to perform an exhaustive set of fully three dimensional, multifrequency simulations of a given design. As an example, for a given version of the SLAC LCLS, hours of NERSC Cray C-90 CPU time are required to perform three dimensional sensitivity studies.

A more relevant question is whether it is the numerical models or the measurement accuracy of beam and undulator parameters that limit present FEL performance predictability. With virtually no experimental data in the high gain short wavelength regime, this question will go unanswered here, save for a few comments in subsequent sections.

## 3. Strengths and weaknesses of the models

The question of what features of an FEL are modeled well by simulations would perhaps be answered differently by experimentalists and theorists: one experimentalist's

\* Corresponding author. Tel. +1 310 206 5584, fax +1 310 206 1091, e-mail travish@uclaph.physics.ucla.edu.

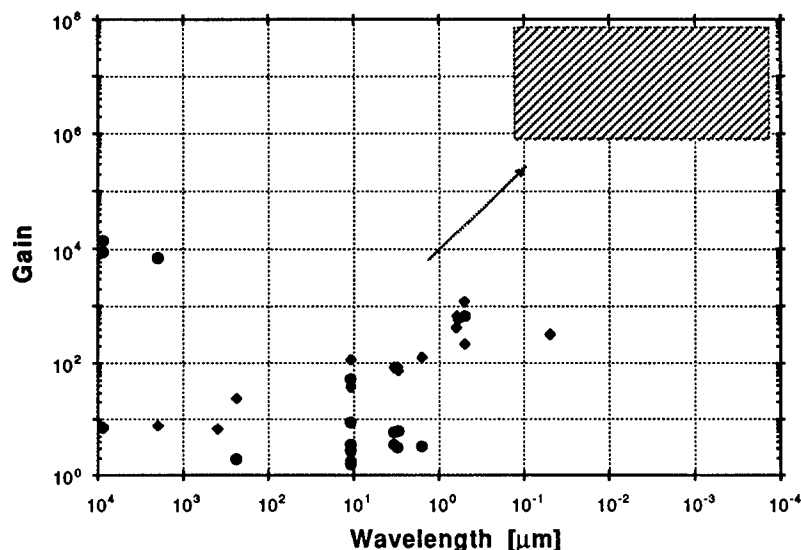


Fig. 1. Gain versus wavelength for a number of past FELs is plotted on a log-log scale. The shaded area represents the regime of the various recently proposed high gain, short wavelength FELs.

answer will be given here. The statements below hold in general for available codes; some comments may not apply to a particular code or set of parameters.

Let us begin with the good news. Simulations can include virtually any theoretically predicted or experimentally measured effect. New phenomena such as optical guiding was first “observed” through the use of numerical codes [8]. Parameters which are experimentally robust or accurately measurable have reliable numerical models. Simulations of high gain amplifiers can include startup from noise, optical guiding, slippage, harmonic generation,

multi-undulator systems, and undulator and alignment errors. However, in order to reduce the complexity and run time of the programs, different codes have been written to incorporate some, but not all of these effects (see Table 1).

Beam current and energy spread are considered well measured experimentally, and hence are well modeled numerically. Some codes can implement current distributions directly from field solvers or experimental data [9]. Another parameter which is in hand is beam steering errors due to mismatch and undulator field errors that are well modeled in three dimensional codes. Furthermore, straight forward BPM and steering magnet corrector schemes are implemented and understood both experimentally and within codes. The saturation regime also is well modeled in numerical codes, while useful analytic theories are still lacking [10]. A significant issue for short wavelength FELs which has received little experimental attention, but appears to be well modeled, is external focusing through quadrupoles, sextupoles, plasmas or other means [11]. Complex simulations including multiple undulators and dispersion sections are also implemented in some codes [12].

The “less good” news is that there are a number of effects which may not be well modeled, but without experimental verification it is difficult to emphatically state if our models are accurate. Emittance is both difficult to measure and model, as mathematical models for, e.g., rms emittance do not contain information about distribution function correlations. As a result, few analytic models make claims about slice emittance versus cooperation length emittance or beam core emittance versus the emittance within an optical mode. The lack of theoretical guidance makes a study of emittance effects incomplete

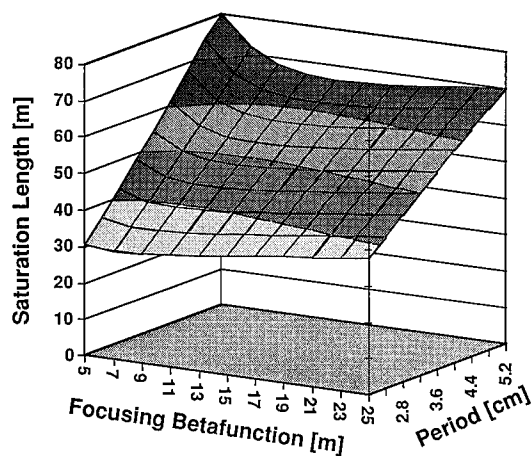


Fig. 2. An example of a multivariable optimization using a three dimensional semi-analytic model [26]. The parameters used here are similar to recent LCLS studies. The saturation length is plotted as a surface of the focusing beta function of the undulator period (assuming a fixed wavelength).

Table 1

A sample of FEL codes and some of their features [19–24]. Some codes have features not listed, others have limited capability in unmarked categories. For example, most codes have external focusing implements, but only ones with discrete focusing channels (not smooth approximations) were indicated.

|                    | Code name |        |        |        |       |       |
|--------------------|-----------|--------|--------|--------|-------|-------|
|                    | FELEX     | FRED3D | GINGER | NUTMEG | SARAH | TDA3D |
| 1D/2D/3D           | 3         | 3      | 2      | 2      | 1     | 3     |
| Time dependent     | yes       |        | yes    |        | yes   |       |
| Multiundulator     | yes       | yes    | yes    | yes    |       | yes   |
| Dispersion section |           |        |        | yes    |       |       |
| Startup model      | yes       |        | yes    |        | yes   |       |
| Steering errors    | yes       | yes    |        |        |       |       |
| Undulator errors   | yes       | yes    |        |        |       | yes   |
| Focusing           | yes       | yes    |        |        |       | yes   |
| Harmonics          | yes       |        |        | yes    |       |       |
| Optical modes      | yes       | yes    |        |        |       | yes   |

and time consuming. Multifrequency codes can model various emittance distributions, but only with azimuthal symmetry or with extensive run times. Issues such as fluctuations, startup from noise and superradiance are also not well tested nor sufficiently sophisticated [13]. As an example, startup from noise is often simulated by assuming an input signal equal to the spontaneous emission within one power gain length. Multifrequency codes also generate particle distributions with the correct Poisson statistics to emulate spontaneous emission levels which agree with analytic models. However, neither of these models may be sufficient to account for experimental conditions where a beam distribution may not be completely uncorrelated. As is discussed in Section 5, startup levels have yet to be well modeled.

The disparity between the  $\sim 10^4$  particles used in simulations and the  $\sim 10^{10}$  particles in a beam may present a formidable problem. At issue is the number of particles,  $N_\lambda$ , within a cubic (resonant) wavelength. For particle distributions with  $N_\lambda > 1$  higher spontaneous emission levels are expected due to coherent emission. Codes can model such distributions by simulating only a slice of the beam, and hence reduce the effective beam volume. Whether such approximations underestimate the actual startup level, or even contain the appropriate effects, is unclear without experimental measurements of SASE.

#### 4. Model verification

Assuring the validity of a simulation requires both programming skills and physical insight. Codes often differ in the numerical methods used to solve a model and in the assumptions made in the model [14]. Agreement between two codes often lends credence to both programs; discrepancies often lead to improvements. Simulation results can also be checked against simplified models. Using parameter sets within one dimensional limits (no energy spread, smooth focusing, no diffraction or other assumptions) allows rapid comparison with analytic results. Additionally, numerical diagnostics (phase space plots, energy conservation checks, bunching parameters, etc.) can be generated within a program allowing for further verification of model performance. Nevertheless, numerical comparisons and verifications do not substitute for experimental authentication.

#### 5. Comparison with experiment

A pessimist's version of this section would be very short: there are no short wavelength, high gain experi-

Table 2

Comparison of the predicted and experimentally measured effective startup power for some of microwave FELs [25].

| FEL name | $\lambda_s$ (f)       | $I_b$<br>(kA) | $\rho \times 10^2$ | $\epsilon$ | Predicted<br>noise (mW) | Measured<br>noise (mW) |
|----------|-----------------------|---------------|--------------------|------------|-------------------------|------------------------|
| ELF      | 8 mm (35 GHz)         | 1             | 5.0                | 1.0        | 0.4                     | 1.5                    |
| ELF      | 3 mm (94 GHz)         | 1             | 3.5                | 1.4        | 0.5                     | 30                     |
| ELF      | 2 mm (140 GHz)        | 1             | 2.8                | 2.5        | 0.4                     | 175                    |
| PALADIN  | 10.6 $\mu$ m (30 THz) | 1             | 0.8                | 1.5        | 40                      | ?                      |
| IMP      | 1.2 mm (250 GHz)      | 3             | 4.0                | 0.8        | 5.3                     | ?                      |

ments. Still, a number of other FEL experiments can be used to evaluate the predictive powers of our codes.

Oscillator experiments have operated from microwave to UV wavelengths with a variety of beam energies and currents. Good agreement has been reported between experiments and simulations [15]. “After the fact” simulations have the best agreement since deviations from design are included. The previous statement is not trite; the errors and practical problems involved in an experiment often dominate over the errors caused by simplifications made in a model. This fact implies that simulations must include all known sources of error such as undulator field errors, beam parameter variations, misalignments and steering errors.

High gain experiments have been performed at microwave frequencies and in the IR at the LLNL ATA Paladin [16]. The microwave results lend credence to the simulations ability to predict growth rates, saturation, performance variation with current and undulator specifications. Little consistent agreement is available for self-amplified spontaneous emission (SASE) (see Table 2). The Livermore IR FEL also showed good agreement with simulations on growth, optical guiding and saturation, but no SASE results were measured. While few measurements have been made, those that have indicate that theoretical predictions underestimate the startup power level. Relevant experimental work is clearly lacking especially in two major areas: SASE and short wavelengths (beyond visible).

## 6. Conclusions on extrapolating to short wavelengths

Extrapolating results is at best a questionable practice. Extrapolating FEL results is particularly difficult due to the limited knowledge of electron beam characteristics in even the most carefully controlled experiments. The added complexity of simulating the various tolerance and errors further reduces the reliability of projections. And there is always the possibility of new physics unaccounted for in present simulations.

The need for staged experiments to address the issues relevant to short wavelength, high gain systems has been stressed throughout this paper. In response to this need, initial experiments are being prepared at BNL [17] and UCLA [18]. Both Brookhaven and UCLA are developing and improving the codes needed to simulate their respective systems. The results from these experiments, and hopefully others to follow, should allow for the verification and improvement of our codes to a level sufficient to design the next generation of FELs.

At present, simulations are not sufficiently well tested to rely on their predictive power for the short wavelength, high gain regime.

## Acknowledgements

This work was supported by the Department of Energy Grants DE-FG03-90ER40796 and DE-FG03-92ER40693 and by the UCLA Department of Physics. The author gratefully thanks Kwang-Je Kim and the other members of the FEL '94 organizing committee. Bill Fawley, John Goldstein, Mark Hogan, Heinz-Deiter Nuhn, Claudio Pellegrini, James Rosenzweig, Ted Scharlemann and Ming Xie provided many useful comments and discussions.

## References

- [1] C. Pellegrini et al., Proc. 14th Int. FEL Conf., Kobe, Japan, Aug. 24–28, 1992, Nucl. Instr. and Meth. A 331 (1993) 223.
- [2] DUV Conceptual Design Report, BNL (1994).
- [3] I. Ben-Zvi and H. Winick (eds.), BNL Report 49651 (1993).
- [4] R. Bonifacio, C. Pellegrini and L. Narducci, Opt. Commun. 50 (1984) 373.
- [5] L.H. Yu, S. Krinsky and R.L. Gluckstern, Phys. Rev. Lett. 64 (1990) 3011.
- [6] W.A. Barletta, A.M. Sessler and L.H. Yu, Proc. 14th Int. FEL Conf., Kobe, Japan, Aug. 24–28, 1992, Nucl. Instr. and Meth. A 331 (1993) 491.
- [7] Y.H. Chin, K.-J. Kim and M. Xie, Phys. Rev. A 46 (1992) 6662; M. Xie, to be published.
- [8] E.T. Scharlemann, A.M. Sessler and J.S. Wurtele, Nucl. Instr. and Meth. A 239 (1985) 29.
- [9] J.C. Goldstein, B.E. Carlsten and B.D. McVey, Nucl. Instr. and Meth. A 296 (1990) 273.
- [10] R.L. Gluckstern, S. Krinsky and H. Okamoto, Proc. 1993 IEEE Particle Accelerator Conf., p. 1545.
- [11] G. Travish and J. Rosenzweig, Proc. 1993 IEEE Particle Accelerator Conf., p. 1548.
- [12] See studies in Ref. [2].
- [13] R. Bonifacio et al., Nucl. Instr. and Meth. A 341 (1994) 181.
- [14] T.M. Tran and J.S. Wurtele, Phys. Rep. 195 (1990) 1.
- [15] L. Thode et al., Proc. Conf. Computer Codes and Linear Accelerators, LANL report LA-11857-C (1990).
- [16] J.T. Weir et al., Proc. SPIE 1133 (1989) 97.
- [17] I. Ben-Zvi et al., Nucl. Instr. and Meth. A 318 (1992) 208.
- [18] See G. Travish et al., these Proceedings (16th Int. Free Electron Laser Conf., Stanford, CA, USA, 1994) Nucl. Instr. and Meth. A 358 (1995) ABS 75.
- [19] FELEX: B.D. McVey, Nucl. Instr. and Meth. A 250 (1986) 449.
- [20] FRED: E.T. Scharlemann et al., J. Appl. Phys. 58 (1985).
- [21] GINGER: W.M. Fawley, private communication.
- [22] NUTMEG: W.M. Sharp, E.T. Scharlemann and W.M. Fawley, Nucl. Instr. and Meth. A 296 (1989) 335.
- [23] SARAH: P. Pierini, private communication.
- [24] TDA3D: T.M. Tran and J.S. Wurtele, Comput. Phys. Commun. 54 (1989) 263.
- [25] This table was provided by W.M. Fawley.
- [26] The data for this graph was produced by M. Xie.



ELSEVIER

# Milestone experiments for single pass UV/X-ray FELs <sup>☆</sup>

Ilan Ben-Zvi <sup>\*</sup>*Brookhaven National Laboratory, Upton NY 11973, USA*

## Abstract

In the past decade, significant advances have been made in the theory and technology of high brightness electron beams and single pass FELs. These developments facilitate the construction of practical UV and X-ray FELs and has prompted proposals to the DOE for the construction of such facilities. There are several important experiments to be performed before committing to the construction of dedicated user facilities. Two experiments are under construction in the IR, the UCLA self-amplified spontaneous emission experiment and the BNL laser seeded harmonic generation experiment. A multi-institution collaboration is being organized about a 210 MeV electron linac available at BNL and the 10 m long NISUS wiggler. This experiment will be done in the UV and will test various experimental aspects of electron beam dynamics, FEL exponential regime with gain guiding, start-up from noise, seeding and harmonic generation. These experiments will advance the state of FEL research and lead towards future dedicated users' facilities.

## 1. The need for new experiments

In the past decade, significant advances have been made in photoinjectors with emittance compensation [1], transport, acceleration and compression of high brightness beams without emittance dilution [2], in high precision undulators [3] and in FEL theory and simulations [4]. Thus single-pass, high-gain FEL operation may be extended to wavelengths a few orders of magnitude shorter than that achieved to date.

Several groups in the USA are developing plans for such short wavelength single-pass FEL facilities [5,6], and thus it would be highly desirable to carry out proof-of-principle experiments to increase confidence that the shorter wavelength devices will indeed perform as calculated. The need for such experiments has been the main focus of a recent workshop [7]. Recommendations for the direction of research in FEL amplifiers made at this workshop as a description of the single pass FEL experiments that are in progress are the subject of this report.

Other workshops [8–14] have begun to address the scientific opportunities such FELs would create. The Department of Energy commissioned a comprehensive study of these opportunities by the National Research Council [15]. There are various approaches to the construction of short wavelength FELs. One can discuss oscillators and

amplifiers in various combinations and with diverse particle accelerators. In the following we will limit the discussion to single-pass, linac-based FELs in the optical regime.

## 2. The PALADIN experiment

The first (and so far only) single-pass, optical-regime FEL amplifier experiment was conducted at Lawrence Livermore National Laboratory [16]. The accelerator used in these experiments was the ATA, a 45-MeV, 3-kA induction linac. The actual current used was filtered with an emittance selector to about 500–700 A. This increased the beam brightness, since the beam had a bright core with most of the current in a low brightness halo.

The undulator in this experiment was the 8 cm period, 2.5 kG, 3 cm gap, 25 m long PALADIN wiggler. This is a high-precision electromagnetic wiggler with parabolic pole face focusing, independent excitation of sections of two periods and binomial coefficient windings. Thus its length and its tapering could be varied on line.

The FEL experiments that were carried out were single pass amplification of a 10.4  $\mu\text{m}/\text{CO}_2$  laser. The experimental results were compared to LLNL simulation codes with reasonable agreement. The launching and exponential growth in the high gain regime and saturation were measured, and gain guiding was convincingly demonstrated. Unfortunately the beam brightness was not sufficient for demonstrating tapering. Also neither Self-Amplified Spontaneous Emission (SASE), nor issues of fluctuations and temporal structure were measured. Previous SASE experiments in the exponential-growth regime were conducted at

<sup>☆</sup> Work supported by the US Department of Energy under contract No. DE-AC02-76CH00016

<sup>\*</sup> Corresponding author. Tel. +1 516 282 5143, fax +1 516 282 3029, e-mail: benzvi@bnlls1.nsls.bnl.gov.

LLNL at millimeter wavelengths. It was noted that noise was higher than expected in these cases.

### 3. "Towards Short Wavelength FELs" Workshop

Reviewers of facility plans for short-wavelength FELs realized there is need for "proof-of-principle" experiments beyond PALADIN. The Workshop "Towards Short Wavelength FELs" (TSW-FEL) was organized to address this concern. The objectives of this workshop, as distributed to the attendees, were:

- 1) Define measurements needed to gain confidence that short wavelength FELs will perform as calculated.
- 2) List possible hardware that could be used to carry out these measurements.
- 3) Define a prioritized FEL physics experimental program and suggested timetable.
- 4) Form collaborative teams to carry out this program.

The TSW-FEL Workshop included a panel discussion of *Defining Critical Experiments and Their Parameters*, chaired by A. Sessler (LBL). The panel, along with contributions from workshop participants, led to a definition of the most important measurements that should be carried out in proof-of-principle experiments.

The panel called for further development of photoinjector guns, including emittance compensation. After the gun, the beam must be accelerated and the bunch length must be compressed to attain the required energy and peak current. During these processes, the emittance must be kept small with a high degree of stability. Bunch compression increases the sensitivity to jitter, making the stability difficult to achieve. A demonstration experiment is desirable for verification.

The Sessler Panel concluded that it is critical to study, at a wavelength intermediate between millimeter waves and ultraviolet or shorter, the start-up of an FEL from noise, exponential growth over several gain lengths, and saturation. Information is needed about such issues as optical guiding and transverse mode structure; the saturation length and power; spatial and temporal coherence; and fluctuations in position, wavelength, and power. Two IR experiments are directed at these questions. A SASE FEL at UCLA (10  $\mu\text{m}$ ) and harmonic generation at BNL (10.5  $\mu\text{m}$ , converted to 3.5  $\mu\text{m}$ ). This infrared work should then be followed by a similar demonstration of SASE in the VUV, at about 100 nm or shorter. The longer wigglers required in the VUV will allow tests of the sensitivity to field and steering errors, and the effect of external focusing. Techniques for building and aligning long, high-field wigglers, and for steering, focusing, and diagnosing beams within them, must be developed.

A session on the *Availability of Resources*, chaired by G. Neil (CEBAF), followed. In this session, various groups described existing equipment that could be used to carry out proof-of-principle experiments. The equipment that

might be used was described in detail, and included available injectors, accelerators and wigglers. In most cases the equipment located at any single site was inadequate to carry out a full program of proof-of-principle experiments. This led to consideration of collaborations to collect at one site enough equipment from several sites to minimize the cost of constructing new equipment. This phase of the workshop started as a group discussion, chaired by B. Newnam (LANL).

During this session, the workshop participants reached consensus on several criteria that would be useful in establishing a prioritized FEL experimental program for extending FEL operation into the extreme ultraviolet and beyond. It was agreed to focus our efforts on a few key experiments that would make maximum impact with limited funds.

Three working groups were established to meet during subsequent sessions to develop experimental programs based on collaborations among the various institutions who could contribute hardware and/or expertise. The working groups were assigned the task of assembling relevant experiments utilizing, to the greatest extent possible, existing equipment and facilities.

Of these groups, the most relevant for this presentation was the one on linac-driven amplifiers (both injection-seeded and self amplified spontaneous emission) led by A. Fisher (BNL) and K.-J. Kim (LBL). Some of the scenarios studied by this group are described below.

### 4. The UCLA SASE experiment

A compact, infrared, high-gain, FEL amplifier is being constructed at UCLA to verify the FEL physics relevant for future X-ray FELs [17]. In this experiment, a 4 MeV beam generated by an RF photocathode gun with a copper cathode (Brookhaven-type gun, at 2856 MHz) will be accelerated by a plane-wave transformer (PWT) linac to  $\sim 17$  MeV. The expected beam parameters are summarized in Table 1. When sent through the existing Kurchatov undulator, which has a 1.5-cm period, a 60 cm length (40 periods) and a peak field of  $\sim 7.25$  kG ( $K \sim 1$ ), this beam will produce 10  $\mu\text{m}$  radiation. The system operates with single bunches. The expected FEL performance is given in Table 1.

All the components for this experiment are in place and rf tests are being conducted on the linac. Initially, UCLA will study gain length as a function of the beam parameters, start-up from noise and lethargy, and saturation starting from a seed-laser pulse. Further studies will include optical guiding, coherence, slippage effects, and additional saturation studies (i.e., superradiance). In particular it will be interesting to study the fluctuation level and temporal structure of the radiation [18]. Calculations done for the SLAC LCLS project at 4 nm predict that fluctuations in intensity of up to 10% may be possible, therefore it is

Table 1  
Parameters for the UCLA FEL

|                          |                         |             |
|--------------------------|-------------------------|-------------|
| Energy                   | ~ 17                    | MeV         |
| Emittance (norm., rms)   | $\sim 5 \times 10^{-6}$ | $\pi$ m-rad |
| Energy spread (rms)      | 0.1                     | %           |
| Peak current             | 200                     | A           |
| Pulse length (rms)       | 2                       | ps          |
| Repetition rate          | 0–5                     | Hz          |
| Power gain length        | < 7.6                   | cm          |
| FEL parameter ( $\rho$ ) | $\sim 10^{-2}$          |             |
| SASE saturation length   | 160                     | cm          |
| Saturated power          | ~ 20                    | MW          |
| Peak power at 60 cm      | ~ 1                     | kW          |

Table 2  
Parameters for the HGHG experiment

|                             |                     |             |
|-----------------------------|---------------------|-------------|
| Energy                      | 30.6                | MeV         |
| Emittance (norm., rms)      | $7 \times 10^{-6}$  | $\pi$ m-rad |
| Energy spread (rms)         | 0.04                | %           |
| Peak current                | 110                 | A           |
| Wiggler length              | $0.31 + 0.12 + 1.5$ | m           |
| Wiggler period              | 2.6, 12, 1.8        | cm          |
| Wiggler field               | 0.8, ~ 0.9, 0.52    | T           |
| Tapered length              | 1.2                 | m           |
| Maximal taper               | 10                  | %           |
| Input power at 10.5 $\mu$ m | 1.6                 | MW          |
| Gain length (radiator)      | 0.215               | m           |
| Output power, 3.5 $\mu$ m   | 30                  | MW          |

important to provide experimental verification of the theory. A second undulator would make possible studies of saturation from SASE, operation in an optical-klystron configuration, and e-beam focusing between the undulators.

### 5. The high gain harmonic generation FEL

The BNL HGHG [19] experiment (see Table 2) will test the principle of high-gain harmonic generation from a 10  $\mu$ m seed laser. The experiment will demonstrate in the infrared the essential physics underlying BNL's DUV-FEL proposal. In the DUV-FEL, a tunable beam in the near IR is converted to the near UV using conventional harmonic-generation crystals. This radiation is then used to seed an FEL designed to radiate into the VUV (down to 75 nm), where conventional high-power laser sources are unavailable. Unlike FEL oscillators, there is no need for a UV resonator and its problems of mirror losses and damage. Unlike SASE or oscillators, the tunability, bandwidth, wavelength stability, pulse length, pulse format and op-

tional frequency chirp of the resulting beam will be determined by the source laser.

The HGHG experiment uses BNL's Accelerator Test Facility (ATF). A 10.6  $\mu$ m, 1.6 MW, CO<sub>2</sub> laser input will generate a 3.53  $\mu$ m, 30 MW output in a three-stage wiggler magnet. The seed beam will modulate a 30 MeV electron beam in the first, 31 cm long wiggler, synchronous at 10.6  $\mu$ m. The electrons will bunch in a 12 cm long dispersive section, then radiate in the third section, a 150 cm wiggler synchronous at 3.5  $\mu$ m. The radiator wiggler has parabolic pole-face focusing and includes an adjustable taper over its final 125 cm.

The experiment will allow detailed measurements of harmonic generation, exponential growth, saturation, tapering, and bandwidth. Furthermore, the rather long (1.5 m) radiator wiggler can be used without the modulator for SASE studies. The design, construction, alignment, and operation of a long, high-field, superferic wiggler [20] will be demonstrated.

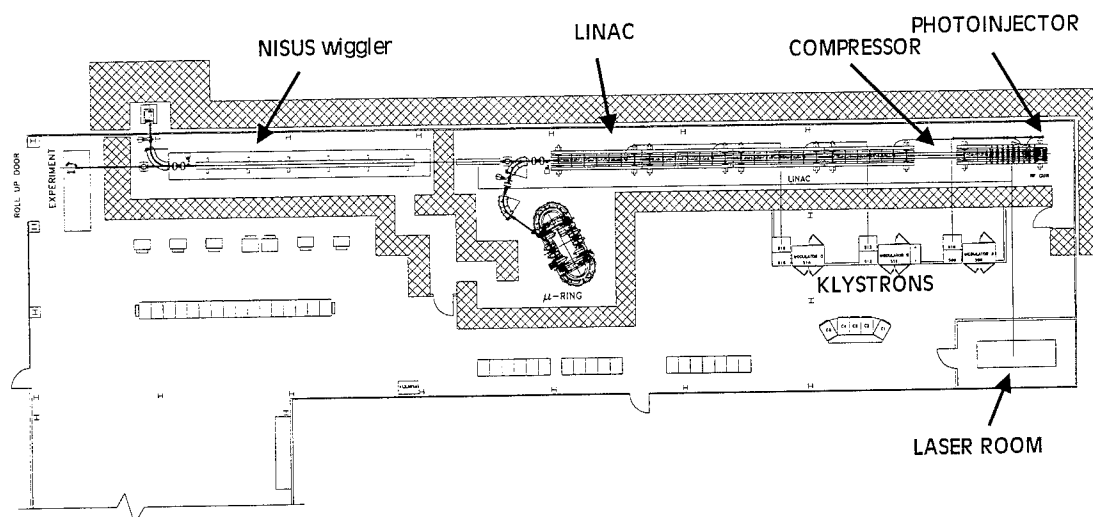


Fig. 1. The layout of the UV project 210 MeV linac with the NISUS wiggler.



## 6. Further experiments

Following the initiative of the TSW-FEL Workshop, collaborations comprising laboratories, industry and universities with interest in this direction of research are being organized.

A highly informal collaboration called “Gun III Collaboration”, comprising BNL, SLAC and UCLA started about one year ago. The objective of this collaboration is to design an improved version of the BNL photoinjector gun. The planned improvements are a simpler construction, improved cathode replacement cover, larger aperture, improved rf coupling port and higher radial symmetry.

Another collaboration is being formed right now to carry out the short wavelength experiments recommended by the TSW-FEL Workshop. The major pieces of equipments, including the linear accelerator, the wiggler and building, will be in place shortly. The linac is a 210 MeV S-band linac at the National Synchrotron Light Source at BNL. The wiggler is NISUS, built by STI Optronics for Boeing under a SDI contract. This wiggler is 10-m long, with a period of 3.9 cm. With the addition of a photoinjector, it will be possible to carry out most of the recommended research at a short wavelength, down to 150 nm and thus provide a much needed benchmark. The layout of this facility is shown in Fig. 1.

Possible demonstration experiments on this linac include the production of high-brightness electron beams, and the exploration of short-wavelength FEL physics issues relevant to VUV and soft X-ray devices: startup from spontaneous radiation, coherence, saturation and seeding. Calculations were made [21] for the performance of NISUS at 0.33 T, resonating at 200 nm with a 210-MeV beam. A current of 300-A, rms normalized emittance of  $6.5 \pi$  mm-mrad and rms energy spread of 0.043% were assumed. The result is a power e-folding length of 1.23 m, betatron wavelength of 26 m and a Raleigh-range over power gain-length ratio of 10.4. The power gain-length is not short enough to reach saturation in the 10-m long wiggler, but it is possible that with bunch compression and better emittance saturation can be reached.

Another exciting possibility is the application of the Chirped Pulse Amplification (CPA) technique. The performance has been calculated for a CPA FEL with HGHG amplification of a chirped Ti:sapphire laser, using a 2-m long modulator wiggler and the NISUS wiggler as a radiator. The result is a power output of 30 GW at 200 nm with a pulse length of 10 fs [22].

Other experiments should also be undertaken. One is beam conditioning [23], the technique that introduces momentum variations correlated with betatron amplitude. This correlation will correct the deleterious effects of the beam's emittance. Ultimately this technique may lead to extremely short wavelength FELs with relatively low energy linacs.

Another valuable experiment would be the demonstration of a wiggler that incorporates strong focusing, as the optimal focusing strength (for best growth rate) increases beyond natural focusing at short wavelengths.

## References

- [1] P. O'Shea, these Proceedings (16th Int. Free Electron Laser Conf., Stanford, CA, USA, 1994) Nucl. Instr. and Meth. A 358 (1995) 36.
- [2] T. Raubenheimer, *ibid.*, p. 40.
- [3] R. Schlueter, *ibid.*, p. 44.
- [4] G. Travish, *ibid.*, p. 48.
- [5] The BNL DUV FEL Conceptual Design Report, ed. S. Krinsky, BNL-49713 (1994).
- [6] C. Pellegrini et al., Nucl. Instr. and Meth. A 341 (1994) 326 and presented at this Conference (16th Int. Free Electron Laser Conf., Stanford, CA, USA, 1994).
- [7] I. Ben-Zvi and H. Winick (eds.), Towards Short Wavelength Free-Electron Lasers Workshop, May 21–22, 1993, BNL, Upton, NY, BNL 49651 (1993).
- [8] Application of Coherent XUV Radiation Workshop, Los Alamos Nat. Lab., Feb. 7, 1986, ed. B.E. Newnam.
- [9] FEL Applications in the Ultraviolet, Opt. Soc. Amer. Topical Meeting, Cloudcroft, New Mexico, March 1988, eds. D.A.G. Deacon and B.E. Newnam J. Opt. Amer. 8 May (1989).
- [10] Report from the NSLS Workshop on Sources and Applications of High Intensity UV-VUV Light, eds. E.D. Johnson and J.B. Hastings, January 1990, BNL 45499.
- [11] Scientific Applications of Short Wavelength Coherent Sources Workshop, SLAC, Oct 21, 1992, SLAC Report 414, eds. W. Spicer, J. Arthur and H. Winick.
- [12] Prospects for a 1 Å Free-Electron Laser Workshop, Sag Harbor, NY, April 22–27, 1990, BNL 52273, ed. J. Gallardo.
- [13] Soft X-ray Science with the Duke FEL Lab Radiation Sources Workshop, Durham, NC, March 1993, ed. L. Knight, X-ray Science and Technology.
- [14] Scientific Applications of Coherent X-Rays Workshop, SLAC, February 12, 1994, SLAC Report 437, eds. J. Arthur, G. Materlik and H. Winick.
- [15] D. Levy, National Research Council Report Summary, presented at this Conference (16th Int. Free Electron Laser Conf., Stanford, CA, USA, 1994).
- [16] T.J. Orzechowski, AIP Conf. Proc. 249 (1992) p. 1939, eds. 6M. Month and M. Dienes.
- [17] G. Baranov et al., Nucl. Instr. and Meth. A 331 (1993) 228.
- [18] R. Bonifacio, L. De Salvo, P. Pierini, N. Piovella and C. Pellegrini, Nucl. Instr. and Meth. in Phys. Res. A 341 (1994) 181.
- [19] I. Ben-Zvi, A. Friedman, C.M. Hung, G. Ingold, S. Krinsky, L.H. Yu, I. Lehrman and D. Weissenburger, Nucl. Instr. and Meth. A 318 (1992) 208.
- [20] L. Solomon, W.S. Graves and I.S. Lehrman, Ref. [1], p. 411.
- [21] L.H. Yu, private communication.
- [22] L.H. Yu, private communication.
- [23] A.M. Sessler, D.H. Whittum and L.H. Yu, Phys. Rev. Lett. 64 (1992) 309.

# Particle beam modulation techniques for the generation of subfemtosecond photon pulses in the VUV/soft X-ray range

Roman Tatchyn \*

Stanford Synchrotron Radiation Laboratory, Stanford Linear Accelerator Center, Stanford, CA 94305, USA

## Abstract

In this paper we consider the energy modulation of a short subinterval of an electron bunch at the scale length of visible/UV laser light. Possibilities for converting this modulation into a high-gain FEL-type density fluctuation to produce a coherently-enhanced subfemtosecond radiation pulse in the VUV/soft X-ray range are discussed.

## 1. Introduction

The photon pulse length generated by a single relativistic electron passing through an accelerating field of length  $l$  can be approximated by  $l/2\gamma^2$ , where  $\gamma$  is the Lorentz contraction factor [1]. For example, for  $l = 0.25$  m and  $\gamma = 1000$ , the pulse length is  $0.125$   $\mu\text{m}$ , which translates into a duration of  $0.42$  fs. The straightforward attainment of these and substantially shorter temporal lengths, however, is ordinarily inhibited by two related factors. First, since a single electron typically emits on the order of 1 photon per pass (pulse), bunches with large numbers of electrons must be employed to emit a useful number of photons. Second, since multi-electron bunches in conventional machines are typically much longer than  $10^{-4}$  m, the temporal pulse length in the case of spontaneous emission becomes defined by the convolution of the bunch density profile (of effective width  $\sqrt{2\pi}\sigma_B$ ) with the single-electron photon pulse profile. Since for readily available values of  $l$  and  $\gamma$  this pulse is typically a delta function, viz.,

$$\sqrt{2\pi}\sigma_B \gg l/2\gamma^2,$$

the temporal pulse length becomes approximable by  $\sqrt{2\pi}\sigma_B/c$ , where  $c$  is the velocity of light. In coherence-enhanced emission, such as, e.g., generated by Gaussian bunches in single-pass Free-Electron Lasers (FELs), the temporal profile of the output radiation can be significantly sharper than the bunch density profile, but in many cases of practical interest it still encompasses an appreciable fraction of the bunch length.

In prior work, pulse-compression techniques based on real or reciprocal space-time modulation of both the particle and photon bunches have been considered [2]. Among the more direct methods based on particle bunch modulation are: 1) schemes for reducing the total bunch length  $\sigma_B$  [3,4]; and 2) selective energy modulation of subintervals of the bunch [5,6] followed by the density modulation, or microbunching, of the beam on a scale  $\lambda_r$  (with  $\lambda_r \ll \sigma_B$ ) via, e.g., the FEL or Optical Klystron (OK) process [7]. Since the radiation is a non-linear function of the microbunch density, strong enhancement of the output pulse in the central region of the (macro) bunch can lead to sharpened temporal profiles. In the present paper we examine a limiting case of this latter approach, viz., the modulation of the energy of an isolated subregion of the particle bunch at the scale length of visible/UV laser light and the conversion of this modulation into a density fluctuation which is then further longitudinally compressed via a high-gain FEL-type bunching process to provide a short coherently-enhanced radiation pulse in the VUV/soft X-ray range.

## 2. Single-pulse energy modulation

As in the cited prior analysis of the OK [7], the present method can be separated into three steps [5]: 1) energy

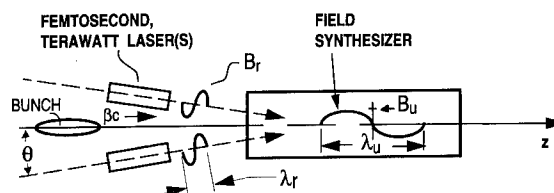
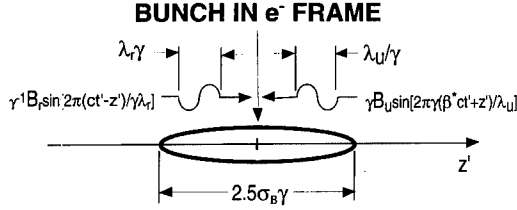


Fig. 1. Energy modulation system using a femtosecond laser(s) and a field synthesizer.

\* Tel. +1 415 926 2731, fax +1 415 926 4100, e-mail tatchyne@ssrl750.

Fig. 2. Field interaction in  $e^-$  frame.

modulation; 2) bunching in a dispersion section; and 3) coherence-enhanced radiation. The basic length scale of the modulated region of the electron bunch is determined by the energy modulator, shown schematized in Figs. 1

and 2. For simplicity, the visible/UV femtosecond (fs) laser(s) can be assumed to emit single cycles of radiation which arrive in conjunction with the beam into the field region of a field synthesizer (FS) [8] with a  $K$  parameter substantially smaller than 1. Both the laser and undulator fields are assumed to be plane polarized with the magnetic components lying in the same plane, with their first field integrals equal to 0. Departures from these idealizations and assumptions can be accounted for in a more general analysis. As shown in Fig. 2, in the rest frame of the electron bunch the transformed fields of the laser(s) and the FS move through each other with practically equal velocities, inducing a maximum energy modulation in selected intervals of the region where they intersect. Away

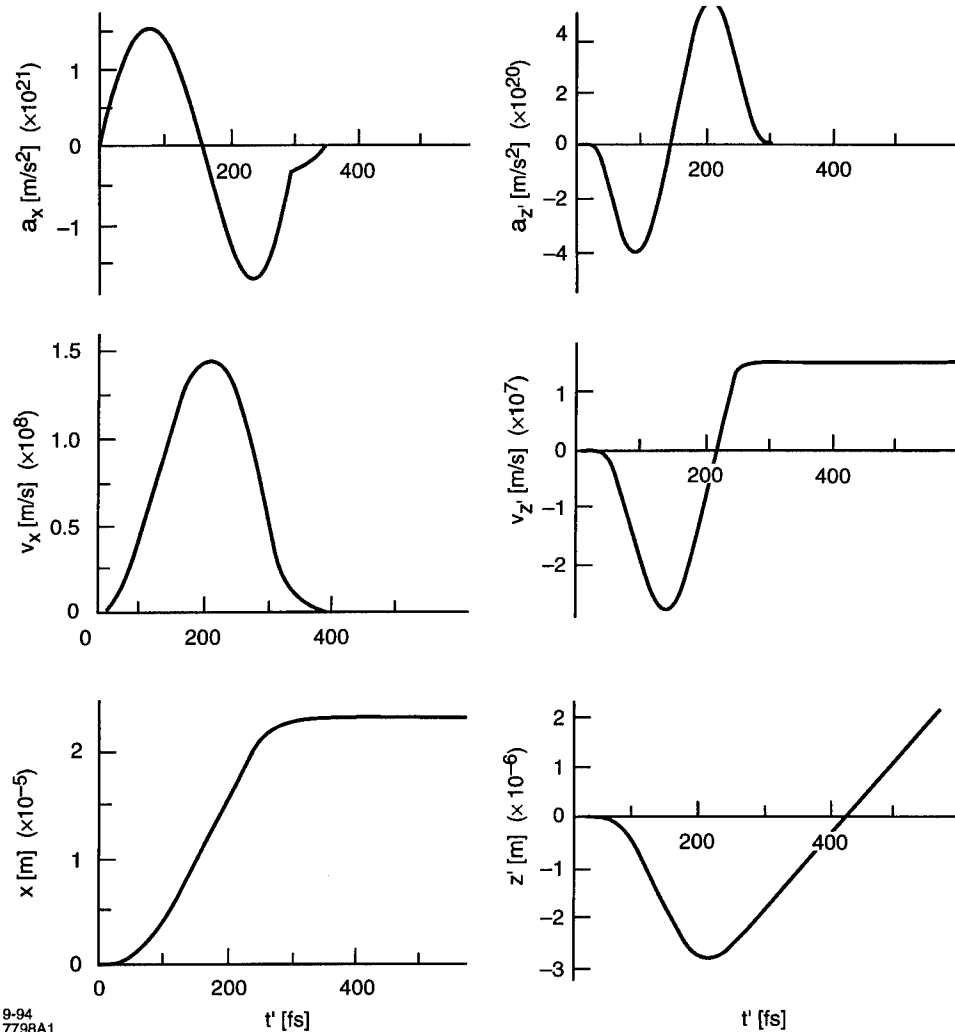


Fig. 3.  $x$  (left) and  $z'$  (right) components of electron motion in the  $e^-$  frame. Assumed parameters:  $\gamma = 300$ ;  $\lambda_L = 4800 \text{ \AA}$ ; laser waist  $0.1 \text{ mm}$ ; laser power  $4.3 \text{ TW}$ ;  $\lambda_u = 8 \text{ cm}$ ;  $B_u = 0.032 \text{ T}$ ,  $v_x(0) = v_z(0) = 0$ .

from the intersection area, the net energy modulation of any electron averages to 0, by symmetry. Viewed in the lab frame, the necessary conditions for maximal modulation are:

$$\lambda_r \equiv (\lambda_u/2)(\gamma^{-2} + \theta^2), \quad (1)$$

and

$$B_r \equiv 0.6B_u/(\gamma^{-2} + \theta^2). \quad (2)$$

The temporal length,  $\Delta\tau$ , of the spontaneous pulse emitted by the maximally modulated section of the bunch, for small  $\theta$ , is approximable by  $\Delta\tau \approx 2\lambda_u(1 - \beta \cos \theta)/c \cos \theta$ . Assuming the transformed fields to be represented by single cycles of a sinusoidal function, as in Fig. 2, the  $x'$  and  $z'$  components of electron motion in the bunch are modulated according to the equations

$$\ddot{x}' = -\left(\frac{qc}{m}\right)\{\gamma B_u \sin(\omega_u t' + k_u z' + \phi_u) + B_r \gamma^{-1} \sin(\omega_r t' - k_r z' + \phi_r)\}, \quad (3)$$

and

$$\ddot{z}' = \left(\frac{q}{m}\right)^2 \left(\frac{1}{2k_u}\right)\{\gamma^2 B_u^2 \sin 2(\omega_u t' + k_u z' + \phi_u) - B_r^2 \gamma^{-2} \sin 2(\omega_r t' - k_r z' + \phi_r) + 2B_r B_u \sin((k_u + k_r)z' + (\phi_u - \phi_r))\}. \quad (4)$$

Here  $k_u$ ,  $k_r$ , and  $\omega_r$  are defined in Fig. 2 and  $\phi_u$  and  $\phi_r$  are the phases of the two fields with respect to the electron in question.

In considering the mechanism of energy transfer for selected electrons in the bunch, we will assume: 1) the bunch to be cold, and 2) the energy transfer to be dominated by radiative interactions. Exactly midway between two converging waves fulfilling condition (2), their magnetic components will cancel and an electron will only experience transverse motion with no net transverse or longitudinal kick. For an electron a distance  $\pm \lambda_u/8\gamma$  away from this position, however, motion in the  $z$  direction will be induced by its transverse velocity coupling to the net magnetic component of the superimposed undulator and laser fields. Electrons at these two locations will experience maximal kicks toward the nearest minima of the superimposed undulator and laser fields. More generally, net (albeit weaker) longitudinal kicks will be generated when  $B_r \neq 0.6B_u/(\gamma^{-2} + \theta^2)$ . In Fig. 3 numerical solutions for the  $x(=x')$  and  $z'$  motions of an electron interacting with the electric and magnetic components of the field synthesizer and laser fields are shown for a particular set of laser and undulator parameters.

### 3. Compression

Following the energy modulator, a subinterval of the bunch will have a gamma distribution describable by

$\gamma + \Delta\gamma(z)$ . For the parameters utilized in this paper, we can assume that any  $z'$ -displacements of the modulated electrons are negligible with respect to the FS modulation period in the bunch frame. The whole bunch is then passed through a dispersion section consisting of a single FS period of length  $L_D$  and strength  $K$  where compression of the modulated subinterval will occur. The functional form of  $\Delta\gamma$  vs.  $z$  prior to compression will depend on a number of factors, including the ratio of  $B_r$  vs.  $B_u$ , their magnitudes, and the detailed density profile of the bunch in the modulated region. For our present discussion we assume that special modulation techniques can be applied to the bunch (e.g., by introducing a correlated energy spread in the accelerator or by shaping the laser and FS field profiles) and in the dispersion section to make the net energy modulation approximately linear in  $z$ , allowing the derivation of simple figures of merit.

If the modulated region is partitioned into  $N$  increments in the longitudinal direction we can write the net modulated gamma difference between the 1st and  $N$ th increments as  $\Delta\gamma_{1N}$ . In terms of this figure the required parameters for the dispersion section are defined by

$$L_D(1 + (K^2/2)) = \lambda_u(\gamma/2\Delta\gamma_{1N}). \quad (5)$$

For a real beam with a homogeneous (uncorrelated) energy spread  $\sigma_e$ , and vertical and horizontal angular spreads  $\sigma'_v$  and  $\sigma'_H$ , a straightforward calculation yields the following estimate for the minimal attainable ratio of the length,  $\Delta_{\min}$ , of the compressed region to the wavelength of the laser:

$$\frac{\Delta_{\min}}{\lambda_r} \approx \frac{\gamma}{\Delta\gamma_{1N}} \sqrt{2\pi\sigma_e^2 + \frac{(\pi(\sigma_v'^2 + \sigma_H'^2))^2 \gamma^4}{(1 + K^2/2)}}. \quad (6)$$

For example, assuming typical bunch and dispersion section parameters  $\sigma_e = 0.1\%$ ,  $\sigma'_v = \sigma'_H = 0.0001$  rad, and  $K = 4$ , a relative (and linear) energy modulation of 5% is seen to allow a compression of the modulated region down to approximately 5% of its initial length.

Following compression down to this length ( $\Delta_{\min}$ ), a coherence-enhanced radiation pulse is induced by a final FS section, e.g., a single-period field tuned to a wavelength  $\lambda$  fulfilling the condition  $\Delta_{\min} < \lambda < \lambda_r$ . For example, for  $\lambda_r = 4800$  Å and  $\lambda = 480$  Å, a temporal pulse length of 0.16 fs can be attained.

### 4. Summary

A method for preparing subfemtosecond pulses in the VUV/soft X-ray range has been described. Recent developments in visible/UV laser and electron beam technologies [4,9] indicate that the physical requirements for attempting the proposed scheme could be met. In principle, the method is not limited to shorter wavelength ranges, but

can be used, e.g., to generate compressed visible pulses starting from modulation by short IR or microwave pulses. Further variations of the method, such as sequential compressions at successively shorter wavelengths within the same bunch, or more sophisticated bunch modulation based on the flexibility allowed by the FS for generating arbitrary field profiles are also of interest and merit further study.

### Acknowledgements

This work was supported in part by the Department of Energy, Office of Basic Energy Sciences and High Energy and Nuclear Physics and Department of Energy Contract DE-AC03-76SF0015.

### References

- [1] J.D. Jackson, *Classical Electrodynamics* (Wiley, New York, 1975) chap. 14
- [2] R. Tatchyn, Proc. PEP Workshop on PEP as a Synchrotron Radiation Source, eds. R. Coisson and H. Winick, SSRL Report 88/06, p. 97.
- [3] H. Wiedemann, P. Kung and H.C. Lihn, *Ultra Short Electron and Photon Pulses*, SSRL ACD-Note 116 (1991).
- [4] H. Winick, K. Bane, R. Boyce, J. Cobb, G. Loew, P. Morton, H.-D. Nuhn, J. Paterson, P. Pianetta, T. Raubenheimer, J. Seeman, R. Tatchyn, V. Vylet, C. Pellegrini, J. Rosenzweig, G. Travish, D. Prosnitz, E.T. Scharlemann, K. Halbach, K.-J. Kim, R. Schleuter, M. Xie, R. Bonifacio, L. De Salvo and P. Pierini, Proc. 8th Synchrotron Radiation Instrumentation Conf., Gaithersburg, MD, August 23–26, 1993, Nucl. Instr. and Meth. A 347 (1994) 199.
- [5] R. Tatchyn, Proc. Workshop on Fourth Generation Light Sources, eds. M. Cornacchia and H. Winick, SSRL Report 92/02, p. 482.
- [6] K.-J. Kim, S. Chattopadhyay and C.V. Shank, Nucl. Instr. and Meth. A 341 (1994) 351.
- [7] P.L. Csonka, *Particle Accelerators* 11 (1980) 45.
- [8] R. Tatchyn, Proc. Workshop on Fourth Generation Light Sources, eds. M. Cornacchia and H. Winick, SSRL Report 92/02, p. 417.
- [9] C.P.J. Barty, C.L. Gordon III and B.E. Lemoff, Multiterawatt 30-fs Ti:sapphire laser system, Opt. Lett., to be published.

## Parametric study of an X-ray FEL

G. Travish <sup>a,\*</sup>, W.M. Fawley <sup>b</sup>, K.-J. Kim <sup>b</sup>, H.-D. Nuhn <sup>c</sup>, C. Pellegrini <sup>a</sup>, H. Winick <sup>c</sup>,  
M. Xie <sup>b</sup>

<sup>a</sup> *UCLA Department of Physics, Los Angeles, CA 90024, USA*

<sup>b</sup> *Lawrence Berkeley Laboratory, University of California, Berkeley, CA 94720, USA*

<sup>c</sup> *Stanford Linear Accelerator Center, Stanford University, CA 94309, USA*

### Abstract

An FEL utilizing a high energy, high current and low emittance beam to produce radiation shorter than 2 Å is investigated in this paper. This device is an extension of the previously proposed 40 Å Linac Coherent Light Source based on the Stanford linear accelerator. Here we investigate the performance characteristics and parameter sensitivities of this single pass, high gain FEL amplifier operating by self-amplified spontaneous emission (SASE). We begin by comparing various approaches to this short wavelength source and justify our choice of a helical undulator operating on the fundamental frequency. Numerical simulations as well as extensions of previous studies are used to show performance as a function of undulator parameters, startup noise, emittance, focusing, current and energy spread. Further studies and parameter modifications are proposed where needed.

### 1. Introduction

The Linac Coherent Light Source (LCLS) was conceived as a high gain, single pass, SASE FEL amplifier operating in the “water window” near 40 Å [1]. It was proposed to combine the emerging RF photocathode gun technology with the high energy Stanford linear accelerator and a long undulator to obtain a new, powerful short wavelength light source. After two application workshops were held, it became clear that the demand for a < 2 Å device was far greater than for the water window source [2,3]. Spurred by these demands a study began on how to lower the wavelength by more than an order of magnitude.

Our study began with a general survey of the parameter space. Various constraints exist on the beam parameters (emittance, current, energy spread, etc.) as well as the undulator (period, gap, field strength, etc.). These constraints serve to define an operating regime. Using a semi-analytic 3D model to rapidly explore this regime allows us to find a base parameter set which is nearly optimal [4]. The optimization can minimize undulator (saturation) length or maximize output power. Generally, these devices provide several orders of magnitude more brilliance, average and peak power than existing devices so that power is not a concern. Rather, minimizing the undu-

lator length is a higher priority. All cases require the FEL to saturate in order to minimize output fluctuations. The results of this model are a useful starting point for numerical simulations which can be more carefully account for 3D effects (diffraction, optical guiding, startup, etc.). Additionally, a comparison of helical, planar, harmonic and multiundulator generation schemes was done. The helical case offers shorter saturation lengths compared to a planar undulator, desirable circularly polarized light to users, and simplicity over multiundulator schemes. Nevertheless, these other concepts need further investigation before a final comparison can be made. Here we only consider the helical case.

The base set of parameters chosen for the helical case using the semi-analytic model is presented in Table 1. The following sections of this paper discuss the FEL performance as functions of various parameters.

### 2. Undulator requirements

The undulator for a one angstrom LCLS presents a technical challenge due to its length, high field, short period and high field quality. The need to incorporate strong focusing quadrupoles, steering magnets and beam diagnostics adds to the engineering challenge. Various technologies are under consideration including permanent magnet [5], electromagnet [6] and superconducting structures. At present, the superconducting bifilar (double helix) solenoid geometry [7] seems promising. Regardless of the

\* Corresponding author. Tel. +1 310 206 5584, fax +1 310 206 1091, e-mail travish@uclaphysics.ucla.edu.

Table 1  
The approximate base parameters for the 1.4 Å LCLS FEL

|                                   |   |
|-----------------------------------|---|
| Electron beam                     |   |
| Energy                            | 15 GeV                                  |
| Energy spread (rms, uncorrelated) | 0.02%                                   |
| Peak current                      | 5 kA                                    |
| Bunch charge                      | 1 nC ( $6 \times 10^9$ e <sup>-</sup> ) |
| Normalized emittance (rms)        | 1 mm-mrad                               |
| Bunch length (rms)                | 15 μm (~ 60 fs)                         |
| Repetition rate                   | 120 Hz                                  |
| Helical undulator                 |   |
| Period                            | 2.7 cm                                  |
| Undulator parameter (K)           | 2.9                                     |
| Magnetic field                    | 1.6 T                                   |
| External focusing betafuncion     | 6 m                                     |
| FEL                               |   |
| Wavelength                        | 1.4 Å                                   |
| Output power                      | > 10 GW                                 |
| FEL parameter ( $\rho$ )          | $1 \times 10^{-3}$                      |

geometry chosen, certain constraints such as the field strength (or undulator parameter), period, gap size and field quality must be satisfied.

The length of the undulator (~ 40 m) requires that the beam steering be corrected along the device. Combinations of BPMs and steering coils can accomplish this and could be integrated into the chosen undulator design. Both past simulations of a 40 Å device and 1D theory indicate that correcting the beam steering on the scale of the beam radius within each gain length is sufficient to maintain FEL performance within a factor of two of the perfect steering case [8]. This would suggest BPMs and steering magnets every 2.5 m with an accuracy of ~ 10 μm. Poorer correction is expected to degrade performance; however, BPMs with sufficient accuracy are being designed for Next Linear Collider (NLC) applications [9].

Undulator errors have traditionally been stated in terms of rms field error. Simplistic arguments (using effective energy spread) show that a ~ 0.1% rms field error can be tolerated (again with the nominal factor of 2 reduction in output power). Undulators and wigglers meeting this field quality have been built as third generation insertion devices.

### 3. Startup level and fluctuations

The LCLS has been proposed to operate in SASE mode because of the lack of a short wavelength source to act as a “seed” and the lack of high reflectance mirrors to form a cavity at these wavelengths and powers. This introduces the need to understand the startup regime in this high gain FEL. Various analytic models have been proposed, but none have been tested due to the lack of operating experi-

ments [10]. Upcoming experiments at UCLA [11], BNL [12] and other institutions will address the startup regime at longer wavelengths. Presently, however, we must rely on models and simulations.

The effective startup power is the spontaneous emission within the first gain length of the FEL which acts as an input to the remaining undulator amplifier. Three methods have been used to estimate the effective startup power of the LCLS: a simplistic 1D model, integration of the spontaneous emission of a single electron over the appropriate (FEL) solid angle, and numerical simulations using the code GINGER [13]. Perhaps the most realistic model was the simulation which yielded ~ 10 kW. Regardless, the results of the three methods agreed with a factor of two. This is in agreement with past comparisons of the startup level from numerical simulations and 1D theory.

Unfortunately, we still do not know if any of the above models are correct. Certainly, precise numbers for the startup level cannot be predicted with confidence. Thus, it is important to study the sensitivity of the LCLS to effective input power. The code TDA3D [14] was used for this and subsequent simulation results. The results are presented in Fig. 1. The saturation power is similar from 1 kW to 20 kW, however the saturation length becomes longer for lower input powers; the saturation length scales logarithmically with input power.

Fluctuations in the saturation power due to statistical variations in the effective startup power have been studied for the 40 Å LCLS [15]. The conclusion was that these fluctuation would be on the ~ 10% level. For the 1 Å LCLS these fluctuations may be reduced to the ~ 1% level since the number of cooperation lengths in a bunch is > 1000.

### 4. Emittance and focusing requirements

Failure of past FELs has often been blamed on poor beam quality with high emittance being the primary prob-

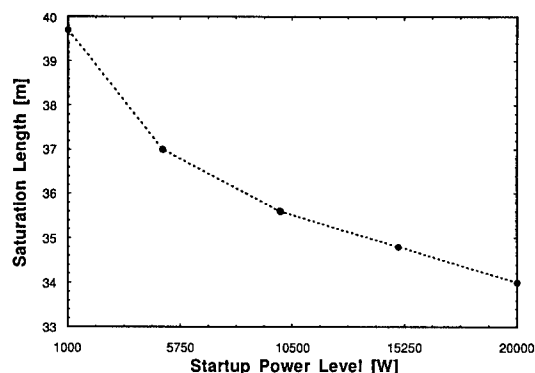


Fig. 1. Saturation length as a function of effective input (startup) power is plotted. All other parameters are as given in Table 1. The line connecting the simulation data serves only to aid in viewing.

lem. The pioneering work of Los Alamos on RF photocathode guns has produced beams of unprecedented brightness. Normalized rms emittances of  $\sim 2$  mm-mrad have been reported at 1 nC of charge [16,17]. Extrapolating these achieved performances to the near future leads us to assume a 1 mm-mrad emittance is achievable. Preserving the beam emittance through transport, compression and acceleration would also be required. An important point which has been emphasized by some authors is that an FEL is sensitive to the “slice” emittance rather than the overall (“bulk”) emittance [18]. It is possible that present RF photocathode guns already produce slice emittances of 1 mm-mrad at 1 nC of charge. Careful simulations of the FEL performance as a function of different emittance profiles are yet to be done.

With the above statements in mind, it is possible to simulate the FEL performance as a function of overall (uniform) beam emittance. Fig. 2 shows the results of these simulations. The performance of the FEL is seriously degraded by higher emittances; the saturation length increases while the saturated power is relatively unaffected. This is somewhat expected since the 1D constraint on the emittance and wavelength is not satisfied. Thus, it is critical that emittance dilution effects in the transport lines, compressors and linac be minimized.

Two options may alleviate severe emittance sensitivity. First, the slice emittance may not be effected as much as the bulk emittance. Second, higher beam energy could be used to lower the (normalized) emittance requirement. A further issue is that of optimizing the focusing for a given emittance.

The previously presented results assume a fixed quadrupole focusing channel. A strong focusing channel is required to propagate the beam over distances of tens of meters while maintaining high beam densities necessary for peak FEL performance. In reality, the focusing channel would be tuned to the achievable emittance. The 1D theory states that the focusing betafunction ( $\beta$ ) should be equal

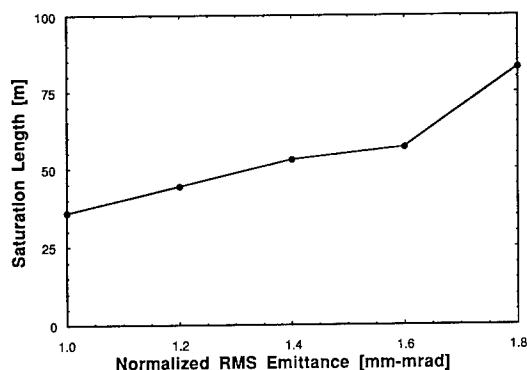


Fig. 2. The saturation length as a function of emittance is plotted from results of numerical simulations. Other parameters are fixed as in Table 1.

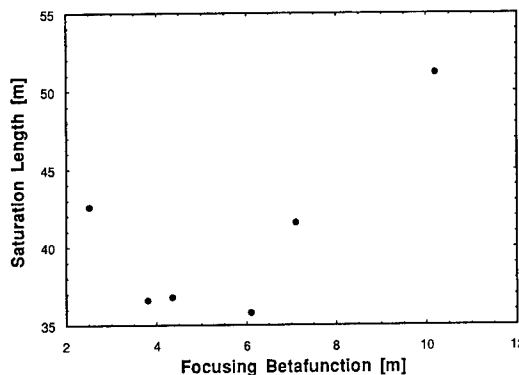


Fig. 3. Variation of the external focusing betafunction and its effect on the saturation length is plotted. The strong alternating focusing is simulated with a realistic lattice (no smooth approximation) and the deviation of the data points from a smooth curve is due to the different phase advances of each case. The remaining parameters are given in Table 1.

to or larger than the field gain length ( $L_g$ ) for optimal performance. For a fixed emittance of 1 mm-mrad, we plot the saturation length versus the betafunction in Fig. 3. The optimal focus is near 6 m. Sensitivity to beam mismatch does not seem to be an issue for the precision achievable at the Stanford linear accelerator.

## 5. Current and energy spread

A typical RF photocathode gun produces a beam of one to a few nC with a pulse length of a few picoseconds [19]. Thus, peak currents of a few hundred amperes are produced with higher currents excluded (at low emittance) by space charge problems. The LCLS requires much higher currents to operate. Bunch compression has been extensively developed at SLAC to meet the needs of lepton linear colliders, and can be applied to FEL beams to produce short pulses with high peak currents  $\sim$  kA [20]. The LCLS may employ two stage compression to achieve peak currents  $\sim$  5 kA with uncorrelated rms energy spreads  $\sim$  0.02%. The compressors are susceptible to fluctuations in the beam current from the gun and timing jitter from the RF and gun drive laser. Hence, the sensitivity of the FEL to current variation is relevant (see Fig. 4).

Simulations reveal that beam current fluctuations as large as 10% cause less than a 5% difference in the saturation length and about 9% variations in the saturated power. The undulator should be designed long enough to still saturate with a reduced beam current.

The uncorrelated energy spread is related to the beam current through the compressor. Larger beam currents generally imply larger energy spreads. However, the 1D theory predicts that energy spreads as large as  $\sim$  0.1% would not be detrimental. Simulations and experience at



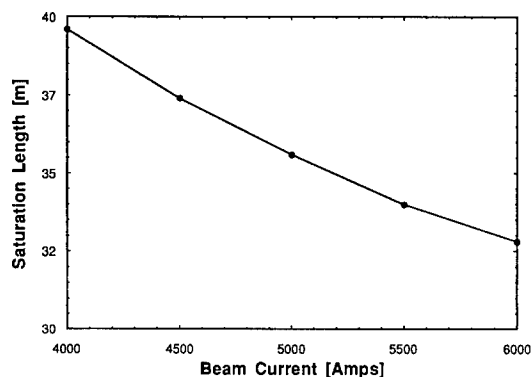


Fig. 4. Simulations of the effect of current variation on the saturation length of the LCLS with the effective startup level varied in proportion to the current. Parameters other than current are given in Table 1.

SLAC show that energy spreads of 0.02% at 5 kA should be obtainable [21]. Hence, achievable uncorrelated energy spreads should not be detrimental to the FEL.

The correlated energy spread contributes to the line width of the FEL and this may be a factor for some users. However, due to the high photon fluxes the use of a monochromator could be possible. Other coherence and line width issues have been studied for previous parameter sets and indicate general agreement with 1D theory with the exception of a “spiky” time structure to the radiation pulse. Again users will have to contend with this issue, but with a time scale of femtoseconds this may be a non-issue [22].

#### Acknowledgements

The authors thank the other members of the LCLS collaboration. This work was supported by the Office of Basic Energy Sciences, Department of Energy Contract DE-AC03-76SF0015 (SLAC); Department of Energy Grant DE-FG03-92ER-40493 (UCLA); Director, Office of En-

ergy Research, Office of Basic Energy Sciences, Materials Sciences Division, of the U.S. Department of Energy under contract No. DE-AC03-76SF00098 (LBL).

#### References

- [1] C. Pellegrini et al., Proc. Int. FEL Conf., Kobe, Japan, Aug. 24–28, 1992, Nucl. Instr. and Meth. A 331 (1993) 223.
- [2] W. Spicer, J. Arthur and H. Winick (eds.), Stanford, CA, SLAC Report 414.
- [3] J. Arthur, G. Materlick and H. Winick (eds.), Stanford, CA, SLAC Report 437.
- [4] M. Xie, LBL-36038, Berkeley, CA (1994).
- [5] R. Tatchyn et al., Proc. 1993 IEEE Particle Accelerator Conf., p. 1608.
- [6] G.A. Deis et al., IEEE Trans. Magnetics 24(2) (1990) 986.
- [7] C.A. Brau, Free-Electron Lasers (Academic Press, Boston, 1990) p. 269.
- [8] G. Travish et al., Proc. 1993 IEEE Particle Accelerator Conf., p. 1533.
- [9] J. Seeman, Advances of Accelerator Physics and Technologies, ed. H. Schopper (World Scientific, 1993) p. 219.
- [10] K.-J. Kim, Phys. Rev. Let. 57 (1986) 1871.
- [11] G. Travish et al., these Proceedings (16th Int. Free Electron Laser Conf., Stanford, CA, USA, 1994) Nucl. Instr. and Meth. A 358 (1995) ABS 75.
- [12] I. Ben-Zvi et al., Nucl. Instr. and Meth. A 318 (1992) 208.
- [13] E.T. Scharlemann and W.M. Fawley, SPIE Proc. 642 (1986) p. 2.
- [14] T.M. Tran and J.S. Wurtele, Comput. Phys. Commun. 54 (1989) 263.
- [15] R. Bonifacio et al., Nucl. Instr. and Meth. A 341 (1994) 181.
- [16] R.L. Sheffield, Proc. 1989 IEEE Particle Accelerator Conf., vol. 2. p. 1098.
- [17] I. Ben-Zvi, Proc. 1993 Particle Accelerator Conf., p. 2962.
- [18] R. Sheffield, Proc. 1993 IEEE Particle Accelerator Conf., p. 2970.
- [19] J. Rosenzweig et al., Nucl. Instr. and Meth. A 341 (1994) 379.
- [20] See Ref. [9].
- [21] K. Bane, T. Raubenheimer and J. Seeman, Proc. 1993 IEEE Particle Accelerator Conf.
- [22] US/Japan LCLS Collaboration Meeting, May 27–28, 1994.



ELSEVIER

# Multisectional FELs with dispersion and undulator sections

V.A. Bazylev<sup>\*</sup>, M.M. Pitatelev

*Russian Research Center "Kurchatov Institute", Moscow 123182, Russian Federation*

## Abstract

A free electron laser scheme consisting of a large number of identical parts is considered. Each part consists of an undulator and a dispersion section. The dispersion equation describing the process of radiation is derived in a one dimensional approach. The gain dependence on the dispersion section parameters is investigated. The regime having maximum radiation gain is found. The well known TDA code was modified for 3-D simulation of a multisection FEL. Stanford linac parameters were used in simulation. A total power gain exceeding  $4 \times 10^8$  can be achieved at a wavelength of 4.2–4.3 nm and a total length of the magnetic system of 20 m. Thus the gain of uniform FELs can be substantially exceeded in multisection FELs.

## 1. Introduction

It is well known that for the creation of UV and X-ray FELs the gain must be high because of the absence of good quality mirrors. It is also well known that gain decreases with the decrease of the radiation wavelength. In order to increase the gain the scheme of the optical klystron can be used [1–10]. Some years ago a FEL scheme with a large number of alternate undulator and dispersion sections was proposed [11]. This multisection scheme is an evolution of the optical klystron in which there is one dispersion section between two undulators. The study of the multisectional scheme in Ref. [11] was done on a qualitative level and under the assumption of small amplification within every element of the system.

In the present paper a theoretical investigation of X-ray FELs with alternate undulators and dispersion sections is reported. X-ray radiation and modulation of the electron energy takes place in the undulators. Transfer of the energy modulation into phase modulation takes place in the dispersion sections. It is shown that high amplification can be achieved with proper choice of the dispersion section parameters. Analytical work was carried out in the framework of a 1-D model. Raman effects and the mode structure of radiation were not taken into account. In addition, the results of 3-D computer simulations are presented in this paper.

## 2. Magnetic system and the conditions of the calculations

Let the relativistic electron beam pass along the  $z$  axis of the Magnetic System (MS) (see Fig. 1) consisting of the alternating Undulator (US) ( $L_w$ ,  $\lambda_w$  and  $K$  are the length, period and parameter of the undulator.) and Dispersion (DS) Sections. Every dispersive section is similar to the usual dispersive section of the optical klystron. It consists of three magnets of lengths  $s/4$ ,  $s/2$  and  $s/4$  with magnetic fields  $B_d$ .

After the passage through the DS, the phase of an electron changes according to:

$$\Delta\Phi = \Delta\Phi_0 + 2\pi N_d \frac{\gamma - \gamma_0}{\gamma_0}, \quad (1)$$

where  $\Delta\Phi_0$  is the change of the phase of the electron with the energy  $mc^2\gamma_0$ , and  $N_d$  is the effective number of periods of the DS:

$$N_d = \frac{B_d^2 s^3 e^2}{24\lambda_w \left(1 + \frac{K^2}{2}\right) m^2 c^4}. \quad (2)$$

The assumption  $N_d \gg L_w/\lambda_w$  assures a large phase modulation of the electron beam inside the DS compared to a small inertial grouping inside the US.

The 1-D theory of radiation without diffractive effects is valid if

$$|G_0| \lambda_s L_w \ll |G_0 - 1| R^2, \quad (3)$$

<sup>\*</sup> Corresponding author. Tel. +7 095 196 7679, Fax +7 095 943 0073, e-mail [x1144@cpuv1.net.kiae.su](mailto:x1144@cpuv1.net.kiae.su).

where  $\lambda_s$  is the radiation wavelength,  $G_0$  is the gain within one element of the MS (US + DS), and  $R$  is the radius of the electron beam.

### 3. Dispersive equation in 1-D theory

Let us assume that the MS is infinite and that there are no saturation of radiation effects. The field of the radiation  $E(z)$ , and the amplitudes of the energy and density modulation of the electron beam  $\Delta\gamma$ ,  $\Delta\rho$  satisfy the equations

$$\begin{aligned} E(z + L_t) &= G_0 E(z); \\ \Delta\gamma(z + L_t) &= G_0 \Delta\gamma(z); \\ \Delta\rho(z + L_t) &= G_0 \Delta\rho(z). \end{aligned} \quad (4)$$

As mentioned above, the amplitude of the modulation  $\Delta\rho$  is constant inside an US and changes only inside a DS.

The dependence of the amplitude of the radiation field upon the longitudinal coordinate  $z$  can be found from Maxwell equations

$$E(z) = E(z = z_n) - \frac{\pi K \rho_n (z - z_n) j_0 L_w}{\gamma}, \quad (5)$$

where  $\rho_n$  is the amplitude of the density modulation inside section  $n$  and  $j_0 = i/\pi R^2$  is the current density of electron beam.

One can obtain the following equation from Eqs. (4) and (5):

$$(G_0 - 1)E(z = z_n) = - \frac{\pi K \rho_n j_0 L_w}{\gamma}. \quad (6)$$

The total change of an electron's energy is the sum of the changes inside every section and can be found with the help of the perturbation theory at radiation

$$\gamma^j(z = z_n) - \gamma_0^j = \frac{KE(z = z_n) e^{i\Phi_n^j} L_w (G_0 + 1)}{4E_0 \gamma_0} F_1(\gamma_0^j), \quad (7)$$

where  $\gamma^j$  is the energy of the electron of number  $j$ ,  $\gamma_0$  is the middle energy of the electron beam,  $E_0 = mc^2/e$ ,  $\Phi_n^j$  is the phase of the electron of number  $j$  inside the US of number  $n$ , and

$$\begin{aligned} F_1(\gamma_0^j) &= \sum_{s=1}^{\infty} G_0^{-s} e^{-is(2\pi N_d(\gamma_0^j - \gamma_0)/\gamma_0 + \Delta\Phi_0)} \\ &= \frac{1}{G_0 e^{-i(2\pi N_d(\gamma_0^j - \gamma_0)/\gamma_0 + \Delta\Phi_0)} - 1}. \end{aligned} \quad (8)$$

The total change of the phase of an electron after passing through all DS can be found with the help of the perturbation theory at the radiation. In first order one can obtain

$$\Phi_n^j = N_d \frac{\pi KE(z = z_n) e^{i\Phi_n^j} L_w (G_0 + 1)}{2E_0 \gamma_0^2} F_1(\gamma_0^j) F_2(\gamma_0^j), \quad (9)$$

where

$$\begin{aligned} F_2(\gamma_0^j) &= \sum_{s=0}^{\infty} G_0^{-s} e^{-is(2\pi N_d(\gamma_0^j - \gamma_0)/\gamma_0 + \Delta\Phi_0)} \\ &= \frac{G_0 e^{-i(2\pi N_d(\gamma_0^j - \gamma_0)/\gamma_0 + \Delta\Phi_0)}}{G_0 e^{-i(2\pi N_d(\gamma_0^j - \gamma_0)/\gamma_0 + \Delta\Phi_0)} - 1}. \end{aligned}$$

The amplitude of the density modulation is defined by the expression

$$\begin{aligned} \rho_n &= \langle e^{-i\Phi_n^j} \rangle_n \\ &= -iN_d \frac{\pi KE(z = z_n) L_w (G_0 + 1)}{2E_0 \gamma_0^2} \langle F_1(\gamma_0^j) F_2(\gamma_0^j) \rangle_j, \end{aligned} \quad (10)$$

where  $\langle \rangle_j$  means averaging over the electrons.

With the help of expressions (6) and (10) one can obtain the following dispersive equation, describing the radiation process in the MS

$$iN_d \frac{\pi^2 K^2 L_w^2 j_0 (G_0 + 1)}{2\gamma_0^3 i_A (G_0 - 1)} \langle F_1(\gamma_0^j) F_2(\gamma_0^j) \rangle_j = 1, \quad (11)$$

where  $i_A = mc^3/e = 17$  kA.

### 4. Computer simulation; 1-D model

Let the distribution function of the electrons have the form

$$f(\gamma) = \begin{cases} 0 & \text{if } \gamma < \gamma_0 - \sigma, \\ 1/(2\sigma) & \text{if } \gamma_0 - \sigma < \gamma < \gamma_0 + \sigma, \\ 0 & \text{if } \gamma > \gamma_0 + \sigma. \end{cases} \quad (12)$$

To obtain the solution of Eq. (11) one must find the roots of the following equation:

$$\begin{aligned} G_0^3 + G_0^2 \left( -1 + i\kappa N_d e^{-i\Delta\Phi_0} \frac{\sin \mu}{\mu} - 2 e^{-i\Delta\Phi_0} \cos \mu \right) \\ + G_0 \left( e^{-2i\Delta\Phi_0} + i\kappa N_d e^{-i\Delta\Phi_0} \frac{\sin \mu}{\mu} - 2 e^{-i\Delta\Phi_0} \cos \mu \right) \\ - e^{-2i\Delta\Phi_0} = 0, \end{aligned} \quad (13)$$

where  $\kappa = \pi^2 K^2 L_w^2 j_0 / 2\gamma_0^3 i_A$ ,  $\mu = 2\pi N_d \sigma$ .

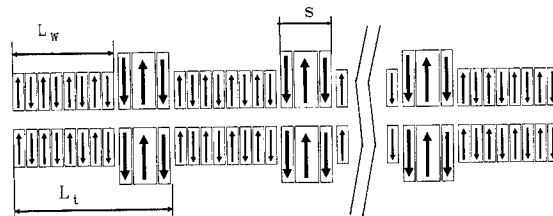


Fig. 1. Principal scheme of the multisectional FEL.

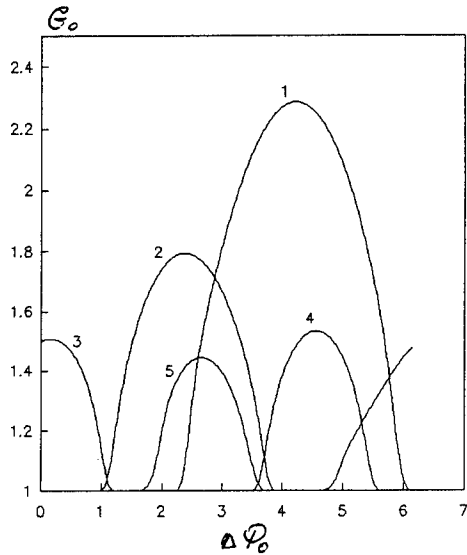


Fig. 2. Dependence of the gain  $G_0$  upon  $\Delta\Phi_0$  at different values of  $\mu$  ( $0.6 < \mu < 3.0$ ) and  $\kappa = 1.5$ .

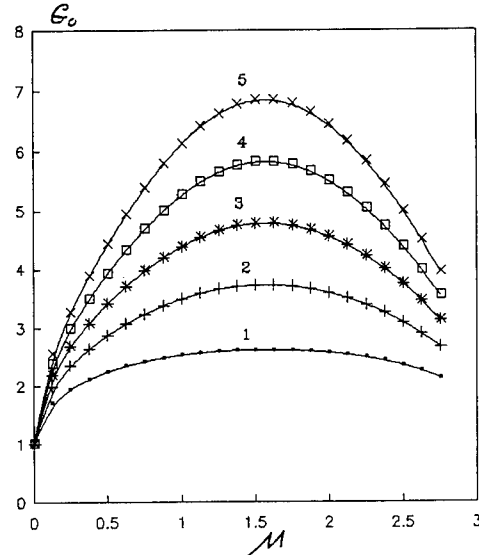


Fig. 3. Dependence of the optimized gain upon  $\mu$  at different  $N_d\kappa$ .  $N_d\kappa = 1.0$  (1); 2.0 (2); 3.0 (3); 4.0 (4) and 5.0 (5).

Eq. (13) has three complex roots. The gain is defined by the root with the largest magnitude of the modulus. The dependence of the gain  $G_0$  upon  $\Delta\Phi_0$  at different values of  $\mu$  ( $0.6 < \mu < 3.0$ ) and  $\kappa = 1.5$  is shown in Fig. 2. The same calculations were also completed at other values of  $\kappa$  and  $\mu$  in order to find the optimum. The dependence of the optimized gain upon  $\mu$  (at different  $\kappa$ ) is shown in Fig. 3. Maximum amplification is reached at  $\mu = \pi/2$  and  $\Delta\Phi_0 = 3\pi/2$ . So the gain after passing the electron beam through one section of the MS is described by the formula

$$G_0 = 1 + \frac{\kappa}{4\pi\sigma} + \sqrt{\frac{\kappa}{2\pi\sigma} + \left(\frac{\kappa}{4\pi\sigma^2}\right)^2}. \quad (14)$$

It is clear from Eq. (14) that there is a possibility of significant amplification inside every element of the MS at a relatively small energy spread of electron beam.

### 5. Computer simulation of radiation; 3-D model

For the 3-D calculations the well-known code TDA [12] presented by the Massachusetts Institute of Technol-

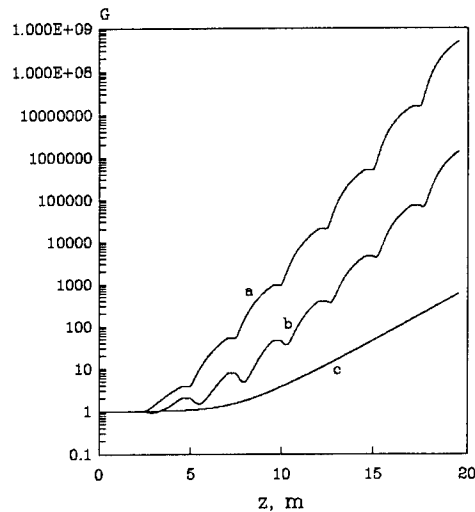


Fig. 4. Dependence of total amplification upon the longitudinal coordinate  $z$ . (a)  $\lambda_s = 4.264$  nm, (b)  $\lambda_s = 4.269$  nm (c) 1-sectional undulator.

Table 1  
Parameters of the electron beam, undulator and dispersion sections

| Electron beam   |      | Undulator section   |     | Dispersion section  |    |
|-----------------|------|---------------------|-----|---------------------|----|
| Energy [GeV]    | 7    | Length [cm]         | 200 | Work length [cm]    | 40 |
| Current [A]     | 2500 | Period [cm]         | 8.3 | Magnetic field [kG] | 12 |
| Emittance [rad] | 3    | Undulator parameter | 6   |                     |    |
| Energy Spread   | 0.1% |                     |     |                     |    |

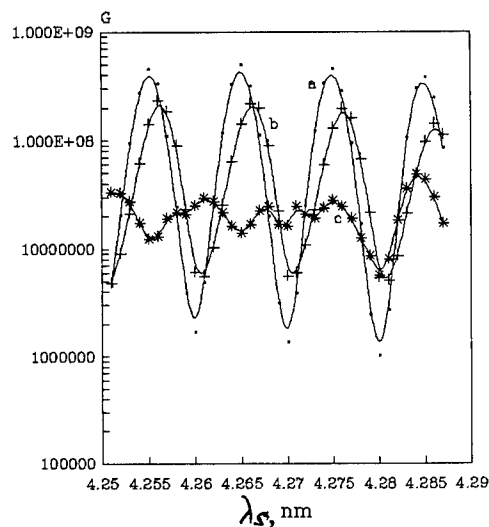


Fig. 5. Dependence of the amplification upon the radiation wavelength for an ideal MS. (curve (a)) and nonideal MS (curves (b) and (c) correspond to two occasional sets of DS parameters within 5% accuracy of the preparation of the DS).

ogy was modified in order to be able to simulate an FEL with any number of undulator and dispersion sections. The simulations were carried out for the electron beam of the Stanford linac [13]. The parameters of the electron beam, undulator and dispersion sections are given in Table 1.

The distance between undulator and dispersion sections is equal to 5 cm. The radiation wave length is equal to 4.2–4.3 nm. There are 8 undulator and 7 dispersion sections. The total length of the magnetic system is equal to 19.5 m.

The dependence of total amplification upon the longitudinal coordinate  $z$  is shown in Fig. 4, which displays the results for  $\lambda_s = 4.264$  nm (maximum of amplification; curve (a)) and  $\lambda_s = 4.269$  nm (minimum of amplification; curve (b)). In the first case, buckets of electrons formed in a DS are in a radiation phase at the entrance of the US. In the second case the buckets are in an absorption phase at

the entrance of the US. Nevertheless the total amplification is much higher than for a homogeneous undulator (without DS, curve (s)). The curve of amplification for a nonideal DS should be between curve (a) and curve (b).

The dependence of amplification upon the radiation wavelength is shown in Fig. 5 for an ideal MS (curve (a)) and nonideal MS (curves (b) and (c) corresponding to two occasional sets of DS parameters within 5% accuracy of the preparation of the DS). It is useful to indicate that the gain is approximately equal to  $\sqrt{G_{\max} G_{\min}}$  for an imperfect MS.

Every element of the MS provides a factor of 10 amplification. The total amplification is equal to  $3 \times 10^7$ – $4 \times 10^8$ , 4 orders of magnitude more than a one-sectional FEL with the same length.

## Reference

- [1] N.A. Vinokurov and A.N. Skrinsky, Preprint of Institute of Nuclear Physics 77–59, Novosibirsk (1977).
- [2] G.N. Kulipanov, I.V. Pinaev, V.M. Popik et al., Nucl. Instr. and Meth. A 331 (1993) 98.
- [3] K. Yamada, T. Yamazaki, S. Sugiyama et al., Nucl. Instr. and Meth. A 318 (1992) 33.
- [4] C.M. Tang and W.P. Marable, Nucl. Instr. and Meth. A 318 (1992) 675.
- [5] S. Takano, H. Hama and G. Isoyama, Nucl. Instr. and Meth. A 331 (1993) 20.
- [6] M.E. Couprie, V. Litvinienko, D. Garzella et al., Nucl. Instr. and Meth. A 331 (1993) 37.
- [7] Y. Wu, V.N. Litvinienko, E. Forest et al., Nucl. Instr. and Meth. A 331 (1993) 287.
- [8] J. Gallardo and C. Pellegrini, Opt. Commun. 77 (1990) 45.
- [9] I. Ben-Zvi, L.F. Di Mauro, S. Krinsky et al., Nucl. Instr. and Meth. A 318 (1992) 201.
- [10] A.S. Fisher, J.C. Gallardo, H.D. Nuhn et al., Nucl. Instr. and Meth. A 318 (1992) 730.
- [11] V.N. Litvinienko, Nucl. Instr. and Meth. A 304 (1991) 463.
- [12] T.M. Tran and J.S. Wurtele, Comput. Phys. Commun. 54 (1989) 263.
- [13] C. Pellegrini, J. Rosenzweig, H.-D. Nuhn et al., Nucl. Instr. and Meth. A 331 (1993) 223.

## Simulations of a klystron undulator for the SLAC X-ray FEL

G.H. Winter<sup>\*</sup>, J. Hall, R.K. Wong, W.B. Colson

Physics Department, Naval Postgraduate School, Monterey, California 93943, USA

### Abstract

The Stanford Linear Accelerator Center (SLAC) linac has been proposed as an electron beam source for a high power X-ray FEL. A klystron design with an enclosed dispersive section allows a shorter undulator to achieve bunching in a weak radiation field. Single-mode phase-space simulations are used to investigate the effectiveness of electron bunching and the onset of saturation. A longitudinal multimode simulation shows the resulting coherence development.

Holography and high resolution imaging of DNA base pairs are potential applications for an X-ray laser [1]. The “water window”, where water becomes transparent, can be explored by soft X-rays in the 20–40 Å wavelength range. The Free Electron Laser (FEL) appears to be a viable source for an X-ray laser due to its ability to create coherent radiation from noise through Self-Amplified Spontaneous Emission (SASE). The X-rays are created by a single pass of electrons through an undulator which eliminates the need for resonator mirrors. A proposed design combines the SLAC linac with an undulator to produce X-rays. Wavelengths are proposed down to the hard X-ray region of a few Angströms [2].

A large portion of the FEL cost is in the production of the undulator; reducing the length of the undulator reduces the FEL cost. A method of reducing the length of the undulator introduces a dispersive section in the undulator making an FEL klystron. A penalty resulting from the klystron design is the onset of saturation at weaker fields than without the klystron.

The FEL klystron can be described by phase-space simulations using classical FEL theory with dimensionless parameters [3]. The phase of the electron with respect to the optical field is  $\zeta(t) = (k + k_0)z(t) - \omega t$ , where the optical frequency is  $\omega = ck$ , the undulator wavenumber is  $k_0 = 2\pi/\lambda_0$ , and the optical wave number  $k = 2\pi/\lambda$ . The electron phase velocity is  $v(\tau) = d\zeta/d\tau$ , where the dimensionless time  $\tau = ct/L$ ,  $c$  is the speed of light, and  $L$  is the undulator length. The dispersive section shifts the electrons far off-resonance so that the electrons do not interact with the optical field, and there is no change in the phase velocity,  $v$ . The electron phase change,  $\Delta\zeta$  is

proportional to the velocity modulation in the first undulator section, so that the net effect of the dispersive section is [3]

$$\Delta\zeta = \nu D, \quad \Delta\nu = 0,$$

where  $D$  is the dimensionless dispersive strength of the klystron.

Phase-space simulations are used to study a soft X-ray FEL at 40 Å. The initial radiation field is  $a_0 = 0$ ; the optical field grows from noise as a result of spontaneous emission from 200 000 electrons with random initial phase. An FEL design at  $\lambda = 40$  Å has an undulator length of  $L = 17$  m, electron beam energy of 5 GeV and a peak current of 5000 A which corresponds to a dimensionless current density [3] of  $j = 932$ . This FEL was examined without a klystron and then with a klystron. The case without the klystron is shown in Fig. 1. The electron bunch is at a phase where it gives energy to the optical field at the end of the undulator. The dimensionless power  $P$  corresponds to a peak power of 15 GW. In Fig. 2, the use of the klystron FEL with the same parameters and  $D = 0.5$  shows that electrons have bunched in the lower half of the

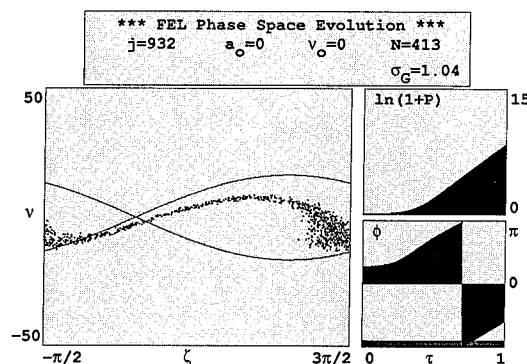


Fig. 1. 40 Å laser, without klystron, single-mode phase-space plot.

<sup>\*</sup> Corresponding author. Tel. +1 408 656 3114, fax +1 408 656 3114, e-mail winter@physics.nps.navy.mil.

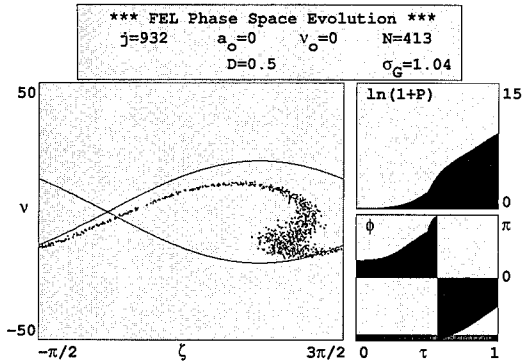


Fig. 2. 40 Å laser, with klystron, single-mode phase-space plot.

separatrix and at the optimal phase relation,  $\zeta + \phi = \pi$ , for maximum gain. The peak power calculated for the klystron FEL is 51 GW. Saturation occurs earlier than without the klystron reducing the length of the undulator.

Longitudinal multimode simulations with the same parameters study the coherence development of the optical field. Simulations without a klystron and before saturation resulted in an X-ray linewidth of  $\Delta\lambda/\lambda = 0.1\%$ . Using the klystron and after saturation, simulations resulted in a linewidth of  $\Delta\lambda/\lambda = 0.2\%$ .

Hard X-ray FELs [2] at 1.5 and 4.5 Å have also been

proposed. Single-mode phase-space simulations without a klystron indicate the production of an X-ray beam with undulator lengths of 46 and 45 m, respectively. Simulations show that the use of a klystron with both FELs did not reduce the undulator saturation length. The simulations were run at resonance with various values of dimensionless drift time  $D$ . The peak gain may be off-resonance and further research is being performed to determine optimum conditions.

### Acknowledgements

The authors are grateful for support of this work by the Naval Postgraduate School, Stanford University (N00014-91-C-0170), and SURF/CEBAF

### References

- [1] Proc. Workshop on Scientific Applications of Short Wavelength Coherent Light Source, SLAC-414, SLAC/SSRL-0007, CONF-9210278 (1993).
- [2] LCLS Technical Group Meeting Notes (July 27, 1994).
- [3] W.B. Colson and C. Pellegrini, Laser Handbook, Vol. 6 (1990) chap. 5.

## Mock-up of the focusing undulator for the SLAC X-ray FEL project <sup>☆</sup>

A.A. Varfolomeev <sup>\*</sup>, V.V. Gubankov, A.H. Hairetdinov, S.N. Ivanchenkov,  
A.S. Khlebnikov, N.S. Osmanov, S.V. Tolmachev

*CRL, Russian Research Center 'Kurchatov Institute', 123182 Moscow, Russian Federation*

### Abstract

A small prototype of the undulator requested for the SLAC X-ray FEL project was designed and manufactured. Experimental results on the magnetic fields obtained with the five period model show that the hybrid scheme using side magnet arrays is very promising. It can provide the specified magnetic field profiles in a small area near the undulator axis, focusing fields are easily adjustable, and the construction is compact.

### 1. Introduction

For the X-ray FEL on the SLAC linac [1], based on self-amplified spontaneous emission (SASE), a special undulator must be constructed. It should be very long (50–60 m) and should provide high magnetic fields and large focusing strengths for both transverse directions. One of the first of several possibilities for the undulator construction [2] was based on the use of an iron-free pure permanent magnet undulator inserted into external quadrupole lenses. These lenses need to provide a specified large field gradient up to 50 T/m. But as the external quadrupole system surrounding the undulator cannot be small, construction appears to be expensive.

We have analyzed different approaches to the undulator design and have found that the best results can be obtained with the hybrid scheme and side magnet arrays [3]. The experimental results, obtained with the fabricated undulator [4] having tunable focusing strength, can be considered as an approval of this scheme. With the proper orientation of the side magnets the scheme can provide very high quadrupole focusing strengths along with limited undulator dimensions [5]. A similar approach to the scheme was suggested by Tatchyn [6].

### 2. Undulator scheme and basic parameters

A schematic layout of a single undulator cell (period) is shown in Fig. 1. Permanent magnets 1 with steel poles 2 compose a conventional hybrid structure. Side permanent magnets 3 provide the transverse magnetic field gradient. With the side magnet magnetizations oriented in opposite directions as shown, the most efficient quadrupole focusing in the XZ-plane (defocusing in the YZ-plane) is ensured. By changing both magnetization directions one can get focusing in the YZ-plane (defocusing in the XZ-plane) respectively.

Here we consider the specifications for the most recent version of the above project [7] and use as objectives the following parameters: undulator period  $\lambda_w = 27$  mm, gap  $g = 5$  mm, on-axis focusing magnetic field gradient 50

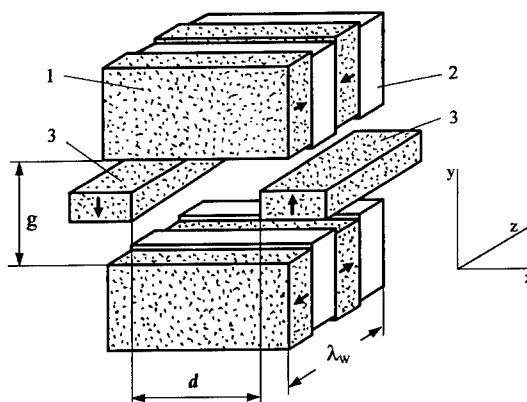


Fig. 1. Schematic of the undulator cell. 1 – main SmCo<sub>5</sub> magnet; 2 – steel pole; 3 – additional NdFeB magnet.

<sup>☆</sup> The research described in this publication was made possible in part by Grant No. MQH000 from the International Science Foundation.

<sup>\*</sup> Corresponding author. Tel. +7 095 196 7764, fax +7 095 196 7764, e-mail: x1065@cpuv1.net.kiae.su.



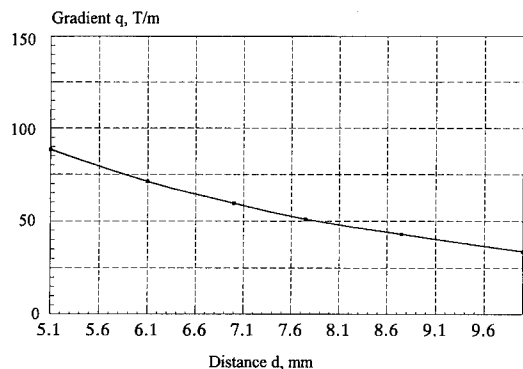


Fig. 2. Dependence of the on-axis magnetic field gradient  $q = dB_y(x)/dx$  on the distance  $d$  between the side magnet arrays.

T/m, and undulator magnetic field amplitude  $B_{y0} = 1.4$ – $1.6$  T. The mock-up undulator was designed according to the above scheme and undulator requirements. The prototype model contains five cells. It was assembled from  $\text{SmCo}_5$  main magnet blocks, steel poles and NdFeB side magnet blocks with the following dimensions respectively:  $40 \times 40 \times 10 \text{ mm}^3$ ,  $25 \times 3.5 \times 28 \text{ mm}^3$  and  $50 \times 25 \times 4.5 \text{ mm}^3$ .

### 3. Results of mock-up tests

The transverse magnetic field profiles were experimentally tested with the above mock-up. The dependence of the on-axis magnetic field gradient  $q = dB_y(x)/dx$  on the distance between the side magnet arrays is shown in Fig. 2. The required value of 50 T/m is achieved for a horizontal gap of 8 mm. The shape of the profile  $B_y(x, y = 0)$  corresponding to this case is presented in Fig. 3.

It was found from the experiment that the field amplitude on the undulator axis does not depend strongly on the side magnet array positions. The field amplitude was actu-

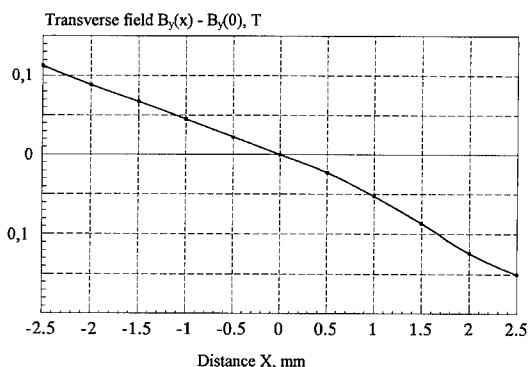


Fig. 3. Profile  $B_y(x, y = 0)$  as a function of  $x$ -coordinate for the distance  $d$  equal to 8 mm.

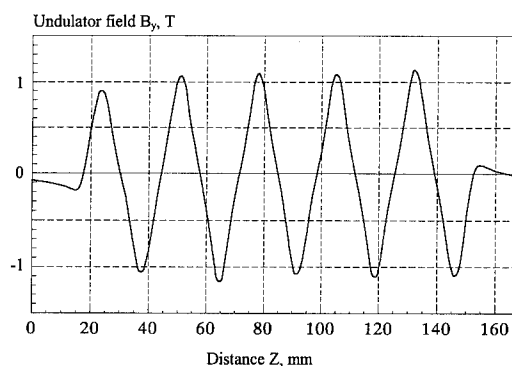


Fig. 4. Profile  $B_y(z)$  measured along the central undulator axis.

ally decreased by up to 5% when the distance between the side magnets was reduced to 7 mm. A magnetic field amplitude of 1.1 T for a 5 mm gap was achieved (see Fig. 4). This value can be increased by several percent by replacing the  $\text{SmCo}_5$  main magnets by NdFeB magnets and the steel poles by vanadium permendur.

### 4. Conclusion

The proposed undulator scheme with side magnets can provide the required field gradients for achieving the focusing strengths specified by the project [1,7]. The use of the hybrid type of undulator allows one to reach high enough magnetic field amplitudes as well. As a whole the undulator construction can be very compact in the transverse directions.

### References

- [1] C. Pellegrini, J. Rozenzweig, H.-D. Nuhn et al., Nucl. Instr. and Meth. A 331 (1993) 223.
- [2] R. Tatchyn, R. Boyce, K. Halbach et al., Design considerations for a 60 meter pure permanent magnet undulator, Proc. Particle Accelerator Conf. (PAC 93), Washington, DC, May 17–20, 1993.
- [3] W.H. Urbanus, R.W.B. Best, A.G.A. Verhoeven, M.J. van der Wiel, M. Caplan, L. Bratman, G. Denisov, A.A. Varfolomeev and A.S. Khlebnikov, Proc. 3rd Europ. Particle Accelerator Conf., Berlin, March 24–28, 1992, vol. 1, p. 629.
- [4] A.A. Varfolomeev, S.N. Ivanchenkov, A.S. Khlebnikov et al., Nucl. Instr. and Meth. A 341 (1994) 466.
- [5] A.A. Varfolomeev, Yu.P. Bouzouloukov, V.V. Gubankov, S.N. Ivanchenkov, A.S. Khlebnikov, N.S. Osmanov and S.V. Tolmachev, Development of focusing undulator on the basis of side magnets, Proc. Synchrotron Radiation Conf. (SR-94), Novosibirsk, Russia, 1994.
- [6] R. Tatchyn, Nucl. Instr. and Meth. A 341 (1994) 449.
- [7] C. Pellegrini, private communication.

## Coherent spontaneous emission in FELIX

D. Oepts<sup>\*</sup>, D.A. Jaroszynski<sup>1</sup>, H.H. Weits, P.W. van Amersfoort

*FOM Instituut voor Plasmafysica 'Rijnhuizen', P.O. Box 1207, 3430 BE Nieuwegein, The Netherlands*

Spontaneous undulator radiation, which provides the seed field in a free-electron laser oscillator, results from density variations in the injected electron beam on the scale of the resonance wavelength. For a macroscopically homogeneous beam, the relevant variations are the result of statistical fluctuations in the electron density, associated with the discrete nature of the electrons. The superposition of the incoherent fields generated by the individual electrons then leads to a radiated power proportional to the number density of the electrons. When the electron beam is pulsed with a bunch length less than the resonance wavelength, the fields add coherently, resulting in a power proportional to the square of the density [1,2].

The power emitted by a bunch of  $N$  electrons can be written as [3]

$$P(k) = NP_1(k) + N^2 P_1(k) f(k), \quad (1)$$

where  $P_1(k)$  is the power emitted by a single electron at wavenumber  $k = 2\pi/\lambda$ , and  $f(k)$  is a form factor depending on the macroscopic longitudinal density distribution,  $S(z)$ , of the bunch,

$$f(k) = \left| \int \exp(ikz) S(z) dz \right|^2. \quad (2)$$

Here,  $S(z)$  is normalized such that  $\int S(z) dz = 1$ . For a smooth bunch with a characteristic length  $l_b$ , there will be little constructive interference for wavelengths much smaller than  $l_b$ . This corresponds to the value of  $f$  dropping from unity at  $k = 0$  to small values for  $k > 2\pi/l_b$ . In FELIX, the electron beam consists of a train of micropulses with a duration of the order of 3 ps, corresponding to a length of 1 mm. The pulses are repeated at a frequency of 1 GHz and contain  $1.2 \times 10^9$  electrons. The wavelength of operation of FELIX extends from 100  $\mu\text{m}$  down to 5  $\mu\text{m}$ . At these wavelengths, much shorter than the electron bunch length, one would not expect coherent

effects to be important. However, even when  $f(k)$  is very small, the coherent part in Eq. (1) can be larger than the incoherent one because of the large additional factor  $N$  in the second term. The coherent spontaneous emission can therefore have a noticeable effect on the operation of the laser, specifically on the start-up and coherence properties.

Measurements of coherent spontaneous emission effects in the long-wavelength branch of FELIX have been reported earlier [4]. More recently, similar measurements have been performed using the short-wavelength branch of the machine. As absolute calibration of measurements of the spontaneous emission power is difficult to realize, we compared the spontaneous power with the saturated laser output. Diffractive attenuators [5] were used to enable measurement of the spontaneous power and the saturated power with the same detector and the same optical geometry. At a wavelength of 80  $\mu\text{m}$ , the spontaneous power was found to be a factor of  $5 \times 10^4$  lower than the saturated power (see Fig. 1), whereas for incoherent spontaneous emission one would expect a factor of  $10^8$  to  $10^9$ . A coherent enhancement by a factor of order  $10^4$  is thus observed. At 12  $\mu\text{m}$  wavelength, the spontaneous emission power was a factor of  $3 \times 10^6$  below the saturated power. The enhancement is much smaller, as expected at this short wavelength, but still noticeable.

In addition to accelerated start-up of the laser, we observed consequences of the coherent spontaneous emission on the spectral properties of the laser. The coherent emission is determined by the shape of the electron bunches, and has a fixed phase relative to the electron pulses. Consequently, there is a fixed phase relation between the emission from successive bunches. This is in contrast to the incoherent emission, which has a random phase as a result of the independent shot noise variations in each bunch. The round-trip time for the optical cavity of FELIX is 40 ns, while the electron micropulses are repeated at 1 GHz. Therefore, 40 optical pulses circulate concurrently in the cavity. There is no interaction between these light pulses. Nevertheless, we observe stable interference fringes when successive optical pulses are made to overlap, both for the spontaneous emission and for the saturated laser output, and at 12  $\mu\text{m}$  as well as at 80  $\mu\text{m}$ .

<sup>\*</sup> Corresponding author. Tel. +31 3402 31224, fax +31 3402 31204, e-mail [oepts@zeus.rijnh.nl](mailto:oepts@zeus.rijnh.nl).

<sup>1</sup> Permanent address: Heriot-Watt University, Riccarton, Edinburgh, UK.

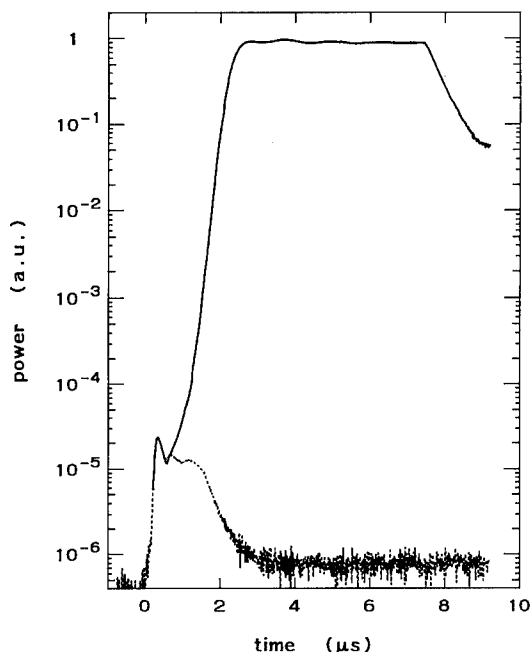


Fig. 1. Full line: growth of the optical output power during a FELIX macropulse, at a wavelength of  $81 \mu\text{m}$ . Data obtained from a series of measurements using progressively longer electron macropulses and increasing attenuation. Dotted line: spontaneous emission only, obtained by desynchronising the optical cavity to eliminate the gain. The electron beam attains its peak current at about  $t = 0.6 \mu\text{s}$ , and becomes stable after  $t = 1.4 \mu\text{s}$ .

This shows that there is indeed a fixed phase relation between successive pulses already in the seed field, which is maintained during the amplification process. The coherence between pulses can also be interpreted as meaning that the optical field consists of discrete harmonics of the electron repetition frequency [6]. A wavelength of  $12 \mu\text{m}$  contains harmonics around the 25 000th. The fact that the harmonics are well separated in the spectrum, as follows from the interference measurements, means that the short

term stability of the pulse repetition rate, or jitter, is better than 1 in 50 000, and that the pulse shape reproduces on the scale of a wavelength. We have also found that the harmonics of the pulse repetition frequency must coincide with longitudinal modes of the optical cavity for the radiation to build up most effectively in the start-up phase of the laser power.

Recently, we observed a component with a wavelength around  $90 \mu\text{m}$  in the spontaneous emission of the short-wavelength branch of FELIX, set for operation at  $12 \mu\text{m}$ . The radiation was found to have a fixed phase with respect to the electron bunches, and hence to be coherent emission. At wavelengths far from resonance, where  $P_1(k)$  is small, coherent emission can again be important when  $f(k)$  is large, i.e. for long wavelengths. This does not explain the radiation in question, however, as its power was found to be almost independent of the undulator strength, and therefore not related to  $P_1(k)$ . An alternative explanation has not yet been found.

#### Acknowledgements

This work has been performed as part of the research program of the Stichting voor Fundamenteel Onderzoek der Materie (FOM), and was made possible by financial support from the Nederlandse Organisatie voor Wetenschappelijk onderzoek (NWO).

#### References

- [1] H. Motz, J. Appl. Phys. 22 (1951) 527.
- [2] Y.U. Jeong, C.H. Nam, S.S. Lee, Y. Kawamura and K. Toyoda, Phys. Rev. E 47 (1993) 1313.
- [3] J.S. Nodvick and D.S. Saxon, Phys. Rev. 96 (1954) 180.
- [4] D.A. Jaroszynski, R.J. Bakker, A.F.G. van der Meer, D. Oepts and P.W. van Amersfoort, Phys. Rev. Lett. 71 (1993) 3798.
- [5] F. Keilmann, Proc. SPIE 666 (1985) 213.
- [6] A. Doria, R. Bartolini, J. Feinstein, G.P. Gallerano and R.H. Pantell, IEEE, J. Quantum Electron. QE-29 (1993) 1428.



ELSEVIER

## Femtosecond deep UV pulse by high gain harmonic generation from a chirped seed <sup>☆</sup>

Li Hua Yu <sup>\*</sup>

Brookhaven National Laboratory, Upton, NY 11973, USA

### Abstract

In this work we show that the techniques of high gain harmonic generation and chirped pulse amplification (CPA) can be combined to generate deep-uv radiation with peak power of order of 100 GW and pulse width of 5 fs. The resulting pulse would have wide range of applications.

In this paper we combine two techniques [1]: the high gain harmonic generation or the subharmonically seeded single pass free electron laser (FEL), and the chirped pulse amplification (CPA).

The harmonic generation technique has been developed since the early stages of the history of the free electron laser [2]. One promising approach on this line pursued at Brookhaven National Laboratory is that of the subharmonically seeded FEL [3,4]. A detailed description of this technique is given later in this paper. In the seeded beam approach, the radiation produced in the FEL has the coherence properties and relative bandwidth of the seed laser.

In the CPA technique [5], developed first for the conventional laser systems, the stored energy from a short pulse oscillator is extracted and stretched prior to amplification. By stretching the pulse, the input fluence to the amplifier remains constant while the intensity is reduced, which mitigates the problem of phase distortion incurred in the amplification of high intensity beam. The amplified pulses are then compressed to produce an extremely high peak power, short pulse. Stretching and compressing are achieved by utilizing gratings to disperse the frequencies of the pulse in such a manner that their path lengths prior to entering the amplifier differ.

An essential condition for the amplification of a short pulse is that the bandwidth of the laser system be broad enough to accommodate the spectrum of frequencies from which it is comprised. The relationship between the pulse duration  $\tau$  and bandwidth  $\Delta\nu$  is given by the Fourier

transform limit  $\Delta\nu\tau \sim 0.5$ . Using this relation, we find that for wavelength  $\lambda = 88$  nm, the required bandwidth for a 5 fs pulse, is  $\Delta\nu/\nu = 3\%$ . In the deep-uv regime (below 100 nm), the lack of a conventional amplifier medium with such large bandwidth makes it difficult to apply CPA technique to generate high power (in the order of 100 GW) and short (order of below 10 fs) pulses, which would have a very wide range of applications [1].

However, the FEL is a candidate for this medium. In this paper we turn our attention to the properties of the FEL required to exploit CPA to produce ultrashort pulses of deep-uv radiation. The pulse compression can be carried out externally to the FEL, with essentially the same techniques in the conventional CPA.

Without chirping the electron beam energy, a high gain FEL's gain bandwidth of 0.1% would be typical [3]. Therefore, to amplify a chirped pulse with a few percent bandwidth, the energy of the electron pulse should be chirped to match the resonance condition. The subject of energy chirped FELs has been previously explored in an oscillator configuration [6,7]. However, to create a chirped output radiation pulse that can be compressed to a short pulse of the order of femtoseconds duration, the pulse must be very accurately chirped, i.e., from the head to the tail of the pulse the optical phase relationship should be as coherent as if it had been originally stretched from a femtosecond pulse. Hence, from the standpoint of phase coherence, the choice of a chirped pulse seeded single pass FEL seems the most promising configuration to pursue. The subharmonically seeded beam approach developed for the Brookhaven National Laboratory Deep Ultra-Violet Free Electron Laser (DUV-FEL) [3,4], provides a framework for the present discussion, with the overall scheme shown schematically in Fig. 1. For the FEL, pulses from a solid state laser will be stretched to provide a 5 ps chirped pulse to seed the FEL.

<sup>☆</sup> Work performed under the auspices of the U.S. Department of Energy, under contract DE-AC02-76CH00016.

<sup>\*</sup> Corresponding author. Tel. +1 516 282 5012, fax +1 516 282 3029, e-mail yu@bnlls1.nsls.bnl.gov.

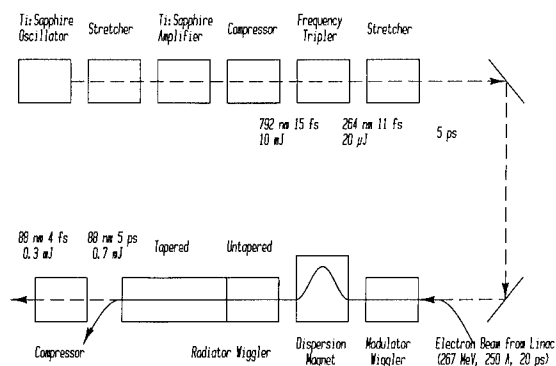


Fig. 1. A schematic diagram showing the experimental arrangement.

In this case, the electron source is an RF photocathode gun providing up to 4 nC of charge in a nominal 20 ps pulse. The electrons are accelerated to an energy of up to 310 MeV by 5 SLAC type linac sections. The last linac section is used to tune the electron beam energy, or alternatively to generate energy chirping to match the chirped input seed laser beam. By introducing the energy chirp right in front of the wiggler the complexities associated with transport and emittance preservation of electron beams with a relatively large energy spread are eliminated. In our example the electron beam has an energy centered at 267 MeV, a peak current of 256 A and a normalized rms emittance of  $6.4\pi$  mm mrad.

This high brightness electron beam is transported to an initial 2 m long wiggler, with period of  $\lambda_{w1} = 3.9$  cm and maximum on-axis field of 0.76 T, where it interacts with the seed laser radiation. This so called “modulator” is designed to be resonant to 264 nm, the wavelength of the seed radiation, and introduces a small energy modulation on the electron beam. The electron beam then enters a dispersion section 20 cm in length with a 0.32 T magnetic field.

The function of this magnet is to convert the energy modulation of the beam into a spatial bunching with a strong third harmonic component at 88 nm. After it is micro-bunched, the beam enters a second wiggler, known as the “radiator” resonant for 88 nm radiation having a maximum on-axis field of 0.75 T and  $\lambda_{w2} = 2.2$  cm. When the coherently bunched beam enters the second wiggler magnet, there is a rapid coherent generation of 88 nm radiation within the first meter where the intensity of the radiation has a characteristic quadratic dependence on the distance traversed in the wiggler. There is then a transition to exponential growth which continues until 6 m into the wiggler where the 88 nm radiation approaches saturation. At this point the magnetic field of the wiggler is tapered to extract more energy from the electron beam. Here we have used 264 nm seed as an example to obtain 88 nm output radiation. The system is actually tunable over a wide

wavelength range determined by the chirped pulse laser used to generate the seed radiation.

We now turn to the key issue in the system: the preservation of the phase coherence and hence the accurate wavelength chirp of the seed pulse in the FEL. According to the theory of chirped pulse amplification [8], the phase distortion should be maintained below  $\pi$ , so that after compression the different frequency components of the chirped pulse will be coherently superimposed together at the center of the pulse.

The phase and amplitude of the output radiation depend on the current and energy detuning of the electron beam and, within a bunch, both the current and energy are functions of time. Although the energy of the electron beam is linearly chirped to match the linear chirp of the seed laser pulse wakefields generated during the acceleration introduce an additional nonlinear chirping, which results in energy detuning. Further, because of its finite bandwidth, the input chirped laser pulse intensity is also a function of time. Each of these factors contributes to phase and amplitude distortion in the FEL. To minimize the collective impact of these effects we only use the central 5 ps part of the electron bunch, where the current is near the maximum and varies only a few percent, and the energy detuning is also minimized. During this 5 ps, the seed laser wavelength  $\lambda$  is chirped through a 4% bandwidth. To resonantly match the seed laser, the electron beam energy  $\gamma$  is chirped through 2%. These parameters form the basis of our calculations.

The electron distribution (current as a function of time within the pulse) is based on the BNL DUV-FEL design operating in a configuration that provides a 20 ps long pulse with peak current of 256 A and a relatively flat top, suitable for chirped pulse amplification. The current as a function of time is given in Fig. 2. To include wakefield effects we assumed an energy chirp of 0.8% in 20 ps with cubic time dependence in addition to the applied linear chirping. The local energy spread (the energy spread within a slice of the electron pulse thin enough so that the energy

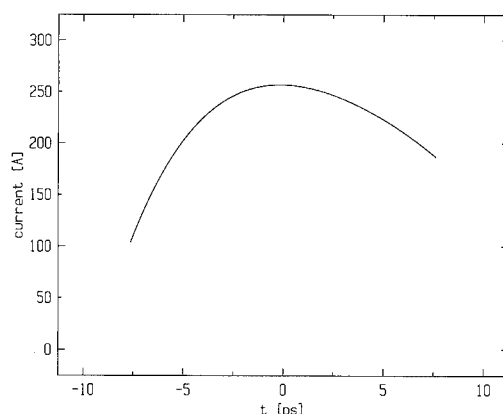


Fig. 2. Electron pulse current as a function of time.

chirping within the slice is negligible) is less than 0.1% FWHM. The laser pulse is assumed to be Gaussian and linearly chirped through 4% in the central 5 ps with a FWHM bandwidth of 2%, and a peak power of 4.6 MW. The generation of this pulse is within the state of the art of the laser technology. For the FEL simulation, we used a modified TDA code to calculate the output phase and amplitude [9,4]. For a more detailed description of the simulation, we refer to Ref. [4].

For the calculation we make an approximation related to the impact of slippage on ultrashort pulse amplification in an FEL. The slippage problem arises from the fact that the electron pulse moves more slowly than the laser pulse. If the laser pulse is much shorter than the slippage distance, the electrons interacting with the laser pulse at the beginning of the wiggler would slip away from the laser pulse before the end of the wiggler, and the FEL efficiency would be reduced significantly. The slippage in our example scales to roughly a 0.1 ps transit time difference for the electrons and photons. Within this 0.1 ps the energy of the electrons that interact with the laser light changes due to chirping. However, 0.1 ps is much smaller than either the laser pulse or electron bunch, so the variation of current and energy are negligible, and therefore are not included in our analysis. This is also related to the validity of using TDA code which is a time independent single frequency 3D code; in principle, we should use 4D code with full time dependence. However, the variation of wavelength within the slippage distance is also small, so the phase shift variation within the slippage should be negligible. If we divide the pulse into many slices with each slice length less than the slippage distance, we are justified in our use of 3D code to calculate the phase shift within each slice independently. A more rigorous calculation should compare a 1D chirped pulse calculation with a 2D time dependent calculation using a simulation code such as GINGER [10].

To describe the phase relation between the input laser and output laser, we write the input field as:

$$A_1 = a_1(t) \cos[k_1 z - \omega_1 t + \phi_1(t)], \quad (1)$$

while the output field is:

$$A_2 = a_2(t) \cos[k_2 z - \omega_2 t + \phi_2(t)], \quad (2)$$

where  $k_1$ ,  $k_2$ ,  $\omega_1$ ,  $\omega_2$  are the wavenumber and frequency for the center of the chirped input and output pulses respectively for  $\lambda_1 = 264$  nm, and  $\lambda_2 = 88$  nm. The output phase distortion is then given by the nonlinear time dependent part of the phase  $\phi(t) = \phi_2(t) - n\phi_1(t)$ , where  $n = \omega_2/\omega_1$  is the frequency multiplication ratio (in our example  $n = 3$ ). Any term in  $\phi(t)$  which is linear in  $t$  only represents a frequency shift.

The phase difference  $\phi$  between  $\phi_1$  and  $\phi_2$  is determined by the complicated FEL interaction and the electron microbunching process in the dispersion section through the electron phase shift. And it is convenient to write  $\phi$  as

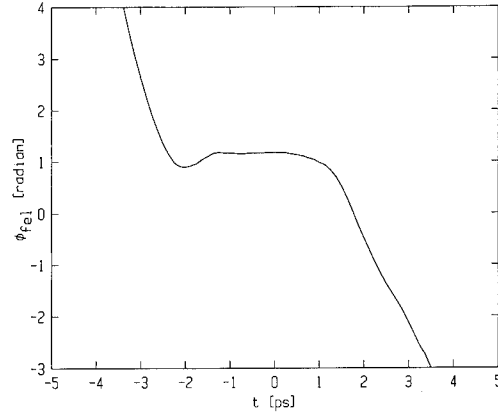


Fig. 3. Phase shift as a function of time.

a sum of two terms:  $\phi = \phi_{\text{disp}} + \phi_{\text{fel}}$ . The first term  $\phi_{\text{disp}}$  is determined by the electron phase shift in the dispersion section. We have:

$$\phi_{\text{disp}} = \frac{d\psi}{d\gamma} (\overline{\gamma(t)} - \gamma_0) + \phi_0, \quad (3)$$

where  $d\psi/d\gamma$  is the dispersion strength defined in Ref. [4], which is the electron phase shift per unit energy deviation from a reference energy  $\gamma_0$  in the dispersion section. If the  $j$ th electron passes the dispersion section delayed by  $dt_j$  because its energy is less than the reference energy  $\gamma_0$  by  $d\gamma$ , then the phase delay is  $d\psi_j = \omega_2 dt_j$  (in our example  $d\psi/d\gamma = 3$ ).  $\overline{\gamma(t)}$  is the average electron energy at time  $t$ , and  $\phi_0$  is a constant determined by the distances between the dispersion section and the wigglers. It is easily seen that a linear chirping in energy  $d\gamma/dt$  introduces a frequency shift  $\delta\omega = d\psi/d\gamma \cdot d\gamma/dt$ , while a nonlinear chirping (nonlinear energy time dependence generated, e.g., by wakefield) introduces a phase distortion. The second term  $\phi_{\text{fel}}$  is the phase shift referenced to the phase of the electrons with the average energy  $\overline{\gamma(t)}$ , and is a function of current, energy detuning, and the input laser intensity. The output power and  $\phi_{\text{fel}}$  on the axis are calculated for each individual slice of the electron pulse using the modified TDA code providing the results shown in Fig. 3. A calculation of  $\phi_{\text{fel}}$  off axis by an rms electron beam radius yields similar results.

Our calculations show that under these conditions, the 4 ps center slice provides most of the FEL gain while maintaining the intensity variation below 25%, phase distortion (the nonlinear part of  $\phi_{\text{fel}}$ ) within 0.6 rad, with less than 0.2 rad of nonlinear phase distortion introduced by  $\phi_{\text{disp}}$ . As previously mentioned, the seed laser pulse wavelength is chirped through 4% bandwidth within the central 5 ps, and the chirping rate is  $4\%/(5 \text{ ps}) = 0.8\%/ps$ , hence the central 4 ps output radiation chirped through  $0.8 \times 4 = 3.2\% \approx 3\%$  of bandwidth. This means that the output radiation has a 3% bandwidth, and can be compressed to 5

fs. The chirped pulse has a peak power 150 MW and 4 ps pulse length with a pulse energy of about 0.6 mJ, so when it is compressed to 5 fs, the resulting peak power approaches 120 GW.

Many important technical issues remain which require further study, e.g., the electron pulse timing jitter, and the stretcher-compressor pair at 88 nm, etc. However, a preliminary analysis of these issues shows that the scheme presented here is entirely feasible [1].

### Acknowledgements

We would like to thank J. Gallardo for providing the electron beam parameters of the BNL-ATF for the calculations, and S. Krinsky, I. Ben-Zvi, L. DiMauro, D. McWhan, G. Mourou, G. Korn, and E. Esarey for their useful comments and suggestions.

### References

- [1] L.H. Yu, E. Johnson, D. Li and D. Umstadter, *Phys. Rev. E* 49 (1994) 4480.
- [2] Csonka, *Particle Accelerators* 8 (1978) 225;  
V. Stagno, G. Brautti, T. Clauser and I. Boscolo, *Nuovo Cimento B* 56 (1980) 219;
- W.B. Colson, *IEEE J. Quantum Electron* QE-17 (1981) 1417;
- R. Coisson and F. DeMartini, *Physics of Quantum Electronics* (Addison-Wesley, 1982) p. 9;
- P. Elleaume, *Physics of Quantum Electronics* (Addison-Wesley, 1982) p. 8;
- I. Schnitzer and A. Gover, *Nucl. Instr. and Meth. A* 237 (1985) 124;
- R. Bonifacio, L. De Salvo Souza, P. Pierini and E.T. Scharlemann, *Nucl. Instr. Meth. A* 296 (1990) 787;
- R. Prazeres et al., *Nucl. Instr. and Meth. A* 304 (1991) 72.
- [3] Brookhaven National Laboratory DUV Free Electron Laser Conceptual Design Report, ed. S. Krinsky, December 1993, BNL-49713.
- [4] L.H. Yu, *Phys. Rev. A* 44 (1991) 5178.
- [5] P. Maine, D. Strickland, P. Bado, M. Pessot and G. Mourou, *IEEE J. Quantum Electron.* QE-24 (1988) 398.
- [6] G.T. Moore, *Nucl. Instr. and Meth. A* 272 (1988) 302.
- [7] F. Glotin et al., *Phys. Rev. Lett.* 71 (1994) 2587;  
D.A. Jaroszynsky et al., *Phys. Rev. Lett.* 71 (1994) 3798.
- [8] A.E. Siegman, *Lasers*, Chap. 10 (University Science Books, 1986) p. 386.
- [9] T.M. Tran and J.S. Wurtele, *Comp. Phys. Commun.* 54 (1989) 263.
- [10] W.M. Fawley, A.M. Sessler and E.T. Scharlemann, Coherence and linewidth studies of a 4-nm high power FEL, *Proc. Particle Accelerator Conf.*, Washington, 1993, Lawrence Berkeley Laboratory Report LBL-33285, to be published.

## Coherence effects in FEL radiation generated by short electron bunches

G.P. Gallerano <sup>\*</sup>, A. Doria, E. Giovenale, G. Messina

*ENEA, INN-FIS, P.O. Box 65, 00044 Frascati, Italy*

### Abstract

In the last few years there has been a growing interest in the study of coherent radiation from short electron bunches. The possibility of realizing compact FEL devices in the far-infrared and millimeter wave regions utilizing small to medium size radio-frequency (RF) accelerators has stimulated a number of theoretical and experimental investigations to clarify basic physics issues in this process.

Coherent emission experiments will be reviewed in this paper. Measurements on the temporal and spectral characteristics of the coherent emission from a single bunch and on the coherence between consecutive bunches will be presented along with an analysis of the influence of coherence on the dynamics of the laser.

### 1. Introduction

The idea of generating coherent radiation in the far infrared and millimeter wave region utilizing bunched electron beams goes back to the early fifties. Experimental and theoretical investigations were carried out to extract energy at a harmonic of the frequency used to modulate the beam current [1,2]. In the early work by Motz on the emission of radiation by fast electrons passing through a undulator [3] the question of coherence was raised, and it was observed that the coherent radiated power should increase with the square of the current for a bunch length less than one half wavelength, while a power proportional to the current is expected for randomly phased electron bunches. Shortly after that, experimental evidence of coherent radiation was demonstrated at wavelengths around 8 mm [4], and a few years later the first experiment to relate beam current to output power was successfully carried out [5].

The advent of the laser in the sixties greatly reduced the effort in extending the operating region of microwave electron devices into the sub-millimeter and infrared regions. The main effort was instead devoted to the search on gaseous, liquid and solid state materials to be used as an active medium at any frequency in the spectrum of electromagnetic radiation. The successful development of the first free electron laser in 1976 at Stanford in the near-infrared [6] triggered a gradual move toward both shorter and longer wavelengths, in particular for a class of

FEL which utilizes the well assessed technology of RF accelerators in an extremely wide range of electron energies. The peculiar temporal structure of the electron beam generated by these devices, which is composed of a train of short electron bunches with a length of the order of a millimeter, has led back to the original question of coherence in the long wavelength operation, and to the search of new original solutions which could fully exploit the potential of these accelerators.

Coherent radiation generated through different types of beam-wave interaction schemes has been investigated in recent years: transition radiation generated by electrons passing through thin foils [7,8], synchrotron radiation from bending magnets, Cherenkov and Smith-Purcell radiation, and most extensively undulator radiation [9–19]. A summary of these experiments is reported in Table 1, where the spectral range of emission, the type of accelerator and the electron bunch duration are also shown.

The shortest electron bunch duration has been recently obtained at the SUNSHINE facility at Stanford [8], where a  $1 + \frac{1}{2}$  cell RF gun and an alpha magnet are used to compress electron bunches down to 100 fs. The shortest wavelength reached so far in the observation of coherent emission from a pre-bunched beam has been measured around 30  $\mu\text{m}$  in the FELIX experiment at FOM. Correlation between consecutive bunches has also been observed [9,10].

At the ENEA compact FEL facility, with a simple geometry of the interaction, and without the presence of a resonator, power of the order of several watt was detected from both Cherenkov- [11] and undulator- [12] type FELs. This power level is several orders of magnitude greater than the expected incoherent spontaneous emission and

<sup>\*</sup> Corresponding author. Tel. +39 6 94005223, fax +39 6 94005334, e-mail gallerano@efr419.enea.it.



clearly shows the occurrence of coherent emission due to the short bunch duration, which results in adding in phase the fields of the individual electrons in the bunch. An FEL oscillator with a power level the order of 1 kW in 4  $\mu$ s pulses has been built [13] in the millimeter wave region, which utilizes the coherent spontaneous emission as a seed. A powerful method of calculating the coherent emission and its dependence on the actual bunch duration and shape has been provided [12], showing that, in case of an RF accelerator, coherence between a great number of consecutive bunches is also expected. This results in emission at discrete frequencies which are harmonics of the RF. In the following we will describe and analyze in detail the experimental evidence of these features.

## 2. Coherence from a single bunch and coherence between bunches

In considering the emission of radiation from a rectangular electron bunch of duration  $\tau$  (length  $\Delta x$ ) and charge  $Q$ , the total radiated power will be proportional to the square of the sum of the fields, with their relative phase, generated by individual electrons in the bunch. If the bunch length is much longer than the wavelength of the radiation (typically:  $\tau = 10$  ps implies 100 optical cycles at  $\lambda = 30 \mu\text{m}$ ) the average over the phase distribution will in general approach zero apart from a contribution from a small fraction of the total charge,  $\Delta q = fQ$ , which is assumed to be distributed over a length scale of half a wavelength or less. The total radiated power will then be:

$$P \propto N + (fN)^2, \quad (1)$$

where  $N$  is the number of electrons in the bunch. The first term in Eq. (1) represents the incoherent spontaneous emission, while the second term represents the coherent one. The coherent emission will dominate if:

$$f^2 N \gg 1. \quad (2)$$

For a typical bunch of duration  $\tau = 10$  ps and peak current  $I_p = 1.6$  A, the total charge is  $Q = 1.6 \times 10^{-11}$  C, and the number of electron is  $N = 10^8$ . The condition (2) will then require:  $f \gg 10^{-4}$ . Such a small “excess” charge will be distributed over a fraction of the bunch length according to:  $f\Delta x \leq \lambda/2$ , where the relational operator  $<$  holds true for a bunch shape with smoother edges than a rectangular one. This implies that coherent radiation will in general overcome incoherent radiation already at wavelengths in the medium infrared.

Another important question is the presence or absence of a definite phase relationship between consecutive bunches generated in an RF accelerator. Assuming regularly spaced electron bunches, observation of the emitted radiation over a time interval of several bunches will show emission at discrete frequencies which are harmonics of the fundamental  $\nu_{\text{RF}} = 1/T_{\text{RF}}$ . The upper limit to the range of harmonics over which coherent emission occurs will be set by the phase and amplitude stability of electron bunches over the macropulse. As a typical number, in an S-band linac, a phase stability of  $10^{-4}$  yields a jitter in position between bunches of  $\sim 10 \mu\text{m}$ , so that again coherence between bunches is expected in the far infrared.

A model for coherent emission in a waveguide has been described in Ref. [12] assuming an “infinite” train of regularly spaced electron bunches moving through an undulator. According to this picture radiation is emitted at discrete frequencies  $\nu_l = l/T_{\text{RF}}$ , where  $l$  is an integer, and

Table 1  
Recent experiments on coherent emission

| Laboratory                      | Radiation                             | Spectral range         | Accelerator                        | Bunch duration |
|---------------------------------|---------------------------------------|------------------------|------------------------------------|----------------|
| Cornell                         | Transition rad. harmonic gen.         | 0.25–3 mm              | 300 MeV RF linac                   | 3 ps           |
| ENEA-Frascati, compact FEL      | Cherenkov undulator                   | 0.8–1.6 mm             | 5 MeV microtron                    | 15 ps          |
| FOM-Institute, Nieuwegein       | undulator                             | 1.5–4 mm               | 2.3 MeV microtron                  |                |
| Korea Ad. Inst. Science & Tech. | undulator                             | 20–100 $\mu\text{m}$   | 25 MeV RF linac                    | 3–6 ps         |
|                                 | undulator                             | 7.4 mm                 | Photocathode gun electrostatic     | 35 ps          |
| ILE-Osaka, Tohoku               | undulator bending magnet              | 1.5–4 mm               | 6.85 MeV RF linac                  | 5 ps           |
| Pantell's group, Stanford       | Synchrotron undulator                 | 1–2 mm                 | 3–4 MeV                            | 10 ps          |
|                                 | undulator                             | 100–200 $\mu\text{m}$  | 1 + 1/2 cell RF gun                |                |
| SCA FIR-FEL, Stanford           | undulator                             | 30–50 $\mu\text{m}$    | Superconducting RF linac           | 1–3 ps         |
| SUNSHINE, SSRL, Stanford        | Synchrotron transition rad. undulator | 50 $\mu\text{m}$ –1 mm | 1 + 1/2 cell RF gun + alpha magnet | 100 fs         |
|                                 | undulator                             |                        | 30 MeV RF linac                    |                |
| UCLA, Los Angeles               | undulator                             | 1–2 mm                 | 1 + 1/2 cell RF gun                | 10–100 ps      |
|                                 |                                       |                        | 4 MeV RF linac                     |                |

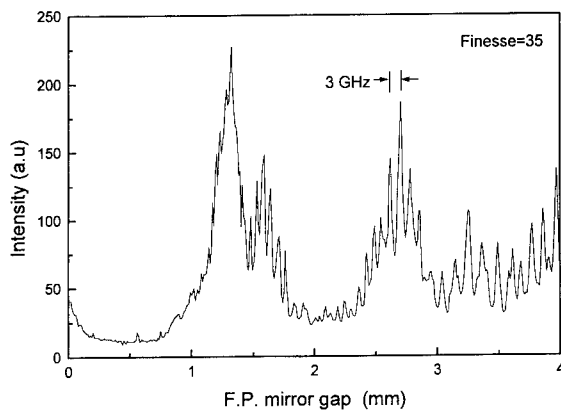


Fig. 1. Fabry-Perot interferogram of the coherent spontaneous emission.

the radiated power in the  $TE_{0,n}$  mode at the harmonic  $l$  is calculated as:

$$P_{l,0,n} = \frac{Z_0}{\beta_g} I_p^2 \frac{C_l^2}{8} \frac{a_w^2}{\beta^2 \gamma^2} \mathcal{F}^2 \frac{L^2}{ab} \left[ \frac{\sin(\theta/2)}{\theta/2} \right]^2, \quad (3)$$

where  $Z_0 = 377 \Omega$  is the free-space impedance,  $\beta_g$  is the group velocity in the guide,  $I_p$  is the bunch peak current,  $C_l$  is the Fourier coefficient of the bunch current profile at the  $l$ th harmonic,  $a_w$  is the usual undulator parameter,  $\mathcal{F}$  is the filling factor of the e-beam distribution over the waveguide transverse mode,  $L$  the undulator length,  $a$  and

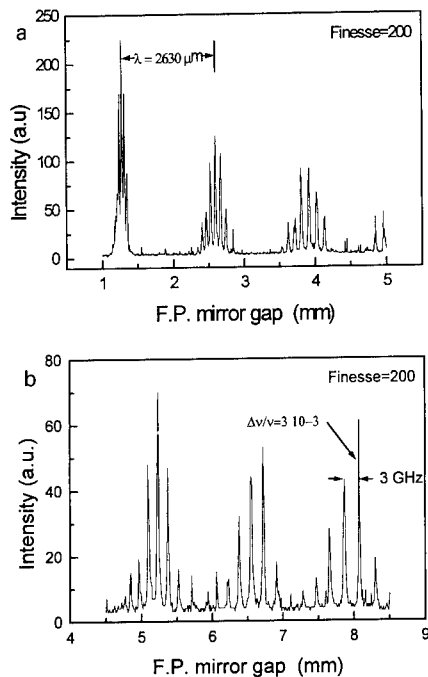


Fig. 2. Fabry-Perot interferogram of the FEL oscillator output at increasing resolution: (a) scan of the mirror gap from 1 to 5 mm; (b) scan from 4.5 to 8.5 mm

$b$  the waveguide transverse dimensions, and  $\theta$  the usual FEL phase-shift parameter.

Eq. (3) represents a multiple line spectrum with a

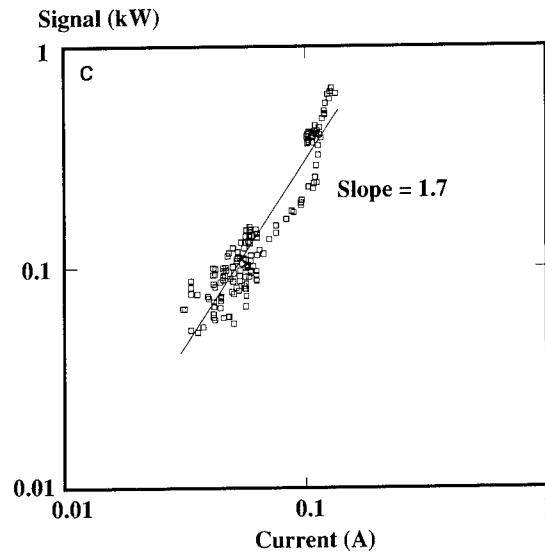
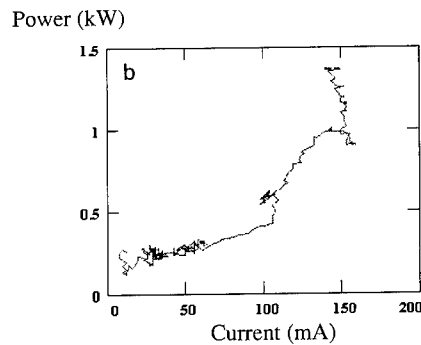
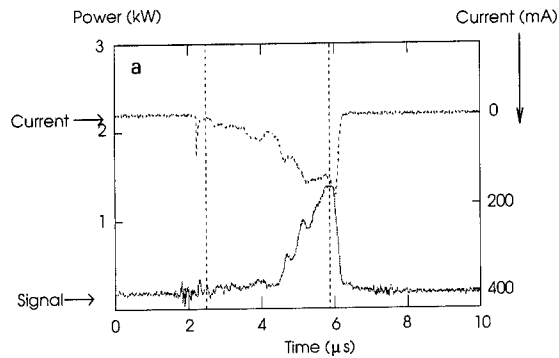


Fig. 3. Signal growth in the FEL resonator: (a) temporal profile of electron current (upper trace) and mm-wave detector signal (lower trace); (b) dependence of power on electron beam current; (c) dependence of power on electron beam current on a double log scale. Squares: experimental data; line: best fit of the experimental data with a straight line.

radiated power at the harmonic frequency  $\nu_l$  proportional to the square of the electron current and to the square of the undulator length. The frequency dependence of the radiated power has the usual  $\sin^2(\theta/2)$  behaviour of the undulator spontaneous emission around the resonant frequency  $\nu_r$  given by  $\theta(\nu_r) = 0$ . The width of the individual lines will be related to the number of correlated bunches. In practice, if correlation between bunches is assumed to occur over the whole macropulse duration  $T_M$ , typically 1–10  $\mu$ s, a relative linewidth  $\Delta\nu_l/\nu_l \approx T_{RF}/T_M \approx 3 \times 10^{-4}$ – $3 \times 10^{-5}$  is expected. On the other hand, current amplitude fluctuations during the macropulse over a time interval of  $\sim 100$  ns would increase the linewidth to:  $\Delta\nu_l/\nu_l \approx 3 \times 10^{-3}$ .

### 3. Experimental results

Coherent spontaneous emission measurements at millimeter wavelengths were performed on the ENEA FEL at Frascati and reported in Ref. [12]. Although experimental results were in good agreement with theory, the spectral resolution of the Fabry–Perot (FP) interferometer employed in the measurements was not enough to resolve individual harmonics of the 3 GHz RF and measure their linewidth. The same type of measurement has been repeated more recently utilizing free-standing metal meshes as mirrors in the FP interferometer with a resulting finesse  $F = 35$ . This corresponds to a spectral resolution of about 1 GHz at a mirror gap of 0.4 cm. The measured FP interferogram is shown in Fig. 1. Two bands characteristic of FEL emission in a waveguide close to the “zero slippage” condition [12] can be observed at the first interferometric order for values of the mirror gap in the range between 1 and 2 mm. A “line” structure is clearly present within these bands and is well resolved at the second interferometric order (mirror gap between 2 and 4 mm). A separation of 3 GHz between the individual lines is measured, which shows the emission at harmonics of the RF. The measured linewidth is in this case limited by the spectral resolution of the interferometer.

A more detailed spectral analysis has been performed on the emission from the FEL oscillator once mirrors were installed in the FEL resonator (see Ref. [13] for detailed characteristics of the resonator). Taking advantage of the large signal to noise ratio, due to the relatively high output power, it has recently been possible to set up a metal-mesh FP interferometer with a finesse  $F = 200$  and a spectral resolution of about 0.1 GHz at a mirror gap of 0.8 cm. The “line” structure is extremely clear in this case (Fig. 2), even at low interference orders, within a measured relative bandwidth of the FEL emission  $\Delta\nu/\nu \approx 7\%$  FWHM. The relative width of the individual harmonics is measured to be  $\Delta\nu_l/\nu_l \approx 3 \times 10^{-3}$ . This number is in agreement with a correlation between bunches over 100 ns time duration, and it is also close to the width of the longitudinal modes in the FEL resonator.

Finally, the growth of the FEL output power during the macropulse has been investigated to study the effect of coherent spontaneous emission in the start-up of the oscillator. Utilizing a “ramped” current pulse and a fast n-Ge photon drag detector it has been possible to measure the correlation between the output power and the electron beam current. The time evolution of FEL power and e-beam current, and their correlation is shown in Fig. 3a and 3b respectively. A non-linear dependence of signal on current, which on a double log scale is well fitted by a straight line with slope 1.7 (Fig. 3c), is observed up to a threshold region, where the onset of gain and exponential growth is established.

Prebunching has proven to be an interesting feature in the realization of mm-wave and far infrared FELs, which provides a faster start-up of the laser and new spectral characteristics important for the use of FELs in spectroscopic applications.

### References

- [1] P.D. Coleman and M.D. Sirkis, J. Appl. Phys. 26 (1955) 1385.
- [2] R.H. Pantell, P.D. Coleman and R.C. Becker, IEEE Trans. Electron Devices ED-5 (1958) 167.
- [3] H. Motz, J. Appl. Phys. 22 (1951) 527.
- [4] H. Motz et al., J. Appl. Phys. 24 (1953) 826.
- [5] H. Motz, D. Walsh, J. Appl. Phys. 33 (1962) 978.
- [6] D.A.G. Deacon, L.R. Elias, J.M.J. Madey, G.J. Ramian, H.A. Schwettman and T.I. Smith, Phys. Rev. Lett. 38 (1977) 892.
- [7] U. Happek, A.J. Sievers and E.B. Blum, Phys. Rev. Lett. 67 (1991) 2962.
- [8] P. Kung, H. Lihn, H. Wiedemann and D. Bocek, Phys. Rev. Lett. 73 (1994) 967.
- [9] D. Oepts, R.J. Bakker, D.A. Jaroszynski, A.F.G. van der Meer and P.W. van Amersfoort Phys. Rev. Lett. 68 (1992) 3543.
- [10] D.A. Jaroszynski, R.J. Bakker, A.F.G. van der Meer, D. Oepts, W. van Amersfoort, Phys. Rev. Lett. 71 (1993) 3798.
- [11] F. Ciocci, A. Doria, G.P. Gallerano, I. Giabbai, M.F. Kimmitt, G. Messina and A. Renieri, Phys. Rev. Lett. 66 (1991) 699.
- [12] A. Doria, R. Bartolini, J. Feinstein, G.P. Gallerano and R.H. Pantell, IEEE J. Quantum Electron. QE-29 (1993) 1428.
- [13] F. Ciocci, R. Bartolini, A. Doria, G.P. Gallerano, E. Giovenale, M.F. Kimmitt, G. Messina and A. Renieri, Phys. Rev. Lett. 70 (1993) 928.
- [14] T. Nakazato et al., Phys. Rev. Lett. 63 (1989) 1245.
- [15] Y.U. Jeong, Y. Kawamura, K. Toyoda, C.H. Nam, S.S. Lee, Phys. Rev. Lett. 68 (1992) 1140.
- [16] M. Asakawa, N. Sakamoto, N. Inoue, T. Yamamoto, K. Mima and S. Nakai, Nucl. Instr. and Meth. A 341 (1994) 72.
- [17] J. Lewellen et al., these Proceedings (16th Int. Free Electron Laser Conf., Stanford, CA, USA, 1994) Nucl. Instr. and Meth. A 358 (1995) 24.
- [18] K.W. Berryman and T.I. Smith, *ibid.*, p. ABS 93.
- [19] F.V. Hartemann et al., presented at this Conference (16th Int. Free Electron Laser Conf., Stanford, CA, USA, 1994).



ELSEVIER

## Free electron maser experiment with a prebunched beam

M. Cohen<sup>\*</sup>, A. Kugel, D. Chairman, M. Arbel, H. Kleinman, D. Ben-Haim, A. Eichenbaum,  
M. Draznin, Y. Pinhasi, I. Yakover, A. Gover

*Department of Electrical Engineering–Physical Electronics, Faculty of Engineering, Tel-Aviv University, Ramat-Aviv, 69978, Israel*

### Abstract

An experimental project aimed at demonstrating Free Electron Maser (FEM) operation with prebunching is under way at Tel-Aviv university. The FEM utilizes a 1.0 A prebunched electron beam obtained from a microwave tube. The electron beam is bunched at 4.87 GHz and is subsequently accelerated to 70 keV. The bunched beam is injected into a planar wiggler ( $B_w = 300$  G,  $\lambda_w = 4.4$  cm) constructed in a Halbach configuration with 17 periods. The wiggler utilizes a new scheme for horizontal focusing based on the use of two long permanent magnets at the sides of the wiggler. We plan to study FEM gain enhancement and radiation features due to the prebunched (superradiant) mode of operation. In an oscillator configuration the experiment should be enable study of seed injection by prebunching. Simulation of FEL operation shows an expected gain of approximately 100% and an rf output power of 5 kW. In this paper we review the design of the main parts of the experimental set-up, and present recent analytical, numerical, and experimental results.

### 1. Introduction

The emission of coherent radiation from a FEL can be enhanced if the e-beam is prebunched prior to entrance into the interaction region [1–4]. Such a scheme should allow for operation at high harmonic frequencies for high harmonics components of the beam current [3–11]. A linear theory for this scheme operated in the superradiant and stimulated superradiant mode was presented in Ref. [1] for both the low and the high gain regimes. A table top low-energy and high-current Free Electron Maser (FEM) is under development in Tel-Aviv university for experimental study of prebunched FEM physics. The basic scheme is shown in Fig. 1.

In the present scheme the electron beam is prebunched by a microwave tube operated at 10 kV, 1.0 A and driven at 4.87 GHz to produce a bunched e-beam. Upon exit from the prebuncher, the beam is accelerated to 70 keV. After a short acceleration region, the e-beam drifts, is focused and is injected into the wiggler. Tables 1, 2, and 3 contain the main FEM characteristics.

The FEM device will be operated as an amplifier in the low-gain, space-charge dominated regime. We plan to study the FEM gain enhancement and radiation features in the prebunched (superradiant) mode of operation of the single-pass FEL with a long electron pulse. If one closes

the rf out–rf in loop (Fig. 1) the device becomes an oscillator. The oscillator configuration will be used to study seed injection by e-beam prebunching and amplified superradiant oscillation [1].

In this paper we describe the design of the main parts of the experimental set-up and present recent analytical, numerical, and experimental results including a novel scheme for lateral focusing in the wiggler as described in Section 2.

### 2. Wiggler field design

The planar wiggler consists of a stack of Sm–Co permanent magnets comprising 17 periods, in a Halbach arrangement. The wiggler parameters are presented in Table 2.

To attain e-beam focusing in the lateral dimension of the planar wiggler a novel scheme was developed based on two longitudinal magnets, which provide a lateral field gradient on the axis of the wiggler. To attain a circular beam ( $k_{\beta x} = k_{\beta y}$ ), equal focusing strength is required in the vertical and horizontal dimensions. The horizontal gradient of the vertical magnetic field required to satisfy this condition is given by the following expression [12]:

$$\alpha = \frac{e}{2mc} \frac{B_w^2}{\gamma\beta_z}, \quad (1)$$

where  $B_w$  is the peak value of the vertical component of the wiggler field. For the present experiment  $\alpha \equiv \partial B_w / \partial x$

<sup>\*</sup> Corresponding author. Tel. +972 3 640 8148, fax +972 3 642 3508, e-mail: moshec@eng.tau.ac.il.

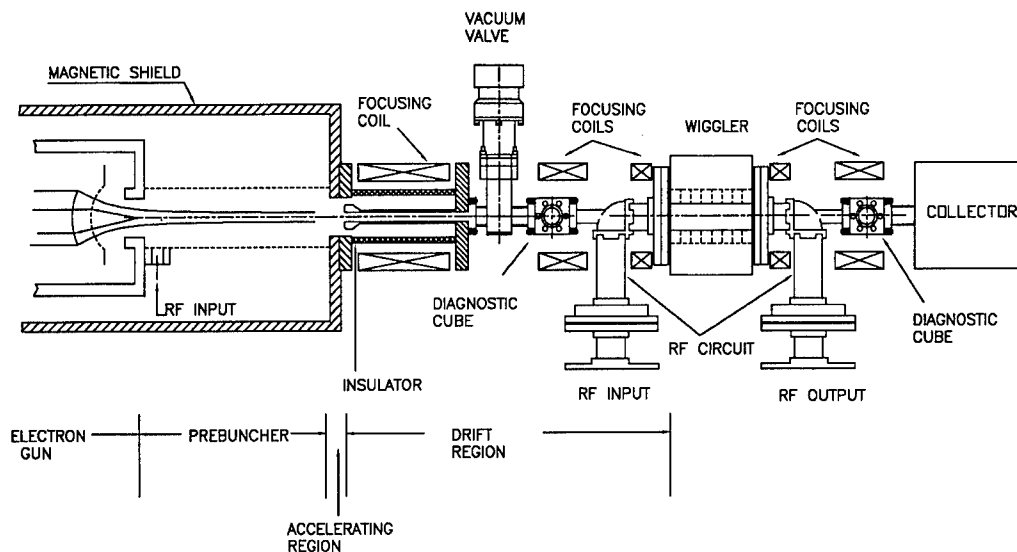


Fig. 1. The basic scheme of the prebunched beam experiment at TAU.

$= 0.49$  G/mm. The wiggler also includes matching magnet sections at the wiggler entrance and the wiggler exit. The magnetic field of the wiggler in three dimensions was calculated numerically using Biot–Savart’s law, following Ref. [14].

For the magnets we use, the distance between the longitudinal magnets is determined theoretically [12]:  $D = 10.42$  cm. The same result is obtained by solving the 3D

problem numerically and measuring the beam parameters experimentally. The electron beam cross-section measurements for various cases of horizontal focusing inside the wiggler are presented in Fig. 2. Good agreement is found between experimental results, theoretical calculation and numerical simulations. We used the pulsed-wire technique [13] to construct and measure the proper wiggler field and to minimize random field errors.

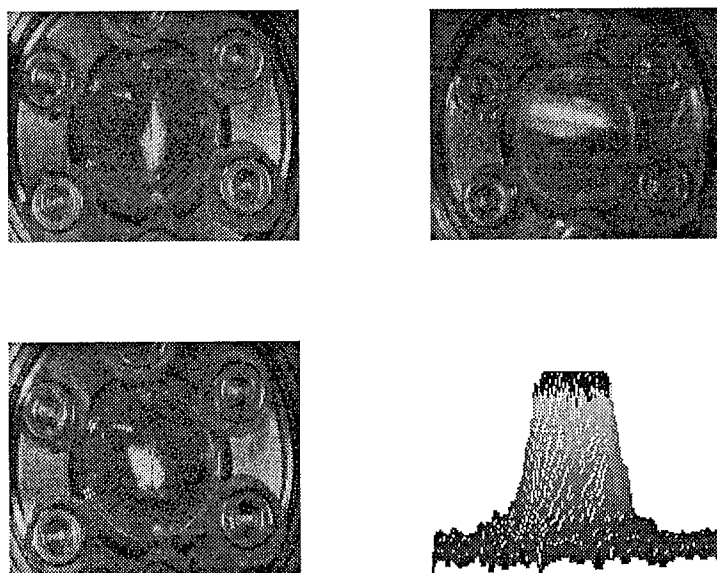


Fig. 2. Measurements of e-beam cross section inside the wiggler. (a) e-beam cross-section with horizontal overfocusing, (b) without horizontal focusing, (c) with horizontal focusing. (d) The current density of the e-beam inside the wiggler.

Table 1  
Electron beam parameters

|                         |                               |
|-------------------------|-------------------------------|
| Electron beam energy    | $E_k = 70$ keV                |
| Beam current            | $I_0 = 1.0$ A                 |
| Beam diameter           | $r_b = 2.0$ mm                |
| Plasma frequency        | $f_p = 0.5$ GHz               |
| Macropulse duration     | $\tau = 1\text{--}20$ $\mu$ s |
| Electron bunch duration | $\tau_{eb} = 0.2$ ns          |
| Energy spread           | $\sigma_E / E \approx 0.5\%$  |

Table 2  
Planar wiggler parameters

|                     |  |
|---------------------|--|
| Wiggler field       | $B_w = 300$ G ( $a_w = 0.12$ )           |
| Period length       | $\lambda_w = 4.4$ cm                     |
| Number of periods   | $N_w = 17$                               |
| Wiggler length      | $L_w = 0.748$ m                          |
| Gap                 | $g = 5.1$ cm                             |
| Betatron wavenumber | $k_{\beta x} = k_{\beta y} = 23.4$ rad/m |

### 3. Microwave interaction region

The parameters of the waveguide operating in the TE<sub>10</sub> mode which has been chosen for FEL interaction are given

Table 3  
Microwave (TE<sub>10</sub> mode) parameters

|                      |   |
|----------------------|---|
| Waveguide dimensions | $a \times b = 47.55 \times 22.15$ mm <sup>2</sup> |
| Cutoff frequency     | $f_{co} = 3.15$ GHz                               |
| Frequency            | $f_s = 4.87$ GHz                                  |
| Signal wavelength    | $\lambda_s = 6.2$ cm                              |
| Losses               | $\alpha = 0.04$ dB/m                              |
| Power filling factor | $A_e / A_{em} = 0.063$                            |

in Table 3. The fundamental mode TE<sub>10</sub> of a WR-187 rectangular waveguide ( $47.55 \times 22.15$  mm<sup>2</sup> cross section) is used for the FEM interaction. The cutoff frequency of this mode is 3.15 GHz and the system is operated in a frequency range of 4 to 6 GHz. In this frequency range, the only mode that can propagate in the waveguide is the fundamental mode (TE<sub>10</sub>), all the higher order modes are cut off. The dispersion curves are given in Fig. 3d.

The electron beam enters the interaction region through a 9 mm diameter hole in the waveguide bend. This hole is followed by a cylindrical section below cutoff so that it allows injection of the beam with no rf power loss and with rf power reflection of less than 5% of the total input power in the 4–6 GHz frequency range [15]. In order to increase the power filling factor we may insert profiles

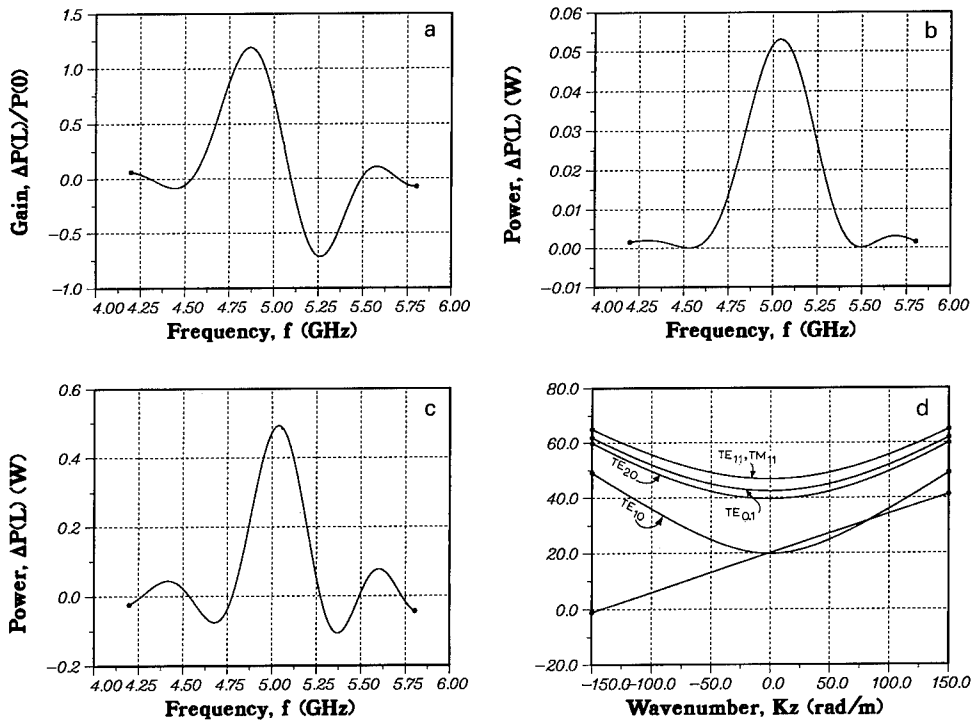


Fig. 3. Predicted radiation emission from prebunched beam. (a) The gain vs. the signal frequency. The maximum gain is achieved at 4.87 GHz. (b) The power generated due to prebunched beam as a function of frequency. The peak power appears at 5 GHz. (c) The power generated due to stimulated prebunched beam emission as a function of frequency. The peak power appears at 5 GHz. (d) The dispersion curves and the electron beam line. The electron beam is synchronized with the fundamental mode TE<sub>10</sub>. In a frequency range of 4–6 GHz, all the waveguide modes except TE<sub>10</sub> are cutoff.

along the waveguide walls. This lowers the cutoff frequency and enables reduction of the waveguide dimensions for the same cutoff frequency. Consequently, the wiggler gap can be decreased and the wiggler field increases resulting in higher gain.

#### 4. Gain and power calculation

The FEL gain and radiated power were calculated for a linear model of a prebunched cold beam [1]. This model yields the following gain–dispersion equation:

$$C_s(s) = \left\{ \left[ (sL - i\bar{\theta})^2 + \bar{\theta}_{pr}^2 \right] LC_s(0) + \left[ (sL - i\bar{\theta})M_j e^{i\bar{\phi}_j} - iM_v e^{i\bar{\phi}_v} \right] \left[ \frac{P_B}{\mathcal{P}_s} \right]^{1/2} \right\} / \left\{ sL \left[ (sL - i\bar{\theta})^2 + \bar{\theta}_{pr}^2 \right] - i\bar{Q} \right\}, \quad (2)$$

where  $\bar{\theta}$ ,  $\mathcal{P}_s$ , and  $k_z$  are the normalized detuning parameter, the normalization power and the wavenumber of the propagating waveguide mode, respectively. The reduced plasma frequency parameter is:

$$\bar{\theta}_{pr} = \frac{\omega'_p}{v_{0z}} Lr, \quad (3)$$

where  $\omega'_p = [e^2 n_0 / (\epsilon_0 \gamma_0 \gamma_{0z}^2 m)]^{1/2}$  and  $r$  is the plasma frequency reduction factor. For our FEM design parameters  $r$  is in the range of 0.2–0.5. The bunching power parameter  $P_B$  is given by:

$$P_B = \frac{1}{16 A_{em} \beta_{ph}} \sqrt{\frac{\mu_0}{\epsilon_0}} \left[ \frac{\bar{a}_w}{\gamma_0 \beta_{0z}} I_0 L \right]^2, \quad (4)$$

where  $\beta_{ph}$  is the phase velocity. The amplitude of the generated radiation due the prebunched beam is proportional to the velocity and current indices of modulation which are defined as  $M_j e^{i\bar{\phi}_j} = \tilde{J}_z(0)/J_0$ ,  $M_v e^{i\bar{\phi}_v} = \tilde{V}_z(0)/v_{0z} kL$ , where  $\bar{\phi}_j$  and  $\bar{\phi}_v$  are the phases of the current density and axial velocity modulation waves with respect to the ponderomotive wave phase. The gain parameter is given by:

$$\bar{Q} = \frac{1}{4} \frac{A_e}{A_{em}} \left[ \frac{\bar{a}_w}{\gamma_0 \beta_{0z}} \beta_{ph} \right]^2 \left[ \frac{\omega}{v_{0z}} \right]^2 L^3 k_z. \quad (5)$$

The field amplitude  $C(L)$  is derived by taking the inverse Laplace transform of the gain Eq. (2):  $C(L) = \mathcal{L}^{-1}\{C(s)\}$  and the output power is found from the relation  $P_{out} = |C(L)|^2 \mathcal{P}_s$ . The square of the absolute value (after transformation) of the two parts in Eq. (2) produce three

terms corresponding to three different radiation emission processes. The curves of gain and radiated power of the various radiation processes are shown in Figs. 3a, 3b, and 3c. The gain of a conventional FEL (without prebunching) is obtained from the first part on the r.h.s. of Eq. (2), the pure prebunched beam emission (zero input signal) is due to the second term (squared) in this equation.

The last emission process results from the mixed term which involves the input signal and the bunched beam parameters. We define the radiation due to this term as a stimulated prebunched beam emission. The curves in Figs. 3 are obtained with the FEM design parameters which are presented in Tables 1, 2, and 3, and with the assumptions that  $\bar{\phi}_v = \bar{\phi}_j = 0$ ,  $M_v = 0$  and  $M_j = 0.01$ . The device will be operated by inserting an rf signal to either or both input ports as shown in the experimental scheme (Fig. 1). We shall experimentally verify the three radiation processes described by theory and measure the corresponding emission curves (Figs. 3).

#### References

- [1] I. Schnitzer and A. Gover, Nucl. Instr. and Meth. A 237 (1985) 124.
- [2] C. Leibovitch, K. Xu and G. Bekefi, IEEE J. Quantum Electron. QE-24 (1988) 1825.
- [3] D.A. Jaroszynski, R.J. Bakker, A.F.G. van der Meer, D. Oepts and P.W. van Amersfoort, Phys. Rev. Lett. 71 (1993) 3798.
- [4] D.A. Jaroszynski, R.J. Bakker, A.F.G. van der Meer, D. Oepts and P.W. van Amersfoort, Nucl. Instr. and Meth. A 341 (1994) ABS 24.
- [5] B. Girard, Y. Lapierre, J.M. Ortega, C. Bazin, M. Billardon, P. Elleaume, M. Bergher, M. Velghe and Y. Petroff, Phys. Rev. Lett. 53 (1984) 2405.
- [6] J.M. Ortega, Y. Lapierre, B. Girard, M. Billardon, P. Elleaume, C. Bazin, M. Bergher, M. Velghe and Y. Petroff, IEEE J. Quantum Electron. QE-21 (1985) 909.
- [7] A. Gover, A. Friedman and A. Luccio, Nucl. Instr. and Meth. A 259 (1987) 163.
- [8] R. Bonifacio, L. De Salvo and P. Pierini, Nucl. Instr. and Meth. A 293 (1990) 627.
- [9] M. Billardon, R. Coisson and Y. Lapierre, Appl. Phys. B 39 (1986) 9.
- [10] R. Coisson, IEEE J. Quantum Electron. QE-19 (1982) 306.
- [11] B.M. Kincaid, Nucl. Instr. and Meth. A 250 (1986) 212.
- [12] M. Cohen and A. Gover, Internal Report PBFEM5 (1993).
- [13] R. Kost, M. Rafaeli, M. Cohen and A. Gover, Annual Meeting of the Israel Physical Society, Tel-Aviv, April 1993.
- [14] L. Elias, R.-C.J. Hu and G. Ramian, Quant. Inst. Rep. UCSB, QIFEL023 (1983).
- [15] D. Ben-Haim, M.Sc. Thesis, Tel-Aviv University (1994).

# Mode-locked super-radiant free-electron laser oscillator

Y. Pinhasi<sup>\*</sup>, A. Gover

Faculty of Engineering, Department of Electrical Engineering–Physical Electronics, Tel-Aviv University, Ramat Aviv 69978, Israel

## Abstract

Evolution of the time domain fields and the spectral power of super-radiant radiation in a free-electron laser oscillator (e-beam pulses shorter than a wavelength) are investigated. We consider a finite train of  $N$  short bunches of electrons propagating through the undulator. The coherence of the synchrotron radiation emitted from the bunched beam grows with the number  $N$  of the e-beam pulses entering the interaction region. When  $N$  grows to infinity, the radiation becomes perfectly coherent at all harmonic frequencies of the pulse injection (bunching) frequency.

When the super-radiant emission takes place inside a resonator, the coherence of the emitted radiation is enhanced. Under the condition of mode-locking, the fields add in phase and the spectral energy distribution becomes narrow. When the finesse  $F$  of the resonator is small  $F < N$ , the spectral width of the out-coupled radiation emitted from the resonator is limited by  $N$ , and in the opposite case  $F > N$ , it will be limited by  $F$ . If the number of pulses  $N$  grows to infinity, the out-coupled radiation reaches a steady state of perfect coherence with reduced harmonic contents (determined by the Finesse of the resonator). There is no threshold for emission of this kind of coherent radiation.

## 1. Introduction

Electrons passing through a magnetic undulator emit partially coherent radiation called undulator synchrotron radiation [1]. The radiation from different electrons, which enter the undulator at random, adds up incoherently, unless the electrons are inserted as a single short bunch (shorter than the oscillation period of the emitted radiation) [2–7] or enter as a periodic train of bunches at the frequency of the emitted radiation [8–11]. Only in these cases do the electrons radiate in phase with each other (super-radiant) and the radiation is coherent.

Super-radiant emission from a short pulsed electron beam has recently been observed experimentally in synchrotron radiation [12,13], in Cherenkov radiation [14] and in undulator radiation [15–17]. Most recently Asakawa et al. reported the emission of enhanced super-radiant undulator radiation from a train of short electron beam pulses within a mm-wave cavity [18].

The purpose of this article is to present a rigorous time and frequency domain analysis of super-radiant undulator radiation by a train of electron beam short pulses inside a waveguide resonator (see Fig. 1).

This scheme is of interest as a realizable source of a long or even of a continuous train of coherent radiation

pulses. Contrary to conventional laser oscillators, this kind of super-radiant oscillator does not have an oscillation threshold and can produce coherent radiation at any power level.

## 2. Excitation of the electromagnetic field

Our analysis is based on modal expansion of the total electromagnetic field presented as a superposition of transverse eigen-functions of the uniform cavity in which the radiation propagates [20]. In the angular frequency domain  $\omega$ , the field of each mode can be written as:

$$\begin{aligned}\tilde{E}_q(r, \omega) &= \tilde{C}_q(z, \omega) \tilde{\mathcal{E}}_q(x, y) e^{+jk_{zq}(\omega)z}, \\ \tilde{H}_q(r, \omega) &= \tilde{C}_q(z, \omega) \tilde{\mathcal{H}}_q(x, y) e^{+jk_{zq}(\omega)z}.\end{aligned}\quad (1)$$

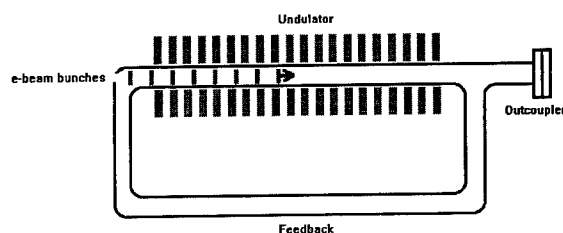


Fig. 1. Schematic illustration of a super-radiant free-electron laser oscillator.

<sup>\*</sup> Corresponding author. Tel. +972 3 640 8271, fax +972 3 642 3508, e-mail yosip@eng.tau.ac.il.



$\tilde{\mathcal{E}}_q(x, y)$  and  $\tilde{\mathcal{H}}_q(x, y)$  are complex vectors representing the transverse profile and polarization of the electric and magnetic fields of transverse eigenmode  $q$ , with wave-number  $k_{zq}(\omega)$ .  $\tilde{C}_q(z, \omega)$  is the Fourier transform of the mode's amplitude, which in the case of a propagating (non-evanescent) mode, satisfies the following excitation equation:

$$\begin{aligned} \frac{d}{dz} \tilde{C}_q(z, \omega) \\ = -\frac{1}{4\mathcal{P}_q} e^{-jk_{zq}(\omega)z} \iint \tilde{\mathbf{J}}(r, \omega) \cdot \tilde{\mathcal{E}}_q^*(x, y) dx dy, \end{aligned} \quad (2)$$

where  $\mathcal{P}_q = \frac{1}{2} \iint [\tilde{\mathcal{E}}_{q\perp}(x, y) \times \tilde{\mathcal{H}}_{q\perp}^*(x, y)] \cdot \hat{z} dx dy$  is the normalization power of the  $q$ th propagating mode. For a radiation signal of finite energy, the spectral energy density carried by the excited propagating mode is given by:

$$\frac{d\mathcal{W}_q(z)}{d\omega} = |\tilde{C}_q(z, \omega)|^2 \mathcal{P}_q. \quad (3)$$

### 3. Super-radiant emission from a train of e-beam bunches

Consider first the case of a train of electron bunches passing through a wiggler field, emitting super-radiant synchrotron radiation without a resonator. The electron beam is composed of  $N$  short bunches, entering the interaction region with time intervals  $T$  between each other. The duration of each bunch is small compared to the period of the emitted electromagnetic field. The current density is a product of the space-charge density and the velocity  $\mathbf{v}$  field of the electrons:

$$\mathbf{J}(r, t) = -\hat{q} \sum_{n=0}^{N-1} \mathbf{v} f(x, y) \delta[z - z_n(t)], \quad (4)$$

where  $f(x, y)$  is the transverse space-charge distribution of the bunch of total charge  $\hat{q}$ . In the space-frequency domain the current density of the train of bunches is the Fourier transform of (4):

$$\begin{aligned} \tilde{\mathbf{J}}(r, \omega) &= \int_{-\infty}^{+\infty} \mathbf{J}(r, t) e^{+j\omega t} dt \\ &= -\hat{q} \sum_{n=0}^{N-1} \frac{\mathbf{v}}{v_z} f(x, y) e^{+j\omega t_n(z)}, \end{aligned} \quad (5)$$

where

$$t_n(z) = nT + \int_0^z \frac{1}{v_z(z')} dz' \quad (6)$$

is the time passed until the  $n$ th bunch, which entered the interaction region at time  $nT$  and moves at an instantane-

ous axial velocity  $v_z(z)$ , arrives at a point  $z$ . Substitution of the expression for the transverse current density  $\tilde{\mathbf{J}}(r, \omega)$  into Eq. (2), results in [21]:

$$\begin{aligned} \frac{d}{dz} \tilde{C}_q(z, \omega) &= \frac{\hat{q} \zeta_q}{8\mathcal{P}_q} \sum_{n=0}^{N-1} \frac{1}{v_z} e^{+j[n\omega T + \int_0^z \theta_q(z') dz']} \\ &\quad \times \iint f(x, y) \tilde{\mathbf{v}}_{\perp}^w \cdot \tilde{\mathcal{E}}_q^*(x, y) dx dy, \end{aligned} \quad (7)$$

where we define:

$$\zeta_q \equiv \begin{cases} 1 & \text{for TE modes} \\ 1 - \frac{k_{\perp q}^2}{k_{zq} k_w} & \text{for TM modes} \end{cases}$$

and  $\theta_q(z) = \omega/v_z(z) - (k_{zq} + k_w)$  is the detuning at point  $z$ .  $k_w = 2\pi/\lambda_w$ , where  $\lambda_w$  is the wiggler period and  $\tilde{\mathbf{v}}_{\perp}^w$  is the amplitude of the transverse wiggling velocity.

Neglecting the interaction effect of the radiation on the electrons in the bunch, it is assumed that the electrons in the beam all move at a constant (averaged over wiggler period) axial velocity  $v_z(z) = v_{z0}$  and keep their initial detuning parameter  $\theta_q$  constant along the wiggler. Consequently, the solution of the excitation Eq. (7) at the exit of a wiggler of length  $L_w$  is found to be:

$$\begin{aligned} \tilde{C}_q(L_w, \omega) &= \mathcal{A}_q \text{sinc}\left(\frac{1}{2}\theta_q L_w\right) \frac{\sin\left(\frac{1}{2}N\omega T\right)}{\sin\left(\frac{1}{2}\omega T\right)} \\ &\quad \times e^{j\frac{1}{2}[\theta_q L_w + (N-1)\omega T]}, \end{aligned} \quad (8)$$

where

$$\mathcal{A}_q = \frac{\hat{q} \zeta_q}{8\mathcal{P}_q} \frac{L_w}{v_{z0}} \iint f(x, y) \tilde{\mathbf{v}}_{\perp}^w \cdot \tilde{\mathcal{E}}_{q\perp}(x, y) dx dy$$

and  $\text{sinc}(x) \equiv (\sin(x))/x$ . In the case of two well-separated solutions, where the respective frequency bandwidths of the emission are smaller than the spectral range between the resonance frequencies, it is sufficient to use a first order approximation  $k_{zq}(\omega) \simeq k_{zq}(\omega_s) + (1/v_g)(\omega - \omega_s)$  of the dispersion relation of the propagating mode  $q$ . The time domain picture of the field of the mode emitted by the e-beam bunches near the synchronism frequency  $\omega_s$  is found to be [7]:

$$\begin{aligned} E_q(x, y, z = L_w, t) &= \Re \left\{ \frac{\mathcal{A}_q}{\tau_{sp}} \sum_{n=0}^{N-1} \text{rect}\left(\frac{t - t_d - nT}{\tau_{sp}}\right) \right. \\ &\quad \left. \times \tilde{\mathcal{E}}_q(x, y) e^{-j[\omega_s t - k_{zq}(\omega_s)L_w]} \right\}. \end{aligned} \quad (9)$$

It consists of  $N$  rectangular pulses modulating a carrier at frequency  $\omega_s$ . The temporal duration of each of the pulses is the slippage time  $\tau_{sp} = L_w/v_{z0} - L_w/v_g$ , and the rate of

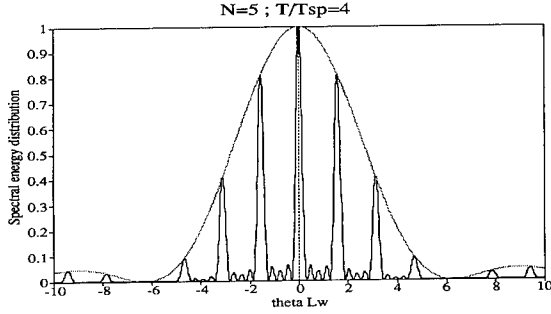


Fig. 2. The normalized spectral energy distribution of a super-radiant emission from  $N = 5$  bunches. The duty-cycle of radiation pulses is  $\tau_{sp}/T = 25\%$ .

pulse appearance is given by the spacing  $T$  between the electron bunches.  $t_d = \frac{1}{2}(L_w/v_{z0} + L_w/v_g)$  is the time delay of the center of the first pulse.

The spectral density of the radiation energy emitted by a train of  $N$  bunches is calculated from Eq. (8) according to Eq. (3):

$$\frac{d\mathcal{W}_q(L_w)}{d\omega} = |\mathcal{A}_q|^2 \mathcal{P}_q \text{sinc}^2\left(\frac{1}{2}\theta_q L_w\right) \frac{\sin^2\left(\frac{1}{2}N\omega T\right)}{\sin^2\left(\frac{1}{2}\omega T\right)}. \quad (10)$$

It constitutes a comb of line-peaks separated by the free-spectral range  $\Delta\nu_{\text{radiation}} = 1/T$  and weighted by a  $\text{sinc}^2$  function with a main lobe width of approximately  $\Delta\nu \approx 1/\tau_{sp}$ . The typical width of each line-peak is  $\delta\nu_{\text{radiation}} = 1/(NT)$ , becoming narrower as the number  $N$  of bunches increases. Fig. 2 shows a normalized line-shape of radiation energy emitted when  $N = 5$  bunches pass through a wiggler. The duty-cycle of the emitted radiation in this example is chosen to be  $\tau_{sp}/T = 25\%$ .

The ratio of the separation between peaks to the bandwidth of each radiation peak  $\Delta\nu_{\text{radiation}}/\delta\nu_{\text{radiation}} = N$ , measures the degree of radiation coherence. In the limit  $N \rightarrow \infty$ , the radiation becomes perfectly coherent at all harmonic frequencies of the pulse injection (bunching) rate. The temporal field then becomes a periodic signal with spectral power distribution:

$$\frac{dP_q(L_w)}{d\omega} = \left(\frac{2\pi}{T}\right)^2 |\mathcal{A}_q|^2 \mathcal{P}_q \text{sinc}^2\left(\frac{1}{2}\theta_q L_w\right) \times \sum_{n=-\infty}^{+\infty} \delta\left(\omega - \frac{2\pi n}{T}\right). \quad (11)$$

This should be compared to the result obtained in Refs. [10,11], for the power emitted in a prebunched free-electron laser.

#### 4. Super-radiant emission in a resonator

Now we consider the super-radiant emission of a finite train of e-beam bunches inside a waveguide resonator, the

radiation is reflected by the end mirrors and is circulating in the cavity. In the frequency domain, the field of the transverse mode  $q$  inside the resonator is found from the summation of an infinite number of reflected waves:

$$\tilde{E}_q(x, y, z = L_w, \omega) = \tilde{C}_q(L_w, \omega) \tilde{\mathcal{E}}_q(x, y) \times \sum_{m=0}^{\infty} \rho^m e^{imk_{zq}l_c}, \quad (12)$$

where  $\rho$  is the complex field combined reflectivity of all the mirror in the round-trip feedback loop and  $l_c$  is the round-trip length of the cavity. The summation (12) forms an infinite geometric progression, which can be written in the form:

$$\begin{aligned} \tilde{E}_q(x, y, z = L_w, \omega) &= \frac{\mathcal{A}_q}{1 - \rho e^{ik_{zq}l_c}} \text{sinc}\left(\frac{1}{2}\theta_q L_w\right) \\ &\times \frac{\sin\left(\frac{1}{2}N\omega T\right)}{\sin\left(\frac{1}{2}\omega T\right)} e^{i\frac{1}{2}[\theta_q L_w + (N-1)\omega T]} \tilde{\mathcal{E}}_q(x, y). \end{aligned} \quad (13)$$

The spectral density of the out-coupled energy in a steady-state operation is found from Eq. (3):

$$\begin{aligned} \frac{d\mathcal{W}_q^{\text{out}}(L_w)}{d\omega} &= |\mathcal{A}_q|^2 \mathcal{P}_q \frac{\mathcal{T}}{(1 - \sqrt{R})^2 + 4\sqrt{R} \sin^2\left(\frac{1}{2}k_{zq}l_c\right)} \\ &\times \frac{\sin^2\left(\frac{1}{2}N\omega T\right)}{\sin^2\left(\frac{1}{2}\omega T\right)} \text{sinc}^2\left(\frac{1}{2}\theta_q L_w\right), \end{aligned} \quad (14)$$

where  $R = |\rho|^2$  and  $\mathcal{T}$  is the power transmission coefficient of the outcoupler. We notice that the spectral energy distribution of the transmitted wave is the line-shape of the radiation emitted by the  $N$  wiggling bunches (10), multiplied by a transfer function of the Fabry–Perot resonator. The maximum transmission of a Fabry–Perot resonator occurs when  $k_{zq}l_c = 2m\pi$  (where  $m$  is an integer), which defines the resonant frequencies for the longitudinal modes of the resonator. The intermode frequency separation is  $\Delta\nu_{\text{resonator}} = 1/t_r$ , where  $t_r = l_c/v_g$  is the round-trip time of the radiation. The width of the transmission peaks is given by  $\delta\nu_{\text{resonator}} = \Delta\nu/F$  where  $F = \pi\sqrt{R}/(1 - R)$  is the finesse of the resonator.

Fig. 3 shows the line-shape of the spectral energy distribution of the out-coupled radiation when a super-radiant emission of a single bunch ( $N = 1$ ) is circulating in the resonator. In that case the width of the line-peaks of the transmitted radiation is determined by the resonator quality. Improvement of the finesse of the resonator increases the spectral resolution between the peaks.

For the case of multi-bunching, line-peaks appear already in the spectrum of the radiation inside without feedback. The ratio between the separation of the line-peaks

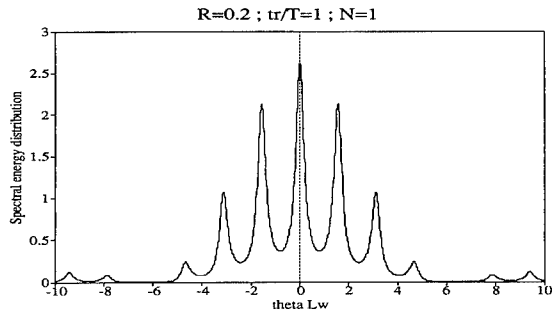


Fig. 3. The line-shape of the out-coupled radiation when synchrotron radiation from a single bunch is circulating in a resonator.

of the radiation emitted by the  $N$  wiggling bunches and the free-spectral range of the resonator  $\Delta\nu_{\text{radiation}}/\Delta\nu_{\text{resonator}} = t_r/T$  determines whether and which of the peaks will be coupled out. When this ratio is equal to unity (i.e. the time  $T$  between the pulses is tuned to be equal to the round-trip time  $t_r$  of the radiation in the resonator), all of the radiation line-peaks are coupled out of the resonator. Under such a condition of “mode-locking” [19], the circulating waves add in phase resulting enhancement of the temporal coherence of the radiation.

Examination of the ratio between the line-widths of the radiation and those of the transmission curve of the resonator  $\delta\nu_{\text{radiation}}/\delta\nu_{\text{resonator}} = (F/N)t_r/T$ , shows that the

bandwidth of the out-coupled radiation at each line becomes narrower as the finesse of the resonator increases. When the finesse of the resonator is small relative to the number of bunches  $F < N$ , the bandwidth of each line is limited by the number of bunches  $N$ . In the example demonstrated in Fig. 4a, the Finesse of the resonator was chosen to be  $F = 1.8$ , smaller than the number  $N = 5$  of the e-beam pulses. The transmission characteristics of the resonator (which is illustrated in dashed line), is observed to have wide bandpass regions, corresponding to the poor finesse. The spectral width of the out-coupled radiation peaks (shown as a solid line) is narrower, determined by the number of bunches  $N$ . In the opposite case, shown in Fig. 4b, the finesse of the resonator  $F = 14$  is higher than the number of pulses ( $N = 5$ ) in the e-beam. The bandwidth of the spectral lines of the out-coupled radiation becomes narrow, and their energy peaks in the frequency domain are intensified, as the result of the enhancement of their temporal coherence.

## References

- [1] H. Motz, J. Applied Phys. 22 (1951) 527.
- [2] R. Bonifacio, C. Maroli and N. Piovella, Optics Commun. 68 (1988) 369.
- [3] R. Bonifacio, B.W.J. McNeil and P. Pierini, Phys. Rev. A 40 (1989) 4467.
- [4] S. Cai, J. Cao and A. Bhattacharjee, Phys. Rev. A 42 (1990) 4120.
- [5] N.S. Ginzburg and A.S. Sergeev, Optics Commun. 91 (1992) 140.
- [6] F. Ciocci, R. Bartolini, A. Doria, G.P. Gallerano, M.F. Kimmit, G. Messina and A. Renieri, Phys. Rev. Lett. 70 (1993) 928.
- [7] A. Gover, F.V. Hartemann, G.P. Le Sage, N.C. Luhmann, R.S. Zhang and C. Pellegrini, Phys. Rev. Lett. 72 (1994) 1192.
- [8] M.P. Sirkis and P.D. Coleman, J. Appl. Phys. 28 (1957) 527.
- [9] R.M. Pantell, P.D. Coleman and R.C. Becker, IRE Trans. Electron Devices ED-5 (1958) 167.
- [10] I. Schnitzer and A. Gover, Nucl. Instr. and Meth. A 237 (1985) 124.
- [11] A. Doria, R. Bartolini, J. Feinstein, G.P. Gallerano and R.H. Pantell, IEEE J. Quantum Electron. QE-29 (1993) 1428.
- [12] G. Williams et al., Phys. Rev. Lett. 62 (1989) 261.
- [13] T. Nakazato et al., Phys. Rev. Lett. 63 (1989) 1245.
- [14] J. Ohkuma, S. Okuda and K. Tsumori, Phys. Rev. Lett. 66 (1991) 1967.
- [15] Y.U. Jeong et al. Phys. Rev. Lett. 68 (1992) 1140.
- [16] Y. Jeong et al., Phys. Rev. E 47 (1993) 1313.
- [17] R. Zhang et al., Nucl. Instr. and Meth. A 341 (1994) 67.
- [18] M. Asakawa et al., Nucl. Instr. and Meth. A 341 (1994) 72.
- [19] E. Jerbi and G. Bekefi, IEEE J. Quantum Electron. QE-29 (1993) 1192.
- [20] Y. Pinhasi et al., Nucl. Instr. and Meth. A 318 (1992) 523.
- [21] Y. Pinhasi and A. Gover, Three-dimensional coupled-mode theory of free-electron lasers in the collective regime, Phys. Rev. E, to be published.

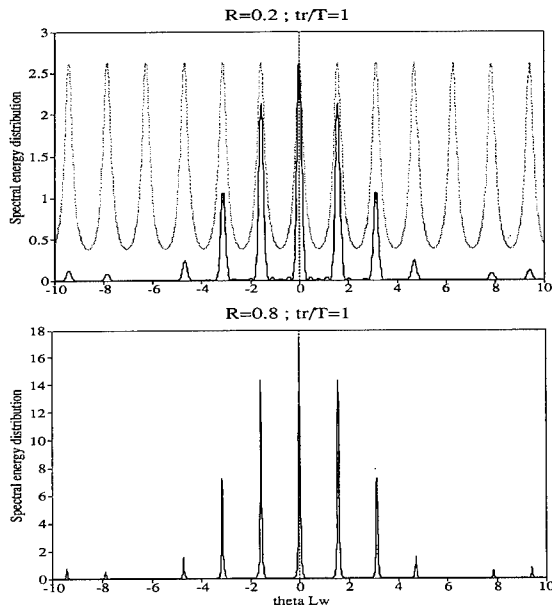


Fig. 4. The line-shape of the out-coupled radiation when a super-radiant emission (of  $N = 5$  bunches, duty-cycle  $\tau_{sp}/T = 25\%$ ) is circulating in a resonator ( $t_r = T$ ). (a) Finesse  $F = 1.8$  smaller than the number of bunches  $N = 5$ . (b) Finesse  $F = 14$  higher than the number of bunches  $N = 5$ .

# Simulation of radiation build-up in an FEL oscillator: the effect of the electron beam micropulse shape

S. Kuruma <sup>a</sup>, K. Mima <sup>b,\*</sup>, K. Imasaki <sup>a</sup>, S. Nakai <sup>b</sup>, C. Yamanaka <sup>a</sup>

<sup>a</sup> *Institute for Laser Technology, Suita, Osaka 565, Japan*

<sup>b</sup> *Institute of Laser Engineering, Osaka University, Suita, Osaka 565, Japan*

## Abstract

Using a one-dimensional multi-frequency simulation code, we have investigated how the radiation build-up time in an FEL oscillator depends upon the electron beam micropulse width and micropulse shape. From the simulation, it is found that in the Gaussian electron beam case when the electron beam micropulse width is shorter than the radiation wavelength, the radiation in the cavity builds up faster than in longer cases (because of the coherent spontaneous emission). But in the square electron beam pulse case, the spontaneous emission at the edge is much stronger than in the case of a Gaussian electron beam pulse, so the effect of coherent spontaneous emission is reduced. The radiation spectral intensity and temporal profiles have been evaluated for super Gaussian pulse shapes of a bunched electron beam.

## 1. Introduction

A free electron laser using an RF linac as an electron beam source is suitable for generating radiation in the visible, infrared or sub millimeter regimes [1]. The electron beam from RF linac has a time dependent structure. The macro pulse is composed of series of micro pulses. In previous work [2], it was shown that the characteristics of radiation build up in an FEL resonator depend upon the width of the electron beam micropulse. In addition the spontaneous emission from an electron beam pulse depends upon the temporal electron beam pulse shape [3]. Therefore, the characteristic of radiation build up in an FEL resonator has to depend upon both electron micropulse width and temporal shape. In this paper, the effects of micropulse width and temporal shape for radiation build up in an FEL resonator are investigated using the super Gaussian distribution as the electron beam micropulse shape.

## 2. Model configuration and outline of the simulation code

The configuration is almost the same as in the previous work [2]. But the 1-D multi-frequency simulation code [4] is improved to introduce the super Gaussian function as

the temporal profile of the electron beam micropulse. The electron beam current density  $n_b$  is assumed as follows,

$$n_b \propto \exp\{-\ln 2(\psi/\tau_b)^{2m}\}, \quad m = 1, 2, \dots, \quad (1)$$

where  $\tau_b$  is the FWHM of electron beam micro pulse and  $\psi$  is the ponderomotive phase. The case  $m = 1$  corresponds to a Gaussian shape and  $m = \infty$  corresponds to a square shape. Spontaneous emission is introduced as the same manner of previous work [4] by adding small perturbations on electron phases around the quiet start positions and adjusting this numerical noise to the actual spontaneous emission power.

## 3. The characteristic of radiation build up in an FEL resonator

In this section, we present numerical examples using parameters which correspond to the FEL experiment at ILE. The parameters are shown in Table 1.

Fig. 1 shows the temporal evolution of the radiation power in the resonator for a Gaussian electron beam micro pulse ( $m = 1$  at Eq. (1)). In this case, the wavelength of radiation is 500  $\mu\text{m}$ , so the slippage distance is about  $1.6 \text{ ps} \times 30 = 48 \text{ ps}$ . As the peak current is fixed in this simulation, the total charge is proportional to the micropulse width. The micropulse width  $\tau_b$  is a) 1 ps, b) 5 ps and c) 50 ps respectively. Case of c) corresponds to the usual FEL oscillation. The electron beam is bunched after about 70 or 80 passes and the radiation builds up exponentially after that. In case b) the radiation does not build up

\* Corresponding author. Tel. +81 6 879 8724, fax +81 6 877 4799, e-mail mima@ile.osaka-u.ac.jp.

Table 1  
Simulation parameters

|                      |  |
|----------------------|--|
| <b>Electron beam</b> |  |
| Beam energy          | $E_{b0} = 6 \text{ MeV}$<br>( $\gamma = 12.74$ ) |
| Beam current         | $I_b = 10 \text{ A}$                             |
| Beam radius          | $r_b = 3 \text{ mm}$                             |
| <b>Laser</b>         |  |
| Fundamental mode     | $\lambda_{s0} = 500 \text{ } \mu\text{m}$        |
| Frequency resolution | $\Delta\omega/\omega_0 = 1/200$                  |
| Longitudinal mode    | $n = -40 \text{ to } 40$                         |
| <b>Wiggler</b>       |  |
| Wiggler period       | $\lambda_w = 6 \text{ cm}$                       |
| Wiggler field        | $B_w = 3200 \text{ G}$                           |
| Wiggler number       | $N_w = 30$                                       |
| <b>Cavity</b>        |  |
| Resonator length     | $L = 3.6 \text{ m}$                              |
| Reflectance          | $R = 99\%$                                       |
| Resonance wavelength | $482 \text{ } \mu\text{m}$                       |
| $K$ parameter        | 1.8  |

because the total charge in a micropulse is too small. In case a) the radiation builds up faster than b) and c) although the total charge is smaller than in the other cases. The reason is that the electron micropulse length is shorter than the radiation wavelength. In this case, the electron micropulse can be considered to be bunched at the entrance of the wiggler. The radiation in the resonator builds up as a superposition of the emission from electron micropulses. It is called coherent spontaneous emission. The radiation does not build up exponentially, so the saturation level is lower than normal FEL oscillation.

Fig. 2 shows the temporal evolution of the radiation power in the resonator for a square electron beam micropulse ( $m = \infty$  at Eq (1)). The micro-pulse width  $\tau_b$  is a) 1 ps, b) 5 ps and c) 50 ps respectively. Comparing with Fig. 1, in case a), the radiation builds up almost the same except for a factor of 2 in intensity, but in case b), the radiation builds up exponentially so the radiation power after 150 passes is 7 orders of magnitude greater. It seems that the reason is due to emission from the edge of the square electron beam pulse which is much stronger than that from a Gaussian electron beam pulse, since the scattering of the wiggler magnetic field is greater when the

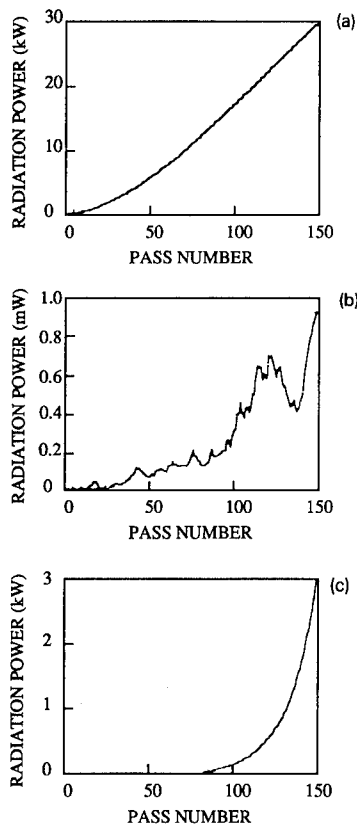


Fig. 1. Temporal evolution of the radiation power for a Gaussian electron micropulse ( $m=1$ ), (a)  $\tau_b = 1 \text{ ps}$ , (b)  $\tau_b = 5 \text{ ps}$ , (c)  $\tau_b = 50 \text{ ps}$ .

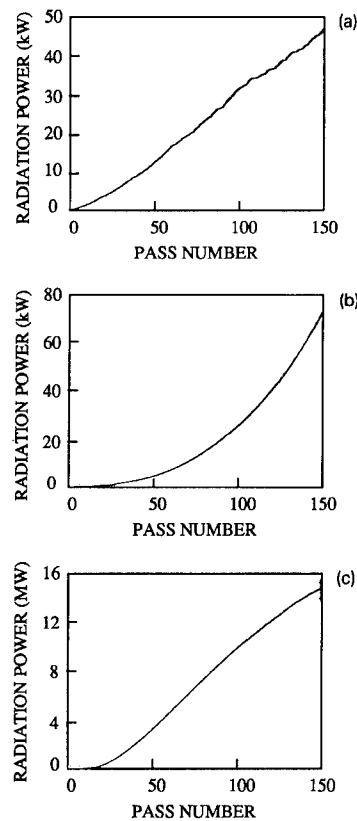


Fig. 2. Temporal evolution of the radiation power for a square electron micropulse ( $m=\infty$ ), (a)  $\tau_b = 1 \text{ ps}$ , (b)  $\tau_b = 5 \text{ ps}$ , (c)  $\tau_b = 50 \text{ ps}$ .

electron beam has a sharp boundary. Thus, the emission from the electron beam edge plays the role of the input radiation, and bunching of the electron beam occurs even though the total charge in the micropulse is small. In case c), because of strong emission at the electron pulse edge, the electron beam is bunched faster, i.e. stimulated emission occurs after about 20 passes, so the radiation builds up to about  $1.5 \times 10^7$  W, 4 orders of magnitude greater than that of the Gaussian electron pulse case (Fig. 1c).

Fig. 3 shows snap shots of the frequency spectrum of radiation at the end of the wiggler after one pass for the case of Fig. 2b. The shape of the frequency spectrum is interesting. It seems that it originates from interference between the radiation from the electron pulse front edge and that from the rear edge.

Fig. 4 shows the electron micropulse width and shape dependence of the radiation power after one pass (solid line) and after 150 passes (dotted line). In this figure, the electron micropulse temporal shape is varied from Gaussian to square using a super Gaussian distribution, i.e. a)  $m = 1$ , b)  $m = 2$ , c)  $m = 5$ , d)  $m = 10$  and e)  $m = \infty$ , respectively. The radiation wavelength is  $500 \mu\text{m}$  which corresponds to  $1.6 \text{ ps}$  and the slippage distance corresponds to  $48 \text{ ps}$ . The effect of coherent spontaneous emission is obvious for case a), but as the order of the super Gaussian is increased i.e. the profile of the electron pulse

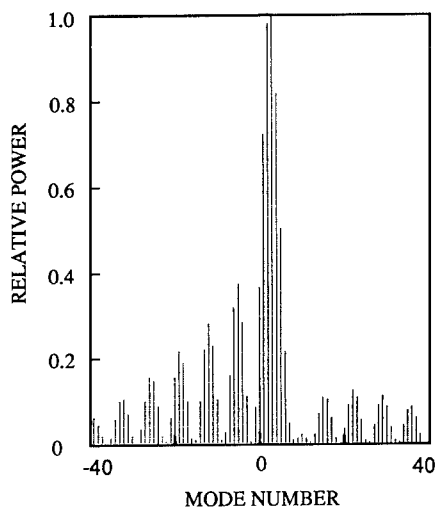


Fig. 3. Snap shot of the frequency spectrum of radiation at the end of the wiggler after one pass for a square electron micropulse of  $\tau_b = 5 \text{ ps}$ .

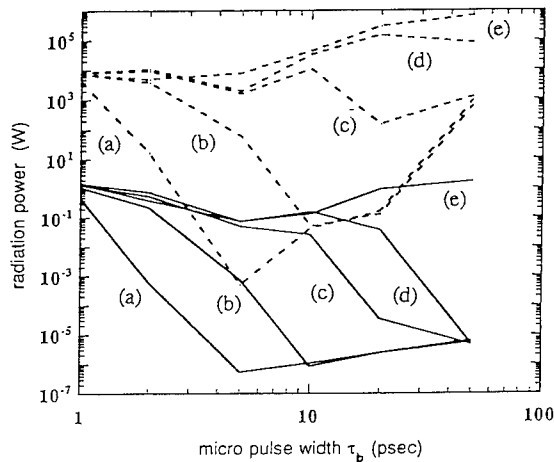


Fig. 4. The electron micropulse width vs. radiation power after one pass (solid line) and the 150th pass (dotted line) for various super Gaussian modes ((a)  $m = 1$ , (b)  $m = 2$ , (c)  $m = 5$ , (d)  $m = 10$ , (e)  $m = \infty$ ).

approaches a square (the case e)), the effect of emission from the electron pulse edge is greater, and the effect of coherent spontaneous emission is smaller.

#### 4. Summary

Using 1-D multi-frequency simulation code, we have shown how the characteristics of the radiation build up in an FEL resonator depend upon the electron beam micropulse length and temporal shape. The super Gaussian distribution is assumed for the electron beam micropulse and it is shown that as the electron micropulse temporal profile steepens the emission from the electron micropulse edge increases, reducing the relative effect of coherent spontaneous emission.

#### References

- [1] C.A. Brau, *Free Electron Laser* (Academic Press, 1990).
- [2] S. Kuruma, M. Naruo, K. Mima, S. Nakai and C. Yamanaka, *Nucl. Instr. and Meth. A* 341 (1994) 289.
- [3] S. Kuruma, M. Naruo, K. Mima, C. Yamanaka and S. Nakai, *Nucl. Instr. and Meth. A* 318 (1992) 707.
- [4] S. Kuruma, M. Naruo, K. Mima, K. Imasaki, S. Nakai and C. Yamanaka, *Nucl. Instr. and Meth. A* 331 (1993) 421.



ELSEVIER

# Finite pulse effects in self-amplified-spontaneous-emission <sup>☆</sup>

Kwang-Je Kim <sup>\*</sup>, Sang June Hahn

*Lawrence Berkeley Laboratory, University of California, Berkeley, CA 94720, USA*

## Abstract

We study the effects of the electron density profile on self-amplified-spontaneous-emission (SASE). A general formalism in the linear regime is developed by deriving the coupled Maxwell–Klimontovich equations for an arbitrary density profile including the effects of the energy spread, diffraction, and the betatron oscillation. An explicit solution is obtained for the one-dimensional (1-D) case. The temporal and the spectral intensity profiles of SASE depend linearly on the initial electron correlation function. The correlation function consists of two terms, a term giving rise to the usual spontaneous radiation and its amplification to SASE, and a term representing the coherent bunched beam effect. The latter term has been neglected so far in the treatments of SASE, but it could be significant when there is a variation in the electron density at a length scale comparable to the wavelength. The theory reproduces the well-known results when the electron density is uniform. It also reproduces a recent theory for a finite top-hat density profile and a vanishing energy spread.

## 1. Introduction

The theory of SASE in the linear regime has been treated before for the case of an infinitely long, uniform electron beam [1,2]. Recently, Bonifacio et al. [3] have presented a theory of SASE for a finite, top-hat density profile with a vanishing electron energy spread. In this paper, we extend the theory to a general density profile including the effects of electron energy spread, diffraction and the betatron oscillation.

The Maxwell–Klimontovich equations describing the linear evolution of the radiation amplitude and the electron distribution function is derived in Section 2. The crucial step in this derivation is the specification of the electron coordinate relative to the bunch center with two variables, the macroscopic variable  $\zeta$  and the microscopic phase variable  $\theta_j$ . A  $\zeta$ -dependent Klimontovich distribution function for the electron phase is introduced. The distribution function enters as a source term in Maxwell's equation, and satisfies an equation describing the evolution of the microscopic variables at fixed  $\zeta$ .

The equations are solved explicitly for the 1-D case in Section 3. The solution reproduces the known results in the appropriate limits. The temporal and the spectral intensity

profiles of SASE depend linearly on the initial electron correlation function. The correlation function consists of two terms, a term giving rise to the usual spontaneous radiation and a term representing the coherent bunched beam effect. The latter could be significant when there is a variation in the electron density at a length scale comparable to the radiation wavelength. Section 4 contains the concluding remarks.

## 2. Interaction of radiation field with finite pulse electron beam

The slowly varying part  $\mathcal{E}$  of the electric field  $E$  is defined by

$$E(\mathbf{x}, t, z) = \mathcal{E}(\mathbf{x}, t, z) e^{ik_s(ct-z)} + \text{c.c.} \quad (1)$$

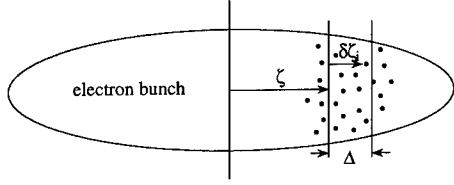
Here  $\mathbf{x}$ ,  $t$ ,  $z$  are respectively the two dimensional transverse, time, and longitudinal coordinates,  $k_s = 2\pi/\lambda_s$  is the radiation spatial frequency,  $\lambda_s$  is the wavelength,  $c$  is the speed of light, and c.c. implies complex conjugate.

To describe the source term in the Maxwell equation, the electron bunch is divided into bins of width  $\Delta$ . The bin size  $\Delta$  is normally taken to be the order of  $\lambda_s$  to be consistent with the slowly varying phase and amplitude approximation. However  $\Delta$  is really the resolution of the macroscopic electron distribution, which could be much smaller than  $\lambda_s$ . The coordinate of the electron is written as

$$z = v_{\parallel} \tilde{t}_j(z) + \zeta + \delta\zeta_j. \quad (2)$$

<sup>☆</sup> This work was supported at LBL by the Director, Office of Energy Research, Office of Basic Energy Sciences, Materials Sciences Division, of the US Department of Energy, under Contract No. DE-AC03-76SF00098.

<sup>\*</sup> Corresponding author. Tel. +1 510 486 7224, fax +1 510 486 7981, e-mail kwangje@lbl.gov.

Fig. 1. Illustration of the coordinates  $\zeta$  and  $\delta\zeta_j$ .

Here we choose  $z$  as the independent variable,  $v_{\parallel}$  is the average longitudinal velocity,  $\tilde{t}_j(z)$  is the time the electron arrives at  $z$  (averaged over the velocity oscillation in the case of a planar undulator). In the above, the variable  $\zeta$  is the macroscopic variable specifying the bin, while  $\delta\zeta_j$  is the microscopic variable specifying the electron position within the bin. The phase  $\theta_j$  is introduced via

$$\theta_j = (k_s + k_u)(\zeta + \delta\zeta_j) \approx k_s(\zeta + \delta\zeta_j), \quad (3)$$

where  $k_u = 2\pi/\lambda_u$  and  $\lambda_u$  is the undulator period. Fig. 1 illustrates the coordinates  $\zeta$  and  $\delta\zeta_j$ . Following the standard derivation [4] and changing the variable from  $(t, z)$  to  $(\zeta, z)$ , we obtain (MKS units are used throughout this paper)

$$\left( \frac{\partial}{\partial z} + (1 - \beta_{\parallel}) \frac{\partial}{\partial \zeta} + i \frac{\nabla_{\perp}^2}{2k_s} \right) \mathcal{E}(\mathbf{x}, \zeta; z) = - \frac{eK_1}{4\epsilon_0\gamma_0} \frac{1}{\Delta} \sum_{j \in [\Delta, \zeta]} e^{i\theta_j} \delta^{(2)}(\mathbf{x} - \mathbf{x}_j). \quad (4)$$

Here  $e$  is the electron charge,  $\beta_{\parallel} = v_{\parallel}/c$ ,  $K_1 = K(J_0(\xi) - J_1(\xi))$ ,  $K = eB_0/mck_u$ ,  $B_0$  is the peak undulator magnetic field,  $m$  is the electron mass,  $\xi = K^2/4(1 + K^2/2)$ ,  $J$ 's are Bessel functions,  $\gamma_0$  is the energy of the reference electron in units of  $mc^2$ , and  $\epsilon_0$  is the vacuum dielectric constant. The summation in Eq. (4) is over the electrons belonging to the bin specified by  $\zeta$ .

We introduce an electron distribution function as follows:

$$\begin{aligned} \hat{f}(\theta, \eta, \mathbf{x}, \dot{\mathbf{x}}, \zeta; z) \\ = \frac{1}{N_{\Delta}} \sum_{j \in [\Delta, \zeta]} \delta(\theta - \theta_j) \delta(\eta - \eta_j) \delta^{(2)}(\mathbf{x} - \mathbf{x}_j) \\ \times \delta^{(2)}(\dot{\mathbf{x}} - \dot{\mathbf{x}}_j), \end{aligned} \quad (5)$$

where  $\eta_j = (\gamma_j - \gamma_0)/\gamma_0$ ,  $\gamma_j$  is the energy of  $j$ th electron in units of  $mc^2$ ,  $\dot{\mathbf{x}} = d\mathbf{x}/dz$  is the transverse angle, and  $N_{\Delta}$  is the total number of electrons inside the bin of length  $\Delta$  at the location of maximum density (which is taken to be at  $\zeta = 0$ ). The source term in Maxwell's equation is proportional to the quantity

$$f_1(\mathbf{x}, \dot{\mathbf{x}}, \eta, \zeta; z) = \int d\theta e^{i\theta} \hat{f}. \quad (6)$$

$f_1$  is essentially the  $\zeta$ -dependent bunching factor.

The equation for  $f_1$  can be found from the Vlasov equation for  $\hat{f}$ , obtained by considering the change of  $\hat{f}$  for a fixed  $\zeta$ . The result to the lowest order in  $\mathcal{E}$  is given by

$$\begin{aligned} \left( \frac{\partial}{\partial z} - i2\eta k_u - \frac{ik_u}{2} (\dot{\mathbf{x}}^2 + k_{\beta}^2 \mathbf{x}^2) + \dot{\mathbf{x}} \frac{\partial}{\partial \mathbf{x}} + \ddot{\mathbf{x}} \frac{\partial}{\partial \dot{\mathbf{x}}} \right) f_1 \\ = - \frac{eK_1}{2mc^2\gamma_0^2} \mathcal{E}(\mathbf{x}, \zeta; z) \frac{\partial}{\partial \eta} \tilde{f}(\mathbf{x}, \dot{\mathbf{x}}, \eta, \zeta). \end{aligned} \quad (7)$$

Here we have assumed a constant betatron focusing with

$$\ddot{\mathbf{x}} \equiv \frac{d\dot{\mathbf{x}}}{dz} = -k_{\beta} \mathbf{x}, \quad (8)$$

where  $k_{\beta}$  is the betatron wave number. In Eq. (7),  $\tilde{f}$  is a smooth background distribution obtained by taking an ensemble average of  $\int d\theta \hat{f}$  at  $z = 0$  with the normalization

$$\int \tilde{f}(\mathbf{x}, \dot{\mathbf{x}}, \eta, \zeta = 0) d^2\mathbf{x} d^2\dot{\mathbf{x}} d\eta = 1. \quad (9)$$

In the above equation, the point  $\zeta = 0$  may be conventionally chosen to be the bunch center. Eqs. (4) and (7) completely specify the free-electron laser interaction for the case of a finite pulse electron beam.

### 3. Solution for 1-D case

Let us now consider the 1-D equation obtained by neglecting the transverse dependence:

$$\left( \frac{\partial}{\partial z} + (1 - \beta_{\parallel}) \frac{\partial}{\partial \zeta} \right) \mathcal{E}(\zeta; z) = -\kappa_1 \int f_1(\eta, \zeta; z) d\eta, \quad (10)$$

$$\begin{aligned} \left( \frac{\partial}{\partial z} - i2\eta k_u \right) f_1(\eta, \zeta; z) \\ = -\kappa_2 \mathcal{E}(\zeta; z) \chi(\zeta) \frac{d}{d\eta} V(\eta), \end{aligned} \quad (11)$$

where  $\kappa_1 = eK_1 n_0 / 4\epsilon_0 \gamma_0 \Sigma$ ,  $\kappa_2 = eK_1 / 2mc^2 \gamma_0^2$ ,  $n_0 = N_{\Delta}/\Delta$  is the peak linear density, and  $\Sigma$  is the beam cross section. Here we have assumed that the function  $\tilde{f}(\eta, \zeta)$  is factorized in the form

$$\tilde{f}(\eta, \zeta) = V(\eta) \chi(\zeta), \quad (12)$$

with the normalization

$$\int V(\eta) d\eta = 1, \quad \chi(0) = 1. \quad (13)$$

The coupled equations (10) and (11) can be solved by the Laplace transform technique in the variable  $z$ . The result consists of two terms, the coherent amplification term proportional to the initial coherent field  $\mathcal{E}(\zeta; 0)$  and the self-amplified spontaneous emission (SASE) term pro-



portional to the initial electron beam noise represented by  $f_1(\eta, \zeta; z=0)$ . The SASE term is given by

$$\mathcal{E}(\zeta; z) = i \frac{k_s \kappa_1}{2k_u^2} \int d\eta \int_{-\infty}^{\zeta} d\zeta' G(\zeta, \zeta', \eta; z) \times f_1(\eta, \zeta'; 0), \quad (14)$$

where

$$G(\zeta, \zeta', \eta; z) = \frac{1}{2\pi} \oint d\lambda \frac{e^{i[\lambda z - \psi_\lambda(\zeta) + \psi_\lambda(\zeta')]} }{\lambda/2k_u - \eta}. \quad (15)$$

Here the  $\lambda$ -integration is along a straight path parallel to the real axis, above all singularities in the integrand. The function  $\psi_\lambda(\zeta)$  in Eq. (15) is

$$\psi_\lambda(\zeta) = \frac{k_s}{k_u} \lambda \zeta + 2k_s \rho^3 \int d\eta \frac{dV/d\eta}{\lambda/2k_u - \eta} \int_0^{\zeta} \chi(\zeta') d\zeta', \quad (16)$$

where  $\rho = (\kappa_1 \kappa_2 / 4k_u^2)^{1/3}$  is the fundamental scaling parameter.

Eq. (14) reduces to the result in Refs. [1,2] for the case of  $\chi(\zeta) = 1$  (uniform pulse profile), and to the result in Ref. [3] for the case of a top-hat pulse profile with a vanishing energy spread. The case of a general pulse profile with a vanishing energy spread was also treated by Moore [5].

The temporal intensity profile of the SASE radiation is proportional to

$$\begin{aligned} & \langle |\mathcal{E}(\zeta; z)|^2 \rangle \\ &= \left( \frac{k_s \kappa_1}{2k_u^2} \right)^2 \int d\eta \int d\eta' \int_{-\infty}^{\zeta} d\zeta' \int_{-\infty}^{\zeta} d\zeta'' \\ & \times G(\zeta, \zeta', \eta; z) G^*(\zeta, \zeta'', \eta'; z) \\ & \times \langle f_1(\eta, \zeta'; 0) f_1^*(\eta', \zeta''; 0) \rangle, \end{aligned} \quad (17)$$

where the brackets  $\langle \rangle$  imply the ensemble average. The electron correlation function appearing in the integrand is

$$\begin{aligned} & \langle f_1(\eta, \zeta; 0) f_1^*(\eta', \zeta'; 0) \rangle \\ &= \frac{1}{n_0} \delta(\zeta - \zeta') \delta(\eta - \eta') V(\eta) \chi(\zeta) \\ & + \chi(\zeta) \chi(\zeta') V(\eta) V(\eta') |\langle e^{i\theta} \rangle|^2, \end{aligned} \quad (18)$$

where

$$\langle e^{i\theta} \rangle \equiv \frac{\int \chi(\zeta) e^{ik_s \zeta} d\zeta}{\int \chi(\zeta) d\zeta}. \quad (19)$$

The first term in Eq. (18) represents the usual shot noise with a vanishing correlation length, while the second term represents the coherent bunched beam effect. Normally, the second term is negligible, and the radiation field evolves from the stochastic undulator radiation with the correlation length increasing as  $\sqrt{\lambda_s z / \rho}$  [1,2]. The second term could become large when the density varies significantly in a length of the order of  $\lambda_s$  or shorter. This term gives rise to the so called coherent synchrotron radiation (see for example Ref. [6]), and may explain the large effective noise term observed in the LLNL experiment [7].

#### 4. Conclusion

We have presented a general formulation of the start-up from noise for a general electron beam density profile including the effects due to diffraction, electron beam focusing, and energy spread. Our treatment for the finite pulse profile takes into account the coherent bunched beam effect for  $L_e \leq \lambda_s$ . Based on the formalism presented here, we will carry out a detailed calculation of the radiation characteristics for the proposed short wavelength FEL scheme based on SASE [8].

#### References

- [1] K.-J. Kim, Nucl. Instr. and Meth. A 250 (1986) 396; Phys. Rev. Lett. 57 (1986) 1871.
- [2] J.M. Wang and L.H. Yu, Nucl. Instr. and Meth. A 250 (1986) 484.
- [3] R. Bonifacio et al., Phys. Rev. Lett. 73 (1994) 70.
- [4] W.B. Colson, in: Laser Handbook, eds. W.B. Colson, C. Pellegrini and A. Renieri (North-Holland, 1990) Vol. 6, p. 115.
- [5] G.T. Moore, Nucl. Instr. and Meth. A 239 (1985) 19.
- [6] T. Nakazano et al., Phys. Rev. Lett. 63 (1989) 1245.
- [7] T.J. Orzechowski et al., Phys. Rev. Lett. 54 (1985) 889.
- [8] H. Winick et al., Nucl. Instr. and Meth. A 347 (1994) 199.



ELSEVIER

# Turbulent FEL theory and experiment on ELSA at Bruyeres-le-Chatel

P. Chaix \*, P. Guimbal

*Commissariat à l'Energie Atomique, BP 12, 91680 Bruyères le Châtel, France*

## Abstract

We consider the asymptotic behaviour of long pulse high current Compton free electron laser oscillators. It is known that if the current is high enough and the cavity losses low enough, sideband instabilities and non-linear mode couplings eventually lead to a strong broadening of the radiated spectrum, and to a strong efficiency enhancement. In this “post-sideband” regime, the electron dynamics along the wiggler is intrinsically stochastic, and the efficiency is due to chaotic diffusion of the electrons toward lower energies, rather than to standard synchrotron oscillations. This results in new scaling laws for saturation properties. We have obtained simple analytical estimates for the extracted efficiency and for the spectral width, in very good agreement with numerical simulations. The infrared ELSA free electron laser at Bruyères-le-Châtel has been used to obtain experimental evidence for these new scaling laws. In particular it has been verified that in the post-sideband regime, the ratio of the extracted efficiency to the relative spectral width is independent of the operating parameters, and close to  $\sqrt{3}/2$  as predicted by theory.

## 1. Introduction

The physics of FELs in the small signal regime is by now well understood. This is also the case for the non-linear regime and saturation as long as the radiation remains monochromatic, and the wiggler is uniform [1] or has a simple structure [2]. Much more remains to be understood when the wiggler has a non-trivial structure (multi-section, tapered, or multi-frequency wigglers [3]), or when the radiated spectrum cannot be considered as monochromatic. We will concentrate here on this last issue, in the continuous beam limit where spectral broadening is essentially due to the sideband instability. Note that this problem is also of broader interest: the dynamics of FEL oscillators is dissipative on the time scale of many cavity round trips, and cavity losses allow the system to evolve toward an equilibrium (if the radiation remains monochromatic), or at least toward some asymptotic regime. Along the wiggler the dynamics is conservative and a Hamiltonian of the following form can be written to describe the energy transfer between electrons and radiation:

$$H(\zeta, \delta; \phi, E) = \sum_n \omega_n E_n + \sum_i \frac{1}{2} p_i^2 + G \sum_{i,n} \frac{1}{k_n} E_n^{1/2} \cos[k_n(\zeta_i - \phi_n)], \quad (1)$$

where  $\phi_n$  and  $E_n$  are the laser variables, and  $\zeta_i$  and  $\delta_i$  are

the electron variables. This Hamiltonian, which describes the coupled dynamics of a set of electrons and a set of ponderomotive waves, can also be considered as a paradigm Hamiltonian for plasma turbulence [4,5]. Travelling wave tubes are ruled by a similar Hamiltonian and just like free electron lasers can be said to provide plasma physics experiments with no plasma. The general problem of plasma turbulence is difficult; however, we will be interested here in saturation properties; now saturation is a strong field but low gain regime, so that it will be legitimate to consider as a first step, that the fields are slowly varying. Therefore it will be legitimate to restrict ourselves to the non-self-consistent dynamics of electrons in a given set of waves. A detailed analysis of this dynamics is still missing, but we will take advantage of the fact that approximate descriptions can be given to obtain a simple but non-trivial description of the post-sideband FEL dynamics.

On the other hand, the saturation properties can be studied experimentally, provided that one delivers sufficiently intense electron pulses to enter the post-sideband regime, and at the same time sufficiently long macropulses so that the system has time to actually reach saturation. As we will indicate in Section 3, the ELSA FEL in Bruyères-le-Châtel is able to meet these requirements. Simultaneous energy and spectral measurements then allowed us to obtain confirmation of the theoretical scale laws.

## 2. Theoretical framework

We will be interested in the asymptotic regime of high current Compton FEL oscillators in the continuous beam

\* Corresponding author. Tel. +33 1 6926 4712, fax +33 1 6926 6094, e-mail chaix@bruyeres.cea.fr.

limit. The standard model relevant for this problem [6] can be generalized to describe multifrequency regimes [7] involving  $N_e$  electrons interacting with  $N_L$  laser modes of discrete wave numbers  $q_n = q_0(1 + nh)$ . With the wiggler and radiated vector potentials

$$A_w(z) = (mc/e)a_w \cos(k_w z),$$

$$A_L(z, t) = (mc/e) \operatorname{Re}\{a_n(t) e^{iq_n(z-ct)}\}, \quad (2)$$

the dynamics along the wiggler is ruled by the Hamiltonian given in Eq. (1), where we have used the following notation:

$$\omega_n = nh, \quad k_n \equiv k_w(1 + nh),$$

$$a_n(t) \equiv (\mu_0 e^2 \gamma_0 E_n / m q_n^2)^{1/2}$$

$$\times \exp -ik_w[(1 + nh)\phi_n - nhct],$$

$$p \equiv (\gamma^2 - \gamma_0^2) / \gamma_0^2 \ll 1$$

with

$$q_0 \equiv 2k_w \gamma_0^2 / (1 + a_w^2/2),$$

$$\zeta \equiv z + (q_0/k_w)(z - ct),$$

$$G \equiv a_w K_1 \langle ST \rangle (\mu_0 e^2 / m)^{1/2} (q_0(1 + a_w^2) / 2k_w)^{-3/4}.$$

Here  $\gamma_0$  is the reduced energy of the incoming electrons, and the coupling constant  $G$  involves the filling factor  $\langle ST \rangle$  taking into account the radial overlap between the electron and laser transverse profiles  $T(r)$  and  $S(r)$ .

The use of the Fourier representation for the radiated field does not imply a continuous beam: the discreteness of the spectrum merely induces a period  $2\pi/q_0 h$  in the variable  $z - ct$ , and allows the numerical analysis of finite pulse effects for pulses shorter than this period. On the other hand, the number of modes  $N_L$  taken into account must be large enough to allow spectral broadening until saturation. Note that long but finite pulse numerical simulations are rather expensive, since they require a small  $h$  (long pulse) and a large  $N_L h$  (broad spectrum). However the continuous beam limit is relevant to understand the physics of saturation in the case of pulses much longer than the slippage length. Indeed, in this case saturation is due to the very nature of the interaction, while for short pulses slippage plays a dominant role, and saturation is rather due to the escape of radiation from the interaction zone [1].

In the continuous beam limit, the electrons enter the wiggler with  $p = 0$  and uniformly distributed  $\zeta$ . During the first passes they feed the fundamental FEL instability, and then the sideband instability. Although the asymptotic gains (that is for an infinitely long wiggler) for symmetrical sidebands are equal, the gain for one pass in a finite length wiggler is larger for the lower sideband [8]. This scenario repeats itself (one has sidebands of sidebands and mode couplings), so that the spectrum broadens toward lower wave numbers [7] (this is energetically natural since

the gain can be positive only if the electrons lose a fraction of their energy and thereby become resonant with lower wave number modes). Numerical simulation shows that this spectral broadening eventually stops, and the system reaches an asymptotic regime where non-linear mode couplings make the energy of each given mode fluctuate from pass to pass, but where global quantities such as the radiated energy or the spectral width remain quite constant. Let us consider this saturation in some detail. In this regime, the gain is equal to the losses (the order of a few percent), so that the electromagnetic field may be considered as constant during one pass:

$$E_n = \text{const.}, \quad \phi_n = \text{const.} + \omega_n ct. \quad (3)$$

As we will see, our final result will hardly depend on the detailed shape of the spectrum. We may then consider that the spectrum is flat, that  $E_n$  is non-zero and constant for  $-2\sqrt{3}\Sigma < nh = \omega_n < 0$  ( $\Sigma$  is the relative rms spectral width) and zero otherwise. Each non-empty mode  $n$  creates a pendulum-like resonance in the electronic phase space, at the resonant energy  $p_n = \omega_n$  determined by the stationary condition of the phase:  $\zeta - \phi_n = \text{const.}$  These resonances overlap, so that the electrons are not trapped, but experience a chaotic motion. This chaotic motion rapidly decorrelates the phase  $\zeta$ , so that one can replace it by a uniform stochastic variable (this is known as the random phase approximation [9]). The remaining variable, the conjugate momentum  $p$ , then obeys a stochastic differential equation, so that the momentum distribution obeys a Fokker–Planck equation [10] of the form:

$$\partial_z g(z, p) = \frac{1}{2} \partial_p D(p) \partial_p g(z, p). \quad (4)$$

The diffusion coefficient  $D$  depends on the momentum  $p$  via the spectral density, and is non-zero only between 0 and  $p_{\min} = -2\sqrt{3}\Sigma$ . However, the asymptotic distribution does not depend on the precise shape of the diffusion coefficient, and is uniform between 0 and  $p_{\min}$ . Therefore the extracted efficiency, which is identical at saturation with the relative energy loss of the electrons, is  $\rho = -p_{\min}/4 = \sqrt{3}\Sigma/2$ : in the post-sideband regime, the efficiency is proportional to the relative spectral width, and their ratio is the spectral brightness  $B$ :

$$B \equiv \frac{\rho}{\Sigma} = \frac{\sqrt{3}}{2} \approx 0.8. \quad (5)$$

It is a remarkable result that this ratio does not depend on any of the control parameters, as long as these parameters allow one to enter the post-sideband regime.

Moreover, due to the strong regularizing properties of the diffusion equation, the rate of convergence toward this equilibrium depends very little on the shape of the diffusion coefficient  $D(p)$ , that is on the shape of the spectrum: this is why it can be modelled as a flat spectrum, and

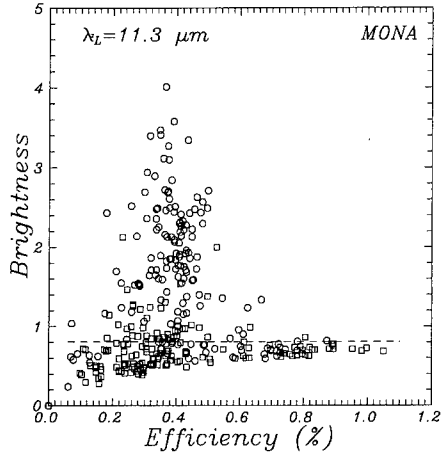


Fig. 1. Spectral brightness  $B = \rho/\Sigma$  plotted against the efficiency  $\rho$ , operating with the hybrid wiggler Tria ( $\lambda_w = 3.2$  cm,  $N_w = 31$ ). Circles correspond to negative cavity detunings, and squares to positive cavity detunings. The threshold for turbulence occurs here around  $\rho = 1\%$ ; above this value, the spectral brightness remains essentially constant, and close to the value predicted by theory (Eq. (5)).

the diffusion coefficient can be taken to be a constant between 0 and  $p_{\min}$ . Then the average momentum distribution evolves like the square root of time,  $\langle p(z) \rangle = -(2Dz/\pi)^{1/2}$ , which leads to an efficiency proportional to the square root of the wiggler length:

$$\rho = -\frac{1}{2} \langle p(z = L_w) \rangle = (DL_w/2\pi)^{1/2}. \quad (6)$$

One can go further with this approach, and derive a closed form formula for the diffusion coefficient [11] and hence for the extracted efficiency at saturation  $\rho$  which can be written:

$$\rho \approx 0.11 B_w \lambda_w^2 \gamma_0^{-3/2} (QN_w J/R^2)^{1/2}, \quad (7)$$

where  $B_w$  is the wiggler maximum magnetic field (T),  $\lambda_w = 2\pi/k_w$  is the wiggler period (m),  $\gamma_0$  is the reduced energy of the incoming electrons,  $Q$  is the cavity quality factor,  $N_w$  is the number of wiggler periods,  $J$  is the current (A) and  $R$  is the rms radius of the interaction region (m). Eq. (7) is in very good agreement with numerical simulations. One may remark in particular that the efficiency is predicted to be proportional to the square root of the number of wiggler periods (this is a signature of the diffusive character of the dynamics), contrary to the standard monochromatic  $\rho \propto 1/N_w$  prediction of the monochromatic analysis [1]. But in the following we will concentrate on the spectral brightness law  $B \equiv \rho/\Sigma \approx \sqrt{3}/2$ . Indeed, it is not necessary to have a complete knowledge of all the operating experimental parameters to verify whether or not the number  $B \equiv \rho/\Sigma$  is actually “universal”, so that it is certainly the first theoretical result to test.

### 3. Experimental issues

The experimental problem is to measure simultaneously the efficiency and the spectral width in the post-sideband regime. We reached this regime by operating with currents ranging from 50 A to 100 A, total losses of the order of 5% (with an out coupled fraction of 10 to 20%), and with 500 to 1000 micropulses in a macropulse (to be compared with a rise time less than 50 micropulses). We operated with two different wigglers, corresponding to wavelengths around 20  $\mu\text{m}$  and around 10  $\mu\text{m}$ .

The spectral information, integrated over the macropulse, has been obtained from a spectrometer coupled with a pyroelectric array (note that one has to care for water absorption lines when lasing around 20  $\mu\text{m}$ ).

The efficiency has been measured by using both electron and radiation diagnostics. A time resolved electron spectrometry within the macropulse, using a rotating mirror and an OTR screen, provided us with an absolute measure of the efficiency. However this diagnostic is rather heavy to handle, and has a small dynamic range. We therefore added an optical measurement of the laser energy, involving an absolute measurement integrated over the macropulse and a time resolved relative measurement. (Detailed information about the diagnostics and operating parameters is available in [12]).

We used the cavity length as a tuning parameter. At the optimum cavity length, the observed spectrum is large and the efficiency is significantly enhanced compared to the monochromatic efficiency. A detuning of the cavity reduces both the efficiency and the spectral width. For negative detunings (shorter cavity), the efficiency goes to the usual limit  $\propto 1/N_w$ , with a Fourier limited spectral width, which leads to a low efficiency high spectral brightness FEL output beam. For positive detunings, the asymp-

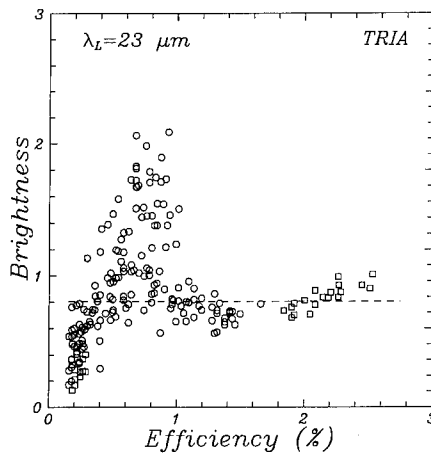


Fig. 2. The same as Fig. 1, but operating with the Halbach wiggler Mona ( $\lambda_w = 1.82$  cm,  $N_w = 34$ ). One again observes a good agreement between theory and the measured spectral brightness in the turbulent regime ( $\rho > 0.5\%$ ).

otic regime is more unstable, and the efficiency decreases faster than the spectral width, so that one obtains a low efficiency low spectral brightness FEL output beam. Note that this behaviour is observed with both wigglers (Fig. 2), as well as with numerical simulation [13]. We plotted the spectral brightness  $B$  against the efficiency  $\rho$ , for both wigglers (Figs. 1 and 2). The turbulent regime with  $B \sim 0.8$  appears clearly, in good agreement with theory.

#### 4. Conclusion and perspectives

We have given in this paper both a simple theoretical description of the FEL dynamics in the post-sideband regime, leading to scale laws for saturation properties, and a description of experimental evidence for the first of these laws Eq. (5). Therefore FELs provide a new class of devices where the concepts of intrinsic stochasticity find applications.

The second of our scale laws Eq. (7) still deserves experimental tests, which are part of the future program of the ELSA facility. These experiments will be more difficult, since they will require that we vary one parameter at a time, and free ourselves of fluctuations to be able to make relevant comparisons. Note that beyond the academic interest, the results of these experiments may have operational consequences in the future. Indeed by verifying the prediction that in the post sideband regime, longer wigglers lead to both gain and efficiency enhancement,

they may promote the development of long wiggler oscillators.

#### References

- [1] W.B. Colson, in: Free Electron Lasers, eds. Colson et al. (Elsevier, 1990) p. 115.
- [2] D. Iracane, D. Touati and P. Chaix, Nucl. Instr. and Meth. A 341 (1994) 220.
- [3] P. Chaix, D. Iracane and F. Desrayaud, Nucl. Instr. and Meth. A 341 (1994) 215.
- [4] D. Escande, in: Large Scale Structures in Nonlinear Physics, Villefranche-sur-mer, January 1991, Lecture Notes in Physics (Springer).
- [5] H.E. Mynick and A.N. Kaufman, Phys. Fluids 21 (1978) 653.
- [6] N.M. Kroll, P.L. Morton and M.N. Rosenbluth, IEEE J. Quantum Electron. 17 (1981) 1436.
- [7] D. Iracane and J.L. Ferrer, Phys. Rev. Lett. 66 (1991) 33.
- [8] D. Iracane, P. Chaix and H. Delbarre, Phys. Rev. E 49 (1994) 815.
- [9] A.J. Lichtenberg and M.A. Lieberman, Regular and Stochastic Motion (Springer, New York, 1983).
- [10] H. Risken, The Fokker–Planck Equation (Springer, Berlin, 1984).
- [11] P. Chaix, D. Iracane and C. Benoist, Phys. Rev. E 48 (1993) R3259.
- [14] P. Guimbal et al., these Proceedings (16th Int. Free Electron Laser Conf., Stanford, CA, USA, 1994) Nucl. Instr. and Meth. A 358 (1995) 240.
- [13] D. Iracane et al., Phys. Rev. Lett. 72 (1994) 3985.



ELSEVIER

## A Cherenkov free electron laser with high peak power

P.J.M. van der Slot <sup>a,\*</sup>, J. Couperus <sup>a</sup>, W.J. Witteman <sup>b</sup>, A.N. Lebedev <sup>c</sup>, E.G. Krastelev <sup>c</sup>,  
A.V. Agafonov <sup>c</sup>, V.S. Voronin <sup>c</sup>, V.A. Krasnopolsky <sup>d</sup>

<sup>a</sup> *Nederlands Centrum voor Laser Research, P.O. Box 2662, 7500 CR, Enschede, The Netherlands*

<sup>b</sup> *Department of Applied Physics, University of Twente, P.O. Box 217, 7500 AE, Enschede, The Netherlands*

<sup>c</sup> *P.N. Lebedev Physical Institute, Leninsky Prosp. 53, Moscow 117924, Russian Federation*

<sup>d</sup> *Moscow Radiotechnical Institute, Varshavskoe Sh. 132, Moscow 113519, Russian Federation*

### Abstract

A Cherenkov FEL can be a suitable source for radiation from the millimeter wavelength region down to the far infrared. With only a few different dielectric materials the laser can range from 6 mm down to  $\approx 600 \mu\text{m}$ . Nonlinear theory shows, for an amplifier configuration, power levels of about 100 kW in the far infrared up to several MW at millimeter wavelengths. Good coupling with the evanescent wave supported by the dielectrically lined waveguide requires a thin walled annular beam of good quality. The characteristics of such an electron gun, a special design for a Cherenkov FEL with parameters given in this paper, will be presented.

### 1. Introduction

Different types of sources are available in the far infrared and millimeter wavelength region [1]. They all have the disadvantage that they are only tunable over a relative small region or have a low to very low power. To cover the complete wavelength region many different devices are needed. The Free Electron Laser (FEL) could provide an alternative. Of the different types of FELs, the Cherenkov FEL (and related devices) [2] seem suitable for producing radiation in the far infrared and millimeter wavelength region. Some characteristics of such a device will be presented here. A Cherenkov FEL is a reasonably compact device due to the fact that the generated wavelength decreases with decreasing electron beam energy. However, it requires a good quality thin annular electron beam. A special thermionic electron gun was designed and constructed to produce such an electron beam. This gun will be presented in the last section. All parameters given in this paper reflect design parameters of the laser under construction. Much of the pioneering work on Cherenkov FELs has been done by Walsh and his coworkers (see, e.g. Refs. [3,4]).

### 2. Basic properties

Consider a dielectrically lined waveguide with inner radius  $r_d$  of a dielectric medium with thickness  $d$ , the waveguide radius being  $r_d + d$ . Two types of waves are supported by this waveguide. A more or less normal waveguide mode whenever the phase velocity of the wave is above and an evanescent wave in the vacuum region for waves with a phase velocity below the speed of light in vacuum. This can be seen in Fig. 1 where the dispersion relation [4] is plotted for a dielectrically lined waveguide for the three lowest modes, together with the radial profile of the axial electric field component of the  $\text{TM}_{01}$  mode at two different frequencies corresponding to the two different types of waves. It should be noted at this point that dividing the waveguide modes into two classes (TE and TM) is only possible for axisymmetric modes (which we are considering here). The parameters are  $\epsilon_r = 2.1$ ,  $r_d = 3.25 \text{ mm}$  and  $d = 0.25 \text{ mm}$ . Also shown as dotted lines in Fig. 1 are the two asymptotes corresponding to  $\omega/(ck) = 1$  and  $\omega/(ck) = \epsilon_r^{-1/2}$ , i.e. the light lines in vacuum and a dielectric medium and the beam line ( $\omega = c\beta k$ ). Several properties can be concluded from this figure. First of all, interaction between the electron beam and a wave is only possible if the beam energy  $\gamma$  is above a threshold value  $\gamma_T^2 = \epsilon_r/(\epsilon_r - 1)$ . As the scale of decay for the evanescent waves is the radiation wavelength, good coupling can only be maintained for a beam moving closely along the dielectric medium. A hollow beam would have a larger growth rate compared to a solid beam due to a better overlap with

\* Corresponding author. Tel +31 53 893 965, fax +31 53 338 065, e-mail peter@qe.tn.utwente.nl.

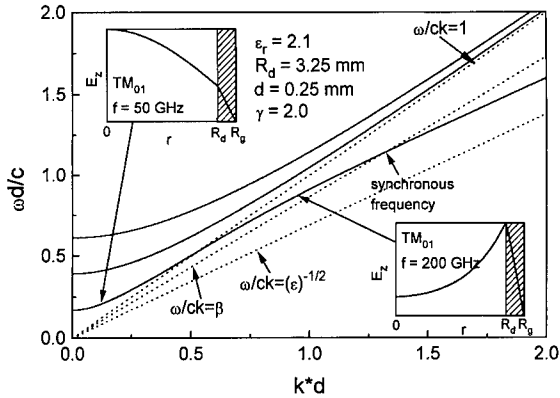


Fig. 1. Solution of the dispersion relation. The inserts show the radial dependence of the longitudinal component of the electric field for a  $TM_{01}$  mode at two different frequencies.

the radiation field. Finally, the synchronous frequency (see Fig. 1) increases with decreasing beam energy.

This synchronous frequency has been calculated [4] as a function of the beam accelerating voltage. These calculations show that for  $\epsilon_r = 2.1$ ,  $d = 0.25$  mm and a fixed geometry the laser can be tuned from  $\approx 220$  GHz to  $\approx 450$  GHz by changing the beam energy from 500 to 260 kV. Interaction is only possible with the  $TM_{01}$  mode. Taking  $\epsilon_r = 8.6$ , the laser can be tuned from 44.9 to 49.5 GHz ( $TM_{01}$ ), from 151 to 162 GHz ( $TM_{02}$ ) and from 262 to 275 GHz ( $TM_{03}$ ) when the beam voltage decreases from 500 to 250 kV. Increasing the thickness of the dielectric liner results in a decrease of the synchronous frequency for a specific mode ( $f \propto 1/d$ ).

### 3. Non-linear simulation

To estimate the performance of the Cherenkov FEL in the far infrared and millimeter wavelength region, nonlinear calculations were performed using a three dimensional model [5]. The parameters used in the calculations reflect the design parameters for the Cherenkov FEL under construction. They are shown in Table 1.

At two typical beam energies the maximum output power was calculated as a function of the frequency for a single pass amplifier configuration. The parameters used are shown together with the results in Fig. 2. For both beam energies only interaction with the lowest order  $TM_{01}$  is possible. At the first beam energy of  $\gamma = 1.80$ , and using  $d = 0.5$  mm, a maximum output power of about 2.25 MW at 138 GHz was found, resulting in an efficiency of 5.5%. With an input power of 100 W, this maximum power is reached with an interaction length of 33 cm. The output power drops sharply towards zero for higher frequencies and much slower for decreasing frequency. The FWHM is

Table 1

Overview of the main parameters of the Cherenkov FEL under construction.  $\tau$  is the electron pulse duration,  $f_{\text{rep}}$  is the repetition frequency for the electron pulses,  $l$  is the length of the dielectric medium and  $d_b$  is the thickness of the annular beam. Other symbols are explained in the text.

|                    |               |               |
|--------------------|---------------|---------------|
| $V_b$              | kV            | 300–500       |
| $r_b$              | mm            | $\approx 3.0$ |
| $d_b$              | mm            | $< 1$         |
| $I$                | A             | 100           |
| $\delta p_z / p_z$ |               | $< 1\%$       |
| $\tau$             | $\mu\text{s}$ | 10            |
| $f_{\text{rep}}$   | Hz            | $\leq 10$     |
| $\epsilon_r$       |               | 2.1–10        |
| $r_d$              | mm            | 3.5           |
| $d$                | mm            | 0.25–0.5      |
| $l$                | cm            | 30            |
| $\delta$           | mm            | 0.5           |

about 10 GHz resulting in a linewidth of  $\delta f/f = 7.2\%$ . At the other beam energy of  $\gamma = 1.587$  a thickness of  $d = 0.25$  mm was used for the dielectric liner. Here a maximum output of 58 kW was obtained at a distance of about 69 cm. The frequency is 356 GHz. Again the power drops rather sharply for higher frequencies and less quickly for lower frequencies. A FWHM of about 5 GHz is found which corresponds to a relative linewidth of  $\delta f/f = 1.4\%$ . The maximum output power increases for lower frequencies, e.g. a maximum power of 7.1 MW (20% efficiency) was found at 53.5 GHz with the following parameters:  $\gamma = 1.685$ ,  $\epsilon_r = 7.0$  and  $d = 0.5$  mm. To investigate the influence of the thickness  $d_b$  of the electron beam, the

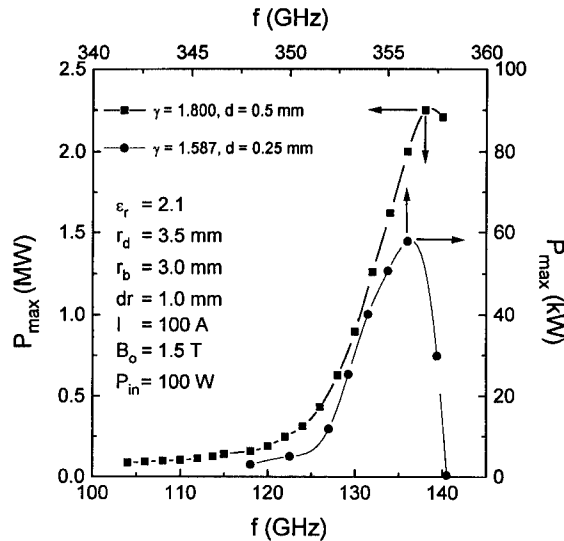


Fig. 2. Maximum power versus input frequency for two different beam energies.

maximum output power was calculated as a function of  $d_d$ . It was found that the maximum power dropped with a factor of 4 in going from an annular beam with  $d_b = 0.5$  mm to a solid electron beam. The frequency used was 138 GHz (see Fig. 2). Reducing  $d_b$  to smaller values results in even higher powers than presented in Fig. 2. However, it becomes extremely difficult to produce high current, hollow electron beams of good quality with very small thickness.

Further calculations (not presented here) show that the laser is sensitive to the beam quality as found for other Cherenkov FELs [5]. Therefore a special electron gun was designed to produce a good quality, thin walled annular beam to be used in the Cherenkov FEL under construction.

#### 4. Thermionic electron gun

Apart from the quality of the electron beam, the electron source must be reliable, reproducible, and operate at a maximum repetition rate of 10 Hz. Therefore a thermionic gun powered by a modulator was designed for this project [6]. A lanthanum hexaboride thermoemitter was chosen in view of its good reproducibility, high repetition rate and well developed technology, insuring a long pulse with a current density up to  $10 \text{ A/cm}^2$ . The limited emissive power makes a rather large cathode surface necessary and a high degree of magnetic compression ( $\approx 10$ ) at a short inter-electrode distance.

A simplified electrode configuration with magnetic coils, the magnetic field produced by these coils and the corresponding beam behaviour are presented in Fig. 3. The coil at the exit is necessary to test the gun separately and compensates for the solenoid which produces a constant magnetic field in the interaction region of the Cherenkov

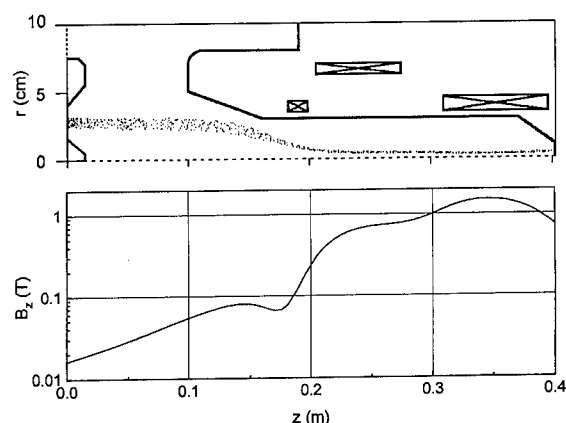


Fig. 3. Schematic layout of the electron gun showing the beam behaviour. Also shown is the magnetic field required for beam compression.

FEL. The first coil provides an opposite magnetic flux to create a correcting bump in the magnetic field profile. The low magnetic field at the cathode surface is not strong enough to link the electrons to the magnetic force lines. At the entrance of the anode hole (adiabatic region) they must be put on a particular force line to prevent transverse oscillations. The calculated microperveance was  $0.525 \mu\text{A/V}^{3/2}$ .

The longitudinal momentum spread (see Table 1) was found to be rather sensitive with respect to coil position and currents.  $\pm 1$  mm displacement of one of the first two coils led to a significant increase in the spread and in the beam wall thickness. About the same effect was induced by  $\pm 1\%$  current variations in the coils. The effect of common displacements of the coils or common variations of the currents was weaker. The position of the third coil and current variations in it are not so crucial. An interesting feature of the chosen scheme is the scaling of coil exciting currents when changing accelerating voltage. For a fixed anode–cathode separation and variation of voltage from 200 to 500 kV, the beam structure remains practically unchanged if the coil currents are varied proportionally to the total momentum of particles corresponding to the applied voltage. This feature can turn out to be useful in creating an overall control system.

Gun tests are currently carried out in a single-pulse regime on a special test facility based on a 10-stage open-air generator. The maximum test voltage of 300 kV with a pulse flat top of  $10 \mu\text{s}$  duration is limited by the electric strength of the dividing transformer for the heater current. So far an emission current of over 100 A is reached for 1.8 kW consumed power (20 V, 90 A). In normal operation the gun will be powered by a modulator delivering voltage pulses up to 500 kV at a maximum repetition rate of 10 Hz. Low voltage tests of the modulator show a ripple of less than 0.5% during the flat part of the pulse. Preliminary results of the test confirm the main design considerations of the gun as far as they concern generation of a high current annular beam of a small diameter. However, peculiar problems are foreseen at a fine tuning stage because of an unprecedently small longitudinal momentum spread to be measured and corrected.

#### Acknowledgements

The development of the electron gun has been supported by a grant from the Netherlands Organization for Scientific Research (NWO).

#### References

- [1] K.J. Button (ed.), *Infrared and Millimeter Waves*, Vol. 13 (Academic Press, 1985).



- [2] J. Walsh, B. Johnson, G. Dattoli and A. Renieri, *Phys. Rev. Lett.* 53 (1984) 779.
- [3] S. Jacobs (ed.), *Physics of Quantum Electronics*, Vol. 7 (Addison Wesley, 1980).
- [4] E. Garate and J. Walsh, *IEEE Trans. Plasma Phys.* PS-13 (1985) 524.
- [5] H.P. Freund and A.K. Ganguly, *Phys. Fluids B* 2 (1990) 2506.
- [6] A.V. Agafonov, E.G. Krastelev, A.N. Lebedev, V.S. Voronin, A.M. Bishaev, V.A. Krasnopolsky and P.J.M. van der Slot, 10th Int. Conf. on High Power Particle Beams, San Diego, CA, USA, 1994, to be published.



ELSEVIER

## Amplifier performance of the NRL ubitron <sup>☆</sup>

D.E. Pershing <sup>\*,1</sup>, R.D. Seeley <sup>1</sup>, R.H. Jackson, H.P. Freund <sup>2</sup>*Naval Research Laboratory, Washington, DC 20375, USA*

### Abstract

Operation of the Naval Research Laboratory  $K_u$ -band ubitron has successfully demonstrated a high power/efficiency and broad bandwidth. This device employs a helical wiggler/axial guide field configuration. Performance levels achieved at 16.6 GHz can be summarized as a peak power of 4.2 MW for an efficiency of 17.5% and a gain of 29 dB, and an instantaneous bandwidth of 22%. Substantial beam loss was observed. The specific loss rate was correlated with output power, and reached a level of 50% beam loss at the 4.2 MW level. Nonlinear simulations of the experiment are in good agreement with these observations.

### 1. Introduction

The NRL ubitron [1] has demonstrated operation as a high power, broad band, and efficient amplifier with a maximum output power of 4.2 MW for an efficiency of 18%, a 29 dB gain, and a large signal bandwidth (not saturated) greater than 22%. The experiment met the performance goals for the fundamental mode amplifier; specifically, an output power of 1–5 MW, an efficiency greater than 15%, a large-signal gain of 25–30 dB, and a large-signal bandwidth greater than 20%. Experimental results are in good agreement with theoretical predictions using the 3-D nonlinear code ARACHNE [2–4]. It is important to note in this regard that, in contrast to earlier devices operating in the Raman regime [3], the DC self-fields of the beam played an important role in the interaction.

### 2. Experimental results

An extensive description of the experiment is given in Ref. [1]. The wiggler is a pulsed bifilar helix with a period of 2.54 cm and a length of 33 wiggler periods. The first five and the last three periods represent an adiabatic entrance and exit. Amplification was measured over the

following parameter ranges: wiggler amplitude  $\approx 175$ –320 G, axial field  $\approx 1.75$ –2.54 kG, beam voltage  $\approx 212$ –254 kV, and beam current  $\approx 67$ –100 A. The beam radius upon wiggler entry is  $\approx 0.4$  cm and the waveguide radius is 0.815 cm. The FWHM of the beam pulse is  $\approx 2.4$   $\mu$ s, with a flat top of  $\approx 1$   $\mu$ s. Operation is largely in the  $TE_{11}$  mode at  $K_u$  band (12.4–18 GHz). The experimental configuration is shown in Fig. 1. Note that the solenoid is split to accommodate a gate valve separating the gun and the interaction/diagnostics sections which necessitated additional solenoid coils to maintain the field profile.

Amplification has been measured over a wide parameter range. Although the nominal beam and axial field values are 250 kV/100 A and 2.2 kG, these do not necessarily represent the optimal parameter range, and equivalent output power has been obtained for several different parameter sets. The maximum power measured is 4.2–4.5 MW at 16.6 GHz. Typical waveforms showing the essential characteristics of ubitron operation are given in Fig. 2. In this case, an output power of  $\approx 4.5$  MW (4.2 MW from calorimeter) was measured for a 245 kV/94 A beam, with axial guide field and wiggler field amplitudes of 2.47 kG and 270 G, respectively. This represents a gain of 29 dB and an efficiency of 18%.

It is important to observe the beam loss on the rising and falling edges of the pulse at the voltage resulting in gyroresonance for the fixed magnetic fields, as well as the high beam loss during the interaction. The ripples on the two beam current traces are due to current monitor ringing. It should also be noted that the output power shown does not represent saturation. Indeed, for most parameters we have been unable to drive the system to saturation.

The ubitron has also demonstrated a wide instantaneous bandwidth. However, there are two factors which render this measurement difficult. Specifically 1) the modulator

<sup>☆</sup> This work is supported by the Office of Naval Research.

<sup>\*</sup> Corresponding author. Tel. +1 703 339 6500, fax +1 703 339 6953.

<sup>1</sup> Permanent address: Mission Research Corp., Newington, VA 22122, USA.

<sup>2</sup> Permanent address: Science Applications International Corp., McLean, VA 22102, USA.

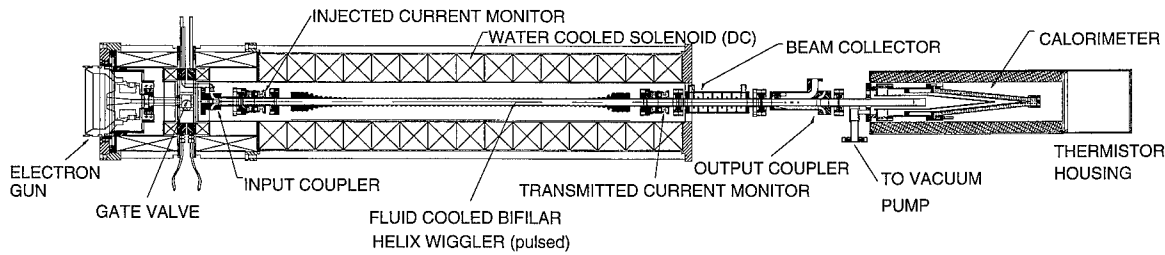


Fig. 1. Experimental configuration.

exhibits a slow time scale voltage drift, and 2) in order to accommodate high input power, the phase splitting circuitry utilizes two sets of short slot hybrids to cover most of the  $K_u$  band and several hours are required to switch between them. Hence, the bandwidth measurements are not always made with the identical parameters, but are indicative of ubitron bandwidth potential. Fig. 3 shows the bandwidth characteristics for a case in which the output power exceeds 600 kW. This represents a bandwidth in excess of 22%.

The NRL ubitron exhibits is highly sensitive to variations in the beam voltage and the axial and wiggler magnetic fields. An example of the output power sensitivity to beam voltage is shown in Fig. 4. Output power is seen to reach a maximum in excess of 4 MW at 245 kV, and to increase from 2–4 MW as the voltage increases about 4.5% from 234–245 kV. This sensitivity points to the need for very tight modulator voltage control. Similar sensitivity to variations in the axial and wiggler magnetic fields has also been observed. In order to illustrate the sensitivity of the interaction to variations in the axial magnetic field, we consider a 250 kV/83 A beam with a wiggler field amplitude of 275 G. Experimentally, the output power varies from 2–4.4 MW at 16.6 GHz as the axial magnetic field increases from 2.4–2.54 kG. Observe that the output power nearly doubles for an axial field increase of 5.5%. Somewhat less sensitivity is measured for wiggler field variations. With a 247 kV/83 A beam and an axial magnetic field of 7.6 kG, the output power

increases from 0.4 to 2.6 MW at 16.6 GHz as the wiggler field increases from 160–280 G (i.e., a field increase of  $\approx 25\%$  is required to double the output power). Part of this parametric sensitivity arises because the system is not driven to saturation; hence, small changes in the growth rate can result in relatively large variations in the output power.

### 3. Comparison with theory

A key feature of the NRL ubitron program is the integration of theoretical and experimental efforts which leads to the development and validation of a design and simulation capability. To demonstrate this capability, we compare experimental measurements with theory. We use the 3-D nonlinear simulation code ARACHNE, which in its latest version [3,4] includes both RF and DC beam space charge effects, under the assumption of an initial axial energy spread of 1.5%. It is also important to, the inclusion of the DC space-charge fields is important for the current experiment.

In general, experimental performance follows theoretical predictions as far as trends with wiggler field, axial field, beam voltage, and beam transmission are concerned. However, we usually measure a somewhat higher power than predicted. Typically, we find that a 5% increase in both the wiggler and axial fields in ARACHNE, over the experimental calibration, results in good agreement with

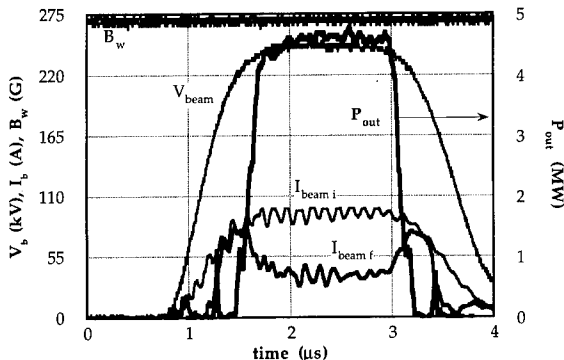


Fig. 2. Typical waveforms.

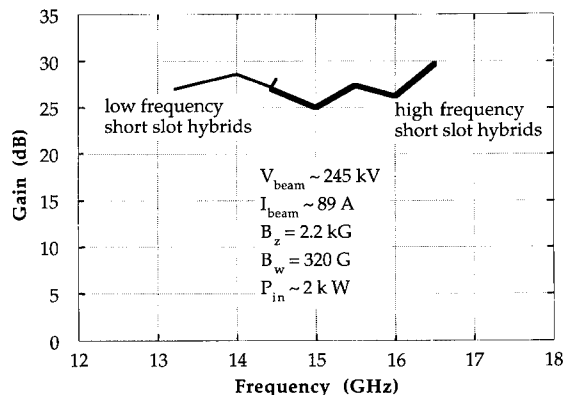


Fig. 3. Ubitron bandwidth characteristics.

the experiment. This is slightly outside our estimated 2–3% experimental uncertainty. Although this is not a large discrepancy, it is an issue that is still under investigation, and there are several possible contributory factors. On the theoretical side, possible reasons for the discrepancy include unavoidable differences between the experimental implementation and theoretical model, such as mechanical and field misalignments or actual injected beam conditions. Although these factors normally have a deleterious affect on output power, they cannot be ruled out. Experimentally, the presence of internal reflections could increase the effective input power, and thereby increase the output power over that expected for a single pass amplifier. In addition, although the solenoid and wiggler fields were carefully measured with calibrated diagnostics and compared with simulations prior to assembly, a final confirmation of the field calibrations must await the ultimate dismantling of the apparatus.

The first comparison between theory and experiment deals with the dependence of output power on input power. Power measurements are typically higher than predicted by ARACHNE for single-pass amplification with no reflections and for the nominal experimental parameters. To explain the discrepancy, we first assume the presence of a small amount of internal reflections. Note that the beam flat top is about 1  $\mu$ s wide and more than 100 round trips of the radiation are possible. Hence, even a small degree of reflection can substantially alter the output power. In order to describe the effect of internal reflections using ARACHNE we adopt the following procedure. A single-pass drive curve is first computed to obtain a gain function  $P_{\text{out}} = G(P_{\text{in}})$ . Using this gain function, we define a repetitive map for the output power over each roundtrip of the radiation through the cavity, i.e.  $P_{n+1} = G(P_{\text{inj}} + \epsilon P_n)$ , where  $P_{\text{inj}}$  is the injected power and  $\epsilon$  is the roundtrip reflection coefficient. As expected, the output power over the total pulse time increases with the reflection coefficient, and good agreement can be found with the experi-

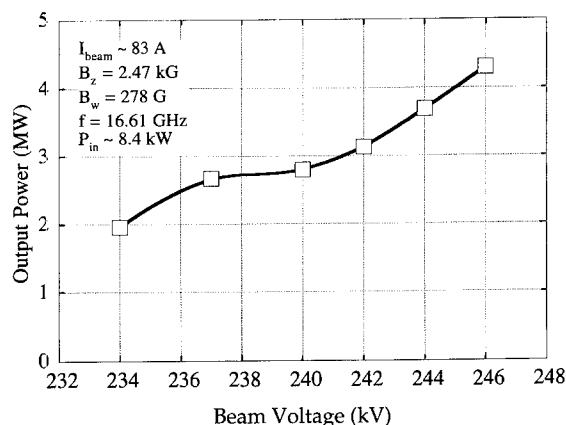


Fig. 4. Variation in the output power with beam voltage.

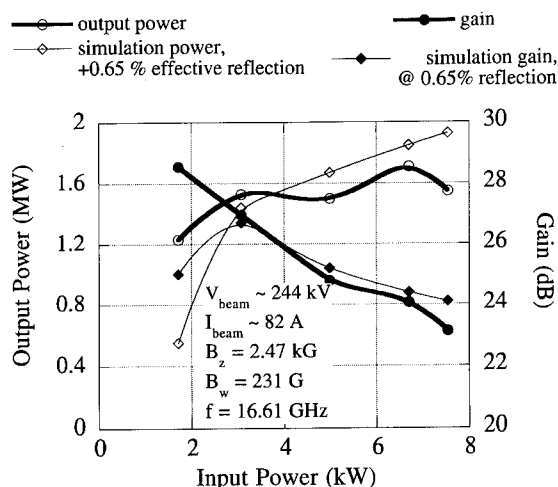


Fig. 5. Drive curve showing the output power and gain as a function of the input power.

ment for an effective reflection coefficient of 0.65%. This is illustrated in Fig. 5 showing drive curves obtained from the experiment and from the above-mentioned procedure for a 244 kV/82 A beam and for wiggler and guide magnetic fields of 231 G and 2.47 kG at 16.6 GHz. However, based on cold tests and measurements of reflected power during operation, we expect round trip reflections of the order of 0.1–0.3%.

It is also possible that the actual injected power is underestimated. However, the uncertainty in the injected power is thought to be < 20% and this is not sufficient to explain the discrepancy over a single-pass; internal reflections affect output power much more strongly. Therefore, we expect that other factors must be involved.

A second possible explanation for the discrepancy between the theory and experiment is in the diagnostic calibration accuracy of 2–3%. The strong dependence of the output power on beam voltage for several values of the

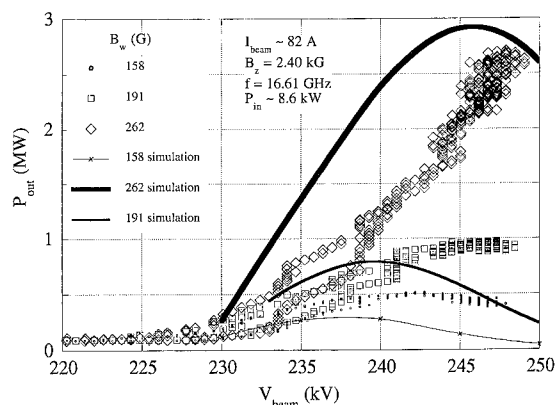


Fig. 6. Variation in the output power with beam voltage for several values of wiggler amplitude.

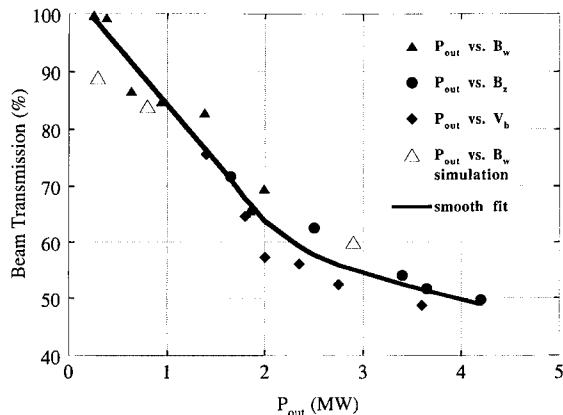


Fig. 7. Variation in beam loss with output power.

wiggler field is shown in Fig. 6. The data for this figure are presented as output power vs. beam voltage. The simulation results from ARACHNE are shown with the solid curves, with the curve thickness matching the corresponding point thickness of the experimental measurement. Reasonable agreement is shown in the voltage where the peak power occurs and in the overall voltage dependence, although the output power peaks as predicted by ARACHNE are at voltages 2–3% less than observed. However, both the wiggler and axial magnetic field values used in ARACHNE were 5% higher than the nominal experimental values.

In view of these comparisons, we expect that the bulk of the discrepancy between theory and experiment is accounted for by the assumptions of 1) a small degree of internal reflections, and 2) small changes from the nominal values of the magnetic fields and beam voltage.

One final issue important for a production device is beam loss. Both simulation and experiment show high beam loss in the interaction region at multimewatt power levels. This is demonstrated in Fig. 7 in which we plot the variation in beam loss with output power for a variety of different beam, wiggler and axial field parameters. The solid triangles in the figure represent data collected from experimental runs in which the variation in output power versus wiggler amplitude was studied. Similarly, the solid circles (diamonds) represent data collected from studies of the variation in the output power versus the axial guide field (beam voltage). The hollow triangles represent ARACHNE simulations of output power dependencies on wiggler and axial guide fields. The solid line is simply a smooth fit to all of these points. It is evident that the fraction of transmitted beam falls fairly uniformly with output power and reaches about 50% transmission at a 4 MW power level. Observe that all the points from both the

experiment and the simulation cluster fairly closely about the fitted curve, and represent good agreement between the theory and the experiment. Two factors contribute to the high beam loss: operation near gyroresonance, and large beam orbits at high output power. Note that gyroresonant beam loss begins at a voltage reduction of  $\sim 20\%$ , which is comparable to the measured 18% efficiency.

Although this degree of beam loss is clearly undesirable for high duty factor operation, it does not necessarily result in tube damage. The NRL ubitron was disassembled after many hours of operation at 6 pps and examined for damage. For this experiment it was found that the beam loss is sufficiently distributed axially to result in little or no tube damage. This effect could probably be reduced by simply reducing the initial beam diameter, or operation further from gyroresonance.

#### 4. Summary

In conclusion, results from the NRL ubitron experiment demonstrate that the performance potential of the ubitron/FEL has been realized. A configuration using a fundamental mode circularly polarized rf wave and a helical wiggler results in a relatively compact, high power, and efficient amplifier with wide instantaneous bandwidth and without the necessity of wiggler field tapering. Performance levels compare quite favorably with those from other pulsed, high power microwave amplifier designs.

In general, there is good agreement between theory and experiment. Both theory and experiment show a high degree of output power sensitivity to beam voltage and axial magnetic field. Some differences exist, with the experimental power levels typically higher than predicted. We are examining the questions of internal reflections, magnetic field calibrations, and beam modeling as sources of the discrepancy. Further attention to the beam loss issue is required for higher duty factor operation. Future work will include more extensive measurements of noise and phase characteristics, as well as utilization of our theory/design capability for designs at higher frequency and lower voltage regimes.

#### References

- [1] D.E. Pershing, R.H. Jackson, H. Bluem and H.P. Freund, Nucl. Instr. and Meth. A 304 (1991) 127.
- [2] A.K. Ganguly and H.P. Freund, Phys. Fluids 31 (1988) 387.
- [3] H.P. Freund, R.H. Jackson and D.E. Pershing, Phys. Fluids B 5 (1993) 2318.
- [4] H.P. Freund and T.M. Antonsen, Jr., Principles of Free-electron Lasers (Chapman & Hall, London, 1992) Chap. 5.



ELSEVIER

## The groove guide as an interaction structure for a microwave FEL

P. Arcioni <sup>a</sup>, M. Bressan <sup>a</sup>, F. Broggi <sup>b,\*</sup>, G. Conciauro <sup>a</sup>, L. Perregrini <sup>a</sup>, P. Pierini <sup>b</sup>

<sup>a</sup> *Dip. di Elettronica, Univ. di Pavia e INFN Sezione di Pavia, Via Abbiategrasso 209, 27100 Pavia, Italy*

<sup>b</sup> *LASA-INFN Sezione di Milano, Via Fratelli Cervi 201, 20090 Segrate (Milano), Italy*

### Abstract

Microwave FELs need a waveguide to confine the radiation and to control the group velocity of the radiation. If the electron bunches are short (some tens of ps), the control of the group velocity allows the FEL to operate in different regimes (steady-state or superradiant) [1].

The Groove Guide (GG) is a low loss, laterally open structure; it consists of two parallel conducting planes with two grooves trapping the electromagnetic energy. The dimensions of the GG are of the order of some wavelengths, and, differing from the “standard” oversized waveguide, the GG supports a single TE<sub>01</sub>-like mode, if suitably designed.

Moreover, the electromagnetic energy density, trapped by the grooves, is higher than in the rectangular oversized guide, for the same amount of power flowing, leading to a stronger coupling between the electrons and the radiation.

In this paper the advantages of using a GG as a FEL interaction structure are discussed. Experimental measurements and characterization in the Ka band of prototypes of straight section, bend, transition from/to standard WR-28 rectangular waveguide are presented.

### 1. Introduction

The waveguide is a very, if not the most, important component of a microwave FEL. As a matter of fact beyond the confinement of the radiation, in a FEL with short electron bunches, like an RF accelerator driven one, the waveguide allows control of the group velocity of the radiation, leading to different FEL operation, the Steady-State (SS) (when the group velocity is equal to the electron beam velocity) or the SuperRadiance (SR) (when the radiation slips away from the electron bunch) [1]. If a rectangular waveguide is considered, its transverse dimensions must be large enough to host the electron beam size and wiggling motion, leading to dimensions of many wavelengths (oversized or overmoded guide). Such a waveguide allows the propagation of many (even hundreds) higher order modes, excited by discontinuities or imperfections of the waveguide, or by the beam itself. Many of these modes can couple with the beam and be amplified [2].

Such a big number of higher order modes precludes the use of standard components in the circuitry for the input of the triggering power into the waveguide (in an amplifier configuration) and in the output circuitry, for the radiation diagnostics. In order to avoid all these problems we sug-

gest the use of a groove-guide as interaction structure. The work on this kind of waveguide has been carried out for the ELFA project [3,4] and the data presented refer to this experiment. This paper summarizes the feasibility studies of the groove guide for FEL applications and presents the experimental data of characterization of prototypes of groove guide components dimensioned for the ELFA project [3,5].

### 2. The properties of the groove guide

The GG consists of two parallel conducting planes with a rectangular longitudinal groove in each. The guide supports a TE mode and the energy is concentrated in the groove region. Despite the short wavelength, the dimensions of the guide are large, of the order of some wavelengths, and an accurate choice of the dimensions of the guide allows the trapping of a *single* mode while the higher order modes are laterally radiated. In this way the electron–radiation interaction can take into account only the trapped mode, since its field is the only one giving a continuous interaction along the guide.

Fig. 1 shows a section of the guide with the dominant mode electric field lines and the energy distribution.

Being laterally open, the groove guide eases beam/radiation diagnostics during the interaction, and the coupling/decoupling of the beam with the radiation. Moreover the pumping problems related to the low conductance of an oversized guide are overcome.

\* Corresponding author. Tel. +39 2 239 2541, fax +39 2 239 2543, e-mail broggi@mvlasa.mi.infn.it.

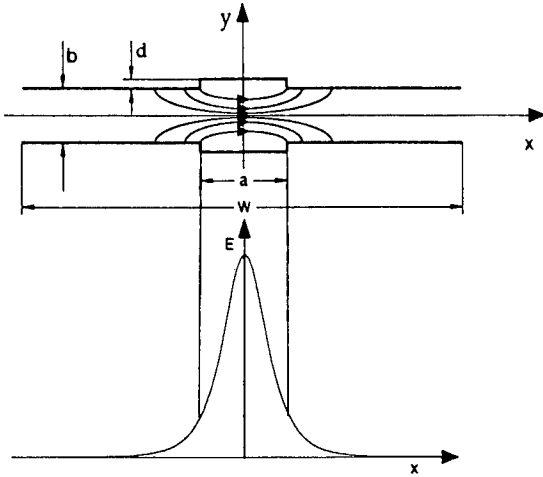


Fig. 1. Cross section of the groove-guide with the field lines and the electric field amplitude in the  $x$  direction at  $y = 0$ .

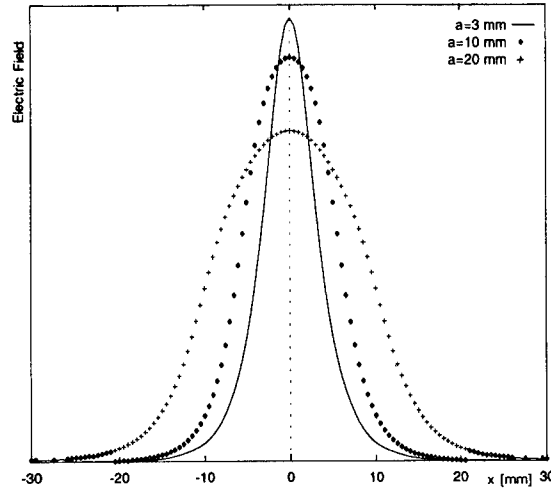


Fig. 2. Electric field distribution for different groove width.

The characteristics of propagation in the groove guide are determined by its dimensions, the groove width  $a$ , the spacing  $b$ , and the groove depth  $d$ , so the group velocity can be adjusted in order to explore the different FEL regimes (SS or SR) simply by changing the spacing of the planes of the *same structure*.

Numerical evaluations of the tolerances on the dimensions of the guide show that good control of the group velocity, consequently of the slippage between the electron bunch and the radiation, can be achieved with ordinary machining precision.

In the ELFA experiment the height of a rectangular oversized waveguide was 8.7 mm for the SS regime, and 9.0 mm for the SR, the other transverse dimension was 50 mm. The corresponding groove guide had dimensions of  $a = 16$  mm,  $b = 7.2$  mm,  $d = 1$  mm for the SS, and  $b = 7.5$  mm for the SR operation.

### 3. Optimization of the guide

The dimensions of the groove guide reported above guarantee the equivalence of the groove guide with the rectangular oversized waveguide, concerning only the propagation constant. Different combinations of the dimensions can give the same characteristics.

Since the width of the groove  $a$  affects the concentration of the energy, an optimization of the groove dimensions has been carried out, in order to get the maximum coupling between the wiggling electrons and the electric field (see Fig. 2).

To this aim the code PAGODA [6], giving the propagation constant and the field of arbitrarily shaped waveguide, was used. Afterwards the coupling coefficient of the fields with the electron motion, normalized to the coupling of a

reference rectangular waveguide was calculated. Hence the coupling coefficient is defined as

$$C = \frac{\langle E^{GG}_v \rangle \lambda_w}{\langle E^{RW}_v \rangle \lambda_w} = \frac{\langle E^{GG}_x v_x \rangle \lambda_w}{\langle E^{RW}_x v_x \rangle \lambda_w}, \quad (1)$$

where  $E^{GG}$  and  $E^{RW}$  are the normalized modal electric field of the groove guide and of the rectangular waveguide respectively,  $v$  is the velocity of the electrons and the average is performed over the wiggler period  $\lambda_w$ . In Fig. 3 the coupling coefficient as a function of the groove width  $a$ , for different spacing of the guide planes  $b$  referring to the ELFA experiment [5], is shown. In order to get the same propagation characteristics the groove depth and/or the plane spacing must be set accordingly.

In consequence of this optimization the dimensions of the groove guide for the ELFA experiment have been set as follows:  $a = 6$  mm,  $b = 7$  mm,  $d = 1.52$  mm for the SS regime. A trim of the spacing  $b$  to 7.34 mm allows the SR operation.

As a consequence of the enhancement of the coupling factor  $C$ , in a 1D FEL model [7], the FEL gain parameter  $\rho$ , which determines the scaling laws and the operating

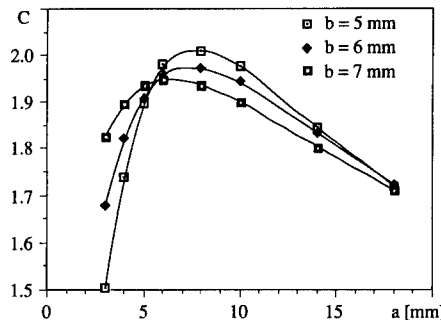


Fig. 3. Coupling coefficient as a function of the groove width.

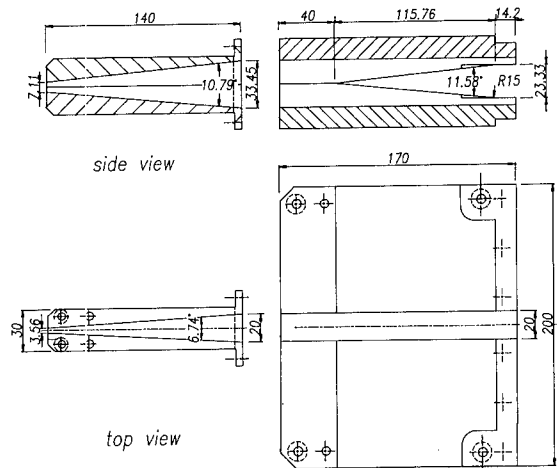


Fig. 4. Schematic view of the transition from standard to groove guide.

constraints of an FEL, is increased by a factor  $C^{2/3}$  [8]. As an example, for the ELFA parameters  $C = 1.95$  [5] and  $\rho$  is increased by a factor of 50%; all the quantities related scale consequently. It is important to note that the gain length is reduced by about 30%, leading to a shorter wiggler length necessary to reach saturation. The power at saturation is increased by the same factor as  $\rho$ .

#### 4. Experimental measurements

In order to check the mechanical feasibility and the electrical characteristics of a groove guide, some experimental tests have been carried out on prototypes of groove guide components. In particular the transition from stan-

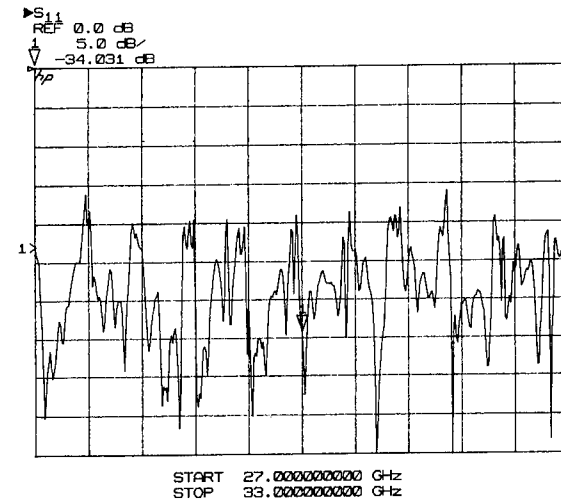


Fig. 6. Reflection coefficient for the transition system.

dard waveguide and a straight section of groove guide has been investigated. The tests have been done at a center frequency of 30 GHz. In Fig. 4 a sketch of the transition from the standard WR-28 to the groove guide is shown.

It consists of two elements. The first one is a tapered transition matching the standard waveguide dimensions to the groove. It is 140 mm long, consequently the tapering angles are  $6.74^\circ$  in the horizontal plane and  $10.8^\circ$  in the vertical plane. The second part opens laterally. The measurements were performed with an Hewlett Packard network analyzer mod. 8510B. Figs. 5 and 6 show the transmission and the reflection coefficient of the double transition from the standard waveguide to the groove guide and back to the standard waveguide, as a function of the frequency.

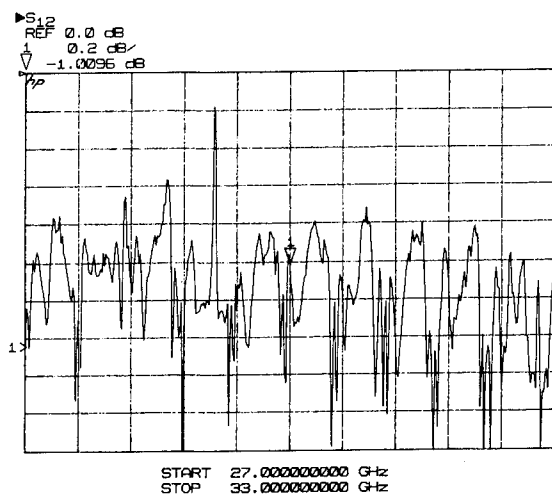


Fig. 5. Transmission coefficient for the transition system.

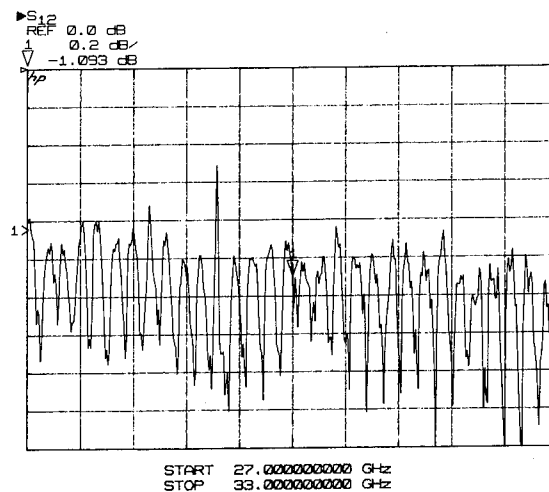


Fig. 7. Transmission coefficient for the transition-straight section system.



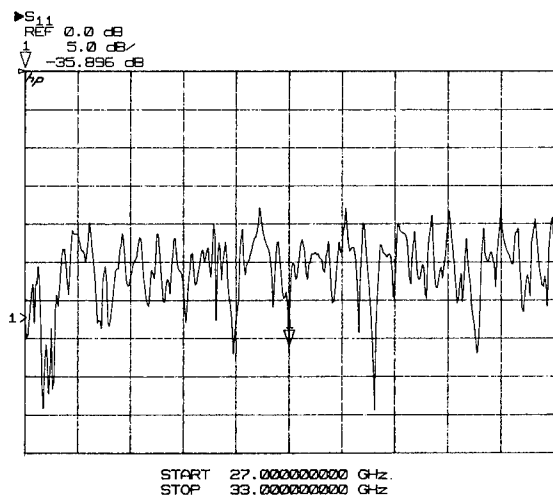


Fig. 8. Reflection coefficient for the transition-straight section system.

At the frequency of 30 GHz a loss of 1 dB (about 20% of the power) and a reflection of  $-34$  dB has been measured, showing a good matching between the standard waveguide and the entry of the groove guide.

In Figs. 7 and 8 the transmission and the reflection coefficient of the double transition measured before with an inserted straight section of groove guide 50 cm long are shown.

At the center frequency of 30 GHz the system shows an attenuation of 1.1 dB and a reflection coefficient of about  $-36$  dB, leading to an attenuation of 0.2 dB/m for the straight section of the groove guide, according to Ref. [9].

Experimental tests varying the contact strength between the components have not shown a significant difference with the normal mechanical mounting and locking, confirming the possibility of having long interaction structures composed by several short sections without degrading the performance of the structure itself.

Preliminary tests on a  $90^\circ$  bend have been done, but better optimization must be carried on.

## 5. Conclusions

The components needed to create a complete transmission system, i.e. directional couplers, detectors, attenuators, and so on have been studied [10,11] and can be readily obtained. The groove guide with its low-loss and relaxed machining and mounting tolerances, together with the shorter wiggler length needed, due to the stronger coupling, seems to be a very promising interaction structure. The higher order mode power, laterally radiated, must be monitored (for example with resistive sheets or liquid crystal sensors) if precision measurement of the FEL efficiency are needed.

## Acknowledgement

The authors are indebted to Mr. D. Agnetti for the technical drawings and his assistance in machining the prototypes.

## References

- [1] R. Bonifacio et al., Nucl. Instr. and Meth. A 296 (1990) 358.
- [2] W.M. Sharp, S.S. Yu, P. Pierini and G., Cerchioni, Nucl. Instr. and Meth. A 296 (1990) 535.
- [3] E. Acerbi et al., Electron Laser Facility for Acceleration, Design Report (1992).
- [4] E. Acerbi et al., Proc. 1993 IEEE Particle Accelerator Conf., IEEE, Piscataway, NJ, 1993, p. 1524.
- [5] P. Arcioni, M. Bressan, F. Broggi, G. Conciauro and P. Pierini, Proc. 1993 IEEE Particle Accelerator Conf., IEEE, Piscataway, NJ, 1993, p. 1569.
- [6] P. Arcioni, M. Bressan and G. Conciauro, PAGODA: a Computer Code for the Analysis of Waveguides – Operating Manual, Technical Report 03/90, Dept. of Electronics of Pavia (1990).
- [7] R. Bonifacio et al., Riv. Nuovo Cimento 9 (1990).
- [8] R. Bonifacio, C. Pellegrini and L. Narducci, Opt. Commun. 50 (1984) 313.
- [9] D.J. Harris and K.W. Lee, Electron. Lett. 14 (1978) 101.
- [10] J. Meissner, Electron. Lett. 20 (1984) 460.
- [11] D.J. Harris and S. Mak, Electron. Lett. 17 (1981) 516.



ELSEVIER

## Ribbon-FEL experiments at one-dimension distributed feedback

A.V. Arzhannikov<sup>a</sup>, V.B. Bobylev<sup>a</sup>, S.L. Sinitsky<sup>a</sup>, A.V. Tarasov<sup>a</sup>, N.S. Ginzburg<sup>b,\*</sup>,  
N.Yu. Peskov<sup>b</sup>

<sup>a</sup> Institute of Nuclear Physics, Novosibirsk, Russian Federation

<sup>b</sup> Institute of Applied Physics, Nizhny Novgorod, Russian Federation

### 1. Introduction

A FEL driven by a 1 MeV electron beam, with a strongly elongated cross section (i.e. with a so called sheet or ribbon beam), seems to us a suitable device to generate power in the gigawatt range at a few mm wavelength (see Refs. [1,2]). Ribbon beam generation and transport through a plane magnetic undulator were studied not only theoretically but also experimentally at the U-2 device [1–3]. The problem of providing synchronism between radiation emission from different parts in the beam cross section has been solved in a theory only [2,4,5]. To realize a feedback, which is necessary for providing radiation synchronism, use of two-dimensional Bragg gratings has been suggested in these papers. However in the experiment at the U-2 device feedback has been realized by using one-dimensional Bragg gratings. Results of these experimental studies will be described in this paper.

### 2. Experimental setup

A schematic drawing of the experiment is shown in Fig. 1. A resonator for a 4 mm TEM-mode electromagnetic wave is made of two pairs of one-dimensional copper Bragg gratings and a copper waveguide located between them. The inner cross section of the waveguide is  $1 \times 20$  cm and the length is 32 cm. Selection properties of the resonator has been tested by injecting microwave power with a wavelength near 4 mm from a commercial generator. The dependence of the maximum microwave energy density in the resonator on the wavelength of the input microwave power is shown in Fig. 2. This figure shows that this resonator can be really used for selection of waves in the region near 4 mm wavelength.

### 3. Results and discussion

The experiments on transporting the ribbon electron beam through the plane undulator, with the one-dimensional Bragg gratings installed, have shown that a maximum power at 4 mm wavelength is reacted a certain value of the longitudinal magnetic field in the plane undulator. In our experiments this optimal value is 6 kG, which corresponds to an approximate resonance between the gyro and

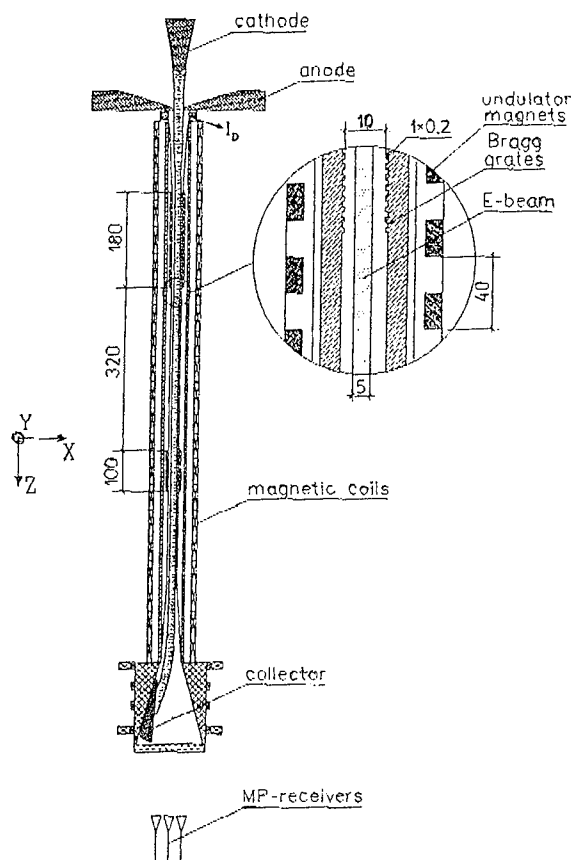


Fig. 1. Schematic view of the experiment.

\* Corresponding author. Tel. +7 8312 384 552, e-mail ginzburg@appl.nnuu.su.

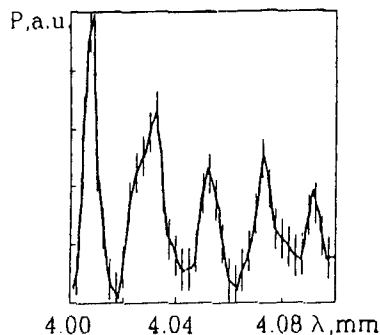


Fig. 2. Dependence of the maximum microwave energy density in the resonator on the wavelength of the input microwave radiation.

bounce motions of the beam electrons. Signals registered in the experiment at this optimal magnetic field are shown in Fig. 3. In this figure one can see that 4 mm radiation is generated in the form of a single spike with a duration of about 1  $\mu$ s. However, under the same conditions, there are

a few shots in which the number of spikes has reached 4–5. It should be pointed out that in spite of the resonator, radiation at 8 mm has been registered as can be seen in Fig. 2. On the other hand, 2 mm wavelength power was observed with very small amplitude in the experiments. A 10% deviation of the longitudinal magnetic field from the optimal value leads to a decrease in the output power at 4 mm of at least an order of magnitude.

An absolute value for the microwave power has been estimated from measurements of the temperature change of a special gum when the microwave power is absorbed during a shot. By means of this calorimeter, the energy content of the microwave pulse has been measured to be 30–50 J. Taking into account the waveform of the microwave power signals we may estimate the peak power in the range of a few tens of megawatt. The fact that the microwave power was not as high as expected and measured in a previous experiment [3], is explained by the length of the undulator which is only 0.5 m in this experiment instead of 1 m in the previous one.

Measurements of the polarization of the microwave radiation have shown that the electric field of the waves is mainly directed along the transverse magnetic field ( $X$ -axis in Fig. 1). Taking into account this fact and the result shown in the Fig. 2 one can conclude that even with one-dimensional Bragg gratings wavelength selection is possible.

## References

- [1] A.V. Arzhannikov, S.L. Sinitsky and M.V. Yushkov, Book of abstracts of FEL'90 Conf., Paris, France, 1990, p. 105.
- [2] A.V. Arzhannikov, N.S. Ginzburg, V.S. Nikolaev, N.Yu. Peskov, A.S. Sergeev, S.L. Sinitsky and R.P. Zotkin, Technical Digest FEL'92 Conf., Kobe, Japan, 1992, p. 214.
- [3] A.V. Arzhannikov et al., Proc. BEAMS'90 Conf., Novosibirsk, USSR, 1990, Vol. I.
- [4] N.S. Ginzburg, N.Yu. Peskov and A.S. Sergeev, Pis'ma v ZhTF 18, N:9 (1992) 23.
- [5] N.S. Ginzburg, N.Yu. Peskov and A.S. Sergeev, Opt. Commun. 96 (1993) 254.

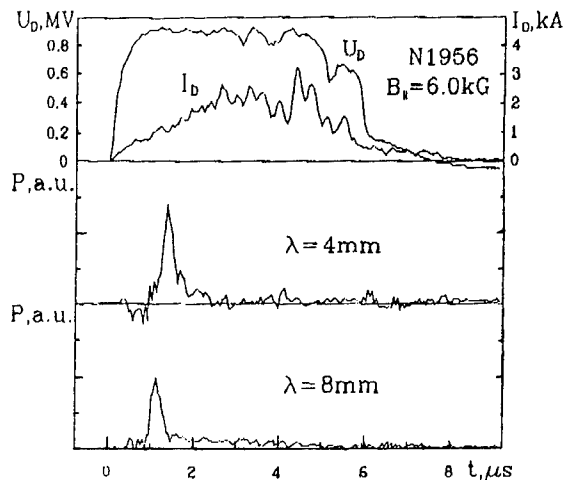


Fig. 3. Set of signals characterising the generation of the microwave radiation with the wavelengths 4 mm and 8 mm during the beam pulse.  $U_D$ : diode voltage;  $I_D$ : current at the entrance of the resonator.

# Analysis of chaotic behaviour in a Raman FEL

S. Kawasaki <sup>a,\*</sup>, H. Ishizuka <sup>b</sup>, T. Koarai <sup>c</sup>, A. Watanabe <sup>c</sup>, M. Shiho <sup>c</sup>

<sup>a</sup> Faculty of Science, Saitama University, Urawa 338, Japan

<sup>b</sup> Fukuoka Institute of Technology, Wajiro, Higashi-ku, Fukuoka 811-02, Japan

<sup>c</sup> Japan Atomic Energy Research Institute, Fusion Research Establishment, Naka-machi, Ibaraki, 311-02, Japan

## Abstract

To compare with the experiment of Raman FEL carried out at JAERI, extensive data of the simulation have been compiled and behaviours of particle orbits in the phase space relative to rf field were studied in detail to get a phenomenological understanding of the effects of beam space charge on FEL performance. Although an ordinary Hamiltonian analysis cannot rigorously be applied to the Raman FEL due to its dissipative character, it is found that the orbits in the phase space become chaotic on going up in beam intensity. The effect of the tapering on the behaviour of the orbits was also discussed.

## 1. Introduction

FEL oscillations and amplifiers are based on a non-linear process and chaotic phenomena in FEL performance are expected for many aspects involved therein. So far chaos in FELs was studied in the following two aspects. Firstly, in the single particle dynamics in a wiggler in which the motion of electrons is determined self-consistently including the effect of the beam field. The energy conservation of the particles makes it possible to analyse the evolution of the particle orbits with the Hamiltonian formalism. Contour maps of the orbits in the phase plane could show the existence of chaos for a particular parameter presenting the non-linearity of the system [1–3]. Secondly, there is another kind of treatment of the chaos in FEL, where the process of an rf oscillator/amplifier is analysed considering that the rf field absorbs energy of electrons coherently excited with the rf itself, and the system is intrinsically dissipative. Therefore, a Hamiltonian formalism is invalid because the total energy is not preserved [4]. Ginzburg and Antonsen carried out studies for a Compton FEL in this regime using one dimensional return maps with regard to an electron slippage [5,6].

We have studied a Raman FEL at JAERI experimentally [7], and also with 1D and 3D numerical simulations [8,9], where the effects of beam space charge and of tapering of the wiggler field on the performance are of principal concern. Interaction between the particles and rf fields is reflected in the orbits in the phase plane as a time

history of particle motion relative to the rf. The simulation is consistent with the our experiments [7]. In order to make a further study on FEL amplification, we investigated a chaotic aspect of the phase motion of the electrons relative to the rf in  $\psi$ - $d\psi/dt$  phase space (a Poincaré surface-of-section) using a 1D simulation code, taking notice that the system being considered is quasi-preservable at least in the saturation regime.

## 2. Simulation programme

The algorithm of the numerical code was described elsewhere in detail [9]. It is similar to that developed by Freund and Ganguly [10], while ours includes a longitudinal space charge term, so that the beam intensity can be treated directly as one of the main parameters. The effect of the modulation of the wiggler field strength with accord to the evolution of the particle energy, or tapering, on the intensity and evolution of the output rf were intensively studied with the code. The tapering pattern was optimized for various cases of particle energy and current intensity [8]. The equations used are

$$d^2\delta a_{\text{in}}/dz^2 + [\omega^2/c^2 - k^2 - k_{\text{in}}^2]\delta a_{\text{in}} = 8(\omega^2/c^2)F_{\text{in}}\langle(\cos \alpha/|v_z|)e_{\text{in}} \cdot v\rangle, \quad (1)$$

$$2k^{1/2} d(k^{1/2}\delta a_{\text{in}})/dz = -8(\omega^2/c^2)F_{\text{in}}\langle(\sin \alpha/|v_z|)e_{\text{in}} \cdot v\rangle, \quad (2)$$

$$v_z dP/dz = -e(\delta E_{\text{rf}} + \delta E_{\text{sc}}) - (e/c)v \times (B_w + B_z + B_r). \quad (3)$$

and

$$E_{\text{sc}} = -d\phi/dz = -2(\omega_b^2/c\omega)\langle\sin \alpha\rangle. \quad (4)$$

\* Corresponding author. Tel. +81 48 858 33 71, fax +81 48 858 33 71.

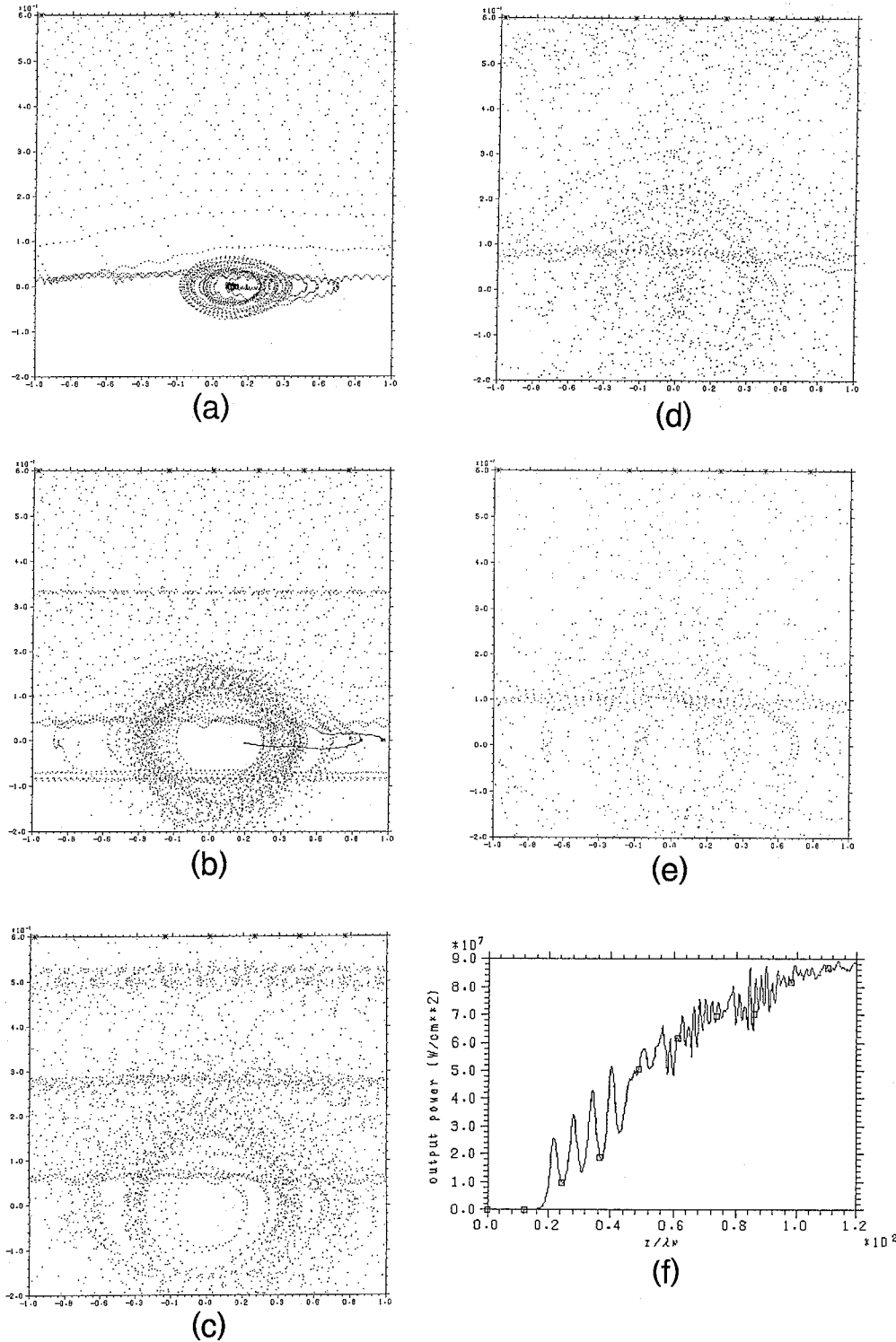


Fig. 1. (a)–(e) Orbits in  $\psi$ - $d\psi/dt$  plane with tapering. Abscissa is  $\pi$  to  $-\pi$ . Ordinate is  $d\psi/dz/k_w$ . Beam intensity  $I$  = (a) 10 A, (b) 100 A, (c) 300 A, (d) 600 A, (e) 1 kA. (f) Evolution of rf power along the wiggler with tapering, where  $\lambda_w$  is the wiggler period.

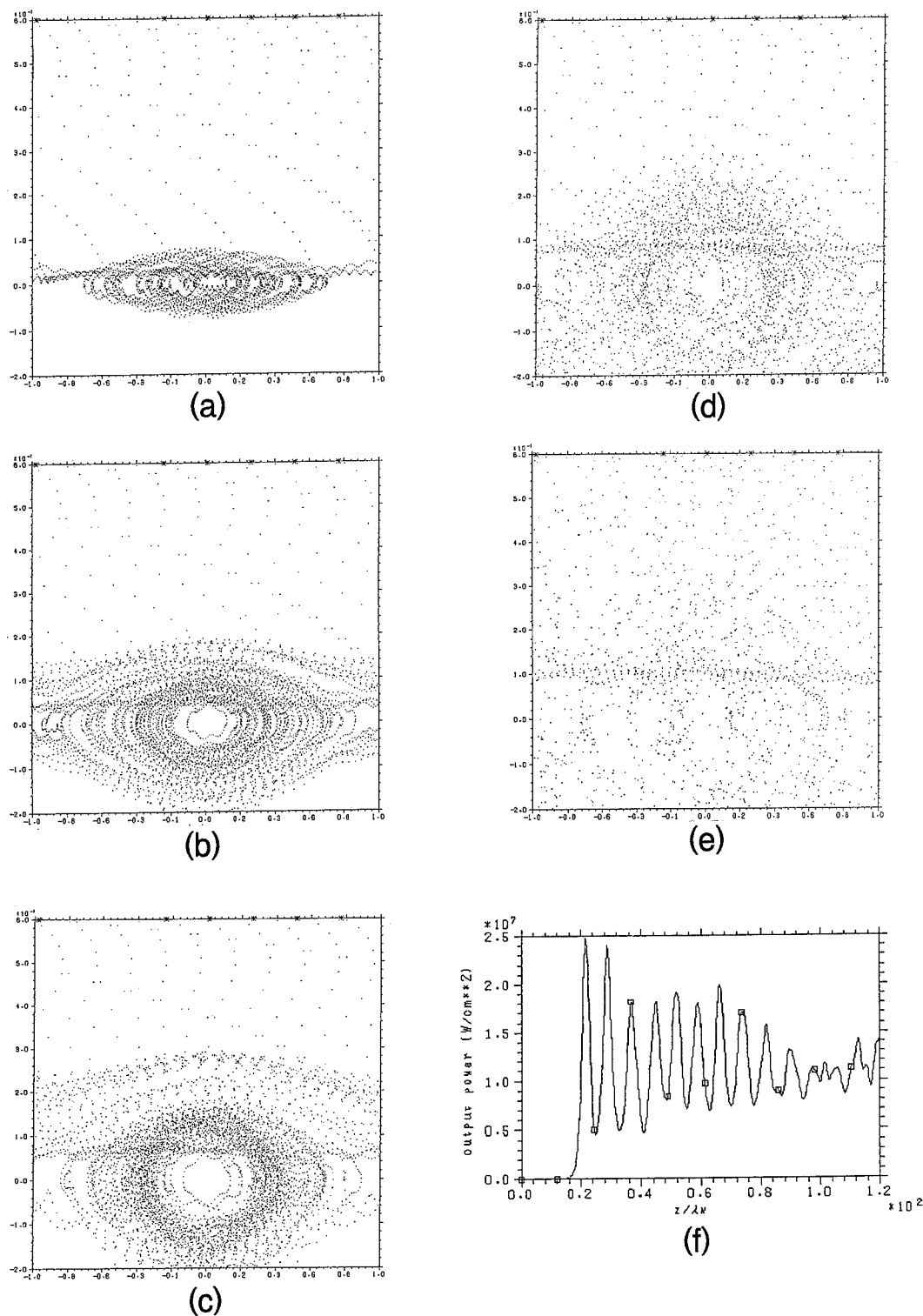


Fig. 2. Orbits in  $\psi$ - $d\psi/dt$  plane without tapering. Beam intensity  $I$  = (a) 10 A, (b) 100 A, (c) 300 A, (d) 600 A, (e) 1 kA. (f) Evolution of rf, without tapering.

Table 1  
Simulation parameters

|                                  |                   |
|----------------------------------|-------------------|
| Particle energy (MeV)            | 1.6               |
| Ref. frequency (GHz)             | 80                |
| Longitudinal magnetic field (T)  | 0.3               |
| Wiggler field (focusing type, T) | 0.19547           |
| Boundary dimension (cm)          | rectangular (2×2) |

The notations used here are to be referred to Ref. [9]. The phase of the particle motion relative to rf,  $\psi$ , is calculated indirectly by integrating  $k + k_w - \omega/v_z$  with the space co-ordinate  $z$  along the wiggler.

Instead of proceeding with a more exact treatment of the equations as was done in Ref. [4], we simply demonstrate  $\psi$  and  $d\psi/dt$  of the electron particles for various beam intensity. The beam and wiggler parameters used in the simulation are listed in the Table 1.

### 3. Orbits in phase space of $\psi$ and $d\psi/dt$

Figs. 1a–1e show the orbits traced for several test particles in the phase space for various beam intensity from 10 A through 1 kA, with the wiggler tapering and Fig. 1f gives the evolution of the rf power along the wiggler through the pitch number of 130. Figs. 2a–2f are the corresponding data without tapering. The parameters of the beam, wiggler and tapering are taken to be identical for all cases except the beam intensity.

When the beam intensity is low enough, the particles come to form a bunch and oscillate around an equilibrium

phase, reflecting the FEL pendulum equation. Increasing the intensity up to an order of 600 A, the bunch will diverge while the structure is kept in a similar pattern as a whole. Finally when the intensity goes up to 1 kA, the orbits diverge randomly in the phase space and the bunch structure disappears. Fig. 3 shows the distance of the two orbits which have slightly different initial conditions (Lyapunov exponent). For the beam intensity  $I = 10$  A, the distance remains small through the whole wiggler periods, while it diverges nearly exponentially for  $I = 1$  kA. These facts strongly suggest that a certain physics leading to chaotic behaviour in FEL operation on the phase space  $\psi$ – $d\psi/dt$  lies behind and its key parameter should be the beam intensity, or the self-electric field.

On the other hand, comparison of the orbits with/without tapering makes clear that the tapering tends to increase the rf by enhancing the bunching of the beam and keeping it around an equilibrium phase. As shown in Figs. 1f and 2f, the effect of tapering on the efficiency of conversion to rf is fairly demonstrated, while the orbits in the phase space dissipate more rapidly for tapered operation than for non-tapered. It is still unknown whether and how the tapering does relate to the onset of chaos or not.

### 4. Summary

It is found that the operation of a Raman FEL has chaotic characteristics in the phase space in its operation as an rf amplifier when the beam intensity goes up to the level of 1 kA. The simulation code itself should be reliable and the apparent chaos could not be due to the numerical calculation method, since it can provide the results consistent with the experiment at least until the saturation regime. The effect of the tapering on the chaotic behaviour is not definitely determined, although phenomenologically it seems that application of the tapering accelerates the transition to the chaos.

### References

- [1] C. Chen and R.C. Davidson, Phys. Rev. A 43 (1991) 5541.
- [2] L. Michel et al., Nucl. Instr. and Meth. A 304 (1991) 465.
- [3] G. Spindler and G. Renz, Nucl. Instr. and Meth. A 304 (1991) 492.
- [4] The Hamiltonian formalism can be applied to the system with a dissipation if rf field is included in the Hamiltonian: D. Farina et al., Phys. Rev. E 49 (1994) 1603.
- [5] N.S. Ginzburg and M.I. Petelin, Int. J. Electron. 59 (1985) 291.
- [6] T.M. Antonsen, Jr., AIP Conf. Proc. 230, Nonlinear Dynamics and Particle Acceleration, eds. Y.H. Ichikawa and T. Tajima (New York, 1991) p. 106.
- [7] K. Sakamoto et al., J. Appl. Phys. 75 (1994) 36.
- [8] S. Kawasaki et al., Nucl. Instr. and Meth. A 341 (1994) 316.
- [9] Y. Kishimoto et al., Phys. Rev. Lett. 65 (1990) 851.
- [10] H.P. Freund and A.K. Ganguly, Phys. Rev. 28 (1983) 3438.

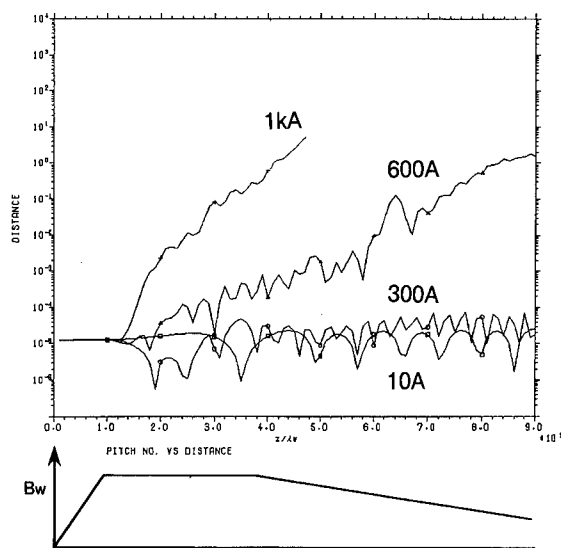


Fig. 3. Distance in the phase space between two orbits having close initial conditions, for various beam intensity. The pattern of wiggler tapering is shown below.

# Strong coupling operation of a FEL amplifier with an axial magnetic field

J.L. Rullier<sup>\*</sup>, J. Gardelle, J. Labrousche, P. Le Taillandier

CEA / CESTA, P.O. Box 2, 33114 Le Barp, France

## Abstract

This paper presents the results of a FEL experiment at 35 GHz, using a highly relativistic electron beam ( $T = 1.75$  MeV). The electron pulse length is 30 ns FWHM with a peak current of 400 A. The FEL is designed to operate in the high-gain Compton regime, with a negative coupling parameter ( $\Phi < 0$ ) leading to a strong growth rate. More than 50 MW of RF power in the TE11 mode (43 dB gain) has been obtained with good reproducibility. The experimental results are in good agreement with predictions made using the 3D stationary simulation code SOLITUDE.

## 1. Introduction

Free electron lasers (FELs) are currently under investigation because of their remarkable properties, which include their high efficiencies and output powers, their potential as sources of coherent short wavelength radiation, and their inherent frequency tunability. Several experiments have been carried out using a helicoidal wiggler [1–3]. Some of them operate at moderately high beam current and use a magnetic guide field  $B_0$  to steer the electron beam in the axial direction. For that experimental set-up, the FEL operation displays a resonance [1] when the cyclotron wavelength  $\lambda_0$  in the axial magnetic field approaches the wiggler periodicity  $\lambda_w$ . Thus the FEL can run either in the group I regime, with  $\lambda_0 > \lambda_w$ , or in the group II regime, with  $\lambda_0 < \lambda_w$ .

Such experiments can be made to operate in the high gain regimes. In that way, previous works by Freund and Sprangle [5,6] have shown the importance of the coupling parameter defined by:

$$\Phi = 1 - \frac{\Omega_0 \beta_{\perp}^2 \gamma_{\parallel}^2}{(1 + \beta_{\perp}^2) \Omega_0 - k_w \beta_{\parallel} c}. \quad (1)$$

In Eq. (1),  $\Omega_0 = eB_0/(m\gamma)$  is the relativistic cyclotron frequency,  $\gamma_{\parallel} = (1 - \beta_{\parallel}^2)^{-1/2}$ ,  $k_w = 2\pi/\lambda_w$  and  $\beta_{\perp}$  and  $\beta_{\parallel}$  are the dimensionless transverse and axial velocities corresponding to the helical trajectories.

There is interest in operating with a negative value of  $\Phi$  even though the electrostatic beam oscillation mode is more unstable [5]. In this paper we report an experiment

using a strongly relativistic electron beam, with parameters which may be adjusted so as to run in the strongly negative  $\Phi$  configuration. Fig. 1 shows this regime of FEL operation. The longitudinal velocity from a particle trajectory calculation and the coupling parameter are plotted as a function of the axial magnetic field.

Experimental results for various values of the wiggler field and the axial guide field have been obtained. In the amplifier operation regime a maximum output power radiation of 50 MW has been reached which corresponds to an efficiency of 7%. A study of the saturation as a function of the wiggler length has been carried out. All these experimental results have been compared with numerical computations from the particle simulation code SOLITUDE [7], and good agreement has been found.

## 2. Experiment

A schematic of the FEL amplifier experiment is shown in Fig. 2. The main components of the device are the pulsed-line generator EUPHROSYNE, the graphite diode, the axial guiding magnetic coil and the bifilar wiggler.

The accelerating voltage for the experiment is supplied by a Marx capacitor bank with a Blumlein transmission line delivering a 1.75 MV, 50 kA, 50 ns pulse to a 36  $\Omega$  matched load diode. The strongly relativistic electron beam is emitted from a hemispherical graphite cathode by field emission (micro-explosive emission process). The graphite anode, with its 3.5 mm radius aperture, is 60 mm long. It allows only a small fraction of the current to propagate and acts as an emittance selector. Using the calculation of Ref. [8] we can estimate the normalized emittance to be  $\epsilon_n < 2500 \pi \text{ mm} \cdot \text{mrad}$ .

<sup>\*</sup> Corresponding author.



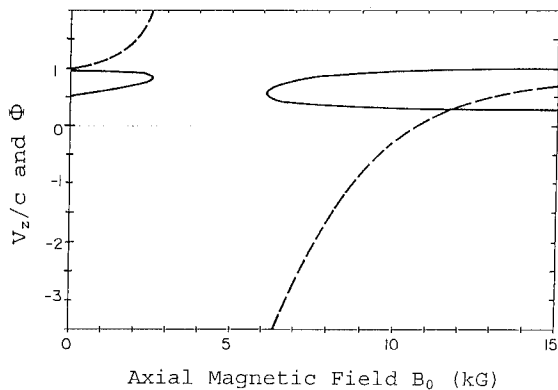


Fig. 1. Coupling parameter  $\Phi$  (dashed line) and  $V_z/c$  (solid line) as a function of the axial guide magnetic field  $B_0$  with a constant wiggler field  $B_w = 0.95$  kG.

The 28 period bifilar helical wiggler has a period of 8 cm and provides a magnetic field with magnitude  $B_w$  adjustable up to 3 kG on axis. The wiggler field is slowly up-tapered, by using metallic straps between helical wires, over the eight first periods. This provides an adiabatic input into the interaction region for the electron beam.

The gun and the wiggler, plus the diagnostics, are immersed in a uniform axial magnetic field generated by a solenoid. The intensity of this field  $B_0$  can be varied up to 10.5 kG. The electrons are propagated in a stainless-steel drift tube with an internal diameter of 39 mm. The fundamental  $TE_{11}$  mode of the cylindrical wave guide has a cutoff frequency of 4.56 GHz. The entire system is designed to operate in this lowest waveguide mode. The electron beam current from the emittance selector is illustrated in Fig. 3 as a function of the axial guide field  $B_0$ . At the resonance when  $\lambda_0 = \lambda_w$ , the electrons have a large transverse excursion, strike the drift tube wall and are lost. From the experimental data we evaluate this resonance to be maximum at 4.7 kG. We observe in Fig. 3 that at high  $B_0$  we have a good diode performance whereas the emis-

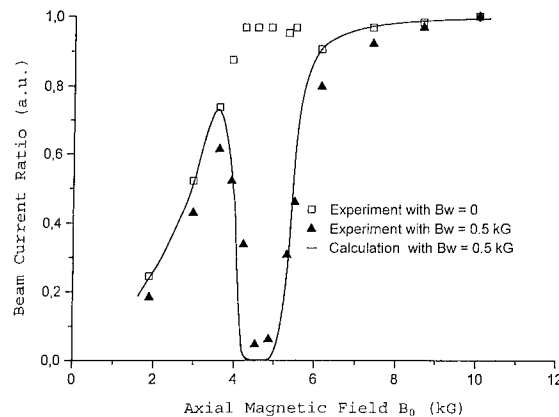


Fig. 3. FEL transmitted electron beam current as a function of the axial guide magnetic field  $B_0$  with a constant wiggler field  $B_w = 500$  G.

sion is perturbed when  $B_0$  is less than 3.5 kG. Consequently we ran our experiment in group II regime.

A high-power magnetron operating at 35.1 GHz is used as the input power source for the amplifier regime. The initial  $TE_{10}$  mode is propagating through a standard Ka-band rectangular waveguide, then converted toward a circular waveguide. This section of circular waveguide supports only the fundamental  $TE_{11}$  mode for the operating frequency. Its radius is then adiabatically up-tapered to the radius of the drift tube. A tungsten wire grid launches the wave, without perturbing the electron orbits in the interaction region. The wave is linearly polarized, so that only half of the incident power, with the correct rotation of the electric field vector, participates in the FEL interaction. An attenuator allows us to reduce the usable power from the maximum of 20 kW to zero.

Just after the passage through the wiggler, a second tungsten wire grid deflects the RF power out of the drift tube, permitting the use of a Cherenkov diagnostic of the beam after its interaction with the electromagnetic wave.

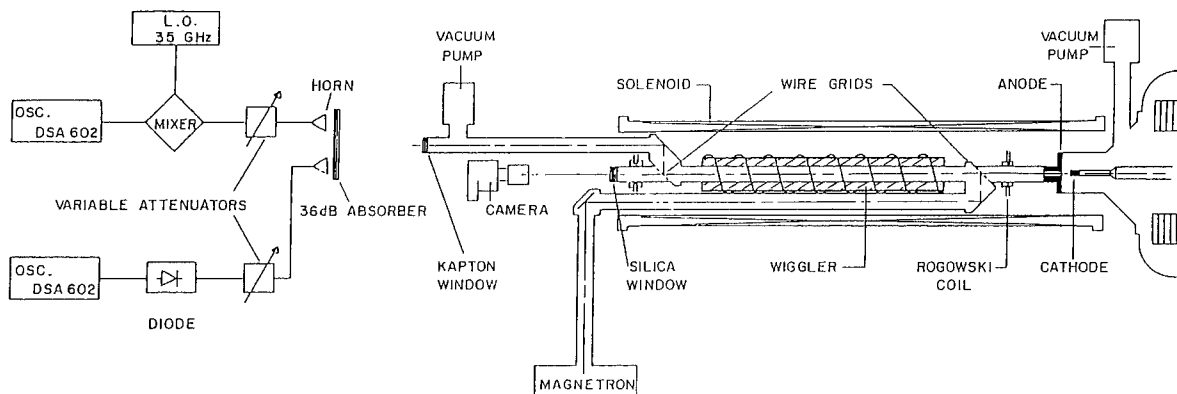


Fig. 2. Free electron laser experimental configuration.

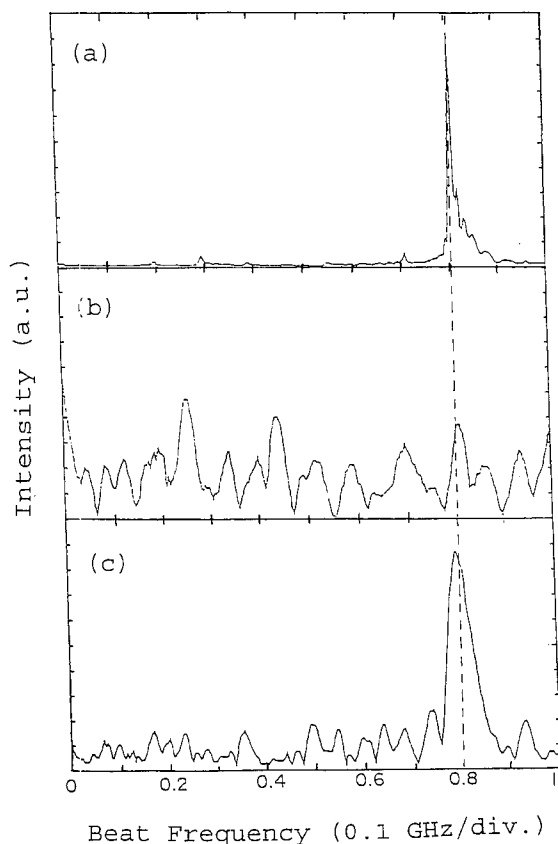


Fig. 4. Frequency spectrum: (a) magnetron alone; (b) superradiant regime; (c) amplifier regime.

We also use this diagnostic to align the guiding coil with the beam when the wiggler is turned off.

The output power from the FEL is transmitted through a Kapton window which maintains the vacuum. After attenuation by propagation in the air and through a 36 dB absorber, a small fraction of the radiation is collected by a rectangular horn (Ka-band). Then a variable attenuator (0–10 dB) reduces the power to the desired level for the diode detector whose response on the oscilloscope (DSA, 602) determines the power level. The entire system is calibrated using the known input power of the magnetron.

A second channel with identical horn and attenuator is used to measure the frequency. Less than 2 mW of the 35 GHz FEL radiation is mixed with radiation from a variable frequency 34–36 GHz local oscillator (LO). It is a Gunn-type diode which generates 10 mW at 35.9 GHz. The response of the mixer gives rise to the beat wave of the two signals, and by varying the LO frequency we can explore a wider spectrum. This beat wave is then recorded by a 1 GHz band-pass oscilloscope and by Fourier transformation we obtain the frequency spectrum. Results are shown in Fig. 4. The magnetron curve (a) exhibits a peak at 800 MHz corresponding to 35.1 GHz frequency. We observe that the FEL in the amplifier regime (c) peaks

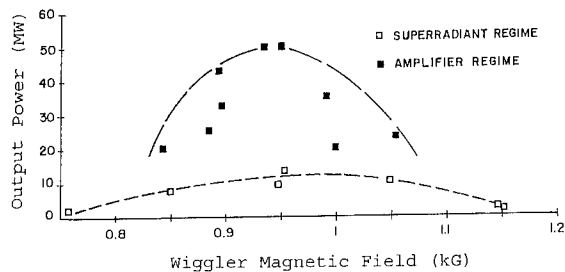


Fig. 5. FEL output power as a function of  $B_w$  for  $B_0 = 8$  kG.

exactly at 35.1 GHz just like the input magnetron. On the other hand in the superradiant regime (b) this main operating frequency is still present but mixed with other frequencies. The FWHM is less than 10 MHz for the magnetron corresponding to the 500 ns pulse length, and is approximately 100 MHz for the FEL radiation in consequence of the short pulse ( $\approx 10$  ns) emitted. To find the optimum operating conditions a measurement of the output power with parameter variation has been carried out for both superradiant operation (without the magnetron) and amplifier operation. The FEL output power as a function of  $B_w$  at constant  $B_0$  is illustrated in Fig. 5. Obviously the maximum output power is reached at the same parameter value for both operation regimes and the amplification factor is higher at this maximum. One of the best shots in amplifier operation is represented in Fig. 6. Since 50 mV diode response corresponds to 5 mW and the variable attenuator was set for 100 dB in total line attenuation (from the wiggler exit to the diode), this RF signal describes an output power level of 50 MW corresponding to an efficiency of 7% (total electron beam power = 700 MW).

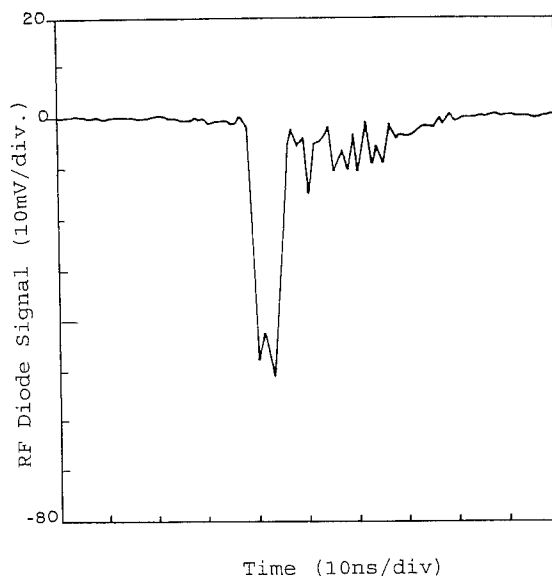


Fig. 6. RF diode signal for  $B_0 = 8$  kG and  $B_w = 0.95$  kG.

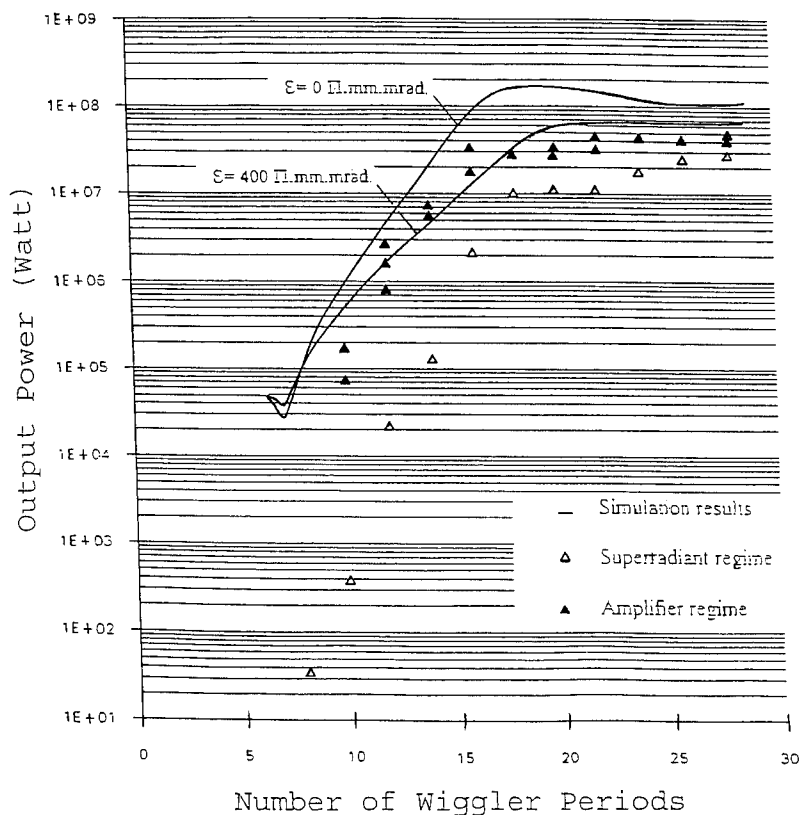


Fig. 7. Saturation studies for  $B_0 = 8$  kG and  $B_w = 0.95$  kG.

The study of the electromagnetic wave saturation is carried out by the measurement of the output power as a function of the interaction length in the wiggler. This length is varied by deflecting the electron beam into the drift tube wall. For this purpose, we use a movable coil which generates a transverse magnetic field greater than 1 kG. Fig. 7 shows a measured gain curve, along with simulation results for the optimum operating parameters defined previously. Comparison is made with the superradiant operation mode. The output power is observed to saturate at a length of 1.4 m, in good agreement with the simulation. As expected, after saturation the power decreases.

Saturation studies in the amplifier regime as a function of the input power have also been carried out. We have found that less than 3 kW is enough to reach saturation, which corresponds to an amplification of 43 dB.

### 3. Summary

In summary, we have carried out a successful high-power FEL experiment with a large negative coupling

parameter  $\Phi$ . Operation in the amplifier mode at 35.1 GHz gave rise to 50 MW of output power with an efficiency of 7% for 43 dB of gain. The experimental results are in good agreement with predictions made using the 3D stationary simulation code SOLITUDE.

### References

- [1] J.A. Pasour and S.H. Gold, IEEE J. Quantum Electron. QE-21 (1985) 845.
- [2] Y. Su, S. Huang et al., Nucl. Inst. and Meth. A 272 (1988) 147.
- [3] M.E. Conde and G. Bekefi, Phys. Rev. Lett. 67 (1991) 3082.
- [4] H.P. Freund and T.M. Antonsen Jr., Principles of FEL (Chapman & Hall, 1992).
- [5] H.P. Freund and P. Sprangle, Phys. Rev. A 26 (1982) 2004.
- [6] H.P. Freund and P. Sprangle, Phys. Rev. A 28 (1983) 3438.
- [7] Ph. Gouard and J. Gardelle, CEA, R-5617 (1992).
- [8] D. Prosnitz and E.T. Scharlemann, LLNL AT&A note 229 (1984).



ELSEVIER

## Experimental results on the 1.5 MeV ion-channel guided X-band free-electron laser

K. Takayama<sup>a,\*</sup>, J. Kishiro<sup>a</sup>, K. Ebihara<sup>a</sup>, T. Ozaki<sup>a</sup>, S. Hiramatsu<sup>a</sup>, H. Katoh<sup>b</sup>

<sup>a</sup> National Laboratory for High Energy Physics in Japan (KEK), Oho 1-1, Tsukuba, Ibaraki, 305 Japan

<sup>b</sup> Dynamic Numerical Simulation (DYNUS), Shin-Kohoku, Yokohama, Kanagawa, 222 Japan

### Abstract

Experiments on the ion-channel guided X-band free-electron laser amplifier (IXFEL) generated peak microwave power exceeding 100 MW at 9.4 GHz with a gain of 21 dB/m. Saturation in the evolution curve has been achieved and a frequency spread of 0.9% was observed. The amplified microwaves were separated from the driving beam line and extracted without breakdown.

### 1. Introduction

A microwave FEL has been regarded as a possible candidate power source for future linear colliders [1] since the successful demonstration at LLNL. The Livermore 34.6 GHz experiment [2] triggered extensive theoretical studies on a multi-stage microwave FEL ( $\mu$ -FEL) in the so-called two-beam scheme at KEK and LBL/LLNL/MIT. Other attractive applications of the  $\mu$ -FEL such as a planetary radar [3], thunder-bolt control by atmosphere ionization [4], or power transfer in space [3] have come to be discussed on various occasions [5]. These applications shall utilize its characteristics of extremely high peak power, very short wavelength, relatively small frequency spread, and pure mode, which have not been simultaneously satisfied in conventional microwave sources.

Subsequent beam transport is crucial in the multi-stage regime. Ion Channel Guiding (ICG) in the regime was proposed [6], expecting Landau damping of beam break-up instability (BBU) and resistive-wall instability which occur in such long distance transport [7]. The ICG technique was employed in the weakly relativistic X-band FEL (800 keV) [8] in our preliminary set-up. Other crucial problems are seed power injection into the beam line and amplified-power extraction from it with sufficient efficiency. In fact a large seed power has been theoretically proved to mitigate output phase's sensitivity to injection errors in driving beam current or accelerating voltage [9]. Recently we have developed over-sized input and output couplers with efficiencies of nearly 90% in the  $TE_{01}$  mode which can minimize reflection and mode conversion. The present

IXFEL integrates ICG, conventional planar wiggler and RF handling system with efficient  $\mu$ -couplers.

### 2. Experimental set-up

As schematically shown in Fig. 1, the microwave source is a pulsed magnetron (EEV Model M5188), capable of nominally generating an output power of 91 kW. The input signal is fed into the over-sized Rectangular Waveguide (RW, WRJ-2, 5.5 cm  $\times$  11 cm) with a miter-bend which was designed so as to minimize reflection and mode-conversion. This input coupler has a passing small 20 mm diameter aperture for electron beams. The amplified microwaves through the 3 m-long RW are coupled out from the driving-beam line with the other miter-bend connected with the over-sized ceramic window. The transmitted  $\mu$ -wave is eventually emitted into the anechoic room with a horn-antenna and a fraction is received with the basic-size open-RW placed in the well-aligned forward direction. The radiation signal is attenuated down to the milliwatt level and monitored by a crystal diode. The attenuators used were periodically checked for reproducibility. Mode-conversion in over-sized RF components was measured in the full lineup as well as component-by-component by the phase interference method where a far-field pattern of the transmitted reference signal from a Gunn-oscillator is monitored as a function of the straight-RW length being varied over a wavelength of the beatwave between the dominant  $TE_{01}$  mode and any possible higher mode such as  $TE_{03}$ . Both of the input and output coupler demonstrated a transmission efficiency of 85% in  $TE_{01}$  mode, giving a net seed-power of 77 kW, which is consistent with the MAFIA simulation [10].

Diethylaniline (DEA) gas is fed into the beam line from three reservoir flasks. The gas pressure is monitored by

\* Corresponding author. Tel. +81 298 64 5240, fax +81 298 64 3182, e-mail: takayama@kekvox.kek.jp.

four Shultz and BA gauges calibrated to a Baratron capacitance manometer. An KrF excimer laser ( $\lambda = 248$  nm) with 18 ns pulse length is used to ionize the DEA by the two-photon resonant process. Laser pulse energy is measured by a joulemeter and typically is 140 mJ/20 mm diameter, with shot-to-shot jitters of 5 mJ. Plasma density in operation was determined from three independent informations [11]: a magnitude of ion-channel relaxation in the Langmuir–Child limited beam current, a critical pressure at which beam's envelope in straight transport hits the waveguide wall 2.5 m downstream from the emittance selector, a gas pressure leading to cut-off of 9.4 GHz  $\mu$ -waves; nominally,  $2 \times 10^{10} \text{ cm}^{-3}$ .

A 1.5 MeV driving electron beam was generated in the induction gun mounted with a carbonized felt-cathode. Details of the induction gun energized with two magnetic switches were given elsewhere [12]. Nominally 600 A of the 1.3 kA e-beam arriving at the emittance selector entrance was carved out with this emittance selector which is simply a combination of an ion channel and a narrow 1-m-long aluminum pipe of 20 mm in diameter. The emittance selector has an acceptance of 0.06–0.04 cm rad [11] for a nominally fixed gas pressure and laser intensity. In the maximum amplification regime mentioned later, a beam current of 450 A was monitored at the wiggler end.

Beam energy measurement was not done by using an analyzer magnet with a slit because such a narrow slit interrupts ion-channel guiding. The maximum beam energy was known with a set of well calibrated  $\text{CuSO}_4$  voltage-divider mounted in each of induction modules.

Each unit of the air-core planar wiggler magnet ( $\lambda_w = 16$  cm and 15 periods) is independently energized with a pulse power-supply and the eddy-current assisted field-uniformity ( $\Delta B_w/B_w = 1.5\%$  at the RW's horizontal edge) [13] is provided with thick copper bars inserted in both sides of the wiggler gap. In addition to the ICG, a set of

air-core quadrupole magnets was excited for further focusing in the horizontal direction. In order to minimize a coherent betatron amplitude in the wiggler, a steering magnet locating slightly upstream was slightly excited.

### 3. Amplification experiment

*Resonant structure in signal.* Typical examples of the amplified signal for two different wiggler fields (1.21 kG and 0.93 kG) are shown in Fig. 2. Resonant structure in the pulse duration clearly indicates the existence of resonant beam energy. Two resonant portions in time merge at the central position of the pulse beyond  $B_w = 1.2$  kG which corresponds to the peak energy position.

*Frequency spectrum.* The frequency spectrum of the amplified signal was measured by a low- $Q$  transmission-type frequency counter. The filling time of the counter cavity,  $2Q/\omega$ , is about 4 ns which is much shorter than the pulse duration of 10–15 ns. Fig. 3 represents the frequency spectra of the injected magnetron and amplified signals at  $B_w = 1.21$  kG. The frequency spread of  $\Delta f/f = 0.9\%$  within 3 dB of the peak power is found for the amplified signal, while that of the injected magnetron signal is  $\Delta f/f = 0.6\%$  which is set by a finite  $Q$ -value of the frequency counter, that is, 120. The actual frequency spread of the magnetron obtained by a spectral analyzer is less than 0.1% in FWHM [14]. Another notable result of frequency measurements was a shift in the frequency spectrum for the resonant portion which corresponds to FEL interaction of lower-energy beams in a lower wiggler field just mentioned above. We observe that in a case of  $B_w = 0.93$  kG the spectrum is downshifted from the magnetron frequency by  $\sim 60$  MHz, as seen in Fig. 3. A reasonable explanation for the shift has not been found yet.

*Detuning.* Dependence of the gain on the wiggler field

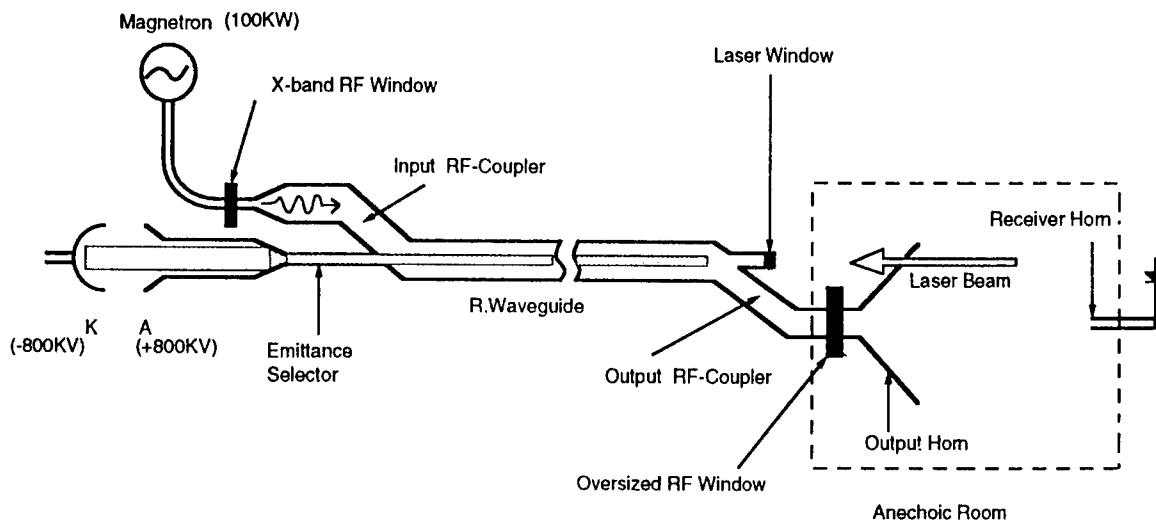


Fig. 1. Schematic view of the IXFEL.

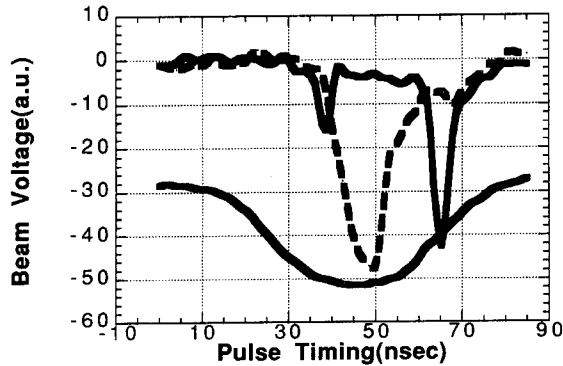


Fig. 2. Amplified signals at  $B_w = 1.21$  kG dashed and  $0.93$  kG (solid), beam voltage profile in time (bottom).

was measured at the wiggler position just before saturation (see below). In Fig. 4, the magnitude of the amplified power is shown as a function of the wiggler field. Indicated data here were taken at the same pulse timing that gives the peak power for  $B_w = 1.2$ – $1.25$  kG. Within 3 dB of the peak power, the fractional magnetic field “bandwidth”,  $\Delta B_w/B_w$ , is about 8.1%. Beam transmission efficiency gradually degraded beyond  $B_w = 1.2$  kG. Therefore, the detuning curve should be somewhat different from the case without beam loss. This speculation seems to be consistent with some estimation from the theoretical detuning curves shown in the same figure where a lower beam current certainly gives much small gain in the region of higher wiggler field. Assuming possible transmission beam currents ( $I = 450, 200$  A) and energy-spread of 1.5%, these detuning curves are derived from a cubic dispersion relation taking account of geometrical coupling with  $TE_{01}$  mode, vertical betatron motion and quadratic

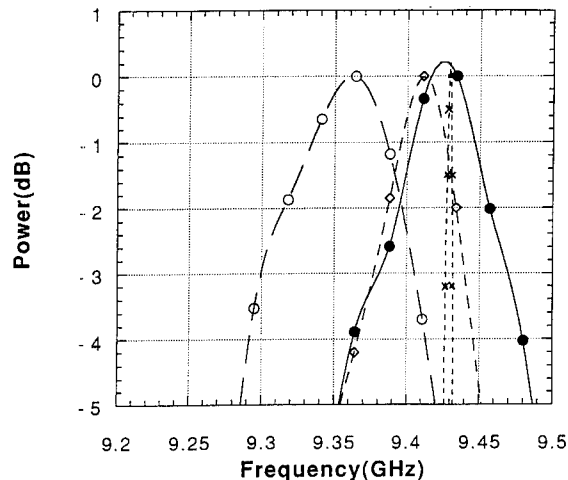


Fig. 3. Frequency spectrum of the amplified signal at  $B_w = 1.21$  kG (solid) and at  $B_w = 0.93$  kG (long dash), magnetron signal (short dash), by a spectral analyzer (shortest dash).

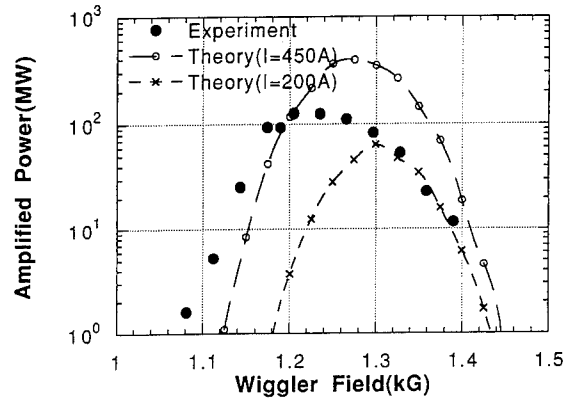


Fig. 4. Experimental detuning curve and theoretical calculations for  $I = 450$  A (long dash) and  $200$  A (short dash).

wiggler field variation in the vertical direction which depend on a spatial size in the RW effectively occupied by beams [11]. A beam size of  $2r_0 = 4$  cm which is obtained by numerical tracking with the realistic magnetic fields was assumed in calculation.

**Evolution.** The evolution curve was obtained by simply turning on the wiggler unit in order. Evolutions for RW-length covering a beatwave length between  $TE_{01}$  and  $TE_{03}$  are depicted in Fig. 5. The evolution curve adjusted by the phase interference method which places roughly in the middle of scattered points indicates the exponential gain of 21 dB/m. Apparently, the  $TE_{01}$  mode dominates the received power. A small fraction of the received power originates from the  $TE_{03}$  mode converted in the output coupler including the RF-window but the  $TE_{21}$  mode which is a possible one evolving through the interaction region rarely contributes to the received fraction of the

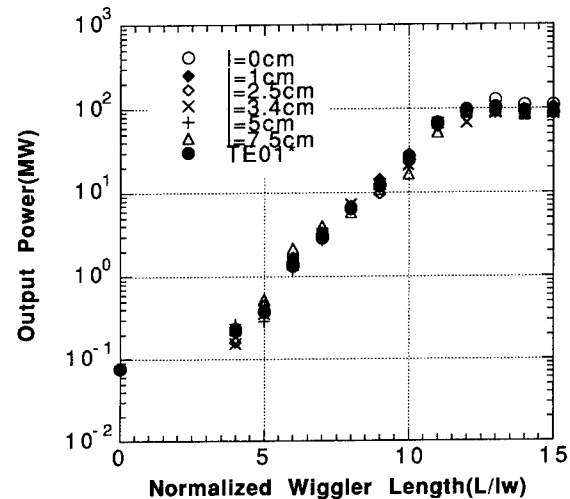


Fig. 5. Evolution for different RW-lengths and the adjusted  $TE_{01}$  evolution curve.

amplified power in our forward receiving system. The experimentally obtained size of the gain is in good agreement with theoretical estimation mentioned in the previous paragraph.

**Higher mode evolution.** For an amplified power measurement of the  $TE_{21}$  mode, the receiver horn was positioned at  $\theta = 20^\circ$ , less than the ideal location of  $\theta = \lambda/b \approx 33^\circ$  because of the finite-size of the anechoic room. The signal level was not distinguished, being hidden by the dominant mode. At theoretical calculation [11] based on the cubic dispersion relation tells us that the gain for the pure  $TE_{21}$  mode is quite small, that is, less than a few dB/m in the wiggler field region of current interest because of the lower resonant field and small geometrical coupling due to an effectively expanded beam size, assuming a uniform particle distribution within the diameter of  $2r_0 = 4$  cm. A power fraction of the  $TE_{21}$  mode should be negligible in the total output power.

#### 4. Discussion

An effect of the ion channel density on FEL amplification has not been systematically studied; nonetheless, the gain was notably reduced, accompanied with further beam-loss, in a higher pressure region than the nominally operating pressure. This indicates that beam transport through the wiggler region takes a trivial but practical role in FEL amplification; the amplitude of the coherent betatron motion in the FEL interaction region as well as phase-space matching depends on the upper magnetic field environment where a beam having been guided through the continuous ion-channel alone sees different guiding fields (tapered input wiggler field + rising  $Q$ -field + ion-channel). The experimental fact that beam-loss is notable in the higher wiggler field region strongly suggests the beam size is expanding. This is consistent with our preliminary numerical FEL simulation [11]. Such a diffusion of a driving-beam in the physical space seems to suppress evolution of the  $TE_{21}$  mode as numerically demonstrated by Freund et al. [15].

#### 5. Summary

By integrating ion-channel guiding, ion-channel guided emittance selection, the eddy-current assisted wiggler, and miter RF-bends, reasonable  $\mu$ -FEL amplification was achieved with effective saturation. The experimental re-

sults were well explained by theoretical considerations; particularly, they, displayed an important aspect of the geometrical coupling between  $TE_{01}$ ,  $TE_{21}$  modes and a driving beam largely expanding in the RW. The IXFEL has demonstrated the viability of the ICG for future interesting applications beyond two proceeding ICG experiments [16]. Seed power injection and amplified-power extraction required in realistic applications of the  $\mu$ -FEL were realized with high efficiency.

#### Acknowledgements

The authors wish to thank Associate Director, Prof. Y. Kimura, for his continuous support of our R & D works. K. Saitoh and S. Hashimoto contributed to early works of magnetic field measurement and  $\mu$ -wave calibration, respectively.

#### References

- [1] A.M. Sessler, Proc. Conf. on Laser Acceleration of Particles, Los Alamos, 1982, AIP Proc. 91, ed. P.J. Channel (AIP, New York, 1982) p. 163.
- [2] T.J. Orzechowski et al., Phys. Rev. Lett. 57 (1986) 2172.
- [3] K. Takayama, S. Hiramatsu and M. Shiho, J. British Interplanetary Soc. 44 (1991) 573.
- [4] M. Shiho et al., Proc. 19th Int. Conf. on Infrared and Millimeter Waves in Sendai, 1994, p. 254.
- [5] See, e.g., J. Benford and J. Swegle, High-Power Microwaves (Artech House, Boston/London, 1991).
- [6] K. Takayama and S. Hiramatsu, Phys. Rev. A 37 (1988) 173.
- [7] K. Takayama, Phys. Rev. A 39 (1989) 184; D.H. Whittum, A.M. Sessler and V.K. Neil, Phys. Rev. A 43 (1991) 294.
- [8] T. Ozaki et al., Nucl. Instr. and Meth. A 318 (1992) 101; T. Monaka, Ph.D. Thesis (1992).
- [9] K. Takayama, Part. Accel. 39 (1992) 65.
- [10] K. Takayama et al., Nucl. Instr. and Meth. A 341 (1994) 109.
- [11] K. Takayama et al., to be published.
- [12] J. Kishiro et al., Proc. 1993 Accelerator Conf., Washington, 1993, p. 673.
- [13] K. Takayama et al., KEK preprint 89-152 (1989), unpublished.
- [14] M. Brady (English Electric Valve Co.) private communication (1994).
- [15] H.P. Freund, P.H. Jackson and D.E. Pershing, Phys. Fluids B 5 (1993) 2318.
- [16] W.E. Martin et al., Phys. Rev. Lett. 54 (1985) 685; G.J. Caporaso et al., Phys. Rev. Lett. 57 (1986) 1591; S.L. Shope et al., Phys. Rev. Lett. 58 (1987) 551.

# Experimental study of the spatial evolution of the spectrum of a Raman FEL

P. Zambon<sup>a,\*</sup>, W.J. Witteman<sup>a</sup>, P.J.M. van der Slot<sup>b</sup>

<sup>a</sup> Department of Applied Physics, University of Twente, P.O. Box 217, 7500 AE Enschede, The Netherlands

<sup>b</sup> Nederlands Centrum voor Laser Research, P.O. Box 2662, 7500 CR Enschede, The Netherlands

## Abstract

For a specific set of parameters, corresponding to an operating point near magneto-resonance, the evolution of the spectrum generated by a Raman FEL was investigated. It is shown that in several frequency bands radiation is emitted. These different frequencies are identified as belonging to the FEL instability and another mechanism, probably the gyrotron instability. The measurements show apparently a competition between these mechanisms. The experimentally determined growth rate is somewhat larger than the theoretical one, indicating that the FEL does not operate as a true amplifier.

## 1. Introduction

A standard diagnostic for an experimental study and comparison with theory is the measurement of the spatial evolution of the emitted power by changing the interaction length (e.g. by stopping the electrons, as described below) [1,2]. More information can be obtained by measuring the evolution of the spectrum as well, which is the subject of this paper. The settings chosen for the magnetic fields (see below) correspond to an average steady state perpendicular velocity  $\beta_{\perp} = 0.17$  at a total beam energy  $\gamma$  of 1.974. It is found that this point is not far away from magneto-resonance. Earlier experiments [3] have indicated that in such a case the FEL as well as the gyrotron interaction is possible. In this region, proper injection of the electron beam becomes very important because oscillations around the steady state axial velocity are easily excited.

## 2. Experimental set-up

The general set-up of the Twente Raman FEL has already been thoroughly described elsewhere [4]. The laser uses a pulsed bifilar undulator consisting of 40 periods of 3 cm each, with a tapering of 6 periods at the entrance. A Marx generator produces voltage pulses of 100 ns duration with a nominal value of 500 kV. The current is approximately 190 A.

In order to study the spectral evolution, the interaction length was varied by stopping the electron beam along the undulator using a kicker magnet. Calculations show that a kicker magnetic field of 0.3 T is sufficient to stop the electron beam within 2 cm. This has been confirmed by experiments. The diagnostic of the produced radiation consists of a Joule meter and a set of high pass filters covering the  $K_{\alpha}$ -band [4]. The filters produce equidistant wavelength bands with a width of 1 mm. The two detection methods cannot be used simultaneously. All measurements reported here are obtained for an axial guide field of  $B_z = 1.02$  T and an undulator field  $B_u = 0.19$  T. Linear theory [5] predicts the FEL interaction with the  $TE_{11}$  to occur at 30 GHz (10 mm) for these settings.

The Marx generator has an inherent spread between successive shots. In analyzing the results only shots were selected with a maximum spread of 2% in the accelerating voltage during the pulse. The field emission diode produces an inherent increase in the current during a shot. This was limited to a maximum increase of 10%. Shot to shot fluctuations were 2% and 10% for voltage and current respectively.

## 3. Spatial evolution of the spectrum

In the first experiments the total emitted energy was measured using the Joule meter and a high-pass filter with a cut-off frequency of 21 GHz. In the case of the cut-off filter the time dependent signal was integrated to obtain the total received energy. The results are shown in Fig. 1 where the energy is plotted versus the interaction length of the electron beam. Below an interaction length of 60 cm

\* Corresponding author. Tel. +31 53 833 969, fax +31 53 338 065, e-mail: paolo@qe.tn.utwente.nl.



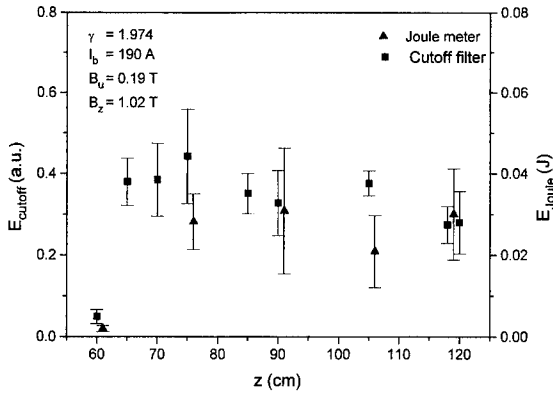


Fig. 1. Total energy measured with the Joule meter (triangles) and with a high pass filter with a cutoff frequency of 21 GHz (squares) as a function of the interaction length.

no signal was found above the background noise. The general behaviour of the two types of measurement is quite the same apart for an increase in output energy observed at the end of the undulator by the Joule meter and not by the cut-off filter. This indicates that the radiation shifts to longer wavelengths at the end of the undulator. It is clear from Fig. 1 that a large growth appears up to about 65 cm and the laser output seems to be more or less constant for larger interaction lengths. Assuming exponential growth between 60 and 65 cm a “power” growth rate of  $\sim 0.41 \text{ cm}^{-1}$  is obtained for the total radiation field.

The spectral evolution was measured in the same way as the total energy, however here only cut-off filters were used. The difference in energy as measured by two filters with successive cut-off frequencies was attributed to radiation emitted in the frequency band between these cut-off frequencies. The first observation which can be made from these measurements is that all frequency bands show a local maximum for an interaction length between 65 and 80 cm. Second the different frequencies show more than one local maximum at different values for the interaction length. Some examples are given in Fig. 2. A typical example of the complete spectrum (also indicating a typical spread in the measurements) is shown in Fig. 3. Note that the measurements in Fig. 2 (represented by symbols) are connected by straight lines for convenience only. For example the 33.3 GHz line grows from approximately zero to a maximum when the length increases from 60 to 65 cm and drops back to zero for larger lengths. Only at the end of the undulator (120 cm) some energy is again emitted at this frequency. It is further observed that the growth in some frequency bands is complementary to that in other frequency bands. It is found that at the 25 GHz band the energy increases when it decreases for the 30 GHz and 23 GHz bands (as is shown in Fig. 2). It seems that some kind of competition between the different frequencies is present.

Assuming that for an interaction length less than 60 cm the radiation is growing from noise and is in the exponen-

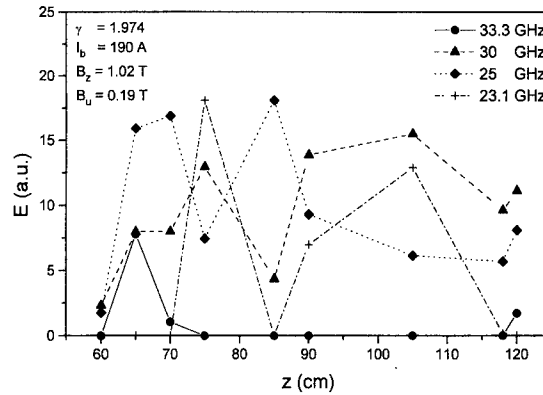


Fig. 2. The energy  $E$  emitted in different frequency bands as a function of the interaction length. The center frequency is indicated. All bands have a spectral width of 1 mm (i.e. they vary in the frequency domain).

tial growth regime up to the first local maximum, the growth rate can be derived from it. Fig. 2 already indicates that the different frequency bands have different growth rates. At 65 cm the largest contribution to the total energy comes from the 25 GHz band. This band shows a “power” growth rate of  $\sim 0.44 \text{ cm}^{-1}$ , which is somewhat larger than the one found for the total energy. The 30 GHz band has at this position a “power” growth rate of  $\sim 0.24 \text{ cm}^{-1}$ . For other frequency bands the growth rates cannot be determined as the signal could not be distinguished from noise in the detectors at 60 cm interaction length.

The undulator did not contain a taper at the exit. As a result the magnetic field will show a spike at the exit [6]. The question arises whether this spike can excite electron orbits required for gyrotron type interaction in the region after the undulator. To study this experimentally the electron beam was stopped just before the end of the undulator using the kicker magnet. In another series of measurements

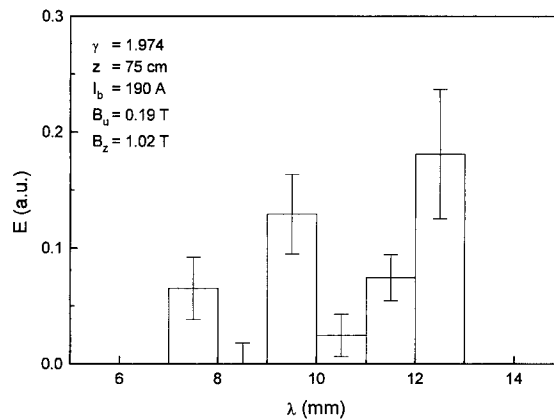


Fig. 3. Typical example of spectrum measured at an interaction length of 75 cm. The error bars indicate the shot to shot spread in the measured energy.

it was allowed to propagate through the undulator into the region with only the axial guide field. No significant differences were found in the output energy as well as in the measured spectra. The spike will most likely disturb the electron beam at the exit of the undulator but the beam seems not to couple to the radiation field any more. The guide field starts to diverge just behind the exit of the undulator. This will also make it difficult to couple the electron beam to the radiation field through a gyrotron-like interaction.

#### 4. Preliminary comparison with non-linear theory

To compare the measured results with theory a non-linear model describing an amplifier set-up was developed. This model is basically the one described in Ref. [7]. However, it was modified to include the complete three dimensional electron orbits. At the moment the code only allows interaction of the electron beam to take place with the  $TE_{11}$  mode. Higher order modes will be included in the future.

Calculations were performed for the experimental parameters given above. Only interaction was found around 30 GHz. No interaction with the  $TE_{11}$  was found at other frequencies within the  $K_a$ -band. The saturated power level was about 12 MW. The exponential (power) growth rate found was  $0.182 \text{ cm}^{-1}$ . The growth rate derived from the measured spectral evolution is somewhat larger. This could well be explained by a small reflection from the outcoupling window used in these experiments [3,4]. From the Joule meter measurements the maximum total energy emitted was about 30 mJ. Using the pulse duration of the electron beam (100 ns) an average power of about 0.03 MW is found. The time structure of the radiation pulse shows many spikes so that the peak power within the radiation pulse can be an order of magnitude higher. This is still far below the levels predicted by the numerical code. Two explanations can be given. First we have observed growth at frequencies different from 30 GHz which is not predicted by the numerical code. Two possibilities arise. Interaction takes place with higher order modes or a second type of interaction not described by the non-linear model takes place. The latter could be gyrotron interaction which has been found before [3]. For the experimental parameters this interaction could very well be initiated by the injection of the electron beam in the undulator [4]. A second explanation could be found in the quality of the electron beam. To reduce the increase of the current with time, which results from the expanding plasma in the field

emission diode, the anode–cathode distance was increased. This may have influenced the quality of the electron beam more than was expected. A reduced quality will affect the growth rate and maximum power which can be obtained. It does not explain, however, the growth observed at other frequencies. Comparison between the experimental and theoretical growth rate seems not to indicate a serious beam degradation. However this needs to be checked. Most likely the measurements are a result of a combination of the two effects. Furthermore it is not clear how the apparent competition which we observe between growth in different frequency bands will influence the saturation levels.

#### 5. Discussion

For the parameters investigated a complex evolution of the spectrum was found. This evolution seems to indicate a competition between radiation emitted in several frequency bands, one of which is identified as corresponding to the FEL interaction. As the operating point was rather close to magneto-resonance the complicated electron orbits could very well couple to the FEL as well as the gyrotron instability. The growth rate found experimentally was somewhat larger than the theoretical one, which indicates that some of the radiation is reflected at the outcoupling window. The system is therefore not a true amplifier. The frequencies which could not be identified as FEL interaction are generated inside the undulator as no significant difference was found when the beam was allowed to propagate to the end of the axial guide field and when it was stopped just before the exit of the undulator.

#### References

- [1] J. Fajans, J.S. Wurtele, G. Bekefi, D.S. Knowles and K. Xu, *Phys. Rev. Lett.* 57 (1986) 579.
- [2] A. Bhattacharjee, S.Y. Cai, S.P. Chang, J.W. Dodd, A. Fruchtman and T.C. Marshall, *Phys. Rev. A* 40 (1989) 5081.
- [3] P.J.M. van der Slot and W.J. Witteman, *Nucl. Instr. and Meth. A* 331 (1993) 140.
- [4] P.J.M. van der Slot, Ph.D. Thesis, University of Twente, The Netherlands (1992).
- [5] J. Fajans, G. Bekefi, Y.Z. Yin and B. Lax, *Phys. Fluids* 28 (1985) 1995.
- [6] J. Fajans, *J. Appl. Phys.* 55 (1984) 43.
- [7] J.S. Wurtele, R. Chu and J. Fajans, *Phys. Fluids B* 2 (1990) 1626.

# A microwave inverse free-electron-laser accelerator (MIFELA)

J.L. Hirshfield <sup>a,b</sup>, T.C. Marshall <sup>a,c</sup>, T.B. Zhang <sup>a,c,\*</sup>, A.K. Ganguly <sup>a,d</sup>, P.A. Sprangle <sup>a,d</sup>

<sup>a</sup> Omega-P, Inc., 2008 Yale Station, New Haven, Connecticut 06520, USA

<sup>b</sup> Physics Department, Yale University, New Haven, CT 06520, USA

<sup>c</sup> Applied Physics Department, Columbia University, New York, NY 10027, USA

<sup>d</sup> Physics Division, Naval Research Laboratory, Washington, DC 20375, USA

A microwave inverse FEL accelerator (MIFELA) is now under construction at Yale University. This paper reports on some initial studies regarding the construction of this compact accelerator with output energy  $\sim 20$  MeV based upon the IFEL principle [1], driven by high power microwaves obtained from a 2.85 GHz klystron and its associated harmonic converter [2]. We imagine that a high- $Q$  multimode resonant structure will fill with microwaves (14.25 GHz in this study), building up a high intensity field for electron acceleration. An rf gun will inject a short pulse of electrons at an optimized phase into the MIFELA section, which includes an undulator and a guiding field surrounding a smooth bore drift tube (Fig. 1a).

The theoretical model for the acceleration process in the MIFELA we use here is based on the well-known FEL equations under waveguide boundary conditions [3]. The parameters used in the simulation are listed in Table 1 and are close to those of the proposed accelerator at Yale. The  $TE_{11}$  mode was chosen since it has a lowest cut-off frequency. To get the optimum accelerating gradient, we vary the undulator period  $l_w(z)$  and the undulator parameter  $a_w(z)$ , so as to gradually increase the resonant energy of the trapped electrons and put most of the beam electrons into an accelerating bucket. The gradient of the axial field is determined so that the accelerator works with the stable Group I electron orbits [4]. Fig. 2 shows the electron energy as a function of axial distance along the MIFELA. The electrons are injected monoenergetically from the gun at  $\gamma = 4$  in a small initial “phase window” between  $-\pi/8$  and  $-3\pi/8$ . The resonant energy of the design structure is shown as a dotted line. It can be seen from Fig. 2 that the beam energy and the resonant energy matches well along the acceleration section, using a change of linear taper rate at  $z = 75$  cm (Table 1).

The idea of small initial “phase window” is significant

in this application since once injected, all the electrons are located in the accelerating buckets. Experimentally, this can be done by gating the injected electron beam emerging from a rf gun and buncher cavity as it enters the MIFELA (Fig. 1b); the  $\pi/4$  spread corresponds to a pulse length of  $\sim 6$  ps. Fig. 3 shows the phase plot and the energy spectrum of the accelerated electrons at the end of the accelerating section. Because of this small “phase window”, all the electrons we simulated are trapped in the accelerating bucket. In the phase plot there is no spread of the particles, and the electron energy distribution in this case is also narrow ( $\Delta\gamma/\gamma \sim \frac{1}{2}\%$ ).

At the end of the MIFELA, we allow the guide field to decrease gradually, while maintaining the strong undulator field. With a sufficiently gentle gradient, one can show that the defocusing effect of the decreasing guide field can

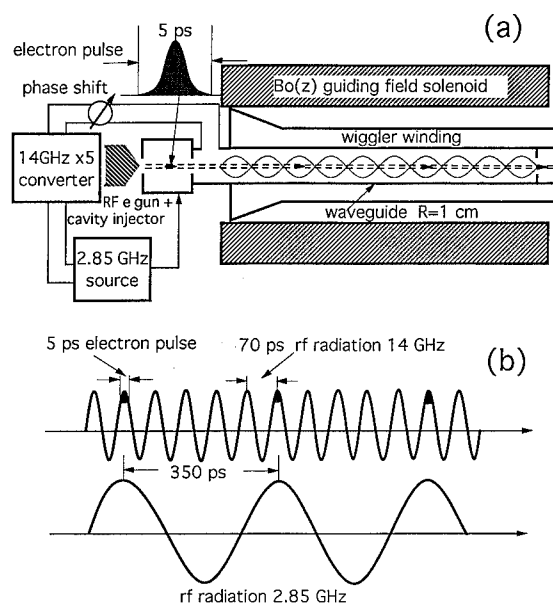


Fig. 1. (a) Schematic of the MIFELA, showing the microwave feed to the gun and accelerator. (b) Rf wave forms, showing how a bunch is injected into the MIFELA.

\* Corresponding author. Tel. +1 212 854 6672, fax +1 212 854 8257, e-mail tzhang@cuplvx.hp.columbia.edu.

Table 1  
MIFELA simulation parameters

|                               |  |
|-------------------------------|--|
| Electron beam energy          | 1.5–22.0 MeV   |
| Electron beam current         | 10.0 A   |
| Electron beam radius          | 0.2 cm   |
| Undulator magnetic field      | 2.7–13.4 kG  |
| Guiding field                 | 0.35–1.64 kG; linear ramp  |
| Undulator period              | 5.1–8.0 cm, linear ramp,<br>$0 < z < 0.75$ cm<br>8.0–8.7 cm, linear ramp,<br>$75 < z < 150$ cm |
| Effective undulator parameter | 1.8–11.6   |
| Driving field wavelength      | 2.1 cm   |
| Driving field intensity       | 0.45 (circular polarized)  |
| Waveguide mode                | TE <sub>11</sub>   |
| Waveguide radius              | 1.0 cm   |

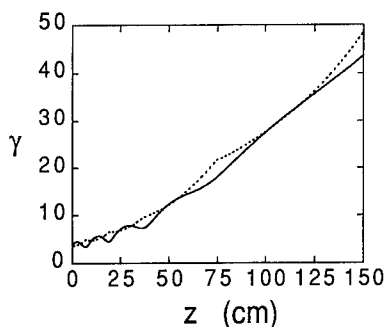


Fig. 2. Electron energy as a function of the axial distance along the undulator. The dotted line is the resonant energy of trapped particles for the given MIFELA parameters. Initial injection is a cold beam at  $\gamma = 4$  with phase between  $-\pi/8$  and  $-3\pi/8$ .

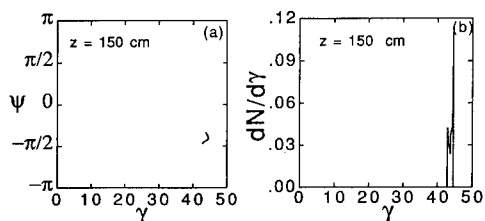


Fig. 3. The electron distribution in phase space (a) and energy spectrum (b). The initial phase distribution is between  $-\pi/8$  and  $-3\pi/8$ .

be overcome by the natural focusing of the helical undulator. If the rf field continues on in this end section of the MIFELA, we find there is still a small increase of electron energy since the electrons remain in the accelerating buckets. After that, with the decrease of guide field,  $a_w/\gamma$  drops, and the electrons fall out of resonance. Since the electrons have random phase with respect to the driving field, no net energy increase occurs in the end section. In this way, the output beam of the MIFELA can be extracted to zero guide field. The accelerating gradient we have obtained in this example is  $\sim 13$  MeV/m, comparable with the best rf linac performance.

Before construction, numerical results will be obtained from use of a fully nonlinear 3D FEL code ARACHNE developed at the Naval Research Laboratory [4,5]. The results obtained from the code described above have been “calibrated” against the results of the 3D code, so that our preliminary estimates of the MIFELA performance should be fairly reliable. The 3D code will permit prediction of the beam emittance.

The device will use the power at the fifth harmonic of a 24 MW, 2.856 GHz XK-5 SLAC klystron as the rf pump. Calculations [2] indicate that a conversion efficiency of  $\sim 70\%$  is to be expected for a cold beam, and  $> 50\%$  efficiency for a beam with velocity spread of 1%. We envision the use of a TE<sub>11m</sub> cavity to increase the rf pump parameter in the MIFELA by approximately a factor of five compared with the value for a free travelling wave. The loaded  $Q$  would then be  $\sim 4000$ ; however, the real power flow to the beam is limited to the available 12 MW. This will determine the amount of charge that can be accelerated as well as the pulse repetition rate.

### Acknowledgement

This work is supported by the Department of Energy.

### References

- [1] I. Wernick and T.C. Marshall, Phys. Rev. A 46 (1992) 3566.
- [2] A.K. Ganguly and J.L. Hirshfield, Phys. Rev. Lett. 70 (1993) 291.
- [3] T.B. Zhang and T.C. Marshall, Phys. Rev. E 50 (1994) 1491.
- [4] A.K. Ganguly and H.P. Freund, Phys. Rev. A 32 (1985) 2275.
- [5] A.K. Ganguly and H.P. Freund, Phys. Fluids. 31 (1988) 387.

# Experimental mode analysis of the circular free electron laser

Takahide Mizuno <sup>a,\*</sup>, Takashi Ootuki <sup>b</sup>, Tsutomu Ohshima <sup>a</sup>, Hirobumi Saito <sup>a</sup>

<sup>a</sup> Institute of Space and Astronautical Science, 3-1-1 Yoshinodai, Sagami-hara, Kanagawa, Japan

<sup>b</sup> Musashi Institute of Technology, Japan

## Abstract

A single mode oscillation on the circular free electron laser has been studied. The operation mode was  $TM_{81}$  (11.77 GHz) whose frequency width was 0.3% ( $= \Delta f/f$ ) and the total radiation power was about 600 kW using a rotating hollow electron beam (442 kV). The observed permissible detuning between the oscillation frequency and the beam mode was 3% at  $TM_{81}$  oscillation.

## 1. Introduction

A circular version of a free electron laser, proposed by Bekefi [1], has been explored theoretically [2,3]. It has the advantage of being very compact because of the use of a rotating electron beam. Several other potential advantages of a circular FEL as compared with a conventional linear FEL have been treated theoretically by Saito and Kawai. They reported that a circular FEL has a higher growth rate and wider permissible detuning than a linear FEL. These distinctive features are produced by the negative mass effect in the rotation motion of the relativistic electrons. Some experimental studies [4–9] have been reported, but details of the oscillation mode and of mode competition have never been reported.

We report on the oscillation mode in the circular FEL. The theoretical dispersion relation is described in Section 2. In Section 3, we describe the experimental apparatus and results of the experiment, i.e. a detailed measurement of oscillation modes changing and of the spectrum. In addition, we report on a measurement of the stored energy in the coaxial waveguide in order to estimate the quality factor due to the diffraction. Finally, we discuss the oscillation mode on the circular FEL and a permissible detuning in Section 4.

## 2. Theory

The configuration of the circular FEL is shown in Fig. 1. In this device, a relativistic electron beam is subject to synchrotron motion with large Larmor radius under a

uniform axial magnetic field in the gap of a coaxial waveguide. The electron motion is modified by an azimuthally periodic wiggler magnetic field whose direction is radial. The electron wiggling motion in the axial direction. As a result, the electron beam interacts with an axial electric field of a TM coaxial waveguide mode.

The bunched electron beam supports a synchronous mode described by Eq. (1):

$$\omega_0 = (P + N) \frac{\Omega_c}{\gamma} + (k_z v_z). \quad (1)$$

This mode is composed of a high-harmonic cyclotron upshift and an axial Doppler upshift. Here,  $\Omega_c = eB_z/m_0$  is the cyclotron frequency, and  $e$ ,  $B_z$ ,  $m_0$ ,  $\gamma$ ,  $N$ ,  $p$ ,  $k_z$  and  $v_z$  are the electron charge, the axial uniform magnetic field, the electron rest mass, the Lorentz factor, the wiggler period, the azimuthal harmonic number of the radiation, the axial wave number of the radiation and the axial component of the electron velocity, respectively. This equation suggests that the synchrotron frequency is the essential factor in the circular FEL operation, as axial

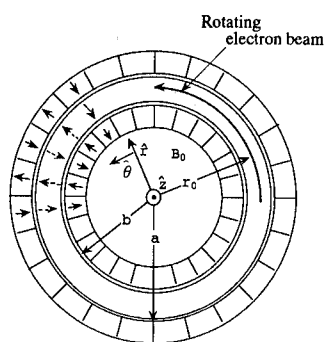


Fig. 1. Front view of the circular wiggler.

\* Corresponding author. Tel. +81 427 51 3911 (ext. 2420), e-mail tmizuno@net202.newsian.isas.ac.jp.

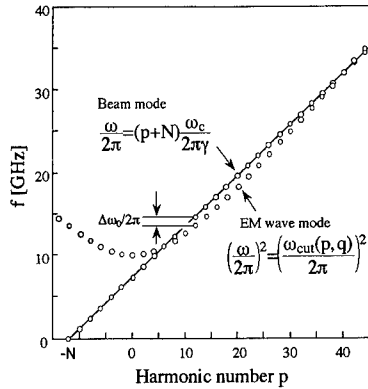


Fig. 2. The dispersion relation of the circular FEL.

velocity is in a conventional linear FEL. The waveguide mode is described by the following equation:

$$\omega_s^2 = \omega_c(p, q)^2 + (k_z c)^2. \quad (2)$$

Here  $q$  and  $\omega_c$  are the radial harmonic number and the cutoff frequency of the TM( $p, q$ ) mode, respectively. The dispersion relation that is described by Eqs. (1) and (2) is illustrated in Fig. 2. We assume the axial wave number is  $k_z = 0$ . This figure indicates that two resonance frequencies can be observed simultaneously.

### 3. Experiment

The experimental configuration is illustrated in Fig. 3. A Marx capacitor bank directly energizes a cathode that

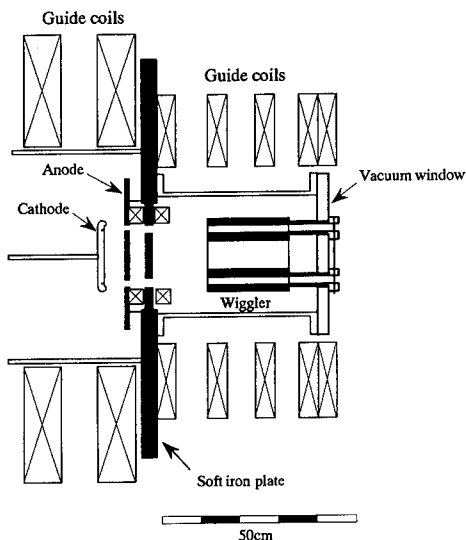


Fig. 3. The schematic diagram of the experimental apparatus.

has a region of hollow velvet cloth. A hollow electron beam is accelerated from the cathode plasma with the diode voltage. The relativistic hollow beam starts rotating at the cusped magnetic field and, after the cusp region, forms a rotating electron beam whose Larmor radius and axial current are about 63 mm and 100–150 A, respectively.

The circular wiggler field, whose direction is radial, is generated by an assembly of Nd–B–Fe permanent magnets (Fig. 1) in the coaxial waveguide. The wiggler has 12 periods in a revolution 0.09 T peak intensity. Inner radius, outer radius and axial length of the wiggler are 55 mm, 70 mm and 200 mm, respectively. In this wiggler, the electron spiral motion involves the wiggling motion in the axial direction due to the radial wiggler field. The rotation motion and axial perturbed motion of the electron contribute to the interaction with the TM waveguide mode [10].

The spectrum of the radiation frequency is observed with a FFT (Fast Fourier Transfer) system and YIG tunable band-pass filters. The FFT system can sweep the Ku and Ka bands by means of two broad band mixers. The IF signal of the Ku band mixer is DC–4 GHz and the Ka band mixer is 0.1–5 GHz. We use the FFT capability of a DSA602 (Tektronix) in order to obtain a frequency spectrum of the IF signal. The FFT is defined by the sampling rate (2 Gs/s) and the record length (512 points). Thus the frequency resolution of this system is 3.9 MHz and sweep-time is 256 ns. The main purpose of this system is measurement of mode competition. For other measurements we have two YIG filters. One can sweep the Ku and Ka bands whose 3 dB band width is 30 MHz, and the other one can sweep the Ka band whose 3 dB band width is 50 MHz. The main purpose of the filters is the observation of the time dependence of oscillation modes and timings.

Fig. 4 shows the electron energy dependence of the oscillation mode that was measured with the YIG filter system. The first wave form from the top is the cathode voltage, the other curves are the output power from the YIG filter tuned to 12.18, 11.77, 11.25 and 10.77 GHz. The electron energy decreases monotonically because the cathode is directly connected to the Marx capacitor bank. The azimuthal harmonic mode number of the mode  $p$  (TM $_{p1}$ ) decreases with decreasing cathode voltage. We can explain this phenomena from Fig. 2 which shows the theoretical dispersion relation. Fig. 2 suggests that the inclination of the beam mode line increases as the energy decreases; as a result the harmonic number should decrease.

From Fig. 4, we can find the strongest mode is TM $_{81}$  and with a pulse width of about 400 ns. We measured the spectrum of the radiation with the FFT system in order to investigate mode competition. The sample trace of the FFT output is shown in Fig. 5. From this experiment, we found five different modes that were TM $_{p1}$  ( $p = 5, 6, 7, 9, 10$ ) competing modes of the TM $_{81}$ . However, the magnitude of

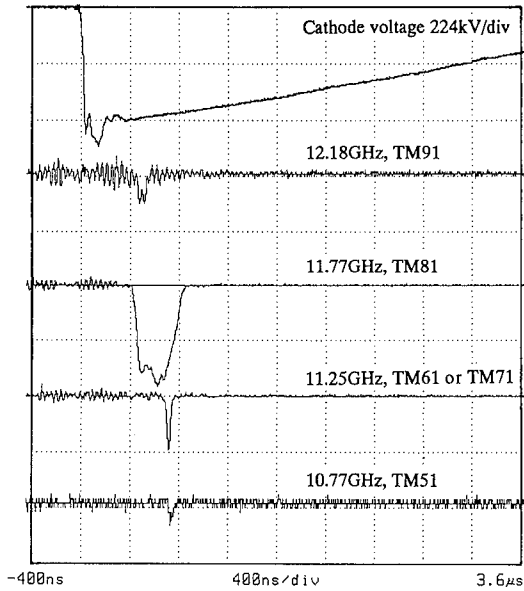


Fig. 4. Wave forms of the cathode voltage and radiations (guide field 0.0380 T).

each mode was 20–30 dB less than the  $TM_{81}$  mode, as seen in Fig. 5. As a result, the  $TM_{81}$  mode oscillation was almost single mode. The total radiation power of the single mode oscillation was measured in the far field. In the far field pattern shown in Fig. 6, the solid line is the theoretically predicted curve and the solid circles are the experimental results. Both main lobes of the theory and experiment are at about  $40^\circ$  and the side-lobes are at about  $55^\circ$ . From these results we obtain a total radiation power of about 600 kW at 11.77 GHz. We also measured the Ka band radiation power simultaneously, but it was less than 1 kW.

The stored energy in the coaxial waveguide (cavity) is important in order to understand the interaction between the electrons and the wave and to obtain the quality factor of the cavity. We use a loop antenna whose diameter is 1.0

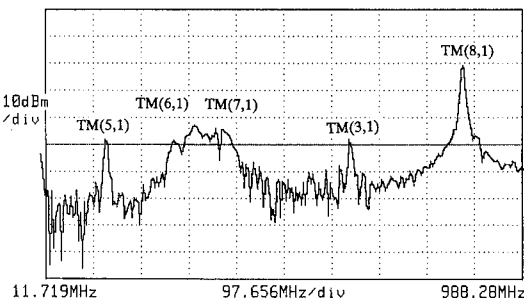


Fig. 5. The frequency spectrum of the radiation ( $f_{L0} = 10.90$  GHz, FFT: 2 Gs/s, 512 points).

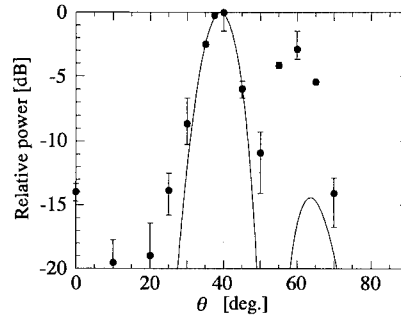


Fig. 6. The far field pattern. Solid line: theoretical curve; solid circle: experiment.

mm in order to pick up the azimuthal component of the magnetic field ( $H_\theta$ ) around the outside of the conducting wall in the waveguide. The stored energy can be calculated from  $H_\theta$ . The sensitivity of the  $H_\theta$  probe was calibrated using the  $TE_{10}$  mode of a rectangular wave guide. As a result of the  $H_\theta$  measurement, we obtained a stored energy of about 6.2 mJ. Thus we can find the quality factor due to diffraction using the stored energy and total radiation power. The diffraction  $Q$  ( $Q_{\text{diff}} = \omega U / (dU/dt)$ ) was about 400. Here, we assumed the axial wave number  $k_z$  was negligible, because the oscillation frequency was almost the same as the cutoff frequency. Since the ohmic  $Q$  can be calculated theoretically as  $Q_{\text{ohm}} = 3.1 \times 10^4$ , the quality factor of the cavity is limited by the diffraction  $Q$ .

#### 4. Discussion

As shown in Fig. 4, the oscillation mode number (lower branch) decreases as the electron energy decreases at constant magnetic field. However, the cathode voltage is decreasing from 447 kV to 415 kV during the  $TM_{81}$  mode oscillation (about 400 ns). This suggests that the oscillation occurred with 3% frequency detuning. The cavity decay time  $\tau = Q/f$  is about 30 ns.

In conclusion, we obtained single mode oscillation of the circular FEL at  $TM_{81}$  (11.77 GHz). The frequency width was about 0.3% and the radiation power was about 600 kW.

#### References

- [1] G. Bekefi, Appl. Phys. Lett. 40 (1982) 578.
- [2] H. Saito and J.S. Wurtele, Phys. Fluids 30 (1987) 2209.
- [3] Y. Kawai, H. Saito and J.S. Wurtele Phys. Fluids B 2 (1991) 1485.
- [4] G. Bekefi, R.E. Shefer and W.W. Destler, Appl. Phys. Lett. 44 (1984) 280.

- [5] F. Hartemann, G. Bekefi and R.E. Shefer, IEEE Trans. Plasma Sci. PS-13 (1985) 484.
- [6] W.W. Destler, F.M. Aghamir, D.A. Boyd, G. Bekefi, R.E. Shefer and Y.Z. Yin, Phys. Fluids 28 (1985) 1962.
- [7] E. Chojnacki and W.W. Destler, IEEE J. Quantum Electron, QE-23 (1987) 1605.
- [8] F. Hartmann and G. Bekefi, Phys. Fluids 30 (1987) 3283.
- [9] T. Mizuno, H. Sekita, K. Takagi, T. Ohshima, H. Saito and T. Sekiguchi, Nucl. Instr. and Meth. A 318 (1992) 749.
- [10] T. Mizuno, T. Ohshima and H. Saito, Nucl. Instr. and Meth. A 331 (1993) 117.



## Concept of a submillimeter wavelength CARM

V.L. Bratman<sup>\*</sup>, G.G. Denisov, M.M. Ofitserov, M.I. Petelin, S.V. Samsonov

*Institute of Applied Physics, Russian Academy of Sciences, 603600, 46 Ulyanov Str., N. Novgorod, Russian Federation*

### Abstract

The main problems in the advance of the CARM from the millimeter wavelength range into the submillimeter range are discussed. Methods of realization of an electron-optical system forming an intense spiral electron beam with low velocity spread as well as a low-loss, high-selective microwave system are proposed. Results of calculations and the first stage of modeling a CARM experiment at millimeter wavelengths are presented. A submillimeter wavelength CARM for  $\alpha$ -particle diagnostics in ITER is designed.

### 1. Introduction

The Cyclotron Autoresonance Maser (CARM) [1,2,5–12] is a variety of FEM with the simplest pumping in the form of a homogeneous magnetic field. Due to the highly developed technique for the creation of strong homogeneous magnetic fields, in the submillimeter wavelength range, significantly lower particle energies are required for the CARM than for the “usual” FEM-ubitron with spatio-periodical magnetic pumping. So in this range the CARM can be simpler and cheaper than the ubitron. The correctness of these general statements became clear to us again when we estimated the possibility to create a powerful pulsed source of coherent radiation at a wavelength of 0.2 mm (frequency 1.5 THz). Such a source has been announced to be necessary for  $\alpha$ -particle diagnostics in ITER. According to the calculations, a rather low electron energy (2–2.5 MeV) and an attainable magnetic field (100–120 kG) are sufficient for the CARM; in the case of the ubitron, however, the electron energy must be at least twice as high (for example, the ubitron [13] operating at this range uses an electron beam of 6 MeV energy produced in an electrostatic accelerator).

The experience obtained with CARMs of a millimeter wavelength range [6–12] indicates that the most important problems are as follows: 1) the formation of an electron beam with a rather high rotary velocity and small spread in longitudinal velocity; 2) the discrimination of parasitic modes, especially, the modes near cut-off (gyrotron modes at different cyclotron harmonics) and backward waves. In the submillimeter wavelength range, the problem of ohmic losses of the wave in the microwave system walls can also be significant. A possible way to solve all these problems

is to use in the CARM a quasi-optical, open-from-sides cavity (or waveguide) in which a thin solid electron beam excites a mode having small diffraction and ohmic losses. This paper describes electron-optical and microwave systems suitable for the submillimeter CARM and also represents preliminary results of modeling experiments at millimeter wavelengths.

### 2. Main problems

CARM operation is based on stimulated bremsstrahlung radiation of electrons moving along helical trajectories in a homogeneous magnetic field  $\mathbf{H} = H\mathbf{z}_0$ . The electrons interact with a wave propagating nearly along the magnetic field direction under the cyclotron resonance condition:

$$\omega \approx \omega_H + h v_{\parallel}, \quad (1)$$

where  $\omega$  and  $h$  are the frequency and the longitudinal wave number, and  $\omega_H$  and  $v_{\parallel}$  are the cyclotron frequency and the longitudinal velocity of the electrons. Correspondingly, as in the FEM-ubitron, the Doppler frequency upshift  $\Gamma = \omega/\omega_H$  is high:  $\Gamma \sim \gamma^2$  ( $\gamma = (1 - \beta_{\perp}^2 - \beta_{\parallel}^2)^{-1/2}$  is the relativistic factor of electrons,  $\beta = v/c$ ) if the phase velocity of the wave  $v_{ph} = \omega/h$  and the longitudinal velocity of electrons  $v_{\parallel}$  are close enough to the speed of light  $c$ . According to the theory [1,2], in order to obtain high electronic efficiency in the CARM, unlike the ubitron, a rather large rotary velocity of the particles is necessary:  $\beta_{\perp} \sim \gamma^{-1}$  (initially, electrons must be situated at the high Landau levels). It is important to note that not only the rotary but also the longitudinal momentum of electrons changes in the course of emission of radiation (the electrons emit photons and undergo a recoil). But, if the phase velocity of the wave is close to the speed of light, then the cyclotron resonance condition (1) is sustained automati-

<sup>\*</sup> Corresponding author. Tel +7 8312 384 552, fax +7 8312 362 061.

cally for a long time in spite of the large changes in electron energy  $\Delta\gamma$  and in longitudinal velocity  $\Delta v_{\parallel}$ , because the variations of the cyclotron frequency  $\Delta\omega_H$  and the Doppler shift  $\Delta(hv_{\parallel})$  are mutually compensated (auto-resonance [3,4]). It is obvious, that for high efficiency condition (1) has to be fulfilled to a definite accuracy, for all electrons of the beam. The respective requirement can be formulated as follows:

$$\frac{\delta\beta_{\perp}}{\beta_{\perp}} \leq \frac{1}{4bN}, \quad (2)$$

where  $N$  is the number of gyrorotations,  $b = \beta_{\perp}^2 / (2\beta_{\parallel}\beta_{ph}(1 - \beta_{\parallel}/\beta_{ph}))$  is a parameter characterizing the electron recoil. Numerical calculations confirm estimation (2).

Different ways can be used to form an electron beam satisfying the above mentioned conditions. For example, for relatively low electron current, it is possible to employ the usual (for gyrotrons) magnetron-injection gun followed by acceleration of particles to relativistic velocities and strong magnetic field compression. Besides, the necessary electron beam can be provided by means of nonadiabatic pumping of an initially rectilinear thin solid beam in the magnetostatic field of a short wiggler or kicker [7,8]. Let us discuss the last way, being applicable for both thermo- and field-emission guns, in more details.

If the electron current is not very high, then the particle energies are almost the same and the spread in rotary velocity after pumping in the kicker (Fig. 1) is determined by the ratio of initial chaotic transverse velocity to its value in CARM operating space and by the position spread of the particles. In the case where the electron beam diameter is much less than the Larmor step of the particles, the kicker is weakly sensitive to the position spread, so that the main electron-optical problem remains forming a rectilinear electron beam with minimum oscillations. To solve this problem it is possible, like the experiment [8], to use a simple two-electrode field emission gun with a selecting hole in the anode that retains only the central part of the whole beam with the most “rectilinear” electrons (Fig. 1). But in this case, the anode hole operates like an electrostatic lens. Correspondingly, the maximum parasitic transverse velocity of particles in the beam before the kicker is determined by the ratio of the anode hole radii  $r_h$  to the distance between electrodes  $d_{C-A}$  (for ideal axial

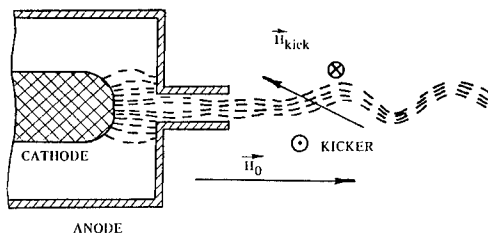


Fig. 1. Electron-optical system of the CARM.

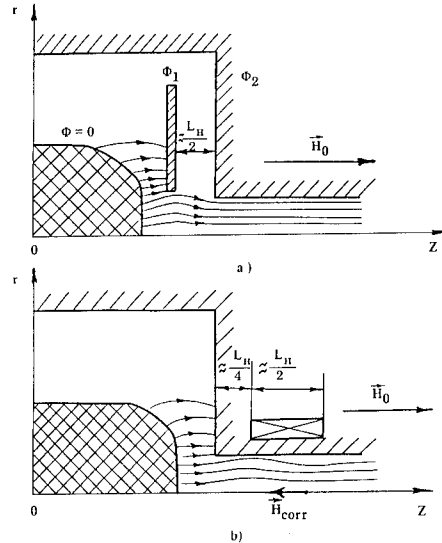


Fig. 2. Electron trajectories (schematically) in electron guns with (a) correcting high-voltage electrode and (b) correcting coil.

symmetry)  $\beta_{\perp \text{ in}} \sim r_h/d_{C-A}$ . It is obvious that a too small a hole will allow the passage of only a very small electron current, which is proportional to the area of the hole  $I \sim (r_h/d_{C-A})^2$ . Estimates and detailed calculations demonstrate the possibility of decreasing the undesirable influence of the anode lens and diminishing considerably the amplitude of the parasitic electron oscillations using additional elements that compensate non-adiabatically the parasitic gyro-rotation of all particles of the paraxial beam. Such a compensation can be provided by an additional high-voltage electrode or (which is significantly simpler) by an additional coil with definite direction and value of current (Fig. 2). These correcting elements should allow us to simultaneously decrease the spread in velocity and to enhance the current efficiency of the electron gun many times.

As the CARM is advanced from the millimeter wavelength range into the submillimeter range, the microwave system of the CARM should inevitably become more overmoded and the problem of parasitic generation will be more acute. In these circumstances it seems to be more expedient to give up the axial symmetry and develop a more selective, open-from-sides microwave system, namely, a cavity where quasi-plane waveguide (Figs. 3 and 5) and quasi-plane reflectors of various types (including the Bragg reflectors) (Fig. 5) are used. As the operating mode of this cavity, low-loss TE mode with the electric field parallel to the plane of symmetry (Fig. 3) should be used. Diffraction losses of the mode with one Gaussian variation along the  $x$ -axis and  $n$  sinusoidal variations along the  $y$ -axis are determined by its Fresnel parameter

$$N_F = \frac{b^2 n}{8a^2}, \quad (3)$$

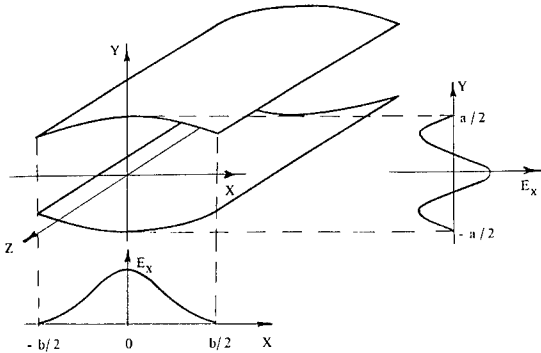


Fig. 3. Operating section of CARM in the form of open waveguide and the  $TE_{1,3}$  mode.

where  $a$  and  $b$  are waveguide cross-section dimensions (see Fig. 3). Choosing the high mode with  $N_F > 1$ , possessing small diffraction losses, as the operating mode, we may have simultaneously  $N_F < 1$  and, correspondingly, very high diffraction losses for the most dangerous low-frequency (gyrotron) modes.

Such an open microwave system gives one flexibility in choosing an appropriate scheme of the CARM. For example, there is a simple possibility to provide high reflection (close to 100%) of the operating wave propagating at a small Brillouin angle from the cathode side. For this purpose one can bend the open waveguide in the plane of symmetry with a comparatively small radius without operating wave losses, which allows the electron beam and the wave to be separated; after that the wave can be effectively reflected by a simple metal mirror (Figs. 4 and 5).

### 3. Modeling experiments

In order to check the main ideas above-mentioned regarding the electron-optical and microwave system of a submillimeter CARM-oscillator, the experiments at millimeter wavelengths using a mildly relativistic electron beam are being carried out. The “hot” experiments are performed at the Sinus-6 direct-action accelerator with a field emission, magnetically insulated injector that permits one to obtain an electron beam with an energy up to 600

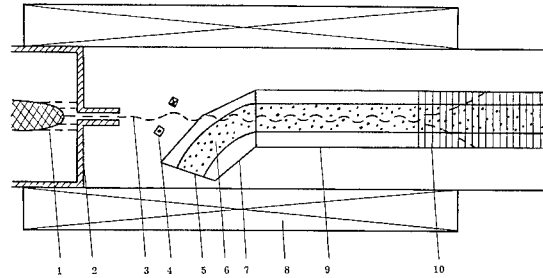


Fig. 4. Scheme of the modeling CARM experiment. (1) cathode, (2) anode, (3) electron beam, (4) kicker, (5) metal mirror, (6) wave beam, (7) reflector with the turn, (8) solenoid, (9) operating section of cavity, (10) Bragg reflector.

keV, a whole beam current of  $\sim 5$  kA and a pulse duration of  $\sim 20$  ns.

At the first stage, the simplest configuration of the electron gun without any correcting elements was used (Fig. 4). The CARM-oscillator parameters (Table 1) were chosen in accordance with the preliminary, combined numerical analysis of an electron-optical and a microwave system and with the preliminary experimental data.

An electron beam of 500 keV energy and of about 3 kA whole current is produced from a graphite, magnetically insulated cathode, 7 mm in diameter. A 2.5 mm hole in the anode selects the most “rectilinear” part of the beam with a current of 120 A for magnetic fields of 8–12 kG. The rotary velocity up to  $\beta_{\perp} \approx 0.7$  is imparted to electrons by means of a kicker in the form of a rectangular frame with current sloping at some angle to the longitudinal axis (Figs. 4 and 5).

The  $TE_{1,3}$  mode with one Gaussian variation along the  $x$ -axis and three sinusoidal variations ( $n = 3$ ) along the  $y$ -axis of an open waveguide (see Fig. 3) was chosen as the operating mode. In this case, the electrons are synchronous (except for the operating mode at the operating frequency) to the  $TE_{1,2}$  mode at a frequency near the cut-off one and to the  $TE_{1,1}$  backward wave. The parasitic gyrotron  $TE_{1,2}$  mode has a zero electric field at the waveguide center, so it weakly interacts with the thin electron beam propagating along the  $z$ -axis. Another parasitic  $TE_{1,1}$  mode, according to formulae (3), has the Fresnel parameter less than unity

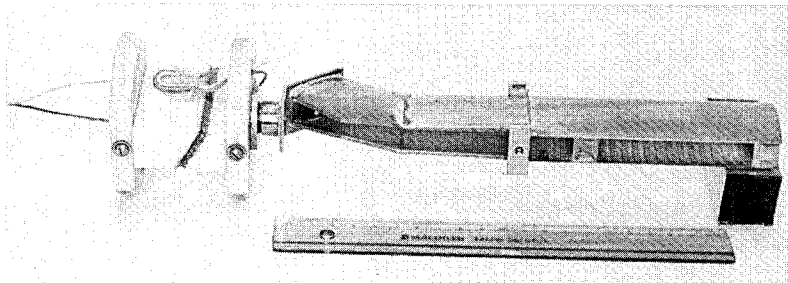


Fig. 5. Kicker and microwave system of the CARM in the modeling experiment.

Table 1  
CARM parameters in the modeling experiment

|   |                      |
|---|----------------------|
| Electron beam   |                      |
| Energy  | 500 keV <sup>b</sup> |
| Current   | 120 A <sup>b</sup>   |
| Pulse duration  | 15 ns <sup>b</sup>   |
| Diameter  | 2.5 mm               |
| Operating rotary velocity $\beta_{\perp}$                   | 0.5                  |
| Velocity spread $\delta\beta_{\perp} / \beta_{\perp}$ (rms) | 0.06 <sup>a</sup>    |
| Magnetic field  | 11 kG                |
| Microwave system  |                      |
| Operating frequency   | 36 GHz <sup>a</sup>  |
| Operating mode  | TE <sub>1,3</sub>    |
| Height  | 20 mm                |
| Width   | 32 mm                |
| Operating section   |                      |
| Length  | 70 mm                |
| Cathode-side reflector with the turn                        |                      |
| Length  | 60 mm                |
| Angle of the turn   | 25°                  |
| Reflection coefficient                                      | 98% <sup>a</sup>     |
| Frequency band  | 8% <sup>b</sup>      |
| Collector-side Bragg reflector                              |                      |
| Length  | 108 mm               |
| Period of corrugations                                      | 5.4 mm               |
| Depth of corrugations                                       | 1 mm                 |
| Reflection coefficient                                      | 80% <sup>a</sup>     |
| Frequency band  | 2% <sup>a</sup>      |
| CARM operation  |                      |
| Electronic efficiency                                       | 12% <sup>a</sup>     |
| Radiation power   | 7.2 MW <sup>a</sup>  |

<sup>a</sup> Calculated value.

<sup>b</sup> Measured value.

and, therefore, large diffraction losses. Thus, the most dangerous parasitic modes are effectively discriminated in the operating section of the CARM.

Two reflectors are used in the CARM-oscillator for selective feedback of the operating mode. In the cathode-side reflector (Figs. 4 and 5) the wave beam turns, separates from the electron beam and reflects from a metal mirror. This wave beam turn, proposed and verified experimentally in Ref. [14], is performed non-adiabatically at a very short distance, almost without diffraction losses. Effective operation of the cathode-side reflector at the operating frequency was confirmed in the “cold” experiments. The collector-side reflector (Figs. 4 and 5) is one of the Bragg-type reflectors with periodically corrugated walls.

As a result of the first experimental stage, effective parasitic mode discrimination was obtained. In the case where a smooth waveguide section was placed instead of the Bragg reflector we did not indicate microwave radiation at operating rotary velocity of the electrons. For

stronger pumping of the electron beam ( $\beta_{\perp} > 0.5$ ), rather powerful (probably, gyrotron modes) radiation with a wavelength longer than 10 mm, was observed.

In order to check operation of the reflectors and of the whole cavity in the “cold” experiments, a mode converter from the fundamental mode of a rectangular waveguide into the TE<sub>1,3</sub> mode of the open waveguide is being developed now. We also plan to use a correcting coil behind the anode hole to enhance the electron beam quality.

### Acknowledgements

The research described in this publication was made possible in part by Grant No. R85000 from the International Science Foundation and Grant No. 93-02-842 from the Russian Foundation of the Fundamental Research. The authors are very grateful to E.V. Suvorov, V.V. Rostov, I.V. Pegel and B.V. Raisky for useful discussions.

### References

- [1] M.I. Petelin, Radiophys. Quantum Electron. 17 (1974) 686.
- [2] V.L. Bratman, N.S. Ginzburg, G.S. Nusinovich, M.I. Petelin, and V.K. Yulpatov, Relativistic HF Electronics, vol. 1, ed. A.V. Gaponov-Grekhov (Gorky, USSR, 1979) p. 157.
- [3] A.A. Kolomenskij and A.N. Lebedev, A.N. Dokl. Acad. Nauk SSSR, 145 (1962) 1259.
- [4] V.Ya. Davydovskij, Pis'ma Zh. Eksp. Teor. Fiz. 43 (1962), 886.
- [5] V.L., Bratman, G.G. Denisov, N.S. Ginzburg, and M.I. Petelin, IEEE J. Quantum Electron. QE-19 (1983) 282.
- [6] V.L. Bratman, and G.G. Denisov, Int. J. Electron. 72 (1992) 969.
- [7] V.L. Bratman, G.G. Denisov, and S.V. Samsonov, Proc. 2nd Int. Workshop on “Strong Microwaves in Plasmas”, N. Novgorod, 1993, vol. 2, p. 690.
- [8] G. Bekefi, A. DiRienzo, C. Leibovitch, and B.G. Danly, Appl. Phys. Lett. 54 (1989) 1302.
- [9] M. Caplan, and B. Kulke, Proc. 14 Int. Conf. Infrared and MM Waves, Conf. Digest SPIE (1989) 420.
- [10] B.G. Danly, J.A. Davies, K.D. Pendergast, R.J. Temkin, and J.S. Wurtele, Microwave and Particle Beam Sources and Directed Energy Concepts, SPIE vol. 1061 (1989) p. 243.
- [11] Q.S. Wang, A.T. Lin, N.S. Luhmann Jr., et al., Proc. 13th Int. Conf. on IR and MM Waves, Conf. Digest, SPIE (1988) 1039.
- [12] R.B. Mc Cowan, A.W. Fliflet, S.H. Gold, W.M. Black, A.K. Kinkead, V.L. Granatstein, and M.S. Sucey, IEEE, Trans. Electron Devices ED-36 (1989) 1968.
- [13] J.P. Kaminski, et al., Proc. 15th Int. Free Electron Laser Conf., 1993, Nucl. Instr. and Meth. A 341 (1994) 169.
- [14] N.L. Alexandrov, G.G. Denisov, Int. J. of Infr. and MM Waves, 8 (1994) 1373.



ELSEVIER

# Theory of the free-electron laser based upon a coaxial hybrid wiggler

H.P. Freund <sup>\*,1</sup>, R.H. Jackson, D.E. Pershing <sup>2</sup>, J.M. Taccetti <sup>3</sup>

*Naval Research Laboratory, Washington, DC 20375, USA*

## Abstract

A 3D nonlinear FEL formulation based upon a Coaxial Hybrid Iron (CHI) wiggler is described. The CHI wiggler is created by insertion of a central rod and an outer ring (composed of alternating ferrite and nonferrite spacers) along the axis of a solenoidal. Relatively high field strengths can be achieved with the CHI wiggler at shorter wiggler periods than is possible in many other conventional wiggler designs. The formulation is a slow-time-scale analysis of the interaction of an annular electron beam with the CHI wiggler in a coaxial waveguide. Simulations are presented for W-band operation. The results indicate that operation over a wide bandwidth is practical, and that the uniform- and tapered-wiggler bandwidths are comparable.

## 1. Introduction

The FEL wavelength depends upon the beam energy and the wiggler parameters as  $\lambda \approx (1 + a_w^2) \lambda_w / 2\gamma_0^2$ , where  $\lambda_w$  is the wiggler period,  $\gamma_0$  is the bulk relativistic factor, and  $a_w \approx 0.0934 B_w \lambda_w$  for an rms wiggler amplitude  $B_w$  in kG and  $\lambda_w$  in cm. In the exponential Compton regime, both the gain and efficiency scale as  $a_w^{2/3} / \gamma_0$ . Hence, the wavelength, gain, and efficiency of the interaction all decrease as the beam energy increases for fixed wiggler parameters. A great deal of effort has been devoted to the design of short period wigglers to operate at short wavelengths with low beam energies. However, this is a self-defeating process since reductions in  $\lambda_w$  often result in reductions in  $B_w$  as well with a deleterious impact on the efficiency and gain.

We analyze an FEL based upon a Coaxial Hybrid Iron (CHI) wiggler [1] which is a configuration where a central rod and a coaxial ring of alternating ferrite and nonferrite spacers are inserted into a solenoid. The ferrite (nonferrite) spacers on the central rod are aligned opposite to the nonferrite (ferrite) spacers on the outer ring (see Fig. 1).

This produces an azimuthally symmetric field where the amplitude can be increased by increasing the strength of the solenoid. Since the radial component of the field has a minimum at the center of the gap, the field focuses the beam against self-field induced spreading. In addition, the CHI wiggler results in an azimuthal bulk transverse velocity; hence, the interaction is strongest for waves with an azimuthal component.

The ease of construction of this design permits the development of wigglers with extremely short periods by the simple expedient of using thin spacers. In most wiggler designs this is offset by the fact that shorter periods typically result in lower amplitudes and increased field gradients. This is not necessarily the case for the CHI wiggler since high amplitudes can be achieved by using a stronger solenoid. Note also that the gyroresonance between the periodic and axial components can enhance the FEL interaction as well [2].

## 2. The general formulation

In a source-free region the divergence and curl of the magnetic field vanish, and the field of the CHI wiggler is found by solution of Laplace's equation  $\nabla^2 \mathbf{B}(r, z) = 0$  for appropriate boundary conditions. We assume that the ferrite spacers result in a step function in the axial field at  $r = R_{in}$  and  $R_{out}$  such that  $B_z(R_{in}, z) = B_{in}$  and  $B_z(R_{out}, z) = B_{out}$  along the surface of the dielectric and zero along the surface of the ferrite. Each wiggler period corresponds to the combined length of two spacers, and we

\* Corresponding author. Tel. +1 703 734 5840, fax +1 703 821 1134, e-mail: freund@mmace.nrl.navy.mil.

<sup>1</sup> Permanent address: Science Applications International Corp., McLean, VA 22102, USA.

<sup>2</sup> Permanent address: Mission Research Corp., Newington, VA 22122, USA.

<sup>3</sup> Permanent address: University of Maryland, College Park, MD 20742, USA.

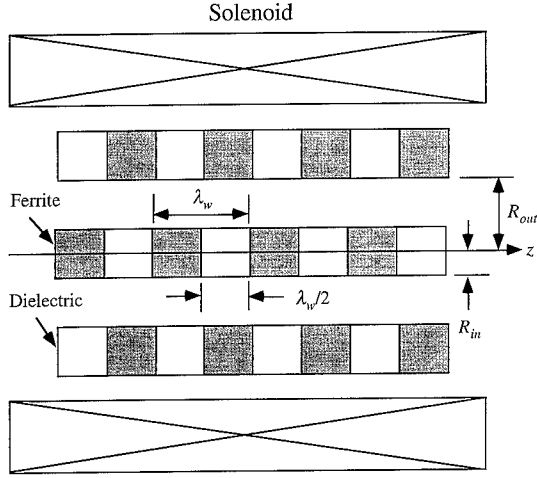


Fig. 1. Schematic illustration of the CHI wiggler configuration.

assume that the length of each spacer is  $\lambda_w/2$ . The solution which results is [3]

$$B_z(r, z) = B_0 + B_w \sum_{n=1}^{\infty} \cos(nk_w z) \times \frac{[S_n I_0(nk_w r) - T_n K_0(nk_w r)]}{G(nk_w R_{out}, nk_w R_{in})}, \quad (1)$$

and

$$B_r(r, z) = B_w \sum_{n=1}^{\infty} \sin(nk_w z) \times \frac{[S_n I_1(nk_w r) + T_n K_1(nk_w r)]}{G(nk_w R_{out}, nk_w R_{in})}, \quad (2)$$

where  $B_w \equiv 2B_0$ ,  $G(\xi, \zeta) \equiv I_0(\xi)K_0(\zeta) - I_0(\zeta)K_0(\xi)$ ,

$$S_n \equiv \left(\frac{2}{n\pi}\right) \sin\left(\frac{n\pi}{2}\right) [K_0(nk_w R_{in}) + K_0(nk_w R_{out})] \quad (3)$$

and

$$T_n \equiv \left(\frac{2}{n\pi}\right) \sin\left(\frac{n\pi}{2}\right) [I_0(nk_w R_{in}) + I_0(nk_w R_{out})]. \quad (4)$$

This is in agreement with the results of the Poisson/Superfish family of magnetics codes [4].

Now consider the dynamical equations which govern the electromagnetic fields and the electron beam. Consider propagation in a coaxial waveguide with inner and outer radii  $a$  and  $b$ . The neglect of space-charge effects is valid as long as  $\omega_b/ck_w < \gamma_z^3 v_w^2/8\gamma_0 c^2$ , where  $\omega_b$  is the ambient plasma frequency,  $v_w$  is the bulk transverse wiggler velocity, and  $\gamma_z = (1 - v_{||}^2/c^2)^{-1/2}$  for a bulk stream-

ing velocity  $v_{||}$ . Space-charge effects can also be neglected if (1) the wavelength is less than the Debye length and the space-charge waves are subject to strong Landau damping, or (2) the bandwidth of the interaction is greater than the plasma frequency [5].

The boundary conditions at the walls of the coaxial waveguide are satisfied by a superposition of the TE, TM, and TEM modes of the waveguide. We limit the discussion here to the TE modes. As such, the vector potential can be expressed as

$$\delta A(x, t) = \sum_{l=0}^{\infty} \sum_{m=1}^{\infty} \delta A_{lm}(z) \left[ \frac{l}{\kappa_{lm} r} Z_l(\kappa_{lm} r) \hat{e}_r \sin \alpha_{lm} + Z'_l(\kappa_{lm} r) \hat{e}_\theta \cos \alpha_{lm} \right], \quad (5)$$

where for angular frequency  $\omega$  and wavenumber  $k_{lm}$

$$\alpha_{lm} \equiv \int_0^z k_{lm}(z') dz' + l\theta - \omega t, \quad (6)$$

and  $\omega^2 = c^2 k_{lm}^2 + c^2 \kappa_{lm}^2$  for a given cutoff  $\kappa_{lm}$ . The cut-offs are given by solution of the dispersion equation  $J'_l(\kappa_{lm} a) Y'_l(\kappa_{lm} b) = J'_l(\kappa_{lm} b) Y'_l(\kappa_{lm} a)$ , where  $J_l$  and  $Y_l$  denote the regular Bessel and Neumann functions of order  $l$ . The radial polarization functions are  $Z_l(\kappa_{lm} r) \equiv J_l(\kappa_{lm} r) + \Delta_{lm} Y_l(\kappa_{lm} r)$ , where  $\Delta_{lm} \equiv -J'_l(\kappa_{lm} b)/Y'_l(\kappa_{lm} b)$ .

The dynamical equations have been described in detail [2] and the results for the TE modes are

$$\left[ \frac{d^2}{dz^2} + \left( \frac{\omega^2}{c^2} - k_{lm}^2 - \kappa_{lm}^2 \right) \right] \delta a_{lm} = \frac{\omega_b^2}{c^2} H_{lm} \left\langle \frac{v_r}{|v_z|} \frac{l}{\kappa_{lm} r} Z_l(\kappa_{lm} r) \sin \alpha_{lm} + \frac{v_\theta}{|v_z|} Z'_l(\kappa_{lm} r) \cos \alpha_{lm} \right\rangle, \quad (7)$$

$$2k_{lm}^{1/2} \frac{d}{dz} (k_{lm}^{1/2} \delta a_{lm}) = \frac{\omega_b^2}{c^2} H_{lm} \left\langle \frac{v_r}{|v_z|} \frac{l}{\kappa_{lm} r} Z_l(\kappa_{lm} r) \cos \alpha_{lm} - \frac{v_\theta}{|v_z|} Z'_l(\kappa_{lm} r) \sin \alpha_{lm} \right\rangle, \quad (8)$$

where  $\delta a_{lm} \equiv e \delta A_{lm} / m_e c^2$  is the normalized amplitude of the modes, and

$$H_{lm} \equiv \frac{2\kappa_{lm}^2 (b^2 - a^2)}{(\kappa_{lm}^2 b^2 - l^2) Z_l^2(\kappa_{lm} b) - (\kappa_{lm}^2 a^2 - l^2) Z_l^2(\kappa_{lm} a)}. \quad (9)$$

The electron beam is assumed to be monoenergetic with an axial energy spread determined by an initial (i.e., at  $z = 0$ ) pitch angle spread, and the averaging operator is

$$\langle (\cdots) \rangle \equiv \frac{A}{4\pi A_g} \int_0^{2\pi} d\phi_0 \int_0^{p_0} dp_{z0} \beta_{z0} \times \exp\left[-(p_{z0} - p_0)^2 / \Delta p_z^2\right] \times \int_{A_g} dx_0 dy_0 \sigma_{\perp}(x_0, y_0) \times \int_{-\pi}^{\pi} d\psi_0 \sigma_{\parallel}(\psi_0) (\cdots), \quad (10)$$

where  $A_g \equiv \pi(b^2 - a^2)$  is the area of the waveguide,  $\beta_{z0} \equiv v_{z0}/c$  for the initial axial velocity  $v_{z0}$ ,  $\phi_0 \equiv \tan^{-1}(p_{y0}/p_{x0})$ ,  $(p_{x0}, p_{y0}, p_{z0})$  denote the initial beam momenta,  $p_0$  and  $\Delta p_z$  denote the initial total momentum of the beam and axial momentum spread respectively,  $\psi_0$  ( $\equiv -\omega t_0$ , where  $t_0$  is the time at which the particle crosses the  $z = 0$  plane) is the initial ponderomotive phase,  $\sigma_{\perp}$  and  $\sigma_{\parallel}$  are the initial distributions of the beam in cross-section and phase, and

$$A \equiv \left[ \pi \int_0^{p_0} dp_{z0} \exp\left[-(p_{z0} - p_0)^2 / \Delta p_z^2\right] \right]^{-1} \quad (11)$$

is a constant. This results in an axial energy spread

$$\frac{\Delta \gamma_z}{\gamma_0} = 1 - \left[ 1 + 2(\gamma_0^2 - 1) \frac{\Delta p_z}{p_0} \right]^{-1/2}. \quad (12)$$

The equations for the fields are solved simultaneously with the orbit equations for an ensemble of electrons. We integrate the complete 3D Lorentz force equations

$$v_z \frac{d}{dz} \mathbf{p} = -e\delta \mathbf{E} - \frac{e}{c} \mathbf{v} \times (\mathbf{B}_{\text{ext}} + \delta \mathbf{B}), \quad (13)$$

for each electron, where  $\mathbf{B}_{\text{ext}}$  is the magnetostatic field due to the CHI wiggler, and  $\delta \mathbf{E}$  and  $\delta \mathbf{B}$  denote the aggregate electromagnetic fields for all the wave modes. By specifying the initial beam conditions and integrating the Lorentz force equations, we model the injection of the beam into the wiggler by means of a tapered wiggler amplitude. This describes any increase in the effective beam emittance in a

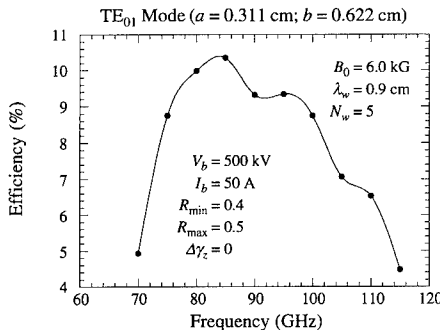


Fig. 2. Variation of the efficiency with frequency in the W-band.

TE<sub>01</sub> Mode ( $a = 0.311$  cm;  $b = 0.622$  cm;  $f = 85$  GHz)

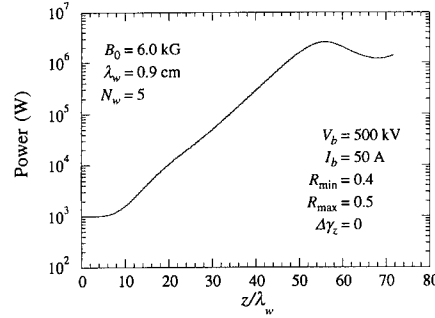


Fig. 3. Evolution of the power with axial position at 80 GHz.

self-consistent way. In addition, we also consider amplitude tapering for the purpose of efficiency enhancement. In order to describe these effects, we assume that the overall coefficient of the periodic component of the field varies as

$$B_w = \begin{cases} 2B_0 \sin^2\left(\frac{k_w z}{4N_w}\right); & z \leq N_w \lambda_w, \\ 2B_0; & N_w \lambda_w < z \leq z_0, \\ 2B_0[1 + k_w \epsilon_w(z - z_0)]; & z > z_0, \end{cases} \quad (14)$$

where  $N_w$  denotes the number of wiggler periods in the entry taper region, and  $\epsilon_w$  is the normalized slope of the taper for purposes of efficiency enhancement.

### 3. Numerical analysis

The dynamical equations are solved for an amplifier configuration in which several modes may propagate at a fixed frequency  $\omega$ . The initial conditions on the fields are chosen to model the injection of an arbitrary power level for each mode. The initial wavenumbers are chosen by the vacuum state, and the growth rates are initially zero since the amplitude of the periodic component of the CHI wiggler is also initially zero. The initial state of the beam models the injection of a continuous, axisymmetric beam

TE<sub>01</sub> Mode ( $a = 0.311$  cm;  $b = 0.622$  cm;  $f = 85$  GHz)

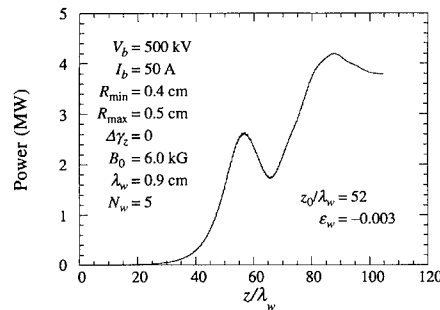


Fig. 4. Evolution of the power with axial distance for an optimized taper at 85 GHz.

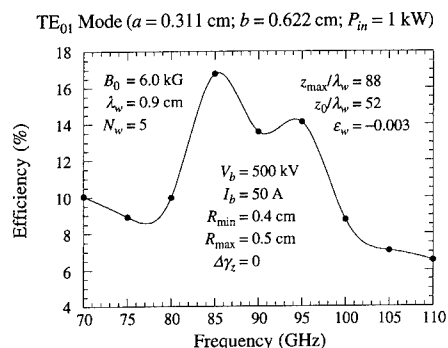


Fig. 5. Variation in the efficiency as a function of frequency in the W-band.

with a uniform density and annular cross-section. For convenience, we choose  $R_{in} = a$  and  $R_{out} = b$ . While we shall be concerned with the fundamental resonance in this paper, both the first and third spatial harmonics of the CHI wiggler are included.

We consider W-band (80–100 GHz) operation and assume the beam has an energy of 500 keV, a current of 50 A, and inner and outer radii of 0.4 cm and 0.5 cm. The CHI wiggler has  $B_0 = 6.0$  kG with a period of 0.9 cm and  $N_w = 5$  and inner and outer radii of 0.311 cm and 0.622 cm respectively. The mode of interest is the  $TE_{01}$  mode with a drive power of 1 kW. Amplification is found over a frequency band from  $\approx 70$  to 115 GHz although the peak efficiencies are found from 80 to 100 GHz. This is illustrated in Fig. 2 in which we plot the saturation efficiency versus frequency for an ideal beam with  $\Delta\gamma_z = 0$ . As is evident, the maximum efficiency is approximately 10.3% at 85 GHz for an output power of almost 2.6 MW. However, the efficiency varies relatively little over the entire W-band and the interaction bandwidth is about 33%.

The evolution of the power is shown in Fig. 3 for the case of the peak efficiency at 85 GHz, and exponential growth is evident from the end of the entry taper region to the saturation point at  $z/\lambda_w \approx 56$  for an interaction length of 50 cm. The decline in efficiency with increases in the initial axial energy spread is relatively benign, and decreases by less than a factor of two as the energy spread increases to somewhat beyond  $\Delta\gamma_z/\gamma_0 \approx 1.25\%$ . Thus, good operational efficiencies are expected for axial energy spreads less than 0.5%.

The performance of a tapered wiggler amplifier is sensitive to both the start-taper point and the slope of the taper. Optimization of the efficiency for operation at 80 GHz indicates that peak efficiency is found for a start-taper point at  $z_0/\lambda_w \approx 52$  and a slope of  $\epsilon_w \approx -0.003$ . The evolution of the power versus distance for this case is shown in Fig. 4. It is evident that the output power peaks at approximately 4.2 MW over a total length of 88 wiggler periods. This translates into a total wiggler length of only 79 cm including the entry taper region.

The variation in the power versus frequency over the W-band is shown in Fig. 5 for parameters that optimize the device for operation at 80 GHz (i.e.,  $z_0/\lambda_w = 52$ ,  $\epsilon_w = -0.003$ , and a total length of 88 wiggler periods). As shown, the curve of the efficiency versus frequency is double-peaked. The larger peak is, as might be expected, at 85 GHz and the secondary peak is at the upper end of the W-band at 95 GHz representing an output power of about 3.5 MW. Hence, we conclude that it is possible to design a W-band MW amplifier using the CHI wiggler.

#### 4. Summary and discussion

We have presented an analytical description of an FEL based upon the CHI wiggler. The nonlinear simulation is a slow-time-scale model for the self-consistent evolution of the modes of a coaxial waveguide with the trajectories of an ensemble of electrons [2]. We emphasize that no wiggler-period-average is applied to smooth the orbital dynamics. Hence, we treat the full particle dynamics and model the injection of the beam into the wiggler.

Specific examples have been discussed for W-band operation with uniform and tapered wigglers. Operation over a wide bandwidth is found to be practical for CHI wiggler-based FELs for both the uniform and tapered-wiggler examples. It is of interest that the bandwidth of the interaction for a tapered wiggler is found to be large. This contrasts with the commonly accepted belief that tapered-wiggler interaction results in a narrow bandwidth. Note that this conclusion is not confined to the CHI wiggler [5].

Our overall conclusion is that the CHI wiggler represents a design in which the limitations of conventional wigglers to reach high field strengths at short wiggler periods are overcome to some degree. The CHI wiggler, therefore, permits the construction of high frequency FELs at relatively low beam voltages.

#### Acknowledgement

This work was supported by the Office of Naval Research.

#### References

- [1] R.H. Jackson, H.P. Freund, D.E. Pershing and J.M. Taccetti, Nucl. Instr. and Meth. A 341 (1994) 454.
- [2] H.P. Freund and T.M. Antonsen, Jr., Principles of Free-electron Lasers (Chapman & Hall, London, 1992).
- [3] H.P. Freund, R.H. Jackson, D.E. Pershing and J.M. Taccetti, Phys. Plasmas 1 (1994) 1046.
- [4] A.M. Winslow, J. Comp. Phys. 2 (1967) 149.
- [5] H.P. Freund, Nucl. Instr. and Meth. A 331 (1993) 496.
- [6] B. Levush, H.P. Freund and T.M. Antonsen, Jr., Nucl. Instr. and Meth. A 341 (1994) 234.





ELSEVIER

# Cyclotron resonance maser experiment in a non-dispersive waveguide

A. Shahadi <sup>a</sup>, E. Jerby <sup>a,\*</sup>, M. Korol <sup>a</sup>, R. Drori <sup>a</sup>, M. Sheinin <sup>a</sup>, V. Dikhtiar <sup>a</sup>,  
V. Grinberg <sup>a</sup>, I. Ruvinsky <sup>a</sup>, M. Bensal <sup>a</sup>, T. Harhel <sup>b</sup>, Y. Baron <sup>b</sup>, A. Fruchtman <sup>c</sup>,  
V.L. Granatstein <sup>d</sup>, G. Bekefi <sup>e</sup>

<sup>a</sup> High-Power Microwave Laboratory, Faculty of Engineering, Tel Aviv University, Ramat Aviv 69978, Israel

<sup>b</sup> Technical College, Tel Aviv University, Ramat Aviv 69978, Israel

<sup>c</sup> Faculty of Physics, Weizmann Institute, Rehovot, Israel

<sup>d</sup> Maryland University, College Park, Maryland, USA

<sup>e</sup> Department of Physics and Research Laboratory of Electronics, Massachusetts Institute of Technology, Cambridge, MA 02139, USA

## Abstract

A cyclotron-resonance maser (CRM) experiment with a transverse electromagnetic (TEM) wave is presented in this paper. A nonrelativistic electron beam is spiraling in this device in a non-dispersive parallel-line waveguide. The CRM oscillator output frequency is tuned by the axial magnetic field in the range of 3.2–4.8 GHz.

## 1. Introduction

The cyclotron resonance interaction with transverse electromagnetic (TEM) modes is known to be weaker than cyclotron interactions with other waveguide modes [1,2]. Ref. [3] describes a CRM oscillator experiment operating in a Fabry–Perot cavity. The condition for amplification in this case is defined as [3]

$$V_{\perp}^2 > 2V_z c, \quad (1)$$

where  $V_{\perp}$  and  $V_z$  are the electron perpendicular and axial velocity components. Other CRM experiments in Fabry–Perot resonators are reported in Refs. [4,5]. Theoretical studies of CRM interactions with TEM waves are devoted mainly to quasioptical devices with open resonators [6,7].

The tuning relation of the cyclotron interaction is given in general by

$$\omega = \omega_c \pm V_z k_z, \quad (2)$$

where  $\omega$  is the em wave angular frequency, and  $k_z$  is the axial wavenumber. The  $\pm$  signs correspond to interactions with forward and backward waves, respectively. The angular cyclotron frequency is

$$\omega_c = \frac{e}{\gamma m} B_0, \quad (3)$$

where  $e$ ,  $m$ , and  $\gamma$  are the electron charge, mass, and relativistic factor, respectively, and  $B_0$  is the axial mag-

netic field. The approximate tuning relation of the TEM-CRM interaction results from Eq. (2) for  $k_z \cong k$  as

$$\omega = \frac{\omega_c}{1 \mp V_z/c}. \quad (4)$$

For a nonrelativistic electron beam ( $|v| \ll c$ ), the amplification condition in Eq. (1) dictates a very small axial velocity of the electron beam. Hence, the Doppler shift in Eq. (4) is relatively small, and  $\omega \cong \omega_c$ . In addition, the slow electron velocity increases the effective space-charge density.

In this paper we describe a nonrelativistic table-top CRM oscillator in which a long-wavelength TEM wave is supported by a nondispersive parallel-line waveguide [8]. Radiation is observed in the cyclotron frequency whenever the electron beam acquires a large transverse velocity by a magnetic kicker.

## 3. Experimental setup

The TEM cyclotron device used in our experiment is shown in Fig. 1. The metallic waveguide consists of a WR90 rectangular tube with two parallel wires along it. They support odd and even TEM modes in frequencies below the empty waveguide cutoff. A low-energy electron beam is orbiting in an externally applied axial magnetic field. The orbiting motion of the electrons couples them synchronously to the electromagnetic wave in the non-dispersive waveguide.

The experimental apparatus is based on the setup of the periodic-waveguide CRM experiment at Tel Aviv Univer-

\* Corresponding author. Tel. +972 3 6 408 048, fax +972 3 6 423 508, email: jerby@taunivm.tau.ac.il.

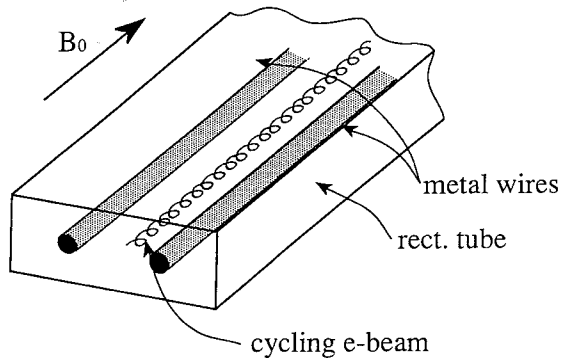


Fig. 1. Schematic of the TEM-mode cyclotron maser device.

sity [9,10]. The oscillator tube consists of a planer-diode electron gun, a non-dispersive parallel-line waveguide (shown in Fig. 1), a solenoid, and a kicker coil. A low-energy, low-current electron beam ( $< 5$  keV,  $< 1$  A) is injected into the waveguide and interacts with the TEM

wave. The uniform solenoidal magnetic field maintains the electron cyclotron motion along its axis. The electron beam is dumped at the exit of the interaction region onto a collector which is also used to measure the electron current.

Three synchronized pulsers generate the solenoid, the e-gun, and the kicker pulses, as described in Ref. [10]. The electron gun high-voltage pulser (1 ms pulse width) [11] and the high-current kicker pulser are triggered at the peak of the 25 ms width solenoid pulse.

The impedance of the parallel-line waveguide in the odd TEM mode is  $\sim 200 \Omega$ . The waveguide is terminated in the CRM oscillator cavity by two partial mirrors at both ends. The mirror near the electron gun has a hole at the center for the electron beam entrance. The mirror at the collector has an SMA ( $50 \Omega$ ) RF connector attached to each wire. These terminations form a cavity with a low quality factor ( $Q < 200$ ).

The low-energy solid electron beam is generated by a simple planar diode electron gun, which consists of a

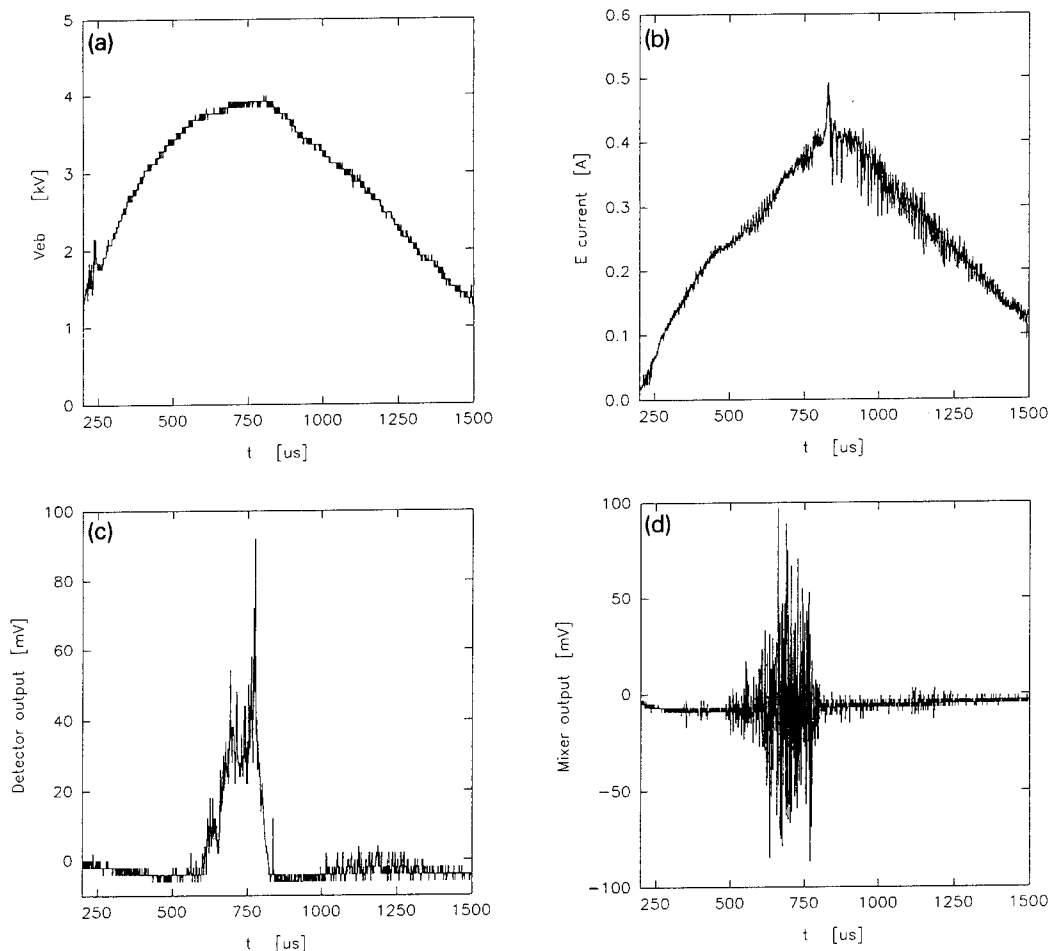


Fig. 2. Typical experimental results of the TEM-CRM oscillator. (a) The electron gun voltage. (b) The electron beam current measured in the collector. (c) The microwave detected output power. (d) The heterodyne mixer output.

dispenser thermionic cathode (Spectra-Mat, STD200) and a planar anode. The electron beam diameter is 4 mm and its filling factor for the odd TEM-mode is estimated to be 2.5%. A kicker coil spins up the electron beam at the entrance to the solenoid. The axial solenoid field is 1–2 kG. The waveguide is terminated by a collector section connected to ground by a 10  $\Omega$  resistor which measures the electron current.

The RF power generated in the cyclotron oscillator is coupled by a small dipole antenna into a WR187 waveguide section which acts as a high-pass filter (its cutoff frequency is 3.15 GHz). The signal is coupled out by a coaxial probe and is split into two arms, as in Refs. [9,10]. In the power measurement arm, the signal is attenuated and detected by an HP424A power detector. In the heterodyne measurement arm, the signal is mixed with a fixed LO signal from an external RF oscillator. The mixer output is filtered by the internal 20 MHz low-pass filter of a Tektronix TDS 540 digital oscilloscope. This heterodyne measurement shows the spectral contents of the CRM oscillator output shifted by the LO frequency. Typical output signal measurements are presented in the next section.

#### 4. Experimental results

Typical results of the TEM-CRM oscillator experiment are shown in Figs. 2a–2d. Figs. 2a and 2b show the electron gun voltage variation during the pulse and the corresponding electron beam current measured in the collector section, respectively. Figs. 2c and 2d show the detected microwave power and the corresponding microwave heterodyne detection output, respectively.

The output signal of the mixer shown in Fig. 2d is observed with an LO frequency of 4.5 GHz and a solenoid field of  $\sim 1.6$  kG. Hence, the corresponding cyclotron frequency is close to the radiation frequency within the accuracy limit of the experimental setup. According to the tuning relation of Eq. (4), the result  $\omega \cong \omega_c$  indicates that  $V_z \sim 0$ , and, consequently, the CRM operates with a large pitch ratio  $V_\perp \gg V_z$ . The total electron velocity in this experiment is  $0.12c$ , and it turns out that most of it is imparted to the transverse cyclotron motion.

The oscillator frequency is tuned by varying the solenoid field. The heterodyne results in Fig. 3 show the mixer output (RMS) for various LO frequencies, with different solenoid fields. The CRM tunability in this setup is demonstrated in the frequency range of 3.2–4.8 GHz. Lower frequencies are measured as well without the high-pass filter at the exit of the cavity. The spectral contents of the TEM-CRM emission for each value of the solenoid field is close to the corresponding cyclotron frequency (3), with some line widening. The bandwidth observed is  $\sim 10\%$ . It is considerably larger than expected from the axial velocity spread of the spiraling electron beam ( $\sim 2\%$

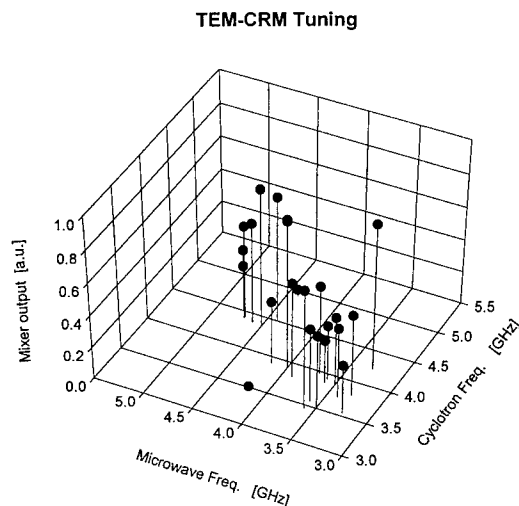


Fig. 3. Output heterodyne signal (RMS) measurements for various LO and cyclotron frequencies.

to satisfy the condition in Eq. (1)). This line widening is explained by the nonuniformity of the solenoid field at its ends, and by the narrow spikes observed in the oscillator output. A tunability range of over one octave in the range 2–5 GHz is observed in this experiment without the high-pass filter.

#### 5. Conclusions

The cyclotron maser oscillator experiment presented in this paper shows a strong cyclotron interaction between a low-energy electron beam orbiting in an axial magnetic field and a TEM wave propagating in a nondispersive waveguide. The coupling occurs only with a considerable kicker field. The kicker induces a large transverse electron velocity component, as required by Eq. (1). A wide tunability of the TEM-CRM is demonstrated in this experiment.

Further studies of the TEM-CRM device are needed in order to investigate the effects of the electron velocity spread, and to examine novel kicker mechanisms. Our recent experimental results show, however, the feasibility of a long-wavelength nonrelativistic CRM device in a non-dispersive metallic waveguide.

#### Acknowledgements

This research is supported by the Israeli Ministry of Energy and by the Belfer Foundation for Energy Research.

**References**

- [1] S.K. Ride and W.B. Colson, Appl. Phys. 2050 (1979) 41.
- [2] A. Fruchtman, J. Appl. Phys. 54 (1983) 4289.
- [3] F.A. Korolev and A.F. Kurin, Radio Eng. Electron. Phys. 15 (1970) 1868.
- [4] E.C. Morse and R.V. Pyle, J. Vac. Sci. Technol. 3 (1985) 1239.
- [5] N.A. Ebrahim, Z. Liang and J.L. Hirshfield, Phys. Rev. Lett. 49 (1982) 1556.
- [6] A.F. Kurin, G.A. Kurina and V.V. Novikov, Radiophys. Quantum Electron. QE-19 (1976) 742.
- [7] P. Sprangle, J.L. Vomvoridis and W.M. Manheimer, Appl. Phys. Lett. 38 (1981) 310.
- [8] E. Jerby et al., Cyclotron resonance maser experiment in a non-dispersive waveguide, in preparation.
- [9] E. Jerby, G. Bekefi and A. Shahadi, Nucl. Instr. and Meth. A 341 (1994) 115.
- [10] E. Jerby, A. Shahadi, V. Grinberg, V. Dikhtiar, M. Sheinin, E. Agmon, H. Golombek, V. Trebich, M. Bensal and G. Bekefi, Cyclotron maser oscillator experiments in a periodically loaded waveguide, IEEE J. Quantum Electron, to be published.
- [11] V. Grinberg, E. Jerby and A. Shahadi, these Proceedings (16th Int. Free Electron Laser Conf., Stanford, CA, 1994) Nucl. Instr. and Meth. A 358 (1995) 327.

# Green function analysis of a Raman FEL

G. Shvets<sup>\*</sup>, J.S. Wurtele

*Department of Physics and Plasma Fusion Center, Massachusetts Institute of Technology, Cambridge, MA 02139, USA*

## Abstract

This paper derives, in closed form, the Green function of an FEL operating in the strongly Raman regime. This Green function allows for the calculation of the temporal and spacial evolution of an arbitrary input radiation pulse. For the first time superradiance, originally studied in Compton regime by Bonifacio and co-workers [Phys. Rev. Lett. 73 (1994) 70; Nucl. Instr. and Meth. A 239 (1985) 36], has been seen numerically in a strongly Raman FEL.

## 1. Introduction

The desire to build compact free-electron lasers and to develop high-power microwave sources often requires operation in the Raman regime. To date many of the experiments in the Raman regime have not had significant effects from slippage. There are applications, such as RF accelerator power sources, where detailed knowledge and control of the phase and amplitude of the free-electron laser (FEL) output is of critical importance. With the improving performance of photocathode guns, FEL experiments, using RF linacs as drivers, with modest beam energies and high currents, may operate in the high gain Raman regime with strong slippage.

Most theoretical research for the free-electron laser (FEL) operating in the Raman regime has concentrated on either the linear growth in an amplifier, the derivation and solution of nonlinear equations for the self-consistent coupling between particles and fields, and comparison of simulations with experiments. The desire to build compact FELs and to develop high-power microwave sources often requires operation in the Raman regime.

The approach used here is to first formulate the linear FEL equations, including space-charge, in integral form, solve the equations by Fourier–Laplace transform in the limit of a strongly Raman FEL and perform an inverse transform to find the Green function. An exact expression for the Raman regime Green function is obtained in the limit of a long electron pulse. The expression is fully causal, is valid for high and low gain and includes all launching losses. Effects similar to Compton regime superradiance are found.

## 2. Integral equation

This paper follows the formalism of Ref. [1], where the normalized independent variables are

$$\bar{s} = \frac{2\gamma_z^2 c}{N_w \lambda_w} \left( t - \frac{z}{v_g} \right), \quad (1)$$

$$\bar{z} = z / (N_w \lambda_w). \quad (2)$$

These variables are chosen so that  $\bar{s}$  propagates with the optical pulse and is measured in units of the slippage length, and interaction length  $z$  is normalized to the wiggler length; thus  $d\bar{s}/d\bar{z} = 1$ . The free-streaming phase of a particle in the ponderomotive wave is given by

$$\theta_0 = 2\pi N_w (\bar{z} - \bar{s}) + \bar{s} (k_w - k_z / 2\gamma_z^2) N_w \lambda_w, \quad (3)$$

where  $N_w$  is the number of wiggler periods,  $\lambda_w$  is the wiggler period,  $\gamma_z$  is the electron relativistic factor calculated from the parallel velocity,  $c$  is the speed of light, and  $v_g$  is the group velocity of light and the normalized detuning over the wiggler is

$$y_0 = (k_w - k_z / 2\gamma_z^2) N_w \lambda_w.$$

Within the context of a cold beam fluid model valid prior to saturation, the FEL evolution equations for an arbitrary gain during a single pass through the wiggler can be written as:

$$\frac{\partial \hat{a}}{\partial \bar{z}} = \frac{2\pi i a_w L_w r_e \delta n \exp(-i\theta)}{\gamma k}, \quad (4)$$

$$\begin{aligned} \frac{d^2 \theta}{d\bar{z}^2} = & i \frac{8\pi^2 N_w^2 a_w}{1 + a_w^2} \hat{a}[\bar{s}(\bar{z}), \bar{z}] \exp(i\theta) \\ & - i \frac{\omega_p^2 N_w^2 \lambda_w^2}{c^2 \gamma_z^2} \frac{\delta n}{n_0}, \end{aligned} \quad (5)$$

$$y_0 = \frac{d\theta}{d\bar{z}}(\bar{z} = 0), \quad \theta_0 = \theta(\bar{z} = 0). \quad (6)$$

<sup>\*</sup> Corresponding author. Tel. +1 617 253 5952, fax +1 617 258 7864, e-mail gena@ilm.pfc.mit.edu.

In this notation the normalized slowly varying complex amplitude of the field is  $\hat{a}(\bar{s}, \bar{z})$ , the detuning is  $y_0$ , the Lagrangian phase variable is  $\theta$ , the wiggler amplitude is  $a_w$ ,  $L_w = N_w \lambda_w$ ,  $k = 2\pi/\lambda$  is the radiation wavenumber,  $\omega_p^2 = 4\pi e^2 n_0/m$  is the non-relativistic beam plasma frequency, and the density perturbation  $\delta n$  can be expressed in terms of the phase as:

$$\delta n = -n_0(\bar{s} - \bar{z}) \left( \frac{\partial \theta(\theta_0, \bar{z})}{\partial \theta_0} - 1 \right), \quad (7)$$

where  $n_0$  is the beam density. Note that  $t - z/v_z = (N_w \lambda_w/c)(\bar{s} - \bar{z})$ . We will assume here that the unperturbed beam density  $n_0$  is constant. A related analysis with a nonuniform beam density is presented in another paper [2]. The second term in Eq. (5) is due to the space-charge force.

In linear theory, the phase can be expanded as:

$$\begin{aligned} \theta = \theta_0 + y_0 \bar{z} + \int_0^{\bar{z}} d\bar{z}' \int_0^{\bar{z}'} d\bar{z}'' \\ \times \left( \frac{i8\pi^2 a_w N_w^2}{1 + a_w^2} \exp[i(y_0 \bar{z}'' + \theta_0)] \hat{a}(\bar{s} - \bar{z} + \bar{z}'', \bar{z}'') \right. \\ \left. - i \frac{\omega_p^2 N_w^2 \lambda_w^2}{c^2 \gamma \gamma_z^2} \frac{\delta n}{n_0} (\bar{s} - \bar{z} + \bar{z}'', \bar{z}'') \right). \end{aligned} \quad (8)$$

Note that  $\bar{s} - \bar{z} = \bar{s}_0$  is the Lagrangian entrance time of a particle into the wiggler.

An integro-differential equation for the field can be obtained:

$$\begin{aligned} \frac{\partial \hat{a}(\bar{z}, \bar{s})}{\partial \bar{z}} + \frac{\omega_p^2 N_w^2 \lambda_w^2}{c^2 \gamma \gamma_z^2} \int_0^{\bar{z}} d\bar{z}' \int_0^{\bar{z}'} d\bar{z}'' \frac{\partial \hat{a}}{\partial \bar{z}''} (\bar{s} - \bar{z} + \bar{z}'', \bar{z}'') \\ \times \exp[iy_0(\bar{z}'' - \bar{z})] \\ = i j_c \int_0^{\bar{z}} d\bar{z}' \int_0^{\bar{z}'} d\bar{z}'' \hat{a}(\bar{s} - \bar{z} + \bar{z}'', \bar{z}'') \\ \times \exp(iy_0(\bar{z}'' - \bar{z})), \end{aligned} \quad (9)$$

where  $j_c = 4\pi a_w^2 N_w^3 \lambda_w^2 I / (\gamma^3 r_b^2 I_A)$ ,  $I$  is the beam current,  $r_b$  is the beam radius, and  $I_A = 17$  kA. An integral equation formulation was used for the Compton FEL in Ref. [3].

### 3. Dispersion relation

Eq. (9) can be solved by a Fourier transform in  $\bar{s}$  to arrive at

$$\begin{aligned} \frac{\partial \hat{a}(\omega, \bar{z})}{\partial \bar{z}} + \frac{\omega_p^2 N_w^2 \lambda_w^2}{c^2 \gamma \gamma_z^2} \int_0^{\bar{z}} d\bar{z}' \int_0^{\bar{z}'} d\bar{z}'' \frac{\partial \hat{a}}{\partial \bar{z}''} (\omega, \bar{z}'') \\ \times \exp[i(y_0 - \omega)(\bar{z}'' - \bar{z})] \end{aligned}$$

$$= i j_c \int_0^{\bar{z}} d\bar{z}' \int_0^{\bar{z}'} d\bar{z}'' \hat{a}(\omega, \bar{z}'') \times \exp[i(y_0 - \omega)(\bar{z}'' - \bar{z})], \quad (10)$$

and then a Laplace transform in  $\bar{z}$  using

$$\hat{a}(\omega, \Gamma) = \int_0^\infty d\bar{z} \exp(i\Gamma \bar{z}) \hat{a}(\omega, \bar{z}) \quad (11)$$

with the requirement that the initial field derivatives vanish:

$$\frac{\partial \hat{a}(\bar{z} = 0, \bar{s})}{\partial \bar{z}} = \frac{\partial^2 \hat{a}(\bar{z} = 0, \bar{s})}{\partial \bar{z}^2} = 0. \quad (12)$$

The result can be found in the literature (for example, a Green function approach was used to study start-up in a Raman regime oscillator [4] and superradiance and growth from noise in a high gain amplifier [5]) so we omit the details here. The main point of this paper is to show that for a strongly Raman FEL a closed form for the Green function can be derived and to study Raman superradiance.

After an inverse Laplace transform, one obtains:

$$\begin{aligned} \hat{a}(\omega, \bar{z}) = j_c \hat{a}(\omega, \bar{z} = 0) \left( \frac{e^{i\Gamma_1 \bar{z}}}{\Gamma_1(\Gamma_1 - \Gamma_2)(\Gamma_1 - \Gamma_3)} \right. \\ \left. + \frac{e^{i\Gamma_2 \bar{z}}}{\Gamma_2(\Gamma_2 - \Gamma_3)(\Gamma_2 - \Gamma_1)} \right. \\ \left. + \frac{e^{i\Gamma_3 \bar{z}}}{\Gamma_3(\Gamma_3 - \Gamma_2)(\Gamma_3 - \Gamma_1)} \right). \end{aligned} \quad (13)$$

where the roots  $\Gamma_j$  satisfy the cubic dispersion relation:

$$\Gamma((\Gamma + y_0 - \omega)^2 - k_b^2) = -j_c. \quad (14)$$

Here the relativistic beam plasma frequency is  $k_b^2 = N_w^2 \lambda_w^2 \omega_p^2 / c^2 \gamma \gamma_z^2$ . The usual steady-state complex gain is recovered by taking  $\omega = 0$ .

For an FEL in the strong Raman regime the above cubic reduces to a quadratic, in the usual way, by assuming the detuning is near to the slow space-charge wave and the growth rate is much smaller than the beam plasma frequency. In this approximation,

$$\Gamma(\Gamma + y - k_b) = -\mu^2/4, \quad (15)$$

where  $\mu^2 = 2j_c/k_b$  and  $y = y_0 - \omega$ . The Green function is then:

$$\begin{aligned} G_{\bar{z}}(\bar{s}) = \frac{\mu^2}{4} \int_{-\infty + i\delta}^{\infty + i\delta} d\omega \exp(i\omega \bar{s}) \\ \times \left\{ \frac{e^{i\Gamma_1(y)\bar{z}}}{\Gamma_1(y)(\Gamma_1(y) - \Gamma_2(y))} \right. \\ \left. + \frac{e^{i\Gamma_2(y)\bar{z}}}{\Gamma_2(y)(\Gamma_2(y) - \Gamma_1(y))} \right\}, \end{aligned} \quad (16)$$

and the roots

$$\Gamma_1 = \frac{y - k_b}{2} + \frac{1}{2} \sqrt{(y - k_b)^2 - \mu^2}, \quad (17)$$

$$\Gamma_2 = \frac{y - k_b}{2} - \frac{1}{2} \sqrt{(y - k_b)^2 - \mu^2}. \quad (18)$$

#### 4. Explicit Green function

Carefully performing the inverse Laplace transform (Eq. (16)) yields an explicit expression for the Green function for the field evolution from a given initial field, and a parallel analysis yields the evolution of the field from the input noise in  $\delta n$ . The result is

$$\begin{aligned} a_1(\bar{z}, \bar{s}) &= a_1(\bar{s})|_{\bar{z}=0} + \int_{\bar{s}-\bar{z}}^{\bar{s}} d\bar{s}' G_a(\bar{z}, \bar{s} - \bar{s}') a_1(\bar{s}')|_{\bar{z}=0} \\ &\quad + \frac{2\pi i L_w a_w r_e}{\gamma k} \int_{\bar{s}-\bar{z}}^{\bar{s}} d\bar{s}' G_n(\bar{z}, \bar{s} - \bar{s}') \frac{\delta n}{n_0}(\bar{s}') \end{aligned} \quad (19)$$

with the Green functions  $G_a$  and  $G_n$  given by

$$\begin{aligned} G_a(\bar{z}, \bar{s}) &= \frac{\mu}{2} \frac{(\bar{z} - \bar{s})^{1/2}}{\bar{s}^{1/2}} \\ &\quad \times \exp(i\bar{s}(k_b - y_0)) I_1(\mu \bar{s}^{1/2} (\bar{z} - \bar{s})^{1/2}), \end{aligned} \quad (20)$$

$$G_n(\bar{z}, \bar{s}) = \exp(i\bar{s}(k_b - y_0)) I_0(\mu \bar{s}^{1/2} (\bar{z} - \bar{s})^{1/2}). \quad (21)$$

Here  $I_1$  and  $I_0$  are the usual modified Bessel functions. As is expected from causality, both functions vanish for  $\bar{s} < 0$

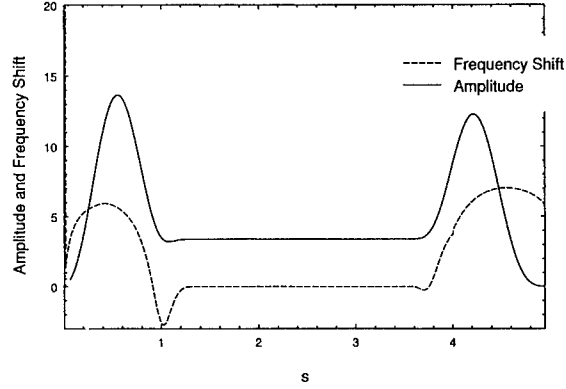


Fig. 2. Field amplitude and frequency shift (with respect to the initial detuning) at the end of the wiggler. As can be seen, superradiant spikes have formed at the pulse edges and have grown by frequency shifting the initial pulse into the gain bandwidth (peak gain corresponds to a frequency shift of 10.5).

and  $\bar{s} > \bar{z}$ . In the absence of initial density perturbation, and in the limit that the coupling goes to zero, i.e.,  $\mu = 0$ , the field amplitude propagates unaltered for any pulse shape (since  $G_a = 0$ ). The expression is fully causal, is valid for high and low gain and includes slippage, all launching losses, and start up from noise (SASE in the Raman regime).

We can recover the steady-state case with an initially time independent radiation field of the form

$$\hat{a}(\bar{s}, \bar{z} = 0) = a_0,$$

and no density perturbation. The steady-state amplified field can be found, using some well known Bessel function relations, to be:

$$\hat{a}(\bar{s}, \bar{z}) = a_0 \cosh(\mu \bar{z}/2).$$

#### 5. Superradiance

Superradiance has been studied in the Compton regime [5]. It is also present in the Raman regime. Superradiant spikes are seen when an initially flat-top pulse enters the wiggler detuned out of the growth bandwidth. The pulse evolution is shown in Figs. 1 and 2. In Fig. 1 the initial field amplitude is shown at the entrance of the wiggler. The gain corresponds to  $\mu = 10$  and  $y_0 - k_b = 10.5$ , or a 5% detuning from the gain bandwidth around the slow space-charge wave. Thus in steady state there would be no exponential growth. In Fig. 2 the amplitude and frequency shift (with respect to the initial detuning) at the end of the wiggler are plotted. As can be seen, superradiant spikes have formed at the pulse edges and have grown by frequency shifting the initial pulse into the gain bandwidth (peak gain corresponds to a frequency shift of 10.5 in Fig. 2). This shifting is gradual, rather than instantaneous – the

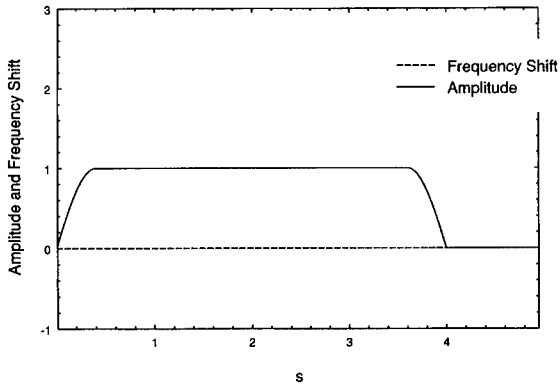


Fig. 1. The initial field amplitude is shown at the entrance of the wiggler. The gain corresponds to  $\mu = 10$  and  $y_0 - k_b = 10.5$ , or a 5% detuning from the gain bandwidth around the slow space-charge wave.

superradiant process involves both growth and frequency shifts. The peak gain frequency is reached only asymptotically, after many  $-e$ -foldings.

The calculated Green functions are responses to delta-function perturbations. One can show that the maximum of the Green function occurs at  $\bar{s} = \bar{z}/2$ , corresponding to a group velocity of  $v_g = (c + v_b)/2$ . This is a manifestation of laser lethargy in the strongly Raman regime.

#### Acknowledgements

This work is supported by the US Department of Energy, Division of High-Energy Physics and the Air Force Office of Scientific Research.

#### References

- [1] G. Shvets and J.S. Wurtele, Phys. Plasmas 1 (1994) 157.
- [2] S. Ishii, G. Shvets and J.S. Wurtele, these Proceedings (16th Int. Free Electron Laser Conf., Stanford, CA, USA, 1994) Nucl. Instr. and Meth. A 358 (1995) 489.
- [3] W.B. Colson, IEEE J. Quantum Electron. QE-17 (1) (1981) 417.
- [4] E. Jerby, G. Bekefi and J.S. Wurtele, Phys. Rev. Lett. 66 (1989) 2068; E. Jerby, G. Bekefi and J.S. Wurtele, IEEE J. Quantum Electron. QE-27 (1991) 2512.
- [5] R. Bonifacio et al., Phys. Rev. Lett. 73 (1994) 70 and references therein; R. Bonifacio and F. Casagrande, Nucl. Instr. and Meth. A 239 (1985) 36.





ELSEVIER

# Free-electron maser oscillator experiment in the UHF regime

R. Drori, E. Jerby \*, A. Shahadi

*High-Power Microwave Laboratory, Faculty of Engineering, Tel Aviv University, Ramat Aviv 69978, Israel*

## Abstract

A nonrelativistic electron beam (< 4 keV) travels in this experiment in a non-dispersive waveguide along a planar undulator and an axial magnetic fields. The electron beam has a Gaussian pulse shape with a 1 ms pulse width. Two distinct radiation bursts are observed during the electron energy sweep. Each burst contains a different range of microwave frequencies. One burst corresponds to the FEM interaction, at ~ 0.8 GHz. The other burst corresponds to the cyclotron resonance interaction, at ~ 5 GHz. This experiment demonstrates an FEM operation in an extremely long wavelength (37.5 cm) in the UHF regime.

## 1. Introduction

A free-electron maser (FEM) experiment in the UHF regime (< 1 GHz) is presented. This FEM operates also in a mode of a cyclotron resonance maser (CRM) at ~ 5 GHz.

The static magnetic field is produced in this experiment by a combination of a solenoid and a planar undulator [1] as shown in Fig. 1. The total magnetic field on-axis is given by  $B_0 \cong \hat{x}B_w \cos k_w z + \hat{z}B_0$ , where  $B_0$  and  $B_w$  are the axial magnetic field and the wiggler amplitudes, respectively, and  $k_w$  is the wiggler periodicity. The electron trajectory is, consequently, a superposition of a wiggling motion and a cyclotron motion. The cyclotron wavenumber is  $k_c = \omega_c / \bar{v}_z$ , where  $\bar{v}_z$  is the electron average axial velocity component.  $\omega_c = eB_0 / \gamma m$  is the angular cyclotron frequency, and  $e$ ,  $m$ , and  $\gamma$  are the electron charge, mass, and relativistic factor, respectively.

The superposition of the cyclotron and the wiggling motions results in two corresponding conditions for synchronism between the electrons and a TEM-wave in the non-dispersive waveguide. The FEM resonance condition is

$$\omega_{\text{FEM}} = \frac{\bar{v}_z k_w}{1 \pm \bar{v}_z / c}, \quad (1a)$$

and the cyclotron resonance condition is

$$\omega_{\text{CRM}} = \frac{\omega_c}{1 \pm \bar{v}_z / c}, \quad (1b)$$

where the  $\pm$  signs correspond to forward and backward waves in the oscillator cavity.

During the electron energy sweep in the Gaussian pulse, the undulator and the cyclotron interactions may excite different radiation frequencies according to Eqs. (1a) and (1b). These interactions are expected in different electron energies and longitudinal cavity modes.

## 2. Experimental setup

A general view of the FEM experimental device with the non-dispersive waveguide is shown in Fig. 1. The experimental setup is based on the CRM experiment [2] at Tel Aviv University. The oscillator tube consists of a planar-diode electron gun, a coplanar waveguide, a solenoid, and a planar folded-foil undulator. A low-energy electron beam is injected into the waveguide and interacts with the TEM wave. The electron beam is dumped at the exit of the interaction region onto a collector which is also used to measure the electron current. The experimental parameters are listed in Table 1.

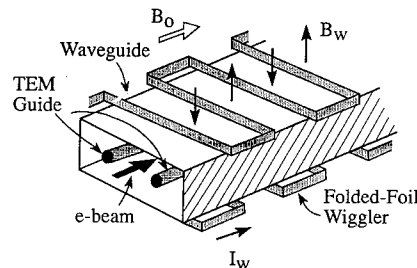


Fig. 1. A scheme of the low-voltage FEM in a non-dispersive waveguide.

\* Corresponding author. Tel. +972 3 6408048, fax +972 3 6423508, e-mail jerby@taunivm.tau.ac.il.

Table 1  
Experimental parameters

|                            |         |                     |
|----------------------------|---------|---------------------|
| Electron beam              |         |                     |
| Energy                     | < 4     | [keV]               |
| Current                    | < 0.5   | [A]                 |
| Pulse width                | ~ 1     | [ms]                |
| Magnetic field             |         |                     |
| Uniform solenoid           | 2.0     | [kG]                |
| Folded-foil undulator:     |         |                     |
| Strength                   | 0.2     | [kG]                |
| Period                     | 2.0     | cm                  |
| TEM waveguide              |         |                     |
| Rectangular tube           | 0.9×0.4 | [in. <sup>2</sup> ] |
| Parallel wires:            |         |                     |
| Wire diameter              | 1.9     | [mm]                |
| Distance between centers   | 11      | [mm]                |
| Cavity length              | 75      | [cm]                |
| Microwave output frequency |         |                     |
| Pulse A – Cyclotron        | ~ 5     | [GHz]               |
| Pulse B – FEM              | ~ 0.8   | [GHz]               |

Three synchronized pulsers generate the solenoid, the e-gun, and the wiggler pulses, as described in Ref. [2]. The e-gun pulser [3] and the high-current wiggler pulser are triggered at the peak of the 20 ms solenoid pulse.

The undulator used in this experiment is a coaxially-fed folded-foil wiggler as described in Ref. [4]. The wiggler strength  $B_w$  depends on the current  $I_w$  in its windings and is given by  $B_w = (2\mu_0 I_w N / \lambda_w) \text{sech}(k_w h / 2)$ , where  $\lambda_w$  is the wiggler period,  $N$  is the number of winding layers, and  $h$  is the wiggler gap. In this experiment,  $\lambda_w = 2$  cm,  $h = 1.4$  cm,  $I_w \leq 400$  A, and  $N = 3$ . The maximum wiggler magnetic field on-axis is 0.33 kG.

The non-dispersive waveguide shown in Fig. 1 consists of two metal wires stretched along a standard WR90 rectangular tube. The wires are supported by two small ceramic (Macor) holders at the center of the waveguide. The impedance of the coplanar waveguide is  $\sim 200 \Omega$ . The cavity is terminated at both ends by two partial mirrors. The mirror near the electron gun has a hole at the center for the electron beam entrance. The mirror at the collector has two SMA (50  $\Omega$ ) RF connectors connected outside the cavity by a wire which forms a small antenna for the output detection as shown in Fig. 2. These terminations form a cavity with a low quality factor ( $Q \sim 200$ ). Cold measurements of the 75 cm cavity show resonance frequencies separated by  $\sim 200$  MHz, with small deviations related to the reactive loads of the partial mirrors at the ends of the waveguide.

The RF power generated in the oscillator is detected by the apparatus shown in Fig. 2. The output signal is sampled by a small dipole antenna and is split into two arms. In one arm, the signal is attenuated and detected by an HP8474 barrier detector. In the other arm, the signal is

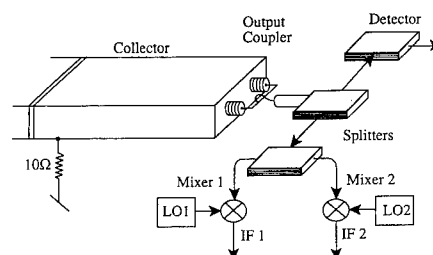


Fig. 2. The microwave diagnostic setup.

split again into two mixers. It is mixed with two local oscillator (LO) signals generated by two external RF oscillators. The mixer outputs are filtered by the internal 20 MHz low-pass filter of a Tektronix TDS 540 digital oscilloscope. This arrangement enables the simultaneous heterodyne measurement of two frequencies in the maser radiation output. In particular, the mixer heterodyne outputs can show the spectral contents of the FEM and the

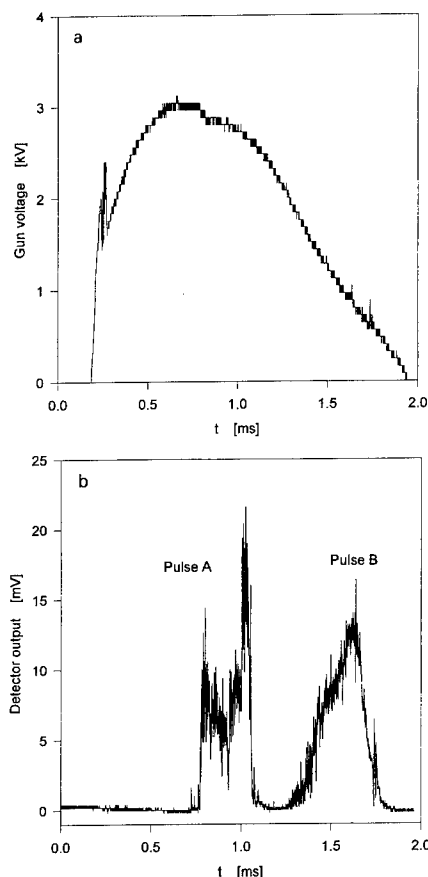


Fig. 3. Typical experimental measurements of two radiation bursts in a single shot. (a) The electron gun voltage. (b) The microwave detected power.

CRM interactions shifted by the corresponding LO frequency.

### 3. Experimental results

Typical signal measurements of the FEM oscillator are presented in this section. Fig. 3a shows the voltage variation of the electron pulse vs. time. The microwave power excited in the oscillator is shown in Fig. 3b as the power detector output. Two microwave pulses, denoted by A and B, are observed in the detector output in Fig. 3b in the energy levels 2.7 keV and 0.9 keV, respectively. Similar signals have been obtained in over one hundred shots in this experiment. The double heterodyne detection provides a simultaneous measurement of the center frequencies of the two microwave pulses. Each mixer output correlates clearly with each RF pulse. The results show that a 4.93 GHz mixer output coincides with pulse A, and a 0.80 GHz mixer output coincides with pulse B.

A parametric analysis shows an agreement between the

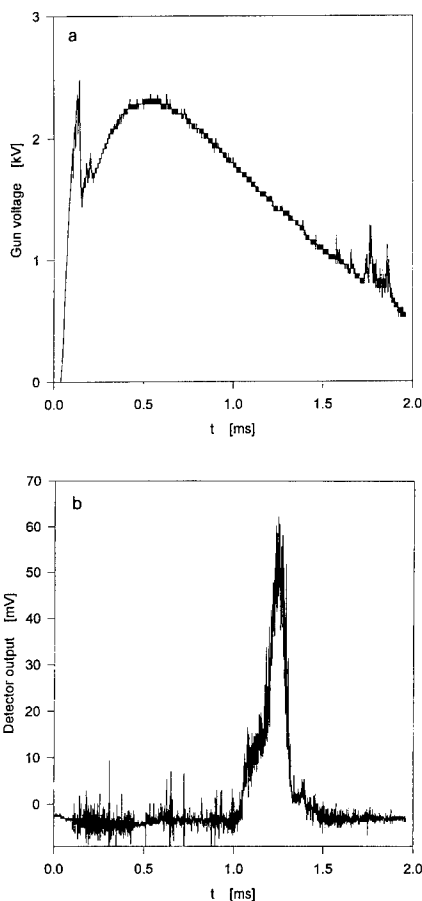


Fig. 4. Typical experimental measurements of one radiation burst in a low-energy electron beam. (a) The electron gun voltage. (b) The microwave detected power.

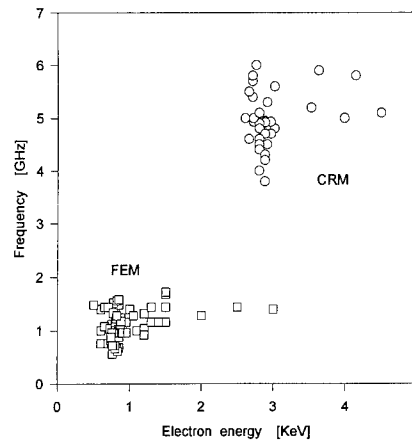


Fig. 5. A frequency–energy map of the FEM and CRM bursts in a 0.4–6.0 GHz LO scan.

tuning relations in Eqs. (1a) and (1b) and the operating conditions of pulses B and A, respectively. Hence, pulse A corresponds to the cyclotron resonance interaction, and pulse B corresponds to the FEM interaction.

A solely FEM interaction is presented in Figs. 4a and 4b, which show the electron gun voltage, and the detector output, respectively. The FEM emission is observed at 825 MHz, without an accompanied CRM interaction. The peak energy in this case, 2.5 keV, is too small to excite the CRM interaction, as observed in the previous example shown in Fig. 3.

A summary of runs performed in this experiment with various LO frequencies in the range of 0.4 GHz to 6 GHz is presented in Fig. 5 in a form of a frequency–energy map. The circles and squares denote observations of mixer outputs in pulse A and pulse B, respectively, with various LO frequencies. Two distinct groups are clearly observed in the map. The spectral content of pulse A is centered around 5 GHz ( $\pm 1$  GHz) with an electron beam energy centered around 3 keV. The other group in the map, related to pulse B, is centered around 1 GHz and 1 keV. The average values of the two groups (5 GHz at 3 keV for pulse A, and 1 GHz at 1 keV for pulse B) agree well with the corresponding tuning conditions of Eqs. (1b) and (1a). Hence, pulses A and B obtained in many shots are related to the CRM and FEM interactions, respectively. The spectral line widening of the radiation observed might be related to various causes including the axial velocity spread of the electrons, the solenoid field non-uniformity at its ends, and the narrow spikes observed in the detected power.

### 4. Conclusions

This experiment demonstrates FEM and CRM interactions with TEM modes in a non-dispersive waveguide. The operating FEM frequency is measured in the UHF regime

(< 1 GHz) with an electron energy around 1 keV. In higher energies, around 3 keV, the cyclotron interaction is excited at  $\sim 5$  GHz, in addition to the FEM interaction. For the CRM interaction, the undulator acts as a distributed kicker which rotates the electron beam, as described in Ref. [5].

The FEM operates in this experiment in an exotic operating regime, in which  $\lambda \gg \lambda_w$ . To the best of our knowledge [6], this is a first demonstration of a low-voltage FEM operation in the UHF regime.

### Acknowledgement

This work is supported in part by the Abraham Shechterman Foundation.

### References

- [1] Y.Z. Yin and G. Bekefi, J. Appl. Phys. 55 (1984) 33.
- [2] A. Shahadi, E. Jerby, M. Korol, R. Drori, M. Sheinin, V. Dikhtiar, V. Grinberg, I. Ruvinsky, M. Bensal, T. Harel, Y. Baron, A. Fruchtman, V.L. Granatstein and G. Bekefi, these Proceedings (16th Int. Free Electron Laser Conf., Stanford, CA, USA, 1994) Nucl. Instr. and Meth. A 358 (1995) 143.
- [3] V. Grinberg, E. Jerby and A. Shahadi, *ibid.*, p. 327.
- [4] A. Sneh and E. Jerby, Nucl. Instr. and Meth. A 285 (1989) 294.
- [5] A.C. DiRienzo, G. Bekefi, C. Chen and J.S. Wurtele, Phys. Fluids B 3 (1991) 1755.
- [6] H.P. Freund and V.L. Granatstein, Ref. [2], p. 551.



ELSEVIER

## A 130–260 GHz, 1 MW free electron maser for fusion

W.H. Urbanus <sup>a,\*</sup>, W.A. Bongers <sup>a</sup>, G. van Dijk <sup>a</sup>, C.A.J. van der Geer <sup>a</sup>, J.P. van Ieperen <sup>a</sup>,  
A. van der Linden <sup>a</sup>, P. Manintveld <sup>a</sup>, A.B. Sterk <sup>a</sup>, A.V. Tulupov <sup>a</sup>, A.G.A. Verhoeven <sup>a</sup>,  
M.J. van der Wiel <sup>a</sup>, V.L. Bratman <sup>b</sup>, G.G. Denisov <sup>b</sup>, A.A. Varfolomeev <sup>c</sup>,  
S.N. Ivanchenkov <sup>c</sup>, A.S. Khlebnikov <sup>c</sup>, M. Catellino <sup>d</sup>, A. Salop <sup>d</sup>, M. Caplan <sup>e</sup>

<sup>a</sup> FOM Instituut voor Plasmafysica “Rijnhuizen”, Association EURATOM–FOM, P.O. Box 1207, 3430 BE Nieuwegein, The Netherlands

<sup>b</sup> Institute of Applied Physics, Uljanova Ulitsa 46, Nizhny Novgorod, 603600, Russian Federation

<sup>c</sup> Russian Research Centre Kurchatov Institute, Ulitsa Kurchatova 46, Moscow, 123182, Russian Federation

<sup>d</sup> Varian Associates, Inc., 811 Hansen Way, Palo Alto, CA 94304, USA

<sup>e</sup> Lawrence Livermore National Laboratory, POB 808, L-626, Livermore, CA 94550, USA

### Abstract

We report on design work and testing of several main components of the FOM-Fusion-FEM project. Measurements on the electron gun are presented, showing a uniform beam current profile and a low halo current. A time-dependent simulation study of the interaction between the electron beam and the mm-waves shows that, for proper undulator tapering, longitudinal mode competition results in a quasi single-mode regime. Further, some high power and detailed low power measurements on mock-ups of the waveguide system are presented, showing that the reflection and outcoupling systems perform well.

### 1. Introduction

The FOM Fusion Free-Electron Maser (FEM) is the pilot experiment to develop a tunable mm-wave source for plasma heating and control in future fusion experiments such as ITER. In such reactors plasma is confined by magnetic fields of the order 6 T, which sets the frequency range for electron cyclotron resonance heating to 130–260 GHz. Unit power level should be at least 1 MW at a system efficiency (grid to mm-wave power) of over 35%. Fast frequency tuning over several percent is required to follow and suppress plasma instabilities. Most of these parameters cannot be met by present day gyrotrons.

The aim of the FOM-FEM project is to generate 1 MW of output power, in the frequency range 130–260 GHz, in 100 ms pulses, with a tunability on the ms-scale of  $\pm 5\%$  and a system efficiency of over 50%.

The FEM design is presented elsewhere [1,2]. The FEM injector is a 12 A, 80 keV electron gun followed by a 2 MV dc accelerator. The accelerator voltage is used to set the mm-wave frequency. The dc accelerating voltage is supplied by a 2 MV, 25 mA Insulated Core Transformer (ICT). Because of the limited current, and to keep the generation of X-rays and thermal effects on beam line

components to a sufficiently low level, at least 99.8% of the beam current must be recovered. For this reason, a completely straight beam line will be used and a decelerator and depressed collector will recover the charge and energy of the unspent electron beam. The cathode of the gun is at ground potential, the undulator and mm-wave cavity are mounted inside a high voltage terminal at 2 MV, and the collector is near ground potential.

### 2. Electron gun tests

The electron beam emittance and the beam current distribution are crucial in this FEM. The reason is that a current loss of less than 20 mA is required in the entire beam line. The emittance is limited to  $150 \pi$  mm mrad, for 99.8% of the beam, by the acceptance of the beam line, which is set by the  $15 \times 20$  mm<sup>2</sup> cross section of the waveguide inside the undulator and the focusing properties of the undulator [3–5]. The interaction between the electron beam and the mm-waves requires a smaller normalised emittance, between 50 and  $90 \pi$  mm mrad [6]. Further, to prevent emittance growth down the beam line, the beam should have an homogeneous current density, or “top-hat profile”.

A triode-type thermionic gun has been produced by Varian [7]. A modulation electrode is located between the spherical-surfaced cathode at ground potential and the

\* Corresponding author. Tel. +31 3402 31224, fax +31 3402 31204, e-mail urbanus@rijnh.nl.

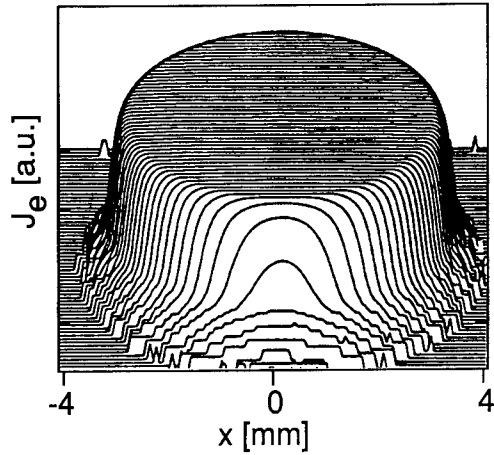


Fig. 1. Three-dimensional plot of the electron beam current density,  $J_e$ , as measured on a prototype gun, at  $z = 55$  mm behind the cathode. The plot is logarithmic.

anode at 80 kV. Beam profile measurements, shown in Fig. 1, have been performed at a number of longitudinal positions from the cathode. A top-hat profile is achieved for 85% of the total current. The normalised beam emittance is calculated to be  $60 \pi$  mm mrad for 99% of the beam current and less than  $150 \pi$  mm mrad for 99.8% of the beam current [7,8].

### 3. Simulations of the FEM mechanism

The FEM is a high gain oscillator using a two section, step-tapered undulator with 34 periods of 40 mm. The field strength is 0.2 T in the first 20 periods and 0.16 T in the subsequent 14 periods. Between the two sections is a drift gap. Further, the undulator has extra arrays of side magnets for electron beam focusing in both transverse directions [4,5]. Inside the undulator a rectangular corrugated waveguide is mounted, which carries a  $HE_{11}$  mode.

Numerical studies, using a single-frequency amplifier code, on the interaction of the electron beam with the transverse waveguide modes have shown that the FEM starts up in the main  $HE_{11}$  mode and operates steadily with more than 1 MW output power for a 25–30% reflection coefficient of the mm-wave system [6]. The reflection coefficient is the fraction of output power fed back to the entrance of the system (see also Section 4). These simulations have also shown that the linear gain curve has a peak at a higher frequency than the saturated gain curve. This implies an evolution of the spectrum until the FEM reaches saturation.

The competition of the longitudinal resonator modes has been the subject of recent simulations. The detailed results are presented separately at this Conference [9,10]. Here we summarize some main results.

The step in the undulator field has a strong influence on the frequency behaviour of the non-linear gain, as is

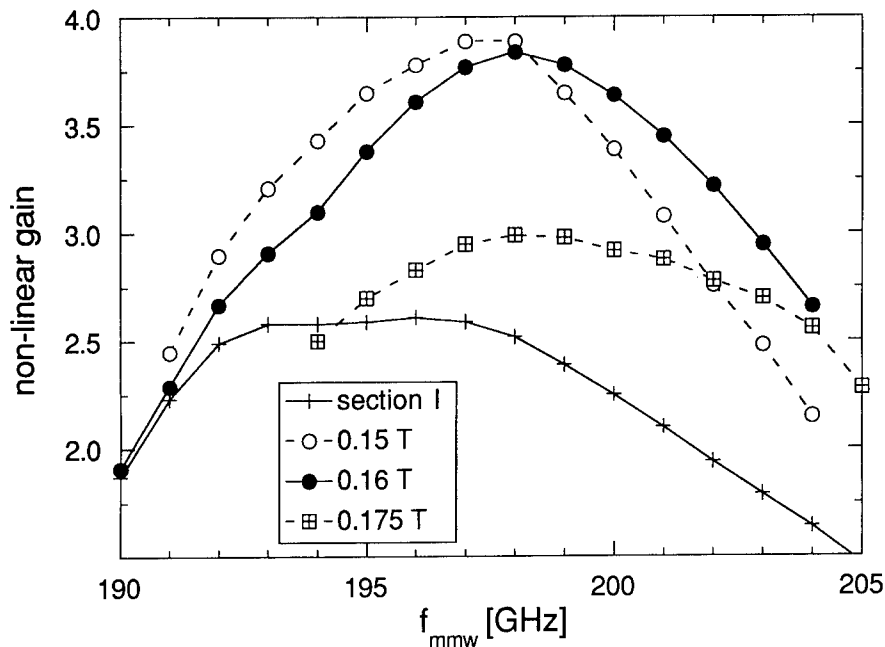


Fig. 2. The non-linear gain versus frequency,  $f_{\text{mmw}}$ , for different undulator strengths of Section 2. The lower curve gives the non-linear gain for section I only, where the undulator field is 0.2 T. The input power is adjusted such that saturation takes place at the end of the undulator. The electron beam current, energy and emittance are 12 A, 2 MeV and  $50 \pi$  mm mrad, respectively.

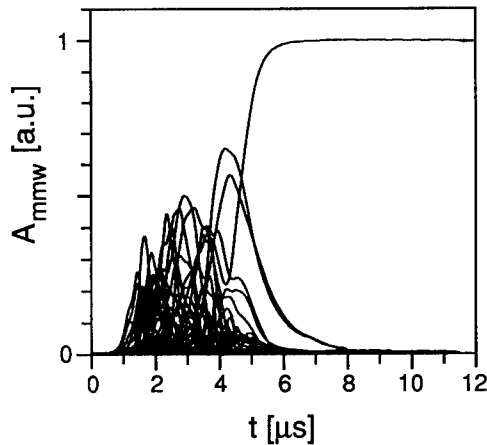


Fig. 3. Multi-frequency, time-dependent simulation of the evolution in time of the mm-wave field amplitude,  $A_{\text{mmw}}$ , at the exit of the undulator. Forty longitudinal resonator modes are taken into account, ranging from 190 to 210 GHz. The reflection coefficient is 24% for all frequencies. The electron beam parameters are as in Fig. 2. The undulator field in section 2 is 0.16 T.

illustrated in Fig. 2. The input signal is chosen such that saturation is just reached at the undulator exit. For an untapered undulator the curve is flat and broad, which means that a number of modes have roughly the same gain. A steady-state single-mode regime will not be reached. Instead, the evolution in time will show spiking. Adding a second undulator section with a slightly lower undulator field (0.2 T in section 1 and 0.175 T in section 2) makes the non-linear gain curve narrow and removes the flat part. Due to a small difference in gain for different modes there is a possibility of single-mode operation. The situation is improved further when the undulator strength is reduced to 0.16 T. In this case the gain curve has a prominent peak and one can find a stable single-mode regime. This analysis shows that, generally, step-tapering the undulator results in a peaked gain curve and stabilizes the FEM.

The reflection coefficient, the length of the drift gap and the beam current density have influence on the longitudinal mode competition too. A variation of these three parameters at the optimum values of the undulator fields allows one to suppress overbunching and to find single-mode regimes with an output power above 1 MW. The output power evolution in such a regime is shown in Fig. 3, where steady state is reached after 6  $\mu\text{s}$ . The drift gap between the undulator sections is 50 mm, i.e., 1.25 undulator periods. For this drift gap the linear gain has a minimum value and the saturated power has a maximum value, as obtained from single-frequency simulations [9]. A reflection coefficient of 24% was used for all frequencies taken into account. In reality the FEM will have frequency discrimination because of the finite bandwidth of the mm-

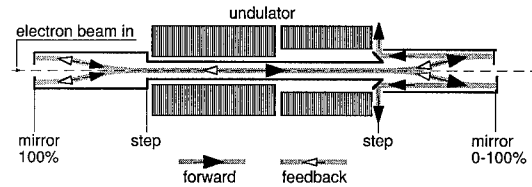


Fig. 4. Schematic layout of the mm-wave system. At both ends of the undulator the mm-wave beam is split into two off-axis beams. The straight electron beam passes between the mirrors, which are used for reflection and outcoupling of the mm-wave beams.

wave system (see Section 4). It is expected that in this case the single-mode regime sets in more quickly [9].

#### 4. mm-wave system tests

Inside the undulator is a corrugated rectangular waveguide, which carries a  $\text{HE}_{11}$  mode. Since the electron beam line will be completely straight, the mm-wave beam has to be coupled out sideways. Using stepped waveguides located on either end of the undulator, which split an on-axis mm-wave beam into two off-axis beams, hitting off-axis mirrors, a mm-wave cavity is created (see Fig. 4). The mirrors at the downstream side are adjustable and are set such that they reflect 24% of the power back towards the upstream mirror. This is the feedback power. The remaining 76% of the power is coupled out. The upstream mirror reflects 100% of the feedback power back into the undulator waveguide.

For testing the stepped waveguides a low-power  $\text{HE}_{11}$  beam is injected into the waveguide. Measurements have been done at the position of the mirrors, which are now removed, to check whether the  $\text{HE}_{11}$  beam is separated properly into two off-axis beams. The beam profile was measured by scanning a small horn antenna across the

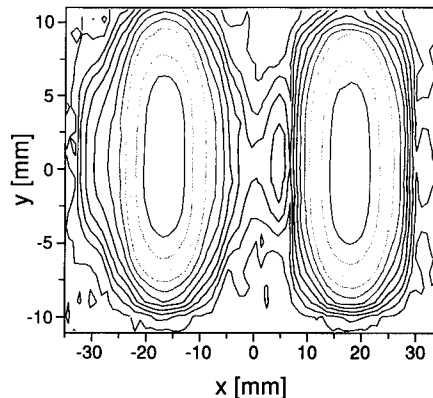


Fig. 5. Power pattern of a 200 GHz beam at the position of the mirrors at the end of the stepped waveguide. Contour levels of power are given at 4 dB intervals.

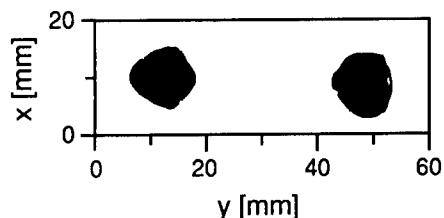


Fig. 6. High power measurement on the stepped waveguide, for a 140 GHz, 400 kW beam. In this simple, preliminary experiment, the beam patterns were recorded using thermographic paper.

waveguide, which measures the power at a large number of points and at a large frequency range. This way, the bandwidth of the waveguides and the mechanical adjustment could be checked. In Fig. 5 the antenna pattern is shown for a 200 GHz beam. It shows that 99.5% of the mm-wave power is contained in the two beams. This means that for 1 MW power level, 5 kW would leak between the mirrors.

With the mirrors mounted in position the power reflected by the stepped waveguide has been measured. This way it can be checked whether recombination of the two off-axis beams works well. First measurements show that over 97% of the power is reflected by the system. The 3% power loss is due to alignment errors and tolerances of the test waveguide.

High power measurements using a 140 GHz, 600 kW gyrotron have been carried out at the Institute for Applied Physics in Nizhny Novgorod. A preliminary result on the stepped waveguide is shown in Fig. 6. In this case, thermographic paper was used to record the beam profiles. For technological reasons, the experiment was carried out in open air, instead of in vacuum. Nevertheless, up to 400 kW no sparking occurred. Taking into account that the breakdown voltage in open air is roughly a factor of 10 lower than in vacuum, sparking is not expected to be a problem in our FEM at MW power level.

## 5. Conclusions

Measurements of the gun show a sufficiently small halo current, a sufficiently small emittance and a uniform current density.

The optimum drift gap between the undulator sections and the optimum step-tapering in the undulator field

strength have been determined for simulations taking a large range of possible operating frequencies into account. Single-mode operation is expected to be reached within a few microseconds.

Both low power and high power experiments on the mm-wave system show that splitting one mm-wave beam into two off-axis beams using a stepped waveguide works well. Recombination of two beams back into one beam has also been demonstrated successfully. No sparking problems are expected at 1 MW power level.

The system is now under construction. Major components, such as the undulator, the accelerator tubes and the ICT power supply have been delivered. All remaining components will be delivered in fall 1994. The system is expected to be operational in 1995.

## Acknowledgements

The work described here was performed as part of the research programme of the association agreement between the "Foundation for Fundamental Research on Matter" (FOM) and EURATOM with financial support from the "Dutch Organisation for Scientific Research" (NWO) and EURATOM.

## References

- [1] W.H. Urbanus et al., Nucl. Instr. and Meth. A 331 (1993) 235.
- [2] W.H. Urbanus et al., Nucl. Instr. and Meth. A 341 (1994) ABS 53.
- [3] A. van der Linden, C.A.J. van der Geer and W.H. Urbanus, to be published in Proc. 4th Europ. Particle Accelerator Conf., London, 27 June–1 July, 1994.
- [4] A.A. Varfolomeev et al., these Proceedings (16th Int. Free Electron Laser Conf., Stanford, CA, USA, 1994) Nucl. Instr. and Meth. A 358 (1995) 396.
- [5] A.A. Varfolomeev et al., *ibid.*, p. 197.
- [6] A.V. Tulupov, M.J. van der Wiel, W.H. Urbanus and M. Caplan, Nucl. Instr. and Meth. A 341 (1994) 305.
- [7] M.J. Cattelino and J. Atkinson, Low Emittance Electron Gun for FOM 1 MW 200 GHz CW FEM, Varian Interim technical report (1993).
- [8] M. Caplan et al., private communication (1993).
- [9] M. Caplan, T.M. Antonsen, B. Levush, A.V. Tulupov and W.H. Urbanus, Ref. [4], p. 174.
- [10] P. Eccen, T.J. Schep and A.V. Tulupov, Ref. [4], p. 178.



# CEBAF UV/IR FEL subsystem testing and validation program

G.R. Neil \*, S.V. Benson, H.F. Dylla, H. Liu

*Continuous Electron Beam Accelerator Facility, 12000 Jefferson Avenue, Newport News, VA 23606, USA*

## Abstract

A design has been established for IR and UV FELs within the Laser Processing Consortium's (LPC) program for development and application of high-average-power FELs for materials processing. Hardware prototyping and testing for the IR portion of the system are underway. The driver portion has been designed based on the superconducting radio-frequency (SRF) technology now seeing large-scale application in the commissioning of CEBAF, the Continuous Electron Beam Accelerator Facility, where LPC activities are centered. As of July 1994, measurements of beam performance confirm SRF's benefits in beam quality and stability, which are applicable to high-average-power FELs.

## 1. Introduction

The Continuous Electron Beam Accelerator Facility (CEBAF), a DOE nuclear physics laboratory, has joined with industrial corporations and universities to form the Laser Processing Consortium (LPC) to develop a new capability for production-scale processing of polymer, ceramic, and metal surfaces using UV and IR light from high-average-power free electron lasers [1]. While conventional lasers have limited application for industrial-scale surface processing – with cost per photon 100 to 1000 times too high and available wavelengths fixed and few – numerous compelling applications exist if high-average-power FEL technology can be demonstrated [2].

The initial stages of the LPC program include a kilowatt-level IR FEL and involve DOE-funded injector hardware and Commonwealth of Virginia-funded wiggler and optical cavity. Injector fabrication is underway, and driver component testing is proceeding using CEBAF superconducting radio-frequency (SRF) linac performance to qualify hardware designs. The data accumulated through mid-1994 represents substantial progress in quantifying the large-scale performance of SRF accelerators in daily use, thereby providing validation of SRF's potential for driving high-average-power FELs. This paper, after summarizing the laser design, addresses subsystem testing and validation status.

## 2. FEL design overview

Fig. 1 shows the LPC/CEBAF FEL, driven by a cost-efficient SRF three-cryomodule linac similar to CE-

BAF's two 20-module linacs [3]. The accelerating gradient will be 8 MV/m for a net energy gain of approximately 96 MeV. A photocathode gun designed at the University of Illinois will produce the electron beam [4]. The first-pass accelerated beam will recirculate back to the injection point for a second acceleration pass, enter the wiggler at up to 200 MeV energy, yield laser light, and finally decelerate through two energy-recovery passes in the linac before its remaining energy is absorbed in a copper beam dump at about 10 MeV. The UV FEL will use a taperable high-field wiggler similar to those recently purchased by several synchrotron light sources and FEL projects around the world. (See Robinson et al., this conference.) The IR FEL wiggler will be an electromagnet similar to a half-length version of the highly successful OK-4 undulator used at the Novosibirsk FEL project [5]. The UV FEL optical cavity will consist of a retro-reflecting reimaged ring resonator (R5) cavity [6,7]. Table 1 summarizes the machine specifications for both the driver accelerator and the laser. The predicted output power vs. wavelength shown in Fig. 2 is based on a scaling model by Benson [3] with tuning achieved by varying the wiggler field strength.

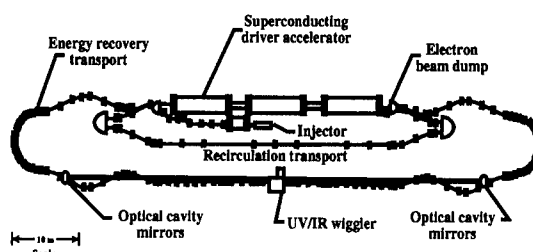


Fig. 1. Layout of the kilowatt demonstrator FEL.

\* Corresponding author. Tel. +1 804 249 7443, fax +1 804 249 5024, e-mail neil@ceba.gov.

### 3. Subsystem testing and validation status

The sections below discuss FEL subsystems, for which a number of hardware elements have been tested in prototype or in CEBAF accelerator commissioning. In most cases we have found their demonstrated performance exceeds the FEL requirements.

#### 3.1. Injector

The design goals for the FEL injector require electron bunches of 200 pC delivered at a 24.95 MHz repetition rate, for an average beam current of 5 mA. This precludes the use of RF guns using room-temperature RF systems, since these structures in CW operation cannot support the high fields required to deliver the necessary bunch charge within the specified emittance and energy spread. (An SRF gun has been demonstrated, but this technology is insufficiently mature.)

Our baseline gun design is to operate at 500 kV DC with 10 MV/m field at the cathode, leading to less than 13 MV/m maximum field on the cathode electrode structure. We have modeled the single-electron-bunch perfor-

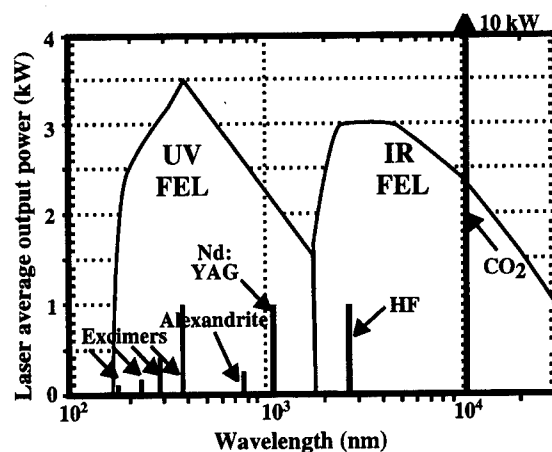


Fig. 2. Predicted output power vs. wavelength for the FEL with energy recovery, assuming the electron beam parameters listed in Table 1. The power output of conventional commercial lasers is also shown.

Table 1

Machine specifications

|  |  |
|--|--|
| Driver accelerator                             |  |
| Electron kinetic energy                        | 50–200 MeV                               |
| Pulse repetition frequency (design goal)       | 24.95 MHz                                |
| Charge/bunch (design goal)                     | 200 pC                                   |
| Momentum spread ( $\sigma_p/p$ ) <sup>a</sup>  | $2 \times 10^{-3}$ to $1 \times 10^{-3}$ |
| Bunch length ( $\sigma_t$ )                    | 0.4 ps                                   |
| Peak current ( $I$ )                           | 100–200 A                                |
| Normalized emittance ( $\epsilon_N$ )          | $12 \pi$ mm mrad                         |
| Beta functions at wiggler center               | 88 cm (round beam)                       |
| UV wiggler and UV optical cavity               |  |
| Wiggler length ( $L$ )                         | 1.44 m                                   |
| Wiggler wavelength ( $\lambda_w$ )             | 3 cm                                     |
| Maximum field ( $B_{max}$ )                    | 0.8 T                                    |
| Wiggler gap ( $2h$ )                           | 7.5 mm                                   |
| Effective Rayleigh range                       | 79 cm                                    |
| Optical mode waist ( $w_0$ )                   | 0.20 mm at 200 mm                        |
| Optical cavity length ( $L_{cav}$ )            | 60.08 m                                  |
| Output radiation characteristics               |  |
| Optical tuning range (UV)                      | 150–1000 nm                              |
| Optical tuning range (IR)                      | 2–28 $\mu$ m                             |
| Pulse duration                                 | 1 ps (FWHM), 2 ps IR                     |
| Pulse repetition rate                          | 2.5, 4.99, ... 24.95 MHz                 |
| Spectral bandwidth ( $\delta\lambda/\lambda$ ) | < 0.5% FWHM                              |
| Polarization                                   | linear                                   |
| Peak power                                     | 100–160 MW                               |
| Transverse mode quality                        | < $2 \times$ diffraction limit           |

<sup>a</sup> Since absolute energy spread should remain constant as the energy is changed, the range of energy spread shown reflects a factor of two change in energy.

mance of our proposed gun using a version of PARMELA modified by McDonald [8] and adapted to the DC gun case by substituting fields calculated by POISSON (DC gun case) as suggested to us by Herrmannsfeldt [9]. The results of extensive calculations for this DC gun case indicate that this gun will deliver sufficient single-bunch charge suitable for bunching and acceleration by CEBAF SRF cavities. (See Liu et al., this conference.)

The photocathode will be illuminated by a commercial CW mode-locked Nd:YLF laser, operating at 74.85 MHz and frequency doubled to 527 nm in an LBO crystal. The laser provides in excess of 5 W at 527 nm in the mode-locked pulse train at 74.85 MHz. One pulse of every three will be selected electro-optically to provide the 24.95 MHz pulse train to the photoemission gun. The  $\frac{5}{3}$  W of useful laser light will support the required 5 mA average current for cathodes with quantum efficiencies greater than 0.7%. Typical GaAs photoemission cathode quantum efficiencies are an order of magnitude greater than this at the 527 nm wavelength, providing a reasonable operating margin, although the lifetime at these average currents has not been demonstrated. Particular attention will be given to the cathode vacuum environment. The measured auto-correlated output of the laser is 42.9 ps FWHM pulse length. Amplitude stability is excellent: < 0.3% p-p on subsecond time scales and < 0.5% p-p on 30 min time scales. No accurate phase stability data has yet been obtained.

Following the 500 kV photocathode gun, the beam enters a one-cell fundamental-frequency room-temperature prebuncher. A two-cavity cryounit (quarter-cryomodule) follows the prebuncher. These cavities provide an appropriate amount of additional bunching and focusing for suitable injection into the first cryomodule in the driver accelerator while accelerating the electrons to an energy of

10 MeV. Both cavities are operated at an accelerating gradient of 10 to 11 MV/m.

### 3.2. SRF

Performance of the driver accelerator's three cryomodels must be comparable to that routinely achieved during CEBAF's tests of 42 cryomodels:  $Q = 5 \times 10^9$  at a gradient of 8 MV/m. No modifications are necessary for the superconducting cavities, although some modifications to auxiliary components mounted on the cavities are desirable. These modifications are driven by the increase in higher-order-mode (HOM) power resulting from the increase in bunch charge. The power absorbed in each HOM load increases from 0.1 W in the CEBAF case to 30 W in the FEL. A design for taking the HOM power to 50 K (as opposed to 2 K as in CEBAF) has been produced.

CEBAF linac cavity performance has been exemplary and validates the high reliability and beam stability expected of SRF cavities. In a recent accelerator test of these cavities, 600 MeV beam was provided to CEBAF's Hall C for nuclear physics research for the first time. In a subsequent test with 286 cavities operating (of 338 total in the injector and both linacs), maximum energy was 808 MeV, with an average gradient of 5.65 MV/m. For this test RF power (and consequently beam energy) was limited due to our desire not to set a high demand charge on electricity during the rest of the year.

Reliability was excellent; in an initial 65-h run beam was on target 69.7% of the time. During a typical 8 h shift during this run, trips from various interlocks and hardware safety systems occurred approximately once an hour and were quickly reset by the operators. No re-steering of the beam was required. It should be noted, finally, that in over a year of operation no degradation of cavity performance has been observed. Since the number of components in the FEL will be less than 1/10 the number in CEBAF, we expect to achieve excellent beam availability.

### 3.3. RF

Driver linac cavities will use energy recovery to reduce RF requirements to  $< 5$  kW, a level comparable to demonstrated CEBAF performance. Thus each will use a standard CEBAF 5 kW klystron. Injector cavities, operating without energy recovery, will each require about 30 kW including the reactive load. An appropriate source is presently being procured.

The RF phase and amplitude control requirements are strict in the FEL; however, we have succeeded in demonstrating in most cases our ability to meet and exceed these requirements, although with low beam loading and on resonance. Table 2 shows the requirements and the demonstrated performance of this system. Further information on the design and performance of this control module is available in Ref. [10].

It must be noted that the RF control in the recirculated, energy-recovered system has some elements which are not fully tested in the present system. In the FEL injector, beam loading will occur which exceeds our experience base. In the linac, the average detuning angle will need to be around  $-64^\circ$  rather than zero so that there is substantial phase/amplitude coupling. A modification of the control circuitry will minimize this issue, but beam testing is needed to confirm control algorithms. Further, overall system stability of energy recovery during FEL operation needs further study. (See Edighoffer, this conference.)

### 3.4. Cryogenics

An SRF FEL needs a capable and reliable refrigerator system, and at 1500 MHz this system must operate subatmospheric. Until 1994, experience with subatmospheric compressors had been limited to low total refrigeration power on the TORE-SUPRA tokamak. But in the 6 months between February and August 1994, substantial experience was gained on the CEBAF CHL, which provides in excess of 4800 W of cooling capacity at the 2 K operating

Table 2  
RF requirements and demonstrated performance

| Parameter               | Requirement                        | Demonstrated   |
|-------------------------|------------------------------------|--|
| Power                   | 2 kW linac, 30 kW injector         | 5 kW   |
| Amplitude stability     | $\sigma_A/A \leq 1 \times 10^{-3}$ | $2 \times 10^{-4}$ correlated and<br>$3 \times 10^{-5}$ uncorrelated |
| Phase stability         | $\sigma_\phi \leq 1^\circ$         | $\leq 0.10^\circ$  |
| Microphonic noise       | less than $20^\circ$ peak-peak     | $< 13^\circ$ peak-peak typical                                       |
| Operating gradient      | 8 MV/m $\pm 5\%$                   | 8 MV/m   |
| Loaded $Q$              | $6.6 \times 10^6$                  | $6.6 \times 10^6 \pm 20\%$   |
| He-pressure sensitivity | $< 10$ Hz/mbar                     | $< 10$ Hz/mbar   |
| Lorentz force           | 3 Hz/(MV/m) $^2 \pm 10\%$          | 3 Hz/(MV/m) $^2$   |
| HOM power               | $< 30$ W/load                      | $< 0.5$ W/load   |

temperature of CEBAF. Continuous runs exceeding 800 h were achieved.

The CHL system has demonstrated the 2 K capacity to maintain operation of the FEL simultaneously with the CEBAF linac. The heat load due to all of CEBAF is only about 3000 W at 2 K. The FEL will contribute less than an additional 500 W at 2 K. During commissioning of the system over 5000 W of cooling capacity was demonstrated. An additional liquefier will be needed for the FEL to support the 2300 W of 50 K cryogenic loads. This will be achieved with a minor upgrade on the 12000 W capacity already in existence.

### 3.5. Transport

The two-pass FEL design with energy recovery requires considerable manipulation of longitudinal and transverse beam dynamics to provide the bunch lengths required at the wiggler and to make stable energy recovery feasible. Two recent tests on the CEBAF accelerator provide guidance for the FEL beam transport. In one, total path length was accurately set to better than 4 parts in  $10^7$  out of a total length of 1.4 km by comparison of beam arrival times with a pickup loop. Recent operational experience has also shown that  $M_{56}$  (energy-path length interdependence) control to the level required in the FEL driver is feasible.

By modulating the beam energy and measuring the arrival phase of the beam using a precision phase detector between a reference signal from the final RF control module and a beam position monitor at the  $90^\circ$  point of one arc, the linear transfer matrix can be determined. In the recent commissioning work, setting nominal values of currents into the arc magnets resulted in an  $M_{56}$  of 18.5 cm. After application of small corrections on the order of 3% to the compaction control quadrupoles, the  $M_{56}$  was measured to be 1.8 cm over a path of approximately 125 m, more than 1.5 times the corresponding FEL path length. The technique can probably be used to measure  $M_{56}$  to an accuracy of better than 3 mm, giving us confidence that the  $M_{56}$ 's required in the FEL to bunch and decompress the electron beam before and after the wiggler can be properly set to their design values of order 1 m.

### 3.6. Optical systems

The UV FEL optical cavity will consist of a retro-reflecting reimaged ring resonator (R5) cavity [6,7]. This design allows the cavity to be rather long (60 m) without the requirement of state-of-the-art active angular controls for the mirrors. The resonator has a number of useful properties including uniform mirror loading and insensitivity to spherical aberration. The UV FEL will use commercially available high-power dielectric coatings on cooled silicon carbide substrates. The IR FEL mirrors will use protected silver coatings on silicon carbide substrates. The

IR cavity will use a more conventional near-confocal resonator due to the relaxed angular tolerances at the longer wavelengths. Both optical cavities will use scraper mirror output coupling.

## 4. Conclusions

A design has been established for the CEBAF IR and UV FELs as standalone systems. The IR portion of the system – consisting of the injector,  $1\frac{1}{4}$  cryomodels, IR wiggler, and optical system – is funded and work is proceeding in construction, prototyping and testing of the hardware components. Measurements of beam performance have been made using the CEBAF linacs, which support the chosen design parameters. The benefits of the superconducting design in terms of beam quality and stability are evident. The crucial performance tests will come this year as the injector is commissioned.

## Acknowledgements

This work was supported by the Virginia Center for Innovative Technology and by the US Department of Energy. In addition to gratitude to the CEBAF staff in general, the authors thank members of the Laser Processing Consortium for their participation in the planning and development of the CEBAF FEL program. Acknowledgement is also made of FEL photocathode gun design at the University of Illinois under NSF grant number PHY-89-21146.

## References

- [1] Proposal: High-Power Ultraviolet and Infrared Free-Electron Laser for Industrial Processing, Laser Processing Consortium, May 1994, available from CEBAF, 12000 Jefferson Avenue, Newport News, VA 23606.
- [2] M.J. Kelley et al., Proc. Int. Conf. on Radiation Processing, Orlando, 1994 (Radtech, 1994).
- [3] Reference Design Report: High-Power Ultraviolet and Infrared Free-Electron Laser for Industrial Processing, Laser Processing Consortium, May 1994, available from CEBAF.
- [4] C.K. Sinclair, Nucl. Instr. and Meth. A 318 (1992) 410.
- [5] I.B. Drobyazko et al., Nucl. Instr. and Meth. A 282 (1989) 424.
- [6] Chun-Ching Shih and Su-Miau Shih, Nucl. Instr. and Meth. A 304 (1991) 788.
- [7] C.C. Shih, G.J. Linford, S.W. Quon and A.J. Schmit, SPIE Proc. 1224 (1990).
- [8] K.T. McDonald, IEEE Trans. Electron Devices ED-35 (1988) 2052.
- [9] W. Herrmannsfeldt, private communication.
- [10] S. Simrock, Proc. 1991 IEEE Particle Accelerator Conf., San Francisco, May 1991, p. 2515.



ELSEVIER

## Design study of a G-band FEL amplifier for application to cyclotron resonant heating in magnetic fusion reactors

H.P. Freund<sup>a,\*</sup>, M.E. Read<sup>a</sup>, R.H. Jackson<sup>b</sup>, D.E. Pershing<sup>b,2</sup>, J.M. Taccetti<sup>b,3</sup>

<sup>a</sup> *Physical Sciences, Inc., Alexandria, VA 22314, USA*

<sup>b</sup> *Naval Research Laboratory, Washington, DC 20375, USA*

### Abstract

A G-band (140–150 GHz) free-electron laser is described using a coaxial hybrid iron (CHI) wiggler. The CHI wiggler is produced by insertion into a solenoid of a central rod and an outer ring composed of alternating ferrite and nonferrite spacers. The position of the spacers is such that the ferrite (nonferrite) spacers on the central rod are opposite the nonferrite (ferrite) spacers on the outer ring. The field is cylindrically symmetric and exhibits minima in the center of the gap providing for enhanced beam focusing. We describe a tapered wiggler amplifier for plasma heating applications. Preliminary design studies using a nonlinear simulation indicates that output powers of 3.5 MW are possible using a 690 kV/40 A electron beam for a total efficiency of 13%. It is important to note that no beam loss was observed even for realistic values of beam energy spread.

### 1. Introduction

Auxiliary sources of plasma heating for currently-planned thermonuclear fusion reactors employ both ion and electron cyclotron schemes. The electron cyclotron heating schemes necessitate approximately 20 MW of CW power at frequencies ranging from 140 to 280 GHz depending upon whether it is desired to use the fundamental or second harmonic resonance [1]. At the present time no source under consideration, or even anticipated, is expected to produce the full power requirement in a single module, and a system composed of several similar sources is envisioned. In this paper, we describe the design and operation of a G-band (140–150 GHz) free-electron laser (FEL) amplifier based upon a coaxial hybrid iron (CHI) wiggler [2–4] which can meet these requirements.

The CHI wiggler is produced by insertion into a solenoid of a central rod and an outer ring composed of alternating ferrite and nonferrite spacers. A schematic representation

of the structure is shown in Fig. 1. The position of the spacers is such that the ferrite (nonferrite) spacers on the central rod are opposite the nonferrite (ferrite) spacers on the outer ring. The field is cylindrically symmetric and exhibits minima in the center of the gap providing for enhanced beam focusing. Since high fields at short wiggler periods can be achieved with this design by the relatively simple expedient of using narrow spacers and a ferromagnetic material with a high saturation level in a strong solenoid, a CHI wiggler-based FEL is capable of producing power at the required wavelengths using a relatively low energy electron beam.

The analysis and design of a CHI-wiggler FEL herein is based upon a 3-D slow-time-scale nonlinear simulation. Interested readers are referred to Refs. [3,4] in which the formulation is described in detail. In this formulation a set of second order nonlinear differential equations is derived for the evolution of the amplitudes and phases of an arbitrary ensemble of the TE, TM, and TEM modes of a coaxial waveguide. These equations are simultaneously integrated with the complete 3-D Lorentz force equations for an ensemble of electrons using an analytic model of the CHI wiggler [2,3]. The orbit equations are not averaged over a wiggler period; hence, we model the adiabatic injection of the beam into the wiggler self-consistently, and can specify the initial conditions of the beam prior to injection. This is advantageous since the design codes for electron guns and beam diagnostics generally give information on the beam conditions outside the wiggler.

\* Corresponding author. Tel. +1 703 734 5840, fax +1 703 821 1134, e-mail freund@mmace.nrl.navy.mil.

<sup>1</sup> Permanent address: Science Applications International Corp., McLean, VA 22102, USA.

<sup>2</sup> Permanent address: Mission Research Corp., Newington, VA 22122, USA.

<sup>3</sup> Permanent address: University of Maryland, College Park, MD 20742, USA.

The wiggler amplitudes and periods which can be achieved have been determined using the POISSON/SUPERFISH group of codes [5]. To this end, we have specified vanadium permendur spacers and found that a 4 kG solenoid would saturate the ferrite for spacers with inner and outer radii of  $R_{in} = 0.7$  and  $R_{out} = 1.5$  cm, and a wiggler period of  $\lambda_w = 1.5$  cm. For convenience, we shall also assume that  $R_{in}$  and  $R_{out}$  are also the inner and outer radii of the coaxial waveguide. Using these wiggler dimensions, we choose to operate with a 10 kG solenoid which provides a wiggler amplitude of  $\sim 2$  kG at the center of the gap (corresponding to a maximum of the periodic field amplitude of  $\sim 4$  kG at the pole faces) and a uniform axial field component of  $\approx 6$  kG to provide for additional focusing. Note that a magneto-resonant enhancement in the gain and efficiency is also present when the Larmor period associated with the uniform axial field component is close to the wiggler period. We also assume an entry taper region of  $N_w = 5$  wiggler periods in length. This is found to be sufficiently long to preserve the initial electron beam quality through the injection process.

Since the performance of an FEL is critically dependent upon the electron beam quality, we must design an electron gun which produces an annular beam with a low energy spread. The design tool we used for this is the EGUN code [6]. In designing the electron beam, we first need to specify the energy, current, and inner and outer radii of the beam. Bearing in mind that the wiggler period is 1.5 cm and that operation in G-band is desired, we choose an electron beam voltage in the neighborhood of 690 kV and a current of 40 A. Assuming that the inner and outer radii of the beam at the exit of the gun were 1.05 cm and 1.15 cm respectively, it was found to be possible to design a gun which produced a beam with an axial energy spread of substantially less than 0.1%.

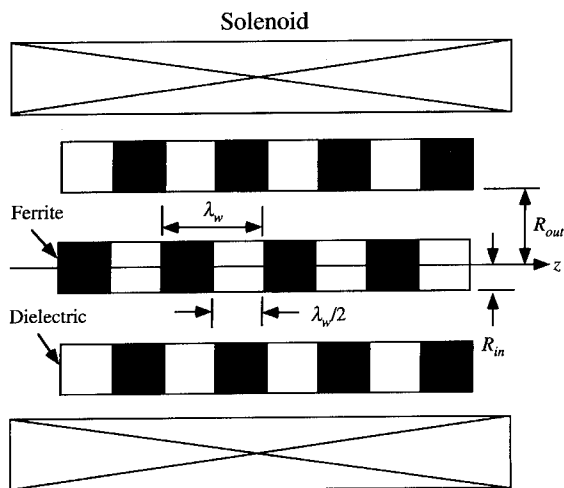


Fig. 1. Schematic illustration of the CHI wiggler configuration.

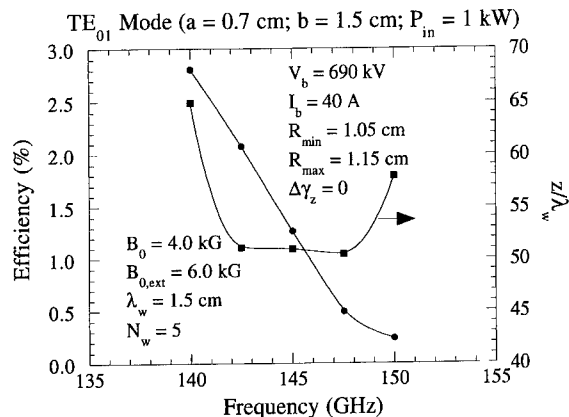


Fig. 2. Efficiency and saturation distance versus frequency at 690 kV.

Finally, throughout the paper we shall deal with the  $TE_{01}$  mode and an injected power level of 1 kW.

## 2. Uniform wiggler case

We first address the interaction for the case of a uniform wiggler, and consider the above-mentioned wiggler, waveguide and beam parameters for the case of an ideal beam in which the axial energy spread  $\Delta\gamma_z = 0$ . The first issue to be addressed is the frequency tuning for these parameters. To this end, the efficiency and saturation distance is plotted in Fig. 2 versus frequency. It is clear from the figure that the efficiency decreases with frequency over this entire band from 140 to 150 GHz. Since the saturation distance is relatively constant over the range of 142–147 GHz, this implies that the peak gain is found in the vicinity of 142 GHz for an efficiency of  $\approx 2.2\%$ . As such, we consider the highest gain and efficiency possible and assume a frequency of 142.5 GHz in the remainder of the paper. Note that this type of tuning is expected to occur at all beam voltages and wiggler periods. Thus, it should be possible to retune to 150 GHz just as readily if you are willing to go to higher beam voltages or shorter wiggler periods.

The interaction is sensitive to the beam position. In the first place, we hold the cross-sectional beam area fixed at that used in Fig. 2 and vary the mean beam radius  $R_0$ . The results of this study are shown in Fig. 3 in which the variation in efficiency and saturation distance is plotted versus  $R_0$ . As seen in the figure, a beam center of 1.10 cm (which is that used previously) seems to be the optimum. Although the efficiency is somewhat higher at  $R_0 = 1.12$  cm, this is near the edge of a steep decrease in efficiency with increasing  $R_0$ . Therefore, we use the more conservative choice of  $R_0 = 1.10$  cm henceforth.

In the second place, the interaction is sensitive to the thickness of the beam. In order to illustrate this, consider

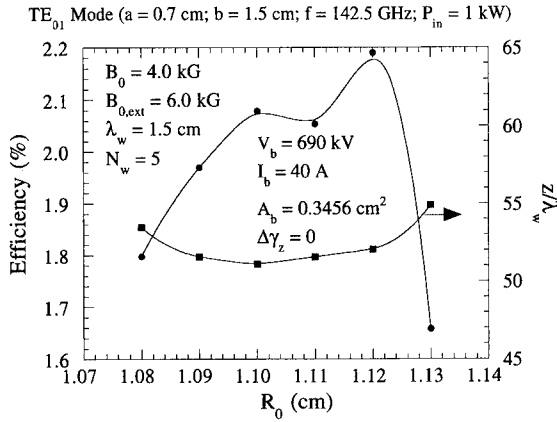
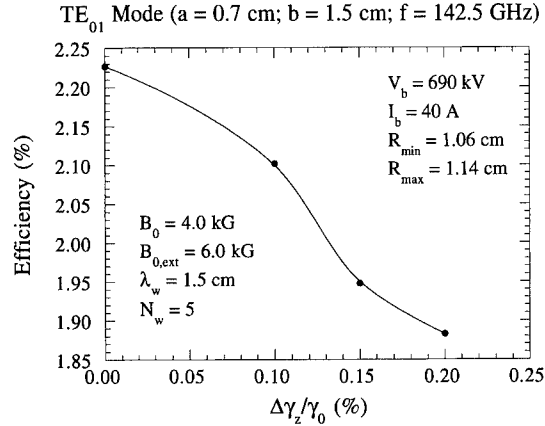
Fig. 3. Efficiency and saturation distance versus  $R_0$ .

Fig. 5. Variation in the efficiency and saturation distance versus beam thickness.

the variation in the efficiency as a function of beam thickness  $\Delta R$  for a mean beam radius fixed at  $R_0 = 1.10$  cm. The efficiency and saturation distance are shown in Fig. 4 as a function of beam thickness. It is clear from the figure that the gain remains relatively constant for  $\Delta R \leq 0.6$  cm and that the efficiency decreases with increasing  $\Delta R$  over the entire range surveyed. Since it is difficult to focus the beam down to an extremely narrow thickness, we make a conservative choice of  $\Delta R = 0.4$  cm which maximizes the gain and still yields a respectively high efficiency. This is the value of the beam thickness which we shall use for the remainder of the paper.

Before proceeding to the study of the tapered wiggler interaction, we turn to the effect of the axial beam energy spread. The variation in the efficiency as a function of  $\Delta \gamma_z$  is shown in Fig. 5. Observe that the efficiency falls from about 2.24% to 2.10% as the axial energy spread increases to 0.10%. This is a relatively modest decrease in efficiency, and a beam quality within this range has been demonstrated with the gun design code.

Finally, since CW operation is required, the amount of beam loss during the course of the interaction is an important consideration. Since the total beam power is in the neighborhood of 28 MW, even 1% beam loss could pose an insurmountable problem. As a result of the favorable focusing properties of the CHI wiggler, however, no beam loss was found in the simulation prior to saturation for the uniform wiggler cases studied.

### 3. Tapered wiggler case

Turning to the case of a tapered wiggler, it should be remarked that there is an optimum both in the start-taper point and in the slope of the taper for the efficiency enhancement process. We have optimized both of these parameters and found that for a 1 kW input power that the optimal start-taper point is given by  $z_0/\lambda_w = 46$  and the optimal slope of the taper is  $\varepsilon_w = -0.001$  (where  $\varepsilon_w \equiv$

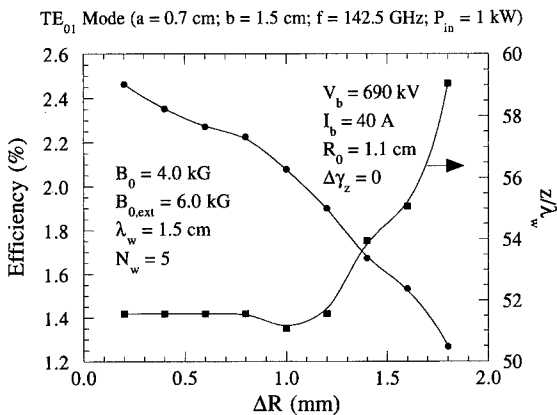


Fig. 4. Variation in efficiency versus the axial energy spread of the beam.

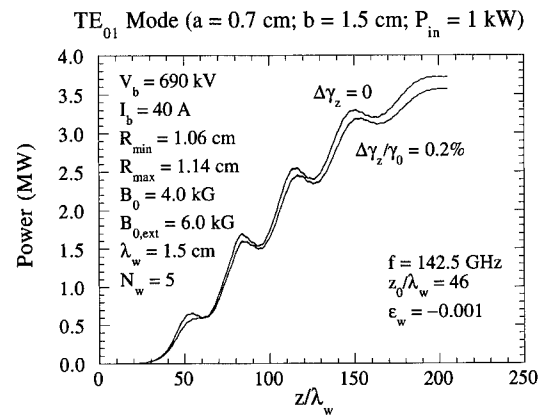


Fig. 6. Evolution of the power with axial position for two choices of the energy spread.

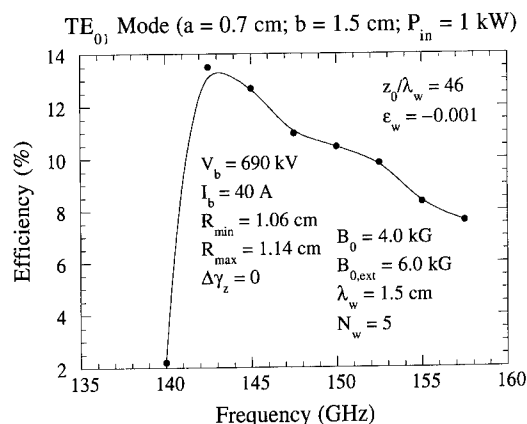


Fig. 7. The bandwidth for the tapered wiggler interaction.

$k_w^{-1} d \ln B_w / dz$ ). The evolution of the power with axial distance for this choice is shown in Fig. 6 for the cases of an ideal beam with  $\Delta\gamma_z = 0$  and for  $\Delta\gamma_z/\gamma_0 = 0.2\%$ . Note that the interaction is shown over a length of  $\approx 200\lambda_w$  which represents the length required to taper the wiggler amplitude to zero for this choice of the taper. It is clear from the figure that the efficiency does not change a great deal with the decrease in beam quality over this range, and that the efficiency rises to a value over 13% for an output power of better than 3.5 MW. This represents a substantial improvement over the uniform wiggler efficiency, and occurs due to the relatively high wiggler field strength.

We now turn to the bandwidth of the tapered wiggler interaction, and find that the bandwidth can be quite large. Consider the case in which we start with the optimum parameters for the interaction at 142.5 GHz including the total length of the system. The bandwidth will then be determined by the response of the identical system to different drive frequencies. The result of this study is shown in Fig. 7 in which the efficiency at the end of the interaction region is plotted as a function of frequency. As is evident from the figure, the efficiency remains high over a frequency range of approximately 142.5 GHz through 160 GHz, which represents a rather large instantaneous bandwidth. This is in accord with an earlier study made using a simpler FEL model [7].

Finally, it should be noted that despite the extended interaction length for the tapered wiggler cases shown, no beam loss was found in simulation for any of these parameters.

#### 4. Summary

The results of this study of a G-band amplifier based upon the CHI wiggler can be summarized rather simply. In the first place, no beam loss was found to occur for either

the uniform or tapered wiggler runs. This is a requirement from the standpoint of designing a CW device. In the second place, the efficiencies were found to be fairly high. In the uniform wiggler case, efficiencies are in the neighborhood of 2–3% for the chosen parameters, while the tapered wiggler interaction produced efficiencies of 13–14% at 142 GHz. These conclusions hold for both an ideal beam and for one with the more realistic beam energy spread of less than or of the order of 0.2%. It should be remarked here that beam qualities of this order are quite reasonable with careful gun design. We also observe that, given the sensitivity of the interaction to the beam dimensions, careful gun design is required.

The principal source of concern with the above-mentioned design is the length of the tapered wiggler interaction. At 200 wiggler periods in length, the support of the central rod becomes a serious design issue. However, we feel that it is not insurmountable. Most importantly, a vertical mount would be preferable. Secondly, it is not necessary to taper the wiggler to saturation. A shorter tapered wiggler would sacrifice some output power but facilitate the support of the central rod. Lastly, it should be emphasized that this study represents an initial design only. On the basis of this work, we can now undertake to optimize the design for higher gain and shorter interaction length. This might include several variations in the parameters. Shorter wiggler periods and lower beam voltages would help to shorten the overall interaction length. In addition, operation closer to the magneto-resonance can also enhance the gain. Finally, it should be noted that a 1 kW source at these frequencies might require the design of a gyrotron oscillator as a source of the drive power.

#### Acknowledgement

This work was supported by the Department of Energy and the Office of Naval Research.

#### References

- [1] V.L. Granatstein and R. Colestock (eds.), *Wave Heating in Plasmas* (Gordon & Breach, New York, 1986).
- [2] R.H. Jackson, H.P. Freund, D.E. Pershing and J.M. Taccetti, *Nucl. Instr. and Meth. A* 341 (1994) 454.
- [3] H.P. Freund, R.H. Jackson, D.E. Pershing and J.M. Taccetti, *Phys. Plasmas* 1 (1994) 1046.
- [4] H.P. Freund, R.H. Jackson, D.E. Pershing and J.M. Taccetti, these Proceedings (16th Int. Free Electron Laser Conf., Stanford CA, USA, 1994) *Nucl. Instr. and Meth. A* 358 (1995) 139.
- [5] A.M. Winslow, *J. Comp. Phys.* 2 (1967) 149.
- [6] W.B. Herrmannsfeldt, SLAC Report No. 226 (1979).
- [7] B. Levush, H.P. Freund and T.M. Antonsen, Jr., *Nucl. Instr. and Meth. A* 341 (1994) 234.





ELSEVIER

# Time-dependent multi-dimensional simulation studies of the electron output scheme for high power FELs <sup>☆</sup>

S.J. Hahn <sup>\*</sup>, W.M. Fawley, K.-J. Kim, J.A. Edighoffer

*Lawrence Berkeley Laboratory, University of California, Berkeley, CA 94720, USA*

## Abstract

We examine the performance of the so-called electron output scheme recently proposed by the Novosibirsk group [G.I. Erg et al., 15th Int. Free Electron Laser Conf., The Hague, The Netherlands, 1993, Book of Abstracts p. 50; Preprint Budker INP 93-75]. In this scheme, the key role of the FEL oscillator is to induce bunching, while an external undulator, called the radiator, then outcouples the bunched electron beam to optical energy via coherent emission. The level of the intracavity power in the oscillator is kept low by employing a transverse optical klystron (TOK) configuration, thus avoiding excessive thermal loading on the cavity mirrors. Time-dependent effects are important in the operation of the electron output scheme because high gain in the TOK oscillator leads to sideband instabilities and chaotic behavior. We have carried out an extensive simulation study by using 1D and 2D time-dependent codes and find that proper control of the oscillator cavity detuning and cavity loss results in high output bunching with a narrow spectral bandwidth. Large cavity detuning in the oscillator and tapering of the radiator undulator is necessary for the optimum output power.

## 1. Introduction

Recently, the Novosibirsk group [1] has proposed a novel outcoupling scheme, called the electron output scheme, for high power FEL application. In this approach, shown schematically in Fig. 1, the role of the FEL oscillator is to induce the bunching of the electron beams at low optical power, while outcoupling is achieved by extracting the bunched electron beam out of the oscillator via an achromatic transport into a single pass undulator, called the radiator, where it generates intense coherent radiation. The main advantage of the scheme is that the oscillator can be operated at a low intracavity power level by employing a transverse optical klystron (TOK) configuration. This consequently avoids excessive thermal loading on the cavity mirrors. Fig. 1 shows a TOK configuration consisting of three undulators and two dispersive sections.

The SELENE proposal [2] employs this scheme with a goal of a high power FEL serving as a ground-based power source for several space applications. Previous, time-independent simulation studies [3,4] of the SELENE proposal indicated that the radiator output power could be as great as 500 times the oscillator intracavity power.

The fact that intracavity power can be made small in an optical klystron oscillator can be understood from the fact that the effective length  $L_{\text{eff}}$  of the undulator increases due to the inclusion of the dispersive sections and that the synchrotron oscillation frequency is proportional to the quarter power of the intracavity power. Since an FEL oscillator with low-to-moderate single pass gain reaches saturation when the beam particles execute about one half of synchrotron rotation, one would expect that  $P \propto L_{\text{eff}}^{-4}$ . On the other hand, the dispersive sections also increase the single pass gain, which lowers the threshold for the onset of the sideband instability. This instability induces significant temporal fluctuations on the outgoing electron beam which should be avoided for the steady-state operation in the final radiator. To counter this instability, one detunes the cavity length and/or increases the single pass cavity loss, which can be treated only in the time-dependent approach. Another source of time-dependent phenomena occurs when the pulse length of the electron beam is comparable to the slippage distance in the FEL oscillator (which is increased by the inclusion of the two dispersive sections). Hence, we believe it is important to carry out time-dependent simulations for a reliable evaluation of the electron outcoupling scheme.

In order to explore all these effects plus those due to instantaneous energy spread, emittance, and diffraction (all of which reduce gain), we have carried out 1- and 2-D, time-dependent simulations with the FEL1D [6] and GINGER [7] codes. Our goal was temporally stable, low power

<sup>☆</sup> This work was supported at LBL by the Director, Office of High Energy and Nuclear Physics, U.S. Department of Energy, under Contract No. DE-AC03-76SF00098.

<sup>\*</sup> Permanent address: Department of Physics, POSTECH Korea.

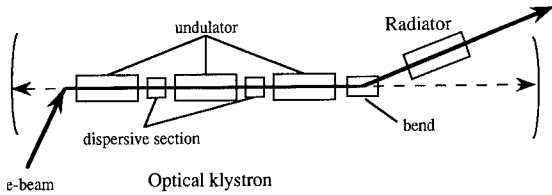


Fig. 1. Schematic diagram of the "electron output" FEL system.

operation within the oscillator while simultaneously obtaining the high output bunching of the electron beam required for high power radiator performance.

## 2. Oscillator simulation results

For our study, we have chosen parameters corresponding to the current Novosibirsk experiment [1]:  $I_b \sim 10$ – $100$  A,  $E_b = 58$  MeV,  $\lambda_s = 8$   $\mu\text{m}$ ,  $\epsilon_n = 20\pi$  mm-mrad, and a micropulse duration  $\tau_p = 1000\lambda_s \approx 27$  ps. The 79-m long optical resonator (corresponding to a minimum micropulse repetition rate of 1.9 MHz) contains an optical klystron consisting of three helical undulators, each with 40 periods of 9-cm period length ( $a_w \approx 1.2$ ), separated by two dispersive sections (see Fig. 1).

It is well known [6,5] that cavity detuning and mirror losses play a crucial role for short-pulse FEL oscillators in determining the output spectrum, which can range from a multi-mode chaotic state to a (preferred) single mode stationary state, in between which lies the LCO (limit-cycle oscillation) state [6]. Another important parameter is the strength  $D$  of the two dispersive sections. Following Colson, we define  $D$  as the ratio  $N_d/N_w$  where  $N_w (= 120$  in the present study) is the total number of undulator periods in the oscillator and  $N_d$  is the number of undulator periods necessary to produce the drift of each dispersive section. Thus, the effective undulator length is given by  $L_{\text{eff}} = (1 + 2D)N_w\lambda_w$ .

As mentioned in the previous section, in the low current (i.e. low gain) regime when  $D$  and thus  $L_{\text{eff}}$  increase, we expect that the intracavity saturation power will decrease. This is confirmed by the results of 1D, time-dependent simulation shown in Fig. 2 where the average cavity power (within the micropulse) for three different values of  $D$  are plotted versus cavity detuning parameter  $-\delta L/\lambda_s$ . These simulations adopted  $I_b = 8.8$  A,  $\delta\gamma/\gamma = 0$ , and a mode filling factor of 0.11. We have plotted points corresponding to stationary states only; smaller values of  $\delta L$  lead to chaotic or LCO behavior while larger values result in single pass gain below the chosen cavity loss value (10%). Due to the increase of the single pass gain with larger  $D$ , the detuning necessary for stationary state behavior also increases with  $D$  as is evident from the figure. The average output bunching  $b$  which, for the 1D runs, varies inversely with average cavity power, reaching a maximum

value of 0.3–0.4 near the point of FEL threshold. Here  $b = |\langle \exp(-i\theta_n) \rangle|$  where the brackets indicate averaging over the particles' positions in phase space.

Fig. 2 also plots the results from 2D time-dependent simulations which include the effects of diffraction, beam emittance, and also instantaneous energy spread ( $\pm 0.2\%$ ). The equilibrium e-beam radius  $r_b \approx 0.6$  mm is  $\approx 5$  times smaller than the optical mode radius. The instantaneous energy spread is comparable to  $1/2N_w^{\text{eff}}$  leading to a reduction of the net gain per pass to about 2.8 for  $D = 0.2$ . This reduction suggests that one must be careful in minimizing the instantaneous energy spread (and output beam emittance if operation at short wavelengths is desired) from the accelerator and transport sections to the undulator. The 2D simulations resulted in stationary states with average output bunching values of  $\approx 0.35$  for appropriate values of  $\delta L$ , which are about a factor of two smaller than for the 1D runs due to the lower gain per pass. When  $-\delta L$  is too small (equivalent to too small a cavity loss), the trapped particle instability becomes evident after 30 passes or so.

In the high current (i.e. high gain) regime, the intracavity power and average bunching can show different sensi-

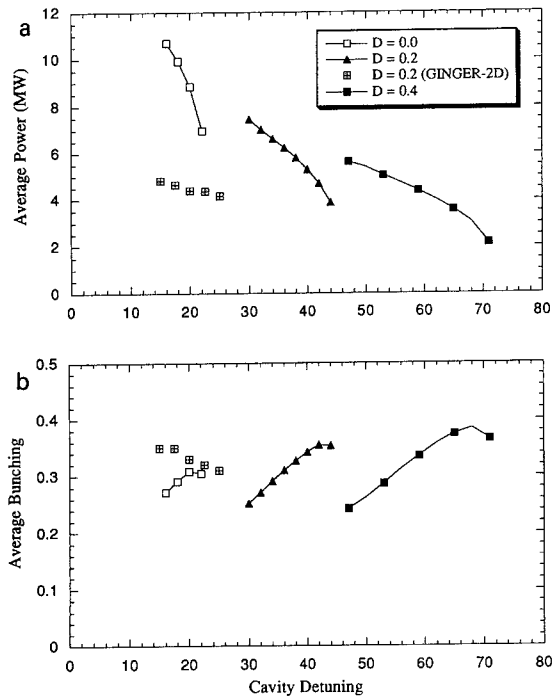


Fig. 2. 1D simulation results for the average intracavity laser power and average output e-beam bunching as a function of the cavity detuning for three different optical klystron dispersion strengths  $D$  for a low current case ( $I_b = 8.8$  A). The single pass cavity losses were 10% for these results. For the case of  $D = 0.2$ , we have also plotted time-dependent, 2D results that include effects such as diffraction and emittance.

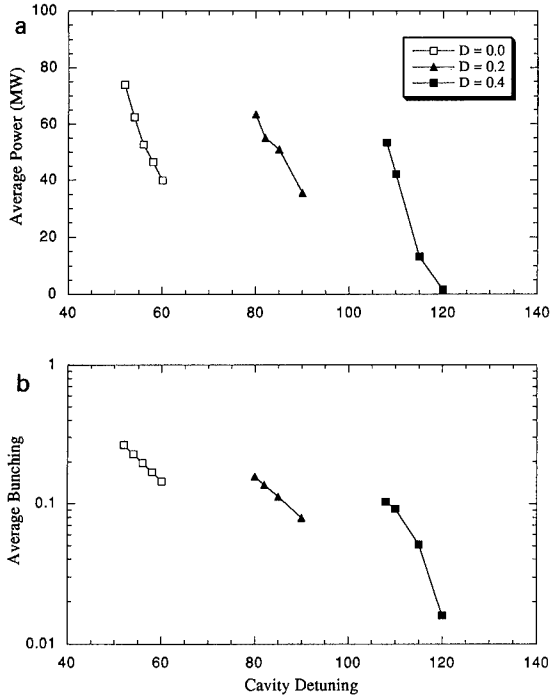


Fig. 3. High gain peak intracavity power and output bunching as a function of the cavity detuning for three different  $D$  values for high current ( $I_b = 88$  A) runs with 10% single pass cavity loss.

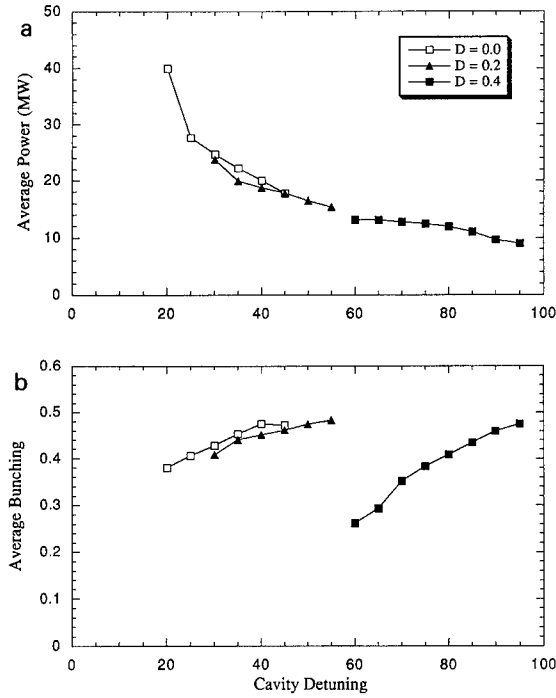


Fig. 4. High gain peak intracavity power and output bunching as a function of the cavity detuning for three different  $D$  values for high current ( $I_b = 88$  A) runs. Here the single pass cavity losses were increased to 80%.

tivity to  $D$ . For small cavity loss values, as  $D$  increases, the average bunching in stationary states decreases as shown in Fig. 3 in contrast to the low gain results. These results were obtained with  $I_b = 88$  A, a mode filling fraction of 0.11, and a 10% single pass cavity loss. The negative effects produced by the dispersive sections are

due to the total phase advance of the particles becoming excessive for large  $D$ . Another phenomenon that differs in the high current, high single pass gain regime is that the number of passes necessary to reach nominal power saturation is less than that necessary to reach the single-mode,

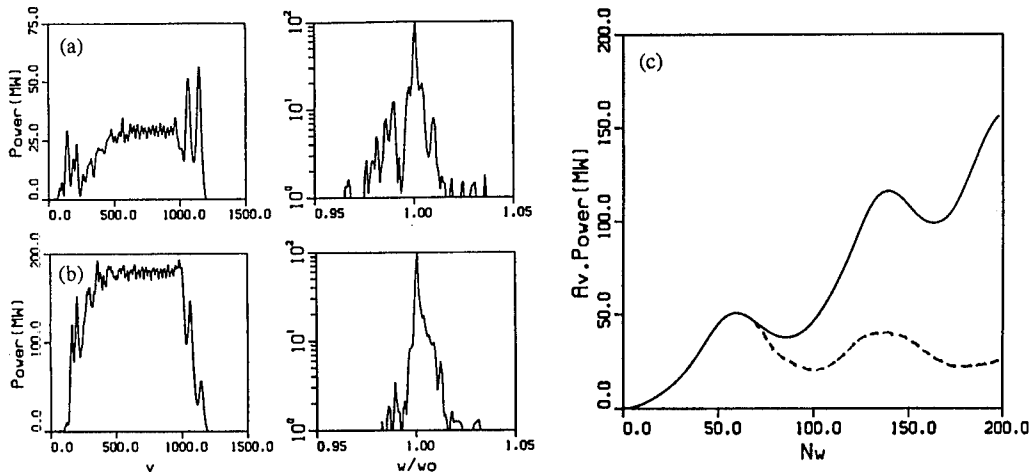


Fig. 5. 1D simulation of the radiator for the high current case with  $D = 0.2$ ,  $\delta L = -50\lambda$ , and single pass cavity losses of 80%. (a) Optical pulse profile and its spectrum with constant  $a_w = 1.187$  at  $N_w = 200$ , (b) tapered case, (c) average power as a function of the undulator period with (solid line) and without (dotted line) tapering.

stationary state. In the low current regime, the situation is reversed. Furthermore, we have noticed that while the start point (in pass number) of the stationary state increases in the low gain regime as the cavity detuning increases, it decreases in the high gain regime.

In order to utilize the advantages of the dispersive sections for high current cases, we found it necessary to increase the single pass cavity losses to 80%. As shown in Fig. 4, the sensitivity to  $D$  and  $\delta L$  then becomes quite similar to what was found in the low gain, low current regime. More importantly, the output electron beam is now well bunched for good energy extraction in the radiator undulator.

### 3. Radiator simulation results

We modeled the time-dependent radiator performance using as our initial condition the bunched electron beam from the low gain oscillator and a zero amplitude laser signal. Fig. 5 shows 1D results for a high current case with 80% cavity losses where  $D = 0.2$  and  $\delta L = -50\lambda_s$  were adjusted to achieve a stationary output state from the oscillator. Both untapered and tapered undulators were considered. For the latter, a simple 5% linear taper in  $a_w$  began after  $N_w = 55$  which increased the power by a factor of 5 and strongly suppressed sideband growth and narrowed the output spectrum. The average output power of 156 MW corresponds to an extraction efficiency of 3.0%. These results illustrates the possible advantages of a taper; it may well be possible to increase the output power another factor of two or greater by a more optimal tapering strategy. We also note that an additional dispersive section could be placed between the oscillator and radiator which may further improve the radiator performance.

### 4. Conclusion

In summary, we have the following observations. The electron output scheme works quite well for systems with moderate single pass gain. In this case, one can optimize output bunching and limit intracavity power in the oscillator by judicious choice of cavity detuning and dispersive section strengths. The oscillator then operates in a stationary mode with a narrow spectrum without sidebands and large energy extraction is possible from the radiator. Systems with high intrinsic single pass gain may require additional modifications such as large single pass cavity losses before stable, low power oscillator operation is possible.

### References

- [1] G.I. Erg et al., 15th Free Electron Laser FEL Conf., The Hague, The Netherlands, 1993, Book of Abstracts p. 50; Preprint Budker INP 93-75.
- [2] H.E. Bennett et al, Nucl. Instr. and Meth. A 341 (1994) 124.
- [3] D.D. Quick, J. Blau, R.K. Wong and W.B. Colson, Nucl. Instr. and Meth. A 341 (1994) ABS 92.
- [4] J. Blau, R.K. Wong, D.D. Quick and W.B. Colson, Nucl. Instr. and Meth. A 341 (1994) ABS 94.
- [5] See, e.g. R.W. Warren, J.C. Goldstein and B.E. Newnam, Nucl. Instr. and Meth. A 250 (1986) 19; K.-J. Kim and M. Xie, Nucl. Instr. and Meth. A 304 (1991) 146.
- [6] D.A. Jaroszynski et al, Nucl. Instr. and Meth. A 331 (1993) 52; S.J. Hahn and J. K. Lee, Phys. Rev. E 48 (1993) 2162.
- [7] R.A. Jong, W.M. Fawley and E.T. Scharlemann, SPIE 1045 (1989) 18.



ELSEVIER

# Chaotic particle deceleration and FEL efficiency enhancement with an incoherent pump wave or a stochastic undulator

Ya.L. Bogomolov, N.S. Ginzburg<sup>\*</sup>, E.R. Golubyatnikova

*Institute of Applied Physics, Russian Academy of Sciences, 46 Ulyanov Str., 603600 Nizhny Novgorod, Russian Federation*

## Abstract

For efficiency enhancement of FELs driven by high-current low-quality electron beams we propose the use of incoherent pump waves or stochastic undulators.

## 1. Introduction

It is known that the efficiency of an FEL is not large and is inversely proportional to the number of oscillations of electrons along the length of the interaction space [1,2]. The most developed method of efficiency enhancement consists in tapering of an undulator, resulting in an adiabatically smooth variation of the velocity of the combination wave [3,4]. This method is effective only for beams with a small dispersion of parameters on the scale of the combination wave amplitude. In the present work it is shown that the use of an incoherent pump or stochastic undulator is effective for the efficiency enhancement of an FEL driven by beam with a large dispersion of parameters. For this pump the enrichment of the spectrum of the combination waves, which are synchronous with the electrons, and, as consequence, realization of the mechanism of diffusive stochastic particle deceleration take place. As a result, the efficiency of energy extraction from the beam to the short-wave radiation is proportional to the width of pump spectrum and exceeds the value that is realized for the case of a monochromatic pump wave. It is important to note that the efficiency of energy transformation is practically independent of the beam quality.

## 2. The basic equations

Let the monochromatic signal wave propagating with the electron beam be given by a vector-potential

$$A_s = \text{Re} [x_0 A_s(z) \exp(i(\omega_s t - k_s z))].$$

The frequency of this wave is fixed by an external master

oscillator. Suppose that the pump field represents a set of discrete lines with uncorrelated phases

$$A_i = \text{Re} \left[ \sum_{n=0}^{\infty} x_0 A_{in}(z) \exp(i(\omega_{in} t + k_{in} z)) \right].$$

The average motion of a relativistic electron in the field of the signal and pump waves may be described by the kinetic equation for a one-dimensional distribution function

$$\frac{\partial f}{\partial t} + v_z \frac{\partial f}{\partial z} + F_z \frac{\partial f}{\partial p_z} = 0,$$

where

$$F_z = -\frac{e^2}{2\mathcal{E}} \text{Re} \left[ \sum_{n=0}^{\infty} i k_{cn} A_s A_{in}^*(Z) \times \exp(i(\omega_{cn} t - k_{cn} z)) \right]$$

is the ponderomotive force,  $k_{cn} = k_s + k_{in}$ ,  $\omega_{cn} = \omega_s - \omega_{in}$  are the wave numbers and frequencies of the ensemble of combination waves, and  $p_z = mv_z \gamma$ ,  $\mathcal{E} = mc^2 \gamma$ .

In the framework of the quasi-linear approximation, the equation for the slowly-varying distribution function  $\tilde{f}(z, p)$ , after averaging over ensemble of combination waves, has form

$$v_z \frac{\partial \tilde{f}}{\partial z} = \frac{\partial}{\partial p_z} \left( D(z, p_z) \frac{\partial \tilde{f}}{\partial p_z} \right), \quad \tilde{f}|_{z=0} = \tilde{f}^0(p_z) \quad (1)$$

with diffusion coefficient

$$D = \frac{8\pi^3 e^4 c^2 k_c^2 I_s I_i}{\omega_s^2 \omega_i^2 (v_z + c) \mathcal{E}^2} \Big|_{k_i = k_s(c - v_z)/(c + v_z)}$$

Here  $\tilde{f}^0(p_z)$  is the initial electron distribution function,  $I_s = |A_s|^2 / 8\pi c$  is the signal wave intensity, and  $I_i =$

<sup>\*</sup> Corresponding author. Tel. +7 8312 384 552, e-mail ginzburg@appl.nnov.su.

$|A_i|^2 \omega_i^2 / 8\pi c \delta k$  is the intensity of the pump wave spectrum.

Amplification of the signal wave by an electron beam moving in the field of the incoherent pump (or stochastic undulator) is described by equations

$$\frac{dI_s}{dz} = \frac{\pi^2 e^2 \omega_p^2}{mc^5} \frac{I_s}{k_s} \int_0^\infty \frac{I_i}{\omega_i^2} \left( \mathcal{E} \frac{\partial \tilde{f}}{\partial p_z} \right) \bigg|_{v_z=v_c} dk_i, \quad (2)$$

$$I_s|_{z=0} = I_s^0.$$

In the case of an ultrarelativistic beam Eqs. (1) and (2) reduce to

$$\frac{\partial P_s}{\partial z} = \frac{\pi}{2} \frac{\omega_p^2}{\omega_s^2} \int_1^\infty \frac{4P_s P_i k_s^2 \gamma^2}{\pi} \frac{\partial F}{\partial \gamma} d\gamma, \quad P_s|_{z=0} = P_s^0. \quad (3)$$

$$\frac{\partial F}{\partial z} = \frac{\partial}{\partial \gamma} \left( \frac{4P_s P_i k_s^2 \gamma^2}{\pi} \frac{\partial F}{\partial \gamma} \right), \quad F|_{z=0} = F_0(\gamma),$$

where  $\omega_p = (4\pi e^2 N_0 / m)^{1/2}$  is the plasma frequency,  $N_0$  is the density of the electron beam.  $F(\gamma, z)$  is the average distribution function over electron energy,  $P_s = |A_s|^2 \pi c / 2P_*$  is the normalized power of the signal wave,  $P_i = |A_i|^2 \pi c / 2P_* \delta k$  is the normalized spectrum power of the pump wave, and  $\delta k = k_{n+1} - k_n$ , and  $P_* = m^2 c^5 / e^2 = 8.7$  GW.

### 3. The results of computer simulation

Let the initial distribution function be given by

$$\hat{F}^0 = \frac{2}{\delta} \cos^2 \left[ (u-1) \frac{\pi}{\delta} \right],$$

in the interval  $[-\delta/2, \delta/2]$  in the neighborhood of the energy of the central fraction  $\bar{\gamma}$ , where  $\delta = \Delta\gamma/\bar{\gamma}$  is the relative width of the distribution function,  $u = \gamma/\bar{\gamma}$  is the normalized electron energy.

The spectrum distribution of the pump field is approximated by the Gaussian function:  $P_i = P_i^{\text{tot}} g(k_i)$ , where  $P_i^{\text{tot}}$  is the total intensity, and

$$g(u) = \frac{1}{\sqrt{\pi} \sigma} \exp \left[ - \left( \frac{u_i^2}{u^2} - 1 \right)^2 / \sigma^2 \right],$$

where  $\sigma = \Delta k_i / \bar{k}_i$  is the pump spectrum width and  $u_i = \gamma_i / \bar{\gamma}$  ( $\gamma_i = \sqrt{k_s / 4k_i}$ ) corresponds to the center of the spectrum in electron energy space.

Taking into account energy conservation, Eqs. (1) reduce a diffusion equation

$$\frac{\partial \hat{F}}{\partial \zeta} = \frac{\partial}{\partial u} \left( (\eta + P_s^0) g(u) u^2 \frac{\partial \hat{F}}{\partial u} \right), \quad (4)$$

where

$$\zeta = \frac{\omega_p^2 \lambda_i \bar{\gamma}}{4\pi c^2} \frac{\lambda_s^2 P_i^{\text{tot}}}{S_\perp P_*} z, \quad P_s^0 = \frac{2P_s^0 \omega_s^2}{\pi \omega_p^2 \bar{\gamma}}.$$

$$\eta = 1 - \int_0^\infty u \hat{F} du$$

is electron efficiency.

The results of computer simulation show that energy extraction efficiency grows with increasing pump spectrum width,  $\sigma$ . At the same time, the length of the interaction space, in which maximum efficiency is realized also increases. Computer simulation demonstrates that electron efficiency depends only to a small degree on parameter  $\delta$ , characterizing the dispersion of electron energy (cf. Figs. 1a and 1b). The saturation of amplification is indicated by the formation of a plateau in the distribution function (see Fig. 2). Its width and maximum efficiency are determined by the width of the pump spectrum and the distance between the center line of the pump field and the center of the electron distribution function. The pump intensity and the beam density influence the growth rate and the length of interaction space.

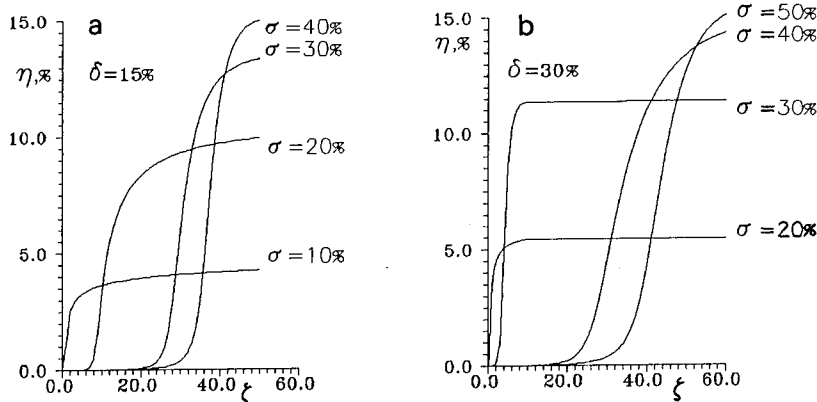


Fig. 1. Electron efficiency vs normalized longitudinal coordinate  $\zeta$  for (a) energy dispersion 15%; (b) energy dispersion 30%.

Let us estimate the parameters of an FEL-amplifier with wavelength  $\lambda_s = 0.3$  mm driven by an electron beam with current  $I = 5$  kA and particle energy 4.5 MeV ( $\bar{\gamma} = 10$ ). The beam moves through a stochastic undulator with characteristic period  $\bar{d} = 3$  cm, magnetic field intensity of 3 kOe, and interaction cross-section  $S_i = 0.5$  cm<sup>2</sup>. The solid curve in Fig. 3 shows the dependence of efficiency on the longitudinal coordinate for the case where the electron energy dispersion and the width of the pump field spectrum are both 30%. The maximum efficiency of  $\sim 10\%$  is reached after about 3 m. With an input power of 100 kW, the output power of about 1.2 GW of short-wave radiation corresponds to a gain of 40 dB. Note that a gyrotron may be used as a master oscillator [5].

The dashed curve in Fig. 3 represents a simulation of amplification of a monochromatic wave by the same electron beam as above passing through a regular wiggler with period  $\bar{d} = 3$  cm, and magnetic field intensity 3 kOe. Comparison of the curves shows that for an electron beam

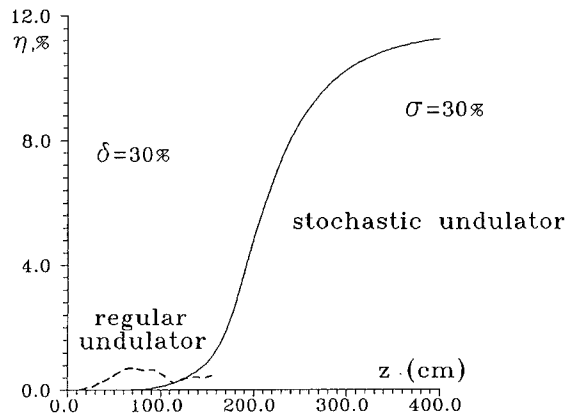


Fig. 3. Comparison of efficiency of an FEL driven by the electron beam with an energy dispersion of 30% in the case of a stochastic undulator (solid curve) and a regular undulator (dashed curve).

with a large energy dispersion (30%), the efficiency with an incoherent pump is a factor of 10 greater than with the regular wiggler. Thus, an incoherent pump wave may be used for efficiency enhancement of FELs driven by low-quality high-current electron beams.

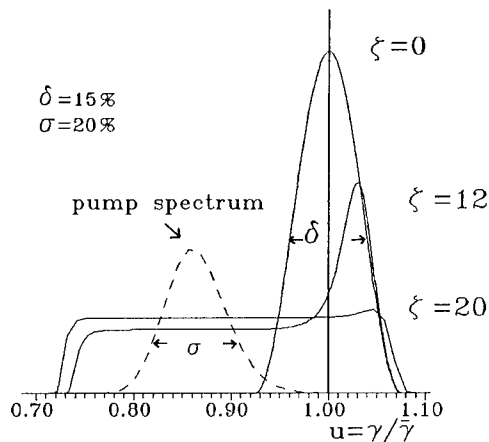


Fig. 2. Evolution of the electron distribution function.

## References

- [1] P. Sprangle, C.M. Tang and W.M. Manheimer, Phys. Rev. A 21 (1980) 302.
- [2] V.L. Bratman, N.S. Ginzburg and M.I. Petelin, JETP 76 (1979) 930.
- [3] A.T. Lin and J.M. Dawson, Phys. Rev. Lett. 42 (1979) 1670.
- [4] N.M. Kroll, Ph.L. Morton and M.N. Rosenbluth, Physics of Quantum Electronics, eds. S.F. Jacobs and M.O. Scully (Addison-Wesley, 1980), vol. 7, p. 113.
- [5] A.G. Luchinin and G.S. Nusinovich, Gyrotrons, IAP AN SSSR, Gorky (1989) p. 55.



ELSEVIER

## Predicted operating conditions for maintaining mode purity in the 1 MW 200 GHz FOM free electron maser <sup>☆</sup>

M. Caplan <sup>a,\*</sup>, T. Antonsen <sup>b</sup>, B. Levush <sup>b</sup>, A. Tulupov <sup>c</sup>, W. Urbanus <sup>c</sup>

<sup>a</sup> Lawrence Livermore National Laboratory, P.O. Box 808, L-637, Livermore, CA 94551, USA

<sup>b</sup> University of Maryland, Institute for Plasma Physics, College Park, Maryland 20742, USA

<sup>c</sup> FOM Instituut voor Plasmafysica, Rijnhuizen, P.O. Box 1207, 3430 BE Nieuwegein, The Netherlands

### Abstract

A Free Electron Maser (FEM) oscillator is now under construction at the FOM Institute (Rijnhuizen), Netherlands with the goal of producing 1 MW long pulse to CW microwave output in the range 130 GHz to 250 GHz with application to plasma heating. A newly developed multi-frequency FEM simulation code (MALT1D) using the windows approximation in the high gain regime and including AC space charge is used to model possibilities for longitudinal mode competition and resulting non-stationary chaotic output. The code predicts that stationary single frequency output can be obtained by taking advantage of the frequency dependence of the feedback reflection coefficient and by optimizing the gap spacing between the two wiggler sections.

### 1. Introduction

A Free Electron Maser (FEM) is now under construction at the FOM Institute, Netherlands which was designed with the long term goal of producing 1 MW microwave power long pulse to CW in the range 130 GHz to 250 GHz for application to heating of fusion plasmas. The first tests to be performed next year will be operated short pulse (10–20  $\mu$ s) at 200 GHz to verify the physics design. The overall FEM design concept has been discussed elsewhere [1] and consists of using a 2 MeV, 12 A DC beam with low stray body current so as to eventually make use of the depressed collector concept for high wall plug efficiency (40–60%). The essentials of the physics design is shown in Fig. 1 which consists of an electron beam interacting with HE<sub>11</sub> corrugated waveguide mode in a two section step tapered wiggler in order to achieve the required 5–6% electronic efficiency. The step waveguide concept allows for an adjustable feedback reflection coefficient and provides for separation of the microwave beam and electron beam. The long pulse or CW requirement requires a design with relatively high gain per pass (4–10) in order to reduce the feedback reflection and circulating microwave power.

The design parameters given in Table 1 were deter-

mined using a fully 3D non-wiggler averaged single frequency code developed at LLNL (CRM-FEL) which included effects of emittance, non-linear focusing, transverse betatron oscillators and AC space charge fields (and harmonics) [2]. A summary of the predicted performance is shown in Fig. 2 indicating 1.3 MW output. The assumption was that the FEM would operate at the peak of the linear gain curve and that there would be no longitudinal mode competition in the final steady state. In order to verify these assumptions, a multi-frequency non-stationary computer code was developed based on previous low gain/pass FEM oscillator codes developed at the University of Maryland [3]. The new codes (MALT1D, MALT 3D) combine features of both the Livermore and Maryland codes resulting in a high gain/pass multi-frequency oscillator simulation model including effects of slippage, AC space charge fields (including harmonics) emittance and transverse betatron motion.

### 2. Computer model

The electromagnetic fields are first expanded in known transverse waveguide modes whose amplitudes  $V(z, t)$  vary slowly in time and space about the centre frequency  $\omega$  and wavenumber  $k$ . The axial longitudinal space charge field is calculated separately:

$$E = \text{Re}\{V(z, t)e^{j\omega t - jkz}\}\epsilon(x, y) + \hat{z}E_z(\text{AC space charge}),$$

$$B = \text{Re}\{V(z, t)e^{j\omega t - jkz}\}(\hat{z} \times \epsilon(x, y)).$$

<sup>☆</sup> Work performed under the auspices of the U.S. Department of Energy by Lawrence Livermore National Laboratory under Contract W-7405-Eng-48.

\* Corresponding author. Tel. +1 510 423 6466, Fax +1 510 424 6401, e-mail u21567@f.nersc.gov.



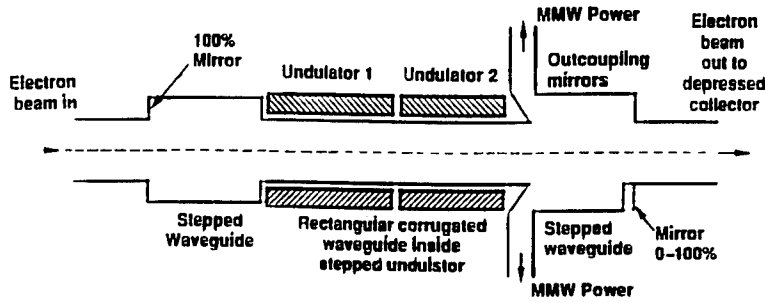


Fig. 1. Schematic of the FEM interaction circuit showing the step undulator, the waveguide and the reflection/outcoupling system.

The following wave equation for  $V(z, t)$  is obtained after averaging Maxwell's equations over the transverse cross section weighted by the normalized transverse mode function  $\epsilon$ :

$$\left[ \frac{\partial}{v_g \partial t} + \frac{\partial}{\partial z} \right] V(z, t) = \frac{4\pi I_0}{c} \frac{1}{N_p} \sum_p e^{-j\psi_p} \frac{U_{\perp}^p}{U_z^p} \cdot \epsilon(x_p, y_p) = \frac{4\pi I_0}{c} \left\langle e^{j\psi} \frac{U_{\perp}}{U_z} \cdot \epsilon \right\rangle_{t,z},$$

where  $v_g$  is the group velocity,  $\psi_p = (\omega t_p - kz)$  is the particle phase,  $\epsilon(x_p, y_p)$  is the transverse mode function, and  $I_0$  is the beam current. This equation is solved in the "windows approximation" which assumes that the radiation is locally periodic in time with period  $T_w = 2\pi/\Delta\omega$  where  $\Delta\omega$  is the frequency resolution. The amplitude is thus represented by

$$V(z, t) = \sum_n V_n(z) \exp[jn\Delta\omega(t - z/v_g)],$$

Table 1  
FEM design parameters

|                     |                      |
|---------------------|----------------------|
| Voltage             | 1.75 MeV             |
| Current             | 12 A                 |
| Wiggler period      | 4 cm                 |
| Length section 1    | 20 full periods      |
| Wiggler field 1     | 2000 G               |
| Length section 2    | 14 full periods      |
| Wiggler field 2     | 1600 G               |
| Inter-wiggler gap   | 6 cm                 |
| Waveguide size      | 20 × 15 mm           |
| Waveguide mode      | HE <sub>11</sub>     |
| Feedback reflection | 29%                  |
| Beam Size           | 1.2 mm               |
| Beam emittance      | 50–80 $\pi$ -mm-mrad |

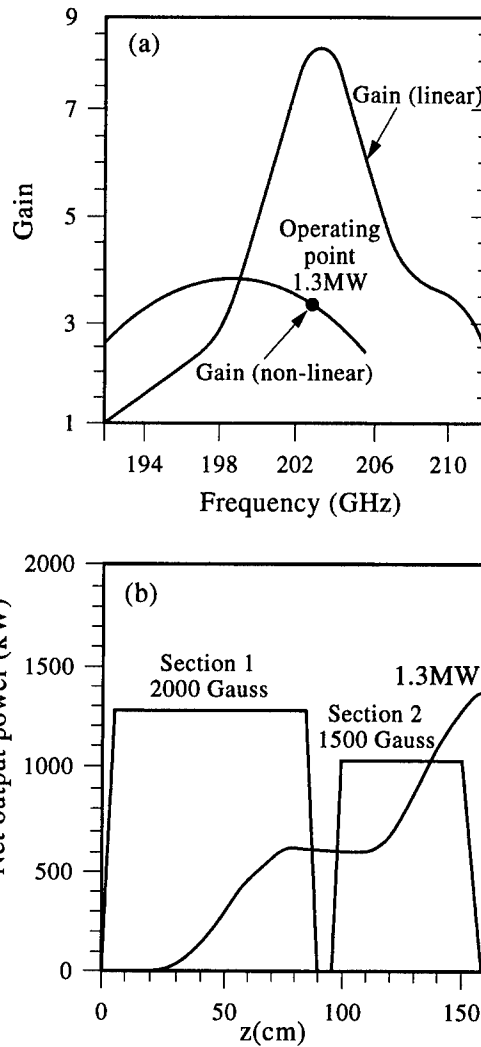


Fig. 2. Predicted FEM performance using stationary code. (a) Linear gain and non-linear gain versus frequency. (b) Net power generated versus distance.

where  $V_n(z)$  is the amplitude of a particular longitudinal mode whose frequency is  $\omega + \Delta\omega$ .

The equation for each longitudinal mode is obtained by Fourier transforming the wave equation in the slow time variable  $t$  and injecting multiple buckets  $N_q$  of particles throughout the window duration. One obtains

$$\frac{dV_n}{dz} = \frac{4\pi I_0}{c} \frac{1}{N_q} \sum_q \left\langle e^{-j\psi} \frac{U_{\perp}}{U_z} \cdot \epsilon \right\rangle_{t_q, z} \times \exp \left[ -jn\Delta\omega \left( t_q + \int_0^z dz' \left( \frac{1}{\bar{v}_z^q} - \frac{1}{v_g} \right) \right) \right]$$

average over entrance times and phases

The radiation is re-injected after each pass, but reduced by the frequency dependent reflection coefficient (assumed to be Lorentzian) giving rise to the following boundary condition:

$$V_n^{\text{new}}(z=0) = \rho_n V_n^{\text{old}}(z=z_L),$$

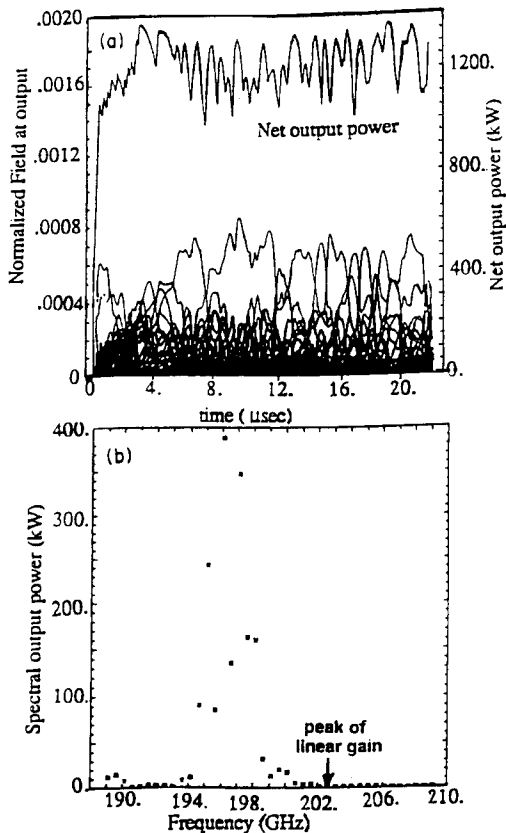


Fig. 3. Predicted FEM performance using multi-frequency code and original parameters of Table 1 with reflection independent of frequency. (a) Normalized output field for each frequency and total output power versus time. (b) Power (before reflector) versus frequency at 20  $\mu$ s after startup.

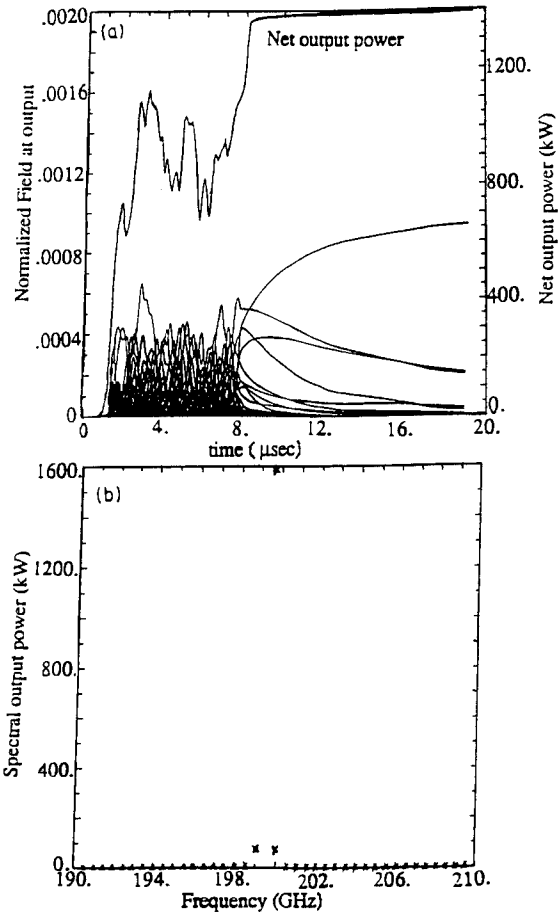


Fig. 4. Predicted FEM performance taking into account the frequency dependence of the reflection coefficient. Peak reflection: 20% at 199 GHz. (a) Normalized output field for each frequency and total output power versus time. (b) Power (before reflector) versus frequency at 20  $\mu$ s after startup.

where

$$\rho_n = \rho_{\text{max}} / [1 - j(n\Delta\omega)/\Delta\omega_R].$$

Finally, the axial AC space charge field is given by:

$$E_z(t_q, z) = \frac{16I_0}{r_b^2 c(k + k_w)} \text{Re} \left\{ \sum_{m=1}^{N_H} (R_m/m) e^{jm\psi} \langle e^{-jm\psi} \rangle_{t_q, z} \right\},$$

where  $N_H$  is the number of space charge harmonics and  $R_m$  is the space charge reduction factor. The 3D code MALT3D is obtained by supplementing the field equations with exact 3D non-wiggler averaged equations of motion. If the equations of motion and field equations are wiggler averaged and only  $\gamma$ ,  $\psi$  equations are kept, the MALT1D code is obtained. However, even in this code an effective average radius is used to take into account transverse effects (scalping, betatron oscillations) by calibrating in

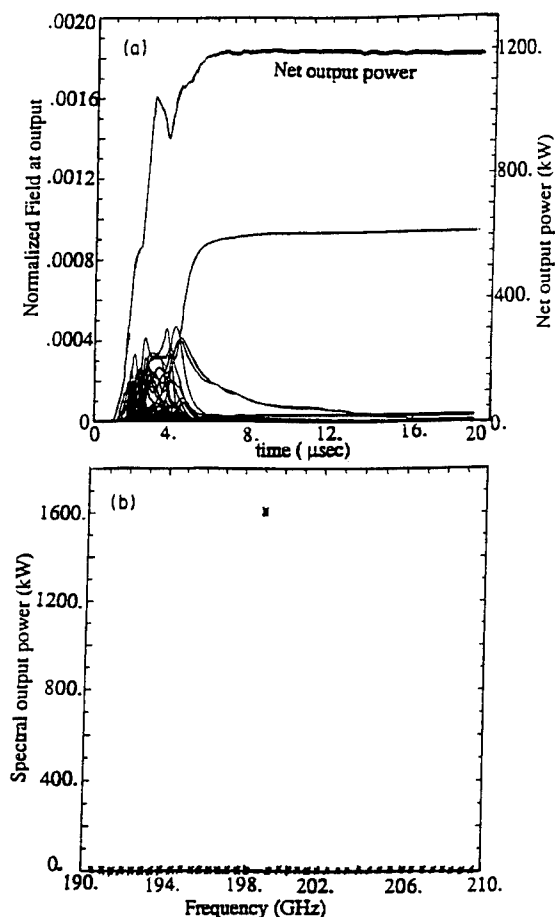


Fig. 5. Predicted FEM performance with wiggler gap optimized at 5 cm. Peak reflection: 25% at 200 GHz. (a) Normalized output field for each frequency and total output power versus time. (b) Power (before reflector) versus frequency at 20  $\mu$ s after startup.

the single frequency limit against the 3D stationary code in order to ensure similar interaction strengths.

### 3. Performance predictions for FEM using the multi-frequency code MALT1D

Computer simulations were performed for the original design parameters in Table 1. The frequency range simulated was from 190 GHz to 210 GHz using 41 modes separated by 0.5 GHz, all having initial power of 1 mW. The effective radius used in calculating AC space charge was 1.5 mm rather than 1.2 mm since comparison with the 3D simulations showed that the scalloping beam caused by

imperfect matching through the two wiggler sections was equivalent to an ideal beam of larger radius. The results are illustrated in Fig. 3 and immediately showed that there was substantial longitudinal mode competition with resulting non-stationary output.

The operating frequency of maximum power was not at the peak of the linear gain curve as earlier assumed, but shifted to near the peak of the non-linear gain curve. However, the net output power was in the range 1.1 MW to 1.3 MW, in agreement with the stationary results. These simulations assumed that the reflection coefficient was independent of frequency. However, recent measurements indicated that reflection was frequency dependent over the region of gain and could be represented as a Lorentzian with a half width to half maximum of  $\pm 7$  GHz. Simulations were performed with Lorentzian frequency dependence of the reflection coefficient and optimization was done varying the peak value of reflection and the frequency separation between the peak of the Lorentzian and the peak of the linear gain curve. Fig. 4 illustrates that greatly improved mode purity as well as steady output could be obtained by choosing a peak reflection of 20% centered at 199 GHz. The output power was 1.4 MW.

Further improvement was done by optimizing the inter wiggler gap. Previous stationary simulations indicated that a 5 cm gap rather than a 6 cm gap would reduce linear gain but increase non-linear gain. Simulations were performed using the 5 cm gap as well as the frequency dependent reflection coefficient with a peak of 25% centered at 200 GHz. The results are illustrated in Fig. 5 showing almost pure mode operation at 1.2 MW occurring with a rise time of roughly 6  $\mu$ s.

### 4. Conclusions

Mode purity in the original FEM design can be improved by optimizing the adjustable experimental parameters which include inter-wiggler gap, reflection coefficient and frequency separation between the peak of the linear gain curve and the peak of the reflection versus frequency curve. In all cases, a net output power of over 1 MW is achieved.

### References

- [1] W.H. Urbanus et al., Nucl. Instr. and Meth. A 331 (1993) 235.
- [2] M. Caplan, Nucl. Instr. and Meth. A 331 (1993) 243.
- [3] B. Levush and T. Antonsen, Nucl. Instr. and Meth. A 285 (1989) 136.

# Spectral dynamics of the FEM

P.J. Eecen<sup>\*</sup>, A.V. Tulupov, T.J. Schep

*FOM-Instituut voor Plasmafysica "Rijnhuizen", Associatie EURATOM–FOM, Postbus 1207, 3430 BE Nieuwegein, The Netherlands*

## Abstract

The FOM Fusion FEM project involves the construction and operation of a 1-MW, 100 ms pulse, rapidly tunable FEM in the 130–250 GHz range for fusion applications. The undulator is a novel step-tapered undulator, consisting of two sections with different strengths and lengths and equal periodicities, and separated by a fieldfree gap. The purpose of this novel proposal is to enhance the efficiency at high output power. The associated high gain in the linear and in the non-linear regime provide a unique oscillator.

The spectral dynamics of the high-current FEM with a low-quality cavity is calculated with a multi-pass, multi-frequency code. In this code the electrons are described 3D. The equations in the model are not averaged over a wiggler period. The continuous beam limit is considered. The radiation field is described as a sum over discrete frequencies. The millimeter wave field has the transverse radial dependence of the  $HE_{11}$ -mode in the rectangular corrugated waveguide.

The linear gain curve of the step-tapered undulator has a completely different spectrum than the single undulator. Furthermore the gain of the FEM is so high that non-linear interaction already occurs within a few passes. In the fully non-linear regime the gain is still relatively high and the output power reaches the required high level. Already in an early phase the spectral dynamics is strongly influenced by non-linear competition between the various maser modes. This non-linear mode competition is investigated, in particular the evolution of the sidebands is analyzed.

It is observed that the spectral signal at the resonant frequency of the second undulator is suppressed. This suppression is observed for several gap lengths. Furthermore the spectrum can change with the variation of the gap length from quasi-stable to chaotic.

## 1. Introduction

The FOM Institute for Plasma Physics at Rijnhuizen is now undertaking the development and construction of a free electron maser (FEM) [1] which will be used in future plasma experiments. The most important application of electron cyclotron (EC) processes in next generation tokamaks is plasma heating and current drive. For this purpose the high-power tunable millimeter wave source should fulfil the following requirements: a fast tunable frequency between 130 and 250 GHz, a narrow frequency spectrum, 1 MW cw output power and a overall efficiency not less than 35%.

The undulator in the present design is a novel step-tapered undulator. The undulator consists of two sections with different strength and length. The two sections have the same undulator period and are separated by a fieldfree gap. The first section consists of 20 periods and a peak magnetic field of 2.0 kG and the second section of 14

periods and a peak magnetic field of 1.6 kG. At both ends of the two undulators there are two matching cells of half an undulator period with strengths of  $\frac{1}{4}$  and  $\frac{3}{4}$  the nominal undulator strength. The beam enters the undulator on axis and the wiggle motion is symmetrical with respect to the undulator axis. The undulator fields of both sections have equal focussing forces in both directions. The planar undulators have both the same polarisation. The electrons wiggle in the horizontal plane.

The oversized, rectangular, corrugated waveguide with internal dimensions of 15 mm  $\times$  20 mm has corrugations at the vertical sides. This waveguide has low losses, as required for the high average power of the FEM. The radial structure of the millimeter waves is the one of plane polarised  $HE_{mn}$  modes.

This new idea of the step-tapered undulator has to provide a high linear gain and a high efficiency at the same time, which cannot be done with a normal undulator. For the present design the reflection coefficient is a profile with half width of about 7 GHz and with a maximum of only 29%. The peak value of the reflection coefficient can easily be changed in the design. From the physical point of view the study of results with the reflection coefficient

<sup>\*</sup> Corresponding author. Tel. +31 3402 31224, fax +31 3402 31204.

profile requires initially the understanding of the basic non-linear dynamics. So in this paper a rectangular reflection coefficient profile will be taken for the considered frequency window. In that way, the effect of the non-linear interaction on the total spectrum can be followed. The resonator is a low quality cavity because of the low reflection coefficient. This means, there is another unique feature in this design: in the steady-state regime the step-tapered undulator operates still with a high gain. In this case the field may not be considered nearly constant during one pass in saturation.

An important question is the evolution of the spectrum of the step-tapered undulator compared to the problems with the spectrum of a single undulator. The linear gain spectrum of the step-tapered undulator is expected to deviate from the single undulator. Not one peak, but at least two peaks are expected, because of the different resonance conditions of the two sections. In fact, the single pass, linear gain curve is even found to have four peaks. This does not look encouraging for a single mode operation in the steady-state. The danger is that these multiple peaks in the linear gain curve can all grow into the steady-state regime. Furthermore, each of these peaks is in principle capable of generating sidebands.

In the next section a brief description of the multi-frequency code MFF [2] is given. With this code, the dynamics of the frequency spectrum, starting from noise, is followed into the non-linear regime. In Section 4 it is observed unexpectedly that only the peak in the gain curve, which is at resonance with the first undulator remains to grow into saturation, while the peaks at higher frequencies are suppressed by non-linear interaction.

One of the surprising results is that after the power grows beyond a certain value a sideband is generated only at the lower frequency side of the peak. There are no sidebands generated at higher frequencies which seems a direct result of the non-linear interaction in the step-tapered undulator. The evolution of the sideband is discussed and a comparison is made with sidebands generated with a single undulator. Also the effect on the sideband by changing the gap-length is investigated.

## 2. Description of the multi-frequency field

Multi-pass calculations of the spectral evolution of the FEM can be done with the multi-frequency code MFF (Multi-Frequency FEM). As a first step in investigating the spectral dynamics of a step-tapered undulator the space-charge forces have been disregarded. Normally the space-charge forces slow down the development of spectral instabilities and therefore important peculiarities of the spectral dynamics are less pronounced. This contradicts to the purpose of the study in this paper to clarify the main features of the non-linear dynamics and to find the most dangerous spectral instabilities.

The radial structure of the maser field  $a_L$  is that of the  $HE_{mn}$  modes,

$$a_L(x, y, z, \bar{z}) = \hat{e}_x a(z, \bar{z}) \sum_{m,n} a_{mn}(x, y), \quad (1)$$

where  $a_{mn}(x, y) = \cos(m\pi x/b)\cos(n\pi y/a)$  and  $a$  and  $b$  are the dimensions of the rectangular waveguide. The multi-frequency field is expanded over the cavity modes. Each of these modes is given as a product of rapid phase factors and slowly varying envelopes

$$a(z, \bar{z}) = \sum_{l \ll N} a_l(z) e^{i(1+l/N)k_{z0}\bar{z}}, \quad (2)$$

where  $\bar{z} = z - v_{ph}t$ ,  $k_u$  is the undulator wavenumber,  $l$  labels the mode and  $N$  is a large number given by the number of wavelengths that fit in the cavity. The field  $a(z, \bar{z})$  is  $N\lambda_{z0}$ -periodic and the minimal distance between two maser frequencies is  $\omega_0/N$ . The phase velocity is defined as  $v_{ph} = \omega_0/k_{z0}$ , so the phase for the central frequency is  $k_{z0}\bar{z} = k_{z0}z - \omega_0 t$ . The phase velocity is taken to be the same for all different modes in this model. This means that the dispersion relation for each frequency for each  $HE_{mn}$  mode is fixed

$$\left(1 + \frac{l}{N}\right)^2 k_0^2 \approx \left(1 + \frac{l}{N}\right)^2 k_{z0}^2 + \left(\frac{m\pi}{b}\right)^2 + \left(\frac{n\pi}{a}\right)^2, \quad (3)$$

up to order  $(l/N)^2$  which is a small number.

Standard averaging over a wiggler period is not applied, which is appropriate for a high gain FEM. The electron dynamics is calculated three dimensionally. Emission and energy spread are taken into account. It should be noticed, that since the radiation field is calculated in the Fourier space, slippage is automatically included. This effect is important for the proper description of the phase mixing.

Typical parameters of the calculations are  $N = 200$ , which gives a frequency spacing of about 1 GHz, when the central frequency is about 200 GHz. The number of modes is typically 50 and the number of particles about  $80N$ .

## 3. Results and conclusions

The study of the basic spectral dynamics of the step-tapered FEM performed with the multi-frequency code MFF with parameters given in Table 1 is going to clarify the role of the step-tapered undulator on the evolution of the spectrum. The reflection coefficient is taken to be equal for all the frequencies in order to have results which give direct information about the interaction in the step-tapered undulator itself.

When the power is relatively small, the FEM is in the linear gain regime. If we disregard the prebunching of the electrons in the first section to emphasize the difference of the step-tapered undulator and the single undulator, both sections of the step-tapered undulator act like independent

Table 1

Design parameters of the FOM FEM for Fusion applications, as implemented in the code MFF.

|                                 |                             |
|---------------------------------|-----------------------------|
| Beam voltage                    | 1.75 MV ( $\gamma = 4.42$ ) |
| Beam current                    | 12 A                        |
| Beam emittance                  | $49 \pi$ mm mrad            |
| Beam radius                     | 0.92 mm                     |
| Peak wiggler field section 1    | 2.0 kG                      |
| Peak wiggler field section 2    | 1.6 kG                      |
| No. undulator periods section 1 | 2.0                         |
| No. undulator periods section 2 | 1.4                         |
| Wiggler period                  | 4.0 cm                      |
| Gap between wigglers            | 6.0 cm                      |
| Waveguide mode                  | HE <sub>11</sub>            |
| Waveguide dimensions            | 20 × 15 mm                  |
| Reflection coefficient          | 29%                         |

FEMs. Since their undulator strengths are different, also their resonance conditions are different and two peaks in the linear gain curve can be expected. The peaks in the gain curves for the first or the second section are 203 GHz and 220 GHz respectively and are well separated. These peaks are shown as the dashed lines in Fig. 1. The peak values of the linear gain curves are 30 and 4.5. However, the gap and the prebunching of the electrons, because of the interaction in the first section modifies the gain curve. The linear gain curve for the step-tapered undulator is shown in Fig. 1 and is drastically changed with respect to the linear gain curves of the separate sections. The gain curve given by the solid line has four peaks. The two peaks with the lowest frequencies (200 GHz and 208 GHz) result from the peak of the first undulator, modified by the gap and the second undulator. The peak at 220 GHz is generated by the second undulator, enhanced by the pre-bunched electrons. One can conclude that the system is not

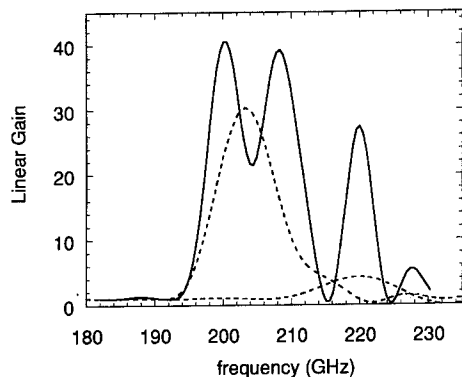


Fig. 1. The solid line is the linear gain for the different frequencies at the end of the first pass through both undulators. The two dashed lines are the linear gain curves for the two sections separately as a comparison.

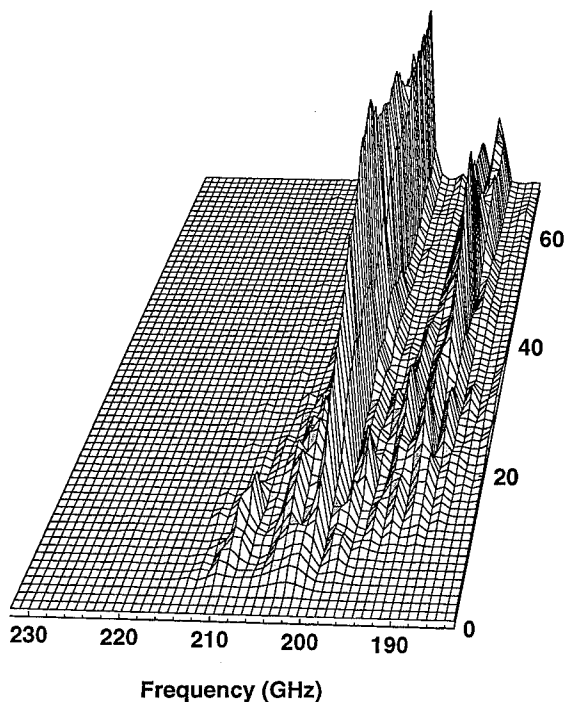


Fig. 2. The evolution of the power for the different frequencies during the first 70 passes.

a sum of two separate systems, but the step-tapered undulator operates as a whole system with a significant klystron effect.

From the single pass gain curve one could suspect that the spectrum evolves into a discrete spectrum with well distinguished lines with about 10 GHz spacing; however, this is not the case. When a certain power level has been arrived, the step-tapered undulator begins to operate as a non-linear system. This starts already in an early stage,

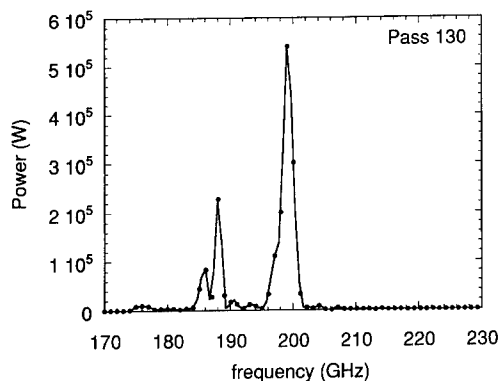


Fig. 3. The power for the different frequencies at the end of the 130th pass.

well before the power of the stationary state is reached. The operation is drastically changed by the non-linear internal dynamics. The dynamics of the second section is totally determined by the coherent bunching of the electrons in the first section, in which case the second section operates as a pure amplifier section and not as an oscillator.

This is shown in Fig. 2, where the evolution of the spectrum for the first 70 passes is shown. The power in each mode is plotted at the end of each pass just before the reflection. We recall that 71% of this signal is coupled out. In Fig. 2 the important result is observed, that the peaks with frequencies higher than the first one at 200 GHz, are suppressed by the system. This is clearly shown in Fig. 3, where the profile of the power is plotted for the 130th pass. The figure shows that the power for the frequencies beyond the main peak are effectively zero. This is due to the internal dynamics of the electrons in the step-tapered undulator. The coherent bunching in the first section is enough to make the second section an amplifier of the main peak. This suppression of higher frequencies also occur when the gap length is changed. At this point it should be stressed that we did not introduce any frequency discrimination or filtering.

Before discussing the sideband, which is clearly visible in Figs. 2 and 3, the results of multi-frequency calculations are shown for only a single-section undulator in Fig. 4. The undulator has the same parameters as the first section in the FEM, but here 30 undulator periods are taken in order to get overbunching faster and higher saturated power to show the sideband behaviour more pronounced. The field is plotted after some passes. There are clearly two sidebands generated at each side of the main signal. The position of the sidebands can be estimated analytically by assuming that the electrons are deeply trapped within the ponderomotive well. When applying the resonance condition for a low energy electron beam to the well

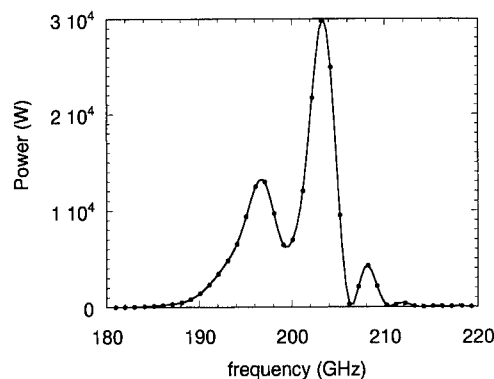


Fig. 4. Power for the different frequencies for an one section undulator. The undulator has 30 periods and the parameters of the first section of the FEM.

known result for the sideband position, one finds that the position for the sideband is approximately given by

$$\Delta k \approx \pm \frac{k_{\text{pon}}}{k_u} \frac{\Omega_{\text{syn}}}{c} \approx \pm \frac{2k_{\text{pon}}}{\beta_z \sqrt{1 + a_u^2}} \sqrt{a_u a_s}, \quad (4)$$

where  $k_{\text{pon}} = k_u + k_{z0}$  and  $a_u$  and  $a_s$  are the normalised undulator and radiation fields. When the estimate of Eq. (4) is applied to Fig. 4, we find that  $\Delta \nu \approx \pm 5$  GHz, which is exactly the case in the picture. In the following passes, the spectrum is becoming chaotic and more and more peaks are generated.

Returning to Figs. 2 and 3, the most striking result is that the sidebands only grow at frequencies lower than the frequencies in the main peak. This behaviour is quite different than that of a single undulator where sidebands grow at both sides of the main peak. The main peak in the power at 199 GHz in Fig. 3 is very narrow and contains a power of 1.15 MW within 4 GHz spacing. The estimate for the frequency spacing of the sideband (4) gives 10.2 GHz, which is very close to the observed 11 GHz.

Another observation that can be made from Fig. 2 is that a regime is reached where sidebands gain and lose energy at a regular interval at the cost of the main signal, but stay at the same position in frequency space. This regime can be called a quasi-stable regime. Whether the regime is stable or not can only be concluded after calculations on a longer time scale. This quasi-stable operation regime, with the two distinct spectral lines, may be an interesting option for fusion applications.

Some calculations have been done with different gap lengths to investigate the effect on the spectrum. It is clear that the linear gain curves depend on the gap length. The influence of the gap length on the spectrum in the non-linear regime is quite diverse. Chaotic spectral behaviour was observed at an early stage with a  $1\lambda_u$  gap. With a gap of  $1\frac{1}{4}\lambda_u$ , the system generates a sideband at much higher pass numbers. The power in the main peak stays approximately the same and the peak position changes much less than in the case of the  $1\frac{1}{2}\lambda_u$  gap length.

### Acknowledgement

This work was performed as a part of the research programme of the association agreement of EURATOM and the "Stichting voor Fundamenteel Onderzoek der Materie" (FOM) with financial support from the "Nederlandse Organisatie voor Wetenschappelijk Onderzoek" (NWO) and EURATOM.

### References

- [1] W. Urbanus et al., Nucl. Instr. and Meth. A 318 (1992) 16;  
W. Urbanus et al., Nucl. Instr. and Meth. A 331 (1993) 235.
- [2] P.J. Eecen, A.V. Tulupov and T.J. Schep, Nucl. Instr. and Meth. A 341 (1994) 309.

# Competition of longitudinal modes and the scenario of single-mode regime build-up for the FOM-Fusion-FEM project

V.L. Bratman <sup>\*</sup>, A.V. Savilov

*Institute of Applied Physics, Russian Academy of Science, 603600, 46 Ulyanov Str., Nizhny Novgorod, Russian Federation*

## Abstract

The temporal dynamics of excitation of a free-electron maser with a prolonged and low- $Q$  microwave system is studied taking into account the feedback frequency dispersion, the HF space charge, and the undulator tapering. It is shown that in spite of a great many longitudinal modes excited at the small-signal stage, even a rather broadband feedback dispersion significantly shortens the transient time and provides a stable single-frequency operating regime.

## 1. Introduction

The free-electron maser (FEM), which is under construction at the FOM-Institute Rijnhuizen, The Netherlands, in the framework of the FOM-Fusion-FEM project [1], has to provide in a long-pulse (CW in perspective) regime at output powers of 1 MW in a very broad frequency range, from 130 to 260 GHz, with fast frequency tuning over 10%. In accordance with the design described in Refs. [1–3], the FEM represents an auto-oscillator with a low- $Q$  microwave system consisting of an amplifier with a relatively low gain and a broadband feedback system (Fig. 1). In order to decrease ohmic losses, the microwave system of the amplifier is an overmoded rectangular waveguide with corrugated walls. The original feedback system suggested by Denisov [2] is based on the phenomenon of multiplication of the quasi-optical wave beams. The system is formed by two quasi-optical stepped reflectors, each terminated by simple mirrors. The reflector splits the wave beam, injected from the relatively narrow operating waveguide, into two beams which are reflected by mirrors. The reflection coefficient of the input reflector is 100% and the output reflection coefficient is widely controlled by a shift between the mirrors.

In order to obtain the necessary HF power at a rather small electron current 12 A at a voltage about 2 MeV one was forced to use, in particular, both a long interaction space and a tapered undulator [3]. However, as in any resonant TWT, the long length and complexity of the system can lead to both a multi-frequency operating regime and a long duration of the transient process due to compe-

tition of longitudinal modes. Many of these modes located in the band of the single-pass amplification and of the feedback arise from initial noises during the small-signal stage of the auto-oscillator excitation. The result of their rather complicated interaction and the character of the operating regime should be described in the framework of the nonstationary spatio-temporal approach [4–6]. Developing the 1-D code, designed for low- $Q$  systems in Ref. [5], as well as the considerably simpler two-mode approach [7], we study the generation regime of the FEM taking into account such significant factors as HF space charge, undulator tapering, and feedback frequency dispersion. It is shown that a rather wide ( $\sim 5\%$ ), but finite, frequency band of the feedback provides the stable single-frequency regime and considerably decreases the transient time in comparison with an infinitely wide band.

## 2. Spatio-temporal approach

The FEM excitation can be described by means of nonstationary equations [4–6] for electrons

$$\frac{\partial u}{\partial \zeta} = \text{Im}((a_n + q^2 p) e^{i\theta}), \quad \frac{\partial \theta}{\partial \zeta} = u - \delta(\zeta), \quad (1)$$

and for the HF field

$$\frac{\partial a_n}{\partial \zeta} + \frac{\partial a_n}{\partial \tau} = 2i\rho, \quad \rho = \langle e^{-i\theta} \rangle_\varphi, \quad (2)$$

where  $u = \mu C^{-1}(1 - \mathcal{E}/\mathcal{E}_0)$  is the normalized energy loss of a particle,  $\zeta = h_0 C z$  is the normalized coordinate,  $a_n$  is the normalized amplitude of the HF field at its  $n$ th trip over the interaction space,  $q$  is the space charge parameter,  $\theta = \omega_0 t - h_0 z$  is the electron phase with respect to the synchronous combination wave,  $\tau = \omega_0 C(t - z/v_{z0})(c/v_{gr}$

<sup>\*</sup> Corresponding author. Tel. +7 8312 384552, fax +7 8312 362061.



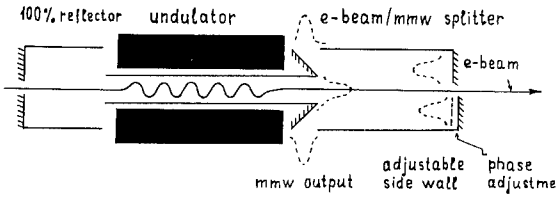


Fig. 1. FOM-Fusion-FEM microwave system.

$-c/v_{z0})^{-1}$ ,  $\omega_0 = v_{z0} h_0(\omega_0)$  is the synchronous frequency,  $\delta(\zeta) = (\omega_0/h_0 v_z(\zeta) - 1)C^{-1}$  is the mismatch describing the undulator tapering,  $v_z(\zeta)$  is the unperturbed longitudinal electron velocity changed due to the undulator tapering,  $C^3 = e\mu\kappa^2/mc^3 N\gamma_0$  is the Pierce amplification parameter, and  $\mu = \gamma_0^{-2}$  and  $\kappa = eA_u/mc^2\gamma_0$  are the parameter of the inertial bunching of particles and the coefficient of the electron-wave coupling. The initial conditions for the electron beam, being unmodulated at the input, can be written in the following way

$$u(\zeta=0, \tau) = 0, \quad \theta(\zeta=0, \tau) = \varphi, \quad (3)$$

where the initial phases  $\varphi$  are distributed homogeneously over the interval  $[0, 2\pi)$ . The simplest boundary condition for the HF field (not taking into account the effect of the feedback frequency dispersion, important for the FOM-FEM) can be represented in the following form [5]

$$a_{n+1}(\zeta=0, \tau) = \sqrt{R} a_n(\zeta=L, \tau-T), \quad (4)$$

where  $R$  is the product of the reflection coefficients,  $T$  is the feedback time, and  $L$  is the normalized length of the interaction space. The analysis including such additional factors as HF space charge and the tapered undulator shows that, as in the simplest situation [5], at a fixed  $R$  the parameter  $L$  primarily defines the type of the operating regime. The auto-oscillator is excited if  $L$  is larger than the starting value  $L_{st}(R)$ . If the parameter  $L$  does not significantly exceed the starting value, then the operating regime is the single-frequency one with the only excited mode being that which has the largest small-signal single-pass gain (the “main” mode). But if  $L$  exceeds a some

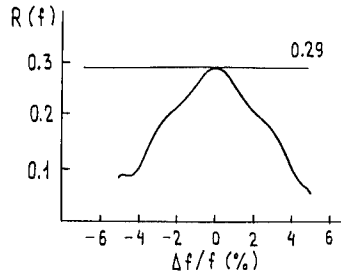


Fig. 3. Frequency dispersion of the real FOM-FEM feedback at 200 GHz.

critical value,  $L_{cr}(R)$ , then many longitudinal modes are represented at the operating regime; too long  $L$  leads also to a very long transient time. Such operating regimes were obtained for the FOM-FEM at various frequencies on the basis of Eqs. (1)–(4) (e.g. Fig. 2 illustrates maser dynamics at 200 GHz). It is clear that the existence of the limited frequency band of the feedback (Fig. 3) should be able to simplify both the transient process and the spectrum of the operating regime. Further we study this problem by means of both the simplest two-mode approach [7] and the spatio-temporal one.

### 3. Two-mode approach

For the FOM-FEM the excess over the critical length  $L_{cr}$  is not too high and the operating regime includes, besides the main mode, only a few of other parasitic modes with small amplitudes (Fig. 2b). Then the operating regime of an auto-oscillator with a rather low quality, having an essentially non-equidistant spectrum of eigenmodes, can be studied using the two-mode approach [7], when excitation of any parasitic mode is assumed to be defined only by the main mode independently of all other parasitic ones because of their small amplitudes. The two-mode approach permits us to obtain some analytical results and to divide the process of maser excitation into the five following stages (Fig. 2a).

1) The linear stage. A lot of modes arise from small initial noise independently of each other.

2) Suppression of slow-growing modes by fast growing ones. A few fast-growing modes reach the nonlinear regime and suppress slow-growing modes.

3) Fast-growing mode competition. One of the fast-growing modes suppresses all the others.

4) Excitation of a parasitic mode. At the beginning of this stage the regime is close to the single-frequency one of the main mode. However, if there is an excess over the critical value,  $L > L_{cr}$ , this regime proves to be unstable with respect to excitation of parasitic modes.

5) Two-mode regime. The stable regime of the main mode and basically one parasitic mode.

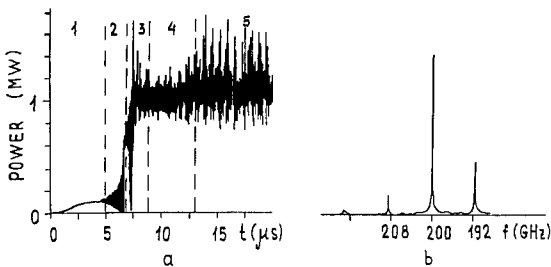


Fig. 2. Dynamics of the FEM excitation (the feedback frequency dispersion is absent). Net output HF power versus time and the five stages of the excitation process (a), and the spectrum at the saturated regime (b).

So the type of the operating regime should be single-mode if generation of the main mode is stable with respect to excitation of any other mode. This problem can be studied by means of the following rather simple set of equations:

$$\frac{du}{d\zeta} = \text{Im}\{(a + q^2 p) e^{i\varphi + i\Phi} + (\tilde{a} + q^2 \tilde{p}) e^{i\tilde{\varphi} + i\Phi}\},$$

$$d\Phi/d\zeta = u - \delta(\zeta), \quad (5)$$

$$\frac{da}{d\zeta} + i\Delta a = 2i\rho, \quad \rho = \langle e^{-i\varphi - i\Phi} \rangle_{\varphi, \tilde{\varphi}},$$

$$\frac{d\tilde{a}}{d\zeta} + i\tilde{\Delta}\tilde{a} = 2i\tilde{\rho}, \quad \tilde{\rho} = \langle e^{-i\tilde{\varphi} - i\Phi} \rangle_{\varphi, \tilde{\varphi}}, \quad (6)$$

where  $a$  and  $\tilde{a}$  are the amplitudes of the main and parasitic modes respectively,  $\Delta = (\omega - \omega_0)/\omega_0(1 - v_{gr}/v_{z0})C^{-1}$  is the mismatch of the main mode corresponding to the maximal single-pass gain in the small-signal regime and being close to the space charge parameter  $q$  for rather large  $L$  ( $e^L \gg 1$ ),  $\tilde{\Delta}$  is an arbitrary mismatch of the parasitic mode,  $\varphi$  and  $\tilde{\varphi}$  are the independent initial electron phases with respect to each of the modes, and  $\Phi$  is the electron phase change.

At the beginning of the fourth stage the regime is close to the single-frequency one of the main mode. Correspondingly, the boundary conditions for the modes are as follows:

$$a(L) = \sqrt{R(\Delta)} a(0), \quad |\tilde{a}(0)| \ll |a(0)|. \quad (7)$$

Single-mode generation should be maintained if for any parasitic mode mismatch  $\tilde{\Delta}$  the small-signal gain  $g(\tilde{\Delta}) = |\tilde{a}(L)/\tilde{a}(0)|^2$  of this mode under the condition of the main mode generation proves to be smaller than the losses:  $g(\tilde{\Delta}) < R^{-1}(\tilde{\Delta})$ .

When dispersion  $R(\Delta)$  is absent, the parasitic mode with the frequency 192 GHz is excited (Fig. 4), another parasitic mode at 208 GHz is excited too, but its admixture is very small (Fig. 2b). However, the account of the real

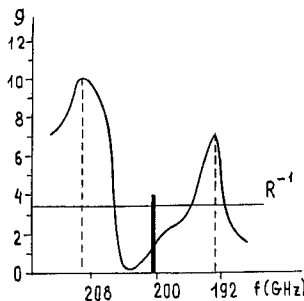


Fig. 4. Two-mode approach. Small-signal single-pass amplification of parasitic longitudinal modes  $g(f)$  at the regime of the excited main mode versus frequency (the main frequency is shown by the bold column).

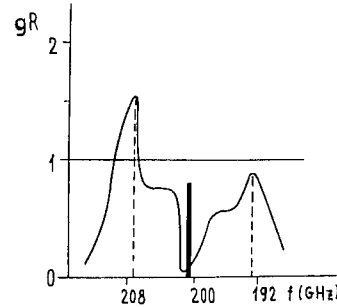


Fig. 5. Two-mode approach. Suppression of the most dangerous parasitic longitudinal modes in the presence of the real feedback.

feedback dispersion (Fig. 3) permits us to expect suppression of the most dangerous 192 GHz-mode (Fig. 5) and obtain almost single-frequency operation with the admixture  $|\tilde{a}/a| \approx 0.1$  of the 208 GHz-mode.

#### 4. Feedback frequency dispersion in the spatio-temporal approach

The two-mode approach has been confirmed after the account of the dispersion  $R(f)$  in the framework of the more correct spatio-temporal approach which permits us to study the influence of the dispersion not only on the operating regime but also on the transient process. Simulating the wave traveling through the real output reflector and representing the HF field inside the reflector as a sum of transverse modes of the wide waveguide we obtain the following two-dimensional boundary condition:

$$a_{\leftarrow}(t) = \sum_{m,n} b_m r_{m,n} \sin(\pi n/2) \times e^{-i\psi_m - i\psi_n} a_{\rightarrow}(t - \Delta t_m - \Delta t_n), \quad (8)$$

where  $a_{\rightarrow} = a(L, \tau)$  is the field at the input of the reflector (at the output of the interaction space),  $a_{\leftarrow}$  is the reflected field,  $b_m = (2/D) \int_0^D g(x) \sin(\kappa_m x) dx$  are the Fourier coefficients of the transverse structure  $g(x)$  of the narrow waveguide field over the transverse mode of the reflector waveguide,  $D$  is the width of the reflector waveguide,  $\kappa_m = \pi m/D$ ,  $x$  is the transverse coordinate,

$$r_{m,n} = \frac{2}{D} \int_0^D r(x) \sin(\kappa_m x) \sin(\kappa_n x) dx,$$

$r(x)$  is the reflector function describing the two mirrors of the output reflector ( $r = 1$  for one reflector mirror,  $r = e^{i\chi}$  for another reflector mirror and  $r = 0$  between the mirrors,  $\chi$  is the phase shift controlling the reflection coefficient),  $\psi_m = k_{m0} l$ ,  $k_{m0} = (\omega_0^2/c^2 - \kappa_m^2)^{1/2}$ ,  $l$  is the reflector length,  $\Delta t_m = l/v_{gr,m}$  is the delay time of the  $m$ th transverse mode, and  $v_{gr,m} = c^2 k_{m0}/\omega_0$  is the group velocity of the  $m$ th mode at the synchronous frequency.

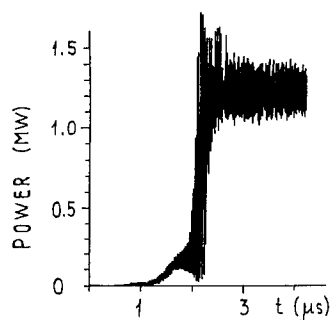


Fig. 6. Temporal dynamics of the FOM-FEM excitation (the real feedback frequency dispersion is included).

The account of the feedback dispersion, using Eq. (8) as the boundary condition for the spatio-temporal equations (1)–(3), significantly changes the excitation picture (Fig. 6). In spite of the rather broadband ( $\sim 5\%$ ) feedback frequency dispersion, the operating regime proves to be stable and single-mode. The feedback frequency dispersion considerably simplifies the process of the excitation and decreases the transient time. This effect should make the frequency tuning which is to be provided during the experiment easier.

## 5. Conclusion

Even a rather broadband frequency dispersion of the feedback proves to greatly influence the process of maser excitation. Because of the decrease of the number of longitudinal modes arising at the small-signal stage, the

dispersion significantly shortens the transient time. Besides, in the case of a small excess over the critical length, a rather broadband dispersion can provide the stable single-frequency operating regime due to suppression of the most dangerous parasitic longitudinal modes with frequencies considerably different from the frequency of the main mode.

## Acknowledgements

The authors are grateful to N.S. Ginzburg, G.G. Denisov, A.S. Sergeev, W.H. Urbanus, A.G.A. Verhoeven, M. Caplan, and A.V. Tulupov for useful discussions.

## References

- [1] A.G.A. Verhoeven et al., Proc. 17th Int. Conf. on IR and MM Waves, Pasadena, 1992.
- [2] A.G.A. Verhoeven et al., Proc. 2nd Int. Conf. on Strong Microwaves in Plasmas, Nizhny Novgorod, Russia, Vol. 2. (1993) 616.
- [3] A.V. Tulupov, M.J. van der Wiel, W.H. Urbanus and M. Caplan, Proc. 15th Int. Conf. on Free Electron Lasers, Nucl. Instr. and Meth. A 341 (1994) 305.
- [4] Ya. L. Bogomolov, V.L. Bratman, N.S. Ginzburg, M.I. Petelin and A.D. Yunakovsky, Opt. Commun. 36 (1981) 209.
- [5] N.S. Ginzburg and A.S. Sergeev, Zh. Tekhn. Fiz. 61 (1991) 133.
- [6] T.M. Antonsen, Jr. and B. Levush, Phys. Fluids B 1 (1989) 1097.
- [7] V.L. Bratman and A.V. Savilov, Zh. Tekhn. Fiz. 64 (11) (1994).



ELSEVIER

## Electrostatic-accelerator FELs for power beaming

Isidoro Kimel, Luis R. Elias \*

*CREOL and Department of Physics, University of Central Florida, Orlando, FL 32826, USA*

### Abstract

We propose the use of electrostatic-accelerator free-electron lasers (EAFELs) to generate intense, CW, single-mode, laser radiation for space power beaming applications such as envisioned by the project SELENE. We discuss two basic FEL configurations employing present electrostatic accelerator technology ( $\leq 25$  MV), together with the electron gun and electron collector beam recovery technology first developed for the UC Santa Barbara FEL.

### 1. Introduction

An ideal radiation source for space power beaming, as envisioned by the project SELENE [1], would generate a truly CW output since that is the best operating regime for photovoltaic (PV) cells. The only known type of FEL that has the potential of operating CW is an electrostatic accelerator driven FEL (EAFEL) [2]. Other accelerators produce electron beams with a complicated time structure consisting of macropulses which in turn are made of very short micropulses.

Also, EAFELs tend to operate in a single mode [3] in contrast to the micropulse FELs with bandwidths consisting hundred of longitudinal modes. This is an added advantage of our type of FEL for space power beaming, since it should be easier to propagate a single mode beam in a controlled way over long distances, rather than a highly multimoded beam.

Another big advantage of EAFELs is the potential of reaching much higher efficiencies than RF-FELs. With RF machines efficiencies of 1%, or even lower, are typical. The overall efficiency loss is compounded by power losses in the klystrons, imperfect coupling of the radiation to the electrons in the accelerating cavities (plus radiation losses in the cavities) and by dumping of the electron beam. On the other hand in an EAFEL, the electron beam is accelerated by electrostatic fields and is recovered to a very large degree. Also, the power supplied to EAFELs is in the form of efficient DC power, mainly at the electron collector. As a consequence, efficiencies levels of 25% and higher are not difficult to achieve in practice, while there is no theoretical reason why it cannot be as high as 70–80%.

In the present paper we present two possible scenarios of EAFEL sources for power beaming. The first and simplest will generate 1.54  $\mu\text{m}$  radiation for GaSb PV cells. In its lowest power version the output will be 100 kW combining existing technology: a 25 MV accelerator similar to the Oak Ridge machine, a 2 A electron gun and collector like we used in previous work and a 7.6 mm period undulator not very different from the 8 mm one we are constructing at present. The second requires the use of two accelerators to reach higher energies and it is justified on the grounds that it will provide the best solution for the SELENE problem.

### 2. True CW versus pulsed FELs for PV illumination

Most existing FELs generate radiation consisting of short pulses. This is the reason why it is generally believed that FELs are only capable of producing such type of radiation. However, one kind of FELs actually generates long pulses and has the potential of operating in a true CW regime. These are electrostatic-accelerator FELs (EAFELs) in which the electron beam is fully recovered. Such a CW EAFEL is under construction at CREOL, University of Central Florida [2].

When considering FELs for power beaming it is important to analyze how the radiation is going to be processed by the photovoltaic cells in satellites. Existing solar cells were designed, of course, for CW operation. It is only recently that the behavior of PV cells under short-pulsed radiation started to be investigated [4]. For the proposed average intensity of 5 suns or 6.8 kW/m<sup>2</sup> for the project SELENE, the peak intensity of a typical RF-FEL output is, conservatively, about 2400 times that average, or about 16 MW/m<sup>2</sup>. It is not known how such high peak intensities can affect the long term performance or the lifetime of a

\* Corresponding author. Tel. +1 407 658 6800, fax +1 407 658 6890, e-mail elias@fel.

PV cell. Besides that, there are several factors that decrease the efficiency of pulsed-laser as compared to CW illumination. Three of these factors are [4]:

a) Series resistance. In a PV cell illuminated with radiation consisting of high intensity micropulses the instantaneous current  $I_{\text{ins}}$  output can be much larger than the average current. Then, the ohmic losses  $RI_{\text{ins}}^2$  can severely reduce the cell performance.

b)  $I$ - $C$  ringing. The large p-n junction capacitance of a PV cell combined with the inductance of the output wiring confronts alternating currents with a LC circuit. The resulting oscillations have the effect of shifting cell operation from the optimum bias point. This further reduces the cell efficiency.

c) Output inductance. For high instantaneous current, its product with the output inductance is formally larger than the open circuit voltage during a certain length of time. During all that time the cell is practically held at open-circuit voltage with negligible power generation.

These recent studies [4] show that the efficiency decrease is much more serious for induction-FEL than for RF-FELs. This seems to have already ruled out induction-FELs as candidates for space power beaming, while further studies are being performed on efficiency reduction by the RF-FELs pulse structure.

### 3. Single electrostatic-accelerator FELs

The highest voltage electrostatic accelerator in operation is the 25 MV machine at Oak Ridge National Laboratory. An EAFEL can be based on a positive terminal (Fig. 1) or negative terminal accelerator (Fig. 2). In the positive terminal system the radiation has to be extracted through the terminal but the electron beam line is simpler.

In Fig. 1 the tank E encloses the whole system. G is the electron gun with the cathode at ground potential. After leaving the gun the electrons enter the acceleration tube AT towards the positive terminal T at 25 MV. The radiation is generated in the undulator sandwiched between the rows of magnets of the resonator. The resonator-undulator UR is located at the terminal. After exiting the resonator the electrons enter the deceleration tube DT. In traversing the deceleration tube the electrons lose most of their kinetic energy. The slowed down electrons then enter the collector C where they are captured.

An essential ingredient in EAFELs is electron beam recovery at the collector. The electrons arrive at the collec-

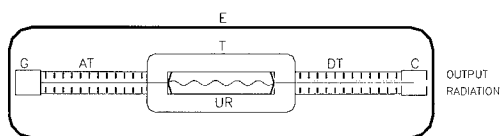


Fig. 1. FEL with a single positive-terminal electrostatic accelerator.

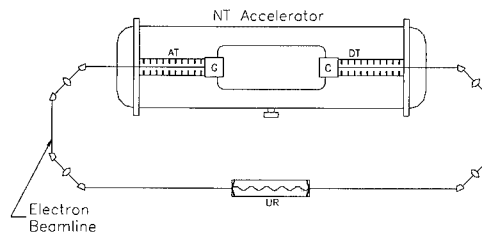


Fig. 2. FEL with single negative-terminal electrostatic accelerator.

tor with a certain energy spread. For this reason the collector consists of several stages for collection of electrons with different energies. With several stages, energy collection efficiency in the 70–80% range can be achieved. The energy lost by the electrons to radiation is accounted for by a difference between the weighted mean voltage of the collector and the guns cathode voltage. The energy lost by the electrons is replenished very efficiently in the form of power supplied to the collector by DC power supplies.

Very high recovery levels can be accomplished. A 99.99% level of recovery was achieved with a current across an accelerator. In the only EAFEL in operation at the present time, the negative terminal system at the University in California at Santa Barbara (UCSB), the recovery level with the FEL in operation is 99.7%. With carefully designed electron beam transport we believe much higher recovery levels can be achieved, approaching 99.99%.

In the negative terminal system of Fig. 2, we encounter the same elements but, with a different location in relation to the accelerator. Now the electron gun and collector are in the terminal while the undulator/resonator is outside the accelerator.

A 6 MV negative terminal EAFEL, essentially as in Fig. 2, is in operation at UCSB providing far infrared radiation at a users facility for scientific experiments. Another negative terminal 1.7 MV EAFEL is presently under construction at CREOL/UCF.

### 4. 25 MeV EAFEL for GaSb illumination

The highest efficiency ( $\eta$ ) PV cells are based on GaAs with a maximum  $\eta = 0.58$  at 840 nm. Easier to reach is the peak  $\eta = 0.26$  of GaSb at 1.54  $\mu\text{m}$ . GaSb's lower

Table 1  
Design parameters for three FELs with 25 MV and  $\lambda = 1.54 \mu\text{m}$

|                       |      |      |      |
|-----------------------|------|------|------|
| Current (A)           | 2    | 20   | 45   |
| Optical power (MW)    | 0.1  | 3.1  | 10   |
| Undulator period (mm) | 7.6  | 7.6  | 7.6  |
| Number of periods     | 250  | 80   | 54   |
| Undulator length (m)  | 1.9  | 0.61 | 0.41 |
| Magnetic field (G)    | 1836 | 1836 | 1836 |
| Gain per pass (%)     | 9.1  | 9.3  | 9.5  |

efficiency and poor temperature coefficient make it less attractive than GaAs, but it has the advantage of being in the “eyesafe” region of wavelengths longer than  $1.4 \mu\text{m}$ .

For the FEL at UCSB we developed two different sets of electron guns and collectors: an electron gun and collector for a 2 A beam current [5] and a much larger gun and collector for a 20 A current [6]. Both guns were designed to generate very high quality electron beams and the collectors were designed for high efficiency energy collection. Due to the existence of these guns and collectors, 2 and 20 A currents were chosen for preliminary FEL designs. A larger current of 45 A was also considered to reach the eventual goal of 10 MW power. Thus, three different FEL design parameters are listed in Table 1. In the three cases a hybrid, planar undulator is used with the period, number of periods, and peak magnetic field as listed. As we can see from Table 1, with a 25 MV, 2 A EAFEL, 100 kW of  $1.54 \mu\text{m}$  very high quality radiation can be produced. In the next section we will consider the generation of shorter wavelengths.

## 5. Two-accelerator FEL

In order to reach  $0.84 \mu\text{m}$  with very high power and moderate currents of the order of  $\sim 10$  A, a higher voltage than 25 MV is required. Thus, our second proposal is to combine two accelerators, one with negative terminal NT and the other with positive terminal PT as shown in Fig. 3. The negative terminal machine will have to be slightly larger than the other, to handle the negative voltage. In this way we can combine a 10 MV and a 25 MV and reach a

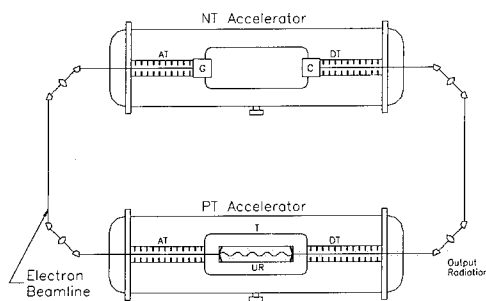


Fig. 3. FEL with two electrostatic accelerators.

Table 2

Design parameters for  $\lambda = 0.84 \mu\text{m}$  with 35 and 50 MV FELs

|                       |      |       |       |       |
|-----------------------|------|-------|-------|-------|
| Energy (MeV)          | 35   | 35    | 50    | 50    |
| Current (A)           | 2    | 30    | 2     | 12    |
| Optical power (MW)    | 0.11 | 9.72  | 0.78  | 10.7  |
| Undulator period (mm) | 8    | 8     | 16    | 16    |
| Number of periods     | 320  | 54    | 66    | 28    |
| Undulator length (m)  | 2.56 | 0.432 | 1.056 | 0.448 |
| Magnetic field (G)    | 1622 | 2402  | 5269  | 5269  |
| Gain per pass (%)     | 9.3  | 8.6   | 9     | 9.7   |

35 MeV acceleration, or two 25 MV for a total of 50 MeV. A technical detail that will have to be worked out is finding the best way for providing the collector with the required voltage and power at the 25 MV terminal.

The difference with Fig. 1 is that now the electron gun G and collector C are in the terminal of the first accelerator NT. Here the electrons are accelerated to 25 MV and then enter the second accelerator PT where they are accelerated 25 MV more. PT is as in Fig. 1 except that the gun and collector are not at its ends but, rather, inside the other accelerator NT. In Table 2 we list parameters of two 35 MeV and two 50 MeV systems.

Although a combination of two accelerators as proposed here was never tried before, there is no fundamental reason why it cannot successfully be done.

## References

- [1] H.E. Bennett, J.D.G. Rather and E.E. Montgomery, Nucl. Instr. and Meth. A 341 (1994) 124.
- [2] L.R. Elias, I. Kimel, D. Larson, D. Anderson, M. Tecimer and Z. Zephu, Nucl. Instr. and Meth. A 304 (1991) 219.
- [3] I. Kimel and L.R. Elias, Phys. Rev. A35 (1987) 3818; Nucl. Instr. and Meth. A 272 (1988) 368; Phys. Rev. A 38 (1988) 2889; Nucl. Instr. and Meth. A 285 (1989) 132; Nucl. Instr. and Meth. A 296 (1990) 528.
- [4] R.A. Iowe and G.A. Landis, The efficiency of photovoltaic cells exposed to pulsed laser light, presented at the 11th Space Photovoltaic Research and Technology Conf., NASA Lewis Research Center, Oct. 21, 1992.
- [5] L.R. Elias and G. Ramian, in: Free-Electron Generators of Coherent Radiation, SPIE vol. 453 (1984) p. 137.
- [6] I. Kimel, L.R. Elias and G. Ramian, Nucl. Instr. and Meth. A 250 (1986) 320.

# Super-power free electron lasers with two-dimensional distributed feedback

N.S. Ginzburg<sup>a,\*</sup>, N.Yu. Peskov<sup>a</sup>, A.S. Sergeev<sup>a</sup>, A.V. Arzhannikov<sup>b</sup>, S.L. Sinitsky<sup>b</sup>

<sup>a</sup> Institute of Applied Physics Russian Academy of Sciences, 46 Ulyanov str., 603600 Nizhny Novgorod, Russian Federation

<sup>b</sup> Institute of Nuclear Physics Russian Academy of Sciences, 11 Lavrent'ev str., 630090 Novosibirsk, Russian Federation

## Abstract

Using time domain analysis we have studied the processes of oscillation build-up and spatial synchronization in FELs with two-dimensional distributed feedback driven by large size sheet and tubular relativistic electron beams. It is proved that the proposed feedback mechanism ensures powerful spatially coherent radiation when the ratio between the transverse sized of the electron beam and the wavelength is up to  $10^2$ – $10^3$ .

## 1. Introduction

For generation of super-power microwave radiation it is proposed to drive free electron lasers (FEL) by intense sheet and tubular (hollow) relativistic electron beams with particle energy 1–2 MV, total current up to 100 kA and power up to 100 GW. However, the typical transverse size of such beams runs up to  $10^2$  cm [1–3]. As a result, providing spatial coherence of emission from different parts of electron beams, is a problem. For solving this problem we have proposed the use of two-dimensional distributed feedback, which may be realized in planar and coaxial 2-D Bragg resonators [4,5]. The additional transverse electromagnetic energy fluxes arising in these resonators should synchronize the radiation of large size electron beams.

In the present work, using time domain analysis, we study the processes of oscillation build-up and spatial synchronization of radiation in FELs with two-dimensional distributed feedback driven by sheet and tubular relativistic electron beams.

## 2. FEL with planar 2-D Bragg resonator and sheet electron beam

Let a planar 2-D Bragg resonator be formed by two metal plates with width  $l_x$ , length  $l_z$  and separation  $a_0$  (Fig. 1a), which are corrugated as

$$a = a_1(\cos(\bar{h}x - \bar{h}z) + \cos(\bar{h}x + \bar{h}z)), \quad (1)$$

where  $\bar{h} = \sqrt{2}\pi/d$ ,  $d$  is the corrugation period, and  $a_1$  is the corrugation depth. Assuming  $\bar{h}a_1 \ll 1$  we will seek the field in the resonator in the form of four coupled waves:  $\mathcal{A}_\pm$  propagating in the  $\pm z$  direction and  $\mathcal{B}_\pm$  propagating in the  $\pm x$  direction:

$$E = \text{Re} \left[ E_p(y) (\mathcal{A}_+(x, z, t) e^{-i\bar{h}z} + \mathcal{A}_-(x, z, t) e^{i\bar{h}z} + \mathcal{B}_+(x, z, t) e^{-i\bar{h}x} + \mathcal{B}_-(x, z, t) e^{i\bar{h}x}) e^{i\omega_0 t} \right], \quad (2)$$

where  $\mathcal{A}_\pm(x, z, t)$ ,  $\mathcal{B}_\pm(x, z, t)$  are slow functions of coordinates and time and  $E_p(y)$  is a function describing

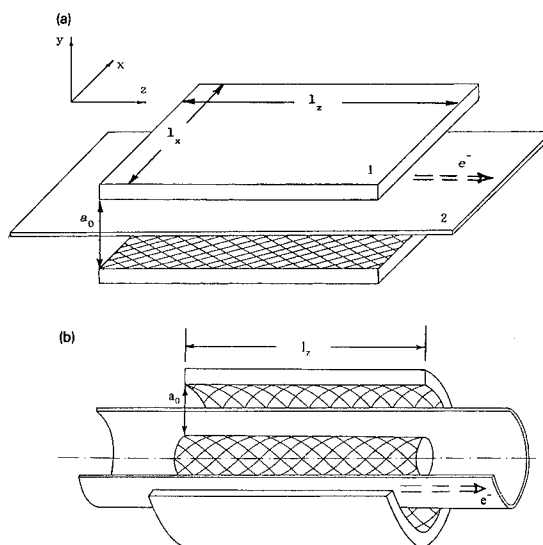


Fig. 1. The schemes of FEL-oscillators with 2-D Bragg resonators driven by (a) sheet and (b) tubular electron beams.

\* Corresponding author. Tel. +7 8312 384 552, fax +7 8312 387 552, e-mail ginzburg@appl.nnuu.su.

the wave's profile along the  $y$  coordinate (the last function coincides with one of the eigenmodes of a planar waveguide). As the carrier we can take the Bragg frequency.  $\omega_0 = \hbar c$ .

Let us investigate excitation of the 2-D Bragg resonator by a sheet relativistic electron beam. Suppose that electrons oscillate either in an undulator field (ubitron) or in a uniform axial magnetic field (cyclotron autoresonance maser – CARM). We assume that only the  $\mathcal{A}_+$  wave is synchronous with the electrons moving in the  $+z$  direction and the other waves do not interact with the beam. The resonance condition can be written in the form

$$\omega - \hbar v_{\parallel} = \Omega, \quad (3)$$

where  $v_{\parallel} = \beta_{\parallel} c$  is electron axial velocity and  $\Omega$  is the electron oscillation frequency (for ubitrons  $\Omega = 2\pi v_{\parallel}/d_u$  is the bounce frequency, where  $d_u$  is the undulator period; for CARM  $\Omega = eH_0/mc\gamma$  is the gyrofrequency, where  $\gamma$  is the relativistic mass factor). Only the synchronous forward wave  $\mathcal{A}_+$  will be amplified by an electron beam. On the grating this wave scatters into waves  $\mathcal{B}_{\pm}$ , which propagate in the transverse directions and synchronize (after scattering back into the wave  $\mathcal{A}_+$ ) radiation of different parts of an electron beam. Simultaneously waves  $\mathcal{B}_{\pm}$  scatter into the backward wave  $\mathcal{A}_-$ , thus forming the feedback circle.

The excitation of the 2-D Bragg resonator by the electron beam and oscillation build-up can be described by the following system of equations:

$$\left( \frac{\partial}{\partial Z} + \beta_{\text{gr}}^{-1} \frac{\partial}{\partial \tau} \right) A_+ + \hat{\sigma}_{\parallel} A_+ + i\hat{\alpha}(B_+ + B_-) = \frac{1}{\pi} \int_0^{2\pi} e^{-i\theta} d\theta_0, \quad (4a)$$

$$\left( -\frac{\partial}{\partial Z} + \beta_{\text{gr}}^{-1} \frac{\partial}{\partial \tau} \right) A_- - \hat{\sigma}_{\parallel} A_- + i\hat{\alpha}(B_+ + B_-) = 0, \quad (4b)$$

$$\left( \pm \frac{\partial}{\partial X} + \beta_{\text{gr}}^{-1} \frac{\partial}{\partial \tau} \right) B_{\pm} \pm \hat{\sigma}_{\perp} B_{\pm} + i\hat{\alpha}(A_+ + A_-) = 0, \quad (4c,d)$$

$$\left( \frac{\partial}{\partial Z} + \beta_{\parallel}^{-1} \frac{\partial}{\partial \tau} \right)^2 \theta = \text{Re}(\hat{A}_+ e^{i\theta}). \quad (4e)$$

Boundary conditions for Eqs. (4) take the form

$$A_+(X, -L_z/2, \tau) = 0, \quad A_-(X, +L_z/2, \tau) = 0, \quad (5a,b)$$

$$B_+(-L_x/2, Z, \tau) = 0, \quad B_- (+L_x/2, Z, \tau) = 0, \quad (5c,d)$$

$$\theta|_{Z=-L_z/2} = \theta_0 \in [0, 2\pi), \quad \left( \frac{\partial}{\partial Z} + \beta_{\parallel}^{-1} \frac{\partial}{\partial \tau} \right) \theta|_{Z=-L_z/2} = -\Delta. \quad (5e)$$

Here we have used the following dimensionless parameters and variables:  $Z = \hbar z C$ ,  $X = \hbar x C$ ,  $\tau = \omega_0 t C$ ,  $\hat{\alpha} = a_1/2Ca_0$  is the wave coupling parameter,  $v_{\text{gr}} = \beta_{\text{gr}} c$  is the group wave velocity,

$$A_{\pm}, B_{\pm} = \frac{e\kappa\mu}{mc\omega\gamma C^2} \mathcal{A}_{\pm}, \mathcal{B}_{\pm},$$

$$C = \left( \frac{eI_0 \lambda^2 \kappa^2 \mu}{8\pi\gamma_0 mc^3 a_0} \right)^{1/3}$$

is the gain parameter (Pierce parameter),  $\theta$  is the electron phase relative to synchronous wave,  $\Delta$  is the initial mismatch of synchronism,  $\kappa$  is the parameter describing the coupling between the wave and the electrons (this parameter is proportional to the particle's oscillatory velocity),  $\mu$  is the bunching parameter,  $I_0$  is the electron current per unit transverse size,  $L_{x,z} = \hbar l_{x,z} C$ , and  $\hat{\sigma}$  is the ohmic losses (these losses are important for FELs with a coaxial Bragg resonator. In this section we suppose  $\hat{\sigma} = 0$ ).

The electron efficiency is given by the relations

$$\eta = \frac{C}{\mu(1 - \gamma_0^{-1})} \hat{\eta}, \quad \hat{\eta} = \frac{1}{2\pi L_x} \int_{-L_x/2}^{+L_x/2} \int_0^{2\pi} \left( \frac{\partial \theta}{\partial Z} + \Delta \right) \Big|_{Z=L_z/2} d\theta_0 dX. \quad (6)$$

Dependences of efficiency on time for various parameters which allow the establishment of a stationary regime of generation are presented in Fig. 2. At the stationary regime spatial profiles of partial waves  $A_{\pm}$  and  $B_{\pm}$  are close to the profiles of the corresponding waves for the highest  $Q$  mode of a "cold" resonator (compare Fig. 3 and Fig 3 in Ref. [5]). The frequency of this mode as well as the oscillation frequency coincides with the Bragg frequency. It is important to note that the amplitude of the

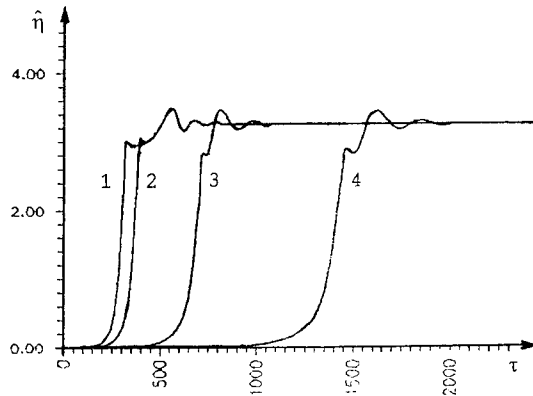


Fig. 2. Establishment of the stationary regime of oscillation, in an FEL with a planar 2-D Bragg resonator. Normalized efficiency versus time:  $L_z = 4$ ,  $\Delta = 1.82$ ,  $\hat{\alpha}^2 L_x = 1.25$ ; (1)  $L_x = 0.8$ ,  $\hat{\alpha} = 1.25$ ; (2)  $L_x = 3.2$ ,  $\hat{\alpha} = 0.625$ ; (3)  $L_x = 12.8$ ,  $\hat{\alpha} = 0.315$ ; (4)  $L_x = 28.8$ ,  $\hat{\alpha} = 0.208$ .



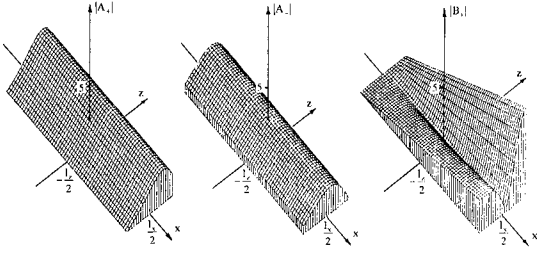


Fig. 3. Spatial profile of partial waves amplitude  $|A_{\pm}(X, Z)|$ ,  $|B_{\pm}(X, Z)|$  in the stationary regime of oscillation:  $L_z = 4$ ,  $\Delta = 1.82$ ,  $L_x = 12.8$ ,  $\hat{\alpha} = 0.315$ .

synchronous wave  $A_+$  does not depend on the transverse coordinate  $x$ . Therefore equal energy is extracted from all parts of the electron beam.

From Eqs. (2) it can be shown that under stationary conditions ( $\partial/\partial\tau = 0$ ), when the fundamental mode is excited, the distribution of waves along the longitudinal coordinate, as well as efficiency, does not change when the conditions  $\alpha^2 L_x = \text{const.}$  and  $L_z = \text{const.}$  are satisfied. Such a scaling gives us the possibility of increasing the width of the interaction space while simultaneously decreasing the coupling parameter (for example, decreasing the corrugation depth). Computer simulation of nonstationary equations (2) confirms this conclusion. If  $L_z \leq 5$  the synchronization regime is stable at least up to  $L_x \leq 30$ . However, the transitional time increases with increasing systems width (see Fig. 2).

Using the above theoretical consideration, let us estimate the possibility of an FEL with wavelength  $\lambda = 4$  mm driven by a relativistic electron beam with transverse size 140 cm, electron current 1 kA/cm, particle energy 1 MeV and pulse duration  $10^{-6}$  s. Such beams are formed by the U-2 accelerator (Novosibirsk, Nuclear Physics Institute RAS) [1,2]. Let the undulator period be 4 cm, transverse oscillatory electrons velocity  $\beta_{\perp} \approx \kappa \approx 0.3$ , and parameter  $\mu = \gamma_0^{-2} \approx 0.1$ . In this case, when the distance between the cavity plates  $a_0 = 5$  cm, the gain parameter is  $C \approx 0.0065$ . Curve 3 in Fig. 2 ( $\hat{\alpha} = 0.315$ ,  $L_z = 4$ ,  $L_x = 12.8$ ) corresponds to a corrugation depth  $a_1 = 0.4$  mm, a cavity length of 36 cm and a cavity width of 140 cm. The transitional time is about 150 ns. With an efficiency of 15% the radiation power amounts to 20 GW. Thus, the 2-D distributed feedback provides spatially coherent radiation with the oversize coefficient  $L_x/\lambda \approx 350$ .

### 3. FEL with coaxial 2-D Bragg resonator and tubular electron beam

The scheme of an FEL with a tubular electron beam and a coaxial 2-D Bragg resonator is presented in Fig. 1b.

In this case a doubly periodic corrugation of the walls of the resonator

$$a = a_1 (\cos(\bar{h}R\varphi - \bar{h}z) + \cos(\bar{h}R\varphi + \bar{h}z)) \quad (7)$$

couple the  $\mathcal{A}_{\pm}$  waves propagating in  $\pm z$  directions and the  $\mathcal{B}_{\pm}$  waves propagating in the azimuthal  $\pm\varphi$  directions. Let us assume that the resonator  $R$  significantly exceeds the distance between the plates ( $R \gg a_0$ ) and the wavelength ( $R \gg \lambda$ ). Under these conditions, neglecting the curvature of the plates, we can describe the excitation of a coaxial 2-D Bragg resonator by a tubular electron beam with the help of Eqs. (4), where  $X = R\varphi C$  is the coordinate along the perimeter of the resonator. Boundary conditions in the longitudinal direction (5a, b) for waves  $\mathcal{A}_{\pm}$  and for electrons (5e) do not change, while in the transverse direction the conditions of cyclicity are valid

$$\begin{aligned} \mathcal{A}_{\pm}(-L_x/2, Z, \tau) &= \mathcal{A}_{\pm}(+L_x/2, Z, \tau), \\ \mathcal{B}_{\pm}(-L_x/2, Z, \tau) &= \mathcal{B}_{\pm}(+L_x/2, Z, \tau), \end{aligned} \quad (8)$$

where  $L_x = 2\pi RC$  is the normalized perimeter of the resonator. According to relations (8) it is possible to expand solutions of Eqs. (4) in a Fourier series:

$$\begin{aligned} A_{\pm}(X, Z, \tau) &= \sum_{m=-\infty}^{\infty} A_{\pm}^m(Z, \tau) e^{imX}, \\ B_{\pm}(X, Z, \tau) &= \sum_{m=-\infty}^{\infty} B_{\pm}^m(Z, \tau) e^{imX} \end{aligned} \quad (9)$$

and consider every term as a mode with azimuthal index  $m$ .

An important specific of the coaxial 2-D Bragg resonator is the existence of a non-disappearing azimuthal-symmetric eigenmode (i.e. a mode with infinite quality factor), if we do not take into account ohmic or diffraction losses for the partial waves  $\mathcal{B}_{\pm}$ . Under the same approximations azimuthally non-symmetric eigenmodes ( $m \neq 0$ ) have finite losses (finite quality). For this reason, under excitation of such a resonator by an electron beam, selective discrimination of azimuthal non-symmetric modes arises. For the establishment of a stationary generation regime ohmic or other losses are of prime importance.

The initial transient may be divided into two stages when  $\sigma \neq 0$ . In the first, relatively short stage, an azimuthally symmetric distribution of the waves amplitudes is formed during several passes of the partial waves over resonator. In the next, much longer, stage, storage of electromagnetic energy in the resonator occurs. At the end of this stage either the stationary generation regime (moderate excess beam current over the threshold) or self-modulation regime (large excess over the threshold) is established. In both regimes the symmetric mode is excited. This conclusion is illustrated by Fig. 4 which represents the time dependence of different azimuthal harmonics in spectrum  $B_+$  at the cross-section  $Z = L_z$ . At  $\tau = 0$ , as an

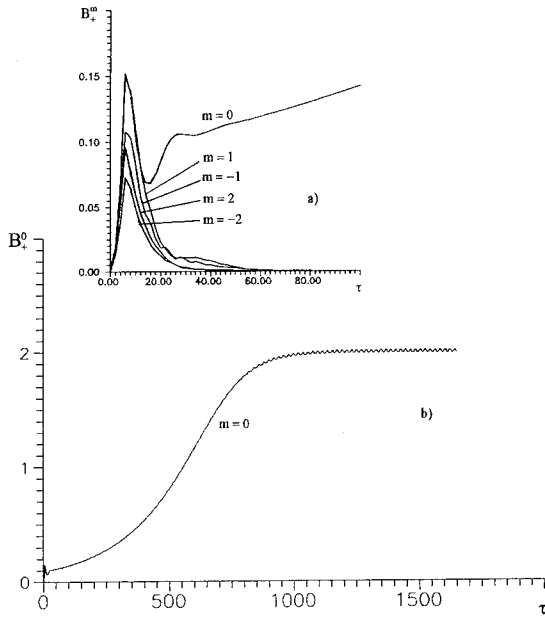


Fig. 4. Amplitudes of azimuthal harmonics in the spectrum of the partial wave  $B_+$  versus time: (a) establishment of the azimuthally-symmetric structure in the initial stage of the transient, (b) electromagnetic energy storage in the resonator in the second stage;  $L_z = 6.8$ ,  $L_x = 12.8$ ,  $\Delta = 0.65$ ,  $\hat{\alpha} = 0.1$ ,  $\hat{\sigma} = 0.095$ .

initial perturbation we took the wave  $A_+$  to have equal amplitude of different harmonics with indexes  $m \in [-2, 2]$ . At first, transformation of the wave  $A_+$  into the waves  $B_{\pm}$  takes place and the amplitudes of all of the harmonics in the spectrum of  $B_+$  growth. But then, amplitudes of all the harmonics beside  $m = 0$  fall practically to zero.

As is clear from comparison of Fig. 4a and Fig. 4b, the main part of the transient occupies the second stage (stage of energy storage), when the distribution of amplitudes is

azimuthally symmetric and equal energy extraction from different parts of the electron beam takes place. For this reason, the total transitional time depends only to a small degree on the perimeter of the system,  $L_x$ . Characteristics of the stationary regime of generation (we suppose that the current per unit of the azimuthal size is constant) also do not depend on the full perimeter.

Note in conclusion that establishment of the stationary regime was observed in the computer simulation at least up to the magnitude of normalized perimeter  $L_x \cong 30$  which with gain parameter  $C \approx 0.01$  corresponds to  $R/\lambda \cong 10^2$ . This confirms the possibility of using 2-D distributed feedback for generation of spatially coherent radiation in FELs driven by high power large size tubular electron beams.

### Acknowledgements

The authors wish to acknowledge partial support from grant R8B000 from International Science Foundation and grant 94-02-04481-a from Russian Foundation of Fundamental Research.

### References

- [1] A.V. Arzhannikov, V.T. Astrelin, V.A. Kapitonov, M.P. Lamzin, S.L. Sinitsky and M.V. Yushkov, Preprint INP RAS 89-81, Novosibirsk, Russia (1989).
- [2] A.V. Arzhannikov, V.S. Nikolaev, S.L. Sinitsky and M.V. Yushkov, J. Appl. Phys. 72 (1992) 1657.
- [3] A.N. Baskrikov, S.P. Bugaev, I.N. Kiselev, V.I. Koshelev and K.N. Sukhuskin, ZhTF 58 (1988) 483.
- [4] N.S. Ginzburg, N.Yu. Peskov and A.S. Sergeev, Pis'ma v ZhTF 18 (9) (1992) 23 (Sov. Tech. Phys. Lett. 18 (5) (1992) 285).
- [5] N.S. Ginzburg, N.Yu. Peskov and A.S. Sergeev, Optics Commun. 96 (1993) 254.



ELSEVIER

## Design and performance calculations for a $K_a$ -band CHI wiggler ubitron amplifier

J.M. Taccetti<sup>1</sup>, R.H. Jackson, H.P. Freund<sup>2,\*</sup>, D.E. Pershing<sup>3</sup>, M. Blank,  
V.L. Granatstein<sup>1</sup>

*Naval Research Laboratory, Washington, DC 20375, USA*

### Abstract

Design and performance calculations for a coaxial hybrid iron (CHI) wiggler free-electron laser configuration are presented. The capability of generating high fields at short periods, as well as good beam focusing properties, make it a desirable configuration for high power coherent radiation sources in relatively compact systems. In addition to a description of the geometry, numerical calculations detailing the magnetostatic wiggler fields, the beam dynamics, and the interaction of the beam with the electromagnetic waves in the  $K_a$ -band (26–40 GHz) will be presented. Key considerations for the experimental design will be outlined and discussed.

### 1. Introduction

Fast-wave interaction devices, i.e. gyrotrons and FEL/ubitrons, have many attractive properties for the generation of high power, high frequency microwaves. However, practical devices have been elusive because of magnetic field, voltage, and size requirements. For FELs/ubitrons the disadvantage can be partially overcome by the utilization of short period ( $\lambda_w < 5$  mm) magnetic wigglers. Several micro-wiggler configurations have been investigated, each having its own advantages and disadvantages in the areas of achievable field strength and uniformity, ease and cost of fabrication, control, tuning, and beam acceptance and focusing.

The coaxial hybrid iron (CHI) wiggler is a short-period compatible configuration which offers several advantages relative to the above issues. The CHI wiggler is a coaxial configuration constructed by insertion of ferromagnetic and non-ferromagnetic elements into a solenoidal field [1,2]. Other wiggler configurations derived from a solenoidal field have also been discussed in the literature

[3–6]. This paper will present design and performance calculations for a CHI wiggler based  $K_a$ -band FEL amplifier under development at the Naval Research Laboratory. The goal is an output power of 100 kW at 35 GHz while reducing the voltage to approximately 150 kV. A companion paper appearing in this issue discusses the application of the CHI wiggler to a high power FEL designed for the cyclotron resonant heating of fusion plasmas [7].

### 2. CHI wiggler configuration

The CHI wiggler consists of alternating rings of ferro- and nonferromagnetic materials, surrounding a central rod consisting of cylinders of the same materials as the rings but shifted axially by half a period. As shown in Fig. 1, a wiggler period consists of only two ferromagnetic pieces (an inner cylinder and an outer ring) along with their respective non-ferromagnetic spacers. The width of the two ferromagnetic pieces need not be the same, as long as the combined length is the same for both inner and outer sections. This entire structure is placed inside a solenoid (the axes of the solenoid and the wiggler are coincident) and causes a deformation of the solenoidal field into a combination of periodic radial and axial components. Having the magnetic field source external to the wiggler offers advantages for coil cooling and field tapering. Large wiggler fields are possible while maintaining a relatively simple and low-cost design.

The electron beam is annular and travels down the gap

\* Corresponding author. Tel. +1 703 734 5840, fax +1 703 821 1134, e-mail freund@mmace.nrl.navy.mil.

<sup>1</sup> Permanent address: University of Maryland, College Park, MD 20742, USA.

<sup>2</sup> Permanent address: Science Applications International Corp., McLean, VA 22102, USA.

<sup>3</sup> Permanent address: Mission Research Corp., Newington, VA 22122, USA

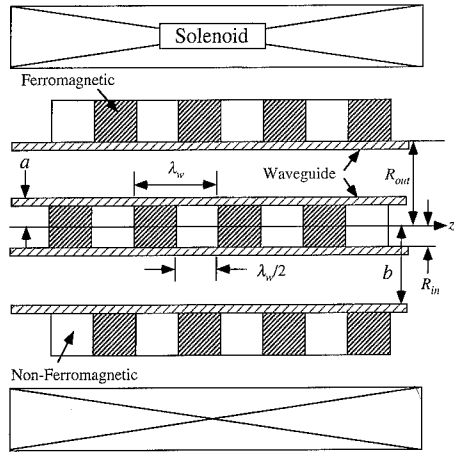


Fig. 1. CHI wiggler geometry.

between the outer rings and the central piece. The radially undulating magnetic fields cause this annular beam to wiggle azimuthally. The electrons may then exchange energy with coaxial modes which contain an azimuthal electric field component, for example the  $TE_{01}$  mode. Note that for the experiment under construction the primary interaction is with this mode. Simulations using the formulation described in Ref. [2] indicate that the interaction with the TEM and TM modes is much weaker at the frequencies of interest.

The magnetic fields in the gap can be found analytically by solving Laplace's equation with the boundary conditions that the axial component of the magnetic field be zero along the faces of the ferromagnetic pieces and some constant value  $B_z$  along the faces of the non-ferromagnetic ones. The resulting equations for both the axial and radial components of the field (and accompanying figures) are described in earlier publications [1,2]. In essence, the radial component varies sinusoidally along the axial direction and has a minimum at the center of the gap. The axial component consists of a constant term and oscillating terms which are small at the gap center.

### 3. Magnetostatic wiggler analysis

The magnetic field profile of a CHI wiggler may be modified by changing or tapering several parameters of the basic configuration. Multiple variations of the basic CHI wiggler geometry were studied in order to optimize the configuration for the highest periodic field. This search also detailed ways in which the field may be tailored by varying the parameters of the geometry. These parametric variations were performed using the POISSON simulation codes. The ferromagnetic material was assumed to be low-carbon steel, and the  $B$ - $H$  table provided with the codes was used. Only one quarter of the actual wiggler is

input because the codes take advantage of cylindrical symmetry. The configuration used in POISSON also allows the study of the entrance fields. Parameters varied in the standard configuration include: gap height; inner pole height, width, taper angle; outer pole height, width, taper angle; and axial phase offset of inner and outer pieces.

The ultimate field strength of the periodic component is limited by the saturation of the ferromagnetic material. The variation in the maximum radial field at saturation has been studied in Ref. [1] as a function of gap height. As shown in Fig. 5 in that paper, the maximum radial field at saturation decreases monotonically with increasing gap spacing. Fig. 2 shows how varying the height of the outer rings can also be used to change the value of the peak radial field. These and other results show that variations of pole shapes increased the peak radial field by only a few percent, and also show various ways to taper the field.

### 4. Beam dynamics

The dynamics of electrons in the CHI fields were studied both analytically and computationally. For the analytic solution, it was assumed that the particle did not stray far from the gap center – its original position (i.e.  $\delta r \ll \lambda_w$ ); hence an idealized field model is used for the analytic orbit treatment. The simplified form used for the field is:

$$B_r = B_w \sin k_w z, \quad B_z = B_0, \quad (1)$$

In the above equations  $k_w = 2\pi/\lambda_w$  and  $B_w$  and  $B_0$  are constants. Assuming a constant bulk axial velocity  $v_{\parallel}$  and solving the equations of motion to lowest order in wiggler amplitude, one obtains the quasi-steady-state solutions:

$$v_{\theta} = \left[ \frac{B_w (\beta_z/\beta_0) B_T}{B_0^2 - (\beta_z/\beta_0)^2 B_T^2} \right] v_{\parallel} \cos k_w z, \quad (2)$$

$$v_r = \left[ \frac{B_0 B_w}{B_0^2 - (\beta_z/\beta_0)^2 B_T^2} \right] v_{\parallel} \sin k_w z, \quad (3)$$

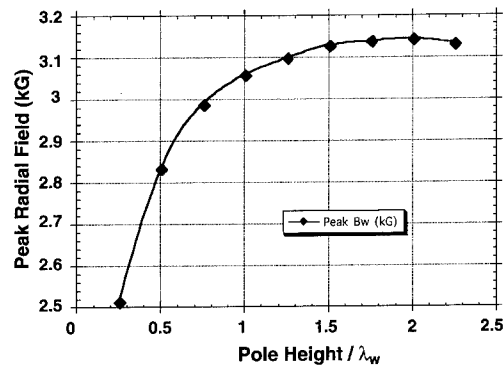


Fig. 2. Peak radial field versus the height of the outer rings.

where  $\beta_z = v_{||}/c$  and  $B_T$  is a constant field in the axial direction, called the transition field, and is given by:

$$B_T = \frac{mc^2}{e} \gamma \beta_0 k_w, \quad (4)$$

where  $\gamma$  is the relativistic factor and  $\beta_0$  is the magnitude of the total particle velocity (a constant) in units of  $c$ . The transition field is a constant value of the axial field which delineates the transition from group I orbits to group II orbits as  $B_z$  is increased. These equations describe an electron performing an elliptical orbit in the  $r$ - $\theta$  plane (with a period equal to the wiggler period) while streaming at a constant axial velocity. These results are analogous to those of a simplified planar wiggler field with a constant axial guide field [8].

Using energy conservation and the quasi-steady state solutions for  $v_\theta$  and  $v_r$  obtained above, one may obtain a quartic polynomial in  $v_{||}$ , which may be solved numerically. The existence of a constant field in the axial direction causes the transverse velocities to increase about a certain resonant value of the axial field. The azimuthal component of the velocity (Eq. (2)) (as well as the radial component) is seen to depend strongly on this gyroresonance effect, from the fact that the fields are squared in the denominator.

A figure of merit of the strength of the wiggler is  $\alpha$  (the ratio of azimuthal to axial velocity). A plot of  $\alpha$  against the applied field is given in Fig. 3 showing the gyroresonant gap. Notice that orbits below  $B_T$  (Group I) are more sensitive as  $B_z$  approaches  $B_T$  than those above  $B_T$  (Group II). This sensitivity indicates that tapering of parameters will be very important for achieving maximum performance. It also shows the enhancement possible in the interaction due to the existence of the axial field. In preparing this figure, single and multi-particle three-dimensional orbits were simulated using the TRACK-3 code to integrate trajectories using the realistic three-dimensional field model described in Refs. [1,2]. Results of the simulations agree very well with simplified analytic values

away from the gyroresonant gap, as the electron remains very near the wiggler gap center.

An examination of the trajectories shows a drift in the  $\theta$ -direction, but this is acceptable in the CHI FEL case since it remains in the interaction region due to the cylindrical geometry. Calculations have shown that this drift can be explained using Busch's theorem and depends on the entrance conditions used in the simulation. Actual CHI wiggler axial fields decrease in magnitude at the entrance into the wiggler (due to the iron pieces), and may partially cancel out this drift. Future plans include running simulations with PIC (particle in cell) codes utilizing 2-D simulations of the CHI wiggler field including entrance conditions.

## 5. The experimental design

The experiment to be built at the Naval Research Lab will be a CHI-wiggler FEL operating as an amplifier at a frequency of 35 GHz in the K<sub>a</sub>-band. The principal goal of the experiment is to operate at lower voltages while still generating high power, high frequency microwaves. Current plans call for operation at approximately 150 kV with an output power of 100 kW.

The major components of the FEL are the gun, the wiggler section (including the solenoid and the waveguide), the beam collector, and the input and output couplers. The gun will operate at around 150 kV and produce a 10 A annular beam for the CHI wiggler. The wiggler assembly will be placed horizontally within the bore of an existing superconducting magnet. The central rod of the wiggler will be supported by radial struts located near the gun and the collector. The coaxial waveguide consists of the (electroplated) faces of the inner and outer pieces of the wiggler. This waveguide will contain a central sever to reduce rf reflections. The diameter of the wiggler, and therefore of the waveguide, is limited by the bore of the magnet, 6.4 cm, and places a lower bound on our operating frequency. The wiggler will have a period of about 1 cm and will be about 60 periods in length.

A SLAC klystron gun will be modified to produce the necessary annular beam. The superconducting magnet, with an axial field of up to 30 kG, will permit an extensive study of the full performance range of the CHI FEL. The bore size of the magnet is 6.4 cm and its total length is 78.3 cm.

Preliminary calculations using untapered configurations (using a previously described nonlinear three-dimensional slow-time-scale formulation [2]) have shown gains on the order of 0.3 dB/cm and efficiencies in excess of 10% in this frequency range. Studies are currently under way to lower the voltage required while still retaining performance. Fig. 4 shows the gain profile for a specific set of parameters, for which a saturated gain of about 30 dB (0.26 dB/cm) with a gain bandwidth of around 20% was

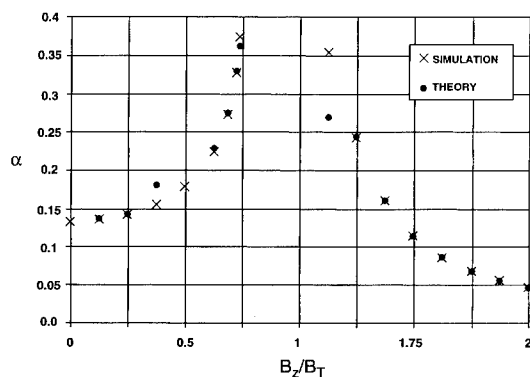


Fig. 3. Variation of  $\alpha$  versus the applied field for  $B_w/B_T = 0.135$  (comparison of theory and TRACK-3 simulation results).

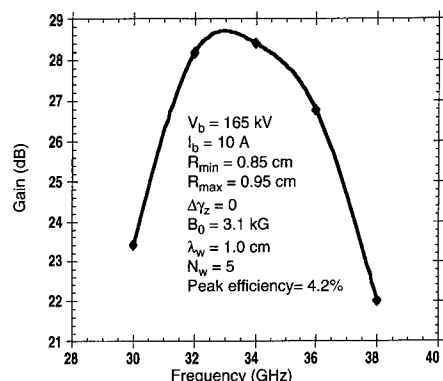


Fig. 4. Preliminary simulation results for a  $K_a$ -band amplifier utilizing a coaxial  $TE_{01}$  mode.

achieved. In this figure,  $R_{\min}$  and  $R_{\max}$  are the inner and outer radii of the coaxial waveguide (i.e. the wiggler gap), and  $N_w$  is the number of adiabatic entrance periods. It must again be stressed that these results are very preliminary since optimization of parameters was not performed.

## 6. Summary and conclusions

The above results indicate interesting potential for high frequency amplifiers based on the CHI wiggler configuration. Work is in progress on the design of a CHI wiggler ubitron amplifier in the  $K_a$ -band. A Pierce-type electron gun is being modified to produce a hollow beam for the

device, which will have a period of about 1 cm and will consist of about sixty periods with a central sever. An existing superconducting magnet ( $B_z \leq 30$  kG) will be used to produce the axial field in order to allow exploration of the full performance range of the CHI wiggler.

## Acknowledgement

This work was supported by the Office of Naval Research.

## References

- [1] R.H. Jackson, H.P. Freund, D.E. Pershing and J.M. Taccetti, Nucl. Instr. and Meth. A 341 (1994) 454.
- [2] H.P. Freund, R.H. Jackson, D.E. Pershing and J.M. Taccetti, Phys. Plasmas 1 (1994) 1046.
- [3] K.D. Jacobs, G. Bekefi and J.R. Freeman, J. Appl. Phys. 52 (1981) 4977.
- [4] A.H. Ho, R.H. Pantell, J. Feinstein and Y.C. Huang, IEEE J. Quantum Electron. QE-27 (1991) 2650.
- [5] A.A. Varfolomeev, S.N. Ivanchenkov, A.S. Khlebnikov and N.S. Osmanov, Nucl. Instr. and Meth. A 318 (1992) 809.
- [6] H. Golombek, E. Agmon and E. Jerby, Nucl. Instr. and Meth. A 331 (1993) 775.
- [7] H.P. Freund, M.E. Read, R.H. Jackson, D.E. Pershing and J.M. Taccetti, these Proceedings (16th Int. Free Electron Laser Conf., Stanford, CA, USA, 1994) Nucl. Instr. and Meth. A. 358 (1995) 163.
- [8] H.P. Freund and T.M. Antonsen, Jr., Principles of Free Electron Lasers (Chapman & Hall, London, 1992).



ELSEVIER

# Beam transport through undulators designed for high power FEMs

A.A. Varfolomeev<sup>\*</sup>, A.V. Smirnov

*Coherent Radiation Laboratory, RRC “Kurchatov Institute”, Moscow 123182, Russian Federation*

## Abstract

The problem of extremely low loss electron beam transport through an undulator is common to high power FEM projects. It is complicated by the fact that the undulator is usually tapered or sectioned, the gap is limited, and the electron beam energy is variable. We report simulation results for two mm-wave FEL projects, and show how the electron beam transport problem can be solved.

## 1. Introduction

For FEMs driven by electrostatic accelerators with electron beam (e.b.) recovery, high average power can be obtained if there are very low electron beam losses in the devices. These losses directly limit the efficiency of the facilities. For high efficiency other conditions are required as well: tapered or sectioned undulators, reasonable acceptance, easy control of the current losses, etc. As a result the e.b. transport becomes a complicated problem which can be resolved only by the optimization with respect to many factors. We have made simulations on e.b. transport for two FEM projects: FOM-Fusion-FEM [1] and KAERI-FEL [2]. Extremely low losses ( $\leq 0.2\%$ ) are specified for each project. The results show what kinds of problems arise and how they can be solved.

Some aspects of focusing scheme options, undulator acceptance, phase synchronism and beam mismatch and misalignment were analyzed earlier [3,4] for the FOM project. Here we consider the optimal focusing conditions for various e.b. energies using realistic beam transport simulations made using quasi-3D magnetic field data obtained from the KIAE-4 undulator. For the KAERI-FEL we describe transport of the low-energy electron beam through the short-period undulator including nonlinear behavior caused by violation of the paraxial approximation.

## 2. Beam transport through the two-section undulator

The first goal of the calculations was to find the optimal focusing of the KIAE-4 undulator [5] for various nominal e.b. energies. We first used modified Kapchin-

skij-Vladimirskij equations [6] and then made more accurate multi-particle simulations using the code [7]. It includes the effects of different kinds of focusing fields, measured undulator magnetic fields and transverse space charge forces using a particle-in-cell (PIC) method.

For the general case, when a superposition of the quadrupole and the periodic sextupole type fields is used (see Ref. [5] for example), we introduce the following expression for the relative focusing strength:

$$(k_{\beta y}/k_{\beta x})^2 = \frac{(K_w k_w / \beta_{\parallel} \gamma)^2}{qe / (\beta_{\parallel} \gamma m c^2) + (K_w k_x / \beta_{\parallel} \gamma)^2} - 1. \quad (1)$$

Here  $K_w$  is the r.m.s. undulator strength,  $k_w = 2\pi/\lambda_w$  is the undulator wavenumber,  $\gamma$  is the electron relativistic factor,  $q = -dB_y/dx$  is the transverse magnetic field gradient ( $q > 0$  is focusing for XOZ plane and right hand frame), and  $\beta_{\parallel} = v_z/c$  is the dimensionless longitudinal electron velocity. We assume that the usual relationship between  $k_w$  and field curvatures in the XOZ and YOZ transverse planes holds:  $k_w^2 = k_y^2 + k_x^2$ .

To shorten the numerical calculation process only beams which were slightly convergent in the both the XOZ and YOZ planes at the exit of the first section were considered [4]. For the two-section undulator the e.b. transport is sensitive to the beam current. The space charge effect is most noticeable at relatively low generalized beam perveance  $S$ . For the FOM project  $S$  is equal to 0.05.

Results on the beam confinement obtained for the FOM-Fusion-FEM parameters [1] are presented in Table 1. It is seen, that for one of the energies two focusing options give identical confinement results.

For other e.b. energies the corresponding focusing strengths are different. Thus, in the general case focusing strengths should be adjusted with energy.

<sup>\*</sup> Corresponding author. Tel. +7 095 196 7764, fax +7 095 196 7764, e-mail x1065@cpcuv1.net.kiae.su.

Table 1

The optimum focusing for various electron beam energies

| Kinetic energy<br>$E$ (MeV) | Optimal relative<br>focussing strength<br>$k_{\beta y}/k_{\beta x}$ | Beam confinement area<br>$\Delta x_{\max}, \Delta y_{\max}$ (mm) |
|-----------------------------|---|--|
| 2                           | 2.7   | $\pm 2.7, \pm 1.7$   |
| 1.75                        | 1   | $\pm 2.6, \pm 1.8$   |
| 1.75                        | 1.7   | $\pm 2.6, \pm 1.72$  |
| 1.35                        | 1   | $\pm 3.06, \pm 1.83$   |

Electron beam envelopes obtained for different focusing and matching conditions are presented in Figs. 1 and 2. It is evident from Fig. 1 that the entire two-section undulator cannot be optimized if the beam matching is made only at the first section entrance. The optimal Twiss parameters for the entire undulator are half those for the first section alone.

Fig. 2 presents beam envelope calculation results for two cases: an “idealized” undulator and “real” undulator. For the “ideal” undulator the parameters  $q$ ,  $k_x^2$  and field amplitude  $B_w$  were assumed to be step functions. For the real undulator these parameters were described by quasi-3D field data including stray undulator fields. It is clear that the electron beam transport is sensitive to the stray fields, i.e. the fields in the region of the intersection gap and near the undulator ends. These stray fields should be taken into account to obtain reliable results on e.b. transport.

Another important result of the calculations is information about the growth of the effective transverse emittance of the electron beam. At an energy  $E = 1.35$  MeV, the effective emittance containing 99.2% of the current grows by 30% if equal sextupole focusing is used ( $k_{\beta y}/k_{\beta x} = 1$  and  $q = 0$ ). The effective emittance growth for 100% of

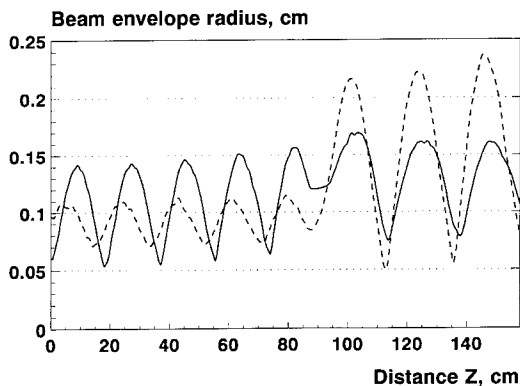


Fig. 1. Circular beam radius obtained by simulations for input beam parameters optimal for the entire two section undulator (solid curve,  $\beta_{bx,by} = 3$  cm/rad) and for input beam parameters matched to only the first section (dashed curve,  $\beta_{bx,by} = 6.2$  cm/rad). The electron beam energy is  $E = 1.35$  MeV.

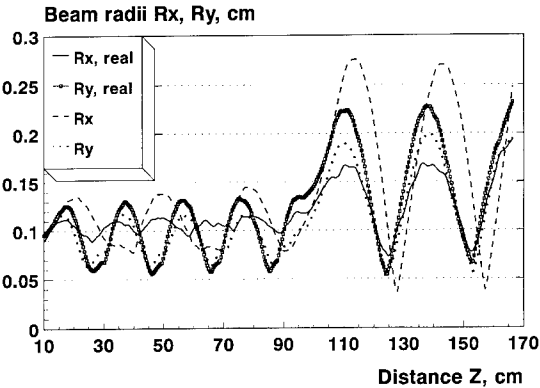


Fig. 2. Beam envelopes calculated for real undulator fields, including stray fields (solid curves), and an idealized undulator (dashed curves). The following focusing parameters were used:  $\langle q \rangle = 74.5$  G/cm,  $\langle k_x^2 \rangle = 0.184$  cm $^{-2}$ ,  $k_{\beta y}/k_{\beta x} = 1.37$  for the first section and  $\langle q \rangle = 68.5$  G/cm,  $\langle k_x^2 \rangle = 0.230$  cm $^{-2}$ ,  $k_{\beta y}/k_{\beta x} = 0.988$  for the second section. The electron beam energy is  $E = 1.75$  MeV.

the beam is 70%. This growth is caused by beam optics aberrations which are most significant when equal focusing is used [3,8]. It is another reason why equal focusing cannot be considered optimal.

### 3. Low-energy beam transport for the short-period single section undulator

We shall now consider the KAERI-FEL project [2] based on a single section undulator with a rather small period,  $\lambda_w = 1.5$  cm, and equal focusing fields. A field

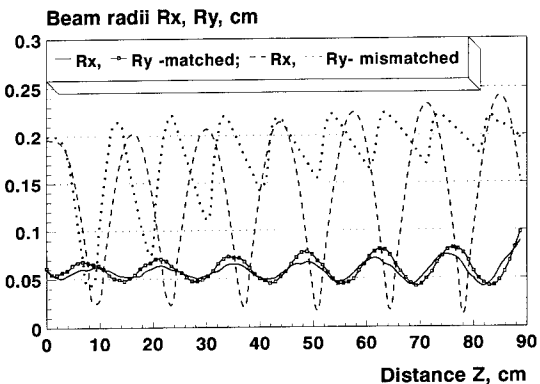


Fig. 3. Beam envelopes obtained by simulations for the KAERI-FEL project [2] for the matched beam (solid curves,  $\beta_{bx,by} = 5.93$  cm/rad,  $\alpha_{x,y} = 0.65$ ) and mismatched beam (dashed and dotted curves,  $\beta_{bx,by} = 61.8$  cm/rad,  $\alpha_{x,y} = 0$ ). The following parameters were used:  $B_w = 1.2$  kG,  $q = 0.143$  kG/cm,  $I = 2$  A,  $\epsilon_n = 10$   $\pi$  mm mrad. Electron beam energy is  $E = 0.43$  MeV.



gradient was used for providing the equal focusing:  $q(z) = eB_w^2(z)/4mc^2\beta_{\parallel}\gamma$  (see Eq. (1)).

Beam envelope plots depicted in Fig. 3 were calculated using the code [7] and the input beam parameters specified by the project [2] (dashed curves). As it is seen, such an input beam is badly mismatched, resulting in anharmonic motion in the vertical plane and in non-circular beam propagation. The envelopes for an optimally injected beam are presented in the Fig. 3 (solid curves).

An analytical approach can be used to estimate optimum input beam parameters. For the paraxial ( $k_{x,y}R_{x,y} \ll 1$ ) and smooth ( $\lambda_w k_{\beta y, \beta x} \ll 1$ ) approximations the appropriate matching conditions are given by theory [6]:

$$\beta_{bx,by} = \beta_{x,y} \left( S_{x,y} + \sqrt{1 + S_{x,y}^2} \right), \quad \alpha_{xb,yb} = 0. \quad (2)$$

Here  $\beta_{bx}$ ,  $\beta_{by}$  are the Twiss parameters,  $S_{x,y}$  are the generalized perveances (scaling factors):  $S_{x,y} = \pi I \beta_{bx,by} c / (\gamma^2 v_z \epsilon_{nx,y} I_A)$ ,  $\epsilon_{nx,y}$  are the transverse normalized emittances,  $I_A = mc^3/e$ ,  $\beta_{x,y} = 1/k_{\beta x,y}$ . Note, that for the KAERI-FEL project [2] the beam perveance parameter equals to  $S = 0.22$ . As this is comparable with unity, space charge effects cannot be neglected.

The Twiss parameters  $\beta_{bx}$ ,  $\beta_{by}$  estimated analytically according to Eq. (2) and determined numerically (see Fig. 3) have coincided. This is not surprising, since the paraxial and smooth conditions are valid and there is no intersection gap.

#### 4. Conclusion

Electron beam transport through high power FEL undulators with specified low beam losses is possible if undulators with adjustable focusing are used and the focusing and field matching as well as beam matching optimizations are made for each nominal beam energy.

#### References

- [1] W.H. Urbanus, R.W.B. Best, A.G.A. Verhoeven, M.J. van der Wiel, M. Caplan, L. Bratman, G. Denisov, A.A. Varfolomeev and A.S. Khlebnikov, Nucl. Instr. and Meth. A 331 (1993) 235.
- [2] S.K. Kim, S.O. Cho, Y.Uk Jeong, B.C. Lee and J.M. Lee, Nucl. Instr. and Meth. A 341 (1994) ABS 95.
- [3] A.A. Varfolomeev and A.V. Smirnov, Preprint IAE-5656/14, Moscow, Russia (1993).
- [4] A.A. Varfolomeev and A.V. Smirnov, Nucl. Instr. and Meth. A 341 (1994) ABS 123.
- [5] A.A. Varfolomeev, S.N. Ivanchenkov, A.S. Khlebnikov, N.S. Osmanov, M.J. van der Wiel, W.H. Urbanus and V.F. Pavluchenkov, Nucl. Instr. and Meth. A 341 (1994) 466.
- [6] I.M. Kapchinskij, The Theory of Linear Resonance Accelerators (Energoizdat, Moscow, 1982) in Russian.
- [7] A.V. Smirnov, Preprint IAE-5655/14, Moscow, Russia (1993).
- [8] J.J. Barnard, Nucl. Instr. and Meth. A 296 (1990) 508.



ELSEVIER

# High power operation of a wiggler-focused sheet beam free electron laser amplifier

S. Cheng<sup>\*</sup>, W.W. Destler

*Department of Electrical Engineering and Institute for Plasma Research, University of Maryland, College Park, MD 20742, USA*

## Abstract

The proof-of-principle millimeter-wave free electron laser amplifier at the University of Maryland has been operated at an input power level of  $\sim 1$  kW at a frequency of 86 GHz, following successful operation at smaller input power levels at 94 GHz. Significant gain has been achieved at high rf power level with 56 period uniform wiggler in these preliminary studies. The experiments have been performed at 530–570 kV voltages, 5–19 A beam currents, and 2.1–3.65 kG wiggler magnetic fields. Experimental results are in good agreement with theoretical calculations from a one-dimensional simulation code. The discrepancy between the results of 86 GHz and 94 GHz are analysed in terms of electron beam quality, wiggler period error, and waveguide dimension error.

The 56 period wiggler has been extended to 74 period with the addition of a 18 period section. Sheet electron beams have propagated through the 74 period wiggler with a newly adjusted wiggler entrance taper. Completion of the proof-of-principle experiments will include saturation studies and the addition of a tapered wiggler section for efficiency enhancement.

## 1. Introduction

Millimeter-wave free electron lasers (FELs) find many potential applications in areas such as electron cyclotron resonance heating of plasmas for magnetic fusion, high-resolution long-range radar, and advanced accelerators [1]. The advantages of using a sheet electron beam and a small period wiggler have been discussed previously [2–5]. A proof-of-principle (PoP) millimeter-wave FEL amplifier embodying these features has been operated successfully at 94 GHz at the University of Maryland, and up to 15–17 dB gain has been achieved at several Watt rf input power with a 56 period uniform wiggler [5].

Operation of this device at  $\sim 1$  kW input rf power levels has recently been studied at a frequency of 86 GHz. Significant gain has been obtained in these preliminary studies. Gain at 86 GHz frequency with several Watts of input rf power has also been measured, which is comparable with the high power gain. However, the observed device gain at 86 GHz is lower than that achieved in the previous studies at 94 GHz. This discrepancy is not caused by saturation effects, but rather is attributed to structural errors associated with the PoP device. It can be shown that the same amount of structural error results in a larger value of  $\Delta\gamma_z/\gamma_z$  at 86 GHz than that at 94 GHz. This relative

axial energy spread is also dependent on the rf frequency even if the injected electron beam has the same initial momentum spread. These frequency dependences favor 94 GHz operation rather than 86 GHz for those amplifier parameters chosen for our PoP experiments.

## 2. High power FEL amplifier experiments

The setup of the high power FEL amplifier experiments is similar to that used for the studies at 94 GHz [5]. A schematic of the experiment is shown in Fig. 1. Electrons are generated from an explosive field emission diode [7], which is driven by a pulse-line accelerator. Tungsten graphite was used as the cathode material. The two anode plates are spaced 4.0 cm apart with a 1.0 mm by 2.0 cm slot in the center of each anode plate. Electrons drift 1.0 cm further through a 1.0 mm by 2.0 cm slot in the beam/wave coupler before entering into the wiggler. This double anode structure scrapes off most of the electrons allowing only a small portion of the beam to come out in the form of a sheet or ribbon. The electromagnetic wiggler [2] is pulsed by a charged capacitor bank. The ferromagnetic laminations are offset alternatively in the opposite directions with respect to each other to generate a magnetic field gradient on the wide transverse sides of the wiggler. This offset-pole technique [3] is important for sheet electron beam confinement in the wide transverse direction, since no axial magnetic field is utilized in this

<sup>\*</sup> Corresponding author. Tel. +1 301 405 5016, fax +1 301 314 9437, e-mail scheng@eng.umd.edu.

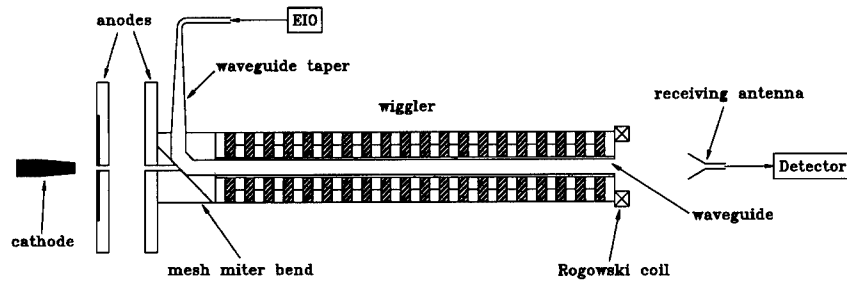


Fig. 1. Schematic of experimental setup.

device. Electron confinement along the narrow dimension of the sheet beam is provided by the strong focusing effect of the wiggler magnetic field. The propagated beam current is monitored using a calibrated Rogowski coil situated at the down-stream end of the amplifier waveguide. An extended interaction oscillator (EIO) generates about 1 kW of peak power with a duration of up to 2  $\mu$ s. An electro-formed waveguide taper converts the rf output of the EIO from the fundamental  $TE_{10}$  mode of the standard WR-10 waveguide (2.54 mm by 1.27 mm inner dimension) to the  $TE_{01}$  mode of the FEL amplifier waveguide (2.8 mm by 4.0 cm inner dimension). The electron beam and rf signal are coupled through a 45° mesh miter bend acting as a beam/wave coupler, which has about 90% reflectivity for the rf power and 90% transparency for the electron beam current. The amplified rf signal is sampled in the far radiation field region using a horn antenna. The antenna is oriented in such a way that it can pick up only the radiation with its electric field parallel to the wide dimension of the rectangular amplifier waveguide. When such an orientation was rotated 90° around the axis of the FEL amplifier system, there was no signal pickup observed. The experimental parameters are summarized in Table 1.

Fig. 2 shows a typical trace of an amplified rf signal together with the corresponding beam voltage, beam current, and input rf signal. Amplification or absorption occurs when certain voltage, current, and wiggler field conditions are satisfied. The measured gain versus beam voltage for 3.1 and 3.5 kG wiggler magnetic fields are plotted in Figs. 3 and 4, respectively. Superimposed with these plots

are the predictions from a 1-D simulation code [6]. It can be seen that there is an optimal voltage corresponding to each case for the FEL amplifier to achieve high gain.

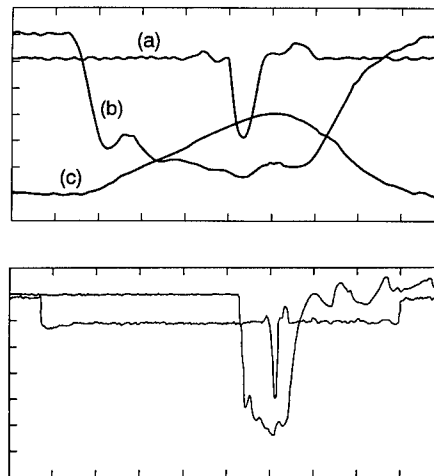


Fig. 2. Typical traces of (a): Amplified rf signal, 5 mV/div; (b): Beam voltage, 103.5 kV/div; (c): Beam current, 5 A/div. Time scale: 20 ns/div (upper), 100 ns/div (lower).

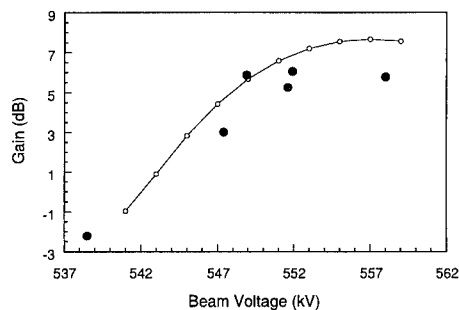


Fig. 3. A plot of gain at 86 GHz vs beam voltage. Filled circles are experimental points with 1.0 kW input power, 3.1 kG peak wiggler magnetic field, and 11.5–14.0 A current. Superimposed is the 1-D simulation result with 13.0 A beam current and  $\theta = 5$ .

Table 1  
Experimental parameters

|                                   |                  |
|-----------------------------------|------------------|
| RF input frequency                | 86 GHz           |
| RF input power                    | 1.0 kW           |
| Beam voltage                      | 530–570 kV       |
| Beam current                      | 5–19 A           |
| Wiggler period                    | 9.6 mm           |
| Wiggler peak magnetic field       | 2.1–3.65 kG      |
| Wiggler length                    | 56 periods       |
| Wiggler entrance taper            | 3 periods        |
| Amplifier waveguide cross-section | 2.8 mm by 4.0 cm |
| Electron beam cross-section       | 1.0 mm by 2.0 cm |

### 3. Analysis

The preliminary experiments have shown high power amplifications at 86 GHz. Compared with the results obtained previously at 94 GHz with small input signals, however, observed gain is lower. We have also conducted amplification experiments at 86 GHz frequency with several Watts of input power. The small signal gain measured is comparable with the results observed at high input rf power levels and is also consistent with the 1-D simulation, which indicates that the amplifier is not yet saturated because of the high rf input power. The experimental results at both frequencies are in reasonable agreement with the simulations, provided the only free parameter in the simulation is appropriately chosen. This parameter,  $\bar{\theta}$ , represents a characteristic electron momentum spread, which is assumed to have a Gaussian profile. In the simulations,  $\bar{\theta}$  was chosen to be 3 for the 94 GHz experiments, while  $\bar{\theta}$  was chosen to be 5 for the 86 GHz experiments.

Let us first look at the effect of structural errors. The FEL resonance condition can be obtained considering waveguide mode dispersion relation

$$\omega^2 = (k_c^2 + k_z^2)c^2 \quad (1)$$

and FEL beam/wave phase matching condition

$$\omega \approx (k_w + k_z)\beta_z c. \quad (2)$$

In the above relations,  $k_c$  (equals  $\pi/b$  for  $TE_{01}$  mode, where  $b$  is the narrow dimension of the rectangular amplifier waveguide) is the waveguide cutoff wavenumber,  $k_w$  (equals  $2\pi/\lambda_w$ , where  $\lambda_w$  is the wiggler period) is the wiggler wavenumber,  $k_z$  is the axial propagation wavenumber, and  $c$  is the speed of light. Differentiation

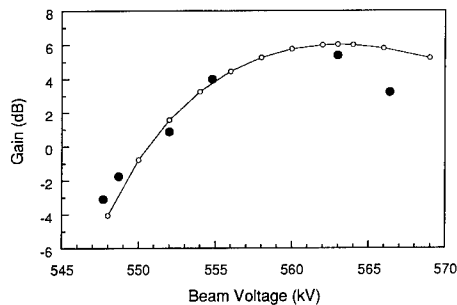


Fig. 4. A plot of gain at 86 GHz vs. beam voltage. Filled circles are experimental points with 1.0 kW input power, 3.5 kG peak wiggler magnetic field, and 6.0–8.0 A beam current. Superimposed is the 1-D simulation result with 7.5 A beam current and  $\bar{\theta} = 5$ .

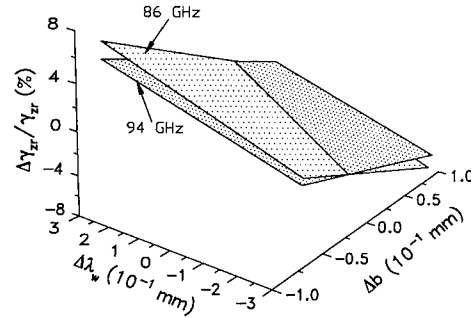


Fig. 5. A 3-D plot of  $\Delta\gamma_{zr}/\gamma_{zr}$  vs. waveguide narrow dimension error and wiggler period error for 86 GHz and 94 GHz. Waveguide narrow dimension  $b = 2.8$  mm.

with respect to  $b$  and  $\lambda_w$  and straightforward mathematical manipulation lead to the following explicit relation

$$\Delta\gamma_z = -\left(\frac{\pi c \gamma_z^3 \beta_z^3}{\omega}\right) \times \left\{ \left[ \frac{c \beta_z \lambda_w}{(\omega \lambda_w - 2\pi \beta_z c) b^3} \right] \Delta b - \left( \frac{2}{\lambda_w^2} \right) \Delta \lambda_w \right\}, \quad (3)$$

which is plotted in Fig. 5. Here, the analysis assumes constant errors throughout the FEL interaction length for both waveguide dimension and wiggler period. In reality, the errors are randomly distributed. The effects of random wiggler imperfections have been studied. While the constraint imposed by wiggler errors is more serious for shorter wavelength FELs it is less important than the problem of electron beam quality [8]. While the issues of beam quality and wiggler imperfections are different, wiggler period error and amplifier waveguide error are similar in the sense that they both cause changes in the resonance energy  $\gamma_{zr}$  and irregularities in the phase of the ponderomotive-wave.

The structural errors in the PoP experiments are estimated to be  $\pm 0.1$  mm for the waveguide narrow dimension and  $\pm 3\%$  for the wiggler period. According to the analysis here, the maximum  $|\Delta\gamma_{zr}|/\gamma_{zr}$  is calculated to be up to 8% at 86 GHz and 6% at 94 GHz. These different values of energy spread can provide a qualitative explanation of the discrepancy between the achieved gains at the two different frequencies. It also reinforces the importance of achieving high structural quality.

The importance of beam quality has been emphasized in many papers relevant to FELs. For electrons with a given pitch angle  $\theta$ , the axial energy spread can be expressed as:

$$\frac{\Delta\gamma_z}{\gamma_z} = -\frac{1}{2} \gamma_z^2 \beta_z^2 \theta^2. \quad (4)$$

The operation of a FEL at different frequencies utilizing the same wiggler requires different beam energies. This results in a frequency dependence of  $\Delta\gamma_z/\gamma_z$ , which becomes stronger as the electron pitch angle becomes larger. Depending on the working regime defined by the intersection of the dispersion curves (described in Eqs. (1) and (2)), the operating voltage needs to be either raised or lowered as frequency goes up/down. For the experimental parameters described in Table 1, the same beam velocity spread yields a larger  $\Delta\gamma_z/\gamma_z$  for the FEL amplifier at 86 GHz than at 94 GHz.

Another possible reason responsible for the lower gain observed at 86 GHz might be a change of the beam matching condition at the input of the wiggler as a result of the voltage dependence of beam propagation on the not optimized wiggler entrance taper profile. Although the dependence is not significant for a  $\sin^2(k_w z/4N_{\text{tap}})$  entrance taper profile, in reality an optimal entrance taper is difficult to achieve. Therefore the effect can be substantial, as we have observed in our experiments.

For a future device, the use of a thermionic electron gun can expect a better quality electron beam. Reasonable manufacturing errors can be held within  $\pm 1$  mil ( $\pm 0.025$  mm) for the waveguide narrow dimension and  $\pm 3$  mils ( $\pm 0.076$  mm) for the wiggler period. With these estimated values, the maximum  $|\Delta\gamma_z|/\gamma_z$  will be 1.9% at 86 GHz and 1.6% at 94 GHz for the waveguide narrow dimension of 2.8 mm which does not represent the optimal design. An optimal waveguide dimension will give a less value of maximum  $|\Delta\gamma_z|/\gamma_z$  at these frequencies. This will make structural imperfection a less serious issue than the problem of beam quality. If a superconducting magnetic wiggler [10] is adopted, the core saturation problem will be solved, the amplifier waveguide size can be easily optimized, and the beam propagation difficulty will be alleviated.

#### 4. Beam propagation through 74 period wiggler

Experimental and numerical studies on the sheet beam propagation through 56 period uniform wiggler has been reported [9]. Theoretical analysis and computer simulations show that an additional section of uniform wiggler is needed to drive this FEL amplifier into saturation. For this purpose, another 18 period uniform wiggler section has been fabricated. The wiggler entrance taper profile has also been adjusted in order to maximize electron beam propagation through the wiggler. The measured entrance taper profile is close to  $\sin^2(k_w z/4N_{\text{tap}})$  with  $N_{\text{tap}} = 4$ , where

$N_{\text{tap}}$  is the number of tapered period. Beam propagations through the 56 and 74 period wiggler with the newly adjusted wiggler entrance taper have been measured and compared. Interception of electrons in the additional 18 period wiggler section is not excessive. High power amplification experiments will next be conducted with the insertion of a new amplifier waveguide.

#### Acknowledgements

We would like to thank Dr. Rich Fischer for the loan of the EIO millimeter-wave source. The authors are also grateful to J. Rodgers, J. Pyle, and K. Diller for their technical assistance, Dr. B. Levush and Dr. P.E. Latham for their help in the initial running of the simulation code, and Dr. V.L. Granatstein for his encouragement.

This work was supported by the U.S. Department of Energy.

#### References

- [1] G. Bekefi, B. Chen, I. Mastovsky, P. Volfbeyn, I. Wilson and W. Wuensch, ICOPS'94, Abstracts 94CH3465-2, 2D10-11, p. 114.
- [2] W.W. Destler, V.L. Granatstein, I.D. Mayergoyz and Z. Segalov, J. Appl. Phys. 60 (1986) 521.
- [3] V.L. Granatstein, T.M. Antonsen, Jr., J.H. Booske, W.W. Destler, P.E. Latham, B. Levush, I.D. Mayergoyz, D.J. Radack, Z. Segalov and A. Serbeto, Nucl. Instr. and Meth. A 272 (1988) 110.
- [4] J.H. Booske, W.W. Destler, Z. Segalov, D.J. Radack, E.T. Rosenbury, J. Rodgers, T.M. Antonsen, Jr., V.L. Granatstein and I.D. Mayergoyz, J. Appl. Phys. 64 (1988) 6.
- [5] W.W. Destler, S. Cheng, Z.X. Zhang, T.M. Antonsen, Jr., V.L. Granatstein, B. Levush and J. Rodgers, Phys. Plasma 1 (1994) 1708.
- [6] B. Levush, H.P. Freund, T.M. Antonsen, Jr., Nucl. Instr. and Meth. A 341 (1994) 234.
- [7] S. Cheng, W.W. Destler, V.L. Granatstein and J. Rodgers, Proc. 10th Int. Conf. on High Power Particle Beams, San Diego, CA, USA, June 20–24, 1994, to be published.
- [8] H.P. Freund and R.H. Jackson, Nucl. Instr. and Meth. A 341 (1994) 225.
- [9] Z.-X. Zhang, V.L. Granatstein, W.W. Destler, S.W. Bidwell, J. Rodgers, S. Cheng, T.M. Antonsen, Jr., B. Levush and D.J. Radack, IEEE Trans. Plasma Sci. PS-6 (1993) 760.
- [10] S.W. Bidwell, D.J. Radack, T.M. Antonsen, Jr., J.H. Booske, Y. Caemel, W.W. Destler, V.L. Granatstein, B. Levush, P.E. Latham, I.D. Mayergoyz and Z.X. Zhang, Nucl. Instr. and Meth. A 304 (1991) 187.

# Free-ion lasers with radiative ion cooling

E.G. Bessonov \*

*Lebedev Physical Institute of the Russian Academy of Sciences, Moscow, Russian Federation*

## Abstract

Application of Radiative Ion Cooling (RIC) developments in the field of Free-Ion Lasers (FILs) are considered.

## 1. Introduction

Electron beams are considered to be the most suitable active media for Free-Particle Lasers (FPLs) because the electron mass is small. Electrons can be accelerated easily to a necessary relativistic factor  $\gamma$ , and they will emit powerful electromagnetic radiation in given fields. However, the optimal conditions for radiation by ions can be obtained in undulators with acceptable periods  $\lambda_u \sim 1$  m. Moreover, under conditions of equal relativistic factors which define the hardness of the emitted radiation, ion beams possess many orders of magnitude higher stored energy and much less emittance than electron beams. For example, the electron beam of the APS possesses two orders higher emittance and five orders less stored energy than the proton beams of the LHC at nearly the same relativistic factors [1]. The stored beam energy of the LHC will exceed 500 MJ. It follows that under the conditions of optimal deflecting parameters  $p_\perp$  and equal efficiencies for both electron and ion beams the limiting power of FILs will be many orders higher than that of FELs. Hence the more complicated and expensive FIL may be preferable when extremely high power sources are required [2–4]. The limiting hardness of the FIL will be higher as well. By analogy with synchrotron radiation, a Radiative Ion Cooling (RIC) method on non-fully stripped ion beams in storage rings can be used at the top energy of the rings [5]. RIC may make it possible to store very high current low-emittance ion beams using multiple injection of ions in high energy storage rings.

This article attempts to adopt RIC techniques to high power FILs. Quantum X-ray generators on moving ions [6,7] and high power hard quasi-monochromatic spontaneous incoherent backward Rayleigh scattering sources [6,8] can also be developed with cooled ion beams.

## 2. Main consequences from the FPL theory

The minimum wavelength  $\lambda_n$  of electromagnetic radiation emitted by a relativistic charged particle in an undulator on the  $n$ th harmonic in free space and in a waveguide is defined by  $\lambda_u$ ,  $\gamma$ ,  $p_\perp$  and the cutoff wavelength  $\lambda_c$  of the waveguide mode:

$$\lambda_n^{\text{fs}} = \frac{\lambda_u}{2n\gamma^2} (1 + p_\perp^2),$$

$$\lambda_n^{\text{wg}} = \frac{\lambda_u \left( 1 \pm \sqrt{1 - (1 + p_\perp^2)(1 + \lambda_u^2/n^2\lambda_c^2)/\gamma^2} \right)}{n(1 + \lambda_u^2/n^2\lambda_c^2)}, \quad (1)$$

where  $p_\perp = (|\mathbf{p}_\perp|^2)^{1/2} = (|\mathbf{B}_\perp|^2)^{1/2}/B_c$ ,  $p_\perp = \gamma\beta_\perp$ ,  $\beta_\perp = v_\perp/c$ ,  $v_\perp$  is the transverse velocity of the particle,  $\mathbf{B}_\perp$  is the transverse magnetic field strength of the undulator,  $B_c = 2\pi mc^2/n^+ e\lambda_u$ ,  $e$  is the electron charge,  $m$  is the mass of the particle,  $n^+$  is the number of the ion charge state, the coefficient  $2\pi mc^2/e \approx 19.7$  A [MG cm], and  $A$  is the atomic weight.

The maximum rate of energy loss in free space, or in a circular waveguide, per particle in a parametric FPL using a helical undulator and a beam consisting of a series of short ( $< \lambda_1$ ) microbunches spaced an integral number of wavelengths  $\lambda_1$ , apart is,

$$\left( \frac{d\varepsilon}{dy} \right)_{\text{max}}^{\text{fs}} = \frac{\pi^2 mc^2}{\lambda_u} \frac{p_\perp^2}{1 + p_\perp^2} \frac{i}{i_A},$$

$$\left( \frac{d\varepsilon}{dy} \right)_{\text{max}}^{\text{wg}} = \frac{2mc^2 p_\perp^2 l^d}{k\gamma^2 r^2} \frac{i}{i_A}, \quad (2)$$

where  $\pi^2 mc^2/i_A \approx 0.3n^+ \text{ MeV/kA}$ ,  $2mc^2/i_A \approx 0.061n^+ \text{ MeV/kA}$ ,  $i_A = mc^3/en^+$ ,  $l^d$  is the e-folding damping length of the electromagnetic wave field strength in the waveguide,  $r$  is the waveguide radius, coefficient  $k$  is determined by the waveguide mode, and  $\beta_{\text{ph}}$  and  $\beta_g$  are the phase and group velocities [3]. The rates of the particle energy loss ( $d\varepsilon/dy$ ) in free space when the wide beam of the radius,  $\sigma_p \gg \lambda\gamma/(1 + p_\perp^2)^{1/2}$ , is used, and in the

\* Tel. +7 095 334 01 19, fax +7 095 938 22 51 e-mail: bessonov@sci.fian.msk.su.

waveguide, tend to (2) at the distances from the beginning of the undulator,  $l_p = 2\pi\sigma_p^2/\lambda_1$  and  $l^d$ , respectively.

### 3. Main consequences from the RIC theory

The RIC method is similar to synchrotron damping [9] in its physics, but is like laser cooling [10] in technique (when laser photons are used). In this method ion excitation by means of real photons (thermal, laser), or in the ultrarelativistic case by means of equivalent virtual photons from an undulator, is used. The photon energy is chosen so that in the ion beam coordinate system it is close to the transition energy  $\hbar\omega'_0$  between definite electron states in the ions. A broadband photon beam is used in order to excite ions with different energies and momenta effectively. The radiofrequency system of a storage ring is used to compensate longitudinal momentum loss. Since the scattered radiation is directed mainly along the direction of the ion's velocity, it leads to damping of both betatron and phase oscillations of the ions in the storage ring.

The spectral width needed for an ion beam with angular and energy spreads of the value  $\theta_b$ , and  $(\Delta\gamma)_b$ , is

$$\frac{\Delta\omega_1}{\omega_1} > \frac{\theta_b^2}{4} + \frac{(\Delta\gamma)_b}{\gamma}. \quad (3)$$

The damping times for vertical and radial betatron oscillations and for phase oscillations are

$$\tau'_z = \tau'_{z\min} \frac{2\pi R(1+D)}{n_{\text{int}} l_{\text{eff}} D}, \quad \tau'_x = \tau'_z, \quad \tau'_s = \tau'_z/2. \quad (4)$$

where  $\tau'_{z\min} = g_2 \gamma \lambda_0^2 P_A / 2\pi^2 c^2 g_1 f_{1,2} \hbar \omega'_0$ ,  $P_A = m_e m_i c^5 / e^2$ ,  $m_i$ ,  $m_e$  are the ion and electron mass respectively,  $g_{1,2}$  are the statistical weights of the states 1 and 2,  $f_{1,2}$  is the transition strength,  $D = I/I_c$  is the saturation parameter,  $I_c = (\pi c g_1 \hbar \omega'_0 / \gamma^2 g_2 \lambda_0^3)$  ( $\Delta\omega_1/\omega_1$ ,  $l_{\text{eff}} = \min(l_{ss}, l_R)$ ) is the effective interaction length of the laser and photon beams,  $l_{ss}$  is the length of a straight section of the storage ring,  $l_R = S/\lambda_1$  is the Rayleigh length (within the limits of the length  $2l_R$ , the laser area exceeds the minimum area by less than a factor of two),  $S$  is the cross-section area of the laser beam,  $n_{\text{int}}$  is the number of photon and ion beam interaction regions, and  $R$  is the mean radius of the storage ring orbit [5].

The quantum nature of the photon scattering will lead to an equilibrium radial dimension and energy spread of the ion beam [5]

$$\sigma_x = \alpha R \sqrt{\frac{1.4 \hbar \omega'_0}{m_i c^2}}, \quad \frac{\sigma_\gamma}{\gamma} = \sqrt{\frac{0.7 \hbar \omega'_0}{m_i c^2}}. \quad (5)$$

Here  $\alpha \approx \nu_x^{-2}$  and  $\nu_x$  are the momentum compaction factor and radial betatron oscillation tune of the storage ring, respectively [10].

The equilibrium vertical dimension of the ion beam  $\sigma_z = \sigma_x / \alpha \gamma \nu_z$ . The radial dimension of the ion beam defined by the energy spread  $\sigma_\gamma$  is equal to  $\sigma_s = \sigma_x = R \alpha \sigma_\gamma / \gamma$ . The equilibrium radial angular spread and emittance of the ion beam are

$$\sigma_{\theta x} = \frac{1}{\nu_x} \sqrt{\frac{1.4 \hbar \omega'_0}{m_i c^2}}, \quad \epsilon_x = \frac{1.4 \pi R}{\nu_x^3} \frac{\hbar \omega'_0}{m_i c^2}. \quad (6)$$

The cooled ion beam parameters (5) and (6) do not depend on the ions' energy (laser wavelength).

The transition from the first excited level to the ground state of hydrogen-like and approximately for sodium-like ions corresponds to  $f_{1,2} = 0.42$ ,  $g_1 = 1$ ,  $g_2 = 4$ ,  $\lambda'_0 = 4/3 Z_{\text{eff}}^2 R'$ ,  $\hbar \omega'_0 = 3 \alpha'^2 m_e c^2 Z_{\text{eff}}^2 / 8 \approx 10.19 Z_{\text{eff}}^2$  [eV],  $\tau'_{z\min} = (8^4/3^3 f_{1,2} \alpha'^7) (m_i/m_e) (\gamma \Lambda_e / c Z_{\text{eff}}^6) \approx 0.775 A \gamma / Z_{\text{eff}}^6$  [s], where  $R' = e^4 m_e / 4 \pi c \hbar^3 = 109678 \text{ cm}^{-1}$  is the Rydberg constant,  $\alpha' = e^2 / \hbar c$ ,  $\Lambda_e = \hbar / m_e c \approx 3.86 \times 10^{-11} \text{ cm}$ ,  $Z_{\text{eff}} = n^+ + 1 \leq Z$ , and  $Z$  is the atomic number.

The damping time  $\tau_s$  can be decreased by a factor of  $(\Delta\gamma)_b/\gamma$  when a highly monochromatic laser beam is used in combination with a sweep (chirp) of the laser frequency. In this case the laser bandwidth (3) can be narrowed to  $\Delta\omega_1/\omega_1 \geq \theta_b^2/4$ . Using the synchro-betatron resonance [5], the damping time of betatron oscillations can be shortened by the phase oscillation damping.

For nearly fully stripped high energy ions beam loss due to residual gas interaction at pressures  $\leq 10^{-10}$  mbar is negligible compared to that caused by high current inelastic intrabeam interaction processes involving ion charge-exchange and ionization [11–13]. But inelastic intrabeam processes have a threshold energy which can be estimated as follows. The minimum distance which can be reached between two similar ions of the kinetic energy  $\Delta T'$  is  $r_{\min} = n^+ e^2 / 2 \Delta T'$ . For an inelastic process to take place the value  $r_{\min}$  must be less than  $\approx a_0 n^2 / Z_{\text{eff}}$ , where  $a_0 = \hbar^2 / m_e e^2$  is the Bohr radius, and  $n$  is the main quantum number. Hence, the threshold energy  $\Delta T'_{\text{thr}} \approx n^+ Z_{\text{eff}} e^2 / 2 a_0$ . As the transverse momentum is an invariant,  $\langle \Delta T'_\perp \rangle \approx m_i c^2 (\theta_b \gamma)^2 / 2$ . The value  $\langle \Delta T'_\perp \rangle|_{\theta_b = \sigma_{\theta x}} \approx 0.26 \alpha'^2 \gamma^2 m_e c^2 Z_{\text{eff}}^2 / \nu_x^2$  can be less than  $\Delta T'_{\text{thr}}$  if the energy of the ions

$$\gamma < \gamma_{\text{thr}} = 1.38 n^+ \nu_x / \sqrt{Z_{\text{eff}}}. \quad (7)$$

Losses of ions through inelastic beam interactions are absent in this case. The problem is to cool the ion beams in a short interval  $\tau_z < \tau_1$ , where

$$\tau_1 = \frac{2\sqrt{2} \pi^2 R^{5/2} \sqrt{\epsilon_x / \pi}}{N_i c \nu_x^{3/2} \sigma_1}, \quad (8)$$

$N_i$  is the number of ions in the beam,  $\sigma_1$  is the total beam loss cross-section determined by both electron capture and ionization of the beam ions [14]. Expression (8) is valid for the case of  $\epsilon_x \approx \epsilon_z$ ,  $\nu_x \approx \nu_z$ . The beam life time  $\tau_1 \sim 1.44$  s when  $R = 10^3 \text{ m}$ ,  $N_i \sim 10^{15}$ ,  $\sigma_1 \sim 10^{-17} \text{ cm}^2$ , ( $\gamma > \gamma_{\text{thr}}$ ).

Relativistic ions can lose their electrons in a strong external magnetic field. The relative energy of the relativistic ions determined by this process cannot exceed the value [5]

$$\gamma = \gamma_{cn} = \frac{E_0 Z_{\text{eff}}^3 \xi}{H n^4} \bigg|_{\xi=0.012} \approx \frac{2.06 \times 10^6 Z_{\text{eff}}^3}{H n^4}. \quad (9)$$

A list of dimensionless beam parameters for some ions, the values  $\gamma$ ,  $m_i c^2 \gamma$ ,  $\tau_{z\text{min}}$  and  $I_c$  at  $\lambda_1 = 6 \times 10^{-5}$  cm,  $\Delta \omega_1 / \omega_1 = 10^{-3}$  and the values  $\gamma_{\text{thr}}$ , and  $\gamma_{cn}$  at  $H = 10^5$  Gs,  $n = 1, 2$  are presented in Table 1.

The current which can be stored in a ring is limited by an additional self-defocusing force determined by a Laslett limiting current  $i_{\text{lim.m}}^L \sim \Delta \nu_{x,z} \sigma_x (\sigma_x + \sigma_z) \gamma^3$ . A second, particularly important, limiting average current is determined by a Keil–Schnell limiting current of the longitudinal instability  $i_{\text{lim.m}}^{K-Sch} \sim (\gamma/Z_n)(\Delta \gamma/\gamma)^2$ , where  $Z_n$  is the longitudinal impedance [5,14].

The limiting currents determined by transverse and longitudinal oscillations can be increased by the use of transverse feedback and by an extended tail in the momentum distribution [11,15].

#### 4. Possible parameters of the FILs

The main parameters of the staging storage rings for FILs using RIC of  $^{10}\text{B}^{4+}$  ions when  $\Delta \nu_{x,z} = 0.25$ ,  $|Z_n|/n = 1.0 \Omega$ ,  $(\Delta \gamma)_b/\gamma = 10^{-3}$ ,  $\nu_x \approx \nu_z$ ,  $\sigma_x \approx \sigma_z$  are given in Table 2.

The following example illustrates possible parameters of an FIL in the centimeter wavelength region. A beam of  $^{10}\text{B}^{4+}$  ions passes through a waveguide which in the form of a smooth pipe of radius  $r = 1.5$  cm with an e-folding length  $l^d = 30$  m. The waveguide is installed in a helical undulator with a period  $\lambda_u = 0.5$  m and magnetic field strength  $B_\perp = 100$  kG. The  $H_{11}$  mode is excited ( $\lambda_c = 3.41r$ ) and  $k \approx 0.5$ . The energy of ions  $\varepsilon_1 \approx 579$  GeV

Table 1  
Dimensionless beam parameters for some ions

|   | Ion                  |                        |                             |                             |
|---|----------------------|------------------------|-----------------------------|-----------------------------|
|   | $^3_2\text{He}^{1+}$ | $^{10}_5\text{B}^{4+}$ | $^{238}_{92}\text{U}^{10+}$ | $^{91}_{40}\text{Zr}^{39+}$ |
| $10^5 \nu_x^3 \varepsilon_x / (1.4 \pi R)$  | 1.44                 | 2.7                    | 0.55                        | 19                          |
| $10^4 \sigma_x / (\sqrt{1.4} \alpha R)$     | 1.2                  | 1.64                   | 0.74                        | 4.36                        |
| $10^4 \sigma_{\theta x} \nu_x / \sqrt{1.4}$ | 1.2                  | 1.64                   | 0.74                        | 4.36                        |
| $10^4 \sigma_y / \gamma$                    | 1.00                 | 1.37                   | 0.62                        | 3.65                        |
| $\gamma$                                    | 9.87                 | 61.7                   | 299                         | 3947                        |
| $mc^2 \gamma$ [GeV]                         | 27.7                 | 579                    | $6.7 \times 10^4$           | $3.4 \times 10^5$           |
| $\tau_{x\text{min}}$ [ms]                   | 358                  | 30.6                   | 41.6                        | 0.067                       |
| $I_c$ [MW/cm <sup>2</sup> ]                 | 0.056                | 2.195                  | 51.12                       | $9.05 \times 10^3$          |
| $\gamma_{\text{thr}} / \nu_x$               | 0.98                 | 2.47                   | 4.16                        | 8.51                        |
| $\gamma_{c1}$                               | 165                  | $2.6 \times 10^3$      | $2.7 \times 10^4$           | $1.3 \times 10^6$           |
| $\gamma_{c2}$                               | 10.3                 | 160                    | $1.69 \times 10^3$          | $8.2 \times 10^4$           |

Table 2

The main parameters of the staging storage rings for FILs using RIC of  $^{10}\text{B}^{4+}$  ions

|                                | Machine               |                       |                       |
|--------------------------------|-----------------------|-----------------------|-----------------------|
|                                | SR1                   | SR2                   | SR3                   |
| $R$ [m]                        | $10^2$                | $10^3$                | $10^4$                |
| $\nu_x$                        | 10                    | 25                    | 250                   |
| $\gamma_{\text{thr}}$          | 24.7                  | 61.7                  | 617                   |
| $\lambda_1$                    | $2.4 \times 10^{-5}$  | $6 \times 10^{-5}$    | $6 \times 10^{-4}$    |
| $\sigma_x$ [mm]                | 0.19                  | 0.31                  | 0.031                 |
| $\sigma_{\theta x}$ [mrad]     | $1.94 \times 10^{-2}$ | $7.76 \times 10^{-3}$ | $7.76 \times 10^{-4}$ |
| $\epsilon_c$                   |                       |                       |                       |
| [mm mrad]                      | $3.78 \times 10^{-3}$ | $2.4 \times 10^{-3}$  | $2.5 \times 10^{-5}$  |
| $\sigma_y / \gamma$            | $1.37 \times 10^{-4}$ | $1.37 \times 10^{-4}$ | $1.37 \times 10^{-4}$ |
| $i_{\text{lim.m}}^L$           | 11.07                 | 11.07                 | 11.07                 |
| $i_{\text{lim.m}}^{K-Sch}$ [A] | 580                   | 232                   | 23.2                  |

( $\gamma = 61.7$ ) and the current of the ion beam is  $i = 5$  kA (see Tables 1 and 2).

In this case  $B_c \approx 10^6$  G,  $p_\perp \approx 0.1$ ,  $\lambda_c = 5.115$  cm,  $n = 1$ . According to (1) the wavelength of the emitted radiation is  $\lambda_1 \approx 1$  cm, the rate of the energy loss per ion  $d\varepsilon/dy \approx 42 n^+ i$  keV/m kA  $\approx 850$  keV/m and the power emitted by the ion beam per unit length  $dP/dy = (i/n^+ e)(d\varepsilon/dy) \approx 42 i^2$  MW/mkA  $= 1.05$  GW/m.

The ion beam current in the storage ring can be increased by beam bunching techniques [12,15–17]. A high harmonic number RF buncher must be used in the final stage of the manipulations in order to produce short ( $< \lambda$ ) small (a few  $\lambda$ ) period bunches. Short period bunching can be produced in an external RF system as well. The limiting current  $i_{\text{lim.m}}^L$  can be increased by increasing of transverse dimensions of the beam in the process of a beam manipulations.

In order to cool ion beams in SR2 a dye laser or a free-electron laser of power  $P_1 \approx 100$  W, and wavelength  $\lambda_1 \approx 6 \times 10^{-5}$  cm can be used. If  $\Delta \lambda_1 / \lambda_1 = 10^{-3}$ , the laser beam area  $S = 1$  cm<sup>2</sup> and the reflectivity coefficients of the resonator mirrors  $R_r \approx 0.99$ , then the intensity of the laser beam in the resonator and the saturation parameter will be  $I_1 = 2P_1 / S(1 - R_r) \approx 20$  kW/cm<sup>2</sup>,  $D \approx 0.43$ . In this case the damping time  $\tau_z \approx 16.6 \tau_{z\text{min}} \approx 0.51$  s when  $n_{\text{int}} I_{\text{eff}} / 2 \pi R = 0.2$ .

A centimeter wavelength source of such power could be used in Linear Colliders (LC) where the  $E_{01}$  mode could be excited and electrons accelerated at the same time in a rippled waveguide. Harder ( $\sim 1$  mm) continuous radiation from an undulator installed in a storage ring could be generated by short ( $< 1$  mm) ion bunches for fusion and other applications. Increased energy high charge state heavy ion beams could allow the generation of VUV (and harder) high power radiation for laser fusion and other applications.



## 5. Conclusion

The energy stored in the ISR beam has reached  $5 \times 10^6$  J, in the form of a beam of 50 A at 31.5 GeV for a duration of 3.3  $\mu$ s. Peak currents in excess of  $10^3$  A have been focused to submillimeter spots without problems [12]. Recent developments in high energy particle accelerators are making it much easier to generate high power cm to X-ray electromagnetic radiation which can be used in different fields of science and technology.

## Acknowledgements

The author would like to thank A.G. Molchanov, E. Yukov and A.N. Skrinsky for helpful discussions.

## References

- [1] S.K. Dutt, Proc. Workshop on Fourth Generation Light Sources, SSRL/SLAC, February 24–27, 1992, p. 170.
- [2] E.G. Bessonov and Ya.A. Vazdik, Proc. 15th Int. Accelerator Conf., Hamburg, DESY, 20–24 July 1992, Int. J. Mod. Phys. A, Suppl. 2A, 2b, 1 (1993) 540.
- [3] E.G. Bessonov, Nucl. Instr. and Meth. A 341 (1994) 355.
- [4] R. Coisson, SSC as a powerful coherent source of radiation from X-Ray to IR written in Dec. 1991 in response to a question of H. Winick (private communication).
- [5] E.G. Bessonov, Preprint FIRAN No 6, Moscow (1994); E.G. Bessonov, submitted to Phys. Rev. Lett.; E.G. Bessonov, J. Russian Laser Res. 15 (5) (1994) 403.
- [6] K.A. Ispirian and A.T. Margarian, Phys. Lett. 44A (1973) 377.
- [7] L.D. Miller, Opt. Commun. 30 (1979) 87; G.C. Baldwin and N.J. DiCiacomo, IEEE Trans. Nucl. Sci. NS-30 (1983) 981.
- [8] N.G. Basov, A.N. Oraevsky and B.N. Chichkov, Sov. Phys. JETP 62 (1985) 37.
- [9] A.A. Kolomensky and A.N. Lebedev, Theory of Cyclic Accelerators (North-Holland, 1966); H. Bruck, Accélérateurs Circulaires de Particules (Press Universitaires de France, 1966).
- [10] P.J. Channel, J. Appl. Phys. 52 (1981) 3791; S. Schröder, R. Klein, N. Boos et al., Phys. Rev. Lett. 64 (1990) 2901; J.S. Hangst, K. Berg-Sorenson, P.S. Jessen et al., Proc. IEEE Particle Accelerator Conf. Accelerator Science and Technology, San Francisco, May 6–9, 1991 vol. 3 (1991) p. 1764; W. Petrich, M. Grieser, R. Grimm et al., Phys Rev A 48 (1993) 2127.
- [11] B. Franzke, K. Beckert, F. Bosch et al. Proc. 15th Int. Accelerator Conf., Hamburg, DESY, 20–24 July 1992, Int. J. Mod. Phys. A, Suppl. 2A, 2B, 1 (1993) 60.
- [12] C. Rubbia, Nucl. Instr. and Meth. A 278 (1989) 253.
- [13] F. Melchert, E. Salzborn, I. Hofmann et al., Nucl. Instr. and Meth. A 278 (1989) 65.
- [14] N.S. Dikansky and D.V. Pestrikov, Physics of the Intense Beams in the Storage Rings (in Russian) (Nauka, Novosibirsk, 1989).
- [15] I. Hofmann, Nucl. Instr. and Meth. A 278 (1989) 271.
- [16] R.C. Arnold, Nucl. Instr. and Meth. A 278 (1989) 163.
- [17] R.C. Arnold, Nucl. Instr. and Meth. 199 (1989) 557.



ELSEVIER

## Time-resolved study of sideband generation and transition to chaos on an infrared FEL <sup>☆</sup>

W.P. Leemans <sup>a,\*</sup>, M.E. Conde <sup>a</sup>, R. Govil <sup>a</sup>, B. van der Geer <sup>a</sup>, M. de Loos <sup>a</sup>,  
H.A. Schwettman <sup>b</sup>, T.I. Smith <sup>b</sup>, R.L. Swent <sup>b</sup>

<sup>a</sup> Center for Beam Physics, Lawrence Berkeley Laboratory, University of California, Berkeley, CA, USA

<sup>b</sup> Hansen Experimental Physics Laboratory, Stanford University, Stanford, CA, USA

### Abstract

We report observations on sideband generation and transition to chaos in an infrared free electron laser operating at a wavelength  $\lambda_r$  of 4  $\mu\text{m}$  with a low loss optical cavity. The temporal evolution of the radiation spectrum through the complete macropulse has been measured on a micropulse to micropulse basis [1]. Stable sidebands are observed for small cavity detuning with frequency offsets in good agreement with calculations. For even smaller cavity detuning, self-oscillations occur with the main laser wavelength varying by up to 2%. Using a wavelength stabilization system based on RF feedback [2], we have suppressed these wavelength fluctuations without loss of peak power.

### 1. Introduction

Free electron lasers operating in a high power regime can be unstable to trapped particle instabilities when slippage between the light pulse and the electron bunch causes different longitudinal slices of the electron bunch to be coupled. In the sideband instability [3], large optical wave amplitudes will cause the electron bunch to undergo synchrotron oscillations in phase space during its passage through the undulator. Simulations as well as time-integrated experiments [4] indicate that radiation spectra can exhibit a narrow spectral sideband at relatively low power operation or very complex broad band spectra at high power operation. Theoretical studies [5] have furthermore indicated that FELs can evolve from regular towards chaotic behavior via a period doubling cascade, intermittency and quasi-periodicity.

To study the dynamical behavior of the instability we have developed a diagnostic system [1] capable of measuring the spectrum of every single micropulse in a macropulse with a duration long compared to the growth time of the instability. Using this diagnostic system we have obtained

the first time-resolved radiation spectra, on a micropulse-to-micropulse basis, from an infrared FEL for a cavity detuning parameter  $D$  ( $= \delta L / \lambda_r$ ) ranging between  $-0.5$  and  $0.2$ . Here  $\delta L$  is the change in cavity length from perfect synchronism. Micropulse spectra have been obtained for FELs operating in the visible wavelength range by the use of optical streak cameras [6] and for near infrared FELs [7] ( $< 1.8 \mu\text{m}$ ) by the use of high digitizing speed array systems.

In addition, we have performed a time-resolved measurement demonstrating suppression of the wavelength instability through modulation of the electron beam energy. Although the sideband instability can lead to enhanced extraction efficiency for uniform wigglers [8], the consequential reduction in the temporal coherence often makes this mode of operation undesirable. With the exception of group velocity control [9], most sideband suppression techniques [10] such as cavity detuning, and wavelength dependent cavity loss invariably have led to reduced FEL efficiency [11].

### 2. Experimental setup and parameters

The experiment used the Stanford SCA/FEL operating at  $\lambda_r = 4.08 \mu\text{m}$  with a measured optical cavity  $Q$  of 229. The wiggler used in this experiment had 120 periods ( $N_w$ ), a period  $\lambda_w = 3.6 \text{ cm}$ , and an RMS normalized wiggler strength  $a_w = 0.7$ . The linac produced 1.8–2.0 ms long macropulses at 10 Hz, containing electron bunches at a repetition frequency of 11.8 MHz and a bunch duration on

<sup>☆</sup> This work was supported in part by the Director, Office of Energy Research, Office of Basic Energy Sciences, Material Sciences Division, of the U.S. Department of Energy under contract No. DE-AC03-76SF00098 and by the Office of Naval Research, Contract No. N00014-91-C-0170.

\* Corresponding author. Tel. +1 510 486 7788, fax +1 510 486 7981, e-mail leemans@lbl.gov.

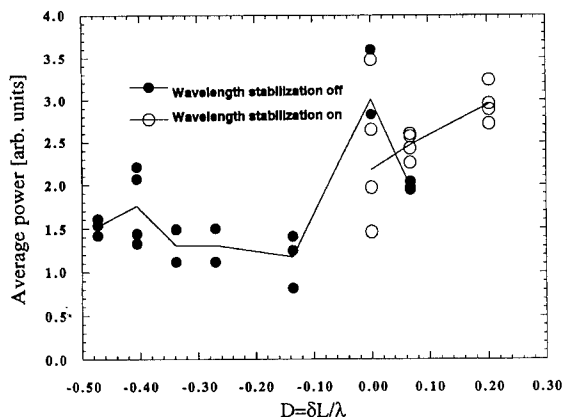


Fig. 1. FEL output power as a function of normalized cavity detuning  $D$  with (circles) and without (dots) RF feedback wavelength stabilization. We have adopted  $D = 0$  as the cavity length resulting in maximum output power without stabilization. The line through the data connects average power levels for each detuning.

the order of 1–4 ps. The peak current was on the order of 5 A. As a function of optical cavity detuning, the optical pulses, repeating also at 11.8 MHz, had a measured duration of 1.5–3.4 ps and a pulse energy of 0.05–0.2  $\mu$ J. The average output power for various cavity detuning lengths ranged between 0.5 and 1.5 W resulting in an average intracavity power on the order of 240–730 W.

The SCA/FEL feedback system allows stabilization of the FEL wavelength through changes in the electron beam energy. The time scale for changes in the electron beam energy is 6–12  $\mu$ s [12], faster than the cavity life time of 190  $\mu$ s in this experiment. The measured bandwidth of the feedback is on the order of 10 kHz. The wavelength is monitored using a two-element detector at the output of a spectrometer; the output is then used to modulate the energy of one of the accelerating structures so as to correct for any wavelength drift.

The spectral diagnostic, which consists of a 1 m focal length spectrometer with a 150 grooves/mm grating and a previously described image dissector readout system [1], had a measured spectral resolution of 5 nm/bin and a spectral coverage range of 100 nm (20 bins), equivalent to 2.5% of  $\lambda_r$ . A bin refers to a slice of the spectrum.

### 3. Sidebands and chaotic transition

In Fig. 1 we show the measured FEL output power as a function of normalized cavity detuning  $D$ . We have adopted  $D = 0$  as the cavity length resulting in maximum output power without wavelength stabilization.

Fig. 2 displays time-resolved FEL spectra for four different cavity detuning lengths without wavelength stabilization. The initial wavelength chirp from longer wavelengths towards shorter wavelengths is somewhat surpris-

ing but is believed to be due to an electron beam energy change in the beginning of the macropulse. It is important to note that the present diagnostic does not have enough dynamic range or sensitivity to measure the transition from initial start up, seeded by spontaneous emission, to saturation with an expected red shifting of the wavelength. For  $D = -0.41$  (Fig. 2b), a sideband is seen to grow after saturation of the main frequency, separated from the fundamental by  $0.98 \pm 0.06\%$ . The sideband saturates in typically 10–20  $\mu$ s, i.e. 100–200 passes. The theoretical sideband frequency is given by [9]

$$\Delta\omega = \frac{ck_{\text{synch}}}{1 - v_{\parallel}/v_g} = \frac{c\sqrt{2k_w k_r a_w a_r}}{\gamma_r} \frac{\lambda_w}{\lambda_r} \quad (1).$$

Here  $k_{\text{synch}}$  is the synchrotron wavenumber,  $v_{\parallel}$  is the longitudinal electron velocity,  $v_g$  is the group velocity of the light pulse,  $k_w$  and  $k_r$  are the wavenumbers of the wiggler and the FEL radiation light respectively,  $a_w$  and  $a_r$  are the normalized wiggler and radiation vector potential respectively, and  $c$  is the speed of light in vacuum. Using the measured average macropulse power level of 0.43–1.5 W, Eq. (1) predicts  $\Delta\omega/\omega = 0.93$ –1.02%, in good agreement with measurements.

For even smaller detuning ( $D = -0.36$ ), periodic self-oscillations are seen in the wavelength (Fig. 2c) as well as the output power (Fig. 3). The typical oscillation frequency observed in our experiment varies in the range of 1–25 kHz. Although we cannot rule out cavity length changes due to mirror vibrations or fluctuations in the electron beam parameters as the cause of these fluctuations, similar limit cycle behavior, characterized by such periodic oscillations, has recently also been observed in the FELIX experiment [13]. The observed periodicity is in reasonable agreement with an estimate for the limit cycle oscillation frequency given by [5]

$$f = f_c \frac{L_{\text{syn}}}{2|\delta L|}. \quad (2)$$

Here  $f_c$  is the cavity frequency (11.8 MHz),  $L_{\text{syn}}$  is the slippage distance in a synchrotron period and  $\delta L$  is the cavity length detuning.

For an even longer optical cavity, the main frequency varies more widely over the 2.5% wide spectral range of the diagnostic (Fig. 2d). Whether this behavior is chaotic cannot be definitively answered because the macropulse length is too short to follow the spectrum over many oscillation periods. However, in a preliminary attempt to catalogue the behavior, we next estimate various branching parameters and compare with calculations of chaotic FEL behavior by Hahn et al. [5]. The branching parameters of interest are the slippage parameter  $S (= L_e/L_c)$  and the scaled synchrotron slippage distance  $\mu (= L_s/L_{\text{syn}})$ . Here  $L_e$  is the electron bunch length and  $L_s$  the usual slippage length. For our experiment,  $S = 0.74$ –0.85,  $\mu = 1.12$ –1.43 and  $D = -0.12$ –0.02 are ranges for the branching param-

ters where stochastic behavior has been observed. For a higher gain system, allowing longer detuning lengths ( $D = -2.0$ ), simulations by Hahn et al. [5] indicate that routes to chaos via quasi-periodicity and intermittency exist for identical  $\mu$  and  $S$  parameter ranges.

#### 4. Instability suppression using RF feedback system

Fig. 4 shows the dramatic change in spectrum for the same cavity detuning with the wavelength stabilization off and on. Wavelength drift as well as power fluctuations are

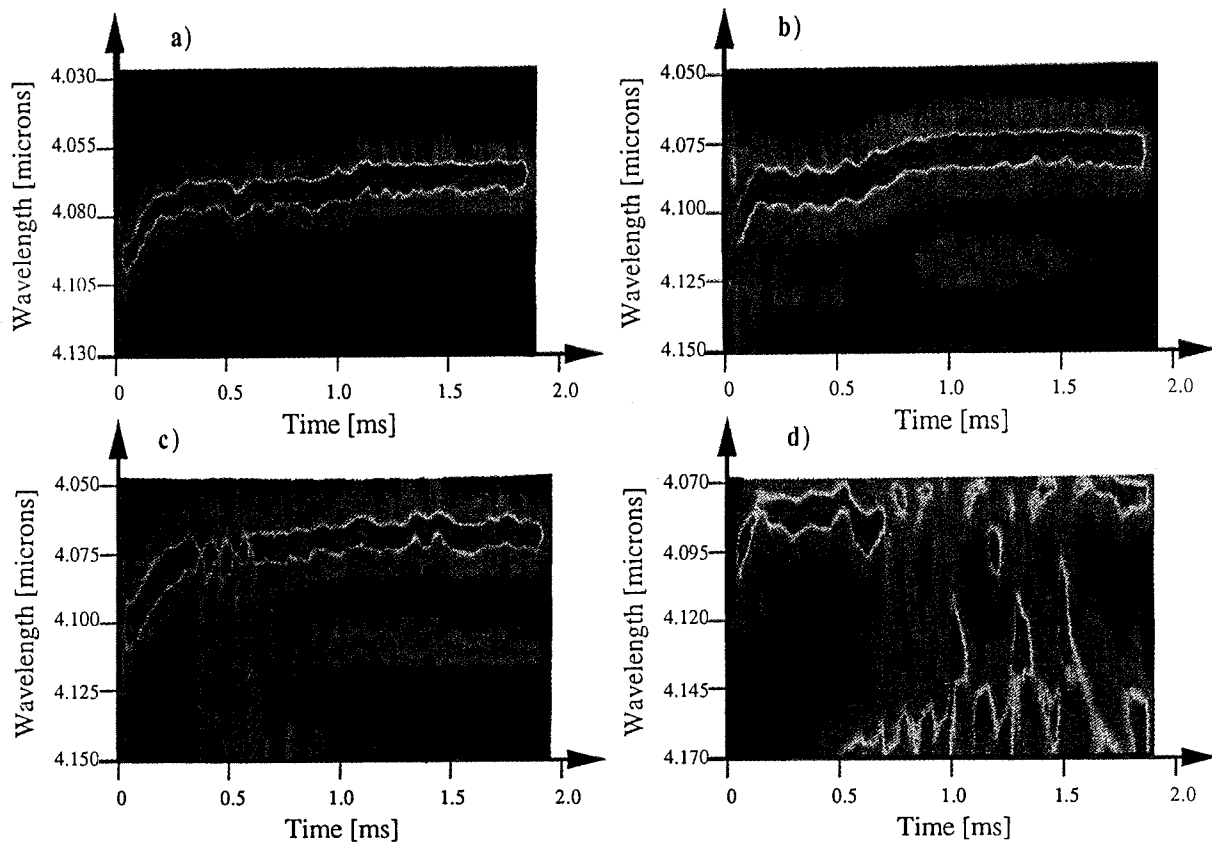


Fig. 2. Measured FEL spectrum as a function of time for  $D = -0.47$  (a),  $D = -0.41$  (b),  $D = -0.36$  (c), and  $D = -0.27$  (d).

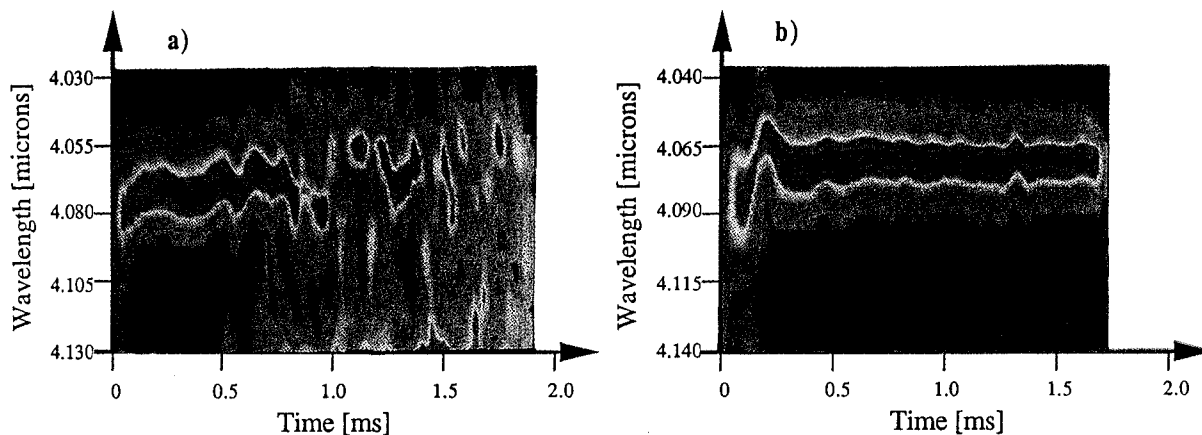


Fig. 4. Measured FEL spectrum as a function of time for  $D = 0.065$  without (a) and with (b) RF feedback wavelength stabilization.

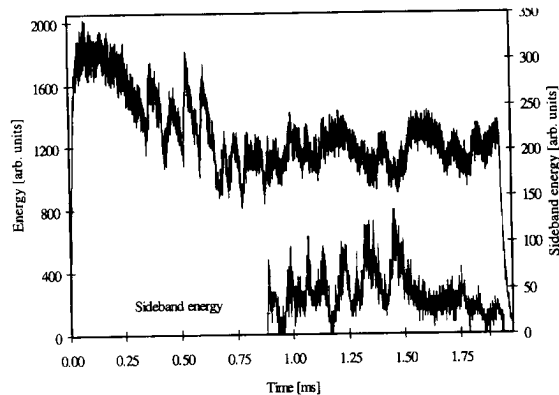


Fig. 3. Output power as a function of time for case c in Fig. 2. The self-oscillation which lasts about 700  $\mu$ s has a frequency on the order of 10 kHz.

greatly suppressed. We also note that the output power with stabilization on is about equal to the maximum output power (Fig. 1).

The details of the instability suppression depend upon the FEL operation regime: either narrow band sideband generation (Fig. 2b) or center wavelength drift (Figs. 2d and 4a). Whereas the latter case is intuitively simpler to understand, the former case depends on the wavelength coverage of the wavelength monitor since in this case (low power) the center wavelength does not shift. Since the two-element detector of the feedback loop covers more than a 1% wavelength interval, it will sense the centroid of the spectrum shifting towards longer wavelength as soon as a sideband grows. This then causes an increase in beam energy as compensation. In Fig. 2b it can be seen that a change in center wavelength does indeed lead to suppression of the sideband. We are currently carrying out detailed simulations to further study the details and potential of this technique and plan to report on our findings in a subsequent paper.

## Acknowledgements

We would like to thank Bill Fawley for many useful discussions and insightful comments, the Stanford SCA/FEL crew for their dedication in running the FEL, and Swapan Chattopadhyay for his encouragement and support.

## References

- [1] W.P. Leemans et al., Nucl. Instr. and Meth. A 331 (1993) 615; A 341 (1994) 473.
- [2] A. Marzali and T.I. Smith, Nucl. Instr. and Meth. A 331 (1993) 59.
- [3] N.M. Kroll, P.L. Morton and M.N. Rosenbluth, IEEE J. Quantum Electron. QE-17 (1981) 1436.
- [4] R.W. Warren, B.E. Newman and J.C. Goldstein, IEEE J. Quantum Electron. QE-21 (1985) 882; Bhattacharjee et al., Nucl. Instr. and Meth. A 285 (1989) 153.
- [5] S.J. Hahn and J.K. Lee, Phys. Rev. E 48 (1993) 2162; S.J. Hahn et al., Nucl. Instr. and Meth. A 341 (1994) 200.
- [6] A.H. Lumpkin, N.S.P. King and M.D. Wilke, Nucl. Instr. and Meth. A 285 (1989) 17.
- [7] J.C. Frisch, Ph. D. dissertation, Stanford University (1990); J.C. Frisch and J.E. Edighoffer, Nucl. Instr. and Meth. A 296 (1990) 9.
- [8] D. Iracane et al., Phys. Rev. Lett. 72 (1994) 3985.
- [9] J. Masud et al., Phys. Rev. Lett. 58 (1987) 763; S.S. Yu et al., Nucl. Instr. and Meth. A 259 (1987) 219.
- [10] J.E. Sollid, D.W. Feldman and R.W. Warren, Nucl. Instr. and Meth. A 285 (1989) 153.
- [11] Recent work by D.A. Jaroszynski et al., (these Proceedings (16th Int. Free Electron Laser Conf., Stanford, CA, USA 1994) Nucl. Instr. and Meth. A 358 (1995)) indicates the possibility of using a step-tapered undulator for sideband control without efficiency loss.
- [12] A. Marzali, T.I. Smith and H.A. Schwettman, these Proceedings (16th Int. Free Electron Laser Conf., Stanford, CA, USA, 1994) Nucl. Instr. and Meth. A 358 (1995) 252.
- [13] D.A. Jaroszynski et al., Phys. Rev. Lett. 70 (1993) 3412.

## Sub-picosecond laser pulse generation on the CLIO FEL

R. Prazeres<sup>\*</sup>, J.M. Berset, F. Glotin, D. Jaroszynski, J.M. Ortega

*LURE, bât. 209d, Université de Paris-Sud, 91405 Orsay cedex, France*

### Abstract

Laser pulse length measurements have been carried out on the CLIO infrared free-electron laser using a Michelson interferometer with a Te crystal as a second order autocorrelation device. Simultaneously spectral measurements have been carried out showing that the laser pulse is close to the Fourier transform limit. A minimum laser pulse length of  $\delta t = 400$  fs, and a line width of  $\delta\lambda = 500$  nm have been found for  $\lambda = 9.2$   $\mu\text{m}$ , giving a peak power of 70 MW in the full spectral bandpass. We also examine, in this paper, the laser spectral brightness as a function of the cavity length detuning, and the laser pulse length with the linac operating off the crest of the accelerating wave.

### 1. Introduction

The CLIO infrared Free Electron Laser (FEL) of Orsay is now operating as a high performance and reliable user facility, in the wavelength range 1.8–17.5  $\mu\text{m}$  [1]. The electron beam is produced by a 30–60 MeV RF linear accelerator, designed and constructed specially for the FEL facility. The undulator is of the planar type with SmCo permanent magnets and 48 periods of  $\lambda_0 = 4$  cm. The deflection parameter can be adjusted from  $K = 0$  to  $K = 2$ . The mirrors of the optical cavity are protected silver coatings on 38 mm diameter silicon substrates, with a radius of curvature of 3 m. The mirrors are separated by 4.8 m, giving a Rayleigh length of  $Z_R = 1.2$  m. The light is partially extracted from the cavity by a ZnSe plate set at  $60^\circ$ , close to the Brewster angle. The use of ZnSe allows operation from  $\lambda = 0.6$  to 18  $\mu\text{m}$ , with an extraction coefficient of 1.5% per face. The Brewster plate extraction creates two exit laser beams, each consisting of two parallel beams. The temporal separation between the two parallel laser pulses is about 50 ps (for ZnSe), which is larger than the laser pulse length (0.5–6 ps). After extraction, the laser beam passes through a telescope and then through a 15 m long transport line. To avoid infrared absorption in the air (by  $\text{H}_2\text{O}$ ,  $\text{CO}_2$ , ...), the infrared transport line may be filled with dry,  $\text{CO}_2$  free, air.

The CLIO optical beam consists of micro-pulses, with an adjustable temporal spacing of 4, 8, 16 or 32 ns. These micro-pulses form macro-pulses of 10  $\mu\text{s}$ , with an adjustable repetition rate between 6.25 Hz and 50 Hz. The

electron micro-pulses are about 10 ps long. However, the laser pulses are not of the same length as the electron bunch; the overlap and length depend on the cavity detuning and on the effect of lethargy [2]. The knowledge of the laser pulse length is essential for the users interested in time resolved studies. Knowledge of pulse length also allows calculation of the peak power.

Measurement of the laser pulse length has been carried out with a Michelson interferometer and a frequency-doubling crystal [3]. This system measures the second order auto-correlation spectrum and further allows calculation of the laser pulse length and an estimate of the pulse coherence length. Wavelength spectra have been taken at same time. The information in both time and frequency allows calculation of the proximity to the Fourier limit.

Using this diagnostic, interest in the production of sub-picosecond laser pulses has lead us to explore operation with “chirped” electron bunches, which might lead to shorter laser pulses [4,5].

### 2. The accelerator

The injector of the linac is a 90 keV thermionic gun, followed by a 0.5 GHz sub-harmonic prebuncher (SHB) and a 3 GHz fundamental buncher (FB). The electron beam, at 3.6 MeV, is then accelerated in a 4.5 m long travelling wave accelerating section, to the nominal energy. The electron energy is presently in the range 32–60 MeV, but it will be extended to 25–70 MeV. Due to the large electron phase extent ( $180^\circ$ ) of the SHB output, the electron bunch has a low energy “tail”, which is filtered in an energy analysing slit. In normal conditions for FEL lasing, the slit width is adjusted to deliver sufficient beam

<sup>\*</sup> Corresponding author. Tel. +33 1 6446 8091, fax +33 1 6446 4148.

current in  $\Delta\gamma/\gamma < 0.7\%$  of FWHM energy spread. Energy selection by the slit also allows a measurement of the energy spectrum and the pulse length of the electron beam [6]. To measure the pulse length, the phase of the accelerator is shifted by a few degrees ( $25\text{--}30^\circ$ ) to produce a chirping of the electron energy along the longitudinal axis of the electron pulse. Therefore, the spectrum obtained with the slit corresponds to the longitudinal electron bunch shape.

### 3. Chirped electron beam experiment

With the goal of producing sub-picosecond laser pulses, the phase between the RF accelerator field and the injector field was shifted by about  $30^\circ$ . This method has also been used for electron bunch length measurements, as explained in Section 2. The phase shift, creates a chirp in the electron energy along the longitudinal axis of the electron pulse. Two methods of producing short laser pulses in this configuration have been explored. In the first “crude” method, the chirped electron bunch is truncated longitudinally when crossing the energy analysing slit, and only a short part is sent to the undulator. This leads to short laser pulses; however, the efficiency is strongly reduced because of the decrease of the electron beam current. In the second method, the energy analysing is left open, and, in principle, the longitudinally chirped electron bunch produces a chirped laser pulse. Using a double-grating time compressor, the laser pulse length can be reduced while still conserving the average power and the full laser efficiency.

The autocorrelation measurements of laser pulse length after the compressor device, however, did not show any time reduction. This negative result was supported by numerical simulations, which have shown that chirping of the electron micro-pulse washes out at saturation, and is not suitable for time compression.

Nevertheless, with the “chirping configuration” for the linac, but without the compressor device, a substantial reduction of laser pulse length has been observed. This result was not understood at this time. A pulse length of 700 fs FWHM has been measured compared to 1 ps for normal (non-dephased) operation of the linac. This result is obtained with a fully opened analysing slit which means that the length reduction is not due to truncation of the electron bunch, as proposed in the “first crude method” explained above.

### 4. Recent measurements

The anomalous laser pulse reduction has been explained during the second set of measurements that have been carried out after modification of the Pulse Forming Network (PFN) of the linac [7]. The modification was undertaken to improve the flatness of the electron current

and to reduce the electron energy fluctuation during the macro-pulse. One consequence is that the central laser wavelength is more stable than before, and the FEL saturates uniformly along the macro-pulse. The auto-correlation measurements now give a minimum laser pulse length of 400 fs (see Section 5). This pulse length depends on cavity length, and can be varied between 6 ps and 400 fs. Also, the “chirping configuration” of the linac no longer influences the laser pulse length, as before. This result has led us to the conclusion that the laser pulse length before PFN modification was abnormally large because of electron beam fluctuations, and that the effect of the “dephased configuration” was only to smooth electron energy fluctuations. The laser wavelength was then more stable during the macro-pulse, and saturation was more uniform along the macro-pulse. The pulse reduction to 700 fs was present with the fully opened analysing slit, because the smoothing effect on the electron beam was independent of the size of the slit [8]. After PFN modification the minimum laser pulse measured is 400 fs for a stable electron beam, and reduction in the “chirping configuration” of the linac is no longer observable.

### 5. Fourier analysis

The main question arising from these measurements, which is still not resolved is that the laser pulse length is more than an order of magnitude shorter than the electron bunch. One hypothesis is that the dispersive effect of the ZnSe intracavity extraction plate induces a filtering of the optical pulse as the laser builds up to saturation. Numerical simulations are now being undertaken to explore this explanation.

Another important question is to know how close the laser is to the Fourier transform limit. The auto-correlation spectra give only partial information on the laser pulse. Wavelength spectra are also needed to estimate the proximity of the optical pulse to the Fourier transform limit, and to exhibit any additional spectral components such as side-bands [2]. The recent measurements of time and wavelength spectras have been carried out at  $\lambda = 9.2 \mu\text{m}$ . Two pairs of spectra are displayed in Figs. 1 and 2. Each pair displays both the auto-correlation (a) and the wavelength (b) associated spectra. Fig. 1 corresponds to a measurement at optimum cavity length, corresponding to the largest average laser power of 380 mW (at 32 ns/25 Hz of repetition rate) and to the shortest laser pulse. The width of the smoothed autocorrelation spectrum (Fig. 1a) is 550 fs FWHM. It is possible to extract the real laser pulse length from the auto-correlation width, but only an assumption of the shape. If we assume that the shape is Gaussian, this value corresponds to a real laser pulse width of  $550/\sqrt{2} = 390$  fs FWHM. The linewidth of the wavelength spectrum (Fig. 1b) is  $\Delta\lambda/\lambda = 5.4\%$  FWHM (for  $\lambda = 9.2 \mu\text{m}$ ). This gives a Fourier coefficient of  $\Delta t \Delta\nu = 0.69 \pm 0.18$ , rather

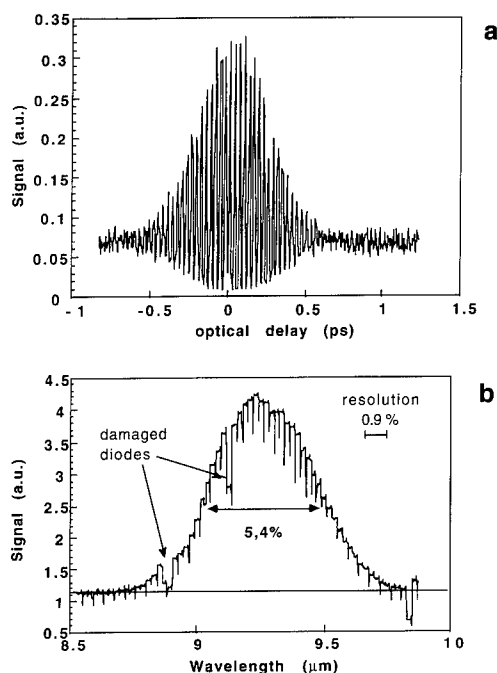


Fig. 1. Auto-correlation (a) and wavelength (b) spectra, at optimum tuning cavity length ( $\Delta L = 0$ ), corresponding to maximum laser power and minimum pulse length.

close to the Fourier coefficient of 0.44 for a Gaussian pulse shape. On the other hand, the interference fringes in Fig. 1a are observable all along the autocorrelation spec-

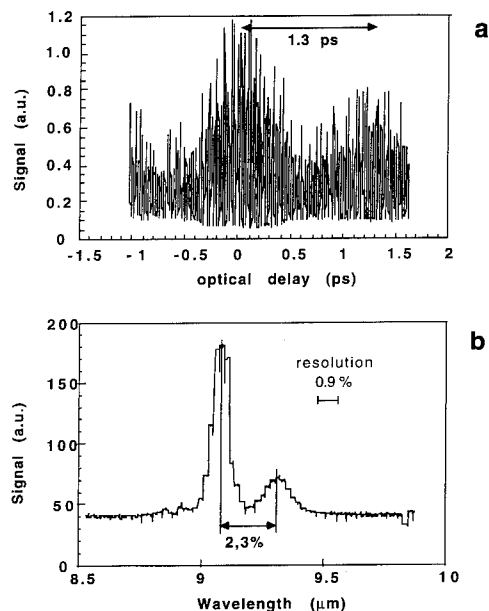


Fig. 2. Auto-correlation (a) and wavelength (b) spectra, at detuned cavity length corresponding to lower laser power, and showing side-bands clearly.

trum, showing that the coherence length is close to the pulse length. These results also indicate that the laser pulse is close to the Fourier limit.

For a detuned operating point of the cavity length, corresponding to lower laser power and longer pulse length, a clear side-band component is observed in the spectrum (Fig. 2b). The distance between the side-band peak and the main peak is  $\Delta\lambda/\lambda = 2.3\%$ , which is close to the theoretical value  $1/N = 2.1\%$  for  $N = 48$  undulator periods. The corresponding auto-correlation spectrum in Fig. 2a shows a modulated time structure which corresponds to the side-band structure in the wavelength spectrum [9]. The modulation period is 1.3 ps, which is close to the theoretical slippage length  $N\lambda/c = 1.5$  ps.

The smallest Fourier coefficient that we have observed experimentally has been obtained with a cavity length shortened by about  $\delta L = 40$  μm, corresponding to the flat region of the detuning curve. The wavelength and auto-correlation spectra lead to a Fourier coefficient of  $\Delta t \Delta \nu = 0.32 \pm 0.14$  which shows that the laser is very close to the Fourier limit.

No side-band components are present in the spectrum that corresponds to the optimum cavity length for largest laser power (Fig. 1). The side-band components evident in Fig. 2, for a detuned cavity length and lower laser power seem to be in contradiction with the fact that side-bands are normally generated when the laser power increases, and therefore are expected at the optimum cavity length. It is our opinion that the lack of side-bands, in our measurements at largest laser power, can be explained by the dispersive effect of the ZnSe intracavity extraction plate. The suppression of side-band components, for optimum cavity length, is also consistent with the short duration of the laser pulse ( $\Delta t = 400$  fs) measured at the optimum cavity length.

Note that the excellent quality of the auto-correlation spectra is due partly to the excellent stability of the FEL. The stability has been enhanced by improving the temperature feedback of the water cooling system. In addition, the auto-correlation spectra quality has been improved by normalizing the auto-correlation signal by the square of a linear signal (proportional to the energy of the laser).

## 6. Conclusion

Our measurements have shown that the CLIO laser pulse length can be continuously adjusted between 400 fs and 6 ps (at  $\lambda = 9.2$  μm), and that the laser is close to the Fourier limit. Taking into account the measurement of the average laser power, the shortest pulse length of 400 fs corresponds to a peak power of about 70 MW.

The acquisition of auto-correlation spectra requires very good stability of the FEL during the scan (5–30 min). This stability has been obtained after improvements of the temperature feedback of the water cooling system, and the



Pulse Forming Network (PFN) of the accelerator. This demonstrates the good reliability of CLIO for users experiments.

The brevity of the laser pulse,  $\Delta t = 400$  fs, relative to the electron pulse length (10 ps), is not fully explained. However, the hypothesis of the dispersive effect of the intra-cavity extraction plate holds some promise. Numerical simulations are now in progress to confirm the hypothesis.

The “chirped electron beam” experiment did not produce shorter laser pulses after the pulse compressor device, because the effect of chirping washes out at saturation. Nevertheless, our studies on these matters are still continuing.

## References

- [1] F. Glotin et al., Proc. 3rd EPAC Conf., Berlin, 1992; J.M. Ortega et al., Nucl. Instr. and Meth. A 311 (1993) 267; R. Prazeres et al., Nucl. Instr. and Meth. B 89 (1994) 54.
- [2] W.B. Colson, Laser Handbook, vol. 6, eds. W.B. Colson, C. Pellegrini and A. Renieri (North-Holland, Amsterdam, 1990).
- [3] E.P. Ippen and C.V. Schank, Ultra-Short Light Pulses, Ed. S.L. Shapiro (Springer, New York, 1977).
- [4] G.T. Moore, Phys. Rev. Lett. 60 (1988) 1825.
- [5] F. Glotin et al., Phys. Rev. Lett. 71 (1994) 2587.
- [6] R. Chaput et al., Nucl. Instr. and Meth. A 311 (1993) 640.
- [7] R. Chaput et al., Proc. 4th EPAC Conf., London, 1994.
- [8] F. Glotin et al., Proc. 4th EPAC Conf., London, 1994.
- [9] D. Jaroszynski et al., Phys. Rev. Lett. 70 (1993) 3412.



ELSEVIER

## Sub-picosecond FEL micropulse length and electron bunch measurements

E.R. Crosson<sup>a,\*</sup>, K.W. Berryman<sup>a</sup>, T.I. Smith<sup>a</sup>, R.L. Swent<sup>a</sup>, H.C. Lihn<sup>b</sup>,  
H. Wiedemann<sup>b</sup>

<sup>a</sup> *Stanford Picosecond FEL Center, W.W. Hansen Experimental Physics Laboratory, Stanford University, Stanford, CA 94305-4085, USA*

<sup>b</sup> *Applied Physics Department and SLAC, Stanford University, Stanford, CA 94309, USA*

### Abstract

Recently, transform limited optical micropulses with lengths of less than 600 fs FWHM have been produced at the Stanford Picosecond Free Electron Laser (FEL) Center. These sub-picosecond FEL optical pulses are important for many types of experiments, especially those investigating fast kinematic processes. In an effort to understand the details of short optical micropulse production, we have made measurements of the electron beam's micropulse structure with sub-picosecond resolution using a newly constructed electron beam diagnostic which uses transition radiation.

### 1. Introduction

From a user's perspective, three valuable characteristics of the Stanford picosecond infrared free electron laser (FEL) are its high peak power, variable sub-picosecond optical micropulse length, and variable transform limited optical bandwidth. Precise control of the FEL optical pulse has been essential for many time-resolved measurements performed at Stanford, particularly photon-echo experiments investigating the dynamics of liquids and glasses and pump-probe experiments studying the vibrational dynamics of proteins [1,2].

In an effort to optimize temporal resolution, a search of electron beam accelerator parameters was performed to minimize the optical micropulse length. The results were FEL micropulses shorter than 600 fs FWHM. This is considerably less than the slippage distance in our wiggler (1.2 ps at 5  $\mu\text{m}$ ). In an effort to understand the physics of creating short optical micropulses in our FEL, we have measured spectral and temporal observables associated with the electron and FEL optical beams as a function of accelerator settings.

### 2. Methods

The center's accelerator is a linac which consists of a 100 keV thermionic gun, 260 MHz subharmonic buncher,

and six superconducting accelerating structures operating at 1300 MHz. Electron beam micropulses are on the order of a few picoseconds in duration at a repetition rate of 11.8 MHz. FEL micropulse data in this paper were obtained with a permanent magnet wiggler with 72 periods and a wiggler wavelength of 3.1 cm. It has operated between 3  $\mu\text{m}$  and 10  $\mu\text{m}$  in wavelength.

To extract temporal information about the electron micropulse we have constructed an electron beam diagnostic which uses transition radiation to measure electron bunch shape with sub-picosecond resolution [3]. Transition radiation can be thought of as a second-order Cherenkov effect produced whenever uniformly moving charges cross the boundary between two media with different dielectric constants. The emitted transition radiation is linearly polarized; the electric vector is in the plane defined by the normal to the interface and the direction of the emitted radiation [4,5]. The opening angle of the cone of radiation is given by  $2/\gamma$ , where  $\gamma$  is the Lorentz factor. The transition radiation intensity for a single, highly relativistic electron is of the order of the fine-structure constant (i.e. one photon per hundred electrons) and is essentially a delta function in time composed of a very broad spectrum of wavelengths. The radiation emitted from an electron bunch is simply the sum of the delta function contribution from each electron. The resulting transition radiation signal is directly proportional to the electron micropulse charge distribution. Frequency components of the radiation pulse which have wavelengths comparable to, or longer than, the electron micropulse have an amplitude which is proportional to the number of electrons in the micropulse. Short wavelength components have a non-vanishing amplitude

\* Corresponding author. Tel. +1 415 723 0789, fax +1 415 725 8311, e-mail crosson@leland.stanford.edu.

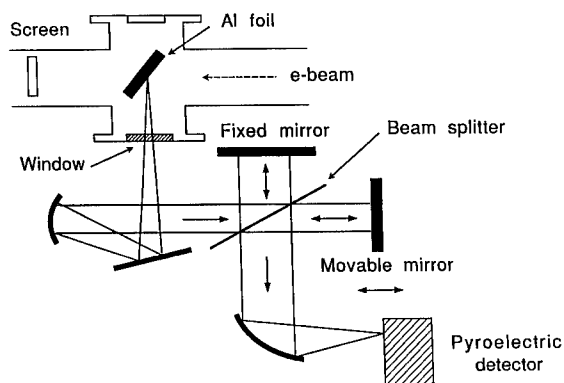


Fig. 1. Experimental set-up for measuring electron beam auto-correlation traces consisting of a thin aluminum foil and a Michelson interferometer with Mylar beam splitter.

only because of shot noise in the beam, and thus have an amplitude proportional to the square root of the number of electrons. The signal power from long wavelength components ( $\sim 100 \mu\text{m}$  and longer for 1 ps microbunches) is quadratic in the electron beam current.

A diagram of the electron beam temporal measuring device is shown in Fig. 1. In this device, located after the last accelerating structure, the relativistic electron beam strikes a thin ( $25.4 \mu\text{m}$ ) aluminum foil at an angle of incidence of  $45^\circ$ . The transition radiation produced exits the vacuum system through a 1 mm thick, high density polyethylene window. The radiation is then collimated and sent through a Michelson interferometer using a Mylar beam-splitter and a Moletron P1-series pyroelectric detector with a 5 mm diameter area. The delay mirror in the interferometer is moved using an optically encoded servomotor with a travel resolution of less than  $1 \mu\text{m}$ . The data acquisition is fully automated and a scan takes approximately 3 min depending on the resolution desired.

The thickness of the Mylar beam splitter has a direct effect on the sensitivity and bandwidth of the autocorrelator. The strength of the signal from a given frequency component is proportional to  $\sin^2(2kt)$ , where  $k = 2\pi n/\lambda$ ,  $\lambda$  is the free space wavelength,  $n$  is the index of refraction of the foil, and  $t$  is the foil thickness. Thus sensitivity to long wavelength components favors thick foils, while high resolution favors thin foils. By trying various foil thicknesses, we found that  $51 \mu\text{m}$  was near optimum for our electron beam lengths.

To determine the longitudinal energy/phase space distribution of the electron beam, a systematic set of measurements of the electron-beam energy spectra were made by dephasing the RF of the last accelerating structure relative to the electron bunch. Measurements were made over a  $60^\circ$  range with a step size of  $4^\circ$ . The electron spectrometer used in these measurements was located downstream of the last accelerating cavity. The energy of the beam enter-

ing the last accelerating structure was approximately 30 MeV.

The FEL optical pulse lengths were determined by standard crossed-beam second harmonic generation auto-correlation technique using a  $500 \mu\text{m}$  thick  $\text{AgSe}_2$  crystal.

### 3. Results and discussion

In this investigation, we measured and analyzed a large set of electron auto-correlation, electron energy spectrum, and optical autocorrelation data taken as a function of electron accelerator parameters. Temporal information about the electron micropulse was extracted from electron auto-correlation data by comparing experimental data with curves calculated from various trial charge distributions and include the effects of the Mylar beam splitter,  $\text{H}_2\text{O}$  and  $\text{N}_2$  absorption, and detector cut-off [6]. Because we are unable to accurately measure the detector spectral response at wavelengths longer than  $500 \mu\text{m}$ , we have included this effect in the calculations by modeling our detector's long wavelength cut-off using a Fermi function with parameters giving a spectral response consistent with information provided by the manufacturer. The parameters of the Fermi function were then varied by 10% with no substantial changes in the calculated autocorrelation results.

In an effort to verify that the data contained no artifacts, several aspects of the auto-correlation device were experimentally investigated. These included testing the sensitivity of results to electron beam and optical alignment, the effect of different thicknesses of polyethylene window, and the effect of apertures at various places along the optical transport system. Except for changes in the overall magnitude, data are relatively unchanged.

Additional temporal information about the electron beam was extracted from electron energy data by measuring the energy spectrum of the electron beam as a function of the phase of the last accelerating structure. This data was analyzed using tomographic techniques [7] to reconstruct the phase space distribution assuming an electron energy dependence of  $E(\varphi) = E_0 + E_{\text{acc}} \cos(\varphi)$ , where  $E_0$  is the energy of an electron entering the last accelerating structure,  $E_{\text{acc}}$  is the peak energy contribution from the last accelerating structure, and  $\varphi$  is the phase between the crest of the RF wave and an electron. Temporal information about the beam was obtained from the phase space distribution by taking the one dimensional projection along the time axis. Preliminary analysis of these data suggest a temporal resolution of  $\sim 1$  ps.

Electron beam auto-correlation traces for three settings of the pre-accelerator phase (second of the six accelerating structures), denoted (a), (b), and (c), are shown in Fig. 2. Figs. (b) and (c) correspond to changes in pre-accelerator phase (with respect to figure (a)) of  $\sim 2^\circ$  and  $\sim 4^\circ$ . Fig. 3 is the calculated electron micropulse distributions, (a), (b),

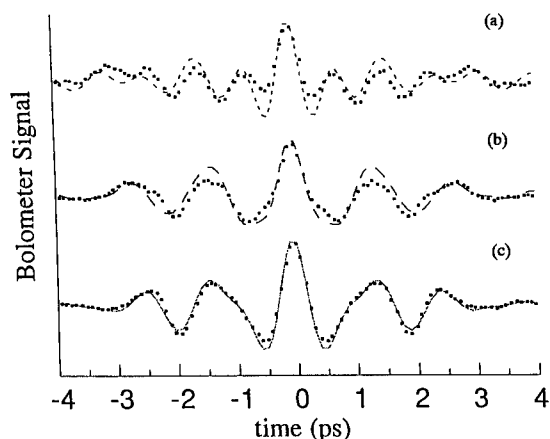


Fig. 2. Electron beam auto-correlation data and calculations (solid lines) as functions of three electron beam accelerator settings.

and (c), extracted from these electron beam auto-correlation data. Contrary to our expectations, these results indicate the presence of three charge bunches within a single RF cycle. Temporal projections of the longitudinal energy/phase space distribution for a single accelerator setting (different from those above) as are shown in Fig. 4. The consistency of this data with the curves of figure 3 confirms the three bunch diagnosis.

The dependence of the electron bunch shape on the pre-accelerator phase shown in Fig. 3 confirms empirical observations made over the years. The pre-accelerator amplitude and phase is generally set so that it provides around 3 MeV to the electron bunch, but at some 30–40° from the maximum. The electron bunch exits the pre-accelerator at approximately 5 MeV. There is thus a substantial energy-phase correlation within the bunch which provides significant velocity modulated bunching in the ~ 6 m drift region before the next accelerating structure.

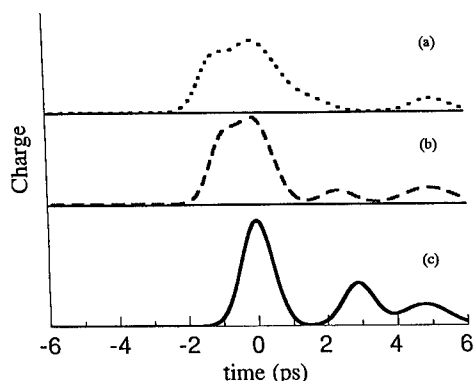


Fig. 3. Calculated electron micropulse distributions extracted from electron auto correlation corresponding to three electron beam accelerator settings.

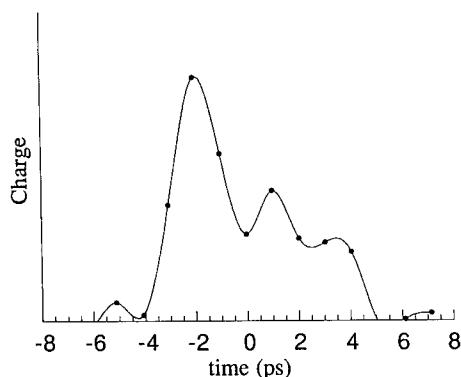


Fig. 4. Calculated electron micropulse distribution extracted from spectral data corresponding to a single electron beam accelerator settings. The solid line is a spline fit to the results.

Clearly, changing the pre-accelerator phase changes the energy–phase correlation, and thus the degree of bunching.

The optical autocorrelation traces corresponding to the same pre-accelerator settings as in Fig. 3 are shown in Fig. 5. Comparing the two figures allows the effect of different electron bunch structures on the optical pulse to be seen. Each charge bunch will interact with the optical field in the wiggler as it passes through, and if the bunches are less than a slippage length apart, the field from one bunch can interact with a different bunch. If the temporal separation between bunches is large enough that they don't interact, then any charge in a bunch which is insufficient for lasing is essentially wasted. If the bunches do interact, then their relative timing and energy centroids can be expected to have a significant impact on the FEL's behavior.

#### 4. Conclusions

We have found that the auto-correlation device described here provides high resolution temporal information about the electron beam micropulse. Simultaneous mea-

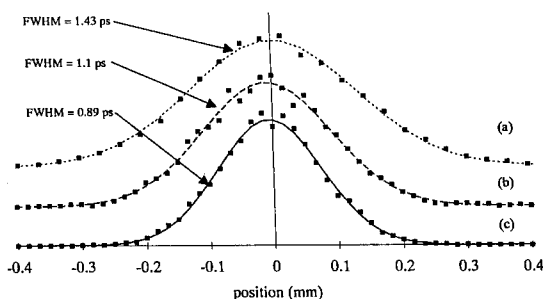


Fig. 5. FEL optical auto-correlation data and fits to Gaussian distributions (solid lines) corresponding to three electron beam accelerator settings.

surements of electron and optical autocorrelations have helped us gain insight into electron beam micropulse structure and corresponding FEL optical micropulse length. We hope to continue to refine this measurement technique and to understand the relationship between electron beam structure and FEL micropulse length, with the objective of applying this to the production of tailored optical micropulses.

### Acknowledgements

The work described here was supported in part by the Office of Naval Research, Contracts No. N00014-91-C-0170.

### References

- [1] D. Zimdars et al., Phys. Rev. Lett. 70 (1993) 2718.
- [2] J.R. Hill, A. Tokmakoff, K.A. Peterson, B. Sauter, D. Zimdars, D.D. Dlott and M.D. Fayer, J. Phys. Chem. 98 (1994) 11213.
- [3] P. Kung, H.T. Lihn, H. Wiedemann and D. Bocek, Phys. Rev. Lett. 73 (1994) 967.
- [4] I. Frank, V. Ginzburg, J. Phys. (Moscow) 9 (1945) 353.
- [5] L. Wartski, S. Roland, J. Lasalle, M. Bolore and G. Filippi, J. Appl. Phys. 46 (1975) 3644.
- [6] D.E. Burch, J. Opt. Soc. Am 58 (1968) 1383.
- [7] J. Radon, Berichte Sachsische Akademie Der Wissenschaften, Leipzig, Math. Phys. K1 69 (1917) 262;  
S.R. Deans, The Radon Transform and Some of its Applications (Wiley, New York, 1983).



ELSEVIER

## Observation and characterization of frequency-chirped optical pulses on the Mark III free-electron laser

Eric B. Szarmes<sup>a,\*</sup>, Angus D. Madden<sup>b</sup>, John M.J. Madey<sup>a</sup>

<sup>a</sup> *FEL Laboratory, Department of Physics, Duke University, Durham, NC, USA*

<sup>b</sup> *Department of Physics, UC Davis, Davis, CA, USA*

### Abstract

In an experimental program to develop and operate a chirped-pulse free-electron laser at Duke University, we have accelerated  $\sim 2$  ps electron bunches in the Mark III rf linac with an offset of  $17^\circ$  from the phase that minimizes the energy spread, and have observed (via optical autocorrelation measurements) compression of the energy-chirped electron bunches in the dispersive elements of the transport system by an amount consistent with theoretical predictions. The resulting 1.0 ps optical pulses from the laser exhibited a spectral width at  $3.2 \mu\text{m}$  equal to 3.6 times the transform limit, and were over-compressed by a factor of 2.7 in a dispersive delay line comprised of four sapphire, Brewster angle prisms. The measured time-bandwidth product and the observed over-compression both indicated a minimum compressed pulse width of approximately 150 fs. We present a detailed description of the experimental methods and results.

Previous theoretical and numerical studies of rf linac free-electron lasers (FELs) have indicated the feasibility of using energy-chirped electron bunches to drive the oscillation of frequency-chirped optical pulses that are susceptible to compression in an external dispersive delay line [1–5]. Electron bunches with the appropriate time–energy correlation are most conveniently produced in the linac by accelerating the bunches on a high-gradient phase of the rf wave, and were originally proposed as an analog of the tapered-wiggler FEL to increase the extraction efficiency of the laser [1,2]. However, the chirped-pulse FEL can in principle produce extremely broad band optical pulses with even relatively modest energy chirps, and for this reason considerable interest has developed at several laboratories for the potential applications to time-resolved spectroscopy. The first reported experiments on energy chirping were performed by the Collaboration for an Infrared Laser at Orsay (CLIO) at  $8.5 \mu\text{m}$  [6]. However, the optical pulses from that laser were transform-limited and were not susceptible to compression.

In this paper, we report the first operation of a chirped-pulse FEL leading to the production of frequency-chirped optical pulses, and the subsequent over-compression of those pulses in an external dispersive delay line. In the experiment,  $\sim 2$  ps electron bunches were accelerated in the Mark III FEL [7] with an offset of  $17^\circ$  from the phase

that minimizes the energy spread, leading to the production of saturated, tophat optical pulses from the laser with a duration of 1.0 ps and a spectral width at  $3.2 \mu\text{m}$  equal to 3.6 times the transform limit. These optical pulses were over-compressed by a factor of 2.7 in a dispersive delay line comprised of four sapphire, Brewster angle prisms whose design has been previously described in the literature [4]. The measured time-bandwidth product and the observed over-compression both indicated a minimum compressed pulse width of approximately 150 fs, with projected peak powers greater than 15 MW (although these were not measured directly).

The Mark III FEL uses a microwave gun and an rf linac driven by the same 2.86 GHz rf source, with a calibrated phase shifter between the gun and linac to adjust the injection phase of the electron bunches. A dispersive chicane in the transport system is used to bend the electron bunches around the resonator mirror and into the laser, and a spectrometer magnet is located between the linac and chicane. The optical cavity is comprised of metal cavity mirrors, with the output coupling in the present experiments provided by a 2.0 mm thick barium fluoride Brewster plate at  $64^\circ$  incidence.

The experiment was performed in four steps in order to benchmark the results. First, the electron bunches were injected into the linac with the phase adjusted for minimum energy spread on the spectrometer magnet, in order to establish the reference phase prior to dephasing the linac. This led to the production of transform-limited optical pulses in the laser which were used to estimate (via

\* Corresponding author.

optical autocorrelation) the duration of the electron pulses from the linac. Second, the phase of the rf linac with respect to the injected electron bunches was shifted by  $17^\circ$  to yield higher energies at the trailing edge of the bunches. This sign of the energy chirp leads to a compression in the chicane and a higher peak current in the laser. Direct autocorrelation measurements on the resulting chirped optical pulses were used at this stage to estimate the duration of the compressed electron pulses, so that the observed compression could be correlated with the phase offset in the linac. Third, spectral measurements on the chirped optical pulses were performed in order to calculate the time-bandwidth product, which was used to estimate the factor by which the pulses would be compressed in the pulse compressor, as well as the dispersion required to achieve the minimum pulse width. Fourth and finally, the chirped pulses were propagated through the pulse compressor, and the resulting pulse duration measured with the autocorrelator.

The experiment was performed at a nominal electron energy of 43.6 MeV for the unchirped electron pulses. The electron macropulse had a duration of 3.3  $\mu\text{s}$  and an average current of 190 mA, yielding an unchirped optical macropulse of roughly 2  $\mu\text{s}$  and a macropulse energy of 19 mJ. After the linac was dephased by  $17^\circ$  and the downstream optics re-adjusted to optimize the laser, the macropulse energy had dropped to 14 mJ, but the optical macropulse also turned on sooner than in the unchirped case. This suggests an increase in the small signal gain, presumably from an enhanced peak current due to electron pulse compression in the chicane, as previously observed in rf linac FELs [8]. The pulse-to-pulse stability of the chirped laser was better than  $\pm 10\%$ .

The results of the spectral and temporal measurements, excluding the final dispersive pulse propagation, are summarized in Fig. 1. Figs. 1a and 1b show the instantaneous optical spectrum and the optical autocorrelation trace of the unchirped optical pulses, and Figs. 1c and 1d show the instantaneous spectrum and autocorrelation trace of the chirped laser operating with a phase offset of  $17^\circ$ . In the former case, the FWHM spectral width is 0.48%, and the pulse duration is 2.2 ps for the tophat pulse shape indicated by the triangular autocorrelation trace. The resulting time-bandwidth product of 1.0 is only slightly larger than the transform limited product of 0.89 for a tophat pulse, so the linac phasing was essentially optimized for zero energy chirp. For the chirped laser, we observe both a shift and a broadening of the instantaneous optical spectrum in Fig. 1c. The broadening is substantial ( $\Delta\lambda/\lambda \sim 3.4\%$ ), and the wavelength shift resulting from the change in the phase of the rf wave (and thus the electron energy) indicates that the phase of minimum energy spread was located not at the peak of the wave, but at a phase offset of  $-6^\circ$  (with the bunch on the trailing edge.) A phase shift of  $17^\circ$  then advances the phase of the bunch to  $+11^\circ$  on the leading edge, and so the electron distribution remains near the

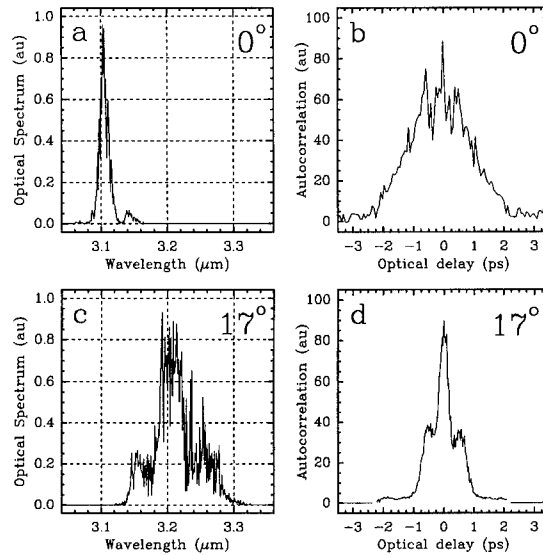


Fig. 1. (a) Instantaneous optical spectrum of a transform-limited optical pulse and (b) corresponding optical autocorrelation indicating a tophat profile with sideband modulations, with negligible energy chirp on the electron bunches. The TTL (times-transform-limit) is 1.1. (c) Instantaneous optical spectrum of a frequency-chirped optical pulse and (d) corresponding optical autocorrelation showing enhanced sideband modulations, for electron bunches with a phase offset of  $17^\circ$  in the rf linac. The TTL is 3.6.

peak of the wave. The inferred phase of minimum energy spread is consistent with direct spectrometer measurements of the energy and energy spread versus phase.

The autocorrelation trace for the chirped laser in Fig. 1d indicates an optical pulse with an enhanced sideband structure and a duration of 1.0 ps (assuming a tophat profile.) This compression of the optical pulse upon chirping the laser (even without transmission through the pulse compressor) is consistent with the compression of the chirped electron pulses in the chicane preceding the laser. If we assume that a change in the optical pulse duration indicates the same change in the electron pulses, then a net phase offset of  $\psi = 17^\circ$  on a  $\tau_p = 2.2$  ps electron pulse induces an energy spread given by

$$\left(\frac{\Delta\gamma}{\gamma}\right)_{\tau_p} = \tau_p \omega_{rf} \tan \psi = 1.2\%. \quad (1)$$

For a dispersion of 0.96 ps per % energy spread in the Mark III chicane, the electron compression is then 1.2 ps, which is indeed consistent with the observed narrowing of 1.2 ps in the optical pulses. It is possible that the phase offset itself can induce intrinsic changes in the electron bunch length in the first few cells of the linac, but this is less likely for electron bunches that remain near the peak of the rf wave (as is the case in the present experiment). We further note that for a chirped electron pulse of  $\sim 1$  ps and an optical slippage at 3.2  $\mu\text{m}$  of 0.5 ps ( $N_w = 47$

periods), the change in resonance parameter within one slippage length is less than the gain bandwidth, given the above energy chirp. Therefore, the gain reduction due to chirping is essentially negligible in this case [9].

The chirped optical pulse indicated in Figs. 1c and 1d has a spectral width equal to 3.6 times the transform limit for a tophat pulse. The spectral width itself is more than a factor of 2 greater than the estimated energy chirp of 1.2%, and is greater than a simple application of the resonance condition would predict. The spectral width and optical autocorrelation can be used to estimate the optimum compression ratio of the pulses and the dispersion required in the delay line according to previously published expressions [4]. If we assume that the spectral width is due entirely to chirp, then the estimated compressed pulse width is 150 fs, and should be obtainable with a prism separation of 2.2 cm for the double pass delay line used in the experiments. Unfortunately, the compressor was designed for a linac configuration [4] providing longer pulses with substantially less chirp than we achieved in the present experiments, and the optimum prism separation could not be realized; the present experiment actually used a prism separation of 9.1 cm, and the results of the pulse propagation are shown in Fig. 2. We see that the 1.0 ps optical pulse actually broadened to 2.7 ps while preserving the modulated substructure. Therefore, given the estimated optimum prism separation, an over-compression is suggested. In fact, if the input pulse were not chirped at all, then a prism separation of 0.9 m would have been required to produce the observed pulse broadening!

The dispersive pulse propagation is most easily analyzed using the space–time analogy with diffracting optical beams, and is illustrated in Fig. 3. If the dispersion is proportional to the prism separation (as in the present experiment) then similar triangles on the observed over-compression indicate an optimum prism separation of 2.5 cm, which is very close to the initial estimate. The analogy also provides an expression relating the pulse width  $\Delta\tau_p$  in the far field and the transform-limited (compressed) pulse

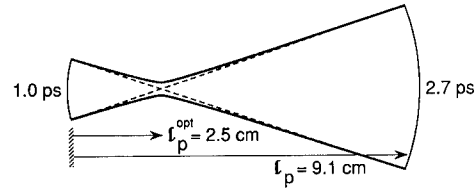


Fig. 3. Space–time analogy for the dispersive pulse propagation of Fig. 2. The indicated optimum prism separation is 2.5 cm, with a compressed pulse width of 155 fs. The measured time–bandwidth product on the uncompressed pulse indicates an optimum separation of 2.2 cm and a compressed pulse width of 150 fs.

width  $\Delta\tau_c$  in terms of the dispersion  $\phi'' = \partial^2\phi/\partial\omega^2$  in the delay line:

$$\Delta\tau_p\Delta\tau_c = 2\pi\phi''\kappa, \quad (2)$$

where  $\kappa$  is the Fourier product for the transform-limited pulse. From the expression for  $\phi''$  given in Ref. [4], we calculate a compressed pulse width of 155 fs, which is again very close to the initial estimate.

The demonstrated pulse broadening immediately suggests that the FEL can be used to produce broadband optical pulses that are susceptible to severe pulse shaping. The main assumption in the projection to optimum compression is that the bandwidth was due primarily to a uniform frequency chirp, and this, of course, may not be the case. The optical pulses did show evidence of sideband modulation and were not extremely long to begin with (only 1 ps). However, the observed bandwidth was considerably greater than both the sideband shift and the transform limit of the pulse, suggesting that substantial chirping was present. In Fig. 2b, we see that the intensity spikes not only broadened individually, but also increased in separation from one another by the same factor by which the entire pulse broadened, while maintaining essentially the same depth of modulation. These observations indicate that the spikes experienced a temporal delay with respect to each other, indicating a uniform frequency chirp throughout the pulse. We note that successful chirping requires that the electron pulses be much greater than the slippage length, so that end effects or super-radiant saturation do not distort the pulse [9]. In the present experiment, the electron pulses were a factor of 2 times longer than the slippage length, and so the frequency chirp induced in the optical pulses should have remained correlated with the electron energy chirp.

### Acknowledgements

The authors wish to thank Jim Widgren for operating the Mark III linac during these experiments. One of us (E.B.S.) would also like to gratefully acknowledge helpful discussions with Foorood Amirmadhl. This work was supported by the Army Research Office under Contract

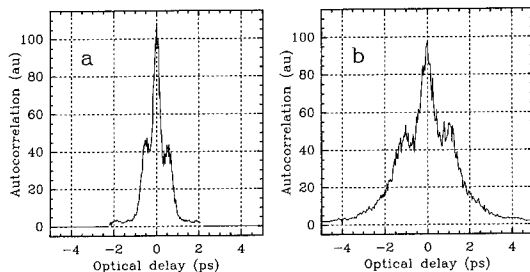


Fig. 2. (a) The optical autocorrelation from Fig. 1d, prior to propagation of the pulse through the dispersive delay line. The pulse duration is 1.0 ps. (b) Optical autocorrelation on the same pulse after propagation through the dispersive delay line. The pulse duration is 2.7 ps.



DAAL03-88-0109 and by the Office of Naval Research under Contract N00014-91-C-0226.

## References

- [1] G.T. Moore, Nucl. Instr. and Meth. A 272 (1988) 302.
- [2] G.T. Moore, Phys. Rev. Lett. 60 (1988) 1825.
- [3] E.B. Szarmes, S.V. Benson and J.M.J. Madey, Nucl. Instr. and Meth. A 296 (1990) 755.
- [4] E.B. Szarmes and J.M.J. Madey, Nucl. Instr. and Meth. A 318 (1992) 914.
- [5] G.T. Moore and J.C. Goldstein, Nucl. Instr. and Meth. A 285 (1989) 176.
- [6] F. Glotin, R. Chaput, D. Jaroszynski, R. Prazeres and J.-M. Ortega, Phys. Rev. Lett. 71 (1993) 2587.
- [7] S.V. Benson, J. Schultz, B.A. Hooper, R. Crane and J.M.J. Madey, Nucl. Instr. and Meth. A 272 (1987) 22; S.V. Benson, W.S. Fann, B.A. Hooper, J.M.J. Madey, E.B. Szarmes, B. Richman and L. Vintro, Nucl. Instr. and Meth. A 296 (1990) 110.
- [8] C.A.J. van der Geer et al., Nucl. Instr. and Meth. A 334 (1993) 607.
- [9] E.B. Szarmes, Ph.D. dissertation, Stanford University (1992).

## Two-colour operation of the free-electron laser using a step-tapered undulator

D.A. Jaroszynski<sup>\*</sup>, R. Prazeres, F. Glotin, J.M. Ortega

*LURE, Bât 209d, Centre Universitaire Paris-Sud, 91405 Orsay Cedex, France*

### Abstract

Two-colour operation of the CLIO free electron laser (FEL) has been demonstrated experimentally. Using a step-tapered undulator which produces two independently tunable resonances we have obtained two-colour FEL operation with a frequency difference over a range of  $\pm 20\%$ . We show that the range is currently limited by the influence of optical dispersion in the dielectric output coupler. We present first order autocorrelation measurements that show 100% modulation due to beating of the two colours over the range of the spectrum. We present power measurements that show that “optical klystron” type of interference effects influence the small signal gain.

The step-tapered undulator of CLIO is a conventional “Halbach” design consisting of two identical independently adjustable planar sections, sequentially arranged such that the deflection strength  $K$  changes in an abrupt step  $\Delta K$ , from  $K_1$  and  $K_2$ , the upstream and downstream undulator deflection parameters respectively [1]. Each undulator section has  $N_u = 24$  periods with a wavelength,  $\lambda_u$  of 4 cm giving a total of 48 periods. The range of operation of the FEL spans the wavelength range 2 to 17  $\mu\text{m}$  and forms part of a user facility serving the needs of a large and varied user community requiring intense subpicosecond [2] to picosecond [3] optical radiation. The FEL [3] is driven by short (10 ps) electron pulses, with 0.7–0.9 nC charge, derived from a 30–60 MeV, S-band, linac. CLIO has a 4.8 m long, nearly concentric, optical cavity with a Rayleigh range of 1.2 m and the optical radiation is coupled out of the cavity using a near Brewster’s angle ZnSe dielectric plate that is slightly dispersive and influences the cavity detuning curves. The output coupling fraction is 6–10% over the operating wavelength range of the FEL. Mirror diffraction and absorption losses give an additional 3% loss at the shorter wavelength end of operation, rising above 5% at wavelengths longer than 12  $\mu\text{m}$  [3]. Because the step-tapered undulator gives rise to two resonances,  $\lambda_1 = \lambda_u(1 + K_1^2)/2\gamma^2$  and  $\lambda_2 = \lambda_u(1 + K_2^2)/2\gamma^2$ , with  $\gamma mc^2$  the electron beam energy, the laser will oscillate at two wavelengths simultaneously when the small signal gain for each section is above threshold for

oscillation. The gain per pass of CLIO is in the range of 100–600% per roundtrip pass [3] and therefore the FEL will oscillate to saturation with one undulator section, i.e., 24 periods only. The high gain of CLIO is the main factor making two-colour operation of the FEL feasible [4]. Two-colour operation has been observed presently over a wide range of wavelengths with well separated wavelengths for two electron energies, 40 MeV and 50 MeV respectively. However, we expect two-colour operation not to depend on the electron energy.

To study two-colour operation of the FEL we have measured optical spectra of the output radiation over a range covering the two resonance wavelengths for a variety of  $\Delta K$  values, with  $|\Delta K| < 0.2$ . For large  $\Delta K$  values the optical spectra are distinct and smooth. An example is shown in Fig. 1 where we show the development of the macropulse spectrum with time for  $K_1 = 1.23$  and  $K_2 = 1.36$  respectively. The wavelength difference,  $\Delta\lambda \approx 0.8 \mu\text{m}$ , is slightly larger than that predicted analytically using the  $\Delta K$ . This is due to the slight shift in the mean energy of the electrons entering the second undulator section after losing energy to the optical field associated with  $\lambda_1$ . In Fig. 1 the dotted line represents the laser wavelength of  $\lambda_2$  when laser action is killed at  $\lambda_1$ . The 0.15  $\mu\text{m}$  difference in wavelength between  $\lambda_2$  with and without laser action at  $\lambda_1$  is consistent with laser action at  $\lambda_1$  causing a reduction of the mean energy of  $\Delta\gamma/\gamma \approx 1/4N_u$ , i.e.,  $(\lambda'_2 - \lambda_2)/\lambda_2 = 2\Delta\gamma/\gamma = 1/2N_u$  at saturation. The shifting of the mean energy of electrons arriving in the second undulator section can also cause reductions in the gain experienced at  $\lambda_2$  because of the shift of the electron energy and therefore the resonance wavelength.

<sup>\*</sup> E-mail dino@lure.u-psud.fr.

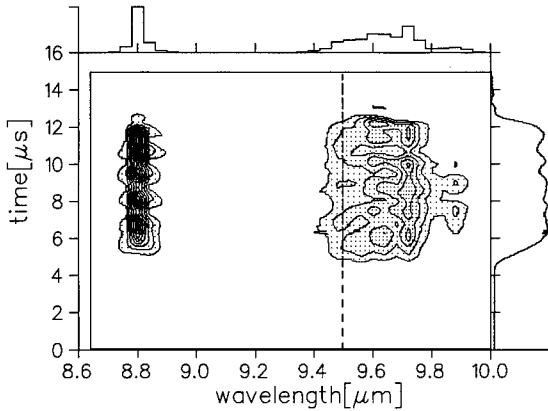


Fig. 1. Contour plot of measurements of the temporal evolution of spectra at 40 MeV.  $K_1 = 1.23$  and  $K_2 = 1.36$  giving  $\Delta\lambda = 0.8$   $\mu\text{m}$  and peak powers of 3.3 MW and 7.6 MW respectively. The dotted line represents the centroid of  $\lambda_2$  for sole operation at  $\lambda_2$ . The integrated spectrum is shown on the right-hand side of the plot.

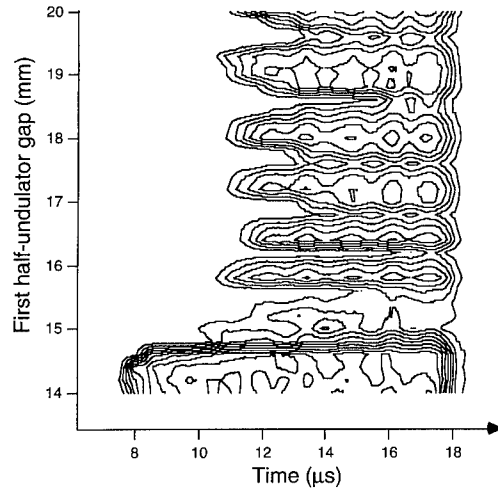


Fig. 2. Optical macropulse temporal evolution measured while varying the upstream undulator gap while keeping the downstream gap fixed at 14 mm. The contour plot shows interference effects in the gain manifesting itself as a delayed saturation.

This, however, remains a small effect as the laser wavelength tracks the resonance energy for slow changes in energy and therefore remains at optimum gain.

We have also observed competition between laser action at  $\lambda_1$  and that at  $\lambda_2$  in the form of quenching or inhibition, depending on  $\Delta K$  and the relative powers at the two wavelengths [4]. At low power, “optical klystron” type of interference effects in the gain [5–7], which depend on the detailed phase changes of the electrons in the two sections, and  $\Delta K$ , occur. The gain can be depressed or enhanced at both or either  $\lambda_1$  or  $\lambda_2$ . The interference effects are largest for small  $\Delta K$  values where the individual gain spectra for the two resonances overlap. This has the effect of delaying saturation as is clearly seen in Fig. 2 which shows measurements of the optical macropulse evolving in time as a function of the gap of the first undulator section while keeping the second undulator gap fixed. The cavity length was also fixed in the measurements. The separation between the minima, where the gain is depressed, correspond to a  $\pi$  change in the phase of the electrons as they pass down the undulator due the step in the phase velocity [7].

In addition to shifts in the wavelength  $\lambda_2$  due to energy shifts there is also an increase in the energy spread of electrons entering the second undulator section due to laser action in the first undulator section. Laser action at  $\lambda_1$  induces an energy spread equal to the height of the potential well which itself is proportional to the square root of the electrical field strength. This is of the order of  $\sigma_\gamma/\gamma \approx 1/N_{u1}$  for CLIO at the onset of saturation. The small signal gain for  $\lambda_2$  is reduced by a factor of  $1/(1 + 4N_{u2}^2(2\sigma_\gamma/\gamma)^2)$  leading to a reduction of two in the gain when the optical field at  $\lambda_1$  begins to saturate. We explic-

itly denote the number of periods for the upstream and downstream undulators is  $N_{u1} = 24$  and  $N_{u2} = 24$  respectively. The optical field at  $\lambda_2$  can be completely quenched when the gain falls below the losses. However, it is possible to control the saturation intensity at  $\lambda_1$  by adjusting the optical cavity length slightly and therefore control the induced energy spread.

The largest  $\Delta\lambda$  where simultaneous two-colour FEL operation currently occurs is 20%. The limit is due to the influence of dispersion in the optical cavity which sets two different synchronism lengths for the cavity. The range of cavity length detunings,  $\delta L$ , where there is synchronism is dependent on gain, lethargy, slippage and the electron pulse duration. Fig. 3 shows a typical measured detuning curve for two colour operation with  $\lambda_1 = 8.1$   $\mu\text{m}$  and

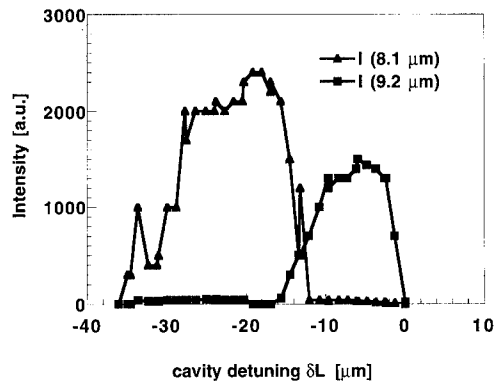


Fig. 3. Measured cavity length detuning curve of the two-colour FEL.

$\lambda_2 = 9.2 \mu\text{m}$ . The curves for  $\lambda_1$  and  $\lambda_2$  were measured separately using a monochromator to discriminate against the other wavelength. As a result of dispersion the detuning curves for  $\lambda_1$  and  $\lambda_2$  only overlap slightly and, in this range it is possible to adjust the relative powers at  $\lambda_1$  and  $\lambda_2$  by adjusting  $\delta L$  and therefore control the influence of heating of the electron beam due to laser action at  $\lambda_1$ . The power at either of the two wavelengths is comparable with that obtainable for  $\Delta K = 0$ . There does not seem to be a large sacrifice in the efficiency of the laser when operating on two-colours simultaneously. To increase the largest wavelength separation a non-dispersive optical cavity should be used. Currently hole output coupling is being installed on CLIO to reduce the dispersion. However, even when there is no dispersion in the optical cavity it is still possible to adjust the relative powers at  $\lambda_1$  and  $\lambda_2$  by adjusting the position and size of the electron beam focal spot in the undulators.

The total energy of the optical micropulses at both wavelengths is comparable with that obtained for monochrome FEL lasing with  $\Delta K = 0$ . We calculate peak output powers of the order of 5–10 MW at each of the wavelengths. For the purposes of the calculation we have assumed an optical pulse length of 3 ps. It should be noted that a higher efficiency consistent with the shorter undulator,  $N_u = 24$ , is expected. However, as the gain for one undulator is lower than for the full length undulator with  $2N_u = 48$  periods it is not possible to obtain laser action to saturation within the electron macropulse duration at small cavity desynchronisms where the efficiency is maximum. The cavity desynchronism is set for optimum small signal gain rather than high power and high efficiency, for two colour operation, to obtain saturation before the end of the electron macropulse. Also, it should be noted that when  $\Delta K$  is small and positive the FEL operates on a single wavelength with an efficiency enhanced over that for a uniform undulator [8,9].

To try and determine the relative temporal and spectral properties of the optical pulse from the two-colour FEL we have carried out first order autocorrelation measurements using a Michelson interferometer. Fig. 4 shows a measured autocorrelation interference pattern that clearly shows the beat pattern with close to 100% modulation, implying that the two colours have similar temporal durations and that the frequency is stable during the 3 ps long optical pulses.

Experiments are also under way using second order autocorrelation and cross correlation techniques to establish whether the two colours are really simultaneous or whether laser action at each of the two wavelengths is constrained to different parts of the electron micropulse. From our numerical simulations it appears that the two colours overlap partially, although we have not included the dispersive dielectric output coupler in the simulations. Measurements of the first order autocorrelation spectrum for  $\lambda_1 = 8.3 \mu\text{m}$  and  $\lambda_2 = 7.9 \mu\text{m}$  using a Michelson interferometer show that the duration of the optical mi-

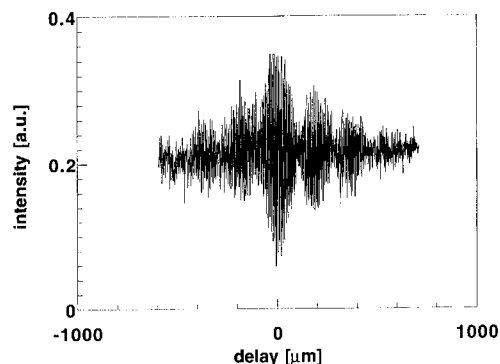


Fig. 4. Measured first-order autocorrelation spectrum of output optical pulse from the two-colour FEL.

cropulses at the respective wavelengths is more or less the same, evident from beats in the interference pattern of Fig. 4. We are also examining in detail, experimentally, the influence of the dispersive dielectric output coupler. In the first instance we will check whether two-colour operation still occurs with hole output coupling.

In conclusion, we have shown that two-colour FEL operation is possible with a simple undulator structure and a single electron source and single optical cavity. Two colours produced in this way have the advantage that they are naturally synchronised with each other and are therefore useful in carrying out time resolved two-colour pump-probe experiments. Two-colour operation has already been used to measure recombination processes in semi-conductors. The two-colour operation of the FEL is likely to greatly enhance its capabilities as a tool. Pump-probe experiments can now be done with an independent choice of the pump and probe wavelengths. Also, various non-linear frequency mixing experiments can be considered to further extend the wavelength to longer wavelengths. Such experiments will be performed in the near future on CLIO. Other applications that may be possible are plasma-beam accelerators, selective two-colour multi-level pumping in atomic, molecular or solid state systems, the study of atomic Rydberg states, etc. Cross polarised undulators, where the first undulator magnetic field is perpendicular to the second, would generate two differently polarised colours that are easily separated using a polariser. The possibility of a polychrome FEL is also of interest.

## References

- [1] P. Bourgeois et al., Nucl. Instr. and Meth. A 304 (1991) 150.
- [2] F. Glotin et al., Phys. Rev. Lett. 71 (1993) 2587.
- [3] R. Prazeres et al., Nucl. Instr. and Meth. A 311 (1993) 15.

- [4] D. Jaroszynski, R. Prazeres, F. Glotin and J. Ortega, *Phys. Rev. Lett.* 72 (1994) 2387.
- [5] C. Pidgeon et al., *Nucl. Instr. and Meth. A* 259 (1987) 31.
- [6] D. Jaroszynski et al., *Nucl. Instr. and Meth. A* 259 (1987) 38.
- [7] B. McNeil and W. Firth, *Nucl. Instr. and Meth. A* 259 (1987) 240.
- [8] D. Jaroszynski, R. Prazeres, F. Glotin and J. Ortega, *Phys. Rev. Lett.*, to be published.
- [9] D. Jaroszynski, R. Prazeres, F. Glotin and J. Ortega, these Proceedings (16th Int. Free Electron Laser Conf., Stanford, CA, USA, 1994) *Nucl. Instr. and Meth. A* 358 (1995) 228.



ELSEVIER

## Free-electron laser operation and self-amplified spontaneous emission using a step-tapered undulator

D.A. Jaroszynski<sup>a</sup>, R. Prazeres<sup>a</sup>, F. Glotin<sup>a</sup>, J.M. Ortega<sup>a</sup>, D. Oepts<sup>b,\*</sup>,  
A.F.G. van der Meer<sup>b</sup>, G. Knippels<sup>b</sup>, P.W. van Amersfoort<sup>b</sup>

<sup>a</sup> LURE, Bât 209d, Centre Universitaire Paris-Sud, 91405 Orsay Cedex, France

<sup>b</sup> FOM-Instituut voor Plasmafysica "Rijnhuizen", Edisonbaan 14, 3439 MN Nieuwegein, The Netherlands

### Abstract

We present an experimental and theoretical evaluation of a new method of enhancing the efficiency and gain of the free-electron laser (FEL) and observations of self-amplified spontaneous emission at start-up of the step-tapered FEL. The stepped undulator is divided into two uniform sections of different deflection strengths, the upstream  $K_1$  and the downstream  $K_2$ , and a step of  $\Delta K = K_2 - K_1 \approx 0.03$  with  $K_1 < K_2$  for mid-infrared operation.

In this paper we review a new method for enhancing the efficiency and improving the spectral brightness and temporal properties of the Compton free-electron laser (FEL) [1] and discuss measurements that show that the step-tapered FEL oscillation commences with self-amplified spontaneous emission when the gain increases above 100%.

Experimental observations, and a theoretical analysis, show that the efficiency of the FEL can be increased by the use of a two section reverse step-tapered (RST) undulator where the undulator deflection parameter,  $K$ , is increased in a single abrupt step between the two undulator sections [1–3]. The undulator structures consist of two identical independently adjustable sections with deflection parameters  $K_1$  and  $K_2$ , the upstream and downstream parameters respectively [4]. In addition, we have also observed that the small signal gain is enhanced [1], that the spectral brightness of the FEL is improved because sidebands are suppressed [1] and that the FEL operates with improved stability at its peak power output producing smooth subpicosecond optical pulses [1]. RST operation of the FEL is now routinely used in applications using the FEL output radiation in other areas of physics [5]. The experimental observations have been carried out on two FELs operating in the infrared: CLIO [6], in France and FELIX, in the Netherlands [7,8].

CLIO operates in the intermediate high gain range

above 100% because of the high peak current [6]. The single pass gain for one undulator section is also large enough for the FEL to reach saturation with one section only, making it possible for the laser to operate on two wavelengths simultaneously [2,3]. FELIX, however, has a lower small signal gain because of a longer wavelength and lower current. In CLIO, the optical radiation is coupled out of the cavity using a slightly dispersive ZnSe plate close to Brewsters' angle [9] while in FELIX hole output coupling is used. Table 1 gives other parameters for CLIO and FELIX.

The maximum efficiency of the FEL is limited to  $\eta \approx 1/2N_u$ , where  $N_u$  is the total number of undulator periods [10]. However, this can usually never be attained in oscillators where saturation of the efficiency commences when the optical field strength is large enough for the electrons to carry out synchrotron oscillations. An instability arising from the synchrotron oscillations causes the oscillator to develop sidebands in its optical spectrum [10,11] and produces optical spikes [12] and limit cycle oscillations of the pulse shape and the optical power [13,14]. The most common method of enhancing the efficiency of the FEL amplifier is by using a tapered undulator [11,15], usually accomplished by varying  $K$  or the undulator period,  $\lambda_u$ , uniformly so that the electrons are trapped in the ponderomotive potential while they traverse the undulator at saturation [10]. The main disadvantage of tapering in an FEL oscillator is that the small signal gain is reduced and, because the optical frequency depends on the evolution of the electrons in the laser field, the wavelength is generally never at a value that leads to efficiency enhancement [16]. The oscillator efficiency depends on the

\* Corresponding author. Tel. +31 3402 31224, fax +31 3402 31204, e-mail oepts@zeus.rijnh.nl.

Table 1  
Laser parameters of FELIX and CLIO

|                              | CLIO  | FELIX |               |
|------------------------------|-------|-------|---------------|
| Electron energy              | 30–50 | 22–45 | MeV           |
| Electron energy spread (rms) | 0.2   | 0.5   | %             |
| Bunch charge                 | 900   | 200   | pC            |
| Bunch length                 | 2.2   | 1     | mm            |
| Normalized emittance (rms)   | 50    | 100   | $\pi$ mm mrad |
| Number of undulator periods  | 48    | 38    |               |
| Undulator period             | 40    | 65    | mm            |
| Wavelength range             | 2–17  | 6–110 | $\mu$ m       |

number of incident electrons trapped in the ponderomotive potential [17] which, in turn, depends on the optical radiation frequency [10].

In CLIO and FELIX we have found that a stepped undulator leads to an enhancement of efficiency [1]. We find from both simulations and measurements that the efficiency can be enhanced by as much as 100% for a positive step in  $K$ ,  $\Delta K \approx 0.03$  [1–3]. Fig. 1 shows typical measurements of the average optical power as a function of  $\Delta K$  for CLIO. Efficiencies, determined from these power measurements, for 40 MeV, and  $\lambda = 8 \mu\text{m}$ , are between 0.7 and 1.0% for a RST undulator with  $\Delta K \approx 0.03$ , nearly a factor of two higher than for  $\Delta K = 0$ . The maximum efficiency with a RST undulator is still only of the order of the natural efficiency,  $\eta = 1/2 N_u \approx 1\%$  expected for CLIO. In FELIX, the optical power and the electron energy spectrum have been measured as a function of  $\Delta K$  for 45 MeV with  $\lambda = 12 \mu\text{m}$ , as shown in Fig.

1b. Efficiencies of 1.2% result. This is 75% larger than the efficiency at  $\Delta K = 0$  and is equal to the expected natural efficiency,  $\eta = 1.3\%$ . However, higher efficiency operation may be possible with dynamic desynchronization of the optical cavity length [18–20] or with longer macropulses.

To simulate step-tapered undulator FEL operation numerically we have solved the coupled Maxwell–Lorentz equations in the slowly varying amplitude approximation and in one dimension [1,10,13]. The influence of inhomogeneous effects is also included and a transverse filling factor [10] describes the optical mode coupling. The influence of dispersion due to the output coupling plate can also be included for comparison with data from the CLIO experiment. The numerical simulations and the measured data shown in Fig. 1 are in good agreement. In our simulations for CLIO we find that a second much larger peak in the enhancement of the efficiency occurs at  $\Delta K \approx 0.06$ , shown in Fig. 1c, when dispersion in the cavity is omitted from the simulation. This second larger peak was not observed in the measurements [1]. However, it may be possible to observe it in CLIO if an alternative non-dispersive method of coupling the radiation out of the cavity is used. In principle saturation should be reachable with  $\Delta K \approx 0.06$  as the gain is more than 100%, as shown in Fig. 1c. Fig. 1c also shows interference fringes in the gain [3,4,21,22], and, surprisingly, that the gain is enhanced by a factor of three or four for  $\Delta K \approx 0.03$  over that for  $\Delta K = 0$ .

From simulations we find that, for  $\Delta K \approx 0.04$ , the electrons enter the first undulator section with a phase velocity above the resonance of the first section but approximately at resonance with the second undulator section for a saturated intracavity field of approximately 1 GW. The first undulator section acts as a buncher and the electrons are very strongly bunched as they enter the second undulator. A large portion of the electrons are at the bottom of the potential and do not have a strong influence on the optical power in the second undulator section. This has the effect of preventing synchrotron oscillations from occurring, and therefore the field amplitude tolerable before synchrotron oscillations start is increased, consistent with the observed enhancement of efficiency. The higher energy electrons, accelerated in the first

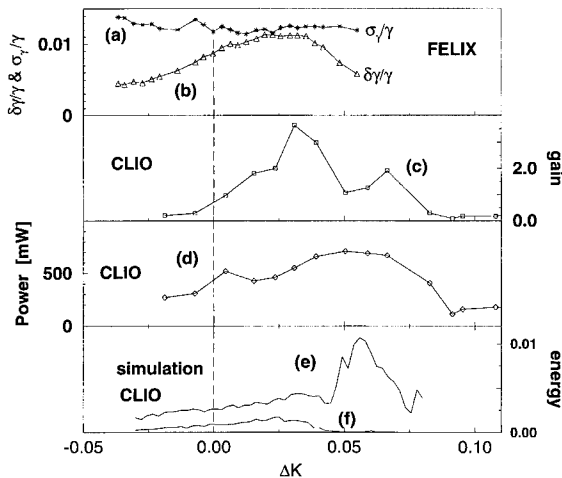


Fig. 1.  $\Delta K$  scans: (a) the electron energy dispersion, after interaction,  $\sigma_\gamma/\gamma$ ; (b) FELIX efficiency, determined from the mean electron energy reduction  $\Delta\gamma/\gamma$ ; (c) the small signal gain of CLIO vs  $\Delta K$ ; (d) CLIO efficiency, determined from the laser power; (e, f) simulations of intracavity optical power, not including dispersion, at 15 and 100 roundtrips respectively for CLIO parameters.

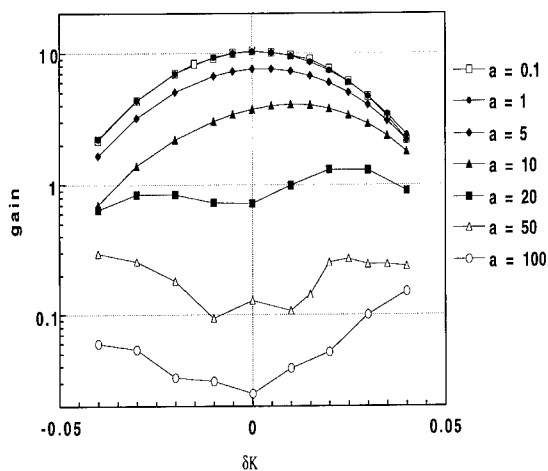


Fig. 2. Simulations of the maximum gain of an amplifier vs  $\Delta K$  for  $0.01 < |a| < 100$ .

section, are captured by the second undulator potential and experience an energy loss which can be seen in the evolution of the electron energy spectrum down the undulator as shown in Fig. 3. Figs. 3a and 3b compare the mean reduction in phase velocity for  $\Delta K \approx 0.04$  and  $\Delta K = 0$ . A beneficial side effect is that the energy spread of the electrons exiting the second undulator is reduced over that for  $\Delta K = 0$  and synchrotron oscillations are suppressed, as is also observed in our measurements of the dispersion of the electrons exiting the undulator shown in Fig. 1a. The dispersion of the electron energy due to interaction does not increase when the FEL operates in the RST mode despite of the increased optical power [1]. This feature of RST operation may have beneficial applications in storage ring FELs.

In Fig. 2 we show the results of a simulation of the gain, for CLIO parameters, of an amplifier as a function of  $\Delta K$  for a number of normalised input field amplitudes

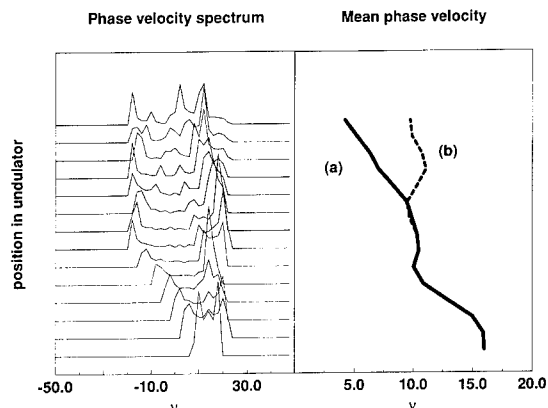


Fig. 3. Simulations of phase-velocity spectra of the electrons passing down the undulator for  $\Delta K \approx 0.04$  (a) and  $\Delta K = 0$  (b) (dotted line).

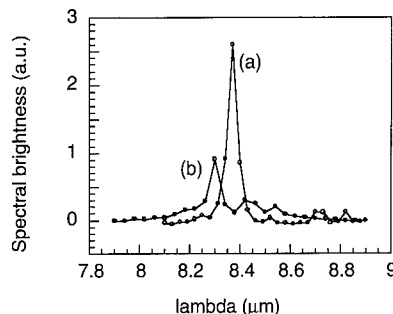


Fig. 4. Measurement of spectral brightness for  $\Delta K \approx 0.03$  (a) and  $\Delta K = 0$ , (b), showing an enhancement for RST undulator operation.

$|a| = 0.1$  to  $100$  (1 MW to 1 GW). For each value of  $\Delta K$  we have varied the input radiation frequency to establish the optimum gain and frequency. We find that, in an amplifier, the gain peaks at  $\Delta K \approx 0.01$  for small amplitudes and, as the amplitude is increased toward saturation, the optimum shifts to positive  $\Delta K$  values. For very high fields the gain for  $\Delta K > 0$  can be considerably higher than that at  $\Delta K = 0$ . This implies that the efficiency will also be higher at these  $\Delta K$  values. We also find that the frequency at which the optimum gain occurs evolves continuously, with no discrete jumps, as the field amplitude is increased for  $\Delta K > 0$ . However, for  $\Delta K < 0$ , there are discontinuities, as  $|a|$  is increased, in the frequency for optimum gain. We therefore expect that in an oscillator with  $\Delta K < 0$  the FEL will saturate at a lower power, as has been observed in our measurements described above.

An added beneficial consequence of RST operation is that the spectral properties of the FEL are improved because synchrotron oscillations and sidebands are suppressed [1]. We observe that the spectral brightness can be increased markedly. Fig. 4 shows measurements of spectra made close to the peak of the cavity detuning curve (i.e. peak power) for CLIO with a RST undulator with  $\Delta K \approx 0.03$ , compared with that for a normal undulator,  $\Delta K = 0$ . The measured spectra, in Fig. 4a for  $\Delta K \approx 0.03$ , are smooth and lack sidebands associated with synchrotron oscillations and spiking. The featureless spectra also indicate smooth temporal envelopes of the optical pulses. We have measured, in CLIO, the optical pulse shape by second-order autocorrelation methods [1] and found smooth subpicosecond optical pulses with no sub-structure and that the laser operates with good amplitude stability at the peak of the detuning curve with a RST undulator.

The measurement of very large enhancements of gain for an RST undulator is surprising. We expect the start-up wavelength of the oscillator to be important in determining the gain of the laser medium. From our simulations of the gain of an amplifier, discussed above, we found that the small signal gain peaked at  $\Delta K \approx 0.01$ . However, in our measurements of the small signal gain we find a larger



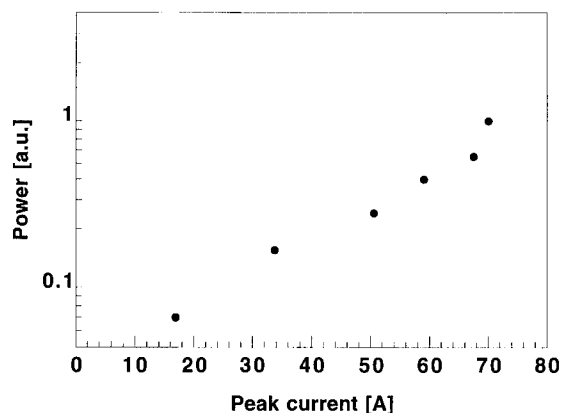


Fig. 5. Measurement of self-amplified spontaneous emission intensity as a function of electron peak current for  $\Delta K \approx 0.03$ .

enhancement at  $\Delta K \approx 0.03$ , as shown in Fig. 1c. By measuring both the spontaneous emission spectrum and the laser spectrum at low and high fields we have established that the wavelength of the radiation in the RST configuration is fixed by the downstream undulator, with the higher  $K$ . In the spontaneous emission measurements we have also observed self-amplified spontaneous emission, where the optical power exhibits a strongly non-linear dependence on the electron charge, for an RST undulator, as shown in Fig. 5 indicating that the first undulator acts as a buncher and the second section as a radiator. The peak in the radiation spectrum occurs at the resonance wavelength of the second undulator.

In conclusion, we have presented a new method of enhancing the efficiency of the FEL using a reverse step-tapered undulator by a combination of detrapping electrons at the bottom of the ponderomotive potential so preventing synchrotron oscillations and trapping of electrons accelerated in the first undulator section. The RST FEL starts up by self-amplified spontaneous emission as confirmed by our measurements. We have also observed gain enhancement and an improvement in the spectral brightness and the stability of the FEL at its highest output powers. We have shown that another benefit of the enhancement of efficiency with a RST undulator is that it does not lead to a

corresponding increase in energy spread of electrons leaving the undulator.

## References

- [1] D. Jaroszynski, R. Prazeres, F. Glotin and J. Ortega, *Phys. Rev. Lett.*, in press.
- [2] D. Jaroszynski, R. Prazeres, F. Glotin and J. Ortega, *Phys. Rev. Lett.* 72 (1994) 2387.
- [3] D.A. Jaroszynski, R. Prazeres, F. Glotin and J.M. Ortega, these Proceedings (16th Int. Free Electron Laser Conf., Stanford, CA, USA, 1994) *Nucl. Instr. and Meth. A* 358 (1995) 224.
- [4] C. Pidgeon et al., *Nucl. Instr. and Meth. A* 259 (1987) 31.
- [5] A. Peremans et al., *J. Electr. Spectr. Relat. Phenom.* 64 (1993) 391.
- [6] R. Prazeres et al., *Nucl. Instr. and Meth. A* 331 (1993) 15.
- [7] P. van Amersfoort et al., *Nucl. Instr. and Meth. A* 318 (1992) 42.
- [8] R.J. Bakker et al., *IEEE J. Quantum Electron.* QE-30 (1994) 1635.
- [9] R. Prazeres, J.B.R. Chaput, F. Glotin and J.M. Ortega, to be published.
- [10] W. Colson, in: *Laser Handbook*, Vol. 6, eds. W. Colson, C. Pellegrini and A. Renieri (North-Holland, Amsterdam, 1990) p. 115.
- [11] P. Sprangle and C. Roberson, *Phys. Fluids B* 1 (1989) 3.
- [12] B. Richman, J. Madey and E. Szarmes, *Phys. Rev. Lett.* 63 (1989) 1682.
- [13] D. Jaroszynski et al., *Phys. Rev. Lett.* 70 (1993) 3412.
- [14] D. Jaroszynski et al., *Nucl. Instr. and Meth. A* 331 (1993) 52.
- [15] N. Kroll, P. Morton and M. Rosenbluth, *IEEE J. Quantum Electron.* QE-17 (1981) 1436.
- [16] E. Saldin, E. Schneidmiller and M. Yurkov, *Opt. Commun.* 103 (1993) 297.
- [17] E. Scharlemann, in: *Laser Handbook*, Vol. 6, eds. W. Colson, C. Pellegrini and A. Renieri (North-Holland, Amsterdam, 1990), pp. 291–343.
- [18] D. Jaroszynski et al., *Nucl. Instr. and Meth. A* 296 (1990) 480.
- [19] D. Jaroszynski et al., *Nucl. Instr. and Meth. A* 318 (1992) 582.
- [20] R.J. Bakker et al., *Phys. Rev. E* 48 (1993) R3256.
- [21] D. Jaroszynski et al., *Nucl. Instr. and Meth. A* 259 (1987) 38.
- [22] B. McNeil and W. Firth, *Nucl. Instr. and Meth. A* 259 (1987) 240.



ELSEVIER

## Electron energy spectral measurements in the large-slippage regime

W.A. Gillespie <sup>a,\*</sup>, A.M. MacLeod <sup>a</sup>, P.F. Martin <sup>a</sup>, G.M.H. Knippels <sup>b</sup>,  
A.F.G. van der Meer <sup>b</sup>, E.H. Haselhoff <sup>b</sup>, P.W. van Amersfoort <sup>b</sup>

<sup>a</sup> University of Abertay, Bell Street, Dundee DD1 1HG, UK

<sup>b</sup> FOM-Institute for Plasma Physics 'Rijnhuizen', Edisonbaan 14, 3439 MN Nieuwegein, The Netherlands

### Abstract

Time resolved electron spectra have been measured at FELIX while lasing in the 8–30  $\mu\text{m}$  range. Over this wavelength range the slippage, given by the longitudinal coupling parameter,  $\mu_c = N\lambda/\sigma_e$ , varies considerably ( $0.5 < \mu_c < 3$ ). Limit-cycle behaviour, previously observed in optical spectra [1], is also evident in the electron spectra. Efficiencies of up to 1.6% have been measured. In these cases the output electron energy distribution has a total width of more than 14%! Also presented are measurements of the electron and optical spectra in the case when the electron energy is swept at a rate of 0.3%/ $\mu\text{s}$  while lasing at 30  $\mu\text{m}$ .

### 1. Introduction

Previous measurements of the effect of the FEL interaction on the electron energy distribution have been rather limited, especially in the regime of strong slippage. Therefore we decided to install a spectrometer downstream of the high energy beam line of FELIX. The wavelengths that can be produced in this FEL currently range from 5 to 30  $\mu\text{m}$  and the longitudinal coupling parameter,  $\mu_c = N\lambda/\sigma_e$ , ranges from 0.5 to 3. At  $\mu_c \approx 1$ , short-pulse effects start to become important so we should be able to probe the transition, if any, from the long-pulse to short-pulse regime. As a first result, we noticed that for large  $\mu_c$  the increase in spectral width due to lasing was much larger than expected. As much as 50% of the current was occasionally lost on the vacuum pipes, and a new housing for the spectrometer had to be built. Due to the delay caused by this modification the number of measurements is still somewhat limited, but nevertheless some interesting observations have been made. During energy ramp runs, the spectrometer was used as a diagnostic to obtain rather linear ramps without introducing additional spectral broadening of the electron energy spectrum. To check the performance of the spectrometer, non-lasing results were compared with earlier measurements [2] and a button position monitor that measures the mean beam energy. The comparison was quite satisfactory.

### 2. Description of the electron spectrometer

In December 1993 the electron spectrometer was installed for the first time and modified in July 1994 to increase the energy acceptance. The system consists of a 90° bending magnet with input and output pole edge rotations of 38° and 32° respectively and a dispersion in the focal plane of 8 mm/%. At this position a 2  $\mu\text{m}$  thick kapton foil, coated with 40 nm of aluminium, is mounted at a 45° angle to the beam. The optical transition radiation (OTR) is focussed on a linear array of 32 detectors by means of a relay lens and a standard zoom objective. The OTR-detector (Hamamatsu S4114-35Q) is sensitive between 190 and 1000 nm, with peak response at 800 nm. The bandwidth of the system is 5 MHz. It is therefore possible to accurately follow the macropulse signal, but the individual micropulses (separated by 1 ns) cannot be observed. The dispersion of the total system, which can be changed from 0.06 to 0.25 by changing the zoom, was set to 0.2%/channel, resulting in a full width of more than 6%. Macropulse-integrated spectra can be monitored in real-time but data archiving is normally manually controlled in view of the large amount of data generated.

### 3. Fixed wavelength lasing

In FELIX the laser output for wavelengths longer than 20  $\mu\text{m}$  generally exhibits stable oscillations during the macropulse with frequency and amplitude depending on the cavity desynchronism [1]. In this regime the slippage of the optical micropulse is of the same magnitude as the electron bunch length, giving rise to “lethargy” effects.

\* Corresponding author. Tel. +44 382 308247, fax +44 382 308877, e-mail eetwag@dct.ac.uk.

Table 1

Measured extraction efficiency and brightnesses.  $\Delta L/\lambda$  is the cavity desynchronism,  $\eta$  is the efficiency and  $\sigma_{es}$  and  $\sigma_{os}$  are the rms widths of the electron energy and optical spectra respectively

| $\lambda$ ( $\mu\text{m}$ ) | $\Delta L/\lambda$ | $\eta$ (%) | $\eta/\sigma_{os}$ | $\eta/\sigma_{es}$ |
|-----------------------------|--------------------|------------|--------------------|--------------------|
| 30                          | -0.30              | 1.6        | 0.8                | 0.55               |
| 30                          | -0.60              | 1.6        | 1.15               | 0.6                |
| 30                          | -1.67              | 1.0        | 2.5                | 0.65               |
| 19                          | -0.85              | 0.7        | 0.6                | 0.5                |
| 12                          | -0.83              | 0.6        | 0.55               | 0.4                |
| 8                           | -0.50              | 0.7        | 0.25               | 0.5                |

During the growth phase the effective “group velocity” of the pulse is reduced which is compensated by a slight decrease in cavity length. Near saturation the “group velocity” increases and the pulse slowly slips ahead of the electron bunch whereafter it decays due to cavity losses. At some point a subsequent pulse starts to grow out of the tail of the previous pulse. Over a wide range of parameters a stable oscillation results.

As expected, these oscillations also clearly show up in the electron energy spectral measurements: both the efficiency and the spectral width show the characteristic modulation (Fig 1). In Table 1 the results of two days of dedicated beam time are summarized.

In view of the rather limited set of experimental parameters it is difficult to draw definite conclusions. The data do suggest however that the ratio between the efficiency and the spectral width of the electron distribution is more or less constant. More surprising are the relatively high efficiencies that are measured at 30  $\mu\text{m}$  during a maximum of the oscillation. Even though the measured value of 1.6% is not much above the theoretical value of  $1/2N$  ( $= 1.3\%$ ), these high values have to our knowledge only been produced at much higher bunch charges (only 200 pC in our case) or with tapered undulators. The efficiencies at the shorter wavelengths, which were obtained at bunch charges of only 140 pC, fall short of the theoretical value by a factor of two, as often seems to be the case [3,4]. At 30  $\mu\text{m}$  the experimental results are well reproduced by simulations based on a simple 1-D code (Fig. 1b), but at shorter wavelengths the code does not predict a lower efficiency. This is not too surprising as the relative importance of transverse effects, which are not taken into account, to longitudinal effects is expected to change quite considerably going from 30 to 8  $\mu\text{m}$ . The total width of the electron spectra can be as large as 14% in which case the complete spectrum has to be recorded in subsequent macropulses as the maximum energy bin covered by the system with reasonable efficiency is limited to 6%. As the macropulses are highly reproducible, this does not introduce significant errors. The maximum power extracted from the beam exceeds the 100 kW level which is almost a factor of four higher than the measured optical output. At

first this outcoupling efficiency seemed surprisingly low in view of the measured cavity loss of 6% and the quoted reflectivity of the gold-coated copper mirrors of  $> 98.5\%$ . Later it was realized that at this wavelength the cavity does

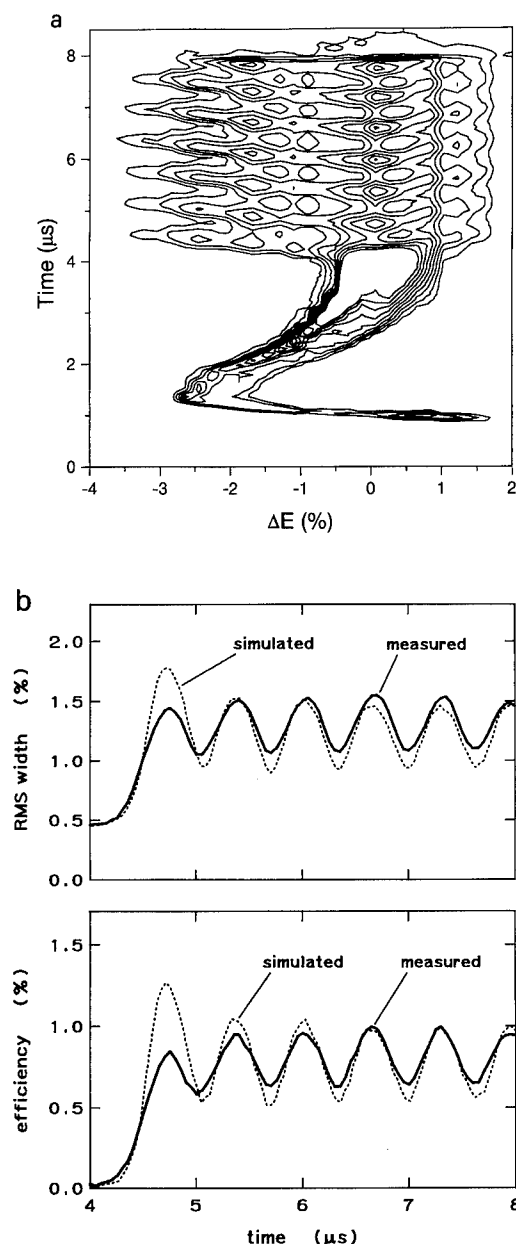


Fig. 1. The measured electron spectrum, efficiency and rms width as a function of time while lasing at  $\lambda = 30 \mu\text{m}$  and -50  $\mu\text{m}$  detuning. The nominal input beam energy is 36 MeV. The limit-cycle oscillations are clearly present and have a period of 0.60  $\mu\text{s}$ . Besides the main peak at resonant energy a sideband is present at  $\Delta E = -1.8\%$ . The initial transient in the beam energy visible in the contour plot is due to beam loading transients.

not support higher-order transverse modes and so the diffraction losses at the outcoupling hole are of the same magnitude as the power coupled out. From the spectral width the micropulse length was estimated to be 1 ps FWHM, which results in a peak intra-cavity power in excess of 1 GW. For completeness we have also listed in Table 1 the “brightness” as defined in [5]. Only at 30  $\mu\text{m}$  do the results seem to be in agreement with the predictions, i.e. the brightness decreasing with decreasing cavity desynchronism down to a level of 0.8.

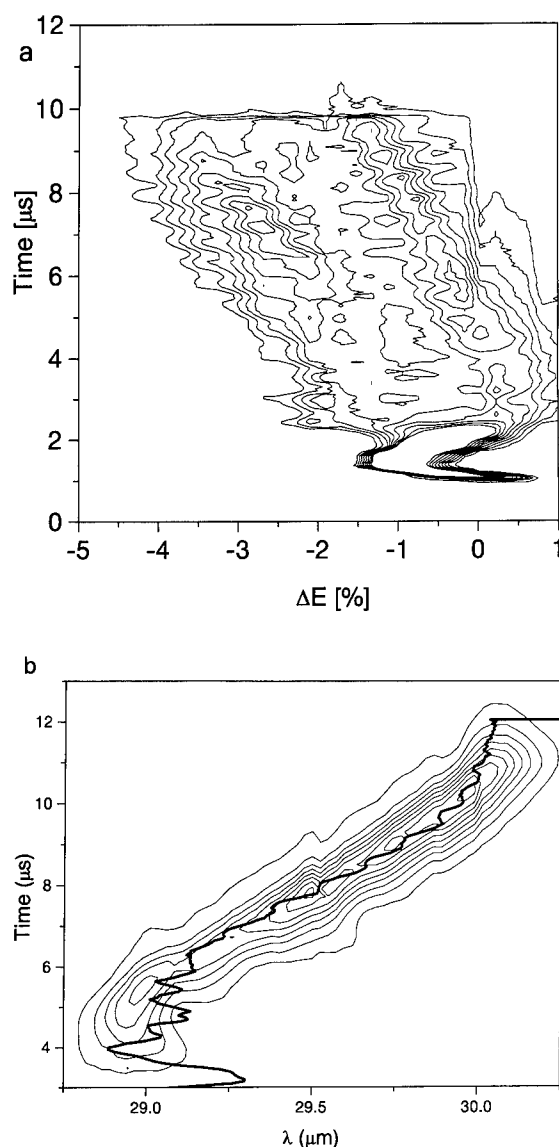


Fig. 2. Electron energy spectrum and optical spectrum in the case of a deliberate down ramp in beam energy. Also shown in the plot of the optical spectrum is the expected wavelength shift that is calculated from the measured beam energy without lasing.

#### 4. Ultra-fast wavelength scans

For some applications it may be advantageous to change the wavelength during the macropulse. A typical example would be the resonant excitation of an anharmonic ladder in a molecule where the decay time of the different energy levels exceeds the micropulse spacing. In FELIX the wavelength can be changed by changing the beam current which, due to the beam loading, results in a change in beam energy. Changing the current from the gun is simply done by applying different waveforms for correcting the current drawn from the gun. Ramping speeds up to 0.3%/μs and maximum energy changes of up to 1.8% can be produced, the limitation at this moment being the waveform-generating electronics. It is clear from fig. 2 that the resulting optical pulse is scanned well outside its spectral bandwidth. The total change in wavelength is 3.7% whereas the FWHM is 0.6%. Fig. 2b shows the expected wavelength shift calculated from the measured mean energy of the electron beam without lasing. The electron signal has been shifted roughly 1.5 μs in time to accommodate for the memory time of the cavity. Both positive and negative ramps have been applied. At these sweep rates the central wavelength follows the input beam energy quite accurately. No asymmetries in up or down ramp as reported by others [3,6] have been observed until now.

#### 5. Conclusions

We have measured time-resolved high-resolution electron spectra under different lasing conditions. The spectra show pronounced short-pulse effects which agree with the measured optical spectra. At 30 μm the spectra can be reproduced using a fairly simple one-dimensional model. Additional experiments over a wider range of experimental conditions are needed to clarify the role of the longitudinal coupling parameter on the spectra. The optical system will be improved to increase the useful energy window of the detector.

At the maximum energy ramping speeds used, 0.3%/μs, the wavelength shifts accordingly with no apparent asymmetry in up or down ramping.

#### Acknowledgements

This work has been performed as part of the research program of the Stichting voor Fundamenteel Onderzoek der Materie (FOM), and was made possible by financial support from the Nederlandse Organisatie voor Wetenschappelijk Onderzoek (NWO).

## References

- [1] D.A. Jaroszynski, R.J. Bakker, A.F.G. van der Meer, D. Oepts and P.W. van Amersfoort, Phys. Rev. Lett. 70 (1993) 3412.
- [2] A.F.G. van der Meer, R.J. Bakker, C.A.J. van der Geer, D. Oepts, P.W. van Amersfoort, W.A. Gillespie, P.F. Martin and G. Saxon, Nucl. Instr. and Meth. A 331 (1993) 282.
- [3] R.W. Warren, J.E. Sollid, D.W. Feldman, W.E. Stein, W.J. Johnson, A.H. Lumpkin and J.C. Goldstein, Nucl. Instr. and Meth. A 285 (1989) 1.
- [4] Ph. Guimbal, S. Joly, D. Iracane, J. Fréhaut, P. Balleyguier, A. Binet, J.P. Blésès, J. DiCrescenzo, V. Fontenay, P. Fourdin, G. Haouat, J.G. Marmouget, Y. Pranal, F. Sabary, S. Striby and D. Touati, Nucl. Instr. and Meth. A 341 (1994) 43.
- [5] D. Iracane, P. Chaix and J.L. Ferrer, Phys. Rev. E 49 (1994) 800.
- [6] R.L. Swent, K.W. Berryman, H.A. Schwettman and T.I. Smith, Nucl. Instr. and Meth. A 304 (1991) 272.

## Experimental measurement of short pulse guiding effects in a free-electron laser

Bruce A. Richman <sup>a,\*</sup>, Brian McVey <sup>b</sup>, John M.J. Madey <sup>c</sup>

<sup>a</sup> *Stanford Picosecond FEL Center, Stanford University, Stanford, CA 94305-4085, USA*

<sup>b</sup> *Los Alamos National Laboratory, Los Alamos, NM 87545, USA*

<sup>c</sup> *Department of Physics, Duke University, Durham, NC 27706, USA*

### Abstract

We present the results of computer simulations of the MKIII FEL at Stanford (1988) using the Los Alamos National Laboratories FELEX simulation code. The simulations predict a tapering of the spot size through the length of the optical pulse that results from the effect of slippage on optical guiding. We show that this effect can be measured using optical autocorrelation, and present a simple mathematical model that may be used to calculate autocorrelation functions measured after the beam passes through an aperture, and compare these autocorrelation functions to reveal the effect of the spatial taper. We then present an autocorrelation experiment on the MKIII free-electron laser at Stanford, the inconclusive results of which probably stem from remnant laser instability and drift. However, the maximum difference in normalized autocorrelation functions, under experimental conditions with 50% single pass gain, was 5%. This corresponds to a difference in spot size between the front and back of the pulses of approximately 25%.

### 1. Introduction

Most FEL applications require knowledge of the characteristics of the FEL being used, particularly the structure of the laser pulses. The spot size and, in the case of RF linac driven FELs, the pulse length are needed to determine power density and time resolution. In many instances, the FEL system should be optimized based on the three-dimensional pulse shape of the output of the first FEL.

In this paper, we first analyze the 3-D character of short laser pulses on the MKIII as predicted by the FELEX simulation code developed at Los Alamos National Laboratories [1]. Second, we describe a method to observe such 3-D effects experimentally using optical autocorrelation and an aperture in the output laser beam. To study the effects of the aperture, such autocorrelation functions are calculated from a 3-D optical pulse model based on the FELEX predictions. Third, we present the results of an aperture/autocorrelation experiment performed on the MKIII FEL.

### 2. FEL 3-D guiding

FELEX results [1,2] showed that slippage of the optical pulses over the electron pulses in the wiggler can have a significant effect on the shape of the optical pulses. The optical pulses calculated from simulations which used electron pulses less than three slippage distances long exhibited a strong spatial taper when the laser gain was high, where the slippage distance is the number of wiggler periods multiplied by the optical wavelength. The taper is caused by optical guiding by the electron beam, but which is a function of the longitudinal position within the pulse, a result of the unusual two step gain process. The laser radiation bunches the electrons in the first part of the wiggler, which radiate coherently into the laser field in the remainder of the wiggler, producing optical gain and guiding. Slippage is particularly important for short optical pulses: the leading part of the optical pulse bunches the electrons, but slips over the electron pulse before experiencing gain; whereas the trailing part of the optical pulse undergoes gain from the electrons bunched by the radiation farther ahead. As a result, the back of the optical pulse experiences more gain, and optical guiding, than the front, leading to the development of the spatial taper.

The FELEX code was run using short electron pulses in an effort to find three-dimensional high gain effects. A square electron pulse 375  $\mu\text{m}$  in length and with emittance

\* Corresponding author. Tel. +1 415 723 0209, fax +1 415 715 8311, e-mail: brich@leland.stanford.edu.

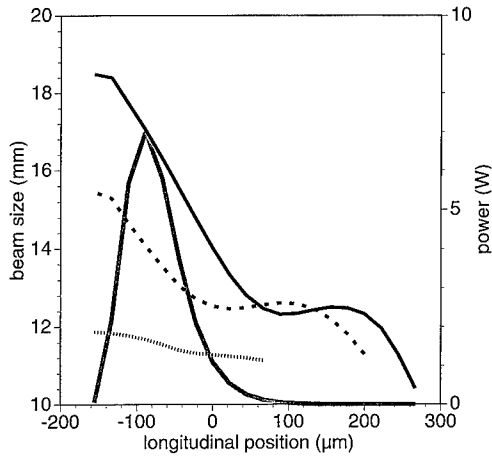


Fig. 1. Beam size as function of position in the pulse for pass 10 (solid), 20 (dashed), and 100 (dotted) of the FELEX simulation. The power for pass 20 is shown in gray.

and beam size to match the operating conditions of the MKIII FEL at Stanford [3] was used as input to FELEX. The optical wavelength was 3  $\mu\text{m}$ . The MKIII laser wiggler has 47 periods, so the electron pulses used in the simulation are approximately two slippage distances long. The simulation indicates that the pulses shorten as they develop through several passes and develop weak and long forward tails. These effects result from slippage and lethargy, and have been observed previously [6]. Fig. 1 illustrates the unusual tapering of the pulses outside the laser in the far field of the resonator (where relative beam sizes are reversed). At pass 10, the transverse size at the front of the pulse is about 30% smaller than at the back. This tapering decreases dramatically as the gain drops progressively from pass 10 to 30. At pass 100, the gain is only 16% (including round-trip losses of 15%), and almost no tapering remains at this point. The taper is almost nonexistent for simulations using an electron pulse length of 4 slippage distances.

### 3. Measuring taper with autocorrelation

The tapering effect can be characterized experimentally by introducing apertures of various diameters into the laser beam and then observing the autocorrelation. An intensity autocorrelator was used in the experiment, and autocorrelation functions of the computed apertured laser pulses were calculated by propagating the output laser beam to the position of the controlling iris (aperture) placed in the far-field of the laser beam, multiplying power densities at

different longitudinal positions, and then integrating over the transverse plane ( $x, y$ ) and longitudinal position,  $z$ ,

$$I_{AC}(\Delta z) = \int_{-\infty}^{+\infty} dz \int_{\text{aperture}} dx dy |E_0^2(x, y, z)| \times |E_0^2(x, y, z + \Delta z)|. \quad (1)$$

We composed a simple mathematical model of the laser pulse power density at the aperture to predict the autocorrelation functions to give physical insight into the behavior of the autocorrelation function of different optical pulses. The model approximated the shape of the cross-sectional power curve generated by FELEX and included a linear taper to a Gaussian transverse power density profile. The pulse length and taper in the model can be varied to study how those quantities affect the autocorrelation function. The model power density is given by

$$I(r, z) = z(z - z_e)^2 \exp\left[-\frac{(z - z_g)^2}{2L_g^2}\right] \times \frac{1}{(R_0 - gz)^2} \exp\left[-\frac{2r^2}{(R_0 - gz)^2}\right] \quad (2)$$

for  $0 \leq z \leq z_e$ , and  $I(r, z) = 0$  otherwise. The linear taper is given by  $(R_0 - gz)$ . The difference between the model and the FELEX result is well within the uncertainty of the actual experiment.

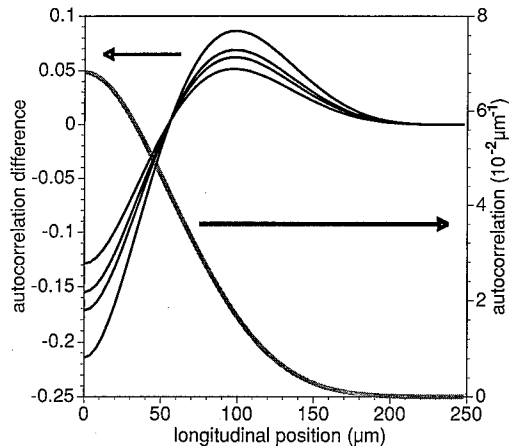


Fig. 2. Model generated autocorrelation curve (gray); and normalized autocorrelations of the apertured model pulses minus that with no aperture. The model laser beam size ranges from approximately 8 mm to 14 mm over the length of the optical pulse, and the aperture sizes range from 7.6 mm in diameter to 14.7 mm. The autocorrelations change monotonically with this diameter, and the largest difference corresponds to the smallest aperture. The peak values of the autocorrelation functions of the smallest aperture and no aperture differ by 3%.

In order to compare them, the autocorrelation functions were normalized so that their integral over  $dz$  was 1. The pulse length could also be calculated from the autocorrelations. Subtraction clearly reveals the differences among the autocorrelation curves. Fig. 2 shows the predicted autocorrelations with various apertures at pass 20 (assuming a square electron pulse) minus the autocorrelation with no aperture, and the autocorrelation with no aperture for comparison. The model predicted a 3% difference between the peak of the autocorrelation curve calculated with no aperture and the curve with a 7.6 mm aperture. The effective pulse length also changed by 3%.

Autocorrelation functions calculated directly using the FELEX results showed smaller differences among the apertures than the mathematical model, about 1%, although the power curve and autocorrelation of the model are quite close to the FELEX results.

#### 4. The autocorrelation experiment

The MKIII FEL system has been described previously in detail [3].

The aperturing iris diameter was varied from a few millimeters to 1.5 cm, or removed entirely. To simplify the interpretation of the results, no focussing was done upstream of this iris. Thus the laser beam could be considered as in the far field limit of the resonator at the iris.

The intensity autocorrelator produced more meaningful information than a Michelson arrangement and required much less optical delay resolution. The decay rate of its detector was too slow to resolve resonator cavity decay phenomena as observed in a previous guiding experiment [4]. The optical focussing between the iris and the doubling was such that any transverse symmetric beam profile would be scaled [5]. Thus, the normalized autocorrelation at the crystal would be the same as at the aperture, simplifying the theoretical analysis.

An AT clone computer controlled the autocorrelation experiment and performed data acquisition. Both macropulse reference and autocorrelator signals were sampled every 10 ns and digitized to 8 bits.

The power in the beam was monitored before the aperturing iris with a 200 MHz detector. This macropulse reference signal primarily served to trigger the electronics in the small signal regime, at about 1/20th of the saturated power level, to eliminate startup jitter in the digitized data.

Under prime operating conditions, each scan took about 20 s and several scans were taken successively for each iris diameter. A complete data set (including many iris diameters) took thirty minutes.

#### 5. Experimental results

The macropulse reference shape detailed the state of the laser as a function of time through the macropulse.

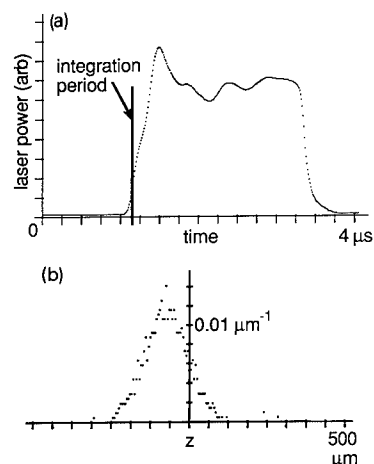


Fig. 3. Macropulse power and one autocorrelation. (a) Macropulse power vs. time, with the integration period used in (b). (b) One of the autocorrelation curves (with no aperture) used in the subtractions.

From this, specific time regions could be selected, such as small signal or build-up, steady state or saturated, and decay or ring down. The gain was calculated for such time segments to check the consistency of a set of scans and to match theoretical calculations.

The autocorrelation data were integrated over the chosen time region. Typical pulse lengths were in the range of 150  $\mu\text{m}$  to 600  $\mu\text{m}$ . Autocorrelation curves taken with the same aperture diameter were averaged to reduce the effects of noise. The macropulse shapes and small signal gain in the time integration domain of the data files were checked for consistency before averaging. Usually one scan was excluded from each average out of a set of three to five scans because it was deemed inconsistent with the others. The averaged data from different aperture diameters were then subtracted from each other for comparison.

Autocorrelation data were obtained with three different cavity detuning lengths: zero detuning (maximum and stable power), short, and long (unstable “noise driven” [6]). The laser resonator length detuning was varied to observe the effect of changing the relative overlap between electron and laser pulses in the wiggler. In all cases, the electron beam parameters were set to give the minimum electron pulse length.

The results for the case of zero detuning are shown in Figs. 3 and 4. Fig. 3a shows the time integration period used in Figs. 3b and 4 relative to the macropulse power as a function of time. This integration period was chosen so that the laser gain during the period (48%) was closest to the gain of pass 20 of the FELEX simulation results. The optical pulse in this period was approximately 140  $\mu\text{m}$  long. Fig. 3b is a typical autocorrelation trace integrated over the time window in Fig. 3a. The signal before this time window was too small and unstable to analyze.



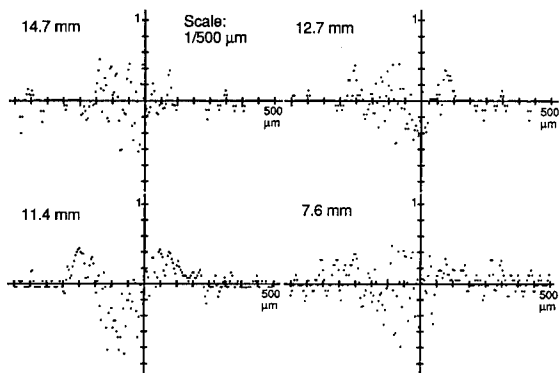


Fig. 4. Subtracted autocorrelation curves. Autocorrelation is integrated over the same time regime as in Fig. 2. Each part of the figure is the subtraction between the autocorrelation obtained with an aperture (diameter shown) and one obtained with no aperture. The laser gain was 48%.

Each plot in Fig. 4 is the difference between the autocorrelation obtained with an aperture and that obtained with no aperture. The aperture diameters were chosen such that the autocorrelation signal was reduced to between  $\frac{7}{8}$  and  $\frac{1}{4}$  of the signal with no aperture, so that there would be a full range of aperture sizes relative to the beam.

As seen in Fig. 4, there do not appear to be any significant differences between the curves with aperture diameter greater than 13 mm and no aperture at all. The smaller apertures, however, seem to have a significant effect on the autocorrelation function. The differences of the 11.4 mm and 10.2 mm aperture curves with the no aperture curve show approximately a 5% change in the peak of the autocorrelation curves. However, the uncertainty of the difference of any point of the curve is also 5% of the peak value, and the 7.6 mm aperture curve shows little difference from the no-aperture curve. Another data set acquired earlier during the same day also showed no significant differences. The large uncertainty in these differences caused by variations from macropulse to macropulse, and the possible long term drifts of the laser pulse length mean that these difference curves are inconclusive. Also, subtractions from later in the macropulse where the gain is markedly lower show similar differences. However, these data sets do indicate an upper limit of the effect of 5% of the peak value of the autocorrelation functions given the optical pulse length and laser gain during the measurement.

The model-based autocorrelation differences show a 1% to 3% change in the peak of the autocorrelation

function with different apertures, which is consistent with the 5% upper limit. The largest difference occurs between the smallest aperture, 7.6 mm, and no aperture.

Autocorrelation curves obtained with short and long detuning indicated pulse length changes but no curve differences above the uncertainty level.

## 6. Conclusion

We have presented a simple mathematical model of the optical pulses designed to match the FELEX simulation results, characterizing the predicted spatial taper of the pulses caused by the longitudinally dependent optical guiding in the laser. Autocorrelation curves of these model pulses passing through various diameter apertures were calculated and compared with each other by normalization and subtraction. The 3-D character of the pulses was evinced in subtractions of the model autocorrelations, with differences of the curves of 1% to 3% of their peak value.

Experimental autocorrelation curves obtained with apertures of several different diameters were compared. The observed differences of 5% were, however, similar to the uncertainty of 5% caused by laser instability and drift. The three-dimensional guiding results are thus inconclusive, but the differences of the autocorrelation curves at 50% laser gain must be less than the 5% uncertainty limit, consistent with the model autocorrelation differences.

## Acknowledgement

The authors wish to thank Dr. Stephen Benson for many helpful discussions concerning the design of the experiment in relation to the behavior of the MKIII FEL.

## References

- [1] B.D. McVey, Nucl. Instr. and Meth. A 250 (1986) 449.
- [2] B.A. Richman, Three-dimensional guiding effects in a free-electron laser, doctoral dissertation, Dept. of Applied Physics, Stanford University (1991).
- [3] S.V. Benson et al., Nucl. Instr. and Meth. A 250 (1986) 39.
- [4] J.E. LaSala, D.A.G. Deacon and J.M.J. Madey, Phys. Rev. Lett. 59 (1987) 2047; J.E. LaSala, Transverse mode evolution in a free-electron laser oscillator, doctoral dissertation, Dept. of Applied Physics, Stanford University (1987).
- [5] H. Kogelnik and T. Li, Proc. IEEE 54 (1966) 1312.
- [6] S.V. Benson, Diffractive effects and noise in short pulse free-electron lasers, doctoral dissertation, Dept. of Physics, Stanford University (1985).



ELSEVIER

## High efficiency results at 23 $\mu\text{m}$ on the ELSA FEL and operation with the MONA wiggler

Ph. Guimbal<sup>\*</sup>, D. Iracane, S. Joly, P. Balleyguier, A. Binet, J.P. Blésès, J. DiCrescenzo, V. Fontenay, P. Fourdin, G. Haouat, J.G. Marmouget, Y. Pranal, F. Sabary, S. Striby, D. Touati

*Commissariat à l'Energie Atomique, BP 12, 91680 Bruyères-le-Châtel, France*

### Abstract

The ELSA FEL at Bruyères-le-Châtel has reached an efficiency above 3% at 23  $\mu\text{m}$ , a performance not previously reported with a uniform wiggler in this wavelength range. So far, the experimental results seem to be in good agreement with both theoretical and numerical predictions made by our group. We also report our first results in the 10–20  $\mu\text{m}$  range with our new wiggler MONA.

### 1. Introduction

The ELSA FEL at Bruyères-le-Châtel has been designed to achieve and to study high efficiencies. For many years, our theory group has been doing pioneer work on the “post-sideband regime” [1,2]. Continuous improvements of machine performance (Section 2) has allowed us to reach this regime experimentally at 23  $\mu\text{m}$  and the first results (Section 3) [3] confirm the prediction of a “universal brightness” of the FEL light above a certain efficiency threshold.

More recently, we lased with a new short-period wiggler ( $\lambda_w = 1.82$  cm) between 9 and 19  $\mu\text{m}$ . Details on its design will be given in Section 4. The first results show the same brightness behaviour at 11  $\mu\text{m}$  as that observed at 23  $\mu\text{m}$ .

### 2. Accelerator status

The ELSA FEL has already been described [4], so we will review here only recent improvements. The present – and not ultimate – operating parameters of ELSA are listed in Table 1. Up to now, the drive laser illuminated the photocathode at an angle of about 65°, producing important e-bunch edge effects for short pulses (15 ps) and large spot sizes (6 mm in diameter). A new laser injection

system at 0.5° has been installed recently. To reduce pulse fluctuations under 1% within the macropulse, a Pockels cell with a polarizer has been successfully tested and will be installed at the end of the drive laser table.

The CsK<sub>2</sub>Sb cathodes are routinely prepared with a quantum efficiency (QE) of 2–3%; however, due to the large residual pressure in the rf-gun cavity under operational conditions ( $5 \times 10^{-9}$  mbar), their lifetime is limited to 1–2 h. When running high charges ( $> 2$  nC), the cathode is moved back in the preparation chamber and heated up to 100°C for a few minutes: the QE is then at 30–50% of its initial value. A new 144 MHz cavity is under construction to improve significantly the photocathode lifetime.

Extensive transverse and longitudinal e-beam emittance measurements have been recently performed (cf. table 1). The transverse emittances are measured by means of the quad-scan technique at the exit of the linac and within the wiggler by means of the three-screens technique [5]. Longitudinal emittance measurements are performed by varying the rf phase and measuring the beam energy spread in the focal plane of the spectrometer [6], and the beam pulse length with a streak camera, detecting the Optical Transition Radiation (OTR) light emitted by a screen.

### 3. FEL operation at 20 $\mu\text{m}$

To check theoretical predictions on the spectral dynamics of a FEL, one ideally needs to have time-and-frequency-resolved photon spectra calibrated in units of

<sup>\*</sup> Corresponding author. Tel. +33 1 69 26 51 36, fax +33 1 69 26 62 18, e-mail guimbal@bruyeres cea.fr.

spectral efficiency (say in % per % bandwidth). Let us describe the actual implementation.

### 3.1. FEL light spectrometry

The FEL light is analysed by a 0.32 m grating spectrometer coupled with a slow pyroelectric 512-element array detector (Spiricon LP512) providing a spectrum integrated over the whole macropulse. The coverage is about 13% and the overall resolution is about 12 nm at 20  $\mu\text{m}$ , limited mainly by optics and not by the detector. It is close to the Fourier-transform limit due to the finite length of the micropulse. The video output of the detector is digitized on 11 bits and stored on disk. After some small calibration corrections, the moments of the spectra are easily deduced from these data. One problem arises from the strong water absorption lines in the 20  $\mu\text{m}$  region. They can locally alter the spectral profile but we checked they only slightly affect the rms width which is of primary concern for the brightness measurements discussed below. The next runs will no longer be affected by this problem because the optical diagnostics setup is now under dry atmosphere.

Another source of bias could be the macropulse integration of the spectra but, as the macropulse is quite long (typically 50–100  $\mu\text{s}$ ) compared to a few  $\mu\text{s}$  for the build-up, it should have only a negligible effect on the momenta as long as there is no collective drift of the spectrum at saturation. To overcome this limitation and to refine our analysis of the saturation, we are building a time-resolved photon spectrometer. Such a tool has not been implemented on many FELs. In the visible, one can use a synchroscan streak camera to obtain picosecond time resolution [7]. In the infrared, the Stanford group on the SCA has proposed an original way to obtain a single-pulse spectrum at 5  $\mu\text{m}$  [8]. We are presently exploring two ways: one where the time resolution is obtained by a fast spinning mirror, a counterpart of our electron spectrometer described below. The detector will be a pyroelectric 128  $\times$  128 focal plane. The time resolution should be a few  $\mu\text{s}$ . A more ambitious project is to use a 64-element HgCdTe array, each detector being connected to its own amplification/acquisition system. Because commercially available systems meeting our requirements are very expensive, we have developed our own acquisition boards. The system is presently under assembly and should run in the next months.

### 3.2. Time-resolved electron spectrometry

We have recently upgraded our electron spectrometer to provide time resolution within the macropulse (Fig. 1). On ELSA, the extraction of the electron beam from the optical cavity is done by a 150° magnet used as a spectrometer. The light of the OTR screen which lies in the spectrometer focal plane is deviated by a fast spinning mirror in a direction orthogonal to the energy axis and sent

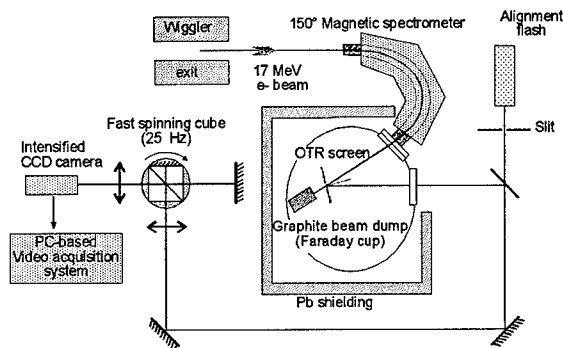


Fig. 1. Scheme of the time resolved electron spectrometer. The light reflected by the two mirrors above and on right of the spinning cube gives an extra electron spectrum on the CCD integrated over the macropulse.

to an intensified CCD camera. The energy and time resolutions depend on the focus of the electron beam at the entrance of the spectrometer. They are respectively about 0.2% and a few  $\mu\text{s}$ . By switching off the laser, we get the micropulse energy spread and average energy stability through the macropulse. Switching it on, we get the efficiency against time directly as the relative difference between the average electron energy at the beginning of the macropulse and within it (cf. Fig. 2).

Actually, for reasons of data storage and processing as well as insufficient energy range at efficiencies above 2%, electron spectra are not continuously acquired. Efficiency is therefore routinely extracted from optical data calibrated

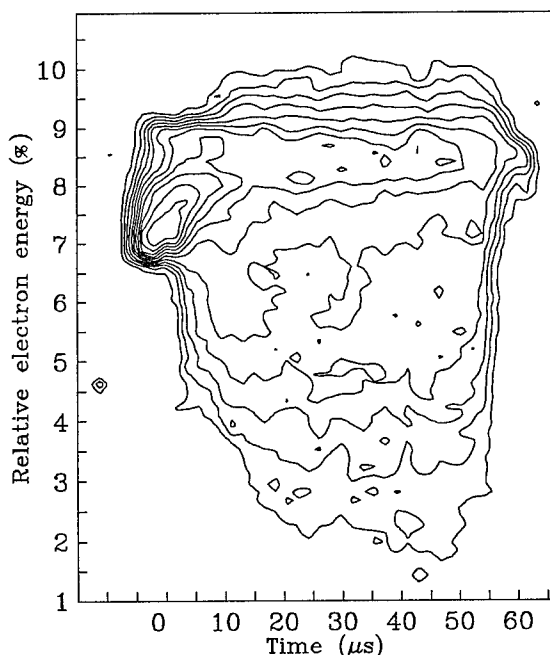


Fig. 2. Time resolved electron spectrum while lasing at 11  $\mu\text{m}$ .

against the electron beam energy loss. Indeed the link between the ELSA efficiency at saturation and the energy incident on the infrared Joulemeter involves numerous measurements and optical propagation simulations. The efficiency is deduced from the ratio, per bunch at saturation, of the laser energy divided by the electron beam energy. The latter is straightforwardly determined from a Faraday cup, while the photon micropulse energy is deduced from a HgCdTe detector (20 ns response time) whose response is calibrated by the Joulemeter after optical transport corrections. These corrections have been carefully measured using the electron spectrometer.

Nonetheless, we tried to check their consistency against the known characteristics of the optical setup. Therefore, we have computed the optical cavity efficiency defined as the ratio of the extracted laser power divided by the power produced by the FEL interaction. The simulations show an efficiency of about 20% at 20  $\mu\text{m}$ , a rather low value due to the small hole-outcoupled fraction compared to the mirrors reflection losses. These simulations have been checked by comparing predicted total losses against measured cavity ringdown in various conditions. Then the photon line transmission has been numerically evaluated and found between 35 and 45%, depending on the wavelength. This large attenuation comes mainly from one KRS-5 lens (respectively window) placed at normal incidence in front (respectively at the end) of the line. The overall transport correction has been found in rather good agreement with its determination by electron data.

### 3.3. First experimental evidence of an universal brightness

Due to improved machine operation, we routinely achieved efficiencies at 23  $\mu\text{m}$ , above 2%, our record

Table 1  
Parameters of the ELSA-FEL (for optical cavity and TRIA wiggler parameters, see Ref. [4])

| MONA wiggler parameters     |   |
|-----------------------------|---|
| Type                        | Halbach, 2 blocks/period  |
| Period                      | 18.2 mm   |
| Number of periods           | 34  |
| Maximum magnetic field      | 0.58 T for a 4 mm gap   |
| Main accelerator parameters |   |
| Photo-injector              | 0.53 $\mu\text{m}$ YAG laser<br>2 MV, 144 MHz rf-gun                          |
| Rf linac frequency          | 433 MHz   |
| Electron energy             | up to 18 MeV  |
| Normalized rms emittance    | 3 $\pi$ $\mu\text{m}$ at 0.2 nC, 10 A<br>5 $\pi$ $\mu\text{m}$ at 2 nC, 100 A |
| Longitudinal rms emittance  | 0.06 ps $\cdot$ MeV at 1 nC   |
| Micropulse repetition rate  | 14.4–72.2 MHz   |
| Micropulse duration         | 10–60 ps (magnetic compression)   |
| Micropulse charge           | up to 4 nC  |
| Macropulse repetition rate  | 0.5–2 Hz  |
| Macropulse duration         | up to 140 $\mu\text{s}$   |

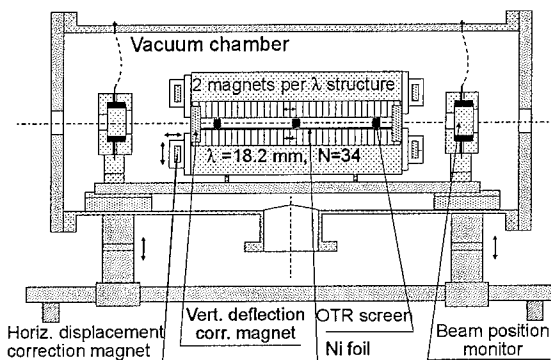


Fig. 3. Scheme of the MONA wiggler. The Nickel foil reduces the energy spread by wakefields inside the wiggler.

being well above 3%. The bunch charge was varied from 1 to 3 nC without any strong effect on the small signal gain which was about 100%. A possible explanation is the decompression of the bunch by space charge effects. Indeed we observed more recently a progressive increase of the pulse length at high bunch charge (exceeding 2 nC). During the runs at 23  $\mu\text{m}$ , the drive laser pulse width was about 20 ps but no measure of the e-pulse length was available. Because we forced a strong magnetic compression in the 180° bend before the wiggler by adjustment of the rf phase in the linac, the peak current for the lowest charge of 1 nC was probably close to 100 A. This hypothesis will be checked in the next runs.

Taking advantage of operation at high efficiency, we tried and verified the prediction of an asymptotic brightness of the FEL spectrum between 18 and 27  $\mu\text{m}$  [3]. To eliminate the effect of e-beam fluctuations from shot to shot on the analysis, the data recorded by several independent systems are labelled by a macropulse number and analyzed macropulse-by-macropulse. The results (cf. Fig. 1 in Ref. [1]) are in good agreement with the theoretical prediction within the limit of experimental error bars (15%). Similar results, at lower efficiency, have been more recently obtained with our new short-period wiggler.

## 4. The MONA wiggler

At the maximum energy of the ELSA accelerator and with our standard TRIA wiggler (see Table 1), our minimum operating wavelength is 18  $\mu\text{m}$ . To lase between 10 and 20  $\mu\text{m}$  on the fundamental and to reach 4  $\mu\text{m}$  on the third harmonic, we built a new short-period wiggler (Fig. 3).

One constraint was to re-use magnets designed for TRIA. The fundamental cell of the TRIA structure [9] is made by one vanadium-permendum pole fed by a stack of 3 SmCo magnets of increasing width from the inner one (close to the gap) to the outer one. The most simple way to reduce the period was “to remove the poles and the two

outer magnets of each triplet''. Thus the period is reduced from 32 to 18.2 mm. This leads to a two blocks/period Halbach structure, very similar to the one adopted by the Los Alamos group to lase in the UV [11]. One difference is that, because of the rectangular section of our magnets ( $9 \times 19 \text{ mm}^2$ ), we had no choice for the direction of magnetization, which is along the wiggler axis.

Because the magnetic harmonics above the third are negligible for the gaps of interest, the wiggler field can be written as:

$$B = (1 - \rho)B_{\max} \cos(k_w z) + \rho B_{\max} \cos(3k_w z + \phi).$$

First calculations with our 2D multifrequency code SPECTRE [10] showed that, for a given total magnetic field  $B_{\max}$  and  $\phi = 0$ , the gain on the third FEL harmonic was rather insensitive to the  $\rho$  value in the range 0–0.3. The expected  $\rho$  value for the 4 mm minimum gap is 0.08. Further simulations have included the effect of the relative phase  $\phi$  without showing any marked dependence with this parameter ( $\phi = 0$  in our case;  $\phi = \pi/2$  corresponds to the case where magnetization is transverse).

Because the MONA wiggler is under vacuum and because it has no flexible tuning possibility, we paid particular attention to the characterization and pairing of its SmCo magnets. In a first step, we carefully measured with Helmholtz coils and a high precision integrating voltmeter, the three components of the magnetic moment  $M$  of each block. The procedure involved five successive four-quadrants rotations of the block placed in different configurations, controlled by a stepper motor. Incorrect handling and voltmeter drifts were detected by the redundancy of the data. Because the complete characterisation of 200 blocks requires several days, the variation of  $M$  with the room temperature has been checked and found to be on the order of  $500 \pm 50 \text{ ppm K}^{-1}$  depending on the block. Total random errors are estimated to be less than 5 parts in 10 000.

Partial demagnetization is another critical issue. We estimated it with the same setup by measuring several magnets one-by-one and then grouped by pairs or by triplets in colinear or opposing configuration. Curiously, the additivity seemed better verified in the opposing configuration which is more representative of the actual assembly (10–20 parts in 10 000) than in the colinear configuration. Because full calculation of the field of a Halbach wiggler is easy, we did the final sort by a computer program with the criterion of a straight electron trajectory inside the wiggler. With these simulations, we also designed correction magnets compensating the well-known horizontal walk-off of the trajectory to keep the beam perfectly on axis.

After assembly, the field on axis has been measured with a Hall probe and final equalization of the magnetic field at the 0.3% level was done with small iron shunts put on top of the blocks (two complementary configurations were necessary to do all the corrections). The straight e-beam trajectory on the three OTR screens inside the wiggler and the FEL small signal gain measurements showed that the method used is dependable. Nonetheless, compared to the pulsed-wire technique [11], it requires time, numerous high precision measurements and offers (as we unpurposely demonstrated once during the first runs) some opportunities for errors.

Lasing has been obtained between 9  $\mu\text{m}$  with the maximum energy of 18 MeV, and 19  $\mu\text{m}$ , thus making the link with the TRIA lasing range. For longer wavelengths, the rapid increase of diffraction losses and decrease of the hole extraction efficiency prevent proper operation. At 11  $\mu\text{m}$ , data taken along a detuning curve have shown the same 0.8 high-efficiency limit for the brightness as we observed with TRIA (cf Fig. 2 in Ref. [1]). A first attempt to lase on the third harmonic at 4  $\mu\text{m}$  with a 6 mm gap has been unsuccessful. Calculations showed that a small signal gain of 100% on the fundamental and an adequate aperture suppress it, would be necessary. These conditions should be met in our next runs with a 4 mm gap.

## References

- [1] P. Chaix and Ph. Guimbal, these Proceedings (16th Int. Free Electron Laser Conf., Stanford, CA, USA, 1994) Nucl. Instr. and Meth. A 358 (1995) 96.
- [2] P. Chaix et al., Phys. Rev. E 48 (1993) R 3259.
- [3] D. Iracane, V. Fontenay, Ph. Guimbal, S. Joly, S. Striby and D. Touati, Phys. Rev. Lett. 72 (1994) 3985.
- [4] Ph. Guimbal, S. Joly et al., Nucl. Instr. and Meth. A 341 (1994) 43 and references therein.
- [5] A. Loulergue et al., Transverse and longitudinal emittance measurements in the ELSA linac, Proc. 4th Int. EPAC Conf., London, UK, 1994.
- [6] S. Joly et al., Brightness measurements of the ELSA electron beam, Proc. Linac-94 Conf., Tsukuba, Japan, Aug. 1994.
- [7] A.H. Lumpkin et al., Nucl. Instr. and Meth. A 296 (1990) 134.
- [8] W.P. Leemans, J.A. Edighoffer and R.L. Swent, Nucl. Instr. and Meth. A 341 (1994) 473.
- [9] A. Binet et al., Nucl. Instr. and Meth. A 304 (1991) 707.
- [10] D. Iracane, D. Touati and P. Chaix, Nucl. Instr. and Meth. A 341 (1994) 220.
- [11] R.W. Warren and C.M. Fortgang, Nucl. Instr. and Meth. A 341 (1994) 444.



ELSEVIER

## Free-electron laser oscillation with a multibunch electron beam of the 38 MeV L-band linear accelerator at ISIR

S. Okuda <sup>a,\*</sup>, Y. Honda <sup>a</sup>, N. Kimura <sup>a</sup>, J. Ohkuma <sup>a</sup>, T. Yamamoto <sup>a</sup>, S. Suemine <sup>a</sup>,  
T. Okada <sup>a</sup>, S. Ishida <sup>a</sup>, T. Yamamoto <sup>a</sup>, S. Takeda <sup>b</sup>, K. Tsumori <sup>a,1</sup>, T. Hori <sup>a,2</sup>

<sup>a</sup> Radiation Laboratory, The Institute of Scientific and Industrial Research, Osaka University, 8-1 Mihogaoka, Ibaraki, Osaka 567, Japan

<sup>b</sup> National Laboratory for High-Energy Physics, 1-1 Oho, Tsukuba, Ibaraki 305, Japan

### Abstract

Free-electron laser oscillation has been achieved with a multibunch electron beam generated with the 38 MeV L-band linear accelerator at The Institute of Scientific and Industrial Research in Osaka University. The wavelengths of the observed FEL are 32 to 40  $\mu\text{m}$  for energies of the electron beams of 17 to 19 MeV. The macropulse length of the beam is 1.8  $\mu\text{s}$ . The net FEL gain measured at a wavelength of 40  $\mu\text{m}$  is 25%. The tuning range of the length of the optical cavity and the FEL spectra have also been measured. The total output FEL energy of 12 mJ has been obtained in the recent experiments at a wavelength of 40  $\mu\text{m}$ . The intracavity peak power of the FEL is estimated to be about 150 MW.

### 1. Introduction

The high-brightness single-bunch electron beam generated with the 38-MeV L-band (1300 MHz) electron linear accelerator (linac) at The Institute of Scientific and Industrial Research (ISIR) [1] has been used for analyzing transient phenomena induced by radiation. In the experiments of free-electron lasers (FELs) self-amplified spontaneous emission from the single-bunch beam has been observed at wavelengths of 20 and 40  $\mu\text{m}$  [2].

The ISIR linac has been optimized for generating the single-bunch beam. In order to generate a multibunch beam necessary for FEL oscillation experiments the operational conditions of the rf components of the linac have been investigated [3,4]. After some improvements of the components of the linac oscillation experiments have been performed. The first FEL oscillation has been achieved in March to April 1994 at wavelengths of 32 to 40  $\mu\text{m}$  and in the very recent experiments considerably higher output FEL energy has been obtained at a wavelength of 40  $\mu\text{m}$ . In this article the optical performance of the FEL measured in these experiments are presented.

### 2. Accelerator system and the operational conditions

The ISIR linac is equipped with a high-current electron gun, three subharmonic prebunchers (SHPBs), fundamental bunchers, and an accelerating waveguide 3 m long. The SHPBs consist of two at the twelfth subharmonic of the fundamental rf frequency and one at the sixth.

A small-sized (8 mm diameter) circular gun cathode is used in the present experiments, with which the emittance of the accelerated beam is reduced to half of the previous one. A pulsed electron beam with a pulse length of 4  $\mu\text{s}$  is injected from the gun at a peak current of 600 mA. The first SHPB is not operated. The second and the third ones are operated at relatively low powers compared with the case for generating a single-bunch beam. The parameters of the multibunch beam thus obtained are listed in Table 1. The macropulse length of the accelerated beam is 4  $\mu\text{s}$ . The latter part in the beam macropulse, which has a pulse length of 1.8  $\mu\text{s}$  and an energy spread of 1.8% in FWHM, is selected with a beam slit and is transported to the optical cavity. The pulse length is 49 times as long as the round-trip time of a FEL in the optical cavity. The details of the accelerator system and the beam conditions are described in Ref. [5].

### 3. Experimental

The experimental setup is schematically shown in Fig. 1. The electron beam is transported with a doubly achromatic beam-bend to the optical cavity. There are three

\* Corresponding author. Tel +81 6 879 8511, fax +81 6 875 4346.

<sup>1</sup> Present address: Harima Laboratory, Sumitomo Electric Industries Corp., Akoh, Hyogo, Japan.

<sup>2</sup> Present address: Spring-8 Project Team, Japan Atomic Energy Research Institute, Ibaraki, Japan.

Table 1  
The parameters of the multibunch beam

| <i>Electron Beam</i>    |                   |
|-------------------------|-------------------|
| Energy                  | 17–19 MeV         |
| Accelerator frequency   | 1300 MHz          |
| Micropulse spacing      | 9.2 ns            |
| Charge/micropulse       | 2 nC              |
| Peak current/micropulse | 50 A              |
| Micropulse length       | 30–40 ps          |
| Macropulse length       | 1.8 $\mu$ s       |
| Energy spread           | 1.8–2%            |
| Normalized emittance    | 200 $\pi$ mm mrad |

beam-current monitors and six beam-profile monitors with ceramic plates. Three of those profile monitors are placed in the wiggler gap. The diameter of the electron beam is about 5 mm in the wiggler. The axis of the electron beam shifts by 2 mm in the wiggler fields at a wavelength of 40  $\mu$ m. A diagnostic system with a He–Ne laser is installed in order to monitor the tilting of the optical cavity mirror. The optical path of the output FEL to the detector is indicated with the laser. Two spherical Au-coated Cu mirrors form the optical cavity. As for the output mirror the angles of tilt and the position on the axis of the cavity are remotely controlled with stepping motors. However, in the present experiments the angles have not been changed during the oscillation experiments. The parameters of the FEL and the optical cavity are listed in Table 2.

The FEL output window is a KRS-5 plate 5 mm thick which has a transmittance of 42% at a wavelength of 40  $\mu$ m. The sensitivity of the liquid-He-cooled Ge:Be detector used for the measurements has been evaluated with a blackbody light source and the incoherent spontaneous emission from a multibunch beam passing through a wiggler. The time resolution of the detector is 3  $\mu$ s. It is too long to observe the time structure of the output FEL. Instead of measuring the time structure directly, the FEL energy is measured by changing the macropulse length of the electron beam. In this case the pulse length of the electron beam injected from the gun is changed. By using Au-coated plane and concave mirrors the output FEL is

Table 2  
The parameters of the FEL and the optical cavity

| <i>Wiggler</i>                           |               |
|--|---------------|
| Magnet                                   | Nd–Fe–B       |
| Length                                   | 1920 mm       |
| Period                                   | 60 mm         |
| <i>K</i>                                 | 1             |
| <i>Optical</i>                           |               |
| Wavelengths                              | 32–40 $\mu$ m |
| Cavity length                            | 5532 mm       |
| Mirror concave radii of curvature        |               |
| M1                                       | 3384 mm       |
| M2 (for output)                          | 2763 mm       |
| Hole radius                              | 0.5 mm        |
| Rayleigh range (at 40 $\mu$ m)           | 915 mm        |
| Radius at wiggler center (at 40 $\mu$ m) | 3.4 mm        |

transported to the detector placed out of the accelerator room through pipes filled with dry nitrogen gas. The intensity of the FEL is attenuated with teflon sheets for detection. The transmittance of the FEL through the sheets and the FEL output window are measured with the output FEL.

#### 4. Results

Fig. 2 shows the dependence of the total FEL energy measured for one beam macropulse at a wavelength of 40  $\mu$ m, on the length of the optical cavity. The width of this tuning curve is relatively large compared with those for the other FEL facilities (a few tens of micrometers in most cases). This can be attributed to the relatively small total number of amplification of the FEL with the electron bunches in the present case. The energy of the FEL emitted from the output mirror of the optical cavity is evaluated by taking into account the transmittance of the output window and the loss in the optical path. The total output FEL energy for one beam macropulse thus obtained is 0.03  $\mu$ J at the cavity length of the best tuning. For about the same conditions the total FEL energy measured for one

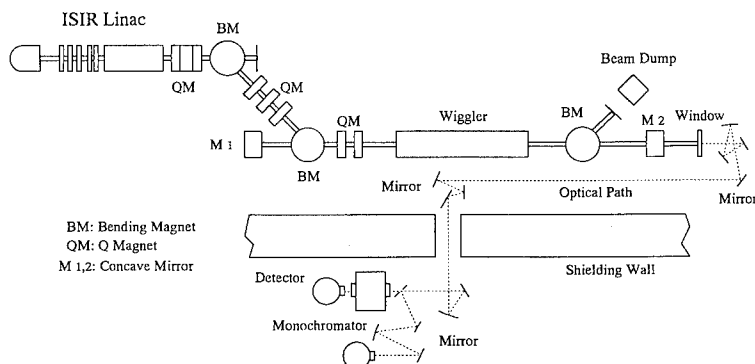


Fig. 1. Schematic diagram of the experimental setup.

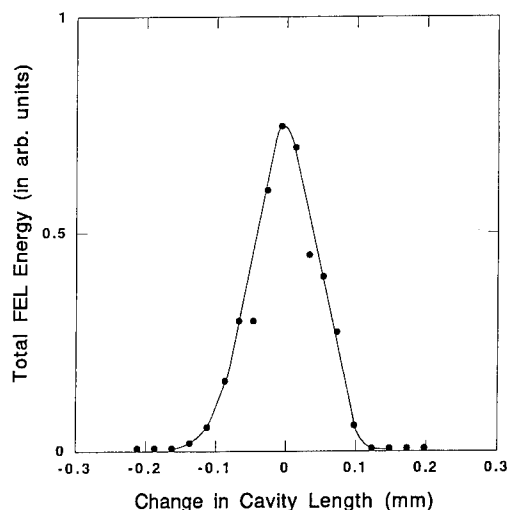


Fig. 2. The dependence of the total FEL energy measured for one beam macropulse, on the length of the optical cavity at a wavelength of 40  $\mu\text{m}$ .

beam macropulse is plotted versus the macropulse length of the electron beam in Fig. 3. The net FEL gain given from the inclination of this curve is 25%. Near the end of the beam macropulse the beam current is slightly lower than the average.

The spectrum of the FEL measured at a wavelength of 33  $\mu\text{m}$  at a total output FEL energy for one beam macropulse of about 0.03  $\mu\text{J}$  is shown in Fig. 4. The width of the spectrum is 1.3% in FWHM. The spectral width of the incoherent spontaneous emission estimated from the

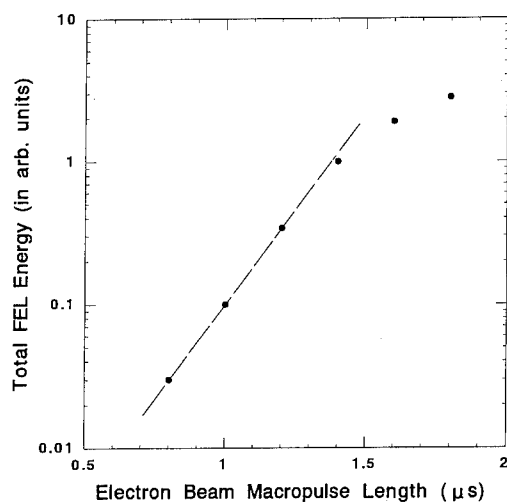


Fig. 3. The dependence of the total FEL energy measured for one beam macropulse, on the length of the beam macropulse at a wavelength of 40  $\mu\text{m}$ .

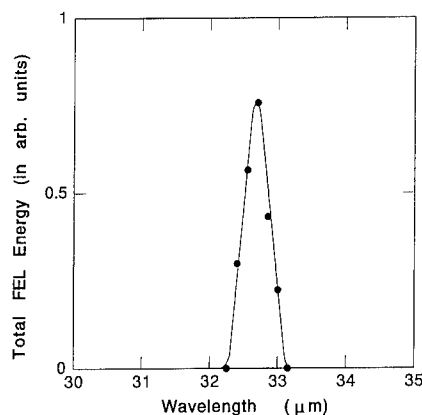


Fig. 4. The spectrum of the FEL measured at a wavelength of 33  $\mu\text{m}$ .

energy spread of the electron beam and the diameter of the beam in the wiggler is 4.0%.

In the first oscillation experiments the highest values of total output FEL energies measured for one beam macropulse have been 0.5 to 2  $\mu\text{J}$  for wavelengths of 32 to 40  $\mu\text{m}$ . Since the micropulse length of the FEL and the loss of the FEL in the optical cavity have not been measured, the peak power of the FEL in the micropulse is not known. Assuming the micropulse length of 30 ps and the loss of 1%, the maximum intracavity peak powers of the FELs are estimated to be about 3 to 10 kW for wavelengths of 32 to 40  $\mu\text{m}$ . In this case the loss and the peak power might be underestimated.

In the recent experiments a total output FEL energy for one beam macropulse of 12 mJ has been obtained at a wavelength of 40  $\mu\text{m}$  by changing the operational conditions of the rf components of the accelerator system. From this result the intracavity peak power is estimated to be 150 MW for the same assumptions as described before. The micropulse shape of the electron beam and the ratio of the satellite electron bunches have not been measured in the experiments. The characterization of the electron beams in these conditions and the time-resolved measurements of output FELs are under preparation.

## 5. Possible wavelengths of FELs

Most of the FEL user facilities are based on S-band linacs. The charge of electrons in a beam micropulse is about 2 nC in the present experiments. Such a large charge, which provides a relatively high FEL gain, is a feature of an L-band linac. The maximum FEL wavelength is limited by the slippage between the electron beam and the FEL micropulse in a wiggler. It is estimated to be a few hundreds of micrometers in the present beam parameters. This suggests that a relatively wide tuning range of FEL wavelengths is possible.



## 6. Conclusions

Oscillation of a FEL has been achieved with a multi-bunch electron beam of the ISIR L-band linac. The optical characteristics of the FELs have been measured. The total output FEL energies measured for one beam macropulse and the estimated intracavity peak powers of the FELs are 0.5 to 2  $\mu\text{J}$  and 3 to 10 kW for wavelengths of 32 to 40  $\mu\text{m}$ . In the recent experiments the total output energy of 12 mJ has been observed at 40  $\mu\text{m}$ . In this case the intracavity peak power has been estimated to be 150 MW.

## Acknowledgements

The authors wish to thank Prof. S. Takamuku and Prof. S. Tagawa for important suggestions to the present work.

## References

- [1] S. Takeda, K. Tsumori, N. Kimura, T. Yamamoto, T. Hori, T. Sawai, J. Ohkuma, S. Takamuku, T. Okada, K. Hayashi and M. Kawanishi, IEEE Trans. Nucl. Sci. NS-32 (1985) 3219.
- [2] S. Okuda, J. Ohkuma, N. Kimura, Y. Honda, T. Okada, S. Takamuku, T. Yamamoto and K. Tsumori, Nucl. Instr. and Meth. A 331 (1993) 76.
- [3] S. Okuda, K. Tsumori, J. Ohkuma, N. Kimura, T. Yamamoto, T. Hori and S. Takamuku, Nucl. Instr. and Meth. A 318 (1992) 81.
- [4] S. Okuda, J. Ohkuma, N. Kimura, Y. Honda, T. Okada, S. Takamuku, S. Ishida, T. Yamamoto and K. Tsumori, Nucl. Instr. and Meth. A 331 (1993) 73.
- [5] S. Okuda, Y. Honda, N. Kimura, J. Ohkuma, T. Yamamoto, S. Suemine, T. Okada, S. Takeda, K. Tsumori and T. Hori, these Proceedings (16th Int. Free Electron Laser Conf., Stanford, CA, USA, 1994) Nucl. Instr. and Meth. A 358 (1995) 248.



ELSEVIER

# Single-bunch and multibunch electron beam generation for FEL experiments with the 38 MeV L-band linear accelerator at ISIR

S. Okuda <sup>a,\*</sup>, Y. Honda <sup>a</sup>, N. Kimura <sup>a</sup>, J. Ohkuma <sup>a</sup>, T. Yamamoto <sup>a</sup>, S. Suemine <sup>a</sup>,  
T. Okada <sup>a</sup>, S. Takeda <sup>b</sup>, K. Tsumori <sup>a,1</sup>, T. Hori <sup>a,2</sup>

<sup>a</sup> Radiation Laboratory, The Institute of Scientific and Industrial Research, Osaka University, 8-1 Mihogaoka, Ibaraki, Osaka 567, Japan

<sup>b</sup> National Laboratory for High-Energy Physics, 1-1 Oho, Tsukuba, Ibaraki 305, Japan

## Abstract

The generation of multibunch electron beams used for FEL oscillation experiments with the 38 MeV L-band linear accelerator at The Institute of Scientific and Industrial Research has been studied. Originally, the components of the accelerator system have been optimized for generating a high-brightness single-bunch beam. The operational conditions of the system have been investigated for a multibunch beam. A multibunch beam with a macropulse length of 4  $\mu$ s has been accelerated at energies of 17 to 19 MeV. The latter part of the pulsed beam with a length of 1.8  $\mu$ s has an energy spread of 1.8%. The charge per bunch is 2 nC. The beam of this part has been successfully used for oscillation experiments at a wavelength of 32 to 40  $\mu$ m.

## 1. Introduction

The 38 MeV L-band (1300 MHz) linear accelerator (linac) of The Institute of Scientific and Industrial Research (ISIR) in Osaka University was constructed in 1978 for generating high-brightness single-bunch electron beams. After the improvement of a subharmonic-prebuncher (SHPB) system, the charge of electrons in the single-bunch beam increased up to a maximum of 67 nC in [1]. The electron beams have been applied to analyzing transient phenomena induced by irradiation. Many beam modes are also available for a variety of basic researches.

In the experiments for free-electron lasers (FELs), self-amplified spontaneous emission (SASE) has been observed at wavelengths of 20 and 40  $\mu$ m [2]. For amplifying the radiation with two different electron bunches succeeding, a high-brightness two-bunch electron beam has been generated [3]. The conditions for generating the beam are being investigated.

For the accelerator system, optimized to generate the single-bunch beam, the operational conditions of the com-

ponents of the system have been investigated to generate the multibunch beam necessary for FEL oscillation experiments [4]. After the improvement of the beam characteristics and the measurement of the spontaneous emission [5], oscillation experiments have been performed [6].

In this article the operational conditions of the ISIR linac for generating single-bunch and multibunch beams and the beam characteristics of multibunch beams used for the FEL experiments are presented.

## 2. Accelerator system

The accelerator system of the ISIR linac is schematically shown in Fig. 1. The parameters of the linac are listed in Table 1. The linac is equipped with a high-current 120-keV triode gun, three SHPBs (two at the twelfth subharmonic of the fundamental and one at the sixth), fundamental bunchers and a 3 m long accelerating waveguide.

For generating a single-bunch beam, a high-current electron gun (Model 12, ARCO) is used. The diameter of the gun cathode is 51 mm. This gun is also used for the ordinary operations. Another gun has a small-sized cathode with an area of 0.5 cm<sup>2</sup> (Y-646B, EIMAC), which is used for generating the multibunch beam in FEL oscillation experiments. The pulse lengths of the injected beams are 3 ns to 4  $\mu$ s. In the case of the single-bunch beam the peak voltage for the grid pulser is about 2 kV maximum. A new

\* Corresponding author. Tel. +81 6 879 8511, fax +81 6 875 4346.

<sup>1</sup> Present address: Harima Laboratory, Sumitomo Electric Industries Corp., Akoh, Hyogo, Japan.

<sup>2</sup> Present address: Spring-8 Project Team, Japan Atomic Energy Research Institute, Ibaraki, Japan.

Table 1  
Parameters of the ISIR linac

|                                   |                        |
|-----------------------------------|------------------------|
| Accelerator frequency             | 1300 MHz               |
| Maximum energy                    | 38 MeV                 |
| Accelerating waveguide            |                        |
| Type                              | travelling wave        |
| Length                            | 3 m                    |
| Rf power                          | 20 MW                  |
| Filling time                      | 2 $\mu$ s              |
| Injector                          |                        |
| High voltage                      | 120 kV                 |
| SHPB (rf frequency, rf power)     |                        |
| The first                         | 108 MHz, 20 kW         |
| The second                        | 108 MHz, 20 kW         |
| The third                         | 216 MHz, 20 kW         |
| Bunchers (rf frequency, rf power) | 1300 MHz, 5 MW (total) |

Table 2

Operational conditions of the accelerator components for generating the single-bunch and the multibunch beams

|                  | Beam mode    |            |
|------------------|--------------|------------|
|                  | Single-bunch | Multibunch |
| Electron gun     |              |            |
| Cathode          | Model 12     | Y646B      |
| Pulse length     | 4.5 ns       | 4 $\mu$ s  |
| Energy           | 100 kV       | 100 kV     |
| Peak current     | 10–30 A      | 0.5–0.8 A  |
| SHPB power level |              |            |
| The first        | 50–100%      | 0%         |
| The second       | 50–100%      | 50%        |
| The third        | 50–100%      | < 10%      |

pulsar has been developed for the two-bunch beam. A burst-mode gun pulsar is being developed.

The SHPB has a coaxial single-gap cavity at one end of the inner conductor. Pulsed rf of 20  $\mu$ s duration is supplied to the SHPB by three 20 kW rf amplifiers independently. An electron beam injected from the gun to the first SHPB at a pulse length shorter than 4.5 ns forms a single-bunch beam.

The accelerating waveguide is driven by a 20 MW L-band klystron (TV-2022B, Thomson-CSF), and the pre-buncher. Two bunchers are driven by a 5 MW L-band klystron (E3775A, Toshiba). The ripple on the flat-top of the klystron-current pulse has been minimized to be smaller than 0.3% by adjusting the pulse-forming network of the modulator, to meet the requirements of the FEL oscillation experiments. The lengths of the rf pulse on the flat-top for the 5 and the 20 MW klystrons are 3.2 and 3.9  $\mu$ s, respectively. The maximum beam energy is 38 MeV for no beam-loading.

### 3. Operational conditions of the linac

When the SHPBs are not operated, a multibunch beam consisting of electron bunches with an interval of 770 ps is generated. The beam is being used for ordinary experiments at a pulse length of 3 ns to 4  $\mu$ s. More complicated

operational conditions required for generating the single-bunch, the two-bunch and the multibunch beams by using the SHPBs are listed in Table 2. In this case the pre-buncher and the buncher are operated in the ordinary conditions.

When a long-pulse beam is injected from the gun to the SHPBs, a multi-bunch beam is generated at a micropulse spacing corresponding to the rf period of the SHPB at the twelfth subharmonic (9.2 ns). The injection currents from the gun are generally 500–800 mA. The results for the calculation shows that one twelfth SHPB effectively forms the multi-bunch beam because the space-charge effect is considerably smaller compared with that of the single-bunch beam. In the present case the first SHPB is not operated. In the cavity of the third SHPB a rf field is induced. So as to keep the rf field nearly constant over the macropulse duration, the timing, the power and the phase of the rf supplied to the third SHPB are controlled. The details of the procedure are described in Ref. [4]. Such a control has given a relatively uniform micropulse train over the macropulse of the electron beam.

The length on the flat-top of the rf pulse is 3.9  $\mu$ s for acceleration and is 3.2  $\mu$ s for the bunchers. The ends of these rf pulses have been made to agree. In order to use the relatively long pulse-length of the electron beam, the injection from the gun has been started at the beginning of the rf pulses.

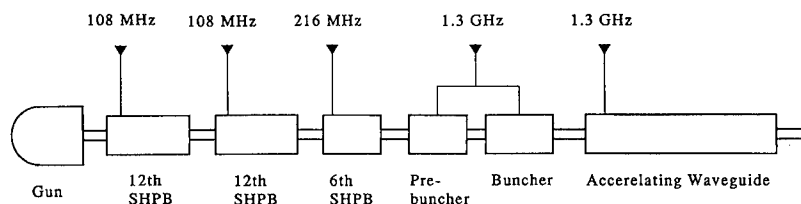


Fig. 1. Schematic diagram of the ISIR linac.

Table 3

Parameters of the multibunch beam used for the oscillation experiments

|                      | Beam mode                   |                               |
|----------------------|-----------------------------|-------------------------------|
|                      | Single-bunch                | Multibunch                    |
| Charge/micropulse    | 67 nC                       | 2 nC                          |
| Micropulse length    | 20–50 ps                    | 30–40 ps                      |
| Micropulse spacing   | —                           | 9.2 ns                        |
| Macropulse length    | —                           | 1.8 $\mu$ s (4 $\mu$ s total) |
| Repetition           | 1–720 s <sup>-1</sup>       | 1–360 s <sup>-1</sup>         |
| Energy spread        | 0.7–2.5%                    | 1.8%                          |
| Normalized emittance | 400 $\pi$ mm mrad (average) | 200 $\pi$ mm mrad             |

#### 4. Beam characteristics

The characteristics of the single-bunch and the multibunch beams of the ISIR linac measured are listed in Table 3. The energy spread of the single-bunch beam has a minimum value at a charge of electrons in a bunch of 33 nC. At higher charges the energy spread increases with the charge.

Fig. 3 shows a typical waveform of the multibunch beam at an energy of 17.1 MeV which corresponds to a FEL wavelength of 40  $\mu$ m in the experiments at ISIR, observed with a beam current monitor placed after the accelerating waveguide. The injection current at the gun is 600 mA. The macropulse length is 4  $\mu$ s, as shown in this figure. Some irregularity is observed in the early part of the waveform. The energy spectrum of the multibunch

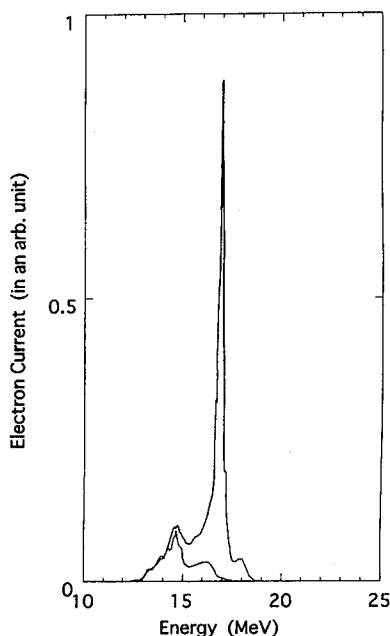
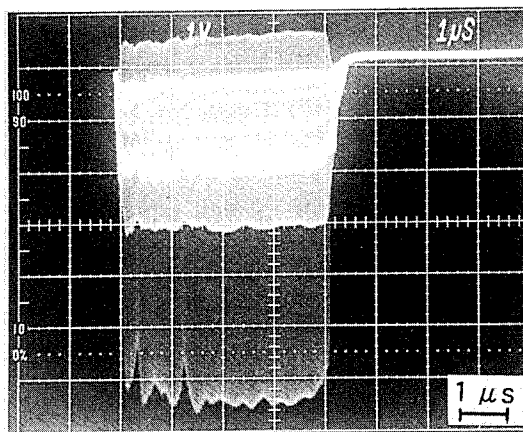
Fig. 2. The energy spectra of the multibunch (2 and 4  $\mu$ s) beams.

Fig. 3. A typical waveform of the multibunch beam measured with a beam current monitor.

beam is shown in Fig. 2. It is divided into two parts, one for a pulse length of 2  $\mu$ s and another for 4  $\mu$ s. This spectrum shows that the early part of the beam with a pulse length of 2  $\mu$ s is not available for the oscillation experiments. In the experiments the latter part with a length of 1.8  $\mu$ s has been selected with a beam slit and has been transported to a FEL optical cavity. The macropulse length is about 50 times longer than the FEL round-trip time in the optical cavity. The length of the rf pulse for the fundamental bunchers on the flattop is shorter than that for the accelerating waveguide. In the early part of the accelerated beam the rf power for the bunchers is relatively low, being deviated from the flattop. The energy spread and the relatively irregular waveform shown in Fig. 3 in the early part can be attributed to the relatively low buncher-power and the distribution of the beam energy due to the acceleration within the rf filling time and to the beam-loading effect.

The emittance of the electron beam has been measured by monitoring the beam profiles while focusing the beam with  $Q$ -magnets. By using the smaller cathode for the electron gun the beam emittance has been improved. The emittance is expected to be improved furthermore by reducing the distance between the gun and the first SHPB.

The micropulse shape of the multibunch beam has been measured with a streak camera. In this measurement the Cherenkov light emitted from the beam passing in air has been observed. The micropulse length strongly depends on the conditions of the bunchers, affecting the FEL gain. However, the micropulse shape has not been measured during the oscillation experiments.

When the injection current of the electron gun increases to above 600 mA, the energy spread and the total charges of the satellite bunches also increase. This is probably due to the beam-loading effect for acceleration, which decreases the length of the beam macropulse used for FEL oscillation.

## 5. Application of the multibunch beam to the FEL oscillation experiments

The multibunch beam generated with the ISIR linac has been used for FEL oscillation experiments. Oscillation has been achieved at wavelengths of 32–40  $\mu\text{m}$  and the intracavity peak power of the FEL has been estimated to be 150 MW at a wavelength of 40  $\mu\text{m}$  [6]. In the experiments the maximum obtainable beam energy is about 25 MeV which corresponds to a FEL wavelength of 20  $\mu\text{m}$ . For the shorter wavelengths the burst-mode injection is necessary. Because the round-trip time of the optical cavity is four times as long as the micropulse spacing of the electron beam in the oscillation experiments at ISIR, the beam-loading can be decreased to 25% by doing the burst-mode injection. However, in this case the operational conditions of the SHPBs become more complicated.

## 6. Summary

The operational conditions of the components of the ISIR linac, which has been optimized for generating the high-brightness single-bunch beam, have been investigated for generating the multibunch beam necessary for FEL oscillation experiments. The multibunch beam with a macropulse length of 4  $\mu\text{s}$  has been accelerated at energies

of 17 to 19 MeV. The latter part of the beam with a length of 1.8  $\mu\text{s}$  has an energy spread of 1.8%. The charge per bunch is 2 nC. The beam in this part has been successfully used for oscillation experiments at wavelengths in the range from 32 to 40  $\mu\text{m}$ .

## References

- [1] S. Takeda, K. Tsumori, N. Kimura, T. Yamamoto, T. Hori, T. Sawai, J. Ohkuma, S. Takamuku, T. Okada, K. Hayashi and M. Kawanishi, IEEE Trans. Nucl. Sci. NS-32 (1985) 3219.
- [2] S. Okuda, J. Ohkuma, N. Kimura, Y. Honda, T. Okada, S. Takamuku, T. Yamamoto and K. Tsumori, Nucl. Instr. and Meth. A 331 (1993) 76.
- [3] S. Okuda, J. Ohkuma, S. Suemine, S. Ishida, T. Yamamoto, T. Okada and S. Takeda, Nucl. Instr. and Meth. A 341 (1994) 59.
- [4] S. Okuda, K. Tsumori, J. Ohkuma, N. Kimura, T. Yamamoto, T. Hori and S. Takamuku, Nucl. Instr. and Meth. A 318 (1992) 81.
- [5] S. Okuda, J. Ohkuma, N. Kimura, Y. Honda, T. Okada, S. Takamuku, S. Ishida, T. Yamamoto and K. Tsumori, Nucl. Instr. and Meth. A 331 (1993) 73.
- [6] S. Okuda, Y. Honda, N. Kimura, J. Ohkuma, T. Yamamoto, S. Suemine, T. Okada, S. Ishida, T. Yamamoto, S. Takeda, K. Tsumori and T. Hori, these Proceedings (16th Int. Free Electron Laser Conf., Stanford, CA, USA, 1994) Nucl. Instr. and Meth. A 358 (1995) 244.



ELSEVIER

## Wavelength shifting in the Stanford FEL ☆

A. Marziali \*, T.I. Smith, H.A. Schwettman

*Stanford Picosecond FEL Center, W.W. Hansen Experimental Physics Laboratory, Stanford University, Stanford, CA 94305-4085, USA*

### Abstract

The time evolution of FEL wavelength in response to small perturbations of the electron energy was measured in the Stanford FEL for a range of operating parameters. The dependence of the wavelength response on the cavity  $Q$ , desynchronism, and electron pulse length was also measured. A simple model of the wavelength shifting mechanism is presented which explains the observed behavior.

### 1. Introduction

Since its realization in 1976 [1], the Free Electron Laser (FEL) has become widely used as a scientific instrument [2]. In such use, the requirements for optical beam quality and stability are stringent. One of these requirements is stability of the FEL wavelength to a small fraction of the optical spectral width. Though this requirement has been met [3] by negative feedback from the optical beam wavelength to the electron beam energy, the dynamic behavior of the FEL wavelength during electron energy changes has not been well understood. In this paper, we present time dependent measurements of the FEL wavelength following sudden changes in electron beam energy. We also present a model of FEL wavelength shifting which provides insight into the observed behavior.

### 2. A simple model for FEL wavelength shifting

A simple model of the wavelength shifting mechanism for short pulse FELs can be generated by considering the evolution of the optical pulse. The FEL resonance condition states that the electron bunch must slip back over the optical field by one optical wavelength each wiggler period. Thus, as the two pulses travel the length of the wiggler, the electron bunch slips backward with respect to the optical pulse by a distance  $N\lambda$  where  $N$  is the number of wiggler periods and  $\lambda$  is the optical wavelength. Since the electrons must be bunched by the optical field before they can efficiently exchange energy into the field, slip-

page leads to preferential optical gain near the trailing edge of the pulse. This effect, known as lethargy, reduces the effective group velocity of the optical pulse. To compensate for this, the FEL cavity length must be slightly detuned from resonance. This detuning, also referred to as desynchronism, shortens the round trip time of the optical pulse in the laser cavity such that, in a reference frame that is co-moving and synchronized with the electron bunches, the optical pulse is moved forward with respect to the electron bunch by a small distance each pass.

As a result of slippage and desynchronism, on each pass there are electrons at the back of the optical pulse which spontaneously radiate into a region of low optical energy. This spontaneous optical field is moved forward into the electron pulse by desynchronism on subsequent passes and is amplified until saturation is reached or until it is moved ahead of the electron pulse and decays from cavity losses. The optical field in the FEL pulse can therefore be viewed as growing from the back of the pulse as it moves forward at the rate of one desynchronism distance per pass.

Considering this description of optical pulse evolution, it seems likely that one mechanism for wavelength shifting is for changes in the electron energy to result in instantaneous changes in the wavelength of spontaneous radiation at the back of the electron pulse, and for this wavelength change to propagate into the pulse one desynchronism distance per pass. Though mode competition in the bulk of the optical pulse may also contribute to wavelength shifting, the FEL gain dependence on wavelength at saturation is so small that this is likely to be a slow process. Therefore, in this model it is assumed that propagation by desynchronism is the dominant mechanism for wavelength shifting in optical pulses that are of length comparable to the slippage distance.

Considering this assumption, the wavelength response as a function of pass number is the convolution of the

☆ Work supported by ONR contract #N00014-91-C-0170-P00003.

\* Corresponding author. Tel. +1 415 723 0291, e-mail: andre@hel.stanford.edu.

electron energy as a function of pass number with the optical pulse shape. If the center wavelength of the optical pulse is defined as

$$\lambda(n) = \frac{\int_0^\infty \lambda(n, z) P(z) dz}{\int_0^\infty P(z) dz}, \quad (1)$$

where  $\lambda(z)$  and  $P(z)$  are the optical wavelength and power as a function of position in the optical pulse, and we define normalized wavelength and energy changes as

$$\Delta\lambda(n) = \frac{\lambda(n) - \lambda(0)}{\lambda(\infty) - \lambda(0)}, \quad \Delta\gamma(n) = \frac{\gamma(n) - \gamma(0)}{\gamma(\infty) - \gamma(0)}, \quad (2)$$

then

$$\Delta\lambda(n) = \frac{\int_0^{nd} \Delta\gamma\left(n - \frac{z}{d}\right) f(z) dz}{\int_0^\infty f(z) dz}, \quad (3)$$

where  $n$  is the number of passes,  $d$  is the desynchronism distance, and  $z$  is distance along the FEL axis in the optical pulse frame.

Eq. (3) can be simplified using a simple approximation of the optical pulse shape  $f(z)$ . One such model is shown in Fig. 1. The region of the optical pulse where the optical field interacts with the electron bunch is modeled as a constant amplitude region of length  $\alpha = \sigma_z + N\lambda$  where  $\sigma_z$  is the width of the electron bunch. Though such a “square” model of what is obviously a rounded region is crude, this approximation keeps the model simple without compromising its essential features. The optical field region ahead of this interaction region consists of an optical field that has been moved forward out of the interaction region by desynchronism, and is attenuated exponentially by the optical cavity loss. The shape of this passive region can be

written as an exponential. The optical pulse shape as a function of longitudinal distance can then be expressed as

$$f(z) = [u(z) - u(z - \alpha)] + u(z - \alpha) e^{-(z - \alpha)/(dQ)}, \quad (4)$$

where  $\alpha = \sigma_z + N\lambda$  is the length of the interaction region,  $d$  is the desynchronism distance,  $Q$  is the optical cavity  $Q$ , and  $u(x)$  is the step function ( $u(x) = 0$  for  $x < 0$ ,  $u(x) = 1$  for  $x > 0$ ).

Using Eqs. (3) and (4), the wavelength  $\lambda(t)$  as a function of time can be predicted for an arbitrary electron energy change  $\gamma(t)$ . For a step change in the electron energy the wavelength response can be written as

$$\Delta\lambda(t) = \frac{t}{\tau(\alpha/d + Q)}, \quad t < \tau \frac{\alpha}{d}, \quad (5)$$

$$\Delta\lambda(t) = \frac{\alpha/d + Q(1 - e^{-t/(\tau Q)})}{\alpha/d + Q}, \quad t \geq \tau \frac{\alpha}{d}, \quad (6)$$

where  $\tau$  is the round-trip time in the optical cavity ( $\tau = 85$  ns in the Stanford FEL).

It is evident from the above equations that the time required for the optical wavelength to respond to a sudden electron energy change will increase with increasing  $Q$ , increase with longer pulses (larger  $\alpha$ ), and decrease with larger desynchronism. For very large desynchronism,  $\alpha/d$  becomes small with respect to  $Q$  and the desynchronism and pulse length dependence of the response time must vanish. In this limit, the response time is only dependent on the optical cavity  $Q$ .

The model is valid in the range of medium to large  $Q$  and electron pulse lengths comparable to, or shorter than, a few slippage distances. For very low  $Q$ , the model of the optical pulse shape we have described no longer resembles the actual shape of optical pulse and some inaccuracy in the model predictions can be expected. For very long electron bunches, wavelength shifting effects which originate in the bulk of the interaction region can no longer be ignored and the model predictions are likely to overestimate the response time.

In the following section, measurements of wavelength response to step changes in electron energy are presented along with the predictions of this model. For the model predictions, the measured electron energy change  $\Delta\gamma(t)$  was substituted into Eqs. (3) and (4) to calculate  $\Delta\lambda(t)$ .

### 3. Wavelength response measurements

Measurements of the FEL wavelength response to electron energy changes were made by suddenly decreasing the electron energy by 0.1%. This was accomplished by electronically changing the set-point for the RF amplitude stabilization loop in one accelerator structure. The RF field amplitude in this structure was measured as a function of

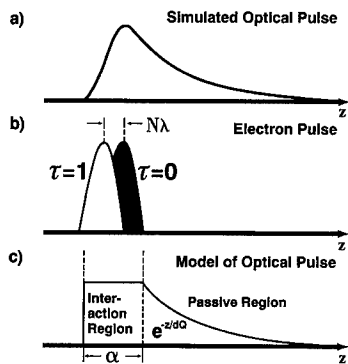


Fig. 1. (a) Simulated [4] optical pulse shape for  $Q = 50$ ,  $d = 0.03N\lambda$  and  $\alpha = 3N\lambda$  with relevant electron pulse shape and position (b). (c) Two-region model of the optical pulse.

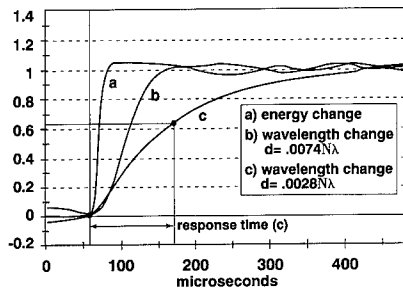


Fig. 2. Measured wavelength response to a sudden perturbation in electron energy as a function of time for  $Q = 190$ ,  $\alpha = 4.6$ . (a) Normalized electron energy. (b) Normalized wavelength as a function of time for  $d = 0.0074N\lambda$ . (c) Normalized wavelength as a function of time for  $d = 0.0028N\lambda$ . The steady state relative wavelength change is approximately 0.2% of  $4.9 \mu\text{m}$ .

time to determine the time evolution of the electron energy during the change. The rate of change of the electron energy is limited by the high loaded  $Q$  of the accelerator structures. The response time of the electron energy, defined in Fig. 2, was typically  $6 \mu\text{s}$  to  $12 \mu\text{s}$ .

The time evolution of the FEL wavelength was recorded using a spectrometer and an array detector [3]. A typical set of measurements is shown in Fig. 2. Trace (a) is the normalized perturbation in the electron energy as a function of time. The relative amplitude of ripple seen on the energy is approximately  $1 \times 10^{-4}$  of the total electron beam energy. Trace (b) and (c) are the normalized FEL wavelength as a function of time for desynchronism  $d = 0.0074N\lambda$  and  $d = 0.0028N\lambda$  respectively. Both wavelength traces were obtained for  $Q = 190$ ,  $\alpha = 4.6N\lambda$ , and  $\lambda = 4.9 \mu\text{m}$ .

To explore the dependence of wavelength response on parameters such as  $Q$ ,  $\alpha$ , and  $d$ , we define a "response time" which is the time interval from the beginning of the energy step to the point where the wavelength has reached 0.63 of its steady state value (see Fig. 2). The optical cavity  $Q$  was varied by appropriate choice of cavity mirrors and was determined by measuring the optical energy decay time. The desynchronism was varied by controlling a motorized mirror and was measured using an LVDT linear motion sensor with  $0.1 \mu\text{m}$  resolution. The position of zero desynchronism was estimated from observation of the sharp decrease in optical power which occurs near  $d = 0$ . All desynchronism values are relative to this point. The length of the interaction region  $\alpha$  was varied by changing the length of the electron bunch. The length  $\alpha$ , however, was estimated by obtaining autocorrelation measurements of the optical pulse length at various values of desynchronism;  $\alpha$  was calculated by extrapolating these measurements to zero desynchronism. All wavelength response measurements were made at  $\lambda = 4.9 \mu\text{m}$  with energy steps that resulted in a  $10 \text{ nm}$  wavelength increase.

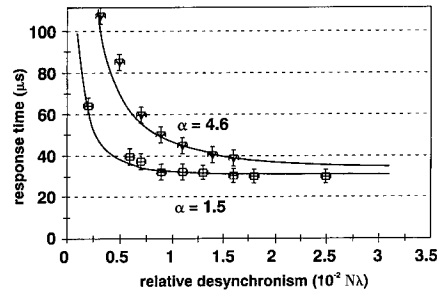


Fig. 3. Response time versus desynchronism for  $\alpha = 1.5N\lambda$  and  $\alpha = 4.6N\lambda$ ,  $Q = 190$ . The crosses represent measured values while the continuous lines represent the predictions of the model.

The response time as a function of desynchronism at  $Q = 190$  is shown in Fig. 3. The continuous lines are the predictions of the model for the wavelength response as calculated using the measured energy step. The measurements and the model show that the response time decreases for larger values of desynchronism. This results from the fact that the wavelength shift must propagate through the optical pulse at a rate of one desynchronism distance per pass; an increase in desynchronism increases the propagation rate and decreases the response time. The two measurement sets shown in Fig. 3 correspond to two different interaction region lengths. The separation between the two curves indicates that the response time increases for longer pulse lengths at a given value of desynchronism. This results from the fact that the time required for the wavelength change to propagate through the optical pulse must increase with pulse length if the propagation rate is fixed. For large desynchronism, the optical pulse length is dominated by the exponential  $e^{-z/dQ}$  and increasing the desynchronism increases both the pulse length and the propagation rate. In this region, the response time is only dependent on the optical  $Q$ .

The response time as a function of desynchronism for large values of  $d$  and for three different values of  $Q$  is shown in Fig. 4. The length of the interaction region is  $1.5N\lambda$ . The response time decreases for smaller values of

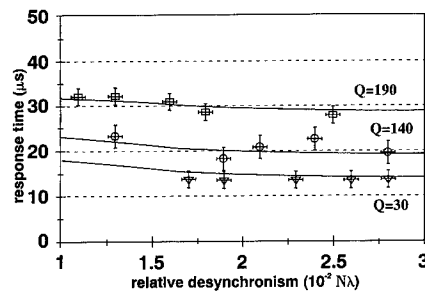


Fig. 4. Response time as a function of desynchronism for  $Q = 30$ ,  $140$ , and  $190$ .  $\alpha = 1.5$ . The crosses represent measured values while the continuous lines represent the predictions of the model.



$Q$  as expected. For the case where  $Q = 30$ , the wavelength response time is limited by the finite slew rate of the energy step. However, as the predicted response time is calculated using the measured slew rate, the comparison is still valid.

#### 4. Conclusion

Time dependent measurements of the FEL wavelength in response to sudden perturbations of the electron energy indicate that lower optical cavity  $Q$ , shorter electron pulses, and large values of desynchronism all lead to a faster wavelength response. A simple analytic model has been shown to be successful in predicting the wavelength response. The electron energy slew rate can in principle be

increased by an order of magnitude over that used in these studies, allowing the validity of the model to be tested with very low optical cavity  $Q$ . An improved approximation of the optical pulse shape may be required to extend the validity of the model to this regime.

#### References

- [1] L.R. Elias, W.M. Fairbank, J.M.J. Madey, H.A. Schwettman and T.I. Smith, Phys. Rev. Lett. 36 (1976) 717.
- [2] T.I. Smith and H.A. Schwettman, Nucl. Instr. and Meth. A 304 (1991) 812.
- [3] A. Marziali and T.I. Smith, Nucl. Instr. and Meth. A 331 (1993) 59.
- [4] W.P. Pinkley, W. Wilkenson, J. Blau, R.K. Wong and W.B. Colson, Nucl. Instr. and Meth. A 341 (1994) ABS 70.



ELSEVIER

## The saturation of the Beijing FEL

Jialin Xie<sup>a</sup>, Jiejia Zhuang<sup>a</sup>, Yongzhang Huang<sup>a,\*</sup>, Yonggui Li<sup>a</sup>, Shaobo Lin<sup>a</sup>,  
Runjie Ying<sup>a</sup>, Yuanyuan Zhong<sup>a</sup>, Lingyi Zhang<sup>a</sup>, Gang Wu<sup>a</sup>, Yuzhen Zhang<sup>a</sup>,  
Chunnong Chao<sup>a</sup>, Lihua Li<sup>a</sup>, Ensheng Fu<sup>b</sup>, Jing Su<sup>b</sup>, Yanshan Wang<sup>b</sup>, Gang Wang<sup>b</sup>

<sup>a</sup> Institute of High Energy Physics, Academia Sinica, P.O.Box 918, Beijing 100039, China

<sup>b</sup> Institute of Optics & Fine Mechanics, Academia Sinica, P.O.Box 800211, Shanghai 201800, China

### Abstract

The first lasing of the Beijing FEL was reported at the 1993 FEL Conference. After improving the performance of some components, saturation of the system was achieved in December 1993. The main measures adopted will be discussed in this report. First, the original undulator was replaced with a new one with better characteristics. Second, back-bombardment of the thermionic cathode microwave gun was reduced by deflecting magnet. With these and other modifications, saturated power output of  $10^8$  over the spontaneous emission was obtained. Saturation over the wavelength range 9–11  $\mu\text{m}$  was achieved.

### 1. Introduction

The Beijing FEL is a rf linac based facility designed to work in the infrared spectra range. In previous papers [1], design, construction and status were reported. This paper will review the upgrade work at BFEL since the 1993 FEL Conference, and will report the experimental results of saturation.

The distinguishing characteristics of the BFEL facility are the use of a thermionic cathode rf gun, a XK-5 klystron driven by a 7  $\mu\text{s}$  modulator with a PFN of 48 sectors, and a 1.5 m, 50 periods NdFeB planar undulator. BFEL began design work in 1986, and construction of a prototype rf gun and modulator in 1987. The first beam test on the prototype rf gun was at the end of 1988. Almost at the same time, design and construction work began on all components of this laser facility, such as rf gun injector, modulator, rf power, beam transport line, undulator, optical cavity, diagnostic devices, and so on. The system was installed on the present site at the end of 1990. Since then, the linear accelerator system has been under continuous improvement. Spontaneous emission was first observed in July 1992. After the optical cavity was mounted, the first lasing signal was obtained in May 1993. The first lasing signal was  $10^3$  times higher than that of spontaneous emission. In November 1993, the undulator was replaced with a new one, and a magnetic deflector was applied on the rf gun to reduce the back-bombardment effect. In

December 1993, saturated lasing was achieved with a power level  $10^8$  times higher than that of spontaneous emission. Up to April 1994, approximately 20 oscillator experiments had been conducted at BFEL, producing an output peak energy from 2 to 10 mJ/pulse, and covering the wavelength range 9–11  $\mu\text{m}$ .

### 2. Description of the machine performance

The BFEL system has already been described in Ref. [1]. We will concentrate on describing the thermionic rf gun, the undulator and the optical cavity. The general layout of BFEL is shown in Fig. 1. The system parameters are shown in table 1. These values are present operating values.

#### 2.1. The thermionic rf gun [2]

As an injector, the rf gun consists of two main parts, the gun cavity and the alpha magnet [3]. The electrons are emitted by a 3 mm diameter LaB<sub>6</sub> cathode. They are accelerated across a 3 cm gap by the rf field in the cavity. The electrons emerge from the cavity through steering and focusing magnets and then pass through the alpha magnet. This magnet selects most of the electrons in some energy range, and bunches them for injection into the accelerator.

Since the electron energy is not very high, the emerging bunches will lengthen as they pass through the drift sections before and after the alpha magnet. The alpha magnet is configured to have a positive momentum compression

\* Corresponding author. E-mail huangyz@vxihep.ihep.cern.ch.

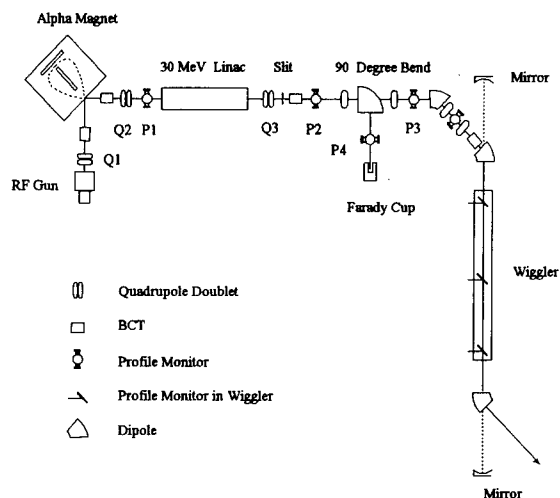


Fig. 1. Schematic view of Beijing FEL facility.

factor, and the debunching of the drift sections must be compensated by the overbunching in the magnet. Since the dimension of the alpha magnet and the length of the drift sections are fixed, in order to increase its bunching effect we must increase the electron energy emerging from the gun cavity while increasing the magnetic field to keep the electron path unchanged in the magnet. It was found that when the rf gun worked with a maximum electron energy of 1.2 MeV, the BFEL lased quite easily. This indicated

Table 1  
BFEL system parameters

|                                     |                  |
|-------------------------------------|------------------|
| Electron beam                       |                  |
| Macropulse length                   | 4.5 $\mu$ s      |
| Macropulse repetition rate          | 3.125 Hz         |
| Micropulse length                   | 3–4 ps           |
| Micropulse repetition rate          | 2856 MHz         |
| Beam energy                         | 24–28 MeV        |
| Energy spread (FWHM)                | 0.7%             |
| Macropulse current                  | 150–200 mA       |
| Normalized emittance at rf gun exit | 20 $\pi$ mm-mrad |
| Undulator II                        |                  |
| Period                              | 3 cm             |
| Number of periods                   | 50               |
| Gap                                 | 1.15 cm          |
| K value                             | 1.17             |
| Electron trajectory deviation       | 50 $\mu$ m       |
| Harmonic contents                   | 1%               |
| Optical cavity                      |                  |
| Cavity length                       | 251.9 cm         |
| Operating wavelength                | 9–11 $\mu$ m     |
| Mirror radii upstream               | 174 cm           |
| down stream                         | 170 cm           |
| Mirror reflectance upstream         | 99.5%            |
| down stream                         | 99%              |
| Rayleigh length                     | 76.5 cm          |

that electron bunches were compressed to just a few picoseconds at the entrance of the linear accelerator.

It is known that the back-bombardment effect could cause beam current to increase within macropulse. This beam is generally not suitable for acceleration because of beam loading. This is the main reason we do not use the full 7  $\mu$ s pulse length of the klystron. A magnetic deflector was adopted to reduce this effect. The first magnet was put near the cathode and it deflected back-bombarded electrons off the cathode. Another magnet was put just after the gun cavity. It bent the electron beam center back to the axis so that the influence on emittance produced by the first magnet could be minimized. Beam tests showed that the current ramp at the exit of the gun cavity was reduced from 40% to 25% but the emittance only increased slightly. This deflector enabled the rf gun to work effectively at 4.5  $\mu$ s.

## 2.2. The undulator

The undulator is of the planar type with NdFeB permanent magnets of 50 periods of 3 cm. The gap can be adjusted and the undulator may be tapered. However, presently all the experiments on BFEL have been done with the same gap and without tapering.

Before November 1993, Undulator I was used. Spontaneous emission (SE) and first lasing were obtained during this period, but we found some problems with it. 1) The linewidth of the spontaneous emission was 4% which is much larger than the theoretical value of 2%. 2) Electron beam spots in the middle and at the end of the undulator were much larger than that of simulation values, and the electron path in the undulator was not a straight line. 3) The small signal gain of the first lasing signal was only 6%; less than the FEL simulation value. Our explanation is that the NdFeB magnets of Undulator I were demagnetized by radiation after about two years' work. The undulator was removed and its field was remeasured. The results showed that the field strength was smaller than the original value. Especially at the positions where the profile monitors were inserted, the field was more than 1000 G smaller. It is now clear that Undulator I was damaged by radiation.

With Undulator II, all above mentioned problems disappeared. The linewidth of spontaneous emission was reduced to 3%, the intensity of SE was several times higher than before, and the second and the third harmonic content was 1.1% of the fundamental value. The beam spot in the middle of the undulator was only a quarter of previous value.

## 2.3. The optical cavity

The optical cavity is a near concentric type consisting of two ZnSe mirrors with a ZnSe/TuF<sub>4</sub> multilayer dielectric coating. After extraction from the downstream mirror,

the laser beam passes through a telescopic beam pipe and is sent to the diagnostic room.

Two ways were used to align the cavity. Before installation, a collimator was adjusted to be coaxial with the undulator. Then the collimator was used to indicate the mounting of mirrors in the cavity, to locate marks on profile monitors along the undulator. These marks are the reference for tuning the electron beam. Two He–Ne lasers were used to monitor the position of the two mirrors by observing the shift of the laser spot reflected from the back of the mirror. Another way was the so called scanning resonant method. A laser beam from a CO<sub>2</sub> laser was sent into the cavity. When the cavity is resonant with the CO<sub>2</sub> laser, which means cavity mirrors are correctly positioned, an interference signal could be received by a HgCdTe detector located in the diagnostic room. Ultimately the cavity was optimized by looking at the lasing signal during experiments.

### 3. Tuning procedure for lasing

After the new undulator was installed, we measured the SE in order to appraise the qualities of electron beam and Undulator II. We found that it could meet the requirements of lasing in the infrared region. Then we began to install the optical cavity, to align mirrors coincident with the undulator axis, and to align all of optical diagnostic detectors. When we began lasing experiments again, the output laser power soon reached the level of  $10^5$  times the SE power. Then, we used the magnetic deflector at the rf gun to reduce back-bombardment and to enlarge the macropulse width. This made the charge and the energy of electron bunches more homogeneous within the macropulse. As a result, the power increased by a factor of 100. Finally, through fine adjustment of cavity mirrors, saturated lasing was obtained. Its power was  $10^8$  times higher than that of SE. This is shown in Fig. 2 where both the electron pulse and the laser pulse are shown. It is seen that after 2  $\mu$ s, corresponding to about 100 round trips, the output power saturated. The measured output energy in the optical macropulse was 3 mJ. The power was deduced from the energy by taking into account the time structure of the laser. The corresponding average intracavity power in the

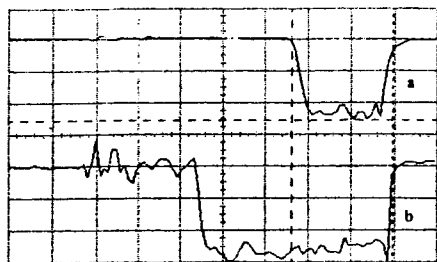


Fig. 2. (a) Laser macropulse shape at saturation; the horizontal axis is 1  $\mu$ s/div. (b) Electron beam macropulse of rf gun.

Table 2

Summary of the laser characteristics

|                                     |                  |
|-------------------------------------|------------------|
| Total spectral range                | 9–11 $\mu$ m     |
| Output energy in optical macropulse | 2–10 mJ          |
| Average power in macropulse         | 200 kW           |
| Peak power                          | 20 MW            |
| Spectral width                      | 0.3–2%           |
| Small signal gain                   | 32%              |
| Optical extraction efficiency       | 0.48%            |
| Optical mode                        | TM <sub>00</sub> |
| Optical divergence                  | 2 mrad           |

optical macropulse was 200 kW, the peak intracavity power was 20 MW.

The tuning procedures used daily to achieve best lasing were as following:

- 1) A scanning CO<sub>2</sub> laser was used as crude indication of the alignment of the cavity mirrors and detectors.
- 2) The rf gun was adjusted to provide the desired bunches with expected current and energy, and optimum bunching at the entrance of the accelerator.
- 3) The phase of the accelerator was adjusted to have a minimum energy spread.
- 4) If the electron energy was not the expected value, we changed the klystron output power, then went back to step 2.
- 5) The electron beam was focused to be a circular spot at the center of the undulator with a divergence matching that of the fundamental optical mode. The marks on three profile monitors were the reference for coarse positioning.
- 6) Spontaneous emission was monitored with the sensitive HgCdTe detector while the cavity length was adjusted until lasing started.
- 7) Fine adjustment of the position and the envelope of the electron beam and fine adjustment of the cavity mirror alignment and the cavity length were used to optimize the laser power.
- 8) The above adjustments, steps 5–7, were repeated to obtain maximum optical power.

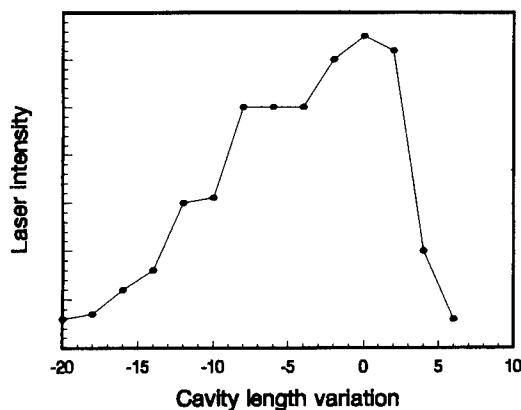


Fig. 3. FEL detuning curve at  $\lambda = 10.68 \mu$ m, optical power intensity vs. cavity tuning  $\Delta z$  (1  $\mu$ m/div).

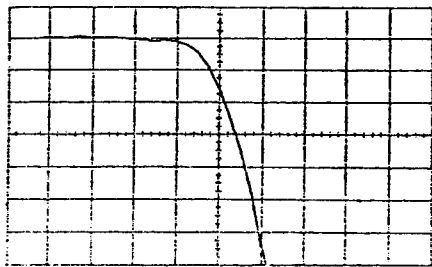


Fig. 4. Optical power build-up at small signal, horizontal axis is 200 ns/div.

#### 4. Optical results

The general optical characteristics are summarized in table 2.

The spectral range 9–11  $\mu\text{m}$  is presently covered by using different electron energy values. This range is restricted by the effective spectral range of the cavity mirrors' reflectance. The total energy produced in a train of optical bunches was measured with a calorimeter for each shot. Fig. 3 shows a typical measurement of optical power versus cavity detuning length. The zero of the horizontal scale corresponds to the length at which laser power and energy are maximum. At this length, the laser spectrum is wide. For a shorter cavity length, there is a rather flat range where the laser power is stable with a narrow spectrum. The stable tuning range width is 6–8  $\mu\text{m}$ . In this range, the laser power saturates earlier, which is an indication of improved small signal gain.

Small signal gain was routinely measured from the exponential rise of the lasing power from spontaneous emission to saturation at the start of the laser macropulse. A trace of the turn-on on a digital oscilloscope is shown in Fig. 4. The net gain from this curve is 24%. Cavity loss

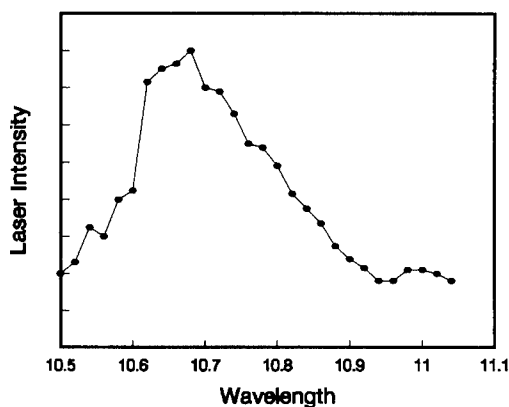


Fig. 5. Laser spectrum at  $\lambda = 10.68 \mu\text{m}$ .

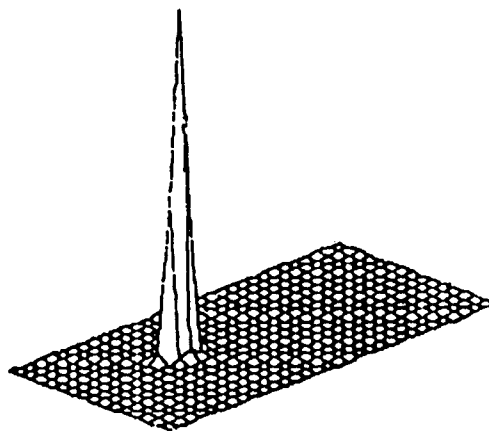


Fig. 6. Spatial distribution of the laser beam.

was measured from the exponential decay of the laser output power after the end of the electron beam macropulse.

The optical extraction efficiency was calculated from conservation of energy. During saturation, the optical power loss in the cavity is equal to the power transmission from electron beam to optical beam. Typical extraction efficiency was 0.48%. The spectral output is shown in Fig. 5, the FWHM measured is 2%. However, this spectrum represents the integrated output measured over many macropulse trains. It is possible that some of the width was due to variation of the wavelength caused by electron energy variation between pulses. It should be noted that the spectra are closely associated with cavity tuning. A minimum width of 0.3% was observed in experiment.

A LMP-32\*36 element pyroelectric detector has been used to measure the spatial quality of laser beam. The detector was located in the focal plane of a lens 10 m from the optical cavity. A 3-D profile of optical beam in the focal plane is shown in Fig. 6. The corresponding beam divergence is 2 mrad which is close to the diffraction limit.

#### Acknowledgement

The authors want to acknowledge the collaboration of Dr. V. Kushnir, Kharkov Institute of Physics and Technology, Ukraine, on the microwave gun performance upgrading during his visit.

#### References

- [1] J. Xie, J. Zhuang et al., Nucl. Instr. and Meth. A 272 (1988) 40; A 296 (1990) 244; A 331 (1993) 204; A 341 (1994) 34.
- [2] Y. Huang, Ph.D. thesis, Institute of High Energy Physics, Academia Sinica (1991).
- [3] H.A. Enge, Rev. Sci. Instr. 34 (1963) 385.

# FEL cavity length measurement with an external laser <sup>☆</sup>

K.W. Berryman <sup>\*</sup>, P. Haar, B.A. Richman

*Stanford Picosecond FEL Center, W.W. Hansen Experimental Physics Laboratory, Stanford University, Stanford, CA 94305-4085, USA*

## Abstract

The nature of linac-driven free electron laser (FEL) operation requires that the length of the laser optical resonator be matched to the repetition rate of the accelerator in order for the returning optical pulse to overlap the newly arriving electron bunch. The range of cavity lengths over which oscillation will occur is limited in typical FEL designs to a few tens of microns, while the total resonator length is often many meters. The task of correctly setting the length of a new FEL resonator is therefore quite difficult, particularly if the cavity geometry contains more than a single line segment. We have demonstrated that such an absolute length measurement with micron accuracy over many meters in any cavity configuration is possible by establishing resonances in the cavity with an external laser of known repetition frequency. This technique was successfully applied in the development of two new FELs at the Stanford FEL Center. We will discuss the advantages of this method over conventional measurement schemes.

## 1. Introduction

All Free Electron Lasers (FELs) must have three elements: an optical cavity, an energetic electron beam, and a spatially varying magnetic field. The magnetic field accelerates the electrons, causing them to radiate a spectrum peaked at a wavelength determined by their energy and the periodicity of the field. The radiated light is stored in the optical cavity, where it can interact with other electrons to produce gain. If the gain exceeds the cavity losses, the optical field will build up to saturation, and the device can properly be called a laser.

Most FELs to date have been constructed with pulsed electron sources, based either on linacs or storage rings. The pulsed nature of the electron beam is determined by the operating frequency of the accelerator, which in the Stanford Superconducting Accelerator (SCA) results in electron bunches with picosecond duration separated by 85 ns. The separation of the electron bunches determines the length of the optical cavity, as the circulating optical pulse must arrive at the front of the cavity coincident with the arriving electrons. With the SCA, the optical cavity must be a multiple of 12.7 m long. Most other FELs have cavity lengths on the order of a few meters. Any FEL, however, will only operate over a narrow range of cavity lengths – some as short as a few microns. Constructing an FEL therefore requires a precise length measurement over a large distance.

Setting an optical cavity length coarsely can be accomplished by a wide variety of methods, ranging from tape measure to optical interferometry. While the latter method is capable of relative length measurement to sub-micron accuracy, absolute measurement over many meters is generally not possible. It is also usually not practical to measure directly from the front surface of one mirror to the next; instead, an arbitrary reference point near the center of each mirror must be established, which introduces additional uncertainty. If the cavity contains more than two mirrors this problem is especially troublesome. Finally, none of these techniques address the question of mirror alignment, which is equally crucial to establish when building a new FEL.

We have decided to adopt a different approach, one which uses a conventional laser with variable repetition frequency to establish resonances directly in the optical cavity. This method allows a rapid and accurate determination of both cavity length and alignment. It has been successfully employed to measure the optical cavities of two new FELs at the Stanford FEL Center.

## 2. Description of technique

The method we have used to establish absolute measurements of length in a long optical cavity uses a conventional laser which is stabilized to a multiple of the FEL micropulse repetition rate. The repetition frequency is adjusted until resonances are observed in the optical cavity. The resonances will be present only when the length of the passive cavity is a subharmonic of the corresponding

<sup>☆</sup> Work supported in part by the Office of Naval Research, Contract No. N00014-91-C-0170.

<sup>\*</sup> Corresponding author.

repetition frequency of the conventional laser cavity. By monitoring and scanning the repetition frequency of the laser, we can therefore make an absolute length determination of the passive cavity. The precision of this method is limited only by the pulse width of the exciting laser, its own repetition frequency stability, and the degree of its pulse to pulse coherence.

We can readily estimate the magnitude of the uncertainty in the length measurement. Finite pulse width implies a finite range of lengths over which resonance will occur. A simple estimate is that the uncertainty is determined by  $\tau/c$ , where  $\tau$  is the pulse width and  $c$  is the speed of light. In fact, this overestimates the uncertainty, as Fig. 1 illustrates. The results in this figure assume complete pulse to pulse coherence of the conventional laser. In this figure we see that resonances occur with a spacing of the laser wavelength, within an envelope determined by the pulse length and the cavity  $Q$ . The width of the resonances, which depend upon wavelength and cavity  $Q$ , are extremely narrow, as even a small phase mismatch will destroy the coherent buildup of radiation. This implies that the cavity length could be determined to within a few tens of nanometers if the resonance heights could be measured with enough accuracy. The laser pulse width is then irrelevant. Unfortunately, determination of resonance heights will be obscured by mirror vibrations and imperfections in the laser. The actual measurement accuracy, nonetheless, can easily reach down to the micron level.

There are also practical limits on the allowable losses within the optical cavity. If the losses are large enough to prevent the storage of multiple pulses, then there will be no detectable difference in the outcoupled power at reso-

nance. For a given experimental geometry, the ratio of the resonant to the non-resonant signal is given simply by [1]

$$\frac{I_{\text{res}}}{I_0} = \frac{1 - e^{-1/Q}}{(1 - e^{-1/2Q})^2}.$$

Here the optical cavity  $Q$  is defined as the inverse of the fractional cavity power losses in a single round trip. In practice, this formula indicates that a detectable increase in the outcoupled power is present even with small coupling or large losses.

The precision of the final measurement also depends ultimately on the accuracy of the repetition frequency measurement of the driving laser. With standard electronics modern commercial lasers are stabilized with a repetition frequency that can be determined to better than 10 Hz. When these numbers are combined with the above estimates, we see that measurements in excess of the actual mechanical stability of the passive cavity are possible. In other words, ambient changes in the length of the cavity due to mirror vibrations are greater than the theoretical measurement limit afforded by this method.

As an aside, we note that in principle one can also perform this measurement by monitoring the temporal distribution of energy leaving the passive cavity. If the cavity has small losses, then energy from a single pulse will be visible many round-trips later. It will appear at a time offset from the next pulse equal to the product of the number of round trips and the relative cavity length error. Then if one monitors the output pulse with an autocorrelator or a sufficiently fast photodetector, as the passive cavity is scanned towards the correct length, the observed

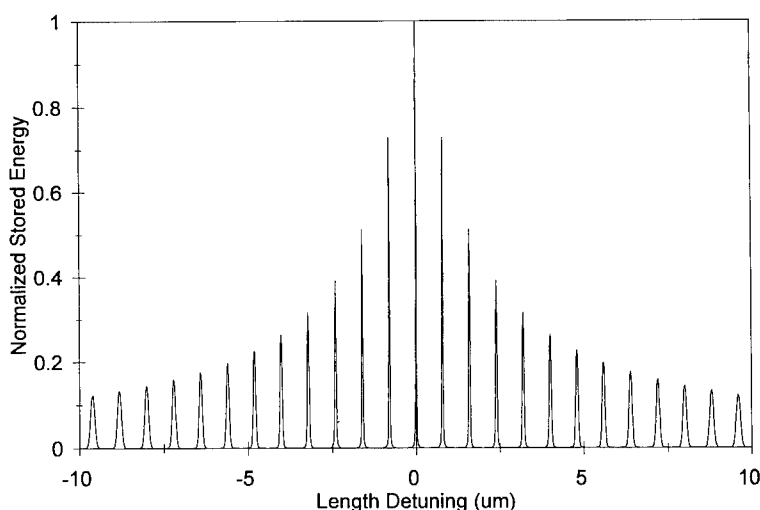


Fig. 1. Calculation of the ratio of stored energy to resonant stored energy expected in the cavity at different cavity lengths, with an 80 fs FWHM pulse at 800 nm, and a cavity  $Q$  of 10.

pulse width will shrink, reaching a minimum when the cavities are in synchronism. This method could be employed in cases where the driving laser frequency cannot be measured conveniently. It does, however, require an extremely low-loss cavity for practical application. Since the frequency of the laser we chose to use was well characterized, we chose not to adopt this approach.

### 3. Experimental method

We have used the method of external laser coupling to measure the length of two separate cavities at the Stanford

FEL Center. We use a Ti:sapphire laser which is actively stabilized to operate near 82 MHz and can be locked to an external frequency source. As our FEL operates with a micropulse frequency of 11.818 MHz, the Ti:sapphire was locked to the seventh harmonic of the FEL repetition rate. The relative timing jitter between the Ti:sapphire and the operating FEL has been measured to be less than 2 ps [2], which provides an upper limit on the jitter of the Ti:sapphire with respect to the frequency source. The laser produces approximately 10 nJ in an 80 fs pulse at a wavelength tunable from 700 to 1000 nm.

The experimental geometries are illustrated in Figs. 2a and 2b. The first cavity is a traditional, symmetric two

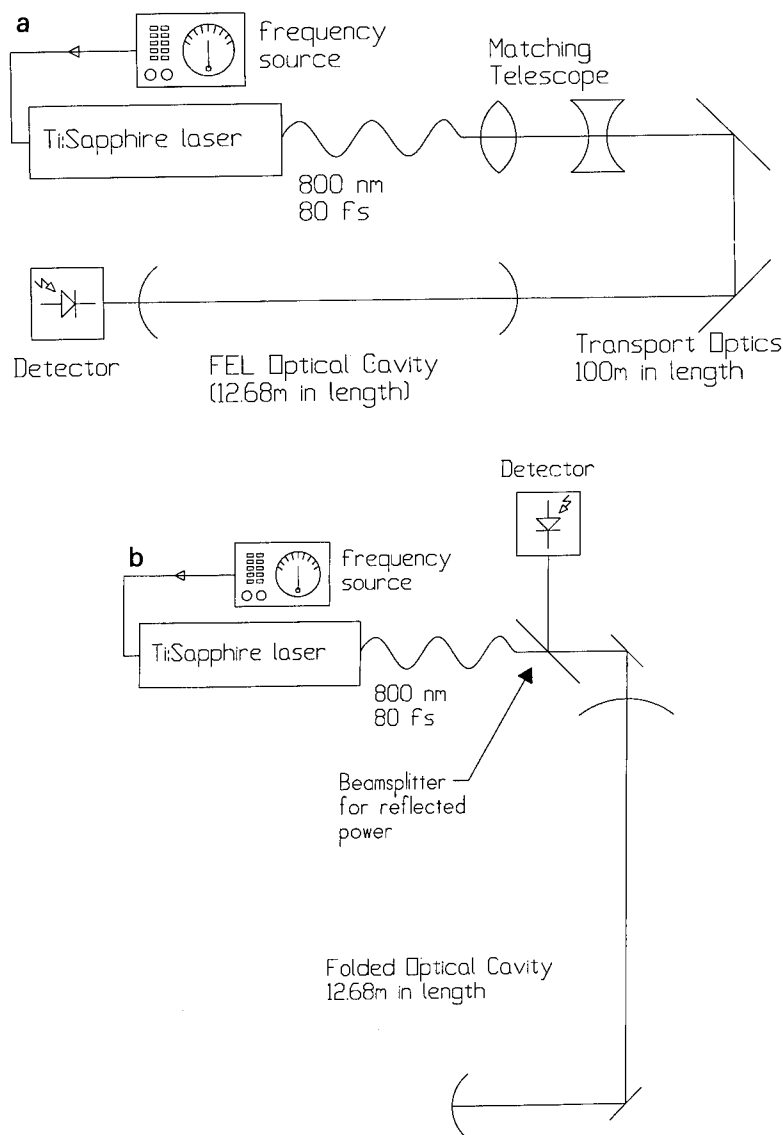


Fig. 2. (a) Layout of the first optical cavity measured with the external laser technique. Coupling was achieved through a partially transparent dielectric mirror. (b) Layout of the folded cavity measured with the external laser technique. Coupling was achieved through a small hole in one mirror.



mirror optical resonator with a length of 12.7 m. The cavity was measured with the same dielectric mirrors which were to be used to establish lasing. They were ZnSe substrates, multilayer coated for high reflection at 4.0  $\mu\text{m}$ . The Ti:sapphire was adjusted to lase at 810 nm, at which wavelength the reflectivities of the mirrors were measured to be 80%, for a cavity  $Q$  of 2.5. The Ti:sapphire was approximately mode matched into the passive cavity. The transmitted signal was monitored with a germanium photodiode, and one of the passive cavity's mirrors was scanned until resonances were observed. The resonance heights were 30% above the background transmitted power, as compared to a calculated value of 50%, assuming perfect steering, mode matching, and complete filling.

The second cavity measured employs a more complicated geometry, and illustrates the advantages of this technique. The cavity is asymmetric, containing two curved mirrors and a 90° bend flat fold mirror. The mirrors are gold coated copper, thus the only coupling available was through a 1.6 mm hole centered on one mirror. A beam-splitter was used to deflect part of the outcoupled radiation onto the germanium detector. The bare gold coating should provide a reflectivity of approximately 98% at 810 nm. In this case we scanned the frequency of the Ti:sapphire until resonances occurred, and then walked both cavities together to the correct frequency for FEL operation. The resonance peaks were approximately 3–5 times the background, compared to a predicted factor of 10, based on a numeric simulation of energy storage.

#### 4. Experimental results

The first optical cavity was set to the proper length for FEL action at the beginning of our February/March experimental run. Once the electron beam was steered properly, the cavity length was scanned, and the FEL turned on within a few microns of the measured set point. The second optical cavity was set to the proper length at the beginning of our June/July experimental run. The maxi-

mum length enhancement of the spontaneous radiation again occurred just a few microns from the measured length. In both cases the task of setting the correct cavity length was reduced from slow scanning over several millimeters to a rapid adjustment over a few tens of microns.

#### 5. Conclusion

The technique we have described here provides one solution to a problem which has affected the construction of many FELs – setting the cavity length. The traditional approach has been to measure the cavity length crudely and then attempt to scan it to the proper length while hoping for laser signal, or at least for enhancement of spontaneous radiation. Our method, in contrast, does not require an electron beam or sensitive detectors for weak spontaneous radiation. It provides a direct measurement of the length with high precision, and requires only a short-pulse conventional laser with repetition frequency near the FEL frequency. Any linac-based FEL with a photoinjector automatically has such a synchronized laser, or, as in our case, a conventional laser may have been synchronized for other purposes. The laser requirements necessary for high precision measurements are not extreme.

This method has been successfully employed to preset the length of two new FEL cavities, eliminating much of the usual uncertainty regarding the proper cavity length, and reducing the time necessary to achieve laser operation. We believe the technique will be generally valuable to anyone constructing a linac or storage-ring FEL.

#### References

- [1] P. Haar, T.I. Smith and H.A. Schwettman, these Proceedings (16th Int. Free Electron Laser Conf., Stanford, CA, USA, 1994) Nucl. Instr. and Meth. A 358 (1995) 319.
- [2] R.J. Stanley, R.L. Swent and T.I. Smith, Synchronization of a femtosecond modelocked Ti:sapphire laser to the Stanford SCA/FEL, submitted to Opt. Commun.



ELSEVIER

## Phase space tomography of relativistic electron beams <sup>☆</sup>

C.B. McKee <sup>\*</sup>, P.G. O'Shea, J.M.J. Madey

*Free Electron Laser Laboratory, Department of Physics, Duke University, Durham, NC, USA*

### Abstract

The performance of an FEL depends on the characteristics of the electron beam used to drive it. Heretofore it was not possible to measure the details of the transverse phase space distributions of high-energy electron beams with the precision required to predict FEL performance. Standard techniques for measuring the transverse phase space of relativistic electron beams treat the phase space distributions as ellipses and only measure the sigma matrices that define the ellipses. These techniques give no information about the detailed structure of the phase space distributions. We have developed a new technique to measure transverse phase space that combines quadrupole-scanning techniques with tomographic image reconstruction to measure the actual phase space distributions while making no a priori assumptions about the distributions. This process is capable of reconstructing phase space distributions that are not elliptical. Both computer simulations and experiments verify that phase space tomography makes the detailed measurement of the phase space distributions possible at high energies. Detailed reconstructions of the phase space distribution of a 44 MeV electron beam from the Mark III FEL are presented.

### 1. Introduction

Measurement of the transverse phase space distribution of the electron beam is important to the understanding of the particle dynamics in accelerators and thus to creating bright electron beams to drive free electron lasers. Standard techniques of phase space measurements that involve placing apertures in the beam are not practical at particle energies beyond a few MeV [1]. Quadrupole-scanning techniques are useful at much higher energies, but these techniques make the a priori assumption that the phase space distributions are Gaussian and measure only the emittance and orientation of the phase space ellipse [2].

The purpose of the research covered in this paper is to measure the transverse phase space distribution of the beam while making no a priori assumption about the distribution. We accomplish this goal by measuring the spatial projections of the electron beam and by applying tomographic techniques to reconstruct the original distribution [3,4]. Radon has shown that an object may be completely reconstructed from the infinite set of all of its projections [5]. Tomographic imaging exploits this idea to reconstruct a two dimensional image from its one dimensional

projections. These techniques are well known in the medical imaging community [6].

In the case of a charged particle beam, we are interested in determining the two dimensional transverse phase space distribution,  $\mu(x, x'; z)$  at a given location,  $z$ , on the beam line. We first measure the one dimensional spatial projection of the electron beam,  $\mu(x, f)$ , as a function of quadrupole strength ( $f$ ). A simple scaling equation relates these spatial projections to the Radon transform of the transverse phase space. Using the same reconstruction techniques as used in Computer Assisted Tomography (CAT scans), we reconstruct the original phase space distribution  $\mu(x, x'; z)$ . This technique assumes no prior knowledge of the distribution of the beam in phase space. However, it does assume that the motion of the particles can be completely described using only the first order transport matrix.

Tomographic image reconstruction techniques have been used before to map the phase space of charged particle beams [7]. However, these previous techniques measure the transverse projection of the beam at different positions along the beam line limiting the number of views to usually no more than three, and therefore limiting information about the beam. Even in computer simulations non-Gaussian distributions do not resemble their original distributions when only three views are used [8]. In the technique described in this chapter we combine quadrupole-scanning with tomographic image reconstruction. The advantages of our technique are that it provides a large number of views of the beam, it requires no a priori

<sup>☆</sup> This research is supported in part by Army contract number DASG60-89-C-0028 and by AASERT award DAAH04-93-G-0309.

<sup>\*</sup> Corresponding author. Tel. +1 919 660 2644, fax +1 919 660 2671, e-mail cbm@phy.duke.edu.

assumptions about the phase space distribution, and it is a single station measurement. We are able to reconstruct the transverse phase space distribution from both computer simulated and experimental data.

## 2. Theory

Let  $\mu(x, x'; z)$  be the distribution of the beam in phase space at the axial beam line position  $z$ . The transverse phase space coordinates are  $x$  and  $x' = dx/dz$ . We will use the vector notation,  $\mathbf{X} = x\hat{i} + x'\hat{j}$ . The spatial projection of the phase space distribution at  $z$  is

$$A(x; z) = \int dx' \mu(\mathbf{X}; z). \quad (1)$$

One can express the projection as a two dimensional integral over phase space,

$$A(l; z) = \iint dx dx' \mu(\mathbf{X}; z) \delta(l - x). \quad (2)$$

According to Liouville's theorem, the density about a representative point in phase space is constant as that point moves in phase space [9];

$$\mu(\mathbf{X}; z) = \mu(\mathbf{X}_0; z_0) \quad \text{where} \quad \mathbf{X} = \mathbf{R}(I; z) \cdot \mathbf{X}_0. \quad (3)$$

$\mathbf{R}(I; z)$  is the transport matrix between  $z_0$  and  $z$ . For current purposes, the transport line consists of a drift section followed by a thick quadrupole and then another drift; thus  $\mathbf{R}(I; z)$  is a function of the quadrupole current. An insertion screen or some other device measures the beam's transverse profile at  $z$ . Varying the current to the quadrupole rotates the beam in phase space at the screen. Using Eq. (3), we can write Eq. (2) as

$$A(l, I; z) = \iint dx_0 dx'_0 \mu(\mathbf{X}_0; z_0) \delta(l - R_{11}x_0 - R_{12}x'_0). \quad (4)$$

Defining the new vector  $\boldsymbol{\zeta}(I; z) = R_{11}\hat{i} + R_{12}\hat{j}$  as a function of quadrupole current and axial position, one can now write the spatial projection as

$$A(l, \boldsymbol{\zeta}) = \int d\mathbf{X}_0 \mu(\mathbf{X}_0; z_0) \delta(l - \boldsymbol{\zeta} \cdot \mathbf{X}_0). \quad (5)$$

Eq. (5) is the Radon transform of the transverse phase space by an arbitrary rotation. This transform is related to the Cartesian rotation transform by [4]

$$\tilde{\mu}(p, \hat{\xi}) = sA(l, \boldsymbol{\zeta}), \quad (6)$$

where  $\boldsymbol{\zeta} = s\hat{\xi}$ ,  $|\boldsymbol{\zeta}| = s$  and  $p = l/s$ .  $\hat{\xi}$  is the Cartesian rotation vector,  $\hat{\xi} = \cos \phi \hat{i} + \sin \phi \hat{j}$ . In terms of the transport matrix elements, the rotation angle is given by  $\tan \phi = R_{12}/R_{11}$  and the scaling factor is given by  $s = R_{11}^2$

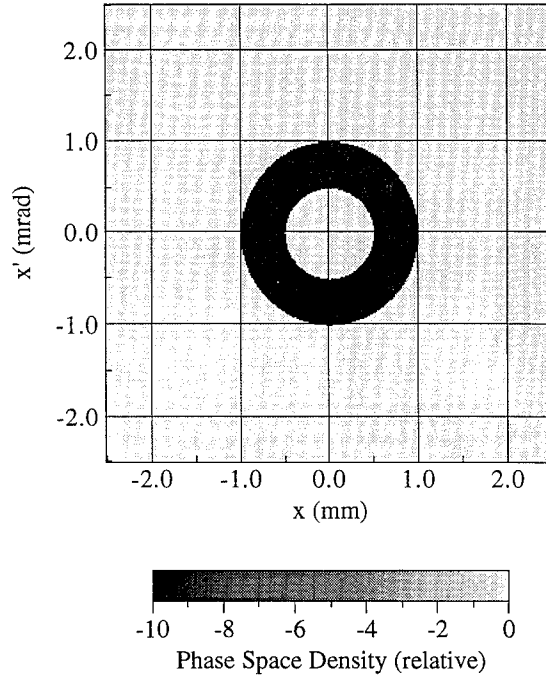


Fig. 1. Initial phase space distribution for computer simulations.

+  $R_{12}^2$ . Since the matrix elements are functions of the quadrupole current, so are the rotation angle and the scaling factor.

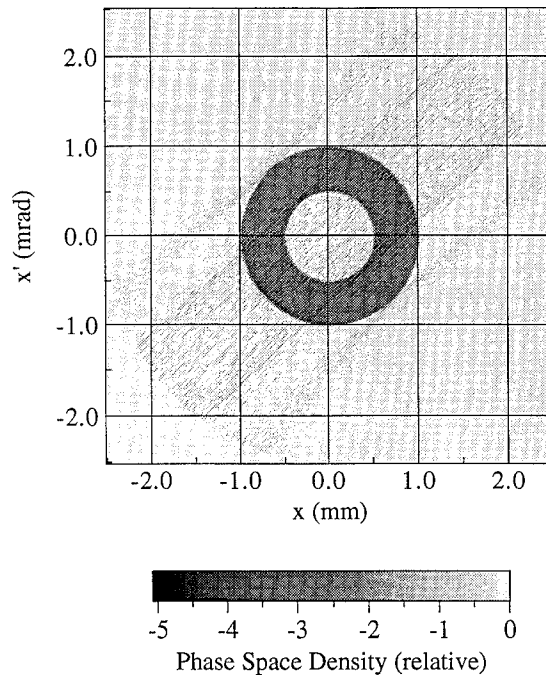


Fig. 2. Reconstructed phase space distribution from computer simulations.

By scaling the phase space projections, we obtain the Radon transform of the phase space distribution of the electrons. There are several methods to invert the Radon transform in order to recover the original function. Filtered backprojection is the most widely used algorithm for computer reconstruction. The inverse equation of the Radon transform is

$$f(\mathbf{x}) = \frac{1}{2} \int_{|\hat{\xi}|=1} d\hat{\xi} \int_{-\infty}^{\infty} dk |k| e^{i2\pi k \hat{\xi} \cdot \mathbf{x}} \times \int_{-\infty}^{\infty} dp e^{-i2\pi kp} \tilde{f}(p, \hat{\xi}). \quad (7)$$

We use the program RECON for the numerical implementation of the filtered backprojection. RECON is a very accurate filtered backprojection reconstruction program borrowed from the medical community [10]. This program requires the rotation angle,  $\phi$ , to be variable over a full  $\pi$  rad.

Before undertaking the actual experiments, we used a computer model to simulate the measurement and reconstruction process. First we create an initial phase space distribution in the shape of a doughnut. This shape is ideal to test the measurement and reconstruction algorithms since it is very non-Gaussian (Fig. 1). The simulation then transports the distribution through the initial drift section, the thick quadrupole, and the final drift section. The program calculates the beam's spatial projection by integrating the final distribution over its angular spread. By

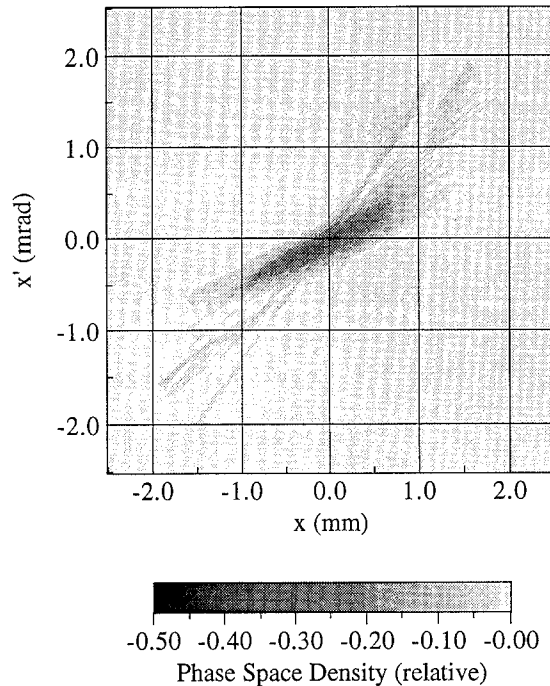


Fig. 4. Reconstructed phase space distribution for a 0.2  $\mu$ s bunch length.

varying the current to the quadrupole, we obtain the spatial projection versus distance and rotation angle. Scaling this two dimensional distribution according to Eq. (6) returns the Radon transform. RECON then reconstructs the original phase space distribution from its transform (Fig. 2).

### 3. Experiment

We conduct the tomography experiment on the Duke University Mark III electron linac. This linac is a small SLAC type linac capable of electron energies up to 44 MeV at currents of 0.2 A. The electron macropulse is normally 4.0  $\mu$ s long with a 10 Hz repetition rate. We measure the beam's vertical profile by integrating the transverse distribution over the horizontal plane. A frame grabber captures and digitizes the image of the beam hitting a phosphor screen observed by a closed circuit vidicon camera (Fig. 3). Subtracting the background leaves only the beam image. The macropulse is shortened to ensure a linear response from the screen with respect to the electron density. The screen is 1 m downstream from the quadrupole used to rotate the phase space distribution. The present beam line allows a  $0.96\pi$  rotation in phase space. We extrapolate the data for the last  $0.04\pi$ . Presently the major sources of error in the reconstruction process are the shadows cast by the crosshairs. The crosshairs are thick lines on the screen where the phosphor material has been removed to allow the machine operators a fixed reference

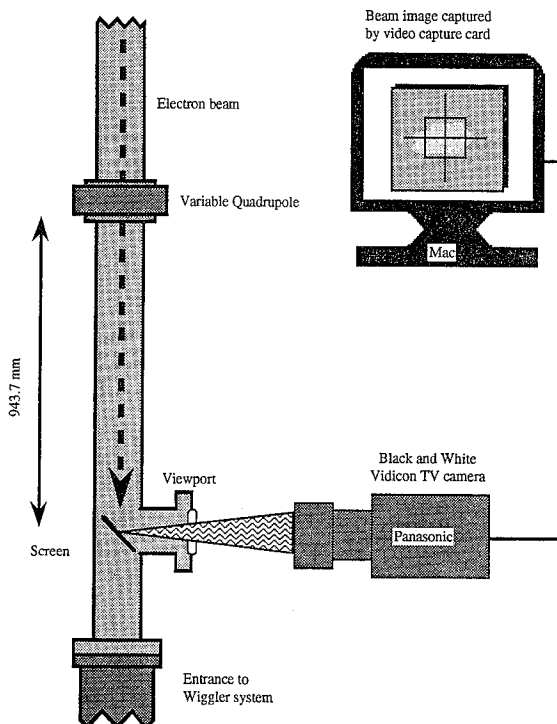


Fig. 3. Experimental apparatus to measure the transverse profile.

grid on the screen. The shadows give rise to the faint diagonal striations in the reconstructed phase space.

Fig. 4 shows a typical reconstructed phase space. We calculate an emittance of 0.153 mm-mrad by fitting the reconstructed phase space to a two dimensional Gaussian. This is the  $1/e$  emittance and is not normalized. Using the standard technique for calculating the Twiss parameters from the beam's width versus quadrupole current [1], we measure an emittance of 0.146 mm-mrad. Again the  $1/e$  width is used. Fig. 5 shows a Gaussian distribution with the Twiss parameters calculated from the experimental distribution. The bunch length for the above experiment is 0.2  $\mu$ s. As the macropulse is lengthened, time variations in the electron current and in the power to the linac moves the beam around in phase space increasing the time averaged emittance. Fig. 6 shows the reconstructed phase space for a 1.0  $\mu$ s bunch length. The emittance calculated from this reconstructed phase space is 0.262 mm-mrad and 0.294 mm-mrad for the standard emittance measurement. Additional experiments show good agreement between the two emittance measurements and reconstruct physically reasonable distributions.

In summary, we reconstruct the transverse phase space distribution for a high energy electron beam using computer tomography. The emittance calculated from the reconstructed phase space is in good agreement with stan-

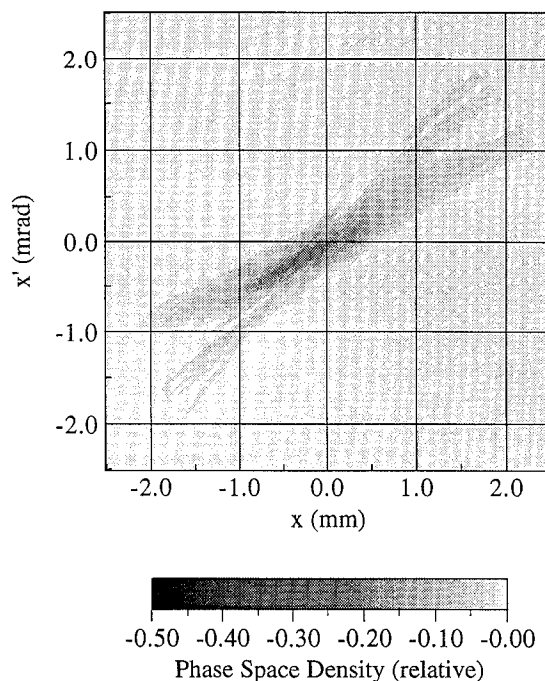


Fig. 6. Reconstructed phase space distribution for a 1.0  $\mu$ s bunch length.

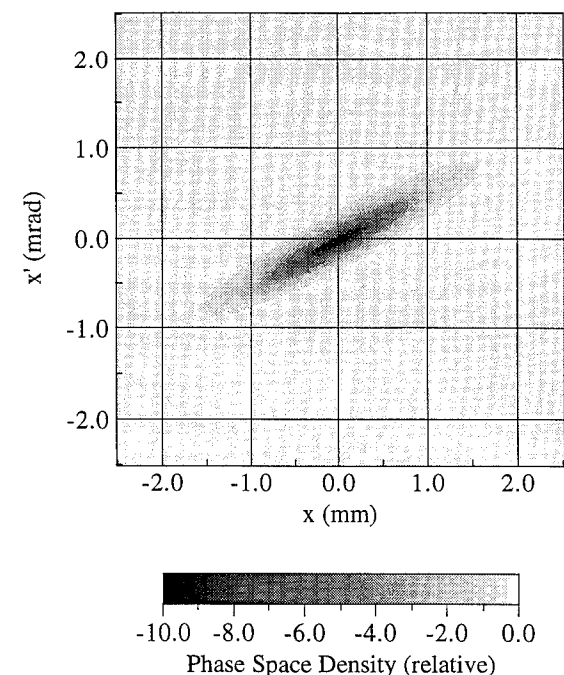


Fig. 5. Gaussian distribution using the Twiss parameters calculated from Fig. 3.

dard emittance measuring techniques. Present efforts consist of creating and reconstructing non-Gaussian beams and improving the resolution.

## References

- [1] C. Lejeune and J. Aubert, *Applied Charged Particle Optics*, ed. A. Septier (Academic Press, New York, 1980).
- [2] B.E. Carlsten, J.C. Goldstein, P.G. O'Shea and E.J. Pitcher, *Nucl. Instr. and Meth. A* 331 (1981) 791.
- [3] C.B. McKee and J.M.J. Madey, *Laser and Particle Beams*, Vol. 12, No. 1 (1994).
- [4] C.B. McKee, *Creation, Transport and Measurement of Bright Relativistic Electron Beams*, Ph.D. Dissertation, Duke University (1994).
- [5] J. Radon, *Berichte Sachsische Akademie der Wissenschaften, Leipzig, Math.-Phys. Kl.* 69 (1917) 262, translated in: S.R. Deans, *The Radon Transform and Some of Its Applications* (Wiley, New York, 1983).
- [6] S.R. Deans, *The Radon Transform and Some of Its Applications* (Wiley, New York, 1983).
- [7] O.R. Sander, G.N. Minerbo, R.A. Jameson and D.D. Chamberlin, *Proc. 1979 Linac Accelerator Conf.*, ed. R.L. Witkov (1979).
- [8] J.S. Fraser, *IEEE Trans. Nucl. Sci.* NS-26 (1) (1979) 1641.
- [9] A.P. Banford, *The Transport of Charged Particle Beams*



ELSEVIER

# Temporal characterization of the Stanford mid-IR FEL micropulses by “FROG” ☆

B.A. Richman <sup>a,\*</sup>, K.W. DeLong <sup>b</sup>, R. Trebino <sup>b</sup>

<sup>a</sup> Stanford Picosecond FEL Center, W.W. Hansen Experimental Physics Laboratory, Stanford University, Stanford, CA 94305-4085, USA

<sup>b</sup> Combustion Research Facility, Sandia National Laboratory, Livermore, CA 94551, USA

## Abstract

We present the results of frequency resolved optical gating (FROG) measurements on the Stanford mid-IR FEL. FROG is a recently developed method to acquire complete and uniquely invertible amplitude and phase temporal dependence of optical pulses. Unambiguous phase and amplitude profiles are recovered from the data. Experimental examples of near-transform-limit, chirped, and atmospheric absorption perturbed pulses are discussed.

## 1. Introduction

Frequency resolved optical gating (FROG) is a technique originally developed in 1992 at Sandia National Laboratory (CA) to characterize the complete amplitude and phase profile of near IR ultrashort Ti:sapphire laser pulses [1,2], and dye laser pulses [3]. FROG is related to autocorrelation but provides a two dimensional set of data, a type of spectrograph, which qualitatively measures optical frequency as a function of time. The most important aspect of this spectrograph is that it is uniquely invertible to the optical pulse field amplitude and phase, both as functions of time within the pulse. Whereas seemingly smooth, Gaussian autocorrelation traces can be generated by severely asymmetric or otherwise pathological pulses, FROG reveals the exact pulse character.

RF linac driven FELs are inherently mode-locked to the linac pulse repetition rate. Most of the mid-IR FELs generate picosecond optical pulses, containing approximately 100 optical cycles. In this paper, we present experimental data for near-transform-limit optical pulses, chirped pulses, and pulses perturbed by narrow atmospheric water vapor absorption. All measurements were performed on the mid-IR FEL at Stanford.

## 2. Theory

The “polarization gate” variation of FROG was used for this paper [1]. A material with significant  $\chi^{(3)}$  is used

to “gate” the optical pulse, and the spectrum of the gated “signal” pulse is analyzed with a spectrometer. The signal pulse complex electric field profile (for the polarization gate) takes the form

$$E_{\text{sig}}(t, \tau) = E(t) |E(t - \tau)|^2, \quad (1)$$

where  $E(t)$  is the complex field profile of the initial laser pulse,  $|E|^2$  is the “gate”, and  $\tau$  is the optical delay between them. In polarization gate geometry, the gate beam polarization is at 45° to the input, and the signal polarization is generated at an additional 45° rotation, perpendicular to the input. Then the signal can be isolated with a polarizer crossed to the input [1]. Note that for a Gaussian pulse, the gate is  $\sqrt{2}$  shorter than the initial pulse, and the signal pulse is  $\sqrt{3}$  shorter. The gate samples a large fraction of the pulse, centered at time  $\tau$ , shorter than the initial pulse so that temporal information may be extracted, but long enough so that spectral information is maintained. The above expression is invertible since integrating over  $\tau$  yields a quantity directly proportional to the initial field profile.

The FROG trace is the spectral intensity of the signal,

$$I_{\text{FROG}}(\omega, \tau) \propto \left| \int_{-\infty}^{\infty} E_{\text{sig}}(t, \tau) \exp(-i\omega t) dt \right|^2 \quad (2)$$

That the spectrum is dependent on the delay is the key to FROG; it is a spectrogram of the pulse, just as a musical score is a spectrogram of a composition. Since Eq. (1) is already invertible, we need only find  $E_{\text{sig}}$  from  $I_{\text{FROG}}$  using Eq. (2). This is a phase retrieval problem. Although unique phase retrieval is not possible with a spectrum and autocorrelation of the initial pulse, it is possible with the FROG spectrogram [1,4]. As a simple example, consider a pulse with a frequency chirp. Since the gate samples only a fraction of the initial pulse, the average frequency of the

☆ Work supported in part by the Office of Naval Research, Contract #N00014-91-C-0170.

\* Corresponding author. Tel. +1 415 723 0209, fax +1 415 715 8311, e-mail: brich@leland.stanford.edu.

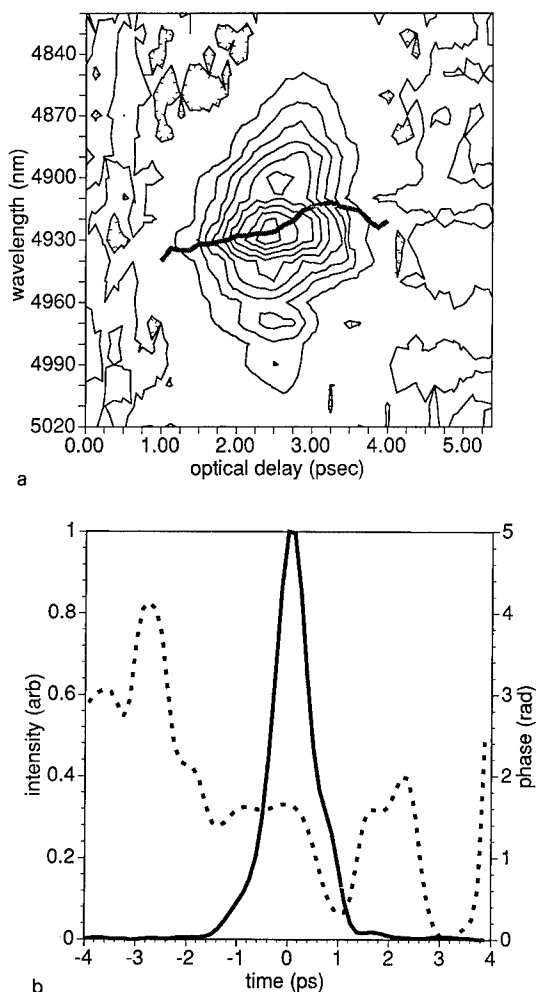


Fig. 1. (a) Experimental FROG trace for nearly transform limited pulse. The black line traversing trace is the average wavelength as a function of time, which indicates a chirp of  $\approx 10$  nm/ps. (b) Electric field amplitude (solid) and phase (dotted) as computed with the inversion algorithm from trace in (a). The computed rms time-bandwidth product is 0.88.

signal should shift as a function of the optical delay. The chirp in units of frequency per delay is given by the slope of the curve frequency vs. delay, as demonstrated by the experimental results shown in Fig. 1 and discussed later.

The inversion is achieved computationally by an iterative process of Fourier transforming  $E_{\text{sig}}$  back and forth between the time (not delay) and frequency domains until the computed FROG trace matches (within acceptable error) the input trace [1].

At each iteration, the square magnitude of  $E_{\text{sig}}$  is forced to match the FROG signal while preserving its phase,

$$|E_{\text{sig}}(\omega, \tau)| = \sqrt{I_{\text{FROG}}(\omega, \tau)}. \quad (3)$$

At the first iteration, the phase of  $E_{\text{sig}}$  is set randomly.  $E_{\text{sig}}$  is then transformed to the time domain, and the original pulse is derived from it (Eq. (1)):

$$E(t) = \int_{-\infty}^{\infty} E_{\text{sig}}(t, \tau) d\tau, \quad (4)$$

and renormalized over time. A new  $E_{\text{sig}}$  is computed from this pulse (with different phase from the previous iteration):

$$E_{\text{sig}}(t, \tau) = E(t) |E(t - \tau)|^2. \quad (5)$$

$E_{\text{sig}}$  is transformed back to the frequency domain, and the loop repeats until an error function based on the difference between the square magnitude of  $E_{\text{sig}}$  and the FROG trace is within a set tolerance. This algorithm, described in detail in Ref. [1], converges for most pulse shapes but does not perform well for complex, multi-peaked pulses. A combination algorithm has been developed more recently to handle complex cases [2].

### 3. Experiment

The first half of the experimental apparatus is a general purpose pump/probe set-up and the second half is a monochromator with a single element detector. Unlike the work reported in Ref. [3], we had neither a detector array nor an imaging spectrometer. Therefore we acquired the complete FROG traces by scanning both the optical delay (with a stepper motor driven translation stage), and the wavelength (with the manual crank of the monochromator).

The gate beam polarization was set and the signal beam was filtered using ZnSe Brewster plate polarizers. A small portion of the beam was picked off before the monochromator so that beam steering could be optimized and the necessary scan length determined. The monochromator slits were typically set for 5 nm resolution and the laser wavelength was 5  $\mu\text{m}$ . A 1 mm diameter indium antimonide detector with 1 MHz bandwidth amplification was used to measure the FROG signal.

A 486 PC computer running "LabView<sup>®</sup>" data acquisition software controlled the motorized delay and digitized the detector signal. The signal was averaged over 600 to 1200 micropulses selected from the same time interval within each of the FEL macropulses. Four to ten macropulses were averaged for each point in the trace. The 600 to 1200 pulse gate was used in case the optical pulse evolved during the FEL macropulse. The noise level was about 5% of the trace peak after averaging. The computer scanned the delay over the set range, and then the monochromator was advanced manually to the next wavelength. Each complete scan of  $\approx 50$  delays by  $\approx 25$  wavelengths took about half an hour.

A 1 mm thick germanium plate provided the  $\chi^{(3)}$  for the gate. We chose germanium because it has a relatively high  $\chi^{(3)}$  and does not have a competing  $\chi^{(2)}$ . Semicon-

ductors with a band-gap of slightly more than twice the photon energy are ideal, and Ge has a band-gap equivalent to a 1.8  $\mu\text{m}$  wavelength. The conversion efficiency was

high enough with our pulse peak power of 200 kW that we needed only the amplifier provided with the detector ( $10^6$  V/A).

#### 4. Analysis and results

Ideally, the data obtained by the procedure described above would be noise free and have zero background. However, laser fluctuations contribute approximately 5% noise uncertainty to the FROG values. And since germanium is not an ideal material, it slightly scatters and depolarizes the laser beam even in the absence of a gate beam. A background spectrum results. If the scattering depolarization is incoherent, then this spectrum may be subtracted out from the entire FROG trace. If it is coherent, then it must be included in the inversion computation. In the analysis presented here, we simply averaged the first few points of each delay scan (where pulse and gate did not overlap) and subtracted that out. We noted that the background appears to be partly coherent and partly incoherent. The magnitude of the coherent part, and the effect of subtracting it out, can be estimated from the size and depth of negative signal regions in the FROG trace after the subtraction. In the worst case, the peak of the trace was five times the depth of the deepest negative region. Since the background is linear in laser power and the true FROG signal is cubic, care should be taken to minimize power losses and to optimize gating conversion efficiency. The two-dimensional data array was then splined into a  $64 \times 64$  array required by the inversion software.

Fig. 1a shows the experimental FROG trace for a nearly transform limited pulse. The spectrum rms half-width measured by the diagnostics [5] was 0.36% at 4.92  $\mu\text{m}$  or  $\Delta\omega = 1.4$  THz-rad. The rms half-width pulse length (measured by autocorrelation) was 0.51 ps. So the measured time-bandwidth product is 0.71 and the theoretical minimum is 0.5. The spectrum and autocorrelation appear in Ref. [6]. A truly transform limited pulse would have a non-rotated elliptical FROG trace. The actual trace is slightly rotated and somewhat elliptical. The background subtraction worked well in this case as there are no significant negative regions in the area of interest. The jaggedness of the contours is probably caused by a minor

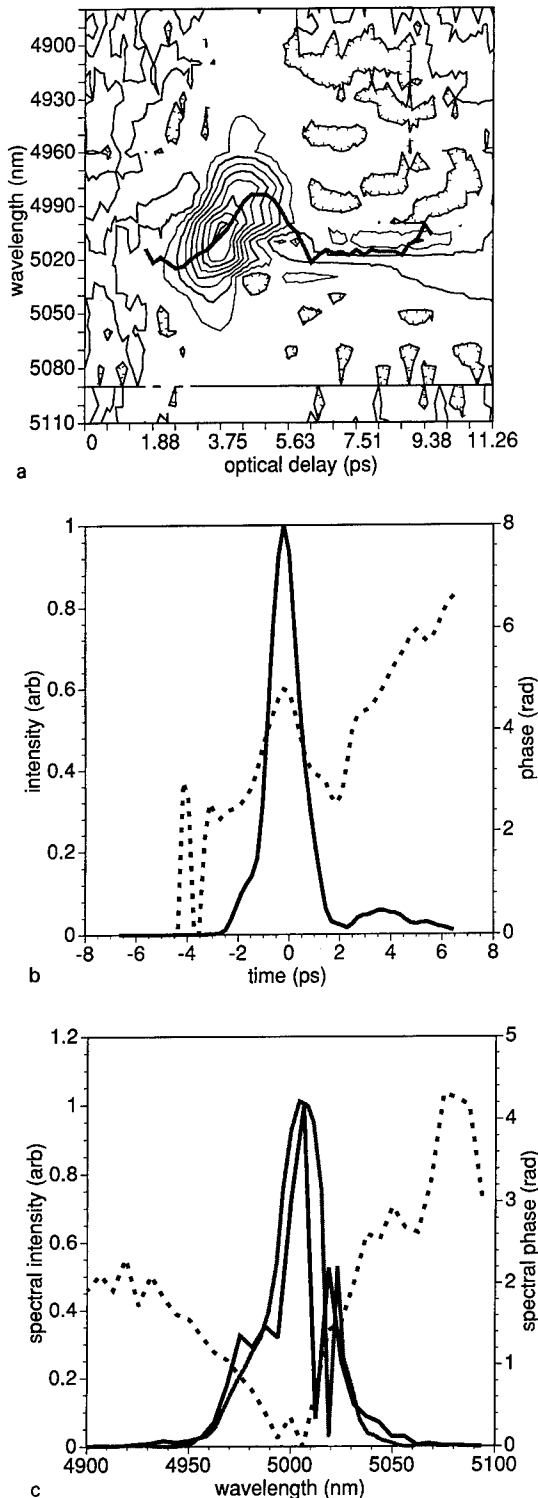


Fig. 2. (a) Experimental FROG trace showing both a significant chirp and perturbation caused by atmospheric absorption. Note large slope of average wavelength curve and non-zero signal at large time delays. (b) Electric field amplitude (solid) and phase (dotted) vs. time as computed with the inversion algorithm. The chirp is 1% over the rms pulse full width. The tail is a result of water vapor free induction (absorption). (c) Computed field amplitude (solid) and phase (dotted) in the spectral domain and experimentally measured spectrum (gray). The absorption line is evident in both computed and experimental traces.



pulse shape change during the course of the scan. Wavelengths were interleaved so that such problems could be easily detected. The black line traversing the trace is the average wavelength as a function of optical delay in the FROG trace. In the polarization gate geometry, this average is the instantaneous wavelength as a function of time within the pulse. In Fig. 1, the function is linear over most of the pulse, and the slope of the line is the “chirp” of the pulse:  $\approx 10$  nm/ps or about 0.2% over the rms full-width of the pulse. This is small compared with the spectral rms full-width of 0.72%.

Fig. 1b shows the electric field amplitude and phase both as functions of time, computed using the inversion algorithm. The rms spectral half-width of the computed pulse (not shown) is 1.5 THz-rad, and the rms half-width pulse length is 0.59 ps. Then the computed time–bandwidth product is 0.88. These values compare well with the diagnostic spectral and autocorrelation measurements. The instantaneous frequency and the chirp can be obtained by differentiating the phase vs. time (and dividing by 2):  $\approx 1.5$  THz-rad/ps or 0.2% over the pulse length. Again, this agrees with the value calculated directly from the FROG trace.

Fig. 2a is an example of a FROG trace of a pulse with a chirp and also perturbed by a water absorption line. The spectral rms half-width was 0.3% with a center wavelength of  $5.00 \mu\text{m}$  and the rms pulse length half-width (from autocorrelation) was 0.62 ps. The time–bandwidth product is then 0.77. This pulse has a stronger chirp than the pulse in Fig. 2:  $\approx 30$  nm/ps (from average wavelength) or 0.9% over the rms pulse full-width. This is one half of the spectral width, and contributes most of the increase in the non-ideal time–bandwidth product. The long tail of signal extending out to 10 ps is caused by the water absorption free induction.

Fig. 2b shows the electric field amplitude and phase as functions of time. The quadratic phase indicates a chirp of  $\approx 0.9\%$ /ps or 1% over the pulse rms full-width, in approximate agreement with the direct calculation from the trace. Also note the tail from the water free induction.

Fig. 2c illustrates the computed spectrum amplitude and phase from the inversion data in Fig. 2b, and the experimental spectrum for comparison. The water absorption is quite evident. Since the absorption line is much narrower than the FEL spectrum, the FEL pulse is almost like an

impulse excitation, and the water resonates, re-emits coherently, and decays in a time determined by its line width, much longer than the initial pulse. This tail can effectively reduce the time resolution of pump/probe and photon echo experiments.

The negative area in Fig. 2a in the plot around (5.5 ps, 5010 nm) is one sixth as deep as the main peak is high, a result of the background subtraction. Most such ratios were about one tenth.

## 5. Conclusion

We have performed FROG measurements on the mid-IR FEL at Stanford. We have obtained results for nearly transform limited pulses, chirped pulses, and pulses perturbed by narrow atmospheric absorption lines. Basic pulse properties such as approximate pulse shape and chirp can be deduced directly from the FROG trace. Exact results are obtained by computational inversion. Our FROG inversions agree with our diagnostic measurements. We have also obtained preliminary FROG results when the FEL has strong sidebands, and we intend to perform more sideband measurements in the future.

## Acknowledgements

The authors wish to thank C. Rella for use of his optical pump/probe apparatus and data acquisition software.

## References

- [1] R. Trebino and D. Kane, *J. Opt. Soc. Am. A* 10 (1993) 1101 and references therein.
- [2] K.W. DeLong and R. Trebino, *J. Opt. Soc. Am. A* 9 (1994) 2429, and references therein.
- [3] D.J. Kane and R. Trebino, *Opt. Lett.* 18 (1993) 823.
- [4] H. Stark, *Image Recovery: Theory and Application* (Academic Press, Orlando, FL, 1987).
- [5] K.W. Berryman et al., these Proceedings (16th Int. Free Electron Laser Conf., Stanford, CA, USA, 1994) *Nucl. Instr. and Meth. A* 358 (1995) 300.
- [6] B.A. Richman et al., *ibid.*, p. ABS 32.



ELSEVIER

## Photocathodes for free electron lasers <sup>☆</sup>

S.H. Kong <sup>\*</sup>, J. Kinross-Wright, D.C. Nguyen, R.L. Sheffield*Los Alamos National Laboratory, Los Alamos, NM, USA*

### Abstract

Many different photocathodes have been used as electron sources for FELs and other electron accelerator systems. In choosing one, a compromise between lifetime and quantum efficiency has been unavoidable. High quantum efficiency photocathodes such as  $K_2CsSb$ ,  $Cs_3Sb$ , and cesiated GaAs have short operational lifetimes and require an ultrahigh-vacuum environment. Long lifetime photocathodes such as  $LaB_6$ , Cu, and Y have relatively low quantum efficiencies. However, recently, cesium telluride was found to be an exception. Initial results from CERN and now at Los Alamos have shown that  $Cs_2Te$  is reasonably rugged with a high quantum efficiency below 270 nm. Further studies carried out at Los Alamos have determined that its performance as an electron source for the Los Alamos Advanced FEL is excellent.

### 1. Introduction

The accelerator and FEL communities have considered many different photocathodes for use in photoinjectors. However, the ideal photocathode has been illusive. The main problem has been finding a fast photocathode that is robust in an operating accelerator and has good quantum efficiencies ( $> 1\%$ ) for photoemission by visible or soft UV light. In 1993,  $K_2CsSb$  and Cu photocathodes were used the most in photoinjectors around the world [1].  $K_2CsSb$  photocathodes, which last about a day, are typically driven with 527-nm light with a QE of a few percent. In contrast Cu photocathodes, which last almost indefinitely, are typically driven with 266-nm light with a QE on the order of  $10^{-4}$ . This clearly illustrates the large gap that exists between robust photocathodes and high QE photocathodes that are being used for photoinjectors. Y, Sm, and Mg have QEs of  $0.5\text{--}1.0 \times 10^{-3}$  and may replace Cu as the dominant metallic photocathode, but still fall short of bridging the gap.

Recently, it has been shown at CERN that cesium telluride photocathodes are reasonably robust while operated in a dc gun with a 266-nm QE of a few percent [2]. We have further characterized the properties of  $Cs_2Te$  photocathodes inside the fabrication chamber and while operated in the photoinjector of the Los Alamos Advanced FEL. The results are given in this paper and show that a good quantum efficiency with a reasonable lifetime is

achieved, helping to bridge the gap between rugged metal photocathodes and fragile alkali-antimonide photocathodes. Several properties of  $Cs_2Te$  photocathodes will be compared with many of the photocathodes being used or being considered for use in photoinjectors. First a survey of these photocathodes will be presented.

### 2. Overview of photocathodes

A large variety of materials have been considered for use or have been used as photoinjector photocathodes and they include:  $K_2CsSb$ ,  $Cs_3Sb$ , cesiated GaAs, CsI,  $Cs_2Te$ , diamond, Cu, Y, Sm, Mg, Ba, ferroelectric cathodes, and thermionic cathodes. The relevant properties that characterize a photoinjector photocathode are: spectral response, operational lifetime, temporal response, saturation level, damage threshold, voltage hold-off, and the transverse energy spread of the emitted electron beam. A comparison between photocathodes of many of these properties is shown in Table 1. The readers are directed to this table for references on specific photocathodes. They will not be recited in this section. A brief survey of the strengths and weaknesses of these photocathodes with the exception of  $Cs_2Te$  will be presented in this section.  $Cs_2Te$  photocathodes will be compared with other photocathodes in Section 4.

#### 2.1. Metallic photocathodes

Of the proven photocathodes, metal photocathodes are the most robust against degradation due to surface contamination, damage due to conditioning or heating, and electric breakdown due to high surface fields. However, the QEs are low because of the high reflectivity, electron-

<sup>☆</sup> Work supported by LANL Laboratory Directed Research and Development under the auspices of the U.S. Department of Energy.

<sup>\*</sup> Corresponding author.

electron scattering that keeps the escape depth very shallow, and a large barrier at the surface [3,4]. Cu photocathodes have been widely used. It is very robust and can be transferred in air. Recently, magnesium, yttrium, samarium, and barium have also been considered. Barium has one of the best spectral response for a metal ( $\sim 0.1\%$  at 334 nm), but is less robust than other metals and may not be able to withstand high electric fields since its work function is  $\sim 2.5$  eV. Yttrium and samarium have work functions of 2.9 eV and 2.7 eV and 266-nm QEs of  $5 \times 10^{-4}$  and  $7 \times 10^{-4}$ , respectively. They are expected to handle up to 100 MV/m and should be more robust than Ba. Magnesium has a relatively high work function of 3.66 eV (4.3 eV for Cu), but still retains a respectable 266-nm QE of  $6 \times 10^{-4}$ . This is currently the most promising metal photocathode.

## 2.2. Semiconductor photocathodes

Semiconductor photocathodes with high QEs for visible light are very sensitive to contamination.  $K_2CsSb$ ,  $Cs_3Sb$ , and cesiated GaAs require ultra-high vacuum conditions and still have short lifetimes.  $K_2CsSb$  and  $Cs_3Sb$  photocathodes need to be changed almost on a daily basis. Cesium GaAs is typically used as a polarized electron source and therefore has a special niche. Careful handling and the ability to reactivate the surface with more cesium has made its use practical [5]. However, despite the improvements, GaAs still requires extremely good vacuum conditions. Furthermore, cesiated GaAs is a negative-electron-affinity photocathode, which typically has long response times [4].

Wide band gap semiconductor photocathodes with high QE for uv light are relatively robust. CsI and (111) NEA diamond photocathodes both require light very close to

vacuum uv, which is typically achieved by frequency quintupling the fundamental of a YLF or YAG laser. This requirement is quite undesirable. Furthermore, CsI photocathodes exhibit unexpected behavior in a rf gun resulting in premature saturation and satellite bunches [2], and diamond photocathodes may have a poor response since it is a NEA photocathode. Diamond photocathodes are still in the developmental stage so a definitive verdict cannot be made at this time.

## 2.3. Thermionic cathodes

Thermionic trioxide cathodes and B-type thermionic dispenser cathodes can operate as photocathodes with 266-nm QEs of  $3.5 \times 10^{-4}$  and  $2.3 \times 10^{-3}$ , respectively. Both require slight heating to keep the QE from degrading too quickly. The trioxide cathodes are not suitable for ps applications due to their long response times. The QE of the dispenser photocathode degrades at a rate of about 3.6% per hour, but can be rejuvenated by heating to 700°C. However, since the QEs of these photocathodes are comparable with that of metals, they are not very competitive.

$LaB_6$  is a metallic-like substance recognized for its thermionic properties. With proper cleaning, a QE of about  $10^{-3}$  may be achieved for 355-nm light incident at a 45° angle. Oxygen can be removed from  $LaB_6$  by heating to 1600°C [6]. The material can be exposed to air and reactivated in vacuum. To keep the surface clean, the photocathode needs to be heated. It remains to be seen if  $LaB_6$  will be superior to metal photocathodes.

## 2.4. Ferroelectric photocathodes

Ferroelectric photocathodes are still in the developmental stage. The emission process is different from that of

Table 1

| Material              | $\lambda$<br>(nm) | QE at $\lambda$      | Operational<br>life times | Vacuum<br>(Torr)       | Response<br>time | $E_{max}$<br>(MV/m) | References |
|-----------------------|-------------------|----------------------|---------------------------|------------------------|------------------|---------------------|------------|
| $Cs_2Te$              | 263               | 13%                  | $T_{1/e} > 100$ h *       | $10^{-10}$ – $10^{-9}$ | $< 3$ ps         | $> 20$              | [2,8,9]    |
| CsI                   | 209               | 2%                   | $T_{1/2} > 150$ h         | $10^{-10}$ – $10^{-9}$ | ( $> ps$ )       |                     | [2]        |
| Diamond               | $< 210$           | $> 1\%$              | (very long)               |                        | ( $> ps$ )       |                     | [10]       |
| $K_2CsSb$             | 527               | 8%                   | $T_{1/2} < 4$ h           | $10^{-10}$ – $10^{-9}$ | $\sim ps$        | $> 20$              | [11]       |
| $Cs_3Sb$              | 527               | 4%                   | $T_{1/2} < 4$ h           | $10^{-10}$ – $10^{-9}$ | $\sim ps$        | $> 20$              | [11]       |
| 0.3 $\mu m$ GaAs (Cs) | 750               | 1.5–6%               | (short) *                 | $10^{-11}$             | $< ns$           |                     | [12,13]    |
| Cu                    | 266               | $1.4 \times 10^{-4}$ | very long                 | $10^{-7}$              | $< ps$           | $> 100$             | [14]       |
| Y                     | 266               | $5 \times 10^{-4}$   | (long)                    | ( $< 10^{-7}$ )        | $< ps$           | $\sim 100$          | [14]       |
| Sm                    | 266               | $7 \times 10^{-4}$   | (long)                    | ( $< 10^{-7}$ )        | $< ps$           | $\sim 100$          | [14]       |
| Mg                    | 266               | $6 \times 10^{-4}$   | $> 5000$ h                | ( $10^{-7}$ )          | $< ps$           |                     | [14,20]    |
| Ba                    | 337               | 0.1%                 | (short-long)              | ( $< 10^{-7}$ )        | $< ps$           |                     | [15]       |
| $LaB_6$               | 355               | 0.1%                 | $\sim 1$ day *            | $< 10^{-7}$            |                  |                     | [16]       |
| Thermionic dispenser  | 266               | $3.5 \times 10^{-4}$ | $T_{1/2} = 12$ h *        | $3 \times 10^{-10}$    | $< 380$ ps       |                     | [17]       |
| Trioxide thermionic   | 355               | 0.1%                 | $T_{1/2} = 10$ h *        | $3 \times 10^{-10}$    | $< 400$ ps       |                     | [18]       |
| Ferroelectric         | 355               | $6 \times 10^{-4}$   | very long                 | ( $10^{-7}$ )          | $< ns$           |                     | [19]       |

standard photocathodes. The incident light induces polarization switching resulting in a macroscopic charge separation in the ferroelectric sample that causes self-emission of energetic ( $> 10$  keV) electrons. 355-nm pulsed laser light has been used in experiments to study this effect, with an effective QE of about  $6 \times 10^{-4}$ . At a nanosecond time scale, no time lag was observed between the laser and the electron-beam pulse. It is also postulated that laser light pulses of any wavelength will suffice assuming the energy is absorbed at the surface layer. For the emission to be sustained at a constant level, the polarization of the sample must be regularly switched by high voltage pulses. This requires electrodes on the photocathode surface. Since the makeup and physics of ferroelectric photocathodes are totally different, tests in a photoinjector are necessary to fully evaluate its performance. Response time, hold-off voltage, and the emittance of the extracted beam need to be examined.

### 3. Characterization of cesium telluride photocathodes

Cesium telluride is a p-type semiconductor with a band gap of about 3.3 eV and an electron affinity of roughly 0.2 eV [7]. Several cesium telluride photocathodes were fabricated and characterized in the fabrication chamber and in the photoinjector of the Los Alamos Advanced FEL. The fabrication process is similar to that of cesium antimonide and is explained elsewhere [8].

#### 3.1. Characterization in the fabrication chamber

The 263-nm QE for  $\text{Cs}_2\text{Te}$  photocathodes is about 13%. 263 nm is the wavelength of the pulsed laser beam used to drive the photocathode when operated in the Advanced FEL. The ruggedness was tested by observing the effects of putting them in  $10^{-7}$  Torr and  $10^{-4}$  Torr vacuum environments.

A  $\text{Cs}_2\text{Te}$  photocathode was stored in  $1\text{--}4 \times 10^{-7}$  Torr vacuum for several hours. The 251-nm QE dropped from 15.7% to 5.2% after the initial 17 hours of exposure. Further exposure dropped the QE to 3.1% after 91.5 hours. The rate of QE decay decreases with time, so the photocathode should retain a QE above 1% in a  $10^{-7}$  Torr vacuum for a long time.

We observed that heating contaminated photocathodes above  $100^\circ\text{C}$  partially rejuvenated their spectral response in the uv. The photocathode mentioned above, with a residual 251-nm QE of 3.1%, was heated to  $110^\circ\text{C}$  for about 12 hours. After cooling to room temperature, the 251-nm QE was measured to be 11.3%. After storing the photocathode in  $10^{-9}$  Torr vacuum for three weeks, the 251-nm QE dropped to 4.7%.

Similar experiments were made by exposing another  $\text{Cs}_2\text{Te}$  photocathode to  $2 \times 10^{-4}$  Torr of air by using a variable leak valve. After five minutes of exposure, the

251-nm QE dropped from 17.8% to 0.70%. After sixty minutes the 251-nm QE dropped to 0.50%. Upon heating to  $175^\circ\text{C}$  for several hours, the QE peaked at 15.0% while hot and stabilized at 10.4% after cooling to room temperature. It was determined that the best temperatures for rejuvenating air contaminated  $\text{Cs}_2\text{Te}$  photocathodes are between  $150^\circ\text{C}$  and  $200^\circ\text{C}$ .

Further details can be found in Ref. [8].

#### 3.2. Characterization in the photoinjector of the Los Alamos Advanced FEL

Cesium telluride photocathodes were transported from the fabrication chamber to the photoinjector of the Advanced FEL under high vacuum. The best 263-nm QE measured for a  $\text{Cs}_2\text{Te}$  photocathode operated in the photoinjector was  $12.5 \pm 3\%$ .

The  $\text{Cs}_2\text{Te}$  photocathodes were typically operated with a 20 MV/m accelerating field and is driven with 263-nm light by  $7.7 \pm 1.5$  ps laser pulses from a frequency quadrupled Nd:YLF laser. We observed no problems with breakdown of the film or dark current due to the accelerating field. However, these fields are modest and do not seriously test the hold-off voltage of these photocathodes. We were able to extract  $2.0 \pm 0.2$  nC/micropulse from a  $1.75 \pm 0.25$  mm radius area on a  $\text{Cs}_2\text{Te}$  photocathode, which is comparable to the space charge limit of  $1.7 \pm 0.5$  nC/micropulse.

The lengths of electron micropulses were measured downstream of the linac by using a Hamamatsu model M1955 streak camera to look at the optical transition radiation (OTR) generated promptly by electrons striking a metal screen. The measured pulse lengths compared well with the results obtained from PARMELA simulations [9]. Therefore, any increase in pulse length due to the photoemission process from  $\text{Cs}_2\text{Te}$  is less than the uncertainties in our pulse length measurements, which is about  $\pm 4$  ps. No discernible tail was observed in the temporal response.

The emittance of the electron beam was estimated by measuring the waist of the electron beam core at the first OTR screen as a function of the field strength of a magnetic quadrupole that is 27 cm upstream. The emittance value measured for  $\text{Cs}_2\text{Te}$  divided by the value measured for  $\text{K}_2\text{CsSb}$  gives a ratio of  $0.9 \pm 0.3$ . Therefore, we see no significant difference in the measured emittance.

The Los Alamos Advanced FEL has successfully lased at wavelengths of 5–6  $\mu\text{m}$  with cesium telluride photocathodes. The operational lifetime of these photocathodes is much greater than that of the  $\text{K}_2\text{CsSb}$  photocathodes normally used and is probably well beyond 100 hours if the photocathodes are considered dead if the QE is less than 1%. The shelf life appears to be excellent even after partial degradation due to operations. In the past, we observed that the shelf life of partially degraded  $\text{K}_2\text{CsSb}$  photocathodes was about a day. Due to the relatively long

life of  $\text{Cs}_2\text{Te}$  photocathodes, more running time will be required before they are well established.

Further details can be found in Ref. [9].

#### 4. Discussion and conclusion

Cesium telluride is clearly a superior photocathode to  $\text{K}_2\text{CsSb}$ . It is much more robust, has a 263-nm QE of about 13%, and can be partially rejuvenated. Furthermore, the response time is sufficiently fast for picosecond operations, the dark current at 20 MV/m is negligible, current near the space charge limit was extracted, and the emittance of the extracted beam is comparable. The only disadvantage is the requirement of using a uv drive laser beam.

The comparison between  $\text{Cs}_2\text{Te}$  and several other photocathodes is summarized in Table 1. What is not reflected in the operational lifetime is the initial drop in QE that occurs during the transfer to the photoinjector. For  $\text{K}_2\text{CsSb}$ ,  $\text{Cs}_3\text{Sb}$ , and GaAs, this may be substantial if ultra-high vacuum is not maintained. With our current system, the QE of  $\text{K}_2\text{CsSb}$  photocathodes typically dropped by more than a factor of two during transfer.

In this table,  $\text{Cs}_2\text{Te}$  photocathodes have the highest QE at its operating wavelength. If we exclude photocathodes that require light with wavelengths less than 250 nm,  $\text{Cs}_2\text{Te}$  is also the most robust photocathode that has a QE greater than 0.1%. The only advantage with thermionic photocathodes is that it can be exposed to air and still be activated. The response times of these photocathodes are probably not sufficiently fast for our applications. Concerning ferroelectric photocathodes, there is insufficient data to make a good comparison.

It remains to be seen if  $\text{Cs}_2\text{Te}$  can replace applications that require rugged metal photocathodes. Cu, Mg, Y and Sm photocathodes have superior lifetimes, faster response, and can better sustain damage from arcing or very high currents. However, since the QE is less by two to three orders of magnitude, any application that does not absolutely require a photocathode material as rugged or as fast as metals may benefit from a  $\text{Cs}_2\text{Te}$  photocathode.

#### Acknowledgements

Work supported by LANL Laboratory Directed Research and Development under the auspices of the U.S. Department of Energy.

I would also like to acknowledge Steven Gierman, John Plato, Steven Russel, Boyd Sherwood, Floyd Sigler, Robert Springer, and Michael Weber for their assistance in the project.

#### References

- [1] C. Travier, Nucl. Instr. and Meth. A 340 (1994) 26.
- [2] E. Chevallay, J. Durand, S. Hutchins, G. Suberlucq and M. Wurgel, Nucl. Instr. and Meth. A 340 (1994) 146.
- [3] A.H. Sommers, Photoemissive Materials (Krieger, New York, 1980).
- [4] W.E. Spicer and A. Herrera-Gomez, Modern Theory and Applications of Photocathodes, 1993 Int. Symp. on Imaging and Instrumentation, San Diego, CA, July 11–16, 1993.
- [5] R.E. Kirby, G.J. Collet and K. Skarpaas, Invited talk presented at the Particle Accelerator Conf. Washington, DC, May 17–21, 1993.
- [6] P.R. Davis, and S.A. Chambers, Appl. Surf. Sci. 8 (1981) 197.
- [7] R.A. Powell, W.E. Spicer, G.B. Fisher and P. Gregory, Phys. Rev. B 8 (1973) 3987.
- [8] S.H. Kong, D.C. Nguyen, R.L. Sheffield and B.A. Sherwood, these Proceedings (16th Int. Free Electron La Conf., Stanford, CA, USA, 1994) Nucl. Instr. and Meth. A 358 (1995) 276.
- [9] S.H. Kong, J. Kinross-Wright, D.C. Nguyen, R.L. Sheffield and M.E. Weber, *ibid.*, p. 284.
- [10] C.P. Beetz, B. Lincoln, K. Segall, D. Wall, M. Vasas, D.R. Winn, D. Doering and D. Carroll, Applications of Diamond Films to Photocathode Electron Guns and Accelerators, IEEE, 0-7803-0135-8/91 (1991).
- [11] The data for  $\text{K}_2\text{CsSb}$  and  $\text{Cs}_3\text{Sb}$  were acquired over the years these photocathodes were used at Los Alamos.
- [12] D. Schultz et al., Nucl. Instr. and Meth. A 340 (1994) 127.
- [13] R. Calabrese et al., Nucl. Instr. and Meth. A 340 (1994) 109.
- [14] T. Srinivasan-Rao, J. Fischer and T. Tsang, J. Appl. Phys. 69 (1991) 3291.
- [15] M.E. Conde, S. Chattopadhyay, K.-J. Kim, S.-I. Kwon, K.-N. Leung and A.T. Young, IEEE Particle Accelerator Conf., Washington, DC, May 1993.
- [16] M. Boussoukaya, H. Bergeret, R. Chehab and B. Leblond, Nucl. Instr. and Meth. A 264 (1988) 131.
- [17] B. Leblond, Nucl. Instr. and Meth. A 317 (1992) 365.
- [18] B. Leblond and G. Rajaonera, Nucl. Instr. and Meth. A 333 (1993) 524.
- [19] H. Riege, Nucl. Instr. and Meth. A 340 (1994) A 80.
- [20] X.J. Wang, T. Srinivasan-Rao, K. Batchelor, I. Ben-Zvi and J. Fischer, Measurements on photoelectrons from a magnesium cathode in a microwave electron gun, preprint, submitted to J. Appl. Phys.



ELSEVIER

## Fabrication and characterization of cesium telluride photocathodes: A promising electron source for the Los Alamos Advanced FEL <sup>☆</sup>

S.H. Kong <sup>\*</sup>, D.C. Nguyen, R.L. Sheffield, B.A. Sherwood*Los Alamos National Laboratory, Los Alamos, NM, USA*

### Abstract

The Advanced FEL at Los Alamos embodies a  $K_2CsSb$  photocathode as an electron source. The photocathode consists of a  $K_2CsSb$  film deposited on a molybdenum plug that can be inserted into the linac of the FEL. However, because  $K_2CsSb$  is easily contaminated and has a half-life of less than a day when in use, switching to a more rugged high quantum efficiency (QE) material such as  $Cs_2Te$  is considered as a means to lengthen the beam time.  $Cs_2Te$  films were deposited on molybdenum plugs in an ultrahigh-vacuum research chamber. Several  $Cs_2Te$  films were measured in situ for their spectral responses with a bias voltage of 90 V; the resulting QEs were 15–18% at a wavelength of 251 nm, 0.3–1% at 334 nm,  $1-3 \times 10^{-4}$  at 365 nm, and  $10^{-7}$ – $10^{-6}$  at 546 nm. For this cathode to be useful, we need to frequency quadruple the 1053 nm line of the Nd:YLF laser to achieve a wavelength of 263 nm. Initial studies showed that the 251-nm QE of  $Cs_2Te$  is much less sensitive to contamination than the 526-nm QE of  $K_2CsSb$ . We exposed  $Cs_2Te$  photocathodes to air at  $10^{-4}$  Torr for five minutes. As a result, the QEs at 254 nm dropped from 16–18% to 1–2%. However, heating the cathode to 165°C revived the QE to about 10%. We conclude that  $Cs_2Te$  is a very rugged photocathode material for use in an rf photoelectron source.

### 1. Introduction

The Los Alamos Advanced free electron laser uses a photocathode driven by a Nd:YLF modelocked laser as a source for 1–3 nC electron pulses of 10–30 ps length. The electrons liberated from the photocathode are accelerated in an rf linear accelerator to an energy of 14–20 MeV. Initially, we have used  $K_2CsSb$  photocathodes, because they have high quantum efficiencies in the green. However, the operational lifetime of these cathodes is very short, about one to three days of normal operations. Photocathode materials used by other groups as electron sources for electron accelerators include Cu and  $LaB_6$ , which are very rugged but have relatively low quantum efficiencies and must be driven by uv light [1,2].

Recently, cesium telluride photocathodes have been successfully used in the operation of the Los Alamos Advanced FEL [3]. In this paper we report on their fabrication technique, and on the experiments performed in the fabrication chamber concerning their contamination and rejuvenation properties.

### 2. Experimental setup

Cesium telluride photocathodes were fabricated in a separate ultra-high vacuum research chamber with an ambient pressure in the middle  $10^{-10}$  Torr range that rose to the low  $10^{-9}$  Torr range during the fabrication. The tellurium source consisted of a small molybdenum can of 99.9999% pure tellurium pieces. The can was heated by thermocoax heater wires wound around the can. The Te atoms escaped through a small hole on the top of the can. Cesium was dispensed from a similar can packed with a powdered mixture of cesium chromate and titanium. The substrate is a molybdenum plug that can be inserted into the linac. The sources were positioned about 1.25 in. from the face of the plug so that simultaneous deposition was possible. Due to this geometry, the deposition occurred at an angle of about  $10^\circ$  from normal. A mask was used to confine the deposition to a  $1 \text{ cm}^2$  area.

The deposition rate of the Te boat was calibrated by using a quartz crystal thickness monitor. The quartz crystal can be placed in front of the sources in place of the Mo plug. Several thicknesses were calibrated by exposing the cathode to the Te source at a given temperature for a given amount of time and noting the resulting thickness reading. However, we cannot monitor or control the temperature of the quartz crystal. A systematic error may arise from the variation of the sticking coefficient with the substrate temperature. Since the fabrication of the  $Cs_2Te$  films was

<sup>☆</sup> Work supported by LANL Laboratory Directed Research and Development under the auspices of the U.S. Department of Energy.

<sup>\*</sup> Corresponding author.

carried out at an elevated temperature, the calibration numbers were probably high. The Cs source was not calibrated.

A battery was used to bias the cathode by  $-90$  V relative to the chamber over a distance of about 1–2 in. resulting in an accelerating field of 1.8–3.6 kV/m. The photocurrent was measured with a picoammeter. An Oriel 350W Hg arc lamp followed by a f1 condenser lens, a dichroic mirror, and a bandpass interference filter were used to illuminate the photocathode with light at several different wavelengths. The light transmitted through the bandpass filter was reimaged onto the photocathode through an uncoated fused silica vacuum window. When accurate measurements of QE were required, the light intensity after the f4 focusing lens was measured with a calibrated silicon photodiode before measuring the photocurrent. The transmission of visible and uv light through the fused silica viewport was taken to be  $90 \pm 3\%$  in the calculations for the incident light intensities. The absolute uncertainty of the QE measurements is about  $\pm 15\%$ . The relative uncertainty between measurements made at the same wavelengths is about  $\pm 5\%$ .

### 3. Fabrication procedure

We precleaned the Mo plugs with soap and water and rinsed them with ethanol before mounting them in a ladder that holds up to seven plugs in a vacuum transport chamber. This pack of cathodes was mounted onto a six-way cross that served as the vacuum interlock. The cross and the cathode pack were pumped out and baked at  $200^\circ\text{C}$ . After the bake, a single cathode was inserted into a portable oven on the end of an actuator and moved to the

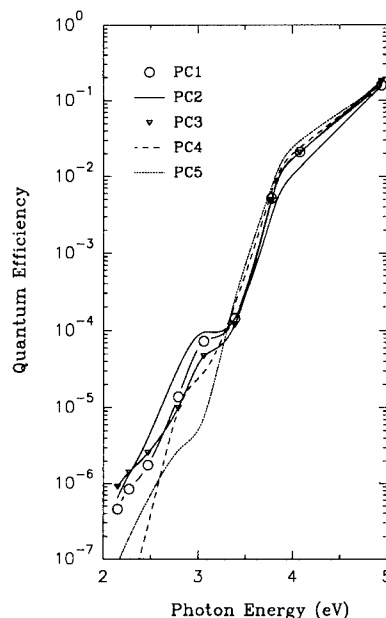


Fig. 2. Spectral response data for  $\text{Cs}_2\text{Te}$  photocathodes, PC1, PC2, PC3, PC4, and PC5.

main chamber. The Mo plug was baked at  $300^\circ\text{C}$  for several hours to further clean the cathode surface.

The fabrication procedure is similar to that for cesium antimonide,  $\text{Cs}_3\text{Sb}$  [4]. First, we deposited a film of Te with a thickness between 100 Å and 300 Å onto the surface of the Mo plug. While monitoring the photocurrent at 251 nm, the film of Te was reacted with Cs until the photocurrent peaked and has decreased by 10–20%. Then the deposition of Cs was stopped by turning off the boat heater. The photocurrent started to recover and eventually reached a level near where it peaked. During the entire process, the substrate temperature was maintained between 100 and  $110^\circ\text{C}$  to help prevent excess Cs and contaminants from condensing on the film and to facilitate the reaction of Cs with Te. The fabrication starting from the deposition of Te typically took about one hour. As a precaution against Cs contamination in the linac, some photocathodes were heated to about  $170^\circ\text{C}$  to ensure removal of any free Cs from the surface. This step is probably necessary only when fabricating near room temperature.

### 4. Spectral response

The QEs of the five  $\text{Cs}_2\text{Te}$  photocathodes were measured at several wavelengths using a 350 W Hg arc lamp and several band pass filters. These cathodes will be designated as PC1, PC2, PC3, PC4, and PC5. They were all fabricated with the same level of exposure to Te vapor, which resulted in a Te layer of about 130 Å on a quartz crystal thickness monitor positioned in place of a cathode.

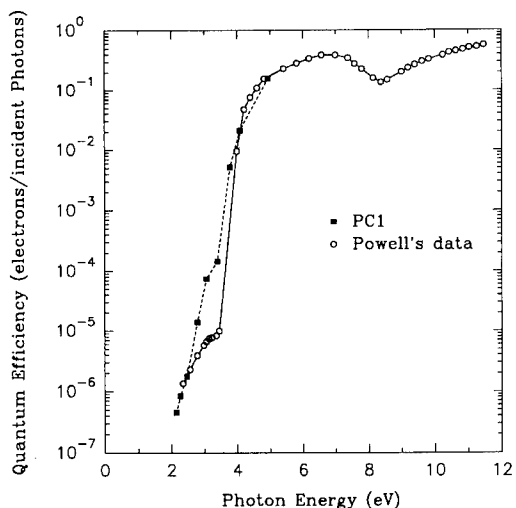


Fig. 1. Spectral response data measured for  $\text{Cs}_2\text{Te}$  photocathode PC1 are compared with Powell's data from Ref. [5].

PC1, PC2, PC3, and PC4 were fabricated at a temperature between 100°C and 110°C. PC5 was fabricated at room temperature to determine if an elevated temperature is necessary. PC4 was the only photocathode in this set heated to 170°C at the end of the fabrication.

The uv spectral response of PC1 compares well with data taken by Powell (Fig. 1) [5]. However, the PC1 data have a broader cutoff below 4 eV due to the relatively large spectral width of the incident light (8–35 nm). The PC1 data also have a larger low energy shoulder. This discrepancy is expected since the low energy shoulder varies in size significantly from different data sources and even among our Cs<sub>2</sub>Te photocathodes (Fig. 2).

In Fig. 2, we see that the quantum efficiencies of the five photocathodes compare very well at 251 nm. Variations are progressively larger at lower photon energies. In particular, the response to visible light is significantly less for PC4 and PC5, which were fabricated differently from the other photocathodes in the set, as described above. The smaller variations in the spectral response among PC1, PC2, and PC3 are probably due to variations in the cesium content.

## 5. Exposure to air

An important issue is the level of vacuum necessary to keep Cs<sub>2</sub>Te QE from degrading below the usable point. Of particular interest is their tolerance to vacuum levels on the order of 10<sup>-7</sup> Torr, which can easily be achieved without requiring a bakeout of a vacuum chamber. Also of interest is the tolerance to vacuum conditions greater than 10<sup>-4</sup> Torr, which will determine the degree of care needed when transferring the photocathode from the fabrication chamber to the photoinjector.

PC1 was exposed for 17 hours to an average vacuum of 1 × 10<sup>-7</sup> Torr. This was accomplished by isolating the photocathode in the vacuum interlock cross and pumping on this section with a turbo pump through a partially closed valve. During the exposure, the vacuum pressure dropped from 4 × 10<sup>-7</sup> Torr to 5 × 10<sup>-8</sup> Torr. After the exposure, the PC1 was transferred back to the main chamber and the spectral response was remeasured (Fig. 3). The 251-nm QE dropped from 15.7% to 5.2% and the shoulder

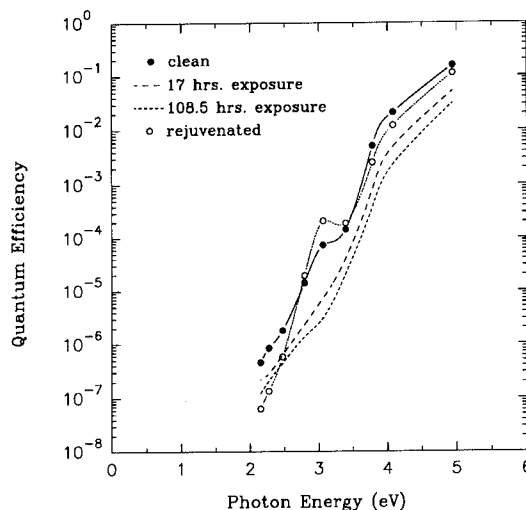


Fig. 3. Spectral response data for photocathode PC1 before and after 17 hours of exposure to 1 × 10<sup>-7</sup> Torr of outgassing followed by 91.5 hours of exposure to 4 × 10<sup>-7</sup> Torr of outgassing. The spectral response data for PC1 after rejuvenation are also displayed.

at 3 eV was no longer well defined. With the same procedure, PC1 was exposed for 91.5 more hours to a vacuum with an average pressure of 4 × 10<sup>-7</sup> Torr. Afterwards, the spectral response was measured again (Fig. 3). The 251-nm QE dropped to 3.1%. If an exponential decay in QE is assumed, then a 1/e time constant of 15 hours is obtained for the first stage and 177 hours for the second stage. Clearly the decay in QE is not exponential. This result suggests that as the photocathode is exposed to contamination, the surface becomes passivated. Thus, it is apparent that Cs<sub>2</sub>Te is reasonably rugged and the possibility of its use in a medium vacuum system is promising.

PC3 was exposed to air through a variable leak valve at an average pressure of 2 × 10<sup>-4</sup> Torr for sixty minutes. The 251-nm QE dropped from 17.8% to 0.70% in the first five minutes. After sixty minutes the 251-nm QE fell to 0.50%. Table 1 summarizes the uv spectral response following each exposure. The first five minutes of exposure is quite detrimental and further exposure is of less consequence. Therefore, any attempt to transfer Cs<sub>2</sub>Te in nitro-

Table 1

The quantum efficiencies of PC3, PC4, and PC5 are listed for three different wavelengths. The QEs separated by slashes represent measurements made prior to air exposure, after 5 minutes of air exposure, and after 60 minutes of air exposure. The photocathodes were exposed to 2 × 10<sup>-4</sup> Torr of air

| Photocathodes   | 251-nm QEs (%) | 304-nm QEs (%)  | 328-nm QEs (%)   |
|-----------------|----------------|-----------------|------------------|
| PC3             | 17.8/0.70/0.50 | 2.1/0.050/0.043 | 0.49/0.013/0.012 |
| Rejuvenated PC3 | 10.4/3.0/1.2   | 1.5/0.30/0.070  | 0.26/0.067/0.014 |
| PC4             | 16.4/1.1/0.79  | 2.4/0.063/0.038 | 0.63/0.013/0.009 |
| PC5             | 14.8/2.0/1.1   | 3.0/0.21/0.080  | 0.73/0.041/0.018 |
| Rejuvenated PC5 | 9.4            | 1.7             | 0.46             |



gen will probably require the ability to rejuvenate the photocathode after the transfer.

PC5 and PC4 were also exposed to air for 5 minutes followed by 55 minutes at a level of  $2 \times 10^{-4}$  Torr. The 251-nm QE of PC5 dropped from 15.8% to 2.0% and 1.1%, and the 251-nm QE of PC4 dropped from 16.4% to 1.1% and 0.79% (Table 1). We observe that PC5 appears to be more rugged than PC3 and PC4, and can conclude that fabricating photocathodes at room temperature does not affect their ability to withstand degradation by exposure to air. Furthermore, a small enhancement in durability may be expected, but this is not a firm conclusion since PC5 probably has a thicker film, which may also result in a more rugged photocathode.

## 6. Rejuvenation of degraded photocathodes

We have found that photocathodes that have been degraded by exposure to poor vacuum conditions can be partially rejuvenated by heating them above 100°C for several hours. After PC2 was degraded by the method mentioned in section 5, it was held at 110°C for about 12 hours. A noticeable increase in the 251-nm QE was seen when the photocathode temperature rose above 100°C. The photocathode was allowed to cool to room temperature before the spectral response was measured (Fig. 3). The 251-nm QE recovered to 11.3%, which is a very respectable value. After storing the rejuvenated photocathode in a vacuum of  $10^{-9}$  Torr for three weeks, the 251-nm QE dropped to 4.7%. A virgin photocathode may be stored for weeks in a vacuum of  $10^{-9}$  Torr with little degradation. It appears that rejuvenated photocathodes take time to reach chemical equilibrium.

Similarly, PC3 and PC5 were partially rejuvenated by heating it to 175°C for about 12 hours and 2 hours, respectively (Table 1). After one hour at 175°C, we observed that further heating increases the QE insignificantly. From experience, we have found that the rejuvenation of these heavily contaminated photocathodes is best achieved when heated to 150–200°C. The 251-nm QE of PC3 peaked at 15.0% while hot, and stabilized at 10.4% after cooling to room temperature. The 251-nm QE of PC5 stabilized at 9.4%. Long term stability was not monitored.

In order to evaluate the ruggedness of rejuvenated photocathodes, PC3 was given another round of exposure to  $2 \times 10^{-4}$  Torr of air. After 5 minutes of exposure, the 251-nm QE dropped from 10.4% to 2.74%. Further expo-

sure for 55 minutes resulted in a 251-nm QE of 1.2%. The results are again summarized in Table 1. Clearly, the ultraviolet QE of the rejuvenated PC3 is less affected by exposure to air than the virgin PC3.

## 7. Conclusions

Several Cs<sub>2</sub>Te photocathodes were fabricated with 251-nm QEs ranging from 16 to 18%, which are in agreement with Powell's data. Exposure to  $4 \times 10^{-7}$  Torr vacuum reduces the 251-nm QE to 3.1% after five days. At this point, the surface appears to be passivated by the contaminants so that further degradation in QE is at a much slower rate. Therefore, operations at  $10^{-8}$  to  $10^{-7}$  Torr vacuum levels may be possible. Exposure to  $2 \times 10^{-4}$  Torr vacuum reduces the 251-nm QE to 0.5–1.0% in one hour. This implies that a transfer process will significantly degrade Cs<sub>2</sub>Te unless good vacuum is maintained. However, the rejuvenation results are very encouraging. Cs<sub>2</sub>Te photocathodes degraded by air can be partially rejuvenated by heating them to 150–200°C. This suggests that transfer in poor vacuum or pure nitrogen may be feasible. Furthermore, it may be possible to extend the operational lifetime of Cs<sub>2</sub>Te photocathodes by heating them while in use or after they are contaminated.

## Acknowledgements

Work supported by LANL Laboratory Directed Research and Development under the auspices of the U.S. Department of Energy.

We also acknowledge Floyd Sigler and Robert Springer for their assistance in the project.

## References

- [1] T. Srinivasan-Rao, J. Fisher and T. Tsang, *J. Appl. Phys.* 69 (1991) 3291.
- [2] M. Boussoukaya, H. Bergeret, R. Chehab and B. Leblond, *Nucl. Instr. and Meth. A* 264 (1988) 131.
- [3] S.H. Kong, J. Kinross-Wright, D.C. Nguyen, R.L. Sheffield and M.E. Weber, these Proceedings (16th Int. Free Electron Laser Conf., Stanford, USA, 1994) *Nucl. Instr. and Meth. A* 358 (1995) 284.
- [4] A.H. Sommers, *Photoemissive Materials* (Krieger, New York, 1980).
- [5] R.A. Powell, W.E. Spicer, G.B. Fisher and P. Gregory, *Phys. Rev. B* 8 (1973) 3987.



ELSEVIER

## Photoemission studies on $\text{LaB}_6$ and pure metals using a nanosecond KrF excimer laser

Min-quan Qian <sup>a,\*</sup>, Mao-rong Yang <sup>a</sup>, Qing Pan <sup>a</sup>, Ke-song Hu <sup>a</sup>, Ren-pei Deng <sup>a</sup>,  
Jiang-jun Shi <sup>a</sup>, Zu-cong Tao <sup>a</sup>, Jian-bo Cheng <sup>b</sup>, Qi-jun Ran <sup>b</sup>, Zu-lun Lin <sup>b</sup>

<sup>a</sup> Institute of Applied Electronics, China Academy of Engineering Physics, P.O. Box 523-65, Chengdu, Sichuan, China

<sup>b</sup> University of Electronics Science and Technology, Chengdu, Sichuan, China

### Abstract

The CAEP RF accelerator will use a photocathode rf gun to provide a high brightness electron beam for FEL experiments. To achieve long lifetime, our photocathode development initially concentrates on  $\text{LaB}_6$  and some pure metals. We report experiments on these materials with a pulsed KrF excimer laser. Using surface heating and laser cleaning (surface activation), the quantum efficiency is dramatically enhanced. The quantum efficiencies of  $\text{LaB}_6$ , Y, Ag and Al are about  $6.1 \times 10^{-4}$ ,  $3.8 \times 10^{-4}$ ,  $2.8 \times 10^{-4}$ , and  $1.4 \times 10^{-4}$ , respectively. Using the pepper pot method, the normalized beam emittances for these materials are about  $10 \pi \text{ mm mrad}$  and the corresponding normalized brightnesses are about  $10^{10} \text{ A/m}^2 \text{ rad}^2$ . These photocathodes will be tested on the  $1 + \frac{1}{2}$  cell microwave cavity at CAEP.

### 1. Introduction

Photocathode experiments for FEL can be divided into two categories: (1) semiconductor photocathodes irradiated by a frequency-doubled Nd:YAG laser, and (2) metal compounds and pure metals irradiated by a frequency-quadrupled Nd:YAG laser. Each approach has distinct advantages and disadvantages. Because semiconductor photocathodes have high quantum efficiency, the requirements for source laser power are quite reasonable. However, these materials are subject to poisoning and have a relatively short lifetime under FEL operating conditions. They require very high vacuum, better than  $10^{-10}$  Torr. On the other hand,  $\text{LaB}_6$  and metals have proved to be robust and long lifetime materials. Their primary drawback is a relatively low quantum efficiency, which necessitates the use of a more powerful driving laser with short wavelength to produce a high photocurrent. The goals for high quantum efficiency and long lifetime are somewhat contradictory. Based on the experiments at Stanford University [1] and BNL [2], our photocathode project initially concentrates on the long lifetime materials.

### 2. Experimental arrangement and measurement

Two vacuum cells shown in Fig. 1 have been used in the experiments. The experiments for multicrystalline  $\text{LaB}_6$  and most metal photocathodes are conducted in the oil-pumped cell while the experiments for crystalline  $\text{LaB}_6$  are conducted in the ion-pumped cell.

The laser used in the experiments, a 10 Hz EMG-150ES KrF excimer laser, supplies 25 ns FWHM pulses at 248 nm (photon energy 5.0 eV). The maximum pulse energy is 750 mJ. The laser beam is directed through an optical system onto the cathode at an angle of approximately  $70^\circ$  to the normal of the surface. The photoelectrons emitted from the cathode are accelerated across the cathode–anode gap, and collected by the Faraday cup as the photocurrent ( $I$ ). If the anode drift cylinder is installed instead of the Faraday cup, the photoelectrons will enter a field-free region through the pepper pot holes to a phosphor screen. The images of the beamlets on the screen are recorded by a TV camera. The normalized emittance,  $\epsilon_n$ , is obtained from the size of the images by a computer processing system. The beam brightness is given by  $B_n = I / \pi^2 \epsilon_n^2$ .

Two kinds of photocathode material have been tested in the experiments. One is the metal compound  $\text{LaB}_6$  (crystal and multicrystalline), and the other is a pure metal (such as Y, Ag, Al, Fe, Cu, Nb and Ta). Since the quantum efficiency is sensitive to the surface quality of the photo-

\* Corresponding author. Tel +86 816 225 839 4179 fax +86 816 225851.

cathode, it is necessary to process the photocathode surface before experiment [3]. The surface of the photocathode is lapped with a diamond compound, washed in solvents and ultrasonically cleaned before installing into the cell. After installation, surface heat treatment ( $10^{-8}$  Torr,  $1400^{\circ}\text{C}$ ) is used for  $\text{LaB}_6$ , and surface activation with the KrF laser ( $20 \text{ MW}/\text{cm}^2$ ) is used for metal photocathodes.

The laser energy and profile are measured with an IP-550 pyroelectric detector and a GaAs photoelectric detector, respectively. A Faraday cup is used to measure the peak photocurrent and its pulse shape. The photoelec-

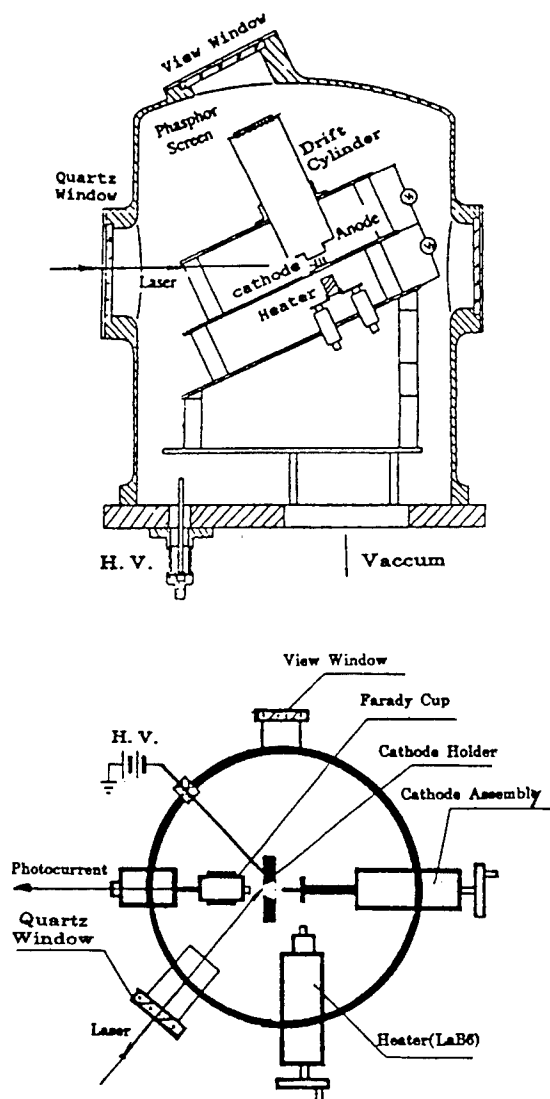


Fig. 1. Schematic of the vacuum photocathode cells. (a) Oil-pumped cell ( $10^{-6}$  Torr). (b) Ion-pumped cell ( $10^{-10}$  Torr).

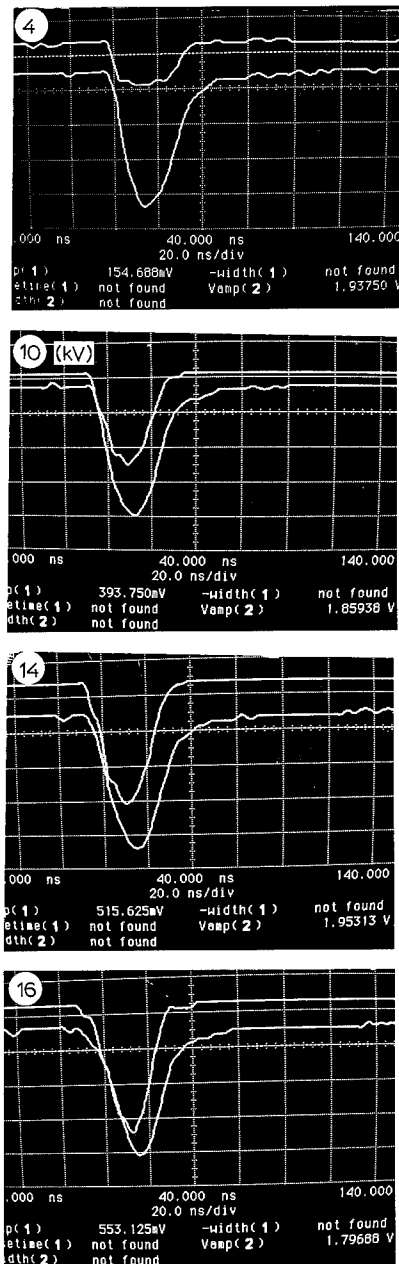


Fig. 2. Photocurrent pulse for  $\text{LaB}_6$  as a function of gap voltage (top: photocurrent; bottom: laser).

tron beam emittance is measured with the pepper pot method [4]. For the photocathode of large radius, five  $r_0 = 0.05 \text{ mm}$  holes in the pepper pot are configured into a cross with the outside four holes equally spaced 3 mm from a central axial hole. For the cathode of small radius, there is one hole on the pepper pot.

### 3. Results and discussions

#### 3.1. Photoemission of $\text{LaB}_6$

The photocurrent pulses at various gap voltages are shown in Fig. 2. The photoelectrons are not completely collected at low voltages due to space charge limitations. Increasing the voltage to 14 kV or higher, the photoelectrons are all collected and the waveforms are the same as that of the laser pulse.

Fig. 3 shows the photocurrent density collected as a function of gap voltage. It is clear from curve 1 that the photocurrent is “emission limited” when the gap voltage is higher than 14 kV. The quantum efficiency is defined as  $\eta = N_e/N_\gamma = (I\Delta t)h\nu/E_\gamma$  in this regime and  $\eta \sim 6.1 \times 10^{-4}$  from curve 1. Curve 2 and curve 3 are space charge limited. From curve 3 the photocurrent density is about 50  $\text{A}/\text{cm}^2$  at a gap voltage of 18 kV and the corresponding photocharge is 25 nC.

Fig. 4 shows photocharge versus irradiated energy. Using a least squares fit the photocharge is linear with energy as  $Q = 3.32 \times 10^{-6}E_\gamma - 6.63 \times 10^{-7}$ , where  $Q$  and  $E_\gamma$  are photocharge in nC and laser energy in mJ respectively. In Fig. 4 we can see the photocharge is not maximum at the highest laser energy. This phenomenon is due to plasma formation on the cathode surface. The plasma absorbs some laser energy and results in the photoemission reduction.

The experimental results show the efficiency of  $\text{LaB}_6$  can be enhanced about an order of magnitude by surface heat treatment. The parameters of the treatment are: vacuum better than  $10^{-8}$  Torr, temperature about  $1400^\circ\text{C}$  and heating time more than 20 min. The key is that the vacuum must be  $10^{-8}$  Torr during treatment. It has been found that an efficiency of  $6.1 \times 10^{-4}$  is achieved after treatment, but it will decrease with a decreasing cathode temperature and stabilize at about  $2 \times 10^{-4}$  after 4 hours. The reason

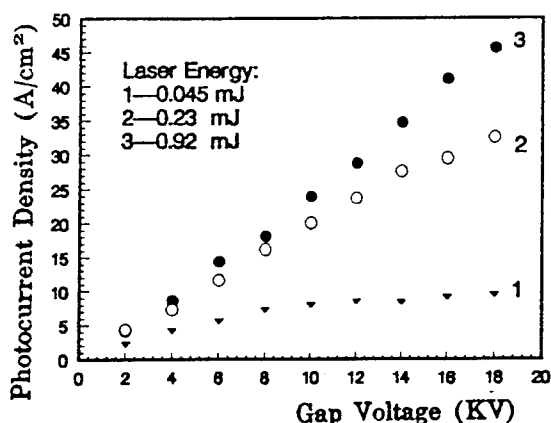


Fig. 3. Photocurrent density for  $\text{LaB}_6$  as a function of gap voltage.

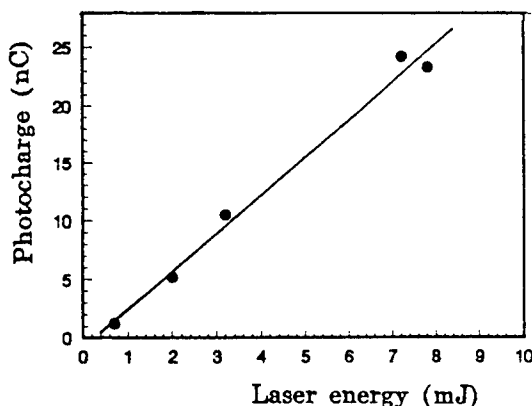


Fig. 4. Photocharge emitted from  $\text{LaB}_6$  versus laser pulse energy.

is that the surface will absorb residual oxygen in the cell while cooling [5].

#### 3.2. Photoemission of metals

Pure metals seem to be interesting materials for laser-driven photocathodes because of the large free electron density, ease of preparation, high damage threshold and almost instantaneous time response. The efficiency of Y, Ag and Al are higher than of the other metals. Fig. 5 shows the photocurrent density of Ag versus gap voltage for the parameters: gap distance  $d = 5$  mm, laser duration  $\Delta t = 25$  ns and emission area of the cathode  $S = 8.8 \times 10^{-2} \text{ cm}^2$ . It is clear from curve 3 that the photocurrent is “emission limited” when the gap voltage is higher than 16 kV. The quantum efficiency is determined to be  $2.8 \times 10^{-4}$ . In Fig. 5 the solid curve is the Langmuir–Child equation;  $j_L = 2.34 \times 10^{-6} V^{3/2}/d^2$ , and the other curves are experimental data. It is apparent that photocurrent driven by a long laser pulse obeys the Langmuir–Child law [6].

In these experiments, the quantum efficiency of metals is found to be  $10^{-6}$  to  $10^{-5}$ . To obtain higher efficiency,

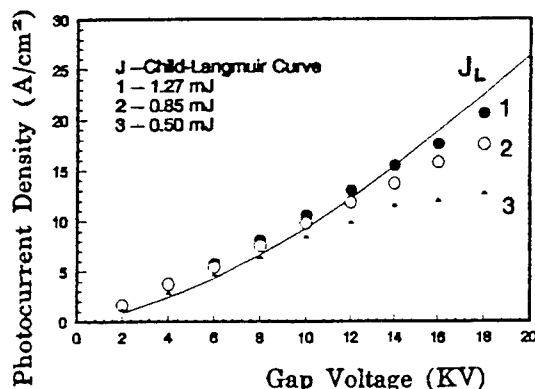


Fig. 5. Photocurrent density of Ag versus gap voltage.

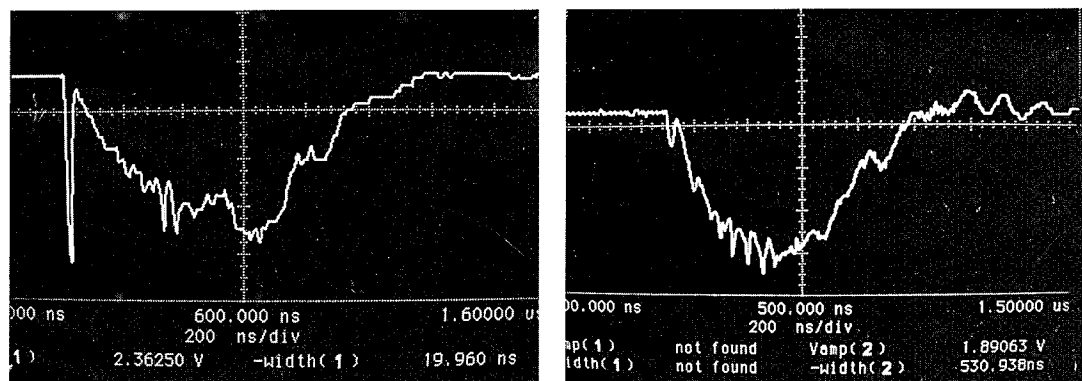


Fig. 6. The current waveform of Nb (left) and Ag (right) with plasma formation.

it is necessary to activate the cathode surface in the cell with the KrF laser at a power of  $20 \text{ MW/cm}^2$ . The activation process is much less effective at power densities less than  $10 \text{ MW/cm}^2$ . Measured efficiencies for various metals are listed in Table 1. It may be seen that the efficiencies increase about an order of magnitude due to activation. The reason for this increase is that residual gases or oxides and impurities at the surface are removed by the intense laser activation. The improved quantum efficiency will decrease when the experiment interrupts for some time or the pressure increases, but the quantum efficiency can be improved again after activation.

For metal photocathodes, inter-electrode breakdown due to cathode surface plasma is quite apparent. Each metal has a characteristic current waveform of its own. The waveforms for Nb and Ag collected by the Faraday cup are shown in Fig. 6. The narrow pulse at the left in each photograph represents the photocurrent. For Nb the temporal pulse shape with a peak current of 2.4 A and a duration of 20 ns is the same as the laser pulse. The long current pulse that follows represents the plasma electron current. The experiments have shown that the photocurrent is apparent for the infusible metals such as Nb, Ta etc, while it is very small for the fusible metals such as Ag, Al etc.

### 3.3. Measurement of beam emittance

The beam emittances of  $\text{LaB}_6$ , Y, Ag and Ta have been measured by the pepperpot method. By comparing mea-

Table 1  
The improvement of efficiency due to activation

|   | Cathode |     |     |     |                |
|---|---------|-----|-----|-----|----------------|
|   | Nb      | Al  | Y   | Ag  | $\text{LaB}_6$ |
| Before activation<br>( $\times 10^{-5}$ ) | 0.15    | 1.6 | 2.7 | 3.9 | 3.0            |
| After activation<br>( $\times 10^{-5}$ )  | 1.5     | 14  | 38  | 28  | 18             |

sured image size with the calculated value at the same conditions, the normalized emittance of  $\epsilon_n = 10 \pi \text{ mm mrad}$  is obtained. It is approximately consistent with the value predicted from equation  $\epsilon_n = r_c (2E_\perp/mC^2)^{1/2}$ , where  $E_\perp = h\nu - \Phi$  and  $\Phi$  is the work function. The emittance of  $\text{LaB}_6$  and metals are about  $10 \pi \text{ mm mrad}$  and their corresponding brightness are  $1$  to  $2 \times 10^{10} \text{ A/m}^2 \text{ rad}^2$ . When the plasma forms on the cathode surface, the whole screen becomes bright, indicating that the emittance is very bad.

## 4. Conclusions

The quantum efficiencies of  $\text{LaB}_6$  and metals can be improved by surface treatment. The vacuum in the cell must be at least  $10^{-8}$  Torr for heat treating  $\text{LaB}_6$ . The efficiency of  $\text{LaB}_6$  is sensitive to surface treatment and vacuum in the cell. We will continue studies to improve its efficiency. To activate metal photocathodes, the laser power density must be more than  $20 \text{ MW/cm}^2$ . We will continue our search for new materials with higher efficiency by studying ion implantation or doping etc.

## References

- [1] M. Curtin, G. Bennet, R. Burke, A. Bhowmik P. Metty and J.M.J. Madey, Nucl. Instr. and Meth. A 296 (1990) 127.
- [2] K. Balchelor et al., Nucl. Instr. and Meth. A 318 (1992) 372.
- [3] T. Srinivasan-Rao, J. Fischer and T. Tsang, J. Appl. Phys. 69 (1991) 3291.
- [4] P.E. Oettinger, SPIE paper 99805, presented at Int. Symp. and Exhibition of Fiber Optics, Optoelectronics and Laser Applications in Science and Engineering, Sep. 6–10, 1989, Boston MA, USA.
- [5] M. Asakama et al., Nucl. Instr. and Meth. A 331 (1993) 302.
- [6] J-P. Girardeau-Montaut and C. Girardeau-Moutaut, J. Appl. Phys. 65 (1989) 1889.



ELSEVIER

## Performance of cesium telluride photocathodes as an electron source for the Los Alamos Advanced FEL <sup>☆</sup>

S.H. Kong <sup>\*</sup>, J. Kinross-Wright, D.C. Nguyen, R.L. Sheffield, M.E. Weber

*Los Alamos National Laboratory, Los Alamos, NM, USA*

### Abstract

The Los Alamos Advanced FEL was successfully operated with a Cs<sub>2</sub>Te photocathode driven by a frequency quadrupled Nd:YLF laser as the electron source. Lasing was achieved at 5–6 μm. Cs<sub>2</sub>Te photocathodes with quantum efficiencies of 15–18% at 251 nm were fabricated in an ultrahigh-vacuum chamber and transferred under high vacuum to the FEL. 263 nm light from the drive laser was focused to an 8 mm spot on the center of the photocathode. We estimated the operational lifetime of Cs<sub>2</sub>Te photocathodes to be at least 20 times that for K<sub>2</sub>CsSb photocathodes. We have found that the dark current, emittance of the extracted beam, and amount of charge extracted is sufficient for FEL applications.

### 1. Introduction

Recently, we have fabricated and tested cesium telluride photocathodes. Cesium telluride, Cs<sub>2</sub>Te, is known for its application in high quantum efficiency UV photocathodes for solar blind photomultiplier tubes. The important question is whether it can be adapted for application as a good electron source for FELs or other systems based on an electron accelerator. We have successfully operated the Los Alamos Advanced FEL with a Cs<sub>2</sub>Te photocathode. This result dismisses any major flaws with this photocathode. However, we still need to consider several other issues: operational lifetime, temporal response, saturation level, quality of the extracted electron beam, and the level of dark current. Any deficiency in these areas may adversely affect the operation of the FEL. The issues of lifetime, saturation level, and dark current have been studied by CERN for a Cs<sub>2</sub>Te photocathode in a 10 MV/m dc gun [1]; a 60 hour half-life for continuous running, a negligible dark current, and a maximum current limited only by the saturation of the gun due to space charge effects have been observed.

### 2. Description of the photoinjector and rf linac

The source of high current electron pulses for the Los Alamos Advanced FEL is a photoinjector that forms the

first half-cell of a high gradient rf linac. The linac is 1.2 m long and capable of accelerating electrons to a maximum energy of 25 MeV. The maximum electric field on the surface of the cathode when operating at 16 MeV is about 20 MV/m.

The drive laser is made up of a Nd:YLF oscillator modelocked at 108.33 MHz (12th subharmonic of the rf) and a double-pass amplifier. A Pockell cell switches out variable length macropulses to be frequency quadrupled by using a LBO crystal followed by a BBO crystal. A typical 10 μs macropulse consists of 1080 micropulses, each 7–14 ps in duration. Typical operations require 1–3 nC of charge per micropulse. A calibrated toroid is used to measure the current, and OTR (Optical Transition Radiation) screens are used to measure the beam profiles.

Further detail on the instrumentation can be found in Refs. [2,3].

### 3. Operation of the Cs<sub>2</sub>Te photocathode in the Los Alamos Advanced FEL

The Los Alamos Advanced FEL has successfully lased at wavelengths of 5–6 μm with cesium telluride photocathodes. We observed no qualitative difference in the quality of lasing when using a Cs<sub>2</sub>Te photocathode in place of a K<sub>2</sub>CsSb photocathode except a deterioration in lasing stability caused by increased fluctuations in the drive laser beam. The necessity of frequency quadrupling the output of the Nd:YLF laser is the one disadvantage in switching to a Cs<sub>2</sub>Te photocathode since it magnifies the instabilities in the drive laser system and requires working with UV radiation. However, the instabilities can be de-

<sup>☆</sup> Work supported by LANL Laboratory Directed Research and Development under the auspices of the U.S. Department of Energy.

<sup>\*</sup> Corresponding author.

creased by upgrading to a diode-pumped and amplifier laser system.

The operational lifetime of Cs<sub>2</sub>Te photocathodes in the Los Alamos Advanced FEL has not been well established at this time since the lifetimes are long. The initial 263-nm QE of new photocathodes is 8–12% at low charge. A small amount of QE degradation from small air leaks sometimes occurs during the transfer of the photocathodes from the fabrication chamber to the photoinjector. The pressure in the linac was in the low  $10^{-10}$  Torr range without beam and rose into the high  $10^{-10}$  Torr to low  $10^{-9}$  Torr range when beam was on. With degradation from the transfer process and initial arcing in the linac, the QE of our first Cs<sub>2</sub>Te photocathode stabilized at about 3–5% while operated in the linac. After 100 hours of operating beam, we observed no significant loss in QE beyond the initial drop. If we consider the photocathode dead when the QE drops below 1%, the lifetime is probably well beyond 100 h.

#### 4. Characterization of the electron beam

The quality of an electron beam is typically characterized by the emittance, brightness, and energy spread. Driving a cathode with photons well above threshold results in a spread in the transverse and longitudinal components (relative to the linac axis) of the photoelectron kinetic energy. However, this energy spread is on the order of an eV, so is not expected to noticeably affect the energy spread of the electron beam. Single pulse measurements yielded a fwhm energy spread of 0.13%, which is limited by the rf system.

The emittance of the electron beam was estimated by measuring the waist of the electron beam core at the first OTR screen as a function of the field strength of a magnetic quadrupole that is 27 cm upstream. The data was fit to a theoretical curve to extract a value that represents the emittance of an electron beam with an ellipsoidal distribution in phase space. However, since the electron beam generated does not have such a distribution, the extracted value is not the true rms emittance. Nevertheless, these values can be used as a figure of merit to compare the quality of electron beams obtained from K<sub>2</sub>CsSb and Cs<sub>2</sub>Te photocathodes. The emittance value measured for Cs<sub>2</sub>Te divided by the value measured for K<sub>2</sub>CsSb gives a ratio of  $0.9 \pm 0.3$ . Therefore, we see no significant difference in the measured emittance.

The pulse lengths of the electron micropulses were measured by using a Hamamatsu model M1955 streak camera to look at the OTR light generated promptly by electrons striking a metal screen. The streak images were processed on a computer to extract the fwhm pulse lengths by generating an intensity profile versus time. The broadening from the finite resolution of the image was removed by subtracting in quadrature,  $(\tau_{\text{actual}})^2 = (\tau_{\text{meas}})^2 - (\tau_{\text{res}})^2$ .

The pulse length of the drive laser beam was also measured with this streak camera.

The measurements were made at several different charge densities (Fig. 1). The pulse length of the UV beam of the drive laser is  $7.7 \pm 1.5$  ps and the resolution of the streak images is  $5 \pm 1$  ps. RF compression in the first cell bunches the electron pulses while the space charge effect expands them. The data compares reasonably well with the results from PARMELA simulations. Therefore, any increase in pulse length due to the photoemission process from Cs<sub>2</sub>Te is less than the uncertainties in our pulse length measurements, which is about  $\pm 4$  ps. No discernible tail was observed in the temporal response.

We were able to extract  $2.0 \pm 0.2$  nC/micropulse over an area of  $9.8 \pm 3$  mm<sup>2</sup> in a rf field of 20 MV/m. This is comparable with the space charge limit of  $1.7 \pm 0.5$  nC/micropulse. The macropulse length is 5  $\mu$ s, which consists of 540 micropulses. This gives a current density of  $2.2 \pm 0.7$  A/cm<sup>2</sup> over the macropulse. More accurate measurements of the drive laser beam diameter is needed to resolve any smaller effects contributing to photocathode saturation.

The observed dark current of Cs<sub>2</sub>Te photocathodes when operated at 16 MeV, which corresponds to a maximum electric field of 20 MV/m, is negligible and less than that observed for K<sub>2</sub>CsSb. The level of dark current is close to the sensitivity limit of our instruments so we can only estimate an upper limit of 0.4 mA/cm<sup>2</sup>.

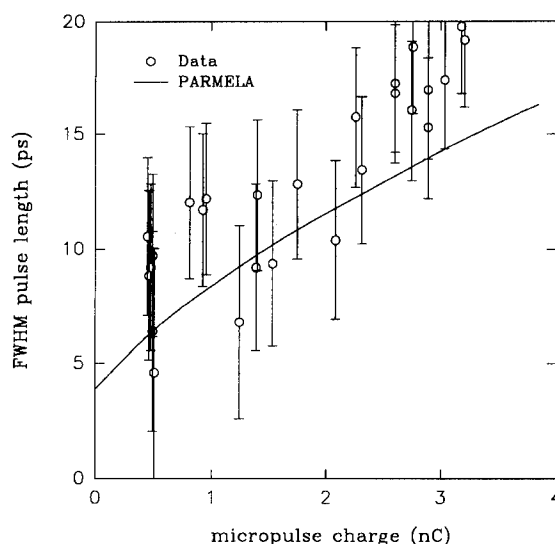


Fig. 1. Pulse length of the electron beam micropulse as a function of charge. The solid curve is the dependence calculated using PARMELA simulations.

## 5. Conclusions

The performance of cesium telluride photocathodes in the Los Alamos Advanced FEL was evaluated. A  $\text{Cs}_2\text{Te}$  photocathode was operated for about 100 h with a 263-nm QE of 3–5%. The emittance of electron beams extracted from a  $\text{Cs}_2\text{Te}$  photocathode is comparable with that of  $\text{K}_2\text{CsSb}$ . Within a measurement uncertainty of 3 ps, we observed no lengthening of the electron pulse except that due to space charge effects. The shortest electron pulse measured was about 5 ps. No discernible tail in the electron pulse was observed. With a surface field of 20 MV/m charge was extracted near the space charge limit. The dark current is also negligible when operating at this field. Therefore, the performance of  $\text{Cs}_2\text{Te}$  photocathodes in the Los Alamos Advanced FEL is excellent.

## Acknowledgements

We acknowledge Stephen Gierman, John Plato, and Steven Russel for their assistance in the project.

## References

- [1] E. Chevallay, J. Durand, S. Hutchins, G. Suberlucq and M. Wurgel, Nucl. Instr. and Meth. A 340 (1994) 146.
- [2] D.C. Nguyen et al., Proc. 1992 Linear Accelerator Conf., Ottawa, Ontario, Canada, Aug. 1992, p. 305.
- [3] D.C. Nguyen et al., SPIE 2118 (1994) 260.



# On the use of CsK<sub>2</sub>Sb photocathodes in RF linacs

Bart M. van Oerle <sup>\*</sup>, Gerard J. Ernst

*Nederlands Centrum voor Laser Research B.V., P.O. Box 2662, 7500 CR Enschede, The Netherlands*

## Abstract

The use of CsK<sub>2</sub>Sb photocathodes in an RF linear accelerator is investigated. Several fabrication techniques for this type of cathodes are reviewed. Measurements are performed on the drop in quantum efficiency due to the use of the cathode in the linac at several wavelengths in the visible. A better lifetime has been found for shorter wavelengths. Finally, the effect of high energy laser pulses on the quantum efficiency in the green is demonstrated.

## 1. Introduction

Recently, alkali-antimonide photocathodes have been used as electron emitters in RF linear accelerators [1]. The advantages of photocathodes as an electron source compared with a thermionic emitter are the expected better beam quality and higher peak current. Although alkali antimonide photocathodes have been intensively studied since their discovery in the early sixties [2–4], little is known about their properties under actual operating conditions in an RF linac. The use of an alkali-antimonide photocathode in an electron gun is completely different from the use in a closed and clean system. For one thing, the peak current drawn from such a cathode is much higher (350 A) than in any other application. Second, in a large system such as a linear accelerator usually more impurities will be produced than in a small glass envelope, and consequently the cathode lifetime is much shorter. Third, since the system is open (vacuum pumps are constantly removing vapours from the linac) any materials that evaporate from the cathode will be removed from the system.

In the present paper, several fabrication techniques for CsK<sub>2</sub>Sb photocathode are reviewed. Also, the drop of the quantum efficiency at several wavelengths in the visible, caused by the use of the cathode in the accelerator, is investigated. Finally, the effect of irradiating the cathode with high energy laser pulses on the quantum efficiency (QE) is discussed.

## 2. Fabrication of CsK<sub>2</sub>Sb cathodes

In Fig. 1, a sketch of the photocathode preparation chamber is given. The cathode itself is placed on an actuator, which is used to move the cathode into the first cell of the linac. The containers with the evaporation materials are mounted on another actuator, perpendicular to the first one. Thus when we wish to evaporate a certain material on the cathode, we move the respective container in front of the cathode. During fabrication, the cathode is kept at a potential of roughly 100 V, so that a green 1.5 mW HeNe laser can be used to illuminate the cathode and monitor the photocurrent with a picoampere meter. The quantum efficiency of the cathode, defined as the number of emitted electrons per incident photon, is given by:

$$QE = \frac{h\nu}{e} \frac{I_{cat}}{P_{las}}, \quad (1)$$

where  $I_{cat}$  and  $P_{las}$  are the cathode current and laser power, respectively. The cathode can also be illuminated with a white halogen source enabling us, by the use of band filters, to measure its spectral sensitivity.

An alkali-antimonide photocathode is prepared by letting a gaseous alkali-metal A react with a pre-deposited layer of antimony [5,6]:

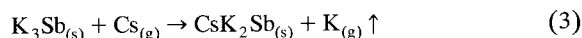


This is an equation of thermodynamical equilibrium, i.e. the process is reversible. The reaction is exothermic, so it is possible to prepare a mono-alkali-antimonide photocathode at room temperature [7]. We have indeed succeeded in preparing cold, single layer Cs<sub>3</sub>Sb cathodes with quantum efficiencies comparable to those of heated cathodes.

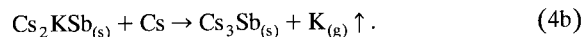
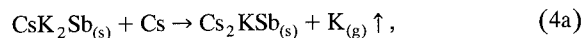
<sup>\*</sup> Corresponding author. Tel. +31 53 89 39 72, fax +31 53 33 80 65, e-mail bart@qe.tn.utwente.nl.

Usually, however, the substrate temperature is kept at 120°C. The main advantage of evaporation on a heated substrate is that it is possible to add multiple layers of alkali-metal and antimony. This is necessary when producing photocathodes that are used in transmission: The efficiency then has an optimum as a function of the thickness of the cathode, so it is necessary to carefully add subsequent layers of Sb and A. On a cold cathode, the second Sb layer does not mix very well with the first A<sub>3</sub>Sb layer, so it remains present as a film on top of the cathode. This causes the QE to drop dramatically, and another layer of alkali-metal is then needed to re-activate the cathode.

When producing CsK<sub>2</sub>Sb cathodes, it is essential to use a high substrate temperature. A CsK<sub>2</sub>Sb cathode is fabricated from a K<sub>3</sub>Sb cathode by the following substitution reaction:



Of course this substitution first occurs near the surface; the Cs atoms next diffuse to the bulk material, trading places with the K atoms that have not yet been substituted. Now suppose that the arrival rate of the Cs atoms is much larger than their diffusion rate into the bulk material. Then we will find multiple substitutions of K atoms near the surface:



Since there now is a stoichiometric excess of Cs near the surface, the QE will drop. This is a signal to the operator to stop the evaporation of the cesium, but there is no way he can be sure that there really is a stoichiometric amount of cesium present in the cathode. Given time, the excess Cs will slowly diffuse into the bulk material.

Between September 1993 and March 1994, photocathodes were daily produced to be used in the RF linac. We have measured the QEs of these photocathodes before they were inserted into the accelerator: The results are shown in Fig. 2. As can be seen, the efficiency of the different K<sub>3</sub>Sb cathodes is relatively constant at about 0.3%, while the QE of the different CsK<sub>2</sub>Sb cathodes varies widely, with an average value of 1.2%. In our experience, there appears to be little correlation between the QE of a K<sub>3</sub>Sb cathode and

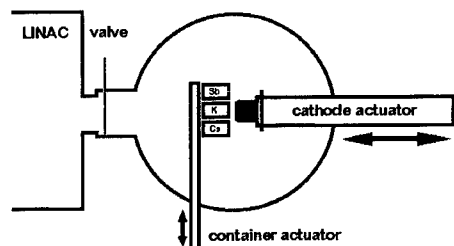


Fig. 1. A sketch of the photocathode preparation chamber.

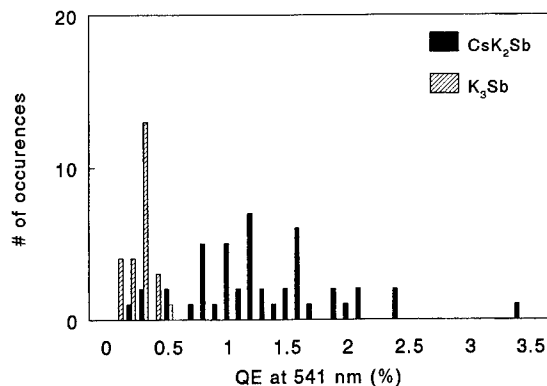


Fig. 2. Statistics of the K<sub>3</sub>Sb and CsK<sub>2</sub>Sb photocathodes that were produced between September 1993 and March 1994.

that of the corresponding CsK<sub>2</sub>Sb cathode. These facts indicate that most contaminations and crystal defects in the cathode are introduced during the substitution of K by Cs. In contrast, we find that after a recent opening of the vacuum (thus, when many contaminants are present) it is very difficult to produce a K<sub>3</sub>Sb cathode with a QE over 0.1%, but that it is very easy to produce high QE (3–4%) CsK<sub>2</sub>Sb cathodes. Apparently the contaminations in CsK<sub>2</sub>Sb cause an energy band shift which have a beneficial influence, whereas in K<sub>3</sub>Sb such a band shift has a harmful effect on the quantum efficiency.

### 3. Spectral sensitivity

In Fig. 3, the dependence of the spectral sensitivity on the fabrication process is shown. Here, we have first produced two K<sub>3</sub>Sb cathodes: one on a substrate at 120°C, and one on a substrate at 180°C. At these temperatures, we expect to produce a cubic and a hexagonal K<sub>3</sub>Sb photocathode, respectively. Clearly, the cubic K<sub>3</sub>Sb has a much

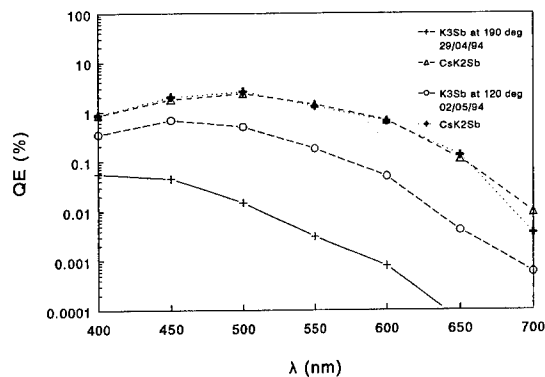


Fig. 3. Spectral sensitivity of a cubic and a hexagonal K<sub>3</sub>Sb cathode, and of the CsK<sub>2</sub>Sb cathodes that were grown on them.

larger quantum yield in the green and red portions of the spectrum than the hexagonal type, as has previously been reported. After completion, a layer of Cs is added to these cathodes. The cesium atoms substitute part of the K atoms in the cathode, thus transforming it into a  $\text{CsK}_2\text{Sb}$  cathode. We found that the spectral sensitivity of the resulting cathode did not depend on the sensitivity of the initial  $\text{K}_3\text{Sb}$  cathode: this can clearly be seen in the figure.

The spectral sensitivity of a typical  $\text{CsK}_2\text{Sb}$  photocathode is shown in Fig. 4. It was measured four times: On completion of the cathode, after a 60 h rest period in the preparation chamber, after a 2 h use in the linac, and after enhancement of the cathode by adding some extra Cs. Note the (with respect to the values given by Sommer [2]) decreased sensitivity in the UV. This is caused by the fact that we did not correct for absorption losses in the preparation chamber window, which we know to be present at wavelengths below 500 nm. We have not yet found a satisfactory explanation for the increased photoyield in the near infrared. As can also be seen, the decrease in quantum yield due to the use of the cathode in the linac is most dramatic in the red part of the spectrum. This suggests the use of shorter wavelength radiation to illuminate the cathode.

#### 4. Effect of laser pulses

To learn more about the decay of the photocathodes while using them in the accelerator, we illuminated  $\text{CsK}_2\text{Sb}$  cathodes with frequency-doubled trains of pulses from a Nd:YLF laser system [8]. The pulse trains, having a length of 15  $\mu\text{s}$ , consisted of 1200 pulses with a 20 ps duration, and an energy contents of 3.5  $\mu\text{J}$  per pulse. These parameters are comparable to those under actual operating conditions of the electron gun. In Fig. 5, the quantum efficiency in the green is plotted versus the number of pulse trains fired on the cathode. The laser pulses initially cause the

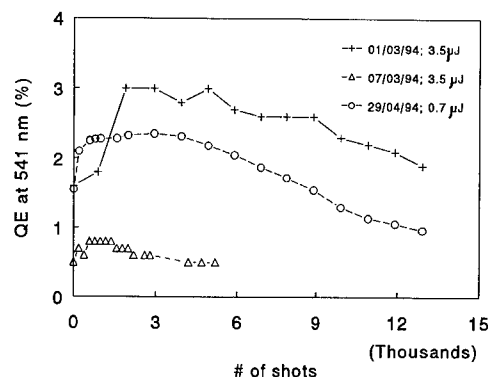


Fig. 5. The effect of high-energy laser pulses on the quantum efficiency of a  $\text{CsK}_2\text{Sb}$  cathode in the green.

QE to increase, until after about 1000 shots (at the repetition rate of 5 Hz, this takes 3 min and 20 s) a maximum is reached. This maximum is roughly twice as high as the initial value. Then, the efficiency starts to decrease. This behaviour is also observed when photocathodes are kept inside the preparation chamber (the maximum QE then typically occurs after one day). A possible explanation of this effect is as follows. Initially the surface material of our cathodes does not correspond to the ideal stoichiometric ratio: there is an excess amount of cesium. Gradually this diffuses into the bulk material, causing the increase of the efficiency of the cathode. This process can be stimulated by irradiating the cathode material with high-energy laser pulses. The fact that the final efficiency is below the peak sensitivity indicates that there is a cesium-deficiency in the cathode as a whole. The material can be described by the stoichiometric formula  $\text{Cs}_{1-x}\text{K}_{2+x}\text{Sb}$ .

#### 5. Conclusions

In our experience, the quantum efficiency of a  $\text{CsK}_2\text{Sb}$  cathode does not depend strongly on the evaporation procedure. That is to say, the variation in QE of several photocathodes that were produced using the same recipe, is larger than the variation between cathodes grown according to different recipes.

Fig. 4 clearly shows that the decay of a multi-alkali photocathode is the most dramatic for wavelengths in the red part of the spectrum. Thus, it will be advantageous to use a shorter wavelength laser for the cathode illumination. Although it is possible to enhance a used cathode (by adding extra Cs) to about half its initial QE in the green, cathode lifetime remains a problem.

When irradiating the cathode with high energy laser pulses, the quantum efficiency initially increases. During operation of a photocathode linac, one can expect that, in the beginning of the experiment, the total beam current increases due to the increase in quantum efficiency. A possible explanation for this increase is the stimulated

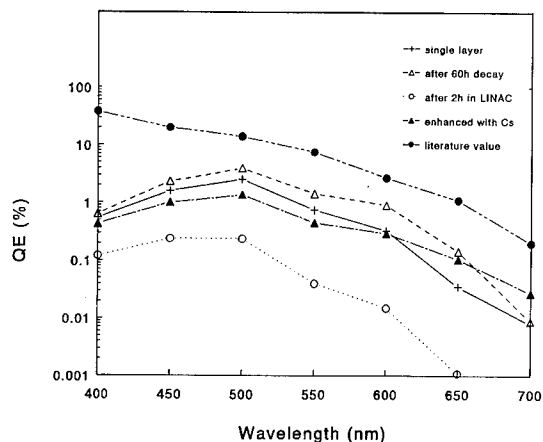


Fig. 4. Spectral sensitivity of a  $\text{CsK}_2\text{Sb}$  cathode, at several moments in its existence.

diffusion of Cs atoms to the bulk material of the photocathode.

### References

- [1] P.G. O'Shea et al., Nucl. Instr. and Meth. A 331 (1993) 62.
- [2] A.H. Sommer, Photoemissive Materials (Wiley, New York, 1968).
- [3] R. Nathan and C.H.B. Mee, J. Phys. E 1 (1968).
- [4] V.P. Beguchev, I.A. Shefova and A.L. Musator, J. Phys. D 26 (1993) 1499.
- [5] E. Kinsky, Adv. EEP 33 A (1972) 357.
- [6] B. Erjavec, Vacuum 43 (1992) 1171.
- [7] E. Chevallay et al., Nucl. Instr. and Meth. A 304 (1994) 146.
- [8] R.F.X.A.M. Mols and G.J. Ernst, Nucl. Instr. and Meth. A 341 (1994) 481.

# Laser cooling of an electron beam by the coherent scattering of a strong laser beam

Toshihiro Taguchi <sup>a,\*</sup>, Kunioki Mima <sup>b</sup>

<sup>a</sup> *Department of Electrical Engineering, Faculty of Engineering, Setsunan University, Neyagawa, Osaka, 572, Japan*

<sup>b</sup> *Institute of Laser Engineering, Osaka University, Suita, Osaka, 565, Japan*

## Abstract

A radiative laser cooling system for electron beams has been investigated numerically. We exactly analyze the motion of charged particles in the strong electromagnetic field of an intense laser pulse. The reduction of the energy spread of the electron beam has been calculated. Since the reduction is very small even if a very high power laser is used, an enhancement of the radiative damping process is important. We consider the use of a coherent radiation process for the enhancement. In order to investigate the motion of particles emitting coherent radiation, we have made a new simulation code to analyze motion of particles interacting with each other with Lienard–Wiechert retarded fields. Using the new code, the enhancement of the reduction of the total energy of a two particle system has been calculated as a function of time, as the two particles approach each other.

## 1. Introduction

Recent topics on accelerator technology have included beam cooling. Accelerators require high brightness and low emittance to increase physical events in elementary particle experiments. In FEL operation, a low emittance electron beam is required for high laser gain.

Generally speaking, cooling is a difficult task. One reason is that cooling needs entropy reduction. Since the total entropy must go up, the excess entropy must be deposited into other media. Particle beams do not contact other materials directly, and hence entropy deposition is a serious problem.

The another difficulty comes from a theorem of classical dynamics known as Liouville's theorem [1]. It says that the total volume occupied by particles in phase space is preserved by the time evolution of the system driven by external electromagnetic forces. Cooling must reduce the phase space volume, and hence some non-conservative forces must be introduced.

Some cooling systems have been proposed and have been successfully operated [2,3]. In the current cooling systems, the cooling rate is small, and they are applied to ring type accelerators only. For a linear accelerator of low energy beams, new fast cooling technologies must be devised.

A laser cooling system utilizes the energy dissipation of accelerated charged particles by means of the emission of radiation. An intense laser has a large electric field and it is possible to accelerate charged particles strongly. In this paper, we show the detailed evaluation of the effect of the laser cooling system originally proposed by Sprangle [4].

Since the use of radiative damping requires very large acceleration of particles, the laser must have a very high intensity. On the other hand, the radiation power is enhanced in coherent radiation processes [5], which take place when the acceleration scale length is greater than the size of the bunched beam. The emitted power of incoherent radiation is proportional to the number of particles,  $N$ , while that of coherent radiation is proportional to  $N^2$ , because the bunch of the particles acts as a single particle. In  $N^2$  radiation, the average force acting on a particle is enhanced by  $N$  times.

To analyze the particle motion with  $N^2$  radiative damping, the retarded field must be solved accurately. For the purpose of the analysis, we have made a new simulation code to calculate the motion of charged particles interacting with each other through the retarded electromagnetic field, and we apply it to the collision process of two particles in a strong external field.

In Section 2, we show the method of including radiative damping and show some results for the cooling method due to a strong laser beam. In Section 3, we show the scheme of the new simulation code and also show some of the collective radiative damping processes for a few particle system. Section 4 is used for discussion.

\* Corresponding author. Tel. +81 720 39 9141, fax +81 720 38 6599, e-mail taguchi@ile.osaka-u.ac.jp.

## 2. Low energy electron beam cooling by counter irradiated strong laser beam

Sprangle et al. proposed a simple cooling method using a strong laser beam [4]. When the laser propagates counter to the electron beam, the higher energy electrons lose more energy than the lower energy electrons. As a result, the initial energy spread is reduced after the laser pulse passes through the beam. In this section, we solve the equations of motion with a radiative damping force, and calculate the reduction of energy spread for a Gaussian laser pulse.

The relativistic equation of motion of a charged particle is as follows:

$$\frac{d\mathbf{p}}{dt} = q \left[ \mathbf{E} + \frac{\mathbf{v}}{c} \times \mathbf{B} \right] + \mathbf{f}_R. \quad (1)$$

Here,  $\mathbf{f}_R$  is the radiative damping force given by the following equation:

$$\mathbf{f}_R = \frac{2q^2}{3mc^3} \left[ \frac{d}{dt} \gamma \frac{d\mathbf{p}}{dt} + \gamma \mathbf{p} \left( \left( \frac{d\gamma}{dt} \right)^2 - \frac{1}{m^2 c^2} \left( \frac{d\mathbf{p}}{dt} \right)^2 \right) \right]. \quad (2)$$

In these equations,  $m$  and  $q$  are the mass and the charge of the particle, which we set to the value of an electron, and  $\mathbf{p}$  and  $\mathbf{v}$  are the momentum and the velocity of the particle, respectively. Since it is difficult to solve Eq. (1) self-consistently, we estimate  $\mathbf{f}_R$  with  $d\mathbf{p}/dt$  driven only by an external field.

For the laser irradiation, the electric field  $\mathbf{E}$  and the magnetic field  $\mathbf{B}$  is set to be the following linear polarized electromagnetic field.

$$\begin{aligned} \mathbf{E} &= E_0(t) \sin(kz + \omega t) \hat{\mathbf{x}}, \\ \mathbf{B} &= -\frac{ck}{\omega} E_0(t) \sin(kz + \omega t) \hat{\mathbf{y}}. \end{aligned} \quad (3)$$

We substitute these formulas into Eqs. (1) and (2) and solve them numerically. We here suppose the shape of the laser pulse is Gaussian,  $E_0(t) = E_p \exp(-(t - t_0)^2/2t_p^2)$ , and the total calculation is done for a time  $4t_p$ , with  $t_0 = 2t_p$ .

Fig. 1 shows the reduction of the energy factor,  $\gamma$ , as a function of the traveling distance of an electron starting with several initial energies. In this case the laser is supposed to be a glass laser (1  $\mu\text{m}$  wavelength). Its intensity  $I_0$  is set to be  $5 \times 10^{18} \text{ W/cm}^2$ , and its pulse length  $\tau (= \sqrt{2} t_p)$  is 7 ps.

After the laser pulse passes, the initial energy spread  $\Delta\gamma = 2$  is reduced to 1.89 and the energy spread  $\Delta\gamma/\gamma$  decreases by about 3%. From a simple calculation of the energy loss, the reduction is calculated as follows [4]

$$\frac{\Delta\gamma}{\gamma} \cong \left( \frac{\Delta\gamma}{\gamma} \right)_{t=0} \left( 1 - \frac{8\pi}{3} \frac{r_e^2 I_0}{mc^2} \left( 1 + \frac{v_0}{c} \right)^2 \gamma \tau \right). \quad (4)$$

Here,  $r_e$  is the classical electron radius, and  $v_0$  is the axial velocity of the electron beam. For the above param-

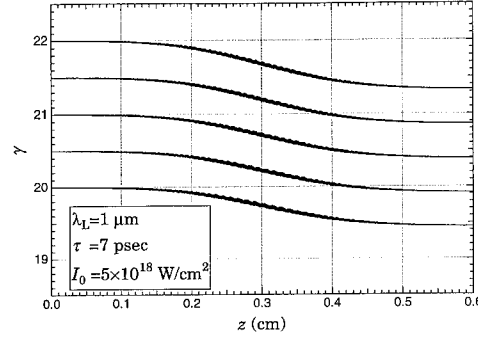


Fig. 1. Energy of electrons interacting with strong laser pulse as a function of the distance traveled.

ter, the reduction is calculated as 2.3%, so the above result agrees well with the simple estimate. Since the reduction is proportional to the laser intensity, a very strong laser is necessary to obtain much cooling.

## 3. Lienard–Wiechert simulation code and its application to analysis of $N^2$ radiative damping

As written in several textbooks of classical electrodynamics [6,7], the radiative damping force is generated by the imbalance of electric repulsive forces acting between every two small segments on a charged sphere. The imbalance results from the finite propagation speed of light, because the retarded time of the force from one segment to the other is different from that of its opposite. In order to analyze the  $N^2$  radiative damping, we must treat the retardation of the interaction force carefully. Conventional particle codes, use a grid method which calculates the interaction between particles by means of field data on mesh points. The effect of retardation is stored in the mesh, but the retarded time of each force is not explicitly expressed.

To calculate the accurate retarded field, we have developed a new simulation code which calculates the retarded time of each force directly. Suppose that orbits of two particles are given by  $\mathbf{r}_1(t)$  and  $\mathbf{r}_2(t)$ , the retarded time  $t'$  of force acted on the particle 1 at time  $t$  exerted by the particle 2 is calculated by the following equation:

$$\frac{|\mathbf{r}_1(t) - \mathbf{r}_2(t')|}{c} + t' = t. \quad (5)$$

Preparing for the calculation of the retarded time, we store the historical data,  $\mathbf{r}$ ,  $\mathbf{v}$ ,  $\dot{\mathbf{v}}$  of all particles at time series,  $t_1, t_2, \dots, t_n (= t)$  calculated in each time step. To calculate the retarded time  $t'$ , we first search a temporal interval  $[t_i, t_{i+1}]$  satisfying the following condition:

$$|\mathbf{r}_1(t) - \mathbf{r}_2(t_i)| + ct_i < ct < |\mathbf{r}_1(t) - \mathbf{r}_2(t_{i+1})| + ct_{i+1}. \quad (6)$$

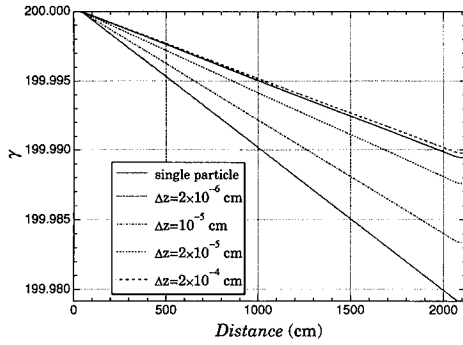


Fig. 2. Reduction of energy of two particles with fixed spacing  $\Delta z$ . The solid curve shows the result of a single particle.

From the data  $r(t_i)$ ,  $r(t_{i+1})$ ,  $v(t_i)$ ,  $v(t_{i+1})$ ,  $\dot{v}(t_i)$ ,  $\dot{v}(t_{i+1})$ , we calculate the coefficients of the fifth order spline interpolating polynomial. We substitute the polynomial into Eq. (5) and obtain a suitable root  $t'$  by Newton's method. When the acceleration is not so large, the iteration of Newton's method finishes in a few steps. After we get the retarded time  $t'$ , we also calculate the position, velocity and the time derivative of the velocity at  $t'$  using the interpolating polynomial. Using those data, we calculate the retarded Lienard–Wiechert field [8] acting on particle 1 at  $t$ .

We use this code to analyze the  $N^2$  radiative damping of particles in a strong external field. For simplification, we use a linear wiggler as an external field instead of a short wavelength laser. We set the parameters as  $\gamma = 200$ , wiggler strength,  $B_w = 2$  kG and wiggler pitch,  $\lambda_w = 10$  cm. The length of the wiggler is 20 m (200 periods) and we put a 50 cm adiabatic section at the entrance and exit of the wiggler. In this simulation, we use macro-particles which have 10000 times the charge and mass of an electron, because the number of particles we can track is limited.

At first, the motion of two particles with a fixed axial spacing  $\Delta z$ , (with same  $x$  and  $y$  coordinates) is calculated. In this case, the calculated retarded forces of two particles are averaged and are redistributed to both of

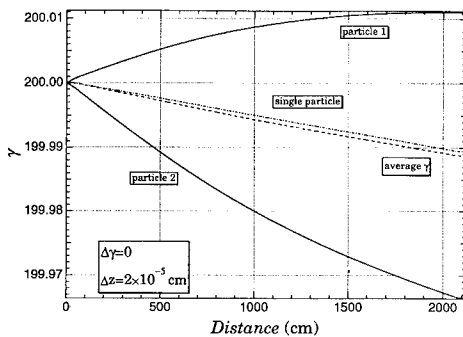


Fig. 3. Reduction of energy of two particles with initial spacing  $\Delta z = 2 \times 10^{-5}$  cm. The dashed curve shows their average.

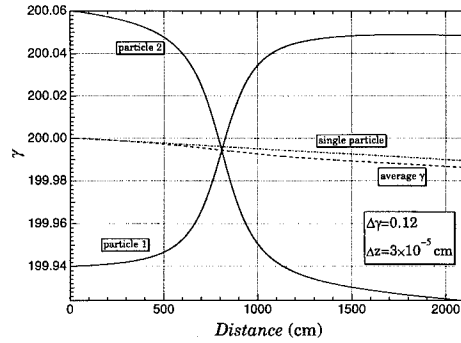


Fig. 4. Reduction of energy of two particles with initial spacing  $\Delta z = 3 \times 10^{-5}$  cm and with initial energy difference  $\Delta\gamma = 0.12$ .

them. Fig. 2 shows the variation of the average  $\gamma$  of two particles as a function of the distance traveled.

As shown in the figure, the energy reduction becomes higher as the spacing decreases. For examples, when  $\Delta z = 2 \times 10^{-6}$  cm, the energy reduction is twice that of a single particle (solid line). On the other hand, the result is almost the same as for a single particle when  $\Delta z = 2 \times 10^{-4}$  cm. When the spacing is less than  $10^{-6}$  cm no more enhancement is obtained.

In the wiggler case, the acceleration scale length is estimated by  $\lambda_w(1 - v_z/c)$ . For the present parameter, this is about  $3 \times 10^{-4}$  cm. The above result is consistent with the critical value.

Fig. 3 shows the energy variation of two free particles which are initially placed with the spacing  $\Delta z = 2 \times 10^{-5}$  cm. Their initial energies are set to be the same. In this case, the repulsive force separates two particles, and the collective energy reduction is very small. Fig. 4 shows the result of two colliding particles. In this case  $\Delta z = 3 \times 10^{-5}$  cm and the energy difference  $\Delta\gamma = 0.12$ . The energy of particle 1 is less than that of particle 2, which is trailing. As shown in the figure, they collide at a distance of about  $z = 800$  cm. Around that moment, the energy reduction is enhanced.

To see the enhancement of energy reduction more clearly, we show the gradient of the average  $\gamma$  as a function of distance in Fig. 5. It shows that the peak

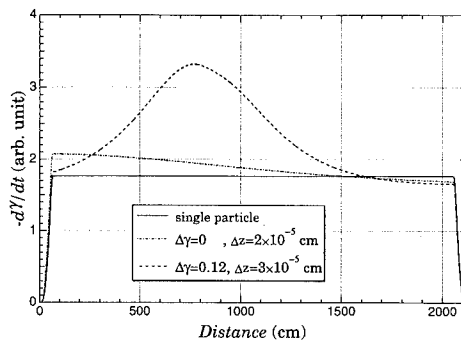


Fig. 5. Spatial gradient of  $\gamma$  as a function of the distance traveled.

gradient in the case of the collision is double that of a single particle.

#### 4. Conclusion and discussion

We have calculated the reduction of an energy spread in a laser cooling system using a strong laser beam, and we have studied the enhancement of radiative damping by virtue of coherent radiation.

For the laser cooling, we solved the equations of motion with a radiative damping force and calculated the reduction of  $\Delta\gamma/\gamma$ . The result was that the beam was cooled, but the cooling rate was not very high, even when a very high power glass laser, ( $5 \times 10^{18}$  W/cm<sup>2</sup>) was used.

In order to study the enhancement of the radiative damping, we next analyzed the coherent radiative process using a new simulation code which accurately calculates the retarded field between particles. We applied the code to calculate the energy reduction at a collision of two particles in a strong external electromagnetic field.

The result was an enhancement of the energy reduction of the average energy when the spacing between two

particle becomes small. This result means that the collision is inelastic, so it could be applied to a cooling system.

In the future we must improve the code to calculate efficiently for many more particles and we must investigate the reduction of phase space volume. Then we will consider an application of the enhancement of the radiative damping to a cooling process. The collective interaction with retarded field is a difficult problem and it has not yet been solved entirely. Our new code will be applied to answer basic electrodynamic questions.

#### References

- [1] H. Goldstein, *Classical Mechanics* 2nd edition (Addison-Wesley, 1981).
- [2] S. van der Meer, CERN/ISR-PO/72-31.
- [3] H. Poth, *Phys. Rep.* 196 (1990) 135.
- [4] P. Sprangle and E. Esarey, *Phys. Fluids B4* (1992) 2241.
- [5] T. Nakazato et al., *Phys. Rev. Lett.* 63 (1989) 1245.
- [6] W. Heitler, *The Quantum Theory of Radiation* (Dover, 1954) Chapter I.
- [7] A.D. Yaghjian, *Relativistic Dynamics of a Charged Sphere* (Springer, 1992).
- [8] L.D. Landau and E.M. Lifshitz, *The Classical Theory of Fields*, 3rd revised English edition (Addison-Wesley, 1971).



# Visualization of spatial profiles of spectra and intensities in FEL simulations

K. Yoshikawa <sup>a,\*</sup>, T. Shinzato <sup>a</sup>, Y. Yamamoto <sup>a</sup>, M. Ohnishi <sup>a</sup>, T. Yamazaki <sup>b</sup>

<sup>a</sup> *Institute of Atomic Energy, Kyoto University, Uji, Kyoto 611, Japan*

<sup>b</sup> *Electrotechnical Laboratory, Tukuba, Ibaraki 305, Japan*

## Abstract

We have developed FEL numerical simulation codes to analyze and examine the FEL experimental results at Electrotechnical Laboratory (ETL) using optical klystrons, and we have reached excellent agreement with experiments so far. To further advance the codes for better and quick understanding, we have tried to visualize the simulation results, especially for spatial profiles of spectra and intensities, using color graphic terminals. Spectral information at each observation point is converted to color graphic data through the modification of a CIE XYZ color system. Simulation results on the color display of the CRT show good agreement with a photo of spontaneous emission spectra taken in the TERAS storage ring at ETL using an optical klystron, and 231 MeV electrons with the fundamental wavelength of 596 nm. Also, the fundamental, 2nd, and 3rd harmonics are separately visualized.

## 1. Introduction

We have developed codes for simulating spontaneous spectra and evaluating gains for the ETL FEL experiments using the TERAS storage ring and the optical klystron. Although we found excellent agreement with the experimental results numerically [1,2], more intuitive comparisons are strongly called for. Therefore, to further advance the simulation results we have tried visualizing the calculated spatial spectral pattern, in particular, in the visible region typical to TERAS. In addition, we have visualized the individual pattern of harmonics for quick understanding and comparison with the actually observed pattern in the experiments on the CRT (cathode ray tube) of the work station (Sun Microsystems, Sparc Station 10-30).

## 2. Calculation of spatial spectra

The magnetic fields of the ETL-TERAS optical klystron, consisting of two 8-period normal undulators with a 608 mm length and a gap of  $g_u = 40.3$  mm ( $K = 2.2$ ) (using Halbach type Neomax permanent magnets with a residual magnetism of 1.17 T), and a dispersive section with a 228 mm length and  $g_d = 57.5$  mm in the

center, were first calculated three dimensionally in the volume where the electrons are transported. Then three dimensional trajectories of electrons with experimentally observed phase distributions and a peak energy of 231 MeV were calculated in the optical klystron magnetic fields with invariant energies assumed. Lienard–Wiebert integrals were then calculated to obtain harmonic spectra using a Fast Fourier Transformation to shorten the computation time. Details are presented in Ref. [1].

The power spectral intensity  $P(\lambda)$  of spontaneous emission observed on the beam axis ( $z$ -axis) 9744 mm away from the entrance of the optical klystron was calculated for an electron beam with the following parameters,  $I_b = 4.34$  mA,  $\gamma = 453.1$ ,  $\Delta\gamma/\gamma = 1 \times 10^{-3}$ ,  $\sigma_x = 0.95$  mm,  $\sigma_y = 0.32$  mm,  $\epsilon_x = \epsilon_y = 1.0 \times 10^{-7}$  mrad.

Spatial intensity profiles proportional to the photon energy flux (power) were also calculated for visualization at the observation ( $x$ – $y$ ) plane for the fundamental, 2nd, and 3rd harmonics.

## 3. Assignment of the calculated colors onto the CRT colors

The visible light tristimulus values ( $X$ ,  $Y$ ,  $Z$ ) are determined, based on the CIE (Commission Internationale de l'Eclairage) criteria using color matching functions of the CIE XYZ color system (CIE 1931 standard colorimetric system [3])  $\bar{x}(\lambda)$ ,  $\bar{y}(\lambda)$ ,  $\bar{z}(\lambda)$ , by integrating  $P(\lambda)$  over the

\* Corresponding author. Tel. +81 774 32 3111 (ext. 2331), fax +81 774 33 1132, e-mail kiyoshi@kuiae.kyoto-u.ac.jp.

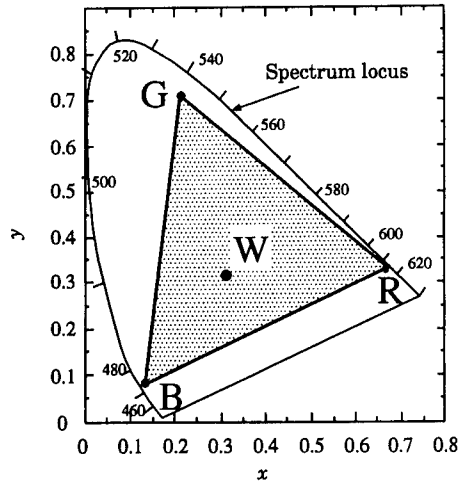


Fig. 1. NTSC standard chromaticity coordinates where R, G, B, W stand, respectively, for red, green, blue and standard white colors.

visible region (380–780 nm) in terms of the maximum luminous efficiency  $K (= 683 \text{ lm/W})$  as

$$X = K \int_{380}^{780} P(\lambda) \bar{x}(\lambda) d\lambda, \quad (1)$$

$$Y = K \int_{380}^{780} P(\lambda) \bar{y}(\lambda) d\lambda, \quad (2)$$

$$Z = K \int_{380}^{780} P(\lambda) \bar{z}(\lambda) d\lambda. \quad (3)$$

The chromaticity coordinates  $(x, y, z)$  are then determined by

$$x = X / (X + Y + Z), \quad (4)$$

$$y = Y / (X + Y + Z), \quad (5)$$

$$z = Z / (X + Y + Z). \quad (6)$$

Any color can be expressed on the  $x$ - $y$  chromaticity diagram, and the chromaticity coordinates of the spectra, which only the laser color can reproduce, are shown by the outer solid curve (spectrum locus) on Fig. 1.

Reproduction of color on a CRT color display is made using additive mixing of three primary colors. The NTSC (National Television Systems Committee) method assigns standard chromaticity coordinates for red (R), green (G), blue (B), and standard white (W) colors corresponding to the R, G, B triangle points, and W in Fig. 1, where any colors in the inner region can be reproduced on the CRT display.

Another set of tristimulus values (R, G, B) based on the NTSC primary stimulus R, G, B can be converted from the tristimulus values  $(X, Y, Z)$  through a fixed matrix [4]. Although the FEL laser color is approximately monochromatic, the spontaneous emission spectra calculated are not, and some of their chromaticity coordinates lie outside the RGB triangle as shown in Fig. 2a. For reproduction on the CRT of such color (A) having the tristimulus values  $(X_A, Y_A, Z_A)$ , the most popular method is the following additive color mixing with the standard white (W) with the resultant chromaticity coordinates  $(x_B, y_B, z_B)$  given by

$$x_B = \frac{X_A + kx_w}{X_A + Y_A + Z_A + k}, \quad (7)$$

$$y_B = \frac{Y_A + ky_w}{X_A + Y_A + Z_A + k}, \quad (8)$$

$$z_B = \frac{Z_A + kz_w}{X_A + Y_A + Z_A + k}, \quad (9)$$

where the constant  $k$  determines the internal dividing point between the color (A) and the standard white (W) having the chromaticity coordinates  $(x_w, y_w, z_w)$ . The appropriate choice of  $k$  can therefore make all the calculated colors

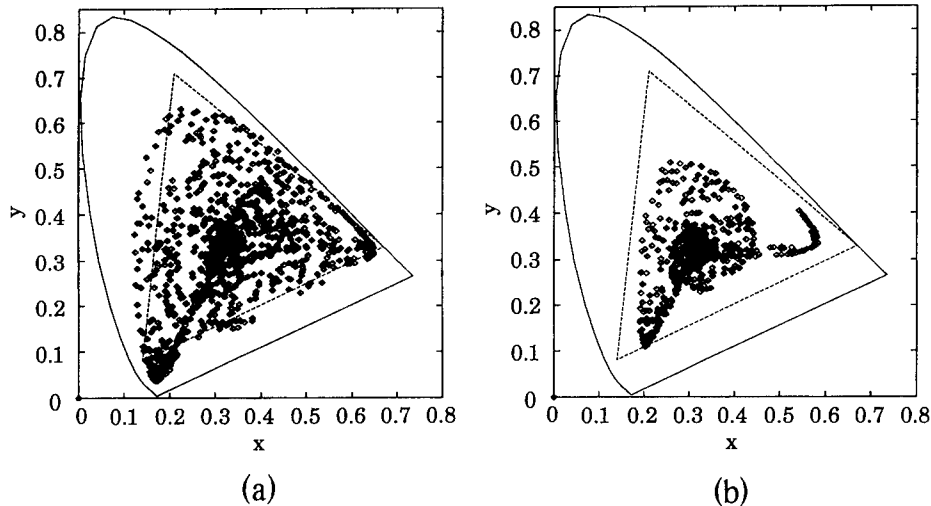


Fig. 2. Calculated chromaticity coordinates on the  $x$ - $y$  chromaticity diagram. (a)  $k = 0$ , (b)  $k = 2 \times 10^{-37}$ .

within the RGB triangle on the  $x$ - $y$  chromaticity diagram for visualization on the CRT color display, as is shown in Fig. 2b for  $k = 2 \times 10^{-37}$ .

#### 4. Visualization results and comparison with experiments

The observation plane (100 mm  $\times$  100 mm) normal to the  $z$ -axis, 9744 mm away from the entrance of the TERAS optical klystron was divided into segments, and 1089 ( $33 \times 33$ ) nodes  $P(\lambda)$  were calculated for one electron incident on and along the  $z$  axis. The results were printed out by a Canon Pixel Jet (a color dot printer, 400 dpi). Also, linear internal extrapolation was adopted to smooth color variations on the plane.

Fig. 3 shows photos of the observed spatial spontaneous emission spectra at the TERAS, the calculated spectra at the observation ( $x$ - $y$ ) plane for one electron with the corresponding visible spectrum band, and the fundamental, 2nd and 3rd harmonic components in the visible spectrum

region. Considering the sensitivity characteristics of the film used (Fuji commercial negative color film) even to the UV light, fairly good agreement of the simulation results with the experimental results on the photo is found. Also, each harmonic component of the pattern and its intensity profile is immediately distinguishable.

To provide further information on the spectra, including those outside the visible region, a pseudo-color assignment to the spectra was made for the 2nd, 3rd, and 4th harmonics for the same parameters as in Fig. 3. Their spectra ranging from 100 nm to 500 nm are shown in Fig. 4. The typical pattern inherent in each harmonic is clearly seen.

For evaluation of the intensity, which is proportional to the integral of  $P(\lambda)$ , a bird's eye view of the color spectra was developed. An example is shown in Fig. 5 for the spectra corresponding to Fig. 3b integrated over the visible spectrum region.

Effects of the number of electron trajectories included in the calculation were examined for 1, 10, and 100 electrons with the phase space distributions as described above (except for 1 electron). Somewhat surprisingly, the displayed results seem almost the same. This is because, in

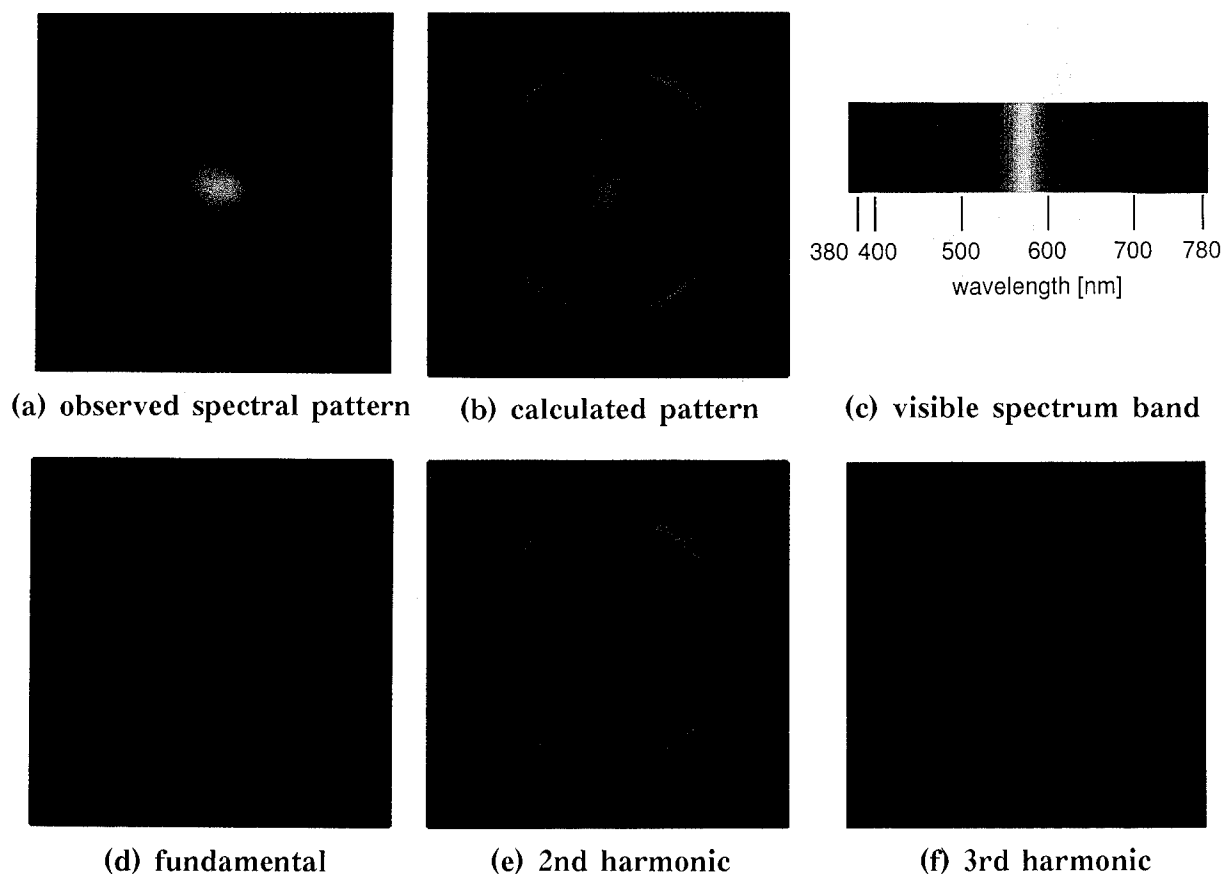


Fig. 3. Visualization results of the spontaneous emission spectra in the visible region for TERAS.

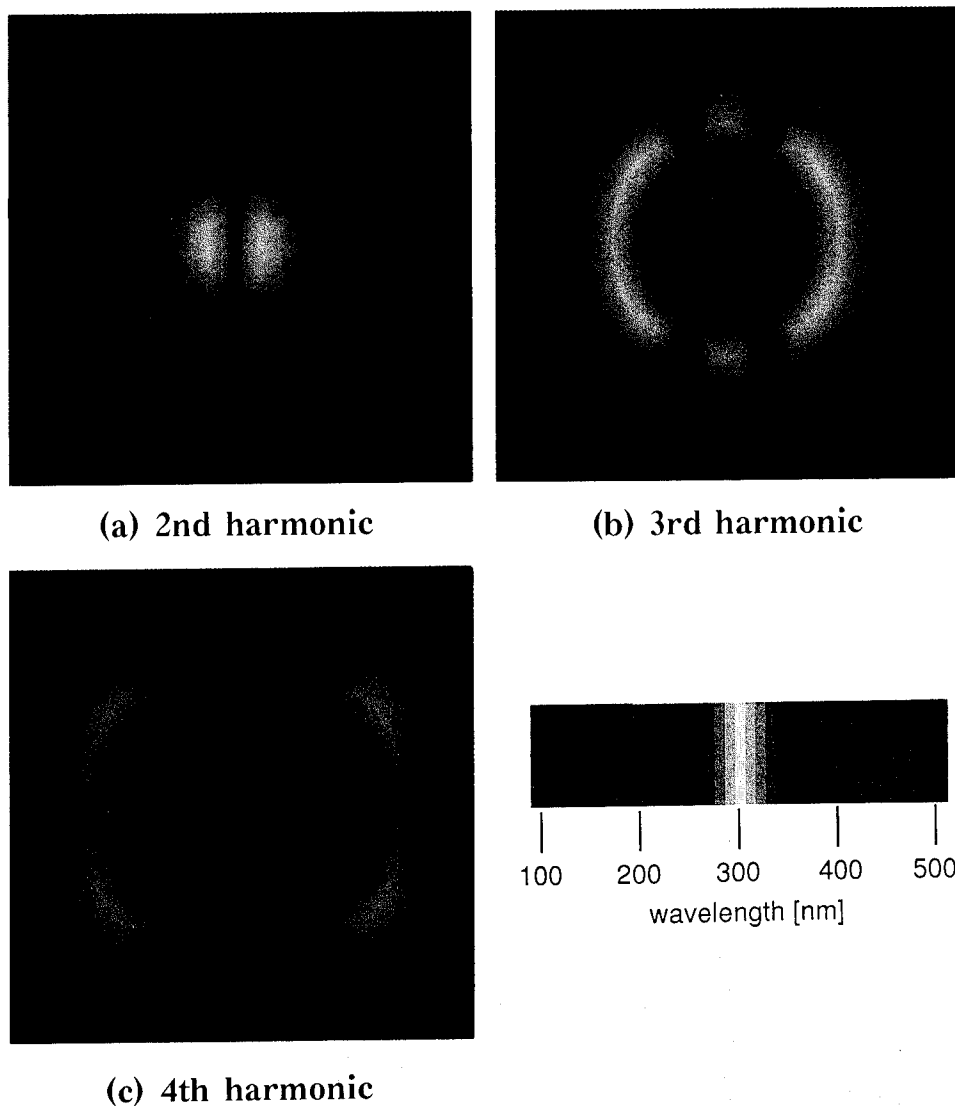


Fig. 4. Pseudo-color visualization of the harmonics including outside the visible spectrum region ranging between 100 nm and 500 nm for the same parameters as Fig. 3.

the process of color reproduction on the color display, the power spectral intensities  $P(\lambda)$  are integrated with weight as in Eqs. (1)–(3), and the color assignment scheme is further adopted into the RGB triangle region, as was described, even though a difference in the fine structure of the spectra is clearly seen in the simulation results. All these schemes reduce the effect of the number of electrons to a great extent.

Considering the computation time of 1 h for one electron from trajectory calculation to visualization by the Sun Sparc Station 10-30 (for  $33 \times 33$  nodes), it would be most advisable to use just one electron for viewing the predicted spectra and intensity profiles in the present case.

## 5. Conclusions

We have developed a visualization method in the simulation code, and found fairly good agreement with the experimental results observed at the ETL-TERAS optical klystron in the visible region. The components of the harmonics are also easily seen by this visualization method. To compensate for the lack of corresponding chromaticity coordinates on the CRT color display, the simple additive color mixture method adopted in this study is found to be reasonable and convenient for the purpose of visualization. The appropriate color or harmonic pattern is found to be obtainable from just one electron trajectory calculation.

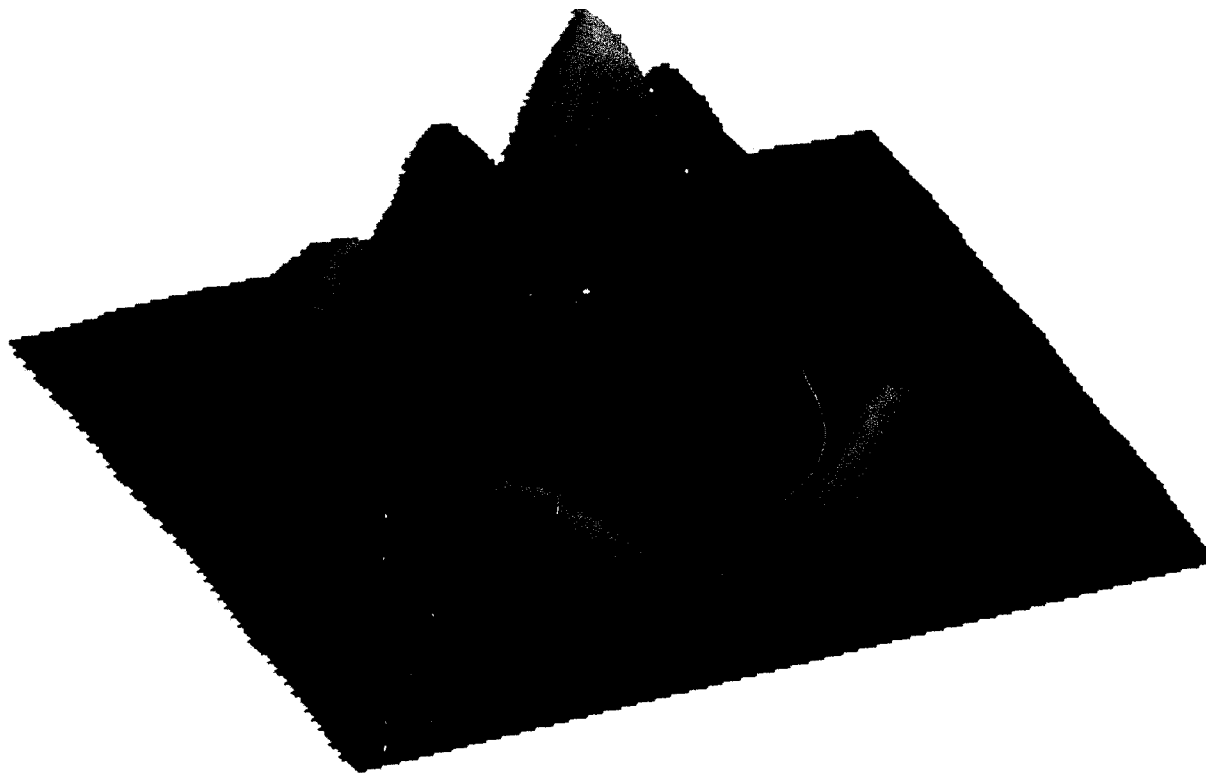


Fig. 5. Intensity profile corresponding to Fig. 3b.

Visualization of this kind would be also effective for quick examinations in FEL oscillator research.

#### Acknowledgements

We would like to express our sincere thanks to Dr. K. Takahama, ETL for his valuable discussions and advises on the color assignment methods.

#### References

- [1] K. Yoshikawa, Y. Inanaga, Y. Yamamoto, M. Ohnishi, T. Yamazaki and K. Yamada, Nucl. Instr. and Meth. A 331 (1993) 416.
- [2] K. Yoshikawa, S. Hashimoto, Y. Yamamoto, M. Ohnishi, T. Yamazaki and K. Yamada, Nucl. Instr. and Meth. A 341 (1994) ABS 5.
- [3] G. Wyszecki and W.S. Stiles, Color Science: Concepts and Methods, Quantitative Data and Formulas (Wiley, 1982) pp. 130–175.
- [4] W.N. Sproson, Colour Science in Television and Display Systems (Adam Hilger, 1983) pp. 29,30.



ELSEVIER

## FEL center user diagnostics and control ☆

K.W. Berryman \*, B.A. Richman, H.A. Schwettman, T.I. Smith, R.L. Swent

*Stanford Picosecond FEL Center, W.W. Hansen Experimental Physics Laboratory, Stanford University, Stanford, CA 94305-4085, USA*

### Abstract

In the past year, the Stanford Picosecond FEL Center has produced more than two thousand hours of beam time dedicated to user experiments. To assure reliable beam delivery and to maximize productivity of our users we have developed a sophisticated system of diagnostics and control. An integrated display is now available in all experimental areas which provides continuously updated measurements of beam spectrum, micropulse duration, power, position, and pointing – all of which may be saved to document beam conditions during an experiment. The beam is actively wavelength and amplitude stabilized to better than 0.01% and 2%, respectively. Direct wavelength control is available to users in every experimental area, allowing changes of wavelength as large as a few percent. Larger wavelength shifts, and adjustments in macropulse or micropulse width or timing, are readily available with operator assistance.

### 1. Introduction

The Stanford Picosecond Free Electron Laser (FEL) Center has been operating as a user facility for almost three years [1]. The challenges of running a user facility are quite different from those involved in building an FEL. A typical user wishes to have a transform limited optical beam free from amplitude and wavelength variation, locked to a unique position and angle in space. The laser should be easily tunable under user control, and should provide flexibility in pulse delivery, spectral and temporal pulse width, and available power. In addition, the user typically desires continuous monitoring of these parameters.

Demands such as these have forced the Center to make a substantial investment in optical diagnostics and control. We have developed both amplitude and wavelength stabilization [2], user wavelength control, and we have explored micropulse width variation [3]. In the course of these developments we have more fully understood the regimes of operation of our FEL.

Once diagnostics and control systems have been developed, the final task is to integrate them smoothly into routine operation. At the Stanford FEL Center a computer continuously and automatically updates a status display visible in every experimental area. In addition, this computer may be controlled remotely, allowing users to change wavelength with the push of a button. Diagnostic data may

be saved and logged, so that FEL operation may be analyzed after the fact. We believe that this system has greatly increased the productivity of the Center.

### 2. Providing the perfect beam

An experimental program will be most productive when the FEL optical beam itself is of the highest quality and is as noise-free as possible. FEL beams produced by RF linacs can be nearly transform and diffraction limited. However, they still exhibit amplitude noise, wavelength noise, errors in position and pointing, and finally, variations in micropulse shape. We have dealt with these problems either through direct stabilization or continuous measurement. The result is an optical beam with quality as good, and in many cases better, than conventional table-top lasers.

The amplitude stabilization is effected by passing the beam through an Acousto-Optic Modulator (AOM), then splitting off a small percentage of the transmitted beam to monitor on a detector. The AOM deflects a fraction of the beam power out of the main beam as a function of its driving RF power. By varying the driving RF in response to the signal on the detector, a uniform amplitude in the transmitted beam may be maintained. Fig. 1 illustrates the result – the optical beam has an rms amplitude variation of only 1.8%. The feedback system also ensures comparable pulse-to-pulse stability over many hours of operation.

Wavelength stabilization is achieved by passing some of the beam through a 0.275 m monochromator and monitoring the signal on a four element linear focal plane array. The signals on the array elements are subtracted and

\* Work supported in part by the Office of Naval Research, Contract #N00014-91-C-0170.

\* Corresponding author. Tel. +1 415 723 9556, fax +1 415 725 8311, e-mail berryman@leland.stanford.edu.

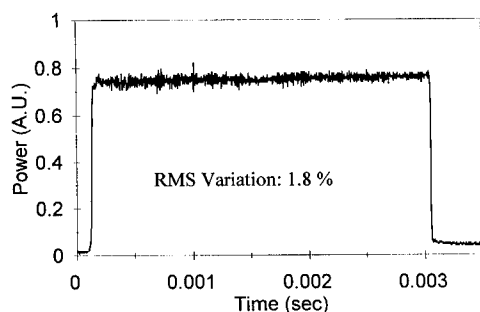


Fig. 1. Amplitude variation within a single macropulse. The operating wavelength was 4.5  $\mu\text{m}$ . The total RMS variation is 1.8%.

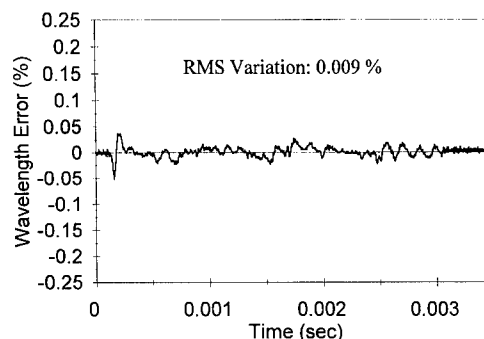


Fig. 2. Wavelength variation within a single macropulse. The center wavelength was 4.5  $\mu\text{m}$ . The total RMS variation is 0.009%.

normalized to provide a wavelength error signal. If the FEL is operating at an average wavelength corresponding to the monochromator setting, an equal amount of power will fall on both sides of the array, and the error signal will be zero. This error signal is then fed back into the driving amplitude in one of the accelerator structures. If the detected wavelength is too short the accelerating energy is reduced, and if it is too long the energy is increased. The resulting stabilization of the center wavelength is evident in Fig. 2. The rms wavelength variation in this case was 0.009%, while the pulse-to-pulse variation over an eight hour experimental shift is comparable. Stabilization to a small fraction of the FEL total bandwidth is necessary for any experiment which involves pumping a narrow absorption line, as otherwise wavelength jitter will translate into population jitter in the pumped state, with corresponding noise in the experimental data.

Beam position and pointing is monitored by a pair of pyroelectric quadrant detectors. Focussing elements in front of these detectors image the beam both at infinity and at the entrance to the table, thereby defining the beam position and angle. At the beginning of an experimental shift, the beam is centered on both quad detectors, assuring that the FEL beam will be aligned properly into the user rooms. The detectors are then monitored by the computer, which displays a history of beam motion. The beam exhibits both fast motion due to mirror vibration and slow drifts due to temperature variation. During a single macropulse, the beam position is stable to within a few tens of microns and the angle to within a few microradians. Over twenty four hours, slow drifts result in misalignments smaller than 100  $\mu\text{m}$  in position and 10  $\mu\text{rad}$  in angle.

The micropulse shape is monitored with an autocorrelator which performs measurements every few minutes. An

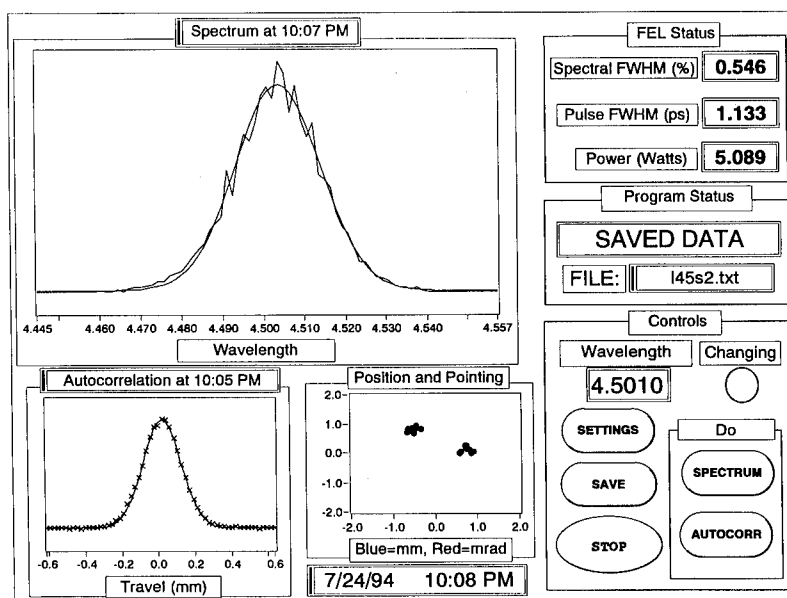


Fig. 3. The computer display for the integrated diagnostics and control program, implemented in the LABVIEW environment.

integrated spectrum is also acquired every few minutes, and together these measurements verify that the beam is operating near the transform limit. The measured FEL pulse shape is extremely stable over many minutes, with the major variation resulting from changes in the optical cavity length due to temperature drift. With operator intervention the variation in pulse duration can be kept to less than ten percent over a period of hours. Also, since the autocorrelations are recorded continuously, any residual variability can be deconvolved from the user's experimental data.

### 3. The diagnostics and control system

The diagnostics system of the Stanford FEL is installed on a dedicated  $5 \times 12$  ft optical table. This table contains two monochromators, an autocorrelator, one AOM, nine infrared detectors of various types, and assorted necessary optics. The beam is transported from the accelerator tunnel to this table via an evacuated pipe, and enters another vacuum tube to be transported from the table to the experimental areas.

Approximately twenty-five percent of the total beam power is split off from the main beam for diagnostic purposes. The present system is compatible with tuning from 3 to 8  $\mu\text{m}$ , and can be extended beyond 8  $\mu\text{m}$  if necessary. The optical table may be purged with dry nitrogen if necessary. Each of the measurement systems are integrated in a single control program which provides continuous monitoring of the diagnostics as well as user control over wavelength, data acquisition, and data logging. A printed version of the screen display for this program is illustrated in Fig. 3. This display is present at all user experimental stations, and the computer may be remotely controlled, allowing for complete remote operation of the diagnostics from any experimental room.

The largest area of the display is dedicated to an FEL spectrum, as this is perhaps the most critical information for typical experiments. The spectrum is obtained by sending a small fraction of the beam through a 1 m monochromator. The monochromator is scanned under computer control, with several macropulses digitized and averaged, producing an integrated macropulse spectrum. The spectrum is then fit to a Gaussian, with the Gaussian FWHM in percent appearing in the numeric indicator for spectral width. The user can specify the range of the scan in percent, the number of points, and the number of macropulses to average. The computer automatically adjusts the scan to the operating wavelength, and repeats every few minutes.

In the bottom left corner of the diagnostics display is a picture of the most recently completed autocorrelation, also with a superimposed Gaussian fit. The pulse FWHM in ps appears in the upper right corner. Our dedicated autocorrelator uses a small percentage of the beam, split

into two pieces and crossed with variable delay in a  $\text{AgGaSe}_2$  crystal. When the two beams are overlapped the crystal produces a frequency-doubled beam with intensity proportional to the product of the intensity in each of the crossed beams. The fundamental is then filtered out and the doubled power recorded as the delay is scanned. Once again, the user can control the width of the scan, number of points, and averaging. Together with the spectral width, the temporal width can be used to check that the FEL is operating near the transform limit.

To the right of the autocorrelation display is a graph providing a history, over the past hour or so, of the beam position and pointing. If the beam should drift, the user can immediately note a shift in position or angle and, if necessary, readjust the alignment. In practice, the long-term drifts in our beam are so small that realignment is only necessary every few days. The diagnostics control program is rounded out with a numeric indicator of beam power in the macropulse, as well as controls which determine data acquisition rates and allow the saving of data to disk.

### 4. Flexibility and reliability

The most obvious advantage of FELs has been their flexibility in the wavelength of operation. FELs with variable-gap undulators are capable of tuning with relative wavelength changes of more than 100% percent in a matter of minutes [4]. At the Stanford FEL Center we tune by changing the linac energy. We are capable of providing twenty-five percent wavelength variation within a few minutes, with larger excursions requiring about an hour to change the dielectric mirrors. We are also able to provide changes of the order of one percent at rates up to a few kHz.

In addition to rapid tunability, the wavelength stabilization system has allowed us to implement user wavelength control. When a user adjusts the wavelength set point, the stabilization system automatically adjusts the energy of the linac. For changes of a few percent or less no operator intervention is necessary at all; the user adjusts the program control and everything else happens automatically. This system has been used successfully by several of our user groups – in one instance, an experimental group studying the phase variation of the nonlinear susceptibility of quantum wells as a function of wavelength was able to make detailed measurements at 24 wavelengths in eight hours [5].

Another important advantage of FELs is their ability to offer variable micropulse lengths and spectral widths through a combination of cavity desynchronization and electron bunch length modification. Several FELs have demonstrated variability in pulse width [6] as well as production of sub-picosecond pulses [7]. At the Stanford FEL Center we are able to vary the micropulse duration from approximately 600 fs to 3 ps. The pulse remains better than 90



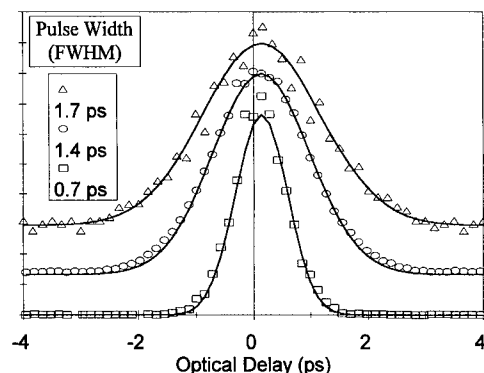


Fig. 4. Autocorrelations acquired consecutively at 4.5  $\mu\text{m}$ , after varying accelerator parameters. Simultaneously measured spectra verified that the pulses remained nearly transform limited throughout this range. The traces are offset for clarity.

percent transform limited throughout this range, so that the corresponding spectral widths range from over one percent to a few tenths of a percent. Fig. 4 illustrates this capability; the three autocorrelations presented were acquired within minutes of each other. In response to user demands, we can choose a micropulse width to within about 100 fs. This capability has proved necessary to characterize multi-level quantum beats in photon echoes produced by the FEL in metal–carbonyl systems [8].

## 5. Conclusions

Users are not interested in the details of FEL physics; they merely wish to have the highest quality optical beam delivered to the experiment in a reliable and well-characterized fashion. A well developed diagnostic system is a necessary prerequisite to fulfill this mission. Good diagnostics serve a further purpose, however. We have found

that as our characterization of the FEL improves, we are able to improve its operation and extend its capabilities. As operation becomes more routine, we have also been able to afford users more direct control over laser parameters. This in turn increases their productivity.

The transformation of a large machine like the FEL into a user-friendly laser system requires a dialog between those who build the machine and those who use it. The construction of our diagnostics and control system has been a powerful catalyst for that cooperation.

## References

- [1] T.I. Smith, H.A. Schwettman, K.W. Berryman and R.L. Swent, SPIE Proc. 1854 (1993) 23.
- [2] A. Marziani and T.I. Smith, Nucl. Instr. and Meth. A 331 (1992) 59.
- [3] E.R. Crosson, K.W. Berryman, H.I. Lihn, T.I. Smith, R.L. Swent and H. Wiedemann, these Proceedings (16th Int. Free Electron Laser Conf., Stanford, CA, USA, 1994) Nucl. Instr. and Meth. A 358 (1995) 216.
- [4] R.J. Bakker, C.A.J. van der Geer, D.A. Jaroszynski, A.F.G. van der Meer, D. Oepts and P.W. van Amersfoort, J. Appl. Phys. 74(3) (1993) 1501.
- [5] E.L. Martinet, H.C. Chui, G.L. Woods, M.M. Fejer, J.S. Harris, Jr., C.W. Rella, B.A. Richman and H.A. Schwettman, Short wavelength (5.36  $\mu\text{m}$  to 1.85  $\mu\text{m}$ ) nonlinear spectroscopy of coupled InGaAs/AlAs intersubband quantum wells, Appl. Phys. Lett., in press.
- [6] R.J. Bakker, D.A. Jaroszynski, A.F.G. van der Meer, D. Oepts and P.W. van Amersfoort, IEEE J Quantum Electron. QE-30 (1994) 1635.
- [7] F. Glotin, R. Chaput, D. Jaroszynski, R. Prazeres and J.-M. Ortega, Phys. Rev. Lett. 71 2587.
- [8] A. Tokmakoff, A.S. Kwok, R.S. Urdahl, R.S. Francis and M.D. Fayer, Multilevel vibrational dephasing and vibrational anharmonicity from infrared photon echo beats, submitted to Chem. Phys. Lett.



ELSEVIER

# The influence of hole-coupling on the transverse structure of intra-cavity light pulses

G.H.C. van Werkhoven<sup>a,\*</sup>, B. Faatz<sup>b</sup>, T.J. Schep<sup>a</sup>

<sup>a</sup> FOM-Instituut voor Plasmafysica 'Rijnhuizen', Postbus 1207, 3430 BE Nieuwegein, The Netherlands

<sup>b</sup> ENEA, Dipartimento Innovazione, Settore Fisica, CRE Frascati, P.O. Box 65, 00044 Frascati, Rome, Italy

## Abstract

The important issue addressed is the spatial structure of the light pulse inside the cavity of a hole-coupled resonator and the fraction of power lost through the aperture. The radial structure of the radiation is determined by the competition between power loss and scattering at the aperture and by the gain due to the interaction with the electrons. The additional effect of slippage couples the transverse and longitudinal profiles of the light pulse. It is shown that, at the back of the pulse, gain and gain-focussing are dominant. The front of the pulse propagates mainly in vacuum. The on-axis field intensity in this region is reduced by scattering. The influence of these mechanisms on the intra-cavity field structure is analyzed using a model that takes the time-dependent spatial dependence of the optical pulse into account. The phenomena are demonstrated numerically for FEL parameters close to those of FELIX.

## 1. Introduction

In this paper, a pulsed beam resonator FEL like FELIX is considered [1], which successfully employs an on-axis aperture to extract the power from the cavity. In case of a continuous electron beam, it has been shown that hole-coupling provides a broad out-coupling scheme [2,3], despite the predicted reduction of the outcoupled power [4].

During each roundtrip in the resonator, the radial profile of the intra-cavity light is determined by two counteracting processes. On the one hand, aperture loss tends to reduce the field intensity on axis. On the other hand, the optical field, in particular on-axis, is amplified by the interaction with the electrons. Therefore, the radial profile of the optical field alters from pass to pass [2,5]. The overlap between the radiation and the electron pulses in the longitudinal direction is determined by their difference in velocity, by the gain and by synchronization of the pulses. In the linear regime, where radiation grows exponentially, gain dominates over losses and scattering, and determines the transverse structure of the optical field. When saturation is reached, the pulse begins to overtake the electrons due to a slight shortening of the cavity. Eventually, the light will run ahead of the electron pulse. This implies that the radial profile of the light will be dominated by power loss and scattering at the aperture. It will be shown that the resulting radial structure yields a

strong reduction of the on-axis field intensity. Behind the pulse, a second pulse will grow as in the linear regime. When saturation is reached, this peak will overtake the electrons and the cycle starts again. This process implies that the intra-cavity field distribution consists of pulses tied to the electrons and of freely propagating pulses. These contributions have an entirely different transverse structure.

The aforementioned effects are investigated using a 4D simulation model that is suitable for pulse propagation in an axisymmetric, hole-coupled resonator. We refer to Ref. [6] for a detailed description of the model. Its main characteristics are described in the next section. In Section 3 numerical results are presented which demonstrate the combined effect of slippage and of the radial mode structure on the energy density distribution of the radiation pulse. The conclusions are summarized in Section 4.

## 2. Description of the simulation model

The simulation model is based upon the set of the paraxial wave equation and the electron equations of motion [7]. The transverse behaviour of the light pulse is modelled by decomposing the field  $u(r, z, t) = \sum_{n=0}^{\infty} u_n(z, t)\Psi_n$  into a set of orthogonal Gauss-Laguerre (GL) modes  $\Psi_n$  which satisfy the vacuum wave equation [8]. The evolution of the radial profile of the light in time and position  $z$  is determined by the coefficients  $u_n$ . In contrast to other spatially three dimensional models, the transverse

\* Corresponding author. Fax +31 3402 31204.

electron motion is only approximately accounted for, whereas the longitudinal motion is calculated exactly. “Warm” electron beam effects as finite beam emittance and undulator focussing are accounted for as far as they lead to a variation of the beam envelope. The model is valid as long as transverse gradients in the radiation field over the cross-section of the electron beam are small [9].

The model is applied to an axisymmetric hole-coupled resonator configuration, which consists of two circular, spherically curved mirrors. The hole is in the upstream mirror. The “scattering” of the radial mode structure of the light on reflection by realistic mirrors, including finite aperture and radius, is accounted for using a reflection matrix formulation [10]. After a complete roundtrip through the cavity, the scattering of each mode  $n$  into itself yields a phase change

$$\phi^r = 2k_0 L_c - 2(2n+1) \arctan \left( \frac{L_c - z_w}{l_r} \right) - 2(2n+1) \arctan \left( \frac{z_w}{l_r} \right), \quad (1)$$

where  $k_0 = 2\pi/\lambda_0$  is the wave number,  $L_c$  is the cavity length and  $l_r$  and  $z_w$  are the Rayleigh length and waist position of the optical field, respectively. For the resonator geometry considered here, this roundtrip phase plays an important role in the radial mode structure of the optical field.

### 3. Numerical results

In this section, the combined influence of the radial mode structure and of slippage effects on the evolution of a light pulse in a hole-coupled resonator is demonstrated numerically. The simulations are performed for the FEL parameters of Table 1 that are characteristic for FELIX. The electron pulse has a parabolic profile in the  $\bar{z}$ -direction. For reasons of simplicity, the electron beam envelope,

the beam emittance, the initial energy detuning and the energy spread are assumed to be constant over the electron pulse. A matched beam is considered. The electron pulse repetition rate is such that the generated optical pulses do not interact. The center of the undulator is shifted towards the downstream mirror by  $\Delta_u$ , with respect to the center of the cavity. A total power loss of 2.5% is assumed for absorption on both mirrors. Furthermore, the radiation wavelength is  $\lambda_0 = 20 \mu\text{m}$ . At this wavelength, mirror edges losses are small. The initial optical pulse has a parabolic longitudinal profile and consists of the Gaussian radial mode ( $n=0$ ). Convergent and reliable results are obtained with maximally five Gauss-Laguerre (GL) modes. The simulations are performed at a fixed de-synchronization  $\Delta L = -2.0\lambda_0$ , where  $\Delta L = 0$  corresponds to synchronization. For this slightly shortened cavity, the gain of the optical field is close to its maximum value.

An example of the energy density of the optical pulse and its decomposition into GL modes is shown in Fig. 1, where the FEL operates in the linear regime. The position in both the light and electron pulses is measure by  $\bar{z} = z - v_{\text{pon}} t$ , where  $v_{\text{pon}} = \omega_0/(k_0 + k_u)$  is the ponderomotive velocity and  $k_u$  is the undulator wave number. The main fraction of the optical power overlaps with the electron pulse, which is located in the region  $(0-60)\lambda_{\text{pon}}$ . Since there is a finite desynchronization, this implies that the effective velocity of the light is reduced. Due to the gain, the energy density is concentrated near the axis. The largest values occur slightly off-axis due to power loss through the hole. The radial mode structure of the pulse consists mainly of the first three even GL modes  $n=0, 2$  and  $4$  of which the Gaussian mode is dominant. The contribution of the odd modes is much smaller. This is also the case in a closed resonator [9]. Apparently, the phase induced by the interaction with the electrons on each mode is small, such that the radial structure is dominated by the roundtrip phase Eq. (1), which is  $\phi^r \propto 3\pi n$ .

Since the energy of the GL modes originates from the Gaussian mode ( $n=0$ ), odd modes see destructive phases each roundtrip. As a result, the energy increase of odd modes is much lower than of even modes, which are in phase each roundtrip.

In the saturated regime, the optical pulse runs ahead of the electron pulse an increase of the effective velocity of the light. A slippage length behind this pulse, a new peak is generated which will grow as large as the first peak. The longitudinal and radial structures of this pulse are similar to those shown in Fig. 1. This is due to the fact that the electrons near the trailing edge of the electron pulse have experienced only a low optical field. This process is repeated periodically and leads to “limit-cycle” oscillations in the outcoupled power [11]. Fig. 2 shows the energy density of the optical pulse near the end of the third cycle. The first two pulses are completely decoupled from the electron beam and are subject to aperture loss and mirror scattering only. The radial profile of these two

Table 1  
Simulation parameters

|                             |             |                  |
|-----------------------------|-------------|------------------|
| Undulator period            | $\lambda_u$ | 0.065 m          |
| Number of undulator periods | $N_u$       | 38               |
| Initial electron energy     | $\gamma_0$  | 46.3             |
| Energy spread               | $\sigma_e$  | 0.35%            |
| Normalized emittance        | $\epsilon$  | 70 $\pi$ mm mrad |
| Peak current                | $I$         | 75 A             |
| Electron pulse length       | $L_b$       | 0.60 mm          |
| Cavity length               | $L_c$       | 6.00 m           |
| Waist position              | $z_w$       | 3.75 m           |
| Rayleigh length             | $l_r$       | 1.20 m           |
| Mirror radii                | $r_{mr}$    | 2.5 cm           |
| Upstream mirror aperture    | $r_{ma}$    | 1.5 mm           |
| Undulator shift             | $\Delta_u$  | 0.90 m           |

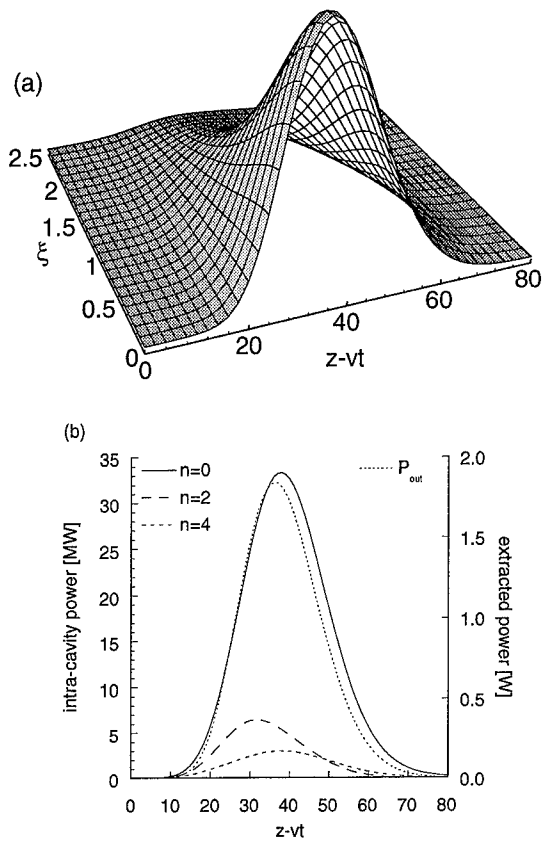


Fig. 1. (a) The energy density of the light pulse in the linear regime as a function of the longitudinal position  $\bar{z} = z - v_{pon}t$  (in units of  $\lambda_{pon}$ ) and the radial coordinate  $\xi = 2r^2/s^2$ , where  $s^2 = (2l_r/k_0) [1 + (z - z_w)^2/l_r^2]$ . The pulse is monitored just before the upstream mirror ( $z = 0$ ) (b) Distribution of the radiation power over the radial modes and the extracted power as a function of the position in the pulse. The electrons are located in the region  $(0, 60)\lambda_{pon}$ . Only the dominant modes are shown ( $n=0, 2$  and  $4$ ). The radiation wavelength is  $20 \mu\text{m}$ . The normalized radii of aperture and mirror are  $\xi = 0.057$  and  $\xi = 16.0$ , respectively.

pulses differs significantly from that of the last pulse, which still overlaps with the electrons, since the field intensity on-axis is strongly reduced. This effect, which is absent in case of a continuous electron beam, has also been demonstrated in Ref. [4], neglecting the influence of edge loss on the radial mode structure.

The scattering of the radial mode structure depends on the radiation wavelength, through the spotsize of the optical field. For the wavelength  $18\text{--}70 \mu\text{m}$ , Fig. 3 shows the extraction ratio  $\eta$ , i.e. the ratio of the extracted and intra-cavity pulse energies, in comparison with the extraction ratio of a single Gaussian radial mode  $\eta_{\text{Gauss}}$ . The wavelength scan is obtained by variation of the undulator strength  $A_{u0}$ , while keeping other parameters fixed. The calculations are performed for a cavity length, optimized for maximum gain at the lowest wavelength in each range.

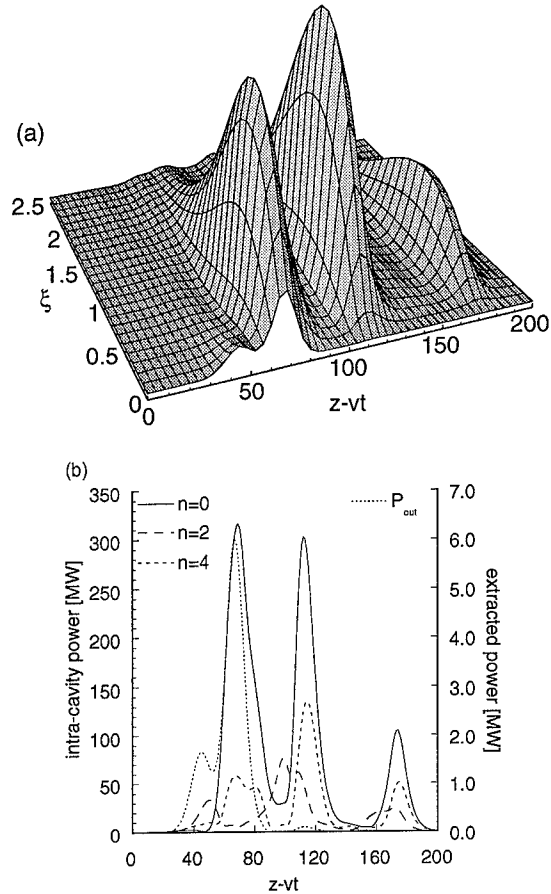


Fig. 2. Energy density and radial mode structure of the optical pulse near the end of the third cycle. All parameters are similar to Fig. 1.

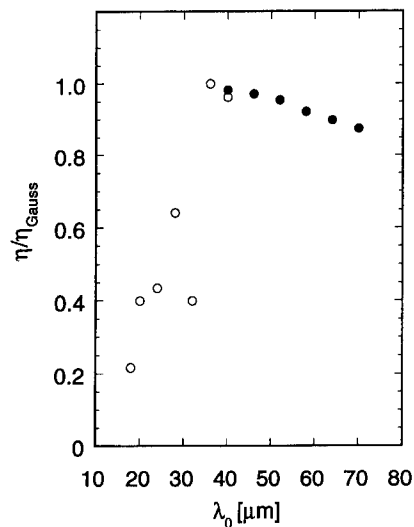


Fig. 3. The extraction ratio  $\eta$  relative to the corresponding value from a spatially one dimensional model as a function of wavelength. The open and solid dots correspond to different initial electron energies,  $\gamma_0 = 46.3$  and  $\gamma_0 = 34.5$ , respectively.

For  $\lambda_0 \leq 32 \mu\text{m}$ , the extraction ratio is significantly lower than that of Gaussian mode. This is due to the fact that a large fraction of the energy density is located off-axis. For these small wavelengths,  $\eta$  depends strongly on the radial mode structure of the light. The irregularity in this range is related to the radial profile which is due to the combined effect of the undulator strength, slippage, desynchronization and scattering at the mirrors, which all depend on the wavelength. These effects can result in small changes in the relative phases of the radial mode structure inside the cavity and can lead to significant changes in the outcoupled power. For larger wavelengths, edge losses become important for higher order GL modes. In this range, the reduction of the on-axis field intensity diminishes and the mode structure consists mainly of the Gaussian mode. Higher-order GL modes are still residually present since they are generated by the electrons each pass.

#### 4. Conclusions

In this paper, we have analyzed the spatial structure of the optical pulse inside the cavity of a hole-coupled resonator FEL and the fraction of power lost through the aperture. The radial profile of the intra-cavity light is determined by gain, power loss through the aperture and by scattering at the mirrors. The additional effect of slippage couples the radial and longitudinal structure of the light pulse.

In the linear regime of FEL operation, the optical pulse is confined to the electron pulse. The radial mode structure consists mainly of the Gaussian radial mode ( $n = 0$ ). After saturation has been reached, the light pulse overtakes the electrons and eventually does not interact with the electrons by more. In this cold cavity region, a substantial fraction of the radiation intensity of the Gaussian mode is transferred to the higher-order GL modes  $n = 2$  and  $n = 4$ . For the cavity geometry investigated here, the contribution of odd modes is small. The mode composition yields a radial profile in which the on-axis field strength can be significantly reduced. This leads to a decrease of the extraction ratio by one order of magnitude, as compared to

a Gaussian radial mode. This reduction can only occur for small values of the wavelength, such that edge losses are small. For larger wavelengths, the higher-order GL modes lose most of their energy at the mirror edge since the radial extension of the modes increases with the number. Eventually, only the Gaussian profile remains.

#### Acknowledgements

This work was performed as part of research programme of the “Stichting voor Fundamenteel Onderzoek der Materie” (FOM) with financial support from the “Nederlandse Organisatie voor Wetenschappelijk Onderzoek” (NWO). One of the authors (B.F) is supported by the “European Infrared FEL Network” (contract number CHRX-CT93-0109).

#### References

- [1] R.J. Bakker, C.A.J. van der Geer, D.A. Jaroszynski, A.F.M. van der Meer, D. Oepts and P.W. van Amersfoort, *J. Appl. Phys.* 74 (1993) 1501.
- [2] B. Faatz, R.W.B. Best, D. Oepts and P.W. van Amersfoort, *IEEE J. Quantum Electron.* QE-29 (7) (1993) 2229.
- [3] M. Xie and K.-J. Kim, *SPIE* 1868 (1993) 150.
- [4] R.H. Pantell, J. Feinstein and A.H. Ho, *Nucl. Instr. and Meth. A* 296 (1990) 638.
- [5] G.A. Barnett, S.V. Benson and J.M.J. Madey, *IEEE J. Quantum Electron.* QE-29 (2) (1993) 479.
- [6] G.H.C. van Werkhoven, B. Faatz and T.J. Schep, *Phys. Rev. E* 50 (1994) 4063.
- [7] P. Jha and J.S. Wurtele, *Nucl. Instr. and Meth. A* 331 (1993) 477.
- [8] A.E. Siegman, *Lasers* (University Science Books, Mill Valley, California, 1986).
- [9] G.H.C. van Werkhoven, B. Faatz and T.J. Schep, *Nucl. Instr. and Meth. A* 331 (1993) 411.
- [10] S. Riyopoulos, P. Sprangle, C.M. Tang and A. Ting, *Nucl. Instr. and Meth. A* 272 (1988) 543.
- [11] D.A. Jaroszynski, R.J. Bakker, A.F.G. van der Meer, D. Oepts and P.W. van Amersfoort, *Phys. Rev. Lett.* 70 (1993) 3412.



ELSEVIER

## Influence of the radial mode structure on the losses in the FELIX hole-coupled resonators

G.M.H. Knippels<sup>\*</sup>, G.H.C. van Werkhoven, E.H. Haselhoff, B. Faatz, D. Oepts,  
P.W. van Amersfoort

*FOM-Institute for Plasma Physics "Rijnhuizen", P.O. Box 1207, 3430 BE Nieuwegein, The Netherlands*

### Abstract

FELIX uses a hole in one of the optical cavity mirrors as a convenient, broadband method of outcoupling. In this contribution we present a preliminary study of the mode structure in the FELIX optical resonators, and compare the results with a computer analysis.

FELIX operates with two separate optical cavities (with identical undulators), to cover the wavelength ranges of 20–110  $\mu\text{m}$  (FEL-1) and 5–30  $\mu\text{m}$  (FEL-2). Both resonators consist of gold-coated copper mirrors, with a hole in the upstream mirror. The relevant parameters for both resonators are listed in Table 1. To obtain insight in the optical mode structure during FEL interaction, we performed a simple experiment by measuring the power coupled out of the hole after the electron beam switches off, with FELIX operating at various wavelengths (the wavelength was scanned by variation of the undulator gap). The decaying optical signal was detected by means of a YBaCuO detector [1], with a rise time of approximately 200 ns. We observed how the ringdown of the optical cavity varied with the FELIX wavelength. To represent the measurements, we converted the  $1/e$  decay time to the loss factor  $\alpha$  of a simple exponential decay  $\alpha \exp(-\alpha t/\tau)$  where  $\tau$  is the cavity round-trip time. For FEL-1, this loss factor has been plotted as a function of the wavelength in Fig. 1a (solid dots). The open dots in Fig. 1a show the loss factor, calculated from the ringdown of a simple TEM<sub>00</sub> mode with 2% absorption losses on the surface of the resonator mirrors. It is seen that the results differ significantly from the measurements. For wavelengths larger than 33  $\mu\text{m}$ , the discrepancy could be eliminated by assuming two times higher absorption losses at the mirrors, however, for shorter wavelengths the discrepancy increases to as much as 15%, which may be related to the existence of higher-order modes. To estimate the effect of higher-order modes, we used an axisymmetric

FEL code [2], which includes both diffraction and slippage. The latter is essential because the slippage distance in FELIX may be as large as ten times the length of the electron pulses. Note that, although we only analyze the radiation field after the electron beam is switched off (i.e. after the FEL interaction), slippage still plays an important role in the build-up of the actual mode structure [3]. The triangles in Fig. 1a show the result of the computer calculation. For wavelengths shorter than 33  $\mu\text{m}$ , it is seen that the measured losses are smaller, which is presumably caused by the fact that the detector was not fast enough to accurately measure decay times at losses exceeding 15%. For wavelengths larger than 33  $\mu\text{m}$ , it is seen from Fig. 1a that the measurements agree well with the computer analysis. In order to explain the anomalously high losses computed for short wavelengths, we used our computer code to investigate the time evolution of the radial energy distribution in the optical cavity. Fig. 2a shows the computed intensity of a micropulse as a function of the longitudinal coordinate  $Z$  and the normalized radial distance  $\xi(\xi \propto r^2)$ , at the moment that the FEL interaction stops. The FEL wavelength is 22  $\mu\text{m}$ , where edge losses are low. The

Table 1  
FELIX resonator parameters

|  | FEL-1  | FEL-2  |
|--|--------|--------|
| Wavelength range ( $\mu\text{m}$ )     | 20–110 | 5–30   |
| Length (m)                             | 6.0    | 6.15   |
| Hole diameter (mm)                     | 3.0    | 2.0    |
| Upstream mirror curvature (m)          | 4.0    | 4.0    |
| Downstream mirror curvature (m)        | 3.0    | 2.783  |
| Mirror diameter (cm)                   | 5.0    | 5.0    |
| Reflectivity at 10.6 $\mu\text{m}$ (%) | > 98.5 | > 98.5 |
| Vacuum tube diameter (mm)              | 27     | 16.7   |

<sup>\*</sup> Corresponding author. Tel. +31 3402 31 224, fax +31 3402 31204, e-mail: knippels@zeus.rijnh.nl.

stored energy is located mainly near the axis of the resonator, with a peak positioned slightly off-axis. Fig. 2b show the situation after an additional 20 roundtrips. Apparently, the on-axis hole has strongly reduced the on-axis intensity, which causes a significant reduction of the out-coupled fraction of intracavity radiation. The “real” cavity losses however do not have to be as high as the through-the-hole measurement of the ringdown would suggest. In fact, there is still a considerable amount of energy inside the cavity, but since the optical energy seems to “avoid” the hole, the power flux through the hole decays rapidly. Such a phenomenon of course affects the measurement of the  $1/e$  power-decay time, as performed during the experiment. This may explain the high discrepancy between the measured cavity losses and the losses for a simple  $TEM_{00}$  mode, which occurs for short wavelengths as seen in Fig. 1a. Also important is the fact that the mode structure may no longer be axisymmetric due to the non-symmetric undulator and electron beam. Such a mode structure has recently been observed in the Mark III FEL. Of course this influences our measurement of the decay time too. At the moment it is impossible to take this effect into account. For wavelengths larger than  $33 \mu\text{m}$ , computer simulations indicate that edge losses at the mirror become large, and prevent the growth of the higher-order

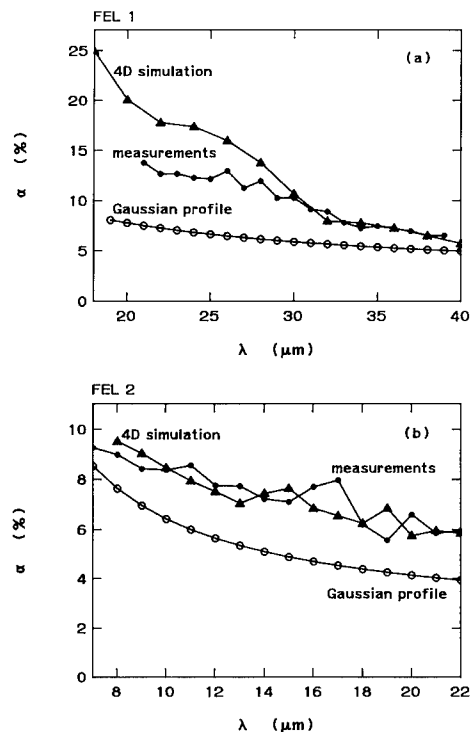


Fig. 1. Cavity losses vs. wavelength, determined from the ringdown of the FELIX resonators FEL-1 (a) and FEL-2 (b). Closed dots: measurements; open dots: analytical result, assuming a  $TEM_{00}$  mode only; triangles: computer simulation.

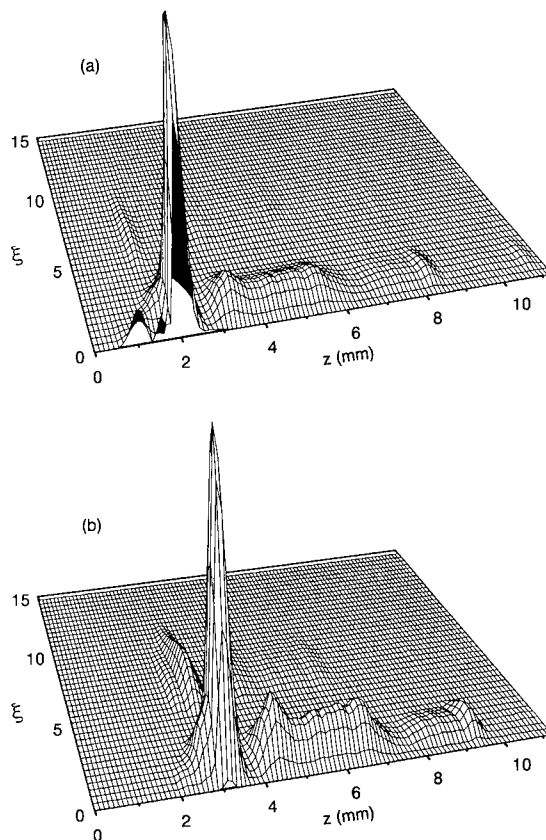


Fig. 2. Computer simulation of the optical micropulse power (just before reflection at the mirror with the hole) vs. radial position ( $\xi \propto r^2$ ) and longitudinal distance ( $z$ ), just before the FEL interaction stops (a), and after 20 additional round trips (b). Radiation wavelength:  $22 \mu\text{m}$ . The radius of the on-axis hole corresponds to  $\xi = 0.0134$ .

modes during FEL interaction. The 2% discrepancy in cavity losses as compared to the case of a single  $TEM_{00}$  mode may now be explained by the losses of higher-order modes. Fig. 1b shows the same analysis for FEL-2. A similar behaviour is seen as in the long wavelength range of FEL-1, i.e. roughly 2% more cavity losses as would result from a  $TEM_{00}$  mode only, presumably caused by higher-order modes. The increasing discrepancy for shorter wavelengths, as seen in Fig. 1a is however not observed. Computer simulations indicate that this is due to the vacuum tube inside the optical resonator which is only 16.7 mm wide, and suppresses the build-up of higher-order modes for wavelengths above  $10 \mu\text{m}$ .

We conclude that in FEL-2 and in FEL-1 for wavelengths above  $33 \mu\text{m}$ , higher order modes cannot grow because of losses at the mirror edges and the vacuum tube (FEL-2). This means that the higher order modes just represent an additional loss factor every roundtrip but do

not significantly change the mode structure in the cavity. However, in FEL-1, for wavelengths below 33  $\mu\text{m}$ , the edge losses at the mirrors are low and the higher order modes grow and change the mode structure in such a way that the power avoids the hole. This is measured as an apparent decrease of the decay time of the out coupled power.

### **Acknowledgements**

This work has been performed as part of the research of Stichting voor Fundamenteel Onderzoek der Materie

(FOM) with financial support from the Nederlandse Organisatie voor Wetenschappelijk Onderzoek (NWO).

### **References**

- [1] We kindly thank Josef Betz from Fortech HTS Austria, who made this detector available.
- [2] G.H.C. van Werkhoven, presented at this Conference (16th Int. Free Electron Laser Conf., Stanford, CA, USA, 1994).
- [3] G.H.C. van Werkhoven, B. Faatz and T.J. Schep, The effect of slippage and scattering on the spatial structure of light pulses in a hole-coupled FEL, Phys. Rev. E, to be published.



# Hole coupling experiments on the Mark III FEL <sup>☆</sup>

G.A. Barnett <sup>a,\*</sup>, S.V. Benson <sup>b</sup>, J.M.J. Madey <sup>a</sup>, E.B. Szarmes <sup>a</sup>

<sup>a</sup> Free Electron Laser Laboratory, Department of Physics, Duke University, Durham, NC, USA

<sup>b</sup> CEBAF, 12000 Jefferson Avenue, Newport News, VA, USA

## Abstract

Hole coupling experiments were performed on the Mark III FEL at Duke University with an experimental configuration allowing access to both the hole coupled and intracavity optical beams. These experiments were performed with two different electron beam configurations. In the first configuration, maximizing optical power through the hole maximized the percent outcoupling. The intracavity optical eigenmode was comprised mainly of the TEM<sub>00</sub> Gauss–Laguerre mode. In the second electron beam configuration, the maximum outcoupled power did not correspond to the maximum percent outcoupling. The intracavity mode was not azimuthally symmetric, nevertheless it enhanced the electronic gain and intracavity power. The maximum percent outcoupling was obtained with an azimuthally symmetric optical eigenmode with power concentrated in the TEM<sub>10</sub> Gauss–Laguerre mode. Experimental outcoupling efficiencies of up to 65.5% were obtained; this is more than three times the 20.0% outcoupling efficiency routinely measured in the Brewster coupled resonator. This paper presents experimental measurements of the outcoupled and total losses, the electronic gain and the mode structure of the hole coupled Mark III FEL at a variety of wavelengths and hole sizes.

## 1. Introduction

Hole coupling experiments provide insight into the relationship between the free electron laser (FEL) gain, the optical resonator and the intracavity mode structure. Computer simulations [1] have determined that the mode selectivity of the gain medium is more critical than the resonator parameters in the determination of the intracavity mode structure. This paper presents the first experimental results that allow us to fully examine the transverse mode structure and gain of a hole coupled FEL.

We have carried out hole coupling experiments on the Mark III FEL at Duke University [2] using the experimental configuration described in detail in Ref. [3]. The experimental configuration is unique because it allows access to both the hole coupled and intracavity beam. Previous hole coupling experiments have not provided access to the intracavity beam [4,5].

The Mark III hole coupling experiments were performed with two different electron beam configurations. The second configuration was obtained by changing the electron beam orbit and bunching characteristics in the microwave gun. The second electron beam was character-

ized by a peak current much larger than the peak current in the first configuration and an emittance comparable to the emittance in the first configuration.

## 2. Configuration one

The experimental results in this section were obtained with a single electron gun configuration. These results are for 0.02 cm radius coupling hole in the upstream cavity mirror. Since the Mark III cavity is not phase degenerate, the optical eigenmode has power predominantly in one free space mode [1]. The dominant mode was experimentally determined from the transverse optical mode profile on a two dimensional pyroelectric array. Higher order mode content can be determined through the presence of beating during the decay of the hole coupled macropulse. For all of the data taken with this electron beam configuration the intracavity mode was the TEM<sub>00</sub> Gauss–Laguerre mode (Fig. 1).

The output coupling, total losses, electronic gain and intracavity energy were measured at wavelengths of 3.024  $\mu\text{m}$  and 3.614  $\mu\text{m}$ . These results are summarized in Table 1. The outcoupling, intracavity energy and electronic gain were changing throughout the data taking sessions. These changes are shown in the table. Two sets of data were taken at a wavelength of 3.024  $\mu\text{m}$ . The intracavity energy in the second data set was larger than in the first data set by a factor of 1.23, but the average percent outcoupled was

<sup>☆</sup> This research is supported in part by Office of Naval Research contract number N00014-91-C-0226.

\* Corresponding author. Tel. +1 919 660 2650, fax +1 919 660 2671.

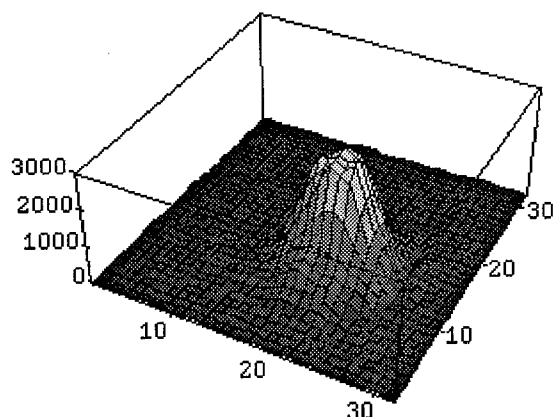


Fig. 1. The intracavity mode structure of the first electron beam configuration. The  $z$  axis is intensity in arbitrary units and  $x$  and  $y$  are the transverse dimensions in  $1/32$  in. The data is from a two dimensional pyroelectric array.

smaller by a factor of 0.86. From the data in the table, it is apparent that as the intracavity power and gain increase, the outcoupling decreases.

The total losses for the second data set at the  $3.024 \mu\text{m}$  wavelength were 16.5%, which are higher than the total losses for the first data set. The mirror was examined between these two data sets, and there was no visible damage on the mirror. Therefore, the increased losses are not attributed to damage.

By replacing the end mirror with the outcoupling hole with a solid mirror, the absorption losses and the losses due to the barium fluoride window that allows access to the intracavity mode were experimentally determined. These losses were 5.3%. Since there are four mirror bounces in the resonator, this gives approximately 1.2% absorption loss per bounce.

### 3. Configuration two

The data of this section were taken with the second electron beam configuration. This configuration drastically

Table 1  
Summary of experimental results for the first electron beam configuration and 0.02 cm radius hole

| Wave-length ( $\mu\text{m}$ ) | Electron energy (MeV) | Outcoupling (%)        | Total losses (%) | Change in intracavity energy (%) |
|-------------------------------|-----------------------|------------------------|------------------|----------------------------------|
| 3.024                         | 44                    | 3.11–2.54 <sup>a</sup> | 14.5             | 10.7 <sup>b</sup>                |
| 3.024                         | 44                    | 2.41–2.68 <sup>b</sup> | 16.5             | 5.0 <sup>a,c</sup>               |
| 3.614                         | 40                    | 2.06–1.70 <sup>a</sup> | 13.2             | 8.6 <sup>b</sup>                 |

<sup>a</sup> Continuously decreasing throughout data taking session.

<sup>b</sup> Continuously increasing throughout data taking session.

<sup>c</sup> The electronic gain was measured to be 68% at the beginning of the run and 55% at the end.

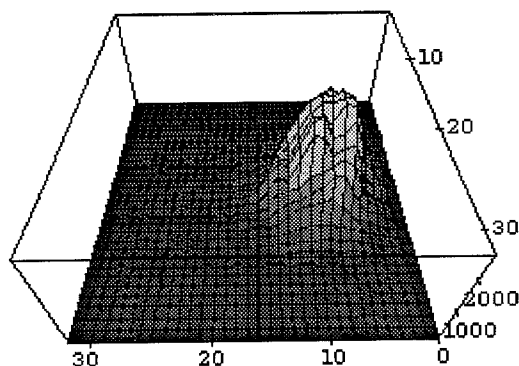


Fig. 2. The intracavity mode structure giving maximum power through the hole in the second electron beam configuration.

changed the optical eigenmode of the laser. In the new electron beam configuration, contrary to the predictions of computer simulations [1], the intracavity eigenmode was not predominantly the  $\text{TEM}_{00}$  Gauss–Laguerre free space mode. The percent outcoupling was first measured with a 0.02 cm hole in the upstream mirror and an optical wavelength of  $2.949 \mu\text{m}$ . With the second electron beam configuration, maximizing the power through the hole by slightly steering the electron beam gave an intracavity mode that was not azimuthally symmetric (Fig. 2). The electronic gain of this mode was 102%, which is larger than the electronic gain of 88.2% measured using Brewster outcoupling with this electron beam configuration at this wavelength. With Brewster coupling the intracavity mode is the  $\text{TEM}_{00}$  Gauss–Laguerre mode; perhaps, as suggested by Pantell et al. [6], the presence of higher order free space modes in the hole coupled cavity allows the optical mode to collapse around the electron beam and enhance the gain.

As the hole coupled signal decayed, it exhibited beating with a frequency of  $19.7 \pm 2$  MHz and an amplitude that was 5% of the signal height. This frequency indicates a mixture of Gauss–Laguerre free space modes whose axial and radial mode numbers each differ by unity, which is reasonable, since the optical eigenmode in Fig. 2 is not azimuthally symmetric. Such free space modes would have a beat frequency in the Mark III resonator of 21.4 MHz. The profile from the two dimensional array suggests a mixture of the  $\text{TEM}_{10}$  and  $\text{TEM}_{11}$  Gauss–Laguerre modes. It is, however, not possible to determine the power in each free space mode since the relative position of the hole and the intracavity mode is not, in this case, known.

The hole coupled macropulse, even with the unusual intracavity mode of Fig. 2, was a lean Airy pattern. The fact that the hole coupled mode always looks the same is a benefit of the hole coupled FEL. This fact, however, emphasizes the need for access to the intracavity beam for a transverse mode analysis.

Slightly resteeing the downstream mirror and the electron beam yielded an azimuthally symmetric optical mode

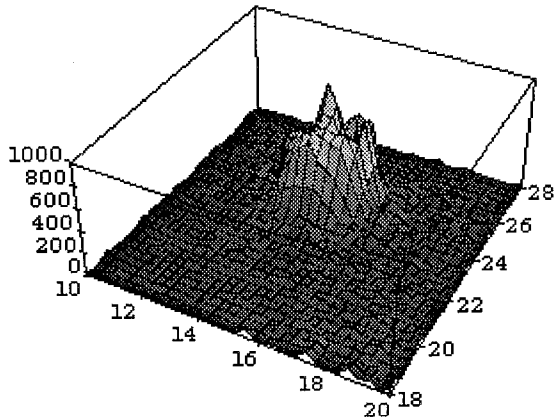


Fig. 3. The azimuthally symmetric mode giving maximum outcoupled percent in the second electron beam configuration.

(Fig. 3). This azimuthally symmetric mode was very difficult to achieve; the laser was very unstable and the intracavity power was much lower than with the non-azimuthally symmetric mode of the section above. Furthermore, the electronic gain was only 60.9%. Since no phase information was contained in the pyrometer profile of the intracavity mode, the expansion of the intracavity eigenmode into the free space Gauss–Laguerre modes cannot be determined. It is possible to determine that such a mode pattern cannot have a large  $TEM_{00}$  contribution. Consequently, such a mode is dominated by some higher order mode; indeed, the profile of the intracavity mode in Fig. 3 suggests the  $TEM_{10}$  Gauss–Laguerre mode.

The decay of the hole coupled macropulse did not exhibit beating. This indicates that there was no power in other azimuthally symmetric modes, which are maximum on axis. However, since the higher azimuthally asymmetric Gauss–Laguerre free space modes are zero on axis, they do not contribute to beating on the hole coupled signal and may have been present. The outcoupled percent is much

larger with the symmetric mode (4.1%) than with the mode that maximizes the power. The losses rose steadily over the course of the run, from 19.6% to 23.0%. At the end of the run the mirror catastrophically damaged and had to be replaced.

Data was also taken at optical wavelengths of 3.551 and 4.381  $\mu\text{m}$ . At a wavelength of 3.551 maximizing the signal through the hole gave a mode similar to Fig. 2. Unlike the results at the previous wavelength of 2.949  $\mu\text{m}$ , the non-azimuthally symmetric mode and the azimuthally symmetric mode had similar electronic gains. At a wavelength of 4.381  $\mu\text{m}$ , the intracavity mode was the  $TEM_{00}$  Gauss–Laguerre mode as seen in the first electron beam configuration. The data from the second electron configuration and a 0.02 cm radius hole is summarized in the first part of Table 2.

The hole size was changed to 0.04 cm radius. It was impossible to obtain an azimuthally symmetric mode at the wavelengths investigated that were shorter than 3.5  $\mu\text{m}$ . The non-symmetric mode is similar to the non-symmetric mode with the 0.02 cm hole. Data was taken for the azimuthally symmetric mode at wavelengths of 3.529 and 4.405  $\mu\text{m}$ . As with the smaller hole size, most power through the hole was achieved with a non-symmetric mode similar to the mode in Fig. 2. At each wavelength, the azimuthally symmetric mode was obtained by slightly steering the downstream mirror and re-optimizing the electron beam. The intracavity mode was similar to the mode with this electron configuration and a 0.02 cm hole (Fig. 3). The results for a 0.04 cm hole are summarized in the second part of Table 2.

The outcoupled percents obtained in the experiments are lower limits for the comparison to theory. This is because we must assume the alignment of the system is not perfect, in which case perfecting the alignment would increase the percent outcoupling. The hole coupled macropulse looked the same as in all of the previous hole sizes and configurations.

Note that with the non-azimuthally symmetric mode at 2.9  $\mu\text{m}$  the electronic gain is comparable to the 88.2% achieved at 2.9  $\mu\text{m}$  with Brewster coupling. At 2.9  $\mu\text{m}$  and a 0.04 cm radius hole, even though the intracavity mode is not symmetric, the hole coupled mode has a nice profile, the outcoupling efficiency is 53.4% and the electronic gain is 87.0%. For the azimuthally symmetric modes, the 62.3% o.c.e. at the 3.529  $\mu\text{m}$  wavelength and the 65.5% o.c.e. at the 4.405  $\mu\text{m}$  wavelength are more than three times the 20% o.c.e. routinely measured in the Brewster coupled resonator and 150% greater than any o.c.e. previously achieved on the Mark III laser.

#### 4. An investigation of the appearance of the $TEM_{10}$ mode

The wiggler gap was opened to reduce the peak gain to see if the  $TEM_{10}$  mode observed in the second configura-

Table 2  
Summary of experimental results for the second electron beam configuration

| Wave-length ( $\mu\text{m}$ ) | Electron energy (MeV) | Out-coupling (%) | Total losses (%) | Electronic gain (%) | Intra-cavity mode |
|-------------------------------|-----------------------|------------------|------------------|---------------------|-------------------|
| 0.02 cm hole                  |                       |                  |                  |                     |                   |
| 2.949                         | 44                    | 3.1              | 15.3             | 102                 | Fig. 2            |
| 2.949                         | 44                    | 4.1              | 19.6             | 60.9                | Fig. 3            |
| 3.551                         | 40                    |                  | 15.0             | 51.0                | Fig. 2            |
| 3.551                         | 40                    | 2.7              | 15.3             | 46.0                | Fig. 3            |
| 4.381                         | 36                    | 2.0              | 13.2             |                     | Fig. 1            |
| 0.04 cm hole                  |                       |                  |                  |                     |                   |
| 2.423                         | 44                    |                  |                  |                     | Fig. 2            |
| 2.919                         | 44                    | 15.5             | 29.0             | 87.0                | Fig. 2            |
| 3.529                         | 40                    | 15.2             | 24.4             | 50.1                | Fig. 2            |
| 3.529                         | 50                    | 15.2             | 24.4             | 56.1                | Fig. 3            |
| 4.405                         | 36                    | 15.4             | 23.6             | 66.7                | Fig. 3            |

tion was due to high gain and guiding. The small signal gain is proportional to the undulator parameter squared,  $K^2$ , times the peak current. Since the peak current in the second configuration was greater than in the first configuration, the gap was opened to reduce the gain by reducing  $K^2$ . The resulting optical wavelength was 3.024  $\mu\text{m}$  and the electronic gain was 47.9%. The optical mode, however, looked the same as the mode in Fig. 3, and so still had most power in the  $\text{TEM}_{10}$  Gauss–Laguerre mode rather than the  $\text{TEM}_{00}$  mode.

The  $\text{TEM}_{10}$  mode appeared one time in the first configuration at a wavelength of 3.0  $\mu\text{m}$  with the smaller radius hole when the mirror damaged at the hole edge. This suggests that the  $\text{TEM}_{10}$  mode appears when the hole is a larger portion of the optical spot size. In the second configuration, the optical mode may be smaller at the hole. In this case, the hole is relatively larger giving the  $\text{TEM}_{10}$  mode. This hypothesis is supported by the fact that the  $\text{TEM}_{00}$  mode is seen in the second configuration at the longest wavelength; as the wavelength is increased, the spot size increases and the hole is a smaller fraction of the optical mode.

## 5. Conclusion

The experiments produced surprising results. Contrary to the predictions of computer simulations, the optical mode structure was strongly dependent upon the presence

of the coupling hole. A non-azimuthally symmetric optical mode structure was discovered that enhanced the electronic gain and maximized the intracavity power; but in this electron beam configuration, an azimuthally symmetric higher order mode maximized the percentage outcoupling. The fact that the transverse intensity profile of the hole coupled signal does not depend on the intracavity mode structure is both a benefit of hole coupling (with other outcoupling methods the outcoupled beam has the transverse profile of the intracavity beam) and a reminder that for a transverse mode analysis, access to the intracavity mode is essential.

## References

- [1] G.A. Barnett, S.V. Benson and J.M.J. Madey, IEEE J. Quantum Electron. QE-29 (1993) 479.
- [2] S.V. Benson, W.S. Fann, B.A. Hooper, J.M.J. Madey and E.B. Szarmes, Nucl. Instr. and Meth. A 296 (1990) 110.
- [3] G.A. Barnett, S.V. Benson and J.M.J. Madey, SPIE Conf. Laser Resonators and Coherent Optics: Modeling, Technology and Applications, Los Angeles, 1993.
- [4] B. Faatz, Ph.D. dissertation, de Vrije Universiteit te Amsterdam (1992).
- [5] B.E. Newnam et al., IEEE J. Quantum Electron. QE-21 (1985) 871.
- [6] R.H. Pantell, J. Feinstein and A.H. Ho, Nucl. Instr. and Meth. A 296 (1990) 638.
- [7] G.A. Barnett, Ph.D. dissertation, Duke University (1994).



ELSEVIER

# Maximization of FEL gain for a hole-coupled resonator

Y.C. Huang<sup>\*</sup>, R.H. Pantell, J.F. Schmerge, J. Feinstein

Department of Electrical Engineering, Stanford University, McCullough 308, Stanford, CA 94305-4055, USA

## Abstract

For a hole-coupled resonant cavity without FEL gain, it is possible to have amplitude cancellation of the optical Gaussian modes at the hole location and, as a result, a null is generated to give very low cavity loss due to the presence of the hole. However, in a warm cavity, i.e. when the electron beam is present and the optical power starts to build up, the FEL gain tends to amplify the modes unequally, and the unbalanced gain for different optical modes results in significant power radiated through the hole. In this paper we present a guideline, based upon variation of the Rayleigh length, for mode selection that maximizes net gain.

## 1. Introduction

The hole-coupled resonator has been studied at several FEL research sites, such as FELIX [1,2], Duke [3], LBL [4–6], Los Alamos [7]. Most conventional lasers operate at narrow band, fixed spectral lines, wherein partially transparent mirrors are sufficient. A hole-coupled cavity has the advantages of reducing the problems of mirror damage from intense FEL radiation, allowing direct entry of the electron beam into the cavity, and providing broad bandwidth coupling for the radiation. The cavity loss due to an on-axis hole can be kept low by having an appropriate mode combination, as was first pointed out in Ref. [8]. Later, it was simulated in Ref. [6] that the hole-coupled scheme can be used to extract radiation from the cavity over a wide frequency range.

Two important concerns are the net gain of the FEL during signal buildup, and the coupling efficiency (see Eq. (3)) of the device at saturation. In this paper, a design procedure is presented for maximizing gain while maintaining high efficiency.

## 2. System and methodology

The system to be considered is the hole-coupled resonator for the Stanford compact far-infrared free-electron laser [9]. Fig. 1 depicts the cavity configuration, in which the optical fields are confined by a 2-mm waveguide in  $y$  and focused by a pair of cylindrical mirrors in  $x$ . There is

a 2 mm  $\times$  2 mm aperture on the up-stream mirror. The mirror diameters (in  $x$ ),  $d_{M1}$  and  $d_{M2}$ , are 3.3 cm, and are the same as the waveguide dimension in  $x$ . The distance between the hole and the optical waist,  $L_r$ , is  $\approx 50$  cm, and the waist is located at the center of a 1 m wiggler. The distance between the optical waist and the down-stream mirror,  $L_l$ , is also about half a meter. By changing  $z_r$ , the Rayleigh length, one can select the optical modes inside the resonator, as will be demonstrated in the following paragraph.

For the cavity configuration in Fig. 1, the optical field is sinusoidal in  $y$  and Hermite–Gaussian in  $x$  [10]. The approach that is used to finding a stable cavity mode is to require that the electrical field reproduces itself to within a constant factor in propagating a round trip in the resonator. Let  $E_{M1}^{+(1)}$  be the starting optical field moving toward the

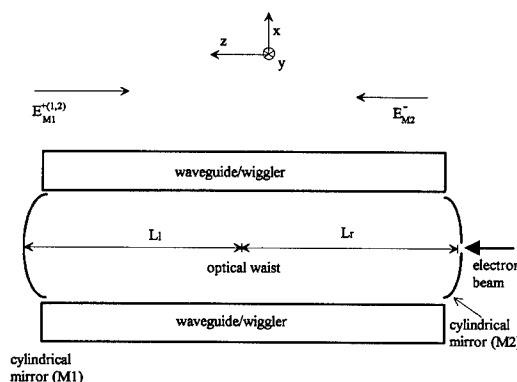


Fig. 1. The hole-coupled resonator. Electrons enter through a 2 mm  $\times$  2 mm hole on the right and pass through a 1 m long wiggler which has a uniform region of 50 cm at the center. The wiggler forms a 2 mm gap waveguide in  $y$ , and has been rotated by 90° about  $z$  for clarity.

<sup>\*</sup> Corresponding author. Tel. +1 415 723 3190, fax +1 415 723 4659, e-mail: huang@loki.stanford.edu.

up-stream mirror M2,  $E_{M2}^-$  be the one reflected from M2, and  $E_{M1}^{+(2)}$  represent the resulting field after completing a round-trip propagation. These fields can be written as linear combinations of Hermite-Gaussian modes

$$E_{M1}^{+(1)}(x, z) = \sum_n a_n^{+(1)} u_n(x, z),$$

$$E_{M2}^-(x, z) = \sum_m a_m^- u_m^-(x, z - 2L_r),$$

and

$$E_{M1}^{+(2)}(x, z) = \sum_n a_n^{+(2)} u_n(x, z - 2L_r - 2L_l),$$

where

$$u_n(x, z) = \left(\frac{2}{\pi}\right)^{1/4} \sqrt{\frac{\exp(-j(2n+1)\tan^{-1}(z/z_r))}{2^n n! w(z)}} \times H_n\left(\frac{\sqrt{2}x}{w(z)}\right) \times \exp\left[-j\frac{k_z x^2}{2R(z)} - \frac{x^2}{w^2(z)} - jk_z z\right] \quad (1)$$

is the  $n$ th Hermite-Gaussian mode. After a round-trip propagation, the coefficient vectors of a stable mode have the following relationship

$$[a_n^{+(2)}] = [S_{nm}^{(2)}][G][S_{mn}^{(1)}][a_n^{+(1)}] = \lambda_e [a_n^{+(1)}], \quad (2)$$

where the scattering matrices,  $S^{(1)}$  and  $S^{(2)}$ , are solved from the mirror boundaries, M1 and M2, respectively,  $[G]$  is the FEL gain and the eigenvalue,  $\lambda_e$ , assures that the optical field resembles itself after a round-trip propagation. The net gain is therefore equal to  $|\lambda_e|^2 - 1$ . The small signal gain for each mode (the diagonal term of  $[G]$ ) is calculated from Ref. [11] including all the inhomogeneous effects. The gain of the second order mode is about 30% of the fundamental mode, and that of the fourth order is less than 1% of the fundamental mode for our parameters. The coupling among modes is assumed to be small and all the off diagonal terms are zero in the gain matrix. For a low loss resonator at saturation,  $[G]$  can be approximated as an identity matrix multiplied by a scalar, which is the reciprocal of the eigenvalue of the cold cavity. Thus at saturation the cold cavity solution is used to determine the loss (for the cavity considered the loss is indeed low as seen in Fig. 5), which by definition is equal to the gain. The coupling efficiency, defined to be the ratio of the output coupling loss to the total loss at saturation, is

$$\int_{-1}^{1} \frac{mm}{mm} |E_{M1}^{+(1)}(x, z = L_r)|^2 dx / (1 - |\lambda_e|^2). \quad (3)$$

Considering a field that is symmetric in  $x$  about the resonator axis, the odd modes are dropped from Eq. (2).

### 3. Design procedures

The coupling efficiency has been a major concern in the aforementioned literature. However, achieving high coupling efficiency at saturation without having a reasonable gain to provide signal buildup is impractical. It was indicated in Refs. [3,4] that the FEL gain tends to focus optical fields on the axis during laser buildup. As a result, the cavity loss can exceed the FEL net gain in a hole-coupled cavity. We suggest a procedure to firstly maximize the net gain by mode selection, and secondly enhance the coupling efficiency.

There are two major sources of loss for a hole-coupled cavity: the diffraction loss due to mode clipping at the mirror edges, and the radiation loss from the hole. Since high order modes give large beam sizes and thus high diffraction loss, one avoids building high order modes in a resonator. In a cold cavity, in general, it is not difficult to generate a null at the hole such that the radiation loss from the hole is small. However, during signal buildup, the unequal gain among modes tends to destroy the amplitude cancellation at the hole and results in a high hole loss. It can be justified from the detuning phase that the farther a mode is from the fundamental mode, the smaller is its gain. Therefore, to reduce both losses, hole and diffraction, it is desirable to minimize the fraction of energy carried by the higher order modes. The optimum situation occurs when only the first two modes appear in the cavity, and they interfere destructively with each other at the hole.

It was pointed out in Refs. [1,2] that the predominant higher order modes appear to have a multiple of  $2\pi$  phase shift with respect to the fundamental mode. However, it is more fruitful to investigate the single-trip phase relationship among modes, since the field amplitude at the plane of the hole is determined by the amplitude and phase of the field in a single transit from the mirror without the hole to the mirror with the hole. From Eq. (1), the single-trip phase difference between a mode of order  $n$  and the fundamental mode is

$$n \left[ \tan^{-1}\left(\frac{L_l}{z_r}\right) + \tan^{-1}\left(\frac{L_r}{z_r}\right) \right]. \quad (4)$$

According to Eq. (4), a symmetric, confocal configuration is likely to have Gaussian modes of  $n=0$  and  $n=2$  interfering each other destructively at the hole, provided they satisfy Eq. (2) to be an eigenmode of the system. Indeed, at an exact confocal configuration, we obtained a null at the hole generated by modes of  $n=0$  and  $n=2$  for the cold cavity case, but very little radiation was coupled out. To enhance the coupling efficiency, we incrementally adjusted the cavity dimensions and the Rayleigh length for a warm cavity such that severe gain degradation did not occur while the coupling efficiency increased. For  $L_r = 51.3$  cm,  $L_l = 53.7$  cm, and  $z_r = 50$  cm, more than 96% of power is contained in the fundamental and second order modes at  $\lambda = 80$   $\mu$ m with 73% coupling efficiency.

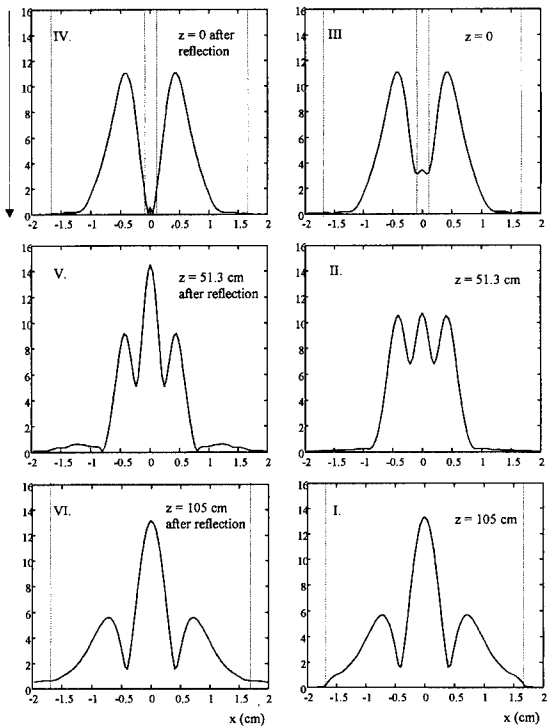


Fig. 2. Optical field evolution for the cold cavity at  $80 \mu\text{m}$ . The dashed lines designate mirror edges. The optical field starts at I and ends at IV. The nonzero power at the hole (III) is coupled out at power saturation.

Fig. 2 (I–VI) illustrate the field evolution of the cold cavity at  $\lambda = 80 \mu\text{m}$  for the near-confocal configuration. The first twenty-five Hermite–Gaussian modes were incorporated into Eq. (2) to derive the lowest loss eigenmode. The dashed lines are edges of the two mirrors. One can imagine that the optical envelope starts (Fig. 2 (I)) at the down-stream mirror, reaches the optical waist in Fig. 2 (II), strikes the upstream mirror in Fig. 2 (III), is reflected from the up-stream mirror in Fig. 2 (IV), and then arrives at the down-stream mirror in Fig. 2 (VI). The nonzero power at the hole of Fig. 2 (III) is coupled out at saturation. Fig. 3 (I–VI) are the field evolution for the warm cavity with the same parameters as in Fig. 2. One sees the growth of the optical power in Fig. 3 (V) and Fig. 3 (VI) due to the FEL gain (predominantly to the  $n = 0$  and  $n = 2$  modes). It is interesting to see that the near-confocal configuration is capable of generating a notch at the hole (Fig. 3 (III)) so as to minimize the cavity loss during laser buildup.

Fig. 4 is a plot of the small signal gain versus wavelength from  $80 \mu\text{m}$  to  $142 \mu\text{m}$ . Curve I in Fig. 4 is the FEL gain without the hole, curve II is the net gain with the hole, and curve III is the minimum gain to reach saturation. The minimum gain,  $G_m$ , is derived from  $(G_m + 1)^n = P_{\text{sat}}/P_0$ , where  $n$  is the number of round-trips determined

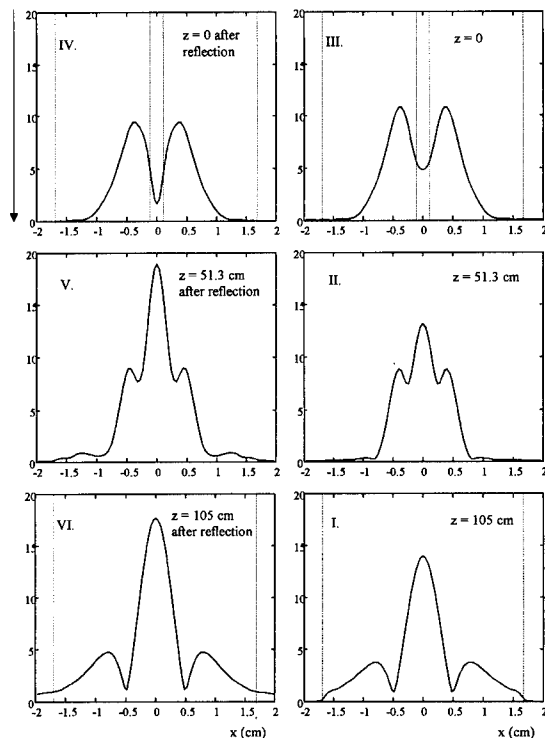


Fig. 3. Optical field evolution for the warm cavity at  $80 \mu\text{m}$ . It is seen that the field intensity at the center (V, VI) is enhanced due to the FEL gain, and a notch at the hole (III) is generated, however. The nonzero field in IV inside the hole is due to the finite number of modes (25) used for the calculation. Increasing the number of modes does make the field inside the hole closer to zero, but does not significantly change the eigenvalue.

from our macropulse duration,  $P_{\text{sat}}$  is the saturation power, and  $P_0$  is the spontaneous emission power. Both curves I and III were calculated by using the parameters in Table 1.

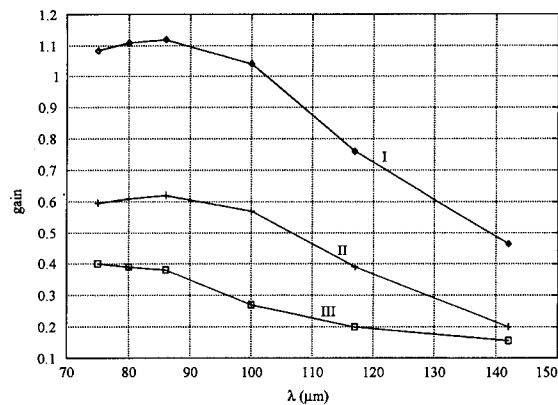


Fig. 4. (I) The FEL gain without the hole, (II) the net gain with the hole, and (III) the minimum gain to reach saturation. A 23% gain reduction results from the presence of the hole, but the net gain is still considerably higher than the minimum gain for saturation from  $\lambda = 80 \mu\text{m}$  to  $\lambda = 142 \mu\text{m}$ .

Table 1

Electron beam parameters, where  $\epsilon_{\text{n rms}}$  is the rms normalized emittance in  $\pi$  mm mrad,  $P_0$  is the noise power, and  $P_{\text{sat}}$  is the saturation power. The wiggler length is 0.5 m and the wiggler period is 1 cm

| $\gamma$ | $\left(\frac{\Delta\gamma}{\gamma}\right)_{\text{rms}}$ | $\epsilon_{\text{n rms}}$ | $I_{\text{peak}}$ [A]<br>( $\mu\text{-pulse}$ [ps]) | $\lambda$ [ $\mu\text{m}$ ] | $P_0$ [mW] | $P_{\text{sat}}$ [kW] | macropulse<br>[ $\mu\text{s}$ ] |
|----------|---|---------------------------|---|-----------------------------|------------|-----------------------|---------------------------------|
| 10.17    | 0.22%   | 5.21                      | 7.6 (14.9)  | 75.3                        | 0.78       | 416                   | 0.4                             |
| 9.85     | 0.22%   | 5.07                      | 8.3 (13.6)  | 80.46                       | 1.1        | 416                   | 0.4                             |
| 9.53     | 0.25%   | 4.98                      | 8.6 (12.2)  | 86.18                       | 2.0        | 418                   | 0.4                             |
| 8.89     | 0.26%   | 4.66                      | 9.4 (8.7)   | 100.0                       | 6.1        | 428                   | 0.5                             |
| 8.22     | 0.25%   | 4.21                      | 10.4 (5.5)  | 117.5                       | 26         | 437                   | 0.6                             |
| 7.53     | 0.27%   | 2.91                      | 9.9 (3.5)   | 141.6                       | 93         | 381                   | 0.7                             |

The presence of the  $2\text{ mm} \times 2\text{ mm}$  hole results in a 23% gain reduction, but the net gain (curve II) is still considerably higher than the minimum gain to reach saturation (curve III).

As a comparison, the lowest loss eigenmode in a resonator ( $L_r = 50\text{ cm}$ ,  $L_1 = 95\text{ cm}$ , and  $z_r = 27.4\text{ cm}$ ) dominated by the Gaussian modes of  $n = 0$ ,  $n = 4$ , and  $n = 8$  was calculated by Eq. (2), and it gave a gain reduction of 38% at  $\lambda = 80\text{ }\mu\text{m}$ . Although the electronic gain is higher for this case, the high diffraction and hole loss result in lower net gain than the near-confocal resonator. When many modes exist in a resonator, the performance of this resonator is more sensitive to the wavelength change. We have 5% cold cavity loss at  $\lambda = 80\text{ }\mu\text{m}$ , and 42% at  $\lambda = 142\text{ }\mu\text{m}$  for this resonator. However, we obtain a fairly smooth tuning range for the near-confocal resonator, as Fig. 5 will show.

Fig. 5 illustrates the total cavity loss (diffraction loss and coupling loss) and coupling efficiency for the near-confocal resonator at power saturation. It shows a coupling

efficiency of 55–75% from  $\lambda = 142\text{ }\mu\text{m}$  to  $\lambda = 80\text{ }\mu\text{m}$  at a total cavity loss of 3–5%.

#### 4. Conclusion

We have pointed that the high loss in a hole-coupled cavity during laser buildup is due to the unequal gain between the fundamental mode and modes far from the fundamental mode. A simple phase rule was proposed to choose modes close to the fundamental mode so as to interfere with the fundamental mode destructively at the hole. By incrementally adjusting cavity parameters for a warm cavity, the coupling efficiency can be enhanced while FEL net gain remains high.

#### References

- [1] B. Faatz, R.W.B. Best, D. Oepts and P.W. van Amersfoort, Nucl. Instr. and Meth. A 331 (1993) 636.
- [2] B. Faatz, R.W.B. Best, D. Oepts and P.W. van Amersfoort, IEEE J. Quantum Electron. QE-29 (7) (1993).
- [3] G.A. Barnett, S.V. Benson and J.M.J. Madey, IEEE J. Quantum Electron. QE-21 (2) (1993).
- [4] S. Krishnagopal, M. Xie and A. Sessler, Nucl. Instr. and Meth. A 310 (1992) 661.
- [5] S. Krishnagopal, M. Xie and K.-J. Kim, Nucl. Instr. and Meth. A 331 (1993) 654.
- [6] M. Xie and K.-J. Kim, SPIE 1868 (1993) 150.
- [7] B.E. Newnam et al., IEEE J. Quantum Electron. QE-21 (1985) 867.
- [8] R.H. Pantell, J. Feinstein and A.H. Ho, Nucl. Instr. and Meth. A 296 (1990) 638.
- [9] Y.C. Huang, J. Schmerge, J. Harris, G.P. Gallerano, R.H. Pantell and J. Feinstein, Nucl. Instr. and Meth. A 318 (1992) 765.
- [10] L. Elias and J. Gallar, Appl. Phys. B 3 (1983) 229.
- [11] E. Jerby and A. Gover, Investigation of the gain regimes and gain parameters of the free electron laser dispersion equation, IEEE J. Quantum Electron. QE-21 (7) (1985).

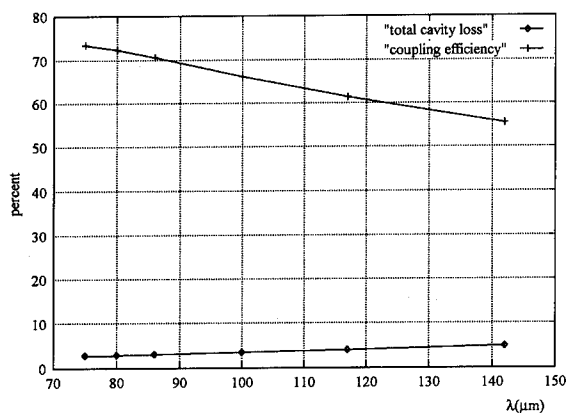


Fig. 5. Total cavity loss and coupling efficiency versus wavelength for the near-confocal resonator. The coupling efficiency is as high as 73% at  $\lambda = 80\text{ }\mu\text{m}$ .



# Pulse stacking in the SCA/FEL external cavity<sup>☆</sup>

P. Haar<sup>\*</sup>, H.A. Schwettman, T.I. Smith

*Stanford Picosecond FEL Center, W.W. Hansen Experimental Physics Laboratory Stanford University, Stanford, CA 94305-4085, USA*

## Abstract

The External Cavity System (ECS) is a passive optical resonator into which we couple the SCA/FEL optical pulse train. We describe measurements of the energy stored in the ECS cavity, where we have routinely observed pulses with 70 times the energy of the incident FEL pulses, near the theoretical maximum for our cavity configuration. We also describe measurements of the stored energy's dependence on cavity length and beam steering. Using these results, we evaluate the potential for increasing the energy of optical pulses delivered by the SCA/FEL to experimenters.

## 1. Introduction

The Stanford Free Electron Laser (FEL) delivers an optical pulse train consisting of picosecond micropulses which occur every 85 ns during millisecond macropulses which repeat at 10 Hz or 20 Hz. When driven by this pulse train, the External Cavity System (ECS) [1], a passive optical resonator can accumulate many micropulses worth of energy. This stored energy can then be extracted to increase the micropulse energy available for experiments. The most direct way to extract energy is to dump the cavity using an intracavity semiconductor switch activated by a high power pulse from an external laser [2]. This technique has the potential to deliver very high energy pulses, but at a low repetition rate (10–100 Hz) limited by the external laser. Alternatively, enhanced micropulse energy can be produced by exploiting the properties of an overcoupled cavity [3]. This approach offers only a modest enhancement in the delivered energy (at most a factor of nine enhancement), but can be operated at very high repetition rates ( $\leq 200$  kHz).

## 2. Theory

Consider a perfectly stable optical pulse train from the FEL coupled into the TEM<sub>00</sub> mode of the ECS. If the temporal spacing between FEL micropulses is matched to the round trip time of the external cavity, energy will accumulate on a time scale given by  $\tau = (2L/c)Q$ , where

$L$  is the length of the cavity and  $1 - \exp[-1/Q]$  is the round trip loss of energy from the cavity. If the loss due to the coupling mirror is  $\delta_e$ , then the steady state stored energy is given by [4][5]

$$U_0 = \frac{\delta_e U_{inc}}{(1 - e^{-1/2Q})^2} \approx 4\delta_e Q^2 U_{inc}, \quad (1)$$

where  $U_{inc}$  is the energy of the incident FEL micropulses. The latter expression is valid if all losses are small.

If there is a constant timing offset  $\Delta t_0$  between the round trip time of the external cavity and the time between micropulses, we can calculate the steady state stored energy to be [1,5]

$$\frac{U}{U_0} = 2 \left( \frac{1-a}{1+a} \right) \left( \frac{1}{2} + \sum_{s=1}^{\infty} a^s \cos(s\phi) \exp \left[ -\frac{\phi^2 s^2}{4\omega^2 \sigma^2} \right] \right), \quad (2)$$

where  $a = \exp[-1/2Q]$  is the round trip field attenuation,  $\phi = \omega \Delta t_0$ , and  $2\sigma$  is the  $1/e$  width of the transform limited FEL micropulses. This function has a local maximum when  $\phi$  is any multiple of  $2\pi$ , with  $U/U_0 = 1$  for  $\phi = 0$ . These maxima tend to be very narrow; for the maximum centered at  $\phi = 0$  the FWHM  $\Delta\phi \approx 1/Q$  for  $Q > 1$ . In general, the timing offset will not be constant, due, for example, to fluctuations in the length of the external cavity. Numerical calculations show that when  $d\phi/dt \ll \Delta\phi/\tau$  the timing error changes slowly enough that the stored energy reaches steady state at each timing error. In this case, we can make the “adiabatic approximation” that Eq. (2) applies at each point in time for each value of  $\phi$ .

To calculate the effects of FEL steering into the cavity, we fix the cavity length at its optimal value and consider only the transverse beam profile of the FEL micropulses which matches the profile of the TEM<sub>00</sub> cavity mode.

<sup>☆</sup> Work supported in part by the Office of Naval Research, contract # N00014-91-C-0170.

<sup>\*</sup> Corresponding author. Tel. +1 415 723 0291, fax +1 415 725 8311, e-mail paulhaar@leland.stanford.edu

Errors in pointing are introduced by adding a linear phase shift across the beam, while positional errors are introduced by displacing the centroid of the FEL pulses from the optical axis of the cavity. The stored energy can be calculated using numerical methods to propagate the stored field as it travels back and forth inside the cavity. If all other beam steering parameters are fixed and the beam pointing ( $\theta$ ) is varied, the calculated stored energy can be fit well to the equation  $U = U_0 \exp[-\theta^2/\Delta\theta^2]$ . The calculation for varying the input position ( $x$ ) also exhibits an approximate gaussian dependence, with characteristic width  $\Delta x$ .

Although they cannot be separated analytically, numerical calculations reveal that, at least for parameters relevant to this experiment, the timing/length effects and steering effects are separable for practical purposes. Thus the two effects can be treated independently and then combined to obtain the correct net effect. This property is essential for interpreting the data.

### 3. Experimental apparatus and procedure

A schematic layout of the ECS is shown in Fig. 1. The length of the external cavity is precisely matched to the length of the FEL cavity (12.68 m) by adjusting the position of the coupling mirror (C1). The cavity mirrors are 38.1 mm diameter, 7.5 m radius, ZnSe mirrors with dielectric coatings; both are partially transmissive in the visible, allowing pre-alignment of the system with a red HeNe laser. The coupling mirror, at  $\lambda = 4.55 \mu\text{m}$ , has a measured transmission coefficient  $\delta_c = 0.0259 \pm 0.0004$ . The other mirror is a high reflector ( $\ll 1\%$  loss). The entire cavity is enclosed and purged with dry  $\text{N}_2$ .

The stored energy ( $U$ ) and  $Q$  are determined by measuring the energy transmitted through and the energy reflected from the cavity. The transmitted energy, which is directly proportional to the stored energy, is measured by detector D1, a 1 MHz  $\text{LN}_2$  cooled InSb detector. The reflected signal,  $U_R$ , is directed by a 10% pick-off plate (P) onto either quad detector QD5, which is used to align both cavity mirrors, or onto detector D2, which is identical to

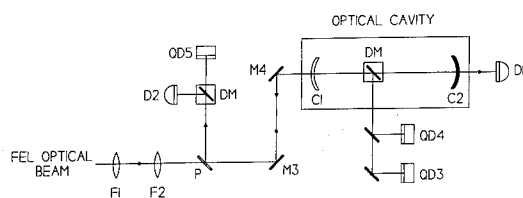


Fig. 1. Schematic layout of external cavity system. Symbols: (M) steering mirror, (F) focussing element, (P) 10% pickoff, (DM) drop-in mirror, (C) cavity mirror, (D) detector, (QD) quadrant detector.

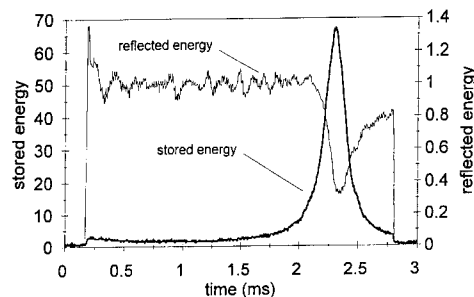


Fig. 2. Stored and reflected energy for a typical macropulse, both in units of  $U_{\text{inc}}$ . The maximum stored energy is  $67U_{\text{inc}}$  with FWHM = 202  $\mu\text{s}$ ; the minimum reflected energy is  $0.32U_{\text{inc}}$ . The spike in the reflected energy at the beginning of the macropulse is due to the “noise eater” AOM.

D1. By conservation of energy, if the stored energy reaches steady state then

$$U \left( \frac{e^{-1/Q}}{1 - \delta_c} \right) + U_{\text{inc}} = U + U_R, \quad (3)$$

where the term in brackets on the left is just the non-coupling losses. Given  $U$  and  $U_R$  we can use Eq. (3) to calculate  $Q$ . An alternative  $Q$  measurement can be made using the non-resonant cavity response. If the cavity length is tuned far enough away from its optimal value, the input FEL micropulses will no longer overlap, and the steady state stored energy will be given by the limit of Eq. (2) as  $\phi \rightarrow \infty$ , which depends only on  $\delta_c$  and  $Q$ .

The FEL optical beam diagnostics provide a frequently updated macropulse spectrum and autocorrelation [6]. In addition, an acousto-optic modulator (AOM) “noise eater” stabilizes the micropulse amplitude. The transverse mode of the FEL optical beam is matched to the  $\text{TEM}_{00}$  mode of the external cavity using a simple telescope (F1 and F2). Quad detectors QD3 and QD4 define the optic axis of the cavity.

### 4. Experimental results and discussion

During the experiment, the FEL was operated at  $\lambda = 4.55 \mu\text{m}$  with 1.1 ps (FWHM) micropulses and 2.5 ms macropulses. Fig. 2 shows the stored and reflected energy for a typical macropulse. Previous ECS experiments [1] have shown that the observed behavior can be explained by a sinusoidally varying timing offset, due, for example, to vibration of the cavity mirrors. The resonant peak seen in the figure occurred when the timing offset passed through zero during the linear portion of the vibrational oscillation. We also commonly observed double peaks, which represent occasions when the timing offset passed through zero twice near an extremum of the oscillation. Due to this timing instability, FEL macropulses with sig-

nificant stored energy appear at an uneven rate, averaging a few Hz.

We recorded the complete time record of the stored and reflected energy for 18 macropulses, and for each of these the adiabatic approximation is valid. The stored energy peaks had FWHM ranging from 113  $\mu$ s to 577  $\mu$ s. If we assume all losses are due solely to the coupling mirror, then  $Q = 38$ , and thus  $\tau = 3.2$   $\mu$ s and  $\Delta\phi = 0.026$  rad for the central ( $\phi = 0$ ) maximum of Eq. (2). We can then estimate  $d\phi/dt$  for the narrowest peak to be 230 rad/s  $\ll \Delta\phi/\tau = 8088$  rad/s. If  $Q < 38$  then  $\Delta\phi/\tau$  will be larger.

The cavity  $Q$  was determined from Eq. (3) for each of the 18 recorded macropulses. Averaging these values gives  $Q = 27.2 \pm 0.4$ . The alternative non-resonant technique gave a consistent result. Combining this  $Q$  with  $\delta_e$  we can calculate from Eq. (1)  $U_0 = 78U_{inc}$ . The energy stored during the recorded macropulses fell between  $63U_{inc}$  and  $73U_{inc}$ , with an average of  $67U_{inc}$ . The most likely source for the discrepancy between the observed and theoretical stored energy is steering. For this cavity configuration and wavelength, theory predicts  $\Delta\theta = 287$   $\mu$ rad and  $\Delta x = 1.98$  mm. If we attribute all the reduction in stored energy to angular steering, the error would average 112  $\mu$ rad and vary from 74  $\mu$ rad to 133  $\mu$ rad. A positional rather than pointing error would average 0.76 mm and range from 0.50 mm to 0.90 mm. To investigate the plausibility of these steering errors, we used quad detectors QD3 and QD4 (see Fig. 1) to record the angle and position of the FEL as it enters the external cavity for consecutive macropulses during a 7.5 minute interval. The measured RMS fluctuations were 10  $\mu$ rad for the vertical angle and 54  $\mu$ m for the vertical position. The range of values covered by these parameters was 72  $\mu$ rad and 367  $\mu$ m, respectively. The horizontal angle and position had similar variations. We also made indirect measurements of the angular stability of the front cavity mirror, indicating RMS angular variations of  $< 21$   $\mu$ rad in the vertical and  $< 9$   $\mu$ rad in the horizontal. These latter measurements are particularly significant since the cavity geometry causes an

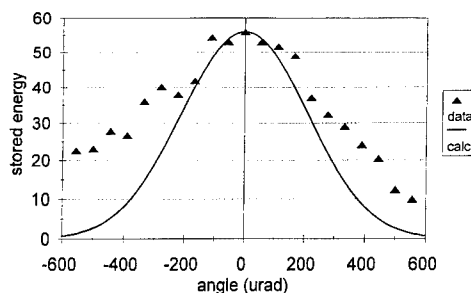


Fig. 4. Stored energy vs input steering. The stored energy is in units of  $U_{inc}$ .

angular deviation of a cavity mirror to be magnified by a factor of 3.2 in the angle of the optic axis. These steering fluctuations are sufficient to account for the observed range of stored energies.

To test the validity of Eq. (2), we measured the stored energy at each local maximum from  $8\lambda$  longer than the optimal length to  $8\lambda$  shorter. Fig. 3 compares the results with calculations. The calculated curve is from Eq. (2) using  $Q = 27.2$ , the average micropulse FWHM = 1.09 ps measured during the scan, and the measured amplitude of the  $\phi = 0$  local maximum. There are no free parameters. Agreement with the data is excellent. During the hour required to acquire the data, the measured long term length drift was linear and shortened the cavity by 6  $\mu$ m. This drift can be explained by a thermal contraction of the concrete floor separating the two cavity mirrors due to a temperature shift  $\Delta T \approx -0.4^\circ\text{C}$ .

We measured the stored energy as a function of FEL pointing by using mirror M4 (see Fig. 1) to vary the vertical input steering angle. The largest stored energy recorded out of 250 sampled macropulses at each angle is plotted in Fig. 4, along with a calculated curve. In combination with the angular fluctuations mentioned above, the procedure of selecting the maximum stored energy at each chosen angle will widen the plotted distribution relative to the calculation. The average displacement in angle of the data points from the theoretical curve is 95  $\mu$ rad, while the maximum displacement is 277  $\mu$ rad. Adding the RMS variation in the vertical input angle and the RMS variation in the vertical angles of the two cavity mirrors in quadrature gives a combined RMS fluctuation of 96  $\mu$ rad, which is sufficient to account for the widening. The asymmetry in the data is due to a systematic error which has since been corrected.

## 5. Conclusions

We have demonstrated significant stored energy in the SCA/FEL external cavity system. With  $Q = 27.2$  and a 2.59% coupling mirror we routinely stored pulses with 70 times the energy of the incident FEL micropulses, nearly

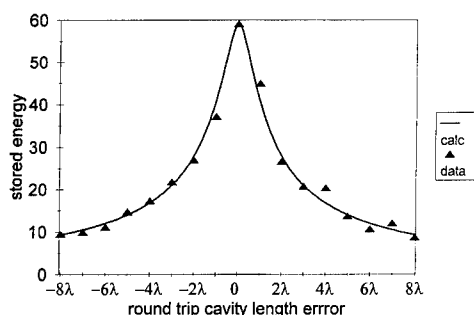


Fig. 3. Stored energy vs cavity length. The stored energy is in units of  $U_{inc}$ . The maximum stored energy in this figure (and the next) differs from the larger values described in the text since this data was taken under slightly different conditions.

90% of the theoretical maximum for these parameters. The main factor limiting this value was steering fluctuations. The dependence of the stored energy on cavity length is in excellent agreement with the theory. Although difficult to measure directly, the dependence of the stored energy on input steering seems consistent with the theory when steering fluctuations are taken into account.

The amount of energy we have stored in the current experiment is adequate for implementing cavity dumping or the enhanced outcoupling schemes described in Ref. [3]. A practical system, however, will require us to eliminate long term length drift and improve the steering stability. The length drift can be corrected directly, using for example an interferometer to monitor the length as part of a feedback loop, or it can be compensated automatically by a system designed to stabilize the stored energy by eliminating timing fluctuations. Steering fluctuations can be reduced by simplifying the ECS optics, thereby reducing the number of optical elements which can contribute to instabilities, and by reinforcing individual optical mounts.

## References

- [1] P. Haar, T.I. Smith and H.A. Schwettman, Proc. 14th Int. Free Electron Laser Conf., Kobe, Japan, 1992, Nucl. Instr. and Meth. A 331 (1993) 621.
- [2] J.P. Kaminski, J.S. Spector, C.L. Felix, D.P. Enyeart, D.T. White and G. Ramian, Appl. Phys. Lett. 57 (1990) 2770.
- [3] P. Haar, T.I. Smith and H.A. Schwettman, these Proceedings (16th Int. Free Electron Laser Conf., Stanford, CA, USA 1994) Nucl. Instr. and Meth. A 358 (1995) ABS 40.
- [4] P. Haar, I.M. Fishman, T.I. Smith and H.A. Schwettman, Proc. 13th Int. Free Electron Laser Conf., Santa Fe, NM, USA, 1991, Nucl. Instr. and Meth. A 318 (1992) 899.
- [5] P. Haar, Effect of instabilities on energy buildup in a passive optical cavity for a pulsed source, HEPL Technical Note #92-3.
- [6] K.W. Berryman, B.A. Richman, H.A. Schwettman, T.I. Smith and R.L. Swent, these Proceedings (16th Int. Free Electron Laser Conf., Stanford, CA, USA, 1994) Nucl. Instr. and Meth. A 358 (1995) 300.

# Resonator design and characterization for the Israeli tandem electrostatic FEL project <sup>☆</sup>

I.M. Yakover, Y. Pinhasi, A. Gover <sup>\*</sup>

*Department of Physical Electronics, Tel-Aviv University, Ramat-Aviv, Israel*

## Abstract

The design and measurements of a resonator operating near 100 GHz and intended for use in a tandem FEL are presented. The designed resonator employs two parallel curved plates as a waveguide. In FEL operation the TE<sub>01</sub> mode is excited. The resonator employs two wave splitters as reflectors. The wave splitters are segments of an overmoded rectangular waveguide which is connected at one end to the waveguide as described above, and is shorted at the other end by a metal plate with an aperture in the center for e-beam passage.

Gain calculations were made in the low gain regime. At the operating frequency the curvature of the plates and the gap size were chosen so as to maximize the gain.

A multimode analysis of the wave splitter was made. Calculations show, that the optimal splitter width and length allow achievement of very low diffraction losses at the aperture (~2%). This means that the aperture can be made sufficiently large to allow efficient beam entrance into the resonator without degrading its *Q*-factor.

A resonator prototype was constructed and its performance was evaluated experimentally.

## 1. Introduction

This paper deals with the theoretical and experimental investigations of the resonator designed for the Israeli tandem electrostatic FEL project. This FEL has the following basic parameters: e-beam energy  $E = 1.5\text{--}2.5$  MeV, e-beam current  $I_0 < 1$  A, wiggler magnetic field  $B_w = 2\text{--}3$  kG, wiggler period  $\lambda_w = 4.4$  cm, wiggler length  $L_w = 88$  cm (20 periods), and the operating frequency is about 100 GHz.

At the beginning of this project several types of overmoded waveguides, i.e. rectangular, circular, and metal-dielectric waveguides [1] and waveguide formed by two parallel curved plates [2], were investigated theoretically in order to determine which of them allows one to reach the optimal performance. Numerical calculations were made taking into account two opposite requirements: that the dimensions of the waveguide cross-section be small enough so as to achieve large gain and be large enough for e-beam passage without interception. It was found that the mentioned set of parameters provides a maximal small signal gain of the order of 100% at the operating frequency of 100 GHz for all types of investigated waveguides.

The relatively low expected gain requires operation

with a waveguide having low losses, which directed our choice to the parallel curved plates waveguide (see Fig. 1) in which the TE<sub>01</sub> mode is excited. This waveguide has small ohmic losses and enables space for electron “wiggling” in the *x*-direction.

The reflector design also meets the difficulties resulting from the linear configuration of the tandem accelerator (see drawing presented in Ref. [3]). The reflectors must have a high reflectivity for the electromagnetic wave and be transparent to the e-beam. We have chosen a wave splitter proposed in Ref. [4] as a main reflector option. The wave splitter is a segment of the overmoded rectangular waveguide which is connected at one end to the parallel plate waveguide (see Fig. 1) and shorted at the other end by a metal plate with an aperture in the center for e-beam passage.

## 2. FEL gain consideration

Gain calculations were made using the following well known single-mode gain-dispersion equation [5] for the FEL operating in the linear regime:

$$G(s) \equiv \frac{(s - i\theta)^2 + \theta_{pr}^2}{s[(s - i\theta)^2 + \theta_{pr}^2] - iQ}, \quad (1)$$

where

$$Q = I_0 \frac{ea_w^2 Z_s (k_z + k_w)^2 L_w^3}{8mcA_{emx} \omega_s \gamma^3 \beta_z^3} [J_0(\rho) - J_1(\rho)]^2 \quad (2)$$

<sup>☆</sup> This work was supported by grants of the U.S.–Israel Bi-National Foundation and the Israeli Ministry of Science.

<sup>\*</sup> Corresponding author. Tel. +972 3 6 408 149, fax +972 3 6 423 508.

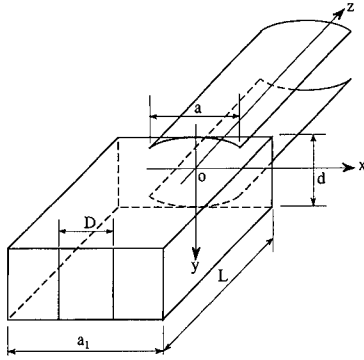


Fig. 1. Junction of wave splitter and parallel plate waveguide.

is the gain parameter,

$$\theta_{pr}^2 = \tilde{r}^2 \frac{eI_0}{\gamma_z^2 m \epsilon_0 V_z^3} L_w^2 \quad (3)$$

is the reduced space-charge parameter,  $\tilde{r}$  is a plasma frequency reduction factor,

$$\theta = \left( \frac{\omega_s}{c} - k_z - k_w \right) L_w \quad (4)$$

is the detuning parameter,  $a_w = eB_w/(k_w mc)$ ,  $\gamma_z = \gamma/\sqrt{1 + a_w^2/2}$ ,  $\beta = \sqrt{1 - 1/\gamma^2}$ ,  $\gamma = 1 + E/(mc^2)$ ,  $\beta_z = \sqrt{1 - 1/\gamma_z^2}$ ,

$$\rho = \frac{\omega_s}{8\beta k_w c} \left( \frac{a_w}{\beta\gamma} \right)^2 \left[ 1 - \frac{1}{2} \left( \frac{a_w}{\beta\gamma} \right)^2 \right]^{-3/2},$$

$J_0, J_1$  are Bessel functions,  $k_w = 2\pi/\lambda_w$ , and  $k_z, Z_s$  and  $A_{emx}$  are the longitudinal wave number, wave impedance and effective mode area of the operating mode respectively. The effective mode area is determined by

$$A_{emx} = \frac{\int |E_x(x, y)|^2 dx dy}{|E_x(0, 0)|^2}, \quad (5)$$

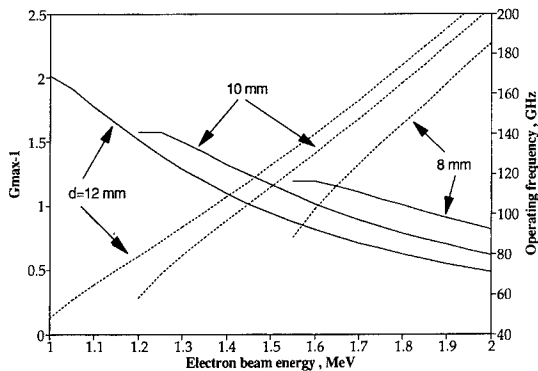


Fig. 2. The calculated dependence of maximal gain (solid curves) and operating frequency (dotted curves) on e-beam energy.

where the integration is carried out over the waveguide cross-section and  $E_x(0, 0)$  is calculated on the waveguide axis.

Electric field expressions were obtained in Ref. [2] analytically in the form of Gaussian–Hermite functions. For the case of a large curvature radius these expressions can be simplified, and the electric field profile of the  $TE_{01}$  mode has the form

$$E_x(x, y) = U_0 \cos\left(\frac{\pi y}{d}\right) e^{-x^2/w_0^2}, \quad (6)$$

where  $U_0$  is the amplitude of the electric field,  $w_0^2 = \sqrt{2Rd - d^2}/\kappa_{01}$ ,

$$\kappa_{01} = \frac{1}{d} \left[ 1 + \tan^{-1} \left( \frac{d}{\sqrt{2Rd - d^2}} \right) \right],$$

$Z_s = 120\pi/\sqrt{1 - (\kappa_{01}c/\omega)^2}$  is the wave impedance of the  $TE_{01}$  mode, and  $R$  is the curvature radius of the plates. Substituting expression (6) into (5) we obtain  $A_{emx} = \sqrt{\pi} w_0 d/2^{3/2}$ .

The calculated dependence of maximal gain (solid curves) and operating frequency (dotted curves) on e-beam energy are presented in Fig. 2. Calculations were made for the following parameters  $R = 14.29$  mm,  $B_w = 2$  kG,  $L_w = 88$  cm,  $\lambda_w = 4.4$  cm,  $I_0 = 0.7$  A. As we may note, an operating frequency of 100 GHz can be obtained at low energies (1.3–1.6 MeV). The maximal gain decreases as the distance  $d$  between waveguide plates increases. Simulations of e-beam transport show that the spacing  $d = 10$  mm is large enough for e-beam passage through the resonator without losses. This value of  $d$  allows achievement of maximal small signal gain of the order of 100% at the operating frequency of 100 GHz. Fig. 3 shows the gain frequency dependence calculated for this case.

### 3. Wave splitter analysis

A multimode analysis of the wave splitter was carried out assuming that the tangential electric field in the plane

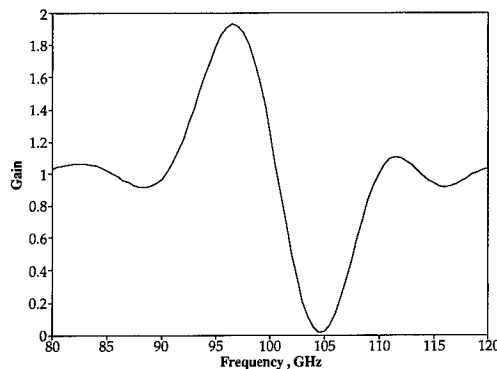


Fig. 3. Gain frequency response.

$z = 0$  has the same profile as the electric field of the  $TE_{01}$  mode of the parallel curved plates waveguide. Further consideration was carried out for the case of a splitter of height equal to the distance between plates. This geometry allows one to assume that only the  $TE_{1n}$  and  $TM_{1n}$  modes are excited in the splitter waveguide. Their electric fields amplitudes are given by the expression (see Ref. [6])

$$U_{1n}^p = \int_{-a/2}^{a/2} dx \int_{-d/2}^{d/2} dy H_{y,1n}^p(x, y) E_x(x, y), \quad (7)$$

where  $H_{y,1n}^p$  is the normalized magnetic field,  $p = h$  for the  $TE_{1n}$  modes, and  $p = e$  for the  $TM_{1n}$  modes.

Substitution of Eq. (6) into Eq. (7) results in

$$U_{1n}^e = U_0 \frac{\alpha_n d}{2\chi_{1n}} \left( \frac{2\delta_n}{a_1 d} \right)^{1/2} (-1)^n V_n, \\ U_{1n}^h = U_0 \frac{\pi}{\chi_{1n}} \left( \frac{2\delta_n}{a_1 d} \right)^{1/2} (-1)^n V_n. \quad (8)$$

Here

$$V_n = \int_{-a/2}^{a/2} dx \cos(\alpha_n x) e^{-x^2/w_0^2}, \quad (9)$$

and  $\alpha_n = 2n\pi/a_1$ ,  $\chi_{1n} = (\alpha_n^2 + (\pi/d)^2)^{1/2}$ ,  $\delta_n = 1$  for  $n = 0$  and  $\delta_n = 2$  for  $n = 1, 2, \dots$ . Using Eq. (7) and (8) the power flow density can be represented in the form of a double series

$$P(x, y, z) = \frac{1}{2} \eta_0 |U_0|^2 \cos^2\left(\frac{\pi y}{d}\right) \\ \times \frac{(\omega/c)^2 - (\pi/d)^2}{a_1^2 \omega/c} \tilde{P}(x, z), \\ \tilde{P}(x, z) = \text{Re} \left\{ \sum_{m=0} \sum_{n=0} \frac{\exp[i(k_{1n} - k_{1m})z]}{k_{1n}} \delta_m \delta_n \right. \\ \left. \times \cos(\alpha_m x) \cos(\alpha_n x) V_m V_n \right\}, \quad (10)$$

where  $k_{1n} = ((\omega/c)^2 - \chi_{1n}^2)^{1/2}$ ,  $\eta_0 = 1/120\pi$ , and only propagating modes are considered.

The results of the computation of  $\tilde{P}(x, z)/\tilde{P}(0, 0)$  for  $d = 10$  mm,  $a = 22$  mm,  $R = 14.29$  mm,  $f = 100$  GHz, and  $a_1 = 25$  mm are shown in Fig. 4 for various lengths of the wave splitter. As we see, at the optimal distance  $z$  the electromagnetic field is negligibly small in a large part of the splitter cross-section. Similar results were achieved in Ref. [4]. This means that the electromagnetic wave and the electron beam can be successfully separated in this plane by shorting the wave splitter by a metal plate having an aperture in its center.

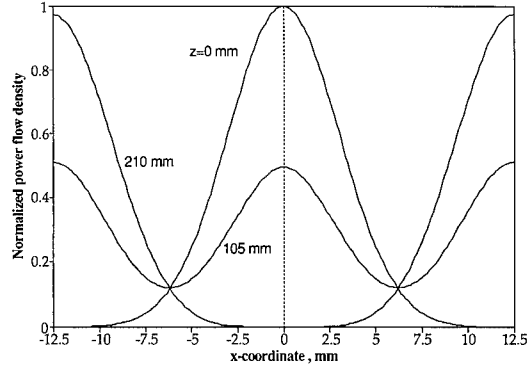


Fig. 4. Calculations of normalized power flow density in a wave splitter.

Diffraction losses in the aperture can be estimated by calculating the ratio

$$\frac{W_a}{W} = \frac{\int_{S_a} P(x, y, z) dx dy}{\int_{-a_1/2}^{a_1/2} dx \int_{-d/2}^{d/2} dy P(x, y, z)}, \quad (11)$$

where  $W_a$  is the power flow through the aperture of area  $S_a$ , and  $W$  is the incident power flow. For the aperture in the form of a rectangular slot of the width  $D$  and of the length  $d$  (see Fig. 1) this ratio can be found analytically:

$$\frac{W_a}{W} = \text{Re} \left\{ \sum_{m=0} \sum_{n=0} \delta_m \delta_n V_m V_n \frac{\exp[i(k_{1n} - k_{1m})z]}{k_{1n}} \right. \\ \left. \times [\varphi(\alpha_{n-m}) - \varphi(\alpha_{n+m})] / \left[ a_1 \sum_{n=0} \frac{\delta_n V_n^2}{k_{1n}} \right] \right\}, \quad (12)$$

where  $\varphi(\alpha_n) = (\sin(\alpha_n D/2))/\alpha_n$ .

Fig. 5 shows the dependence of  $W_a/W$  on frequency, calculated for the parameters  $d = 10$  mm,  $a_1 = 25$  mm,  $L = 210$  mm and various values of the aperture size parameter  $D$ . As we see a slot having a width  $D = 10$  mm

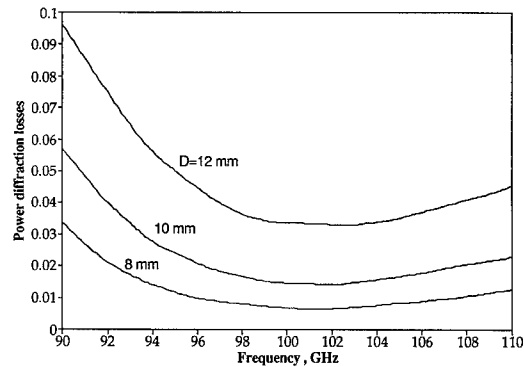


Fig. 5. Calculated diffraction losses in an aperture.

provides very low diffraction losses (of the order of 2% in the frequency band 96–106 GHz).

#### 4. Experimental results

The resonator prototype was designed and built on the basis of theoretical investigations described above. The waveguide samples have a curvature radius of  $R = 14.75$  mm and a spacing between plates of  $d = 10.7$  mm. This value of  $d$  was chosen in order to use the standard tapered transition between W-band and K-band waveguides. The input cross-section of this transition has the dimensions  $2.54 \times 1.27$  mm<sup>2</sup> and the output cross-section is  $10.7 \times 4.3$  mm<sup>2</sup>. It provides for good mode matching in the  $y$ -direction and therefore the TE<sub>01</sub> mode of a parallel plate waveguide can be excited efficiently.

In order to determine the waveguide attenuation constant, the transmission coefficient was measured. Two samples of the same length 400 mm and of different widths of their curved parts  $a = 15$  mm and  $a = 22$  mm were tested. The results of transmission coefficient measurements made for the waveguide with  $a = 15$  mm are shown in Fig. 6. The observed deep oscillations are the result of mismatching between the tapered transition and the tested waveguide in the  $x$ -direction and multiple reflections of the electromagnetic wave. Positions of maxima and minima were measured directly using a frequency meter. Numerical analysis allows one to determine the transverse wave number  $\kappa$  of the observed mode; it was found that  $\kappa = 0.35$  1/mm while the calculated value is  $\kappa_{01} = 0.36$  1/mm. Good agreement between theoretical and experimental values leads to the conclusion that the observed mode is the TE<sub>01</sub> mode.

Further numerical analysis of the experimental results was made in the single mode approximation, and the attenuation constant was determined. The asterisks in Fig. 7 present the attenuation constant of a waveguide having  $a = 15$  mm. As we see the attenuation constant is relatively large of the order of 3 dB/m. This can be understood if one notes that the waveguide width is smaller than the

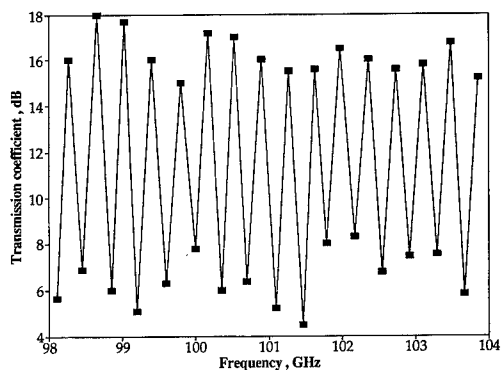


Fig. 6. Measurements of waveguide transmission.

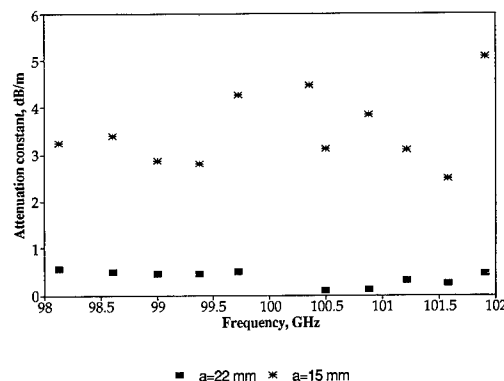


Fig. 7. Waveguide attenuation constant.

TE<sub>01</sub> mode spot size on the curved plate which leads to significant diffraction losses.

Diffraction losses can be reduced by utilizing the wider waveguide. The waveguide sample having  $a = 22$  mm was tested, and its attenuation constant is depicted in Fig. 7 by the squares. This waveguide sample has much smaller losses than the first one, and the lowest attenuation constant of the order of 0.1 dB/m as observed at frequencies of 100.5 and of 100.8 GHz.

A wave splitter having cross-section dimensions of  $10.7 \times 25$  mm<sup>2</sup> and a length of  $L = 210$  mm was built and tested experimentally. First the influence of the aperture in the shorting plate was examined. For this purpose the results of the wave splitter reflection coefficient measurements made for the splitter shorted by a metal plate with a circular aperture of 10 mm diameter were compared with the results obtained for the splitter shorted by a full plate without any aperture. A full coincidence of the results was observed, indicating that the reflectivity of the apertured short is as high as the full short within the measurement accuracy. The return loss of the splitter was also measured. As a reference the return loss of the shorted parallel plate waveguide was used. Very low return loss ( $< 0.1$  dB) was observed at frequencies of 99.8, 100.3, 100.9, 101.3 and 102 GHz. This means that the round trip power loss is of the order of 0.35 dB (8%) for our resonator with a waveguide of 88 cm length. This loss value corresponds to a  $Q$ -factor of the order of 20 000, a very high value for a 100 GHz resonator.

#### References

- [1] Yu.N. Kazantsev, Sov. Radio Eng. Elec. Phys. 15 (1970) 963.
- [2] T. Nakahara and N. Kurauchi, IEEE Trans. MTT-15 (1967) 66.
- [3] A. Gover et al., Nucl. Instr. and Meth. A 341 (1994) ABS 57.
- [4] W.H. Urbanus et al., Nucl. Instr. and Meth. A 331 (1993) 235.
- [5] Y. Pinhasi et al., Nucl. Instr. and Meth. A 318 (1992) 523.
- [6] Kh.L. Garb, P.Sh. Fridberg and I.M. Yakover, Sov. Phys. Collection 22 (1982) 27.





ELSEVIER

# Low-cost electron-gun pulser for table-top maser experiments

V. Grinberg, E. Jerby<sup>\*</sup>, A. Shahadi

*High-Power Microwave Laboratory, Faculty of Engineering, Tel Aviv University, Ramat Aviv 69978, Israel*

## Abstract

A simple 10 kV electron-gun pulser for small-scale maser experiments is presented. This low-cost pulser has operated successfully in various table-top cyclotron-resonance maser (CRM) and free-electron maser (FEM) experiments. It consists of a low-voltage capacitor bank, an SCR control circuit and a transformer bank (car ignition coils) connected directly to the e-gun. The pulser produces a current of 3 A at 10 kV voltage in a Gaussian like shape of 1 ms pulse width. The voltage sweep during the pulse provides a useful tool to locate resonances of CRM and FEM interactions. Analytical expressions for the pulser design and experimental measurements are presented.

## 1. Introduction

Cyclotron resonance masers (CRMs) [1] and free electron lasers (FELs) [2] are considered as relatively complicated and expensive devices, mainly because of the high-energy electron sources required for their operation. A major goal of the Tel Aviv University High-Power Microwave Laboratory is to develop low-voltage, low-cost integrated maser schemes [3] for practical applications. Several new low-voltage experimental masers have been developed in our laboratory during the last two years. These include the traveling-wave FEM [4], the periodic-waveguide CRM oscillator [5], the CRM in a non-dispersive waveguide [6], and the UHF ubitron-FEM oscillator [7].

The experimental CRM and FEM devices described in Refs. [5–7] have been operated successfully with an electron energy lower than 8 keV. The high-voltage pulses for these experiments have been produced by the low-cost pulser described in this paper. This 10 kV, 3 A pulser generates a  $\sim 1$  ms pulse with Gaussian-like shape. The voltage sweep during the pulse provides a useful tool to identify the resonances of the examined maser.

A principle scheme of the pulser [8,9] is shown in Fig. 1. The low-voltage circuit consists of a capacitor bank  $C$ , an SCR switch, a diode  $D_C$  (which prevents a reverse recharging of the capacitor), and the primary winding of the transformer with  $w_1$  turns. The high-voltage secondary winding ( $w_2$  turns) is connected directly to the electron gun. An ordinary car ignition coil can be used as the transformer in this scheme. This simple pulser design is

proposed for small university laboratories who seek a low-budget table-top FEL experiment for fundamental research and for student training. Analytical expressions for the pulser design and examples of its operation are presented in this paper.

## 2. Theory

The pulser shown in Fig. 1 can be implemented in practice with several transformers connected in parallel or in series, in order to increase the output current or voltage, respectively. A pulser scheme with two parallel transformers is shown in Fig. 2a. Its equivalent circuit shown in Fig. 2b includes the resistances  $R_1$ ,  $R_2$  and the inductances  $L_1$ ,  $L_2$  of the transformer primary and secondary windings, respectively. The electron gun response is approximated by a resistor  $R$  and a diode  $D$  in series. We also assume in this model a perfect magnetic coupling between the transformer windings, and ideal SCR and diodes  $D_C$  and  $D$  performance [8–10].

In this section we analyse the effect of the capacitance  $C$  and the number of parallel transformers  $m$  on the pulser characteristics: the initial capacitor voltage  $V_C$ , the pulse duration  $t_p$ , and maximum transformer magnetizing force  $F_m$ .

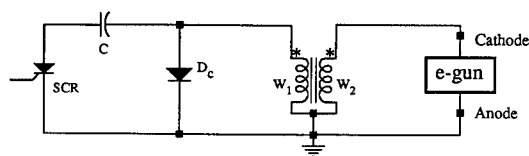
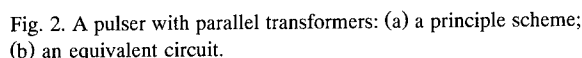


Fig. 1. A principle scheme of the pulser.

<sup>\*</sup> Corresponding author. Tel. +972 3 6 408 048, fax +972 3 6 423 508, e-mail jerby@taunivm.tau.ac.il.



The analysis presented in this paper refers to the first transient interval of the pulser response. It lasts from the SCR ignition to the first zero of the electron-gun current,  $t = t_p$ , in which the magnetizing force attains its maximum. Hence,  $t_p$  is the pulse duration of the electron gun. Two dimensionless parameters are defined to characterize the pulser performance. The parameter  $n$  is related to the normalized capacitance in the pulser circuit by  $n = CR_1(R_2 + mV_g/I_g)/(mL_2)$ . The parameter  $k$  corresponds to the time-constant ratio of the high- and low-voltage loops as  $k = 1 + L_1(R_2 + mV_g/I_p)/(L_2R_1)$ .

In order to find the effect of varying the number of parallel transformers in the pulser, we obtain  $dn/dm = -CR_1R_2/(L_2m^2) < 0$ , and  $dk/dm = L_1V_g/(I_gL_2R_1) > 0$ . Hence, an addition of a parallel transformer to the pulser circuit results in a decrease in the  $n$  parameter, and in an increase in the  $k$  parameter. Consequently, according to the analysis above and Fig. 3, both  $t_p$  and  $F_m$  decrease if  $m$  increases.

### 3. Practical implementation

The pulser scheme described in this paper has been constructed in several versions. It operates successfully in various maser experiments, including a traveling-wave FEM [4], a periodic-waveguide CRM [5], a CRM in a

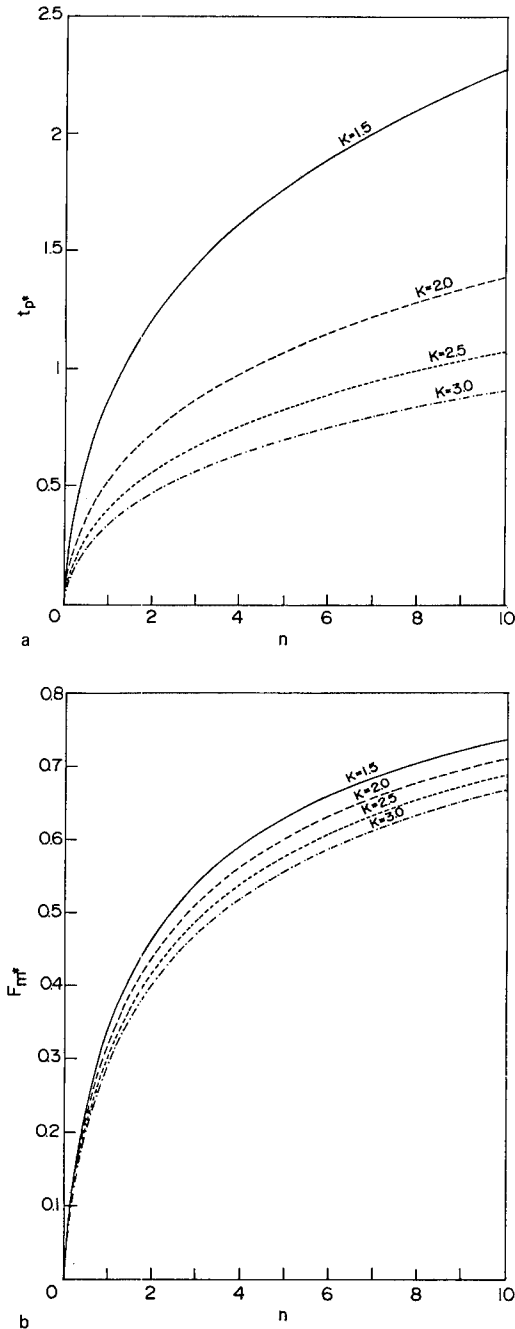


Fig. 3. The effect of the pulser normalized parameters  $n$  and  $k$ : (a) the normalized pulse duration  $t_{p*}$ . (b) The transformer maximum magnetizing force  $F_{m*}$ .

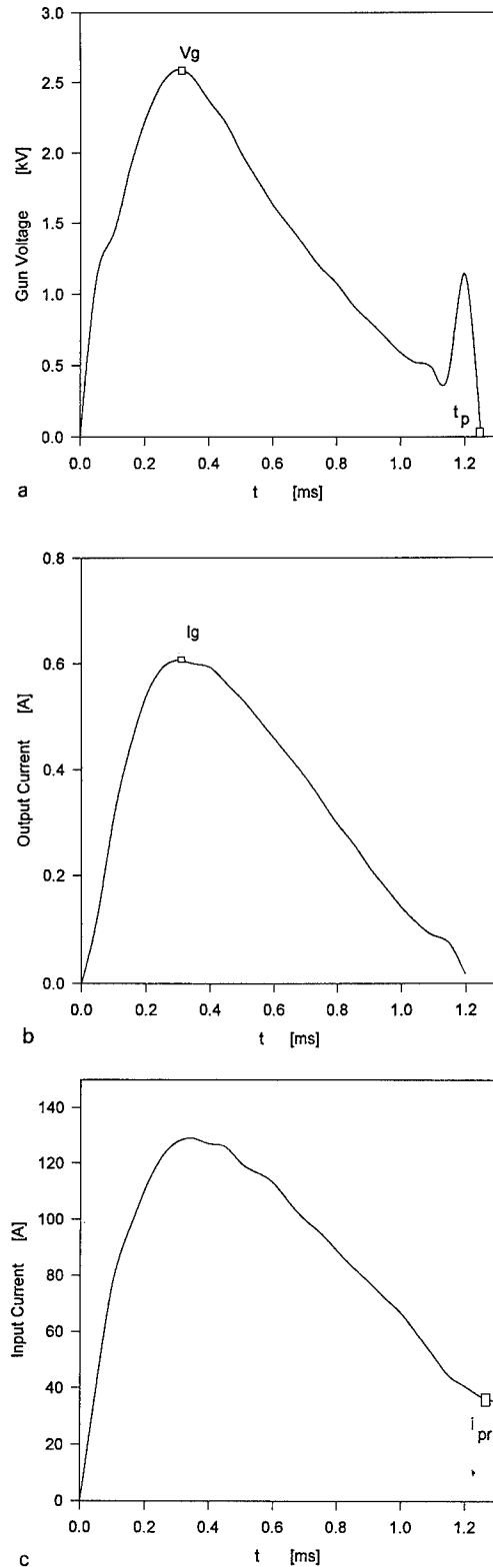


Fig. 4. Typical measurements of a thermionic electron gun pulse: (a) the electron-gun voltage; (b) the electron-gun cathode current; (c) the primary current of the transformer bank.

non-dispersive waveguide, and the FEM experiment in the UHF regime. The pulsers are operated in the range  $V_g = 2\text{--}10$  kV,  $I_g = 0.2\text{--}3.0$  A and  $t_p \sim 1$  ms. As transformers, we use ordinary car ignition coils (Diamand LB-88, with  $R_1 = 2.8\ \Omega$ ,  $R_2 = 11, 150\ \Omega$ ,  $L_1 = 0.003$  H, and  $L_2 = 44.6$  H). The number of parallel transformers  $m$  varies in our experiments from 1 to 3. The capacitances of the capacitor bank is variable in order to enable operation in both the periodic and the aperiodic regimes. The initial voltage of the capacitor bank is controlled in the experiment. The cathode current  $i_g(t)$  is measured by a Rogovski coil and detected with the e-gun voltage  $u_g(t)$  and the primary current of the transformer bank ( $i_{pr} = mi_1$ ) by an oscilloscope. Typical traces are shown for example in Figs. 4a–4c. The remanent primary current at the end of the pulse,  $i_{pr}(t_p)/m$ , is proportional to  $F_m$ , and is used to evaluate a variation in the maximum magnetizing force  $F_m$ .

The effects of the number of parallel transformers  $m$  and the capacitance  $C$  on the parameters  $V_C$ ,  $t_p$  and  $F_m$  has been studied experimentally and compared with the above analysis. The difference between the theoretical and the experimental results is demonstrated in an example in which  $V_g = 2.6$  kV,  $I_g = 0.62$  A,  $C = 350\ \mu\text{F}$ , and  $m = 3$ . The experimental results, shown in Figs. 4a–4c, yield in these conditions  $V_C = 130$  V and  $t_p = 1.24$  ms. The theoretical analysis presented in the previous section results in this case in  $V_C = 110$  V and  $t_p = 0.94$  ms. Hence, the analytical expressions presented in this paper provide a useful estimate for the pulser performance. These can be

used as a simple tool for a preliminary design of pulsers for small-scale nonrelativistic FEM and CRM experiments.

## References

- [1] V.L. Granatstein and I. Alexeff (eds.), High Power Microwaves (Artech House, 1987) and references therein.
- [2] H.P. Freund and T.M. Antonsen, Principles of Free-electron Lasers (Chapman and Hall, London, 1992) and references therein.
- [3] E. Jerby, Nucl. Instr. and Meth. A 331 (1993) ABS 21.
- [4] E. Agmon, A. Golombek and E. Jerby, Nucl. Instr. and Meth. A 331 (1993) 156.
- [5] E. Jerby, G. Bekefi and A. Shahadi, Nucl. Instr. and Meth. A 341 (1994) 115.
- [6] A. Shahadi et al., these Proceedings (16th Int. Free Electron Laser Conf., Stanford, CA, USA, 1994) Nucl. Instr. and Meth. A 358 (1995) 143.
- [7] R. Drori, E. Jerby and A. Shahadi, *ibid.*, p. 151.
- [8] G.N. Glasoe and J.V. Lebacqz, Pulse generators (Dover, New York, 1948).
- [9] B.A. Baginski and Yu.A. Otrubannikov, Elektrotehnika 3 (1980) 48, in Russian.
- [10] R. Rudenberg, Transient Performance of Electric Power Systems (McGraw-Hill, New York, 1950).
- [11] V.S. Grinberg and E.I. Sobko, Elektrichestvo 5 (1988) 42, in Russian; also in Electrical and Electronics Abstracts, Ref. 58808 (1988).
- [12] V.S. Grinberg, Izv. Vyssh. Uchebn. Zaved. Elektromekh 12 (1990) 68, in Russian; also in Electrical and Electronics Abstracts, Ref. 50893 (1991).



ELSEVIER

# First operation and perspectives of the superconducting linac LISA

M. Castellano <sup>a,\*</sup>, M. Ferrario <sup>a</sup>, M. Minestrini <sup>a</sup>, P. Patteri <sup>a</sup>, F. Tazzioli <sup>a</sup>, F. Cevenini <sup>b</sup>,  
L. Catani <sup>c</sup>

<sup>a</sup> INFN-Laboratori Nazionali di Frascati, C.P. 13, 00044 Frascati, Italy

<sup>b</sup> INFN-Sezione di Napoli and Dip. di Fisica, Università di Napoli, Pad 20 Mostra d'Oltremare, 80125 Napoli, Italy

<sup>c</sup> INFN-Sezione di Roma II, Via E. Carnevale, Roma, Italy

## 1. Introduction

The first operation of the whole superconducting (SC) linac LISA has been carried out in March 1994. The beam has been accelerated by the four SC cavities to 18 MeV. The macropulse was 1 ms long with a current of 0.5 mA. The FEL activity is now in stand-by, although both the undulator and the optical cavity are installed or ready for installation at LNF, due to the involvement of the group in the TESLA Test Facility program. In this framework LISA will be mainly used as a test machine for SC accelerator studies and for the development of sophisticated diagnostic tools, exploiting the long macropulse and high average current not far from the TTF design parameters.

In this paper we review the achievements of LISA which could be of interest to the FEL community since a number of choices in the machine design, namely in the injector, were dictated by the FEL requirements.

## 2. Machine performances

### 2.1. The injector

The injector of LISA is composed of a 100 kV DC thermionic gun [1], a double transverse chopper at 50 + 500 MHz, a 500 MHz prebuncher and a 1 MeV capture section. The choice of this rather standard configuration instead of an RF gun was taken to concentrate efforts on the SC linac avoiding further task in developing a new injector. Nevertheless, the design specification, dimensioned for a future CW operation of the machine, implied the construction of a powerful low emittance long macropulse 1 MeV injector.

The injector operation now fulfills average current specifications, providing a 2 ms long macropulse at 2 mA of average current. The beam emittance has been measured both on axis after the 1 MeV capture section and after the U-turn bringing the beam on the axis of the SC linac. The measured emittance in both planes was  $\epsilon < 6 \times 10^{-7}$ , corresponding to normalized emittance  $\epsilon_n < 2 \times 10^{-6}$  at a current of 2 mA. The beam current and emittance measured along the injector are shown in Fig. 1.

The 1 MeV current at the exit of the capture section is measured before any bending magnet, so it was not surprising that a fraction of out-of-phase accelerated electrons with energy different from the main beam, contributing to current at CM3, was lost in the U-turn and was therefore missing in CM4. However, attempts to improve the transport obtained 100% efficiency in some part of the macropulse and much lower in the remaining part, causing a triangular shape of the macropulse. This meant that a variation of parameters along the macropulse affected the capture efficiency and acceleration in the 1 MeV preaccelerator. The position of the transport efficiency peak was found depending on the phase of the prebuncher and on the gun HV. This indicated that voltage drop due to beam loading in the gun power supply allowed for an optimal matching of bunching parameters only for a few hundreds of microseconds; upgrading of the gun HV supply improved the transport efficiency to > 80% and provided a nearly rectangular pulse shape. The last step was the proper setting of the feedback to keep a stable phasing between input power to the capture section and beam; the feedback input is taken from the input power since a pick up sensing the field inside the cavity is not available, however this proved to work effectively raising the transport efficiency up to 100%; a typical shape of the correction signal applied to the phase shifter is shown in Fig. 2; the phase correction applied between the center and the end of the pulse is  $\sim 15^\circ$ .

When routine operation of the machine achieved these performances we were able to use the optical transition

\* Corresponding author. +39 69 40 32 10, fax +39 69 40 35 65.

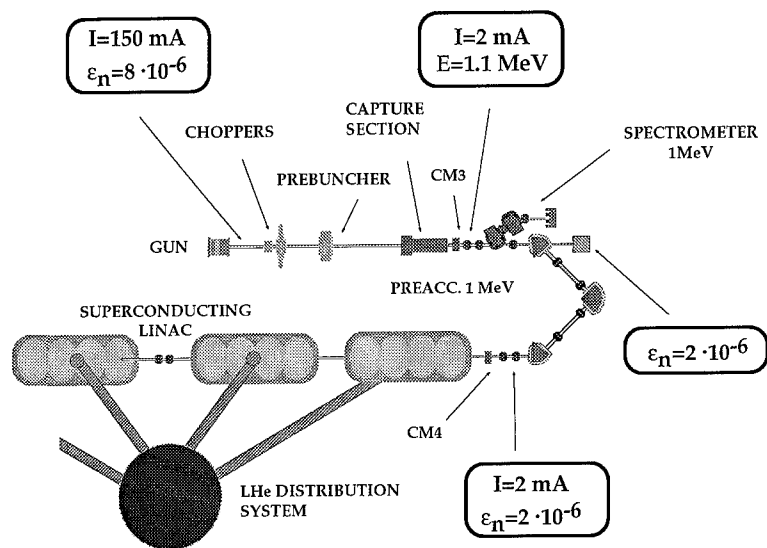


Fig. 1. Schematic layout of LISA.

radiation at 1 MeV to carry out systematic measurement of the beam size [2,3].

## 2.2. The superconducting linac

The operation of the superconducting cavities was obtained for the first time in November 1992. The LISA cavities are strongly coupled to the RF generator to accelerate a high average current in a long macropulse; tuning and locking the cavities within the narrow bandwidth  $\sim 200 \text{ Hz}$  is obtained with a fast electronic phase feedback and a slow mechanical tuning.

In order to reduce the thermal load to the refrigerator the rf power is pulsed. The repetition rate is usually 1 Hz, at a duty cycle  $\sim 2\%$  in beam operation mode, and 25% for conditioning. The pulses are added over a continuous low level drive signal, which helps keeping the tuning locked. A very slow frequency drift (about a few Hz/s) is observed if this feedback is turned off, allowing measurements of beam induced effects on a tuned but unpowered cavity.

The SC cavities were put in operation after a two years long inactivity and without a power conditioning at the construction site. The accelerating field was initially limited to  $< 3 \text{ MeV/m}$  by strong electron emission, evidenced by the intensity of X-rays outside the cavities, but after a few hours of RF conditioning the emission decreased and the cavities safely sustained fields of 4–4.5 MeV/m.

Although the large coupling factor to the generator makes the measurement of the quality factor  $Q_0$  rather cumbersome [4], systematic measurements showed that  $Q_0$  increased during the RF conditioning. Further improvement with respect to the first cooldown have been measured after the last two shifts of operation. This indicates that the best cleaning of the inner surface is not yet achieved; however the average accelerating field now exceeds the design value of 5 MeV/m and the  $Q_0$  vs  $E_{\text{acc}}$  behavior is better than those measured soon after the construction.

The beam transport and acceleration through the superconducting linac was readily obtained in November 1993 with only the first accelerating module powered. In two further shifts in March and May 1994 all the accelerating modules were put in operation simultaneously and phased

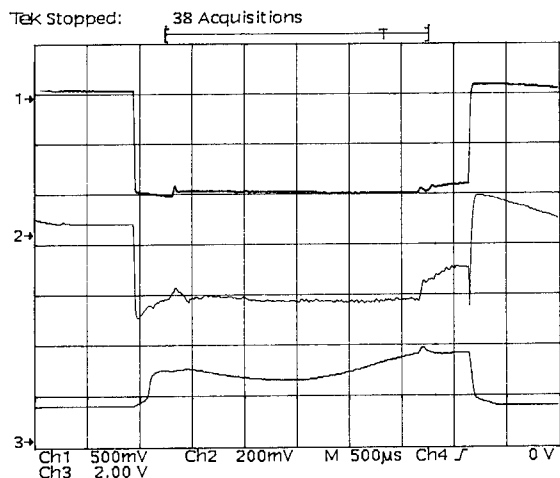


Fig. 2. Plots of the forward power (curve 1), reflected power (curve 2) and phase correction signal at  $15^\circ/\text{V}$  (curve 3) during the capture section rf pulse.

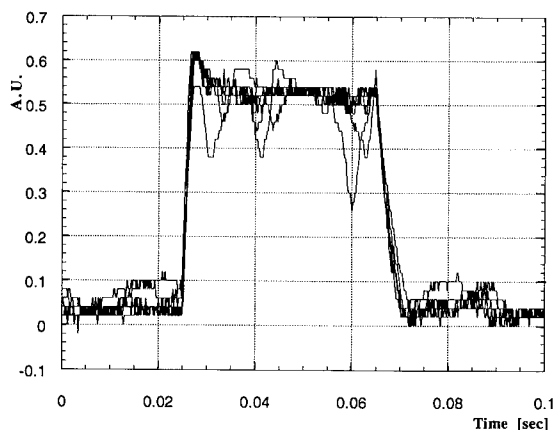


Fig. 3. RF level oscillation in a perturbed SC cavity.

for acceleration up to a final energy of 18 MeV. The beam transport efficiency from one module to the next was improved by maximizing the beam induced signal in the following unpowered module. An accelerated current of  $\sim 0.5$  mA was measured both by the resistive wall current monitor at the linac exit and by the field induced in the last cavity with no RF power input.

Optical and electrical measurement at the linac exit are now disturbed by a strong dark current coming from the last two cavities, which had a shorter conditioning time. This current has of course a much lower energy and a wider direction distribution with respect to the accelerated beam so that it is strongly affected by the focusing and steering elements at the SC linac exit. Measurements are made difficult both by the fluorescence light and the X-ray emission caused by the electrons impinging on the inner vacuum pipe; although a decrease of dark current emission has been already observed, more shieldings are planned to counteract this background.

The main limit to regular operation is the random onset of RF level oscillation, as shown in Fig. 3, apparently related to the average level of He pressure on the LHe bath. A measurement of the vibration spectra rejected the hypothesis of perturbations due to a thermoacoustic oscillation because no well defined line was found; moreover, no significant change of the spectrum was observed changing the length of some potentially resonating structures.

We suspect now that this effect is due to an unstable equilibrium of the cryogenic system as a whole, since this phenomenon, at the beginning apparently more frequent for the cavities 1 and 4, which are farthest from the LHe distribution valve box, showed in the following a tendency to flip randomly from outer to inner cavities. Further work is planned to study this effect more deeply.

### 3. Diagnostics upgrading

OTR based diagnostics will be extensively used at TTF both for high resolution beam profile and for time resolved measurements. The equipment to be used in the 500 MeV line of the TTF will be developed at LNF and previously tested both with LISA and with the 500 MeV injector for the storage ring Dafne. Two systems with design performances defined by different trade-offs between time and spatial resolution are under construction. The fastest diagnostic system is based on a  $16 \times 16$  multianode PMT, followed by a LeCroy FERA charge sensitive ADC system capable of observing the beam evolution during the macropulse at a sampling rate of 40 frame/ms. The slower will be based on a CCD linear array of  $\sim 1000$  pixels; it will provide a detailed section of the OTR emission integrated over a minimum time of  $\sim 50$   $\mu$ s; this performance will make the device useful for time resolved energy measurements at the spectrometer.

The PMT has been intended for high gain, low rate counting per pixel and its biasing is not suited to operation at high repetition rate for rather long time,  $\sim 1$  ms; this asks for a careful optimization of the illumination and gain to avoid exceeding the overall average current limit of 100  $\mu$ A. At such a low current in the maximum gate opening of 1  $\mu$ s the integrated charge per pixel, with a uniformly illuminated cathode, is  $\sim 1$  pC, corresponding to only 4 counts of the ADC. Since digitizing and readout last  $\sim 25$   $\mu$ s, the current at each anode is integrated on a capacitor during this period and the accumulated charge is then reversed, closing an analog switch, in the ADC input during the 1  $\mu$ s gate opening, exploiting at the best the whole dynamical range of the ADC.

Simple Monte Carlo simulations, taking into account any known noise source, have been carried out looking for the best trade-off between the wider field of view and beam position resolution. Assuming that the spot imaging on the PMT photocathode is done so that its  $\sigma$  corresponds to 2 pixels of the cathode grid, a resolution of  $0.01\sigma$  can be obtained for its center position.

### References

- [1] M. Castellano et al., Nucl. Instr. and Meth. A 332 (1993) 354.
- [2] M. Castellano et al., Beam diagnostics with OTR at the SC Linac LISA, presented at the 4th Europ. Particle Accelerator Conf., London, 27/6–1/7 1994.
- [3] M. Castellano et al., Analysis of optical transition radiation emitted by a 1 MeV beam and its possible use as diagnostic tool, to be published in Nucl. Instr. and Meth.
- [4] M. Castellano et al., Nucl. Instr. and Meth. A 332 (1993) 347.



ELSEVIER

# Giant laser pulses in the Duke storage ring UV FEL ☆

V.N. Litvinenko \*, B. Burnham, J.M.J. Madey, Y. Wu

Duke University Free Electron Laser Laboratory, P.O. Box 90319, Duke University, Durham, NC 27708-0319, USA

## Abstract

We have studied the dynamics of giant pulse generation in the Duke UV FEL with peak power of several gigawatts. The giant pulses will be provided by a FEL gain modulation technique developed for the OK-4 UV FEL at Novosibirsk, Russia. A new mechanism for “super-pulse” generation was discovered during these studies. It allows the generation of peak power up to 10 GW using the “phase space” refreshment of the electron beam caused by synchrotron motion [V. Litvinenko et al., to be published]. We have developed a new macro-particle code for giant pulse simulation including all known mechanisms of storage ring FEL interaction. Results of these giant pulse simulations are presented in the paper.

## 1. Introduction

The CW output of short wavelength storage ring FELs is limited by the energy spread growth of the electron beam due to its interaction with the FEL optical field [2]. Nevertheless, this power can be redistributed in time using a Q-switch technique [3] or gain modulation technique [4] to generate giant pulses with 0.1 to 1 GW level of power. The previous projections for the average and peak power performance of the OK-4 FEL, which will be shipped from the Novosibirsk Institute of Nuclear Physics to Duke in January 1995, have been published elsewhere [5].

To test our expectations we have developed a computer program which includes all known phenomena affecting storage ring FEL performance. The theory of storage ring FEL operation implemented in this program is published in these Proceedings [6]. In this paper we present a description of the code and summary of results for the OK-4/Duke UV/VUV FEL achieved using this code. During the study we discovered new phenomena – super pulses with ten to thirty times higher peak power than giant pulses. The theory of these phenomena and the main results on super pulses are presented in Ref. [1].

## 2. Computer model

We have developed a set of computer programs which include all known phenomena influencing operation of

short-wavelength storage ring FELs (SRFEL). The high efficiency algorithms used in the code allow us to track up to 30 000 macro-particles for tens of thousands turns to simulate real-time self-consistent SRFEL operation. A detailed description of the codes is published elsewhere [7]. The model we use here simulates an optical klystron with total length  $2L$  comprised of two planar undulators (each with  $N_u$  periods of  $\lambda_u$  and undulator parameter of  $K_u$ ) and a buncher occupying a length from  $-z_i$  to  $z_i$  [6]. The strength of the buncher can be adjusted to optimize FEL operation. With the buncher turned off the system becomes a conventional FEL.

**Macro-particles.** A macro-particle is described by its energy  $\varepsilon = (E - E_0)/E_0$  and longitudinal position  $s = ct_0$ , where  $t_0$  is the electron arrival time at  $z = 0$ . It represents a cluster of electrons localized in  $(\varepsilon, s)$  phase-space and having standard distribution in transverse phase space. As was shown in Ref. [6], radiation of the macro-particle can be found analytically. This analytical capability makes these simulations possible. The maximum number of macro-particles in the program is 30 000.

**Optical Wavepacket.** We represent the FEL optical field,  $E$ , by a  $TEM_{00}$  mode with slowly varying complex amplitude  $A_0(s)$ .

$$E_0(t, r) = \text{Re} \left\{ \hat{e}_x A_0(s) \frac{\beta_0}{\beta_0 - iz} \exp \left[ iks - \frac{k}{2} \frac{x^2 + y^2}{\beta_0 - iz} \right] \right\}, \quad (1)$$

where  $s = cl - z$  and  $c$  is the speed of light. The Rayleigh length is  $\beta_0$  with waist at azimuth  $z = 0$ ;  $x$  and  $y$  are transverse coordinates and  $k = 2\pi/\lambda$  is the optical wave vector. An optical wave packet is represented by an array (with maximum length of 30 000) of complex wave amplitude  $A[i]$ . The length of one array bin is equal to the total

☆ Work supported by Office of Naval Research Grant #N00014-94-C0818 and Air Force Office of Scientific Research Grant #F49620-93-1-0590.

\* Corresponding author. Tel. +1 919 660 2658, fax +1 919 660 2671, e-mail vl@phy.duke.edu.



slippage in the FEL  $\Sigma_i = \Sigma(L) - \Sigma(-L)$  (see Eq. (3)). This choice limits wavelength bandwidth to  $\Delta k \sim l/\Sigma_i$ . This bandwidth is sufficient to include full width of the FEL gain profile. The program includes the energy detuning parameter which is set to the maximum gain.

**FEL parameters.** We use two complex arrays to represent individual macroparticle induced radiation. It is a well known that the induced radiation (both real and imaginary part of it) is shifted with respect to the optical wavepacket. This effect is essential for optical pulse evolution because it influences the super-mode structure [8]. This shift depends on electron energy. To properly model slippage of induced radiation, we used (in addition to the average value of real and imaginary part of the gain) the first moments of the real and imaginary parts of the gain:

$$G_m = \int_{\Sigma(-L)}^{\Sigma(L)} s A_{\text{ind}}(s) ds,$$

$$A_{\text{ind}}(s_0 + \Sigma(z))$$

$$= -i \frac{k}{E_0 \beta_0} \left( \frac{eK_u J J}{2\gamma} \right)^2 \left( \frac{d\Sigma}{dz} \right)^{-1} \int_{-L}^z dz_1$$

$$\times A_0(s_0 + \Sigma(z_1)) (\Sigma(z) - \Sigma(z_1))$$

$$\times \text{FF}(z, z_1) e^{i(k_u(z-z_1) - k(\Sigma(z) - \Sigma(z_1)))}, \quad (2)$$

where  $\Sigma(z)$  is the FEL slippage function:

$$\Sigma(z) = z \frac{1 + K_u^2/2}{2\gamma^2} \left\{ \begin{array}{l} - \\ + \end{array} \right\} \frac{\Delta s_B}{2} \left( \frac{\gamma_0}{\gamma} \right)^2 \left\{ \begin{array}{l} z < -z_i \\ z > z_i \end{array} \right\}, \quad (3)$$

and  $\Delta s_B$  is the slippage in the buncher. The function  $\text{FF}(z_1, z_2)$  is a complex function derived analytically which takes into account the influence of both horizontal and vertical e-beam emittances and the  $\text{TEM}_{00}$  mode structure [6,10].

The spontaneous radiation is represented by an array with exact values of the radiation amplitude into one bin which is multiplied by the square root of the number of electrons in the macro-particle. We use the exact analytical expressions for spontaneous radiation into the  $\text{TEM}_{00}$  mode, including energy dependence and e-beam emittance [6]:

$$|A_{\text{sp}}|^2 = \frac{2k}{\beta_0} \left( \frac{eK_u J J}{\gamma_0} \right)^2 \int_{-L}^L \int_{-L}^L dz_1 dz_2$$

$$\times \text{FF}(z_1, z_2) e^{i(k(\Sigma(z_1) - \Sigma(z_2)) - k_u(z_1 - z_2))}, \quad (4)$$

where  $k_u = 2\pi/\lambda_u$ . Before adding this expression to the wavepacket, the amplitude of the spontaneous radiation is multiplied by a random number with unit RMS value and complex exponent with random phase. A very similar algorithm is used for the random energy kick caused by the FEL interaction. This energy kick is represented by an array of exact RMS kick values. The amplitude of the kick

depends on the amplitude of the local optical field (see Ref. [6]) and is random in phase:

$$\langle \Delta E^2 \rangle = \frac{1}{2} \left( \frac{eK_u J J}{2\gamma_0} \right)^2 |A_0|^2 \int_{-L}^L \int_{-L}^L dz_1 dz_2$$

$$\times \text{FF}(z_1, z_2) e^{i(k(\Sigma(z_1) - \Sigma(z_2)) - k_u(z_1 - z_2))}. \quad (5)$$

Each of the arrays described above contains 10001 values for a 4% energy deviation range with a step of  $\delta\gamma/\gamma = 4 \times 10^{-6}$ . In order to optimize the FEL performance we provide the capability to interactively change slippage in the buncher and energy detuning. For a chosen FEL geometry, wavelength, and central electron energy, a special program tabulates one real and eight complex double integrals [10] required for the four arrays described above as functions of electron energy, with an energy step of  $4 \times 10^{-6}$ . These integral data are saved in a file. These integral calculations take about one hour of CPU time on a SPARC workstation. The main program reads this file and produces in a few seconds all of the necessary arrays for chosen slippage of the buncher, and recommends the optimum energy detuning parameter.

The main program is composed of four main subroutines:

**FelCoefficients** – Reads tabulated integrals and calculates arrays of real and imaginary values of macro-particle gain and moments. It also recommends the optimum value of energy detuning.

**RingPass** – Includes the exact algorithm for round trip pass of the macro-particle around the storage ring described in Ref. [9].

**FelInteraction** – The main part of the code. It finds the two wavepacket bins the particle is interacting with and calculates the wavepacket optical field using the linear (small signal) approximation. It also calculates the energy bin corresponding to the instantaneous value of the macro-particle energy (including energy detuning). Next it adds the spontaneous radiation (from the proper energy bin) into the wavepacket bins proportional to their overlap (see Fig. 1). The induced radiation is calculated (from the proper energy bin  $\varepsilon$  – bin) using the complex gain  $g_{\text{av}}$ , its first moment  $g_{\text{mom}}$ , and optical wave amplitude  $A_0$ :

$$A_0 = A[i](1 - X) + A[i + 1]X,$$

$$A[i] = A[i] + A_0(1 - X) \{ g_{\text{av}}[e_{\text{bin}}] - g_{\text{mom}}[e_{\text{bin}}] X \},$$

$$A[i + 1] = A[i + 1] + A_0 X \{ g_{\text{av}}[e_{\text{bin}}]$$

$$+ g_{\text{mom}}[e_{\text{bin}}] (1 - X) \}, \quad (8)$$

where  $X$  is the overlap of macro-particle radiation and wave-packet bins (see Fig. 1). Finally, the program varies the electron energy using the energy kick array, optical wave amplitude, and random phase.

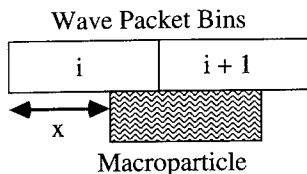


Fig. 1. Optical wave and electron bin overlap.

*CavityPass* – implements exact transformation as described by:

$$A_{n+1}(s) = \sqrt{R} A_n(s - d), \quad (9)$$

where  $R$  is the round trip reflectivity and  $d$  is the detuning of the optical cavity. It accumulates the total value of the detuning from pass to pass and moves the wavepacket array only for the integer part of accumulated detuning. It passes the non-integer part into the *FelInteraction* subroutine. There it is taken into account in the bin search and interaction. The algorithm is described in Ref. [7]. Additional subroutines provide file service and interactive mode of operation. Some of the FEL parameters are used by the program to tabulate integrals. Other parameters in the code can be changed interactively without the one hour delay for tabulation of integrals. While interactive operation complicates the tabulation program (nine integrals instead of three), it gives the very important advantage of flexibility and speed.

### 3. Results of giant pulse simulations

Using the codes described above, we studied laser pulse and e-beam dynamics of the OK-4/Duke UV FEL in Giant pulse mode in the deep UV and VUV range. The parameters of electron beam and layout of the storage ring and OK-4 UV/VUV FEL are published in Refs. [6,11]. We assume an e-beam current of 10 to 100 mA average current (typical value 46 mA) and 10–100 A peak current.

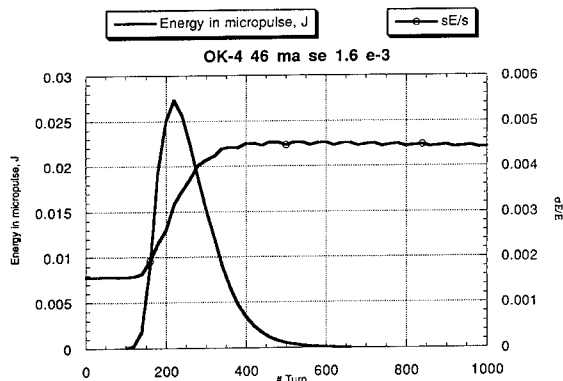


Fig. 2. OK-4 FEL optical micropulse energy and e-beam energy spread evolution during a giant pulse.

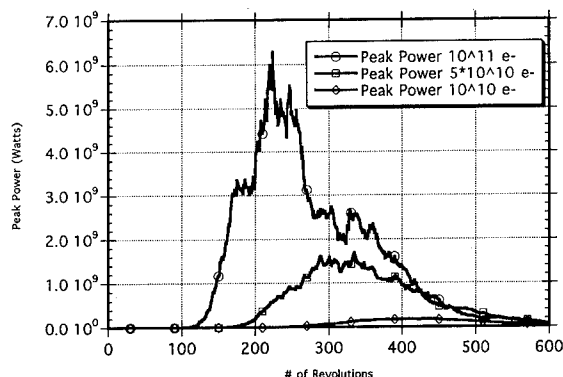
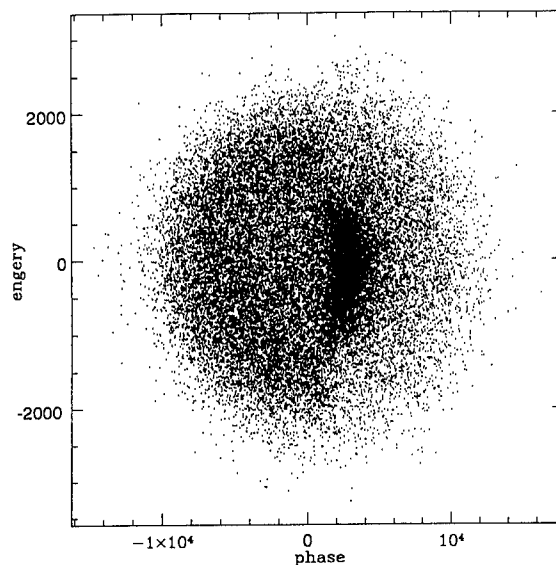


Fig. 3. Peak power in OK-4 FEL at 200 nm for different beam currents (4.6, 23 and 46 mA).

Giant pulse mode in the OK-4/Duke FEL will be realized using gain modulation [4]. The electron beam will be displaced by a special deflector from the axis of the optical cavity to reduce FEL gain below cavity losses. The cooled beam, with energy spread defined by microwave instabilities (see Ref. [6]), will return back to the axis during 50 to 100 e-beam revolutions to ensure adiabatic transition of the closed orbit and absence of residual betatron oscillations. Thus, the FEL will start from noise and the laser power will grow exponentially until it starts to heat the beam. As the energy spread grows, the FEL gain decreases. Maximum power will be reached when FEL net gain is zero. The heated e-beam will be deflected from the axis for 2–4 damping times (15–30 ms for 1 GeV operation) to be cooled. The giant pulse may then be repeated.

Fig. 4. Poincare ( $E, s$ ) phase-space plot for super pulse mode of the OK-4 FEL.

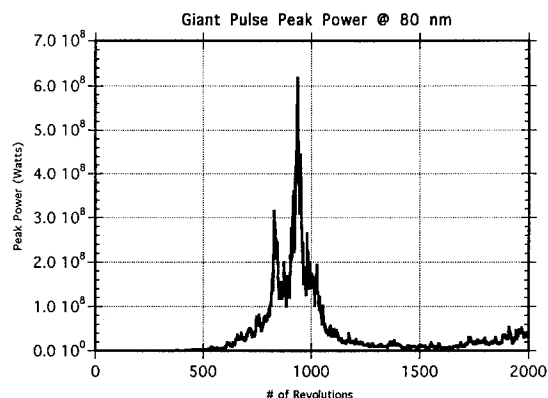


Fig. 5. OK-4 FEL optical micropulse energy at 80 nm.

A typical giant pulse shape for the OK-4/Duke FEL operating at 46 mA ( $10^{11}$  electrons) at 200 nm is shown in Fig. 2. Fig. 3 shows the optical peak for the same beam parameters in the super pulse regime [1]. A typical Poincare plot for this mode of operation is shown in Fig. 4. While the energy in the micropulse in these simulations corresponds to earlier theoretical predictions [5], the peak power is 10 times higher than expected. This fascinating discrepancy is caused by the “super pulse” phenomena [1] and can be exploited for production of very short pulses with exceptionally high peak power.

With more ambitious, but achievable, parameters of electron beam (average current of 92 mA and 1.5 MV RF voltage) the OK-4 can operate in the VUV range at 80 nm. The regular optical cavity must be replaced with a multifacet ring resonator [12]. Fig. 5 shows the OK-4 giant pulse at 80 nm with 14% roundtrip losses in the optical resonator.

We also observed influence of optical cavity detuning on the optical pulse shape and its relative position with respect to the electron bunch.

#### 4. Conclusions

Simulations of giant pulses by a self-consistent storage ring FEL code have confirmed our general projections for the performance of the OK-4 FEL installed on the Duke

Storage Ring. In addition, the new phenomena of super pulses generation was discovered using this code and then explained [1]. Super pulse mode of storage ring operation allows the achievement of 10 to 30 times higher peak power than was predicted by standard models [2].

We plan to continue simulations and improve the code. Improvements of the code will include nonlinear FEL effects, harmonic generation, multiple transverse modes, and intracavity etalons.

#### References

- [1] V. Litvinenko, B. Burnham, J.M.J. Madey and Y. Wu, Super pulses in storage ring FELs, submitted to Phys. Rev. Lett.
- [2] N.A. Vinokurov and A.N. Skrinsky, Preprint INP 77-67, Novosibirsk (1977);  
A. Renieri, Nuovo Cimento B 53 (1979) 160.
- [3] P. Elleaume, Thesis, Universite Paris, Sud (1984);  
M. Billardon et al., Nucl. Instr. and Meth. A 237 (1985) 38;
- [4] V.N. Litvinenko, The optical klystron on VEPP-3 storage ring bypass – lasing in the visible and the ultraviolet, Ph.D., Novosibirsk (1989);  
I.B. Droblyazko et al., Nucl. Instr. and Meth. A 282 (1989) 424.
- [5] V. Litvinenko et al., SPIE Vol. 1552 (1991) 2;  
V. Litvinenko, J.M.J. Madey and N.A. Vinokurov, IEEE PAC 1993, vol 2, p. 1442.
- [6] V. Litvinenko, B. Burnham, J.M.J. Madey and Y. Wu, these Proceedings (16th Int. Free Electron Laser Conf., Stanford, CA, USA, 1994) Nucl. Instr. and Meth. A 358 (1995) 334.
- [7] V. Litvinenko, DFELL report (1994).
- [8] G. Dattoli et al., IEEE J. Quantum Electron. QE-17 (1981) 1371.
- [9] V. Litvinenko, Y. Wu, B. Burnham, G. Barnett and J.M.J. Madey, these Proceedings (16th Int. Free Electron Laser Conf., Stanford, CA, USA, 1994) Nucl. Instr. and Meth. A 345.
- [10] V. Litvinenko, Proc. Nat. Synchrotron Radiation Conf. SR-94, Novosibirsk, July 11–15, 1994, to be published in Nucl. Instr. and Meth.;  
V. Litvinenko, Analytical derivation of 3D FEL time-dependent (complex) gain matrix and spontaneous radiation, to be published.
- [11] Y. Wu et al., Nucl. Instr. and Meth. A 331 (1993) 287;  
Y. Wu et al., IEEE PAC 1993, vol. 1, p. 218.
- [12] B.E. Newnam, SPIE 1227 (1990) 116.

# Theory of the longitudinal dynamics of a storage ring FEL

G. Dattoli \*, L. Giannessi, A. Renieri

*ENEA, Dipartimento Innovazione, Settore Fisica Applicata, Centro Ricerche Frascati, C.P. 65, 00044 Frascati, Rome, Italy*

## Abstract

The longitudinal dynamics of an electron beam circulating in a storage ring and undergoing a FEL interaction is discussed with specific reference to the low gain amplifier case. We exploit the Fokker–Planck equation and analyze the multipolar components of the longitudinal electron motion. One of the major achievements of the analysis is relevant to the longitudinal damping time, which is shown to be interaction dependent, i.e. a function of the FEL detuning parameter and laser intensity.

## 1. Introduction

The operation of a free electron laser (FEL) in a storage ring (SR) strongly modifies the electron beam dynamics. The main effects are [1]:

- i) particle energy variation (gain or loss depending on the phase of the laser field at the time entrance of the electron into the undulator),
- ii) betatron oscillations induced by the jumps between different off-energy closed orbits due to the particle energy variation,
- iii) transverse momentum excitation due to the non-collinear photon absorption or emission process.

Effect iii) can be neglected because, usually, the laser field along the interaction region can be well approximated by a plane wave for TEM<sub>00</sub> operation. Effect ii) can be minimized by a correct choice of the lattice parameters (dispersion free insertion). Effect i) is the more important one and it drives the operating behaviour of a FEL in a SR. Namely the electron energy variation depends critically on a single parameter (the laser field phase at the electron time entrance into the undulator magnet (UM)) which varies in random-like way turn by turn (see Appendix B in the first of refs. [1]). The mean value of the energy variation (averaged over all the phases) accounts for the FEL gain (or losses) and is a function of the electron energy (and of laser and UM parameters), while the random-like component of the energy variation is responsible for the electron beam energy broadening (heating). The saturation process limiting the performances of a storage ring FEL arises just from the competition between this heating and the longitudinal damping due to synchrotron radiation emission. The damping time is also affected by

the FEL interaction [2], but, due to the non-linear dependence of the energy variation on the electron energy, there is not simply a shift of the single particle damping time, but a more complex variation of the collective oscillation mode (dipole, quadrupole, hexapole, etc.) damping times.

## 2. Longitudinal distribution function evolution

In this paper we analyse the damping time modifications due to the FEL interaction in the amplifier case (cw laser field, linearly polarized UM, low gain and low signal regime) under the hypothesis of no electron bunch anomalous lengthening (no microwave instability [3]). In this simple configuration the electron longitudinal distribution function evolution follows a Fokker–Planck equation (FPE), which can be written in the form [1]

$$\frac{\partial f}{\partial t} = \omega_s \left( \frac{c a_c}{\omega_s} \epsilon \frac{\partial f}{\partial z} - \frac{\omega_s}{c a_c} z \frac{\partial f}{\partial \epsilon} \right) + \frac{1}{T} \frac{\partial}{\partial \epsilon} \left( 2 \frac{T}{\tau} \epsilon f + \left( DT + \frac{\langle \delta \epsilon^2 \rangle}{2} \right) \frac{\partial f}{\partial \epsilon} \right) \quad (1)$$

(for the symbols see Table 1).

When the laser is off ( $\langle \delta \epsilon^2 \rangle = 0$ ), Eq. (1) becomes the usual FPE for the SR synchrotron motion and the stationary solution writes

$$f_0(z, \epsilon) = \left( \frac{1}{2\pi\sigma_z\sigma_\epsilon} \right) \exp \left( -\frac{1}{2} \left( \left( \frac{z}{\sigma_z} \right)^2 + \left( \frac{\epsilon}{\sigma_\epsilon} \right)^2 \right) \right), \quad (2)$$

where we have defined the unperturbed r.m.s. energy spread  $\sigma_\epsilon$  and bunch length  $\sigma_z$ :

$$\sigma_\epsilon = \left( \frac{D\tau}{2} \right)^{1/2}, \quad \sigma_z = \left( \frac{c a_c}{\omega_s} \right) \sigma_\epsilon. \quad (3)$$

\* Corresponding author. Tel. +39 6 94001, fax +39 6 9400 5334.

Table 1  
List of the symbols

|                                     |   |
|-------------------------------------|---|
| $f(z, \epsilon; t)$                 | longitudinal electron distribution  |
| $z$                                 | longitudinal displacement of the particle from the synchronous one  |
| $\epsilon$                          | $= (E - E_0)/E_0$ ( $E$ = particle energy, $E_0$ = synchronous energy)                                    |
| $\omega_s$                          | synchrotron frequency   |
| $a_c$                               | momentum compaction   |
| $T$                                 | revolution period   |
| $\tau$                              | longitudinal radiation damping time   |
| $D$                                 | radiation noise diffusion coefficient   |
| $\langle \delta \epsilon^2 \rangle$ | “FEL noise” $= AG(2(\epsilon + \epsilon_0)/(\Delta \omega/\omega)_0), G(x) = (\sin(\pi x/2)/(\pi x/2))^2$ |
| $A$                                 | $= (2\pi r_0/m_0 c^3) \lambda^2 (\Delta \omega/\omega)_0^{-3} K^2/(1 + K^2)^2 JJ^2 I$                     |
| $JJ$                                | $= J_0(\xi) - J_1(\xi), J_n = n$ -th Bessel function, $\xi = K^2/(1 + K^2)$                               |
| $I$                                 | laser power density   |
| $(\Delta \omega/\omega)_0$          | $= 1/(2N)$ homogeneous linewidth, $N$ = number of UM periods  |
| $\epsilon_0$                        | $= (E_0 - E_R)/E_0$   |
| $E_R$                               | $= m_0 c^2 (\lambda_U (1 + K^2)/(2\lambda))^{1/2} = \text{FEL “resonant energy”}$                         |
| $\lambda$                           | laser radiation wavelength  |
| $\lambda_U$                         | UM period   |
| $K$                                 | $= eB\lambda_U/(2\pi m_0 c^2), B = \text{r.m.s. UM magnetic field}$                                       |
| $m_0$                               | rest electron mass  |
| $c$                                 | light velocity in vacuum  |
| $r_0$                               | classical electron radius   |

When the FEL interaction is on, the equilibrium longitudinal distribution is no longer Gaussian and synchrotron frequency and damping time change. In order to analyse this problem, it is convenient to expand the distribution function in terms of Hermite polynomials:

$$f(z, \epsilon; t) = \frac{\exp\left(-\frac{1}{2}\left(\left(\frac{z}{\sigma_z}\right)^2 + \left(\frac{\epsilon}{\sigma_\epsilon}\right)^2\right)\right)}{2\pi\sigma_z\sigma_\epsilon} \times \sum_{n=0}^{\infty} \sum_{m=0}^n h_{n,m}(t) He_{n-m}(z/\sigma_z) He_m(\epsilon/\sigma_\epsilon). \quad (4)$$

By taking into account the properties of the Hermite polynomials, we derive from Eq. (1) the motion equations for the amplitudes  $h_{n,m}(t)$ , ( $n = 0, 1, 2, \dots, m = 0, 1, 2, \dots, n$ ;  $h_{i,j} = 0$  if  $j > i$  or  $i < 0$  or  $j < 0$ ):

$$\frac{1}{\omega_s} h'_{n,m} = (m+1)h_{n,m+1}(n-m+1)h_{n,m-1} - \left(\frac{2m}{\omega_s \tau}\right) h_{n,m} + \left(\frac{2W}{\omega_s \tau}\right) \sum_{r=0}^{\infty} G_{r,m}(\mu_\epsilon, y_0) h_{n-m+r,r}, \quad (5)$$

where the coefficients  $G_{r,m}$  read

$$G_{r,m}(\mu_\epsilon, y_0) = \frac{1}{(m-1)!} \frac{1}{\sqrt{2\pi}} \int_{-\infty}^{+\infty} dy G\left(\frac{y+y_0}{\mu_\epsilon}\right) \times \exp\left(-\frac{y^2}{2}\right) He_{r+1}(y) He_{m-1}(y) \quad (6)$$

and we defined  $W = A(1/(4\sigma_\epsilon^2))(\tau/T)$  is the normalized laser power,  $\mu_\epsilon = 2\sigma_\epsilon/(\Delta\omega/\omega)_0$  is the inhomogeneous broadening parameter,  $y_0 = \epsilon_0/\sigma_\epsilon$  is the detuning parameter, and finally, the prime indicates the derivative with respect to the time.

The amplitudes  $h_{n,m}(t)$  ( $n = 0, 1, 2, \dots$ ;  $m = 0, 1, 2, \dots, n$ ) account for the multipole oscillation modes. Namely, for  $n = 1$  ( $h_{1,0}, h_{1,1}$ ) we have the dipole mode, for  $n = 2$  ( $h_{2,0}, h_{2,1}, h_{2,2}$ ) the quadrupole mode, and so on. Finally the term  $h_{0,0}$  is a constant of motion ( $h'_{0,0} = 0$ ) and, for normalization purposes, we assume

$$h_{0,0} = 1. \quad (7)$$

When the FEL interaction is off (i.e.  $W = 0$ ), Eqs. (5) couple coefficients  $h_{n,m}$  having the same index  $n$ , i.e. different oscillation modes are decoupled. In this condition it is quite easy to derive the normal mode frequencies as the eigenvalues of the  $2 \times 2, 3 \times 3, \dots, n \times n, \dots$ , transport matrices relevant to each mode [4]. The damping time of the  $n$ th oscillation mode is the same for all the  $n$  eigenmodes belonging to this mode and reads

$$\text{damping time} = \tau/n \quad (8)$$

while the oscillation frequencies are a multiple of the fundamental (with the same parity of the mode number  $n$ ) and read

$$\text{oscillation frequency} = m\omega_s \left(1 - \frac{1}{(\omega_s \tau)^2}\right)^{1/2}, \quad (9)$$

with  $0 \leq m \leq n$  and  $m$  has the same parity as  $n$ .

When the FEL interaction is on, all the modes interact with each other and no simple solutions are available. In the next section we will show some numerical results, which indicates that, depending on the operating point, the FEL interaction can enhance (or depress) the longitudinal damping in a relevant way.

### 3. Numerical results

The presence of the FEL interaction modifies the unperturbed mode evolution of the longitudinal distribution. The damping times of the oscillation modes become a function of the laser intensity and of the detuning parameter and the beam reaches a new stationary configuration different from that reported in Eq. (2). The dependence of damping times on laser intensity ( $W$ ) and detuning parameter ( $y_0$ ) is presented in Figs. 1 and 2, where it is shown

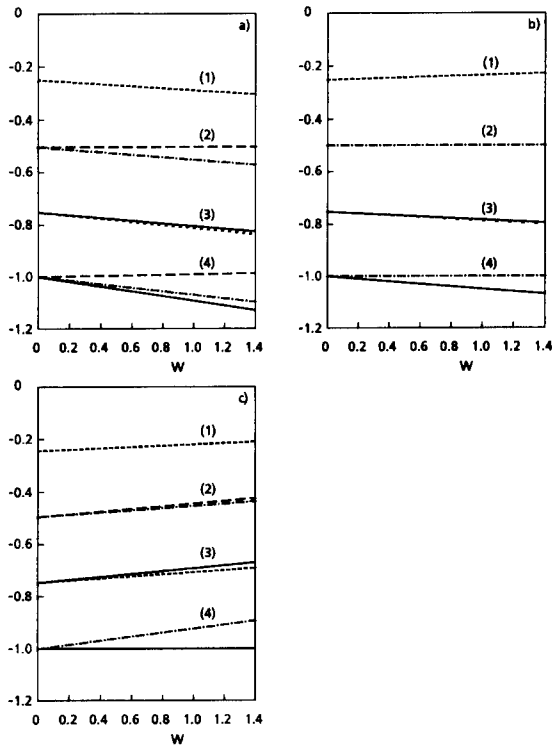


Fig. 1. Real part of the eigenvalues of the dipole (1), quadrupole (2), sextupole (3) and octupole (4) modes as a function of  $W$  for  $\mu_e = 1$ ,  $\omega_s \tau = 4$ , and  $y_0 = 0$  (a), 1.3 (b), 2.6 (c).

that the real part of the mode eigenvalues (which is proportional to the inverse of the damping time) increases or decreases almost linearly with  $W$ , depending on  $y_0$ . Around zero detuning (zero gain value,  $y_0 = 0$ ) the real part of the eigenvalues tend to increase (in absolute value) with increasing  $W$ . This means that the damping time decreases and the beam cooling mechanism is more effi-

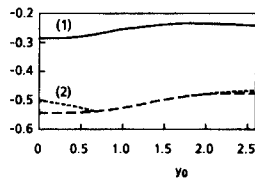


Fig. 2. Real part of the eigenvalues of the dipole (1) and quadrupole (2) modes as a function of  $y_0$  for  $\mu_e = 1$ ,  $\omega_s \tau = 4$  and  $W = 0.8$ .

cient. The situation changes around the maximum gain ( $y_0 = 2.6$ ), where there is a small increasing in the damping time.

#### 4. Conclusions

The analysis presented in this paper is a further step toward the understanding of the SR longitudinal dynamics when the FEL interaction is on. The observed damping enhancement (for some  $y_0$  values) could explain the experimental evidence of some beneficial effects, like bunch cooling and shortening, on anomalous bunch lengthening when a FEL is operating in a SR [5,6]. Namely stronger damping can up-shift the threshold of microwave instability and then a bunch shortening can be observed. A consistent treatment of FEL dynamics and microwave instability could be performed by using again the FPE formalism [7] and it will be exploited in forthcoming papers. We must underline, finally, that the already quoted effects on transverse motion (and transverse damping) require a careful further investigation. In particular it must be investigated if damping partition numbers (Robinson's theorem [8]) are affected by FEL interaction.

#### References

- [1] A. Renieri, *Nuovo Cimento B* 53 (1979) 160;  
G. Dattoli and A. Renieri, *Nuovo Cimento B* 59 (1980) 1.
- [2] M. Sands, *Storage Ring Laser*, ADONE Internal Report T-73, LNF CNEN (Frascati, Italy, 1975);  
See also: L.R. Elias, J.M.J. Madey and T.I. Smith, *Appl. Phys.* 23 (1980) 273.
- [3] A.W. Chao and J. Gareyte, *Scaling Law for Bunch Lengthening in SPEAR II*, SPEAR-197, PEP-224, Stanford Linear Accelerator Center (1976).
- [4] G. Dattoli, L. Giannessi and A. Renieri, *Storage Ring FEL Longitudinal Dynamics*, RT-ENEA 94/23 (Frascati, Italy, 1994), to be published.
- [5] K.E. Robinson, J.M.J. Madey, M.F. Velghe and D.A.G. Deacon, *IEEE Trans. Nucl. Sci.* NS-30 (1983) 3088.
- [6] M.E. Couprie, D. Garzella, A. Delboulbi, M. Velghe and M. Billardon, *Nucl. Instr. and Meth. A* 331 (1993) 84.
- [7] A. Renieri, *Turbulence and Bunch Lengthening in Electron-Positron Storage Rings*, LNF-75/11(R), Laboratori Nazionali di Frascati del CNEN, Frascati (1976).
- [8] K. Robinson, *Phys. Rev.* 111 (1958) 373.

## Dynamic behavior of the Super-ACO FEL micropulse

T. Hara <sup>a,b,\*</sup>, M.E. Couprie <sup>a,b</sup>, A. Delboulbé <sup>a</sup>, D. Garzella <sup>a</sup>, L. Nahon <sup>a,b</sup>, M. Billardon <sup>a,c</sup>

<sup>a</sup> *Laboratoire pour l'Utilisation du Rayonnement Electromagnétique, Bât. 209D, Université de Paris-Sud, 91405 Orsay, France*

<sup>b</sup> *CEA / DSM / DRECAM / SPAM, Saclay, 91191 Gif-sur-Yvette, France*

<sup>c</sup> *ESPCI, 10 rue Vauquelin, 75231 Paris, France*

### Abstract

Recently, we have conducted temporal and spectral studies of the Super-ACO FEL micropulse. These studies are indispensable to supply a stable and well characterized light source for application experiments. The result of the temporal study has already been presented. In this paper, we present the spectral features of the FEL micropulse, including spectral widths, spectral evolution and the relation between temporal width and spectral width of the laser micropulse.

### 1. Introduction

The Super-ACO Free Electron Laser (FEL) is operated at 350 nm and this UV light has been used for application experiments, such as a time resolved fluorescence experiment in biology [1] and two color experiments (FEL + synchrotron radiation), since last year. For the applications, the temporal and spectral features of the laser should be stable, but the behavior of a storage ring FEL is complex, because the same electron bunches are circulated in the ring and reused during the FEL operation, so the performance of the storage ring affects seriously the stability of the laser. For the purpose of supplying a stable light source for the applications, we have studied the dynamic behaviors of the FEL from the temporal and the spectral points of view [2]. These studies are essential for characterization and improvement of the laser light using a longitudinal feedback system [3] or an intra-cavity Fabry–Perot etalon.

The temporal features of the laser micropulse have already been studied using a streak camera and a dissector, which is a stroboscopic picosecond detector [4,5]. The laser micropulse observed with the streak camera sometimes deviates from a Gaussian. This could not be observed by the dissector, since the dissector samples over thousands of micropulses to finish tracing one temporal distribution, and the micropulse shape changes so rapidly. The observation with the streak camera reveals that two or three peaks can be in one micropulse of the laser. A longitudinal jitter of the laser micropulse is observed particularly in the central zone 3 (see below). These phenom-

ena (micropulse deformation and longitudinal jitter) seem to be stabilized with a *Q*-switched operation.

The spectral features are studied with a scanning Fabry–Perot. This device can survey a spectrum in milliseconds with high enough resolution, and we can investigate the dynamic spectral behavior of the laser micropulse. Furthermore, the scanning Fabry–Perot can work in synchronization with the dissector, and thus simultaneous spectral and temporal measurements of the laser micropulse are also possible.

### 2. Operational zones of the Super-ACO FEL

Fig. 1 illustrates the laser behavior as function of the detuning between the positron bunch circulating in the storage ring and the laser micropulse for the case of the Super-ACO FEL. We can distinguish five operational zones depending on the detuning condition.

In zone 3, the micropulse and the positron bunch are perfectly synchronized and the laser has a cw macrotemporal structure at the millisecond time scale.

If we detune the micropulse of the laser and the positron bunch slightly by changing either the optical cavity length or the frequency of the RF cavity of the storage ring, the laser macrotemporal structure becomes pulsed in zones 2 and 4 typically with the period of 3 ms, which is derived from a laser rise time and a damping time of the storage ring.

The macrotemporal structure comes back to cw for larger detuning in zones 1 and 5.

The laser micropulse at the time scale of picoseconds, which comes from the pulsed structure of the positron bunches in the storage ring, has the maximum intensity

\* Corresponding author. Tel. +33 1 6446 8028, fax +33 1 6446 4148, e-mail [hara@lure.u-psud.fr](mailto:hara@lure.u-psud.fr).

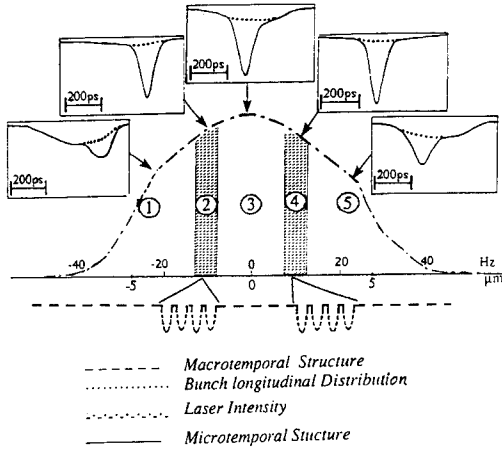


Fig. 1. Five operational zones of the Super-ACO FEL depending on the detuning between the laser micropulse and the positron bunch. The macrotemporal structure is cw in zones 1, 3 and 5, and pulsed in zones 2 and 4.

with a cw macrostructure and presents a longitudinal jitter specially in central zone 3 [6].

### 3. Experimental set-up

The scanning Fabry–Perot (Burleigh) consists of two mirrors, one of them is moved by a few microns using piezo-motors at a frequency up to a few hundreds Hz. According to the distance between the two mirrors, the resonant wavelength of the Fabry–Perot interferometer is given by

$$\lambda = 2nd/N, \quad (1)$$

where  $\lambda$  is the wavelength of the light,  $N$  is an integer,  $n$  is the refractive index of air ( $n \approx 1$ ) and  $d$  is the distance between the two mirrors. When  $d$  is fixed, only light of

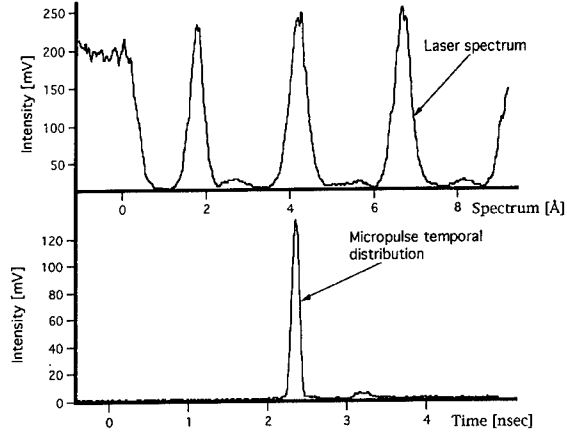


Fig. 2. Temporal distribution and spectrum of the laser micropulse, which are simultaneously measured by the dissector and the scanning Fabry–Perot respectively.

the wavelength  $\lambda$  can transmit through the Fabry–Perot with a width determined by a resolution  $\Delta\lambda_{1/2}$ . If the distance  $d$  is varied and we consider  $N$  such that  $2nd/N \approx \lambda_{\text{laser}}$ ,  $\lambda_{\text{laser}}$  can be scanned and thus we can survey the spectrum of the light. The resolution depends on the mirror reflectivity  $R$ :

$$\Delta\lambda_{1/2} = \frac{(1-R)\lambda^2}{2\pi d\sqrt{R}}. \quad (2)$$

In our case,  $d \approx 0.25$  mm and we use a mirror of  $R = 0.92$ , so the resolution is estimated to be about  $0.07 \text{ \AA}$ . The transmitted light from the Fabry–Perot is measured by a photo multiplier and we can see the observed spectrum on an oscilloscope.

The measured spectrum is shown in Fig. 2. We see several peaks in this figure. This is because, as  $d$  changes, the peaks for different  $N$  appear, while  $\lambda$  is always the same in Eq. (1). The distance between the peaks ( $\Delta d$ ) is

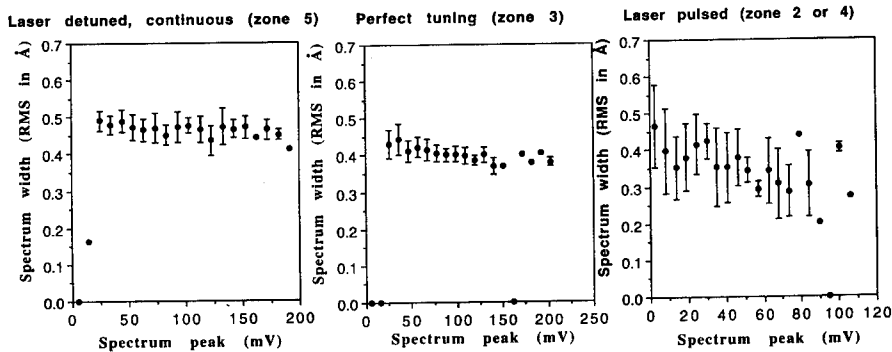


Fig. 3. Laser spectral width as a function of the laser intensity in different operational zones. The errors are calculated by taking the root mean square.



calibrated into the spectral width according to the following formula,

$$\Delta d = \lambda^2 / (2d), \quad (3)$$

where  $\lambda$  is the laser wavelength.

Fig. 2 also shows the temporal distribution of the laser micropulse taken by the dissector simultaneously with the spectrum, thus we can measure the spectrum and the temporal distribution of the laser micropulse at the same time.

#### 4. Spectral features of the laser

A monochromator is an ordinary method of measuring the spectrum, but it takes a few seconds to complete one survey in our case. We find a spectrum of about 1 Å (FWHM) with the monochromator. This value is averaged over a large number of micropulses and no dynamic

Table 1

Measured spectral width in different operational zones

| Operational zone      | Spectral width (FWHM)          |
|-----------------------|--------------------------------|
| Zone 3 (cw)           | 0.4–1 Å                        |
| Zone 1 and 5 (cw)     | 0.8–1.1 Å                      |
| Zone 2 and 4 (pulsed) | 0.5–1.2 Å (spectral evolution) |

behavior is observed. However, by detecting a fringe of a spontaneous emission with the monochromator, we can know the beam energy fluctuation in real time.

To realize a dynamic study of the laser spectrum, we introduce the scanning Fabry–Perot. The measurements have been done in five different synchronization conditions between the positron bunch and the laser micropulse as described before (Fig. 1). The spectrum versus laser intensity is plotted in Fig. 3 for different synchronization conditions.

In zone 5, where the macropulse of the laser is cw, the spectrum stays almost at a constant value. In zone 3, where the positron bunch and the laser micropulse are perfectly synchronized and the macropulse structure is cw, the spectrum stays also almost constant but it is narrower than the spectrum of zone 5. However in zones 2 or 4, where the laser has a pulsed macrotemporal structure, the spectrum becomes thinner as the micropulse intensity grows up. This suggests that the spectrum of the laser is wide when the first micropulse is raised in the optical cavity, and it gets thinner as the micropulse is amplified.

In Fig. 4, the variation of the lasing wavelength during a few tens of minutes is shown. This is done by measuring the resonant peak positions in Fig. 2, and the variation of these positions corresponds to the variation of the lasing wavelength. Normally, the laser wavelength does not change so much as shown in Fig. 4a. But sometimes, the laser presents a gradual wavelength drift (Fig. 4b). The cause of this phenomenon is thought to be the variation of the positron beam orbit at the position of the optical klystron or the variation of the beam energy. We plan a measurement correlating the lasing wavelength and the beam energy by detecting a fringe of a spontaneous emission spectrum with a monochromator as mentioned before.

The laser spectral widths for different synchronization conditions are summarized in Table 1. It should be noted here that the spectral width is sensitive to the laser stability or, in other words, the conditions of the storage ring and the optical cavity. When the laser is very stable, the spectral width reaches the minimum value shown in Table 1.

#### 5. Correlated measurement of temporal and spectral micropulse width

The correlated spectral and temporal measurements of the laser micropulse are carried out by synchronizing the

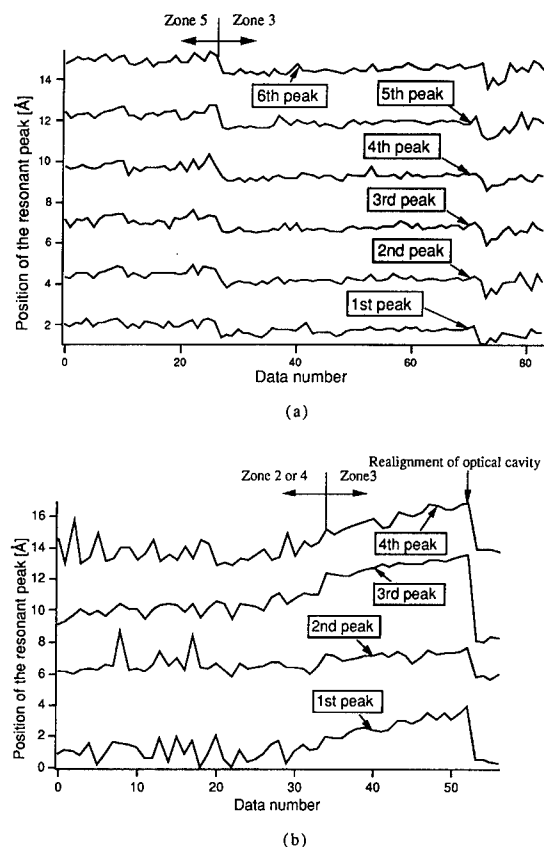


Fig. 4. Drift of the laser wavelength. Data number corresponds to time arbitrarily, about 30 min for full horizontal scale in this figure. As shown in Fig. 2, some peaks appear in one movement of the mirror, each peak has different  $N$  but  $\lambda$  is always the same in Eq. (1). (a) The wavelength variation for the stable laser. (b) The gradual wavelength drift.

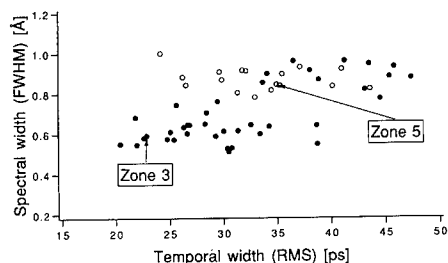


Fig. 5. The relation between temporal width and spectral width of the laser micropulse in zones 3 (filled circles) and 5 (hollow circles).

scanning Fabry–Perot and the dissector (Fig. 2). The preliminary result is shown in Fig. 5. The spectral width does not change or even increases for the larger temporal width. This can be understood by the fact that the coherent length of the UV FEL is much shorter than the micropulse duration. If the coherent length is increased by an intracavity etalon [6], the spectral width approaches the Fourier limit and a relation like Fourier transformation might be observed.

## 6. Discussion

The spectral features of the Super-ACO FEL are studied and we found that the measured spectrum is much narrower than the value obtained previously with the monochromator. The spectrum does not change significantly when the laser macropulse is cw, and the spectral evolution is observed for the pulsed laser when the laser intensity grows up. The drift of the lasing wavelength, which might be due to the variation of the beam energy or the beam orbit, is also observed.

A longitudinal feedback system is developed to maintain perfect synchronization between the laser micropulse and the positron bunch [3]. The laser operates in zone 3 and the laser spectrum is kept narrow for several hours

with this system. The feedback system also suppresses the longitudinal jitter of the laser micropulse, so it succeeds in stabilizing the laser micropulse well both from the temporal and the spectral points of view. We already use this system for the application experiments and the stable cw laser in zone 3 is offered for the two color experiment on a semiconductor surface.

Further experimental studies are planned with an intracavity Fabry–Perot etalon, where the spectral width can be reduced, and in the *Q*-switched mode, where higher peak power can be obtained.

Theoretical studies are being conducted at the same time employing a detailed model including the effects of spontaneous emission, external perturbations and longitudinal micropulse jitter.

## References

- [1] M.E. Couprie, F. Mérola, P. Tauc, D. Garzella, A. Delboulbé, T. Hara and M. Billardon, *Rev. Sci. Instr.* 65 (1994) 1485.
- [2] T. Hara, M.E. Couprie, D. Garzella, A. Delboulbé, L. Nahon and M. Billardon, *Proc. 4th Europ. Particle Accelerator Conf.*, London, UK, 1994, to be published.
- [3] M.E. Couprie, D. Garzella, T. Hara, A. Delboulbé, L. Nahon and M. Billardon, these Proceedings (16th Int. Free Electron Laser Conf., Stanford, CA, USA) *Nucl. Instr. and Meth. A* 358 (1995) 374.
- [4] T. Hara, M.E. Couprie, A. Delboulbé, P. Troussel, D. Gontier and M. Billardon, *Proc. 15th Int. Free Electron Lasers, Conf. The Hague, The Netherlands 1993 Nucl. Instr. and Meth. A* 341 (1994) 21; M.E. Couprie, D. Gontier, P. Troussel, T. Hara, A. Delboulbé and M. Billardon, *Rapport d'expériences, Réf. CEA/DSM/DRECAM/SPAM-93/377*.
- [5] D. Garzella, M.E. Couprie, A. Delboulbé, T. Hara and M. Billardon, *Proc. 15th Int. Free Electron Lasers, Conf. The Hague, The Netherlands, Nucl. Instr. and Meth. A* 341 (1994) 24.
- [6] M.E. Couprie, N.G. Gavrilov, G.N. Kulipanov, V.N. Litvinenko, I.V. Pinaev, V.M. Popik, A.N. Skrinsky and N.A. Vinokurov, *Proc. 12th Int. Free Electron Lasers Conf. Paris, France, Nucl. Instr. and Meth. A* 304 (1991) 47.



ELSEVIER

# mm-wave isochronous FEL and hard X-ray inverse Compton source at the Duke storage ring <sup>☆</sup>

V.N. Litvinenko <sup>\*</sup>, Y. Wu, B. Burnham, G. Barnett, J.M.J. Madey

*FEL Laboratory, Box 90319, Duke University, Durham, NC 27708-0319, USA*

## Abstract

We propose to operate an isochronous mm-wave FEL at the Duke storage ring. Resonant FEL conditions for mm-waves will be provided by the off-axis interaction with an electromagnetic wave. A special optical resonator with holes for the e-beam is proposed for pumping a hard X-ray inverse Compton source with very high brightness. Simulation results for proposed mm-wave FEL operation on the Duke storage ring are discussed in a separate article in these proceedings. The expected performance of the hard X-ray inverse Compton source is presented.

## 1. Introduction

We propose to use a compact nearly-isochronous storage ring with modest (300–700) MeV energy to drive a mm-wave CW FEL and use it as a CW Inverse Compton X-Ray Source (ICXRS). The use of a gigawatt mm-wave pump instead of a dc undulator allows us to reach the hard X-ray range with a spectral brightness comparable with third generation light sources such as ALS and APS. For example, a 725 MeV storage ring with a 1 mm-wave pump will produce a 10 keV bright X-ray beam. To lower the cost of such a facility, we propose to inject the electron beam at very modest energies (25–50 MeV), and then ramp the electron energy to the operational point of several hundred MeV and recirculate the intense electron beam for tens of hours.

In the late 1970s, Madey and Deacon suggested the use of an isochronous storage ring to drive high average power CW FELs [1]. In such devices the circulating electrons pick up energy from the RF cavity and transfer it directly into laser energy. The isochronism of the storage ring is required to preserve the electron beam microstructure. Some elements of the theory of the isochronous storage ring FEL and some stability criteria have been studied and developed by Deacon [2]. The experimental data to document these phenomena includes observations of the well known microwave instability as well as the observations of

the self-excitation of high-harmonic RF cavities used for beam shaping.

The great potential of this device is due to the intrinsic “energy recovery” capability of storage rings and the super-high power attainable using a circulating electron beam. Storage rings with modest energies of 300–1000 MeV have the capability to operate at 0.5–1 A electron beam average current. The average circulating power of electron beams in these storage rings is from 150 MW to 1 GW. Isochronous storage ring mm-FELs can transfer the RF power into very high harmonics of the RF frequency, i.e. into GW level mm-waves. This process is reminiscent of the harmonic generation in classical microwave RF devices.

Microwave instability caused by the impedance of vacuum chambers is a well known effect in storage rings. We intend to exploit this phenomenon for the production of high power mm-waves in a nearly isochronous storage ring FEL system. The term “nearly isochronous” means that the mm-wave modulation of the electron beam density will be preserved from turn to turn (see details in Section 2).

The mm-wave generated in the storage ring resonator will be tightly focused for a head-on collision with the electron beam to produce hard X-ray photons with very high brightness via inverse Compton scattering.

## 2. Isochronous off-axis mm-wave CW FEL

The energy of the Duke storage ring is high for conventional mm-wave FELs. To operate a mm-wave FEL on this storage ring, the off-axis interaction with mm-waves will be used. The electron beam will propagate through the FEL wiggler while a wide mm-wave packet will propagate

<sup>☆</sup> This work is supported by the Office of Naval Research Grant No. N00014-94-C0818 and Air Force Office of Scientific Research Grant No. F49620-93-1-0590.

<sup>\*</sup> Corresponding author. Tel. +1 919 660 2658, fax +1 919 660 2671, e-mail vl@phy.duke.edu.

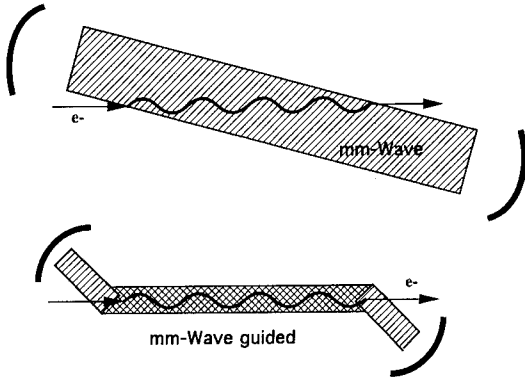


Fig. 1. Two possible mm-wave FEL interaction configurations: (a) with wide mm-wave beam; (b) with mm-wave injected and ejected into/from a waveguide with angle  $\theta$ .

with a  $k$  vector off-axis with an angle  $\theta$ . The resonant condition for the off-axis FEL interaction is:

$$1 - \cos(\theta) = \frac{2 + K^2}{4\gamma^2} - \frac{\lambda}{\lambda_w}, \quad (1)$$

where  $K$  is the wiggler parameter,  $\gamma$  is the relativistic factor,  $\lambda$  is the FEL wavelength and  $\lambda_w$  is the wiggler period. For low  $K$  wigglers with the beam energy under consideration ( $\gamma$  from 600 to 2000), the  $(2 + K^2)/4\gamma^2$  term is usually negligibly small and the FEL wavelength is defined by the wiggler period  $\lambda_w$  and the angle  $\theta$ :

$$\lambda \approx 2\lambda_w \sin^2(\theta/2) \approx \lambda_w \theta^2/2. \quad (2)$$

Two of the many possible schematics of this FEL interaction are shown in Fig. 1.

The off-axis FEL interaction is similar to the conventional FEL but with some differences. The energy change of an electron passing through the FEL is described by:

$$\begin{aligned} \frac{dE_{\text{opt}}}{dz} = & eE_{\text{opt}} \left( \cos(\theta) \frac{K}{\gamma} \cos(k_w z) - \sin(\theta) \right) \\ & \times \cos \left( \delta k z + \frac{K}{\gamma} \frac{k}{k_w} \sin(k_w z) \right. \\ & \left. + \left( \frac{K}{\gamma} \right)^2 \frac{k}{8k_w} \sin(2k_w z) + \varphi \right), \end{aligned} \quad (3)$$

where  $k_w$  and  $k$  are the wiggler and optical wavevectors,  $\delta k = k((2 + K^2)/(4\gamma^2) - 1 + \cos(\theta))$ ,  $E_{\text{opt}}$  is the electric field of the optical wave,  $e$  is the electron charge, and  $\varphi = \omega t$  is the optical phase. The modulation term  $\sin(2k_w z)$  in the cosine argument is typical for planar wigglers [3]. The  $\sin(k_w z)$  term is specific for the off-axis interaction and is caused by the wiggling of the electron trajectory. For individual electrons, the FEL works as a

very high harmonic RF cavity ( $\lambda_{\text{rf}} = \lambda_{\text{fel}}$ ) with an effective voltage of:

$$V_{\text{fel}} = \frac{K}{2\gamma} E_{\text{opt}} L C_{\text{int}}, \quad (4)$$

where  $L$  is the length of wiggler and  $C_{\text{int}} \sim 1$ , a dimensionless interaction coefficient. For the cases we have studied,  $C_{\text{int}}$  was obtained by numerical integration. It is easy to see that the strength of the interaction of the electrons with the mm-wave is proportional to the  $K$  value of the wiggler. An optimized wiggler for mm-wave operation is a one period wiggler with very high  $K$ . The choice of a simple one period wiggler with high  $K$  maximizes the interaction and minimizes the transverse dimensions of the mm-wave size in the interaction region. In earlier studies on the five-period wiggler with a 20 cm long period ( $K_{\text{max}} \approx 20$ ) we find that it has a 4.8 times lower start-up gain than for the one period case [1].

In order to operate a nearly isochronous mm-wave FEL, the storage ring should preserve the mm-microbunch structure. This requirement restricts the maximum phase advance spread caused by the energy deviation and transverse (betatron) oscillations to

$$\Delta l/\lambda < 1, \quad (5)$$

where  $\lambda$  is the FEL wavelength and  $\Delta l$  is the path length difference from the synchronous particle. The energy deviation term gives us  $\lambda > \alpha_c C \sigma_E/E$ , where  $\alpha_c$  is the momentum compaction,  $C$  is the storage ring circumference,  $E$  is the electron energy and  $\sigma_E$  is the electron energy spread. The Duke storage ring has a reasonably low compaction factor of  $\alpha_c = 0.0086$  and a low energy spread ( $\sigma_E/E = 5.8 \times 10^{-4}$ ), which allows nearly isochronous operation with  $\lambda > 1$  mm. The contribution to  $\Delta l$  by transverse oscillations is negligible for the Duke mm-wave FEL ( $\Delta l \sim 0.002$  mm).

The maximum power in an isochronous FEL can be limited by the stability conditions for electron oscillation inside the microbuckets [2]. The nonlinear effects are not essential for the Duke mm-wave FEL [4].

### 3. Inverse Compton hard X-ray source

A mm-wave isochronous FEL with GW levels of peak power can be used as a pump for an ICXRS. The brightness of the inverse Compton X-ray source can be optimized by choosing its time structure and pump waist size (Rayleigh range). In order to maximize the density of pump photons and electrons in the interaction region, the Rayleigh range should be chosen close to half of the electron bunch length. Sharp focusing of the pump wave also yields exceptionally large values of the electromagnetic field in the interaction region. For example, in the suggested experiment on the Duke storage ring, the Rayleigh range of the mm-wave at the interaction point is

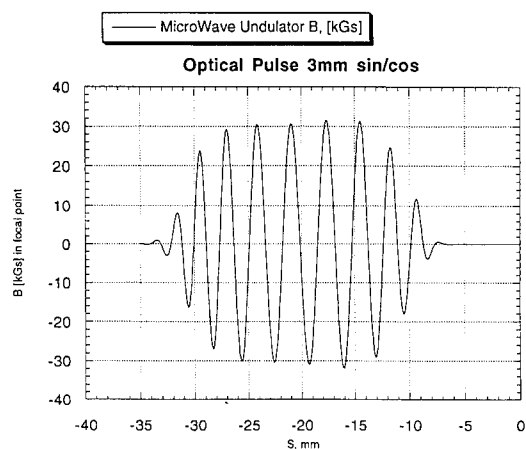


Fig. 2. Reconstruction of a 3 mm-wave pulse focused with 1.5 cm Rayleigh range for X-ray production. The optical field is taken from a simulation of the Duke storage ring 3-mm isochronous FEL operating with 46 mA e-beam current.

0.6–1.5 cm. With the mm-wave FEL parameters described below, 30–50 kG electromagnetic fields can be realized at the center of the interaction waist. Fig. 2 shows the reconstructed 3 mm-wave from simulations at the optical waist (with 1.5 cm Rayleigh range) for the X-ray generation. These exceptionally high field values more than make up for the loss in radiated X-ray power due to the reduced electron energy. Fig. 3 shows the expected performance of the Duke ICXRS for different levels of mm-wave pump powers.

#### 4. Ring resonator design

One possible optical cavity design for the mm-wave FEL and ICXRS is a ring resonator. The ring resonator is designed with 0.5 cm radius holes in the mirrors for

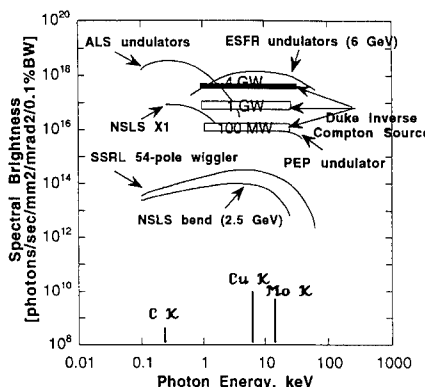


Fig. 3. Spectral brightness of the Duke inverse Compton X-ray source with mm-wave peak power of 100 MW, 1 GW and 4 GW.

passage of the electron beam. This design provides an off-axis FEL interaction, a stable low loss optical mode, a tight focus in the X-ray pump in ICXRS and an optical pulse synchronization with the electron beam.

Fig. 4 shows the configuration of the resonator. The resonator is designed to store the light radiated at an angle  $\theta$  to the electron beam. The X-ray radiation generated by Compton backscattering of electron bunches is outcoupled through the hole in the downstream mirror.

The optical eigenmode of the ring resonator can be described as a linear superposition of azimuthally symmetric Gauss–Laguerre free space modes. Nearly all of the optical power is in the  $TEM_{00}$  Gauss–Laguerre mode; therefore the mode couples strongly with the electron beam. The loss of the second eigenmode is 28 times higher than the  $TEM_{00}$  mode. Thus, this resonator design provides both a low loss eigenmode and good mode selection. Due to the configuration, the resonator is nearly phase degenerate and the losses would be 1.2% per pass for the phase degenerate resonator.

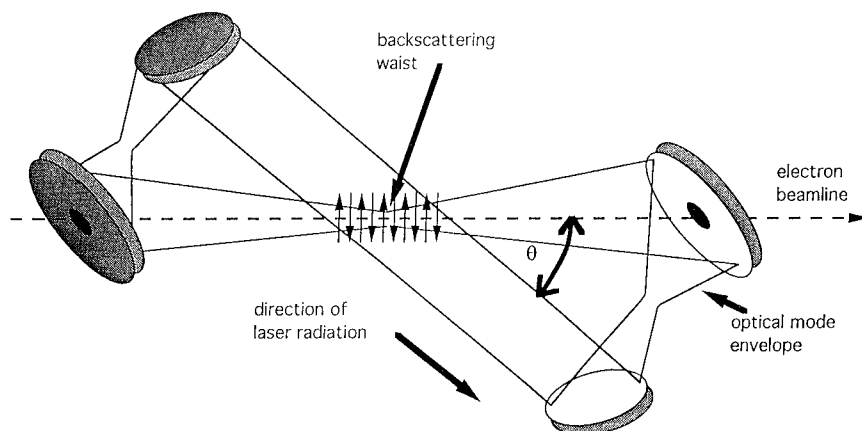


Fig. 4. Optical resonator design for the Duke mm-wave FEL and hard X-ray inverse Compton source.

We intend to study a new design where both legs of the resonator are off-axis and no holes are needed in the mirrors. We hope that it will have even lower losses.

## 5. Conclusion

We propose to operate an isochronous mm-wave FEL at the Duke storage ring with a special optical resonator to pump the hard X-ray inverse Compton source with very high brightness. Simulation results for the proposed mm-wave FEL, which are presented in a separate paper in these proceedings [4], show very promising GW levels of peak power with modest 30–50 mA beam current in the Duke ring. This power is sufficient to pump the very bright hard X-ray inverse Compton source. We intend to continue

these studies to further optimize the performance of the system.

## References

- [1] D.A.G. Deacon and J.M.J. Madey, Phys. Rev. Lett. 44 (1980) 449.
- [2] D.A.G. Deacon, Ph.D. Dissertation, Stanford University (1979);  
D.A.G. Deacon, Phys. Rep. 76 (1981) 349.
- [3] W.B. Colson, Laser Handbook, Vol. 6 (North-Holland, 1990) p. 115.
- [4] V.N. Litvinenko, Y. Wu, B. Burnham and J.M.J. Madey, these Proceedings (16th Int. Free Electron Laser Conf., Stanford, CA, USA, 1994) Nucl. Instr. and Meth. A 358 (1995) 349.



ELSEVIER

# Expected performance of the mm-wave isochronous FEL at the Duke storage ring ☆

V.N. Litvinenko \*, Y. Wu, B. Burnham, J.M.J. Madey

*FEL Laboratory, Box 90319, Duke University, Durham, NC 27708-0319, USA*

## Abstract

We propose to operate an isochronous mm-wave FEL at the Duke storage ring. Resonant FEL conditions for mm-waves will be provided by the off-axis interaction with an electromagnetic wave. The intracavity power of the mm-wave FEL could be used to pump a hard X-ray inverse Compton source with very high brightness. This is discussed in a separate contribution to these proceedings. Simulation results of mm-wave FEL operation on the Duke storage ring are discussed. The expected performance of a mm-wave FEL is presented.

## 1. Introduction

We have discussed the theory of nearly-isochronous FEL, off-axis FEL interaction, stability criteria and expected performance of a hard X-ray inverse Compton X-ray source in another paper published in these proceedings [1]. This paper is focused on the computer program implementing the theory described in Ref. [1] and the simulation results.

## 2. Particle trapping in the external 3 mm FEL fields

To understand the dynamics of the particle interaction with the 3 mm FEL wave, we have studied the dynamics of particle trapping in the external FEL fields in the Duke FEL storage ring. To track the particle around the storage ring, we have used the single particle tracking code DESPOT [2]. DESPOT is capable of studying the 6-dimensional dynamics in the storage ring. The following Hamil-

tonian is implemented in DESPOT using a fourth order symplectic integrator:

$$K(x, y, \delta, p_x, p_y, l; s) \approx \left( -\delta + \frac{p_x^2 + p_y^2}{2(l + \delta)} \right) - \frac{x\delta}{\rho_0} + \frac{x^2}{2\rho_0^2} - \frac{e}{\rho_0} \left( 1 + \frac{x}{\rho_0} \right) V_m(x, y), \quad (1)$$

where  $p_x$  and  $p_y$  are normalized momenta,  $\delta$  is the relative momentum deviation,  $l$  is the path length difference from the synchronous particle,  $\rho_0$  and  $p_0$  are design bending radius and total momentum and  $V_m(x, y)$  are the magnetic multipoles. All orders of transverse nonlinear effects as well as the first and second order momentum compaction effects have been included in DESPOT. We have studied the particle dynamics in the storage ring with an external 3 mm FEL. An additional energy kick will be applied to the particles when passing through the 3 mm FEL field:

$$\delta_{n+1} = \delta_n - \frac{|eV_{\text{fel}}|}{E_0} \sin(kl_{n+1}), \quad (2)$$

where  $V_{\text{fel}}$  is the effective voltage defined in Ref. [1] and  $k$  is the optical wavevector.

A realistic storage ring lattice with high order multipoles obtained from magnetic measurements is used to study the particle trapping in the 3 mm FEL waves. Figs. 1a and 1b show particles trapped in the 0.5 MV 3 mm FEL field, which create stable separatrices 3 mm apart. Islands and chaotic layers around the separatrix indicate the complex dynamics of particle motion. Stable trapping of the particles for a 1 MV 3-mm field is shown in Fig. 1c.

☆ This work is supported by the Office of Naval Research Grant #N00014-94-C0818 and Air Force Office of Scientific Research Grant #F49620-93-1-0590.

\* Corresponding author. Tel. +1 919 660 2658, fax +1 919 660 2671, e-mail vl@phy.duke.edu.

The nonlinear effects due to the storage ring including the first and second order momentum compaction do not significantly affect the particle trapping. It is possible to create 3 mm-size stable traps with energy acceptance close to the e-beam natural energy spread. The maximum mm-

wave field is limited by the over-focusing in longitudinal phase space. The stability condition is  $V_{\text{fel}} < 4E_0 / (ek\alpha_c C)$ , which is 2.0 MV for the Duke storage ring with 1 GeV beam energy and 3 mm FEL wavelength.

### 3. Code description for the mm wave FEL

The simulation code for the mm FEL is written in FORTRAN. All real numbers are in double precision. The code is comprised of three main parts, including the storage ring, the mm-wave FEL and the optical cavity.

The electron motion in longitudinal phase space is described by the following equations

$$S_{n+1} = S_n - \alpha_c C \delta_n, \quad (3a)$$

$$\delta_{n+1} = \delta_n \left( 1 - \frac{1}{N_D} \right) + \sigma_E \sqrt{\frac{24}{N_D}} \mathcal{R} - \frac{|eV_{\text{RF}}|}{E_0} \sin(k_{\text{RF}} S_{n+1}), \quad (3b)$$

where  $s = c(t - t_{\text{syn}})$  is the longitudinal displacement from the synchronous particle,  $\delta = E/E_0 - 1$  and  $E_0$  is the design energy for the storage ring,  $V_{\text{RF}}$  is the RF voltage,  $N_D = (2\Delta E_{\text{SR}}/E_0)^{-1}$ ,  $\Delta E_{\text{SR}}$  is the energy loss through synchrotron radiation and  $\mathcal{R}$  is a random number with a uniform distribution between  $-0.5$  and  $0.5$ . Eqs. (3a) and (3b) describe a self-consistent e-beam with standard energy distribution expressed by  $\exp(-\delta^2/2\sigma_E^2)$ .

Each electron radiates a  $N_w$  period wavelet, where  $N_w$  is the number of wiggler periods. The optical wave built up from the electron radiation therefore has the same plane wave propagation factors as well as amplitude and phase modulation with respect to the longitudinal position. Eq. (4) describes the optical wave packet  $\tilde{A}_0(z, t)$  and the  $N_w$  period wavelet  $\tilde{A}_e(z, t)$  radiated by one electron:

$$\tilde{A}_0(z, t) = \tilde{A}_0(z) e^{i(\omega t - kz)} = |\tilde{A}_0(z)| e^{i(\omega t - kz + \phi_0(z))}, \quad (4a)$$

$$\tilde{A}_e(z, t) = |\tilde{A}_e| e^{i(\omega t - kz + ks)\theta(z)}, \quad (4b)$$

where  $|\tilde{A}_e|$  is the amplitude of the electric field radiated by one electron,  $\phi_0(z)$  and  $|\tilde{A}_0(z)|$  are the optical phase and amplitude of the optical wave, and  $\theta(z) = \eta(z_0) - \eta(z_0 + N_w \lambda)$  is the difference of two step functions.

The electron radiation will change the optical fields according to:

$$\Delta \tilde{A}_0(z, t) = \sum_{n=1}^{N_{\text{particles}}} |\tilde{A}_e| e^{iks_n \theta_n(z)}. \quad (5)$$

At the same time, the electron will interchange energy with the optical wave:

$$\Delta E = -\frac{S}{8\pi} \text{Re} \int dz \tilde{A}_e^* (2\tilde{A}_0 + \sum A_e), \quad (6)$$

where  $S$  is the optical wave cross section.

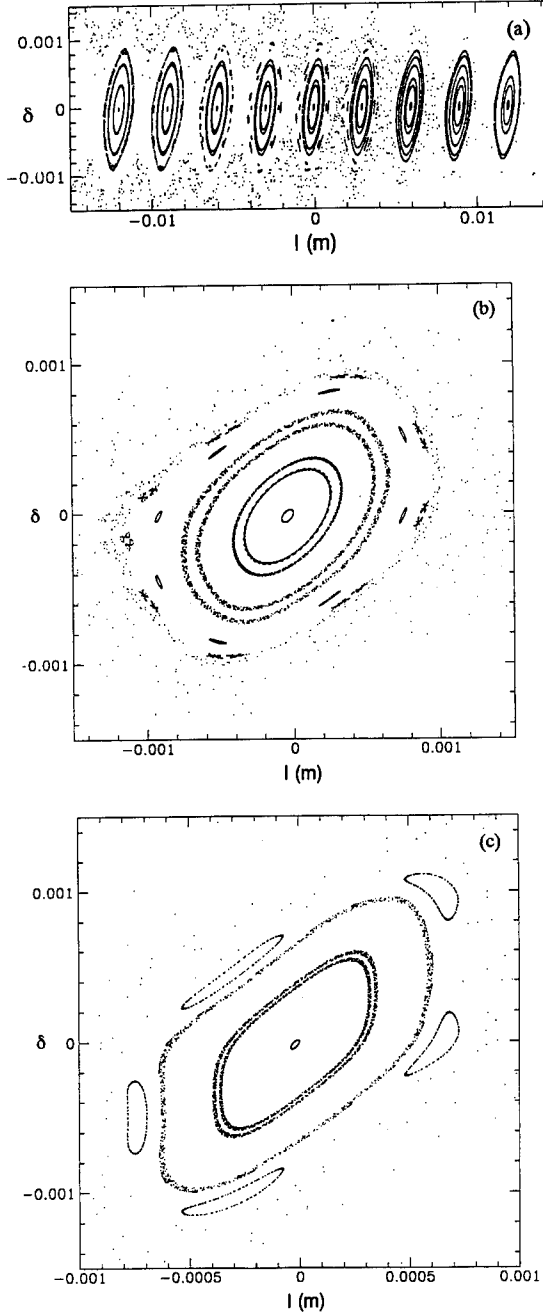


Fig. 1. Tracking results for the Duke storage ring 3 mm FEL: (a) trapping areas with a longitudinal potential of 0.5 MV; (b) a blow-up of one trap area in case (a); (c) a trap area with a longitudinal potential of 1.0 MV.



We represent the optical wave packet by an array of bins. Each bin contains the real and imaginary parts of the mm-wave field. The bin size is equal to one wavelength. Macroparticles are used instead of single electrons in the simulation.

In general, the  $N_w$  period wavelet radiated by a macroparticle will add into  $(N_w + 1)$  bins with the first and last bins receiving only a portion of the radiation which is proportional to their overlap with the wavelet [3]. A form factor for the overlap is

$$\alpha(j + I_b) = \begin{cases} 1 - x, & j = 0 \\ 1, & j = 1, \dots, N_w - 1, \\ x, & j = N_w \end{cases} \quad (7)$$

where  $I_b$  is the first bin where the overlap occurs. The energy loss is handled in a similar fashion by using the same interaction form factor described above.

The optical cavity is represented by a round trip reflectivity and a detuning from the synchronous particles [3]. The cavity detuning is essential to start up the mm-wave FEL. The macroparticles tend to bunch around the stable fixed point of the optical wave where the optical wave has a phase of  $(2n\pi + \pi)$ ,  $n = \text{integer}$ . A cosine wave is radiated by the macroparticle with a phase of  $(\pi/2 + k\Delta s)$ , where  $\Delta s$  is the longitudinal phase displacement relative to the particles at the stable fixed point. The energy loss for this macroparticle can be derived from Eq. (2):

$$\Delta E \propto \cos((2n + 1/2)\pi - k\Delta s) = \sin(k\Delta s). \quad (8)$$

Without cavity detuning the bunched particles will be distributed around the stable fixed point of the optical wave with both positive and negative  $\Delta s$ . In this case, the sum of the energy loss from all macroparticles will be zero. To build up the FEL we use the cavity detuning to provide a positive shift of  $\Delta s$  to all macro-particles and move them to a region where most of them will lose energy to the optical wave.

#### 4. Duke mm wave FEL system

The Duke storage ring, which is a few months from commissioning as of this conference, is ideally suited to drive a high peak power isochronous mm-wave FEL. Its low orbit compaction factor and high average current allow the generation of very high average and peak power with electron beam energies from 250 to 1000 MeV.

The nearly isochronous mm-wave storage ring FEL and inverse Compton X-ray source will be installed in the North straight section of the Duke storage ring. Three meters of this section are dedicated for the source. This area can be expanded to 5–7 m if necessary. The description of the Duke storage ring and the expected beam parameters are published elsewhere [4]. A 0.8 m one period wiggler with  $K = 100$  will be used for this FEL.

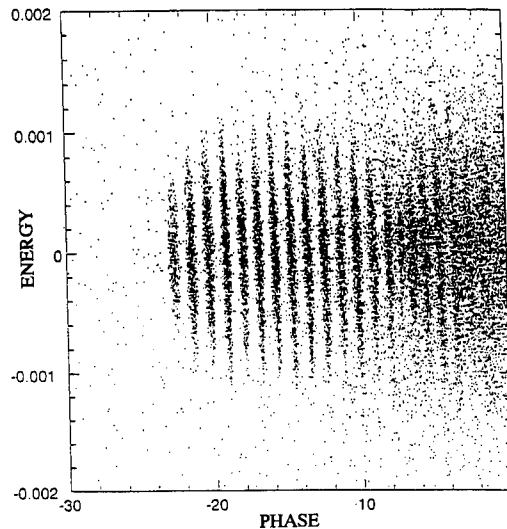


Fig. 2. Poincaré plot of particles trapped in the Duke storage ring 3-mm FEL.

#### 5. Simulation results

The parameters used for most of the simulations are  $10^{11}$  electrons (46 mA) in the storage ring and 800 kV main RF voltage with a RF frequency of 178 MHz. In addition, we have tried more complex RF potential wells with a 4th harmonic RF cavity.

We have studied the dynamics of trapping and detraping of electrons in the self-consistent 3 mm traps. One typical case is shown in Fig. 2 with well defined 3 mm separatrices. When the effective voltage for the 3 mm wave field exceeds 2.0 MV, self-destruction of the traps is observed.

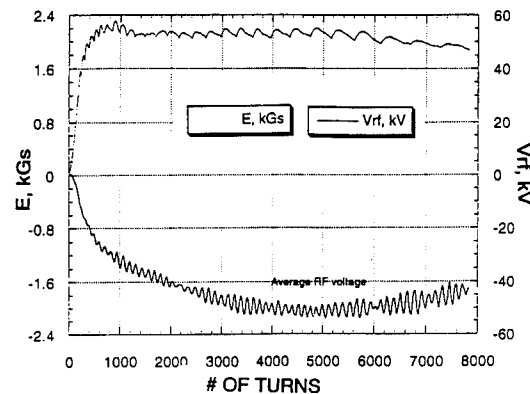


Fig. 3. Start-up and transition in the Duke storage ring 3-mm FEL. The beam current is 46 mA; 800 kV in the main RF and 200 kV in fourth harmonic RF. The upper curve shows the mm-wave peak power, the lower curve shows the power extracted from the RF system.

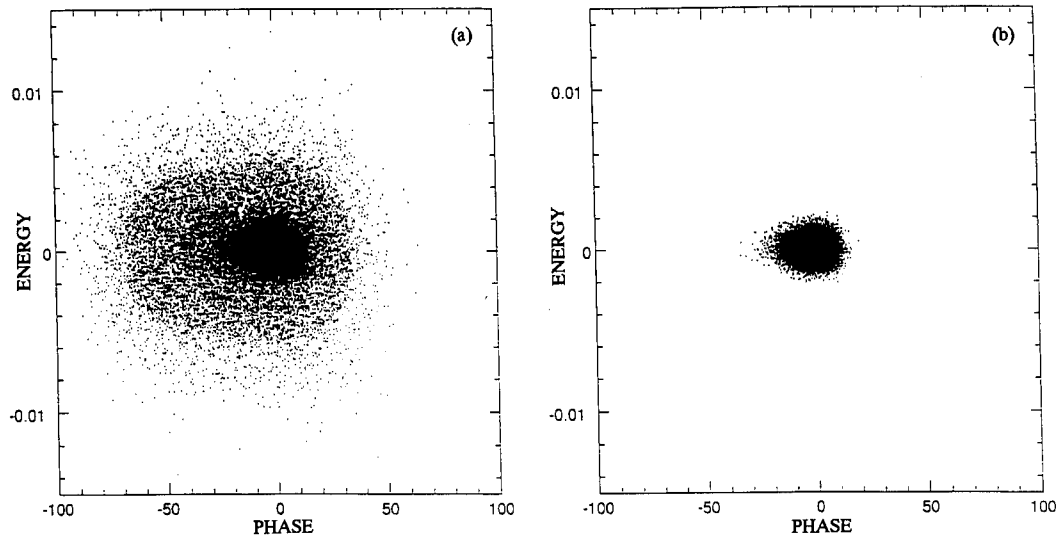


Fig. 4. Electrons distribution in longitudinal phase-space: (a) interacting with a steady self-consistent field in a 3 mm-wave FEL; (b) before interaction.

The start-up gain of the mm FEL as a function of cavity detuning is studied and no discrepancy is found with our theoretical predictions. The mm-wave FEL can start from noise with a typical gain of 1–10% per pass when cavity detuning is negative. Positive detuning causes electrons to absorb energy from the optical wave.

We have studied the transition period and the existence of the steady state. In the study, we have assumed a two-mirror resonator without a wave guide and a round trip loss of 0.2% per pass. The transition period and steady state lasing are illustrated in Fig. 3. Fig. 3 also shows the power transferred from the RF cavity (lower curve) by the e-beam into the 3-mm wave. This power exceeds the Renieri limit [5] by a factor of about 100, clearly indicating the isochronous mode of the FEL operation.

The steady state operations with 1–4 GW intra-cavity power are observed. The self-consistent e-beam distribution is shown in Fig. 4a. The detrapped electrons form a fuzzy cloud around the main core, while the main core with 80–90% of the particles maintains about the same size as the beam without the FEL interaction (Fig. 4b). The electron detrapping is caused by the well known effect of the quantum lifetime.

We have preliminary results on the mm-wave power as a function of the mirror loss. Increasing the mirror loss from 0.2% to 1% reduces the peak power by a factor of 10. Preliminary studies have shown that a 1-mm FEL can also be operated in the Duke storage ring with two to three times lower peak power than a 3-mm FEL.

## 6. Conclusion

We have developed a self-consistent model for a nearly-isochronous mm-wave storage ring FEL. Prelimi-

nary tests have shown that the nearly-isochronous mode of operation is entirely different from standard modes of storage ring FELs. According to our simulations, power lased by the e-beam exceeds the Renieri limit by two to three orders of magnitude (1–10 kW instead of 5–10 W). Stable trapping in self-induced separatrices is additional confirmation for this very new mode of operation.

We have observed FEL start-up from noise. The possibility of such a process was always an unsolved problem for the isochronous FEL. Very promising GW levels of peak power are achievable using a modest (30–50 mA) beam current in the Duke ring. This power is sufficient to pump the very bright hard X-ray inverse Compton source. We intend to continue these studies to further optimize performance of the system.

## References

- [1] V.N. Litvinenko, Y. Wu, B. Burnham, G. Barnett and J.M.J. Madey, these Proceedings (16th Int. Free Electron Laser Conf., Stanford, CA, USA, 1994) Nucl. Instr. and Meth. A 358 (1995) 345.
- [2] E. Forest, DESPOT, Lawrence Berkeley Laboratory, Tracking Code.
- [3] V. Litvinenko, B. Burnham, J.M.J. Madey and Y. Wu, Ref. [1], p. 334.
- [4] Y. Wu, V. Litvinenko, E. Forest and J.M.J. Madey, Nucl. Instr. and Meth. A 331 (1993) 287;  
Y. Wu et al., IEEE PAC 1993, vol. 1, p. 218;  
V. Litvinenko et al., SPIE Vol. 1 552 (1991) 2;  
V. Litvinenko, J.M.J. Madey and N.A. Vinokurov, IEEE PAC 1993, vol. 2, p. 1442.
- [5] N.A. Vinokurov and A.N. Skrinsky, Preprint INP 77-67, Novosibirsk (1977);  
A. Renieri, Nuovo Cimento B 53, 160.



ELSEVIER

## Lasing in the ultraviolet region with the NIJI-IV storage-ring free-electron laser

T. Yamazaki <sup>a,\*</sup>, K. Yamada <sup>a</sup>, N. Sei <sup>a</sup>, H. Ohgaki <sup>a</sup>, S. Sugiyama <sup>a</sup>, T. Mikado <sup>a</sup>,  
R. Suzuki <sup>a</sup>, T. Noguchi <sup>a</sup>, M. Chiwaki <sup>a</sup>, T. Ohdaira <sup>a</sup>, M. Kawai <sup>b</sup>, M. Yokoyama <sup>b</sup>,  
S. Hamada <sup>b</sup>, A. Iwata <sup>b</sup>

<sup>a</sup> Electrotechnical Laboratory, 1-1-4 Umezono, Tsukuba-Shi, Ibaraki 305, Japan

<sup>b</sup> Kawasaki Heavy Industries Ltd., 1-1 Kawasaki-cho, Akashi, Hyogo 673, Japan

### Abstract

Lasing at around 352 nm of the NIJI-IV storage-ring free-electron laser (FEL) was successfully achieved in April 1994, and the tunable wavelength region of the system is now 350–595 nm. The electron-beam energy was 311 MeV, and the beam current was 6–10 mA/bunch. The peak output power was estimated roughly to be higher than 50 mW. After the first lasing at 595 nm and 488 nm with the present system in 1992, the storage ring NIJI-IV was modified to realize the lower-emittance mode, which proved to be quite effective for FEL experiments in the ultraviolet region. The radio-frequency knockout system has been modified to improve the purity of the single bunch. The gain of the 6.3-m optical klystron (ETLOK-II) is about 3.2 times that of a normal undulator of the same length. The optical cavity consists of dielectric multilayer mirrors made of Ta<sub>2</sub>O<sub>5</sub>/SiO<sub>2</sub>. The initial cavity loss was about  $5 \times 10^{-4}$ , but it increased rapidly with ultraviolet and vacuum-ultraviolet irradiation.

### 1. Introduction

NIJI-IV, the first storage ring in the world dedicated to free-electron lasers (FELs), was constructed at the Electrotechnical Laboratory (ETL) in cooperation with Kawasaki Heavy Industries, Ltd [1]. A 6.3-m optical klystron (ETLOK-II) [2] was installed in one of the long straight sections. Lasing at 488–595 nm was achieved in 1992 [3,4]. Since 1993, the ring has been modified to realize the lower-emittance mode. FEL related experiments with the new mode in the ultraviolet wavelength region began in April 1994, and lasing at 352 nm was achieved on April 28, 1994. FEL experiments in the same wavelength region are now under way.

### 2. Modification of the storage ring NIJI-IV

Though lasing in the visible wavelength region was successfully achieved on the storage ring NIJI-IV, the operating mode of the ring was different from that originally designed [5]. Since 1993, the operation mode has

been changed to obtain a stored beam of higher quality [4]. Fig. 1 shows the betatron functions and momentum dispersion functions in the old and new modes. The dispersion function is certainly zero in the long straight section in the new mode, which was not the case in the old mode. The betatron functions with and without the optical klystron (OK) have been measured with a result in fairly good agreement with computer simulations [6].

The reduction of emittance was indirectly confirmed by observing the shape of the spontaneous-emission spectrum from the OK [4]. Also, the horizontal and vertical emittance with the beam current of about 1 mA was roughly estimated from the measurements of the beam sizes and divergence to be  $6 \times 10^{-8}$  m rad and  $8 \times 10^{-9}$  m rad, respectively, which give a total emittance of  $7 \times 10^{-8}$  m rad. The natural emittance according to the computer simulation is  $4.9 \times 10^{-8}$  [4]. Incidentally, the emittance coupling (the ratio of vertical emittance to the horizontal emittance) is only 0.13.

The bunch lengths measured by the use of a streak camera and a fast photodiode in the old and new modes are compared in Fig. 2, which clearly shows the reduction of the bunch length in the new mode. Though the dependence of the bunch length on the stored current, assuming a power law, is shown in the figure, there is some ambiguity about the threshold current. Further systematic measurement is necessary. Actual lasing experiments are made

\* Corresponding author. Tel. +81 298 5541, fax +81 298 52 7944, e-mail: e7127@etlrips.etl.go.jp.

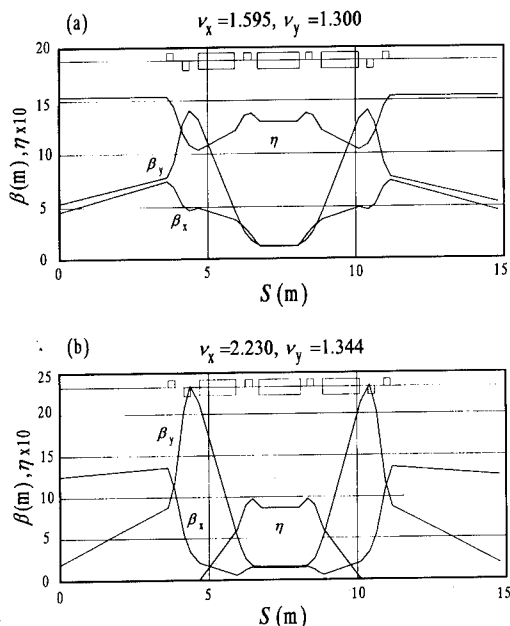


Fig. 1. Betatron and momentum dispersion functions in the old mode (a) and the new mode (b).

with a current of 6–10 mA, so that the bunch length during lasing is 150–180 ps. The natural bunch length according to the simulation is 73 ps [4]. The long bunch length in the full-bunch mode indicates that the coupled-bunch instability is serious in the NIJI-IV.

The maximum average stored current achieved so far is about 250 mA, which is almost twice as high as that in the old mode. The injection efficiency has also been greatly improved. The present injection speed is about 8 mA/s on average. A two-stage radio-frequency knockout (RF-KO) system developed for FEL experiments on the storage ring TERAS [7] which was used on NIJI-IV, has been modified

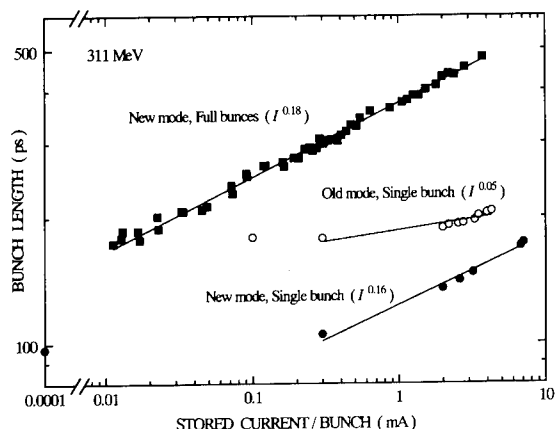


Fig. 2. Bunch length vs. stored current/bunch in the old and new modes.

[8] to improve the purity of the single bunch. A sextupole magnet and reinforced ion clearing operated successfully to increase the peak current. The electron beam was filled at 311 MeV and with the OK gap of 36.2 mm, both of which are the same as those in the oscillation experiment.

### 3. Experimental setup

The experimental arrangement is similar to that for the visible FELs [3]. Each of the normal-undulator section of the ETLOK-II consists of 42 magnetic periods of 72 mm. The length of the central dispersive section (DS) is 216 mm. The undulator gap was 36.2 mm during lasing, and the  $K$  value was 2.27. The energy spread of the electron beam of about  $4.9 \times 10^{-4}$  with 1.8-mA stored current in a quasi-single-bunch mode was estimated from the modulation factors  $f$  of the spontaneous-emission spectra for various widths of the gap of the DS. The energy spread in the pure single-bunch mode should be a little smaller than this because there remained some electrons in other bunches during the measurement.

In the oscillation experiments, most of the central part of the output light is introduced in the presence of air to a monochromator combined with a highly sensitive photodiode array, and the real-time spectrum is observed with an oscilloscope to detect the instantaneous change of the undulator-radiation spectrum which accompanies laser oscillation. The wavelength resolution and the time resolution of the system are 0.2 nm and 33 ms, respectively. The patterns of the resonator light beam and the FEL output are monitored by a CCD camera. A small portion of the output light is led to a streak camera for a rough cavity-length tuning [3,7].

The optical cavity consisted of dielectric multilayer mirrors made of  $\text{Ta}_2\text{O}_5/\text{SiO}_2$ . The cavity loss was measured with a new method by the use of a Nd-YAG laser of the 3rd harmonic [9]. The initial cavity loss was about  $5 \times 10^{-4}$ , but it increased rapidly with the irradiation by the ultraviolet and/or vacuum-ultraviolet.

### 4. Oscillation at around 352 nm

The ratio of the FEL gain  $G_{\text{OK}}$  of the present OK to that of a normal undulator with  $2N$  periods, where  $N$  is the number of periods in a single normal-undulator section of the OK, is plotted in Fig. 3 as a function of the slippage number  $N_d$  [3,7]. The dotted curves in the figure are the theoretical gain curves for typical values of energy spread ( $\sigma_\gamma/\gamma$ ), and the solid line is the optimal curve. The upper point from the experimental data indicates that the OK gain is about 2.3 times that of the normal undulator when the gap of the DS is 38 mm with  $N_d = 97$ . Though  $N$  ( $= 42$ ) of the ETLOK-II is large, still the OK is advantageous owing to the high beam quality.

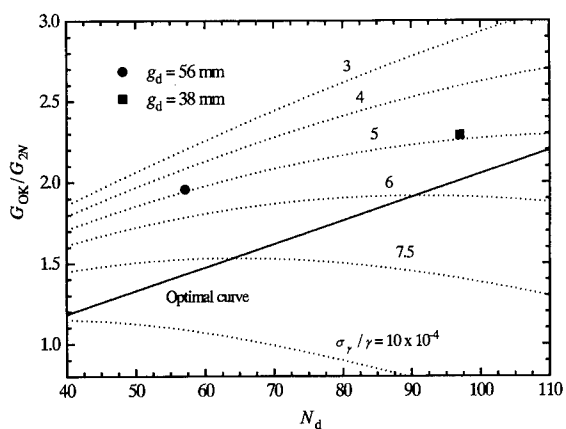


Fig. 3. Ratio of the gain of the ETLOK-II to a normal undulator with  $2N$  periods vs. slippage number.

Fig. 4 shows the output spectra obtained with the photodiode array. Fig. 4a shows a spectrum of the spontaneous emission after penetrating the upstream mirror when the cavity length was detuned, Fig. 4b shows the spectrum near the oscillation threshold, and Fig. 4c shows the

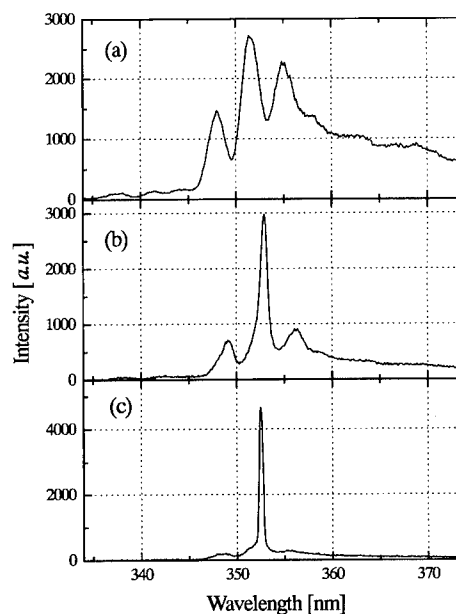


Fig. 4. Output spectra of spontaneous emission (a), near lasing threshold (b), and lasing with a filter in front of the monochromator (c).

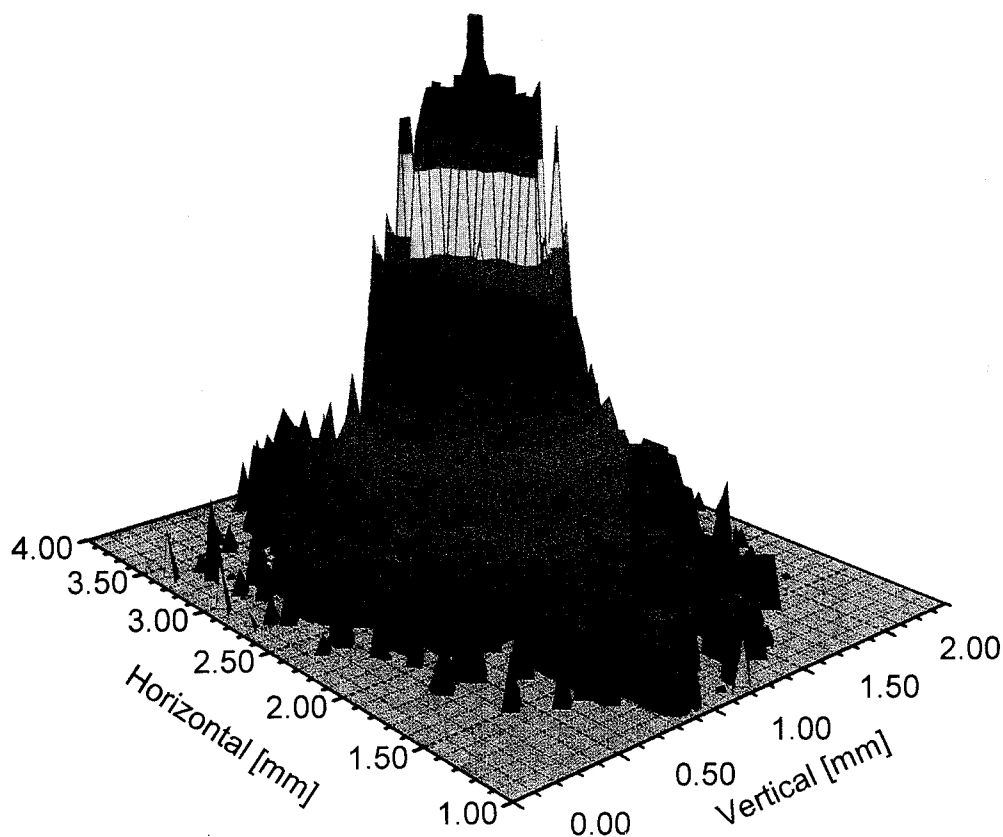


Fig. 5. Intensity pattern of the FEL output.

spectrum during oscillation, when the cavity length was tuned, with a neutral-density filter in front of the monochromator to reduce the intensity. The three spectra were obtained in different runs, and the electron-beam energy was slightly different each time; thus, one cannot precisely compare the peak wavelengths. The peak wavelength and the bandwidth of the spectrum in Fig. 4c are 352.4 nm and 0.4 nm, respectively. If the spectral resolution ( $\sim 0.2$  nm) of the system is taken into account, the actual bandwidth should be much smaller. This means that, though the output power is low, the output light is quite coherent. Lasing continued when the electron-beam current decreased from 10 to 6 mA/bunch. The gap of the OK was varied sometimes during lasing. The peak wavelength of the oscillation varied from 350 to 353 nm owing to the fine structure of the spontaneous-emission spectrum characteristic of the OK.

The optical cavity length was deliberately detuned during lasing. The detuning curve (not shown) was almost Gaussian with one standard deviation of 4.8  $\mu\text{m}$ . The time structure of the output spectrum measured by the system did not show the periodicity of 120 ms which had been seen in the case of the lasing of the lasing at 595 nm [3]. This is probably because the ring damping time was shorter ( $\sim 110$  ms) this time, owing to the higher electron-beam energy compared with that ( $\sim 200$  ms) in the previous experiment. It should be noted, however, that the time resolution of the measurement system was 33 ms. Actually, the time structure of the laser output measured with a PIN photodiode with higher time resolution showed a chaotic behavior with pulse width of about 2 ms. This made the measurement of the output power with the photodiode (after calibration) fairly difficult. The peak output power was deduced to be higher than 50 mW. More precise measurements will be carried out in the near future.

Finally, the output-laser intensity pattern, at the exit optical mirror, observed with a calibrated CCD camera is shown in Fig. 5. The component around the lasing pattern is due to the resonator spontaneous-emission which has penetrated the high-reflectivity mirror. The highest laser peak obtained so far is about 40 times as high as the peak of the latter.

## 5. Conclusion

The operating mode of the storage ring NIJI-IV was modified to accommodate the low-emittance electron beam, which led to successful lasing at 352 nm. Further experiments on lasing are under way.

In order to further increase the peak current of the stored beam, a single-bunch injection system is now being constructed [10]. The overlap of the electron beam and optical beam is very poor because the cross section of the former is ellipsoidal in shape with the long horizontal axis while that of the resonator optical beam is round. The

emittance coupling of the NIJI-IV is very low, as has been mentioned. An experiment to obtain an electron beam with round cross section is under way using a skewed quadrupole magnet. Recovery of the degraded optical-cavity mirrors by plasma treatment and annealing is also being studied [9,11].

## Acknowledgement

This work has been partly supported by the Peaceful Utilization Technology of Nuclear Energy from the Science and Technology Agency of Japan.

## References

- [1] M. Kawai, K. Aizawa, S. Kamiya, M. Yokoyama, Y. Oku, K. Owaki, H. Miura, A. Iwata, M. Yoshiwa, T. Tomimasu, S. Sugiyama, H. Ohgaki, T. Yamazaki, K. Yamada and T. Mikado, Nucl. Instr. and Meth. A 318 (1992) 135.
- [2] T. Yamazaki, K. Yamada, S. Sugiyama, H. Ohgaki, T. Tomimasu and M. Kawai, Nucl. Instr. and Meth. A 318 (1992) 142.
- [3] T. Yamazaki, K. Yamada, S. Sugiyama, H. Ohgaki, N. Sei, T. Mikado, T. Noguchi, M. Chiwaki, R. Suzuki, M. Kawai, M. Yokoyama, K. Owaki, S. Hamada, K. Aizawa, Y. Oku, A. Iwata and M. Yoshiwa, Nucl. Instr. and Meth. A 331 (1993) 27.
- [4] T. Yamazaki, K. Yamada, N. Sei, S. Sugiyama, H. Ohgaki, T. Mikado, T. Noguchi, M. Chiwaki, R. Suzuki, M. Kawai, M. Yokoyama, S. Hamada and T. Tomimasu, Proc. 1st Asian Symp. on FEL, IHEP, Beijing, 1993, to be published; T. Yamazaki, K. Yamada, S. Sugiyama, H. Ohgaki, N. Sei, T. Mikado, T. Noguchi, M. Chiwaki, R. Suzuki, M. Kawai, M. Yokoyama and S. Hamada, Nucl. Instr. and Meth. A 341 (1994) ABS 3.
- [5] T. Tomimasu, S. Sugiyama, H. Ohgaki, T. Yamazaki, K. Yamada, T. Mikado, M. Chiwaki, R. Suzuki, S. Suse, M. Yoshiwa and A. Iwawata, Proc. 7th Symp. on Accelerator Science and Technology, Osaka University, (1989) p. 347; H. Ohgaki, T. Yamazaki, S. Sugiyama, T. Mikado, R. Suzuki, and T. Tomimasu, *ibid.*, p. 284.
- [6] M. Yokoyama, M. Kawai, S. Hamada, T. Yamazaki, K. Yamada, N. Sei, S. Sugiyama, H. Ohgaki, T. Mikado, T. Noguchi, R. Suzuki and M. Chiwaki, these Proceedings (16th Int. Free Electron Laser Conf., Stanford, CA, USA, 1994) Nucl. Instr. and Meth. A 358 (1995) 378.
- [7] T. Yamazaki, K. Yamada, S. Sugiyama, H. Ohgaki, T. Tomimasu, T. Noguchi, T. Mikado, M. Chiwaki and R. Suzuki, Nucl. Instr. and Meth. A 309 (1991) 343; K. Yamada, T. Yamazaki, S. Sugiyama, T. Tomimasu, H. Ohgaki, T. Noguchi, T. Mikado, M. Chiwaki and R. Suzuki, Nucl. Instr. and Meth. A 318 (1992) 33.
- [8] H. Ohgaki, S. Sugiyama, T. Mikado, M. Chiwaki, K. Yamada, R. Suzuki, N. Sei, T. Noguchi and T. Yamazaki, Proc. 9th Symp. on Accelerator Science and Technology, KEK (National Laboratory for High Energy Physics) Tsukuba, 1993, p. 407.

- [9] K. Yamada, T. Yamazaki, N. Sei, N. Shimizu, M. Kawai, M. Yokoyama, S. Hamada, K. Saeki, E. Nishimura, T. Mikado, T. Noguchi, S. Sugiyama, M. Chiwaki, H. Ohgaki, R. Suzuki and T. Tomimasu, these Proceedings (16th Int. Free Electron Laser Conf., Stanford, CA, USA, 1994) Nucl. Instr. and Meth. A 358 (1995) 392.
- [10] M. Yokoyama, M. Kawai, S. Hamada, K. Owaki, T. Yamazaki, T. Mikado, K. Yamada, N. Sei, S. Sugiyama, H. Ohgaki, T. Noguchi, R. Suzuki, M. Chiwaki and T. Tomimasu, Nucl. Instr. and Meth. A 341 (1994) 367.
- [11] K. Yamada, T. Yamazaki, N. Sei and T. Mikado, Nucl. Instr. and Meth. A 341 (1994) ABS 139.

## Expected performance of FELINA, the Dutch VUV-FEL in Amsterdam

R.J. Bakker <sup>a</sup>, R. Maas <sup>a,\*</sup>, G. Luijckx <sup>a</sup>, V.N. Litvinenko <sup>b</sup>, B. Faatz <sup>c</sup>,  
P.W. van Amersfoort <sup>c</sup>

<sup>a</sup> FOM Instituut voor Kernfysica, P.O. Box 41882, 1009 DB Amsterdam, The Netherlands

<sup>b</sup> Duke University, FEL Laboratory, P.O. Box 90319, Durham NC 27708-0319, USA

<sup>c</sup> FOM Instituut voor Plasmafysica "Rijnhuizen", P.O. Box 1207, 3430 BE Nieuwegein, The Netherlands

### Abstract

The FOM Institute for Nuclear Physics (NIKHEF-K) in Amsterdam currently operates the pulse-stretcher and storage ring AmPS as a continuous electron beam source for nuclear physics experiments up to 900 MeV. Here we review the feasibility to use AmPS as a driver for FELINA (Free-Electron Laser IN Amsterdam) for the generation of narrow bandwidth radiation in the (vacuum) ultra-violet spectral range in a two-stage project. For the first stage we consider a relatively low-cost demonstration experiment in the UV, i.e.,  $\lambda \geq 200$  nm, where FEL experiments will be performed in parallel with the nuclear physics research program. Lasing in the VUV requires significant modifications to the ring in order to enhance the gain. From preliminary calculations it can be deduced that lasing down to wavelengths less than 100 nm is then possible.

### 1. Introduction

The Amsterdam Pulse Stretcher project (AmPS) involves the operation of a ring, used as a 250–900 MeV electron beam source for nuclear physics experiments [1]. The ring has been designed for two modes of operation. In stretcher mode the ring is filled every 4 ms in order to provide a continuous external beam with a current up to 25  $\mu$ A. In storage mode the ring can contain up to 200 mA of beam current, used for interaction with an internal gas-jet target. This current in combination with the dimensions of the ring (a circumference of 212 m with 32-m long dispersion-free straight sections) makes the machine a promising driver for a FEL covering the UV and VUV spectral range.

Until 1998, 2500 h/y are designated for nuclear physics purposes. In the remaining time AmPS could be used for FEL physics. However, the design of the ring has not been optimized for FEL operation in the VUV (e.g., the unnormalized emittance is as high as  $160 \pi$  nm rad at 900 MeV). Hence, some modifications are necessary. We consider to do this in two stages. The first stage involves a relatively low-cost demonstration experiment addressing

the UV, i.e.,  $\lambda > 200$  nm. This stage takes place without disruption of the nuclear physics research program. In the second stage more drastic modifications are required in order to construct a FEL, capable of lasing to (at least) 100 nm. In this paper we focus on the requirements for the first stage.

### 2. Machine description

A schematic layout of AmPS is given in Fig. 1 and its parameters are summarized in Table 1. The ring has a "square" shape with a four-fold symmetric structure. The magnetic lattice is of the FODO type and consists of 32 dipoles, 68 quadrupoles, and 32 sextupoles. The electron beam, emerging from the electron linac, is inserted in the east straight section. The north section is occupied by the rf-cavities and extraction devices for the stretcher mode of operation. The west section contains the internal target. At present the south section is still available for the installation of an undulator or optical klystron.

From Table 1 it follows that, for the existing lattice, the FEL gain will be low due to the the low peak current and the high emittance.

**Peak current:** In storage mode 336 bunches circulate in the ring, limiting the peak current by the maximum average current which can be stored in the ring. A decrease of

\* Corresponding author. Tel. +31 20 592 2087, fax +31 20 592 2165.



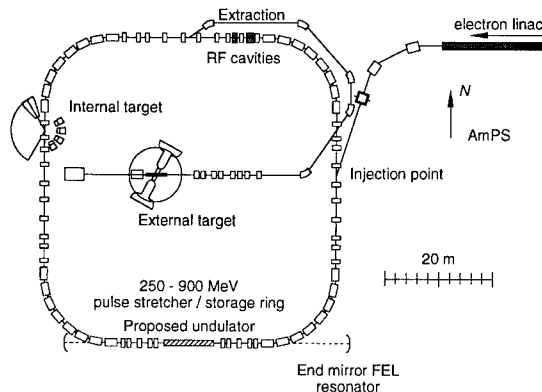


Fig. 1. Layout of AmPS. The 700 MeV injection linac stretches out further to the right.

the number of bunches, while keeping the average current constant, can significantly increase the current per bunch and peak current. With a current of 10–20 mA per bunch, the peak current can easily be increased to 40 A.

**Emittance:** The present usage of AmPS does not require low emittances and the dispersion in the curved sections and the emittance are high. In order to lower the emittance it is necessary to decrease the dispersion function inside the dipoles. The most economic solution requires an alternative powering of the quadrupoles in the curved sections without changing their position. This leads to a reduction of the emittance by a factor of 3.5, i.e., an emittance of  $45 \pi$  nm rad at 900 MeV or  $26 \pi$  nm rad at 700 MeV. A further reduction of the emittance is not possible without installation of additional quadrupoles. From calculations it followed that AmPS can be modified to a high brilliance lattice, i.e., an emittance less than  $5 \pi$  nm rad at 900 MeV, with the installation of 32 additional quadrupole lenses in the arcs [2].

Table 1  
List of important machine parameters of AmPS

|   | Existing   | Update    |
|---|------------|-----------|
| Beam energy $E$ (MeV)                             | 250–900    | 250–900   |
| Circumference $L$ (m)                             | 211.618    | 211.618   |
| Compaction factor $\alpha$                        | 0.027      | 0.010     |
| Average current $I_{av}$ (mA)                     | 200        | 200       |
| Number of bunches $n$                             | 336        | 2         |
| Peak current $I_p$ (A)                            | 0.6        | 40        |
| Horizontal emittance $\epsilon_x$ ( $\pi$ nm rad) | $\leq 160$ | $\leq 45$ |
| Vertical emittance $\epsilon_y$ ( $\pi$ nm rad)   | $< 8$      | $< 2$     |
| RF frequency $f_{RF}$ (MHz)                       | 476        | 476       |
| RF voltage $V_{RF}$ (kV)                          | 350        | 350       |
| Impedance $^b Z/n$ ( $\Omega$ )                   | $< 5$      | $< 5$     |

<sup>a</sup> For  $E = 900$  MeV.

<sup>b</sup> Estimated

### 3. FEL design considerations

**Beam energy:** In order to reduce the effects of intra-beam scattering, it is thought sensible to strive for operation at energies in between 700 and 900 MeV. Here the lower value enables the most gain, while the higher value is more favorable for a high output power and beam lifetime.

**Wiggler period:** The choice of wiggler period will be dictated by the required tuning range. The longer wavelength limit is of special importance for an initial experiment. In this case it is desirable to have the option of lasing in the near visible because of the larger choice of available optical materials for a high- $Q$  resonator. The undulator period must not be too long, however, since this limits the shortest obtainable wavelength for later experiments. For the simulations we have taken an undulator with a 11 cm period. With this undulator, the resonance condition can be satisfied between 25 and 600 nm.

**Undulator scheme:** In order to obtain a flexible but inexpensive device, we consider the use of an optical klystron (OK), i.e., a set of two small undulators, separated by a dispersive section with adjustable magnetic field strength. With an OK, the total undulator length can be reduced significantly while maintaining a high gain. A drawback of the OK, the lower efficiency, can be avoided through adjustment of the magnetic field strength of the dispersive section. During operation both options can be used sequentially. First using a high field strength in the dispersive section to enhance the small-signal gain. In saturation the field strength can be reduced to obtain a higher saturated power level.

**Resonator:** As will be shown in the next section, the gain will be modest and a resonator is required to amplify the spontaneous emission on successive passes. In order to ensure interaction on every round-trip, the cavity length must be chosen such that the round-trip frequency equals a subharmonic of the micropulse repetition frequency. The solution sketched in Fig. 1 corresponds to a regular laser resonator with a length equal to one quarter of the circumference of the ring. This way, the resonator mirror can be positioned on either side of the straight section. In Fig. 1 the center of the cavity has been shifted with respect to the center of the undulator. This has been done to fit the resonator within the existing building. A drawback is the stability of the cavity. For optimum gain the resonator will be close to concentric. For the parameters listed in Table 2 we have, therefore, increased the Rayleigh length with 70% in order to increase the tolerances on the cavity parameters.

### 4. Gain calculations

We calculated the gain for both OK and conventional FEL configurations using rigorous 3-D low gain formulae

[3] and compared our results with results obtained with the 3-D multi-particle simulation code TDA [4]. Since the results were similar, we only present the results obtained with our 3-D formulae.

As regards the OK configuration, we took a interaction region with  $2 \times 24$ , 11-cm long, periods. The two undulators are separated by a dispersive section with a physical length of 0.6 m. The field-strength of this section is always tuned to give maximum gain. A Gaussian distribution of the electrons in the phase space is assumed as well as the TEM<sub>00</sub> optical mode in the cavity. The waist of both the optical mode and the electron beam are taken in the center of the OK. Simulation parameters are given in Table 2. For reasons stated in the previous paragraph these values do not correspond with an optimum filling factor. As a result the calculated gains are 20% less than the optimum value.

For a regular FEL the gain is proportional to the peak current  $I_p$ . In a storage ring, however, there are no direct means to control the peak current since it is determined by the current per bunch ( $I_b$ ) and the relative energy spread ( $\sigma_e$ ):

$$I_p = \sqrt{2\pi} I_b \nu_s / \alpha \sigma_e, \quad (1)$$

where  $\nu_s$  denotes the tune and  $\alpha$  the momentum compaction factor. Both  $\nu_s$  and  $\alpha$  are determined by the lattice. From Eq. (1) it thus follows that  $I_b$  must increase in order to increase the peak current. Unfortunately it is not possible to increase the particle density to infinity. Due to the microwave instability the energy spread and bunch length will increase as soon as the peak current becomes too high:

$$I_p < 2\pi\alpha\sigma_e^2 \frac{E}{e(Z/n)}, \quad (2)$$

where  $E$  is the beam energy in eV,  $e$  is the electron charge, and  $Z/n$  is the longitudinal impedance of the ring. For AmPS the impedance is estimated to be less than  $5\Omega$ . However, there has not yet been an opportunity to measure

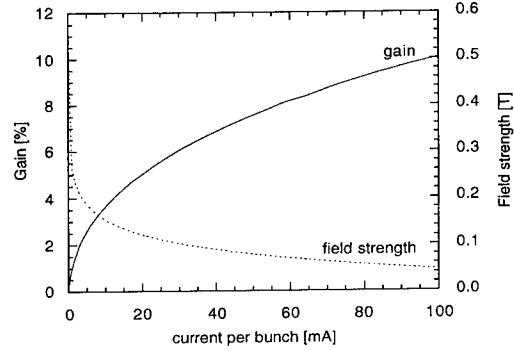


Fig. 2. Gain for  $\lambda = 250$  nm (solid line), and the optimum field strength of the dispersive section (dashed line) as a function of the current per bunch.

the impedance. This will be discussed in Section 5. Due to microwave instability the energy spread becomes:

$$\sigma_e = \left( \frac{1}{\sqrt{2\pi}} \frac{\nu_s I_b e(Z/n)}{\alpha^2 E} \right)^{1/3}. \quad (3)$$

The gain reduction due to energy spread is roughly proportional to  $\sigma_e^2$ . Hence, it remains favorable to increase the current per bunch in order to enhance the small-signal gain. In Fig. 2 the results are shown for the geometry described in the previous section at  $\lambda = 250$  nm. It can be concluded that it is favorable to increase  $I_b$  to an as high as possible current. Specifically an increase to  $I_b = 20$  mA significantly increases the FEL performance. Note that the field strength of the dispersive section must decrease in order to obtain maximum gain. This is due to an increase in energy spread.

Saturation in a storage-ring FEL is induced by gain-reduction self-induced beam heating. The gain formula can thus be used to estimate the equilibrium energy spread, i.e., the energy spread induced by the FEL interaction for the case where the gain equals the threshold losses. Ac-

Table 2  
Simulation parameters

|                                   |                 |
|-----------------------------------|-----------------|
| RMS undulator strength $K$        | $\leq 4.7$      |
| Number of periods $N$             | $2 \times 24$   |
| Undulator period $\lambda_u$      | 11.0 cm         |
| Length dispersive section $L_d$   | 0.6 m           |
| Cavity length $L_c$               | 52.9 m          |
| Stability parameter $g^2$         | 0.93            |
| Raleigh length $\beta_0$          | 3.35 m          |
| Beam energy $E$                   | 700 MeV         |
| Horizontal emittance $\epsilon_x$ | $26 \pi$ nm rad |
| Vertical emittance $\epsilon_y$   | $1 \pi$ nm rad  |
| $\beta$ functions $\beta_{x,y}$   | 3.35 m          |
| Natural energy spread $\sigma_e$  | 0.03%           |
| Synchrotron power $P_{SR}$        | 1.2 kW          |

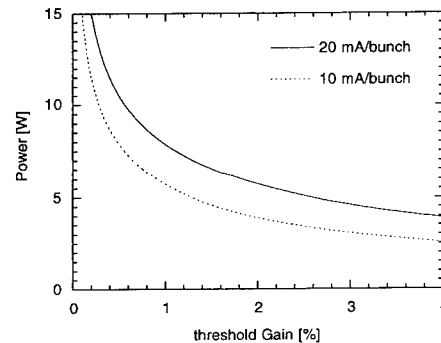


Fig. 3. Power vs the threshold gain for a 700 MeV electron beam at  $\lambda = 250$  nm for micropulses containing 20 or 10 mA per bunch, respectively. The average current is 200 mA.

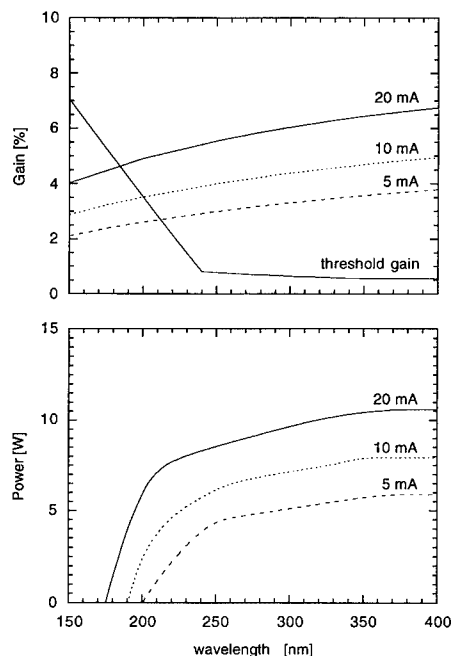


Fig. 4. Power and gain vs wavelength for three different bunch currents.

cording to the Renieri limit the average extracted power is also proportional to the energy spread:

$$P_{\text{FEL}} = 2P_{\text{sr}} \frac{\sigma_e^2 - \sigma_e'^2}{\sigma_e} e^{-1/2}, \quad (4)$$

where  $\sigma_e$  denotes the natural energy spread of the ring.  $P_{\text{sr}}$  denotes the average synchrotron power. It follows that there is a relation between the threshold losses and the maximally extractable average power. In Fig. 3 the results for AmPS are shown. It follows that 5–10 W can be extracted. The extracted optical power is a fraction of this value and depends on the ratio between the total cavity losses and the outcoupling losses.

Finally in Fig. 4 we show the calculated gain and power as a function of the wave-length. Estimates of the threshold gain have been obtained from a combination of results published [5,6] It follows that lasing until  $\lambda = 200$  nm is feasible, provided that there is more than 10 mA per bunch available.

## 5. Discussion

From the calculations presented above we conclude that lasing in the UV and near-visible, i.e.,  $\lambda > 200$  nm, is feasible. Some modifications are required, though.

*Increase of the current per bunch.* At least 10–20 mA per bunch should be reached in order to obtain sufficient

peak current. Here it is important to state that there is some uncertainty regarding the obtainable peak current. Because of microwave instabilities there is, for high peak currents, a relation between the peak current and the longitudinal impedance of the ring (see Eq. (2)). At present we only have an estimate of the impedance. It is our believe that the value quoted,  $5 \Omega$ , is a worst case.

*Reduction of the emittance.* With the present emittance the expected gain would reduce the gain values quoted in Fig. 4 with a factor of approximately 3.

For the above mentioned mode of operation, the average extracted optical power is expected to be of the order of 5–10 W for an electron beam with an energy of 700 MeV and 200 mA of average beam current. Due to an increase in synchrotron power it is expected that at 900 MeV the power will be of the order of 15–25 W.

In order to reach the VUV more gain is required. For this several options are open which are still under discussion, e.g., a further reduction of the emittance or an increase of the undulator length. Preliminary calculations indicate that lasing for  $\lambda > 70$  nm is feasible which makes AmPS competitive with other storage-ring projects, in Dortmund and at Duke University, which are presently in the construction phase.

## Acknowledgements

The work described in this paper is part of the research program of the FOM institute for Nuclear Physics (NIKHEF-K), made possible by financial support from the Foundation for Fundamental Research on Matter (FOM) and the Netherlands Organization for Scientific Research (NWO). The authors want to thank Ying Wu of the Duke University FEL for his contributions.

## References

- [1] G. Luijckx, H. Boer Rookhuizen, P.J.T. Bruinsma, A.P. Kaan, F.B. Kroes, L.H. Kuijer, A. van der Linden, P. Louwrier, R. Maas, J.G. Noomen and J.B. Spelt, Proc. 2nd Europ. Accelerator Conf. (EPAC) 1990, p. 589.
- [2] R. Maas and G. Luijckx, Proc. 3rd Europ. Accelerator Conf. (EPAC), 1992, p. 480.
- [3] V.N. Litvinenko, Proc. National Synchrotron Radiation Conf. SR-94, Novosibirsk, July 11–15, 1994, Nucl. Instr. and Meth. A, to be published.
- [4] T.-M. Tran and J.S. Wurtele, Computer Phys. Commun. 54 (1989) 263.
- [5] B.E. Newnam, SPIE Free-Electron Lasers 738 (1987) 155.
- [6] W.B. Colson, Laser Handbook, Vol. 6, eds. W.B. Colson, C. Pellegrini and A. Renieri (North-Holland, Amsterdam, 1990) pp. 463–484.

# The barrel shaped resonator for the photon storage ring

A.I Kleev <sup>a</sup>, A.B Manenkov <sup>a</sup>, H. Yamada <sup>b,\*</sup>

<sup>a</sup> Institute for Physical Problems, Russian Academy of Science, Kosygina 2, Moscow 117334, Russian Federation

<sup>b</sup> Ritsumeikan University & PRESTO Research and Development Co. of Japan, 2-1-1 Yato-Cho, Tanashi-City, Tokyo 188, Japan

## Abstract

The eigenmodes of a barrel shaped resonator are analyzed to optimize the optical cavity of the photon storage ring. The results are obtained by the Galerkin technique and the quasi-optics approximation. It is shown that there are two types of eigenmodes in the system: the quasi-*E* and quasi-*H* modes. The dependences of the mode losses and the field distribution on the resonator geometry and wall impedances are examined. The effects of intermodal coupling are considered.

## 1. Introduction

The barrel shaped resonator (BSR) is a promising system for the design of the photon storage ring (PhSR) [1]. In the BSR the whispering gallery modes [2,3] (or the modes of similar types) are known to be formed by the superposition of the partial rays, which propagate into the cavity and are repeatedly reflected from a concave wall (Fig. 1). The partial rays of these modes generally form several caustic surfaces [2,3]. There are a few works dealing with the analysis of the mode in the BSR, in which the mode losses are not examined. In general, the ohmic losses are calculated by the perturbation method. In the BSR, however, the incidence angle of partial rays of the whispering gallery modes generally becomes close to the Brewster angle, thus this method cannot be applied.

In the paper the features of the whispering gallery modes (WGM) of the BSR are studied. We examine two geometries: an open resonator with uniform slits (Fig. 1b) and a closed one with parallel plates (Fig. 1c). All the dimensions of the BSR are assumed to be greater than the wavelength  $\lambda$ .

## 2. The characteristic equation

We assume that the mirror surface (the side wall) is defined by the equation  $r = \tilde{R}(z)$ . The electric  $E$  and magnetic  $H$  fields of the eigenmodes can be expressed in terms of two scalar functions:  $\Phi^{(e)}$  and  $\Phi^{(m)}$ . The electro-

magnetic fields on the walls satisfy the following boundary conditions [4]:

$$\mathbf{n} \times \mathbf{E} = \zeta \mathbf{n} \times (\mathbf{n} \times \mathbf{H}), \quad (1)$$

where  $\mathbf{n}$  is the normal unit vector of the wall surface,  $\zeta$  is the wall impedance, which can be different for the mirror and the plates. Later we examine only the even modes, for which  $E_\varphi(z) = E_\varphi(-z)$ . The odd modes can be treated in a similar way.

First we consider the closed BSR (Fig. 1c). The above functions  $\Phi^{(e)}$  and  $\Phi^{(m)}$  are expressed in terms of sums of the functions which describe the waves of a radial transmission line [4]. Using the standard quasi-optics approximation [3] we can write the functions near the mirror surface ( $r \approx \tilde{R}(z)$ ) in the form

$$\Phi^{(e)} = \exp(ip\varphi) \sum_n A_n^{(e)} \sin(w_n^{(e)} z) \cos(\Omega(v_n^{(e)} r)), \quad (2)$$

$$\Phi^{(m)} = \exp(ip\varphi) \sum_n A_n^{(m)} \cos(w_n^{(m)} z) \cos(\Omega(v_n^{(m)} r)),$$

where  $\Omega(x) = p(\tan \theta - \theta) - \pi/4$ ,  $\sin \theta = (1 - p^2/x^2)^{1/2}$ ,  $(v_n^{(e)})^2 + (w_n^{(e)})^2 = (v_n^{(m)})^2 + (w_n^{(m)})^2 = k^2$ ,  $k = 2\pi/\lambda$  is the wavenumber, and  $p$  is the azimuth index of the mode ( $p \gg 1$ ). In deriving Eq. (2) we replace the cylindrical functions by their Debye approximation formulas. The wavenumbers  $w_n^{(e)}$  and  $w_n^{(m)}$  are defined by the boundary condition (1) on the plates  $z = \pm D$ .

To derive the characteristic equation for the wavenumber  $k$ , we take into account the boundary condition (1) on the mirror surface and apply the Galerkin technique [5,6]. After these procedures we transform the initial problem to the algebraic eigenvalue problem:

$$Sa = \Gamma a, \quad a = (A_1^{(e)}, \dots, A_N^{(e)}, A_1^{(m)}, \dots, A_N^{(m)})^T, \quad (3)$$

where  $\Gamma$  is the eigenvalue connected with  $k$  and  $a$  is the eigenvector; the superscript T denotes transposition. As is

\* Corresponding author. Tel. +81 424 68 4479, fax +81 424 76 2057.

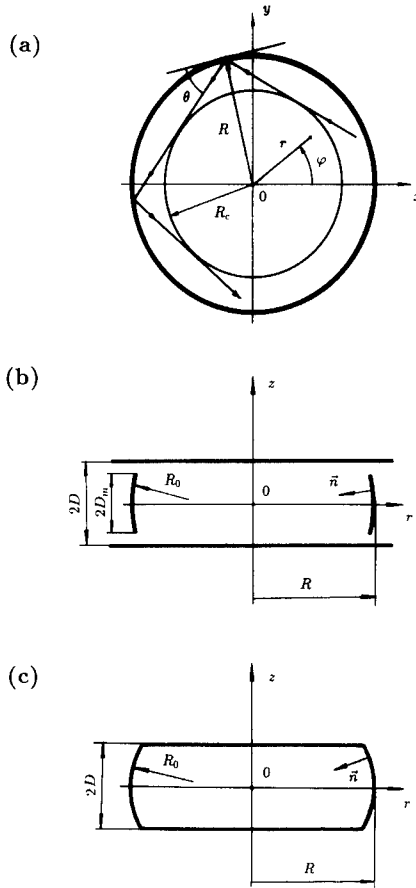


Fig. 1. The cross sections of the BSRs under study and the coordinate systems.

usual in the expansions (2) we retain a finite number  $N$  of the terms. The matrix  $S$  has the symbolic form

$$S = \begin{pmatrix} \mathcal{R}_\perp S^{(e)} & S^{(em)} \\ S^{(me)} & \mathcal{R}_\parallel S^{(m)} \end{pmatrix}. \quad (4)$$

The quantities  $\mathcal{R}_\parallel$  and  $\mathcal{R}_\perp$  are the reflection coefficients for the partial optical rays with different polarizations.

For the open BSR (Fig. 1b) the calculations are made by a similar manner. The slits on the mirror can be considered as parts of the surface, coated by perfectly absorbing material; for these parts ( $|z| > D_m$ ) we have  $R_\parallel = R_\perp = 0$ . The boundary conditions on the other parts of the mirror ( $|z| < D_m$ ) and on the plates have the form (1).

For the cylindrical cavity ( $R_0 = \infty$ ) with perfectly conducting walls the system of eigenmodes is known to be divided into two groups: the  $E$  modes ( $H_z = 0$ ) and the  $H$  modes ( $E_z = 0$ ). In a general case  $E_z \neq 0$  and  $H_z \neq 0$ . Under the condition  $2D \cos \theta \ll R_0$  the mode system can be approximately separated into two groups: the quasi- $E$  modes (or  $qE$  modes) and the quasi- $H$  modes (or  $qH$  modes).

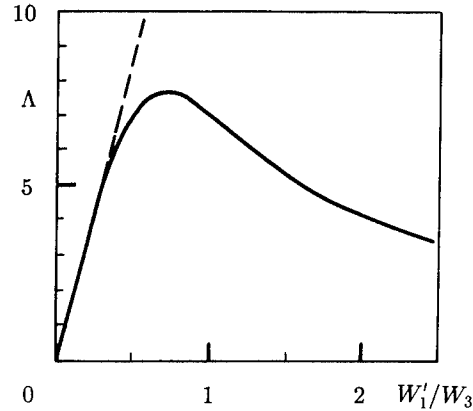


Fig. 2. The losses of the dominant  $qH$  mode ( $l=1$ ) as a function of  $W'_1/W_3$ .

modes). For the first group we have  $|E_z| \gg |H_z|$ , and for the second group we have  $|H_z| \gg |E_z|$ .

Under the conditions mentioned above the mode wavenumber  $k$  is approximately equal to  $kR = \nu'_{pj} + i \ln \Gamma/2 \sin \theta$ , where  $\nu'_{pj}$  is the  $j$ th root of the equation  $J'_p(\nu'_{pj}) = 0$  ( $J'_p$  is the first derivative of the Bessel function). Later on we shall number the modes by the three indices  $p, j, l$ . The “vertical” index  $l$  ( $l=1, 2, \dots$ ) is the number of the eigenvalue (see Eq. (3)) for fixed values of the azimuth index  $p$  and the radial index  $j$  of the mode.

### 3. Numerical results

Below we shall give primary attention to the analysis of the  $qH$  modes, which can be applied in PhSR [1–3]. Considering the mode losses, we shall use the auxiliary parameter  $\Lambda = -20 \log |\Gamma|$ . We shall also use the resonator dimensionless parameters  $\mathcal{N} = kD^2/2R \sin \theta$ ,  $\mathcal{G}$

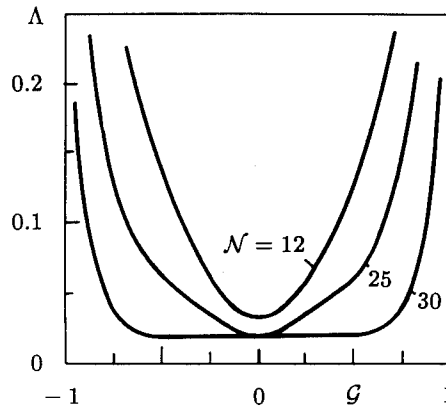


Fig. 3. The losses of the dominant  $qH$  mode ( $l=1$ ) as function of the parameter  $\mathcal{G}$ . The numbers near the curves are the values of  $\mathcal{N}$ .

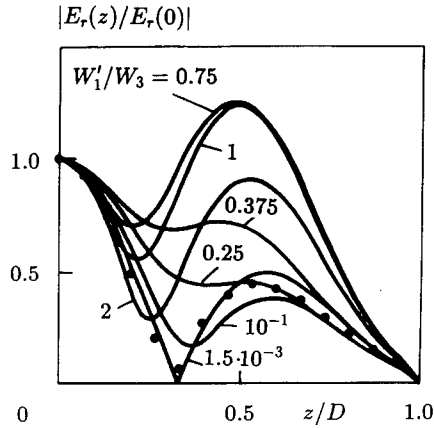


Fig. 4. The field distribution of the dominant qE mode ( $l=1$ ). The numbers near the curves are the values of  $W'_1/W_3$ .

$= 1 - 2R \sin^2 \theta / R_0$ ,  $W_1 = kD\zeta$ ,  $W_2 = \zeta/kD$ ,  $W_3 = kD \sin \theta$ ,  $W_4 = \zeta \sin \theta$ . Note, that  $\theta = \arccos(p/kR)$  is the grazing angle of the partial rays. For simplicity we suppose that the wall impedance is a constant. It can be shown, that the losses of the qH modes are defined by the surface electric currents on the mirror and they do not depend significantly on the conductivity of the plates.

Fig. 2 shows the parameter  $\Lambda$  of the dominant qH modes versus the ratio  $W'_1/W_3$  ( $W'_1 = \text{Re}W_1$ ). Under condition  $\sin \theta \sim |\zeta_1|$  the incidence angle is close to the Brewster angle of the metallic wall and the reflection of the partial rays of the modes is minimal. In Fig. 2 the dashed line gives the same dependence calculated by the perturbation method. The data, obtained by this method, is seen to agree with the above results if  $\sin \theta \gg |\zeta|$ .

In the open BSR the WGMs have both ohmic and radiation losses. The later can be small if the vertical size of the modes caustics are smaller than the mirror dimen-

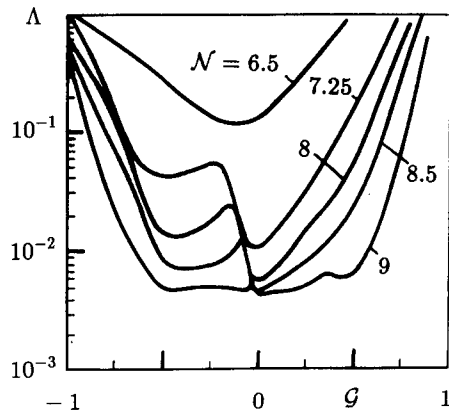


Fig. 5. The losses of the dominant qE modes ( $l=1$ ) as function of the parameter  $\mathcal{G}$ . The numbers near the curves are the values of  $N$ .

sion  $D_m$ . Fig. 3 shows the mode losses as a function of the  $\mathcal{G}$  for the dominant qH mode ( $l=1$ ) of the open BSR. The resonator parameters are:  $W'_1/W_3 = 10^{-3}$ ,  $D/D_m = 2$ .

When the hybridization effects are ignored, the field distribution of the qE modes does not depend significantly on the conductivity of the mirror surface. A finite conductivity changes the fields of the qE modes. Fig. 4 shows the distributions of the component  $E_r$  on the mirror for the dominant qE mode ( $l=1$ ). The parameters of the problem are:  $N=10$ ,  $\mathcal{G}=0$ ,  $W'_2=0.75$ ,  $\alpha = D \sin 2\theta / [R_0(\zeta + \sin \theta)] = 10^{-2}$ . The black circles present the field distribution for the resonator with infinite mirror.

It is known that the losses of the modes can be abruptly changed when intermodal coupling takes place. Such a coupling can arise when the mode frequencies draw closer together. In this case the losses of some modes are usually decreased. This effect is demonstrated by Fig. 5; in this figure the dependences of the  $\Lambda$  on the  $\mathcal{G}$  are presented for the qE-modes. The resonator parameters are:  $W'_2=1$ ,  $W'_4 = 0.25 \times 10^{-3}$ .

#### 4. Conclusion

In the paper we have examined the WGMs of the BSR. The results have been obtained by the characteristic equation which we have solved in the quasi-optics approximation. We have shown that the losses of the eigenmodes are defined by relations between the field magnitudes on the plates  $z = \pm D$  and on the mirror. The losses of the qH modes proved to be large if the incidence angles of the partial rays are close to Brewster angle ( $\sin \theta \sim |\zeta|$ ).

Geometrical imperfections of the resonator can introduce mode coupling, and the parasitic modes may distort the field structure of the operating mode. This distortion can be reduced to a minimum if we filter undesired modes. The results of calculations show that the open BSR with uniform slits (Fig. 1b) has better selectivity properties than the closed BSR. In such a system under specific conditions the losses of the dominant operating qH mode can be smaller than the losses of the other modes.

#### References

- [1] H. Yamada, Nucl. Instr. and Meth. B 79 (1993) 762 and references therein.
- [2] J.B. Keller and S.I. Rubinow, Ann. Phys. 9 (1960) 24.
- [3] L.A. Weinstein, Open Resonators and Open Waveguides (Golem, Boulder, Colorado, 1969).
- [4] N. Marcuvitz, Waveguide Handbook (McGraw Hill, New York, 1951).
- [5] C.A.J. Fletcher, Computational Galerkin Methods (Springer, New York, 1984).
- [6] A.I. Kleev and A.B. Manenkov, Soviet J. Commun. Techn. & Electron. 33 (1988) 115.

## Observation of micro–macro temporal structure and saturation mechanism on the UVSOR free electron laser

H. Hama <sup>a,b,\*</sup>, J. Yamazaki <sup>a</sup>, T. Kinoshita <sup>a</sup>, K. Kimura <sup>b</sup>, G. Isoyama <sup>c</sup>

<sup>a</sup> UVSOR Facility, Institute for Molecular Science, Myodaiji, Okazaki 444, Japan

<sup>b</sup> Graduate University for Advanced Studies, Myodaiji, Okazaki 444, Japan

<sup>c</sup> The Institute of Scientific and Industrial Research, Osaka University, Ibaraki 567, Japan

### Abstract

The dynamic behavior of a free electron laser oscillation on an electron storage ring has been studied. We have measured time dependent micropulse evolution using a streak camera with a dual-sweep. Continuous lasing which appears under detuned condition has been ascertained to consist of discrete evolving groups of micropulses. In the gain-switching mode, bunch lengthening of the electrons due to bunch heating by the interaction with the laser was clearly observed.

### 1. Introduction

Complex properties of storage ring free electron lasers (SR-FEL) have been experimentally and theoretically studied [1–4]. It is a well-known phenomenon that the laser macrotemporal structure depends strongly on the resonator tuning condition, which is one of important characteristics of SR-FEL dynamics. In the UVSOR-FEL, quasi-periodical lasing pulses are seen under the best synchronization between the electron bunch and the optical bunch in the cavity, and cw-like lasing appears as the detuning is increased [5]. Similar behavior has been seen on other storage rings [3,6]. The saturation mechanism of the laser power without any external gain reduction is qualitatively explained by “bunch-heating” due to an interaction of the electron beam with the laser. The bunch heating, that is enhancement of the energy spread of the electrons and lengthening of the longitudinal bunch distribution, causes a reduction of the effective FEL gain. Thus the quasi-periodic lasing is considered to originate from gain oscillations due to bunch heating followed by longitudinal radiation damping of the electron bunch [1]. However, the detuning dependence of the macrotemporal structure has not been completely interpreted, and the transition region from periodic lasing to cw lasing has been studied as a chaotic regime [4]. Experimental data on the bunch heating and the laser macrotemporal structure have been insufficient for complete testing of theoretical models, because only the one-dimensional time dependent structure of the laser and

the time averaged distribution of the electron bunch have been hitherto measured.

In this article, we present experimental results using the dual-sweep streak camera and discuss the nature of the FEL oscillation on the storage ring.

### 2. UVSOR-FEL and experimental arrangement

The UVSOR-FEL has been operated since 1992 at wavelengths around 500 and 300 nm for basic research of the SR-FEL [5,7]. Using a higher harmonic rf cavity to reduce the bunch length and increase the peak current, an FEL gain of 0.6% at 10 mA/bunch has been obtained at wavelength around 500 nm, in good agreement with a theoretical prediction [7]. On-line reflectivities of mirrors in the optical cavity can be measured with a detuned method [7]. The cavity loss is usually in agreement with the theoretical gain at the lasing threshold current except the case of severe misalignment. Other parameters of the UVSOR-FEL are given in Ref. [5].

Time distributions of laser micropulse and the electron bunch lengths have been directly measured with a streak camera (Hamamatsu-C1587). A schematic drawing of the experimental setup is shown in Fig. 1. Using an rf synchronized sweep mode, both single- and multi-revolution exposures are available by varying the MCP gate time. In addition there is a slow sweep at right angles to the fast rf sweep. Selecting an appropriate wavelength region with bandpass filters in front of the streak camera, we can measure profiles of the electron bunch and/or the laser pulse. The projection of the two-dimensional spectrum on the fast sweep axis is the micropulse distribution, and that on the slow sweep axis is the macrotemporal structure.

\* Corresponding author. Tel. +81 564 55 7401, fax +81 564 54 7079, e-mail: hama@kekvox.kek.jp.

Therefore more precise time structure of the laser oscillation can be obtained than in previous one-dimensional measurements. A trigger signal for the MCP gate and the start of the slow sweep is also fed to the measurement of a biplanar photodiode which is put on another exit channel. Because the photodiode has a good rise time response ( $\sim 60$  ps), it is possible to simultaneously measure the macrotemporal evolution.

### 3. Results in the natural lasing mode

The experiment without any rf frequency modulation, usually called “natural lasing”, was performed with the laser wavelength at 479 nm. Fig. 2 shows typical two-dimensional spectra for various detuning conditions obtained by the dual-sweep streak camera, and simultaneous one-dimensional macrotemporal structures measured by the photodiode. The result shows a remarkable aspect of the natural lasing. What had seemed to be CW lasing was in fact discrete groups of micropulses which would appear near the peak of the electron bunch and then drift toward the edge due to detuning (Figs. 2a and 2e). The periodic pulsed lasing appeared only in a very narrow detuning region near the best synchronized condition (Fig. 2c). One can observe that such a macrotemporal evolution does not always consist of one lasing micropulse; occasionally other laser micropulses appear beside the intense one. As the detuning is increased, these satellite pulses become clear and their number increases. From Figs. 2b and 2d, it is seen that the periodic macrotemporal structure still remains but many satellite pulses have evolved close together.

Figs. 3a and 3b show laser micro-macro time structures measured with an expanded slow sweep axis at the best synchronization and the detuned by 10 Hz. Projection spectra derived with narrow gates for the fast sweep axis are shown in Figs. 3c and 3d. Taking into account the response function of the streak camera for a point light source, the width of lasing in Fig. 3c was obtained to be 6 ps (one standard deviation). The spectrum 10 Hz detuning looks wider. However, as one can notice from Fig. 3b, the projection spectrum includes three evolving laser micropulses. The width of each of the micropulses is seen to be narrow and comparable to that at the best synchronization. On the other hand, from the difference of the electron bunch length, the bunch heating at the best synchronization appears to be larger than that at the detuned condition. The nominal bunch length at the current is 95 ps. According to Ref. [1], the minimum possible duration of the laser micropulse for an ideal case of the best cavity tuning and no gain evolution is expressed as  $\sigma_{\text{I}}^{\text{min}} = \sqrt{s\sigma_b/2}$ , where  $s$  is the total slippage length in the optical klystron expressed as  $s = (N + N_d)\lambda_1$ , and  $\sigma_b$  denotes the electron bunch

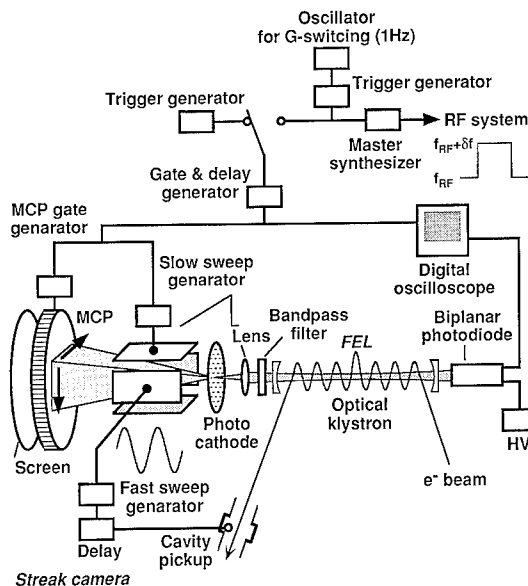


Fig. 1. Schematic layout of the measurement with the dual-sweep streak camera and the biplanar photodiode.

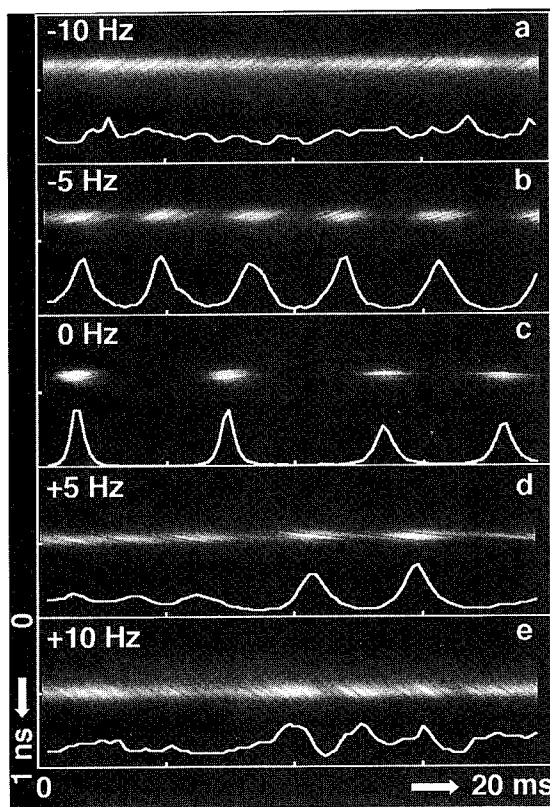


Fig. 2. Measured dual-sweep spectra in the natural lasing mode at various detuning conditions. The frequencies on the left side of the spectra are differences from the nominal rf frequency of 90.108242 MHz. Macrotemporal structures simultaneously measured by the photodiode are also shown.



length. A minimum width of 3 ps is calculated using parameters of  $N + N_d \sim 100$  and  $\sigma_b \sim 100$  ps. Although the measured width is not as small as the calculated minimum value, it is the shortest micropulse width ever reported on a storage ring FEL.

#### 4. Result in the gain-switching mode

##### 4.1. Laser and bunch length evolution

Typical dual-sweep laser spectra measured in the gain-switching mode at various beam currents are shown in Fig. 4a. At high beam currents lasing starts and ends abruptly. At low beam currents one notes that a huge number of revolutions is required for the laser micropulse to grow after the lasing frequency is triggered, and a longer laser evolution is seen. Small satellite laser pulses are also seen beside the main micropulses in every case. More than 80% of the measurements showed the satellite pulses. The figures on the right hand side (Fig. 4b) are measurements of electron bunches, and the bunch-heating phenomenon is clearly seen. It is quite reasonable that bunch heating at the higher gain is more violent and intense than that at the lower gain, and is consistent with the laser macrotemporal structure.

##### 4.2. Bunch heating and gain evolution

Since variations of the laser intensity during a macropulse can be considered to be a result of gain

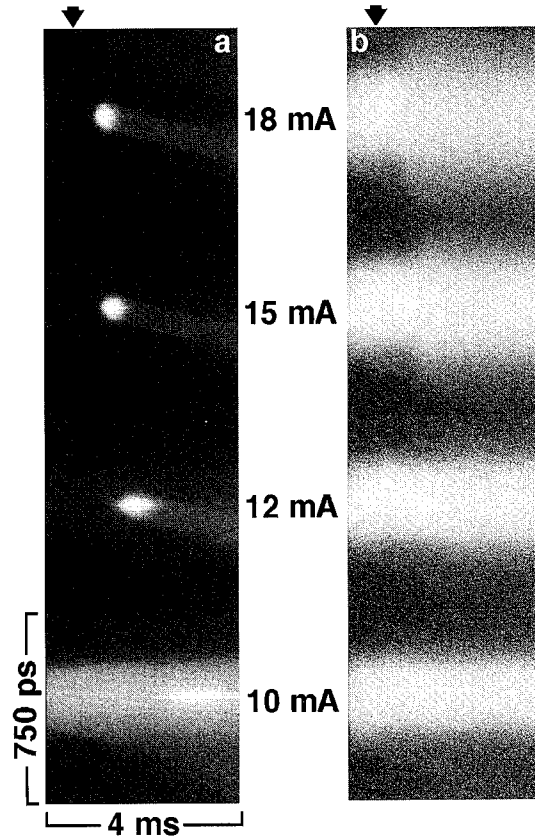


Fig. 4. Measured dual-sweep spectra of the laser (a) and the electron bunch (b) at various beam currents in the gain-switching mode. Arrows indicate the timing start of the gain switching. The lasing threshold current was 9 mA in this measurement.

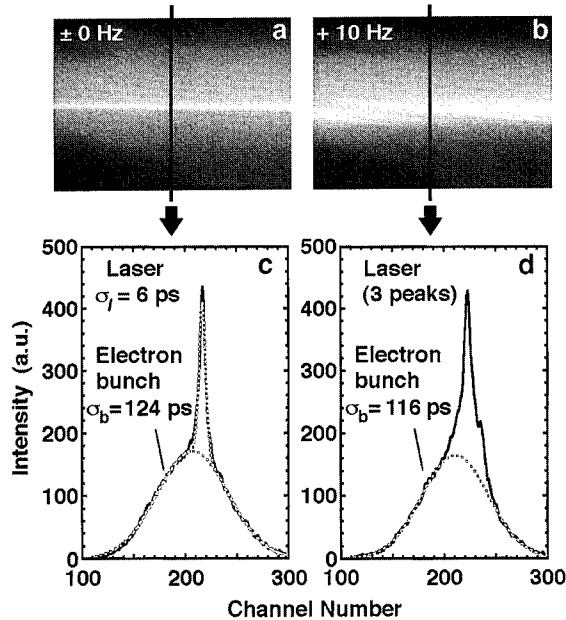


Fig. 3. Dual-sweep spectra measured with an expanded slow sweep axis (0.7 ms), and projection spectra on the fast sweep axis derived with narrow gates indicated by solid lines.

evolution [7], the temporal gain can be written as  $G_t = (P_{t+\delta t}/P_t)^{1/n_r}$ , where  $P_t$  is the intensity of the laser at certain time  $t$  and  $n_r$  is the number of roundtrips during interval  $\delta t$ . An independent relative gain evolution can be deduced from variation of the bunch length  $\sigma_b$  and the energy spread  $\sigma_E/E$ . The gain is proportional to the modulation factor of the spontaneous radiation  $f = \exp[-8\pi^2(N + N_d)^2 (\sigma_E/E)^2]$  and to the peak density of the electron bunch. Thus the relative gain can be written as

$$G_{rel} = \sigma_{ord}/\sigma_b \exp\left\{-8\pi^2(N + N_d)^2 \times [(\sigma_E/E)^2 - (\sigma_E/E)_0^2]\right\}, \quad (1)$$

where  $\sigma_{ord}$  and  $(\sigma_E/E)_0$  are the ordinal bunch length and the energy spread at a lasing beam current without bunch-heating. Although the bunch length at zero beam current is proportional to the energy spread,  $\sigma_b$  at the lasing current is not simply proportional to  $\sigma_E/E$  because of the current dependent bunch lengthening. On the UVSOR, the electron bunch lengthens due to potential-well distortion which does not accompany an increase in the energy spread [8].

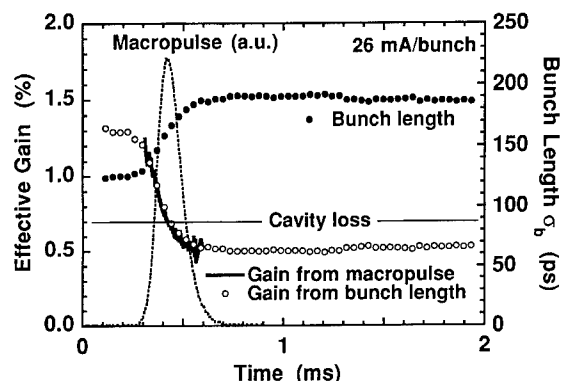


Fig. 5. Evolution of the bunch length and the effective gain in the gain-switching mode. Solid and open circles denote the bunch length and the effective gain derived from the dual-sweep spectrum of the electron bunch, respectively. The solid line shows the gain evolution derived from the laser macropulse measured by the photodiode.

According to potential-well distortion theory, the beam current  $I$  and  $\sigma_b$  is expressed as  $I[Z/n]_{\text{eff}} = C(\sigma_b^3 - \sigma_b^2 \sigma_{z.c.})$ , where  $[Z/n]_{\text{eff}}$  is the effective longitudinal coupling impedance,  $C$  is a constant depending on the ring parameters, and  $\sigma_{z.c.}$  is the zero-current bunch length at a certain energy spread. Therefore  $\sigma_E/E$  at a given  $\sigma_b$  can be written as  $(\sigma_{z.c.}/\sigma_0)(\sigma_E/E)_0$ . Here  $\sigma_0$  is the ordinal zero-current bunch length, i.e., the natural bunch length. The ordinal energy spread  $(\sigma_E/E)_0$  which is calculated from theories of synchrotron radiation on storage rings is  $3 \times 10^{-4}$  for the present experiment. Constants  $[Z/n]_{\text{eff}}$  and  $\sigma_0$  have been derived to be  $3 \Omega$  and  $57 \text{ ps}$  from separate measurements [9].

Fig. 5 shows preliminary results. Gain derived from the bunch length is normalized to the theoretical gain at the beam current. Gain derived from the laser macropulse includes the cavity loss of  $0.7\%$  obtained from the same experiment. Both curves of gain reduction in the region of the laser evolution are in very good agreement with each other.

## 5. Conclusions

We have measured the micro-macro temporal structures in both the natural lasing and the gain-switching mode with the dual-sweep streak camera. In the natural lasing mode, cw-like lasing is found to be made of discrete evolving groups of micropulses. Even in periodic pulsed lasing in the best tuned condition, satellite pulses appear beside the main micropulse. As the detuning increases, these satellite pulses develop and the macrotemporal structure transmutes into the cw-like lasing. A question is, why

do satellite pulses develop with a main micropulse? In other words, why is the cw-lasing not “true” cw-lasing? If lasing seeds can develop any time under the detuned condition, the structure should be cw. However, the micropulses drifting from the top to edge of the electron bunch are always discretely produced. It seems that the start-up of the laser is inhibited, just after one seed begins to develop.

The bunch-heating phenomenon in the gain-switching mode was observed. The electron beam energy spread increasing due to the interaction with the laser photon bunch and damping due to synchrotron radiation was clearly seen. Including bunch lengthening due to potential-well distortion, the effective gain evolution deduced from the bunch length variation agreed very well with that derived from the laser macropulse. More detailed analysis including the relation between the degree of the energy spread and the laser power is under way, and will be reported elsewhere.

## Acknowledgements

We are grateful to the staff of the UVSOR facility for their technical supports and continuous encouragement. One of the authors (H.H.) thanks Dr. S. Takano for variable discussions and comments.

## References

- [1] P. Elleaume, IEEE J. Quantum Electron. QE-21 (1985) 1012.
- [2] V.N. Litvinenko and N.A. Vinokurov, Nucl. Instr. and Meth. A 304 (1991) 66.
- [3] M-E. Couprie, V.N. Litvinenko, D. Garzella, A. Delboulbe, M. Velghe and M. Billardon, Nucl. Instr. and Meth. A 331 (1993) 37.
- [4] M. Billardon, Phys. Rev. Lett. 65 (1990) 713; Nucl. Instr. and Meth. A 304 (1991) 37.
- [5] S. Takano, H. Hama and G. Isoyama, Nucl. Instr. and Meth. A 331 (1993) 20.
- [6] I.B. Drobyazko, G.N. Kulipanov, V.N. Litvinenko, I.V. Pinayev, V.M. Popik, I.G. Silvestrov, A.N. Skirinsky, A.S. Sokolov and N.A. Vinokurov, Preprint 89-118 of the Institute of Nuclear Physics, Novosibirsk, Russia (1989).
- [7] H. Hama, J. Yamazaki and G. Isoyama, Nucl. Instr. and Meth. A 341 (1994) 12.
- [8] A. Lin, H. Hama, S. Takano and G. Isoyama, Jpn. J. Appl. Phys. 31 (1993) 921; B. Zotter, Proc. CERN Accelerator School, General Accelerator Physics, Paris, 1984, CERN 85-19 (CERN, Geneva, 1985) p. 415.
- [9] H. Hama, E. Nakamura, J. Yamazaki and G. Isoyama, Proc. 9th Symp. on Accelerator Science and Technology, KEK, Japan, 1993.

# Dynamics of the Duke storage ring UV FEL ☆

V.N. Litvinenko \*, B. Burnham, J.M.J. Madey, Y. Wu

*Duke University Free Electron Laser Laboratory, P.O. Box 90319 Duke University, Durham, NC 27708-0319, USA*

## Abstract

The Duke 1 GeV storage ring will be commissioned this year with a 280 MeV linac-injector. We intend to ramp the energy to 0.7–1.0 GeV for FEL operation. The OK-4 optical klystron will be shipped from the Budker Institute of Nuclear Physics to Duke in early 1995. The OK-4 will be the first FEL to operate on the Duke storage ring. This paper is dedicated to the study of the OK-4 performance in the CW mode of operation in the UV range, using a 3-D code developed by the authors.

## 1. Introduction

A 1 GeV electron storage ring dedicated for UV–VUV FEL operation is under construction at the Duke University Free Electron Laser Laboratory (DFELL). The main parameters of the DFELL storage ring, of the OK-4 optical klystron, the experimental set-up, and expected performance of UV–VUV FEL are described in Refs. [1,2].

To evaluate the expected performance of the OK-4 FEL on the Duke storage ring, we have developed a new 3-D macro-particle code dedicated to simulating a self-consistent mode of operation of storage ring FELs. This code includes all known mechanisms of storage ring FEL interactions and is described elsewhere [3,16]. In this paper we discuss the 3-D theory of storage ring FEL operation and simulation results for the OK-4/Duke UV/VUV FEL.

## 2. Theory

Short wavelength storage ring FELs have a specific saturation mechanism [4] caused by growth of the electron beam's energy spread due to its interaction with the FEL optical field. The energy spread growth occurs because electrons lose any correlation (on the microscopic scale of an optical wavelength) after one pass around the ring. Thus, an electron has random optical phase on each pass and its interaction with the optical field is chaotic. The first order energy kick received by an electron from the optical

field has a random sign and amplitude. This random kick causes energy diffusion and the resulting energy spread growth reduces optical gain down to the level of the cavity losses and limits the maximum optical field. Because of this, short wavelength storage ring FELs operate in the small signal regime.

Let us consider an optical klystron with total length  $2L$  comprised of two planar undulators (each with  $N_u$  periods of  $\lambda_u$  and undulator parameter of  $K_u$ ) and a buncher occupying a length from  $-z_i$  to  $z_i$ . This system is sketched in Fig. 1. The strength of the buncher can be adjusted to optimize FEL operation. With the buncher turned off, the system becomes a conventional FEL.

We assume that the FEL optical field,  $\mathcal{E}$ , has transverse TEM<sub>00</sub> mode structure with a slowly varying complex amplitude  $A_0(s)$ , where  $s = ct - z$  and  $c$  is the speed of light [5]:

$$\mathcal{E}_0(t, \mathbf{r}) = \text{Re} \left[ e_x A_0(s) \frac{\beta_0}{\beta_0 - iz} \exp \left[ iks - \frac{k}{2} \frac{x^2 + y^2}{\beta_0 - iz} \right] \right]. \quad (1)$$

The Rayleigh length is  $\beta_0$  with waist at azimuth  $z = 0$ ;  $x$  and  $y$  are transverse coordinates and  $k = 2\pi/\lambda$  is the optical wave vector. An electron propagating through the planar undulator wiggles in the horizontal plane:

$$x'(z) \equiv \frac{dx}{dz} = \frac{K_u}{\gamma} \cos(k_u z) + x_0, \quad (2)$$

and the optical wave slips with respect to it [6]:

$$s - s_0 = \Sigma(z) + s_\beta + s_{\text{mod}};$$

$$\Sigma(z) = \Sigma^0(z) \left( \frac{\gamma_0}{\gamma} \right)^2; \quad (3)$$

$$\Sigma^0(z) = z \frac{1 + K_u^2/2}{2\gamma_0^2} \left\{ \begin{array}{l} - \\ + \end{array} \right\} \frac{\Delta s_B}{2} \left\{ \begin{array}{l} z < -z_i \\ z > z_i \end{array} \right\},$$

\* This work is supported by Office of Naval Research Grant #N00014-94-C0818 and Air Force Office of Scientific Research Grant #F49620-93-1-0590.

\* Corresponding author. Tel. +1 919 660 2658, fax +1 919 660 2671, e-mail vl@phy.duke.edu.

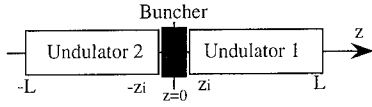


Fig. 1. Schematic layout of FEL/OK.

where  $s_0 = ct_0$  and  $t_0$  is the electron arrival time at  $z = 0$ ;  $\gamma = E/mc^2$  is the relativistic factor of the electron. For ultra-relativistic electrons we will expand the slippage about  $\varepsilon = \delta\gamma/\gamma_0$ :

$$\Sigma(z) = \Sigma^0(z)(1 - 2\varepsilon). \quad (3a)$$

The term  $s_\beta$  in Eq. (3) is the slippage caused by transverse motion of the electron [7,8]:

$$s_\beta = z \left( \frac{x_0'^2}{2} + \frac{y_0'^2}{2} + \frac{y_0^2}{2\beta_u^2} \right); \quad \beta_u = \gamma \frac{\lambda_u}{\sqrt{2\pi} K_u}, \quad (4)$$

where  $2\pi\beta_u$  is the wavelength of the vertical betatron oscillations in the undulator,  $x_0'$  and  $y_0'$  are angles of electron trajectory and  $y_0$  is its vertical position in the FEL at  $z = 0$ . The term  $\Delta s_B$  is an additional slippage introduced by the buncher [9] which is a one period wiggler with wavelength  $\lambda_B$  and wiggler parameter  $K_B$ :

$$\Delta s_B(\gamma) = \lambda_B \frac{1 + K_B^2/2}{2\gamma^2} - 2z_i \frac{1 + K_u^2/2}{2\gamma^2}. \quad (5)$$

The  $s_{\text{mod}}$  term in Eq. (3) is a result of longitudinal velocity,  $v_z$ , modulation caused by the undulating horizontal trajectory:

$$s_{\text{mod}} = \frac{K_u^2}{8k_u\gamma^2} \sin(2k_u z). \quad (6)$$

We assume that the FEL operates at the fundamental harmonic and resonance conditions are satisfied [6]:

$$k' = k_u - k \frac{1 + K_u^2/2}{2\gamma^2}; \quad |k'| \ll k_u. \quad (7)$$

The equation for the energy exchange between the electron and the optical wave in a FEL is [7,9,10]:

$$\Delta \varepsilon(z) = \frac{eK_u JJ}{2E_0\gamma_0} \text{Re} \left\{ e^{ik_s z} \int_{-L}^z dz_1 \times g(z_1) A_0(\Sigma(z_1) + s_0) e^{i[k\Sigma(z_1) - k_u z]} \right\}; \quad (8)$$

where  $e$  is the charge of the electron,  $JJ = J_0(\xi) - J_1(\xi)$ ,  $\xi = K_u^2/(4 + 2K_u^2)$  and  $J_0, J_1$  are Bessel functions of the first kind [6] caused by the  $s_{\text{mod}}$  term in the slippage. The  $g(z)$  term represents a Gaussian wave-packet and the influence of betatron motion of the electron:

$$g(z) = \frac{\beta_0}{\beta_0 - iz} \exp \left[ -\frac{k}{2} \frac{x^2(z) + y^2(z)}{\beta_0 - iz} + ikz \left( \frac{x_0'^2}{2} + \frac{y_0'^2}{2} + \frac{y_0^2}{2\beta_u^2} \right) \right];$$

$$x(z) = x_0 + x_0' z; \quad (9)$$

$$y(z) = y_0 \cos(z/\beta_u) + y_0' \beta_u \sin(z/\beta_u).$$

The integrals in Eq. (8) and below neglect the segment  $-z_i < z < z_i$  where the buncher is out of resonance. This approximation is valid for a long period high  $K$  buncher as usually used in optical klystrons [9].

The short-wavelength radiation of the ultra-relativistic electrons is concentrated inside a small angle  $\sim 1/\gamma$  and is paraxial. Thus, it can be expanded [5] using a set of orthonormal Hermite–Gaussian ( $\text{TEM}_{nm}$ ) functions. As shown in Ref. [11], the wave packet radiated by an electron into the  $\text{TEM}_{00}$  mode is:

$$A_e(s_0 + \Sigma(z)) = -e^{-ik_s z} \frac{2k}{\beta_0} \frac{eK_u JJ}{\gamma} \left( \frac{d\Sigma}{dz} \right)^{-1} g^*(z), e^{i[k_u z - k\Sigma(z)]}, \quad (10)$$

where  $g^*(z)$  is the complex conjugate of  $g(z)$  in Eq. (9). For an unperturbed electron trajectory Eq. (10) gives the spontaneous radiation into the  $\text{TEM}_{00}$  mode. The small signal regime of short wavelength storage ring FELs allows us to use a linear expansion of Eq. (10). Using the well known fact that induced radiation originates from the additional slippage caused by the electrons' energy exchange with the FEL optical field [6], one can find the following:

$$A_{\text{ind}}(s_0 + \Sigma(z)) = -ik\Delta\Sigma(z)A_e, \\ \Delta\Sigma(z) = -2 \int_{-L}^z dz_1 \frac{d\Sigma}{dz_1} \frac{\delta\gamma(z_1)}{\gamma_0} \\ = -2 \int_{-L}^z dz_1 (\Sigma(z) - \Sigma(z_1)) \frac{d\varepsilon(z_1)}{dz_1}. \quad (11)$$

Combined with Eq. (8) this gives a very useful expression (time dependent, real and imaginary part) of the gain of one electron:

$$A_{\text{ind}}(s_0 + \Sigma(z)) = -i \frac{k}{E_0\beta_0} \left( \frac{eK_u JJ}{\gamma} \right)^2 \left( \frac{d\Sigma}{dz} \right)^{-1} \\ \times g^*(z) \int_{-L}^z dz A(s_0 + \Sigma(z_1)) (\Sigma(z) - \Sigma(z_1)) g(z_1) e^{i[k(\Sigma(z_1) - \Sigma(z)) + k_u(z - z_1)]}. \quad (12)$$

One can see that Eq. (12) does not depend on the initial electron phase ( $\varphi = ks_0$ ). The term depending on  $\varphi$  disappears for a non-prebunched electron beam.

We assume that the FEL is installed in a dispersion-free (zero  $\eta$ ) straight section [1]. Zero dispersion decouples the transverse oscillations of the electrons from their energy oscillations. In this case, electron beam emittance does not depend on the FEL interaction and is defined by syn-

chrotron radiation in the storage ring arcs. The electron distribution function is the product of longitudinal  $f_s(\varepsilon, s)$  and transverse  $f_t(X)$  distribution functions:  $f(\varepsilon, s, X) = f_s(\varepsilon, s)f_t(X)$ . The function  $f_t(X)$  is a Gaussian distribution which allows analytical integration of Eq. (12) in the transverse 4-D phase space developed in Refs. [7,8]:

$$\begin{aligned} FF(z, z_1) &= \int dx_0 dx'_0 dy_0 dy'_0 g^*(z_1, X) g(z, X) f(X) \\ &= \frac{\beta_0}{\beta_0 + iz} \frac{\beta_0}{\beta_0 - iz_1} \frac{1}{\sqrt{F_x(z, z_1) F_y(z, z_1)}}; \end{aligned} \quad (13)$$

where  $F_x$  and  $F_y$  represent the influence of horizontal and vertical emittances  $\varepsilon_x$  and  $\varepsilon_y$ . For an electron beam with waist at  $z = 0$  and  $\beta$ -functions of  $\beta_x$  and  $\beta_y$ ,  $F_{x,y}$  are [7,8]:

$$\begin{aligned} F_x(z, z_1) &= \left\{ 1 + k\varepsilon_x \beta_x \left( \frac{1}{\beta_0 + iz} + \frac{1}{\beta_0 - iz_1} \right) \right\} \\ &\times \left\{ 1 + k\varepsilon_x / \beta_x \left( \frac{z^2}{\beta_0 + iz} + \frac{z_1^2}{\beta_0 - iz_1} + i(z - z_1) \right) \right\} \\ &+ \left\{ k\varepsilon_x \left( \frac{z}{\beta_0 + iz} + \frac{z_1}{\beta_0 - iz_1} \right) \right\}^2; \end{aligned}$$

$$\begin{aligned} F_y(z, z_1) &= \left\{ 1 + k\varepsilon_y \beta_y \left( \frac{\cos^2(z/\beta_u)}{\beta_0 + iz} \right. \right. \\ &+ \left. \frac{\cos^2(z_1/\beta_u)}{\beta_0 - iz_1} + i \frac{(z - z_1)}{\beta_u^2} \right\) \\ &\times \left\{ 1 + k\varepsilon_y \beta_u^2 / \beta_y \left( \frac{\sin^2(z/\beta_u)}{\beta_0 + iz} \right. \right. \\ &+ \left. \frac{\sin^2(z_1/\beta_u)}{\beta_0 - iz_1} + i \frac{(z - z_1)}{\beta_u^2} \right\) \\ &+ \left\{ \frac{k\varepsilon_y}{2} \beta_u \left( \frac{\sin(2z/\beta_u)}{\beta_0 + iz} + \frac{\sin(2z_1/\beta_u)}{\beta_0 - iz_1} \right) \right\}^2. \end{aligned} \quad (14)$$

Now we can write the evolution equation for the optical field in the FEL for arbitrary  $f_s(\varepsilon, s)$ :

$$A_{\text{out}}(s) = A_{\text{in}}(s) + \int_{s-\Sigma_t}^s \mathcal{K}(s, s') A_{\text{in}}(s') ds' + A_{\text{sp}}(s); \quad (15)$$

where  $\Sigma_t = \Sigma(L) - \Sigma(-L)$  is the total FEL slippage and the kernel  $\mathcal{K}$  is:

$$\begin{aligned} \mathcal{K}(s, s') &= -i \frac{k}{E_0 \beta_0} \left( \frac{eK_u J J}{\gamma_0} \right)^2 \left( \frac{d\Sigma}{dz} \right)^{-2} \\ &\times (s - s') e^{-ik(s-s')} \int_{-\infty}^{\infty} d\varepsilon \int_{s+\Sigma(-L)}^{s'+\Sigma(L)} \\ &\times ds_0 f_s(\varepsilon, s_0) FF(z_0, z') e^{ik_u(z_0 - z')}; \end{aligned}$$

$$z = \Sigma^{-1}(s - s_0); \quad z' = \Sigma^{-1}(s' - s_0),$$

where  $\Sigma^{-1}$  is the inverse function of  $\Sigma(z)$  (see Eq. (3)). The round trip optical cavity equation of the optical wave is then:

$$A_{n+1}(s) = \sqrt{R} A_n(s - d), \quad (16)$$

where  $R$  is the round trip reflectivity and  $d$  is the detuning of the optical cavity.

The spontaneous radiation of electrons is represented by the term  $A_{\text{sp}}(s)$  in Eq. (15). It can be treated as noise with a correlation function of:

$$\begin{aligned} \langle A_{\text{sp}}(s_1) A_{\text{sp}}^*(s_2) \rangle &= e^{-ik(s_1 - s_2)} \left( \frac{k}{\beta_0} \frac{eK_u J J}{\gamma_0} \right)^2 \left( \frac{d\Sigma}{dz} \right) C_{\text{sp}}(s_1, s_2); \end{aligned} \quad (17)$$

which is zero when the interval is larger than the total slippage  $\Sigma_t$ :

$$C_{\text{sp}}(s_1, s_2) = 0; \quad |s_1 - s_2| > \Sigma_t.$$

The term  $C_{\text{sp}}$  satisfies the standard relation ( $C_{\text{sp}}(s_1, s_2) = C_{\text{sp}}^*(s_2, s_1)$ ) and is described by the following equation on the interval  $s_1 < s_2 < s_1 + \Sigma_t$ :

$$\begin{aligned} C_{\text{sp}}(s_1, s_2) &= \int_{-\infty}^{\infty} d\varepsilon \int_{s_2 - \Sigma(L)}^{s_1 + \Sigma(L)} ds_0 f_s(\varepsilon, s_0) \\ &\times FF(z_1, z_2) e^{ik_u(z_1 - z_2)}, \end{aligned}$$

$$z_1 = \Sigma^{-1}(s_1 - s_0); \quad z_2 = \Sigma^{-1}(s_2 - s_0).$$

The coefficient of energy diffusion can be derived by averaging the square of the energy kick caused by the FEL (Eq. (8)) over transverse phase-space and initial electron phase ( $\varphi = ks_0$ ):

$$\begin{aligned} D_{\text{FEL}}(s, \varepsilon) &= \langle \Delta \varepsilon(L)^2 \rangle \\ &= \frac{1}{2} \left( \frac{eK_u J J}{2E_0 \gamma_0} \right)^2 \int_{-L}^L \int_{-L}^L dz_1 dz_2 FF(z_1, z_2) \\ &\times A_0(s + \Sigma(z_1)) A_0^*(s + \Sigma(z_2)) \\ &\times e^{ik(\Sigma(z_1) - \Sigma(z_2)) - k_u(z_1 - z_2)}. \end{aligned} \quad (18)$$

To find a self-consistent solution for the storage ring FEL one must solve simultaneously a non-linear Fokker–

Planck equation for the electron beam longitudinal distribution function

$$\frac{\partial f(\varepsilon, s)}{\partial t} + \frac{\partial}{\partial \varepsilon} \left\{ \frac{d\varepsilon}{dt} f \right\} + \frac{\partial}{\partial s} \left\{ \frac{ds}{dt} f \right\} = \frac{\partial}{\partial \varepsilon} \left\{ (D_{\text{FEL}}(\varepsilon, s) + D_{\text{SR}}) \frac{\partial f}{\partial \varepsilon} \right\}; \quad (19)$$

and optical field equations Eqs. (15) and (16). The Fokker–Planck equation is accompanied by synchrotron oscillation equations:

$$\frac{d\varepsilon}{dt} = \frac{eV_{\text{rf}}}{E_0} f_0 \left\{ \sin \left( 2\pi h_{\text{rf}} \frac{s}{C_0} \right) - \sin(\varphi_0) \right\} - \frac{\varepsilon}{\tau_c};$$

$$\frac{ds}{dt} = -\alpha_0 C_0 f_0 \varepsilon, \quad (20)$$

where  $C_0$  is the circumference of the ring,  $f_0$  is its revolution frequency,  $\alpha_0$  is the momentum compaction factor,  $V_{\text{rf}}$  and  $h_{\text{rf}}$  are RF voltage and RF harmonic number,  $\tau_c$  and  $D_{\text{SR}}$  are the energy damping time and energy diffusion caused by synchrotron radiation [12].

Some very simplified models of storage ring FELs (SRFEL) were studied, started by Vinokurov and Renieri [4] and followed by many others (see for example the one-dimensional model in Ref. [13] or the Gaussian model in Ref. [8]). These models describe qualitative behavior of SRFELs reasonably well, but fail to predict exact parameters (for example, the exact value of the radiated power or exact profiles of electron and optical bunches). In contrast, real SRFELs have displayed very complex phenomena, including unusual e-beam and optical pulse micro- and macro-structures [14] and even chaotic behavior [15].

### 3. Simulation results

The main parameters of the Duke storage ring and the OK-4 magnetic system are published elsewhere [1,2,8]. The optical cavity for the OK-4 has a length equal to half of the ring circumference. The optical cavity is nearly concentric with a Rayleigh range from 1.85 m for super pulse operation with 10 GW peak power to 3 m for normal operation and a waist located in the center of the OK-4.

Peak current and energy spread in the Duke storage ring are limited by microwave instabilities. We use a longitudinal impedance of  $Z/n = 2 \Omega$  for the simulations.

We studied the performance of the OK-4/Duke UV FEL in different modes: start-up from spontaneous radiation noise, giant and super pulse generation [3] and CW. We have tried to optimize the buncher strength and phase advance, energy detuning and cavity detuning to achieve desirable parameters for the FEL in each of these cases. Page limits for these proceedings allow us to include only a few graphs to demonstrate simulation results. We will

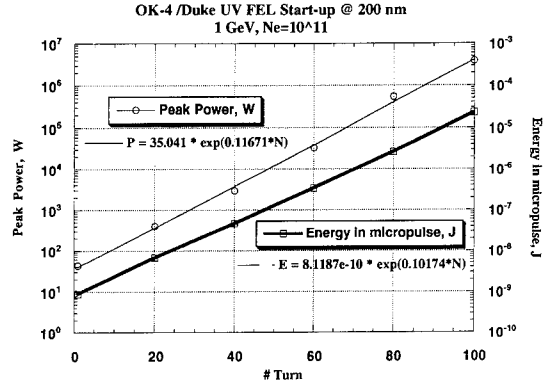


Fig. 2. Typical start-up of OK-4/Duke UV FEL.

publish more figures in a special dedicated paper. Here we present only typical figures.

Typical start-up from noise at a wavelength of 200 nm is shown in Fig. 2. With cavity losses of 4% per pass, the FEL has 11.67% peak and 10.17% average net gain per pass. We used  $10^{11}$  electrons in the bunch and a typical RF voltage of 800 kV for this run.

A beam with  $2 \times 10^{11}$  electrons and RF voltage of 1.5 MV (which has been achieved in the Duke RF cavity) can lase at a wavelength of 80 nm with the OK-4 FEL. A multifaceted optical resonator [17] is required to operate at this wavelength. With round-trip losses of 14% per pass the OK-4 will have 1.3% net gain at this wavelength.

Fig. 3 shows FEL power and electron beam energy spread evolution during the transition period for the OK-4 FEL to CW mode of operation after the giant pulse [3] (the same parameters as Fig. 2).

After transition, the FEL operates in the CW mode with an average power depending on the average beam current. At 200 nm the average power is 6.8 W at an average current of 46 mA (typically used for simulations) and 14.7 W for 100 mA average current. These values are very close to our expectations [1].

Wavepackets display a variety of optical fields. An example of the growing spike is shown in Fig. 4. Finally,

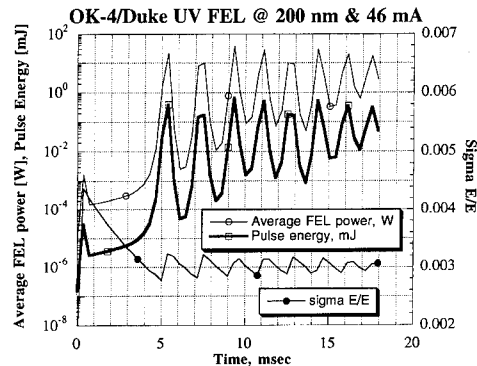


Fig. 3. Transition from start-up to CW mode.

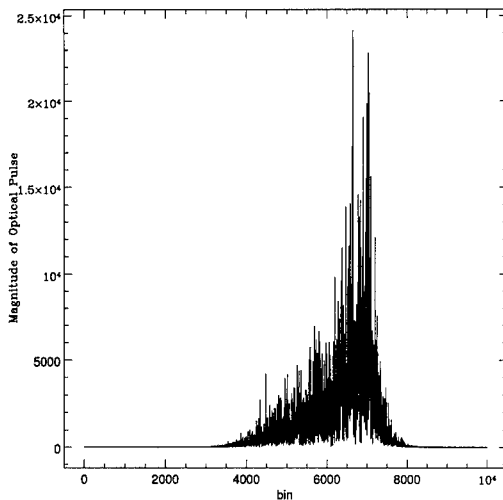


Fig. 4. UV FEL wavepacket with spike.

we observed strong deviations of the electron beam distribution from the Gaussian shape.

#### 4. Conclusions

Simulations of self-consistent storage ring FEL operation using our new code have confirmed our general projections for the average and peak power performance of the OK-4 FEL installed on the Duke Storage Ring. However, these simulations have also displayed a variety of complex behaviors not previously predicted by theory. We plan to continue simulations and improve the code. Improvements of the code will include nonlinear FEL effects, harmonic generation, multiple transverse modes, and intracavity etalons.

#### References

- [1] V. Litvinenko et al., SPIE 1552 (1991) 2;  
V. Litvinenko, J.M.J. Madey and N.A. Vinokurov, IEEE PAC 2 (1993) 1442.

- [2] Y. Wu, V. Litvinenko and J.M.J. Madey, Nucl. Instr. and Meth. A 331 (1993) 287;  
Y. Wu et al., IEEE PAC 1 (1993) 218.
- [3] V. Litvinenko, B. Burnham, J.M.J. Madey and Y. Wu, these Proceedings (16th Int. Free Electron Laser Conf., Stanford, CA, USA, 1994) Nucl. Instr. and Meth. A 358 (1995) 334.
- [4] N.A. Vinokurov and A.N. Skrinsky, Preprint INP 77-67, Novosibirsk, 1977;  
A. Renieri, Nuovo Cimento B 53, 160.
- [5] A.E. Siegman, Lasers (University Science Books) ISBN 0-935702-11-5.
- [6] W.B. Colson, Laser Handbook, Vol. 6 (North-Holland, 1990) p. 115.
- [7] V. Litvinenko, 3D FEL gain for an electron beam with finite emittance and energy spread, Proc. Nat. Synchrotron Radiation Conference SR-94, Novosibirsk, July 11–15, 1994, to be published in Nucl. Instr. and Meth.
- [8] V.N. Litvinenko, The optical klystron on VEPP-3 storage ring lasing in the visible and the ultraviolet, Thesis, Novosibirsk (1989);  
I.B. Drobyazko et al., Nucl. Instr. and Meth. A 282 (1989) 424.
- [9] N.A. Vinokurov and A.N. Skrinsky, Preprint INP 77-59, Novosibirsk (1977);  
N.A. Vinokurov, Optical Klystron – Theory and Experiment, Ph.D. thesis, Novosibirsk (1986).
- [10] J.B. Murphy and C. Pellegrini, Laser Handbook, Vol. 6 (North-Holland, 1990) p. 9.
- [11] V. Litvinenko, Analytical derivation of 3D FEL time-dependent (complex) gain matrix and spontaneous radiation, to be published.
- [12] M. Sands, SLAC 121 (1970);  
J. Murpy, BNL 42333, version 3.0 (1993).
- [13] P. Elleaume, Nucl. Instr. and Meth. A 237 (1985) 38.
- [14] See for example: M. Billardon et al., Nucl. Instr. and Meth. A 237 (1985) 38;  
M.-E. Couprie, Thesis, (1989) Universite Pari-Sud;  
V. Litvinenko et al., Nucl. Instr. and Meth. A 304 (1991) 66;  
D. Garzella et al., Nucl. Instr. and Meth. A 341 (1994) 24.
- [15] M. Billardon, Nucl. Instr. and Meth. A 304 (1991) 37.
- [16] V. Litvinenko, DFELL report (1994).
- [17] B.E. Newnam, SPIE 1227 (1990) 116.



ELSEVIER

# A longitudinal feedback for the Super-ACO free electron laser stability in the UV

M.E. Couprie<sup>a,c,\*</sup>, D. Garzella<sup>c</sup>, T. Hara<sup>a,c</sup>, J.H. Codarbox<sup>b</sup>, M. Billardon<sup>b,c</sup>

<sup>a</sup> CEA DSM DRECAM SPAM, Cen-Saclay, 91191 Gif sur Yvette, France

<sup>b</sup> ESPCI, 10 rue Vauquelin, 75231 Paris Cedex 05, France

<sup>c</sup> LURE Bât. 209 D Université de Paris-Sud, 91405 Orsay cedex, France

## Abstract

To take complete benefit of the FEL's features, longitudinal feedback has been developed for operating the FEL at perfect tuning without jitter. The laser micropulse temporal position is detected and compared to a reference position corresponding to perfect tuning. The time difference is converted into a correcting voltage, which is applied to the RF frequency pilot to adjust the synchronism condition. When the feedback is established, the micropulse jitter is reduced, the intensity fluctuations on the ms scale are damped and wavelength drift is suppressed. It has thus significantly improved the FEL operation at perfect tuning, and provides a stable laser with all its parameters optimized for the users.

## 1. Introduction

The FEL installed on the Super-ACO storage ring now provides 100 mW average power for users at 350 nm with a tunability of 10 nm. The laser operates for more than 10 hours for a given positron beam fill in the ring at 800 MeV. The laser micropulses of 25 ps RMS are reproduced at a high repetition rate, 8 MHz [1,2] and are of the order of  $\frac{1}{5}$  the length of synchrotron radiation pulses from which they are generated. The laser features are rather stable over a long time, depending mainly on the positron beam stability. Nevertheless, the laser stability can be affected by the line. We can observe a micropulse jitter and some intensity fluctuations, and readjusting the FEL is necessary from time to time. Even though on storage ring FELs, where the e beam itself is very stable, because of the recirculation the laser can display some jitter and drift.

Nevertheless, this facility provides a unique source for testing applications of storage ring FELs in the UV. A time-resolved experiment using the Super-ACO FEL was successfully tested in biology, mainly taking advantage of the laser temporal structure, power and polarization [3]. It demonstrated the high quality of the Super-ACO FEL source, comparable to that required for the study of proteins in solution. However, it appears that reducing the micropulse jitter would improve the stability of the FEL, and facilitate user experiments. For newly developing ap-

plications of such a source, especially pump-probe experiments, which use both FEL light and naturally synchronized synchrotron radiation, it is essential to reduce the micropulse jitter.

A longitudinal feedback has been developed for this purpose. Its principle and the preliminary results will be presented here.

## 2. Stability of the Super-ACO free electron laser in the UV

### 2.1. Behaviour of the FEL versus detuning

One can distinguish five zones of FEL operation versus detuning (see Table 1), i.e. the synchronism between the optical pulses bouncing in the optical cavity and the positron beam circulating in the ring (within a relative synchronization range of  $\Delta f_{\text{RF}}/f_{\text{RF}} = 2-3 \times 10^{-6}$ ). Perfect tuning (type 3) corresponds to optimum laser parameters (shorter pulse duration and linewidth, higher power, CW operation) but presents some instability (laser micropulse jitter as great as 200 ps and wavelength drift) [2], which are probably not the most desirable for the users. Zones 1 and 5 correspond to a stable laser (CW, less jitter and intensity fluctuations) but with a lower power and larger pulse duration and linewidth. On the contrary, a pulsed temporal structure at the ms range is observed in types 2 and 4) with consequently high intensity fluctuations, seriously limiting the FEL performance for users. As the natural frequency of oscillation of the Super-ACO FEL

\* Corresponding author. Tel. +33 1 6446 8044, fax +33 1 6446 4148, e-mail couprie@lure.u-psud.fr.



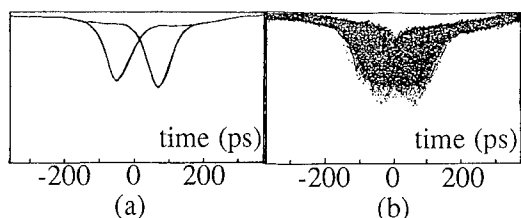


Fig. 1. Laser micropulse jitter observed on the dissector: (a) two FEL micropulses, (b) accumulated.

is between 300 and 400 Hz (unfortunately close to line harmonics), the system is very sensitive to any line excitations.

## 2.2. Methods of dynamical measurements of the FEL features

The microtemporal structure is measured with the dissector [4], a stroboscopic detector with a resolution of 10 ps. The jitter of the FEL micropulse can then be followed at 50–300 Hz (see Fig. 1). It then averages over a large number of micropulses (of the order of 28 000 shots). The FEL has also been characterized with a streak camera, allowing the observation of one single FEL micropulse. Comparison of the results shows that a larger temporal width is obtained with the dissector because of the sampling over the FEL jitter [5].

An additional macrotemporal pulsed structure at the millisecond range is generally observed on storage ring FELs other than on Super-ACO where it presents a stable regime at perfect synchronism. Great advantage can be taken from this so-called “continuous macrotemporal” structure, especially for user experiments. It is unique in the Super-ACO FEL and results from the high stability of the storage ring, and probably from the use of positrons. This macrotemporal structure is monitored with a photomultiplier, showing the resulting intensity fluctuations.

The Super-ACO FEL is not Fourier transformed. The laser wavelength evolution and width are measured with a scanning Fabry–Perot [6], which can even be synchronized with the dissector measurement. A wavelength drift as big as 1 Å can be observed over half an hour of FEL operation.

These phenomena can have various origins. The laser jitter could result from a change in synchronization, due to:

a) an RF frequency change, not very realistic because the pilot frequency is generated by a very stable quartz oscillator, b) a modification of the optical cavity length induced by thermal changes of the mechanics, probably occurring at low frequency, c) a modification of the shape of the longitudinal temporal distribution in the bunch, related to coherent synchrotron oscillations on the beam; it dynamically modifies the gain profile, and can be a rapid change, d) a modification of the beam energy directly coupled with the longitudinal motion of the stored beam. Following some observed transient phenomena, the FEL changes the regime of operation, and the synchronization condition has to be readjusted. The rate of occurrence of these sudden changes is not reproducible, and can vary between a few minutes to one hour without feedback. Wavelength drifts can be induced by a beam energy change, changes of the undulator parameters or a modification of the orbit, or of the local magnetic field.

In consequence, it appeared interesting to try to stabilize the FEL micropulse jitter, the intensity fluctuations and the wavelength drift to improve the source quality. For example, the FEL jitter is not so important for time-resolved fluorescence experiments, where one FEL micropulse is optically separated into two beams, one for the fluorescent solution or sample (start signal) and the other to the triggering photodiode (stop photodiode). However, in that case the photodiode is sensitive to correlated intensity fluctuations, even with a discriminator. On the other hand, two-color experiments involving both FEL and synchrotron radiation depend strongly on delay between the two pulses, even though the FEL jitter is still low in comparison to the duration of the synchrotron radiation pulse (200–400 ps RMS). Perfect synchronisation between the optical pulses and the positrons must be adjusted to within  $10^{-8}$  (i.e. 1 Hz over 100 MHz for the revolution frequency of the positron in Super-ACO). A longitudinal feedback on the temporal position of the laser micropulse was developed for compensating laser micropulse jitter or drifts in the synchronization.

## 3. Principle of the longitudinal feedback

The laser micropulse is sampled at 300 Hz with the dissector which also provides the reference synchronization. A reference position (“reference synchro”) of the

Table 1  
Stability of the laser parameters versus detuning

| Type | Tuning<br>$ \Delta f_{\text{RF}} $ (Hz) | $\sigma_{\text{laser}}$<br>(FWHM) | Jitter   | Macro  | Power | $\Delta\lambda$ [Å] | $\lambda$ drift |
|------|---|-----------------------------------|----------|--------|-------|---------------------|-----------------|
| 1–5  | > 10                                    | 70 ps                             | small    | CW     | < 80% | 0.8–1.1             | < 1 Å           |
| 2–4  | 5–10                                    | 60–65 ps                          | < 50 ps  | pulsed | ≈ 90% | 0.5–1.2             | < 2–3 Å         |
| 3    | 0                                       | 60 ps                             | < 200 ps | CW     | max   | 0.4–1               | < 1 Å           |

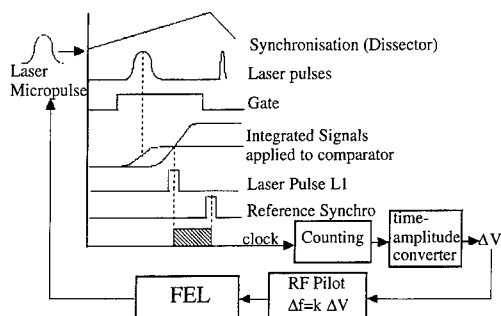


Fig. 2. Principle of the FEL longitudinal feedback: the laser pulse L1 is obtained from the determination of the center of gravity of the laser micropulse, by comparison of its integrals (delayed integral compared to half integral).

laser micropulse is then chosen (for example, for perfect tuning in zone 3) on which the laser micropulse will be controlled. The current laser micropulse position is compared to the reference one, providing a temporal difference. It is then converted into a proportional voltage which is applied to the pilot of the RF cavity with the correct sign to readjust the synchronisation condition with a frequency change (See Fig. 2). In more detail, the synchronization signal generated by the electronics of the dissector is used for generating a wide gate, in order to avoid the return sweep of the dissector. This synchronization is also used for the reference synchronization for the laser micropulse. The position of the laser micropulse is not determined by its peak value, because of sensitivity to intensity fluctuations, but by its centre of gravity. The delay between the "reference synchro" pulse issued from the dissector synchronization and L1 is counted with a clock and applied to a time-amplitude converter which provide a voltage  $\Delta V$  proportional to the delay. The proportionality is adjusted with a potentiometer. A switch system allows choosing the sign for applying the correction to the RF frequency pilot in order to correct the synchronization of the FEL. This

sign can change from one time to another, depending whether the dissector is adjusted on one positive or negative alternance of the RF synchronization.  $\Delta V$  has been recorded with the feedback loop closed, and is illustrated in Fig. 3. The capacitor used for integration limits the speed of the feedback to 10 Hz. This feedback voltage also acts as a detector of the micropulse jitter. Theoretical analysis requires knowledge of the phase-amplitude response of the laser, a second-order non-linear system involving sampled detection. A detailed experimental characterization of the laser response has still to be performed.

#### 4. Results

The feedback system was successfully tested at 50 Hz in December 1993, and then operated at 300 Hz. Various FEL parameters were stabilized, even unexpected ones.

When the feedback is established, the FEL can operate during more than three consecutive hours without the readjustments (mirrors, rather big frequency modification) always required previously. Moreover, its operation is then confined to the central region of the detuning curve (zone 3), desirable for user applications. The laser can then be operated for a longer temporal period.

The slow frequency laser micropulse jitter has been damped, but a jitter of the order of 185 ps at frequencies higher than 10 Hz still remains. Its amplitude has nevertheless been reduced significantly, and the laser remains in zone 3. Without feedback, jitters were intense enough to induce a zone modification for laser operation. Fig. 4 illustrates the FEL micropulse accumulated over 1 min without and with feedback, recorded on the dissector.

The FEL macrotemporal structure is stabilized, and as the FEL remains in zone 3, no pulsed structure appears. Moreover, the intensity fluctuation is significantly reduced, with slow variations of a residual RMS value of 1% (see Fig. 5). Fast 50 Hz (line) excitations can still appear, leading to an RMS value of 2%.

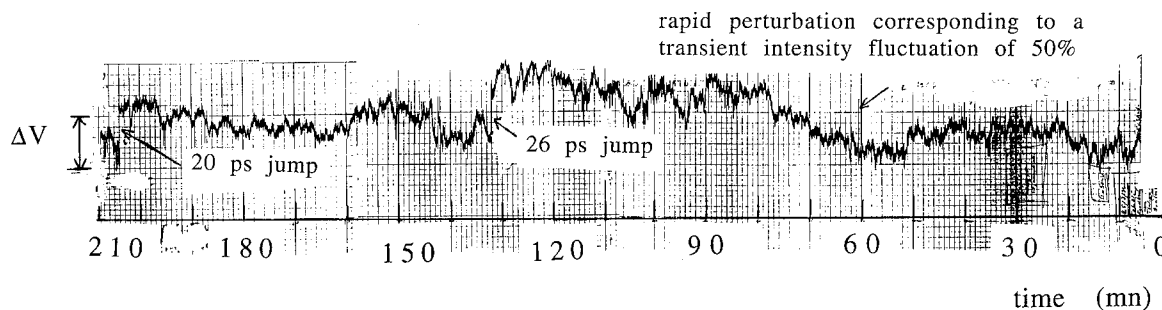


Fig. 3.  $\Delta V$  applied to the RF frequency pilot during operation of the FEL feedback recorded during three and a half consecutive hours. The scale corresponds to a 30 ps displacement leading to a correction of the RF frequency (resp. relative) of 14 Hz (resp.  $1.4 \times 10^{-7}$ ).

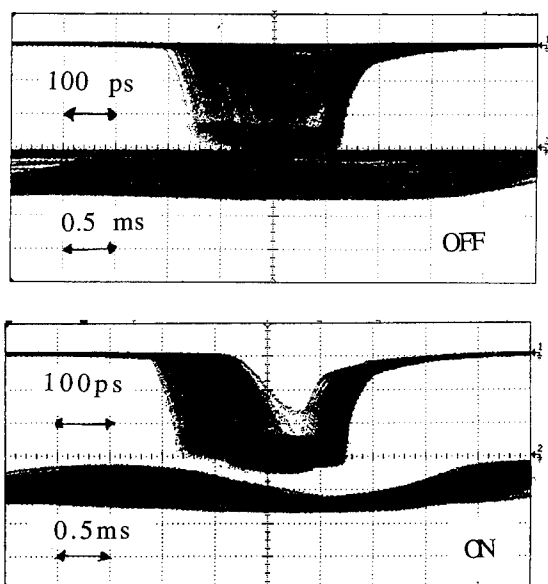


Fig. 4. Laser micropulse accumulated over one min without (a) and with (b) feedback. The upper trace is the laser micropulse measured with the disector, the lower one is the macrotemporal structure.

The more surprising action of the feedback is the stabilization of the wavelength drift. It suggests a common origin for temporal and wavelength drifts.

No modification of the laser transverse modes was observed during the operation of the feedback. Sometimes without feedback, the laser can jump from one transverse mode to another, with some possible relationship with the beam longitudinal motion. For example, for an operation around 90 mA, intermittent coherent hexapolar modes of synchrotron oscillations seem to be correlated with a modification of the laser transverse modes. This would indicate that longitudinal–transverse coupling has to be considered.

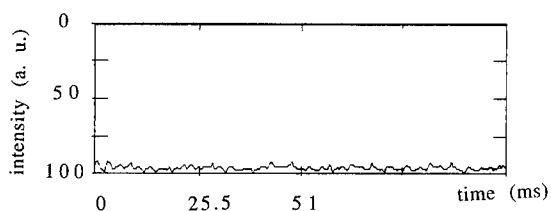


Fig. 5. Laser macrotemporal structure.

## 5. Conclusion

The feedback can stabilize the laser fluctuations up to 10 Hz, and reduce higher frequency changes. It leads to a more reliable operation for optimum characteristics of the laser (smaller spectral and temporal width, highest power) and consequently offers a better source for user applications. It stabilizes not only the expected temporal jitter, but also the intensity fluctuations in the ms range, and even more surprisingly, wavelength drifts of the FEL. The phenomena responsible for such modifications of these FEL parameters have not been fully investigated. The feedback could be used as a dynamical tool for the determination of these complex interactions occurring between the positron beam and the laser.

Further improvements are still required, such as the operation of the feedback at higher frequencies, in order to compensate residual jitter and drifts. It requires a modification of electronics of the disector, and is planned. The theoretical aspects of this sampling feedback on a non-linear system still have to be analysed, together with the determination of its specific action on the sources of instabilities of the FEL.

## References

- [1] M.E. Couprie, M. Velghe, R. Prazeres, D. Jaroszynski and M. Billardon, *Phys. Rev. A* 44(2) (1991) 1301; M.E. Couprie, D. Garzella and M. Billardon, *Europhys. Lett.* 21(9) (1993) 909.
- [2] M.E. Couprie, V. Litvinenko, D. Garzella, A. Delboulbé, M. Velghe and M. Billardon, *Nucl. Instr. and Meth. A* 331 (1993) 37; M. Billardon, D. Garzella and M.E. Couprie, *Phys. Rev. Lett.* 69(16) 2368; M.E. Couprie, V.M. Popik, E.I. Zinine, A. Delboulbé, D. Garzella, M. Velghe and M. Billardon, *Nucl. Instr. and Meth. A* 318 (1992) 59; M.E. Couprie, D. Garzella, A. Delboulbé, M. Velghe and M. Billardon, *Nucl. Instr. and Meth. A* 331 (1993) 37; D. Garzella, M.E. Couprie, A. Delboulbé, T. Hara and M. Billardon, *Nucl. Instr. and Meth. A* 341 (1994) 24.
- [3] M.E. Couprie, P. Tauc, F. Merola, A. Delboulbé, D. Garzella, T. Hara and M. Billardon, *Rev. Sci. Instr.* 65(5) (1994) 1485.
- [4] E.I. Zinine, *Nucl. Instr. and Meth.* 208 (1983) 439.
- [5] M.E. Couprie, D. Gontier, P. Troussel, T. Hara, A. Delboulbé and M. Billardon, *Rapport d'expérience, CEA/DSM/DRECAM/SPAM-93/377*; T. Hara, M.E. Couprie, A. Delboulbé, P. Troussel, D. Gontier and M. Billardon, *Nucl. Instr. and Meth. A* 341 (1994); T. Hara, M.E. Couprie, A. Delboulbé, P. Troussel, D. Gontier and M. Billardon, *Nucl. Instr. and Meth. A* 341 (1994) 21.
- [6] See T. Hara et al., these Proceedings (16th Int. Free Electron Laser Conf., Stanford, CA, USA, 1994) *Nucl. Instr. and Meth. A* 358 (1995) 341.



ELSEVIER

# Effects of an optical klystron on the electron beam of the storage ring NIJI-IV for free-electron lasers

M. Yokoyama<sup>a,\*</sup>, N. Sei<sup>b</sup>, M. Kawai<sup>a</sup>, K. Yamada<sup>b</sup>, S. Hamada<sup>a</sup>, S. Sugiyama<sup>b</sup>,  
H. Ohgaki<sup>b</sup>, T. Mikado<sup>b</sup>, T. Noguchi<sup>b</sup>, R. Suzuki<sup>b</sup>, M. Chiwaki<sup>b</sup>, T. Yamazaki<sup>b</sup>

<sup>a</sup> Kawasaki Heavy Industries, Ltd. 1-1, Kawasaki-cho, Akashi, Hyogo, 673, Japan

<sup>b</sup> Electrotechnical Laboratory, 1-1-4, Umezono, Tsukuba-shi, Ibaraki, 305, Japan

## Abstract

We have simulated the effects of a 6.3-m optical klystron (OK) on the electron beam in the compact storage ring NIJI-IV dedicated to free-electron lasers (FELs) by using the exact treatment of the transfer matrices of the OK. It was found that the focusing force of the OK produced distortion of betatron functions and cuts along resonance lines in the stability region in the betatron-tune diagram. Some of the results derived from the simulations were in reasonable agreement with experimental results. The method of simulation has thus proved to be quite effective in finding a good operating condition of a ring for satisfactory FEL performance especially in the case of a compact storage ring like the NIJI-IV with a long insertion device.

## 1. Introduction

Construction of the storage ring NIJI-IV dedicated to free-electron lasers (FELs) [1] was completed in December 1990 [2], and lasing of the FEL at 595 nm and 488 nm in the visible wavelength region was achieved in 1992 [3,4]. Lasing at 352 nm in the UV region was accomplished in April 1994 [5].

The effects of the insertion device on the electron beam are an important consideration for satisfactory FEL performance in storage-ring FELs. Many authors have discussed the effects on stored beams in high-energy storage rings [6,7], but the approximate methods usually adopted are not very accurate in the case of compact and low-energy storage rings such as the NIJI-IV at the Electrotechnical Laboratory, because the amount of tune shift is large as has been anticipated from a rough simulation [8]. To make the operation of a long optical klystron reliable in NIJI-IV, the stable region of the ring during operation of the OK was obtained by using a numerical analysis with a transfer-matrix method. The results of the simulations were successfully applied to the actual operation of the ring, as described below.

## 2. Calculation of the effects on the stored electron beam

The fundamental parameters of the NIJI-IV [1,9] and the OK [8] are shown in Table 1. Recently, the mode of

operation of the ring has been drastically changed from the old mode with a lower horizontal tune to a higher tune in order to obtain a lower-emittance beam [4,5].

In the case of a planar undulator in a storage ring, the vertical tune shift  $\Delta\nu_y$  is approximately given by

$$\Delta\nu_y = \langle \beta_y \rangle (0.3/E)^2 LB_0^2 / (8\pi), \quad (1)$$

where the  $E$  is the electron energy in GeV,  $B_0$  is the peak magnetic field in T,  $L$  is the total length of the insertion device in m, and  $\langle \beta_y \rangle$  is the average value of the vertical betatron function in m [6]. In the case of the NIJI-IV operated in the old mode, Eq. (1) gave a rather large tune shift of 0.23 since  $\langle \beta_y \rangle$  was 5 m and  $E$  was 240 MeV [9]. The correction for the tune shift resulted in distortion of betatron functions and reduction of the stable region in the tune diagram. In such a case, Eq. (1) is not accurate, and more precise simulation by using a numerical analysis with a transfer-matrix method is necessary to find a good operating mode.

The transfer matrices (TMs)  $M_x$  (horizontal) and  $M_y$  (vertical) of a magnet of bending radius  $\rho$  and orbit length  $\Delta L$ , with entry and exit angles  $\varepsilon$  and  $\gamma$ , respectively, are given as [10]

$$M_x = \begin{pmatrix} 1 & 0 & 0 \\ \tan(\gamma)/\rho & 1 & 0 \\ 0 & 0 & 1 \end{pmatrix} \times \begin{pmatrix} \cos(\Delta L/\rho) & \rho \sin(\Delta L/\rho) & \rho(1 - \cos(\Delta L/\rho)) \\ -\sin(\Delta L/\rho)/\rho & \cos(\Delta L/\rho) & \sin(\Delta L/\rho) \\ 0 & 0 & 1 \end{pmatrix} \times \begin{pmatrix} 1 & 0 & 0 \\ \tan(\varepsilon)/\rho & 1 & 0 \\ 0 & 0 & 1 \end{pmatrix}, \quad (2)$$

\* Corresponding author. Tel. +81 78 921 1606.

$$M_y = \begin{pmatrix} 1 & 0 & 0 \\ -\tan(\gamma)/\rho & 1 & 0 \\ 0 & 0 & 1 \end{pmatrix} \begin{pmatrix} 1 & \Delta L & 0 \\ 0 & 1 & 0 \\ 0 & 0 & 1 \end{pmatrix} \times \begin{pmatrix} 1 & 0 & 0 \\ -\tan(\varepsilon)/\rho & 1 & 0 \\ 0 & 0 & 1 \end{pmatrix}. \quad (3)$$

We assumed that the OK consisted of many rectangular segments of longitudinal length of  $\Delta l$ , and calculated the TM of each segment using Eqs. (2) and (3), and then obtained the total TM by taking the product of the TMs of all the segments along the OK. The magnetic field in a single segment was assumed to be constant, from which the bending radius  $\rho$  and the path length  $\Delta L$  were obtained for a given electron energy. The distribution of the magnetic field in the OK had been measured with a calibrated Hall probe for the undulator gap of 36 mm and the gap in the dispersive section of 56 mm [3]. The magnetic field for the gap wider than 36 mm was deduced using a Halbach formula [11].

The TMs for bending magnets, quadrupole magnets (Q magnets), and drift spaces were calculated by the usual method [10], and thus, the whole TM for the ring was calculated. The structure of the NIJI-IV has been described in previous papers [1,9]. The horizontal ( $\beta_x$ ) and vertical ( $\beta_y$ ) betatron functions were derived from those TMs, from which the betatron tunes  $\nu_{x,y}$  were obtained [10]. The accuracy of the calculation is, of course, better for smaller  $\Delta l$ . To determine the reasonable size of  $\Delta l$ , the dependence of tunes on  $\Delta l$  was calculated, and the result is shown in Fig. 1, which shows that the accuracy is better than 0.002 with  $\Delta l = 4$  mm. Then, we adopted 2 mm for

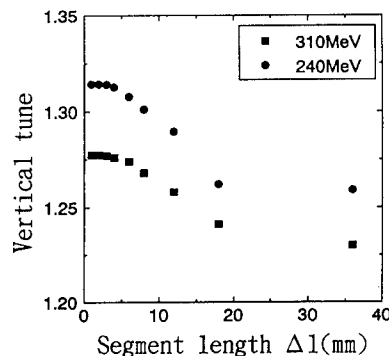


Fig. 1. Dependence of vertical betatron tunes vs. the length of segments  $\Delta l$  in the calculation for two electron-beam energies, with the horizontal tune fixed to 1.60.

$\Delta l$  for the following simulations.

The region of stability in the tune diagram was obtained from the usual condition that the trace of the total TM of the ring is equal or smaller than 2. The resultant regions of stability without and with the OK (with the gap of 36 mm) are shown in Figs. 2a and 2b, respectively. The region of stability for  $0 < \nu_y < 0.5$  has totally disappeared when the OK is inserted. The areas of  $0.5 < \nu_y < 1.0$  and  $1.5 < \nu_y < 2.0$  are reduced owing to the presence of the OK, while the area of  $1.0 < \nu_y < 1.5$  is not changed.

When the gap of the OK is changed in the operation of

Table 1  
The fundamental parameters of the NIJI-IV and the OK

|                                   |                      |
|-----------------------------------|----------------------|
| NIJI-IV                           |                      |
| Lattice type                      | triple-bend achromat |
| Periodicity                       | 2                    |
| Electron beam energy              | 240–500 MeV          |
| Bending radius                    | 1.2 m                |
| Bending angle                     | 60°                  |
| Edge angle                        | 16.1°                |
| Circumference                     | 29.6 m               |
| Effective length of Q magnets     | 0.2475 m             |
| Distance between QF1 and QD       | 0.28 m               |
| Distance between BD and QD        | 0.29 m               |
| Distance between BD and QF2       | 0.29 m               |
| Optical klystron                  |                      |
| Total length                      | 6288 mm              |
| Period in the undulator section   | 72 mm                |
| Number of periods in an undulator | 42                   |
| Minimum gap                       | 36 mm                |
| Peak magnetic field (gap = 36 mm) | 0.34 T               |
| Length of the dispersive section  | 216 mm               |

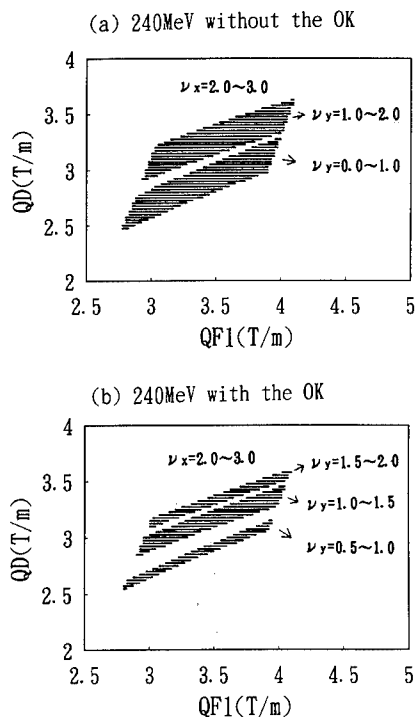


Fig. 2. Calculated region of stability in the tune diagram of the storage ring NIJI-IV without the OK (a) and with the OK (b) with the OK gap of 36 mm.

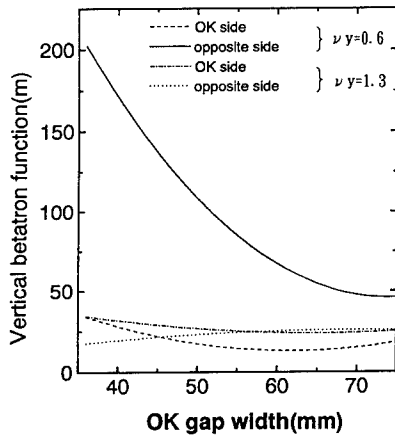


Fig. 3. Dependence of the values of vertical betatron functions on the OK gap from the simulation at the QD on the upstream side of the OK and at the QD at the end of the long straight section of the opposite side with the vertical tune fixed to  $\nu_y = 0.6$  or  $1.3$ . The horizontal tune is fixed to  $\nu_x = 2.3$  in all the cases.

the ring, it is necessary to keep the tunes constant by adjusting the focusing strength of the Q magnets in order to maintain the stored beam. Then, a simulation was carried out to see the variation of the betatron functions during change of the gap with the tunes kept constant for two combinations of ( $\nu_x = 2.3$ ,  $\nu_y = 1.3$ ) and ( $\nu_x = 2.3$ ,  $\nu_y = 0.6$ ).  $\nu_x = 2.3$  gives the lowest emittance. The resultant betatron amplitudes at a defocusing Q magnet (QD) on the upstream side of the OK and the QD at the end of the long straight section of the opposite side [1,3] are shown in Fig. 3. The figure shows that there is at least one point where the betatron function increases from 40 m to 200 m as the OK gap is narrowed with the combination of ( $\nu_x = 2.3$ ,  $\nu_y = 0.6$ ), which is not realistic for the actual ring operation because the closed-orbit distortion becomes large when the FEL wavelength is to be varied. Then, we adopted the combination close to ( $\nu_x = 2.3$ ,  $\nu_y = 1.3$ ). The actual tunes at present are  $\nu_x = 2.230$  and  $\nu_y = 1.344$  [5].

### 3. Comparison with the experimental results

The calculated variation of the magnetic-field gradient of the Q magnets (QF1 and QD) [1,3] for keeping the tunes constant was compared with the experimental values in Fig. 4 for the electron-beam energy of 310 MeV. In the experiment, a 4-element photodiode was used as a tune monitor [9]. The results of calculation are in fairly good agreement with the experimental values. It should be noted that the corrections of the focusing strength are much smaller in the present mode than in the old mode ( $\nu_x = 1.595$ ,  $\nu_y = 1.300$ ).

The betatron amplitude at a Q magnet is obtained by measuring the relation between the variation in the field

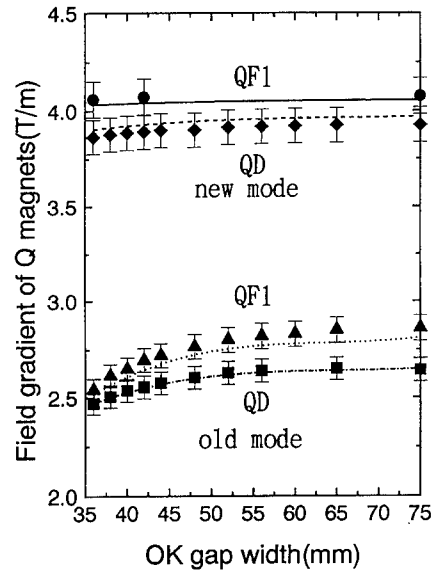


Fig. 4. Variation of the field gradient of QF1 and QD with the OK gap, with the betatron tunes fixed. The electron-beam energy is 310 MeV. ● and ◆ are experimental values for QF1 and QD, respectively, in the present mode. The solid line and the dashed line are those from the calculation. ▲ and ■ are experimental values in the old mode, and the dotted line and the dash-dot line are those from the calculation.

gradient of the Q magnet  $\Delta k$  (in T/m) and the resultant tune shift  $\Delta \nu$  by the relation

$$\beta = 41.9 \Delta \nu E / (\Delta k l), \quad (4)$$

where  $E$  is the electron-beam energy (in GeV) and  $l$  the effective length (in m) of the Q magnet [10]. The variation of the field gradient  $\Delta k$  of each individual Q magnet was applied by the use of an auxiliary power supply through a

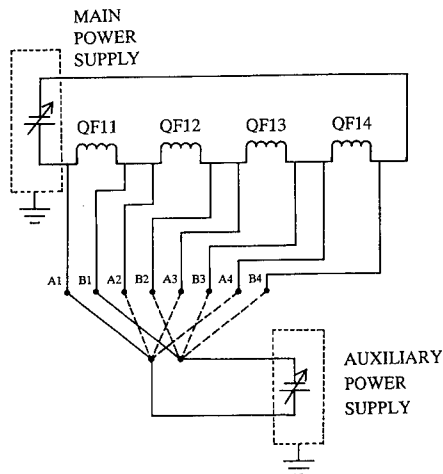


Fig. 5. The main and auxiliary power supply circuit.

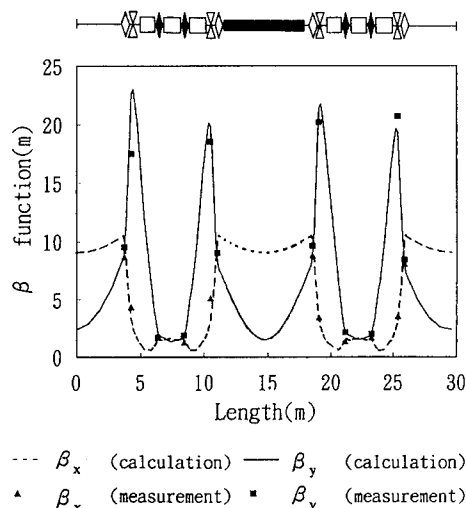


Fig. 6. Comparison of the calculated and experimental betatron amplitudes in the NIJI-IV with the OK gap of 36 mm.

circuit with a switch, as shown in Fig. 5. Main and auxiliary power supplies are isolated electrically. The experimental betatron amplitudes thus measured, with the OK gap of 36 mm, are plotted in Fig. 6. They are in good agreement with the calculated betatron functions.

#### 4. Conclusion

The twiss parameters and the region of stability in the tune diagram of the storage ring NIJI-IV were calculated by the use of a transfer-matrix method in order to find the good operating mode in the presence of the OK. The optimum operation modes of the ring for the FEL experiments were determined according to the results. The corrections to the focusing strengths of the Q magnets and the betatron functions from the simulations are in good agreement with those obtained from experiments. Thus, it is concluded that the present method of calculation is quite

useful for finding a good operating condition of compact storage rings with long insertion devices.

#### References

- [1] H. Ohgaki, T. Yamazaki, S. Suzuki, T. Mikado, R. Suzuki and T. Tomimasu, Proc. 7th Symp. on Accelerator Science and Technology, Osaka University, 1989, p. 284.
- [2] M. Kawai, K. Aizawa, S. Kamiya, M. Yokoyama, Y. Oku, K. Owaki, H. Miura, A. Iwata, M. Yoshiwa, T. Tomimasu, S. Sugiyama, H. Ohgaki, T. Yamazaki, K. Yamada and T. Mikado, Nucl. Instr. and Meth. A 318 (1992) 135.
- [3] T. Yamazaki, K. Yamada, S. Sugiyama, H. Ohgaki, N. Sei, T. Mikado, T. Noguchi, M. Chiwaki, R. Suzuki, M. Kawai, M. Yokoyama, K. Owaki, S. Hamada, K. Aizawa, Y. Oku, A. Iwata and M. Yoshiwa, Nucl. Instr. and Meth. A 331 (1993) 27.
- [4] T. Yamazaki, K. Yamada, N. Sei, S. Sugiyama, H. Ohgaki, T. Mikado, T. Noguchi, M. Chiwaki, R. Suzuki, M. Kawai, M. Yokoyama, S. Hamada and T. Tomimasu, Proc. 1st Asian Symp. on FEL, IHEP, Beijing, 1993, to be published; T. Yamazaki, K. Yamada, S. Sugiyama, H. Ohgaki, N. Sei, T. Mikado, T. Noguchi, M. Chiwaki, R. Suzuki, M. Kawai, M. Yokoyama and S. Hamada, Nucl. Instr. and Meth. A 341 (1994) ABS 3.
- [5] T. Yamazaki, K. Yamada, N. Sei, H. Ohgaki, S. Sugiyama, T. Mikado, R. Suzuki, T. Noguchi, M. Chiwaki, T. Ohdaira, M. Kawai, M. Yokoyama, S. Hamada and A. Iwata, these Proceedings (16th Int. Free Electron Laser Conf., Stanford, CA, USA, 1994) Nucl. Instr. and Meth. A 358 (1995) 353.
- [6] M.W. Poole and R.P. Walker, IEEE Trans. Nucl. Sci. NS-32 (1985) 3374.
- [7] M. Katoh, I. Honjo and Y. Kamiya, Proc. IEEE Particle Accelerator Conf., Tsukuba, Vol. 33 (1990) 123.
- [8] T. Yamazaki, K. Yamada, S. Sugiyama, H. Ohgaki, T. Tomimasu and M. Kawai, Nucl. Instr. and Meth. A 318 (1992) 142.
- [9] M. Yokoyama, M. Kawai, K. Owaki, S. Hamada, K. Aizawa, Y. Oku, A. Iwata, M. Yoshiwa, T. Yamazaki, S. Sugiyama, H. Ohgaki, K. Yamada, N. Sei, T. Mikado, T. Noguchi, R. Suzuki, M. Chiwaki and T. Tomimasu, Nucl. Instr. and Meth. A 331 (1993) ABS 34.
- [10] M. Sands, SLAC-121 Report (1970).
- [11] K. Halbach, Nucl. Instr. and Meth. 187 (1981) 109.



ELSEVIER

## Optical cavities for UV free electron lasers

M.E. Couprie <sup>a,c,\*</sup>, D. Garzella <sup>c</sup>, M. Billardon <sup>b,c</sup><sup>a</sup> CEA DSM DRECAM SPAM, CEN-Saclay, 91191 Gif Sur Yvette, France<sup>b</sup> ESPCI, 10 rue Vauquelin, 75231 Paris Cedex 05, France<sup>c</sup> LURE Bât. 209 D, Université de Paris-Sud, 91 405 Orsay Cedex, France

### Abstract

Several Storage Ring Free Electron Lasers (SRFELs) now operate in the UV and new facilities in the UV and deep UV are near completion. The intense broadband UV–X ray emission from the undulator of an SRFEL leads to degradation and heating of the optics. When the beam energy gets higher and the undulator longer, this radiation becomes more critical, but the laser power and the beam lifetime also increase under these conditions leading to compromise values and specific choices concerning the cavity mirrors. Various schemes of laser extraction and coherent higher harmonics induced by FEL are considered.

### 1. Introduction

Several SRFELs now operate in the UV including VEPP3 (Novosibirsk) [1], Super-ACO (Orsay) [2], UVSOR (Okazaki) [3], and NIJI-IV (Tsukuba) [4]. Oscillation has also been achieved with a linac driven FEL at Los Alamos [5] on the 3rd harmonic on a microundulator. New SRFEL facilities in the UV and deep UV will soon be commissioned on DELTA (Dortmund) [6] and DUKE (North Carolina) [7].

SRFELs have been used to study FEL physics, especially the dynamics of such a source. Consequently, a well designed SRFEL should easily lase in the visible and near UV range. The main justification for building expensive SRFEL systems now relies on the potential they offer for scientific applications due to their tunability, temporal structure, power, polarisation etc. The possibility of using such sources in scientific applications has been demonstrated on Super-ACO in a polarized time-resolved fluorescence experiment in biology [8].

SRFELs cannot be dissociated from synchrotron radiation facilities so their operation should be compatible with the community using synchrotron radiation. This leads to some design constraints; compatibility of the beam optics and longer straight sections for the FEL, leading to low symmetry for the beam lattice. Furthermore, the beam energy for an SRFEL, typically between 500 meV and 1.5 GeV, is rather “low” for the synchrotron radiation community where the tendency is always to increase the energy (ESRF) at 6 GeV, APS at 7 GeV and Spring-8 at 8

GeV). The lower energy range will satisfy the VUV community of synchrotron radiation. The energy should be at least high enough to maintain a reasonable beam lifetime (> 5 hours in the current range of operation), and reasonable synchrotron radiation power (varying as the fourth power of the energy) and FEL power. Operation at these rather “high” energies leads to a more critical environment for the mirrors of the FEL optical cavity. In addition, the number of stored bunches should be low, to avoid coherent longitudinal synchrotron oscillations that prevent proper operation of the laser [9]. The bunches can be stabilized with longitudinal feedback systems. This implies that FEL operation is compatible mainly with the community exploiting the time structure of synchrotron radiation, in biology, and atomic and molecular physics.

Pump-probe experiments coupling both synchrotron radiation and FEL light, are particularly attractive. Such experiments are under way on Super-ACO FEL [10] with adjustable delay between the two light sources.

### 2. Cavity losses and filling factor

In good quality mirrors the absorption and scattering losses are minimized, thus providing the maximum reflectivity for a given mirror transmission. Up to now, high reflectivity multilayer dielectric mirrors have been used, and the FEL optical beam has been extracted by transmission (ranging between 1% and 0.01%), because of the low gain of the present experiments. Additional losses due to diffraction are negligible for a TEM<sub>00</sub> mode because the Fresnel number is larger than 2.

For an FEL, the laser waist and the transverse dimensions of the electron beam should overlap. This constraint

\* Corresponding author. Tel. +33 1 6446 8044, fax +33 1 6446 4148, e-mail couprie@lure.u-psud.fr.



is considered in the “filling factor” term ( $F_f$ ) in the gain [11,12]. Its optimization results in a compromise between the increase of electron density (leading to a rather horizontal flat beam) and a good transverse overlap between the electron and optical beams. For a TEM<sub>00</sub> mode, it can be expressed as:

$$F_f = (1 + (W_0/2\sigma_x)^2)^{-0.5} (1 + (W_0/2\sigma_z)^2)^{-0.5} \times f_c(W_0, \sigma_x, \sigma_z). \quad (1)$$

The first term of Eq. (1) is optimized for a circular cross-section particle beam, with transverse dimensions  $\sigma$ . A factor of 2 difference between  $\sigma_x$  and  $\sigma_y$  reduces the gain by roughly 5%. The correction factor  $f_c$  results from the dynamic change of the particle position relative to the laser beam waist  $W_0$ , and depends on the dimensionless parameters  $\Sigma$  and  $W$  which characterize the transverse dimensions of the particle beams. For a circular cross section beam,  $\Sigma = \sigma(\pi/\lambda L_{OK})^{1/2}$  and  $W = W_0(\pi/\lambda L_{OK})^{1/2}$ ,  $L_{OK}$  being the optical klystron length.  $W$  depends only on the geometry of the optical cavity, and for a symmetrical cavity of length  $d$  and mirror curvature  $R_c$  is given by:

$$W = \sqrt{\frac{d(2R_c - d)}{2L_{OK}}}.$$

The optimum  $W$  is around 0.45 for an optical klystron, though the range is rather large. One must, however, avoid  $W=0$ , the stability limit of the optical cavity. Analytic expressions can be established [13]:

$$\begin{aligned} W \gg \Sigma, \quad F_f &= (1 + (W/2\Sigma)^2)^{-0.5}, \\ 0.6 < W < 0.8 \\ \text{and } 0.05 < \Sigma < 10, \quad F_f &= 0.917 / (1 + 0.1843/\Sigma^2), \end{aligned} \quad (2)$$

A generalized filling factor for a TEM<sub>0n</sub> mode is

$$(F_f)_n = \frac{\rho_M}{\sqrt{\pi} 2^n n!} \int_{-\infty}^{+\infty} \exp\left(-\frac{(x-x_0)^2}{2\sigma_0^2} - \frac{2x^2}{W_0^2}\right) \times H_n^2\left(\sqrt{2} \frac{x}{W_0}\right) dx \quad (3)$$

considering the electric field of the TEM<sub>0n</sub> mode [14] and a Gaussian electron density:

$$E(x) = \sum_n \frac{a_n}{(\sqrt{\pi} 2^n n!)^{1/2}} H_n\left(\sqrt{2} \frac{x}{W_0}\right) e^{-x^2/W_0^2},$$

$$\rho(x) = \rho_M \exp(-(x-x_0)^2/2\sigma_0^2).$$

Here  $x_0$  represents a misalignment with respect to the optical axis,  $H_n$  is the Hermite polynomial of order  $n$  and  $a_n$  is the amplitude of the normalized mode.  $F_f(n)$  can be calculated analytically, and gives the gain reduction with respect to the TEM<sub>00</sub> mode. On Super-ACO, the gain is higher for  $n=1$  (respectively 2 and 3) for a misalignment  $x_0/W_0=0.8$  (respectively 1.2 and 1.6) [11]. Lasing on these specific transverse modes can experimentally be achieved by modification of the mirror axis.

### 3. Available mirrors for short wavelengths

Multilayer dielectric mirrors can be used at wavelengths down to 2000 Å. Although SiO<sub>2</sub>, a low index material ( $n \approx 1.5$  at 3000 Å), is transparent down to 1500 Å, only a few high index materials are transparent in the UV range, and below 2000 Å the absorption coefficient of these increases rapidly. For short wavelengths, metallic mirrors can be used, but they are, of course, not transparent. For soft X-rays, crystals can be employed, and new multilayer mirrors are now being developed.

Ion Beam Sputtered (IBS) multilayer mirrors, initially developed for gyrolasers, were designed to work in the visible with silica and TiO<sub>2</sub>, for example. This latter material is unfortunately absorbant in the UV. These techniques are just now being extended to the UV with new materials such as Al<sub>2</sub>O<sub>3</sub>, HfO<sub>2</sub> and ZrO<sub>2</sub>. The indices, which are different for thin layers and bulk materials, are given in table 1 [15]. The difference in refractive indices between the alternating layers must be as high as possible, to reduce the number of layers and increase the spectral bandwidth [16]. With the oxide of hafnium and silica, a reflectivity of 99.9% at 3500 Å requires about 35 deposited layers and results in a mirror bandwidth of 300 Å [13]. The absorption of the layers can be slightly reduced by a small modification of the stoichiometry (case of HfO<sub>2</sub> and [Hf<sub>x</sub>Si<sub>1-x</sub>]O<sub>2</sub>). The choice of materials is small, and

Table 1  
Optical constants ( $n, k \times 10^{-4}$ ) of oxide layers deposited by reactive sputtering

| $\lambda$<br>(nm) | SiO <sub>2</sub> |          | Al <sub>2</sub> O <sub>3</sub> |          | [Hf <sub>x</sub> Si <sub>1-x</sub> ]O <sub>2</sub> |          | HfO <sub>2</sub> |          | ZrO <sub>2</sub> |          | Ta <sub>2</sub> O <sub>5</sub> |          | TiO <sub>2</sub> |          |
|-------------------|------------------|----------|--------------------------------|----------|--|----------|------------------|----------|------------------|----------|--------------------------------|----------|------------------|----------|
|                   | $n$              | $10^4 k$ | $n$                            | $10^4 k$ | $n$  | $10^4 k$ | $n$              | $10^4 k$ | $n$              | $10^4 k$ | $n$                            | $10^4 k$ | $n$              | $10^4 k$ |
| 200               | 1.5              | 0.00     | 1.83                           | 29.1     | 2.13   | 78.0     | 2.51             | 152      | —                | —        | —                              | —        | —                | —        |
| 300               | 1.47             | 0.00     | 1.70                           | 11.9     | 1.99   | 9.8      | 2.12             | 33.7     | 2.32             | 37       | 2.38                           | 45.6     | —                | —        |
| 400               | 1.46             | 0.00     | 1.65                           | 3.7      | 1.9  | 4.4      | 2.05             | 12.3     | 2.21             | 23.6     | 2.26                           | 5.3      | 2.7              | 21.6     |

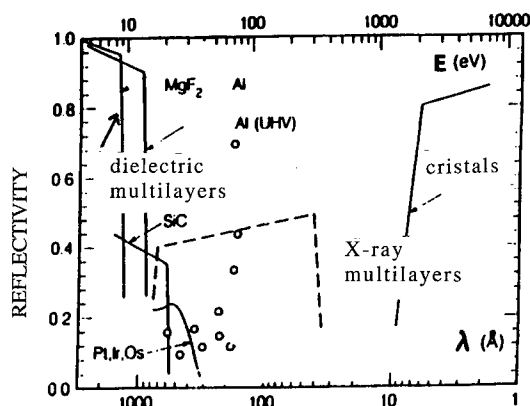


Fig. 1. Mirrors for short wavelengths.

very few materials remain available below 3000 Å.  $\text{MgF}_2$  could also be considered, in spite of its poor stability. The most crucial problem, however, is the degradation induced by the XUV radiation of the undulator. Coatings with high packing density and amorphous structure seem to be the most resistant to radiation. These properties are strongly dependent on the deposition technique [17,18]. Some mirrors were tested on Super-ACO with classical evaporation, Electron Beam Deposition (EBD), Ion Assisted Deposition (IAD) and Ion Beam Sputtering (IBS) [19]. From Fig. 2, IBS seems to be the most suitable deposition technique. Many improvements are being made in IAD [20] and in other new techniques like Ion Plating (IP) [21]. However only IAD techniques offer the best features for FEL operation at shorter wavelengths. Losses can be recovered by oxygen plasma cleaning (removing carbon contamination) and annealing (change of stoichiometry).

Substrates have different requirements: transparency, good optical quality and small roughness. Sapphire and fused silica (suprasil) are transparent over a broad spectral range (down to 1500 Å). The radius of curvature (which

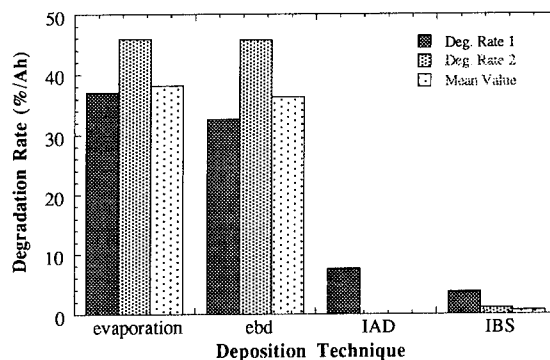
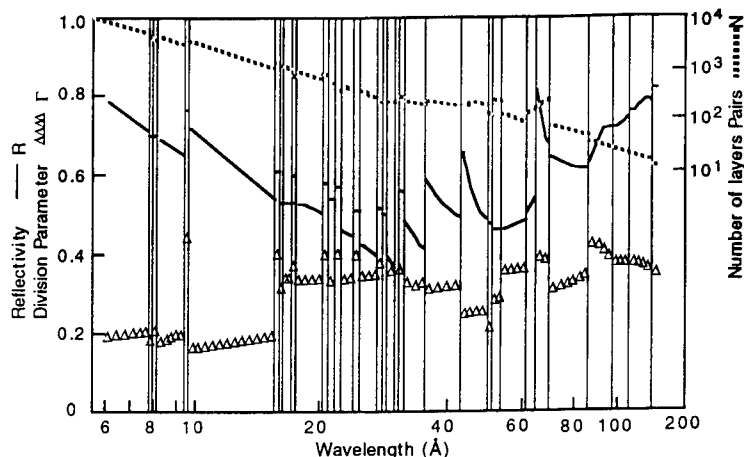


Fig. 2. Summary of the degradation rates for the different deposition techniques, after two irradiation stages, and their weighted average value.

increases for longer optical cavities) must be uniform to prevent optical aberrations. It can be checked by appropriate images reconstructed after reflexion from the mirrors. Roughness and defect spectral density on the substrates and the coated mirrors can be measured with a Zygo interferometer or by an interferential microscopy method [22]. Scattering losses [23] increase with roughness and with shorter wavelengths (1–2 Å for silica and 3–6 Å for sapphire). This roughness difference is mainly due to the higher hardness of sapphire and the consequent difficulty to polish it. Scattering losses are mainly affected by the roughness of the bare substrate.

Metallic mirrors can be used in vacuum down to 200 Å (see Fig. 1). In the UV domain, however, their reflectivity is lower than multilayer mirrors (on the order of 92% for aluminium and 40% for SiC). Al mirrors can be coated with thin layers of silica and alumina. A single layer protects the Al surface, but the reflectivity remains in the range of 92–94%. Higher reflectivities require a combination of several layers. At 2500 Å for example, 24 layers

Fig. 3. X-ray multilayers mirrors: peak reflectivity calculated at normal incidence, corresponding to the best pair of elements in the periodic table and supposes perfect interfaces, with the required number of layers  $N$  and  $G$  the fractional thickness of the most absorbant material in the layers.

lead to 99.3% while 40 layers lead to 99.6% [24]. SiC mirrors are now widely employed for VUV synchrotron radiation beamlines, because of their thermal and mechanical properties.

The development of X-ray multilayers was stimulated by microscopy studies and synchrotron radiation. These optics consist of alternating layers of a heavy material (such as W) (the reflector) and a light material (such as C) (the spacer). The periodicity is related to the wavelength according to the Bragg law. Normal incidence optics has made continuous progress, with direct applications for interferometers in astrophysics and plasma induced lasers. Fig. 3 shows the reflectivities, achieved with various combinations of materials [25]. For example, the range 125–220 Å is covered by molybdenum/silicon mirrors with reflectivities higher than 50%. Other successful mirrors above the carbon K-absorption edge (at 44 Å) use carbon as a spacer and a high atomic-number metal as a reflector (W, Rh). Above 67 Å, Ag/B, Au/B, In/B and Mo/Sr are possibilities. Fe/Ca, V/Ca, Ti/Ca and Pr/Ca can also be used between 36 Å and 67 Å. New pairs, such as Ag/B and Pd<sub>x</sub>B<sub>1-x</sub>/B operate in the water window. It is, however, in this very attractive region, that the reflectivity of the multilayers is the smallest. Below 36 Å, Ni/Ba, Fe/Ba and Fe/Mg could work. Below 20 Å, the high number of layers required (more than 1000) make the mirrors very difficult to produce. Sputtered optics can easily reach 50% of the theoretical reflectivity. The multilayers are tested under synchrotron radiation, in order to know their reflectivity. Of course, the scattering at interfaces is very critical, together with control of the thickness of each layer. Tests have been performed on W/C and W/Si and show that these multilayers seem to be rather stable when exposed to X-ray synchrotron radiation especially if the sample is pre-annealed [26].

#### 4. Geometry of the optical cavity: stability and light extraction

Several optical cavity configurations can be considered, from the concentric ( $R_1 = R_2 = d/2$ ) to the confocal ( $R_1 = R_2 = d$ ) on the edges of the stability region defined as [27]:

$$0 \leq (1 - d/R_1)(1 - d/R_2) \leq 1.$$

Minimizing the average laser transverse mode size along the length of the wiggler leads to an intermediate condition, with  $R_c = d(1 + L_{OK}^2/3d^2)/2$ .

The VEPP3 FEL has been operated in the confocal configuration [28], which minimizes the waist at the center of the resonator. The degeneracy of the optical modes in this case allows great flexibility in the lasing pattern, and makes the geometry appear attractive for hole outcoupling of the FEL beam, its harmonics, or even the microbunched electron beam. However, working close to the stability

limit makes the cavity very sensitive to any modifications of the radius of curvature of the mirrors. Thermal heating, for example, could lead to instability and cessation of lasing.

Coherent harmonics of the undulator can be produced together with the FEL. They constitute an interesting alternative to extend the spectral range by a factor of 5, using the same optical cavity. According to their [29], the coherent harmonics are emitted in a solid angle

$$\Delta\Omega_{\text{coh}} = \frac{\lambda_L^2}{2\pi n^2 \sigma_x \sigma_z}$$

with a spectral width  $\Delta\lambda_{\text{coh}} = \lambda_L^2/2n^2\sqrt{\pi}\sigma_1$  where  $\sigma_1$  is the electron bunch length. The spectral ratio between the coherent emission and the incoherent emission per unit solid angle and pulsation is

$$R_{\text{Spect}} = \frac{1}{2} N_e J_n^2(n\Delta\alpha) \frac{f_n^2}{1 + f_n J_0(n\Delta\alpha)}.$$

The first experiments in the VUV were performed on Super-ACO with an external laser [30]. With the SOLEIL FEL [32] operating at 1500 Å, a new project under design in France,  $2.2 \times 10^4$  coherent photons will be produced at 500 Å in an angle of 80 μrad with relative bandwidth of the order of  $10^{-6}$ . This corresponds to a spectral ratio compared to the spontaneous emission from the undulator of  $1.5 \times 10^3$ .

Up to now, only extraction of the optical beam by transmission or Brewster plate [31] has been tested on SRFELs. Hole extraction could be extrapolated from the IR FELs, especially for harmonic extraction, although preliminary tests on the transverse of the FEL and coherent emission should be performed. Indeed, the Super-ACO FEL has a wide transverse extent [11], and analysis with a Gaussian transverse profile of the gain [32] or cavity modes is not completely satisfactory.

#### 5. Conclusion

The optical cavity appears to be a challenging issue in the development of SRFEL facilities in the UV and VUV. Significant improvements are under way in the synchrotron radiation community, with the new low emittance third generation storage ring. The broadband radiation of the undulator provides a critical environment for the optics. Multilayers should be deposited by ion beam sputtering on a substrate with a high thermal conductivity. User facilities also require a high level of stability of the source. The optical cavity configuration should be designed for stable conditions of operation, taking into account all possible changes under vacuum such as a modification of the radius of curvature of the optics, modification of the electron beam orbit, and coupling between longitudinal and transverse motion etc.

## References

- [1] G.N. Kulipanov et al., Nucl. Instr. and Meth. A 296 (1990) 1.
- [2] M.E. Couprie, D. Garzella and M. Billardon, Europhys. Lett. 21 (1993) 909.
- [3] S. Takano, H. Hama and G. Isoyama, UVSOR activity report (1992) p. 4;  
H. Hama, J. Yamazaki and G. Isoyama, Nucl. Instr. and Meth. A 341 (1994) 12.
- [4] T. Yamazaki et al., Nucl. Instr. and Meth. A 331 (1993) 27;
- [5] P. O'Shea et al., Nucl. Instr. and Meth. A 341 (1994) 7.
- [6] DELTA: a status report DELTA group University of Dortmund Institute of Physics (1990).
- [7] V. Litvinienko, J.M.J. Madey and N. Vinokurov, Proc. Particle Accelerator Conf., Washington, DC, May 17–20, 1993.
- [8] M.E. Couprie, P. Taue, F. Merola, A. Delboulbé, D. Garzella, T. Hara and M. Billardon, Rev. Sci. Instr. 65 (1994) 1485.
- [9] M.E. Couprie, M. Velghe, D. Jaroszynski and M. Billardon, Nucl. Instr. and Meth. A 304 (1991) 58.
- [10] T. Hara et al. and D. Garzella et al., presented at the Users FEL Workshop, Stanford, 1994.
- [11] M.E. Couprie, M. Velghe, R. Prazeres, D. Jaroszynski and M. Billardon, Phys. Rev. A 44 (1991) 1301;  
M.E. Couprie, M. Billardon, M. Velghe and R. Prazeres, Nucl. Instr. and Meth. A 304 (1991) 53.
- [12] W.B. Colson and P. Elleaume, Appl. Phys. B 29 (1982) 101.
- [13] M.E. Couprie, Ph.D. Thesis Laser à Electrons Libres sur anneaux de stockage (1989) Université de Paris-Sud.
- [14] H. Kogelnik and T. Li, Appl. Opt. 5 (1966) 1550.
- [15] S.M. Edlout, A. Smajkiewicz, A. Ghanim and Al-Jumaily, Appl. Opt. 32 (1993) 5601.
- [16] H.A. Macleod, Thin-Film Optical Filters, 2nd edn. (Adam Hilger, Bristol and Boston, 1986).
- [17] J.L. Vossen and W. Kern (eds.), Thin Film Processes (Academic Press, New York, 1978).
- [18] J.L. Vossen and W. Kern (eds.), Thin Film Processes II (Academic Press, Boston, 1991).
- [19] D. Garzella, M.E. Couprie, T. Hara, A. Delboulbe and M. Billardon, to be published in Proc. Int. Symp. on Optical Interference Coatings Grenoble, 1994, SPIE Europto Series; D. Garzella, these Proceedings (16th Int. Free Electron Laser Conf., Stanford, CA, USA, 1994) Nucl. Instr. and Meth. A 358 (1995) 387.
- [20] H. Pulker, W. Haag, M. Buehler and E. Moll, J. Vac. Sci. Technol. A 3 (1985) 2700.
- [21] A.J. Waldorf, J.A. Dobrowolski, B.T. Sullivan and L.M. Plante, Appl. Opt. 32 (1993) 5583.
- [22] P. Gleyzes Contributions à l'amélioration de la résolution en microscopie optique: profilométrie différentielle picométrique et imagerie en champ proche, Ph.D. thesis, University of Paris Sud (1993).
- [23] H.E. Bennett and J.O. Porteus, J. Opt. Soc. Am. 51 (1961) 123.
- [24] A. Fourier, private communication, Laserdot.
- [25] P. Dhez, to be published in the X-Ray Microscopy (XRM'93) Proc., Chernogolovka, Sept. 1993;  
P.A. Kearney, J.M. Slaughter and C.M. Falco, to be published in Opt. Eng.;  
J.M. Slaughter et al., J. Appl. Phys. (1994);  
N.M. Ceglio, Laser and Particle Beams 9 (1991) 71.
- [26] J.B. Kortright, St. Jokseh and E. Ziegler, J. Appl. Phys. 69 (1991) 168.
- [27] A. Yariv, Quantum Electronics (Wiley, New York, 1975).
- [28] G.N. Kulipanov, I.V. Pinayev, V.M. Popik, T.V. Shaftan, A.S. Sokolov and N.A. Vinokurov, Nucl. Instr. and Meth. A 331 (1993) 98.
- [29] R. Prazeres, Génération d'harmoniques cohérentes dans un klystron optique, Thèse de l'Univ. Paris-Sud (1988);  
R. Prazeres et al., IEEE 27 (4) (1991) 1061.
- [30] M.E. Couprie and J.M. Ortéga, Lasers à Electrons Libres, Projet SOLEIL: Argumentation scientifique (Editions de Physique, 1993), Eds. D. Chandesris, P. Morin and I. Nenner, p. 257.
- [31] M.E. Couprie et al., Nucl. Instr. and Meth. A 304 (1991) 47.
- [32] R. Prazeres and M. Billardon, Nucl. Instr. and Meth. A 318 (1992) 889.



ELSEVIER

## Mirror degradation and heating in storage ring FELs

D. Garzella <sup>c,\*</sup>, M.E. Couprie <sup>a,c</sup>, T. Hara <sup>a,c</sup>, L. Nahon <sup>a,c</sup>, M. Brazuna <sup>c</sup>, A. Delboulbé <sup>c</sup>,  
M. Billardon <sup>b,c</sup>

<sup>a</sup> CEA DSM DRECAM SPAM, Cen-Saclay, 91191 Gif Sur Yvette, France

<sup>b</sup> ESPCI, 10 rue Vauquelin, 75231 Paris Cedex 05, France

<sup>c</sup> LURE Bât. 209 D, Université de Paris-Sud, 91405 Orsay cedex, France

### Abstract

Storage Ring Free Electrons Lasers (SRFELs) in the UV are now utilized as laser facilities for time-resolved fluorescence experiments or two-colour experiments with synchronized FEL and synchrotron radiations. Such experiments set new requirements for the laser and, consequently, for the optics such as long duration lasing, high laser power and short wavelengths. As these features imply operation of the storage ring at higher energies, cavity mirrors are subjected to radiation from undulator harmonics under more drastic conditions: increased power leading to heating of the front mirror, and degradation induced by undulator radiation extending towards X-rays. Also, for short  $\lambda$  operation, new difficulties arise: some materials become more absorbant and scattering losses increase.

### 1. Introduction

Since the first lasing on ACO [1], research in Orsay has been carried out with the aim of developing a new source of visible and UV coherent light. This activity has expanded in recent years since the first lasing on Super ACO in the UV range [2] and, principally, since the first experiment of time resolved fluorescence performed with the FEL [3]. Subsequently, two colour experiments coupling the naturally synchronized FEL and synchrotron radiations have been carried out in surface physics and atomic physics [4]. For such use, the duration of lasing must be significant, requiring operation at high beam energy, even though mirror degradation is enhanced. Super ACO is appropriate for such an operation. Moreover, its characteristics [2] have recently been improved by successful operation of a longitudinal feedback system making the laser more stable in position and amplitude [5]. The above requirements, and the low available gain (2% in Super ACO) set constraints on the FEL intracavity mirrors.

### 2. Light environment of the mirrors

#### 2.1. Spectrum of synchrotron radiation

Synchrotron radiation emitted on axis by an undulator has a broadband spectrum characterized by the fundamen-

tal wavelength

$$\lambda = \frac{\lambda_0}{2\gamma^2} \left( 1 + \frac{K^2}{2} \right),$$

and the “critical wavelength” that splits the spectral density into two equal parts [6]:

$$\lambda_c(\text{\AA}) = \frac{18.6}{B_0(\text{T})E^2(\text{GeV})}$$

where  $B_0$  is the magnetic field of the undulator,  $E$  is the beam energy,  $\gamma$  is the relativistic factor and  $K = 0.934 B_0(\text{T})\lambda_0(\text{cm})$ . The “critical wavelength” gives an estimate of the number of harmonics whose photon density is appreciable. The total number of photons per unit area per second per milliamperce emitted for the  $n$ th harmonic is [6]:

$$I(\text{s, cm}^2, \text{mA}) = 4.544 \times 10^9 \frac{\gamma^2 N}{l^2(\text{m})} \times \left[ J_{(n-1)/2}(z) - J_{(n+1)/2}(z) \right]^2 \frac{16z^2}{K^2}, \quad (1)$$

where  $J_n(z)$  are the Bessel functions of order  $n$ ,  $z = nK^2/4(1 + K^2/2)$ ,  $l$  is the distance from the undulator center to the front mirror, and  $N$  is the number of undulator periods. The undulator has off-axis emission, which scales towards longer wavelengths as  $f(\theta^2)$ , where  $\theta$  is the angular distance from the axis. As a consequence of the high  $K$  and the high beam energy required for UV operation there is appreciable emission from the higher

\* Corresponding author.

harmonics (see Table 1). For Super ACO, the number of photons incident on the front mirror in the 19th harmonic at 184 Å (67 eV), is about  $5 \times 10^{13}$ , lower by only a factor of 4 compared to the fundamental at 3500 Å (3.5 eV). In addition, the strong on axis bremsstrahlung emitted in the undulator might have some effect on the front optics, but no studies have been carried out on this aspect yet.

## 2.2. Power

The total power generated by the undulator radiation is given by:

$$P(W) = 7.28 E^2 (\text{GeV}) N I (A) \frac{K^2}{\lambda_0 (\text{cm})}, \quad (3)$$

where  $I$  is the average current. The power increases with higher deflection parameters, longer undulators and greater beam currents and energies. The on axis emission of a helical undulator is centered only on the first harmonic, but higher harmonics are present off axis. This is an attractive solution to minimize the mirror degradation for SRFELs.

The absorbed power is concentrated in the center of the mirror. It leads to a rapid increase of the temperature and to the creation of a thermal gradient from the center to the border of the mirrors. This effect must be taken into account, especially for the next generation of SRFELs where higher power levels are expected.

## 3. Thermal effects

The low gain of Super ACO requires the use of high reflectivity multilayer dielectric mirrors. For the Super ACO FEL at 3500 Å Ta<sub>2</sub>O<sub>5</sub>/SiO<sub>2</sub> mirrors are presently used. Front mirrors have sapphire substrates, while rear mirrors have silica substrates. These materials, either in bulk or as multilayers are totally absorbant below 1500 Å.

Appreciable power can hit the front mirror of the optical cavity. Without care, destruction of the mirror layers can occur, as happened, for example to mirrors

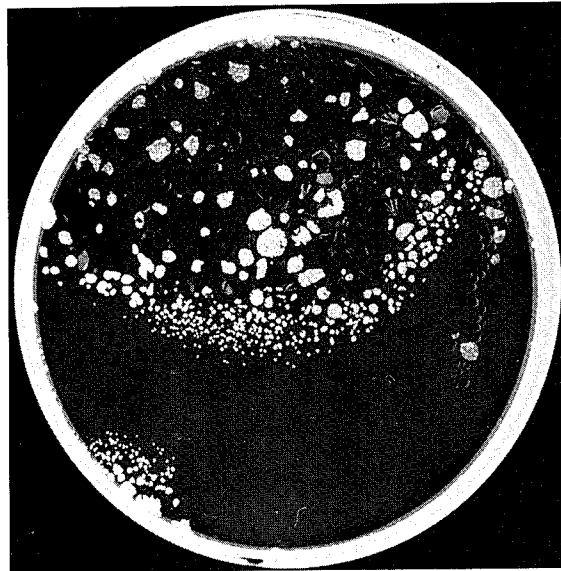


Fig. 1. Silica substrate mirror previously used on ACO FEL exposed to the synchrotron radiation of the Super-ACO SU7 undulator: the layers have been destroyed.

exposed to the Super-ACO undulator synchrotron radiation (see Fig. 1). This can be predicted with a simple model [8,9]. Heating of the layers by absorbed power has also been tested experimentally, using a laser source and an absorbant material deposited on the mirror [8]. Consequently, one should use substrates with high thermal conductivity. For transparent substrates, the choice is limited to sapphire, with a thermal conductivity of 27 W/K m compared to 1.3 for silica. Metallic substrates can also be used, with hole outcoupling. Design of the mirror holder must be performed with care to ensure good thermal contact without stressing the mirror surface and modifying the radius of curvature of the mirror.

The spontaneous power has to be compared to the absorbed laser power. It is generally low on UVSOR, VEPP3 and the visible Super-ACO FEL [7]. Nevertheless,

Table 1  
Undulator radiation and laser power for various SRFEL experiments. In italic the estimated values of the projects

| Experiment | Beam and undulator characteristics |                  |             | Laser characteristics |          |                 |                    |                   |                  |                             |
|------------|------------------------------------|------------------|-------------|-----------------------|----------|-----------------|--------------------|-------------------|------------------|-----------------------------|
|            | <i>E</i><br>MeV                    | <i>I</i><br>(mA) | <i>K</i>    | $\lambda_0$<br>(cm)   | <i>N</i> | <i>P</i><br>(W) | $\lambda_c$<br>(Å) | $\lambda$<br>(nm) | <i>P</i><br>(mW) | <i>P<sub>a</sub></i><br>(W) |
| Super-ACO  | 800                                | 100              | 5<br>4.5    | 12.9                  | 20       | 18<br>15        | 71<br>78           | 350<br>300        | 100              | 1                           |
| UVSOR      | 500                                | 20               | 2.9         | 11.1                  | 16       | 0.4             | 266                | 300               | 0.2              |                             |
| VEPP3      | 350                                | 40               | 1.6         | 10                    | 67       | 0.6             | 893                | 250               | 2.5              |                             |
| DELTA      | 700                                | 100              | 2.1         | 25                    | 17       | 1               | 542                | 213               |                  |                             |
| DUKE       | 1000                               | 100              | 6.6<br>5.35 | 10<br>10              | 67<br>67 | 210<br>138      | 26<br>32           | 300<br>200        |                  |                             |

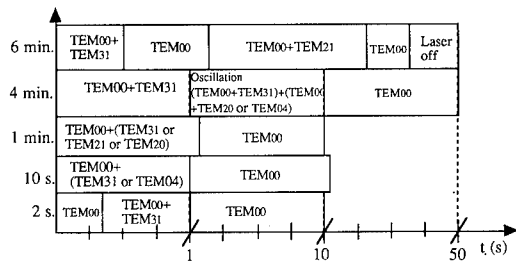


Fig. 2. Sequence of the laser transient resonant transverse modes at the opening of the shutter versus time. y-axis: duration of shutter closing. x-axis: time in a nonlinear scale. y-axis: different time conditions for the closed shutter.

the recent 110 mA operation of Super-ACO, corresponding to a synchrotron power of about 20 W, leads to 0.1 W of transmitted power through one mirror and 1 W of absorbed power. An intracavity average power of 200 W hits both mirrors. Sapphire substrates employed on the Super-ACO FEL allow laser oscillation up to this value, although 5 to 30 minutes are required to reach thermal equilibrium.

When the shutter of the beam line is opened, the undulator power can induce transient, local mechanical modifications of the mirror [10], which lead to a sequence of laser modes (see Fig. 2): high order modes resonant with a  $TEM_{00}$  or  $TEM_{01}$  mode (see Fig. 3). This behaviour results from a small modification of the radius of curvature leading to resonant transverse modes [7]. The mode  $TEM_{nm}$  of phase

$$\Phi_{nm} = \frac{4\pi d}{\lambda} - 4(m+n+1) \cdot \arctg \sqrt{\frac{d}{2R_c - d}}$$

can be resonant with another mode if their phase difference is a multiple of  $2\pi$ . Resonant  $TEM_{nm}$  modes with the  $TEM_{00}$  mode occur for

$$\text{tg}(p\pi/(2(m+n))) = (2/(2R_c - d))^{0.5};$$

with the  $TEM_{01}$  mode they occur for

$$\text{tg}(p\pi/(2(m+n-1))) = (2/(2R_c - d))^{0.5}.$$

For example, the  $TEM_{00}$  and  $TEM_{04}$  (respectively  $TEM_{32}$ ) modes can be resonant for  $R_c = 10.55$  (respectively 9.95) etc. in Super ACO FEL where  $R_c = 10$  m.

To check that heating induced mechanical distortion results from the total power of the undulator and not from the laser itself, the FEL was operated “Q-switched” at 60

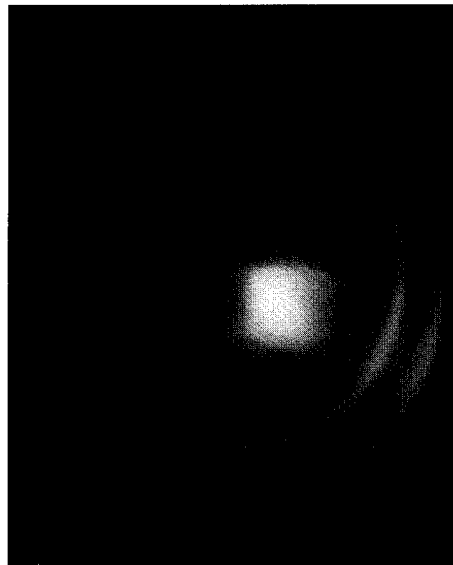


Fig. 3. Photo of the laser taken during the transient mechanical modifications of the mirror profile:  $TEM_{00}$  resonant  $TEM_{31}$  mode.

mA, allowing total relaxation of the saturation of the laser. No transverse mode changes were observed (the laser remains on the  $TEM_{00}$  mode). Nevertheless, the laser power begins to have some influence for operation above 110 mA: at high current after a laser stop generated by detuning, the mirror position for optimizing the stored spontaneous emission has changed. The main effect, however, results from the synchrotron radiation itself.

Tests were made with a visible argon laser illuminating silica and sapphire substrates. The layer absorbs because of a coat of black paint and a thermocouple measures the temperature in the center of the mirror. The results, reported in Fig. 4 for a sapphire substrate, show the temperature behavior when the mirror is an isolated system and when it has good thermal contact with the holder. Temperature achieves equilibrium after 20–30 min in the first case, while only 4 min are needed in the second (see Table 2). The sapphire insures quick thermal equilibrium, with a relatively low elevation of temperature (already  $45^\circ$  for 10 W). These results are compatible with those observed on the FEL cavity, where the situation is intermediate: the same phenomena occur and the behaviour strongly depends on the state of thermal contact with the environment.

High thermal conductivity substrates reduce both the

Table 2  
Measured elevation of temperature/watt and time required for thermal equilibrium

| Sample                  | Isolated                        |                 |               | Good thermal contact            |                 |               |
|-------------------------|---------------------------------|-----------------|---------------|---------------------------------|-----------------|---------------|
|                         | $\Delta T$ ( $^\circ\text{C}$ ) | $t_{90\%}$ (mn) | $t_{eq}$ (mn) | $\Delta T$ ( $^\circ\text{C}$ ) | $t_{90\%}$ (mn) | $t_{eq}$ (mn) |
| $\text{SiO}_2$          | 80                              | 7               | 20–30         | 58                              | 7               | 20–30         |
| $\text{Al}_2\text{O}_3$ | 35                              | 8.4             | 20            | 4.6                             | 2               | 4             |

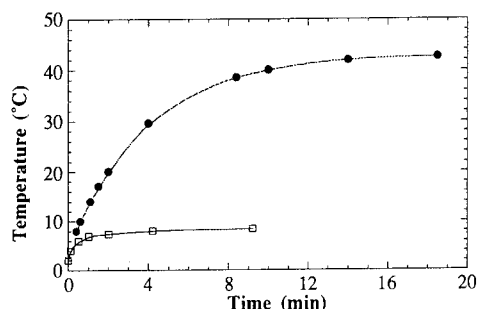


Fig. 4. Temperature growth versus time for a sapphire substrate heated with a 1.96 W argon laser. ● points indicate an isolated system; □ a system with a good thermal contact.

equilibrium temperature and the equilibrium time, but generally better conductivities mean higher thermal expansion coefficients, and more important surface modifications. In addition, good thermal contact between the mirror and its metallic holder must be achieved without mechanical deformations of the mirror, that generate aberrations and additional losses in the cavity. The holder system should guarantee both good thermal and good elastic contact.

#### 4. XUV radiation damage

The UV to X-ray photons produced in the undulator induce mirror degradation and enhanced losses. High reflectivity mirror losses can be measured by a phase shift method [11], absorption by photoacoustics [12] and transmission with a spectrometer. Adopting an empirical approach, one can follow the loss increase for various doses of irradiation. Tests on various mirrors from different manufacturers [10] were performed on the Super ACO FEL providing conditions close to what is imposed by a user facility (high  $E$ ). The most significant effect results from the mirror deposition technology (see Table 3). Clearly the Ion Beam Sputtering (IBS) method, first developed for gyrolasers, provides the best resistance to syn-

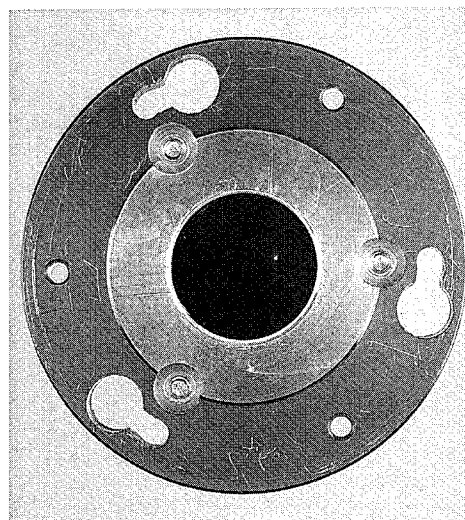


Fig. 5. Photo of a FEL mirror after a normal operation for about 60 hours. We can clearly see the black stain produced by the carbon deposited on the surface. Even a part of the mirror holder is darkened by the pollution.

chrotron radiation. It creates compact amorphous layers. On the contrary, evaporated mirrors, very susceptible to water inclusion, do not behave well when exposed to synchrotron radiation under vacuum. Ion assisted deposition gives intermediate results. The increase of mirror losses probably results from a modification of the stoichiometry of the oxides, leading to a change of the indices (real index  $n$  and absorption) of the materials under various physico-chemical processes [14].

In FEL experiments the optical cavity is under ultra-high vacuum, typically in the range  $10^{-10}$ – $10^{-8}$  Torr; however, a certain quantity of residual hydrocarbon gases is present due to outgassing from the vacuum chamber walls and residual pollution by the solvents used in cleaning the optics. The interaction between the hydrocarbons and the XUV radiation produces cracking of the chemical bonds, and a subsequent progressive contamination of the optics surface by carbon atoms. A striking example is given in Fig. 5. This process has been quantitatively investigated in the past, the results showing a growing rate of the carbon layer dependent on the temperature and, above all, on the residual gas pressure [15].

The carbon contamination can be recovered by use of an RF oxygen plasma apparatus [10,16] composed of a vacuum vessel connected with an oxygen bottle, a power supply for the RF discharge (250 W, 13.5 MHz) and electrodes (placed on the chamber walls). The oxygen flux ( $P = 0.1$  Torr for the experiment) is injected into the chamber from one side, at a grazing angle with respect to the surface of the mirror. Fig. 6 shows the degradation due to carbon contamination which seems to saturate as the dose increases. After the cleaning process mirror losses are

Table 3  
Degradation rates for various materials, techniques and experiments (under the conditions of Table 1)

| Location | Layers   | Technique   | Rate<br>(%/A h) | $\lambda$<br>(nm) |
|----------|--|-------------|-----------------|-------------------|
| S-ACO    | SiO <sub>2</sub> /Ta <sub>2</sub> O <sub>5</sub> | IBS         | 0.12            | 350               |
| S-ACO    | HfO <sub>2</sub> /SiO <sub>2</sub>               | IAD         | 4.43–10.3       | 300               |
| S-ACO    | HfO <sub>2</sub> /SiO <sub>2</sub>               | EBD         | 13.2            | 350               |
| S-ACO    | HfO <sub>2</sub> /SiO <sub>2</sub>               | evaporation | 30.9–43.4       | 350               |
| UVSOR    | HfO <sub>2</sub> /SiO <sub>2</sub>               | EBD         | 7               | 300               |
| VEPP3    | HfO <sub>2</sub> /SiO <sub>2</sub>               | ?           | 0.6–4           | UV                |



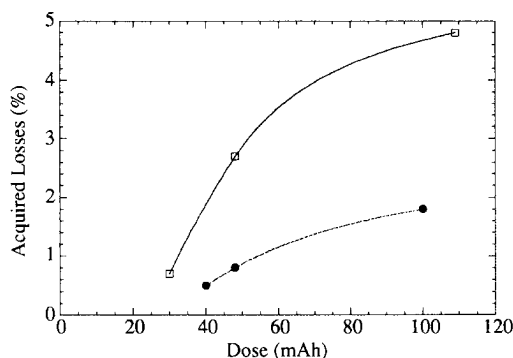


Fig. 6. Behaviour of losses attributed to the carbon contamination versus the received dose. Each set of points corresponds to a group of mirrors coated by the same company with the same deposition technique.

almost recovered, but not totally. This might suggest that another mechanism is involved in the degradation process, such as XUV photoinduced processes (photodesorption, photoionization) changing the stoichiometry of the layers, and, consequently, the imaginary index of materials. To check it, one has to measure the absorption. Mirrors are then annealed in an oven with reactive atmosphere (air), at a temperature of 300°C, for 12 hours, a sufficient time for reestablishing partially or totally the right stoichiometry of the first group layers.

Consequently, the carbon contamination process plays a major role in loss degradation. In any case, the better recovery results from the two combined techniques. With IBS mirrors, the Super-ACO FEL can be operated for three months, with one shift a week, without changing the mirrors. They receive about 5–6 A h and the laser works roughly for 100 hours. After that, the mirrors are recovered and reemployed. On UVSOR, the UV evaporated mirrors have to be changed every two shifts [17].

## 5. Conclusion

Providing a SRFEL UV light source for users requires mirrors resistant to synchrotron radiation from the undulator. Only IBS coatings, at the moment, seem to be ade-

quate for FEL operation at high energy because of its very low degradation rate.

## References

- [1] M. Billardon, P. Eileau, J.M. Ortega, C. Bazin, M. Bergher, M. Velghe, D.A.G. Deacon and Y. Petroff, *Phys. Rev. Lett.* 51 (1983) 1652.
- [2] M.E. Couprie, D. Garzella and M. Billardon, *Europhys. Lett.* 21 (1993) 909.
- [3] M.E. Couprie, P. Tauc, F. Merola, A. Delboulbé, D. Garzella, T. Hara, M. Billardon, *Rev. Sci. Instr.* 65 (1994) 1485.
- [4] T. Hara et al., D. Garzella et al., *Users FEL Workshop*, Stanford, 1994.
- [5] M.E. Couprie, D. Garzella, T. Hara, A. Delboulbé, L. Nahon and M. Billardon, these Proceedings (16th Int. Free Electron Laser Conf., Stanford, CA, USA, 1994) *Nucl. Instr. and Meth. A* 358 (1995) 374.
- [6] S. Krinsky, M.L. Perlman and R.E. Watson, vol. 1A (North-Holland, Amsterdam, 1983).
- [7] M.E. Couprie, M. Velghe, R. Prazeres, D. Jaroszynski and M. Billardon, *Phys. Rev. A* 44 (1991) 1301; M.E. Couprie, M. Billardon, M. Velghe and R. Prazeres, *Nucl. Instr. and Meth. A* 304 (1991) 53.
- [8] M.E. Couprie, Ph.D. Thesis, *Laser à Electrons Libres sur anneaux de stockage*, Université de Paris-Sud (1989).
- [9] M. Velghe, M.E. Couprie and M. Billardon, *Nucl. Instr. and Meth. A* 296 (1990) 666.
- [10] D. Garzella, M.E. Couprie, T. Hara, A. Delboulbé and M. Billardon, *Proc. Int. Symp. of Optical Interference Coatings*, Grenoble 1994, SPIE Europto Series, to be published.
- [11] J.M. Herbelin et al., *Appl. Opt.* 19 (1980) 144; M. Billardon, M.E. Couprie, M. Velghe and J.M. Ortéga, *Appl. Opt.* 30 (1991) 344.
- [12] J.P. Roger, F. Charbonnier, D. Fournier, C. Boccara and P. Robert, *Photothermal Spectroscopy of Laser Materials*, *Proc. Int. Conf. on Lasers '88* (STS Press, McLean, VA, USA, 1989).
- [13] M.E. Couprie et al., *Nucl. Instr. and Meth. A* 272 (1988) 166.
- [14] M.H. Bakashi, M.A. Cecerc and D.A.G. Deacon, *Nucl. Instr. and Meth. A* 296 (1990) 677.
- [15] K. Boller, R.P. Haelrich, H. Hogrefe, W. Jark and C. Kunz, *Nucl. Instr. and Meth.* 208 (1983) 273.
- [16] K. Yamada, T. Yamazaki, N. Sci and T. Mikado, *Nucl. Instr. and Meth. A* 341 (1994) ABS 139.
- [17] H. Hama, Private communication.



ELSEVIER

## Degradation and restoration of dielectric-coated cavity mirrors in the NIJI-IV FEL

K. Yamada <sup>a,\*</sup>, T. Yamazaki <sup>a</sup>, N. Sei <sup>a</sup>, T. Shimizu <sup>a</sup>, R. Suzuki <sup>a</sup>, T. Ohdaira <sup>a</sup>,  
M. Kawai <sup>b</sup>, M. Yokoyama <sup>b</sup>, S. Hamada <sup>b</sup>, K. Saeki <sup>c</sup>, E. Nishimura <sup>c</sup>, T. Mikado <sup>a</sup>,  
T. Noguchi <sup>a</sup>, S. Sugiyama <sup>a</sup>, M. Chiwaki <sup>a</sup>, H. Ohgaki <sup>a</sup>, T. Tomimasu <sup>c</sup>

<sup>a</sup> Electrotechnical Laboratory, 1-1-4 Umezono, Tsukuba City, Ibaraki 305, Japan

<sup>b</sup> Kawasaki Heavy Industries, Ltd., 1-1 Kawasaki-cho, Akashi, Hyogo 673, Japan

<sup>c</sup> Free-Electron Laser Institute, 4547-44 Tsuda, Hirakata City, Osaka 573-01, Japan

### Abstract

In the NIJI-IV free-electron laser (FEL) system, the 6.3-m-long optical klystron generates very intense undulator radiation and its higher harmonics. As a result, the rapid degradation of dielectric multilayer cavity mirrors terminates the laser oscillation in a little while. We reported previously that the mirror degradation was mainly caused by the deposition and/or doping of carbon onto the mirror surface by the undulator radiation in case of the visible FEL and the degraded mirrors were restored to a considerable extent by surface treatment with RF-induced oxygen plasma. However, recent experiments have revealed that the volume degradation inside the dielectric cannot be ignored in the NIJI-IV FEL. Moreover, surface analysis by XPS (X-ray Photoelectron Spectroscopy) indicated that, in the UV FEL around 350 nm, the irradiation of the mirrors by undulator radiation can give rise to the ablation of the top dielectric layer for surface protection. We investigated the relation between the mirror degradation and the condition of both surface and inside of the dielectric for two types of mirrors ( $\text{HfO}_2/\text{SiO}_2$  and  $\text{Ta}_2\text{O}_5/\text{SiO}_2$ ), by using XPS and slow positrons. The degradation mechanism is discussed. The method of restoring the surface- and volume-degraded mirrors are shown.

### 1. Introduction

In the Electrotechnical Laboratory (ETL) free-electron laser (FEL) experiments are in progress, using the storage ring NIJI-IV. This ring has been constructed since 1990 in collaboration between ETL and Kawasaki heavy industries Ltd. in order to realize the UV FEL. This ring has two long straight sections and sufficient laser gain is expected over the wavelength range from the visible to UV by installing a 6.3-m long optical klystron in one of these straight sections. After the first success of lasing in the visible in 1992, the laser wavelength has been successfully extended down to near UV around 350 nm in 1994.

In short wavelength FELs, the degradation of the dielectric-coated cavity mirrors by undulator radiation and its higher harmonics [1–4] is one of the inevitable problems which strongly reduce the advantage of FELs. It was suggested that the mirror degradation is caused by both surface modification and inner damage of the dielectric

layers [1,3]. We reported last year that, in the visible wavelength, the mirror degradation was mainly caused by the deposition and/or doping of carbon atoms onto the dielectric surfaces and the degraded mirrors can be restored by the surface treatment by RF induced  $\text{O}_2$  plasma [5]. However, recent experiments in the UV region suggest that the volumetric mirror degradation caused by the inner damage of the dielectric cannot be ignored. In this case it will be difficult to restore the degraded mirrors only by surface treatment by RF induced  $\text{O}_2$  plasma. We investigated the relation between the mirror degradation and the condition of both surface and inside of the dielectric for two types of mirrors ( $\text{HfO}_2/\text{SiO}_2$  and  $\text{Ta}_2\text{O}_5/\text{SiO}_2$ ). X-ray Photoelectron Spectroscopy (XPS) and a defect detection technique based on electron–positron annihilation  $\gamma$ -rays were used respectively, to observe the surface and inner modification of the dielectric.

The mirror was annealed [3] in addition to the treatment by  $\text{O}_2$  plasma to reduce the volume-degradation component. The XPS and the positron techniques have revealed that the  $\text{O}_2$  plasma and thermal annealing repair the surface and inside of the dielectric. As a result, the degraded mirrors were restored almost perfectly, also in the UV region. In this paper the relation between the mirror degra-

\* Corresponding author. Tel. +81 298 58 5679, fax +81 298 52 7944.

dation and the condition of both surface and inside of the dielectric is shown. The mechanism of the mirror degradation is discussed.

## 2. Experimental

Two types of mirrors ( $\text{HfO}_2/\text{SiO}_2$  and  $\text{Ta}_2\text{O}_5/\text{SiO}_2$ ), delivered from different manufacturers were investigated. Both mirrors have alternating dielectric layers of  $\lambda/4$  thickness with a  $\lambda/2$ -thick  $\text{SiO}_2$  layer on top for surface protection. The initial loss of the new mirrors was observed to be 400–500 ppm and  $\sim 250$  ppm at the optimized wavelength, 350 nm, for the  $\text{HfO}_2/\text{SiO}_2$  and  $\text{Ta}_2\text{O}_5/\text{SiO}_2$  system, respectively. The mirror loss was measured by a cavity-decay-time method [4,6], where the third harmonic of a pulsed Nd:YAG laser was used as a light source for observation. The XPS surface analysis system, whose energy resolution is  $\sim 0.2$  eV, was used to observe the atomic bond near the mirror surface. To get some information about the damage inside the dielectric, a slow positron beam was introduced onto the mirror surface. By observing the  $\gamma$ -ray resulting from electron-positron annihilation, the defect or void inside crystalline or amorphous materials can be detected with very high sensitivity [7].

Fig. 1 shows typical decay curves for the light pulse inside the laser cavity, composed of Hf-based mirrors, before and after the experiment. From the time at the  $1/e$ -fold intensity,  $\tau$ , the round-trip cavity loss,  $P$ , was simply calculated, according to the relation  $\tau = 2d/cP$ , where  $d$  is the cavity length and  $c$  the velocity of light. Although  $d$  is 14.8 m in the actual FEL, it was set to 0.5 m in the loss-measurement system. In Fig. 1 it is shown that the round trip cavity loss rapidly increased by about one order of magnitude, from 986 to 8190 ppm, with the downstream mirror exposed to undulator radiation of 3.6 mA h. It should be noted that the mirror degradation is

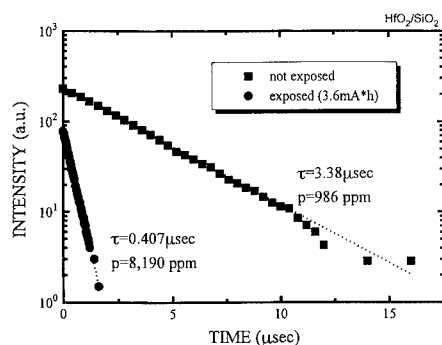


Fig. 1. Typical decay curves for the light pulse inside the laser cavity, composed of Hf-based mirrors, before and after the UV FEL experiment. The cavity length of the loss measurement system is set to 0.5 m.

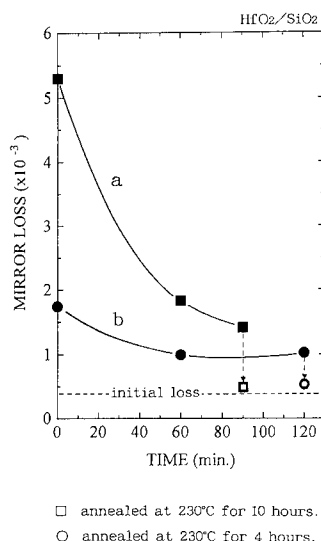


Fig. 2. Dependence of the loss per mirror on the plasma-treatment time for an upstream mirror, a, and a downstream mirror, b.

very serious, considering that exposure of 3.6 mA h corresponds to the time for an experiment of only 20 min.

The  $\text{O}_2$ -plasma treatment was tried to restore the degraded mirrors. Fig. 2 shows the dependence of the loss per mirror on the treatment time for two degraded samples, an upstream mirror, a, and a downstream mirror, b. It is important that the loss before treatment is much larger for sample a than for sample b, although sample a had been set in the FEL system for five times as long a period as sample b. This suggests that the mirror can be degraded not only by the higher harmonics but also by the fundamental of the undulator radiation itself. In both cases, mirror restoration was found, but the loss did not become less than 1000–1500 ppm, which suggest that the mirrors are degraded also by some mechanism other than surface degradation by carbon. Aiming at a perfect restoration, the mirrors were thermally annealed at  $230^\circ\text{C}$ . This successfully reduced the mirror loss down to almost their initial values ( $\sim 400$  ppm).

To elucidate what happened during this process, the surface and inside of the dielectric were observed with XPS and slow positrons. Typical photoelectron spectra are shown in Fig. 3. Figs. 3a, 3b and 3c are those from a new mirror, a degraded mirror, and a mirror treated by  $\text{O}_2$ -plasma, respectively. It is found in Fig. 3b that the carbon 1s peak becomes stronger and asymmetric with a tail toward higher binding energy side, when the mirror is degraded. More detailed observation around C 1s indicates that the asymmetric peak can contain both C–C and Si–C bonds, which means that the carbon atoms are not only deposited, like graphite, on the surface but also doped into the dielectric due to irradiation by the undulator radiation. In Fig. 3c it is found that the carbon 1s peak becomes weaker and symmetric again, which shows the carbon

atoms can be removed by the plasma treatment. Another important point is the appearance of Hf peaks in the degraded mirror as shown in Figs. 3b and 3c. This suggests that the ablation of the  $\text{SiO}_2$  top layer occurs during the experiment. This may limit the repetitive mirror restoration in the Hf-based mirrors. Fig. 4 shows a typical result of the observation of the defect inside the dielectric layers by slow positrons. When the positrons encounter the electrons in a defectless material, positronium whose lifetime is much longer than the lifetime for usual electron–positron annihilation, can be formed. In the case of  $\text{SiO}_2$ , it is well known that the degree of defect formation in atomic bonds can be inferred by measuring the ratio of the long-lifetime component in the electron–positron annihilation  $\gamma$ -rays,  $I_L$ , on the positron energy, which corresponds to the depth of the observation point from the mirror surface. In the present case, the positron energy of

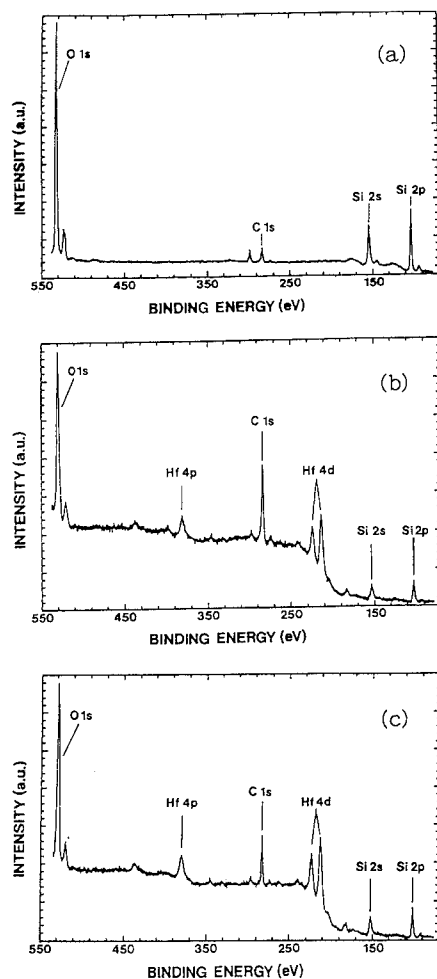


Fig. 3. Typical photoelectron spectra from a new mirror (a), a degraded mirror (b), and a mirror treated by  $\text{O}_2$ -plasma (c).

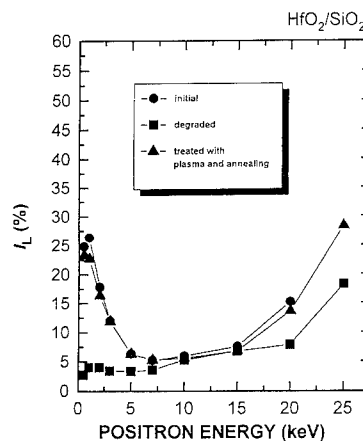


Fig. 4. Dependence of the ratio of the long-lifetime component in the electron–positron annihilation  $\gamma$ -ray,  $I_L$ , on the positron energy. The positron energy corresponds to the depth of the observation point from the mirror surface. In the present case, the positron energy of 3.5 keV is nearly equivalent to the thickness of the  $\text{SiO}_2$  top layer. The sample is a Hf oxide mirror.

3.5 keV is nearly equivalent to the thickness of the  $\text{SiO}_2$  top layer. It is observed at around a few keV that  $I_L$  is much smaller in the degraded mirror than in the new mirror but it returns almost up to its initial value by the mirror treatment. This fact means that a lot of defects are formed inside the  $\text{SiO}_2$  top layer in the degraded mirror but the defects can be repaired by the mirror treatment. As shown later, this change in  $I_L$  occurs only by thermal annealing. Hence, it has been proved that both plasma treatment and thermal annealing are effective separately to the surface degradation and volume degradation.

The behavior of the Ta-based mirrors were also investigated. Ta-based mirrors showed a clearly different character than the Hf-based mirrors. In several mirrors, the loss was decreased only by wiping out the mirror surface carefully with a mixture of alcohol and ether spilled onto a paper. This suggests that the  $\text{SiO}_2$  top layer is fine and hard, and the Si–C formation on its surface is more difficult in Ta-based mirrors than in Hf-based mirrors. It is

Table 1

Change of the loss in a Ta-based mirror by wiping,  $\text{O}_2$ -plasma treatment, and thermal annealing. Almost perfect restoration was obtained by this procedure.

| Procedure                              | Mirror loss (ppm) |
|--|-------------------|
| Initial                                | 247               |
| Final (after experiment)               | 3849              |
| Wipe                                   | 2816              |
| $\text{O}_2$ plasma treatment (60 min) | 802               |
| Thermal annealing (180 min. at 230°C)  | 297               |

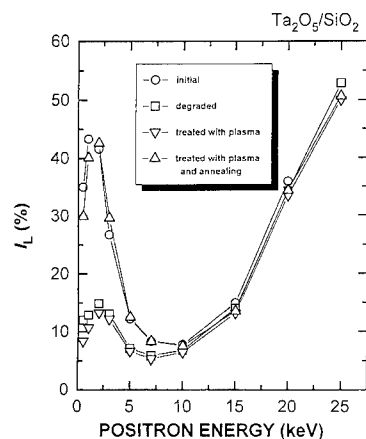


Fig. 5. Dependence of the ratio of the long-lifetime component in the electron-positron annihilation  $\gamma$ -ray,  $I_L$ , on the positron energy at each stage of the mirror treatment. The sample is a Ta oxide mirror.

not clear at present whether this is caused by the difference of the chemical structure in the second dielectric layers or simply by the quality of the  $\text{SiO}_2$  top layer. The degraded Ta-based mirror was treated by the same method as mentioned above. Table 1 shows the result for the sample whose loss reached about 3850 ppm in the FEL experiment. It is found that the sequence of  $\text{O}_2$ -plasma treatment and thermal annealing after the wiping out of the mirror surface successfully decreased the mirror loss down to its initial value almost perfectly. The result for the defect measurement by slow positrons at each stage of the mirror treatment is shown in Fig. 5. It is clearly indicated that the defect in the degraded top layer can be repaired only by the thermal annealing, not by the plasma treatment as mentioned above. It is also found in the figure that the initial defect is much less in Ta-based mirrors than in Hf-based ones (see Fig. 4). Moreover, any photoelectron peak from the second layer was not observed in the XPS measurement during this procedure. These results support the hypothesis that the  $\text{SiO}_2$  top layer is fine and hard in Ta-based mirrors.

### 3. Summary

We investigated the relation between the mirror degradation and the condition of both surface and inside of the dielectric for two types of mirrors ( $\text{HfO}_2/\text{SiO}_2$  and  $\text{Ta}_2\text{O}_5/\text{SiO}_2$ ), to elucidate the degradation mechanisms in dielectric-coated cavity mirrors for VU FEL. The XPS and slow positron technique proved that the mirror degradation contains both effects of surface modification by carbon atoms and inner defects inside the  $\text{SiO}_2$  top layer. The surface and volume degradations have been repaired by  $\text{O}_2$ -plasma treatment and thermal annealing and the mirror performance was restored in the two types of mirrors investigated. However, some results suggested that the  $\text{SiO}_2$  top layer is weak in the Hf system, which may limit the repetitive restoration of the degraded Hf-based mirrors. From the present experimental result, the Ta-based mirror is thought to be more favorable than the Hf-based one at a wavelength around 350 nm. To get a stable FEL in a much shorter wavelength region, it will be necessary to examine the degradation mechanisms for some other dielectric system as well as for the Hf system, because the Ta oxide becomes opaque for wavelength less than 350 nm.

### References

- [1] M. Billardon, P. Elleaume, J.M. Ortega, C. Bazin, M. Bergher, M. Velghe, D.A.G. Deacon and Y. Petroff, IEEE J. Quantum Electron. QE-21 (1985) 805.
- [2] D.A.G. Deacon, Nucl. Instr. and Meth. A 250 (1986) 283.
- [3] P. Elleaume, M. Velghe, M. Billardon and J.M. Ortega, Appl. Opt. 24 (1985) 2762.
- [4] K. Yamada, T. Yamazaki, S. Sugiyama, T. Tomimasu, T. Mikado, M. Chiwaki, R. Suzuki and H. Ohgaki, Nucl. Instr. and Meth. A 304 (1991) 86.
- [5] K. Yamada, T. Yamazaki, N. Sei and T. Mikado, Nucl. Instr. and Meth. A 341 (1994) ABS 139; details will be published elsewhere.
- [6] J.M. Herbelin, J.A. McKay, M.A. Kwok, R.H. Ueunten, D.S. Urevig, D.J. Spencer and D.J. Benard, Appl. Opt. 19 (1980) 144.
- [7] R. Suzuki, Y. Kobayashi, K. Awazu, T. Mikado, M. Chiwaki, H. Ohgaki and T. Yamazaki, Nucl. Instr. and Meth. B 91 (1994) 410.



ELSEVIER

## Magnetic field full test of two-section KIAE-4 undulator

A.A. Varfolomeev <sup>a,\*</sup>, Yu.P. Bouzouloukov <sup>a</sup>, S.N. Ivanchenkov <sup>a</sup>, A.S. Khlebnikov <sup>a</sup>,  
N.S. Osmanov <sup>a</sup>, S.V. Tolmachev <sup>a</sup>, W.H. Urbanus <sup>b</sup>, M.J. van der Wiel <sup>b</sup>

<sup>a</sup> RRC “Kurchatov Institute”, 123182 Moscow, Russian Federation

<sup>b</sup> FOM-Institute for Plasma Physics, Nieuwegein, The Netherlands

### Abstract

Two-sections of the KIAE-4 undulator have been assembled and the magnetic field has been finally tuned. Special attention was paid to focusing strength adjustments in both sections. To obtain this rather strong focusing in both transverse directions a combined focusing scheme was used. Field matching in the intersection gap was controlled using the first and the second integrals of the magnetic field along the entire undulator length. The results of the full test of the undulator have demonstrated a high accuracy of the magnetic field obtained, a wide range of the focusing strength tunability along with a high sensitivity of the electron beam optics to the intersection magnetic field.

### 1. Introduction

It is well recognised that for many types of FELs (high power, long SASE devices, not low e.b. emittance etc.) adjustable focusing undulators are needed. Many theoretical papers were devoted to the problem. The first fabricated undulator with adjustable quadrupole focusing strength was described by authors of Ref. [1].

We have earlier suggested [2,3] a more flexible undulator scheme providing tunable sextupole as well as quadrupole focusing. Using this scheme a complex two-section self-focusing hybrid undulator KIAE-4 [4] has been designed and fabricated for the FOM-Fusion-FEM facility [2,3]. Strict requirements were specified: strong (record for the hybrid systems) magnetic fields, efficient and tunable focusing of the electron beam, wide electron energy acceptance, rather high nominal current, step undulator tapering (two undulator sections with different  $K$ -strengths), end field matching, low weight and compactness, easy access to the channel, etc. Basic parameters of the mechanical constructions as well as preliminary results of the magnetic field measurements obtained with one undulator section can be found in Ref. [4]. Now we report the magnetic field characteristics of the whole undulator installation including the basic undulator fields, end matching and intersection fields, focusing fields and secondary magnetic fields characteristics such as the first and the second integrals. Some analyses are also presented. As far as we know this is the

first operating device with adjustable sextupole and quadrupole focusing over a wide range.

### 2. Approaches for magnetic field measurements

As a whole the undulator KIAE-4 assembly consists of two sections, 20 and 14 periods respectively, which are separated by the intersection gap. Two additional half period cells serve for field matching at each end of the undulator sections. All components are based on one platform and aligned along the common undulator axis with high precision: position error tolerances do not exceed 0.05 mm. Pole tips are positioned with the same accuracy providing the appropriate accuracy in periodicity (see Ref. [4] for details).

To make fast and high precision magnetic field measurements in the assembled undulator a special Hall probe system was designed. A small Hall sensor was fixed on a translation stage which was mounted on a carriage. The translation stage enables the Hall probe to be moved in both directions transverse to the  $Z$ -axis. This carriage cross section was fitted to the gap area profile and could be moved smoothly along the undulator axis conserving its  $X,Y$ -position. Using a stepper motor driver the carriage was moved automatically by  $0.24 \pm 0.005$  mm step with the speed up to 200 steps/min. The accuracy of the Hall sensor position was about 0.05 mm. The accuracy of the above Hall probe magnetometer as a whole was better than  $1 \times 10^{-4}$ . For magnetic field control on the entire undulator length including the intersection gap a wire deflection device was also used. It was specially developed to be applicable for long undulators (see Ref. [5] for details).

\* Corresponding author. Fax +7 095 196 7764, e-mail: x1065@cpuv1.net.kiae.su.

### 3. Undulator performance characteristics

Basic results on magnetic field measurements along the undulator  $Z$ -axis are given in Fig. 1 where the magnetic field  $B_y$  as well as its first and second integrals along the  $Z$ -axis are presented. The amplitudes  $B_{y0}$  in accordance with the specification are equal to 2.025 kG and 1.601 kG for the first section (gap  $g = 26.1$  mm) and for the second section (gap  $g = 29.00$  mm) respectively. Uniformity of the field is evident. This was obtained by fine tuning of the individual cell magnets. The spread  $\Delta B_{y0}/B_{y0}$  does not exceed 0.2%. The contribution of the higher harmonics in the field shape is less than 0.25% for the third harmonic and it is less than 0.1% for the fifth harmonic respectively.

Since the problem of electron beam transport through the undulator directly depends on the second integral of the magnetic field [6] these characteristics were used as criteria during field matching in the intersection gap and at the ends of the undulator sections. The final second integral amplitudes are limited by the value which is comparable with the undulating amplitude of the 1.75 MeV electron ( $\sim 1.1$  mm). The relative spread of the second integral amplitudes from the average value  $(\Delta I_0/\langle J_0 \rangle)_{\text{rms}}$  does not exceed 10%.

The reproducing of the magnetic field properties of the undulator after reassembling of side magnet arrays was also investigated (this reassembling is needed after an access to the waveguide). The differences of the respective second integral amplitudes were found to be less than 5% when the improved wire method [5] was used for the measurements.

Another criterion for the field matching is a slippage  $\Phi$  of the relative phase between the generating electromagnetic wave and the electron produced in the intersection gap. It was found for the project [2,3] that the electron beam interacts with the electromagnetic wave in the second section more effectively if the phase slippage equals to  $\sim \pi$ . The slippage phase can be easily found from the

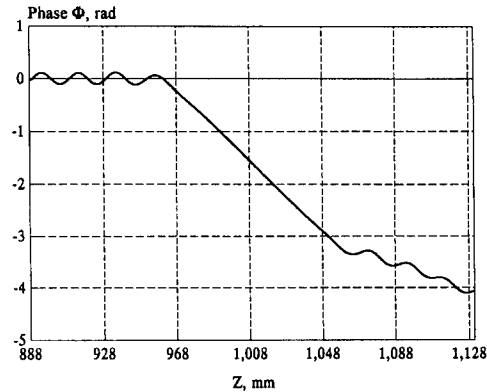


Fig. 2. The phase  $\Phi$  evolution in the intersection gap.

experimental data on the first integral of the magnetic field. The following expression was used for the phase  $\Phi$  evaluation:

$$\Phi = k_w \int dz \left( \left[ 1 + \left( \frac{2\pi}{10.7} \int B_y dz \right)^2 \right] \left( 1 + \frac{K_0^2}{2} \right)^{-1} - 1 \right),$$

where  $k_w$  is the undulator wave number,  $K_0$  is the undulator strength value and the first integral is measured in kG cm.

Fig. 2 shows the phase evolution found between two sections of the KIAE-4 undulator. The nominal intersection distance of 68 mm gives  $\Phi \approx \pi$ . Curve 1 of Fig. 3 gives the phase growth  $\Delta\Phi$  as a function of the distance between the sections. These data can be used for the  $\Phi$ -phase tuning by changing the intersection gap.

### 4. The transverse profiles of the magnetic field

In Ref. [4] we considered only a symmetrical arrangement of the side magnet arrays with equal  $X$ -distances of

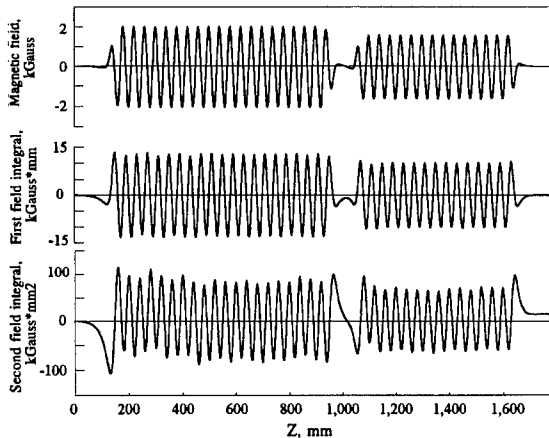


Fig. 1. On-axis magnetic field  $B_y$  with its first and second integrals.

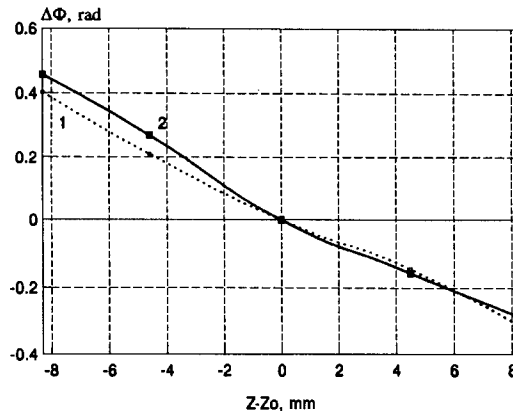


Fig. 3. The phase growth  $\Delta\Phi$  for different intersection gaps (1) with coil current correction for the field matching and (2) without coil current correction.

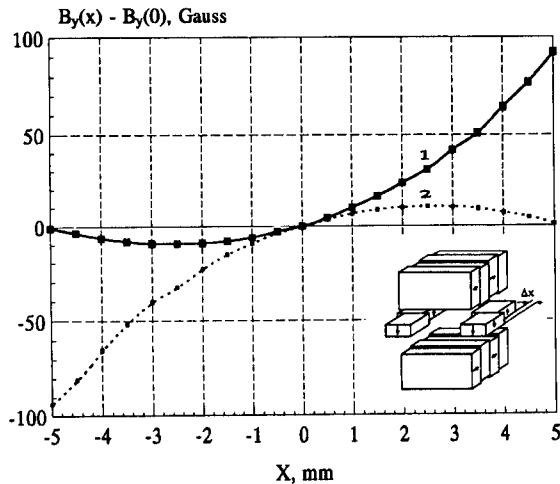


Fig. 4. Transverse profile of the magnetic field  $B_y(x)$  (1) for even poles and (2) for odd poles.

the side magnets from the undulator  $Z$ -axis. This provided periodic parabolic transverse field profiles and thus appropriate sextupole electron beam focusing in the  $X$ - $Z$  plane [6]. To enhance the focusing strength in the horizontal plane for a given limited distance between side magnet arrays (defined by the waveguide size) we use a nonsymmetrical arrangement with displacement side magnets at the distances  $\Delta x$  at chess order (cf. Ref. [1]). This gives an additional nonperiodic field gradient and quadrupole focusing [6]. As a result a superposition of quadrupole and sextupole focusing is provided with adjustable strength. In accordance with the project [2,3] request the distance  $\Delta x = 2.3$  mm was found to be optimal.

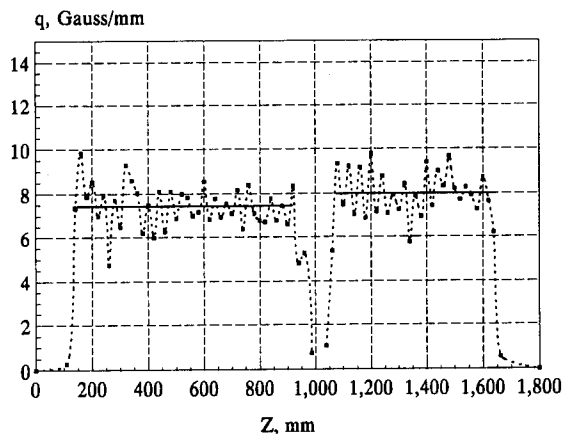


Fig. 5. Transverse gradient of the field  $q$  as a function of  $Z$ -coordinate. ■ experimental results obtained for the points spread under steel poles; — average gradients for the first and the second sections.

The field profiles  $B_y(x)$  obtained for odd and even poles respectively are given in Fig. 4. The respective field shape curves are shifted from the central axis in opposite directions. This asymmetry gives a transverse gradient  $q = dB_y(x)/dx$  [G mm] =  $3 \Delta x$  [mm].

It can be seen from Fig. 5 that the gradient  $q$  is not uniform and depends on  $Z$ . But the focusing strength actually depends on the integral characteristic so the  $q$  spread has no real effect after the field matching is provided. The relative focusing strength defined as  $k_{\beta y}/k_{\beta x}$  (see Ref. [6]) is equal to 1.37 for the first section and to 0.99 for the second one with the above  $\Delta x = 2.3$  mm asymmetry parameter.

## 5. Conclusion

A full test of the magnetic fields of the KIAE-4 undulator has shown that it is fully adequate to meet the strict FOM-Fusion-FEM project requirements. These results can be considered as a practical approval of the novel undulator scheme with side magnet arrays which was firstly developed and used by authors. Compactness, adjustable focusing force, high field strength, tunable tapering, high uniformity of the fields make the scheme and the device attractive for other FEL projects.

## Acknowledgements

Our group appreciates the help received from A.A. Sabelnikov, A.V. Smirnov and A.H. Hairtdinov.

## References

- [1] T. Okazaki, Y. Hosoda, K. Keighi and A. Kobayashi, Nucl. Instr. and Meth. A 331 (1993) 673.
- [2] W.H. Urbanus, R.W.B. Best, A.G.A. Verhoeven, M.J. van der Wiel, M. Caplan, V.L. Bratman, G. Denisov and A.A. Varfolomeev, Proc. 3rd Europ. Particle Accelerator Conf., vol. 1 (1992) p. 629.
- [3] W.H. Urbanus, R.W.B. Best, W.A. Bongers, A.M. van Ingen, P. Manintveld, A.B. Sterk, A.G.A. Verhoeven, M.J. van der Wiel, M. Caplan, V.L. Bratman, G. Denisov, A.A. Varfolomeev and A.S. Khlebnikov, Nucl. Instr. and Meth. A 331 (1993) 235.
- [4] A.A. Varfolomeev, S.N. Ivanchenkov, A.S. Khlebnikov, N.S. Osmanov, M.J. van der Wiel, W.H. Urbanus and V.F. Pavluchenkov, Nucl. Instr. and Meth. A 341 (1994) 466.
- [5] A.A. Varfolomeev, A.S. Khlebnikov, N.S. Osmanov and S.V. Tolmachev, these Proceedings (16th Int. Free Electron Laser Conf., Stanford, CA, USA, 1994) Nucl. Instr. and Meth. A 358 (1995) ABS 46.
- [6] A.A. Varfolomeev and A.V. Smirnov, *ibid.*, p. 197.





ELSEVIER

## Development of a modified wiggler for higher harmonic lasing of a free-electron laser

M. Asakawa <sup>a,\*</sup>, N. Inoue <sup>a</sup>, K. Mima <sup>a</sup>, S. Nakai <sup>a</sup>, K. Imasaki <sup>b</sup>, M. Fujita <sup>b</sup>, J. Chen <sup>b</sup>,  
C. Yamanaka <sup>b</sup>, N. Nakao <sup>c</sup>, T. Agari <sup>c</sup>, T. Asakuma <sup>c</sup>, A. Moon <sup>c</sup>, N. Ohigashi <sup>c</sup>,  
T. Minamiguchi <sup>d</sup>, Y. Tsunawaki <sup>d</sup>

<sup>a</sup> Institute of Laser Engineering, Osaka University, 2-6 Yamada-oka, Suita, Osaka, 565 Japan

<sup>b</sup> Institute for Laser Technology, 2-6 Yamada-oka, Suita, Osaka, 565 Japan

<sup>c</sup> Kansai University, 3-10-11 Yamate-cho, Suita, Osaka, 564 Japan

<sup>d</sup> Osaka Sangyo University, 3-1-1 Daito, Osaka, 574 Japan

### Abstract

A modified wiggler, with enhanced harmonic fields, was developed for free-electron laser higher harmonic lasing. The harmonic wiggler field was produced by arranging high-permeability shims in the gap spacing of a four-block-per-period Halbach design wiggler. By this method, the 3rd harmonic wiggler field exceeded 18% of the fundamental field. The phasing of the harmonic field could be also controlled by the positioning of the shims.

### 1. Introduction

A compact Free-Electron Laser (FEL) program has been running at ILE/ILT using a 6 MeV rf linac. Lasing in the millimeter-range using coherent synchrotron radiation was achieved in 1993 [1]. The key issues of our research for shorter wavelength lasing are a radio-frequency photocathode electron-gun [2–4], a microwiggler with sub-centimeter period [5] and a novel wiggler for multi-order harmonic lasing.

Harmonic operation of FELs has significant implications for compact and short-wavelength FEL systems. Ultraviolet lasing with a low-energy electron beam was demonstrated at LANL and was based on the 3rd harmonic [6]. Taking account into the electron beam energy, this is the shortest wavelength ever achieved by an FEL.

The harmonic gain of an FEL is extremely small compared to that of the fundamental, and it decreases as the harmonic order increases. To improve the harmonic gain, the effect of wiggler harmonics on FEL dynamics has been studied [7–9]. These studies show that the power of the spontaneous emission, the gain and the extraction efficiency can be increased by adding wiggler harmonic fields to the fundamental field in the appropriate ratio and phase. This technique will enable us to operate an FEL at the 5th or higher order harmonic.

In this paper, we will present a modified wiggler, which has considerable harmonic magnetic fields. The modification of the wiggler magnetic field was applied to the wiggler by arranging high-permeability shims in the wiggler gap. The 3rd harmonic component reached 18% of the fundamental component. The FEL dynamics of this modified wiggler will be also discussed.

### 2. Modified wiggler

In a plane-polarized sinusoidal wiggler field, gain on FEL harmonics occurs because the electron motion is not sinusoidal. It travels through the wiggler field with a “figure-eight” trajectory in the rest frame of the beam. One can expect enhancement of the laser harmonics by adding a harmonic field to the fundamental sinusoidal wiggler field. Then the wiggler field with harmonic field, i.e., the modified wiggler field, can be written as follows:

$$B_w(z) = \sum_h B_h \sin(hk_w z), \quad (1)$$

where  $k_w$  is the wavenumber of the fundamental wiggler field,  $h$  is the harmonic order and  $B_h$  denotes the magnetic flux relative to the  $h$ th harmonic wiggler field. When the modified wiggler consist of two harmonic fields, the fundamental and  $h$ th harmonic field, the electron motion is expressed by

$$x = -\frac{1}{\gamma} \left[ \frac{K_1}{k_w} \sin(k_w z) + \frac{K_h}{hk_w} \sin(hk_w z) \right], \quad (2)$$

$$z = \bar{z} + \bar{z}, \quad (3)$$

\* Corresponding author. Tel. +81 6 877 511, fax +81 6 877 4799.

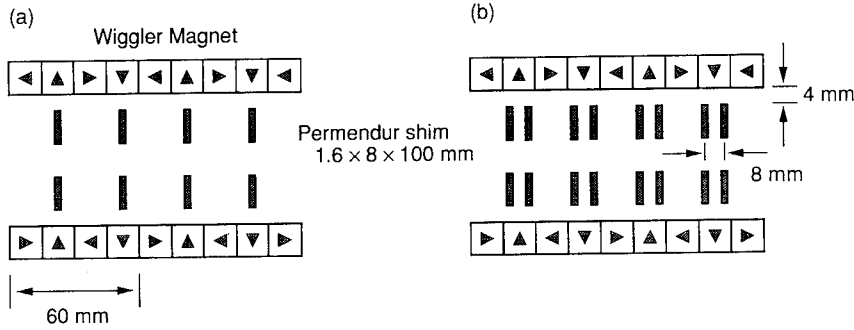


Fig. 1. Schematic view of the modified wiggler.

where  $K_h = eB/hk_w mc$ , and,  $\bar{z}$  and  $\tilde{z}$  denote the axial mean motion and oscillation, respectively, and are given by

$$\bar{z} = \left[ 1 - \frac{1}{2\gamma^2} \left( 1 + \frac{K_1^2}{2} + \frac{K_h^2}{2} \right) \right] ct, \quad (4)$$

$$\begin{aligned} \tilde{z} = & -\frac{1}{4\gamma^2} \left\{ \frac{K_1^2}{2k_w} \cos(2k_w \bar{z}) + \frac{K_h^2}{2hk_w} \cos(2hk_w \bar{z}) \right. \\ & + \frac{2K_1 K_h}{(h+1)k_w} \cos[(h+1)k_w \bar{z}] \\ & \left. - \frac{2K_1 K_h}{(h-1)k_w} \cos[(h-1)k_w \bar{z}] \right\}. \end{aligned} \quad (5)$$

The complex form of the electron motion causes enhancement and suppression of the laser harmonics. The effect on laser gain with variations of the harmonic wiggler fields is significant. To illustrate the effect of the phase of the harmonic wiggler field, let us consider the case of  $h=3$ . When  $B_3$  has an inverted sign to  $B_1$ , gain on the laser harmonics increases, while it decreases when  $B_3$  has the same sign as  $B_1$ . This is because the electron trajectory is more sinusoidal when  $B_3$  has the same sign as  $B_1$ . In order to enhance the laser harmonics, one has to control the phasing of the harmonic wiggler field.

We constructed some trial modified wigglers by arranging permendur shims in the wiggler gap spacing. Fig. 1 shows a schematic view of the modified wiggler. The permanent magnet wiggler was a four-block-per-period Halbach design. The wiggler period was 60 mm and the number of periods was 10. The permendur had a permeability of 800 and saturated magnetic flux of 2.1 T. The shims of permendur were 1.6 mm thick, 8 mm tall and 100 mm long. In Fig. 1a, a permendur shim was placed above the wiggler magnets with magnetization vectors perpendicular to the wiggler axis, while two shims were arranged symmetrically with a spacing of 8 mm in Fig. 1b. These shims were fixed on a substrate with a spacing of 4 mm between the shim and the wiggler magnet in both cases.

Figs. 2a and 2b show the resultant magnetic field profiles obtained from the configurations described in Figs. 1a and 1b, respectively. By the gap, we mean the spacing

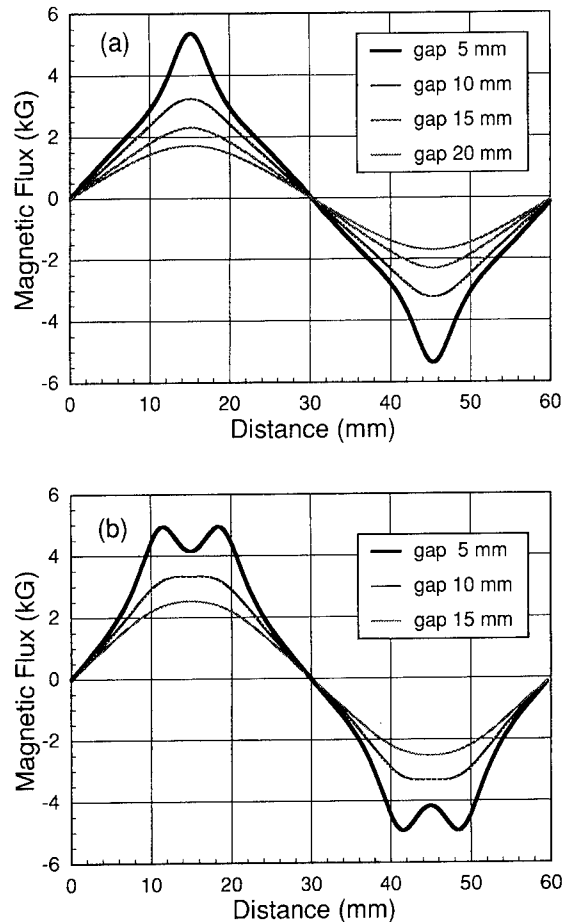


Fig. 2. Resultant magnetic field profiles. Arrangement of the permendur shim is in Fig. 1 (a) and (b) for (a) and (b), respectively. The gap denotes the spacing between the shims opposite to each other.

between permendur shims standing opposite to each other. The magnetic field profiles in Fig. 2 clearly differ from the sinusoidal profile of the non-shim wiggler. The magnetic flux is concentrated at the position where the shim is placed. In Fig. 2a, the magnetic field has a sharp profile, while two peaks appear every half period in Fig. 2b. This difference results from the different phasing of the harmonic wiggler field. As we increased the gap spacing, the magnetic field profile turned into sinusoidal form and the harmonic wiggler field fell off.

Fig. 3 shows the ratio of the harmonic components to the fundamental component,  $B_h/B_1$ , computed from the magnetic field profiles in Fig. 2. The magnetic field was sampled at 128 positions per period, so that we could evaluate up to 64th harmonic field. The error in the sampling position causes the phase noise and the destruction of symmetry to produce even harmonic field. In our

case the ratio of the cosine term to the sine term of 3rd harmonic component was less than  $10^{-4}$ , and the ratio of 2nd harmonic component to the fundamental component was less than  $10^{-6}$ . Thus we neglected these components. In Fig. 3a, the harmonic components of the magnetic field in Fig. 2a, the 3rd harmonic component exceeds 18% of the fundamental component. This is sufficient to enhance the effect of the harmonic wiggler field on the laser gain. In Fig. 3b, the harmonics of the magnetic field in Fig. 2b, the 7th harmonic component is enhanced and is more than 7%. In this case, the phasing of the 5th harmonic component is inverted compared to the result in Fig. 3a. The harmonic components fall off as the gap increases in both cases. Higher order harmonic field decay more rapidly.

### 3. Discussion

From Eq. (4), the resonant condition in the modified wiggler field is expressed relative to the  $K$ -parameters of the harmonic wiggler field:

$$\lambda_r = \frac{1}{2\gamma^2} \left( 1 + \frac{K_0^2}{2} \right). \quad (6)$$

Here we introduced an equivalent  $K$ -parameter,  $K_0$ , which is defined as

$$K_0 = \sqrt{\sum_h K_h^2}. \quad (7)$$

The resonant condition Eq. (6) has the same form as the usual sinusoidal wiggler, so it is reasonable to compare a modified wiggler with a usual wiggler with the same  $K$ -parameters.

The magnetic field profile in Fig. 2a with the gap spacing of 5 mm can be expressed as

$$B_w(z) \approx 3822 \sin(k_w z) - 697 \sin(3k_w z) + 391 \sin(5k_w z) - 196 \sin(7k_w z) \text{ (G)}. \quad (8)$$

Here  $k_w = 2\pi/6 \text{ cm}^{-1}$ . The  $K_0$ -parameter is calculated to be 2.2 in this case. The contribution to the  $K_0$ -parameter from each harmonic field is small, so the modification of the wiggler field does not lengthen the laser wavelength significantly.

By a 3D-simulation [10], the improvement of the gain was estimated to be 18% and 30% for 3rd and 5th laser harmonic, respectively. In this experiment, we used a wiggler which had a large  $K$ -parameter of 2.2. Thus the gain on the laser harmonics was not so small with the sinusoidal field wiggler, and the effect of harmonic wiggler field on the laser gain was small. However, the modification technique can be applied to a small  $K$ -parameter wiggler ( $K < 1$ ), with a short period ( $\sim 10 \text{ mm}$ ), and a small magnetic flux. Then the gain improvement will be more substantial.

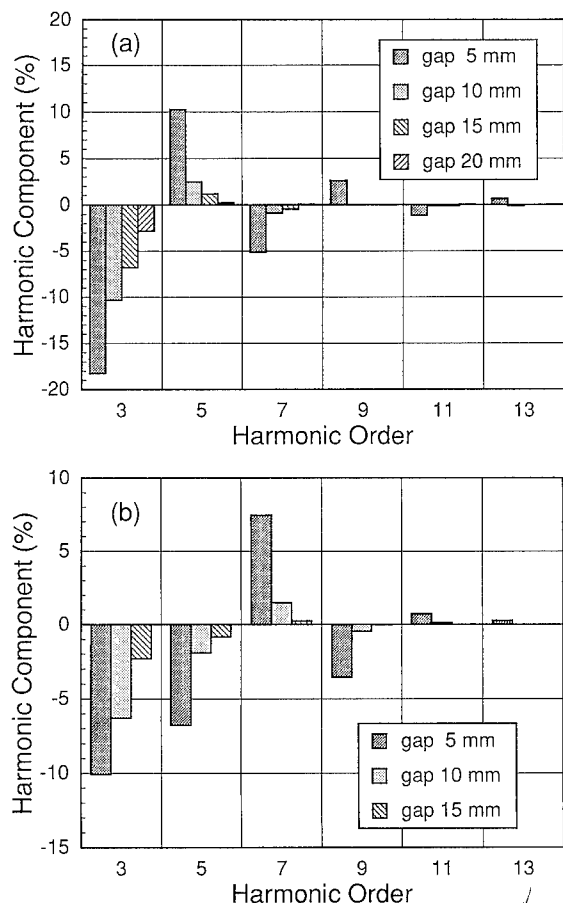


Fig. 3. Ratio of the harmonic wiggler field components to the fundamental component. These results were calculated from the magnetic field profile in Figs. 2; (a) and (b) correspond to the field in Figs. 2a and 2b, respectively.

#### 4. Conclusion

These studies show that modification of the wiggler field by high permeability shims is suitable for modifying a wiggler for higher harmonic lasing. This simple technique can control the magnitude and the phase of the harmonic wiggler field by the shim arrangement. Further, by canting the shim, a transverse focusing force can be produced.

In practice the modified wiggler, consists of many harmonic components. Thus the harmonic gain should be investigated for various combinations of the harmonic wiggler field. The next step is to investigate the optimal field to provide the best wiggler design.

#### References

- [1] M. Asakawa, N. Sakamoto, N. Inoue, T. Yamamoto, K. Mima, S. Nakai, J. Chen, M. Fujita, K. Imasaki, C. Yamanaka, T. Agari, T. Asakuma, N. Ohigashi and Y. Tsunawaki, *Appl. Phys. Lett.* 64 (1994) 1601.
- [2] M. Asakawa, N. Sakamoto, Y. Shimizu, S. Nakai, K. Imasaki and C. Yamanaka, *Nucl. Instr. and Meth. A* 331 (1993) 302.
- [3] M. Asakawa, K. Mima, S. Nakai, M. Fujita, K. Imasaki and C. Yamanaka, *Appl. Phys. Lett.* 64 (1994) 2056.
- [4] M. Fujita, K. Imasaki, J. Chen, H. Furukawa, C. Yamanaka, M. Asakawa, N. Sakamoto, T. Yamamoto, N. Inoue, S. Nakai, K. Nagami, Y. Tsunawaki, T. Agari, T. Asakuma and N. Ohigashi, *Nucl. Instr. and Meth. A* 341 (1994) ABS 35.
- [5] N. Ohigashi, K. Mima, Y. Tsunawaki, S. Ishii, N. Ikeda, K. Imasaki, M. Fujita, S. Kuruma, A. Murai, C. Yamanaka and S. Nakai, *Nucl. Instr. and Meth. A* 341 (1994) 426.
- [6] P.G. O'Shea, S.C. Bender, D.A. Byrd, J.W. Early, D.W. Feldman, C.M. Fortgang, J.C. Goldstein, B.E. Newnam, R.L. Sheffield, R.W. Warren and T.J. Zaugg, *Nucl. Instr. and Meth. A* 341 (1994) 7.
- [7] M.J. Schmitt and C.J. Elliot, *IEEE J. Quantum Electron.* QE-23 (1987) 1552.
- [8] M. Asakawa, K. Mima, S. Nakai, K. Imasaki and C. Yamanaka, *Nucl. Instr. and Meth. A* 318 (1992) 538.
- [9] D. Iracane, D. Touati and P. Chaix, *Nucl. Instr. and Meth. A* 341 (1994) 220.
- [10] Y. Tsunawaki, N. Ohigashi, K. Mima, S. Kuruma, K. Imasaki, A. Murai, C. Yamanaka and S. Nakai, *Nucl. Instr. and Meth. A* 341 (1994) ABS 121.



ELSEVIER

## Performance of the undulator for JAERI FEL project

R. Nagai <sup>a,\*</sup>, H. Kobayashi <sup>c</sup>, S. Sasaki <sup>c</sup>, M. Sawamura <sup>b</sup>, M. Sugimoto <sup>b</sup>, R. Kato <sup>b</sup>,  
N. Kikuzawa <sup>b</sup>, M. Ohkubo <sup>b</sup>, E. Minehara <sup>b</sup>, T. Ikehata <sup>a</sup>, H. Mase <sup>a</sup>

<sup>a</sup> Department of Materials Science, Graduate School of Engineering, Ibaraki University, 4-12-1 Nakanarusawa, Hitachi, Ibaraki, 316, Japan

<sup>b</sup> Free Electron Laser Laboratory, Japan Atomic Energy Research Institute, Tokai, Ibaraki, 319-11, Japan

<sup>c</sup> Department of Synchrotron Radiation Facility Project, Japan Atomic Energy Research Institute, Tokai, Ibaraki, 319-11, Japan

### Abstract

A newly designed hybrid undulator (DFTH-1), whose field termination parts are a novel implementation of the displacement-free termination scheme, has been constructed for the JAERI FEL project. The field termination part of the undulator was designed to minimize the electron trajectory walkoff by using the 3D magnetic field computational code named ELF/Magic. The DFTH-1 undulator could reduce the walkoff by one third of that of the conventional hybrid undulator with non-steering termination.

### 1. Introduction

A free electron laser, JAERI FEL, based on a superconducting rf linac is now under construction to lase in the far infrared region at Japan Atomic Energy Research Institute. Outlines of the JAERI FEL project were reported previously [1,2].

The project was started to realize a high power infrared region FEL. To obtain optimal performance of the FEL, a displacement-free termination scheme hybrid undulator (DFTH-1) has been constructed. Diviacco et al. reported a termination scheme for a pure permanent magnet undulator [3] which optimizes the FEL performance. We applied same termination scheme to a hybrid undulator, solving some technical problems associated with magnetic circuit.

Conventional hybrid undulators tend to use a non-steering termination scheme, which leads to a cancellation of the first integral of the undulator field, and have electron trajectory walkoff in the range of submillimeter in far infrared FELs. In this case, the walkoff depends on the energy of the electron beam and the deflecting parameter  $K$  of the undulator. The walkoff causes misalignment with the electron trajectory in the laser field, and then degrades the FEL performance. In order to reduce the walkoff, the DFTH-1 undulator has a displacement-free termination

scheme which leads to a cancellation of the second integral of the undulator field.

In this paper, the design concept of the DFTH-1 undulator is described, and the performance of the undulator will be discussed.

### 2. Structure of the undulator

The DFTH-1 undulator generates a 52 period sinusoidal undulator field, whose period length and peak amplitude are 33 mm and more than 5000 G at the gap of 15 mm, respectively. A photograph of the DFTH-1 undulator is shown in Fig. 1. Its magnetic circuit consists of wedge-shaped magnets (Ni plated Nd–Fe–B) and poles (annealed permendur). Fluctuation of the longitudinal field pattern was slightly tuned by placing shims on the magnets [4]. The magnetic circuit is mounted on movable jaws, which are made of aluminum and precisely remote-controlled. Tunability of an FEL's radiation depends mainly on the peak amplitude of the field, periodic length of the field and the energy of the electron beam. Since continuously changing the electron beam energy is not so easy for the rf linac system, the undulator field is required to be changed precisely to obtain fine tunability of the radiation wavelength. Therefore, the jaws can control smoothly the peak amplitude of the undulator field. The main parameters of the DFTH-1 undulator are summarized in Table 1.

The field pattern was measured by means of a 3D magnetic probe, and also calculated by using a 3D magnetic field computational code named ELF/Magic. On-axis peak field strength as a function of the gap length of the

\* Corresponding author. Permanent address: Free Electron Laser Laboratory, Japan Atomic Energy Research Institute, Tokai, Ibaraki, 319-11 Japan. Tel: +81 292 82 5464, Fax: +81 292 82 5939.

Table 1  
Parameters of the DFTH-1 undulator

|                           |           |
|---------------------------|-----------|
| Magnet material           | Nd-Fe-B   |
| Periodic length           | 3.3 cm    |
| Gap range                 | 1.5–10 cm |
| On-axis peak field        | 0.5 T     |
| Deflection parameter, $K$ | < 1.54    |
| Field error               | < 1.5%    |
| Number of periods         | 52        |
| Pole width                | 6.2 cm    |
| Magnet width              | 7.8 cm    |

undulator is shown in Fig. 2. The measured and calculated data are represented by the open circles and solid line, respectively. The measured values (open circles) were in good agreement with the calculated ones (solid line). The rms error of the undulator field is shown in Fig. 3. The rms error is determined from the magnitude of difference of the ideal sinusoidal field pattern from the measured/calculated field pattern. Considering sampled magnetic field  $B_i$  at  $i$ -th position  $z_i$ , the rms error of the undulator field  $\Delta B_{\text{rms}}$  is defined as

$$\Delta B_{\text{rms}} = \frac{1}{B_0} \left\{ \frac{1}{n} \sum_i \left( B_i - B_0 \sin \left( \frac{2\pi}{\lambda_0} z_i + \phi_0 \right) \right)^2 \right\}^{1/2}, \quad (1)$$

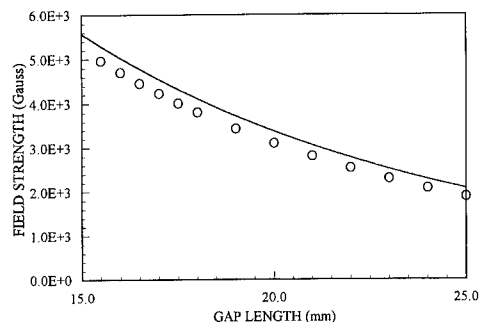


Fig. 2. On-axis peak field as a function of gap length. The measured and calculated data are represented by open circles and solid line, respectively.

where  $B_0$ ,  $\lambda_0$ ,  $\phi_0$  and  $n$  are amplitude, period length, phase of the ideal sinusoidal field and total amount of sampled data, respectively. The rms error includes the error which is attributable to the higher harmonic components of the undulator field. Therefore, the  $\Delta B_{\text{rms}}$  for the calculated field pattern is not equal to zero.

The reproducibility of the field pattern at resetting the same gap length was examined by using the rms difference of the original field pattern from that after resetting. The rms differences for five times resetting are shown in Fig. 4. The reproducibility of the field pattern was found to be

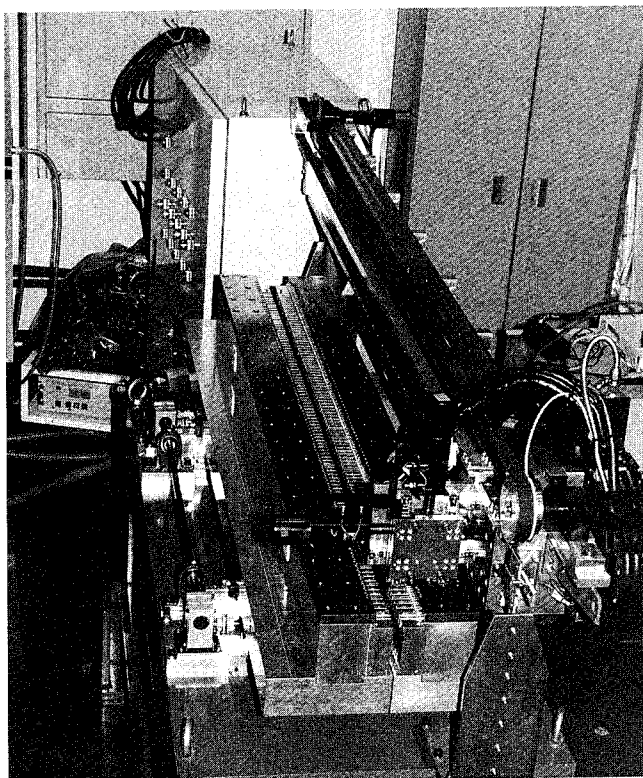


Fig. 1. Photograph of the DFTH-1 undulator.

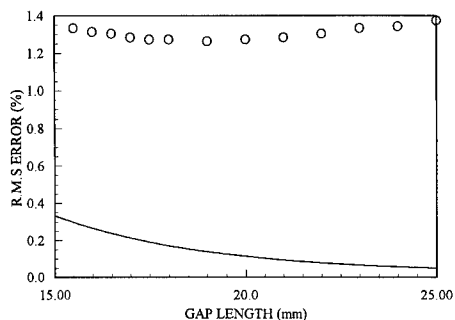


Fig. 3. Rms error of the undulator strength. Open circles are the measured data and solid line is the calculated data.

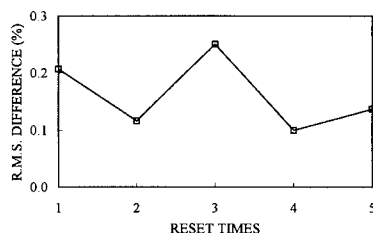


Fig. 4. Reproducibility of the undulator field when the undulator gap was reset.

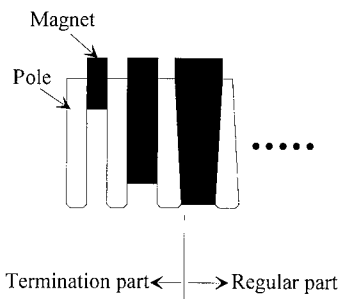


Fig. 5. Schematic drawing of the cross-sectional view of the termination part.

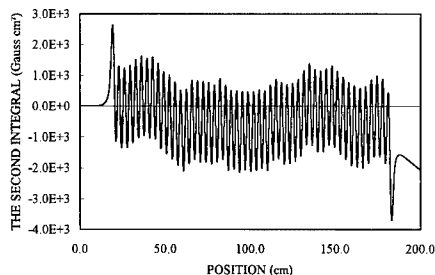


Fig. 6. Typical result of the second integral of the obtained from measured data at the gap length of 17 mm.

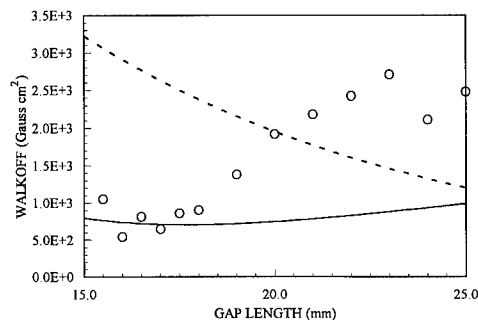


Fig. 7. Walkoff defined as Eq. (2) when gap was varied. The measured, calculated and the ideal usual termination hybrid undulator are represented by the open circles, solid line and dotted line, respectively.

good enough, because the rms difference was sufficiently smaller than the rms error of the undulator field.

### 3. Termination part design and performance

The DFTH-1 undulator is terminated with a novel implementation of displacement-free termination to minimize the electron trajectory walkoff, which affects the FEL performance.

The design of the field termination part focuses on minimizing the electron trajectory walkoff by using the 3D code ELF/Magic. A schematic drawing of the cross-sectional view of the termination part is shown in Fig. 5. In order to realize the termination scheme, two magnet pieces and three pole pieces of the end part were reshaped.

The electron trajectory walkoff is proportional to the second integral of the undulator field. So, the walkoff  $\Delta W_{\text{rms}}$  can be defined as

$$\Delta W_{\text{rms}} = \left\{ \frac{1}{n} \sum_i \left( W_i + B_0 \left( \frac{\lambda_0}{2\pi} \right)^2 \sin \left( \frac{2\pi}{\lambda_0} z_i + \phi_0 \right) \right)^2 \right\}^{1/2}, \quad (2)$$

where  $W_i$  is  $i$ -th sampled data of the walkoff. A typical result of the second integral obtained from measured field pattern at the gap length of 17 mm is shown in Fig. 6. Fig. 7 shows the walkoff when the gap length is varied. Three curves of the walkoff obtained from Eq. (2) using measured field (open circles), calculated field (solid line) and the ideal hybrid undulator field with usual termination (dotted line) were indicated in Fig. 7. The walkoff of the DFTH-1 undulator was sufficiently suppressed, and the measured data were in good agreement with the calculated ones at short gap length.

#### 4. Conclusion

A displacement-free termination scheme hybrid undulator was constructed and the electron trajectory walkoff was sufficiently suppressed and in good agreement with the value of calculation at short gap length. This termination scheme is found to be very useful in the far infrared region free electron laser. the DFTH-1 undulator is expected to provide high performance to the JAERI FEL, because the rms error of the undulator field and the electron trajectory walkoff were small enough and the undulator gap could be reset with good reproducibility.

#### Acknowledgement

The authors would like to thank Dr. M. Takeuchi of Ibaraki university and Dr. Y. Suzuki of JAERI for their continuous encouragement and interests on this work.

#### References

- [1] M. Sawamura, M. Sugimoto, E. Minehara, R. Nagai, J. Sasabe, N. Kikuzawa, M. Takao, K. Mashiko, M. Ohkubo, Y. Kawarasaki and Y. Suzuki, *Nucl. Instr. and Meth. A* 318 (1992) 127.
- [2] E. Minehara, R. Nagai, M. Sawamura, M. Takao, N. Kikuzawa, M. Sugimoto, S. Sasaki, M. Ohkubo, J. Sasabe, Y. Suzuki, Y. Kawarasaki and N. Shikazono, *Nucl. Instr. and Meth. A* 331 (1993) 182.
- [3] B. Diviacco and R.P. Walker, *Sincrotron Trieste Internal Report*, ST/M-TN-92/5.
- [4] S.C. Gottschalk, D.C. Quimby, K.E. Robinson and J.M. Slater, *Nucl. Instr. and Meth. A* 296 (1990) 579.





ELSEVIER

## Development of a short-period hybrid wiggler

F. Inoue<sup>\*</sup>, N. Ikeda, K. Okubo, M. Takahashi, T. Yamanaka*Mitsubishi Heavy Industries, Ltd., 1-1, 1-Chome Wadasaki-cho, Hyogo-ku, Kobe 652, Japan*

### Abstract

A short-period wiggler ( $\lambda_w = 12$  mm,  $g = 6$  mm,  $N_w = 40$ ) was designed and wiggler parameters were optimized by 2-dimensional field analysis to enhance the magnetic field. According to this design, a trial wiggler ( $\lambda_w = 12$  mm,  $g = 6$  mm,  $N_w = 10$ ) was manufactured and its magnetic field was measured. It has a hybrid type structure, with Nd-Fe-B permanent magnets and low carbon steel polepieces. The measured field strength was 0.44 T ( $K = 0.5$ ). We also demonstrated the usefulness of the variable field adjustment method by making a by-pass circuit with a backside shim structure. The maximum adjustment value was 4%.

### 1. Introduction

To realize industrial FELs, it is necessary to reduce their size and cost. One of the best ways to solve this problem is to reduce the energy of the electron beam injected into the wiggler. Under this condition, to get the required FEL wavelength, it is necessary to employ a short-period wiggler. In order to get an infrared FEL (about 10  $\mu\text{m}$ ) with middle electron beam energy ( $< 15$  MeV), the wiggler period length should be around 10 mm. Generally, in a short-period wiggler, the  $K$  parameter is small and it is difficult to realize the gain required for FEL oscillation. To enhance the  $K$  parameter a high magnetic field is needed. Electromagnet wigglers [1–3] create higher fields than permanent magnet wigglers [4] with a short-period, but electromagnet wigglers need stable power supplies to excite the magnetic fields. So using electromagnet wigglers will not reduce the cost.

From the viewpoint of cost reduction, we decided to employ a permanent magnet wiggler and examined how it enhanced the magnetic field. The paper describes the design of a short-period permanent magnet wiggler with a period length of 12 mm, field analysis and the field measurements of a trial wiggler.

### 2. Design considerations

In the short-period wiggler, the  $K$  parameter is generally small. To realize FEL oscillation, it is necessary to enhance the  $K$  parameter. Therefore, development of a

high magnetic field wiggler is one of the most important goals. In this section a comparison of the most typical wiggler, which is a pure magnet wiggler and a hybrid wiggler, is described from the viewpoint of realizing a high magnetic field.

A pure magnet wiggler, called the Halbach wiggler, is the most popular of the wigglers. It has a simple structure, and it is easy to calculate its magnetic field, because it is composed of only permanent magnets. In this type, the magnetic field depends on the characteristics of the permanent magnets; remanent magnetic flux density ( $B_r$ ) and coercive force ( $H_c$ ). So to realize a high magnetic field, it is necessary to use high performance magnets. Under the present conditions, when using a pure magnet wiggler, the magnetic field is limited by the performance of the magnets.

On the other hand, in the hybrid wiggler magnetic poles are created by highly permeable ferromagnets. The magnetic field depends on the saturation field of the ferromagnetic polepiece. In this type, the magnetic field is enhanced to increase the magnetic flux being led into the polepieces.

In this description, the hybrid wiggler has a capability of achieving a higher magnetic field than the pure magnet wiggler by optimizing the magnet and polepiece parameters.

### 3. Field analysis and optimization of wiggler parameters

To enhance the magnetic field, permanent magnet and polepiece parameters were optimized by 2-dimensional field analysis. The calculation model is shown in Fig. 1. In this calculation, the permanent magnet was Nd-Fe-B ( $B_r = 1.2$  T); the polepiece was low carbon steel (S10C);

<sup>\*</sup> Corresponding author. Tel: +81 78 672 2911, fax: +81 78 672 2900.

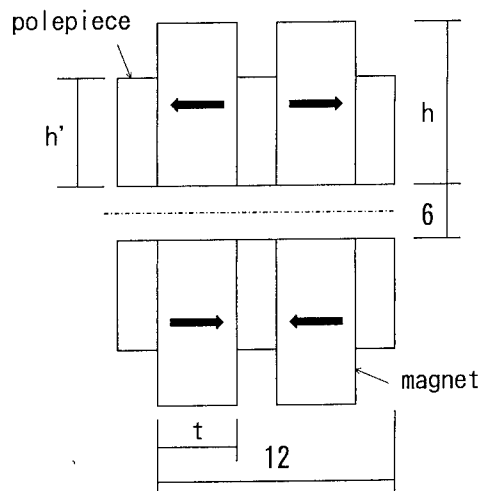


Fig. 1. Calculation model for 2-D field analysis. Optimizing parameters: magnet height  $h$ , magnet thickness  $t$ , polepiece height  $h'$ .

optimized parameters were magnet height, magnet thickness and polepiece height.

The calculation results for optimizing the permanent magnet height are shown in Fig. 2. The magnetic field increases with magnet height and becomes saturated with a height of about 40 mm. In the pure magnet wiggler (Halbach wiggler), the magnetic field is almost constant.

Fig. 3 shows the calculation result for optimizing the permanent magnet thickness. With thin magnets, the magnetic flux is led from the polepiece to the next polepiece not across the gap, because the length between the polepiece and the one next to it is short. On the other hand, with thick magnets, the magnetic field is saturated with minimal magnetic flux being led into the polepiece because the polepiece is thin. The optimized magnet thickness for the magnet is 4 mm with a magnet height of 40 mm. Fig. 4 shows the magnetic flux distribution for the

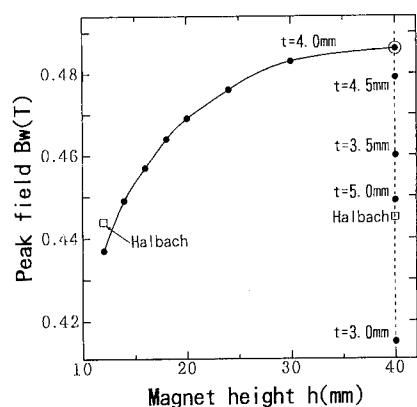


Fig. 2. Optimizing of permanent height with  $\lambda_w = 12$  mm,  $g = 6$  mm.

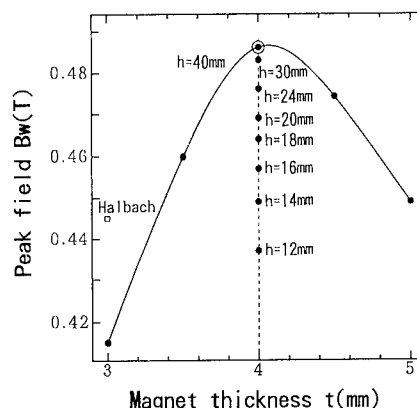


Fig. 3. Optimization of permanent magnet thickness with  $\lambda_w = 12$  mm,  $g = 6$  mm.

hybrid wiggler. With the same height, both the permanent magnets and the polepieces, in Fig. 4a, magnetic flux leaks to the backside of the wiggler. Therefore, the magnetic flux to the side gap is suppressed. With the polepiece which is lower than the permanent magnet in Fig. 4b, the magnetic flux leakage to the backside is reduced and this wiggler has a higher magnetic field than a wiggler with the same height. Fig 5 shows the optimization of the polepiece height. The magnetic field becomes the highest with a polepiece height of 30 mm.

With this wiggler, it is difficult to adjust the magnetic field by moving individual permanent magnets and polepieces because they are very thin. If thin shims are put on the magnetic pole surface, it is difficult to place the shims uniformly and it is necessary to extend the gap length to place the shims correctly. So the variable field adjustment

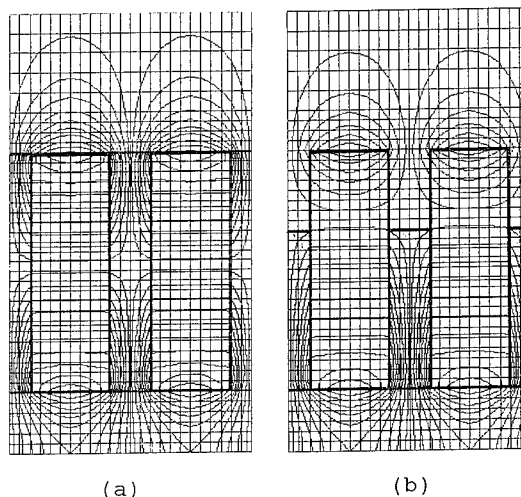


Fig. 4. Magnetic flux distributions: (a) both permanent magnet and polepiece with the same height, (b) polepiece is lower than permanent magnet.

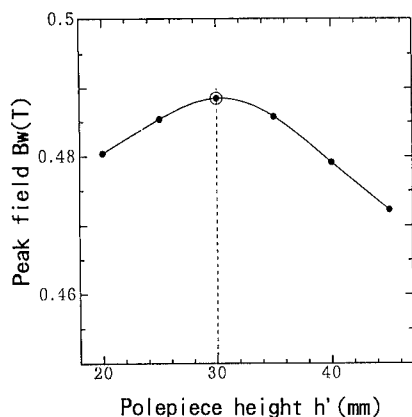


Fig. 5. Optimization of polepiece height with  $\lambda_w = 12$  mm,  $g = 6$  mm,  $h = 40$  mm,  $t = 4$  mm.

method of making a by-pass circuit with a backside shim structure was adopted, as shown in Fig. 6. To choose the shim height and thickness, the maximum adjustment value is 4%, as shown in Fig. 6.

#### 4. Wiggler design and field measurement

We have manufactured a trial wiggler with a period number of 10, shown in Fig. 7. The period length is 12 mm, the gap length is 6 mm. The permanent magnet is Nd-Fe-B, the polepiece is soft magnetic iron (SUY). In the field analysis we used low carbon steel (S10C) because we had no data on the permeability of soft magnetic iron. A vertical polarization structure was adopted to adjust the magnetic field with the backside shim structure easily.

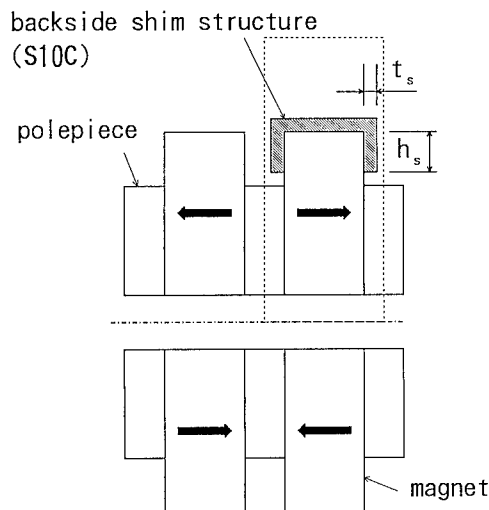


Fig. 6. Variable field adjustment method by making by-pass circuit with a backside shim structure.

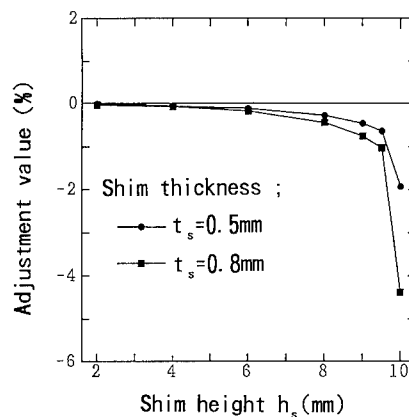


Fig. 7. Calculation of field adjustment method. (●)  $t_s = 0.5$  mm, (■)  $t_s = 0.8$  mm.

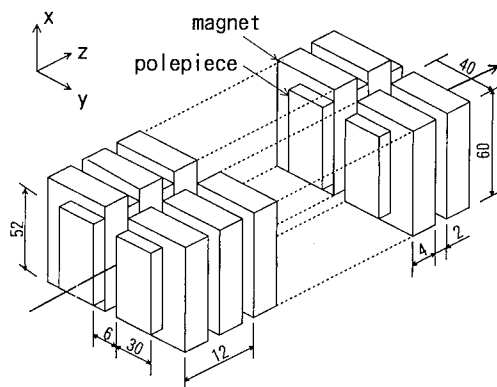


Fig. 8. Short-period hybrid wiggler design.

In Fig. 8, the measured field on the wiggler axis is shown. Arched magnetic field distribution due to the end effect is shown, because the period number is too small

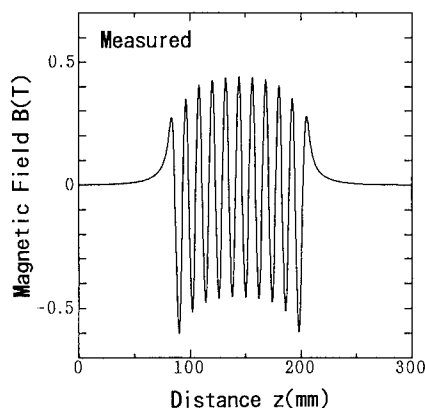


Fig. 9. Measurement of the magnetic field on the wiggler axis.

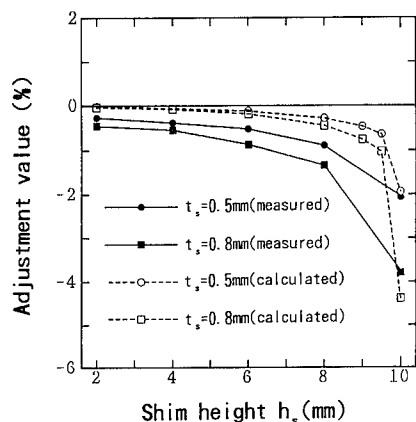


Fig. 10. Measurement of the field adjustment. (●, ○)  $t_s = 0.5$  mm; (■, □)  $t_s = 0.8$  mm; solid line: measured; broken line: calculated.

( $N_w = 10$ ). In the center of the wiggler, the magnetic field strength is 0.44 T ( $K = 0.5$ ). Fig. 9 shows the field adjustment result after making a by-pass circuit with a backside shim structure. To choose the shim height and thickness, a maximum field adjustment value of 4% is possible.

## 5. Conclusions

We designed a short-period hybrid wiggler ( $\lambda_w = 12$  mm,  $g = 6$  mm,  $N_w = 40$ ) by optimizing its magnet and polepiece parameters, and by using field analysis to maximize the wiggler field strength. We also manufactured a trial wiggler ( $\lambda_w = 12$  mm,  $g = 6$  mm,  $N_w = 10$ ). The measured field strength of the trial wiggler on the wiggler center was 0.44 T ( $K = 0.5$ ). We demonstrated the usefulness of the variable field adjustment method by making a by-pass circuit with a backside shim structure. The maximum adjustment value was 4% (shim height: 10 mm; thickness: 0.8 mm).

In this paper, we described a hybrid wiggler with magnetic poles created by S10C or SUY. We expect an even higher field (over 0.5 T) can be achieved if highly permeable materials, like vanadium permendur are used.

## References

- [1] K. Batchelor, I. Ben-Zvi, R. Fernow, J. Gallardo, H. Kirk, C. Pellegrini and A. Van Steenberg, Nucl. Instr. and Meth. A 296 (1990) 239.
- [2] R. Stoner, S.C. Chen and G. Bekeffi, IEEE Trans. Plasma Sci. PS-18 (3) (1990) 387.
- [3] R.W. Warren, Nucl. Instr. and Meth. A 304 (1991) 765.
- [4] K.P. Paulson, Nucl. Instr. and Meth. A 296 (1990) 624.

# Magnetic field measurements of the harmonic generation FEL superconducting undulator at BNL-NSLS ☆

L. Solomon <sup>a,\*</sup>, W.S. Graves <sup>a</sup>, I. Lehrman <sup>b</sup>

<sup>a</sup> National Synchrotron Light Source, Brookhaven National Laboratory, Upton, NY 11973, USA

<sup>b</sup> Grumman Aerospace Corporation, 4 Independence Way, Princeton NJ, USA

## Abstract

A three stage superconducting undulator (modulator, dispersive section, and radiator) is under construction at Brookhaven National Laboratory. Sections of the radiator, consisting of 25 cm long steel yokes, each with 18 mm period, 0.54 T field, and 8.6 mm gap are under test. The magnetic measurements and operational characteristics of the magnet are discussed. Measurement results and analyses are presented, with emphasis on the integrated field quality. The magnet winding and the effects of the various trims are discussed.

## 1. Introduction

A three stage superconducting undulator for use in a high gain, harmonic generation experiment is under construction at the National Synchrotron Light Source at Brookhaven National Laboratory [1–4]. The device triples the frequency of a 10.4  $\mu\text{m}$  CO<sub>2</sub> seed laser using a 30 MeV electron beam. The first stage of the undulator, the modulator section (12 periods, 26 mm, 0.81 T), modulates the energy of the electron beam. The second stage, the dispersive section (12 cm, 0.3–1.2 T), spatially bunches the energy modulated beam. The final stage, the radiator section (84 periods, 18 mm, 0.54 T, tapering possible), extracts energy from the coherently bunched beam at the third harmonic of the modulator.

The magnet yokes for all three stages of the undulator are machined out of ground low carbon steel blocks, and are fabricated by Grumman Corporation. The radiator stage is made up of six contiguous 25 cm long sections, each section consisting of an upper and lower magnet yoke. A series of slots is precision machined ( $\pm 10 \mu\text{m}$ ) into the yokes, and the superconducting wires (SSC wire – Cu/SC = 2.4:1, 0.465 mm OD with Kapton wrapping) are wound within these slots. Machining errors result in 0.1% peak field errors in the unsaturated regime ( $\delta B/B \approx \delta g/g$ ), without trimming or shimming [3]. The process of clamping and aligning the individual magnet yokes into sections

and groups of sections must preserve these tight tolerances, requiring careful assembly and mechanical measurement. The main magnet winding is continuous, with each slot being wound in the reverse direction from its neighboring slots.

Among the attributes of this superconducting undulator technology [5] are high fields at small periods and gaps, an easily varied field and field taper, and magnet entrance and exit conditions modifiable through changes in the wire winding or the end trim currents. The magnets reported on in this paper have all been wound with a binomial current pattern [6] which results in a net displacement but no steering, in the absence of any saturation effects. Work has also addressed higher order windings with reduced saturation effects and lower steering end correction requirements [7].

## 2. Magnet winding

The winding scheme of the radiator magnet has been chosen to permit maximum flexibility in powering of the yoke windings without unnecessary complexity. The yokes are wound identically so that sorting of the magnet yokes is possible. Each radiator yoke has 28 slots, and five independent coils wound on it – the main winding and two entrance and two exit windings. The main winding is a single continuous winding, and is wound as a binomial pattern with 2 wire layers in slot 1 and 28, 6 layers in 2 and 27, and 8 layers in slots 3 through 26. The entrance and exit trims each consist of a single slot trim (4 layers in slot 1, and 4 layers in slot 28) and a double slot trim (2 layers in slot 2 and 3, and 2 layers in slot 27 and 28).

☆ This work has been performed under the auspices of the U.S. Department of Energy

\* Corresponding author. Tel. +1 516 282 5491, e-mail solomon@bnlls1.nsls.bnl.gov.

Thus, all slots have 8 layers of windings. The six radiator sections are assembled contiguously to form the full length radiator. All the windings are connected in series except for the entrance windings on section 1, and the exit windings on section 6. However, the connection points between the various windings are connected to power leads, so that differential powering of the various trims is possible. In this way, the entrance and exit trims on the interior magnet sections of the radiator can function as both joint trims and taper windings. With this scheme, the taper transitions are also binomial. Characterization of the entrance and exit trim windings, the windings in the vicinity of the magnet joints, and the taper transitions is in progress. As the saturation level of the magnet increases, the nominally steering free current distribution pattern at the magnet entrance and exit deviates from the ideal, and the beam is steered off axis. The entrance and exit trim windings are able to correct this steering effect, but higher order windings which reduce the saturation dependence and the required end trim currents are being tested [7].

### 3. Testing and results

The radiator magnets are tested in 50 cm long units, i.e. 2 sections long (4 magnet yokes). A slider supporting a Hall probe array is guided by the gap spacer around which the magnet yokes are clamped. A Helmholtz coil in the test setup permits in situ calibration of the Hall probes at liquid helium temperatures. Details and errors associated with the measurement system are described elsewhere [3]. The nominal operational current for the radiator magnet is 90 A, where the magnet is in a saturated state [5]. The quench current for these magnets, which do not exhibit any training behavior, is  $\approx 180$  A.

As with any iron magnet system, there is concern about hysteresis affecting the reproducibility of a state of the magnet. With the radiator yokes, reliable setpoints are obtained if the magnet is cycled to  $\pm 175$  A, with subsequent setting of the operating current on the approach towards zero current. In order to assess both the reliability

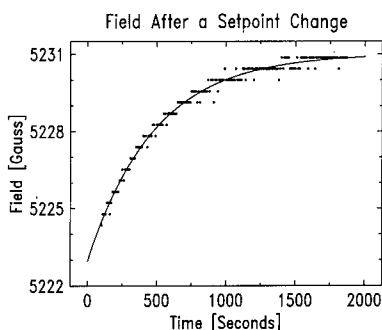


Fig. 1. The time behavior of the magnetic field measured after a change in the current setpoint.

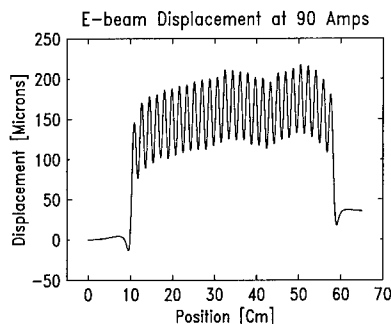


Fig. 2. The electron trajectory through two radiator sections at the nominal operating current of 90 A.

of the setting of a given magnet state and the repeatability of the measurement system, a data set consisting of several field scans at a setpoint of 90 A was taken. The magnet was then cycled several times to  $\pm 175$  A, the magnet current was reset to 90 A, and another data set of several field scans were taken. There were essentially no differences between the intra-set data and the inter-set data in terms of field integral and RMS integral variations (10 G-cm). However, after a current setpoint is reached, the magnetic field approaches equilibrium fairly slowly, as seen in Fig. 1. Though the magnitude of the variation is relatively small, a fit of the data to the form  $1 - \exp(-t/\tau)$  yields  $\tau = 8$  min, shown as the solid line in Fig. 1. To accommodate this time behavior the magnet is stabilized before data acquisition.

Measurements have been taken both with and without field clamps at either end of the test sections, with a dipole loop wrapped around the yokes, and with the end trims powered to straighten the electron beam trajectory. Shown in Fig. 2 is a plot of the electron beam trajectory calculated from twice integrated field data taken at 90 A, with the entrance and exit trims powered symmetrically, and a dipole loop powered to provide  $\approx 12$  G of field. In this data all the interior poles have the same current excitation; none of the coils in the joint area have been powered differentially. Excluding the first and last pole, the total transverse displacement of the electron beam centroid is about  $\pm 25 \mu\text{m}$  peak-to-peak, which is well within the required limit of an RMS variation of  $\pm 20 \mu\text{m}$  (1/10th of the beam radius). Consistent with earlier data, the peak field variation is 0.27% RMS.

Given this high quality trajectory through two sections of the radiator, it is clear that the internal magnet errors are low enough that correctors within the body of the magnet are not required. However, the entrance/exit region, and the joint region requires further investigation. If the end trims can systematically straighten the entrance/exit trajectory, the entire six radiator sections can be assembled with confidence in the resulting trajectory quality. To this end, a parametric study of the effects of the various trims (the double slot trim, the single slot trim, and the joint trim) was carried out. The results of varying the double

slot trim (main winding at 90 A, with field clamps) are shown in Fig. 3. The upper two plots are scans at two different excitations of the double slot trim (21 and 28 A). In order to test how closely the double slot trim approximates a point kick at the entrance of the magnet, a simulated kick was introduced into the data (i.e. a slope is superimposed onto the second integral results). The lowest plot in Fig. 3 shows the result of this manipulation, displaced vertically for clarity. It is clear that the end trim functions as a variable entrance/exit kick, with the deviation from this approximation being localized to the region near the ends of the magnet. In this sense, the trim acts locally to kick the electron beam. The same result is seen in studies of the single slot entrance/exit trim.

The physical joint between two radiator sections is an area of concern due to the possible errors and misalignments which might occur. As mentioned previously, the windings in the region of a physical joint can be powered as joint correction trims. That is, in addition to the main current in the winding, a small current can be superimposed onto the joint area windings to augment or oppose the main current. On one test assembly there was an inadvertent joint field error of  $\approx 2\%$  which resulted in a trajectory error shown Fig. 4, upper trajectory. Though the source of this particular error has not yet been identified, attempts to correct the error through powering the joint windings were highly successful. Shown as the middle and lower trajectories (displaced vertically for clarity) are the results of two attempts to modify the joint region through the joint winding trims. Clearly, the middle plot compensates the joint error quite well, while the lower scan overcompensates. Though precautions will be taken to insure that joint errors are minimized, the existing windings on the yokes can correct the resultant error integrals if they do occur.

Further work includes measurements of the radiator sections with a single period transverse and vertical field coil, additional measurements on the field profile due to the parabolic pole faces, and characterization of the modu-

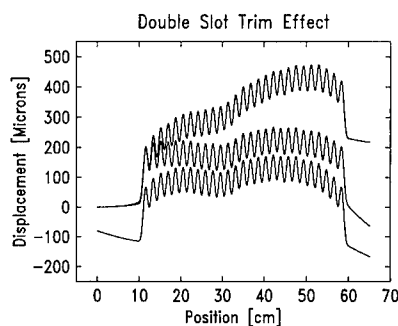


Fig. 3. The effect of the double slot trim on the electron trajectory. (Top): double slot trim at 21 A; middle: double slot trim at 28 amps; bottom: 21 A data with a simulated point kick, displaced vertically for clarity.

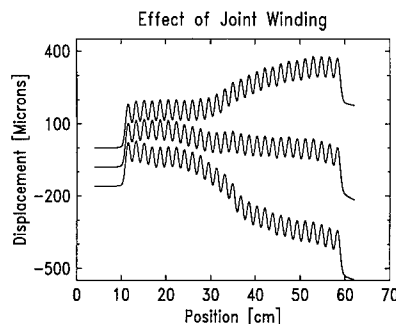


Fig. 4. The electron trajectory through two radiator sections at three different current settings of the joint trims, displaced vertically for clarity.

lator and dispersive stages. The cryostat and full length undulator clamping and alignment assembly is being fabricated by Grumman Co. When all the undulator stages are installed in the cryostat the total assembly will be measured. A measuring fixture which uses both optical and magnetic field measurements to determine the field profile of the device will move inside the 8 mm diameter vacuum chamber. With these measurements, current settings of the various magnet windings will be determined for the operating points of the undulator.

### Acknowledgements

The authors would like to acknowledge discussions with, and contributions of I. Ben-Zvi, K. Halbach, S. Krinsky, G. Rakowsky, and L.H. Yu through the course of the work presented here.

### References

- [1] L.H. Yu, Phys. Rev. A 99 (1991) 5178.
- [2] I. Ben-Zvi et al., Nucl. Instr. and Meth. A 318 (1992) 208.
- [3] L. Solomon, G. Ingold, I. Ben-Zvi, S. Krinsky, L.H. Yu, W. Sampson and K. Robins, Proc. 1993 Particle Accelerator Conf., Washington, DC, IEEE Catalog Number 93CH3279-7, p. 1602.
- [4] G. Ingold, L. Solomon, I. Ben-Zvi, S. Krinsky, D. Li, D. Lynch, J. Sheehan, M. Woodle, X.Z. Qiu, L.H. Yu, X. Zhang, W. Sampson, M. Garber, K. Robins, I. Lehrman, R. Heuer, J. Sheehan and D. Weissenburger, *ibid.*, p. 1439.
- [5] G. Ingold, L. Solomon, I. Ben-Zvi, S. Krinsky, D. Li, D. Lynch, J. Sheehan, M. Woodle, X.Z. Qiu, L.H. Yu, X. Zhang, W. Sampson, M. Garber, K. Robins, I. Lehrman, R. Heuer, J. Sheehan and D. Weissenburger, SPIE 1993 Symposium on Electron-Beam Sources of High-Brightness Radiation, San Diego, CA, SPIE Proc. Vol. 1013, p. 68.
- [6] K. Halbach, Nucl. Instr. and Meth. A 250 (1986) 95.
- [7] W.S. Graves, L. Solomon and I. Lehrman, these Proceedings (16th Int. Free Electron Laser Conf., Stanford, CA, USA, 1994) Nucl. Instr. and Meth. A 358 (1995) 414.

## End fields in the harmonic generation superconducting FEL at BNL-NSLS

W.S. Graves <sup>a,\*</sup>, L. Solomon <sup>a</sup>, I. Lehrman <sup>b</sup>

<sup>a</sup> National Synchrotron Light Source, Brookhaven National Laboratory, Upton, NY 11973, USA

<sup>b</sup> Grumman Aerospace Corp., 4 Independence Way, Princeton, NJ 08540, USA

### Abstract

A study is presented of the end fields in the harmonic generation FEL radiator. This wiggler magnet consists of 6 contiguous 25 cm long steel yokes wound with superconductor, each with 18 mm period, 0.54 T field and 8.6 mm gap. Measurement results and analyses are given for third and sixth order binomial entrance excitations. It is shown that, when the steel cores are driven into saturation, the binomial winding is no longer steering-free, and that higher order entrance windings produce less electron beam steering than do low order windings.

### 1. Introduction

The superconducting magnets for the Harmonic Generation FEL (HGFEL) [1] at BNL are now being built and tested. Previous work discussed the magnet design [2], test setup [3], and initial results. We report measurement results and analysis of the radiator magnet short-section tests with emphasis on the *B*-field properties near the magnet ends.

The entrance winding at the beginning of the magnet was originally chosen to be the lowest order which does not produce steering [4]. This is referred to as the third order binomial winding, and produces a scalar potential pattern at the poles of +1, -2, +2, -2, etc. As previous authors have noted [4,5], differences in saturation level of the steel at high excitation causes steering at the  $\frac{1}{2}$ -strength pole. Detailed study of the electron trajectories and field strengths indicates that the end errors cause nonlocal changes in the magnetic field, and that the trajectory is modified quite far from the ends. The difficulties encountered in properly trimming these poles have led us to consider using entrance windings with higher order binomial coefficients. In addition to the third order winding, sixth order was also measured and simulated. The scalar potential pattern at the magnet poles for this order is +1, -5, +11, -15, +16, -16, +16, etc. In the sections that follow, computer simulations that use both linear and nonlinear *B-H* curves are compared for different order windings, demonstrating the effect of saturation on the

electron beam trajectory. These simulations are then compared to measured data.

### 2. Computer simulation

Simulations of the end windings have been performed with both POISSON and TOSCA in 2D [5] and 3D

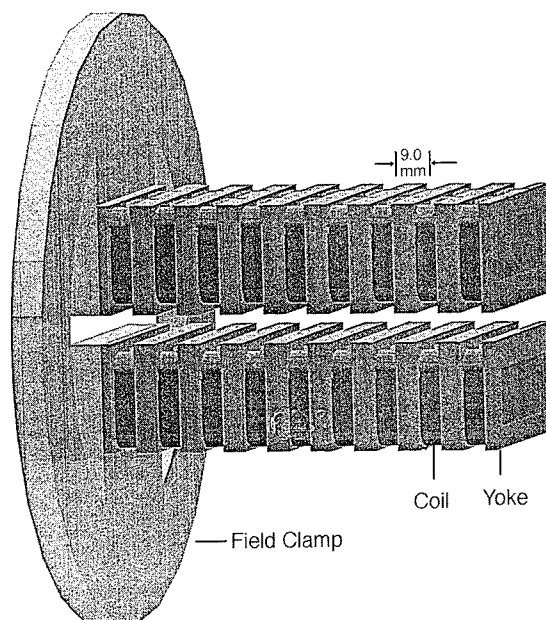


Fig. 1. Geometry of iron yokes and superconducting coils used in computer model.

\* Corresponding author. Tel. +1 516 282 2095, fax: +1 516 282 3238, e-mail: graves@bnl.gov.



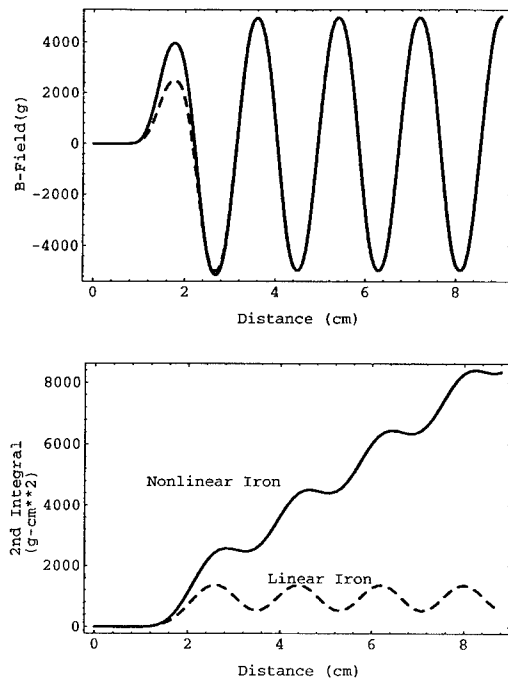


Fig. 2. Upper:  $B$ -field for third order winding. Dashed line shows ideal  $B$ -field (i.e. linear permeability). Lower: electron trajectory through  $B$ -fields above.

respectively. The two dimensional simulation is not accurate near the magnet ends because of the presence of field clamps and also because the finite depth of the third dimension affects the field calculations at the ends. This paper focusses on the 3D results. Fig. 1 shows the geometry used for the iron yokes and superconducting coils. It includes 10 poles and 9 coils, plus surrounding air. For clarity the complete top and bottom yokes are shown, however it was only necessary to model one octant of the yokes shown by using appropriate boundary conditions.

The model differed from the real magnet in several ways. The model used 1010 steel, a 6.0 mm vertical gap, and had no parabolic cut in its pole faces whereas the real

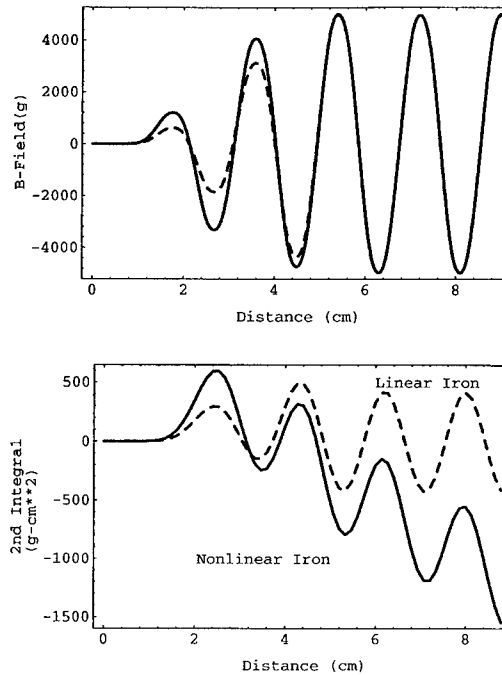


Fig. 4. Upper:  $B$ -field for sixth order winding. Dashed line shows ideal  $B$ -field. Lower: electron trajectory through  $B$ -fields above.

magnet uses 1006 low-carbon steel and, while it also has a 6.0 mm gap, a parabolic cut in the poles increases the gap to 8.6 mm on axis. In addition the operating current in the coils is slightly different for the two cases. In order to facilitate comparisons between the model and measured results, the fields in the simulation are scaled to the measurements by multiplying their magnitude by a constant factor.

Fig. 2 shows the  $B$ -field for the third order winding. The full-strength coil excitation is 6400 A-turns which is near the anticipated operating point. From Fig. 3 the steering due to this error is 1100 g cm. Clearly, the steering is due to the fact that there is only one pole at partial excitation.

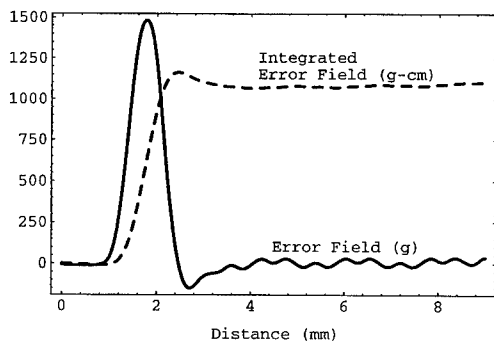


Fig. 3. Error field due to saturation of iron in third order entrance winding. Single partially excited pole causes large steering error.

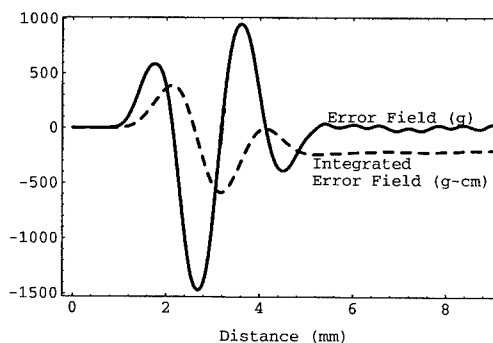


Fig. 5. Error fields due to saturation of iron in sixth order entrance winding. Errors in adjacent poles tend to cancel.

One solution to the steering problem is to use a more gradual entrance winding so that there are several partially excited poles. Fig. 4 shows the magnetic fields and trajectory for the case of sixth order entrance winding.  $B$ -field errors caused by the varying permeability of the steel then tend to cancel one another. From Fig. 5, the error fields are seen to cancel from one pole to the next such that their net integral is about a factor of 5 smaller than the steering in the third order case.

Following the simulation results, yokes have been wound with both third order and sixth order entrance coefficients. Measurement results for these two cases are given in the next section.

### 3. Measurements

The cryogenic test setup is described elsewhere [3,6]. Here we note that four yokes which make up 27 wiggler periods are cooled and tested at one time. The operating current is 90A (6120 A-turns). Fig. 6 shows the measured  $B$ -fields and second integral for the third order winding with no correction trims applied. The dashed line again shows the nonlinear simulation result.

The  $B$ -field and trajectory for the sixth order entrance winding is shown in Fig. 7.

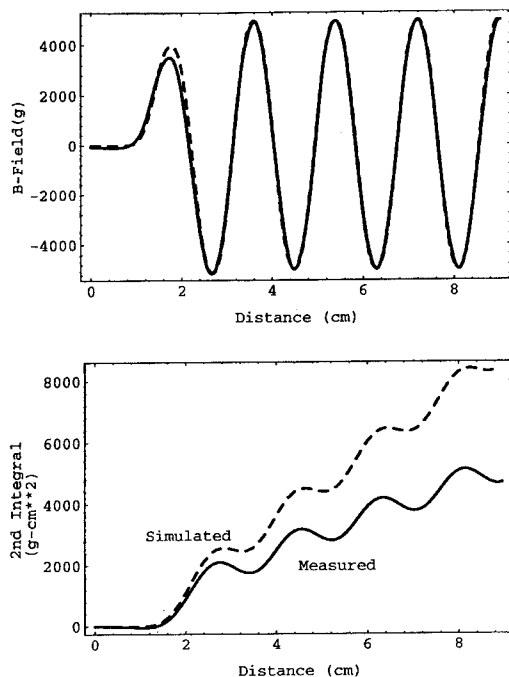


Fig. 6. Upper: measured  $B$ -field of third order entrance winding. Solid line is measured data, dashed line is from simulation. Lower: trajectories through  $B$ -fields above.

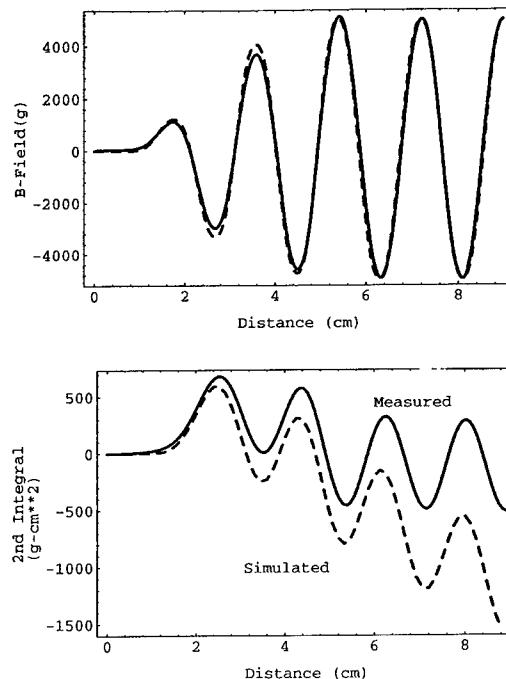


Fig. 7. Upper: measured  $B$ -field of sixth order entrance winding. Solid line is measured data, dashed line is from simulation. Lower: trajectories through  $B$ -fields above.

For both entrance windings, the measured results show less steering than the simulations predict. This may be due to the different permeability of the model (1010 steel) from the real magnet (1006 steel). However, the advantage of using higher order coefficients is clearly demonstrated. Steering is still reduced by a factor of 6 from 600 g cm to 100 g cm.

### 4. Conclusions

Experiment and simulation both show the advantages of using a higher order entrance winding when saturation effects are present in an iron wiggler. For the harmonic generation radiator magnet, steering of the electron beam is reduced by a factor of 6 when changing from the third to the sixth order entrance winding.

### Acknowledgements

We would like to thank George Rakowsky, Li-Hua Yu, Ilan Ben-Zvi, Sam Krinsky, and Klaus Halbach for useful discussions and advice on the measurements and analysis.

## References

- [1] I. Ben-Zvi et al., Nucl. Instr. and Meth. A 318 (1992) 208.
- [2] G. Ingold et al., SPIE Symp. on Electron-Beam Sour of High-Brightness Radiation, SPIE Proc. 2013, p. 68.
- [3] L. Solomon et al., IEEE Particle Accelerator Conf. 1993, Washington DC IEEE CAT#93CH3279-7, p. 1602.
- [4] K. Halbach, Nucl. Instr. and Meth. A 250 (1986) 115.
- [5] X. Zhang et al., Nucl. Instr. and Meth. (1993) 689.
- [6] L. Solomon et al., these Proceedings (16th Int. Free Electron Laser Conf., Stanford, CA, 1994) Nucl. Instr. and Meth. 358 (1995) 411.



ELSEVIER

# Betatron oscillations, undulator acceptance and beam conditioning ( $\beta_{\parallel}(r) = \text{const.}$ ) taking space charge effects into account

V.A. Papadichev \*

*Lebedev Physical Institute, 53 Leninsky Prospekt, 117924 Moscow, Russian Federation*

## Abstract

The use of high-current beams of low and medium energy electrons in infrared and optical FELs makes it necessary to take into account minute effects to balance transverse velocities due to undulator field transverse inhomogeneities and betatron oscillations, and/or longitudinal velocity spread due to a potential drop inside the electron beam. One must calculate the reduction of betatron focusing in the undulator as a function of beam current (i.e. lengthening of the period of betatron oscillations). This effect leads also to diminishing geometric or radiation acceptance of the undulator. The simple analytical treatment given in the paper allows one to calculate electron current limits of beam transport in undulator fields for some beam geometries (ribbon-like beams in a plane undulator and round cylindrical beams in a helical one) and the dependence of the betatron oscillation period in an undulator on beam current. Beam conditioning to obtain  $\beta_{\parallel} = \text{const.}$ , taking into account modified betatron oscillations and the potential drop in the beam due to space charge, is discussed.

## 1. Equations of motion

The equations of motion of electrons in undulators describing orbital and betatron motion (when  $B_{\parallel} = 0$ ) or orbital, cyclotron and drift gyrations (when  $B_{\parallel} \neq 0$ ) and taking into account electric and magnetic fields of the beam can be written in general form as [1,2]:

$$x'' + k_c y' + (k_{\beta x}^2 - k_{s x}^2)x = (eB_y)/(m_0 c^2 \gamma \beta_{\parallel}), \quad (1a)$$

$$y'' - k_c x' + (k_{\beta y}^2 - k_{s y}^2)y = -(eB_x)/(m_0 c^2 \gamma \beta_{\parallel}). \quad (1b)$$

Here  $k_c = \omega/v_{\parallel} = (eB_{\parallel})/(m_0 c^2 \gamma \beta_{\parallel})$  is the cyclotron-motion wave number,  $k_{\beta x}$  and  $k_{\beta y}$  are the wavenumbers of betatron  $x$ - and  $y$ -oscillations, for low current density beams in the absence of an axial magnetic field ( $E_b \approx H_b \approx 0$ ).  $k_{s x}$  and  $k_{s y}$  are the wavenumbers corresponding to space-charge forces of the beam in the  $x$ - and  $y$ -directions. Using appropriate formulae for a chosen type of undulator for  $k_{\beta x}$  and  $k_{\beta y}$ , it is possible to calculate  $k_{s x}$  and  $k_{s y}$  for some simple models of the beam and solve Eqs. (1a) and (1b). Here we employ a model of a solid homogeneous beam of round cross-section for a helical undulator and one of a ribbon-like beam of rectangular cross-section for a plane undulator.

### 1.1. Helical undulator

The equation of the transverse electron motion for the simple model of a round cylindrical beam in a helical undulator and axial magnetic field  $B_{\parallel} \neq 0$ , using the method of [2], can be written as:

$$\begin{aligned} d^2\eta/dz^2 - ik_c d\eta/dz + k_{bs}^2 \eta \\ = -i(e/(m_0 c^2 \gamma \beta_{\parallel}))(B_x + iB_y), \end{aligned} \quad (2)$$

where  $\eta = x + iy$ ,  $i = (-1)^{1/2}$ ,  $v_z = v_{\parallel} = \text{const.}$ ,  $k_c = \omega/v_{\parallel}$  is the cyclotron-motion wave number,  $\omega = (eB_{\parallel})/(m_0 c \gamma)$  is the cyclotron frequency in the longitudinal magnetic field  $B_{\parallel}$ .  $B_x$  and  $B_y$  are undulator field components.  $k_{bs} = (k_{\beta}^2 - k_s^2)^{1/2}$  is the betatron wave number accounting for space-charge forces  $e(E_r - \beta_{\parallel} H_{\theta})$  when  $B_{\parallel} = 0$ .  $k_{\beta} = k_0 \beta_{\perp 0}/(2^{1/2} \beta_{\parallel})$  is the betatron wave number without space-charge influence when  $B_{\parallel} = 0$ .  $k_s = (2I_b/I_0)^{1/2}/(\gamma^{1/2} \beta_{\parallel} \gamma_{\parallel} r_0)$  is the space-charge wave number accounting for electrical and magnetic fields ( $E_r - \beta_{\parallel} H_{\theta}$ ) of the homogeneous cylindrical beam.  $I_b$  is the beam current,  $I_0 = m_0 c^3/e \approx 17$  kA,  $r_0$  is the beam outer radius, and  $\gamma_{\parallel} = (1 - \beta_{\parallel}^2)^{-1/2}$ . The general solution is

$$\eta = A e^{ik_1 z} + B e^{ik_2 z} + C e^{ik_0 z}, \quad (3)$$

where

$$k_{1,2} = k_c/2 \pm ((k_c/2)^2 + k_{bs}^2)^{1/2} \quad (4)$$

are wave numbers of modified cyclotron gyration and

\* Tel. +7 095 132 6300, fax +7 095 938 2251, e-mail vityal@ipnu.flan.msk.su.

azimuthal drift caused by the undulator focusing and beam space-charge forces. Since usually  $k_{bs} \ll k_c$ , one has

$$k_1 \approx k_c \quad \text{and} \quad k_2 \approx -k_{bs}^2/k_c. \quad (5)$$

$A$  and  $B$  depend on initial coordinates and velocities  $R_0 = X_0 + iY_0$  and  $V_0 = V_{0x} + iV_{0y}$ :

$$\begin{aligned} A &= -C(k_0 - k_2)/(k_1 - k_2) - k_2 R_0/(k_1 - k_2) \\ &\quad - iV_0/((k_1 - k_2)v_{||}); \\ B &= C(k_0 - k_1)/(k_1 - k_2) + k_1 R_0/(k_1 - k_2) \\ &\quad + iV_0/((k_1 - k_2)v_{||}). \end{aligned} \quad (6)$$

### 1.2. Plane undulator

Eqs. (1a) and (1b) describe the case of two plane undulators with orthogonal fields, if  $k_{\beta x} \neq 0$  and  $k_{\beta y} \neq 0$ . One should put  $B_x = k_{\beta x} = k_{sx} = 0$  to treat particle motion in a plane undulator with a ribbon beam and axial magnetic field, which results in the following equations:

$$x'' + k_c y' = (eB_y)/(m_0 c^2 \gamma \beta_{||}), \quad (7a)$$

$$y'' - k_c x' + (k_{\beta y}^2 - k_{sy}^2)y = 0. \quad (7b)$$

## 2. Space charge influence in a helical undulator

### 2.1. $B_{||} = 0$

When there is no axial magnetic field,  $B_{||} = k_c = 0$  and Eq. (2) has a simpler solution because  $k_1 = k_2 = \pm k_{bs}$ :

$$\begin{aligned} \eta &= A e^{ik_{bs}z} + B e^{ik_{bs}z} + C e^{ik_0z} \\ &= (A + B) \cos(k_{bs}z) + i(A - B) \sin(k_{bs}z) + C e^{ik_0z}. \end{aligned} \quad (8)$$

Electrons perform independent betatron oscillations along two transverse coordinates  $x$  and  $y$  with a wavenumber  $k_{bs}$ :

$$k_{bs} = (k_{\beta}^2 - k_s^2)^{1/2}, \quad (9)$$

where  $k_{\beta} = k_0 \beta_{\perp 0}/(2^{1/2} \beta_{||})$  and  $k_s = (2I_b/I_0)^{1/2}(\gamma^{1/2} \beta_{||} \gamma_{||} r_0)$ . The maximum transported beam beam current  $I_{max1}$  is determined by  $k_{bs} = 0$ :

$$I_{max1} = I_0 \beta_{\perp 0}^2 \gamma \gamma_{||}^2 k_0^2 r_0^2 / 4. \quad (10)$$

The betatron wavenumber depends on beam current as

$$k_{bs} = k_{\beta}(1 - I_b/I_{max1})^{1/2} \quad (11)$$

as shown in Fig. 1 (curve 1). There is no focusing at  $I_b = I_{max1}$  and the motion is unstable at  $I_b > I_{max1}$ .

$k_b$  when  $I_b = B_{||} = 0$ ; beam current  $I_b$  in units of  $I_{max1}$

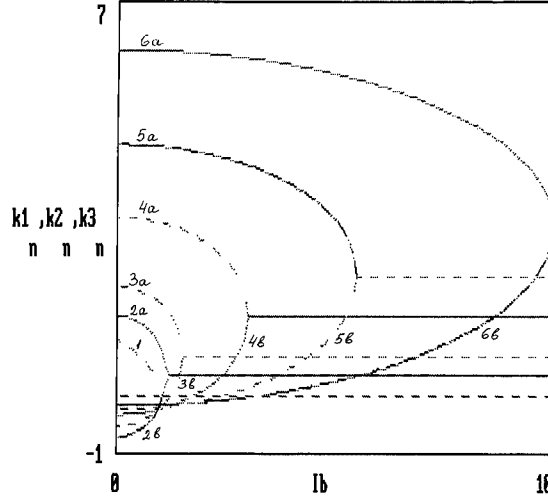


Fig. 1. Betatron oscillation  $k_{bs}$  (curve 1), cyclotron  $k_1$  (curves 2a–6a) and drift  $k_2$  gyration (curves 2b–6b) wavenumbers as functions of beam current  $I_b$  (in units of  $I_{max1}$ ).

### 2.2. $B_{||} \neq 0$

The electron motion becomes more complicated when an axial magnetic field is applied to transport the beam. Wavenumbers of cyclotron ( $k_1$ ) and drift ( $k_2$ ) gyrations in this case are:

$$\begin{aligned} k_{1,2} &= k_c/2 \pm ((k_c/2)^2 + k_{bs}^2)^{1/2} \\ &= (k_c/2) \left\{ 1 \pm \left[ 1 + 4(k_{\beta}^2 - k_s^2)/k_c^2 \right]^{1/2} \right\} \\ &= k_c/2 \left[ 1 \pm (1 + 4k_{\beta}^2/k_c^2)^{1/2} (1 - I_b^2/I_{max2}^2)^{1/2} \right], \end{aligned} \quad (12)$$

with  $k_c/k_{\beta} = 2^{1/2} B_{||}/B_{\perp 0}$ .

The maximum transported beam current is limited by instabilities ( $k_{1,2}$  become imaginary) and depends on the applied axial magnetic field.

$$\begin{aligned} I_{max2} &= I_0 \beta_{\perp 0}^2 \gamma \gamma_{||}^2 (k_c^2/4 + k_{\beta}^2) r_0^2 \\ &= I_{max1} \left[ k_c^2/(4k_{\beta}^2) \right] \gg I_{max1}, \end{aligned}$$

$$I_{max2}/I_{max1} = 1 + (1/2)(B_{||}/B_{\perp 0})^2. \quad (13)$$

The dependence of cyclotron and drift gyration wavenumbers on beam current is shown in Fig. 1 (curves 2–6). The limiting current  $I_{max2}$  can be considerably larger than  $I_{max1}$  if  $B_{||} > B_{\perp 0}$ .

### 3. Space charge influence in a plane undulator

#### 3.1. $B_{\parallel} = 0$

Equations of motion (7a) and (7b) can be further simplified if no axial magnetic field is applied ( $k_c = 0$  and  $k_{\beta y} = k_{\beta}$ ):

$$x'' = (eB_y) / (m_0 c^2 \gamma \beta_{\parallel}), \quad (14a)$$

$$y'' + (k_{\beta y}^2 - k_{\beta s}^2) y = 0. \quad (14b)$$

The first equation (14a) describes plane orbital undulations (in the  $x$ - $z$  plane), the second describes betatron oscillations (in the  $y$ - $z$  plane).

If a ribbon shaped electron beam of height  $2h$  and width  $2d$  is transported in a plane undulator (which is more appropriate for the plane geometry of the beam):

$$k_s = (\pi I_b / I_0)^{1/2} / (\gamma h d)^{1/2} \beta_{\parallel} \gamma_{\parallel} \quad (15)$$

and the betatron oscillation wavenumber  $k_{bs}$  dependence on beam current is similar to Eq. (11), but with another value of the limiting current:

$$I_{\max 3} = I_0 \beta_{\perp 0}^2 \gamma \gamma_{\parallel}^2 k_0^2 h d / (2\pi), \quad (16)$$

$$k_{bs} = k_{\beta} (1 - I_b / I_{\max 3})^{1/2}, \quad (17)$$

so one can use curve 1 of Fig. 1 to determine  $k_{bs}(I_b)$ .

#### 3.2. $B_{\parallel} \neq 0$

If  $B_{\parallel} \neq 0$ , system (7a and 7b) can be solved by finding the orbit:

$$\begin{aligned} x &= -(\beta_{\perp 0} / \beta_{\parallel}) (k_0^2 - k_{bs}^2) \sin(k_0 z) \\ &\quad / [k_0 (k_0^2 - k_c^2 - k_{bsy}^2)], \\ y &= -(\beta_{\perp 0} / \beta_{\parallel}) k_c \cos(k_0 z) \\ &\quad / (k_0^2 - k_c^2 - k_{bsy}^2), \end{aligned} \quad (18)$$

and then integrating the system of two homogeneous equations without the right-hand member. This results in

$$\begin{aligned} k_{1,2} &= \pm (k_c^2 + k_{bsy}^2)^{1/2} \\ &= \pm (k_c^2 + k_{\beta y}^2)^{1/2} (1 - I_b / I_{\max 4})^{1/2}, \end{aligned} \quad (19)$$

$$\begin{aligned} I_{\max 4} &= I_0 \gamma \gamma_{\parallel}^2 \beta_{\parallel}^2 (k_c^2 + k_{\beta y}^2) h d / \pi \\ &= I_{\max 3} (1 + 2B_{\parallel}^2 / B_{\perp 0}^2). \end{aligned} \quad (20)$$

Again, one can use the curve 1 in Fig. 1. The electron movement is a combination of plane undulations  $x = A \sin(k_0 z) + B \cos(k_1 z) + C \sin(k_1 z)$ ,  $y = D \cos(k_1 z) + E \sin(k_1 z)$  and gyration  $x + iy = F e^{ik_0 z}$ .

### 4. Undulator acceptance and beam conditioning

The ideal undulator acceptance is given by  $\alpha = a^2 k_{bs}$  for a beam with a transverse dimension  $a$  (radius or height), so  $\alpha$  scales with beam current in the same way as  $k_{bs}$  (or  $k_1$ ) as it is shown in Fig. 1. Field errors can result in betatron orbit distortion and increased betatron oscillation after axial beam injection [3], thus diminishing the useful aperture of the undulator. In any case, there are limitations on the useful aperture of a transport channel, and  $a = \min\{a_1, a_2, a_3, \dots\}$ . It can be the inner radius of the vacuum chamber or transport channel, maximum permissible particle displacement from the axis or maximum tolerable amplitude of betatron oscillations leading to a large  $\beta_{\parallel}$  shift and knocking electrons out of phase with amplified electromagnetic wave.

To avoid the last effect, a method of beam conditioning was proposed by Sessler and coworkers [4]. By accelerating the off-axis particles so that they acquire additional axial velocity one can then have all beam electrons moving through the undulator with the same longitudinal velocity. A special 10–50 m long focusing lattice consisting of 10–50 periods and having accelerating cavities operating in the  $TM_{210}$  mode are to be employed. This system is most suitable for large FEL facilities to obtain unique ultrashort-wavelength radiation.

On the other hand, many FEL experiments are conducted with high-current electron beams at low and medium electron energies (0.5–15 MeV). Such beams are usually transported in a longitudinal magnetic field to prevent beam blow-up due to space-charge forces. Undulator field inhomogeneity prevents using large-diameter beams and fully exploiting the high-power possibilities of pulsed accelerators. Last years' wide-spread tendency of using microundulators makes the problem more acute since the useful aperture of the undulator becomes too small without beam conditioning. A simple alternative method of beam conditioning in an axial magnetic field can be applied. In this case, the electrons do not experience betatron oscillations and are subjected only to a slight azimuthal drift and undulator orbital motion modified by the longitudinal magnetic field. Cyclotron gyration as a free motion is also possible in addition to those induced orbital and free drift motions. So it is possible to equalize  $\beta_{\parallel}$  across the beam, i.e., to compensate mainly for the increase of the transverse orbital velocity with the radius, by imparting supplementary cyclotron velocities to inner electrons with an appropriate radial profile [1].

Space-charge forces change betatron oscillation wavenumbers (when  $B_{\parallel} = 0$ ), lowering the maximum betatron velocity an electron has on axis. The orbital velocity increase with transverse coordinate is independent of beam current, and the electron total transverse velocity is not constant now as it was in helical or plane undulators with negligible beam current. So the space-charge forces need to be taken into account for high-current, low electron

energy beams (by adding some extra focusing, for example).

It is also necessary to use some correction in the cyclotron velocity profile  $\beta_c(r)$  when  $B_{\parallel} \neq 0$  because of a potential drop in the beam [1].

## 5. Conclusion

It was shown that transverse electron motion parameters (amplitude and periods) depend on beam current, and the motion can become unstable for currents larger than limiting ones (different for various undulator types and axial magnetic field value). The obtained formulae and graphs allow one to calculate needed parameters and to put corrections in beam conditioning to compensate for space-charge effects.

## Acknowledgements

It is a pleasure for the author to express his gratitude to the Physics Department, University of California, Irvine for an opportunity to finish this report during his stay there July–August 1994.

## References

- [1] V.A. Papadichev, these Proceedings (16th Int. Free Electron Laser Conf., Stanford, CA, USA, 1994) Nucl. Instr. and Meth. A 358 (1995) ABS 79.
- [2] V.A. Papadichev, Proc. 12th Int. FEL Conf., Paris, France, 1990, Nucl. Instr. and Meth. A 304 (1991) 749.
- [3] V.A. Papadichev, Ref. [1], p. 429.
- [4] A.M. Sessler, D.H. Whittum and L.-H. Yu, Phys. Rev. Lett. 68 (1992) 309.



ELSEVIER

## Electron trajectories in a helical wiggler with a uniform axial guide field: a comparison of numerical results with results obtained using an approximate but analytical method

J.T. Donohue <sup>a,\*</sup>, Ph. Gouard <sup>b</sup>, J.L. Rullier <sup>c</sup>

<sup>a</sup> *Laboratoire de Physique Théorique, Université de Bordeaux I, 33175 Gradignan, France*

<sup>b</sup> *CEA, Centre d'Etudes de Limeil-Valenton, 94195 Villeneuve-Saint-Georges Cedex, France*

<sup>c</sup> *CEA, Centre d'Etudes Scientifiques et Techniques d'Aquitaine, P.O. Box 2, 33114 Le Barp, France*

### Abstract

A comparison is made between two methods of calculating electron trajectories in a magnetic field consisting of a helical wiggler and a uniform axial guide field. The code SOLITUDE, developed by Gouard, was used to calculate with high precision the trajectories of electrons whose initial positions and velocities were chosen at random from a Gaussian distribution. After propagation through an adiabatic entry, the positions and velocities at the point where the wiggler field becomes steady were used as input to an analytical calculation developed by Donohue and Rullier. Although the calculation is analytic, the method involves truncating the true Hamiltonian, and is therefore not exact. Despite this, generally good agreement is found between the trajectories generated by the two methods, in both the normal and reversed-field configurations. The analytical approach provides physical insight into certain unusual aspects of some of the numerically generated trajectories. Several illustrative examples are compared in detail.

The calculation of the trajectories of electrons in a Free Electron Laser (FEL) with a helical wiggler field and a uniform axial guide field has been the subject of much research, in particular when the spatial dependence of the wiggler field is included. It was established in early work that a particular case of steady motion existed, in which the electrons follow an axially centered helical path with a constant axial velocity in such a way that the transverse velocity vector of the electron is parallel or antiparallel to the transverse magnetic field at each point. Of course, no electron is likely to follow this ideal trajectory, and the question of what the non-ideal trajectories look like arises. Freund and Ganguly [1] have studied the linearized equations of motion about the ideal trajectory, and have obtained two squared frequencies which characterize the oscillations of the electrons about it. Donohue and Rullier [2] (DR) have extended this work by showing that the key quantity (called  $P_z$ ) is a combination of linear and orbital momentum which is conserved along any trajectory as a consequence of the screw-displacement symmetry of the magnetic field. For a given electron, one determines the value of  $P_z$  from the initial conditions, and provided

certain conditions are met, a fixed point of the Hamiltonian exists. The Hamiltonian is then expanded about the fixed point, and the quadratic terms may be reduced by canonical transformation to two uncoupled harmonic oscillators. The squared frequencies are exactly those of Freund and Ganguly, but in addition DR established that in Group I and the reversed field configuration, the frequency of the lesser absolute value is negative. From the initial position and velocity one may obtain the initial moduli and phases of the two oscillators, and the time evolution is then straightforward. The relations among the oscillator variables and the usual position and velocity variables is sufficiently complicated that occasionally rather bizarre trajectories are predicted by the model. The advantage of this approach is that, since the underlying dynamics is simple, one can understand what is going on even for unusual trajectories.

In order to simulate the performance of FELs, a number of workers have written various codes which evaluate numerically the interaction of the electron with the static magnetic field, the electromagnetic field, and the electrostatic fields of the other electrons. One of these codes, SOLITUDE, written by Ph. Gouard, has been extensively used in such simulations. We provide here only a short outline of it, since a detailed description is available [3]. The code embodies a non-linear formulation of the interac-

\* Corresponding author.



tion in FELs with either helical or planar wigglers, and with an electromagnetic field of a single frequency in the wave guide. The wiggler field is assumed to increase linearly in the axial direction in the adiabatic entry, until its nominal value is attained. The trajectories of the electrons are computed using the Lorentz force, while Maxwell's equations are solved in the approximation of a slowly varying amplitude and phase (SVAP). Space charge effects, either longitudinal or transverse, but not both

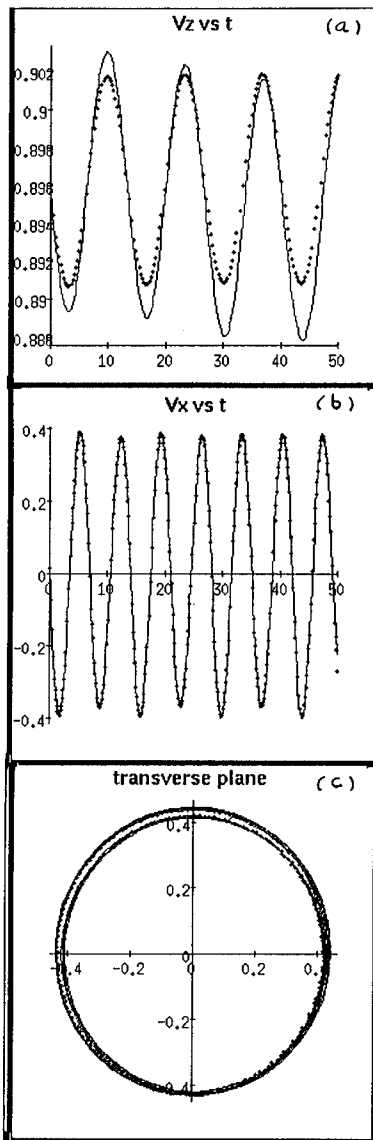


Fig. 1. Electron trajectories as calculated using SOLITUDE (solid curves) and with the analytical model (dashed curves). Beam energy = 1.75 MeV,  $\lambda_w = 8$  cm,  $B_0 = 0.8$  T, and  $B_w = 0.095$  T. (a) The axial velocity  $v_z$  as a function of time. (b) The transverse velocity  $v_x$  as a function of time. (c) The trajectory projected on the transverse plane.

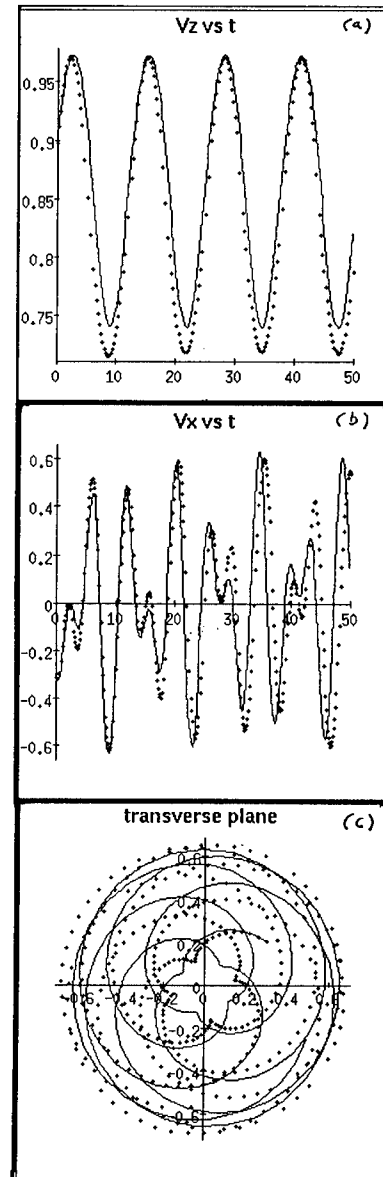


Fig. 2. Same conditions as in Fig. 1, but with an electron whose initial conditions are far from the ideal trajectory. (a) The axial velocity  $v_z$  as a function of time. (b) The transverse velocity  $v_x$  as a function of time. (c) The trajectory projected on the transverse plane.

simultaneously, may be included. The system of coupled non-linear differential equations is solved using the variable step Merson method (fifth-order Runge–Kutta method).

A comparison between the trajectories calculated using SOLITUDE, with electromagnetic and space-charge fields turned off, and those computed using the analytic but approximate approach of DR has been made as follows. For a set of FEL parameters, including guide and wiggler

fields, a number of electron trajectories were generated by SOLITUDE. The initial conditions were chosen at random, but they correspond to a peaked distribution about the nominal beam energy while the spatial distribution is that of a typical transverse beam size. The electrons are propagated through the adiabatic entry until the steady wiggler field is reached. At this point the initial conditions for the DR approach are provided to a simple program written in the MAPLE V [4] language which carries out the steps indicated in Ref. [2]. The trajectories, calculated either by continuing with SOLITUDE or by the DR method, may then be compared visually. In general, rather good agreement is obtained between the two methods, lending credence to the analytic approach. In the figures, we show details of three different trajectories. The solid lines depict simulations made with SOLITUDE, while the predictions of DR are shown as dashed curves. The velocities are relative to  $c$ , the speed of light. Time is in units of  $\lambda_w/(2\pi c)$ , and spatial variables in units of  $\lambda_w/2\pi$ , where  $\lambda_w$  is the wiggler period.

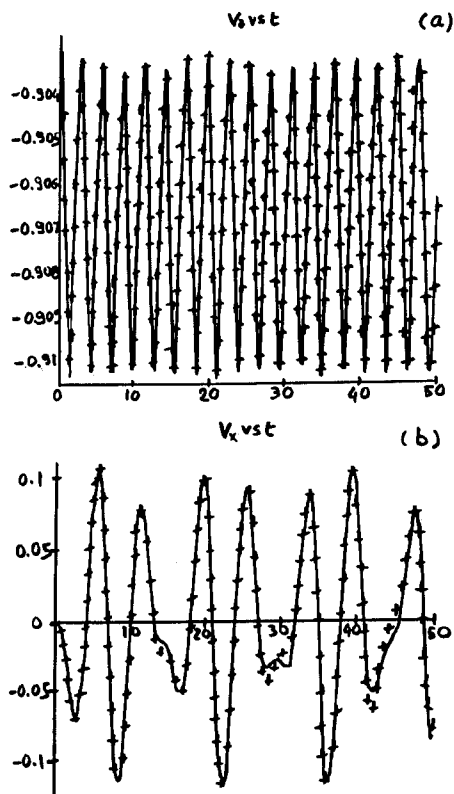


Fig. 3. Electron trajectories as calculated using SOLITUDE (solid curves) and with the analytical model (dashed curves). Reversed field operation ( $v_z < 0$ ). Beam energy = 0.75 MeV,  $\lambda_w = 3.18$  cm,  $B_0 = 1.09$  T, and  $B_w = 0.147$  T. (a) The axial velocity  $v_z$  as a function of time. (b) The transverse velocity  $v_x$  as a function of time.

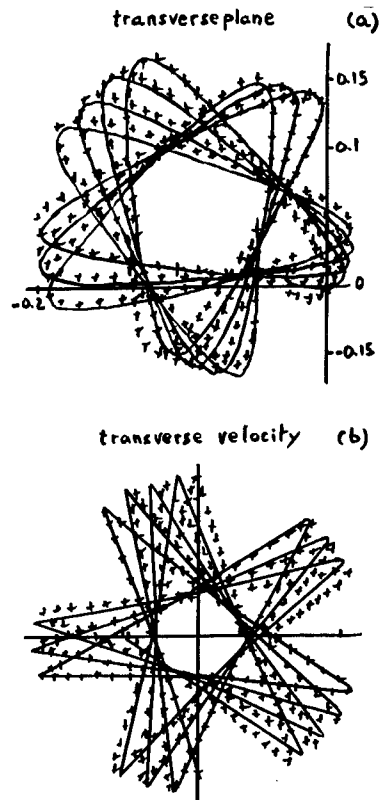


Fig. 4. Same conditions as in Fig. 3. (a) The trajectory projected on the transverse plane. (b) The velocity projected on the transverse plane.

Two examples were chosen using the parameters corresponding to the FEL experiment at CEA-CESTA [5]. The beam kinetic energy is 1.75 MeV,  $\lambda_w = 8$  cm,  $B_0 = 0.8$  T, and  $B_w = 0.095$  T. In the first example, shown in Fig. 1 (type Group II), the passage through the adiabatic entry produced an electron which is not far from the ideal trajectory corresponding to its particular value of  $P_z$ . Consequently the harmonic oscillators in the DR approach have only small amplitudes, and the motion is quite similar to the ideal helical path. It may be noticed that the ratio of transverse to longitudinal velocity is 0.42 in this case, an extremely large value. The nearly circular projection of the trajectory on the transverse plane, shown in Fig. 1c, corresponds closely to the ideal trajectory.

The second example illustrates in Fig. 2 an electron whose initial conditions are far from the ideal trajectory (again in Group II). In particular, the oscillator of frequency  $\Omega_- = 0.485$  (in units  $2\pi c/\lambda_w$ ) has an amplitude  $|A_-| = 0.434$ , which is quite large (the corresponding energy in units of  $mc^2$  is  $\Omega_- |A_-|^2$ , which is approximately 1% of the electron's energy). This is responsible for the very large oscillations in the longitudinal velocity (Fig. 2a), especially as compared with the preceding example. One notices a small difference between the DR predic-

tions and those of SOLITUDE for  $v_z$ , the latter being systematically greater. In turn, this discrepancy causes the predictions for the transverse velocities to drift apart as time increases, although the overall agreement is fairly good, as may be seen in Fig. 2b. The maximum longitudinal velocity possible for this energy is 0.974, and this is reached at the maxima in Fig. 2a. Consequently the transverse velocity falls to zero, which explains the rather surprising appearance of cusps in the projection of the trajectory on the  $x$ - $y$  plane (Fig. 2c). These are predicted by both SOLITUDE and by DR, although the agreement is less than perfect.

The third example, shown in Figs. 3 and 4, was chosen to illustrate results obtained by Conde and Bekefi [6], who have studied the reversed field configuration, where the electron's longitudinal velocity is anti-parallel to the guide magnetic field. We follow Ref. [2] in maintaining the guide field along the positive  $z$ -direction, which means that the axial velocity of the electron is negative. For this example the beam kinetic energy is 0.75 MeV,  $\lambda_w = 3.18$  cm,  $B_0 = 1.09$  T, and  $B_w = 0.147$  T. In general the agreement between SOLITUDE and DR predictions is excellent. It should be mentioned that the exceedingly small ripple in the axial velocity  $v_z$  ( $\pm 0.3\%$ ) in Fig. 3a may be attributed in part to a small oscillator amplitude ( $|A_+| = 0.04$ ,  $\Omega_+ = 2.232$ ), and partly to the fact that the radius of the fixed-point helical orbit in the reversed-field configuration is also small (0.08). However, the transverse velocity  $v_x$  (Fig. 3b) is not a simple oscillation, and the trajectory in the transverse plane (Fig. 4a) does not resemble a circle. In fact, the trajectory in the transverse velocity plane (Fig. 4b) has roughly the shape of a five-pointed star which is slowly rotating. The explanation in terms of the DR oscillator picture is rather simple. The transverse position as a function of time is essentially the superposition of three circular motions of different frequency. One is the fixed-point motion, which has the periodicity of the wiggler field in space and thus  $v_z$  in time. The second is

the  $A_+$  oscillator which sweeps out a circle at effective frequency,  $\Omega_+ + v_z$ , while the third is the  $A_-$  oscillator which sweeps out a circle at effective frequency  $v_z - \Omega_-$ . Since  $\langle v_z \rangle = -0.907$  and  $\Omega_- = -0.904$ , the effective frequencies are  $-0.907$ ,  $1.325$  and  $0.003$ , respectively. The third frequency is so small that nothing is swept out and the only effect is that the center of the fixed-point circle is displaced from the center of the wiggler. One may then notice that the first and second frequencies are almost in the ratio of  $-2:3$ , for which the periodicity would be  $4\pi/5$  producing a trajectory with five-fold symmetry.

The aim of this note is to point out that, while a powerful code such as SOLITUDE is certainly needed to investigate the details of the interaction between the electrons and the non-magnetic effects in an FEL, the approximate but analytical approach of DR is capable of providing a good description of trajectories, and its results can be easily interpreted.

#### Acknowledgements

We express our thanks to P. Le Taillandier for his aid in preparing the graphics and to J. Labrousche for helpful discussions.

#### References

- [1] H.P. Freund and A.K. Ganguly, IEEE J. Quantum Electron. QE-21 (1985) 1073.
- [2] J.T. Donohue and J.L. Rullier, Phys. Rev. E. 49 (1994) 766.
- [3] Ph. Gouard and J. Gardelle, CEA-R-5617 (1992).
- [4] B.W. Char et al., MAPLE V (Waterloo Maple, 1991).
- [5] J.L. Rullier, J. Gardelle, J. Labrousche and P. Le Taillandier, these Proceedings (16th Int. Free Electron Laser Conf., Stanford, CA, USA) Nucl. Instr. and Meth. A 358 (1995) 118.
- [6] M.E. Conde and G. Bekefi, Phys. Rev. Lett. 67 (1991) 3082.

# Focusing properties of an undulator with anharmonic magnetic fields <sup>☆</sup>

A.A. Varfolomeev <sup>\*</sup>, A.H. Hairetdinov

*RRC “Kurchatov Institute”, 123182 Moscow, Russian Federation*

## Abstract

The focusing properties of an undulator are considered for the common case that the undulator magnetic fields are not pure sinusoidal (anharmonic). The exact 3D solution of the Laplace equations for the magnetic field near the axis is found. Using equations of electron motion in the fields it is shown that an admixture of higher harmonics in the undulator fields can significantly increase the focusing strength of the undulator. It is demonstrated that this higher harmonic transverse focusing of the electron beam does not violate the phase synchronism condition between the electron and the field, what is similar to the natural undulator focusing of the basic harmonic field.

## 1. Introduction

Electron beam focusing in FEL undulators while conserving electron phase synchronism is one of the serious problems for short wavelength and long undulators. It is well known that ordinary planar undulators provide natural focusing in one transverse direction only, conserving the phase relations between the optical field and the electron oscillations. Many attempts have been made to provide undulator focusing in both transverse directions (2D focusing). In Ref. [1] profiled pole tips were suggested. Being periodic <sup>1</sup> and of parabolic shape these fields preserve the synchronism conditions, as the longitudinal velocity of an electron averaged over an undulator period is constant over a betatron period. It was demonstrated later [2–5] that the same kind of periodic field structure, resulting in similar focusing properties, can be obtained by adding several rather simple intrinsic magnet elements to the conventional hybrid scheme. The configuration of the *y*-component of

the field near the *z* axis can be described in this case [1] by the expression

$$B_y = B_0 \left( 1 + \frac{k_x^2 x^2}{2} + \frac{k_y^2 y^2}{2} \right) \cos(k_w z),$$

where  $k_w$  is the undulator wavenumber,  $B_0$  is the magnetic field amplitude,  $k_x, k_y$  are the characteristics of the field curvature, the *z*-axis is along the undulator axis, and *x* and *y* are the transverse coordinates.

The above focusing schemes are attractive in terms of synchronism, but have limits for the focusing strengths. They are defined by the betatron wavenumbers  $k_{\beta(x,y)} = b_0 k_{(x,y)} / (\sqrt{2} \gamma k_w)$ , where  $b_0 \equiv cB_0 / (mc^2)$  is the normalized field  $B_0$ . Their natural limits for given field amplitudes are given by the relation  $k_w^2 = k_x^2 + k_y^2$  which follows directly from the requirement that the above basic harmonic undulator field should satisfy Maxwell's equations.

Since the basic harmonic field amplitude  $B_0$  cannot be changed significantly, the above limit on focusing strength has a common character and it has been believed that stronger quadrupole and sextupole focusing can be provided only by some external magnet system without conserving synchronism. There has been no definite answer to the question; does there exist a magnetic field configuration which provides efficient transverse focusing in both directions and also retains synchronism of the interaction? (Simply increasing the field amplitude has penalties in FEL performance and thus is not considered.)

<sup>☆</sup> The research described in this publication was made possible in part by Grant No. MQH000 from the International Science Foundation.

<sup>\*</sup> Corresponding author. Fax +7 095 196 7764, e-mail 1065@cuv1.net.kiae.su.

<sup>1</sup> The necessity of focusing field periodicity first demonstrated in Ref. [1] was analyzed in detail in Ref. [2].

In what follows we demonstrate that the problem can be solved. By applying additional periodic focusing fields which include higher harmonics of the primary undulator, one can obtain stronger focusing in both transverse directions and retain synchronism of the electron beam–radiation field interaction as well.

## 2. Periodical focusing fields

Let us consider a magnetic field which is periodic with space period  $\lambda_w$  but which is not necessarily sinusoidal. We can represent the magnetic field vector on the axis of the anharmonic undulator as follows

$$B_y(x=0, y=0, z) = e_y \sum_{n=1}^{\infty} B_n \cos(nk_w z). \quad (1)$$

Here  $x$  and  $y$  are the transverse coordinates,  $z$  is the undulator axis,  $k_w = 2\pi/\lambda_w$  is the undulator field wave number,  $B_n$  is the amplitude of the  $n$ th harmonic of the magnetic field, and  $e_y$  is the unit vector in the  $y$  direction. Let us also consider the field symmetry corresponding to the equal focusing case  $k_x = k_y$  [1]. This requirement translates into the conditions:

$$\begin{aligned} B_x(\pm x, \mp y) &= -B_x(x, y), \\ B_y(\pm x, \mp y) &= B_y(x, y), \\ B_z(\pm x, \mp y) &= \mp B_z(x, y). \end{aligned} \quad (2)$$

The next step is the solution of the equation for the scalar potential  $\nabla^2 \chi = 0$ . It can be done in the same way as in Ref. [6], i.e. by representing the solution as a Fourier expansion along the  $z$ -axis and expanding into a power series in  $x$  and  $y$ . This expansion is valid due to the fact that we assume the periodicity (1) and limit ourselves to the area near the axis where  $k_w x \ll 1$  and  $k_w y \ll 1$ . Keeping the first terms we obtain for the components of the magnetic field

$$\begin{aligned} B_y &= \sum_{n=1}^{\infty} B_n \cos(nk_w z) \left( 1 + \frac{n^2 k_w^2}{4} (x^2 + y^2) \right), \\ B_x &= \sum_{n=1}^{\infty} B_n \cos(nk_w z) \frac{n^2 k_w^2}{2} xy, \\ B_z &= - \sum_{n=1}^{\infty} nk_w B_n \sin(nk_w z) \left( y + \frac{n^2 k_w^2}{4} \left( x^2 y + \frac{y^3}{3} \right) \right), \end{aligned} \quad (3)$$

where  $B_n$  are the amplitudes of the respective harmonics. These formulae are a more general form of the well-known field of the undulator with profiled pole tips [1] which take into account multiple harmonics of the main undulator period  $\lambda_w$ . In what follows we will evaluate the effect of such a field structure on the motion of the electron beam with special attention to the transverse focusing.

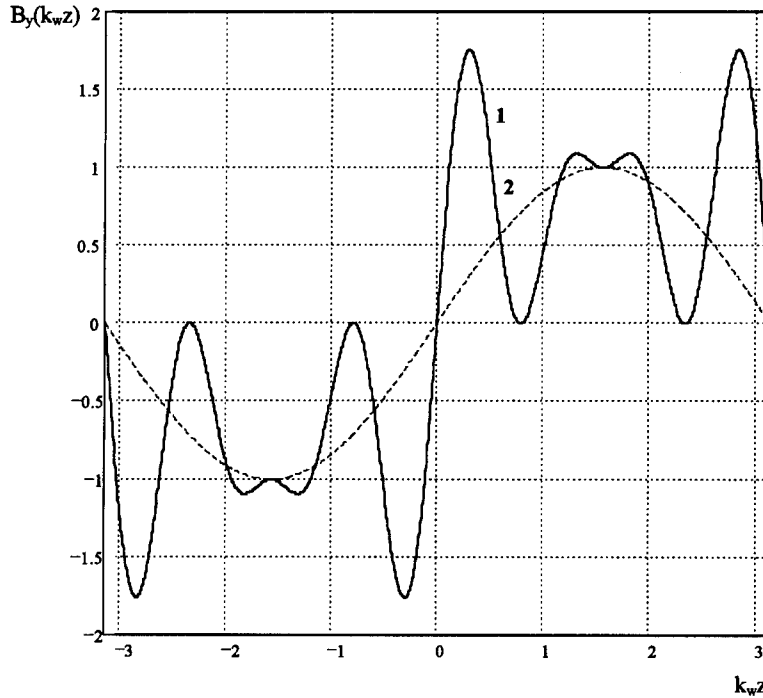


Fig. 1. The plot of the on axis magnetic field  $B_y(k_w z)$ . 1 – field with higher harmonics, up to the 7th; 2 – pure sinusoidal field with the same amplitude  $b_1$ .

### 3. Electron motion in the multiharmonic focusing field

The equations of electron motion in the above magnetic field take the form

$$\begin{aligned}\ddot{x} &= \frac{e}{\gamma mc} (\dot{y}B_z - \dot{z}B_y), \\ \ddot{y} &= \frac{e}{\gamma mc} (-\dot{x}B_z + \dot{z}B_x), \\ \ddot{z} &= \frac{e}{\gamma mc} (\dot{x}B_y - \dot{y}B_x).\end{aligned}\quad (4)$$

Following a procedure similar to that in Ref. [1], we represent the transverse motion by a sum of two terms. One of them is a fast oscillating term over the undulator period. The other one, describing the betatron motion, is nearly constant over the period. Omitting simple, but somewhat lengthy, calculations we present the final equations describing betatron motion:

$$x_0'' + \frac{\sum_{n=1}^{\infty} b_n^2}{4\gamma^2} x_0 = 0, \quad y_0'' + \frac{\sum_{n=1}^{\infty} b_n^2}{4\gamma^2} y_0 = 0. \quad (5)$$

Here the derivatives are taken over  $z$  and  $b_n$  are the normalized harmonic amplitudes.

Eqs. (5) very clearly resemble the ordinary equations of electron motion in a single frequency undulator with profiled pole tips, with one notable exception. Instead of the squared amplitude of the undulator field there is the sum of each of the amplitudes squared. This fact is central to the possibility of enhancing the focusing properties of a multifrequency undulator.

The transverse velocity averaged over an undulator period can be obtained in a manner similar to that described in Ref. [1]. It takes the form

$$\langle \beta_{\perp}^2 \rangle = \frac{1}{2\gamma^2 k_w^2} \sum_{n=1}^{\infty} b_n^2 \left( \frac{1}{n^2} + \frac{k_w^2}{2} (x_{\beta}^2 + y_{\beta}^2) \right), \quad (6)$$

where  $x_{\beta}$  and  $y_{\beta}$  are the amplitudes of the betatron oscillations. This velocity is constant over a betatron period. Thus synchronism is not violated.

We can take a closer look at the betatron wavenumber in this case and compare it to the betatron wavenumber of the single frequency undulator. In general we have  $k_{\beta x}^2 = k_{\beta y}^2 = \sum_{n=1}^{\infty} b_n^2 / (4\gamma^2)$ . In the ordinary equal focusing and single frequency undulator there is just one term  $b_1^2$ , related to the single harmonic of the undulator field. Assuming that the amplitudes of the fundamental are equal in both cases we get for betatron wavelengths the following relation

$$\lambda_{\beta}^{(1)} / \lambda_{\beta}^{(n)} = \sqrt{1 + \left( \sum_{n=2}^{\infty} b_n^2 \right) / b_1^2}. \quad (7)$$

Here  $\lambda_{\beta}^{(1)}$  is the betatron length for the single frequency equal focusing undulator and  $\lambda_{\beta}^{(n)}$  is the betatron length for the multifrequency equal focusing undulator.

### 4. Discussion and conclusion

Examining the expression (7) we see that there is a possibility of decreasing the betatron length, i.e. enhancing the natural focusing strength of the undulator. This can be accomplished if the main undulator field is not purely sinusoidal but has a high enough percentage of harmonics. With enough harmonics amplitudes we can get considerable enhancement of the focusing strength (up to several times) while maintaining synchronism. In considering the conventionally used relation which limits the focusing strength of a planar undulator  $k_w^2 = k_x^2 + k_y^2$ , we note that the term  $k_w^2$  originates from the second derivative over  $z$  of the pure sinusoidal undulator field. In our case the second derivative gives a term like  $n^2 k_w^2$  so this limit does not apply. Thus we have a scheme with stronger focusing applicable to FEL projects where beam transport is difficult (long undulators).

Fig. 1 shows one numerical result for illustration. In this example  $b_1 = 1$ ,  $b_3 = 0.3$ ,  $b_5 = 0.8$ ,  $b_7 = 0.5$  which results in 1.41 times shorter betatron length. The field structure is not optimized. We do not focus here on the problem of providing the magnetic field structure described by Eq. (3) or the performance of the FEL oscillator based on such undulator. Our statement is the following: the focusing strength of an undulator exceeding the so-called natural limit while conserving synchronism is possible. It can be accomplished only by introducing a mixture of harmonics to the undulator field.

### References

- [1] E.T. Scharlemann, J. Appl. Phys. 58 (1985) 2154.
- [2] A.A. Varfolomeev and A.V. Smirnov, Proc. Workshop on FEM-Millimeter Waves, Rijnhuizen, Nieuwegein, The Netherlands, August 1993.
- [3] W.N. Urbanus, R.W.B. Best, A.G.A. Verhoeven, M.J. van der Wiel, M. Caplan, L. Bratman, G. Denisov and A.A. Varfolomeev, Proc. 3rd Europ. Particle Accelerator Conf., vol. 1 (1992) p. 629.
- [4] A.A. Varfolomeev and A.H. Hairtdinov, Nucl. Instr. and Meth. A 341 (1994) 462.
- [5] A.A. Varfolomeev, S.N. Ivanchenkov, A.S. Khlebnikov, N.S. Osmanov, M.J. van der Wiel, W.H. Urbanus and V.F. Pavluchenkov, Nucl. Instr. and Meth. A 341 (1994) 466.
- [6] J.J. Barnard, Nucl. Instr. and Meth. A 296 (1990) 508.



ELSEVIER

## Fourier analysis for the rapid calculation of distorted undulator orbits and their correction

V.A. Papadichev \*

*Lebedev Physical Institute, 53 Leninsky Prospect, 117924 Moscow, Russian Federation*

### Abstract

A simple method of electron trajectory calculation in undulators is proposed. Expanding the field errors in a Fourier series, one can calculate the distorted orbit and electron trajectory, which is a betatron oscillation around the distorted orbit with initial amplitude and velocity opposite in sign and equal in absolute value to those of the distorted orbit at the undulator input. The most dangerous components are “resonant” harmonics of the field distortion with a period close to the betatron oscillation period. Correcting one, two or at most three dangerous harmonics is usually sufficient to obtain an electron orbit acceptably close to the ideal orbital. The above method of trajectory calculation is compared with some examples of numerical calculations published earlier in the literature.

### 1. Introduction

Electron trajectories in the ideal magnetic field of a helical undulator were studied theoretically as early as 1977 by Blewett and Chasman [1]. Orbits and betatron oscillations in a plane undulator were treated theoretically by Scharlemann [2] in 1985.

Some attempts were made to consider the influence of field errors on FEL gain in a rather general approach in 1981 by Gover and Sprangle [3] and Diamant [4]. In 1985 Kincaid studied the influence of random errors in the magnetic field on the radiation spectrum of plane undulators [5]. Large trajectory deviations (up to  $20a$ , where  $a$  is the ideal orbit amplitude) were found even for small rms field errors (0.5%). Subsequent studies principally followed Kincaid's approach [6–11]. The perturbed trajectory is calculated by integrating (analytically or numerically) the equations of motion around the ideal equilibrium orbit using field errors as driving force. A stochastic (random errors) approach is natural for theoretical treatment of the problem since it permits estimation of trajectory drift in the general case, but it has the weakness that it does not indicate how to diminish trajectory distortion.

Another method of trajectory correction, also based on the random error approach, is the use of steering or focusing devices (coils, lenses etc.) to return the beam to the axis step by step. One must use at least two steering elements per period of betatron oscillations to lower the

trajectory deviation by a factor of 3 to 5. One has to double the number of steering elements since there are two transverse degrees of motion.

Since the electrons in more than  $\frac{4}{5}$  of the undulators used in FEL experiments experience more than half a period of betatron oscillation, a simpler, faster and more productive method of trajectory calculation such as that widely used in cyclic accelerators to correct the closed orbit distortions is possible. Expanding the field errors in a Fourier series, one can calculate the distorted orbit and electron trajectory, which is a betatron oscillation around the distorted orbit with initial amplitude and velocity opposite in sign and equal in absolute value to that of the distorted orbit at the undulator input (for particles injected collinear to the undulator axis).

Application of this technique to linear devices such as undulators is justified by the strict periodicity of the undulator field and the constant betatron oscillation period (which is not the case for focusing systems of linear accelerators) and the fact that most undulators used in experiments are long enough in that electrons experience more than half of a betatron oscillation in them.

Field errors in an undulator give rise to orbit distortions and trajectory deviations from the ideal orbit which can be two or three times larger than the orbit distortions. This results in three principal effects: 1) nonoverlapping of the electron beam and radiation, 2) electron beam losses on the walls of the transport system (undulator inner tube) and 3) electron longitudinal velocity deviation from the central (equilibrium, resonant) value and spread. All three effects lead to FEL gain reduction, the first and the third being especially important for long undulator devices and are

\* Tel. +7 095 132 6300, fax +7 095 938 2251, e-mail vitality@lpnu.flan.msk.su.

unavoidable in very short-wavelength FELs because of FEL gain reduction at high electron energies.

Distorted orbit calculation using Fourier analysis is described in Section 2. Particle trajectories are studied in Section 3. Examples of trajectories are given in Section 4 for published undulator parameters. Types of field errors are discussed briefly along with methods of their correction.

## 2. Equations of motion and distorted orbit

### 2.1. Helical undulator

We follow here the well known method of successive approximations used by Blewett and Chasman [1] to determine the ideal orbit and betatron oscillations in a helical undulator, but taking into account errors in the undulator magnetic field.

Using a rectangular (Cartesian) coordinate system and retaining third order terms, we have for the magnetic field of a helical undulator:

$$\begin{aligned} B_x &= -B_0 \left\{ \left[ 1 + \left( \frac{1}{8} \right) k^2 (3x^2 + y^2) \right] \sin(kz) \right. \\ &\quad \left. - \left( \frac{1}{4} \right) k^2 xy \cos(kz) \right\} + \Delta B_x, \\ B_y &= B_0 \left\{ \left[ 1 + \left( \frac{1}{8} \right) k^2 (x^2 + 3y^2) \right] \cos(kz) \right. \\ &\quad \left. - \left( \frac{1}{4} \right) k^2 xy \sin(kz) \right\} + \Delta B_y, \\ B_z &= -B_0 \left[ 1 + \left( \frac{1}{8} \right) k^2 (x^2 + y^2) \right] \\ &\quad \times (x \cos(kz) + y \sin(kz)) + \Delta B_z, \end{aligned} \quad (1)$$

where  $B_0$  is the undulator transverse field amplitude,  $k = 2\pi/l_0$  is the undulator wave number,  $l_0$  is the undulator period, and  $\Delta B_x$ ,  $\Delta B_y$  and  $\Delta B_z$  are magnetic field errors.

The equations of particle motion are:

$$\begin{aligned} \ddot{x} &= -(e/(m_0 c \gamma)) (\dot{y} B_z - \dot{z} B_y), \\ \ddot{y} &= -(e/(m_0 c \gamma)) (\dot{z} B_x - \dot{x} B_z), \end{aligned} \quad (2)$$

where  $e$  and  $m_0$  are the electron charge and rest mass,  $c$  is the speed of light in vacuum and  $\gamma$  is the electron energy in  $m_0 c^2$  units.

The orbit and betatron oscillations in the ideal undulator magnetic field are sought in the form:  $x = r_0 \cos(kz) + u$ ,  $y = r_0 \sin(kz) + v$ . Here,  $r_0 = eB_0/(k^2 m_0 c^2 \gamma \beta_{\parallel}) = \beta_{\perp 0}/(k \beta_{\parallel})$  is the ideal orbit amplitude  $u$  and  $v$  are betatron oscillations in the  $x$  and the  $y$  directions.  $\beta_{\parallel} = v_{\parallel}/c$  is the normalized axial velocity, and  $\beta_{\perp 0} = v_{\perp 0}/c$  is the ideal orbit transverse velocity.

Substituting  $\ddot{u} = u'' v_{\parallel}^2$  and  $\ddot{v} = v'' v_{\parallel}^2$  and neglecting small terms in  $u^2$ ,  $v^2$ ,  $\dot{u}$ ,  $\dot{v}$ , where  $u' = d^2 u/dz^2$  and  $v'' = d^2 v/dz^2$ , and assuming  $v_{\parallel} = \text{const.}$ , we obtain the

final equations of motion in the following form (two independent and similar equations for  $u$  and  $v$ ):

$$u'' + k_{\beta}^2 u = (e \Delta B_y) / (m_0 c^2 \gamma \beta_{\parallel}), \quad (3a)$$

$$v'' + k_{\beta}^2 v = -(e \Delta B_x) / (m_0 c^2 \gamma \beta_{\parallel}), \quad (3b)$$

where  $k_{\beta} = 2\pi/l_{\beta} = \beta_{\perp 0} k / \sqrt{2}$  is the wave number of betatron oscillations.

### 2.2. Plane undulator

A plane undulator has focusing properties only in one transverse direction. Equations of motion are Eqs. (3) with  $k_{\beta} = k_{\beta x} = 0$ . The betatron oscillation wave number in the  $y$  direction,  $k_{\beta y}$ , has the same expression as for the helical undulator,  $k_{\beta y} = 2\pi/l_{\beta y} = \beta_{\perp 0} k / \sqrt{2}$ .

The first equation Eq. (3a) can be easily integrated

$$\begin{aligned} u(z) &= e / (m_0 c^2 \gamma \beta_{\parallel}) \int_0^z \int_0^{z'} \Delta B_y(z') dz' dz'' \\ &\quad + u(0) + z(du/dz)_{z=0}, \end{aligned}$$

resulting in a drift-like trajectory under random field error kicks.

Thus, we need study only one equation of motion, say for  $y$ , i.e., the second one in Eq. (3b). The results can be used for both coordinates of a helical undulator or one of a plane undulator.

### 2.3. Distorted orbit

The Eq. (3b) to be studied is a linear inhomogeneous second order equation (with the right-hand member). Its general solution is a sum of free betatron oscillations,  $v_{\beta} = a_{\beta} \cos(k_{\beta y} z) + b_{\beta} \sin(k_{\beta y} z)$ , and forced oscillations  $v_1$  caused by  $(e \Delta B_x)/(m_0 \gamma \beta_{\parallel})$ . A specific case of random field errors can be very complicated and irregular, making it impossible to find an analytical solution. However, one can use the well-known technique of expanding  $\Delta B_x$  and the distorted orbit of betatron oscillations  $v_1$  in Fourier series:

$$\Delta B_x = a_{x0}/2 + \sum [a_{xm} \cos(mk_L z) + b_{xm} \sin(mk_L z)], \quad (4)$$

$$v_1 = a_{10}/2 + \sum [a_{1m} \cos(mk_L z) + b_{1m} \sin(mk_L z)], \quad (5)$$

where  $L = Nl_0$  is the undulator length,  $N$  is the number of undulator periods,  $k_L = 2\pi/L$  and  $m$  is an integer. Substituting Eqs. (4) and (5) into Eq. (3b) and letting coefficients of  $\cos(mk_L z)$  and  $\sin(mk_L z)$  be zero, one obtains (for  $m = 0, 1, 2, \dots$ ):

$$\begin{aligned} a_{1m} &= r_0 (a_{xm}/B_0) (k^2 / (k_{\beta y}^2 - m^2 k_L^2)), \\ b_{1m} &= r_0 (b_{xm}/B_0) (k^2 / (k_{\beta y}^2 - m^2 k_L^2)). \end{aligned} \quad (6)$$



It is easily seen that the orbit distortion can be large if  $k_{\beta y} \approx mk_L$ , i.e., if the betatron period  $l_{\beta y}$  is roughly equal to  $L/m$ .

### 3. Particle trajectory

The electron trajectory in an undulator is the sum of three motions: the ideal undulator orbit, a distorted betatron orbit due to field errors and free betatron oscillations around this distorted orbit. We subtract (or average) the fast-oscillating ideal orbital motion and analyze only betatron motion, which usually has a much larger deviation from the undulator axis than that of the ideal orbit.

The trajectory is the sum of  $v_{\beta}$  and  $v_1$ ;  $a_{1m}$  and  $b_{1m}$  are taken from Eq. (6);  $a_{\beta}$  and  $b_{\beta}$  are determined from the particle coordinate and angle at the undulator entry:

$$\begin{aligned} Y_{\beta} &= a_{10}/2 + \sum [a_{1m} \cos(mk_L z) + b_{1m} \sin(mk_L z)] \\ &\quad + a_{\beta} \cos(k_{\beta y} z) + b_{\beta} \sin(k_{\beta y} z), \\ a_{\beta} &= Y_{\beta}(0) - a_{10}/2 - \sum a_{1m} \\ &= Y_{\beta}(0) - (r_0 k^2/B_0) \\ &\quad \times [a_{x0}/(2k^2) + \sum a_{xm}/(k_{\beta y}^2 - m^2 k_L^2)], \\ b_{\beta} &= (1/k_{\beta y}) [\beta_y(0)/\beta_{||} - \sum b_{1m} mk_L] \\ &= (1/k_{\beta y}) [\beta_y(0)/\beta_{||} - (r_0 k^2/B_0) \sum b_{xm} mk_L \\ &\quad / (k_{\beta y}^2 - m^2 k_L^2)]. \end{aligned} \quad (7)$$

It is necessary of course to take into account the additional displacement and transverse velocity (angle) acquired by a particle in the stray field at the undulator input, unless its effect is compensated.

### 4. Field errors and trajectory correction

Having measured the magnetic field in a given wiggler, one can calculate the amplitudes of the field error harmonics and then correct the most disturbing ones.

The coefficients  $a_{x0}$ ,  $a_{xm}$ ,  $b_{xm}$  in Eq. (4) for the expansion of  $\Delta B_x$  in a Fourier series are:

$$\begin{aligned} a_{xm} &= (2/L) \int_0^L \Delta B_x \cos(mk_L z) dz \\ b_{xm} &= (2/L) \int_0^L \Delta B_x \sin(mk_L z) dz \end{aligned} \quad (8)$$

Supposing in each half-period of number  $i$  that  $\Delta B_{xi} = \Delta B_i \sin(kz)$  and  $\cos(mk_L z) \approx \text{const.}$ ,  $\sin(mk_L z) \approx \text{const.}$  inside  $l_0/2$ , i.e., for  $(i-1)l_0/2 < z < il_0/2$ , one has

$$\begin{aligned} a_{xm} &= (2/(\pi N)) \sum [\Delta B_i \cos(mk_L l_0 i/2)] \\ b_{xm} &= (2/(\pi N)) \sum [\Delta B_i \sin(mk_L l_0 i/2)]. \end{aligned} \quad (9)$$

It is also possible to calculate the expected harmonic amplitudes assuming that the local errors in each half-period are random. The root-mean-squared values of the harmonic amplitudes normalized to the undulator field amplitude are:

$$\begin{aligned} \langle (a_{xm})^2 \rangle^{1/2} / B_0 &= \langle (b_{xm})^2 \rangle^{1/2} / B_0 \\ &= (2/(\pi N^{1/2})) \langle (\delta B_0/B_0)^2 \rangle^{1/2}. \end{aligned} \quad (10)$$

If  $l_{\beta y} \approx L/m$  (i.e., near the resonance of the betatron orbit distortion), a good approximation is to take into account only  $a_{xm}$  and  $b_{xm}$ . Putting  $Y_{\beta}(0) = \beta_y(0) = 0$ , i.e., injecting electrons along the axis, one has

$$\begin{aligned} a_{\beta} &= -a_{1m} = -(r_0 k^2)(a_{xm}/B_0)(k_{\beta y}^2 - m^2 k_L^2), \\ b_{\beta} &= -b_{1m} mk_L/k_{\beta y} \\ &= -(r_0 k^2)(mk_L/k_{\beta y})(b_{xm}/B_0)(k_{\beta y}^2 - m^2 k_L^2), \\ Y_{\beta} &= -2a_{1m} \sin((mk_L + k_{\beta y})z/2) \\ &\quad \times \sin((mk_L - k_{\beta y})z/2) \\ &\quad + 2b_{1m} \cos((mk_L + k_{\beta y})z/2) \\ &\quad \times \sin((mk_L - k_{\beta y})z/2) \\ &\quad - ((mk_L - k_{\beta y})/k_{\beta y}) b_{1m} \\ &\quad \times \sin(k_{\beta y} z). \end{aligned}$$

Fig. 1 shows the trajectory as calculated in Ref. [9]. We have calculated the trajectory for the same parameters and used rms amplitudes of the first ten harmonics (curve 2). Only three harmonics: the third, fourth and fifth, were used

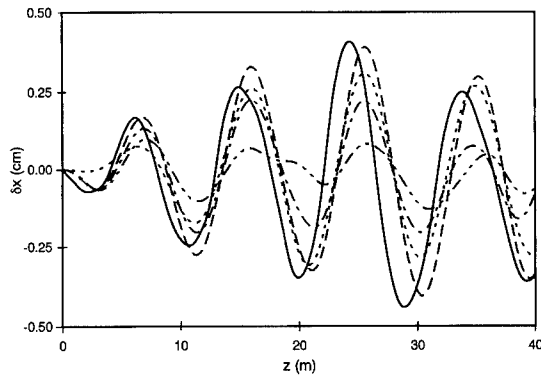


Fig. 1. Electron trajectories in a long undulator: 1 – Numerical integration of the equation of motion with random magnetic field errors [9] (—); 2 – Fourier analysis calculation of the same trajectory using rms values of harmonics and choosing their signs (+ or –) to better fit curve 1 (10 first harmonics used) (----); 3 – The same as for curve 2, but only the 3rd, 4th and 5th harmonics are used (.....); 4 – Trajectory after correction of the 4th harmonic (-.-.-.-); 5 – Trajectory after correction of the 3rd, 4th and 5th harmonics (-.-.-.-)

to calculate curve 3. It is difficult to expect precisely the same result for the trajectory as in Ref. [9] not knowing the exact distribution of random field errors used in the calculation. But the most characteristic features of two trajectories coincide. One can also see the effects of various corrections of the trajectory.

Field errors in plane undulators originate from mechanical tolerances and variation of characteristics of the permanent magnets and iron of poles and yokes from one undulator half-period to another. Transverse displacement of magnets and pole tips is essential in PM and electromagnetic undulators with iron. Degradation of PM strength with time and a limited accuracy of magnetic measurements and correction are also sources of error. Field quality of the helical undulator depends on mechanical precision; the most dangerous source of errors is the radial displacement of winding conductors.

Trajectory correction can be made by using the Fourier analysis of field errors and compensating the effect of the most dangerous harmonics. As a first step, one can move away from resonances by changing the amplitude  $B_0$  of the undulator field. A second step is to decrease the amplitude of dangerous harmonics. This can be done by tuning the field in certain half-periods of the undulator and introducing harmonics of the opposite sign than those of the undulator. A third step (the most difficult one) may be employing a special system of windings for harmonic compensation. Reducing the betatron distorted orbit amplitude (deviation from the axis) results in a nearly double reduction of the trajectory deviation from the undulator axis.

### Acknowledgements

The author is grateful to O.A. Smith for his assistance in preparation of the paper and to I.V. Sinilshikova for trajectory calculations.

It is a pleasure for the author to express his gratitude to the Physics Department, University of California, Irvine for an opportunity to finish this report during his stay there in July–August 1994.

### References

- [1] J.P. Blewett and R. Chasman, *J. Appl. Phys.* 48 (1977) 2692.
- [2] E.T. Scharlemann, *J. Appl. Phys.* 58 (1985) 2154.
- [3] A. Gover and P. Sprangle, *J. Appl. Phys.* 52 (1981) 599.
- [4] P. Diament, *Phys. Rev. A* 23 (1981) 2537.
- [5] B.M. Kincaid, *J. Opt. Soc. Am. B* 2 (1985) 1294.
- [6] C.T. Elliott and B.D. McVey, *World Scientific Proc. of Undulator Magnets for Synchrotron Radiation and Free Electron Lasers*, Trieste, Italy, June 1987, eds. R. Bonifacio, L. Fonda and C. Pellegrini (World Press, 1988).
- [7] H.D. Shay and E.T. Scharlemann, *Nucl. Instr. and Meth. A* 272 (1988) 601.
- [8] S.B. Segall and J.F. Ostiguy, *Nucl. Instr. and Meth. A* 285 (1989) 355.
- [9] E. Esarey and C.-M. Tang, *J. Appl. Phys.* 67 (1990) 2210.
- [10] L.H. Yu, S. Krinsky, A. Friedman, R.L. Gluckstern and J.B.J. von Zejts, *Nucl. Instr. and Meth. A* 318 (1992) 500.
- [11] H. Jiang and L.R. Elias, *Nucl. Instr. and Meth. A* 318 (1992) 830.



ELSEVIER

# On the possibility of the construction of plasma undulators

V. Bazylev <sup>a,\*</sup>, V. Goloviznin <sup>a</sup>, M.M. Pitatelev <sup>a</sup>, A. Tulupov <sup>a</sup>, T. Schep <sup>b</sup>

<sup>a</sup> Russian Research Center “Kurchatov Institute”, Moscow 123182, Russian Federation

<sup>b</sup> FOM-Instituut voor Plasmafysica Rijnhuizen, Postbus 1207, 3430 BE Nieuwegein, The Netherlands

## Abstract

The problem of the creation of a deeply modulated plasma for an FEL by an electron beam is analyzed in a 1-D approximation with of the influence of the exited nonlinear plasma waves upon the electron beam taken into account.

## 1. Introduction

A plasma modulated deeply ( $\delta n/n > 1$ ) by a nonlinear plasma wave would be a possible medium for exciting transverse electromagnetic waves [1]. The reason is that a beam of relativistic electrons moving opposite a nonlinear wave and passing in succession through layers of plasma with a periodically varying electron density would be unstable with respect to the electromagnetic radiation and with respect to the amplification of this radiation at a frequency well above the modulation period. The practical possibilities in this case depend on the development of compact “undulators” (wigglers) for an FEL and on moving into the short-wave region, since the technical capabilities in terms of shortening the period of magnetic wigglers are presently limited to values  $\geq 1$  cm.

The goal of the present report is to identify the conditions which would maximize the amplitude of plasma density modulation created by a relativistic electron bunch and to minimize the negative influence of the plasma wave upon the structure of the electron bunch.

To derive some simple estimates, we restrict the discussion to the 1-D case, and we assume at first that the density of the bunch remains constant over time. We ignore the slowing of the beam electrons and the possible onset of beam–plasma instabilities. We assume that the plasma is cold and collisionless. In this approximation the excitation of plasma waves is described by the following system of equations:

$$\begin{aligned} \frac{\partial E}{\partial z} &= 4\pi e(\delta n + n_b), \\ \frac{\partial E}{\partial t} &= -4\pi e(\delta n + n_0)v - 4\pi en_b v_0, \\ \frac{dp}{dt} &= eE, \end{aligned} \quad (1)$$

where  $E = E_z(z, t)$  is the longitudinal electric field,  $n_b$  and  $v_0$  are respectively the density and velocity of the beam electrons ( $1 - v_0 \ll 1$ ),  $n_0$  is the unperturbed value of the plasma density,  $\delta n$  is the variable part of plasma density,  $v(z, t)$  is the velocity of the plasma electrons, and  $p = mv/(1 - v^2)^{1/2}$  is their momentum. The first two equations of system (1) are Maxwell’s equations for the electric field; the last equation describes the dynamics of plasma electrons.

We are interested below in steady-state solutions which are “traveling” along the  $z$  axis at a velocity  $v_0$ . It is thus convenient to switch to the new variable  $\xi = z - v_0 t$ . In the simplest case, the beam density  $n_b$  can be represented by a step function:

$$n_b(\xi) = \begin{cases} 0 & \text{if } \xi > 0, \\ N & \text{if } -\tau < \xi < 0, \\ 0 & \text{if } \xi < -\tau. \end{cases} \quad (2)$$

where  $\tau$  is the length of the bunch. We are assuming that the initial state of the plasma is unperturbed:

$$E(\xi = 0) = 0, \quad \delta n(\xi = 0) = 0, \quad p(\xi = 0) = 0. \quad (3)$$

We switch to the new variable  $\alpha$  in accordance with

$$d\alpha = d\xi/[v_0 - v(\xi)], \quad (4)$$

and we express  $\delta n$  and  $E$  in terms of  $p$ . We then find the equation

$$\frac{d^2 p}{d\alpha^2} + 4\pi e^2(n_0 - N) \frac{2}{\sqrt{p^2 + m^2}} + 4\pi e^2 N v_0 = 0. \quad (5)$$

It is easy to see that this equation describes the oscillations of a mass point in a potential field

$$U(p) = 4\pi e^2(n_0 - N)\sqrt{p^2 + m^2} + 4\pi e^2 N v_0 p. \quad (6)$$

The change of variables in Eq. (4) is legitimate only under the condition  $v < v_0$ ; i.e., the velocity of the plasma electrons must not exceed the phase velocity of the wave. Otherwise, a “breaking” of the wave will occur, and there can be no solutions which are stationary in terms of  $\xi$ .

\* Corresponding author. Tel. +7 095 196 7679, fax +7 095 943 0073, e-mail x1144@cpuv1.net.kiae.su.

Eq. (5) describes the excitation of a nonlinear plasma wave moving at a phase velocity  $v_0$ . Working from this equation, we can determine how the amplitude of the excited wave varies with the density  $N$  and length  $\tau$  of the electron beam. It turns out that the excitation of the plasma wave occurs in two stages. In the first stage, the electric field generated by the bunch accelerates plasma electrons in the direction opposite the direction in which the bunch itself is moving. After a time  $\tau$ , the electron bunch then moves off in the forward direction. The result is an abrupt change in the potential  $U(p)$  (see Eq. (6)), by an amount

$$U_0(p) = 4\pi e^2 n_0 \sqrt{p^2 + m^2}. \quad (7)$$

The plasma electrons then execute free oscillations, which are described by Eq. (5) with  $N=0$ , while the initial conditions are determined by the values which the variable  $p$  and  $dp/d\alpha$  have reached by the time  $\tau$ . It is easy to see that the amplitude of these wakefield oscillations is at a maximum if the “coordinate”  $p$  is at maximum at the time  $\tau$ , i.e., if  $dp/d\alpha = 0$

By virtue of the obvious conservation law

$$\begin{aligned} \frac{1}{2} \left( \frac{dp}{d\alpha} \right)^2 + 4\pi e^2 \left[ v_0 N p + (n_0 - N) \sqrt{p^2 + m^2} \right] \\ = 4\pi e^2 (n_0 - N) m \end{aligned} \quad (8)$$

the maximum amplitude which we are seeking,  $p_*$ , is determined by the equation

$$v_0 N p_* + (n_0 - N) \sqrt{p_*^2 + m^2} = (n_0 - N) m. \quad (9)$$

We find

$$p_* \approx \frac{-2(n_0 - N)mN}{n_0(n_0 - 2N)}. \quad (10)$$

It is easy to see that the  $N$  dependence of  $p_*$  has a pole  $|p_*| \rightarrow \infty$  as  $N \rightarrow n_0/2$ . The reason is that at  $N > n_0/2$  the potential  $U(p)$  loses its minimum, and the solution ceases to be oscillatory. Since only solutions with  $v < v_0$  are physically meaningful, this circumstance means that “traveling” solutions are generated only by relatively short pulses under condition

$$n_0 - 2N \leq (n_0/2) \sqrt{1 - v_0^2}.$$

Going back, we note that the electric field amplitude, thought of as a function of the plasma density, goes through a relatively sharp maximum at  $n_0 \sim 2N$ . Specifically, at  $n_0 > 2N$  we have

$$E_{\max} \approx 2\sqrt{4\pi Nm} \sqrt{N/(n_0 - 2N)}. \quad (11)$$

The fraction in the second radical can reach the value  $\gamma_0 = (1 - v_0^2)^{-1/2}$  at the maximum. At  $n_0 < 2N$ , the electric field amplitude is determined by the breaking:

$$E_{\max} \approx 2\sqrt{4\pi Nm} \sqrt{\gamma_0 n_0 / N}. \quad (12)$$

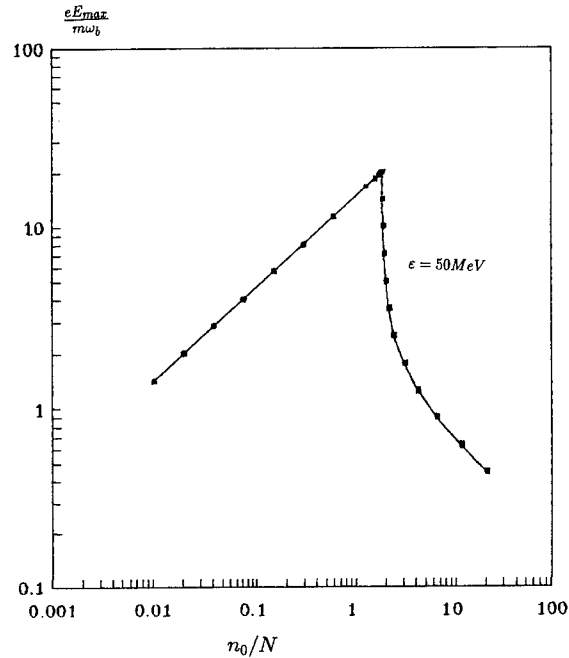


Fig. 1. Amplitude of the accelerating electric field in the wake of an electron bunch as a function of the plasma density. Here and in Fig. 2,  $\omega_b = (4\pi e^2 N / m)^{1/2}$ .

The corresponding length of the bunch is

$$\begin{aligned} \tau_0 = \int_{p_*}^0 dp \left[ v_0 - p / \sqrt{p^2 + m^2} \right] \\ / \sqrt{8ne^2 \left( (n_0 - N) \left[ m - \sqrt{p^2 + m^2} \right] - v_0 N p \right)}. \end{aligned} \quad (13)$$

This length also has a sharp maximum at  $n_0 \sim 2N$ .

Figs. 1 and 2 show curves plotted from Eqs. (11)–(13) for case  $\gamma_0 = 100$  (the energy of the accelerated electrons is 50 MeV.) We again note that reaching the maximum amplitude of the wakefield oscillations of a change at given beam density requires that the length of the bunch be strictly correlated with the plasma density. The amplitude of the wakefield oscillations falls off as the bunch becomes either shorter or longer.

In order to consider the influence of plasma waves upon the electron bunch, computer simulations were carried out. The equations of motion of a large number of electrons of the beam and plasma were solved together with Maxwell's equations.

The results are shown on Figs. 3–5 ( $j = 5$  kA/cm<sup>2</sup>,  $\gamma = 100$ ). The plasma electron density is shown in Fig. 3. The harmonic oscillations of plasma density (Fig. 3a:  $n_0 = 10^{13}$  cm<sup>-3</sup>) become nonlinear ones (Fig. 3b:  $n_0 = 3.3 \times 10^{12}$  cm<sup>-3</sup>; Fig. 3c:  $n_0 = 2.5 \times 10^{12}$  cm<sup>-3</sup>). The optimal dimensions of the bunch are equal to 0.6 cm, 1.7 cm, and 3.6 cm. respectively.

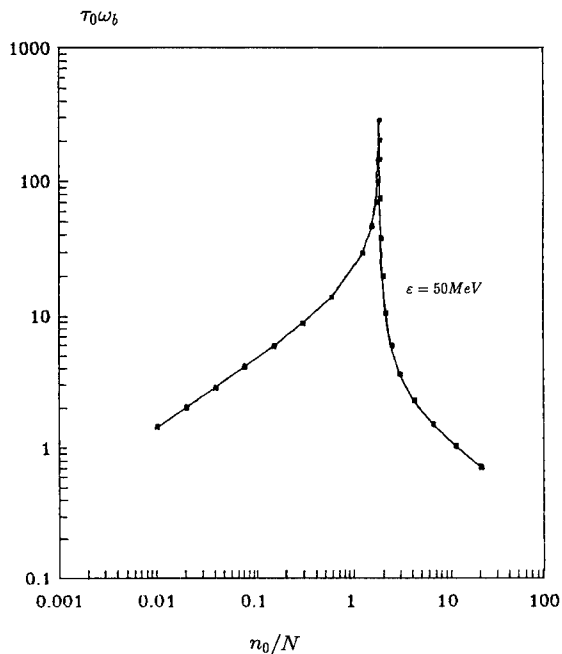


Fig. 2. Optimum bunch length as a function of the plasma density.

The influence of the bunch dimension upon the amplitude of the excited oscillations is shown in Fig. 4 ( $n_0 = 5 \times 10^{12} \text{ cm}^{-3}$ ) (Fig. 4a: the bunch dimension (0.7 cm) is less

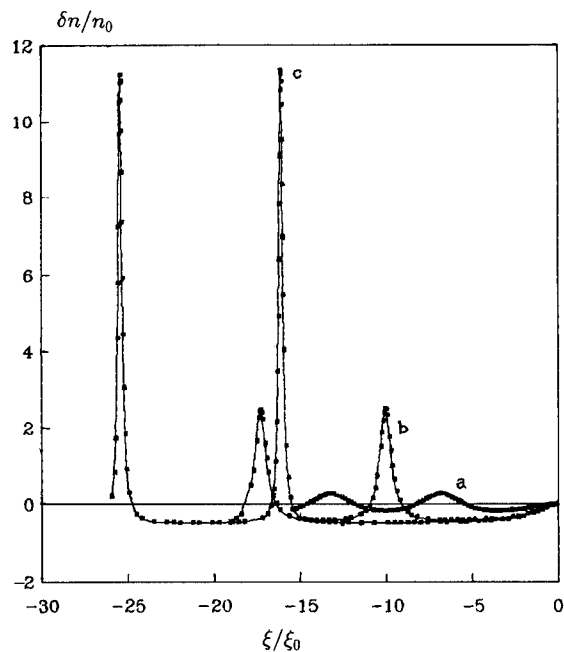


Fig. 3. The profile of the plasma electron density ( $\delta n/n_0$ ) with the parameters of the electron bunch close to optimum. (a)  $n_0 = 10^{13} \text{ cm}^{-3}$ ,  $\tau = 0.6 \text{ cm}$ , (b)  $n_0 = 3.3 \times 10^{12} \text{ cm}^{-3}$ ,  $\tau = 1.7 \text{ cm}$ , (c)  $n_0 = 2.5 \times 10^{12} \text{ cm}^{-3}$ ,  $\tau = 3.6 \text{ cm}$ .

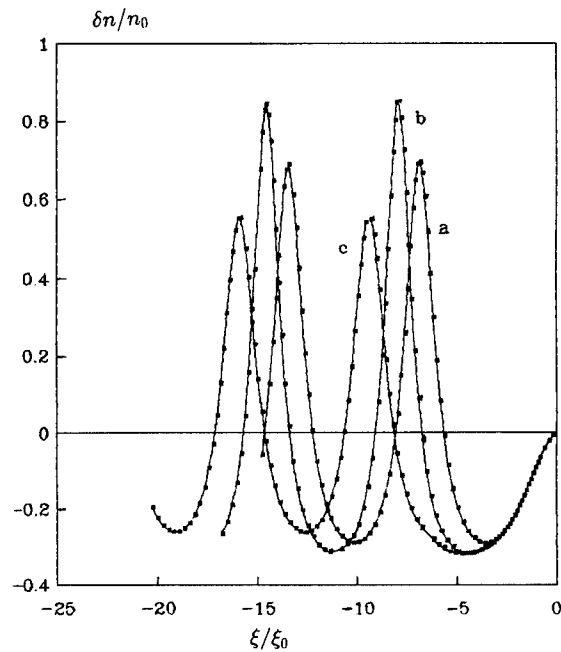


Fig. 4. The profile of the plasma electron density ( $\delta n/n_0$ ) at  $n_0 = 5 \times 10^{12} \text{ cm}^{-3}$  and with different bunch dimensions. (a) 0.7 cm, (b) 1 cm, (c) 1.6 cm.

than the optimal dimension; Fig. 4b: optimal dimension (1.0 cm); Fig. 4c: the bunch dimension (1.6 cm) is more than optimal).

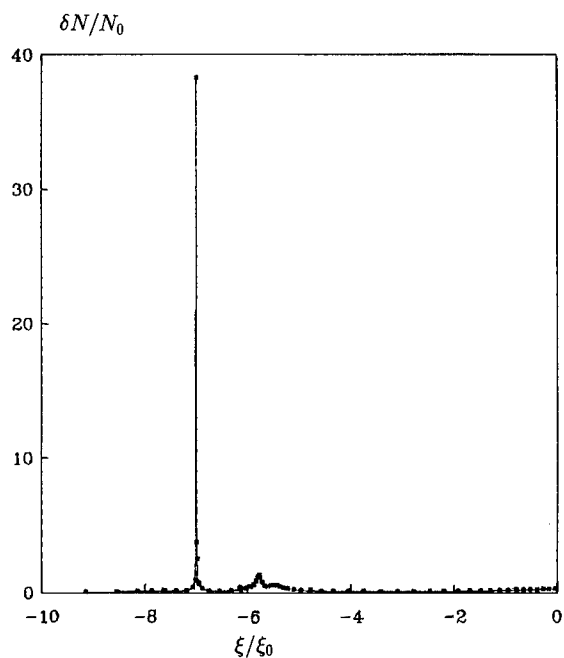


Fig. 5. The final stage of electron bunch evolution. The generation depth is equal to 72 cm. The initial dimension of a homogeneous bunch is equal to 1.7 cm.

The profile of the plasma density and the structure of the bunch are stable up to the moment at which the energy of the most slow electrons of the bunch becomes equal to 1–2 MeV (deep penetration). Then the bunch breaks into pieces. The final stage of this evolution is shown in Fig. 5. (the penetration depth is equal to 72 cm,  $n_0 = 3.3 \times 10^{12} \text{ cm}^{-3}$ ,  $\tau_0 = 1.7 \text{ cm}$ ).

#### Reference

- [1] V.A. Bazylev, Nucl. Instr. and Meth. A 304 (1991) 671.



ELSEVIER

# Free electron lasers with static and dynamic plasma wigglers

N.I. Karbushev

*Moscow Radiotechnical Institute, Varshavskoye shosse 132, 113519 Moscow, Russian Federation*

## Abstract

In free electron lasers, plasma wigglers of static and dynamic types may be used. In the case of a static plasma wiggler a spatially modulated plasma density results in a periodic dielectric permittivity, but pumping electromagnetic fields are absent. A dynamic plasma wiggler arises when an electromagnetic wave propagating in a plasma is scattered by an electron beam. The wave fields act on beam electrons but modulate plasma particles also. Two mechanisms are responsible for the interaction between an electron beam and electromagnetic waves. One of them is analogous to that in usual FELs and exists only in dynamic plasma wigglers. Another mechanism is conditioned by space-temporal modulation of the density and velocity of plasma particles and exist in both static and dynamic plasma wigglers. The contributions of the two mechanisms into the interaction process may be comparable. Both types of magnetized plasma wigglers are considered in a linear approximation.

## 1. Introduction

Different types of plasma wigglers may be used in free electron lasers (FELs) for amplification and generation of electromagnetic waves. In comparison with conventional FELs, a number of advantages can be realized in such wigglers. Plasma parameters can be easily changed and so parameters of plasma wigglers also can be changed easily. Plasma compensates the space charge, and more intense electron beams without decreasing their quality may be used.

Two types of plasma wigglers may exist: static and dynamic ones. The first type of plasma wigglers is made when its density is modulated in space and this modulation is stationary in time. The second type of plasma wigglers arises in the case of propagation of an intense electromagnetic wave in the plasma. This wave is a pumping wave for an electron beam and a modulator for plasma density and velocity.

In static plasma wigglers effective interaction of electron beams with fast electromagnetic waves is possible due to slow space harmonics of the wave which arise in a dielectric medium with periodic permittivity. Such a mechanism is like that in periodic slow-wave structures. In dynamic plasma wigglers two mechanisms of interaction exist. One of them is analogous to that in usual FELs and is conditioned by wave electromagnetic fields acting on beam electrons. Another mechanism is the result of space-temporal plasma modulation by a pumping wave and is the same as in static plasma wigglers.

There are several different branches of electromagnetic waves in plasma [1–5] and they can all be used as pumping waves. Some of them are slow waves with phase

velocities less than the speed of light but there are also fast waves.

The process of interaction of electron beams with amplified or generated electromagnetic waves in static and dynamic plasma wigglers can be described in a general way [6]. A static wiggler will correspond to the particular case of zero velocity of the plasma particles and zero frequency of the pumping wave.

In the present paper, the dispersion equation describing the amplification and generation of electromagnetic waves by an electron beam in an unbounded plasma wiggler is derived and analyzed. An electron beam and plasma are proposed to be strongly magnetized so that motion of their electrons is one-dimensional only in the longitudinal direction.

## 2. Basic equations

The system considered is described by the equation for the axial component of the electric field  $E_z$  and the equations of motion and continuity for electrons:

$$\left( \frac{\partial^2}{\partial x^2} + \frac{\partial^2}{\partial z^2} - \frac{\partial^2}{c^2 \partial t^2} \right) \frac{\partial E_z}{\partial t} + \left( \frac{\partial^2}{\partial z^2} - \frac{\partial^2}{c^2 \partial t^2} \right) 4\pi j_z = 0,$$

$$\frac{\partial v_{p,b}}{\partial t} + v_{p,b} \frac{\partial v_{p,b}}{\partial z} = \frac{eE_z}{(m, m\gamma^3)},$$

$$\frac{\partial n_{p,b}}{\partial t} + \frac{\partial}{\partial z} (n_{p,b} v_{p,b}) = 0, \quad (1)$$

where  $t$ ,  $z$  and  $x$  are the time and axial and transverse coordinates,  $v_{p,b}$  and  $n_{p,b}$  are the axial velocity and the

density of plasma and beam electrons respectively,  $e$  and  $m$  are the charge and mass of the electron, and  $c$  is the speed of light. The density of total current  $j_z$  is directed along the  $z$  axis and is equal to the sum of plasma and beam currents:

$$j_z = j_p + j_b = e(n_p v_p + n_b v_b). \quad (2)$$

When the pumping wave with the axial component of electric field

$$E_{z0} = \text{Re}[E_0 \exp(-i\omega_0 t + ik_0 z + i\kappa_0 x)], \quad (3)$$

where  $E_0$  is its amplitude,  $\omega_0$  is the frequency, and  $k_0$  and  $\kappa_0$  are the axial and transverse components of the wave vector, propagates in a beam-plasma system, the plasma and beam become modulated in space and time. Amplitudes of velocities and densities of the electrons can be found from linearized Eqs. (1):

$$\begin{aligned} v_{p0} &= \frac{ieE_0}{m\omega_0}, \\ v_{b0} &= \frac{ieE_0}{m\gamma^3\omega'_0}, \\ n_{p0} &= \frac{k_0}{\omega_0} \bar{n}_p v_{p0}, \\ n_{b0} &= \frac{k_0}{\omega'_0} \bar{n}_b v_{b0}, \end{aligned} \quad (4)$$

where  $\omega'_0 = \omega_0 - k_0 u$ ;  $\bar{n}_{p,b}$  and  $u$  are average values of electrons densities and the beam velocity. The following dispersion relation for the pumping wave,

$$D(\omega_0, k_0) = 1 - \frac{\omega_p^2}{\omega_0^2} + \frac{\kappa_0^2}{k_0^2 - \omega_0^2/c^2} = \frac{\omega_b^2}{\gamma^3\omega_0'^2}, \quad (5)$$

is valid, where  $\omega_{p,b} = (4\pi e^2 \bar{n}_{p,b}/m)^{1/2}$  are the Langmuir frequencies of the plasma and beam, and  $\gamma = (1 - u^2/c^2)^{-1/2}$  is the relativistic factor.

### 3. Calculation of perturbed values for plasma and beam electrons

If the electromagnetic wave propagates in a beam-plasma system together with a pumping wave, the axial component of its electric field should be written down in the form of the sum of space-temporal harmonics

$$E_{zs} = \sum_{n=-\infty}^{\infty} \text{Re}\{E_{sn} \exp[-i(\omega_s + n\omega_0)t + i(k_s + nk_0)z + i(\kappa_s + n\kappa_0)x]\}, \quad (6)$$

where  $E_{sn}$ ,  $\omega_s$ ,  $k_s$  and  $\kappa_s$  are the amplitudes of harmonics with the numbers  $n$  and frequency and components of a wave vector of an electromagnetic wave. Perturbations of velocities and densities of electrons can be presented as

analog sums, and the amplitudes of all perturbed values are coupled.

In the case of a small enough pumping wave amplitude, we may restrict consideration to only three main harmonics in sum (6) with numbers  $n = 0, \pm 1$ , because the amplitudes of other harmonics are much smaller. Let us define them with the signs “s”, “+” and “−”. Further, when the density of a beam is not too great, so that  $\omega_b^2 \ll \omega_s^2$ , it is sufficient to take into account an electron beam only in terms containing the small values  $\omega'_+$  or  $\omega'_-$  in the denominators (equations  $\omega'_\pm \approx 0$  mean the synchronism of a corresponding wave harmonic with an electron beam). With such assumptions, the following expressions for the amplitudes of the perturbed values can be obtained in a linear approximation:

$$\begin{aligned} v_{ps} &= \frac{ie}{m\omega_s} \left\{ E_s \left[ 1 + \frac{k_s}{\omega_s} \frac{|v_{p0}|^2}{4} \left( \frac{k_+}{\omega_+} + \frac{k_-}{\omega_-} \right) \right] \right. \\ &\quad \left. + \frac{k_-}{\omega_-} \frac{v_{p0}}{2} E_- + \frac{k_+}{\omega_+} \frac{v_{p0}^*}{2} E_+ \right\}, \\ v_{p\pm} &= \frac{ie}{m\omega_\pm} \left[ E_\pm + \frac{k_\pm}{2\omega_s} \left( \frac{v_{p0}}{v_{p0}^*} \right) E_s \right], \end{aligned} \quad (7)$$

$$\begin{aligned} n_{ps} &= \frac{k_s}{\omega_s} \bar{n}_p \left\{ v_{ps} \left[ 1 + \frac{|v_{p0}|^2}{4} \left( \frac{k_s}{\omega_s} + \frac{k_0}{\omega_0} \right) \left( \frac{k_+}{\omega_+} + \frac{k_-}{\omega_-} \right) \right] \right. \\ &\quad \left. + v_{p-} \frac{v_{p0}}{2} \left( \frac{k_0}{\omega_0} + \frac{k_-}{\omega_-} \right) + v_{p+} \frac{v_{p0}^*}{2} \left( \frac{k_0}{\omega_0} + \frac{k_+}{\omega_+} \right) \right\}, \end{aligned} \quad (8)$$

$$\begin{aligned} n_{p\pm} &= \frac{k_\pm}{\omega_\pm} \bar{n}_p \left[ v_{p\pm} + \frac{v_{ps}}{2} \left( \frac{v_{p0}}{v_{p0}^*} \right) \left( \frac{k_0}{\omega_0} + \frac{k_s}{\omega_s} \right) \right], \\ v_{bs} &\approx \frac{ieE_s}{m\gamma^3\omega_s'}, \\ v_{b\pm} &\approx \frac{ie}{m\gamma^3\omega'_\pm} \left[ E_\pm + \frac{k_\pm}{2\omega'_s} \left( \frac{v_{b0}}{v_{b0}^*} \right) E_s \right], \end{aligned} \quad (9)$$

$$\begin{aligned} n_{bs} &\approx \frac{ie\bar{n}_b k_s}{m\gamma^3\omega_s'^2} \left\{ E_s \left[ 1 + \frac{k_s^2 |v_{b0}|^2}{4\omega_-'^2} + \frac{k_+^2 |v_{b0}|^2}{4\omega_+'^2} \right] \right. \\ &\quad \left. + \frac{k_- \omega'_s}{\omega_-'^2} \frac{v_{b0}}{2} E_- + \frac{k_+ \omega'_s}{\omega_+'^2} \frac{v_{b0}^*}{2} E_+ \right\}, \end{aligned} \quad (10)$$

$$n_{b\pm} \approx \frac{ie\bar{n}_b k_\pm}{m\gamma^3\omega_\pm'^2} \left[ E_\pm + \frac{k_\pm}{2\omega'_s} \left( \frac{v_{b0}}{v_{b0}^*} \right) E_s \right].$$

The amplitudes of the plasma and beam current densities can be written down as

$$j_{p,bs} = en_{p,bs} \omega_s/k_s, \quad j_{p,b\pm} = en_{p,b\pm} \omega_\pm/k_\pm. \quad (11)$$



#### 4. Dispersion equation and discussion

Substituting expressions for the current densities (11) with those for the velocities and the densities of electrons (7)–(10) into Eq. (1) for the electric field, one can find the correlation between the amplitudes of harmonics  $E_{s,\pm}$  and the dispersion equation. It follows that the ratio of amplitudes of harmonics is equal to

$$\frac{E_{\pm}}{E_s} = \frac{1}{2} \left[ D(\omega_{\pm}, k_{\pm}) - \frac{\omega_b^2}{\gamma^3 \omega_{\pm}^2} \right]^{-1} \times \left[ \frac{\omega_p^2}{\omega_s \omega_{\pm} v_{\pm}} + \frac{\omega_b^2 k_{\pm} \omega_0'}{\gamma^3 \omega_{\pm}^2 \omega_s'} \right] \left( \frac{v_{p0}}{v_{p0}^*} \right). \quad (12)$$

It is convenient to write down the dispersion equation in the form

$$\left[ D(\omega_s, k_s) - \frac{\omega_b^2}{\gamma^3 \omega_s'^2} - \frac{\omega_p^2 |v_{p0}|^2}{4 \omega_s^2 V^2} \right] \left[ \omega_{\pm}^2 - \frac{\omega_b^2 \gamma^{-3}}{D(\omega_{\pm}, k_{\pm})} \right] = \frac{\alpha_{\pm}^2 \omega_b^2 |v_{p0}|^2}{4 \gamma^3 u^2}, \quad (13)$$

where the function  $D(\omega_{\pm}, k_{\pm})$  is the analog to that introduced in Eq. (5) and

$$V^{-2} = 2 \left( \frac{k_s}{\omega_s} + \frac{k_0}{\omega_0} \right) \left( \frac{k_+}{\omega_+} + \frac{k_-}{\omega_-} \right) + \left( \frac{k_+}{\omega_+} \right)^2 + \left( \frac{k_-}{\omega_-} \right)^2 + \frac{\omega_p^2}{\omega_-^2 v_-^2 D(\omega_-, k_-)} + \frac{\omega_p^2}{\omega_+^2 v_+^2 D(\omega_+, k_+)},$$

$$\alpha_{\pm} = \frac{\omega_0 k_{\pm} u}{\gamma^3 \omega_0' \omega_s'} + \frac{\omega_p^2 u}{\omega_s \omega_{\pm} v_{\pm} D(\omega_{\pm}, k_{\pm})},$$

$$\frac{1}{v_{\pm}} = \frac{k_0}{\omega_0} + \frac{k_s}{\omega_s} + \frac{k_{\pm}}{\omega_{\pm}}. \quad (14)$$

When  $D(\omega_{\pm}, k_{\pm}) \neq 0$  the dispersion equation (13) is equivalent to that of ordinary FELs [6,7]. However, the expression for  $\alpha_{\pm}$  in Eqs. (14) contains two terms of the same order conditioned by two mechanisms of interaction. The first term is determined by direct modulation of an electron beam by a pumping wave and the second is the result of plasma modulation. These two mechanisms can amplify or compensate each other and in general must be taken into account together.

An electron beam interacts with those electromagnetic waves for which

$$\omega_s \pm \omega_0 \approx (k_s \pm k_0)u, \quad D(\omega_s, k_s) \approx 0. \quad (15)$$

Because of the variety of dispersion branches for waves in plasma both synchronism conditions with positive and negative signs in Eqs. (15) can be realized while in usual vacuum FELs only that with negative sign is possible.

The dispersion equation (13) also describes induced (parametric) scattering of electromagnetic waves by the plasma without the electron beam. The conditions of such process are determined by two approximate equations

$$D(\omega_s, k_s) \approx 0, \quad D(\omega_{\pm}, k_{\pm}) \approx 0, \quad (16)$$

which must be fulfilled simultaneously. In the case of induced scattering the solution to the dispersion equation (13) demonstrates an instability without the electron beam. If the plasma-wave system is stable, the resonance conditions (16) correspond to the parametric coupling of electromagnetic and plasma waves accompanied by effective transformation of waves of different types. In the last case the presence of an electron beam and fulfillment of synchronism conditions (15) can lead to a strong beam-plasma instability where one may write down the dispersion equation (13) in form

$$D(\omega_s, k_s) \left[ D(\omega_{\pm}, k_{\pm}) - \frac{\omega_b^2}{\gamma^3 \omega_{\pm}^2} \right] = \left( \frac{\omega_p^2 v_{p0}}{2 \omega_s \omega_{\pm} v_{\pm}} \right)^2. \quad (17)$$

It follows from Eq. (17) that the amplitudes of fast and slow waves increase with the same growth rate [8,9].

For static plasma wigglers, the frequency  $\omega_0$  and the amplitude of the electric field  $E_{z0}$  above, must be replaced with zero but the inhomogeneous perturbation of plasma density  $n_{p0} = k_0 \bar{n}_p v_{p0} / \omega_0$  is finite. So, Eqs. (12)–(14) can be simplified. Only the second term in the expression for  $\alpha_{\pm}$  in Eqs. (14) is non-zero which points to the fact that only one interaction mechanism is present in such cases. In static plasma wigglers, the conditions of synchronism (15) can be fulfilled only with the negative sign, and the resonance conditions (16) for parametric induced scattering or parametric coupling of waves may not be reached, i.e.  $D(\omega_{\pm}, k_{\pm}) \neq 0$ .

#### 5. Conclusion

The interaction of electromagnetic waves with an electron beam in static and dynamic plasma wigglers can be described in a general way. The dispersion equation in such cases is similar to that for usual free electron lasers. There are two mechanisms which are responsible for the amplification and generation of waves by an electron beam in plasma wigglers: that coupled with direct effects of pumping wave fields on beam electrons and one determined by space-time modulation of the density and velocity of plasma electrons. Both these mechanisms must be taken into account.

#### References

- [1] Ya.B. Faynberg, *Fizika Plasmy* 11 (1985).
- [2] V.A. Buts, V.I. Miroshnichenko and V.V. Ognivenko, *Zhurn. Techn. Fiz.* 50 (1980) 2257.

- [3] V.A. Balakirev, *Izv. Vuzov, Radiofizika* 25 (1982) 1198.
- [4] N.I. Karbushev and V.S. Rogov, Abstracts of the 9th All-Union Conf. on Linacs of Charged Particles (1985) p. 95.
- [5] V.A. Balakirev, V.I. Miroshnichenko and Ya.B. Faynberg, *Fizika Plazmy* 12 (1986) 983.
- [6] N.I. Karbushev, V.P. Poponin and A.A. Rukhadze, in: *Generatory Kogerentnogo Izlucheniya na Svobodnykh Elektronakh*, ed. A.A. Rukhadze (Mir, Moscow, 1983) p. 224.
- [7] N.I. Karbushev and A.D. Shatkus, *Nucl. Instr. and Meth. A* 304 (1991) 559.
- [8] G.I. Batskikh, K.G. Gureev, N.I. Karbushev and A.I. Lisitsyn, *Proc. 8th Int. Conf. on High-Power Particle Beams*, Vol. 2 (1990) p. 1173.
- [9] N.I. Karbushev, *Izv. Vuzov, Radiofizika* 34 (1991) 825.



ELSEVIER

## Ultra-short pulse free electron laser oscillators

J. Blau<sup>\*</sup>, R.K. Wong, W.B. Colson

*Physics Department, Naval Postgraduate School, Monterey, California, USA*

### Abstract

An RF linear accelerator can produce ultra-short electron pulses on the order of a picosecond. In a long wavelength FEL, the pulse length can be much less than the slippage distance. Simulations show the effects of such short pulses on weak-field gain, saturated power, and optical pulse structure.

In a free electron laser (FEL) oscillator, the steady state optical pulse length depends on the electron pulse length, but it can be shorter or longer. Other factors such as the cavity  $Q$  and desynchronism affect the steady state optical pulse shape. The FEL weak-field gain and saturated power also depend on the electron pulse length.

It is important to compare the electron pulse length to the slippage distance,  $N\lambda$ , where  $N$  is the number of undulator periods and  $\lambda$  is the optical wavelength. This corresponds to the distance that the slower-moving electron pulse slips back relative to the optical pulse over one pass through the undulator. The slippage distance is typically a few hundred microns, but for a long wavelength FEL it can be greater than a millimeter.

When the electron micropulse length  $l_e$  is less than or equal to the slippage distance, short pulse effects dominate the FEL interaction [1]. Reduced overlap between the electron and optical pulses decreases the weak-field gain. The electron pulse amplifies the trailing edge of the optical pulse, reducing its effective group velocity, and the optical pulse drifts away from the electron pulse over many passes. To counteract this lethargy, the optical cavity length  $S$  is shortened by a desynchronism distance,  $d = \Delta S/N\lambda$ . If  $d$  is too large, the optical pulse eventually moves ahead of the electron pulse and decays according to the cavity  $Q$ , resulting in a broad optical pulse with small amplitude. When  $d$  is much smaller, the optical power can be large, and the optical pulse may be modulated due to the trapped particle instability [1].

An RF linac, such as the Stanford SCA, can produce ultra-short electron micropulses, with length  $l_e \leq 1$  mm. For an FEL operating in the mid to far-IR, this pulse length can be much less than the slippage distance. In that

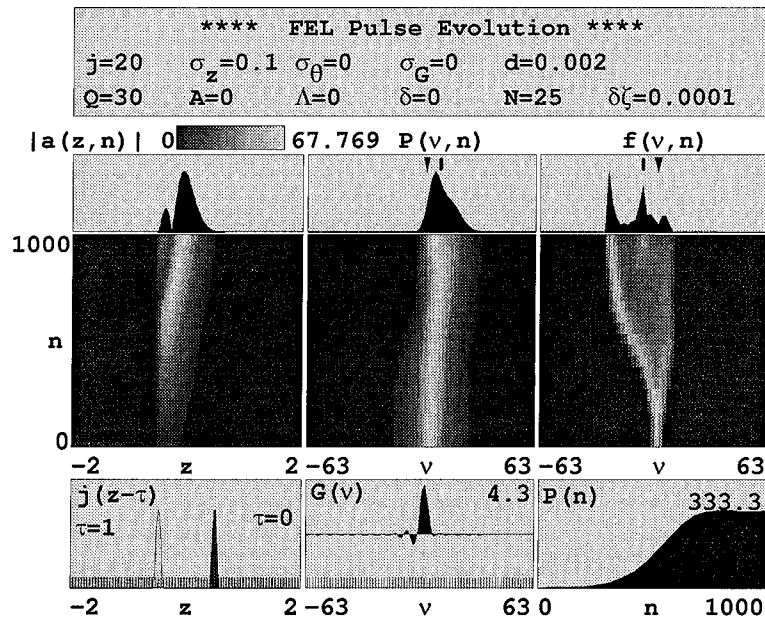
case, the dimensionless electron pulse length  $\sigma_z = l_e/N\lambda \ll 1$ . For example, the FOM FELIX [2] and the Stanford FIREFLY [3] experiments propose to use  $\sigma_z \approx 0.1$ –1.0.

Fig. 1 shows the results of a longitudinal multi-mode simulation of an ultra-short pulse FEL with  $\sigma_z = 0.1$ . The chosen desynchronism was  $d = 0.002$ , and the cavity  $Q = 30$ . The simulation was run for 1000 passes. The power evolution  $P(n)$  is shown in the lower-right corner. The graph in the lower-left corner shows the electron pulse current density  $j(z)$  at the beginning ( $\tau = 0$ ) and end ( $\tau = 1$ ) of the undulator, displaced by the slippage length  $\Delta z = 1$ . Above is an intensity plot of the optical pulse evolution  $|a(z, n)|$ , with the scale shown at the top. In the upper-left is the final optical pulse  $|a(z)|$ , which is longer than the electron pulse length, but shorter than the slippage distance. In the middle is shown the weak-field gain spectrum  $G(\nu)$ , the evolution of the optical power spectrum  $P(\nu, n)$ , and the final spectrum  $P(\nu)$ . On the right is shown the evolution of the electron spectrum  $f(\nu, n)$ .

The optical pulse evolution  $|a(z, n)|$  shows a primary pulse moving ahead due to the desynchronism. As the power grows, the electrons overbunch, causing absorption of light on the trailing edge of the pulse. Meanwhile, a new smaller pulse begins to form and grow behind the primary pulse. If the simulation was carried out farther, it would show a train of subpulses forming, advancing according to the desynchronism, and decaying according to the  $Q$ . This would also cause an oscillation of the optical power  $P(n)$ . Such limit cycle behavior has been observed in previous simulations and experiments [4,5].

Fig. 2 shows the results of another simulation with a smaller desynchronism  $d = 0.0002$  and a larger  $Q = 100$ . The final optical pulse  $|a(z)|$  is now about the same length as the electron pulse  $j(z)$ , and much shorter than the slippage distance. Since the optical pulse is so short, the electron pulse does not “see” much of the light until it is more than halfway down the undulator, leaving less time

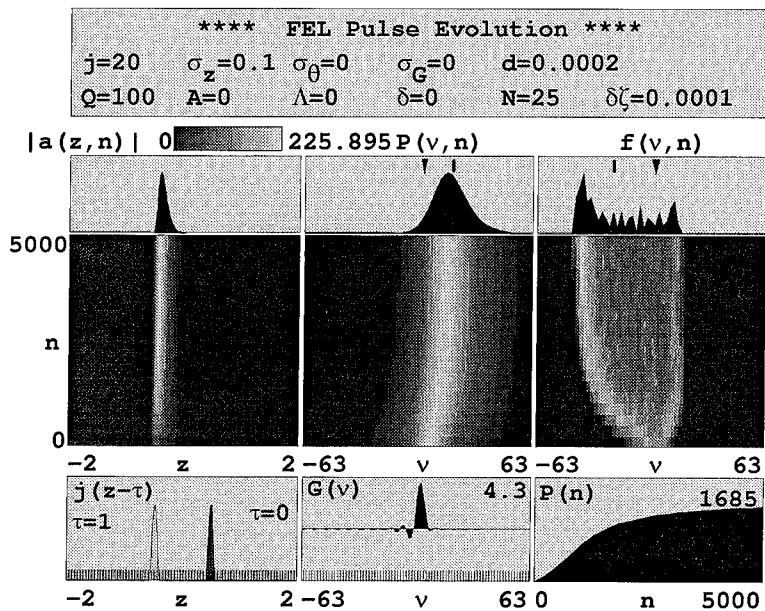
<sup>\*</sup> Corresponding author. Tel. +1 408 656 2886, fax +1 408 656 2834, e-mail: blau@nps.navy.mil.

Fig. 1. Multi-pass evolution of an ultra-short pulse oscillator,  $Q = 30$ .

for bunching and gain. However, the large dimensionless current density  $j = 20$  allows bunching and gain to develop quickly, and the optical field grows to a large amplitude.

Fig. 3 shows the weak-field gain versus the electron pulse length, for fixed  $Q = 30$  and various values of desynchronism  $d$ . The total microbunch charge  $j\sigma_z = 2$  is kept constant as the pulse length  $\sigma_z$  is reduced. It might be

expected that the gain would remain constant, or even decrease slightly, as the pulse length is reduced, because of reduced pulse overlap. However, the simulations show that the gain actually increases slightly as the pulse length is reduced. This was also predicted in previous simulations done at FOM FELIX [6]. Here we show that the trend remains the same as desynchronism is varied, although the slope is greater as  $d$  is increased.

Fig. 2. Multi-pass evolution of an ultra-short pulse oscillator,  $Q = 100$ .

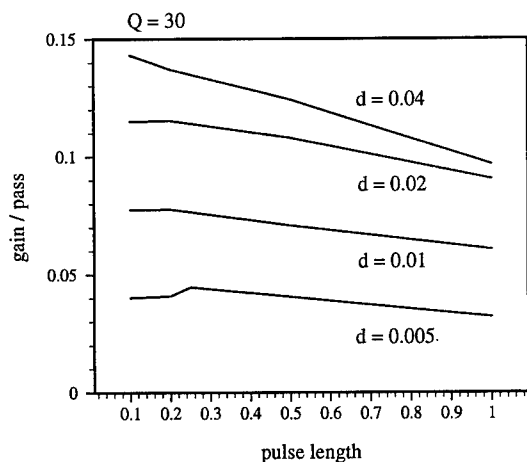


Fig. 3. Weak-field gain versus pulse length, for various values of desynchronism  $d$ .

Fig. 4 shows the saturated power versus electron pulse length, for  $Q = 30$ . Again, the total micropulse charge is kept constant as the pulse length is reduced. The desyn-

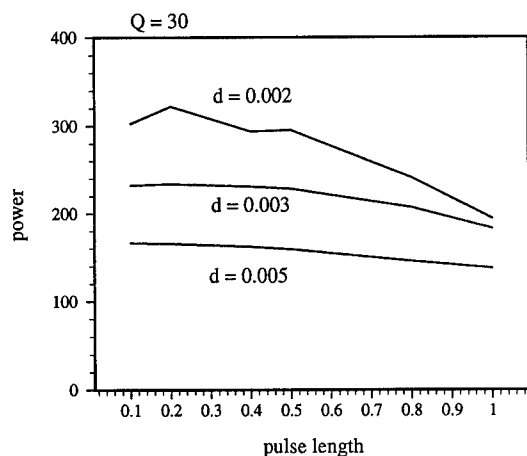


Fig. 4. Saturated power versus pulse length, for various values of desynchronism  $d$ .

chronism values shown here are smaller than the previous figure, because the optimum desynchronism is smaller when the field has reached saturation. For values of desynchronism  $d > 0.003$ , the saturated power is approximately constant as the pulse length is varied, in agreement with previous results [7]. However, when the FEL is operated near the peak of the desynchronism curve,  $d = 0.002$ , the power actually increases as the pulse length is reduced. The ripples in the curve are due to saturation and limit cycle effects.

A comparison was also made of parabolic and Gaussian electron pulses. For short pulses ( $\sigma_z \leq 1$ ), there was very little change in the final saturated power and optical pulse shape.

### Acknowledgements

The authors are grateful for support of this work by the Naval Postgraduate School, Stanford University (N00014-91-C-0170), and SURF/CEBAF.

### References

- [1] W.B. Colson, in: *Free Electron Laser Handbook*, eds. W.B. Colson, C. Pellegrini and A. Renieri (Elsevier, Amsterdam, 1990) chap 5.
- [2] P.W. van Amersfoort et al., *Nucl. Instr. and Meth. A* 318 (1992) 42.
- [3] T.I. Smith et al., presented at this Conference (16th Int. Free Electron Laser Conf., Stanford, CA, USA, 1994).
- [4] D.A. Jaroszynski et al., *Nucl. Instr. and Meth. A* 331 (1993) 52.
- [5] G.A. Cord, W.B. Colson and J. Frisch, *Nucl. Instr. and Meth. A* 304 (1991) 601.
- [6] D.A. Jaroszynski et al., *Nucl. Instr. and Meth. A* 296 (1990) 480.
- [7] D.A. Jaroszynski et al., *Nucl. Instr. and Meth. A* 318 (1992) 582.



ELSEVIER

## Stimulated radiation from an electron beam traversing an inhomogeneous electromagnetic wave

A.V. Koltsov <sup>\*</sup>, A.V. Serov

*P.N. Lebedev Physical Institute Russia Academy of Science, Leninsky Prospect 53, Moscow, Russian Federation*

### Abstract

The time variation of the spatial distribution of an electron beam reflected by an inhomogeneous wave was investigated. The injected beam is perpendicular to the direction of propagation of the wave. The stimulated radiation of the electron beam is calculated. The angular distribution of the radiation and the power density are obtained.

This paper considers the motion and the radiation of electrons in an inhomogeneous electromagnetic wave. To fully describe this process, it is necessary first to determine the electron motion in the field of the wave, and then to calculate the growth of the radiation which results from the electrons moving along given trajectories. The interaction between an electron beam and an electromagnetic wave not only produces electron oscillations but also substantially changes the electron phase and energy distributions. These distributions are responsible for determining the efficiency with which electron energy is converted into radiation.

In order to describe the electron dynamics, the Lorentz force equations are solved for an electron in the electromagnetic wave. When a wave is inhomogeneous, attention is paid to the gradient forces that accompany the motion of particles in a high-frequency inhomogeneous field [1]. When the strength of the electric field of the electromagnetic wave becomes sufficiently high, the electrons are decelerated and reflected backward. The condition for reflection is  $E > \sqrt{2} \pi m c v / e \lambda$ , where  $e$  and  $m$  are the charge and the mass of the particle,  $v$  is the initial particle velocity,  $\lambda$  is the wavelength, and  $c$  is the speed of the light [2]. We have investigated this strong field case. The motion of an electron in an inhomogeneous wave consists of a slow displacement along a smooth path accompanied by simultaneous rapid oscillations with a period  $T = \lambda / c$  relative to this path.

Suppose we have a linearly polarized electromagnetic beam propagating in the  $z$  direction. Let its cross section be a circle of radius  $d$ . The vector potential of the wave  $A$  has only a  $y$  component and can be represented as  $A = (A_x, A_y, A_z) = (0, A_0(x/d) \cos(\omega t - kz), 0)$ , where  $A_0$  is the vector potential amplitude,  $k = 2\pi/\lambda$ ,  $\omega = kc$ . The plane beam of particles with a width  $L$  enters the wave at right angles with respect to the direction of propagation of the wave and the vector  $A$  (see Fig. 1). We assume that the particles are initially uniformly distributed in phase, and we assume a monoenergetic energy distribution. In Ref. [3] it is shown that interaction of an electron with the field of a wave leads to energy and velocity modulation, the process being dependent on the phase of the wave at the time of electron impact on the wave. After a short time, the more-energetic electrons catch up the less-energetic ones, and the electron beam which initially consisted of randomly distributed electrons soon consists of bunches of electrons.

We shall suppose that the initial particle velocity  $v$  is small compared to the speed of the light. In this case the equations of motion are

$$\begin{aligned}\ddot{x} &= -\frac{1}{2} \left( \frac{eA}{mcd} \right)^2 x (1 + \cos 2(\omega t - kz_0)), \\ \dot{y} &= -\left( \frac{eA}{mcd} \right) x \cos(\omega t - kz_0), \\ \ddot{z} &= -\frac{1}{2} \left( \frac{eA}{mcd} \right)^2 x^2 k \sin 2(\omega t - kz_0).\end{aligned}\tag{1}$$

<sup>\*</sup> Corresponding author.

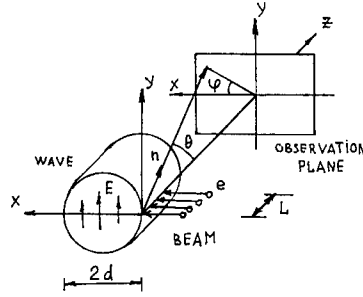


Fig. 1. Wave geometry and coordinate system for analysis of electron motion and induced radiation.

The initial conditions for the time  $\tau$  of the injection of the particles into the wave are given by the expressions  $x = y = 0$ ,  $z = z_0$ ,  $\dot{y} = \dot{z} = 0$ ,  $\dot{x} = v$  at  $t = \tau$ . The solution for the velocities is

$$\begin{aligned}\dot{x} &= v \cos \Omega(t - \tau) \left( 1 + \frac{1}{4} \epsilon^2 (\cos 2(\omega t - kz) - \cos 2(\omega \tau - kz_0)) \right) - \frac{1}{2} v \epsilon \sin \Omega(t - \tau) \sin 2(\omega t - kz), \\ \dot{y} &= -\sqrt{2} v \sin \Omega(t - \tau) \cos(\omega t - kz) \left( 1 + \frac{1}{4} \epsilon^2 (\cos 2(\omega t - kz) - \cos 2(\omega \tau - kz_0) - \frac{1}{4}) \right), \\ \dot{z} &= \frac{v^2}{2c} \left( \left[ 1 - \frac{1}{8} \epsilon^2 \right] \cos 2(\omega t - kz) \sin^2 \Omega(t - \tau) - \frac{1}{2} \epsilon \sin 2(\omega t - kz) \sin 2\Omega(t - \tau) \right. \\ &\quad \left. - \frac{1}{2} \epsilon^2 \cos 2(\omega t - kz) \cos 2\Omega(t - \tau) + \frac{1}{2} \epsilon^2 \cos 2(\omega \tau - kz_0) - \frac{1}{2} \epsilon^2 \cos 2(\omega t - kz) \right. \\ &\quad \left. \times \sin^2 \Omega(t - \tau) \cos 2(\omega \tau - kz_0) + \frac{1}{8} \epsilon^2 \cos 2(\omega t - kz) \sin^2 \Omega(t - \tau) \right)\end{aligned}\quad (2)$$

and the solution for the coordinates is

$$\begin{aligned}x &= \frac{v}{\Omega} \sin \Omega(t - \tau) \left( 1 + \frac{1}{4} \epsilon^2 (\cos 2(\omega t - kz) - \cos 2(\omega \tau - kz_0)) \right), \\ y &= -\sqrt{2} \frac{v}{\omega} \left( \left( 1 + \frac{15}{16} \epsilon^2 \right) \sin \Omega(t - \tau) \sin(\omega t - kz) + \epsilon (\cos \Omega(t - \tau) \cos(\omega t - kz) - \cos(\omega \tau - kz_0)) \right. \\ &\quad \left. + \frac{1}{8} \epsilon^2 \sin \Omega(t - \tau) (\sin(\omega t - kz) \right. \\ &\quad \left. + \frac{1}{3} (\sin 3(\omega t - kz)) - \frac{1}{4} \epsilon^2 \sin \Omega(t - \tau) \sin(\omega t - kz) \cos 2(\omega \tau - kz_0)) \right),\end{aligned}\quad (3)$$

where

$$\Omega^2 = \frac{1}{2} \left( \frac{eA}{mcd} \right)^2 \left[ 1 + \frac{1}{16} \left( \frac{eA}{mcd\omega} \right)^2 \right],$$

$\epsilon = \Omega/\omega$ . The change of the coordinate  $z$  may be neglected, as it is small compared with the wavelength  $\lambda$ .

To describe the distribution function of the beam particles depending on the spatial coordinates and time, it is necessary to calculate the value of the derivative  $\partial x(t, \tau)/\partial \tau$ . The absolute value  $|(1/v)(\partial x/\partial \tau)|$  gives a change in the length of the very small bunch injected in the time  $\tau$ . The electron density is defined by the formula

$$\rho(t) = \rho_0(\tau) \left| \frac{1}{v} \frac{\partial x}{\partial \tau} \right|^{-1},$$

where  $\rho_0(\tau)$  is initial electron density. Differentiation (3) with respect to  $\tau$  gives the following formula

$$\frac{\partial x}{\partial \tau} \propto -\cos \Omega(t - \tau) + \frac{1}{2} \epsilon \sin \Omega(t - \tau) \sin 2(\omega \tau - kz_0) \propto \cos \left[ \Omega(t - \tau) + \frac{1}{2} \epsilon \sin 2(\omega \tau - kz_0) \right]. \quad (4)$$

Fig. 2 shows the dependence of the electron density on the distance  $x/x_0$ , where  $x_0$  is the coordinate of the point of reflection obtained for  $z_0 = 0$  and for different times. It follows from Fig. 2 that the electron density in the wave is  $\sim 100$  times larger than the initial electron density. Stimulated radiation from the electrons is strongest in this the part of the wave.

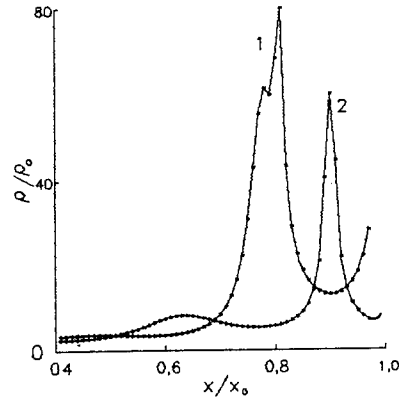


Fig. 2. Electron density distribution.  $x_0$  is the coordinate of the point of reflection; (1)  $t = t_0$ , (2)  $t = t_0 + (\lambda/4c)$ ;  $\epsilon = 0.2$ .

To consider the spectrum of the radiation observed at a large distance from the electron it is necessary to introduce the solution for the particle velocities (2) and coordinates (3) into the radiation formula [4]. After that the spectral-angular intensity distribution of the radiation emitted by accelerated electron is

$$\frac{dI_{\sigma,\pi}}{dO} = \rho_0^2 \frac{(n\omega)^2}{\pi c^3} \frac{\sin^2(nLk(1-n_z)/2)}{(nk(1-n_z))^2} |(M(n\omega) + iN(n\omega), e_{\sigma,\pi})|^2, \quad (5)$$

where  $dI/dO$  is the total energy radiated per unit solid angle,  $\mathbf{n}$  is a unit vector specifying the observation direction ( $\mathbf{n} = (n_x, n_y, n_z) = (\sin \theta \cos \varphi, \sin \theta \sin \varphi, \cos \theta)$ ),  $n$  is the harmonic number,  $n = 1, 2, 3, \dots, e_\sigma$  and  $e_\pi$  are the vector of polarization of the wave. The components of the vector  $\mathbf{M}$  and  $\mathbf{N}$  are given by the expression for the frequency  $\omega$

$$M_x(\omega) = \sqrt{2} \frac{v^2}{c\Omega} \int_0^\pi \exp\left(-in_x \frac{1}{\epsilon} \frac{v}{c} \sin p\right) in_y \epsilon \left( \cos p \left[ \cos p - \cos \frac{1}{\epsilon} p \right] - \frac{1}{4} \sin^2 p \right) dp,$$

$$M_y(\omega) = -\sqrt{2} \frac{v}{\Omega} \int_0^\pi \exp\left(-in_x \frac{1}{\epsilon} \frac{v}{c} \sin p\right) \left( 1 + \frac{1}{16} \epsilon^2 - in_x \frac{1}{8} \frac{v}{c} \epsilon \sin p \right) \sin p dp,$$

$$N_x(\omega) = -\sqrt{2} \frac{v^2}{c\Omega} \int_0^\pi \exp\left(-in_x \frac{1}{\epsilon} \frac{v}{c} \sin p\right) in_y \epsilon \cos p \sin \frac{1}{\epsilon} p dp,$$

$$M_z(\omega) = N_y(\omega) = N_z(\omega) = 0;$$

for the frequency  $2\omega$

(6)

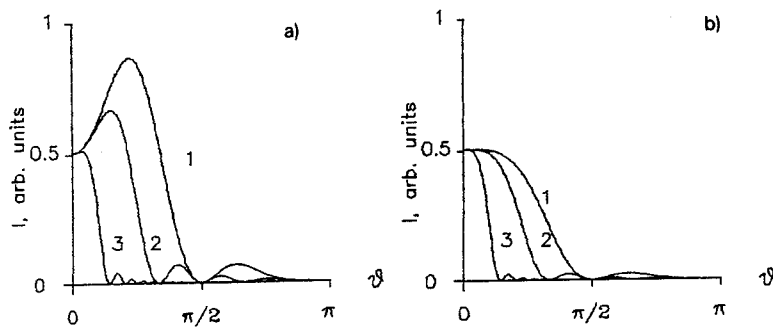


Fig. 3. Angular distribution of  $\sigma$ -component of the radiation in the frequency  $2\omega$ . (a)  $\varphi = 0$ , (b)  $\varphi = \pi/2$ ; (1)  $L = 0.5\lambda$ , (2)  $L = \lambda$ , (3)  $L = 5\lambda$ .



$$M_z(2\omega) = \frac{v^2}{2c\Omega} \int_0^\pi \exp\left(-in_x 2\frac{1}{\epsilon} \frac{v}{c} \sin p\right) \left\{ \left(I + \frac{7}{8}\epsilon^2\right) \sin^2 p - \frac{1}{2}\epsilon^2 \right\} dp,$$

$$N_x(2\omega) = -\frac{1}{2} \frac{v}{\Omega} \int_0^\pi \exp\left(-in_x 2\frac{1}{\epsilon} \frac{v}{c} \sin p\right) \epsilon \sin p dp,$$

$$N_y(2\omega) = -2\frac{v}{\Omega} \frac{v}{c} \int_0^\pi \exp\left(-in_x 2\frac{1}{\epsilon} \frac{v}{c} \sin p\right) in_y \left(1 + \frac{25}{24}\epsilon^2\right) \sin^2 p dp,$$

$$M_x(2\omega) = M_y(2\omega) = N_z(2\omega) = 0.$$

The angular distribution of the  $\sigma$ -component of the radiation for frequency  $2\omega$  is shown in Fig. 3. The distribution was obtained by computation using Eqs. (5) and (6).

### Acknowledgement

The authors are grateful to B.M. Bolotovskii for the useful discussion of the results obtained.

### References

- [1] L.D. Landau and E.M. Lifshitz, *The Classical Theory of Fields* (Pergamon, New York, 1975).
- [2] I.R. Gekker, *Interaction of Strong Electromagnetic Fields with Plasma* (Atomizdat, Moscow 1978) in Russian.
- [3] A.V. Serov, *Kratk. Soobshch. Po Physike FIAN*, N1-2, 31 (1994) (translated by Allerton Press: *Bulletin of the Lebedev Physics Institute*).
- [4] J.D. Jackson, *Classical Electrodynamics* (Wiley, New York, NY, 1975).



ELSEVIER

# Self-oscillations and chaos of free-electron laser oscillators with space charge effects

E.H. Park <sup>a</sup>, J.K. Lee <sup>a,\*</sup>, T.H. Chung <sup>b</sup>

<sup>a</sup> Department of Physics, Pohang University of Science and Technology, Pohang 790-784, South Korea

<sup>b</sup> Department of Physics, Dong-A University, Pusan 604-714, South Korea

## Abstract

We investigate the thresholds of periodic and chaotic oscillations in a free-electron laser oscillator by using self-consistent time-dependent one-dimensional Maxwell–Lorentz equations. We consider a Raman-like case where the space charge effects are pronounced. From the parameter dependence of the limit-cycle oscillation frequency, we modify the previous fitting formulas and specify the regimes for the periodic limit-cycle oscillation and for the chaotic oscillation.

## 1. Introduction

The free-electron laser oscillator, due to its open nature, is a nonlinear dissipative system. In this system, the balance between lethargy and desynchronism plays an important role for effectively overlapping the radiation and the electron beam. The laser lethargy is a well-known effect due to the slippage in the FEL [1]. In the free-electron laser oscillator system, dissipative chaos is possible. The chaos [2–6] arises due to the inherent open nature in multimode free-electron laser oscillators. The dissipative chaos involves the self-consistent action and reaction of the electrons and the radiation in an FEL oscillator.

In previous work on the FELIX system [7], considering the slippage and the cavity detuning, we investigated bifurcation and chaotic transitions [8]. Through self-consistent FEL simulations for varying electron beam currents (but neglecting the space charge effects), we found the chaotic transition routes [9] via period-doubling cascade, intermittency, and quasiperiodicity in a free-electron laser. We observed a weak dependence of various oscillation thresholds [8] on the slippage; namely, the slippage parameter does not directly influence the nonlinear dynamic structures of the system.

In this work, by considering other parameters influencing the dynamic behavior, we examine the thresholds of the periodic and chaotic oscillations. This is done, for example, by varying the cavity detuning and by varying the limit-cycle oscillation frequency as a function of the

principal branching parameter [8] and compare the results with the frequency formula [10] found for the FELIX system. To consider the space charge effect, our model case involves a Raman-like FEL parameter with varying currents.

With the space charge effect [11], our time-dependent equations are

$$\left( \frac{\partial}{\partial z} + \frac{1}{v_{\parallel}} \frac{\partial}{\partial t} \right) \gamma_j = - \frac{k_s a_s a_w}{\gamma_j} \sin \psi_j - \frac{4\eta k_s}{(k_w + k_s)} \times [\langle \sin \psi \rangle \cos \psi_j - \langle \cos \psi \rangle \sin \psi_j],$$

$$\left( \frac{\partial}{\partial z} + \frac{1}{v_{\parallel}} \frac{\partial}{\partial t} \right) \theta_j = k_w - k_s \frac{1 + a_w^2}{2\gamma_j^2},$$

$$\left( \frac{\partial}{\partial z} + \frac{1}{c} \frac{\partial}{\partial t} \right) a_s e^{i\phi_s} = i\eta a_w \left\langle \frac{e^{-i\theta}}{\gamma} \right\rangle,$$

where  $a_w$  is the normalized wiggler parameter ( $\equiv e\lambda_w B_w / (2\pi mc)$ ),  $B_w$  is the wiggler magnetic field strength,  $c$  is the speed of light in vacuum,  $k_w$  ( $= 2\pi/\lambda_w$ ) is the wiggler wavenumber,  $\lambda_w$  is the wavelength of wiggler field,  $a_s$  is the normalized radiation amplitude ( $\equiv e\lambda_s E_s / (2\pi mc^2)$ ),  $E_s$  is the electric field of radiation,  $k_s = 2\pi/\lambda_s$  is the wavenumber of radiation,  $\lambda_s$  is the wavelength of radiation,  $\phi_s$  is the phase of radiation,  $\theta(z, t) = (k_w + k_s)z - \omega t$ ,  $\psi = \theta + \phi_s$  is the ponderomotive phase,  $\omega_p = \sqrt{n_e e^2 / (m\epsilon_0)}$  is the plasma frequency,  $n_e$  is the total electron number density, and  $\eta = \omega_p^2 / 2k_s c^2$ .

\* Corresponding author. Tel. +82 562 279 2083, fax +82 562 297 3099, e-mail: jkl@vision.postech.ac.kr.

## 2. Thresholds of periodic and chaotic oscillations

In describing the thresholds of periodic and chaotic oscillations, we use the dimensionless branching parameters [8], the slippage parameter  $S(=L_s/L_e)$  and the cavity detuning parameter  $D(=\delta L/\lambda_s)$ . Here,  $L_s$  is a slippage distance ( $=N_w\lambda_s$ ,  $N_w$  is the number of the wiggler period),  $L_e$  is the electron pulse length,  $\lambda_s$  is the radiation wavelength, and  $\delta L$  is the cavity detuning length. The parameters used in our work are:  $\gamma$ (relativistic Lorentz factor) = 7.6,  $a_w = 0.354$ ,  $\lambda_w = 6$  cm,  $\lambda_s = 600$   $\mu$ m,  $L_s = 36\lambda_s$ ,  $L_e = 30\lambda_s$ , and the total cavity loss parameter of the FEL oscillator  $R = 0.05$ . In our system with varying currents for pronounced space charge effects, the electron energy is much smaller than the FELIX parameter [7] for a Compton FEL.

Fig. 1 shows the thresholds of the periodic and the chaotic oscillations as the cavity detuning increases, for the cases without and with the space charge effect in the parameter space  $D$  and  $\mu$ . The parameter  $\mu$  is defined as  $L_s/L_{syn}$ , where  $L_{syn}$  is a slippage distance in a synchrotron period. It represents the strength of nonlinear coupling between electrons and radiation. In this simulation,  $S = 1.2$ , which corresponds to a short pulse case. We observe, in Fig. 1, that the threshold lines for periodic oscillations (above which periodic oscillations such as the limit-cycle oscillations [7,8] appear) are not affected by the space charge effect. We have also examined the threshold line for chaotic oscillations. As the current increases, the plasma density becomes large and the space charge effect becomes more pronounced. We note in Fig. 1 that the case with the space charge effect becomes chaotic for smaller currents than the case without the space charge effect. As the cavity detuning is increased, this transition to chaos occurs at a

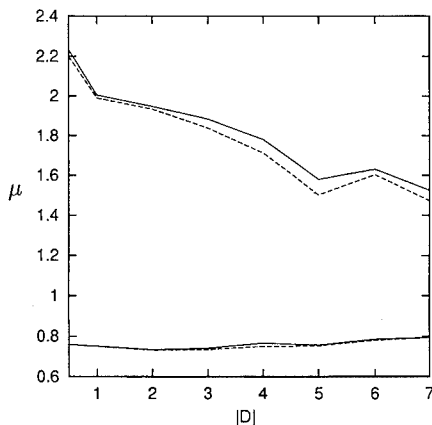


Fig. 1. The thresholds for periodic and chaotic regimes. The solid lines denote the thresholds for the case without the space charge effect and the dotted lines for the case with it.

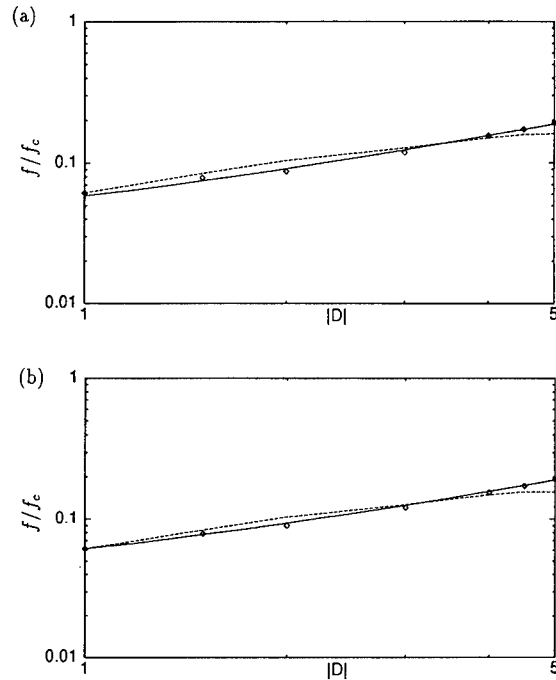


Fig. 2. The comparison between the modified frequency formula and the simulation results for varying cavity detuning. Here,  $S = 1.2$  and  $I = 10$  A for the case (a) without the space charge effect and (b) with it.

smaller value of  $\mu$ , implying an increased nonlinearity of the system.

## 3. The dependence of the oscillation frequency on $\mu$

Fig. 2 shows the frequency dependence on detuning. We modified the previous formulas [7,10] that a coefficient is slightly different from the original formula for better fitting. The modified Jaroszynski [7] formula is  $f/f_c = \sqrt{2}|D|/N_w$  and the modified Hahn formula [10] is  $f/f_c = \sqrt{2}|D|\mu/N_w$ . Here,  $f_c$  is the cavity round trip frequency of the radiation. In Fig. 2, as the cavity detuning varies, the frequency increases linearly. The points denote the results of simulations and the dotted line denotes the values calculated with the modified Hahn formula. The reasonable agreement between the two emphatically demonstrates the linear scaling of the limit-cycle oscillation frequency on  $D$ .

However, Fig. 3 shows that the frequency depends nonlinearly on  $\mu$ . In Fig. 3, the flat lines denote the calculated results with the modified Jaroszynski formula, and the linearly increasing lines with the modified Hahn formula. In a certain region usually for smaller values of  $\mu$ , the modified Jaroszynski formula provides a good fit with the simulation results, while in other region for larger values of  $\mu$  the modified Hahn formula provides a better

fit. As the cavity detuning increases, the modified Hahn formula's fit with simulation results diminishes and the space charge effect becomes more pronounced. For the  $D = -1.0$  case, by using various diagnostic tools, such as Poincare map, Poincare section, and time series of efficiency, we observe the chaotic oscillations in the region  $1.1 < \mu < 1.3$ .

A mode-locked state is when the winding number equals a rational number and the quasiperiodic states are referred to as those with irrational winding numbers [9]. A chaotic state is when the winding number is not defined. In quasiperiodic region, many periodic and quasiperiodic states exist. In describing the route from the mode-locked to quasiperiodic region, the ratio of the frequency of mode-locked state to that of quasiperiodic region is important. As the cavity detuning parameter  $|D|$  increases from 1 to 3, a degree of the square root behavior is decreased and the linear behavior is increased, and a chaotic state, which is between from the mode-locked to quasiperiodic region  $D = -1.0$  case, disappears for the  $D = -2.0$  and  $-3.0$  cases. As the cavity detuning increases, we expect as in Fig. 3 that a chaotic region, which is between from the mode-locked to quasiperiodic region, becomes narrower.

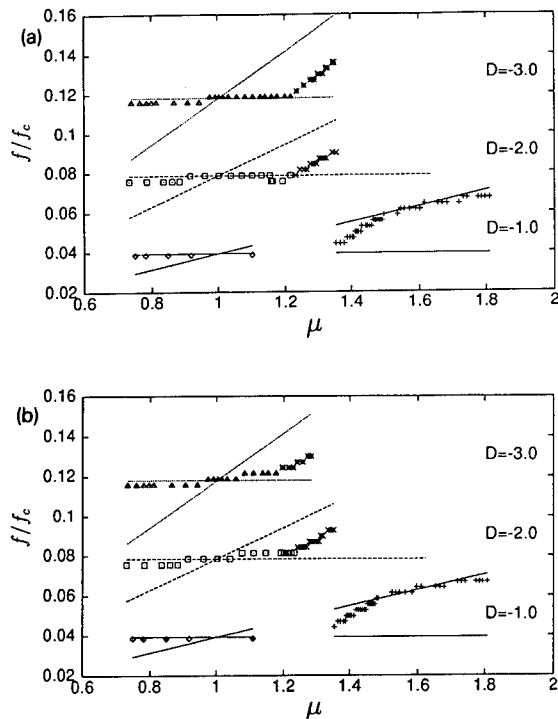


Fig. 3. The frequency  $f$  (normalized to the cavity round trip frequency) of the periodic oscillations for three values of cavity detuning,  $D = -1, -2$ , and  $-3$ .  $S$  is fixed at 1.2 and the linear lines denote the modified Hahn formula, while the flat lines represent the results from the modified Jaroszynski formula for the case (a) without the space charge effect and (b) with it.

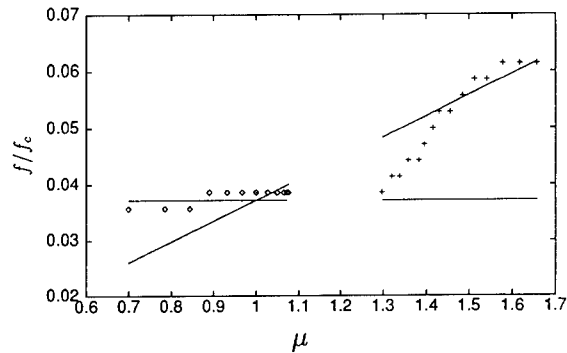


Fig. 4. The main frequency for the FELIX case with  $S = 1.267$  and  $D = -1$ .

Fig. 4 shows the frequency as a function of  $\mu$  for the FELIX system [7,8], where the space charge effect is not significant. Our new modified formulas fit certain regimes of  $\mu$  in a fashion similar to our Raman FEL cases in Fig. 3.

#### 4. Discussion

Through self-consistent time-dependent simulations for a Raman FEL with space charge effects, we have shown global parameter regimes where the periodic and the chaotic oscillations appear. This regime classification is related to the dependences of the oscillation frequencies on various parameters such as the cavity detuning and  $\mu$ .

Our simulation results (both for a Raman and a Compton FEL cases) show that the frequency depends linearly on  $D$  and nonlinearly on  $\mu$ , and that two previous formulas with some modifications fit various regimes.

#### Acknowledgements

We thank Prof. S. Kim and Dr. S.J. Hahn for useful discussions. This work was supported by Research Institute of Science and Technology, Pohang, Korea.

#### References

- [1] H. Al-Abawi, F.A. Hopf, G.T. Moore and M.O. Scully, Opt. Commun. 30 (1979) 235;
- W.B. Colson and A. Renieri, J. Phys. (Paris) Colloq. 44 (1983) C1.
- [2] C. Chen and R.C. Davidson, Phys. Rev. A 43 (1991) 5541.
- [3] L. Michel, A. Bourdier and J.M. Buzzi, Nucl. Instr. and Meth. A 304 (1991) 465.
- [4] G. Spindler and G. Renz, Nucl. Instr. and Meth. A 304 (1991) 492.
- [5] S. Riyopoulos and C.M. Tang, Phys. Fluids 31 (1988) 3387.

- [6] L. Michel, A. Bourdier and J.M. Buzzi, *Phys. Fluids B* 5 (1993) 965.
- [7] D.A. Jaroszynski, R.J. Bakker, D. Oepts, A.F.G. van der Meer and P.W. van Amersfoort, *Nucl. Instr. and Meth. A* 331 (1993) 52; *Phys. Rev. Lett.* 70 (1993) 3412.
- [8] S.J. Hahn, J.K. Lee, E.H. Park and T.H. Chung, *Nucl. Instr. and Meth. A* 341 (1994) 200.
- [9] H.G. Schuster, *Deterministic Chaos: An Introduction* (VCH Verlagsgesellschaft, 1989).
- [10] S.J. Hahn and J.K. Lee, *Phys. Lett. A* 176 (1993) 339; *Phys. Rev. E* 48(3) (1993) 2162.
- [11] H.S. Kim, S.J. Hahn and J.K. Lee, *J. Phys. Soc. Jpn.* 62(7) (1993) 2334;  
T.H. Chung and J.K. Lee, *ibid.*, p. 2501;  
T.H. Chung, H.S. Kim and J.K. Lee, *Nucl. Instr. and Meth. A* 331 (1993) 482.

## Features of operation of a FEL with reversed guide field

A.A. Silivra <sup>\*</sup>, I.A. Goncharov

*Physics Faculty of Kiev University, Kiev, Ukraine*

### Abstract

Features of the nonlinear regime of a FEL with reversed guide field operating in the millimeter wavelength range have been studied numerically by particle techniques. The FEL efficiency for both conventional and reversed guide fields for the case in which the simulating particles were on a steady state trajectory at the entrance to the interaction region was rather high. Taking into account a significant spread of the transverse electron impulses which exists in the experiment due to, for example, a nonadiabatic wiggler field increase at the entrance to the FEL interaction region results in a significant decrease of efficiency for the FEL with conventional guide field orientation while it remains practically unchanged for the FEL with reversed guide field.

For the FEL parameters close to the experimental ones an analysis of electron motion shows that for reversed guide field the period and amplitude of betatron oscillations are significantly less than for the conventional guide field case. Most likely, that is the reason which leads to the substantial changing of the interaction in the two cases.

A FEL with reversed guide field was proposed in Ref. [1], where, in particular, a dispersion equation for such a FEL was derived taking into account steady state trajectories and both polarizations (right- and left-hand) of interacting waves. Although from linear theory there were no considerable differences between the reversed guide field FEL configuration and the conventional one, the first realization of such a FEL [1] was proven to be very successful and showed the nonlinear regime in this configuration should be investigated more carefully. Very impressive experimental results obtained in Ref. [2] has confirmed this necessity and stimulated a flow of theoretical papers devoted to this and related topics (see, for example, Refs. [3–8]). In this article, we try to understand the features of the nonlinear regime of such a FEL in comparison with the conventional FEL configuration.

Let us consider a FEL with a right-hand helical wiggler field and reversed guide field (note, that physically it does not differ from the FEL configuration with forward guide field and left-hand helical wiggler). To simplify the analysis, we restrict ourselves to a one-dimensional case considering wiggler and electromagnetic field as homogeneous in the transverse direction. Near a point of standard FEL synchronism we can take into account only right-hand

polarized electromagnetic wave and, hence, write the nonlinear equations of FEL [9] in the form

$$\begin{aligned} \frac{dp_1}{dz} &= \left( \frac{\Omega_0}{k_w c p_3} - 1 \right) p_2 - \alpha_s \left( \frac{\gamma}{p_3} - \frac{ck}{\omega} \right) \sin \theta, \\ \frac{dp_2}{dz} &= - \left( \frac{\Omega_0}{k_w c p_3} - 1 \right) p_1 - \alpha_s \left( \frac{\gamma}{p_3} - \frac{ck}{\omega} \right) \cos \theta, \\ \frac{d\gamma}{dz} &= - \frac{\alpha_s}{p_3} (p_1 \sin \theta + p_2 \cos \theta), \\ \frac{d\theta}{dz} &= g \left( \frac{\gamma}{p_3} - \frac{ck}{\omega} \right) - 1, \\ \frac{d\alpha_s}{dz} &= \frac{j_0}{mc^3} \frac{\omega}{ck} \int_0^{2\pi} \frac{p_1 \sin \theta + p_2 \cos \theta}{p_3} d\theta_0, \end{aligned} \quad (1)$$

which is applicable for both configurations. Here  $k_w z$  is the normalized longitudinal coordinate,  $\Omega_0 = eB_0/mc$  is the cyclotron frequency in the guide field which must be treated as algebraic value,  $\Omega_w = eB_w/mc$  is the normalized wiggler field strength;  $2\pi/k_w$  is the wiggler spatial periodicity,  $\theta_0 \in [0 \cdot 2\pi]$  are the initial phases with respect to the electromagnetic wave,

$$\alpha_s = \frac{eA}{k_w mc^2} \frac{\omega}{c},$$

where  $A$  is an amplitude of electromagnetic wave vector potential,  $p_{1,2,3} = \gamma v_{1,2,3}/c$  are normalized electron im-

<sup>\*</sup> Corresponding author. Present address: 528 Walker Bldg., Penn State University, University Park, PA 16802, USA. E-mail: silivra@geosc.psu.edu.

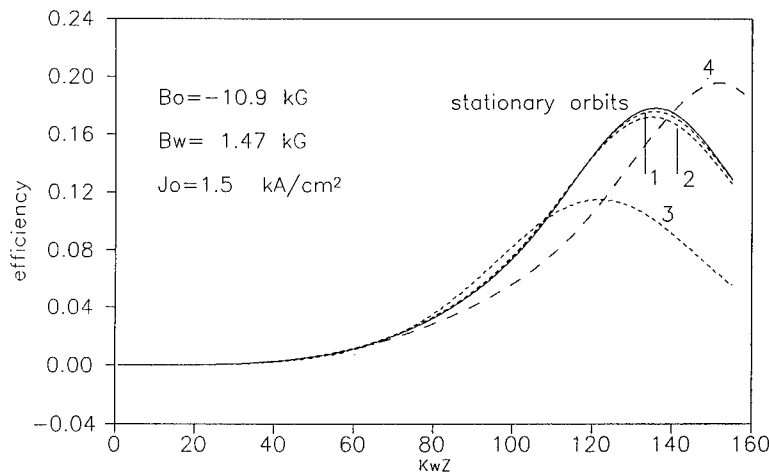


Fig. 1. The dependence of the FEL efficiency versus interaction length for the reversed guide field configuration.  $\alpha_s = 0.02$ ,  $k_w = 2 \text{ cm}^{-1}$ ,  $\gamma = 2.5$ ,  $g = 4.02$ , (1)  $\delta p = p_{\perp}/5$ ; (2)  $\delta p = p_{\perp}/3$ ; (3) “sharp” beginning of wiggler field; (4)  $\delta p = p_{\perp}/3$ ,  $g = 4$ .

pulses which satisfy the relation  $p_3 = (\gamma^2 - 1 - p_1^2 - p_2^2)^{1/2}$ ;  $j_0 = en_0 v_0$  is a density of a beam current and  $g = \omega/(ck_w)$ .

This system of equations allows the simulation of FEL operation by particle techniques. For the simulation, the parameters were close to the experimental ones [2]. The results of simulation are shown in Figs. 1 and 2. The solid curves correspond to the case in which the simulating particles have been on a steady state trajectory at an entrance to the interaction region. As one can see from these figures for both cases of guide field orientation the efficiency of the FEL is rather high.

The crucial change in these dependences arises if the electrons have deviations from steady state orbits at the entrance to the FEL interaction region. A spread in transverse electron velocities takes place in the experiment due

to the nonadiabatic wiggler field increase in the entrance, for example, or due to many other experimental features. In order to simulate this situation the initial conditions for the simulating particles were

$$p_{\perp}(Z=0) = p_{\perp} + \delta p \cos\left(2\pi \frac{\theta_0}{k\Lambda}\right), \quad (2)$$

where  $\delta p$  was  $\frac{1}{3}p_{\perp}$  or  $\frac{1}{5}p_{\perp}$  ( $p_{\perp}$  corresponds to steady state orbit,  $\Lambda$  is a spatial period of betatron oscillations). It assumes that the longitudinal impulse has a corresponding disturbance, although it is relatively much less, while the total energy is considered to be the same as in the previous simulation.

As we can see in Figs. 1 and 2 it results in the fact that the efficiency decreases significantly for positive guide

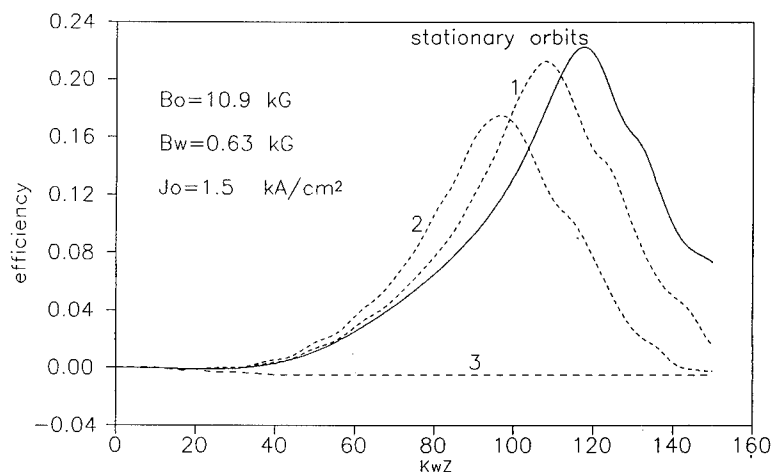


Fig. 2. The dependence of the FEL efficiency versus interaction length for the conventional guide field configuration.  $\alpha_s = 0.02$ ,  $k_w = 2 \text{ cm}^{-1}$ ,  $\gamma = 2.5$ ,  $g = 4.02$ , (1)  $\delta p = p_{\perp}/5$ ; (2)  $\delta p = p_{\perp}/3$ ; (3) “sharp” beginning of wiggler field.

field while it becomes only slightly less for the FEL with reversed guide field orientation.

As a limiting case, we simulated a situation in which the electrons entered the homogeneous wiggler field interaction region having only longitudinal velocity. It means that the section of smooth increase of the wiggler field is removed or the wiggler field is increased from 0 up to a nominal value over the distance which is much less than the period of the wiggler. Results of this simulation are shown by the dashed lines 3 in Figs. 1 and 2. As one can see, such a “sharp” beginning of the wiggler field results in a decrease of efficiency of approximately 1.5 times for reversed guide field FEL while the efficiency of the FEL with conventional orientation of guide field drops to zero.

These results become more understandable if we consider the features of electron motion in a phase space

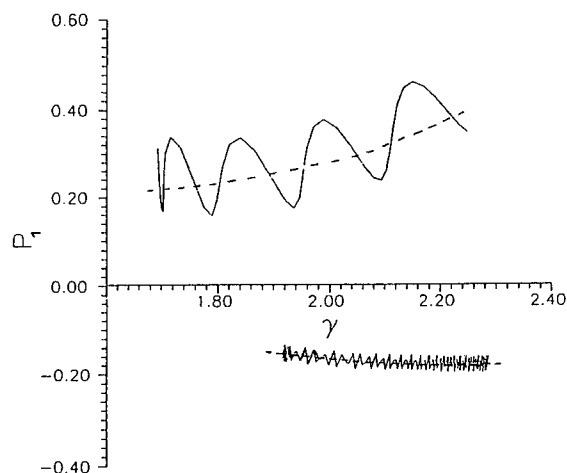


Fig. 3. Trajectories of electrons in the phase space for forward and reversed guide field. Dashed line represents the steady state trajectory.

( $p_1, \gamma$ ). As one can see from Fig. 3, in both cases the electrons move with deviations from the steady state trajectory which is represented by the dashed line. But for the reversed guide field the period and the amplitude of betatron oscillations are rather small and so their influence is effectively averaged. For the conventional orientation of the guide field the situation is opposite. The electron mostly is far enough from the steady state and, thus, cannot contribute to the output effectively.

Thus, the results of the investigation of the nonlinear interaction of the electromagnetic wave with a nonidealized electron beam (i.e. the electron beam in which electrons have deviations from the steady state trajectory right at the entrance to the FEL interaction region) confirm that a FEL configuration with reversed guide field is more effective with regard to the conventional one. These principal results can be explained by taking into account the affect of betatron-like oscillations of electrons.

## References

- [1] Ju.B. Viktorov, A.B. Draganov et al., Opt. Commun. 79 (1990) 81.
- [2] M.E. Conde and G. Bekefi, Phys. Rev. Lett. 67 (1991) 3082.
- [3] C.R. Chu and A.T. Lin, Phys. Rev. Lett. 67 (1991) 3235.
- [4] C. Yashen, D. Zhiwei et al., Nucl. Instr. and Meth. A 331 (1993) ABS 7.
- [5] A.A. Silivra, Nucl. Instr. and Meth. A 331 (1993) 487.
- [6] H.P. Freund and A.K. Ganguly, IEEE Trans. Plasma Sci. PS-20 (1992) 274.
- [7] G. Zhang, G. Shvets and J.S. Wurtele, Nucl. Instr. and Meth. A 331 (1993) 472.
- [8] A.K. Ganguly and H.P. Freund, Nucl. Instr. and Meth. A 331 (1993) 501.
- [9] N.S. Ginzburg and N.Yu. Peskov, Sov. Phys. JTP 58 (1988) 859.



# A proposal for the generation of ultra-short X-ray pulses

Alexander A. Zholents <sup>a,\*</sup>, Max S. Zolotarev <sup>b</sup>

<sup>a</sup> Center for Beam Physics, Lawrence Berkeley Laboratory, University of California, Berkeley, CA 94720, USA

<sup>b</sup> Stanford Linear Accelerator Center, Stanford University, Stanford, CA 94309, USA

## Abstract

In this paper it is shown that optical stochastic cooling in a 150 MeV electron storage ring will allow production of a beam with a longitudinal emittance of  $3 \times 10^{-6}$  MeV/m. Such a small emittance accompanied with a bunch compression technique based upon the transformation in the longitudinal phase space will allow achieving a bunch length of 30  $\mu$ m. This bunch could then be used for the generation of ultra-short X-ray pulses by Compton scattering of laser photons.

## 1. Introduction

In this paper we briefly summarize a feasibility study of an X-ray source capable of producing X-ray pulses with a duration  $\sigma_\tau = 100$  fs, a repetition rate of 714 MHz and an average flux of  $3 \times 10^{11}$  X-rays/s [1]. X-rays are generated by Compton scattering photons from a laser on electrons circulating in the storage ring. The ultra-short duration of the X-ray pulses is due to the short length of the electron bunches in the laser/e-beam interaction region (IR). A compression and decompression of the electron bunches before and after the IR helps to form short bunches in the IR while keeping them long in other sections of the ring. The novel optical stochastic cooling technique [2,3] is implemented in this project in order to ensure a small longitudinal beam emittance. This technique is also used for a weak excitation of transverse emittances in order to decrease heating of the longitudinal emittance by intrabeam scattering. The high repetition rate of the X-ray pulses and the high average flux of X-rays are due to a) many bunches in the storage ring, b) the usage of a powerful cw CO<sub>2</sub> laser, and c) electron-photon interactions inside the optical resonator.

## 2. Storage ring

Fig. 1 shows the layout of the storage ring. Its essential parts are a cooling insertion, a system of bunch compression and decompression, and an interaction region.

The design of the cooling insertion is based on the transit time method of the optical stochastic cooling. Al-

though the working principle of this method is fully described in Ref. [3], for the sake of the self-sufficiency of the paper we will repeat here some basic details.

Optical stochastic cooling is essentially a stochastic cooling method and it obeys the same cooling principles as microwave stochastic cooling. All modifications are associated with the transition to the optical frequency regime. Undulators serve as the pickup and kicker and the amplifier is an optical amplifier, typically dye or Ti:Al<sub>2</sub>O<sub>3</sub>. The cooling insertion by itself includes two undulators, an optical amplifier and a bypass (see the corresponding part of the ring in the Fig. 1). Moving along the insertion, the particle radiates an electromagnetic (EM) wave in the first undulator. This wave goes to the optical amplifier, while the particle follows the bypass trajectory and meets its amplified radiation in the second undulator. A subsequent interaction between the particle and the EM wave from its own amplified radiation results in a change of the particle energy. The amount of the energy change depends on the amplitude and phase of the EM wave at the time when the particle begins to absorb energy in the undulator. In our scheme we hold the amplitude fixed and rely on the phase variation.

The variation of the above mentioned phase from particle to particle is due only to the particle transit time in the bypass, since EM waves radiated by different particles propagate from the first undulator to the second undulator identically. Therefore, in order to have the energy change proportional to, for example, the particle momentum deviation one needs to do the following: i) adjust the propagation time of the EM wave and the traveling time of a particle with a zero momentum deviation so that this particle enters the second undulator at zero electric field and thus does not undergo any energy change; ii) design the bypass optics such that particles with different momenta follow trajectories with different path lengths, so

\* Corresponding author. E-mail: zholents@lbl.gov.

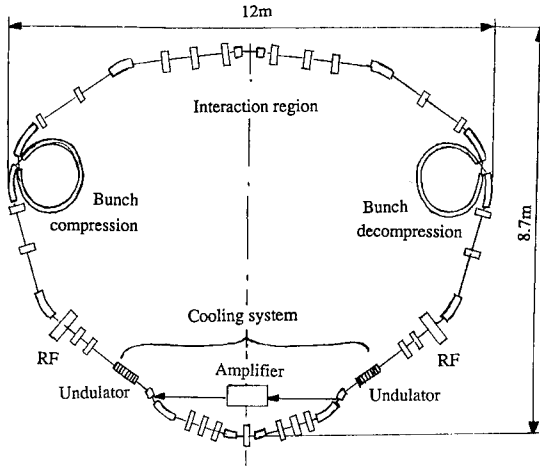


Fig. 1. The layout of the storage ring.

they enter the second undulator with phase shifts (relative to the phase with zero electric field) proportional to their momentum deviation.

A similar approach is applicable to betatron motion. What is required in this case is to link the particle traveling time in the bypass with some quantitative characteristic of the betatron motion (say, the betatron coordinate or angle or a linear combination of them) at the beginning of the bypass and to install undulators in a region with a non-zero dispersion function.

We have so far considered the interaction of the arbitrary test particle with the EM wave of its own radiation – the so-called coherent kick that the particle receives in the second undulator. However, each particle also interacts with the EM waves emitted by other particles that are within a distance defined by the bandwidth,  $\Gamma$ , of the amplifier. These interactions constitute the incoherent kick received by the particle. Choosing the amplification factor of the amplifier one can maintain a proper balance between coherent damping and incoherent heating leading to the minimum damping time. At the optimum and when the amplification factor is not limited by the amplifier power, the damping time of synchrotron oscillations,  $\tau$ , is given by [2]:

$$\tau_s = \frac{N}{\Gamma} \frac{\lambda}{Fl_b} T, \quad (1)$$

where  $N$  is the number of particles in a bunch,  $l_b$  is the bunch length,  $\lambda$  is the wavelength of the undulator radiation,  $T$  is the revolution period (we assume only one cooling insertion in the ring), and  $F$  is the ratio of the beam transverse area in the undulator to the diffraction limited area of the light. Notice, that if  $F > 1$ , then second order chromatic and geometric aberrations need to be corrected with sextupoles in order to fully use this factor for reduction of the damping time.

In the current design we have  $N = 1 \times 10^9$ ,  $l_b = 2.5$  cm,  $\lambda = 0.8 \mu\text{m}$ ,  $\Gamma = 10\%$ ,  $F = 50$ , and  $T = 170$  ns. Thus, optical stochastic cooling could provide damping time  $\tau_d \approx 1$  ms. It will require Ti:Al<sub>2</sub>O<sub>3</sub> amplifier with 0.3 W of the average output power.

It follows from Eq. (1), that the damping time depends inversely on the bunch length. Therefore, a long bunch in the cooling insertion is preferable. At the same time, we need a short bunch in the interaction region (IR) for the generation of short X-ray pulses. The only way to have long and short bunches in one ring is by having bunch compression before the IR and bunch decompression after the IR. Thus, longitudinal phase space transformations similar to the conventional bunching and debunching (which are typical for transfer lines) must be implemented in the ring. Basically, this means that the ring must possess a large momentum compaction factor. This is done in our design by adding  $\alpha$ -rotators to the lattice. Additionally, two high voltage RF cavities, located before and after the cooling insertion, serve as the energy demodulator and modulator. As a result, this system is capable of creating a significant variation of the longitudinal beta-function along the ring with a ratio of the longitudinal beta-function in the cooling system,  $\beta_1$ , to the longitudinal beta-function in the IR,  $\beta_2$ , given by:

$$\beta_1/\beta_2 \approx [\pi(0.5 - Q_s)]^{-2}, \quad (2)$$

where  $Q_s$  is the synchrotron frequency.

We have chosen  $Q_s$  to be close to the half integer resonance with detuning  $\Delta Q_s < 0.001$  in order to explore the beta-beat enhancement near resonance. Long term stability of the magnetic field and accelerating voltage on the level of  $10^{-3}$  seems adequate to maintain this condition, although the resonance harmonics of the magnetic field ripples in the bending magnets and the accelerating voltage ripples in the cavities should be controlled with a better precision of  $10^{-4}$  to  $10^{-5}$ .

Due to a small beam energy spread of  $3 \times 10^{-6}$  in the cooling insertion, the strongest excitation of longitudinal emittance comes from intrabeam scattering. Therefore, we decided to operate in a fully coupled regime with the relatively large horizontal and vertical emittances of  $1 \times 10^{-6}$  m · rad. First, this helps to reduce the growth rates of

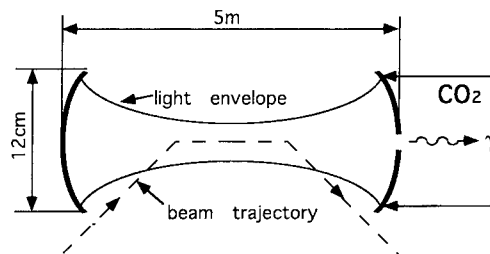


Fig. 2. Schematic of electron-photon interaction inside the optical resonator.

Table 1  
Main parameters of the storage ring

|   |                              |
|---|------------------------------|
| Energy                                    | 150 MeV                      |
| Circumference                             | 50.4 m                       |
| Tunes                                     |                              |
| Horizontal, $Q_x$                         | 4.8                          |
| Vertical, $Q_y$                           | 3.4                          |
| Synchrotron, $Q_s$                        | 0.499                        |
| Momentum compaction factor                | 0.58                         |
| RF frequency                              | 714 MHz                      |
| Accelerating voltage                      | 1.3 MV                       |
| Number of cavities                        | 2                            |
| Emittances                                |                              |
| Horizontal                                | $1 \times 10^{-6}$ m · rad   |
| Vertical                                  | $1 \times 10^{-6}$ m · rad   |
| Longitudinal, $\sigma_E \cdot \sigma_z$   | $4.5 \times 10^{-6}$ MeV · m |
| Damping times                             |                              |
| Transverse                                | 700 ms                       |
| Longitudinal                              | 1 ms                         |
| Intrabeam growth rate                     | $750 \text{ s}^{-1}$         |
| Particles per bunch                       | $1 \times 10^9$              |
| Number of bunches                         | 90                           |
| Empty gap                                 | 12.6 m                       |
| Average beam current                      | 80 mA                        |
| Beam parameters in the interaction region |                              |
| Bunch length, $\sigma_z / c$              | 100 fs                       |
| Energy spread, $\sigma_E / E_0$           | $9 \times 10^{-4}$           |
| Horizontal beam size, $\sigma_x$          | 0.6 mm                       |
| Vertical beam size, $\sigma_y$            | 0.6 mm                       |
| Beam parameters in the cooling insertion  |                              |
| Bunch length, $\sigma_z$                  | 1 cm                         |
| Energy spread, $\sigma_E / E_0$           | $3 \times 10^{-6}$           |
| Compression factor                        | 300                          |

beam emittances from intrabeam scattering. Second, it helps to decrease the stochastic cooling damping time. For a current variant of the ring lattice and for the beam parameters, listed in Table 1, the growth rate of the longitudinal emittance is estimated to be  $750 \text{ s}^{-1}$ .

Radiation damping in the ring is only 0.7 s. Although it is slow, it is sufficient to balance transverse emittance excitation associated with the quantum fluctuations of synchrotron radiation and intrabeam scattering.

Table 1 contains a list of the main storage ring parameters. Table 2 contains parameters of the optical amplifier.

### 3. X-ray generation

Electrons interact with laser photons inside an optical resonator, as is shown schematically in Fig. 2. The res-

Table 2  
Characteristics of Ti:Al<sub>2</sub>O<sub>3</sub> optical amplifier

|                      |                   |
|----------------------|-------------------|
| Central wavelength   | 0.8 $\mu\text{m}$ |
| Bandwidth            | 10 %              |
| Amplification factor | 16                |
| Average output power | 0.3 W             |

Table 3  
Laser and X-ray parameters

|   |                                   |
|---|-----------------------------------|
| Laser parameters                        |                                   |
| Wavelength                              | 10.6 $\mu\text{m}$                |
| Operation regime                        | cw                                |
| Power                                   | 1 kW                              |
| Optical resonator                       |                                   |
| Distance between mirrors                | $\sim 5$ m                        |
| Diameter of the mirrors                 | 12 cm                             |
| Power deposited on mirrors              | $\sim 1$ kW                       |
| Light power inside the resonator        | 300 kW                            |
| Waist size, $\sigma_r$                  | 0.6 mm                            |
| X-ray beam                              |                                   |
| Wavelength in the forward direction     | 0.3 $\text{\AA}$                  |
| Macropulse repetition rate              | 5.95 MHz                          |
| Macropulse duration                     | 126 ns                            |
| Micropulse repetition rate              | 714 MHz                           |
| Micropulse duration, $\sigma_r$         | 100 fs                            |
| Average flux of X-rays                  | $3 \times 10^{11} \text{ s}^{-1}$ |
| Spectral width, $\delta\omega / \omega$ | $\sim 1$                          |

onator is formed by two confocal mirrors. One mirror is semi-transparent. An external cw CO<sub>2</sub> laser is used for a power buildup in the resonator up to 300 kW. The distance between mirrors and their diameter are optimized in order not to exceed  $10 \text{ kW/cm}^2$  of incident power density on the mirror surfaces. The transverse sizes of the electron and photon beams are matched at the waist point. In this case the number of X-rays,  $N_\gamma$ , created in a single pass through the resonator by an electron bunch of  $N_b$  electrons is given by:

$$N_\gamma = \frac{2\pi}{3} \alpha r_e \frac{P}{mc^3} N_b \approx 1.6 \times 10^{-9} P(\text{kW}) N_b, \quad (3)$$

where  $\alpha$  is the fine structure constant,  $r_e$  is the classical electron radius,  $m$  is the electron mass,  $c$  is speed of light, and  $P$  is the power of the light beam inside the resonator.

Table 3 contains laser characteristics and parameters of the generated X-rays.

### 3. Discussion

An average flux of X-rays as high as  $1 \times 10^{12}$  X-rays/s could potentially be achieved with the scheme described in this paper and 1 MW power in the optical resonator. This would require a new optical resonator with larger distance between mirrors and larger mirror diameters and a more powerful cw CO<sub>2</sub> laser for a power buildup in the resonator. It seems also possible that X-ray pulses shorter than described in Table 2 could be generated at the expense of the average flux of X-rays.

A unique feature of the proposal discussed in this paper is an extremely small bunch length in the IR of the storage ring. Accordingly, the bunch is also very short in the bending magnets adjacent to the IR. Therefore, the syn-

chrotron radiation from these magnets that is radiated in the far infrared will be substantially coherent. One can explore this feature for an upgrade of the current scheme into a source of high power far infrared radiation.

#### Acknowledgements

We acknowledge useful discussions with S. Chattopadhyay, K.J. Kim and W. Turner. We express our gratitude to M. Zisman for an extensive introduction to the computer code ZAP [4], which we used for calculations of the intrabeam scattering. This work was supported by Depart-

ment of Energy contracts DE-AC03-76SF00098 (LBL) and DE-AC03-76SF00515 (SLAC).

#### References

- [1] A. Zholents and M. Zolotarev, CBP Tech Note-038, LBL (1993).
- [2] A. Mikhailichenko and M. Zolotarev, Phys. Rev. Lett. 71 (1993) 4146.
- [3] M. Zolotarev and A. Zholents, Phys. Rev. E 50 (1994) 3087.
- [4] M. Zisman et al., ZAP User's Manual, LBL-21270 (1986).



ELSEVIER

# High power self-similar radiation pulse in a free electron laser

T.B. Zhang \*, T.C. Marshall

Department of Applied Physics, Columbia University, New York, New York 10027, USA

## Abstract

Using 1D short wavelength (8  $\mu\text{m}$ ) Compton free electron laser (FEL) equations with slippage, we explore propagation of a high power pulse down a tapered undulator FEL travelling wave amplifier. For an appropriate taper, a short pulse ( $\sim 300$  fs FWHM) with regular features will propagate self-similarly as it grows in power, slipping through a much longer electron pulse. The power spectrum of the pulse is nearly Gaussian with no sidebands. The electron energy is depressed by  $\sim 33\%$ , but slippage causes the peak pulse intensity to be about the same as the electron beam power density,  $\sim 10$  TW/cm<sup>2</sup>.

## 1. Introduction

Under certain conditions, the free electron laser (FEL) oscillator has been found to provide an output of narrow, chaotic high power “spike” pulses of radiation characterized by a wide irregular spectrum [1–3]. Furthermore, in the operation of a FEL oscillator, experiment [4] as well as numerical theory which carries the analysis well into the nonlinear regime [5], shows that the FEL can operate in a mode characterized by low efficiency together with a narrow spectrum, or in a mode that has higher efficiency and a wide spectrum. The latter has to do with the sideband instability [6] which has been observed experimentally [7,8] and which is also found in connection with superradiant spiking studies [9–13] since both [14] arise from slippage. However, there is also evidence that the sideband instability can be stabilized with an appropriately chosen taper of the undulator [15–17].

This paper considers a traveling wave, high gain, Compton FEL which operates at nearly optimal efficiency using a variable-parameter undulator and which produces an intense “clean” output spike pulse with a nearly Gaussian spectrum free of sidebands. The hardware would include a laser “seed” source which supplies a high power pulse having a Gaussian shape, as input to a high efficiency FEL traveling wave amplifier having an appropriately tapered undulator. Our findings are that one might expect to develop an infrared FEL pulse having peak power  $\sim 10$  TW/cm<sup>2</sup> and FWHM  $\sim 300$  fs using an 45 MeV, 150 A electron beam.

## 2. FEL equations and computational model

We now develop a numerical model which establishes how such a FEL pulse can be prepared. We shall study a short optical pulse which is propagating along a much longer pulse of electrons that is traversing an undulator. At FEL resonance, as the light wave moves down one undulator period, it slips ahead of the electrons by one optical wavelength  $\lambda_s$ . We shall study the case where the electron beam pulse is much longer than the overall slippage distance  $L_s = N_w \lambda_s$ , so that essentially no radiation appears ahead of or behind the electron pulse. (A number of recent publications have considered the wealth of interesting effects which occur at the beginning and the end of the electron pulse, which involve “superradiance” [9–13].) We begin by studying a set of 1D equations which are appropriate for the Compton FEL:

$$\frac{\partial \gamma_j(x, y)}{\partial x} = - \frac{2 \rho \gamma_r^2 A_s \sin \psi_j}{\gamma_j \beta_{j\parallel}}, \quad (1)$$

$$\frac{\partial \theta_j(x, y)}{\partial x} = \frac{1}{2 \rho} \left[ 1 - \frac{k_s}{k_w} \frac{(1 - \beta_{j\parallel})}{\beta_{j\parallel}} \right], \quad (2)$$

$$\frac{\partial A(x, y)}{\partial y} = i \gamma_r \left\langle \frac{e^{-i\theta}}{\gamma} \right\rangle. \quad (3)$$

The above equations are derived directly from the original 1D time dependent FEL equations [6] by transforming the variables  $z$  and  $t$  into new independent variables  $x$  and  $y$  [9], i.e.  $x = (ct - z)/l_c$ ,  $y = (z - v_{\parallel}t)/l_c \beta_{j\parallel}$ ; here,  $l_c = \lambda_s/4\pi\rho$  is the cooperation length which is defined as the minimum distance over which an electron may interact cooperatively with the radiation [10],

$$\rho = \frac{1}{\gamma_r} \left( \frac{a_w \omega_p}{4ck_w} \right)^{2/3}$$

\* Corresponding author. Tel: +1 212 854 6672, Fax: +1 212 854 8257, e-mail tzhang@cuplvx.ap.columbia.edu.

is the Pierce parameter;  $\beta_{j\parallel} = [1 - (\mu^2 - 2a_w a_s \cos \psi_j) / \gamma_j^2]^{1/2}$  is the axial velocity of the  $j$ th electron,  $\mu^2 = 1 + a_w^2 + a_s^2$ ,  $a_w$  and  $a_s$  are the normalized vector potentials of the undulator ( $eB_{\perp} / k_w mc^2$ ) and radiation field ( $eE_s / k_s mc^2$ );  $\gamma_j$  is the relativistic factor of the  $j$ th electron,  $\psi_j = \theta_j + \phi$  is the relative phase of the  $j$ th electron with respect to the radiation pulse,  $A(x, y) = A_s e^{i\phi}$  is the complex amplitude of the radiation pulse with

$$A_s = \frac{1}{\sqrt{\gamma_j \rho}} \frac{\omega_s}{\omega_p} a_s,$$

and  $\phi$  is the phase shift of the radiation pulse. For the other quantities:  $k_w = 2\pi / l_w$  is the wave number of the undulator,  $l_w$  is the undulator period;  $k_s = 2\pi / \lambda_s = \omega_s / c$  is the wave number of the radiation pulse,  $\lambda_s$  is the radiation wavelength,  $l_w$  and  $\lambda_s$  satisfy the resonance condition  $\lambda_s = l_w(1 + a_w^2) / (2\gamma_j^2)$ , and  $\omega_p = (4\pi e^2 n_e / m)^{1/2}$  is the plasma frequency for  $n_e$  electrons/cm<sup>3</sup>. The slowly varying amplitude approximation in Eq. (3) has been verified in the application for the short pulse propagation discussed here.

The numerical simulation is based on the computational model described by Eqs. (1) to (3). The FEL works as a traveling wave amplifier. The spatial distribution of simulation electrons has a rectangular profile, the electrons are taken to be monoenergetic, and at the undulator entrance, they are uniformly distributed inside the beam length  $L_b$  with one thousand simulation electrons per radiation wavelength. For each wavelength-size “strip” of electrons, the relative phase location of the electrons with respect to the radiation field is uniformly distributed from  $-\pi$  to  $\pi$ . The input radiation pulse is “seeded” inside the electron beam, with its initial amplitude  $a_{s0} = 10^{-4}$  (200 MW/cm<sup>2</sup> at 8  $\mu$ m wavelength). The pulse profile and width can be varied so that we can study the evolution of various pulses. For the output format of the computational results, the

electron beam pulse and the radiation spike are plotted as the function of independent variables  $x$  and  $y$  respectively, which implies two moving “windows” with the former at the speed of light  $c$  and the latter at the speed of electrons  $v_{\parallel}$ ; both are scaled in the units of the radiation wavelength  $\lambda_s$  from their leading edge. Since all these quantities are recorded at various undulator positions, these results will describe the time evolution of the pulses. In several test runs, we have carried out simulations for different FEL parameters, including different lengths of beam pulses and radiation pulses. Our results for “super-radiant” pulse evolution are in a very good agreement with that of previous authors [9] and provide a calibration of our code.

### 3. Simulation results

Our main interest is to investigate an initial short radiation pulse propagating through a sufficiently long electron pulse. The initial radiation pulse has a Gaussian profile and is injected into the rear part of the electron beam pulse; the peak of the initial pulse is located at  $x = 225\lambda_s$ . The radiation pulse starts from that position at the undulator entrance, and then moves toward the front of the electron pulse as it moves along the undulator. The Fourier-transformed spectrum, has a central frequency  $\omega_s = 2.36 \times 10^{14} \text{ s}^{-1}$ . Other simulation parameters of the FEL amplifier are listed in Table 1, where a representative electron beam pulse length of 2.4 mm ( $\sim 8$  ps) is taken; the beam pulse is 300 wavelengths long, and so the optical pulse moves only halfway through as it traverses 150 undulator periods. (The choice of the 8  $\mu$ m wavelength was arbitrary although this is representative of FEL performance with the chosen beam parameters. The same qualitative features were obtained in another tapered undulator

Table 1  
Simulation parameters

|                                |   |
|--------------------------------|---|
| Beam parameters                |   |
| Electron beam energy           | $\gamma = 89.5$   |
| Electron beam current          | $I_b = 150 \text{ A}$   |
| Beam intensity                 | $5.4 \text{ TW/cm}^2$   |
| Electron beam radius           | $r_b = 0.02 \text{ cm}$   |
| Beam pulse length              | $L_b = 300\lambda_s (2.4 \text{ mm})$                             |
| Undulator parameters           |   |
| Undulator period               | $l_w = 2.5\text{--}1.5 \text{ cm}; \text{ linear ramp}$           |
| Undulator taper                | $\eta = 2.6 \times 10^{-3} \text{ cm}^{-1}$                       |
| Undulator parameter            | $a_w = 2.0 \text{ (constant)}$                                    |
| Undulator length               | $N_w = 150$   |
| Radiation pulse                |   |
| Radiation wavelength           | $\lambda_s = 8.0 \mu\text{m}$                                     |
| Pulse length (FWHM, intensity) | $L_r = 12\lambda_s$   |
| Pulse amplitude range          | $a_s = 10^{-4}\text{--}0.021 (200 \text{ MW--}9 \text{ TW/cm}^2)$ |

FEL simulation for a much lower beam energy and wavelength of 1.5 mm.)

### 3.1. Constant period undulator

Fig. 1 shows the pulse evolution in a constant period undulator ( $l_w = 2.5$  cm). The profiles of electron energy and the radiation spike together with its Fourier-transformed spectrum are shown at two undulator positions  $N_w = 75$  (Figs. 1(a1)–(1a3)) and  $N_w = 150$  (Figs. 1(b1)–(1b3)). In these figures, the electron envelope is at rest and the optical spike propagates from the right to left as  $N_w$  increases. Figs. 1(a2) and 1(b2) show that the optical pulse is amplified while the electron energy is reduced (Figs. 1(a1) and 1(b1)). The “efficiency”, defined from the maximum drop in electron energy corresponding the maximum pulse intensity is  $\sim 10\%$ , compared with the efficiency of a steady-state long continuous wave which is  $\sim 3\%$ . The radiation spike retains the initial profile until approximately 100 undulator periods where the growth becomes saturated. Saturation occurs when the loss of beam energy causes the interaction to drop out of resonance. A flat region and pulses beside the main spike develop from the two edges of the pulse after it propagates

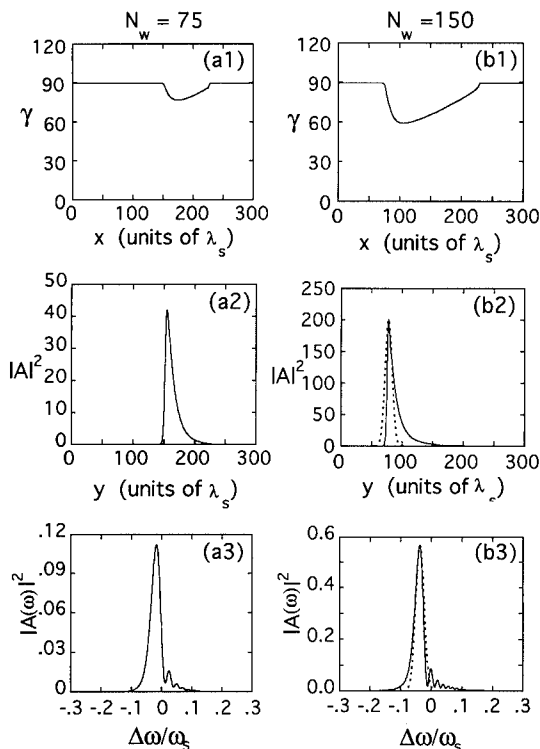


Fig. 2. The parameters are the same as in Fig. 1 except that the undulator period is linearly tapered from 2.5 cm to 1.5 cm. When the radiation spike slips over electron beam, the beam energy is continuously extracted (a1, b1), while the spike keeps a self-similar profile (a2, b2). Its Fourier transformed spectrum (amplitude in arbitrary units) is shown in (a3, b3). A Gaussian comparison pulse (dotted curves) described in the text, is shown in (b2), and its Fourier transform appears in (b3).

a long distance, and this causes a ragged energy profile (Fig. 1(b1)). Fig. 1(b3) shows a powerful long wavelength sideband comparable in intensity to the carrier; it has about the same displacement from the carrier [6] as the sideband instability.

### 3.2. Tapered undulator

If the undulator is tapered, we expect the growth of the sideband can be suppressed, and in Fig. 2 we show the results. The undulator period is linearly tapered from 2.5 cm to 1.5 cm in 150 periods. All other conditions are the same as in Fig. 1 and are obtained from Table 1. In this numerical experiment, we did not optimize the undulator taper to pursue the highest efficiency enhancement: instead, the appropriate taper was chosen for the purposes of obtaining the “cleanest” spike (however, this optimized taper is not very different from the taper which extracts maximum energy from the beam). Unlike the untapered case, the radiation pulse at high amplitude does not radically change its shape, but displays a self-similar profile

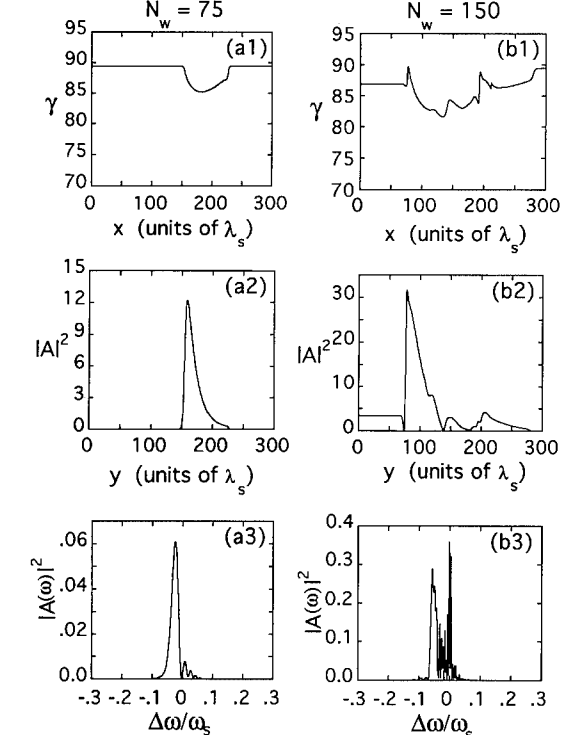


Fig. 1. Constant undulator period simulation. The radiation pulse slips forward into the electron beam from right to left. The beam energy distribution, radiation profile and its Fourier transformed spectrum (ordinate, arbitrary units) are shown in (a1) to (a3) at  $N_w = 75$  and (b1) to (b3) at  $N_w = 150$ .

throughout the slippage region. The width of the initial Gaussian pulse is  $\text{FWHM} \sim 7\lambda_s$  in intensity; it evolves and becomes broadened to about  $\text{FWHM} \sim 12\lambda_s$  during the first 50 periods; it continues to grow in amplitude while keeping a nearly constant profile and width. We have tried various widths of the initial Gaussian pulse, as well as a different initial amplitude profile varying as  $\sim 1/\cosh(\alpha y)$  (a solitary wave solution [18]), and we find the variation of initial choices converges to a similar output pulse profile and width, although the number of undulator periods needed to form the self-similar pulse profile may vary. This suggests that a short optical pulse may eventually evolve to a self-similar spike in the slippage region of the tapered undulator. The characteristic width of the spike is similar to the prediction of the Ginzburg–Landau solitary wave theory [19]. In the constant period undulator, the self-similar feature is lost when the FEL system goes out of resonance.

We should expect an efficiency enhancement in the tapered undulator. Comparing Fig. 2(b2) with Fig. 1(b2), one finds the efficiency is roughly a factor of 3.3 better than the same FEL with constant-period undulator. The maximum value of the normalized field amplitude  $a_s = 0.021$  ( $\sim 9 \text{ TW/cm}^2$ ) corresponds to an intensity of the same order as the beam kinetic energy intensity; this enhancement in power is caused by the slippage of the radiation pulse over “new” electrons as it moves down the undulator. The ragged profile of the electron energy in the constant undulator (Fig. 1(b1)) is found to disappear in tapered undulator (Fig. 2(b1)).

Finally, the sideband is suppressed in the tapered undulator FEL, as shown in Figs. 2(a3) and 2(b3). In this case, we have a comparatively clean spike in both time and frequency domains. Note also there is a frequency shift from the resonance in these spectra. Frequency shifting is an intrinsic characteristic of the time-dependent FEL equations [20]. We may estimate the frequency shift from the computed phase shift  $\phi(x, y) = -i \ln(A/A_s)$ , and  $\Delta\omega/\omega_s = 2\rho\partial\phi/\partial x$ , obtaining the value of  $\Delta\omega/\omega_s = -0.014$ ;  $-0.032$  at the two undulator positions  $N_w = 75$ ;  $150$  which agree approximately with the numerical results. In Fig. 2(b2) is also shown a comparison Gaussian pulse having the same amplitude and FWHM as the self-similar

pulse; in Fig. 2(b3) we find the Fourier transform of this comparison pulse (also Gaussian) is a rather good fit to the spectrum of the self-similar pulse.

### Acknowledgement

This work is sponsored by the Office of Naval Research.

### References

- [1] R.W. Warren, J.C. Goldstein and B.E. Newnam, Nucl. Instr. and Meth. A 250 (1986) 19.
- [2] B.A. Richman, J.M.J. Madey and E. Szarmes, Phys. Rev. Lett. 63 (1989) 1682.
- [3] J.W. Dodd and T.C. Marshall, IEEE Trans. Plasma Sci. PS-18 (1990) 447.
- [4] D. Iracane, V. Fontenay, P. Guimbal, S. Joly, S. Striby and D. Touati, Phys. Rev. Lett. 72 (1994) 3985.
- [5] D. Iracane and J.L. Ferrier, Phys. Rev. Lett. 66 (1991) 33.
- [6] N.M. Kroll, P.L. Morton and M.N. Rosenbluth, IEEE J. Quantum Electron. QE-17 (1981) 1436.
- [7] R.W. Warren, B.E. Newnam and J.C. Goldstein, IEEE J. Quantum Electron. QE-21 (1985) 882.
- [8] F.G. Yee, J. Masud, T.C. Marshall and S.P. Schlesinger, Nucl. Instr. and Meth. A 259 (1987) 104.
- [9] R. Bonifacio, B.W.J. McNeil and P. Pierini, Phys. Rev. A 40 (1989) 4467.
- [10] R. Bonifacio, N. Piovella and B.W.J. McNeil, Phys. Rev. A 44 (1991) 3441.
- [11] W.M. Sharp, W.M. Fawley, S.S. Yu, A.M. Sessler, R. Bonifacio and L. DeSalvo Souza, Nucl. Instr. and Meth. A 285 (1989) 217.
- [12] G.T. Moore and N. Piovella, IEEE J. Quantum Electron. QE-27 (1991) 2522.
- [13] S.J. Hahn and J.K. Lee, Phys. Rev. E 48 (1993) 2162.
- [14] R.M. Caloi, Phys. Rev. A 46 (1992) 7934.
- [15] F.G. Yee, T.C. Marshall and S.P. Schlesinger, IEEE Trans. Plasma Sci. PS-16 (1988) 162.
- [16] B. Hafizi, A. Ting, P. Sprangle and C.M. Tang, Phys. Rev. A 38 (1988) 197.
- [17] R.P. Pila and A. Bhattacharjee, Phys. Plasmas 1 (1994) 390.
- [18] S.Y. Cai and A. Bhattacharjee, Phys. Rev. A 43 (1991) 6934.
- [19] Li-Yi Lin and T.C. Marshall, Phys. Rev. Lett. 70 (1993) 2403.
- [20] G. Shvets and J.S. Wurtele, Phys. Plasmas 1 (1994) 157.



## 3D simulations on output power fluctuation in a short bunch rf-linac FEL

Y. Sentoku <sup>a,\*</sup>, H. Furukawa <sup>b</sup>, K. Mima <sup>c</sup>, T. Taguchi <sup>d</sup>, S. Kuruma <sup>b</sup>, H. Yasuda <sup>a</sup>,  
C. Yamanaka <sup>b</sup>, S. Nakai <sup>c</sup>

<sup>a</sup> Mitsubishi Research Institute, Inc., Tokyo, Japan

<sup>b</sup> Institute for Laser Technology, Osaka, Japan

<sup>c</sup> Institute of Laser Engineering, Osaka University, Japan

<sup>d</sup> Department of Electrical Engineering, Setsunan Univ., Osaka, Japan

### Abstract

A space-time dependent 3D simulation code has been developed in order to analyze the RF-linac FEL oscillator dynamics. Our simulation code employed both the transverse mode spectral method and the longitudinal finite difference method. The electron beam is modeled by a group of super particles which have a density profile in the time domain. In this model the electron beam is able to determine the energy spread and the finite emittance. This simulation code enables us to describe the transverse mode competition and the slippage effects in the resonator cavity.

In this paper, a high power infrared FEL with a short bunch electron beam is investigated. The output power fluctuation with cavity desynchronization is simulated with this code. Especially, we investigated the effects of the transverse mode competition, energy spread, and the finite emittance of the electron beam on the output fluctuation. Using FELIX parameters, the FEL oscillator is simulated for 300 passes. The output power oscillates periodically in the case of single transverse mode and not in the case of multi-transverse modes. In a warm beam with multi-transverse modes, the emission is higher than that with a single mode, and the optical pulse shape is almost the after 100 passes. Furthermore, the phase space motion of the laser field is periodic and stable. As a result of the simulation, we recommend that high power infrared FEL operation should include multi-transverse modes in order to get higher emission and a more stable optical pulse.

### 1. Introduction

Improving the quality of the optical pulse from the FEL is important from the point of application of the optical pulse. It is effective to use a three dimensional simulation code for analyzing the optical pulse and inspecting its quality. There is a 3D FEL simulation code using the transverse mode spectral method and the finite difference method in the longitudinal direction [1]. We extended this code to take into account multi-longitudinal mode effects. With the space-time dependent 3D model, the density profile, the energy spread, and the finite emittance of the electron beam can be included, and we can simulate the more realistic dynamics of the electron and laser pulse in the wiggler. With this code, we will analyze the growth process of the optical pulse and the slippage effects, and the fluctuations of the output emissions of the FEL oscillator.

The electron beam provided by the RF-linac accelerator has several picoseconds in bunch length. In the infrared regime, the slippage length, which is given by  $N_w \lambda$ , where  $N_w$  is the wiggler periods and  $\lambda$  is the wavelength of the laser, is longer than the bunch length of the electron beam, so the peculiar short pulse effects are expected. One of these effects is output power fluctuation, which is called limit cycle oscillation [3]. We simulated the FEL oscillator in this regime and investigated the effects of multi-transverse modes, the energy spread, and the finite emittance of the electron beam on the output fluctuations in order to find the stable operation condition.

### 2. Basic equations

#### 2.1. The wave equation

We consider a linearly polarized wiggler of which the vector potential is expressed by

$$A_w(z) = A_w(z) \cos\left(\int_0^z k_w(z') dz'\right) e_x. \quad (1)$$

\* Corresponding author. Tel. +81 3 3277 0576, fax +81 3 3277 0567.

A dimensionless wiggler parameter  $K(z)$  is defined by  $(e/\sqrt{2}m_e c^2)A_w(z)$ .

When the electron beam passes through the wiggler, the wave equation expanded in transverse modes is described by the following equation:

$$\begin{aligned} & \left( \frac{\partial}{\partial z} + \frac{1}{v_{glm}} \frac{\partial}{\partial t} \right) a_{l,m} \\ &= i \frac{\omega_b^2}{c^2} \frac{1}{2k} \frac{1}{n_e} F_1(z) K(z) \\ & \times \sum_{j=1}^N \left\{ \frac{1}{c} f \left( t - \frac{z}{v_{zj}} \right) G_{lm}^*(x_j, y_j, z) \right. \\ & \left. \times \exp(-i\psi_j(z, t)) / \gamma_j(z, t) \right\}, \end{aligned} \quad (2)$$

where  $a_{l,m} = (e/\sqrt{2}m_e c^2)A_{l,m}$  is a normalised transverse mode amplitude and  $\omega_b$  is the plasma frequency of super-particles.  $\omega_b$  is expressed as  $\omega_b = \sqrt{\chi} \omega_c$  by the plasma frequency  $\omega_c$ , where  $\chi$  is the weight of a super-particle, i.e., the number of electrons in one super-particle.  $n_e$  is the density of electrons,  $f(t - z/v_{zj})$  is the density profile function of the super-particle and  $c$  is the speed of light.  $G_{l,m}$  expresses the Gaussian–Hermite function of an  $l$ - $m$  mode [1]. The wave number in the axial direction and the group velocity of the  $l$ - $m$  mode are given by the following equations:

$$k_{zlm} = k - (l + m + 1) \frac{1}{z_0(1 + \xi^2)}, \quad (3)$$

and

$$v_{glm} = ck_{zlm}/k = \frac{c}{k} \left( k - (l + m + 1) \frac{1}{z_0(1 + \xi^2)} \right), \quad (4)$$

respectively, where  $\xi = (z - \bar{z}_c)/z_0$ ,  $z_0$  is the Rayleigh length and  $\bar{z}_c$  is the axial location of the mode waist.

## 2.2. Electron beam dynamics

The energy change of each electron is expressed by the following equation:

$$\begin{aligned} & \left( \frac{\partial}{\partial z} + \frac{1}{v_{zj}} \frac{\partial}{\partial t} \right) \gamma_j \\ &= - \frac{k}{\gamma_j} F_1(z) K(z) |a_x(x_j, y_j, z, t)| \sin(\psi_j + \phi_j), \end{aligned} \quad (5)$$

where  $\gamma_j$  is the  $\gamma$  value of the  $j$ th super-particle,  $F_1(z) = J_0(K^2/2(1 + K^2)) - J_1(K^2/2(1 + K^2))$ ,  $a_x$  is the normalized vector potential  $\mathbf{a} = (e/\sqrt{2}m_e c^2)\mathbf{A}$  in the  $x$  direction,  $\psi_j$  is the phase of the  $j$ th electron and  $\phi_j =$

$-\log(A_x/|A_x|)$ . We assume that in the  $x$  direction the electrons move with a uniform velocity and in the  $y$  direction their motions exhibit betatron oscillations:

$$x_j(z) = x_{0j} + \frac{p_{x0j}}{\gamma_j m_e c} z, \quad (6)$$

$$y_j(z) = \alpha_j \cos \left( \int_0^z k_\beta(z') dz' + \phi_\beta \right), \quad (7)$$

where  $k_\beta = Kk_w/\gamma_0$ ,  $\phi_\beta = \cos^{-1}(y_{0j}/\alpha_j)$ ,  $\alpha_j = (y_{0j}^2 + \dot{y}_{0j}^2/k_\beta(0)^2 v_{zj}^2)^{1/2}$  and  $v_{zj}$ ,  $p_{x0j}$  are the axial velocity and the initial axial momentum of the  $j$ th particle.

The phase is subject to the following equation:

$$\left( \frac{\partial}{\partial z} + \frac{1}{v_{zj}} \frac{\partial}{\partial t} \right) \psi_j = \bar{k}_w \left( 1 - \frac{\bar{\gamma}_r^2}{\gamma_j^2} \right), \quad (8)$$

where  $\bar{\gamma}_r$  is the resonant energy given by  $\bar{\gamma}_r = \{k(1 + 2K^2)/2k_w \gamma_j\}^{1/2}$  and  $\bar{k}_w = (k - k_{zlm})$ .

## 3. Computational model

When we solve the equations in order to reduce the temporal coordinate space, we introduce the wave frame by

$$\tau \equiv t - z/c. \quad (9)$$

So, the three equations (2), (5) and (8), the wave equation, the energy equation and the phase equation, are rewritten as

$$\begin{aligned} & \left( \frac{\partial}{\partial z} + \frac{1 - v_{glm}/c}{v_{glm}} \frac{\partial}{\partial \tau} \right) \alpha_{l,m} \\ &= i \frac{\omega_b^2}{c^2} \frac{1}{2k} \frac{1}{n_e} F_1(z) K(z) \\ & \times \sum_{j=1}^N \left\{ \frac{1}{c} f \left( \tau + z \left( \frac{1}{c} - \frac{1}{v_{zj}} \right) \right) G_{lm}^*(x_j, y_j, z) \right. \\ & \left. \times \exp(-i\psi_j(z, \tau)) / \gamma_j(z, \tau) \right\}, \end{aligned} \quad (10)$$

$$\begin{aligned} & \left( \frac{\partial}{\partial z} + \frac{1 - v_{zj}/c}{v_{zj}} \frac{\partial}{\partial \tau} \right) \gamma_j \\ &= - \frac{k}{\gamma_j} F_1(z) K(z) |a_x(x_j, y_j, z, \tau)| \sin(\psi_j + \phi_j), \end{aligned} \quad (11)$$

and

$$\left( \frac{\partial}{\partial z} + \frac{1 - v_{zj}/c}{v_{zj}} \frac{\partial}{\partial \tau} \right) \psi_j = \bar{k}_w \left( 1 - \frac{\bar{\gamma}_r^2}{\gamma_j^2} \right). \quad (12)$$

Referring to the FELIX parameters, the parameters used in this simulations are set as shown in Table 1. The

Table 1  
Parameters used in the simulations

|                           |  |
|---------------------------|--|
| Physical parameters       |  |
| Electron energy           | 22.5 MeV                                       |
| Bunch length              | 2.4 ps   |
| Electron energy spread    | 0.0 or 0.5%                                    |
| Normalized rms emittance  | 0.0 or $100 \pi$ mm-mrad                       |
| Beam current              | 60 A   |
| Beam radius               | 1.0 mm   |
| Wiggler period            | 6.5 cm   |
| Number of wiggler periods | 38   |
| Wiggler strength (rms)    | 1.2  |
| Cavity desynchronization  | $-0.5\lambda$                                  |
| Roundtrip loss            | 5%   |
| Rayleigh length           | 1.2 m  |
| Wavelength                | $40 \mu\text{m}$                               |
| Computation parameters    |  |
| Transverse mode           | 0-0 or 2-2                                     |
| Noise factor              | random number which means $ \delta  = 10^{-3}$ |
| Beam shape                | Gaussian profile                               |
| Number of electrons       | 116  |
| Initial phase             | $0, \pi/2, \pi + \delta, 3\pi/2 + \delta$      |

four cases shown in Table 2 are simulated. The first case is for an electron beam which has an energy spread, a finite emittance (called a warm beam), and only one transverse mode. The second case is for a warm beam and nine transverse modes. The third case is for an electron beam which has no energy spread and no finite emittance (called a cold beam) and only one transverse mode. The last case is for a cold beam and nine transverse modes.

#### 4. Output fluctuation

In this simulations, the bunch length of the electron beam is 2.4 ps which is shorter than the slippage length of

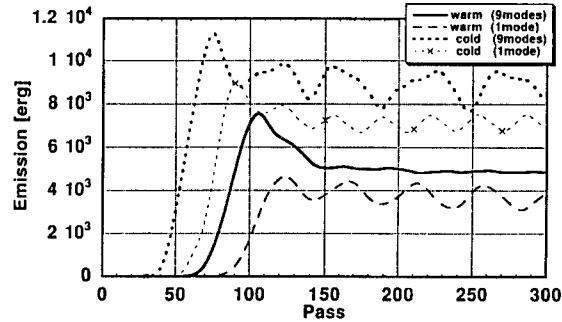


Fig. 1. Comparison of pulse energy fluctuations in the multi-mode case with that in the single mode case.

about 5 ps. So the short pulse effects are significant. As a result of the simulations with cavity desynchronization  $\delta L = -0.5\lambda$ , the output fluctuation is observed as shown in Fig. 1, where the output emission power changes in every pass. In Fig. 1, after superradiant emission is over, the output emission oscillated periodically in the single mode cases, called limit cycle oscillation. On the other hand the emission does not oscillate periodically in the nine mode cases, especially in the warm beam and nine modes cases, where the output emission power approaches a constant.

Next, we investigated the optical pulse shapes at the wiggler end. Fig. 2 shows the pulse shapes for the four cases at the end of 200 passes 240 passes and 280 passes. The relative intensity of the pulse trains are changing with pass number in the warm or cold beam with a single mode. But in the nine modes cases, the pulse shapes are always same, as shown in Fig. 2. From this result, we found that the transverse mode competition tends to make the optical pulse shape stable. In the warm beam and nine modes case, the optical pulse shape is almost identical through 300 passes.

Fig. 3 shows the evolutions of the laser field in phase space through 300 passes. The horizontal axis represents

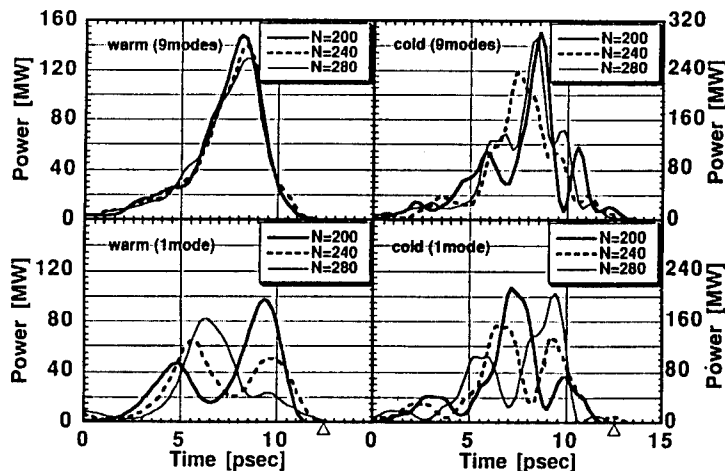


Fig. 2. Optical pulse shapes at the end of wiggler for four cases. The triangle marked at 12.5 ps indicates the center of the electron beam.

Table 2  
Cases of the simulations

| Case                | Energy<br>[spread %] | Emittance<br>[ $\pi$ mm-mrad] | Trans-<br>verse<br>mode |
|---------------------|----------------------|-------------------------------|-------------------------|
| Warm beam & 1 mode  | 0.5                  | 100                           | 0–0                     |
| Warm beam & 9 modes | 0.5                  | 100                           | 2–2                     |
| Cold beam & 1 mode  | 0.0                  | 0.0                           | 0–0                     |
| Cold beam & 9 modes | 0.0                  | 0.0                           | 2–2                     |

the real part and the vertical axis represents the imaginary part of the normalized vector potential  $a$ , and the plots express the phase positions at the center of the optical pulse (8 ps). We could see clearly in the warm beam and nine modes case the Poincare maps have stable motion with one center circle. The one mode case has quasi-periodic motion, namely, the intensity drops two times during one cycle. This intensity modulation causes the limit cycle oscillation of output power. Comparing the warm beam cases with the cold beam cases the output power is lower and the period of rotation in the phase space Poincare maps is smaller, and the orbits in the phase space are regular.

We calculated the Lyapunov exponents in order to investigate the stability against the perturbation of the system for the four cases:

$$\lambda = \lim_{\Delta N \rightarrow \infty} \frac{1}{\Delta N} \log \frac{\sum |A_N(A_{N_0} + \Delta A) - A_N(A_{N_0})|^2}{\sum |\Delta A|^2}, \quad (13)$$

where  $N_0$  is the pass number,  $\Delta N$  is the pass number from the  $N_0$ th pass and  $\Delta A$  is the perturbation added after  $N_0$  passes. Fig. 4 shows the calculated Lyapunov exponents. From Fig. 4 the warm beam and nine modes case and the cold beam and one mode case are stable but the cold beam

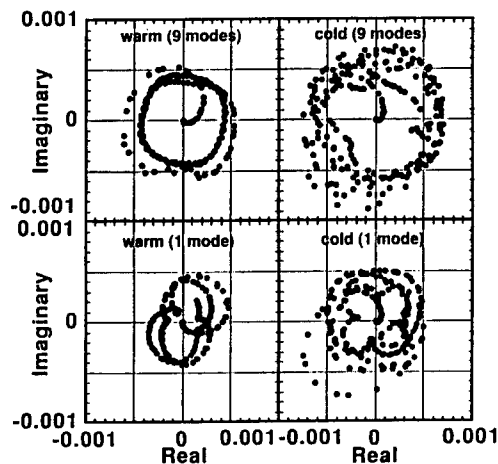


Fig. 3. Poincaré maps on normalized radiation filled phase space at the pulse center (8 ps).

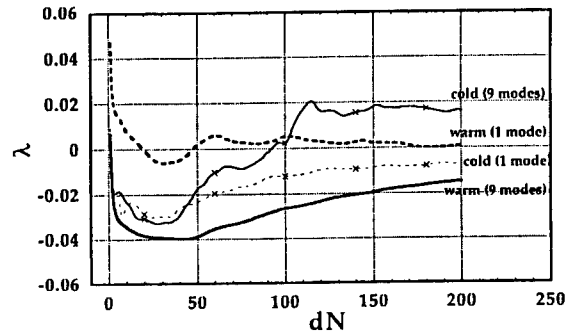


Fig. 4. Lyapunov exponents of laser pulse. The horizontal axis is the pass number from 100 passes.

and nine modes case is unstable. In FEL oscillator theory, it is known that when the gain becomes higher, the system changes from the stable regime to the limit cycle regime and finally to the chaotic regime [4,5]. Because the gain is higher in the cold beam cases than that in the warm beam cases, it is possible that the cold beam cases are in the chaotic regime.

## 5. Concluding remarks

As the result of a simulation using the parameters for infrared high power FEL with a short pulse electron beam, we recommend that high power operation should include high transverse modes, because the output power and optical pulse shape are stable. Furthermore, the system is stable against perturbations with multi-transverse modes as was clearly demonstrated in the warm beam and nine modes case.

## Acknowledgements

Two of authors, Y.S. and K.M., are grateful to Advanced Science Research Center of the Japan Atomic Energy Research Institute for supporting this research, and for fruitful discussion with Dr. T. Tajima and Dr. Y. Kishimoto.

## References

- [1] C.-M. Tang and P.A. Sprangle, IEEE J. Quantum Electron. QE-21 (1985) 970.
- [2] F. Casagrande and G. Cerchioni, Nucl. Instr. and Meth. A 304 (1991) 536.
- [3] W.B. Colson and A. Renieri, J. de Phys. 44 (1983) C1.
- [4] S.J. Hahn, submitted to the Faculty of Pohang Institute of Science & Technology in Partial Fulfillment of The Requirements for the Degree of Doctor of Philosophy in Physics (1993).
- [5] S.J. Hahn and J.K. Lee, Phys. Lett. A, to be published.



ELSEVIER

# Higher harmonic generation in a FEL with an axisymmetric undulator of the induction type

N.I. Karbushev<sup>\*</sup>, V.D. Sazhin, P.V. Mironov

*Moscow Radiotechnical Institute, Varshavskoye shosse 132, 113519 Moscow, Russian Federation*

## Abstract

It is shown that the amplitudes of transverse components of velocities of electrons in an axisymmetric undulator depend resonantly on the value of an axial guiding magnetic field. They increase substantially when the cyclotron frequency is approximately equal to the frequency of the undulator oscillations of the electrons or its higher harmonic, which corresponds to resonance pumping of the undulator motion. Such an effect was observed experimentally in a free electron laser with a hollow kiloampere electron beam of microsecond duration and an axisymmetric undulator consisting of alternating conducting and dielectric rings in an axial magnetic field of a solenoid. The maximum generated microwave power in a FEL reached several megawatts in the centimeter and millimeter ranges of wavelengths.

## 1. Introduction

Higher harmonic generation of microwave radiation in free electron lasers (FELs) is an important problem. It allows the reduction of the beam voltage required at a given frequency of operation or the use of undulators with enhanced periods. Such facilities are equivalent to those using undulators with periods several times less than the fundamental period.

For magnetostatic undulators the existence of odd higher harmonics of a periodic magnetic field is natural [1–3], and they cause the corresponding motion of electrons. Because even harmonics of the undulator magnetic field are absent, the possibility of generation of radiation at even harmonics can be conditioned by velocity harmonics as the result of nonlinearity of motion or by the periodic position interaction [4]. In the last case the interaction of electrons with an electromagnetic wave has only a single resonance with respect to the value of the axial magnetic field when the cyclotron frequency equals the frequency of the fundamental harmonic of the undulator oscillations. The effect of energy exchange between electrons and a wave at a periodic position may be obtained by means of factorization of the wave amplitude on the trajectory of the electrons in powers of the vector of their displacement inside the undulator, when the average value of the scalar product of the fundamental harmonic of the velocity of the electrons and the electric field of a microwave on their trajec-

tory with the frequency and wave vector determined by a higher undulator harmonic is non-zero.

In FELs with an axisymmetric undulator of the induction type consisting of alternating conducting and dielectric rings inside the solenoid [5,6], the non-zero components of a periodic magnetic field are the radial and longitudinal ones, their amplitudes depending on the radius. So, there are two reasons why higher harmonics of undulator motion of electrons may arise. The first one is the result of the nonlinearity of the equations of motion. The second reason is conditioned by the radial inhomogeneity of the amplitude of the undulator field. In both cases the motion of the electrons in the undulator must be resonant with respect to the value of the axial magnetic field, and many resonances exist.

In the present paper the amplitudes of the second harmonic of the electrons velocities in an axisymmetric undulator and a guiding axial magnetic field are calculated analytically, and the experimental results of microwave generation in a FEL [6] are discussed.

## 2. Calculation of the velocity of the electrons in an undulator

The total magnetic field of an axisymmetric undulator of the induction type may be written down in following form:

$$\begin{aligned} \mathbf{B} &= \mathbf{B}_0 + \mathbf{B}_w \\ &= B_0 \mathbf{e}_z + B_w \operatorname{Re} \{ [ \mathbf{e}_z I_0(k_w r) - i \mathbf{e}_r I_1(k_w r) ] \\ &\quad \times \exp(ik_w z) \}, \end{aligned} \quad (1)$$

<sup>\*</sup> Corresponding author.

where  $e_z$ ,  $e_r$  and  $e_\theta$  are the unit vectors in the axial, radial and azimuthal directions,  $B_0$  is the value of the axial magnetic field of a solenoid,  $B_w$  is the value of the periodic component of the axial magnetic field on the axis of an undulator,  $k_w = 2\pi/d$ ,  $d$  is the period of an undulator, and  $I_0$  and  $I_1$  are modified Bessel functions of zeroth and first orders. Equations of motion for electrons in a field (1) in the stationary case are

$$\frac{d\mathbf{v}}{dt} = v_z \frac{d\mathbf{v}}{dz} = \frac{e}{\gamma mc} [\mathbf{v} \times \mathbf{B}] = \left[ \mathbf{v} \times \frac{\boldsymbol{\Omega}}{\gamma} \right], \quad (2)$$

where  $\mathbf{v}$  is the velocity of the electrons,  $\gamma$  is their relativistic factor,  $e$  and  $m$  are the charge and the mass of an electron, and

$$\begin{aligned} \boldsymbol{\Omega} &= e\mathbf{B}/mc \\ &= \boldsymbol{\Omega}_0 + \boldsymbol{\Omega}_w = \Omega_0 e_z + \Omega_w \text{Re} \{ [e_z I_0(k_w r) \\ &\quad - i e_r I_1(k_w r)] \exp(ik_w z) \}. \end{aligned} \quad (3)$$

Let us consider the motion of electrons in an undulator. In the case of adiabatic entrance at its end we may write

$$\begin{aligned} \mathbf{v} &= \mathbf{u} + \tilde{\mathbf{v}} = u e_z + v_{dr} + \text{Re} [v_1 \exp(ik_w z) \\ &\quad + v_2 \exp(2ik_w z) + \dots], \\ \mathbf{r}_\perp &= \mathbf{r}_0 + \tilde{\mathbf{r}} = r_0 e_r + \text{Re} [r_1 \exp(ik_w z) + \dots]. \end{aligned} \quad (4)$$

where  $\mathbf{u}$ ,  $\mathbf{r}_0$  and  $\tilde{\mathbf{v}}$ ,  $\tilde{\mathbf{r}}$  are the constant and variable components of the velocity and transverse displacement of the electrons respectively. In the case of small enough undulator magnetic field amplitude  $B_w$ , when the inequalities

$$|\tilde{v}| \ll u, \quad k_w |\tilde{r}| \ll 1, \quad |\tilde{r}| \ll r_0 \quad (5)$$

are fulfilled, one may factorize the solution to Eq. (2) in powers of  $\Omega_w$ . In the first linear approximation one obtains [7,8]

$$v_1 = -\frac{u}{\gamma} \frac{(\Omega_0/\gamma) \boldsymbol{\Omega}_{w\perp} + i k_w u [e_z \times \boldsymbol{\Omega}_w]}{(k_w u)^2 - (\Omega_0/\gamma)^2}. \quad (6)$$

The velocity (6) has only transverse components while the axial velocity equals zero. Substituting Eq. (3) into Eq. (6) yields:

$$\begin{aligned} v_{1r} &= i u \frac{(\Omega_0/\gamma)(\Omega_w/\gamma)}{(k_w u)^2 - (\Omega_0/\gamma)^2} I_1(k_w r_0), \\ v_{1\theta} &= -u \frac{k_w u (\Omega_w/\gamma)}{(k_w u)^2 - (\Omega_0/\gamma)^2} I_1(k_w r_0). \end{aligned} \quad (7)$$

The variable component of the transverse displacement of the electrons can be determined from the equation

$$v_z \frac{d\mathbf{r}_\perp}{dz} = \mathbf{v}_\perp \quad (8)$$

and in the same approximation it equals to

$$\mathbf{r}_1 = -i v_1 / k_w u. \quad (9)$$

In the second approximation on  $\Omega_w$  the value of the velocity  $v_2$  can be calculated. From Eq. (2), taking account of Eq. (4), it follows that

$$\begin{aligned} 2i k_w u v_2 - \left[ v_2 \times \frac{\boldsymbol{\Omega}_0}{\gamma} \right] \\ = \frac{1}{2} \left\{ e_r \frac{v_{1\theta}^2}{r_0} - e_\theta \frac{v_{1r} v_{1\theta}}{r_0} + \left[ v_1 \times \frac{\boldsymbol{\Omega}_w(r_0)}{\gamma} \right] \right. \\ \left. + \left[ u \times \left( r_1 \frac{\partial}{\partial \mathbf{r}_\perp} \right) \frac{\boldsymbol{\Omega}_w(r_0)}{\gamma} \right] \right\}. \end{aligned} \quad (10)$$

The first three terms on the right-hand side of the Eq. (10) are the result of the nonlinearity of the motion of the electrons and the last one is conditioned by the transverse inhomogeneity of the amplitude of the undulator magnetic field. All these terms are values of the same order and must be included.

It is not too hard to find from Eq. (10) the components of  $v_2$ :

$$v_{2z} = -\frac{u}{4} \frac{(\Omega_w/\gamma)^2}{(k_w u)^2 - (\Omega_0/\gamma)^2} I_1^2(k_w r_0), \quad (11)$$

$$\begin{aligned} v_{2r} &= -i \frac{u}{2} \frac{(\Omega_w/\gamma)^2 I_1(k_w r_0)}{[(2k_w u)^2 - (\Omega_0/\gamma)^2][(k_w u)^2 - (\Omega_0/\gamma)^2]} \\ &\times \left[ \frac{3(k_w u)^2 (\Omega_0/\gamma)^2}{(k_w u)^2 - (\Omega_0/\gamma)^2} \frac{I_1(k_w r_0)}{k_w r_0} \right. \\ &\quad \left. - 2(k_w u)^2 I_0(k_w r_0) - \left( \frac{\Omega_0}{\gamma} \right)^2 I_0(k_w r_0) \right. \\ &\quad \left. - (\Omega_0/\gamma)^2 I_1'(k_w r_0) \right], \end{aligned} \quad (12)$$

$$\begin{aligned} v_{2\theta} &= \frac{u}{2} \frac{k_w u (\Omega_0/\gamma) (\Omega_w/\gamma)^2 I_1(k_w r_0)}{[(2k_w u)^2 - (\Omega_0/\gamma)^2][(k_w u)^2 - (\Omega_0/\gamma)^2]} \\ &\times \left[ \frac{3(k_w u)^2}{(k_w u)^2 - (\Omega_0/\gamma)^2} \frac{I_1(k_w r_0)}{k_w r_0} - 3I_0(k_w r_0) \right. \\ &\quad \left. - 2I_1'(k_w r_0) - \frac{I_1(k_w r_0)}{k_w r_0} \right], \end{aligned} \quad (13)$$

where  $I_1'$  is the derivative of the Bessel function.

In the region of the cyclotron resonance of the second harmonic of the undulator motion of electrons, when

$$\Omega_0/\gamma \approx \pm 2k_w u, \quad (14)$$

the axial component of the velocity (11) is finite but transverse components (12) and (13) can increase very

strongly and exceed the value of the fundamental harmonic velocity (7). In the range (14) the transverse components (12) and (13) may be approximately written in the form

$$\begin{aligned} v_{2r} &\approx \mp i v_{2\theta} \\ &\approx -\frac{5}{3} \frac{i u (\Omega_w / \gamma)^2}{(2 k_w u)^2 - (\Omega_0 / \gamma)^2} I_0(k_w r_0) I_1(k_w r_0). \end{aligned} \quad (15)$$

Simple estimations [9] show that the transverse velocity (15) in resonance conditions (14) is not infinite, although great. Counting the change of the axial velocity from the conservation of energy one can obtain

$$\begin{aligned} |v_{2r}|_{\max} &\approx |v_{2\theta}|_{\max} \\ &\approx \sqrt{2} u \left[ \frac{5}{3} (\Omega_w / \Omega_0)^2 I_0(k_w r_0) I_1(k_w r_0) \right]^{1/3}. \end{aligned} \quad (16)$$

Analogously the transverse drift velocity of the electrons  $v_{dr}$  which appeared in Eq. (4) also can be calculated. From the equations of motion (2) in the second approximation one finds

$$v_{dr} = v_{dr} e_\theta = -e_\theta \frac{v_{1\theta}}{2 \Omega_0} \left[ \frac{\gamma v_{1\theta}}{r_0} + (\Omega_w \cdot e_z) + \frac{|\Omega_{w\perp}|}{k_w r_0} \right]. \quad (17)$$

Substituting Eqs. (3) and (7) into Eq. (17) yields

$$\begin{aligned} v_{dr} &= \frac{k_w u^2}{2 \gamma \Omega_0} \frac{\Omega_w^2 I_1(k_w r_0)}{(k_w u)^2 - (\Omega_0 / \gamma)^2} \left[ I_0(k_w r_0) \right. \\ &\quad \left. - \frac{I_1(k_w r_0)}{k_w r_0} \frac{(\Omega_0 / \gamma)^2}{(k_w u)^2 - (\Omega_0 / \gamma)^2} \right]. \end{aligned} \quad (18)$$

This means changing of azimuthal angle of electrons guiding center  $\vartheta_0$  in correspondence with the formula

$$\vartheta_0(z) = v_{dr} z / u r_0. \quad (19)$$

### 3. Experimental results

The experiments were carried out on the setup described in Ref. [6]. The parameters of the hollow intense electron beam were: energy of electrons  $eU = 400$ – $700$  keV; injected current:  $0.5$ – $1.0$  kA; radius:  $r_0 = 6$ – $12$  mm; pulse duration:  $4$ – $10$   $\mu$ s. The period of the undulator,  $d$ , could be made equal to  $7.2$ ,  $4.8$  or  $2.4$  cm, with the amplitude of the radial component of the magnetic field  $B_{w\perp}$  up to  $500$  G and the axial magnetic field  $B_0$  up to  $8$  kG.

The experimental investigations showed that the power  $P$  of the detected microwave signal reached its maximum values in conditions when the period of the cyclotron

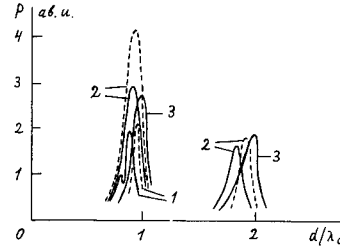


Fig. 1. Dependences of output microwave power on the ratio  $d/\lambda_c$ .

oscillations of electrons,  $\lambda_c$ , was approximately equal to or two times less than the period of the undulator  $d$ . Corresponding dependences are plotted in Fig. 1, where two resonance regions are sharply expressed. Results presented were obtained at the parameters: curves 1:  $d = 2.4$  cm; curves 2:  $d = 4.8$  cm; curves 3:  $d = 7.2$  cm; solid curves:  $U = 600$  kV; dashed curves:  $U = 480$  kV. The values of the microwave power at the fundamental and second resonances were comparable. At the second resonance the greater part of the power was concentrated in the range of higher frequencies than at the fundamental resonance (see also Ref. [6]). The maximum total power generated was of the order of  $10$  MW. At the second resonance good propagation of the electron beam through the waveguide was observed while at the fundamental high losses of the beam current in the undulator were seen.

These experimental results may be explained as follows. The strength of the periodic undulator magnetic field in the experiment was small enough. Because of this the effective interaction of the beam with electromagnetic waves was possible only in resonant conditions when the velocity of the oscillations of the electrons increased. Such resonances are the cyclotron resonances with the fundamental or second harmonics of the undulator motion of the electrons.

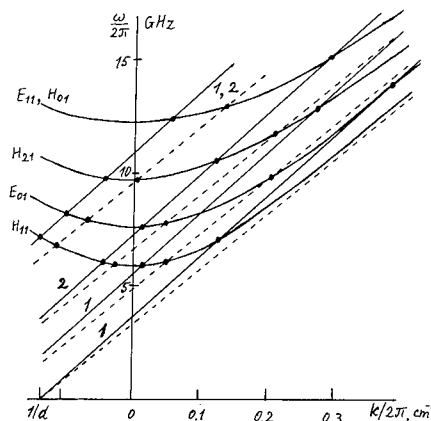


Fig. 2. Dispersion curves of lowest waveguide modes and the lines of synchronism with an electron beam.

In Fig. 2 the dispersion curves for the four lowest modes of the circular metallic waveguide with a diameter of 3 cm are presented. The straight lines correspond to the synchronism with an electron beam for various periods of the undulator (solid lines: for the axial velocity of electrons,  $u = 0.86c$ ; dashed lines: for  $u = 0.81c$ ;  $c$  is the speed of light). The points of intersections of the dispersion curves and straight lines determine the ranges of the frequencies of the waveguide modes generated. For the second undulator resonances (lines 2) the straight lines are upshifted twice in comparison with those for the fundamental resonances (lines 1). Because of this second undulator harmonic resonances lead to increased frequencies of the generated waves.

The periodic position interaction cannot be the reason of the increase of the output microwave power at the second resonance, because the fundamental harmonic of the electrons' velocity is not resonant in such conditions. But the second harmonic of the velocity may increase sufficiently and corresponding estimations can be made.

#### 4. Conclusion

In summary, the experimental results obtained can be explained by resonant increasing of the transverse velocity

of the electrons at the fundamental and second harmonics of the undulator motion, when the period of the cyclotron oscillations of the electrons is approximately equal to or two times less than that of the undulator. The expressions for the second harmonic velocity (12), (13) and (15) obtained in the present paper demonstrate such resonance properties in conditions (14).

#### References

- [1] B. Girard, Y. Lapiere, J.M. Ortega et al., Phys. Rev. Lett. 53 (1984) 2405.
- [2] S.V. Benson and J.M.J. Madey, Phys. Rev. A 39 (1989) 1579.
- [3] R.W. Warren, L.C. Haynes, D.V. Feldman et al., Nucl. Instr. and Meth. A 296 (1990) 84.
- [4] H. Bluem, R.H. Jackson, H.P. Freund et al., Phys. Rev. Lett. 67 (1991) 824.
- [5] K.D. Jacobs and J. Bekefi, J. Appl. Phys. 52 (1981) 4977.
- [6] N.I. Karbushev, P.V. Mironov, V.D. Sazhin and A.D. Shatkus, Nucl. Instr. and Meth. A 318 (1992) 117.
- [7] V.L. Bratman, G.G. Denisov, N.S. Ginzburg and M.I. Petelin, IEEE J. Quantum Electron. QE-19 (1983) 282.
- [8] N.I. Karbushev and A.D. Shatkus, Nucl. Instr. and Meth. A 304 (1991) 559.
- [9] A.A. Kaminsky, A.K. Kaminsky, N.I. Karbushev et al., Nucl. Instr. and Meth. A 331 (1993) 531.





ELSEVIER

# Nonlinear evolution of the equilibrium electron orbits in a helical wiggler with a positive axial guide magnetic field at magnetoresonance

Junsheng Yu<sup>a,b</sup>, W.A. Gillespie<sup>b,\*</sup>

<sup>a</sup> CCAST (World Laboratory), P. O. Box 8730, Beijing 100080, China

<sup>b</sup> Department of Electronic & Electrical Engineering, University of Abertay, Dundee, DD1 1HG, UK

## Abstract

A model of the coupled nonlinear evolution equations is presented for the slow-varying amplitude and phase of the electron perpendicular velocities in a helical wiggler with positive axial guide magnetic field at magnetoresonance. The transverse motion is dominated by the nonlinear effect, which arises from the correlation between the longitudinal and perpendicular velocities. The analytical results are in very good agreement with numerical calculations.

## 1. Introduction

The nonlinear dynamical behaviour of the equilibrium electrons is of importance in an FEL operating in a combined positive guide magnetic field and a helical wiggler field near magnetoresonance [1–4]. The electron orbits become very complicated due to the strong coupling of the longitudinal and transverse motion [3]. Recently, numerical calculations show that the temporal evolution of the  $x$  component of the transverse velocity performs a quasi-harmonic oscillation in terms of an ideal helical wiggle [3,4]. Theoretical analysis also shows that the maximum transverse velocity and orbit excursion are dominated by the Larmor motion [4]. In this work, we have derived the nonlinear evolution equation of the orbit by assuming the transverse velocities are of simple harmonic oscillation with slow-varying amplitude and phase. The scaling for the maximum transverse velocity can also be obtained in a different way in comparison with the previous methods [3,4]. The analytical study is compared with the numerical calculations.

## 2. Evolution equation

We consider a relativistic electron drifting in the field configuration consisting of a helical wiggler magnetic field

$$B_w = B_w(e_x \cos k_w z + e_y \sin k_w z), \quad (1)$$

and a uniform positive guide magnetic field

$$B_0 = B_0 e_z, \quad (2)$$

where  $B_w$  and  $B_0$  are constant amplitudes,  $k_w$  is the wiggler wave number, and  $e_x$ ,  $e_y$  and  $e_z$  are the unit vectors in the  $x$ ,  $y$ , and  $z$  directions, respectively. The relativistic equations of motion can be written as

$$\frac{d\beta_x}{d\tau} = -\beta_y + \epsilon\beta_z \sin k_w z, \quad (3a)$$

$$\frac{d\beta_y}{d\tau} = \beta_x - \epsilon\beta_z \cos k_w z, \quad (3b)$$

$$\frac{d\beta_z}{d\tau} = -\epsilon(\beta_x \sin k_w z - \beta_y \cos k_w z), \quad (3c)$$

where  $\beta_{x,y,z} = V_{x,y,z}/c$ ,  $\tau = \Omega_0 t$ ,  $\Omega_0 = eB_0/(\gamma mc)$ ,  $\gamma = (1 - \beta^2)^{-1/2}$ , and  $e/m$  is the ratio of charge to mass,  $c$  is the light speed in vacuum,  $\epsilon = B_w/B_0$  which is assumed to be smaller than unity. We adopt a nonlinear oscillator representation for  $\beta_x$ ,  $\beta_y$  in Eq. (3) as

$$\beta_x(\tau) = A(\tau) \cos[\tau + \Phi(\tau)], \quad (4a)$$

$$\beta_y(\tau) = A(\tau) \sin[\tau + \Phi(\tau)], \quad (4b)$$

where the amplitude  $A(\tau)$  and the phase  $\Phi(\tau)$  are treated as slowly-varying. Substituting (4) into (3) gives

$$\frac{dA}{d\tau} = \epsilon\beta_z \sin \zeta, \quad (5a)$$

$$A \frac{d\zeta}{d\tau} = -A \left( 1 - \frac{ck_w \beta_z}{\Omega_0} \right) + \epsilon\beta_z \cos \zeta, \quad (5b)$$

$$\frac{d\beta_z}{d\tau} = -\epsilon A \sin \zeta, \quad (5c)$$

\* Corresponding author. Tel. +44 382 308 247, fax +44 382 308 877, e-mail eetwag@ddt.ac.uk.

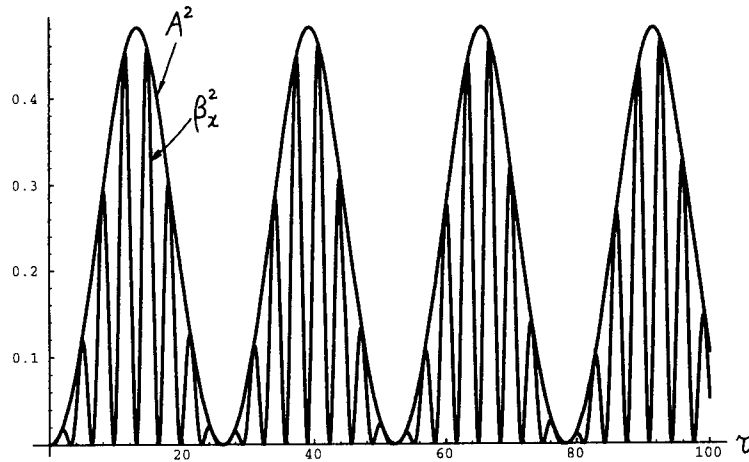


Fig. 1.  $\beta_z^2$  and  $A^2$  vary as the normalised time  $\tau$ , where  $\tau_0 = 0$ ,  $x(0) = 0$ ,  $y(0) = 0$ ,  $z(0) = 0$ ,  $\beta_{x0} = 0$ ,  $\beta_{y0} = 0$  for  $\beta_x^2$ ,  $A(0) = 0$ ,  $\zeta(0) = 0$ , for  $A^2$ ,  $\beta_{y0} = 0.914$ ,  $\lambda_w = 3.18$  cm,  $\epsilon = 0.08$ .

where,  $\zeta = k_w z - (\tau + \Phi)$ . Eqs. (5a)–(5c) represent the nonlinear evolution of the amplitude and phase. Calculations of Eq. (3) for  $\beta_x^2$  and Eq. (5) for  $A^2$  are shown in Fig. 1 for the given parameters. It is found that Eq. (5) is quite successful in describing the nonlinear evolution of the amplitude of the transverse velocity.

From Eq. (5), the scaling for the maximum transverse velocity can be estimated by constructing a potential equation. Multiplying Eq. (5b) by  $\sin \zeta$ , then substituting Eq. (5a) and (5c) into Eq. (5b) gives

$$C = \epsilon A \cos \zeta + \beta_z - \frac{ck_w}{2\Omega_0} \beta_z^2, \quad (6)$$

which is a constant of the motion, i.e.,  $C(\tau) = C(\tau_0)$ . Using the “energy” conservation condition  $A^2 + \beta_z^2 = P_0^2$ , and combining Eq. (5a) and (6) to form the combination  $\sin^2 \zeta + \cos^2 \zeta = 1$ , gives the potential equation:

$$\frac{1}{4} \left( \frac{dA^2}{d\tau} \right)^2 + V(A^2) = 0, \quad (7)$$

where

$$V(A^2) = \beta_z^2 \left[ \left( C - \beta_z + \frac{ck_w}{2\Omega_0} \beta_z^2 \right)^2 - \epsilon^2 A^2 \right],$$

$$\beta_z = \sqrt{P_0^2 - A^2}, \quad P_0 = \sqrt{A_0^2 + \beta_{z0}^2},$$

$$A_0 = A(\tau_0), \quad \beta_{z0} = \beta_z(\tau_0)$$

are the initial values. It can be seen that the potential equation Eq. (7) which describes the amplitude of the transverse velocity is similar to Eq. (6) which describes the transverse velocity in the case of the positive guide field in Ref. [4]. Through a similar derivation from Eq. (7) as in Ref. [4], the maximum value  $A_{\max}$  can be obtained as  $A_{\max} = \epsilon^{1/3}$  at magnetoresonance  $\Omega_0 \cong ck_w \beta_{z0}$ . It is noted that this is another method to determine the maximum transverse velocity in comparison with the previous work [3,4].

## References

- [1] L. Friedland, Phys. Fluids 23 (1980) 2376.
- [2] H.P. Freund and A.T. Drobot, Phys. Fluids 25 (1982) 736.
- [3] G. Spindler and G. Renz, Phys. Plasmas 1 (1994) 389.
- [4] Junsheng Yu, submitted to Phys. Rev. E.



ELSEVIER

## Free gas bubbles acoustic laser

S.T. Zavtrak

*The Institute of Nuclear Problems, Bobruiskaya Str., 11, Minsk 220050, Belarus*

At the present time there are many types of lasers. Their operation is based on the stimulated emission (or scattering) of light by an active medium which is in optical resonance. Lasers are generators of coherent electromagnetic waves in the range from ultraviolet to submillimeters. However, acoustic analogues of such devices have not been created up to now in spite of the progress in laser technology.

The purpose of this report is to suggest a very simple scheme of an acoustic laser which could be easily realized experimentally. This scheme is analogous to that of the free-electron laser (FEL). It is well known that in FEL electromagnetic emission is created by electron beams moving through magnetic periodic systems. These systems are called undulators or wigglers [1]. Undulators play the role of pumping. Initially the emission of the electrons is not coherent. But as the electrons are bunched due to their interaction with the useful electromagnetic wave the emission becomes coherent and leads to amplification of the field.

Analogous results are obtained for the suggested scheme of an acoustic laser, in which a liquid dielectric with gas bubbles is the active medium and bubbles are emitters. The pumping is done by a variable electric field which results in the deformation of bubble volumes. Phase bunching of initially incoherent emitters is realized by acoustic radiation forces.

Consider an acoustic resonator with a liquid dielectric containing gas bubbles as an active medium. For example, we can use different types of oils or distilled water as a liquid dielectric. It is well known that the distilled water has a high dielectric constant.

A static electric field acting on such a system results in the deformation (electrostriction) of dielectrics [2] and hence in changes of the bubble volumes.

The value of the effective pressure acting at the bubble is equal to [2,3]

$$\Delta P = \frac{3\epsilon_1 E^2 (\epsilon_1 - \epsilon_p)}{8\pi(2\epsilon_1 + \epsilon_p)}. \quad (1)$$

Here  $\epsilon_1$  and  $\epsilon_p$  are the dielectric constants of the liquid and bubble respectively, and  $E$  is the electric field strength. As an example, for air bubbles in water ( $\epsilon_p \approx 1$ ,  $\epsilon_1 \approx 81$ )

and at an electric field strength  $E = 10$  kV/cm, the value of  $\Delta P \sim 0.5$  kPa.

Let us suppose that  $E$  is a periodic time function:  $E = E_0 \cos(\Omega t)$ .

The electromagnetic waves propagate through the medium with the velocity of light (for this medium) which is much greater than the velocity of sound. Consequently, the pumping pressure wave may be considered as being independent of the spatial coordinates  $P(t) = P_E \exp(i\omega t)$  (here the angular frequency  $\omega = 2\Omega$  and the pressure-amplitude of the pumping wave  $P_E$  can be easily calculated from Eq. (1), the constant term being omitted).

Under the action of pumping wave bubbles oscillate and emit sound waves. The initial distribution of bubbles is spatially homogeneous. As a result, the waves created by bubbles are added with different phases. Consequently, the resulting pressure of the useful wave is equal to zero.

However, for the active medium in the resonator an acoustic mode can be excited. Then bubbles can be bunched due to the acoustic radiation forces. This leads to self-synchronization of the oscillating bubbles and the amplification of the mode. Thus, the phase bunching of the bubbles is due to the acoustic radiation forces.

The equation for the radii of the pulsating bubbles is given by [4]

$$R_1(t) = -\frac{A}{\rho_1 R_0^2 \omega^2} (P_E \exp(i\omega t) + P'(\bar{r}, t)). \quad (2)$$

The right part of this formula contains the resulting pressure acting at the bubble: the first term corresponds to the pumping wave, the second term describes the pressure created by the oscillations of other bubbles;  $A = R_0 / [(\omega_0/\omega)^2 - 1 + i\delta]$  is the scattering amplitude;  $R_0$  is the mean bubble radius;  $\rho_1$  is the liquid density;  $\omega_0 = \omega_0(R_0)$  is the resonance frequency of the bubble; and  $\delta$  is the absorption constant.

The sound wave  $P'(\bar{r}, t)$  is described by the well known Eq. [4]

$$\Delta P' - \frac{1}{c_1^2} \frac{\partial^2 P'}{\partial t^2} = \rho_1 \frac{\partial^2}{\partial t^2} \int_0^\infty 4\pi n(\bar{r}, R_0, t) R_0^2 R_1(t) dR_0, \quad (3)$$

where  $c_1$  is the speed of sound in the pure liquid (without bubbles) and  $n(r, R_0, t)$  is a function of the bubble size distribution ( $n$  is equal to the number of bubbles per unit liquid volume the mean radii of which range from  $R_0$  to  $R_0 + dR_0$ ). In order to simplify the calculations we assume that all bubbles have equal radii.

The translational motion of the bubble is given by the equation

$$\frac{2\pi}{3} \rho_1 R_0^3 \frac{d\bar{U}}{dt} = \bar{F}_1 + \bar{F}_2 + \bar{D} + \bar{F}_r + \bar{F}_B. \quad (4)$$

Here  $\bar{F}_1 = -2\pi\rho_1 R_0^2 \bar{U} dR_1/dt$  is the drag force due to the bubble volume oscillations (its time-average  $\langle \bar{F}_1 \rangle = 0$ );  $\bar{F}_2$  is the buoyant force which is small for small particles;  $\bar{D}$  is the viscous drag force which for small Reynolds number  $Re = 2R_0 U \rho_1 / \mu_1$  ( $\mu_1$  is the liquid viscosity) is given by Stokes law  $\bar{D} = -4\pi\mu_1 R_0 \bar{U}$  (for gas bubbles [5] the numerical factor is equal  $4\pi$  not  $6\pi$ );  $\bar{F}_r$  is the time-average acoustic radiation force

$$\bar{F}_r = -(4\pi/3) \langle R^3(t) \bar{\nabla} P(\bar{r}, t) \rangle$$

(here  $R(t) = R_0 + R_1(t)$  is the current bubble radius,  $P(\bar{r}, t)$  is the resulting pressure acting at the bubble);  $\bar{F}_B$  is the so-called secondary Bjerkness force due to the interaction between the bubble concerned and the rest (this force is created by the secondary radiation of the bubbles and usually smaller compared to  $\bar{F}_r$ ).

Eqs. (2)–(4) must be supplemented with the balance equation (we shall neglect the coagulation of bubbles)

$$\frac{\partial n}{\partial t} + \text{div}(n\bar{U}) = 0. \quad (5)$$

We shall study the initial stage of the bubble bunching when the deviation  $n'(\bar{r}, R_0, t)$  of the distribution function from the equilibrium value of  $n_0(R_0)$  is small:  $n(\bar{r}, R_0, t) = n_0(R_0) + n'(\bar{r}, R_0, t)$ . The resulting pressure is  $P(\bar{r}, t) = P_0(t) + \Psi(\bar{r}, t)$ , where  $\Psi(\bar{r}, t)$  is the amplitude of the useful acoustic mode which is much less than  $P_0(t)$ .

After linearization of Eqs. (2)–(5) in  $\Psi(\bar{r}, t)$  and  $n'(\bar{r}, R_0, t)$  and substitution

$$\Psi(\bar{r}, t) = -\frac{\partial Z(\bar{r}, t)}{\partial t} \exp(i\omega t) \quad (6)$$

we have a (third order) differential equation for  $Z$ :

$$\begin{aligned} \frac{d^3 Z}{dt^3} + 2i\omega \frac{d^2 Z}{dt^2} + i\beta_0 c_1^2 \frac{dZ}{dt} \\ = \frac{FP_E^2 c_1^2 k_{\text{eff}}^2}{\gamma} (\alpha_0 + i\beta_0) \{ (\alpha_0 - i\beta_0) F^* Z \\ + (\alpha_0 + i\beta_0) FZ^* \} \end{aligned} \quad (7)$$

(we take the spatial dependence of  $Z(\bar{r}, t)$  and  $n'(\bar{r}, R_0, t)$  on  $z$  in the form of a standing wave  $Z(\bar{r}, t) \sim \sin(k_{\text{eff}} z)$ ,  $n'(\bar{r}, R_0, t) \sim \sin(k_{\text{eff}} z)$ , where the effective wave number is  $k_{\text{eff}} = (k_1^2 - \alpha_0^2)^{1/2}$ ).

Here  $\alpha_0 = -4\pi N_0 \text{Re } A$ ,  $\beta_0 = -4\pi N_0 \text{Im } A$ .  $N_0$  is the initial value of full number of bubbles per unit volume,  $F = (1 - (\alpha_0 + i\beta_0)/k_1^2)^{-1}$ , and  $k_1 = \omega/c_1$ .

For the following analysis we suggest some simplifications. Let us assume that the gas content is small, i.e.  $|\alpha_0| \ll k_1^2$ , and the bubbles are far from the resonance. Then  $\beta_0 \ll |\alpha_0|$ ,  $k_{\text{eff}} \approx k_1$ .

We put  $Z = a + ib$ , where  $a$  and  $b$  are real functions. This substitution of  $Z$  into Eq. (7) allows us to obtain the equation for the function  $a$  of the third order (and in the first order of  $\beta_0$ ). We seek a solution to this equation as  $a \sim \exp(Gt)$ , where  $G$  is the time constant of the useful mode. The value of  $G$  is  $\geq 0$  if

$$P_E \geq P_{\text{st}} = \frac{c_1}{|\text{Re } A|} \sqrt{(-6 \text{Im } A) \mu_1 \rho_1 R_0 \omega}. \quad (8)$$

The quantity  $P_{\text{st}}$  corresponds to the starting current in an FEL [1].

From Eq. (8) it follows that  $P_{\text{st}} \sim \mu_1^{1/2}$  and  $P_{\text{st}} \sim \beta_0^{1/2}$ . The physical meaning of these dependences is clear. The viscosity prevents the bunching of bubbles. Therefore, an increase of the viscosity leads to an increase of the quantity  $P_{\text{st}}$ . An increase of  $\beta_0$  results in an increased energy absorption. Accordingly, the starting pumping amplitude also increases.

At the limit  $\omega \ll \omega_0$  we can obtain  $P_{\text{st}} \approx 2c_1 \sqrt{\mu_1 \rho_1 \omega \delta}$ . In the case of air bubbles with the radii  $R_0 = 15 \mu\text{m}$  in water and at a frequency  $f = 1.5 \text{ kHz}$  one obtains  $P_{\text{st}} = 2.8 \text{ kPa}$  ( $E_0 \approx 25 \text{ kV/cm}$ ).

There is thus a deep analogy between an FEL and the suggested scheme of an acoustic laser based on “free” gas bubbles. In both cases we have the same integral parts, such as an active medium, phase bunching and a starting pressure (or current).

## References

- [1] C. Marshall, Free-Electron Laser (Macmillan, New York, 1985).
- [2] L.D. Landau and E.M. Lifshitz, Electrodynamics of Homogeneous Mediums (Nauka, Moscow, 1976) in Russian.
- [3] S.T. Zavtrak and E.V. Korobko, Akust. Zh. 37 (1991) 944.
- [4] K.A. Naugol'nykh and L.A. Ostrovsky, Nonlinear Processes in Acoustics (Nauka, Moscow, 1990) in Russian.
- [5] L.D. Landau and E.M. Lifshitz, Hydrodynamics (Nauka, Moscow, 1990) in Russian.



ELSEVIER

## Modeling of space charge dominated performance of the CEBAF FEL injector

H. Liu<sup>\*</sup>, J. Benesch, S. Benson, J. Bisognano, D. Douglas, G. Neil, D. Neuffer,  
C. Sinclair, B. Yunn

*CEBAF, 12000 Jefferson Avenue, Newport News, VA 23606, USA*

### Abstract

An FEL injector is under development based on the photoemission gun and superconducting radio frequency (srf) technologies established at CEBAF. The injector will deliver  $\sim 10$  MeV CW electron beams having a transverse normalized rms emittance  $< 11 \pi$  mm mrad and a longitudinal rms emittance  $< 35 \pi$  deg-keV with up to 200 pC charge within 8 ps ( $4\sigma$ ) at a repetition rate of 24.95 MHz or 2.495 MHz. Its performance has been modeled using a version of PARMELA with a point-by-point space charge algorithm. The details of modeling and the simulated performance of the injector are presented.

### 1. Introduction

A high brightness electron beam injector is under development at CEBAF for high power industrial FEL applications [1]. It simply consists of a 500 kV dc photoemission gun [2], a room-temperature buncher, a cryounit containing two standard CEBAF srf cavities, and two solenoids. An injection line will transport the beams from the cryounit exit to the main accelerator.

The space charge dominated performance of this injector has been modeled and optimized using a version of PARMELA with a point-by-point space charge algorithm [3]. It has been numerically demonstrated that the design will meet the requirements, although the phase space density distributions bifurcate as the electrons are focused and bunched along the heavily space charge loaded system. The details of modeling and the simulated results are presented and discussed in this paper.

### 2. Space charge algorithm

The design requires an appropriate algorithm for modeling of beam generation, transport and bunching with full space charges included. As an electron pulse is typically as long as 90 ps ( $6\sigma$ ) in the gun region in our case, a particle-in-cell (PIC) code does not apply. PARMELA has

been widely used for photoemission rf gun simulations. However, its conventional space charge algorithm based on the 2-D mesh method does not apply to our case either, since it requires a slow change in the beam envelope and small beam energy spread. These conditions break in our case, as the bunch expands axially from a slice at the cathode to a few centimeters long at the gun exit, and the beam energy spread is large during extraction from the cathode.

Those limitations can be circumvented by using McDonald's point-by-point space charge algorithm [3]. However, it turned out that the results could be noise dominated if a too small particle size factor is chosen [4,5]. Driven by the desire of accurately modeling our injector, we conducted extensive studies on this issue [6]. We assumed that the emittance growths of the free drifting Gaussian beams we were calculating using this algorithm are known from the ISIS simulations [7]. Then we varied the particle size factor in the algorithm to find out its optimal value, that is, giving emittance growth consistent with ISIS. Finally we came up with the concept of a variable particle size factor which is described as a point in the parameter space of  $(\gamma L/a, \nu)$

$$f = 0.16 N_p^{1/3} (\gamma L/a)^{1/6} / \nu^{1/4}, \quad (1)$$

where  $N_p$  is the number of simulated macroparticles,  $\gamma$  is the relativistic energy factor,  $L$  is the bunch length defined as the FWHM of a Gaussian profile,  $a$  is the beam radius, and  $\nu = I/I_A$  with  $I$  being the beam current and  $I_A = 17$  kA the Alfvén current. The scheme of screening the artificial close-encounter effect is described in Refs. [3–6]. We have implemented Eq. (1) into PARMELA. The particle

<sup>\*</sup> Corresponding author. Tel. +1 804 249 6381, fax +1 804 249 5024, e-mail: liu@cebaf.gov.

size factor is calculated at each step of integration according to the beam aspect ratio  $\gamma L/a$  and  $v$  at that instant.

To probe the appropriateness of the algorithms, we modeled our photoemission gun using the two methods. Both longitudinal and transverse emittances were overestimated by a factor of two or so when the mesh method was used, or when the point-by-point method was used with a small particle size factor of 1.75, compared with that from the variable particle size factors around 10.

### 3. Design considerations

In our 500 kV photoemission gun, the dc field gradient at the cathode is 10 MV/m. The space charge field gradient at the cathode can be estimated according to the formula for the terminal space charge field of a slug beam [8,9]

$$E_z = \frac{Q}{2\pi\epsilon_0 a^2} \left( 1 + \frac{a}{\gamma L} - \sqrt{1 + \left( \frac{a}{\gamma L} \right)^2} \right), \quad (2)$$

where  $\gamma$  is the relativistic energy factor,  $a$  is the beam radius and  $L$  is the bunch length. In the limit of  $a/\gamma L \rightarrow \infty$  at the cathode, we have  $E_z = 0.16Q/a^2$  [MV/m] with  $Q$  in nC and  $a$  in cm. With our typical gun parameters of  $Q = 0.2$  nC and  $a = 0.3$  cm,  $E_z = 0.4$  MV/m, which is far below the space charge limited regime.

It is very helpful to take the two extreme limits in Eq. (2) to understand the space charges in general. It leads to

$$2\pi\epsilon_0 a^2 E_z / Q = \begin{cases} 1, & a/\gamma L \gg 1, \\ a/\gamma L, & a/\gamma L \ll 1. \end{cases} \quad (3a)$$

$$(3b)$$

It is clear that: (1) in the gun region, the space charge effect is dominated by the amount of charge, whereas at high energies, it is dominated by the peak current; (2) at high energies  $E_z$  is proportional to  $1/\gamma$  instead of  $1/\gamma^2$ , although this may not be true for the rms energy spread; (3) one should avoid focusing the beam strongly, which was why we made the beam parallel at the exit of the cryounit.

Simulation showed that the beam is strongly divergent out of the gun. This suggests that we place the first solenoid as close to the anode as possible. However, a design constraint is that the field penetration from the solenoid onto the cathode should be low to avoid causing emittance growth. Using our gun parameters, it is estimated that  $B_z$  should be smaller than 1 G to keep the emittance growth below  $0.5 \pi$  mm mrad.

The solenoid configuration is simply scaled down from a design used for 20 keV protons [10]. The major concern is the aberration when the beam goes through it. It was designed using POISSON, and the aberration was checked by substituting the conventional ideal solenoid model in PARMELA with the one calculated by POISSON. It turned

out that the difference between the two is 12% in emittance growth at the exit of the solenoid with the same condition that the beam was focused to a waist at the center of the buncher.

The buncher design is similar to the fourth cell of the CEBAF capture section. The apertures at both ends were enlarged to allow better beam transmission [11]. Usually the rf phase of a buncher should be off zero-crossing towards the deceleration direction to avoid rf nonlinearities for optimal bunching effect. However, the simulation showed that: (1) the beam dynamics is space charge dominated; (2) as the velocity of an electron is  $0.86c$  at 500 kV and the srf cavities inside the cryounit are speed-of-light in phase velocity by design, the beam would always be decelerated before being accelerated at the beginning of the first srf cavity. The latter results in an energy dip which is unfavorable as far as the space charge is concerned. The depth of this energy dip is  $\sim 200$  kV. For these reasons, we set the buncher at the zero-crossing phase.

The beam dynamics is most complicated at the first cell of the first srf cavity in the cryounit. When the gradient is fixed, the focusing and bunching capabilities may change drastically with off-crest phase for an incident beam of 500 kV. When the phase is on-crest, the energy spread is minimum, but the bunching effect is too weak and the focusing effect is too strong. As a compromise, the phase was set to  $20^\circ$  off crest toward the bunching direction. Because of the strong cavity focusing effect, the beam must be divergent going into the cryounit. The second srf cavity was set on crest. In this way, the energy spread can be minimized, which is favorable for the injection line.

### 4. Performance optimization

With those considerations as discussed above in mind, the design was optimized using PARMELA, SUPERFISH and POISSON, with full space charges included. The typical starting parameters used were: voltage 500 kV, charge/bunch 200 pC, bunch length 90 ps ( $6\sigma$ ) and cathode radius 3 mm ( $2\sigma$ ). In this section we summarize the optimized element and beam parameters.

The first solenoid is 13 cm long with a field strength of 360 G to focus the beam to a waist at the center of the buncher. The buncher was set to the zero-crossing phase and a gradient of  $\sim 1.3$  MV/m to bunch the electrons axially to a waist at the beginning of the first srf cavity of the cryounit. The second solenoid is 10 cm long with a field strength of 295 G to match the beam into the cryounit. Usually when the longitudinal performance was optimized, the second lens was tweaked further to minimize the emittance of the beam out of the cryounit.

The bunch length reached slightly above the minimum of  $\sim 15$  ps prior to the cryounit. The first srf cavity was set  $20^\circ$  off crest with a gradient of 10 MV/m in order to

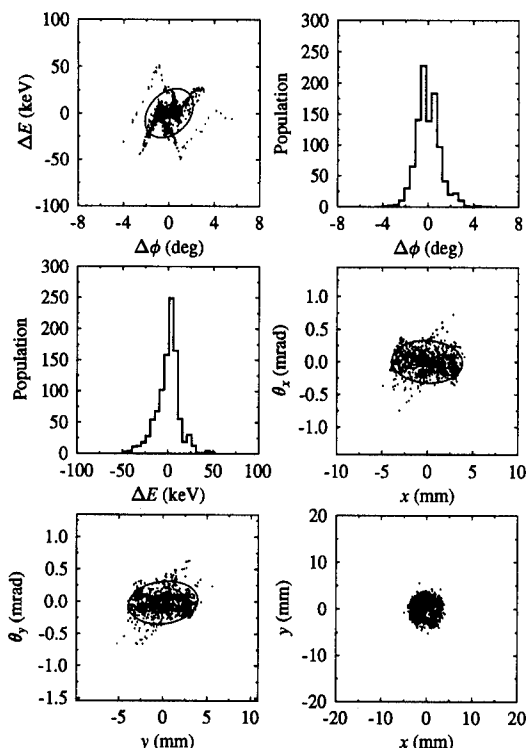


Fig. 1. Beam distributions with optimized performance at the exit of the cryounit. About 10% particles are out of the ellipses in the transverse and longitudinal phase spaces.

optimize both the transverse and longitudinal beam properties. At the exit of the first srf cavity, the bunch length was  $\sim 8$  ps at 5 MeV and the beam was slightly divergent. The second srf cavity was set on crest to accelerate the beam to  $\sim 10$  MeV. At the exit of the cryounit, the beam became parallel.

The optimized beam parameters at the exit of the cryounit are: bunch length 2 ps ( $1\sigma$ ), normalized transverse rms emittance  $7\pi$  mm mrad, and longitudinal rms emittance  $12\pi$  deg-keV. The beam phase space density distributions with optimized performance at the exit of the cryounit are shown in Fig. 1. It is seen that bifurcations appeared in both transverse and longitudinal phase spaces. They are especially conspicuous in the longitudinal phase space.

To track the showing-up of the bifurcations, we show the longitudinal phase space distributions at several different locations in Fig. 2. It is seen that the bifurcations begin to show up after the first srf cavity. The phase space distributions rotate clockwise driven by the space charges. As is known, bifurcation results from focusing a beam to a waist, either transversely or axially. For this purpose, the beam envelopes and bunching process are shown in Fig. 3.

One of the most important parts of our simulations is to understand the bifurcations showing up in the phase space

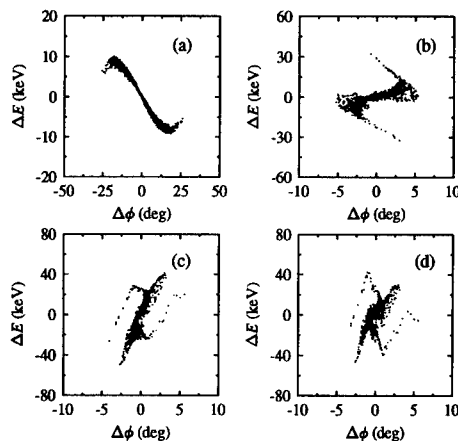


Fig. 2. Longitudinal phase space distributions at (a) entrance to the buncher, (b) entrance to the first srf cavity, (c) exit of the first srf cavity, and (d) exit of the second srf cavity.

density distribution plots. This kind of phenomenon had been discovered and studied as a general topic [12–15] far earlier than when we encountered it here. This issue is so crucial to our injector that it is the dominant factor limiting better performance. It may come from the energy dip discussed previously and the cavity focusing effect from the cryounit, or it may be due to compressing a 200 pC bunch at 500 kV into a few ps at 10 MeV. We intend to investigate this theoretically and experimentally.

## 5. Injection line

The injection line consists of four quadrupoles and five magnets in a staircase configuration. It provides the required optical functions of  $\beta_x = \beta_y = 30$  m and  $\alpha_x = \alpha_y = 0$  prior to the main accelerator. It is achromatic and isochronous by design when the space charge effect is excluded. However, the energy of a particle was modified from magnet to magnet by the space charges, and some emittance growth was caused due to the residual dispersion. The importance of space charge at 10 MeV was

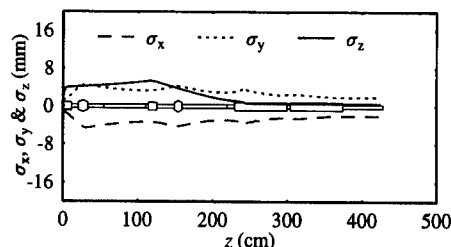


Fig. 3. Beam envelopes and bunching process with the optimized performance. The elements shown on the x-axis are gun, lens 1, buncher, lens 2, srf cavity 1 and srf cavity 2, in sequence.

numerically found earlier [16] and its effect can be estimated by applying tune shift analysis [17] and longitudinal envelope equations [18].

Although the reference design can meet the specifications, several other injection schemes were investigated as well: (1) the chicane proposed earlier [19] for the IR FEL; (2) a U-turn design; (3) a segment-by-segment achromatic design. The dilemma was always to conserve the beam emittance while providing the required beam conditions prior to the main accelerator. Optimization of the projected system performance is continuing.

## 6. Summary

The performance of the CEBAF FEL injector has been modeled using a point-by-point space charge algorithm with variable particle size factors. It is found that the major limitation to the performance of the injector is the bifurcations in phase space density distributions. This issue is being further studied.

## Acknowledgements

We wish to thank B. Carlsten, K. Kim and K. McDonald for discussions. This work was supported by the Virginia Center for Innovative Technology.

## References

- [1] G. Neil et al., these Proceedings (16th Int. Free Electron Laser Conf., Stanford, CA, USA, 1994) Nucl. Instr. and Meth. A 358 (1995) 159.
- [2] C. Sinclair, Nucl. Instr. and Meth. A 318 (1992) 410.
- [3] K. McDonald, IEEE Trans. Electron. Devices ED-35 (1988) 2052.
- [4] H. Liu, Computational Accelerator Physics, AIP Conf. Proc. No. 297, ed. R. Ryne (1994) p. 508.
- [5] H. Liu, CEBAF TN No. 94-020 (1994).
- [6] H. Liu, CEBAF TN No. 94-040 (1994).
- [7] M. Jones and B. Carlsten, Proc. 1987 IEEE Particle Accelerator Conf., IEEE Catalog No. 87CH2387-9 (1987) p. 1319.
- [8] J. Haimson, IEEE Trans. Nucl. Sci. NS-12 (1965) 996.
- [9] J. Haimson, Nucl. Instr. and Meth. 39 (1966) 13.
- [10] K. Mittag and D. Sanitz, 1981 Linear Accelerator Conf., Santa Fe, NM, Oct. 19–23, 1981, LANL report LA-9234-C (1982) p. 156.
- [11] B. Yunn, CEBAF TN No. 94-021 (1994).
- [12] I. Bernstein and S. Trehan, Nucl. Fusion 1 (1960) 3.
- [13] O. Anderson, Particle Accelerators 21 (1987) 197.
- [14] H. Hanerfeld et al., SLAC-PUB-4916 (1989).
- [15] J. Bisognano, High-Brightness Beams for Advanced Accelerator Applications, AIP Conf. Proc. No. 253, eds. W. Destler and S. Guharay (1992) p. 42.
- [16] P. Liger et al., Nucl. Instr. and Meth. A 318 (1992) 290.
- [17] J. Bisognano, unpublished.
- [18] D. Neuffer, to be published.
- [19] P. Liger et al., 1992 Linear Accelerator Conf. Proc., AECL-10728, p. 85.





ELSEVIER

# Nonlinear wave processes during the propagation of a high-current electron beam in an ion-beam undulator

Yu.Ya. Golub, N.E. Rozanov

*Moscow Radiotechnical Institute, Academy of Sci., Russia, Varshavskoye shosse 132, 113519 Moscow, Russian Federation*

## Abstract

The results of investigations of ion beam undulator stability concerning the excitation of nonstationary waves and electron–ion instabilities in two-beam electron–ion system are presented. The instabilities are studied in different regimes by computer simulation. The detrimental influence of the instabilities on the ion undulator's performance is demonstrated. Conditions for minimal influence of the instabilities on the beam's dynamics are found.

In the last five years ion undulators for FELs have been investigated. A principle of the work consists in the excitation of transverse oscillations of a beam's electrons when injected into a region with noncompensated ion charge. To date different types of ion undulators have been considered. We investigate the ion-beam undulator which consists of a nonrelativistic ion beam propagating co-axially with a high-current relativistic electron beam. In principle this undulator can function in the steady-state regime because the disturbed parts of the ion beam are removed from the system by the longitudinal velocity of the ions. The stationary characteristics of ion-beam undulators were investigated in Ref. [1].

We investigate a two-beam electron–ion system consisting of a nonrelativistic ion beam propagating co-axially with a high-current relativistic electron beam. Two cases of beam injection are discussed: equilibrium and nonequilibrium. The kinetic description of both beams is provided by means of solutions of the Vlasov equations for the electron and ion distributions functions,  $f_{e,i}(t, z, r, v_z, v_r, v_\theta)$ . The equations for the scalar potential and the three components of the vector potential are used for finding the electromagnetic fields. The equations are solved in the long-wave ( $\partial^2/\partial z^2 \ll \Delta_\perp$ ), low-frequency ( $\partial^2/\partial t^2 \ll c^2\Delta_\perp$ ), axial-symmetric ( $\partial/\partial\theta \equiv 0$ ) case, where  $\Delta_\perp$  is the transverse part of the Laplace operator. Boundary conditions for the potentials follow from the system's axial symmetry, the presence of conducting tube with radius  $R_w$  and the gauge condition  $\text{div } \mathbf{A} = 0$ . The Vlasov equations are solved by the macroparticle method. It is assumed that the steady-state process is periodic in time set with a frequency  $\omega$ . In this case it is convenient to use the longitudinal coordinate  $z$  as the independent variable, using the relation  $d/dt = (1/v_z)d/dz$ , where  $v_z$  is the velocity of a given macroparticle. The problem is then reduced to the evolution of a periodic-in-time system on  $z$ .

The periodic in time (with frequency  $\omega$ ) potential function are of the form

$$G(t, z, r) = \bar{G}(z, r) + \text{Re} \left\{ \sum_j \tilde{G}_j(z, r) e^{ij\omega t} \right\},$$

which is substituted into the equations for the potential components and integrated over a time period. The equations for the four components of the 4-potential  $A_i(\Delta_{ri}A_i = 4\pi\rho_i, i = 1, 2, 3, 4, \Delta_{ri}$  is the radial parts of the Dalmber operator, and  $\rho_i$  are the components of the 4-density) are solved at every  $z$ -cross-section by the grid method.

First we study the case where both beams are injected in equilibrium into the drift tube.

The strongest of the instabilities in the two-beam electron–ion system are the cyclotron-focusing instability (CFI) [2,3] and the Budker–Chirikov instability (BCI) [4,5]. They are connected with the resonance of the slow-cyclotron wave of the electron beam and the fast Langmuir wave and fast betatron wave of the ion beam, respectively.

The cyclotron-focusing instability is considered first. The dependencies of  $\text{Re } \psi$  and  $\text{Im } \psi$  (real and imaginary parts of the scalar potential normalized to  $m_e c^2/eR_w$ ) on  $\xi \equiv z/R_w$  at  $r = 0$  are shown in Fig. 1a for current  $J_e = 1$  kA, relativistic factor  $\gamma_e = 3$ , longitudinal magnetic field  $B_0 = 1$  kG, ion beam density  $n_{i0} = fn_{e0}$ ,  $f = \frac{1}{9}$ , ion longitudinal velocity  $\beta_{i0} = 0.01c$ ,  $\omega R_w/c = 0.0031$ , beam radii  $a_{i0} = a_{e0} = 0.8R_w$ ,  $R_w = 1.5$  cm. Exponential growth of the potential amplitude, saturation of CFI and further evolution can be seen. The dependence of the space increments of CFI on frequency is shown in Fig. 1b. The instability is displayed in the growth of the amplitude modulation of the electron beam radius and in the longitudinal direction of the ion beam. CFI saturation is due to ion trapping in the slow cyclotron wave of the electron

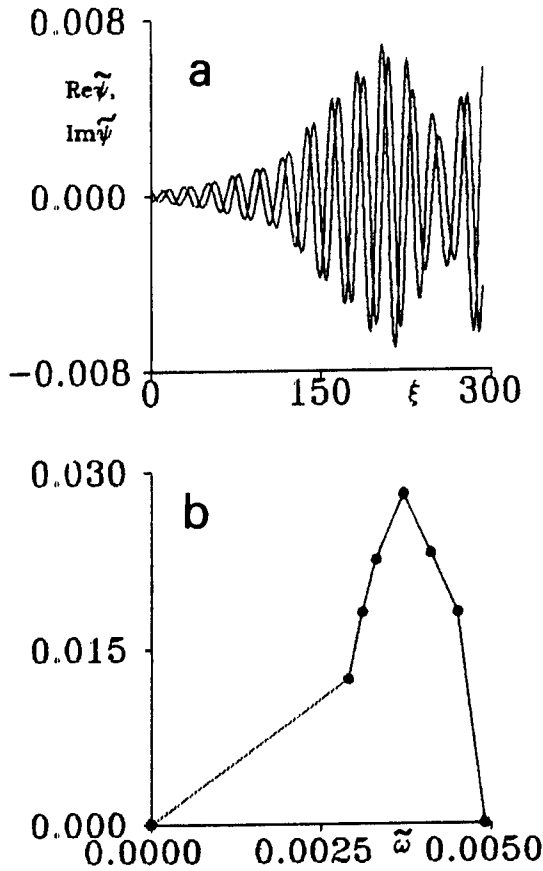


Fig. 1. (a) The dependences of the real ( $\text{Re } \tilde{\psi}$ ) and imaginary ( $\text{Im } \tilde{\psi}$ ) parts of the scalar potential normalized to  $m_e c^2 / e R_w$  on  $\xi$  at  $r = 0$  for current  $J_e = 1$  kA, relativistic factor  $\gamma_e = 3$ , longitudinal magnetic field  $B_0 = 1$  kG, ion beam density  $n_{i0} = f n_{e0}$ ,  $f = \frac{1}{9}$ , ion longitudinal velocity  $\beta_{i0} = 0.01c$ ,  $\omega R_w / c = 0.0031$ , beam radii  $a_{i0} = a_{e0} = 0.8 R_w$ ,  $R_w = 1.5$  cm. The CFI case. (b) The dependence of space increments of CFI from frequencies  $\tilde{\omega} = \omega R_w / c$ .

beam. The phase velocity of the unstable wave is near the phase velocity of the fast Langmuir wave of the ions in the CFI case. The wave amplitude at the moment of saturation is determined largely by the ion trapping condition, but quantitatively can differ for many reasons. The main one is enhancement of the instability development process after the ion trapping owing to radial nonuniformity of the wave amplitude.

The Budker–Chirikov instability is investigated next. The dependences of  $\text{Re } \tilde{\psi}$  and  $\text{Im } \tilde{\psi}$  on  $\xi$  at  $r = 0$  for  $J_e = 0.5$  kA,  $\gamma_e = 3$ ,  $a_{i0} = a_{e0} = 0.6 R_w$ ,  $R_w = 1.5$  cm,  $B_0 = 1$  kG,  $f = \frac{1}{9}$ ,  $\beta_{i0} = 0.05c$ ,  $\omega R_w / c = 0.031$  are shown in Fig. 2a. Exponential growth of the amplitude, saturation of BCI and further evolution can be seen. The dependence of the space increments of BCI on frequency is shown in Fig. 2b for the same parameter as on Fig. 2a, except  $\beta_{i0} = 0.03c$ . The instability in the time periodic regime is seen in

the growth of the radial modulation amplitude of both beams along the longitudinal coordinate. It can be seen that the instability exists in a narrow frequency range which is higher than the frequencies at which CFI is developed at the same parameters. The BCI saturation mechanism is associated with the change of the oscillation wavelength of the separate particles. When the oscillation amplitude grows the beams fall out of resonance. The oscillation wavelength changes due to an increase of non-isochronism with the amplitude growth because of the nonlinear dependence of equilibrium beam fields as a function of radius in the region  $r > a_{i0}$ ,  $a_{e0}$ .

When  $f \gamma_e^2 \approx 1$ , the frequency ranges of the studied instabilities differ from each other. Therefore only one instability is developed in every represented calculation at a given frequency in the one-mode regime. In principle, simultaneous development of both instabilities can be observed in a multimode regime. At  $f \gamma_e^2 \gg 1$ , these instabilities can be merged into one. But calculations at large ion beam density ( $f \gamma_e^2 = 4$ ) show that BCI saturation is not

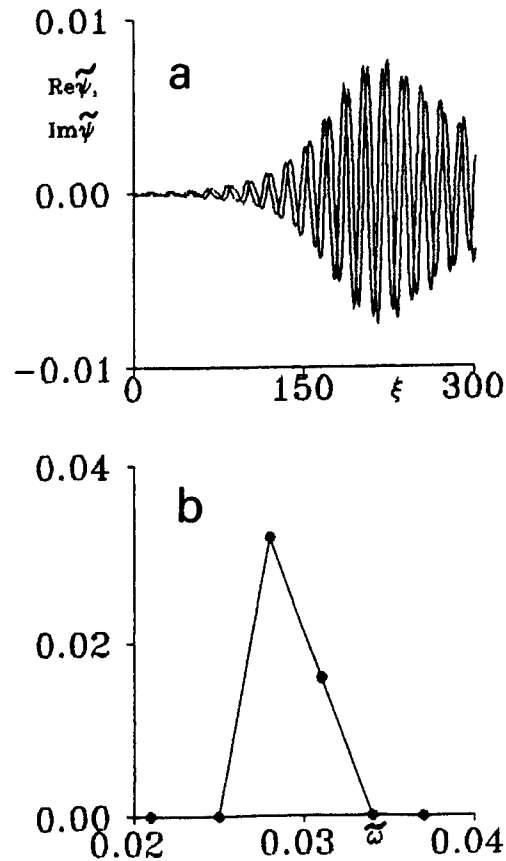


Fig. 2. (a) The dependences  $\text{Re } \tilde{\psi}$  and  $\text{Im } \tilde{\psi}$  on  $\xi$  at  $r = 0$  for  $J_e = 0.5$  kA,  $\gamma_e = 3$ ,  $a_{e0} = a_{i0} = 0.6 R_w$ ,  $R_w = 1.5$  cm,  $B_0 = 1$  kG,  $f = \frac{1}{9}$ ,  $\beta_{i0} = 0.05c$ ,  $\omega R_w / c = 0.031$ . The BCI case. (b) The dependence of space increments of BCI from frequencies with the same parameters as (a), except that  $\beta_{i0} = 0.03c$ .

reached and a large part of the ion beam escapes to the wall of the drift tube.

In this section we study nonlinear wave (nonstationary) processes which take place during nonequilibrium injection of a high-current relativistic electron beam on ion-beam undulator.

The solution of the equations confirms that the electron beam oscillates along  $z$  with large radial amplitude when injected with nonequilibrium transverse velocities. These oscillations are assumed to be useful for generation of electromagnetic waves in an FEL. In Fig. 3 the root-mean-squared, average over a time period, electron beam radius  $R_e$  is shown for current  $J_e = 1$  kA, relativistic factor  $\gamma_e = 3$ , longitudinal magnetic field  $B_0 = 1$  kG, ion beam density  $n_{i0} = fn_{e0}$ ,  $f = \frac{2}{9}$ , ion longitudinal velocity  $\beta_{i0} = 0.01c$ ,  $\omega R_w/c = 0.0035$ , beam radii  $a_{i0} = a_{e0} = 0.8R_w$ ,  $R_w = 1.5$  cm. Over a distance  $\xi \equiv z/R_w < 120$  the vibrations of the electron beam are periodic. Nonstationary processes lead to the growth of electron–ion instabilities and destruction of the  $R_e$  oscillations. The dependences of  $\text{Re } \tilde{\psi}$  and  $\text{Im } \tilde{\psi}$  on  $\xi$  are shown in Fig. 4. The exponential growth of the amplitude and saturation of the instability can be observed.

Analysis of the modeling results shows that these instabilities lead to a decrease in the number of full large-amplitude stationary oscillations of the electron beam along

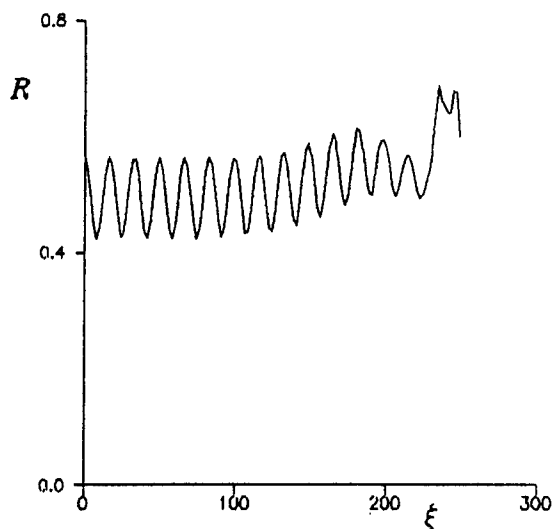


Fig. 3. The dependence of the root-mean-squared, average on time period, radius of electron beam  $R_e$  as a function of  $\xi$  for current  $J_e = 1$  kA, relativistic factor  $\gamma_e = 3$ , longitudinal magnetic field  $B_0 = 1$  kG, ion beam density  $n_{i0} = fn_{e0}$ ,  $f = \frac{2}{9}$ , ion longitudinal velocity  $\beta_{i0} = 0.01c$ ,  $\omega R_w/c = 0.0035$ , beam radii  $a_{i0} = a_{e0} = 0.8R_w$ ,  $R_w = 1.5$  cm.

$\text{Re } \tilde{\psi}, \text{Im } \tilde{\psi}$

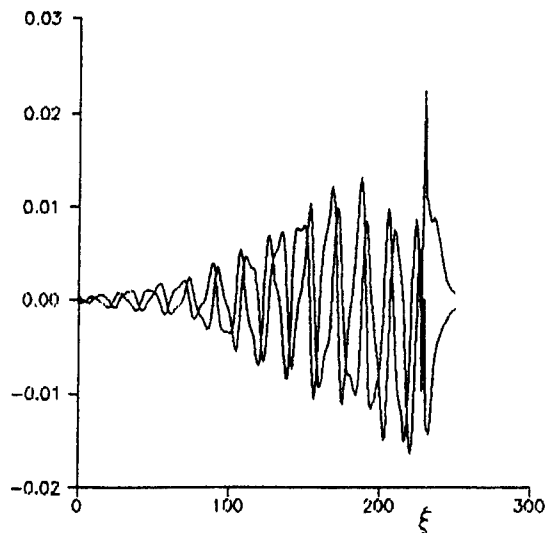


Fig. 4. The dependences of real and imaginary parts of the scalar potential normalized to  $m_e c^2 / eR_w$  as a function of  $\xi$ .

the longitudinal coordinate. This influence of the instabilities depends on many factors: the number of accounted waves, the increments of the instability on a given wave frequency, the initial amplitudes of the waves, etc.

The results of numerical investigation show that optimum parameters of the system, such as electron beam current  $J_e$ , ion beam density  $n_{i0}$ , and longitudinal magnetic field  $B_0$ , exist. The larger  $J_e$  or  $n_{i0}$ , the larger the amplitude of static electron beam oscillations. But the growth of instability increments with increasing of  $J_e$  or  $n_{i0}$  leads to a decreasing number of oscillation due to particles (ion or electron) escaping to the wall of drift tube. Decreasing  $B_0$  gives a larger amplitude of electron beam vibrations, but the number in a given distance also decreases due to lengthening of the period of the vibrations.

## References

- [1] Yu.Ya. Golub and N.E. Rozanov, In: Book of Abstracts of the 15th Int. FEL Conf. (FEL '93), The Hague, The Netherlands, 1993, p. 110.
- [2] V.P. Indykul, I.P. Panchenko, V.D. Shapiro and V.I. Shevchenko, Pis'ma v ZhETF 20 (1974) 153; Fizika plazmy 2 (1976) 775.
- [3] K.V. Khodatyayev and V.N. Tsitovich, Fizika plazmy 2 (1976) 301.
- [4] G.I. Budker, Atomnaya energiya 1 (1956) 9.
- [5] B.V. Chirikov, Atomnaya energiya 19 (1965) 239.



ELSEVIER

# FEL gain calculation for imperfectly matched electron beams <sup>☆</sup>

R.L. Swent <sup>\*</sup>, K.W. Berryman

Stanford Picosecond FEL Center, W.W. Hansen Experimental Physics Laboratory, Stanford University, Stanford, CA 94305-4085, USA

## Abstract

We present here the details of an analytical small-signal gain calculation. The analysis builds on the basic one-dimensional analytical calculation by modeling the effects of finite electron beam size and imperfect matching of the electron beam to the wiggler. The calculation uses TRANSPORT [SLAC-91, Rev. 2 (1977)] parameters to describe the electron beam in order to easily take the output of beam transport calculations and use them as the input for FEL gain calculations. The model accepts an arbitrary TRANSPORT beam and includes the effects of energy spread, beam size, betatron oscillations, and focussing in the wiggler plane. The model has allowed us to calculate the range over which our FEL can be tuned by changing the electron energy alone (i.e., without changing any magnets).

## 1. Introduction

Most analytical calculations of FEL gain assume that the electron beam enters the wiggler with “perfect” matching conditions. The perfect match is that which minimizes the size of the electron beam cross-section throughout the wiggler. This in turn leads to the highest gain. In practice this perfect match is difficult to achieve because it depends on the emittance of the electron beam, a quantity which is notoriously difficult to measure accurately. We wished to investigate the effect of imperfect electron beam matching on the FEL gain. In particular, we were interested in how far one could tune the FEL by changing the electron energy alone before the gain decreased significantly. These results [1] were presented previously, but the details of the calculation have not been published before. There are certainly other cases (e.g., a gas-loaded FEL [2]) where one would like to calculate the FEL gain for other electron beam conditions.

## 2. Gain derivation

The basic formulation is the weak-field, low-gain limit based upon the pendulum equation. This approach was developed by Colson and co-workers [3–5]. The spread of electron phase velocities due to energy spread and betatron oscillations is taken into account using Colson’s techniques. The transverse structure of the optical mode and

the electron beam, both of which are assumed to be Gaussian, are taken into account by the methods of Amir and Greenzweig [6], except that here the electron beam size is allowed to vary along the length of the wiggler.

We use the notation of Ref. [6], which is basically that of Colson, with the difference that transverse coordinates are normalized to  $\sqrt{2L/k}$ , where  $L$  is the wiggler length and  $k$  is the optical wavevector. The gain per pass can be obtained from Eq. (5) of Ref. [3] or Eq. (3.2) of Ref. [6] as:

$$G = \frac{K_f \operatorname{Re} i}{\int |a(\mathbf{r}, -\frac{1}{2})|^2 d^2\mathbf{r}} \int_{-1/2}^{1/2} d\tau \int d^2\mathbf{r} j(\mathbf{r}, \tau) \times \int_{-1/2}^{\tau} d\tau' (\tau - \tau') \times a^*(\mathbf{r}, \tau) a(\mathbf{r}, \tau') \langle e^{-i\nu_f(\tau - \tau')} \rangle. \quad (1)$$

Here the denominator in front is the power at the entrance of the wiggler ( $\tau = -\frac{1}{2}$ ),  $j(\mathbf{r}, \tau)$  is the dimensionless current density, and  $a(\mathbf{r}, \tau)$  is the dimensionless electric field.  $K_f$  is the planar undulator correction factor:

$$K_f = J_0 \left( \frac{\frac{1}{2}K^2}{1 + K^2} \right) - J_1 \left( \frac{\frac{1}{2}K^2}{1 + K^2} \right),$$

where  $K$  is the dimensionless wiggler field strength. The expression in angle brackets is the usual average over the initial distribution of electron phase velocities.

We restrict ourselves here to considering planar wigglers. In this case the electron beam cross-section in the non-wiggle plane (the  $y$ -direction) will be free expansion of a Gaussian. In our calculation the size and location of the waist of this Gaussian are arbitrary. In the wiggle plane (the  $x$ -direction) the electron beam envelope will undergo betatron oscillations, the amplitude of which are deter-

<sup>☆</sup> Work supported by the Office of Naval Research, Contract #N00014-91-C-0170.

<sup>\*</sup> Corresponding author. Tel. +1 415 725 2203, fax +1 415 725 8311, e-mail rlswent@leland.stanford.edu.

mined by the beam size and emittance at the entrance of the wiggler. Then we have

$$j(r', \tau) = \frac{i_0}{2\pi\xi\eta} e^{-(x^2/(2\xi^2)) - (y^2/(2\eta^2))}, \quad (2)$$

where

$$i_0 = \frac{8\pi^2 N e^2 K^2 L^2}{\gamma^3 m c^3} \left( \frac{k}{2L} \right) I,$$

$I$  is the electron beam current (peak),  $\xi = \xi(\tau)$  is the rms size of the electron beam in the  $x$ -direction, and  $\eta = \eta(\tau)$  is the rms size of the electron beam in the  $y$ -direction.

Using the  $\sigma$ -matrix notation of TRANSPORT [7] to describe the electron beam at the entrance to the wiggler we have

$$\eta^2 = \left( \frac{k}{2L} \right) \left( \sigma_{33} - \frac{\sigma_{34}^2}{\sigma_{44}} \right) (1 + q_y^2(\tau - \tau_0)^2),$$

$$\tau_0 = -\frac{1}{2} - \frac{\sigma_{34}}{L\sigma_{44}}$$

= offset of waist from center of wiggler,

$$q_y = L\sigma_{44}/\sqrt{\sigma_{33}\sigma_{44} - \sigma_{34}^2}.$$

In the  $x$ -direction the beam undergoes betatron oscillations, so we have

$$\begin{aligned} \xi^2 = & \left( \frac{k}{2L} \right) \left[ \sigma_{11} \cos^2\left(\omega_\beta\left(\tau + \frac{1}{2}\right)\right) \right. \\ & + \frac{2L\sigma_{12}}{\omega_\beta} \cos\left(\omega_\beta\left(\tau + \frac{1}{2}\right)\right) \sin\left(\omega_\beta\left(\tau + \frac{1}{2}\right)\right) \\ & \left. + \frac{L^2\sigma_{22}}{\omega_\beta^2} \sin^2\left(\omega_\beta\left(\tau + \frac{1}{2}\right)\right) \right], \end{aligned}$$

where  $\omega_\beta = 2\pi NK/\gamma$  is the betatron frequency. Inserting Eq. (2) into Eq. (1) and integrating over the transverse coordinates gives

$$G = -\frac{2qi_0K_f}{\pi} \text{Im} \int_{-1/2}^{1/2} d\tau \int_{-1/2}^{\tau} \frac{(\tau - \tau') \langle e^{-i\nu_0(\tau - \tau')} \rangle}{D_x D_y}, \quad (3)$$

where

$$D_x = [1 + q^2\tau\tau' + 4q\xi^2 - iq(\tau - \tau')(1 + 2q\xi^2)]^{1/2},$$

$$D_y = [1 + q^2\tau\tau' + 4q\eta^2 - iq(\tau - \tau')(1 + 2q\eta^2)]^{1/2},$$

$$q = L/z_0,$$

and  $z_0$  is the Rayleigh length for the optical mode, which is described by

$$a(r, \tau) = \frac{a_0}{1 + iq\tau} e^{-qr^2/(1 + iq\tau)}.$$

The average over initial phase velocities can be written as

$$\begin{aligned} \langle e^{-i\nu_0(\tau - \tau')} \rangle &= \int_{-\infty}^{\infty} f(\nu_i) e^{-i\nu_0(\tau - \tau')} d\nu_i \\ &= e^{-i\nu_0(\tau - \tau')} \int_{-\infty}^{\infty} f(u) e^{-iu(\tau - \tau')} du. \end{aligned} \quad (4)$$

Here  $u$  is the deviation from the central phase velocity  $\nu_0$  and  $f(u)$  is the probability density distribution for  $u$ . Three sources of phase velocity variation will be considered: energy spread, the spread in initial  $y$ -angles, and the betatron oscillations. Since Eq. (4) is the Fourier Transform of  $f(u)$ , we can find the Fourier transforms of the three contributions and multiply them rather than convolving the probability densities themselves. For the energy spread we have (following Ref. [6])

$$f_e(u) = e^{-u^2/(2\sigma_e^2)}/(\sqrt{2\pi}\sigma_e)$$

and its Fourier transform

$$\int_{-\infty}^{\infty} f_e(u) e^{-iu(\tau - \tau')} du = e^{-\sigma_e^2(\tau - \tau')^2/2}, \quad (5)$$

with  $\sigma_e = 4\pi N\sigma_y/\gamma$ , where  $\sigma_y$  is the standard deviation of the Gaussian energy distribution.

A Gaussian distribution of entrance angles in the  $y$ -direction can be analyzed in a manner similar to that of Ref. [4], except that a cylindrically symmetrical distribution was assumed there, while we assume a one-dimensional angular distribution. Introducing  $\sigma_\theta = 4\pi N\gamma^2\sigma_{44}/(1 + K^2)$ , we get the Fourier transform of the phase velocity distribution as

$$\int_{-\infty}^{\infty} f_y(u) e^{-iu(\tau - \tau')} du = \frac{1}{\sqrt{1 - i\sigma_\theta(\tau - \tau')}}. \quad (6)$$

Finally, for the  $x$ -direction the analysis is similar to that leading to Eq. (27) in Ref. [6], except that we need to include correlations between angle and position because we do not wish to restrict ourselves to having a waist at the entrance of the wiggler. By changing to an appropriate coordinate system we can introduce a rotation that causes the correlations to vanish, then proceed as in the uncorrelated case. The resulting Fourier transform is

$$\begin{aligned} \int_{-\infty}^{\infty} f_x(u) e^{-iu(\tau - \tau')} du \\ = \frac{1}{\sqrt{1 - (\tau - \tau')^2\sigma_a\sigma_b - i(\tau - \tau')(\sigma_a + \sigma_b)}}, \end{aligned} \quad (7)$$

where

$$\sigma_a = \sigma_\alpha \cos^2\theta + \sigma_\beta \sin^2\theta + 2\sigma_{\alpha\beta} \sin\theta \cos\theta,$$

$$\sigma_b = \sigma_\beta \cos^2\theta + \sigma_\alpha \sin^2\theta - 2\sigma_{\alpha\beta} \sin\theta \cos\theta,$$

$$\theta = -\frac{1}{2} \tan^{-1} \frac{2\sigma_{\alpha\beta}}{\sigma_a - \sigma_\beta},$$

$$\sigma_\alpha = \frac{4\pi NK^2 k_w^2}{1 + K^2} \sigma_{11},$$

$$\sigma_\beta = \frac{4\pi N\gamma^2}{1 + K^2} \sigma_{22},$$

$$\sigma_{\alpha\beta} = \frac{4\pi NK\gamma k_w}{1 + K^2} \sigma_{12}.$$

Note that if the beam is perfectly matched we have  $\sigma_a = \sigma_b = \sigma_x$  and the Fourier Transform reduces to  $1/(1 - i\sigma_x(\tau - \tau'))$ . If we set  $\sigma_a = 0$  and  $\sigma_b = \sigma_\theta$  the resulting expression is the same as that for  $f_y$ , as is appropriate for the case with cylindrical symmetry and no betatron motion at all.

Combining Eqs. (5), (6) and (7) into Eq. (3) gives the final result:

$$G = -\frac{2qi_0 K_f}{\pi} \text{Im} \int_{-1/2}^{1/2} d\tau \int_{-1/2}^{\tau} \frac{(\tau - \tau') e^{-i\nu_0(\tau - \tau')}}{D_x D_y} \times \frac{e^{-\sigma_x^2(\tau - \tau')^2/2}}{\sqrt{1 - i\sigma_\theta(\tau - \tau')}} \times \frac{d\tau'}{\sqrt{1 - (\tau - \tau')^2 \sigma_a \sigma_b - i(\tau - \tau')(\sigma_a + \sigma_b)}}. \quad (8)$$

This expression gives the gain as a function of  $\nu_0$ . Lasing action will take place at the  $\nu_0$  value with the highest gain. The gain may be further reduced by short-pulse effects, which can be taken into account separately [8].

### 3. Conclusion

We have combined and extended the results of other workers to allow calculation of the FEL gain in the presence of arbitrary electron beam profiles. A useful further extension of this work would be to allow electron beams that are off-center with respect to the optical axis.

### Acknowledgement

This work was supported in part by the Office of Naval Research, Contract No. N00014-91-C-0170

### References

- [1] R.L. Swent, K.W. Berryman, H.A. Schwettman and T.I. Smith, Nucl. Instr. and Meth. A 304 (1991) 272.
- [2] M.B. Reid, J. Feinstein, R.H. Pantell and A.S. Fisher, Nucl. Instr. and Meth. A 272 (1988) 268.
- [3] W.B. Colson, J.C. Gallardo and P.M. Bosco, Phys. Rev. A 34 (1986) 4875.
- [4] W.B. Colson and P. Elleaume, Appl. Phys. B 29 (1982) 101.
- [5] W.B. Colson, SPIE Vol. 738 (1987) 2.
- [6] A. Amir and Y. Greenzweig, Phys. Rev. A 34 (1986) 4809.
- [7] TRANSPORT – a computer program for designing charged particle beam transport systems, SLAC-91, Rev. 2 (1977), also available as NAL-91.
- [8] U. Bizzari et al., Riv. Nuovo Cimento 10 (1987) 1.



ELSEVIER

# Non-linear macroscopic equations for pulse evolution in a high-gain Compton FEL

G.H.C. van Werkhoven<sup>\*</sup>, T.J. Schep

*FOM-Instituut voor Plasmafysica "Rijnhuizen", Postbus 1207, 3430 BE Nieuwegein, The Netherlands*

## Abstract

The non-linear stage of the interaction between electron and light pulses is considered of a high-gain FEL. It is shown that the non-linear oscillations of the radiation intensity can be described analogously to the bouncing motion of a particle in a time-dependent, anharmonic potential. In case the electrons all have the same energy and bunching factor, the potential is constant in the steady state region of the light pulse. In this region, analytical solutions are in good agreement with the full solution. Using the same approximation also in the trailing edge of the light pulse, it is shown that the model provides a surprisingly good description of the physics involved.

## 1. Introduction

Several aspects of the interaction between electron and light pulses in a high-gain FEL can be described by macroscopic equations [1]. In the linear approximation, the macroscopic equations describe the exponential FEL instability. When the laser reaches saturation, higher order moments play a role and a closure relation is required to truncate the series of moments. In case the hierarchy is truncated at the second moment, using the closure relation proposed in Ref. [2] or in Ref. [3], a third order non-linear differential equation is obtained for the complex radiation amplitude  $u$ , which includes the linear regime as well as the oscillatory character of the light in the saturated stage. So far only approximate analytical solutions have been derived for the non-linear regime. In the steady state region of the light pulse, where slippage is negligible, the third order equation is reduced to a first order non-linear equation [4,5] of the Ginzburg–Landau type. However, this equation describes the saturation level but fails to describe the non-linear oscillations of the light, which arise from the sloshing of energy between the electrons and the wave. The collective equations can be closed at the first moment, when the electrons are treated as a single macro-electron [3]. This model is valid only in the non-linear regime and yields a second order differential equation for  $u$ , which reproduces the amplitude and the period of the non-linear oscillations surprisingly well. Another analysis of the oscillatory character of the steady state radiation is

presented in Ref. [6], using linear Vlasov theory of perturbations around a two mode equilibrium saturation field. An approximate solution for the light in the trailing edge of the pulse, where slippage is important, is obtained in Ref. [7]. This solution describes the saturation level and the decrease of radiation due to the slippage, but does not include the non-linear oscillations.

In this paper, the radiation is described analogously to the bouncing motion of a particle in a time-dependent anharmonic potential. This model is analogous to the propagation of non-linear Alfvén waves in plasmas. The model is compared with the full solution of the system of equations, both in the steady state region and in the trailing edge of the light pulse.

## 2. Macroscopic equations for FEL interaction

The amplification of the light  $u$  is described by the wave equation and the electron equations of motion

$$(\partial_z + \partial_{\bar{z}})u(z, \bar{z}) = i\langle b \rangle(z, \bar{z}), \quad (1)$$

$$\frac{d}{dz}b = -ipb, \quad \frac{d}{dz}p = i[ub^* - u^*b], \quad (2)$$

where  $b = e^{-i\psi}$  and  $p$  are the bunching factor and energy of each electron,  $\psi$  is the ponderomotive phase,  $z$  is the position in the undulator and  $\bar{z} \propto (z - v_{\text{pon}}t)$  labels the position in both the light and electron pulses,  $v_{\text{pon}}$  being the velocity of the ponderomotive wave. All quantities are normalized [1].

Upon averaging over all electrons within a  $\bar{z}$ -segment equal to a ponderomotive wavelength, using the average

<sup>\*</sup> Corresponding author. Tel. +31 3402 31224, fax +31 3402 31204, e-mail: gertjan@zeus.rijnh.nl.

$\langle \dots \rangle$ , Eq. (2) yields a set of macroscopic equations of which the lowest four are given below

$$\partial_z \langle b \rangle = -i \langle pb \rangle, \quad (3)$$

$$\partial_z \langle pb \rangle = iu - iu^* \langle b^2 \rangle - i \langle p^2 b \rangle, \quad (4)$$

$$\partial_z \langle p \rangle = i(u \langle b \rangle^* - \text{c.c.}), \quad (5)$$

$$\partial_z \sigma^2 = i[u \langle pb \rangle^* - \langle p \rangle \langle b \rangle^*] - \text{c.c.} \quad (6)$$

Here  $\sigma^2 = \langle p^2 \rangle - \langle p \rangle^2$  is the average energy spread. The evolution of the radiation in the linear regime is described by the linearized version of Eqs. (1), (3) and (4). When the laser reaches the non-linear regime, all higher moments start to play a role.

### 3. Pseudo-potential formulation

The set Eqs. (1 and 2) admit two conservation laws

$$\partial_z \mathcal{E} = -\partial_z |u|^2, \quad \partial_z \mathcal{P} = -i(\partial_z u \partial_z u^* - \text{c.c.}), \quad (7)$$

for the total energy  $\mathcal{E} = \langle p \rangle + |u|^2$  of the electrons and the wave, and for the averaged longitudinal momentum  $\mathcal{P} = \frac{1}{2}(\langle p \rangle^2 + \sigma^2) - (u \langle b \rangle^* + u^* \langle b \rangle)$  of the electrons.

In the steady state region of the light pulse, where  $\partial_z = 0$ , both  $\mathcal{E}$  and  $\mathcal{P}$  are conserved and can be employed to rewrite the problem as follows. Upon writing the complex radiation field  $u = \sqrt{2s} e^{i\phi}$  in terms of a real amplitude  $s$  and phase  $\phi$ , the wave equation Eq. (1) is equivalent to

$$\frac{1}{2}(\partial_z s)^2 + U(s, C, D) = 0, \quad (8)$$

$$2U = s^4 - 2\mathcal{E}s^3 + (2D + \mathcal{E}^2)s^2 - 2(C + \mathcal{E}D)s + D^2, \quad (9)$$

$$\partial_z \phi = -\frac{1}{2}(\mathcal{E} - s) + D/2s, \quad (10)$$

where the quantities

$$C(z) = |\langle b \rangle|^2 \quad \text{and} \quad D(z) = \frac{1}{4}(\sigma^2 + \mathcal{E}^2 - 2\mathcal{P}). \quad (11)$$

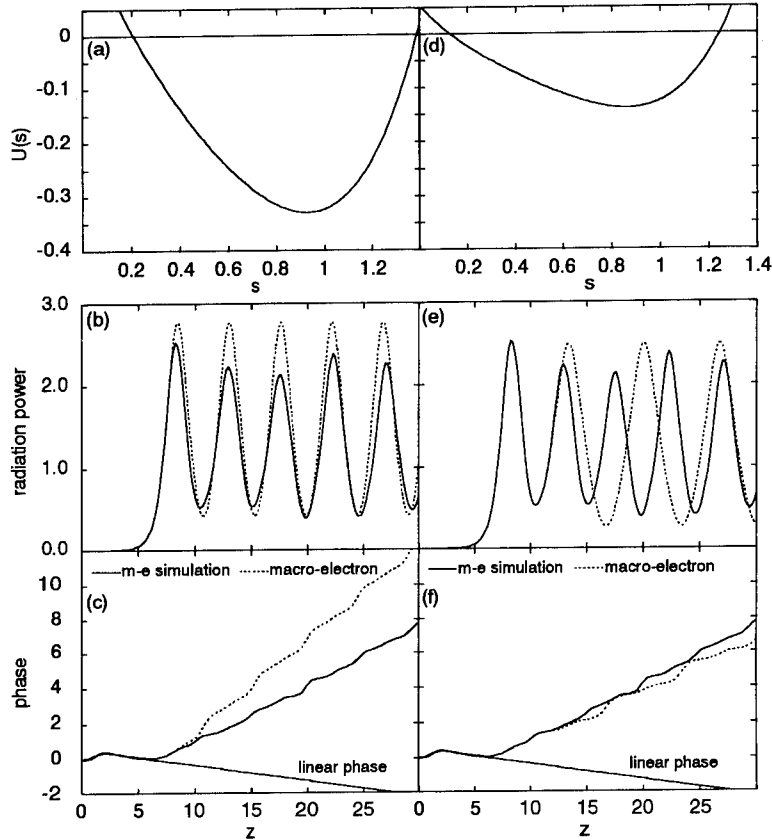


Fig. 1. Comparison of the macro-electron model with the full solution obtained from the m-e simulation. Initial conditions for the macro-electron model are obtained from the m-e results at  $z = 7.7$  (a–c) and at  $z = 11.6$  (d–f), for which  $[C, D]$  are  $[0.57, 0.64]$  and  $[0.20, 0.33]$ , respectively. Despite of these different values, (a) and (d) yield a similar shape of the pseudo-potential. The total energy and longitudinal momentum are  $\mathcal{E} = 2\mathcal{P} = 0.95$ .



We stress that no additional approximations are made to obtain this result. Both  $C$  and  $D$  depend on  $z$  through the average bunching and energy spread. In order to determine  $C$  and  $D$ , a closure relation is required. In case the electrons move as one bunch with single energy  $p$  and bunching factor  $b$ , due to a strong bunching in the non-linear regime, they behave as a macro-electron. This assumption implies the closure relation

$$\langle pb \rangle \simeq \langle p \rangle \langle b \rangle, \quad (12)$$

for which  $C$  and  $D$  are constants. The merit of this pseudo-potential formulation is that the evolution of  $s$  is analogously to the bouncing motion of a particle in a pseudo-potential  $U$ , even if  $C$  and  $D$  are not strictly constant. This implies that no strict closure relations have to be considered.

Taking  $C$  and  $D$  constant, the set Eqs. (8) and (9) is equivalent to the macro-electron model, formed by Eqs. (1), (3) and the closure relation (12), and can be solved analytically. The solutions are characterized by the four complex root  $\{s_1, s_2, s_3, s_4\}$  of  $U(s) = (s - s_1)(s - s_2)(s - s_3)(s - s_4) = 0$ , which depend on the values of  $\mathcal{E}$ ,  $\mathcal{P}$ , and on the constants  $C$  and  $D$ . The solutions are classified in Ref. [8], where a similar method is employed to obtain solutions of the derivative non-linear Schrödinger equation [9] for non-linear Alfvén waves in plasmas. Different types of solutions are described by Eqs. (8) and (9), ranging from purely periodic oscillations to soliton solutions.

For the values of  $C$  and  $D$  considered in this paper, the roots  $\{s_i\}$  are characterized by  $0 < s_1 < s_2$ ,  $s_3 = s_4^*$  and yield the so-called mixed envelope solution for the radiation amplitude in the non-linear regime. This solution is written down below:

$$s = s_2 + \frac{n_+}{1 - \nu_+ \text{sn}^2(\kappa z, k)} + \frac{n_-}{1 - \nu_+ \text{sn}^2(\kappa z, k)}, \quad (13)$$

$$\begin{aligned} \phi = \frac{1}{2s_2} (s_2^2 - \mathcal{E}s_2 + D) \\ + \frac{1}{2\kappa} [n_+ \Pi(\kappa z, \nu_+^2) + n_- \Pi(\kappa z, \nu_-^2)] \\ + \frac{D}{2\kappa} [m_+ \Pi(\kappa z, \xi_+^2) + m_- \Pi(\kappa z, \xi_-^2)], \end{aligned} \quad (14)$$

where  $\text{sn}(\kappa z, k)$  and  $\Pi(\kappa z, \nu^2)$  is Jacobi's elliptic function of the first kind and the elliptic integral of the third kind, respectively. Furthermore,

$$\kappa^2 = q_1 q_2 / 4, \quad (15)$$

$$k^2 = ((s_2 - s_1)^2 - (q_2 - q_1)^2) / (4q_1 q_2), \quad (16)$$

$$n_{\pm} = [\pm(q_2 - q_1) - (s_2 - s_1)] / 2, \quad (17)$$

$$\nu_{\pm}^2 = [(q_2 - q_1) \pm (s_2 - s_1)] / 2q_2, \quad (18)$$

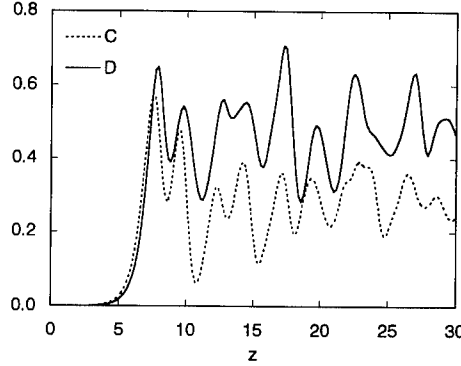


Fig. 2. Spatial variation of  $C$ , the absolute value of the bunching  $\langle b \rangle$ , and  $D$ , which is proportional to the energy spread, as obtained from the m-e simulation. Other parameters are similar to Fig. 1.

$$m_{\pm} = [\mp(s_1 q_2 + s_2 q_1) + (s_2 - s_1)|s_3|] / 2s_1 s_2 |s_3|, \quad (19)$$

$$\xi_{\pm}^2 = [(s_1 q_2 - s_2 q_1) \pm (s_2 - s_1)|s_3|] / 2s_1 q_2, \quad (20)$$

$$q_i^2 = [s_i - \text{Re}(s_3)]^2 + \text{Im}(s_3)^2, \quad i = \{1, 2\}. \quad (21)$$

This solution is compared with the radiation field of the multi-electron (m-e) simulation code [10], which solves the full system of equations Eqs. (1) and (2). The result of the m-e simulation in the saturated stage is used to determine the initial conditions for the pseudo-potential model Eqs. (8)–(10). This is demonstrated in Fig. 1 for two positions in the undulator:  $z = 7.7$  and  $z = 11.6$ . Although  $C$  and  $D$  are quite different, Figs. 1a and 1d show that both cases yield a similarly shaped potential. Figs. 1b and 1c show that the oscillation amplitude and period of the radiation power are reproduced quite well, although the phase  $\phi$  increases faster than predicted. Figs. 1e and 1f show complementary results with regards to the oscillation period and phase of the light. In Fig. 2 the  $z$  dependence of  $C$  and  $D$  is shown, as obtained from the m-e simulation. Although  $C$  and  $D$  fluctuate, the variation of the roots of  $U(s) = 0$  is small for  $z > 5$ , such that the radiation field remains of the mixed envelope type. This implies that the shape of the pseudo-potential changes barely in the entire saturated phase.

#### 4. Behaviour in the trailing edge

In the trailing edge of the light pulse, where slippage plays a role, the radiation is still determined by the pseudo-potential model, upon replacing the  $\partial_z$  by  $\partial_z + \partial_z$ . However, the potential can change drastically on the time-scale of the non-linear oscillations, since  $\mathcal{E}$  and  $\mathcal{P}$  are no longer conserved locally. Therefore we return to the original set of equations for the macro-electron model, which is

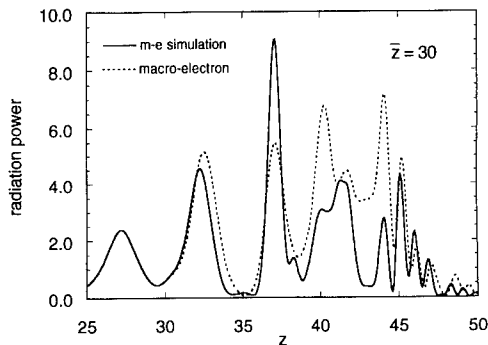


Fig. 3. Radiation intensity as a function of  $z$ , monitored at position  $\bar{z} = 30$  in the electron pulse. The initial conditions are  $u(0, \bar{z}) = 0.01$ ,  $\langle b \rangle(0, \bar{z}) = 0$ ,  $G = 60$  and  $S = 2.0$ . Other parameters are similar to Fig. 1.

expected to hold in most of the trailing edge, as long as the radiation power is sufficiently high to bunch the electrons. The macro-electron equations are solved numerically and are compared with results of the m-e simulation code. In Fig. 3 the evolution of the optical power is monitored at a fixed position  $\bar{z} = 30$  in the electron pulse. The radiation is in the steady state region until  $z = 30$ . At  $z = 30$  the result of the m-e simulation is used to initialize the macro-electron model, since slippage becomes apparent for  $z > 30$ . The results show that the macro-electron model describes the entire  $z$ -dependence of the radiated power, and in particular the first two superradiant high intensity peaks, quite satisfactorily. Hence the macro-electron model accounts for most of the features of the physics involved in the trailing edge of the light pulse.

## 5. Conclusions

The behaviour of the radiation field in the saturated stage of a high-gain FEL can be described analogously to the bouncing motion of a particle in a time-dependent, anharmonic pseudo-potential. In the steady state region of the light pulse, the potential is constant in case the electrons are considered to move as a single bunch, that behaves as a macro-electron with single energy  $p$  and bunching factor  $b$ . The merit of the pseudo-potential formulation is that the non-linear oscillations of the light intensity in the saturated regime can be described even if

the potential is not strictly constant and varies slowly in  $z$ . This implies that no strict closure relations have to be considered.

Using the rigorous macro-electron closure relation, the mixed envelope solutions yield a good representation of the non-linear behaviour of the radiation. In the trailing edge of the light pulse, where slippage is important, the pseudo-potential model begins to lose its applicability, since the total energy and averaged longitudinal momentum are no longer conserved. In this region, the macro-electron equations, equivalent to the pseudo-potential model, are solved numerically.

The macro-electron assumption accounts for most of the features of the interaction between the electron and light pulses, both in the steady state and in the trailing edge region of the light pulse.

## Acknowledgments

The authors like to thank Dr. B.N. Kuvshinov for helpful suggestions. This work was performed as part of the research programme of the "Stichting voor Fundamenteel Onderzoek der Materie" (FOM) with financial support from the "Nederlandse Organisatie voor Wetenschappelijk Onderzoek" (NWO).

## References

- [1] R. Bonifacio, C. Pellegrini and L.M. Narducci, *Opt. Commun.* 50 (1984) 373.
- [2] R. Bonifacio, F. Casagrande and L. De Salvo Souza, *Phys. Rev. A* 33 (1986) 2836.
- [3] G.H.C. van Werkhoven and T.J. Schep, *Nucl. Instr. and Meth. A* 341 (1994) 205.
- [4] R. Bonifacio, C. Maroli and A. Dragan, *Opt. Commun.* 76 (1990) 353.
- [5] A. Bhattacharjee, S.Y. Cai, J.W. Dodd and T.C. Marshall, *Nucl. Instr. and Meth. A* 318 (1991) 99.
- [6] R.L. Gluckstern, S. Krinsky and H. Okamoto, *Phys. Rev. E* 47 (1993) 4412.
- [7] N. Piovella, *Opt. Commun.* 83 (1991) 92.
- [8] T. Hada and C.F. Kennel, *J. Geophys. Res.* 94 (A1) (1989) 65.
- [9] D.J. Kaup and A.C. Newell, *J. Math. Phys.* 19 (1978) 798.
- [10] G.H.C. van Werkhoven, B. Faatz and T.J. Schep, *Nucl. Instr. and Meth. A* 331 (1993) 411.

## Computationally efficient spectral analysis of an FEL oscillator using a Green function analysis

S. Ishii <sup>\*,1</sup>, G. Shvets, J.S. Wurtele

*Department of Physics and Plasma Fusion Center, Massachusetts Institute of Technology, Cambridge, MA 02139, USA*

### Abstract

Previous work on a Green function approach to the evolution of the small gain linear FEL oscillator assumed a long electron pulse. Here this restriction is eliminated and a new expression for the complex amplitude of the optical field at the  $n$ th pass is obtained. The fully causal formalism includes arbitrary temporal profiles of the electron and optical beams and cavity detuning and losses. In our formalism, the solution for the field at the  $n$ th pass requires exponentiating a single matrix rather than sequentially evaluating the field at each pass. Various numerical studies are presented.

### 1. Introduction

The spectral properties of free-electron laser (FEL) oscillators are of critical importance to many applications and have been the subject of numerous investigations. Most of these studies have been made with numerical simulations of the coupled particle–field equations. Here we restrict our analysis to the linear regime, where analytical techniques can be used. There has been a large body of work regarding the FEL as a (time-independent) dielectric medium, but this has been confined mainly to linear gain analysis and optical guiding. The analysis of the linear time-dependent oscillator FEL has received less attention. Colson [1] formulated the Compton FEL interaction as an integral equation for the complex field amplitude. Growth from noise (SASE) in the single pass FEL was examined by Kim [2] and by Bonifacio and co-workers [3]. A Green function approach was used in Ref. [3], and in studies of spiking in oscillators by Jerby et al. [4] and Shvets and Wurtele [5]. Supermode theory by Dattoli et al. [6] and Elleaume [7] addressed the pulse evolution in the FEL oscillator, but required a noncausal approximation. The causal multi-pass Green function for a low gain oscillator was found in Ref. [5]. In general, the above works assumed an electron beam that was infinite, slowly varying on the time scale of the optical pulse, or had a step-function profile. A formulation of FEL oscillator pulse evolution by Fourier transform techniques and matrix multiplication was developed by Tang and co-workers [8]. In this

paper we extend the analysis of Ref. [5] to include arbitrary electron beam profiles.

The Green function approach to the FEL is conceptually appealing. Because of slippage, each slice of the optical pulse leaves a “wake” on the electron beam and experiences a (complex) gain as it propagates. The general form for a single pass Green function would then be expected to depend parametrically on interaction length. The parameters of the electron beam or complex field amplitude can be time-dependent, causing different temporal slices of the radiation pulse to experience unequal gain, which leads to spectral changes. The slippage allows a finite radiation pulse propagating on a uniform electron beam to experience frequency shifting in regions where the radiation pulse varies. In another paper in these proceedings we derive the single pass Green function for the Raman FEL. In an FEL oscillator there is gain, slippage, cavity detuning and losses and multiple passes, so that any analysis is substantially more cumbersome than that used, for example, in studies of the evolution of light in a time-dependent plasma.

The analysis here is fully causal, valid in the low gain regime, and is computationally efficient compared to iterating the single pass Green function. The formulation includes finite electron and optical pulses and cavity detuning and losses. It can be used to examine numerous time-dependent linear phenomena in oscillators, and, in the future, may be (phenomenologically) extended to include nonlinear saturation.

<sup>1</sup> Permanent address: Mitsubishi Heavy Industries Ltd.

<sup>\*</sup> Corresponding author. Tel. +1 617 253 8447, fax +1 617 253 0448, e-mail: ishii@ilm.pfc.mit.edu.

## 2. Theoretical model

This paper follows the formalism of Ref. [1], where the normalized independent variables are

$$\bar{s} = \frac{2\gamma_{\parallel}^2 c}{N_w \lambda_w} \left( t - \frac{z}{v_g} \right), \quad (1)$$

$$\bar{z} = z / (N_w \lambda_w). \quad (2)$$

These variables are chosen so that  $\bar{s}$  propagates with the optical pulse and is measured in units of the slippage length, and interaction length  $z$  is normalized to the wiggler length; thus  $d\bar{s}/d\bar{z} = 1$ . The free-streaming phase of a particle in the ponderomotive wave is given by

$$\theta_0 = 2\pi N_w (\bar{z} - \bar{s}) + \bar{s} (k_w - k_z / 2\gamma_{\parallel}^2) N_w \lambda_w, \quad (3)$$

where the detuning normalized by the wiggler length is  $y_0$ . Also,  $N_w$  is the number of wiggler periods,  $\lambda_w$  is the wiggler period,  $\gamma_{\parallel}$  is the electron relativistic factor calculated from the parallel velocity,  $c$  is the speed of light, and  $v_g$  is the group velocity of light (equal to  $c$  in the numerical example below).

Within the context of a cold beam model prior to saturation, the FEL evolution equations for an arbitrary gain during a single pass through the wiggler can be written as:

$$\frac{\partial \hat{a}}{\partial \bar{z}} = \frac{2\pi i a_w L_w r_e \delta n}{\gamma k} \exp(-i\theta), \quad (4)$$

$$\frac{d^2 \theta}{d\bar{z}^2} = i \frac{8\pi^2 N_w^2 a_w}{1 + a_w^2} \hat{a}[\bar{s}(\bar{z}), \bar{z}] \exp(i\theta), \quad (5)$$

$$y_0 = \frac{d\theta}{d\bar{z}}(\bar{z}=0), \quad \theta_0 = \theta(\bar{z}=0). \quad (6)$$

In this notation the normalized slowly varying complex amplitude of the field is  $\hat{a}(\bar{s}, \bar{z})$ , the detuning is  $y_0$ ,  $r_e$  is the classical electron radius, the Lagrangian phase variable is  $\theta$ , the wiggler amplitude is  $a_w$ ,  $L_w = N_w \lambda_w$ ,  $k = 2\pi/\lambda$  is the radiation wavenumber, and the density perturbation  $\delta n$  can be expressed in terms of the phase as:

$$\delta n = -n_0 (\bar{s} - \bar{z}) \left( \frac{\partial \theta(\theta_0, \bar{z})}{\partial \theta_0} - 1 \right), \quad (7)$$

where  $n_0$  is the beam density. Note that  $t - z/v_z = (N_w \lambda_w / c)(\bar{s} - \bar{z})$ . In linear theory, the phase can be expanded as:

$$\theta = \theta_0 + y_0 \bar{z} + i \frac{8\pi^2 N_w^2 a_w}{1 + a_w^2} \int_0^{\bar{z}} d\bar{z}' \int_0^{\bar{z}'} d\bar{z}'' \hat{a}(\bar{s}_0 + \bar{z}'', \bar{z}') \times \exp[i(y_0 \bar{z}'' + \theta_0)], \quad (8)$$

and an integral equation for the field can be obtained (see Ref. [6]):

$$\begin{aligned} \frac{\partial \hat{a}(\bar{z}, \bar{s})}{\partial \bar{z}} &= i j_c (\bar{s} - \bar{z}) \exp(-i y_0 \bar{z}) \\ &\times \int_0^{\bar{z}} d\bar{z}' \int_0^{\bar{z}'} d\bar{z}'' \hat{a}(\bar{s} - \bar{z} + \bar{z}'', \bar{z}'') \exp(i y_0 \bar{z}''), \end{aligned} \quad (9)$$

where  $j_c = 4\pi a_w^2 N_w^3 \lambda_w^2 I / (\gamma^3 r_b^2 I_A)$ ,  $I(\bar{s} - \bar{z})$  is the beam current,  $r_b$  is the beam radius, and  $I_A = 17$  kA. Integration over the wiggler length yields a difference equation for the multi-pass gain:

$$\begin{aligned} \Delta a(s; n) &= i \int_0^1 d\bar{z} \int_0^{\bar{z}} d\bar{z}' \int_0^{\bar{z}'} d\bar{z}'' j_c (\bar{s} - \bar{z}) \\ &\times \hat{a}(\bar{s} - \bar{z} + \bar{z}'', \bar{z}'') \times \exp[i y_0 (\bar{z}'' - \bar{z})]. \end{aligned} \quad (10)$$

In the limit that the gain is small, the variation of the field with respect to interaction length can be ignored in the integral and a differential equation for the multi-pass gain can be obtained:

$$\begin{aligned} \frac{\partial a(s; n)}{\partial n} &= i \int_0^1 d\bar{z} \int_0^{\bar{z}} d\bar{z}' \int_0^{\bar{z}'} d\bar{z}'' j_c (\bar{s} - \bar{z}) \hat{a}(\bar{s} - \bar{z} + \bar{z}'', n) \\ &\times \exp[i y_0 (\bar{z}'' - \bar{z})]. \end{aligned} \quad (11)$$

The calculation proceeds most readily by a Fourier transform in  $\bar{s}$ :

$$\hat{a}(\omega; n) = \int_{-\infty}^{\infty} d\bar{s} \exp(i\omega\bar{s}) \hat{a}(\bar{s}, n), \quad (12)$$

$$J(\omega) = \int_{-\infty}^{\infty} d\bar{s} \exp(i\omega\bar{s}) j_c (\bar{s} - \bar{z}, n). \quad (13)$$

Then

$$\begin{aligned} \frac{\partial \hat{a}(\omega; n)}{\partial n} &+ \left( i\omega\Delta + \frac{1}{2Q} \right) \hat{a}(\omega; n) \\ &= \frac{1}{2\pi} \int_{-\infty}^{\infty} d\omega' J(\omega - \omega') G(\omega, \omega') \hat{a}(\omega'; n), \end{aligned} \quad (14)$$

where  $\Delta$  is twice the cavity detuning normalized to the slippage length ( $\Delta = 2\delta L_c / (N_w \lambda_s)$ ),  $Q$  is the cavity loss, and the Green function  $G$  is

$$\begin{aligned} G(\omega, \omega') &= i \int_0^1 d\bar{z} \int_0^{\bar{z}} d\bar{z}' \int_0^{\bar{z}'} d\bar{z}'' \exp[i(\omega - \omega')\bar{z}''] \\ &\times \exp[i(y_0 - \omega)(\bar{z}'' - \bar{z})]. \end{aligned} \quad (15)$$

The Green function is a product of exponentials and can be solved straightforwardly in closed form. The multi-pass evolution can now be solved for numerically.

### 3. Numerical method

We solve the equation by isolating the  $n$ -derivative and integrating and using a discrete Fourier transform. The result is a matrix equation for the  $n$ th pass field in terms of the initial field:

$$\begin{pmatrix} \hat{a}(\omega_1, n) \\ \vdots \\ \hat{a}(\omega_N, n) \end{pmatrix} = \exp(n\mathbf{T}) \begin{pmatrix} \hat{a}(\omega_1, 0) \\ \vdots \\ \hat{a}(\omega_N, 0) \end{pmatrix}. \quad (16)$$

Here the transport matrix  $\mathbf{T}$  is readily calculated from the detuning, losses and Green function. The exponential of the matrix can be efficiently calculated by using  $\exp(n\mathbf{T}) = (\mathbf{I} + \epsilon\mathbf{T} + O(\epsilon^2))^{n/\epsilon}$  and choosing  $n/\epsilon$  to be a power of 2. Typically  $n/\epsilon$  is chosen to be 1024 and the Fourier transform is taken with 256 bins.

### 4. Examples

In a previous study [5] of a low gain oscillator, the causal multi-pass Green function was found in the limit of a long electron bunch:

$$\hat{a}(\bar{s}; n) = \int_{\bar{s}-\bar{z}}^{\bar{s}} d\bar{s}' G_n(\bar{s} - \bar{s}') \hat{a}(\bar{s}'; 0),$$

$$G_n(\bar{s}) = \frac{1}{2\pi} \int_c d\omega \exp(-i\omega\bar{s} + nj_c - g(y_0 - \omega)),$$

where the low gain FEL spectral function is

$$g(y_0) = i \int_0^1 dz \int_0^{\bar{z}} d\bar{z}'' \exp(iy_0(\bar{z}'' - \bar{z})).$$

These earlier results can be obtained from the present analysis in the limit of a long electron pulse ( $J(\omega) =$

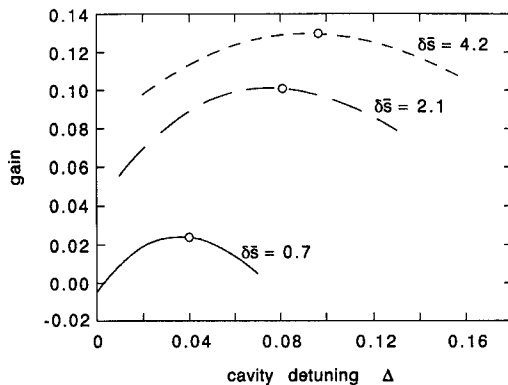


Fig. 1. Dependence of the linear gain on the cavity detuning is shown for normalized electron beam pulse lengths,  $\delta\bar{s}$ , of 0.7, 2.1 and 4.2, with the Colson parameter  $j_c = 1.54$ , and  $Q = 10$ . Detunings are varied between  $\Delta = 0$  and  $\Delta = 0.16$ .

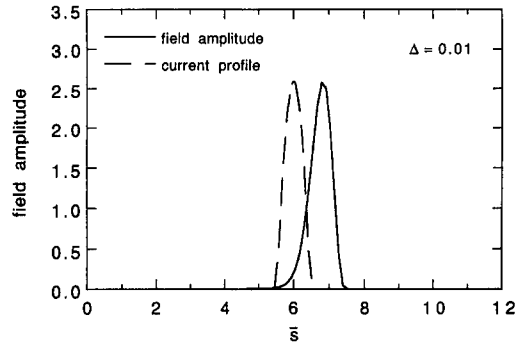


Fig. 2. The electron and optical pulse shapes after 100 passes for an electron beam which is 0.7 slippage lengths long. The electron pulse is shown, in the radiation frame, at the entrance to the wiggler; the electrons would slip by unity to the right in one pass. The cavity detuning is  $\Delta = 0.01$ , the Colson parameter  $j_c = 1.54$ , and  $Q = 10$ .

$2\pi\delta(\omega)$ ). The response to either a jump or a slow modulation of the input electron energy (after the radiation has developed with a spectrum centered around the maximum gain frequency) was investigated. After the energy jumps suddenly, the optical pulse is detuned, the FEL gain cannot compensate for the cavity losses, and the center frequency of the optical pulse shifts to the new peak gain value. Possibly, the frequency shift could occur by amplification of either random beam noise, synchrotron radiation, or a sideband signal. Our numerical and analytic work showed, rather, that the frequency can change through slippage on a finite optical pulse – and that the frequency adjustment requires neither beam nor field noise. For a flat-top pulse the correct frequency appears at the edges, where slippage is significant, and then diffuses into the bulk of the pulse. This was modeled with a diffusion equation:

$$\frac{\partial \hat{a}}{\partial n} = \frac{1}{2} \left( -j_c \frac{d^2 g}{dy^2} \bigg|_{y=y_0} \right) \frac{\partial^2 \hat{a}}{\partial \bar{s}^2} - \left( ij_c \frac{dg}{dy} \bigg|_{y=y_0} - \Delta \right) \frac{\partial \hat{a}}{\partial \bar{s}} + \left( -\frac{1}{2Q} + j_c g(y_0) \right) \hat{a}.$$

It has long been known that the peak gain detuning is such that it compensates for the lethargy. This diffusion equation allows one to find an analytic expression for the optimal cavity detuning. From the diffusion equation, it is clear that, in the limit of a long electron beam,  $-\text{Im}(j_c dg/dy)$  evaluated at peak gain  $y_0 = 2.6$  gives the lethargy. Note that this gives the criterion  $\Delta = 0.7j_c$  (the slope of the imaginary part of the spectral function at peak gain is nearly 0.07, see also Ref. [6]). We examined this criterion for a few examples, corresponding to various values of the pulse length. In these studies, shown in Fig. 1, the cavity detuning was changed for three values of the pulse length. When slippage is unimportant the result agrees with our theoretical prediction ( $-\text{Im}(j_c dg/dy) =$

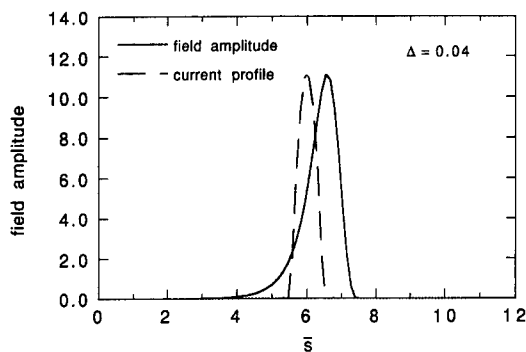


Fig. 3. The same as plot of pulse shapes as in Fig. 2 except the cavity detuning is  $\Delta = 0.04$ .

$\Delta = 0.096$ ) based on the diffusion model. As the pulse is shortened, slippage becomes more significant, and the gain is no longer given by the usual Colson parameter. As a measure of our understanding of the relation between the required cavity detuning and the peak gain, we estimated an effective Colson parameter required to reach the peak gain for each of the shorter pulses. Replacing  $j_c$  by its effective value resulted in good agreement with the theory, as shown by the circles that mark our theoretically estimated peak cavity detuning.

Shown in Figs. 2–4 are the electron and optical pulse shapes after 100 passes for an electron beam length equal to 0.7 slippage lengths. The electron pulse is shown, in the radiation frame, at the entrance to the wiggler; the electrons would slip by unity to the right in one pass. The

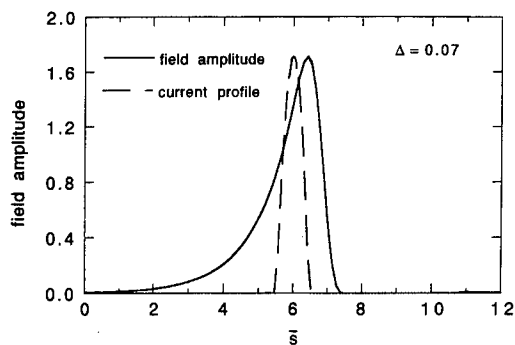


Fig. 4. The same as plot of pulse shapes as in Fig. 2 except the cavity detuning is  $\Delta = 0.07$ .

cavity detuning is increased from 0.01 in Fig. 2 to 0.07 in Fig. 4.

## 5. Discussion

This analysis of the FEL oscillator evolution has so far only been performed in the linear region and in a one-dimensional model. It is straightforward to include gratings, frequency-dependent loss factors, and dynamic cavity detuning. It is less straightforward, but of interest, to include transverse effects (diffraction and guiding) and nonlinear effects (saturation, nonlinear spiking, sidebands). We believe many spectral phenomena, previously suspected as occurring only through nonlinear interactions, can be driven by slippage induced frequency changes in the linear regime.

## Acknowledgement

Work supported by the U.S. DOE, Division of High Energy Physics and the Air Force Office of Scientific Research.

## References

- [1] W.B. Colson, IEEE J. Quantum Electron. QE-17 (1) (1981) 417.
- [2] K.-J. Kim, Phys. Rev. Lett. 57 (1986) 1871.
- [3] R. Bonifacio et al., Phys. Rev. Lett. 73 (1994) 70, and references therein;  
R. Bonifacio and F. Casagrande, Nucl. Instr. and Meth. A 239 (1985) 36.
- [4] E. Jerby, G. Bekefi and J.S. Wurtele, Phys. Rev. Lett. 66 (1989) 2068;  
E. Jerby, G. Bekefi and J.S. Wurtele, IEEE J. Quantum Electron. QE-27 (1991) 2512.
- [5] G. Shvets and J.S. Wurtele, Phys. Plasmas 1 (1994) 157.
- [6] G. Dattoli, J.C. Gallardo, A. Renieri and A. Torre, Phys. Rev. A 35 (1987) 4175;  
G. Dattoli et al., Phys. Rev. A 37 (1988) 4334.
- [7] P. Elleaume, J. Quantum Electron. QE-21 (1985) 1012.
- [8] P. Sprangle, C.M. Tang and I. Bernstein, Phys. Rev. A 28 (1983) 2300;  
C.M. Tang and B. Hafizi, Nucl. Instr. and Meth. A 304 (1991) 497.



ELSEVIER

## Formation of distributed feedback in an FEL under multi-wave diffraction

V.G. Baryshevsky, K.G. Batrakov, I.Ya. Dubovskaya \*

*Institute of Nuclear Problems, 11 Bobruiskaya St., 220050 Minsk, Belarus*

### Abstract

The boundary problem for an X-ray crystal quasi-Cherenkov FEL is solved for the case in which distributed feedback is provided by three-wave coplanar diffraction of the emitted photons. In comparison with two-wave distributed feedback, it is shown in the three-wave case that the necessary interaction region between a particle beam and the electromagnetic wave necessary to reach the oscillation threshold, as well as radiation losses inside the medium, can be reduced with an appropriate choice of parameters. This gives rise to the possibility of relaxing the required parameters of a particle beam necessary for lasing in the X-ray spectral range. At the same time it also allows a reduction in the size of an FEL and the construction of more compact coherent radiation sources in any spectral range.

### 1. Introduction

The advantages of distributed feedback (DFB) in laser resonators was first shown by Kogelnik and Shank [1], and DFB has been widely used in ordinary laser systems [2]. One-dimensional distributed feedback in which the diffracted and transmitted waves propagate along a line in opposite directions was considered by Strauss [3] for a solid X-ray FEL based on channeling radiation in a crystal. In Ref. [4] it was shown that dynamical diffraction of emitted photons by a crystal significantly influences the process of collective radiation by a channeled particle beam. In previous work we have pointed out that a more effective resonator is one in which distributed feedback is formed by the dynamical diffraction of emitted photons by a three-dimensional periodic structure, for example, by a crystal for the X-ray spectral range. This situation is distinguished from the ordinary one-dimensional DFB by the direction of propagation of the diffracted waves. The difference in direction relative to the particle motion is large (but not  $\pi$ ) and, consequently, relative to the radiated wave vectors. The analysis showed that the process of amplification and generation in such a three-dimensional resonator was significantly modified and, under specific conditions, developed more intensively. It was shown that the interaction between a particle beam and the radiated electromagnetic field was strongest near the region of

degeneration of the roots of the dispersion equation describing the electromagnetic modes excited in the resonator. This conclusion was made by considering several kinds of FELs [5–7].

In the present report we show that two-wave DFB (in which only two waves are strongly excited) is not optimal because the region of root degeneration often coincides with the region of strong radiation absorption inside the medium. This is especially important for solid FELs. The most effective resonator is one with multi-wave DFB, where the distributed feedback is formed by multi-wave dynamical diffraction. The advantages of multi-wave DFB are analyzed in detail for the solid quasi-Cherenkov FEL with three-wave coplanar DFB because this analysis can be conducted analytically. Consider, for example, the specific case of a solid X-ray quasi-Cherenkov FEL where the crystal medium provides both a spontaneous radiation mechanism in the X-ray spectral region [8] and diffraction of the emitted X-rays by the crystal forming the three-dimensional distributed feedback. The crystal target is a radiator and a resonator for the X-ray spectral region simultaneously. It should be mentioned that the analysis derived below will be appropriate for other spectral ranges as well. For example, a three-dimensional optical grating can be formed inside a solid target by a laser. Moreover, multi-wave distributed feedback can be formed by surface dynamical diffraction if a particle beam moves over a three-dimensional periodic structure at a distance not more than  $\lambda\gamma$  (where  $\lambda$  is the radiation wave length and  $\gamma$  is the Lorentz factor). In this way multi-wave DFB can be used with an ordinary undulator FEL.

\* Corresponding author. Tel. +7 0172 208 768, fax +7 0172 265 124.

## 2. Generation threshold for quasi-Cherenkov FEL with three-wave coplanar DFB

Let a relativistic particle beam be incident on a crystal plate ( $0 \leq z \leq L$ ) at an arbitrary angle  $\Psi_0$ . The set of Maxwell's equations which describes the interaction of an electromagnetic wave with a crystal and with a particle beam passing through a crystal target can be written in the following form [5]:

$$\begin{aligned} D_\sigma^{(0)} E_\sigma^{(0)} - \omega^2 \chi_1 E_\sigma^{(1)} - \omega^2 \chi_2 E_\sigma^{(2)} &= 0, \\ -\omega^2 \chi_{-1} E_\sigma^{(0)} + D_\sigma^{(1)} E_\sigma^{(1)} - \omega^2 \chi_{2-1} E_\sigma^{(2)} &= 0, \\ -\omega^2 \chi_{-2} E_\sigma^{(0)} - \omega^2 \chi_{1-2} E_\sigma^{(1)} + D_\sigma^{(2)} E_\sigma^{(2)} &= 0, \end{aligned} \quad (1)$$

where  $D_\sigma^{(\alpha)} = k_\alpha^2 c^2 - \omega^2 \epsilon_0^{(\alpha)} + \chi_b^{(\alpha)}$ . We assume a particle beam and a crystal plate oriented so that the three-wave coplanar diffraction condition is satisfied for emitted photons. In this case only three strong waves with the  $\sigma$ -polarization are excited inside the crystal medium (see Ref. [5] for two-wave diffraction geometry). The subscript  $\alpha$  ( $\alpha = 0-2$ ) labels the transmitted wave ( $\alpha = 0$ ) and diffracted waves ( $\alpha = 1, 2$ );  $E_\sigma^{(\alpha)}$  are the  $\sigma$  components of the amplitudes of electromagnetic waves,  $\mathbf{k}_1 = \mathbf{k}_0 + \boldsymbol{\tau}_1$ ,  $\mathbf{k}_2 = \mathbf{k}_0 + \boldsymbol{\tau}_2$  are the wave vectors of photons diffracted by crystal planes with corresponding reciprocal vectors  $\boldsymbol{\tau}_1$  and  $\boldsymbol{\tau}_2$ , and  $\epsilon_0^{(\alpha)} = 1 + \chi_\alpha$  are the dielectric constants of a crystal for transmitted and diffracted waves.

$$\begin{aligned} \chi_b^{(\alpha)} &= \frac{1}{\gamma} (\omega_L / \omega)^2 (u e_\sigma / c)^2 \\ &\times \frac{k_\alpha^2 c^2 - \omega^2}{(\omega - \mathbf{k}_\alpha \mathbf{u})^2 - \frac{\hbar^2}{4m^2 c^4 \gamma^2} (k^2 c^2 - \omega^2)^2} \end{aligned}$$

for the “cold” beam limit and

$$\begin{aligned} \chi_b^{(\alpha)} &= -\frac{i\sqrt{\pi}}{\gamma} (\omega_L / \omega)^2 (u e_\sigma / c)^2 \\ &\times \frac{k_\alpha^2 c^2 - \omega^2}{\delta_\alpha^2} x_\alpha^i \exp[-(x_\alpha^i)^2] \end{aligned}$$

for the “hot” beam limit.  $\chi_b$  represents the part of the dielectric susceptibility produced by the interaction of a particle beam with radiation,  $x_\alpha^i = (\omega - \mathbf{k}_\alpha \mathbf{u}) / \sqrt{2} \delta_\alpha$ ,  $\delta_\alpha^2 = (k_\alpha^2 \Psi_1^2 + k_\alpha^2 \Psi_2^2 + k_\alpha^2 \Psi_3^2) u^2$ , and  $\Psi = \Delta \bar{V} / |\bar{V}|$  is the velocity spread. As was shown in Ref. [5], a comparison of a standard equation of X-ray dynamical diffraction with Eq. (1) leads to the conclusion that the combination of a crystal and a particle beam may be considered as an “active” medium with dielectric susceptibility equal to  $\chi_\alpha + \chi_b^{(\alpha)}$ . It permits the boundary problem of X-ray amplification (lasing) due to the passage of a particle beam through a periodic medium to be reduced to the problem of X-ray diffraction by an “active” periodic medium consisting of a crystal plus radiating particle beam.

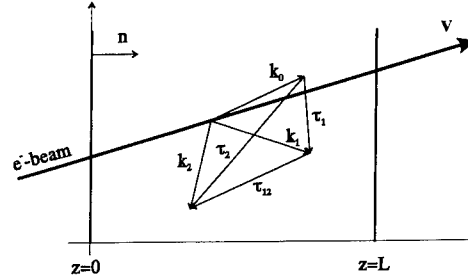


Fig. 1. The geometry of three-wave diffraction.  $V$  is the mean particle beam velocity, and  $z = 0$  and  $z = L$  are two surfaces of a crystal plate.

The geometry of three-wave diffraction is shown in Fig. 1, where  $V$  is the mean particle beam velocity, and  $z = 0$  and  $z = L$  are two surfaces of a crystal plate.

The dispersion equation determining electromagnetic modes inside the “active” medium can be presented in the following form:

$$F_\sigma^{(3)}(\mathbf{k}_0; \mathbf{k}_1; \mathbf{k}_2) = -i \chi_b^{(0)} F_\sigma^{(2)}(\mathbf{k}_1; \mathbf{k}_2), \quad (2)$$

where:  $F_\sigma^{(3)}(\mathbf{k}_0; \mathbf{k}_1; \mathbf{k}_2) = (k^2 c^2 - \omega^2 \epsilon_0^{(0)})(k_1^2 c^2 - \omega^2 \epsilon_0^{(1)})(k_2^2 c^2 - \omega^2 \epsilon_0^{(2)}) - \omega^4 (k^2 c^2 - \omega^2 \epsilon_0^{(0)}) \chi_{1-2} \chi_{2-1} - \omega^4 (k_1^2 c^2 - \omega^2 \epsilon_0^{(1)}) \chi_2 \chi_{-2} - \omega^4 (k_2^2 c^2 - \omega^2 \epsilon_0^{(2)}) \chi_1 \chi_{-1} - \omega^6 (\chi_1 \chi_{-2} \chi_{2-1} + \chi_2 \chi_{-1} \chi_{1-2})$ ;  $F_\sigma^{(2)}(\mathbf{k}_1; \mathbf{k}_2) = (k_1^2 c^2 - \omega^2 \epsilon_0^{(1)})(k_2^2 c^2 - \omega^2 \epsilon_0^{(2)}) - \omega^4 \chi_{1-2} \chi_{2-1}$ .

From Eq. (2) it follows that the root degeneration region (the region of the strongest interaction) and the fulfillment of the Cherenkov condition are possible simultaneously only under the following conditions:

$$\begin{aligned} l_0 l_1 l_2 - l_0 r_{12} - l_1 r_2 - l_2 r_1 - f &= 0, \\ \beta_1 \beta_2 l_1 l_2 + l_0 (\beta_1 l_1 - \beta_2 l_2) - \beta_1 \beta_2 r_{12} - \beta_1 r_1 - \beta_2 r_2 &= 0, \end{aligned} \quad (3)$$

where  $l_0 = \theta^2 - \chi_0 + \gamma^{-2}$ ,  $l_{1,2} = l_0 + \alpha_{B1,2}$ ;  $\alpha_{B1,2} = (2k\tau_{1,2} + \tau_{1,2}^2)/k^2$ .

It is straightforward to show that for the fulfillment of Eq. (3) the system parameters should satisfy the following relationship:

$$\beta_1 \beta_2 (l_0^2 + \beta_1 r_1 + \beta_2 r_2) < 0, \quad (4)$$

where  $f = \chi_1 \chi_{-2} \chi_{2-1} + \chi_2 \chi_{-1} \chi_{1-2}$ ,  $\beta_{1,2} = \gamma_0 / \gamma_{1,2}$  are the asymmetry factors of diffraction  $\gamma_\alpha = (\mathbf{k}_0 \mathbf{n}) / |\mathbf{k}_\alpha|$ ,  $r_1 = \chi_1' \chi_{-1}'$ , and  $r_2 = \chi_2' \chi_{-2}'$ . Expression (4) is more restrictive than the equivalent relation for the two-wave case [5].

In the case of “Bragg–Bragg” diffraction in the X-ray spectral region there is a restriction on the radiation angle

$$\theta_{B-B}^{\max} = \left( \sqrt{-\beta_1 r_1 - \beta_2 r_2} + \chi_0' - \gamma^{-2} \right)^{1/2}. \quad (5)$$

This relation leads to a large value of the diffraction asymmetry factor, which in turn leads to strong radiation absorption inside the medium in the vicinity of the root



degeneration point – just as in the two-wave DFB case [5]. The situation changes in the “Bragg–Laue” geometry. In this case the inequality (4) can be satisfied at angles  $\theta \geq \theta_{B-B}$  which makes it possible to reduce the asymmetry factors  $\beta_1$  and  $\beta_2$  and, consequently, radiation absorption inside the crystal.

The solution of the corresponding boundary problem is presented as a sum:

$$E = \sum_i c_i \exp i k_i r (e_0 + e_1 s_i^{(1)} \exp i \tau_1 r + e_2 s_i^{(2)} \exp i \tau_2 r), \quad (6)$$

where  $s^{(1)} = (\lambda \lambda_2 - r_2) / (\lambda_2 \chi_1 + \chi_2 \chi_{1-2})$ ,  $s^{(2)} = (\lambda \lambda_1 - r_1) / (\lambda_1 \chi_2 + \chi_1 \chi_{2-1})$ , and  $\bar{k}_i$  are the solutions of the dispersion equation and are the coefficients of coupling between the transmitted and diffracted waves,  $E^{(1)} = s^{(1)} E$ ,  $E^{(2)} = s^{(2)} E$ ,  $\lambda_\alpha = [(k + \tau)^2 c^2 - \omega^2 \epsilon_0] / \omega^2$ . To determine the unknown coefficients it is necessary to solve the boundary conditions for the waves on the crystal surfaces. These can be written in the following form for the Bragg–Laue case:

$$\sum_i c_i = 1, \quad \sum_i s_i^{(1)} c_i = 0, \quad \sum_i s_i^{(2)} c_i l_i = 0. \quad (7)$$

Condition (7) is written for the “hot” beam limit. For the “cold” beam limit the corresponding expression can be found in Ref. [9].

It is well known [2] that the oscillation threshold can be determined from the condition that  $\Delta = 0$ , where  $\Delta$  is the determinant of the system (7).

Solving the equation  $\Delta = 0$  we obtain the threshold in the form

$$G = a \chi_0'' + \frac{16}{|\beta_1 \beta_2|} \left[ \frac{\gamma_0 c}{nu} \right]^3 \frac{\pi^2 n^2}{(k l_0 L_*)^2 k L_*} \eta_{B-L} \quad (8)$$

with the phase condition  $(k_{1z} - k_{2z})L = 2\pi n$  ( $n$  is an integer),  $r_{12} = \chi_{1-2} \chi_{2-1}$ , where

$$G = -\frac{\pi^2 n^2}{4\gamma} \left\{ \frac{\omega_L}{\omega} \right\}^2 k^2 L_*^2 (\chi_0' \pm \sqrt{-\beta} | \chi_\tau | - \gamma^{-2}) \times (\chi_0' \pm \sqrt{-\beta} | \chi_\tau |) \sin \phi^2 \times \sin y [(2y + \pi n) \sin y - y(y + \pi n) \cos y] \times y^{-3} (y + \pi n)^{-3}$$

for the “cold” beam limit and

$$G = -\sqrt{\pi} \frac{\omega_L^2}{\gamma \omega^2} \frac{(l_0 + \chi_0' - \gamma^{-2})(l_0 + \chi_0') \sin \phi^2}{\delta_0^2 / k^2} x^4 \times \exp(-(x^1)^2)$$

for the “hot” beam limit.  $a$  and  $\eta_{BL}$  are smooth functions depending on the diffraction geometry and usually are of the order of magnitude of unity,  $y = k \delta L / 2$ , and  $\delta$  is the

deviation from the exact Cherenkov synchronism condition.

Analysis shows that in the coplanar “Bragg–Laue” diffraction geometry of DFB radiation absorption inside the medium can be reduced in the region of root degeneration. For example, under dynamical diffraction by the (111) and (11 $\bar{1}$ ) planes with a symmetry factor of  $\beta_1 = -\beta_2 = \beta = 0.16$  the current density necessary to achieve threshold can be reduced by approximately an order of magnitude in comparison with a two-wave DFB FEL using LiH and an electron energy of 750 MeV with a transverse angular spread  $\Psi_\perp = 5 \times 10^{-6}$  rad [5].

### 3. DFB in the multi-wave diffraction

In principle, in the general case of  $n$ -wave diffraction DFB it is possible to achieve the degeneration of  $n$  roots. In this case the threshold condition has the form [7]:

$$G = \frac{a_n}{(k | \chi_\tau' | L)^{2(n-1)} k L} + b_n \chi_0'', \quad (9)$$

$$r_1 = \chi_1' \chi_{-1}', \quad r_2 = \chi_2' \chi_{-2}',$$

where  $a_n$  and  $b_n$  are functions weakly dependent on the diffraction type.

In this case energy loss through target surfaces can be reduced due to the fulfilment of the inequality  $(k | \chi_\tau' | L) \gg 1$  under dynamical diffraction. As the degree of dispersion root degeneration increases, radiation remains inside the target longer because the group velocity decreases. ( $V_{gr} \sim L^{n-1}$  where  $V_{gr}$  is the radiation group velocity and  $n$  is the degree of dispersion root degeneration.) As a result the region of interaction between a particle beam and the emitted radiation can be reduced. This leads to the possibility of reducing the FEL's dimensions, i.e. of constructing a compact source of coherent radiation.

### 4. Conclusion

It is well known that the use of distributed feedback (DFB) instead of two mirrors for a resonator allows an increase in the efficiency of the generation process in an FEL and a reduction in the size of generator [1,2]. The geometry of the diffraction which provides the DFB can be varied from the simple one-dimensional case [1] to the three-dimensional case [5]. DFB is commonly formed by only two strong excited electromagnetic waves (two-wave DFB). However, by applying a three-dimensional resonator in an FEL it is possible to realize the condition of multi-wave diffraction for emitted photons by orienting a particle beam and a resonator. In this case many waves, depending on the diffraction geometry, are excited by diffraction and multi-wave distributed feedback can occur. We have considered in detail the three-wave coplanar

geometry of diffraction forming distributed feedback in a quasi-Cherenkov crystal FEL. Comparison of the threshold Eq. (8) with its analog in the case of two-wave DFB, for the same kind of FEL studied in Ref. [5], allows us to conclude that favourable conditions may be realized if the distributed feedback is formed in the so-called coplanar “Bragg–Laue” diffraction geometry (see Fig. 1). In this case radiation absorption inside the medium and radiation losses through the target boundary can be suppressed by diffraction. Moreover, the gain  $G$  can be optimized by choosing the diffraction geometry parameters to maximize the interaction time between emitted photons and the particle beam at a fixed resonator length (by decreasing the electromagnetic wave group velocity). As a result, in the case of three-wave coplanar “Bragg–Laue” DFB, the current density of the particle beam necessary for lasing can be reduced by approximately an order of magnitude in comparison with an FEL using two-wave DFB. This is especially important for lasing in the X-ray spectral region where the threshold beam current density is very large. This conclusion is generally applicable, and can be used for any spectral range of coherent radiation. Indeed, the

reduction of the interaction volume in an FEL under multi-wave DFB provides an opportunity to reduce the generator size and to construct a compact source of coherent radiation in any spectral range.

## References

- [1] H. Kogelnik and C. Shank, *Appl. Phys.* 43 (1972) 2327.
- [2] A. Yzriv, *Optical Waves in Crystals* (Wiley, 1884).
- [3] M. Strauss and N. Rostoker, *Phys. Rev.* 39A (1989) 579.
- [4] V.G. Baryshevsky and I.D. Feranchuk, *Dokl. Akad. Nauk Bel. SSR* 27 (1983) 995; 28 (1884) 336.
- [5] V.G. Baryshevsky, K.G. Batrakov and I.Ya. Dubovskaya, *J. Phys. D* 24 (1991) 1250.
- [6] V.G. Baryshevsky, I.Ya. Dubovskaya and A.V. Zege, *Nucl. Instr. and Meth. B* 51 (1990) 368.
- [7] K.G. Batrakov and I.Ya. Dubovskaya, *Izv. Akad. Nauk Bel. SSR* 5 (1990) 82.
- [8] V.G. Baryshevsky and I.D. Feranchuk, *J. Physique* 44 (1983) 913.
- [9] V.G. Baryshevsky, K.G. Batrakov and I.Ya. Dubovskaya, *Izv. Akad. Nauk Bel.SSR* 1 (1991) 53.



ELSEVIER

# A re-examination of scaling laws in the traveling wave interaction

H.P. Freund <sup>\*,1</sup>

Naval Research Laboratory, Washington, DC 20375, USA

## Abstract

A re-examination of traveling wave interactions (in the helix traveling wave tube and the free-electron laser) is performed to investigate the validity of the well-known scaling laws in which the gain varies as the cube (fourth) root of the current when space-charge effects are negligible (dominant). The results indicate that these scaling laws are simplistic generalizations which break down for broad bandwidth interactions, and that the actual variation of the gain with the current can be more complex.

## 1. Introduction

Linear traveling wave devices such as the helix traveling wave tube (TWT) [1–3] and the free-electron laser (FEL) [4,5] have a long history. The TWT interaction is between the axial electric field of a subluminal mode and the axial electron velocity, which results in axial bunching. The FEL interaction is mediated by the ponderomotive force due to the beating of the wiggler and a supraluminal mode also resulting in axial bunching. Similar interactions also occur in devices [6,7] with dielectric linings, gratings, or rippled walls. The equations governing the gain in all such devices bear many similarities.

The particular issue addressed is the scaling of the gain with current in TWTs and FELs. For low currents the maximum gain scales as the cube root of the current. This is called the ballistic (Compton) regime in the TWT (FEL) literature. When the current is large enough that the space-charge potential is important then the maximum gain scales as the fourth root of the current. This is referred to as the space-charge dominated (Raman) regime in TWTs (FELs). The principal purpose of this paper is to show that these simple scaling laws can break down.

The source of these scaling laws lies in the linearized gain. As formulated by Pierce [1] for TWTs, the dispersion equation for frequency  $\omega$  and wavenumber  $k$  is

$$\begin{aligned} & [k^2 - k_0^2(\omega)] \left[ (\omega - kv_{\parallel})^2 - 4QC^3k^2v_{\parallel}^2 \right] \\ & = 2C^3 \frac{\omega}{v_{\parallel}} k_0(\omega) k^2 v_{\parallel}^2, \end{aligned} \quad (1)$$

where  $k_0(\omega)$  is the wavenumber in the absence of the beam,  $v_{\parallel}$  is the axial beam velocity, and the  $Q$  and  $C^3$  parameters describe the effect of the beam on the space-charge wave and on the interaction gain, where  $C^3$  is proportional to the current.

The scaling laws are obtained upon neglect of the backward waves (i.e.,  $k \approx k_0$ ) for which Eq. (1) reduces to

$$(k - k_0)(k - \kappa_+)(k - \kappa_-) = \frac{C^3}{1 - 4QC^3} \frac{\omega}{v_{\parallel}} k_0^2, \quad (2)$$

where

$$\kappa_{\pm} \equiv \frac{\omega/v_{\parallel}}{1 \pm 2\sqrt{QC^3}} \quad (3)$$

describes the positive and negative energy space-charge waves. In the low current regime, the space-charge waves are negligible and

$$\text{Im} \frac{k_{\max}}{k_0} \cong \frac{\sqrt{3}}{2} C. \quad (4)$$

Hence, the gain scales as the cube root of the current. In the space-charge dominated regime, the interaction is with the negative-energy space-charge wave (i.e.,  $k \approx \kappa_-$ ) and the maximum gain is given by

$$\text{Im} \frac{k_{\max}}{k_0} \cong \frac{1}{2} \sqrt[4]{\frac{C^3}{Q}}, \quad (5)$$

which scales as the fourth root of the current.

## 2. Linear theory of the TWT

These scaling laws follow from a complete TWT field theory [8] using a sheath helix model with radius  $R_h$ , and period  $\lambda_h$  which is surrounded by a conducting wall of

<sup>\*</sup> Corresponding author. Tel. +1 703 734 5840, fax +1 703 821 1134, e-mail freund@mmace.nrl.navy.mil.

<sup>1</sup> Permanent address: Science Applications International Corp., McLean, VA 22102, USA.

radius  $R_g$ . The equilibrium model is a thin annulus of radius  $R_b$  and thickness  $\Delta R_b$ ; hence, the equilibrium density is  $n_0(r) = n_b \Delta R_b \delta(r - R_b)$ . The dispersion equation for the azimuthally symmetric subluminal modes is

$$\Lambda_0(k, \omega) \left[ (\omega - kv_{\parallel})^2 + 4QC^3 \beta_{\parallel}^2 \gamma_{\parallel}^2 c^2 \kappa^2 \right] = 2\gamma_{\parallel}^2 C^3 \frac{\omega^2 \kappa^2}{k_h^2 R_h^2} \frac{J_0(\kappa R_h) J_1(\kappa R_g)}{J_0(\kappa R_g) J_1(\kappa R_h)} \frac{W_0(\kappa R_h, \kappa R_g)}{W_1(\kappa R_h, \kappa R_g)}, \quad (6)$$

where  $\beta_{\parallel} \equiv v_{\parallel}/c$ ,  $\gamma_{\parallel}^2 \equiv (1 - \beta_{\parallel}^2)^{-1}$ ,  $k_h \equiv 2\pi/\lambda_h$  is the helix wavenumber,  $\kappa^2 \equiv \omega^2/c^2 - k^2$ ,  $W_n(\zeta, \xi) \equiv Y_n(\zeta)J_n(\xi) - J_n(\zeta)Y_n(\xi)$ ,  $J_n$  and  $Y_n$  denote the regular Bessel and Neumann functions of order  $n$ ,

$$\Lambda_0(k, \omega) = \frac{\omega^2}{c^2} + \frac{\kappa^2}{k_h^2 R_h^2} \frac{J_0(\kappa R_h) J_1(\kappa R_g)}{J_0(\kappa R_g) J_1(\kappa R_h)} \frac{W_0(\kappa R_h, \kappa R_g)}{W_1(\kappa R_h, \kappa R_g)} \quad (7)$$

is the dispersion function of the vacuum helix, and

$$C^3 \equiv k_h^2 R_h^2 \frac{\omega_b^2 \sigma_b^2}{8\gamma_{\parallel}^5 c^2} \frac{J_0^2(\kappa R_b) J_1(\kappa R_h)}{J_0^2(\kappa R_h) J_1(\kappa R_g)} W_1(\kappa R_h, \kappa R_g),$$

$$Q \equiv \frac{1}{2\beta_{\parallel}^2 k_h^2 R_h^2} \frac{J_0(\kappa R_h) J_1(\kappa R_g)}{J_0(\kappa R_b) J_1(\kappa R_h)} \frac{W_0(\kappa R_h, \kappa R_b)}{W_1(\kappa R_h, \kappa R_g)}, \quad (8)$$

where  $\omega_b^2 \equiv 4\pi e^2 n_b/m_e$  denotes the square of the beam plasma frequency, and  $\sigma_b \equiv 2\pi R_b \Delta R_b$  is the cross-sectional area of the beam.

In order to reduce Eq. (6) to the Pierce theory, a near-resonant approximation (i.e.,  $\omega \approx kv_{\parallel}$  and  $\kappa \rightarrow \kappa_e \equiv i\omega/\beta_{\parallel}\gamma_{\parallel}$ ) is made and

$$k_0^2(\omega) \equiv \frac{\omega^2}{c^2} \left[ 1 + k_h^2 R_h^2 \frac{J_0(\kappa_e R_g) J_1(\kappa_e R_h)}{J_0(\kappa_e R_h) J_1(\kappa_e R_g)} \frac{W_1(\kappa_e R_h, \kappa_e R_g)}{W_0(\kappa_e R_h, \kappa_e R_g)} \right] \quad (9)$$

describes the vacuum dispersion relation. In this limit

$$\Lambda_0(k, \omega) = - \frac{(k^2 - k_0^2)}{k_h^2 R_h^2} \frac{J_0(\kappa_e R_h) J_1(\kappa_e R_g)}{J_0(\kappa_e R_g) J_1(\kappa_e R_h)} \frac{W_0(\kappa_e R_h, \kappa_e R_g)}{W_1(\kappa_e R_h, \kappa_e R_g)}, \quad (10)$$

and the Pierce theory is recovered.

A comparison is made of the maximum growth rates from the field theory (6) and the three approximate forms of the dispersion equation: the quartic Pierce theory (1), and the solutions in the ballistic (4) and space-charge dominated (5) regimes. Fig. 1 shows the maximum gain

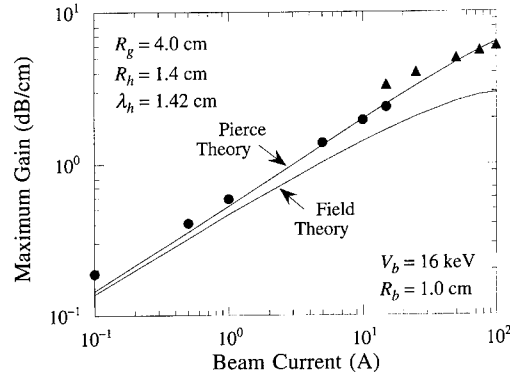


Fig. 1. Scaling of the maximum gain with the current in a helix TWT.

versus current for  $R_g = 4.0$  cm,  $R_h = 1.4$  cm,  $\lambda_h = 1.42$  cm, and a beam with  $V_b = 16$  keV and  $R_b = 1.0$  cm. The circles and triangles in the figure represent the maximum gain from Eqs. (4) and (5) respectively, and the transition between the ballistic and space-charge dominated regimes occurs for  $I_b \approx 20$  A.

The ballistic and space-charge dominated approximations are in reasonable agreement with the Pierce theory over a wide range of currents. In addition, the field and Pierce theories are in reasonable agreement in the ballistic regime. The major discrepancies between the field theory and both the Pierce theory and the ballistic and space-charge dominated approximations are in (1) the scaling of the gain in the ballistic regime, and (2) the magnitude of the gain in the space-charge dominated regime.

In the first case, the gain from the field theory scales closely as  $I_b^{1/2}$  over the entire ballistic regime from 0.1 to 20 A, and not as  $I_b^{1/3}$ . Indeed, the gain increases faster than  $I_b^{1/3}$  even for the quartic Pierce theory in this regime. The reasons for this are twofold. Firstly, since the Pierce theory indicates that the gain scales faster than  $I_b^{1/3}$ , the neglect of the backward wave in the Eq. (3) evidently has broken down. Secondly, the  $Q$  and  $C^3$  parameters are not constants, but vary widely with current since the gain increases with current and the frequency of maximum gain is displaced farther from the exact resonance. This is related to the broad bandwidth of the interaction. Hence, the near-resonant approximation breaks down.

In the second case, the gain in the space-charge dominated regime scales as  $I_b^{1/4}$  for all three analyses for currents between 20 and 100 A, although the field theory predicts lower gains. However, the gain decreases rapidly with increasing current above 100 A due to dispersive shifts in the gain band. In essence, the dielectric effect of the beam shifts the helix mode out of resonance. Hence, while the field theory does predict the  $I_b^{1/4}$  scaling as found in Eq. (5), the predicted gain is much less than that found with the Pierce theory (which breaks down completely for currents in excess of 100 A).

Note that attempt has been made to self-consistently include the effects of DC self-electric and magnetic fields. However, confined flow has been implicitly assumed. In addition, since the equilibrium model is a thin annulus the velocity shear is negligible. Finally, the space-charge limiting current can also be increased under the assumptions that the axial magnetic field is arbitrarily large and that the 16 keV beam energy describes the kinetic energy of the beam after equilibrium has been achieved (i.e., it is not the injection energy).

### 3. Linear theory of the FEL

A waveguide model is assumed for the FEL [9,10]. In contrast with the TWT, the FEL operates with a smooth-bore waveguide (of radius  $R_g$ ) and supraluminous  $TE_{1n}$  or  $TM_{1n}$  modes. The basic analysis employed is 3-D and deals with a thin annular beam propagating through a cylindrical waveguide with a helical wiggler [9,10]. The steady-state orbits describe a velocity  $\mathbf{v} = v_w(\hat{e}_x \cos k_w z + \hat{e}_y \sin k_w z) + v_{||}\hat{e}_z$ , where  $k_w \equiv 2\pi/\lambda_w$  ( $\lambda_w$  denotes the wiggler period). The transverse velocity  $v_w$  is proportional to the product of the wiggler period and amplitude and is related to the axial velocity via  $v_w^2 + v_{||}^2 = (1 - \gamma_0^{-2})c^2$ , where  $\gamma_0$  is the relativistic factor. Further, the radius of the orbit is  $k_w R_b = |v_w/v_{||}|$ . For simplicity, the analysis is limited to the  $TE_{1n}$  modes.

The FEL couples  $TE_{1n}/TM_{1n}$  modes with an azimuthal variation  $\approx \exp(i l \theta)$  to space-charge modes with an azimuthal variation  $\approx \exp[i(l-1)\theta]$ . At the fundamental resonance, the  $TE_{1n}$  dispersion equation is [9,10]

$$\left[ \omega - (k + k_w)v_{||} \right]^2 - \frac{\omega_b^2 \sigma_b}{4\gamma_0^3 c^2} \frac{c^2 \kappa_1^2}{1 + \lambda_b^2} D_0(\kappa_1 R_b, \kappa_1 R_g) \times A_0(k, \omega) = \frac{\lambda_b^2}{1 + \lambda_b^2} \frac{\omega_b^2 \sigma_b}{16\gamma_0^3 c^2} \omega^2 D_1(\kappa R_b, \kappa R_g), \quad (11)$$

where  $\lambda_b \equiv k_w R_b$ ,  $\kappa_1^2 \equiv \omega^2/c^2 - (k + k_w)^2$ ,  $D_0(\xi, \zeta) \equiv J_0(\xi)W_0(\xi, \zeta)/J_0(\zeta)$ ,  $D_1(\xi, \zeta) \equiv -J_0(\xi)J_2(\xi)Y_1'(\zeta)$ , and  $A_0(k, \omega) \equiv J_1'(\kappa R_g)$  denotes the dispersion function for the vacuum  $TE_{1n}$  modes. This notation differs from that used in Refs. [9,10] to more closely match the TWT analysis. Eq. (11) reduces to the Pierce form subject to a near-resonant approximation and replacing  $\kappa \rightarrow \kappa_{co}$  ( $\equiv$  cutoff wavenumber of the mode) in the Bessel functions. However, Eq. (11) will be used in the numerical analysis since this is a more complete form.

The current scaling of the maximum gain is shown in Fig. 2 for  $V_b = 1.3$  MeV,  $R_g = 0.72$  cm,  $\lambda_w = 3.0$  cm, and  $B_w = 625$  G, for which  $k_w R_b \approx 0.052$  and  $\beta_{||} \approx 0.957$ . The dots represent solutions of Eq. (11) for the maximum gain and the solid and dashed lines vary as  $I_b^{1/3}$  and  $I_b^{1/4}$  for comparison. This FEL has a much narrower bandwidth than the TWT and the frequency of maximum gain varies

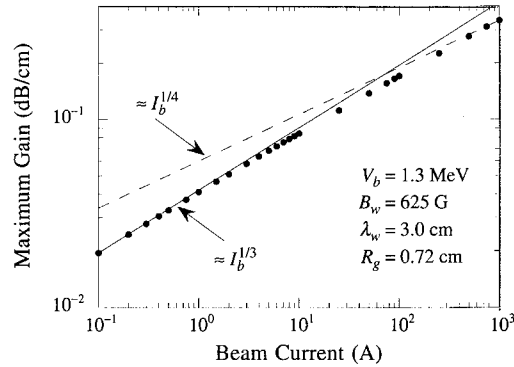


Fig. 2. Scaling of the maximum gain with the current for an FEL.

over 12.7–13.3 GHz over this range of currents. It is evident that, in contrast to the TWT example, the maximum gain follows the expected scaling laws, and for currents below (above) approximately 15 A the gain scales as the cube (fourth) root of the current. The reason for this is that frequency and the  $Q$  and  $C^3$  parameters vary less than for the TWT, and the near-resonant approximation is good. Observe that the analysis represented by Eq. (11) has been verified by comparison with experiment [11–13]. In particular, the  $I_b^{1/4}$  scaling predicted in the Raman regime has been confirmed [12].

This analysis is an idealized treatment of the gain in TWTs and FELs based upon a thin annular beam model and propagation confined by a waveguide. However, small-signal analyses have been conducted for FELs in the Compton [14] and Raman regimes [15] in which alternate scaling laws were obtained. These analyses in both regimes omitted the waveguide so that the radiation is free to diffract away from the electron beam if the gain is not high enough for optical guiding to confine the radiation field within the electron beam. In cases where diffraction is large, the area of the radiation field is much greater than that of the electron beam, and the gain was found to scale as  $I_b$  ( $\ln I_b$ ) $^{1/2}$  in the Compton regime and as  $I_b^{1/2}$  in the Raman regime.

### 4. Nonlinear analysis of the FEL

Nonlinear analyses using more general models of the beam in waveguide-based FELs also exhibit scaling laws which differ from  $I_b^{1/3}$  and  $I_b^{1/4}$ . The particular analysis and simulation code of interest here is referred to as WIGGLIN for convenience, and treats the injection of a solid beam into a rectangular waveguide with a planar wiggler [16,17].

WIGGLIN is a 3-D slow-time-scale description of an FEL. The electromagnetic field is represented as a superposition of the TE and TM modes of a rectangular waveguide, and second order nonlinear differential equations are obtained for the evolution of the amplitude and phase

of each mode. Electron dynamics are treated using the complete 3-D Lorentz force equations. No wiggler average is imposed.

The specific parameters considered correspond to a 35 GHz experiment [18] in which a 3.5 MeV/850 A beam with a 1 cm radius propagated through a rectangular waveguide [9.8 cm  $\times$  2.9 cm] with a planar wiggler with  $B_w = 3.72$  kG and  $\lambda_w = 9.8$  cm. Three wave modes could interact: the  $TE_{01}$ ,  $TE_{21}$ , and  $TM_{21}$  modes. The injected power was  $\approx 50$  kW, the bulk of which was in the  $TE_{01}$  mode. The experiment yielded a saturated power of  $\approx 180$  MW over a length of  $\approx 1.3$  m. WIGGLIN is in good agreement with the experiment for an initial beam energy spread of  $\Delta\gamma_z/\gamma_0 \approx 1.5\%$  [16,17]. We focus here on the predicted scaling of the efficiency with beam current for currents ranging from 100 to 1000 A.

In the present discussion, the efficiency is used rather than the gain. This is because the gain in an experiment, or in the WIGGLIN simulation, is not purely exponential. The instantaneous gain varies widely due to betatron oscillations, multi-mode couplings, velocity shear, and higher order beating between the wiggler and radiation fields to name a few. This makes it more convenient to deal with the efficiency. Since in the case of saturation by phase trapping, the efficiency is also expected to scale as  $I_b^{1/3}$  and  $I_b^{1/4}$  in the Compton and Raman regimes (see Ref. [10], p. 10), this poses no essential difficulty.

Space-charge effects have been shown to be negligible in the ELF experiment [19]; hence, the efficiency might be expected to scale as  $I_b^{1/3}$  in the Compton regime. The efficiency predicted by WIGGLIN is plotted versus beam current in Fig. 3 for both  $\Delta\gamma_z/\gamma_0 = 0$  (circles) and 1.5% (triangles). The solid line increases as the cube root of the current for reference. Evidently, the scaling diverges substantially from  $I_b^{1/3}$  over the range of currents studied, and that no simple power law can approximate the predicted scaling.

The principal reason for this divergence from the  $I_b^{1/3}$  scaling is that, in contrast to the FEL discussed in Section 3, the interaction in this case is extremely broad band. Strong gain is predicted to occur over frequencies ranging

from 30 to 43 GHz [16,17]. Hence, the FEL does not always obey the simple Compton and Raman scaling laws.

## 5. Summary and conclusions

The conclusion is that the well-known scaling laws for the Compton and Raman regimes are overly simplistic. The TWT example shown exhibited an  $I_b^{1/2}$  scaling law in the ballistic regime, and an  $I_b^{1/4}$  scaling in the space-charge dominated regime. The cause of this is that a broad bandwidth interaction exists in which the near-resonant approximation breaks down. The FEL example in Section 3 followed the Compton and Raman regime scaling laws due to a narrower bandwidth than in the TWT example. However, the nonlinear simulation in Section 4 resulted in a scaling law which could not be modeled by a simple power law because of a broader bandwidth than in the example in Section 3. Hence, these scaling laws must be used with some caution for both TWTs and FELs as well as the entire class of linear traveling wave devices.

## Acknowledgments

This work was supported by the Office of Naval Research.

## References

- [1] J.R. Pierce, *Traveling-Wave Tubes* (Van Nostrand, New York, 1950).
- [2] A.H.W. Beck, *Space-Charge Waves* (Pergamon, New York, 1958).
- [3] R.G.E. Hutter, *Beam and Wave Electronics in Microwave Tubes* (Van Nostrand, New York, 1960).
- [4] H. Motz, *J. Appl. Phys.* 22 (1951) 527.
- [5] R.M. Phillips, *IRE Trans. Electron Dev.* ED-7 (1960) 231.
- [6] J.E. Walsh, *Advances Electronics & Electron Devices*, ed. C. Marton (Academic, New York, 1982), Vol. 58, p. 271.
- [7] B. Johnson and J.E. Walsh, *Phys. Rev. A* 33 (1986) 3199.
- [8] H.P. Freund et al., *IEEE Trans. Plasma Sci.* PS-20 (1992) 543.
- [9] H.P. Freund and A.K. Ganguly, *Phys. Rev. A* 28 (1983) 3438.
- [10] H.P. Freund and T.M. Antonsen, Jr., *Principles of Free-Electron Lasers* (Chapman & Hall, London, 1992) Chap. 4.
- [11] J. Fajans, G. Bekefi, Y.Z. Yin and B. Lax, *Phys. Fluids* 28 (1985) 1995.
- [12] J. Fajans and G. Bekefi, *IEEE J. Quantum Electron.* QE-23 (1987) 1617.
- [13] J. Masud et al., *Phys. Rev. Lett.* 58 (1987) 763.
- [14] G.T. Moore, *Nucl. Instr. and Meth. A* 239 (1985) 19.
- [15] A. Fruchtman, *IEEE Trans. Plasma Sci.* PS-18 (1990) 424.
- [16] H.P. Freund, *Phys. Rev. A* 37 (1988) 3371.
- [17] Ref [10], Chap. 5.
- [18] T.J. Orzechowski et al., *Phys. Rev. Lett.* 57 (1986) 2172.
- [19] H.P. Freund, *Nucl. Instr. and Meth. A* 331 (1993) 496.

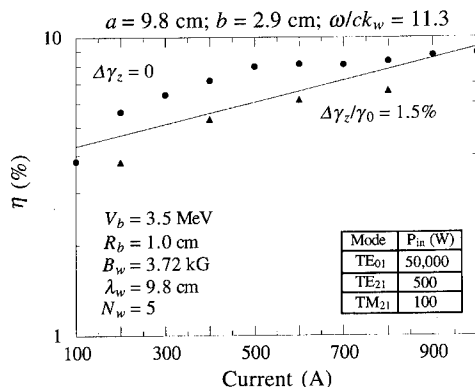


Fig. 3. Plot of the variation in the saturation efficiency versus beam current for parameters consistent with the ELF experiment.



ELSEVIER

# Theoretical investigation of a waveguide application in a FEL with large $\mu_c$

V.I. Zhulin

Scientific Centre "State Optical Institute", Research Institute of Laser Physics, Birzhevaya 12, 199034 St. Petersburg, Russian Federation

## Abstract

A free electron laser with a planar undulator, operating with a train of short electron pulses (3–6 ps) in the far infrared region ( $\lambda = 100\text{--}300\text{ }\mu\text{m}$ ) was studied. The parameter  $\mu_c$  defined as the ratio of the slippage length to the electron pulse length, can be rather large even for  $\lambda = 100\text{ }\mu\text{m}$  ( $\mu_c \approx 10$ ). An increase in the radiation wavelength  $\lambda$  leads to an increase in both  $\mu_c$  and diffraction losses.

The introduction of a waveguide into the optical cavity provides an opportunity to decrease the diffraction losses. To analyze such systems a new code including pulse propagation through a waveguide was used. It was shown that the waveguide dispersion leads to a considerable variation of the pulse shape and an additional shift of the radiation pulse which can be comparable to the slippage length. This effect changes the optimal values of the cavity detuning and can even reduce the output power.

Configurations with both circular and rectangular waveguides were analyzed. Results were compared with corresponding results without waveguides.

A free electron laser with a planar undulator, operating with a train of short electron pulses (3–6 ps) in the far infrared region ( $\lambda = 100\text{--}300\text{ }\mu\text{m}$ ) was studied. The parameter  $\mu_c$ , defined as the ratio of the slippage length to the electron pulse length, can be rather large even for  $\lambda = 100\text{ }\mu\text{m}$  ( $\mu_c \approx 10$ ). An increase in the radiation wavelength  $\lambda$  leads to an increase in both  $\mu_c$  and diffraction losses. Earlier we have shown [1] that in the available range of parameters (for example for the FELIX facility) the growth in diffraction loss is the main factor which causes a rapid decrease in the output power with an increase in  $\lambda \geq 130\text{ }\mu\text{m}$ . Introduction of a waveguide into the optical cavity provides a possibility of decreasing the losses. To analyze such systems we have carried out the following steps:

- consideration of a short pulse propagating through a hollow circular or rectangular waveguide;
- consideration of the degree of coupling between the resonator and the waveguide modes;
- simulation of FEL operation with a waveguide introduced into the optical cavity.

In order to expand an electrical field with axial symmetry and linear polarization in a waveguide it is necessary to use both  $\text{TM}_{0m}$  and  $\text{TE}_{0m}$  circular waveguide modes [2]. The most common representation can be written with the help of an expansion in the roots of Bessel functions of the first order ( $J_1$ ) and their derivatives ( $J_1'$ ). Boundary conditions lead to the determination of these roots for TM modes,  $J_1(U_n^M) = 0$ , and TE modes,  $J_1'(U_n^E) = 0$ . The

simplest representation for the electrical field  $E(r, z)$  with axial symmetry and waveguide radius  $a = 1$  is given by

$$E(r, z) = \sum_{n=0}^{\infty} \left[ a_n J_0(U_n^E r) e^{iz\gamma_n^E} + b_n J_0(U_n^M r) e^{iz\gamma_n^M} \right], \quad (1)$$

where the coefficients  $a_n$  and  $b_n$  are similar to ones in Ref. [2]:

$$a_n = \left[ \left( (U_n^E)^2 - 1 \right) J_0^2(U_n^E) \right]^{-1} \int_0^1 E(r, 0) J_0(U_n^E r) r dr;$$

$$b_n = J_0^{-2}(U_n^M) \int_0^1 E(r, 0) J_0(U_n^M r) r dr. \quad (2)$$

The propagation and attenuation constants are defined from the characteristic equation and have a simple form for the case  $ka \gg nU_n^{E,M}$ ,  $k = 2\pi/\lambda$  [3]:

$$\beta_n = \text{Re}(\gamma_n^{E,M})$$

$$= k \left[ 1 - 0.5 (U_n^{E,M}/ka)^2 (1 + 2 \text{Im}(\nu_{E,M})/ka) \right],$$

$$\nu_E = (\nu^2 - 1)^{-1/2};$$

$$\alpha_n = \text{Im}(\gamma_n^{E,M}) = (U_n^{E,M}/ka)^2 \text{Re}(\nu_{E,M})/a,$$

$$\nu_M = \nu^2 (\nu^2 - 1)^{-1/2}; \quad (3)$$

where  $\nu$  is a refractive index of guide cover. If the electromagnetic field at the entrance of the waveguide is

described by the low order guide modes, then during propagation the losses are very small, especially for a metallic guide. But for a certain range of parameters of the short radiation pulse, the losses cannot be small as for the low order guide modes. This is a consequence of the larger role of higher order modes in the energy balance. We consider a radiation pulse of Gaussian form at the waveguide entrance  $E(r, t) = \exp[-r^2/2\sigma_r^2 - (ct)^2/2\sigma_z^2]$ . The various waveguide modes transport energy with group velocities  $v_n = c\beta_n/k$ . The resulting pulse shape at the waveguide exit ( $z_w$  is the guide length) is found using the formula for the longitudinal shift between guide modes:

$$\Delta z_{nm} = z_w (\beta_n - \beta_m) / k \approx z_w \frac{U_m^2 - U_n^2}{2k^2 a^2}. \quad (4)$$

The waveguide dispersion leads to an additional shift of the radiation pulse which can be comparable with the slippage length (Fig. 1). For a rectangular waveguide the pulse shift is approximately the same as for the circular waveguide (Eq. (4)).

For both rectangular and circular waveguides the problem of coupling between the resonator and the guide modes has a similar solution. There are three low-loss

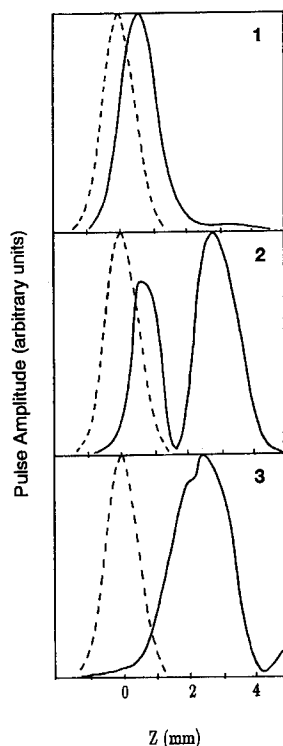


Fig. 1. Pulse shape ( $\sigma_r = 0.2$  cm,  $\sigma_z = 0.07$  cm) at the end of the waveguide (length  $z_w = 5$  m, radius  $a = 2$  cm) in comparison with the start pulse (dashed curve) for various radiation wavelengths: (1)  $\lambda = 100$   $\mu\text{m}$ ; (2)  $\lambda = 150$   $\mu\text{m}$ ; (3)  $\lambda = 200$   $\mu\text{m}$ .

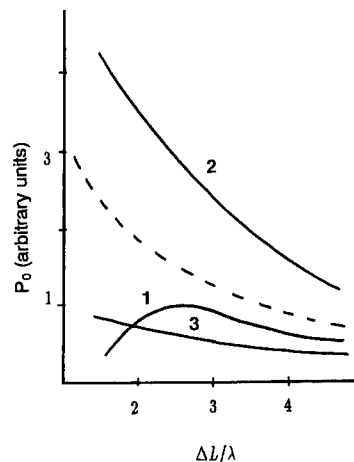


Fig. 2. Dependences of the output power  $P_0$  on the cavity detuning value  $\Delta L/\lambda$  for various values of  $\lambda$  and radius of curvature  $R_1$  of the upstream mirror: (1)  $R_1 = 400$  cm,  $\lambda = 100$   $\mu\text{m}$ ; (2)  $R_1 = 538$  cm,  $\lambda = 100$   $\mu\text{m}$ ; (3)  $R_1 = 538$  cm,  $\lambda = 150$   $\mu\text{m}$ . The dashed line corresponds to the results [1] for the FELIX facility with  $\lambda = 100$   $\mu\text{m}$ .

configurations for the schemes with a waveguide inside the optical cavity as discussed in Refs. [4,5]. However, even for optimal geometry the coupling losses depend on the radiation wave-length  $\lambda$  [5] and significantly affect the exit power of a tunable facility.

In an FEL with very large  $\mu_c$  it is particularly important to optimize the resonator optics with a waveguide and make the correct choice of the cavity detuning value. Using the previously developed 3-D code with pulse propagation [1], we have performed calculations on a configuration with a waveguide inserted between the wiggler and the downstream (flat) mirror. Parameters values considered were close to those for the FELIX facility [1]. The waveguide radius was equal to the mirror radius,  $A = 2.5$  cm. It was assumed that on the pass back to the upstream mirror both the undulator (length  $L_u$ ) and the waveguide serve as an effective guide with length  $z_w + L_u$ . An arbitrary choice of parameters leads to a reduction of the output power (curve 1 in Fig. 2) compared to the case without the waveguide (dashed curve in Fig. 2). The reason for this is poor coupling between the resonator and the guide modes [4]. The correct choice of the mirror radius of curvature reduces the losses (curve 2 in Fig. 2) and provides the opportunity to operate at longer  $\lambda$  (curve 3 in Fig. 2), extending the range of operation to 200  $\mu\text{m}$ .

In conclusion, the applicability of a waveguide to a FEL with a large  $\mu_c$  is restricted by the special losses connected with the guide. Waveguide dispersion leads to considerable variation of the pulse shape and an additional shift of the radiation pulse which can be comparable to the slippage length. This effect changes the optimal values of



cavity detuning and in some cases reduces the output power.

## References

- [1] V.I. Zhulin, R.J. Bakker, A.F.G. van der Meer, D. Oepts and P.W. van Amersfoort, *Nucl. Instr. and Meth. A* 341 (1994) ABS 90.
- [2] K.W. Berryman and T.I. Smith, *Nucl. Instr. and Meth. A* 318 (1992) 885.
- [3] E.A.J. Marcatili and R.A. Schmeltzer, *Bell Syst. Tech. J.* 43 (1964) 1783.
- [4] R.L. Abrams and A.N. Chester, *Appl. Opt.* 13 (1974) 2117.
- [5] S. Avrillier and J. Verdonck, *J. Appl. Phys.* 48 (1977) 4937.



ELSEVIER

# The interaction between low- and high-frequency waves in a waveguide free-electron laser amplifier

William J. Golightly<sup>\*</sup>, Sally K. Ride

*Department of Physics, University of California, San Diego, CA 92093, USA*

## Abstract

We examine the essential physics of the interaction between the downshifted and upshifted radiation fields during a single pass of a waveguide free-electron laser. It is found that after a sufficient period of interaction has elapsed, generally one frequency will predominate over the other. In the case where the lower frequency begins with an infinitesimal amplitude, the outcome may be predicted with a high degree of confidence through a semiempirical formula, given the initial phase velocities and frequency ratio, as well as the initial amplitude and dimensionless current density for the higher frequency. We also discuss an effect in which energy may be exchanged back and forth between the two branches.

## 1. Introduction

Waveguide free-electron lasers are devices that can operate in the submillimeter [1–3] and millimeter [4] regions of the spectrum. In the FEL we are considering, a parallel-plane waveguide confines the radiation and, if the dimension of the guide is chosen properly, the group velocity of the radiation can be reduced until it is comparable to the axial velocity of the electron beam, resulting in a reduction of slip between the radiation and the electrons. The presence of the guide also leads to multiple resonance frequencies [5,6]; i.e., instead of there being a single resonance frequency in the fundamental and in each harmonic, there are now a number of different waveguide modes associated with each harmonic number, and two resonance frequencies within each mode. These frequencies are referred to as the high- and low-frequency waves, or as the upshifted and downshifted radiation branches.

We investigate the interaction that can occur between these different frequencies. In the weak-field limit, there is no interaction at all; all frequencies evolve independently. When the weak-field limit is not applicable, the picture can become quite complex. In this paper we will consider only the case where there are two frequencies present, the high- and low-frequency waves of the first waveguide mode in the fundamental.

This subject has been dealt with in the past by others [7], but the discussion has been confined to the practical question of how a resonator can be designed in such a way

as to suppress the low-frequency wave over the course of many passes through an oscillator. We believe there is also value in approaching the subject from a more intuitive standpoint, relying extensively on the results from computer simulations to gain insights into the basic physics involved.

We can gain insight into this problem by examining the free-space case where a single frequency is allowed to evolve on its own. In this case the field experiences high gain during the linear growth phase; the electron beam then reaches saturation, and synchrotron oscillations occur. We have arrived at a semiempirical formula which may be used to predict the field energy at saturation to a fair degree of accuracy. This will prove to be of use in predicting the outcome of a competition between two interacting frequencies.

## 2. Optical wave evolution in free space

We first present the equations of motion for the system. The field evolves according to [8,9]

$$\dot{a} = -j \langle e^{-i\zeta} \rangle,$$

where  $a$  is a dimensionless field amplitude,  $j$  is a dimensionless current density, and  $\zeta = (k_z + k_0)z - \omega t$  is the electron phase. The brackets indicate an average over the electrons in the beam. The electrons evolve according to the pendulum equation [10]

$$\dot{v} = |a| \cos(\zeta + \phi),$$

where  $v = (k_z + k_0)\beta_z - k$  is the electron phase velocity and  $\phi$  is the optical phase. From these equations it is

<sup>\*</sup> Corresponding author. Tel. +1 619 534 6381, fax +1 619 534 7452.

relatively straightforward to derive an energy conservation relation:

$$|a|^2 - |a_0|^2 = 2j(v_0 - \langle v \rangle), \quad (1)$$

Here  $a_0$  is the initial field amplitude and  $v_0$  is the initial phase velocity of the beam, assumed to be monoenergetic.

As is well known, once saturation is reached the electron beam undergoes an evolution in the phase space formed by the variables  $\zeta$  and  $v$  which is characterized by oscillations in ponderomotive potential wells; these oscillations are responsible for the synchrotron oscillations. Nearly all of the electrons move within a separatrix defined by

$$v = \pm \sqrt{2|a|(1 + \sin(\zeta + \phi))},$$

where the separatrix “separates” the electrons that are trapped in the wells from the electrons that are not trapped.

From semiempirical considerations (whose details are quite involved) it is possible to estimate the energy of the field when it has reached its first maximum, i.e. when the electrons first circulate to the bottom of the separatrix. The result is that when this point is reached we have  $\langle v \rangle \cong -0.9|a|^{1/2} + 0.24|a_0|^{1/2}$ . Eq. (1) may then be written

$$|a|^2 - |a_0|^2 = 2j(v_0 + 0.9|a|^{1/2} - 0.24|a_0|^{1/2}). \quad (2)$$

This formula may be solved for numerically. As a first guess we may assume that  $v_0 = a_0 = 0$  and obtain  $|a| = (1.8j)^{2/3}$ . Convergence normally occurs within a few iterations.

We mention here that Eq. (2) is valid only to first order in  $(|a_0|/|a|)^{1/2}$  and is, therefore, good only when the gain is quite high. The formula also breaks down when  $v_0$  is well below resonance, or when it is so far above resonance that effective coupling between the radiation and the electron beam is not possible. When the conditions are satisfied; however Eq. (2) can be surprisingly accurate, often to within a few percent.

As the electrons circulate in the separatrix their average phase velocity will approximately fluctuate between  $v_0$  and their average value at maximum field energy. For this reason the field energy, averaged over an oscillation, will be approximately halfway between the initial field energy and maximum energy. Use of the energy conservation relation then makes it possible to predict the change in phase velocity of the electron beam, averaged over the beam and over a synchrotron oscillation.

### 3. Coupling in the waveguide FEL

When there are two frequencies present, we have separate parameters  $j$ ,  $v$ , and  $a$  for each. In the discussion that follows we assume for simplicity that the electron beam is perfect; i.e. emittance is negligible, and the beam width is

small compared with the spacing of the waveguide plates. This ensures that variation associated with the transverse mode structure is not important. The electron phases and phase velocities are related by

$$\zeta_2 = \alpha\zeta_1 + \beta\tau, \quad v_2 = \alpha v_1 + \beta,$$

where  $\alpha \cong k_2/k_1$ ,  $\beta = v_{02} - \alpha v_{01}$ , and  $\tau$  is a dimensionless length which varies between 0 and 1 along the length of the wiggler. Here the subscripts 1 and 2 refer to the lower and higher frequencies, respectively. The quantities  $v_{01}$  and  $v_{02}$  are the initial phase velocities for the two branches. The frequencies are coupled via the pendulum equation

$$\dot{v}_1 = |a_1| \cos(\zeta_1 + \phi_1) + \frac{k_1}{k_2} |a_2| \cos(\zeta_2 + \phi_2),$$

so that interaction can occur via the electron beam. There is generally a dramatic difference between the outcome in the coupled and uncoupled cases. When the energies in the two branches are comparable in magnitude, the energy as a function of time in each branch can behave quite erratically. With relatively few exceptions, neither frequency will at any time attain the amount of energy it would have if the other frequency had not been present.

In almost every case, one of the frequencies will come to dominate over the other if they are allowed to interact over a long enough period of time. Normally this occurs quickly, within a few synchrotron oscillations of the start of the simulation. We have found that the following rule nearly always holds: once one of the frequencies has succeeded in saturating the electron beam, the frequency that has the higher phase velocity will come to dominate. Usually the dominant frequency will acquire additional energy at the expense of the other; additional energy may also be extracted from the electron beam.

Using this information and the analytical approach discussed above for the single-mode case, it is possible to predict what the outcome would be if two frequencies were allowed to interact with one another. What if, for example, the higher frequency was excited first and allowed to saturate the electron beam, while the lower frequency was allowed to develop from an infinitesimal amplitude? The lower frequency will be significantly excited if, after saturation has occurred, the phase velocity of the lower frequency exceeds that of the higher frequency. We may use the iterative approach discussed above to compute the changes in the phase velocities. By iterating only once, we may also derive an analytical expression which predicts the difference with reasonable accuracy. We find that once saturation has occurred the difference in phase velocity is given approximately by

$$\begin{aligned} \langle v_2 - v_1 \rangle = & \frac{1}{2} \left( 1 + \frac{1}{\alpha} \right) v_{02} - v_{01} \\ & + \left( 1 - \frac{1}{\alpha} \right) (0.12|a_{02}|^{1/2} - 0.55j_2^{1/3}). \end{aligned}$$

Clearly it is more likely that  $\langle v_2 - v_1 \rangle > 0$ , and that the lower frequency is therefore suppressed, when  $v_{02}$  is larger or  $v_{01}$  is smaller. Since the term

$$\left(1 - \frac{1}{\alpha}\right)(0.12 |a_{02}|^{1/2} - 0.55 j_2^{1/3})$$

is negative, and goes to zero as  $\alpha \rightarrow 1$ , we can see that suppression becomes easier as the frequencies approach one another. This makes intuitive sense, since if the beam is saturated by the higher frequency, and the frequencies are nearly equal, the beam should also be nearly saturated from the point of view of the lower frequency, if  $v_{01}$  is not much greater than  $v_{02}$ . A higher value of  $j_2$  also makes things less stable, since the energy gain is higher, so that  $\langle v_2 \rangle$  is lower, and  $\langle v_2 - v_1 \rangle$  is also lower.

All other things being equal, there is a general tendency for the lower frequency to dominate if given enough time. Although this may be demonstrated mathematically, it is easy to grasp intuitively. Suppose two waves have different wavelengths but the same initial phase velocity. For the longer wavelength, the electron beam would have to undergo a greater reduction in velocity in order to pass through resonance and undergo saturation. Therefore it would yield greater energy to the field than would the shorter wavelength. It is therefore natural for the lower frequency to tend to dominate when the two frequencies are in competition.

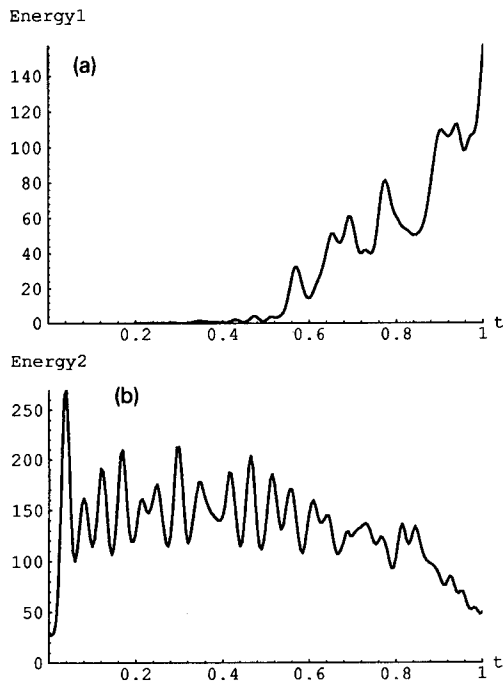


Fig. 1. Energy as a function of time in the coupled case, plotted in dimensionless units for: (a) the lower frequency wave; and (b) the higher frequency wave, for input parameters  $j_1 = 10^6$ ,  $j_2 = 1.8 \times 10^6$ ,  $v_{01} = 50$ , and  $v_{02} = 100$ .

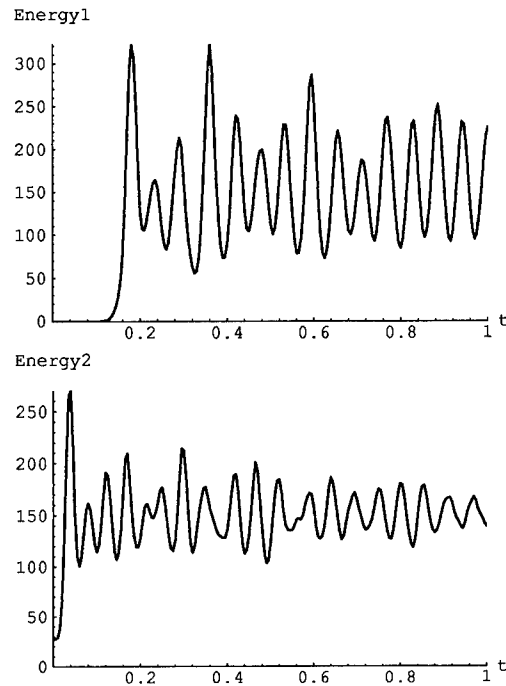


Fig. 2. Energy as a function of time in the uncoupled case, for the same parameters as in Fig. 1.

The kind of behaviour described above can be seen in Fig. 1, where we present the energy evolution for the case where the frequency ratio is 2 to 1 and we assume  $j_1 = 10^6$ ,  $j_2 = 1.8 \times 10^6$ ,  $v_{01} = 50$ , and  $v_{02} = 100$ . The lower frequency is started with infinitesimal amplitude while the higher frequency has significant initial energy. In the uncoupled case (Fig. 2) the lower frequency rises relatively quickly and acquires greater energy than the higher frequency would in its place. In the coupled case, however, the reduction in phase velocity brought about by the higher frequency delays the excitation of the lower frequency. Nevertheless, the lower frequency is clearly coming to dominate, drawing energy from the other wave in the process.

Indeed, it is generally the case that the dominant wave will remove energy from the other wave as it grows. When only one frequency is present and the beam has been saturated, the electrons tend to drift leftward in phase space along with the separatrix, so that for that frequency  $\langle v \rangle = -\phi$ . As the other frequency is excited, the beam becomes less ordered, reducing  $\phi$  and slowing the leftward drift of the separatrix. At the same time the beam is losing energy, accelerating the leftward drift of the electrons. As a result the electrons tend to move into the left half of the separatrix, which corresponds to optical absorption.

#### 4. Optical phase locking

There is another feature of the interaction which is of interest. We find that when neither frequency strongly dominates, it is possible for a situation to arise in which energy is exchanged back and forth between the two branches, while the energy of the electron beam is essentially unaffected. This is reminiscent of the parametric instability in plasma physics [11]. It is best, however, to understand the phenomenon as a form of phase-locking between the optical phases of the waves. Although it occurs for all different frequency ratios, the phenomenon is especially pronounced in the case where the frequency ratio is 2 to 1. Such a case is shown in Fig. 3, where we have  $j_1 = 5 \times 10^4$ ,  $j_2 = 9 \times 10^4$ ,  $v_{01} = 0$ ,  $v_{02} = 36$ , and initial energies are equal. The key to understanding the energy interchange lies in the relative movement of the separatrices for the two frequencies. Suppose we plotted the electron beam in the phase space corresponding to the variables  $\zeta_1, v_1$ , and overlapped the plot with the separatrices. The separatrix for the lower frequency would move at a rate given by  $-\dot{\phi}_1$ , while that for the higher frequency would move at a rate  $-(\dot{\phi}_2 + \beta)/\alpha$ . Over the course of one oscillation in the electromagnetic field the separatrix for the higher frequency will move further backward in phase space than that for the lower frequency, and by an

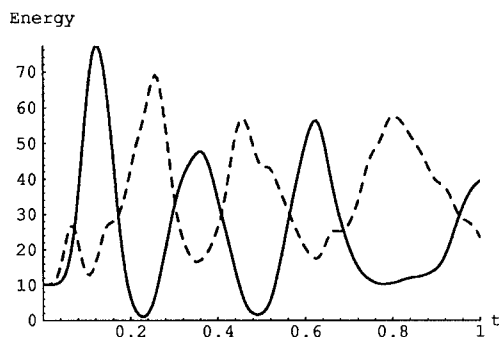


Fig. 3. The effect of phase locking is seen here, where the solid line represents the lower frequency and the dashed line represents the higher frequency. Here  $j_1 = 5 \times 10^4$ ,  $j_2 = 9 \times 10^4$ ,  $v_{01} = 0$ , and  $v_{02} = 36$ .

amount equal to  $\pi$ . This leads to the result that when the electrons are predominantly located in a region of phase space corresponding to absorption for one wave, they also tend to be predominantly located in a region corresponding to emission for the other wave. Hence one wave gains energy while the other loses it.

#### 5. Conclusion

The results presented here could have real practical value. Aside from enhancing our basic understanding of what happens when different frequencies interact in a waveguide FEL, they could also be of use in predicting and explaining observable effects in a tapered waveguide FEL, where energy would be extracted over a large number of synchrotron oscillations. Although we have not included tapering in our analysis, there are no difficulties involved in extending our results to the tapered case.

#### References

- [1] S.K. Ride, R.H. Pantell and J. Feinstein, *Appl. Phys. Lett.* 57 (1990) 1283.
- [2] A. Doria, G.P. Gallerano and A. Renieri, *Opt. Commun.* 80(5-6) (1991) 417.
- [3] R. Bartolini, A. Doria, G.P. Gallerano and A. Renieri, *Nucl. Instr. and Meth. A* 304 (1991) 417.
- [4] R. Bonifacio, I. Boscolo, F. Casagrande, G. Cerchioni, R. Corsini, A. Cucchetti, L. De Salvo Souza, D. Fadini, A. Lombardi, P. Pierini and N. Piovilla, *Nucl. Instr. and Meth. A* 289 (1990) 1.
- [5] A. Amir, E. Boscolo and L.R. Elias, *Phys. Rev. A* 32 (1985) 2864.
- [6] W.J. Golightly and S.K. Ride, *IEEE J. Quantum Electron.* QE-27 (1991) 2656.
- [7] P.E. Latham and B. Levush, *IEEE Trans. Plasma Sci.* 18 (3) (1990) 472.
- [8] W.B. Colson and S.K. Ride, *Phys. Lett. A* 76 (1980) 379.
- [9] W.B. Colson and S.K. Ride, in: *Physics of Quantum Electronics*, Vol. 7, eds. S. Jacobs et al. (Addison-Wesley, Reading, MA, 1980) p. 377.
- [10] W.B. Colson, *Phys. Lett. A* 64 (1977) 190.
- [11] F.F. Chen, *Introduction to Plasma Physics and Controlled Fusion* (Plenum, New York, 1984) p. 309.



ELSEVIER

## Visible surface quasi-Cherenkov FEL

V.G. Baryshevsky, K.G. Batrakov, I.Ya. Dubovskaya<sup>\*</sup>, S. Sytova

*Institute of Nuclear Problems, 11 Bobruiskaya St., 220050 Minsk, Belarus*

### Abstract

A parametric quasi-Cherenkov free electron laser with surface diffraction distributed feedback is studied when an electron beam moves over the target surface. The parameters of such a device using the Los Alamos Advanced Free Electron Laser (AFEL) linac are given.

### 1. Introduction

As shown in Refs. [1,2] induced radiation from a relativistic particle beam can be obtained in a wide spectral region on the basis of parametric (quasi-Cherenkov) radiation (parametric quasi-Cherenkov FEL). Both volume [1] and surface [3] versions of such X-ray FELs were considered. We pointed out that a reduction in the destructive action on the generation process by multiple scattering of the particle beam by atoms can be achieved by transiting to the surface scheme for the FEL, where a particle beam moves over a periodic target at a distance  $d \leq \lambda\gamma$  ( $\lambda$  is the photon wavelength,  $\gamma$  is the Lorentz factor) or at a small angle relative to this target  $\Psi \leq |\chi_0|^{1/2}$  ( $\chi_0 = \epsilon_0 - 1$ ,  $\epsilon_0$  is the medium dielectric constant).

In this case radiation is formed along the whole particle trajectory in vacuum with no multiple scattering. However, even in the best situation the beam current density necessary for achieving the oscillation threshold level in the X-ray spectral region is very high. On the other hand, in the visible spectral region the system parameters considered are available and the analysis shows that a parametric surface visible quasi-Cherenkov FEL can be constructed on the basis of existing accelerators. The basic physical processes for a quasi-Cherenkov X-ray FEL could be modeled with a visible one if an optical grating with  $|\chi_0| \ll 1$  were chosen.

This report is devoted to the consideration of a scheme of a parametric optical quasi-Cherenkov FEL with  $\chi_0/\chi_r \gg 1$  ( $\chi_r$  is the Fourier component of the dielectric susceptibility of the periodic medium), determined by the depth of modulation of a holographic optical diffraction grating.

### 2. Generation equation of the quasi-Cherenkov FEL

Let us consider the scheme of an FEL as shown in Fig. 1.  $h$  is the distance between a particle beam and a target surface,  $\delta$  is the transverse size of a particle beam, the axis  $X$  is chosen along the direction of motion of the beam, the axis  $Z$  is a normal to the target surface, and  $d$  is the width of the dielectric target.  $a$ ,  $b$  and  $c$  are mirrors for the accumulation of energy radiated during the macropulse of an accelerator particle beam. Distributed feedback is formed by dynamical diffraction from an optical holographic diffraction grating. The reciprocal lattice vector characterizing diffraction in this case ( $\tau = (2\pi n_1/a, 2\pi n_2/b, 2\pi n_3/c)$ ) is directed at an angle relative to the particle velocity and to the target surface. The generated radiation frequency is determined by the diffraction process.

The electromagnetic field excited in the system shown in Fig. 1 can be represented in the form:

$$E = a \exp(ik_0 r) + b \exp(ik_0^{(-)} r), \quad (1a)$$

$$E = a \exp(ik_0 r) + c \exp(ik_n r) + d \exp(ik_n^{(-)} r), \quad (1b)$$

$$E = a \exp(ik_0 r) + f \exp(ik_0 r) + g \exp(ik_0^{(-)} r), \quad (1c)$$

$$E = \sum_{i=1}^n c_i \exp(ik_i r) (1 + s_i \exp(i\tau r)) + c_r \exp(ik^{(-)} r) + d_r \exp(ik_r^{(-)} r), \quad (1d)$$

$$E = c_i \exp(ik_0 r) + d_i \exp(ik_r^{(-)} r), \quad (1e)$$

where  $k_0 = (k_\perp, k_{0z})$ ,  $k_{0\tau} = k_0 + \tau$ ,  $k_{0z} = (\omega^2/c^2 - k_\perp^2)^{1/2}$ ,  $k_0^{(-)}$ ,  $k_r^{(-)}$  and  $k_{0\tau}^{(-)}$  are related to the waves reflected from the target surface, while  $k_0^{(-)} = (k_\perp, -k_{0z})$ ,  $k_{0\tau}^{(-)} = (k_{0\perp} + \tau_\perp; -k_{0z\tau})$ ,  $k_{0z\tau} = (\omega^2/c^2 - (k_\perp + \tau_\perp)^2)^{1/2}$ . Obviously the waves reflected from the target

<sup>\*</sup> Corresponding author.

boundary inside the target (this is the boundary between the regions (1d) and (1e) for the transmitted wave  $\mathbf{k}$  and between the regions (1c) and (1d) for the diffracted wave  $\mathbf{k}_\tau$ ) do not fulfill the diffraction condition for the grating. Therefore, for these waves we can assume that the dielectric constant is equal to the ordinary dielectric constant of the medium without diffraction. That is,  $\mathbf{k}^{(-)} = (\mathbf{k}_\perp, -k_z)$ ,  $\mathbf{k}_\tau^{(-)} = (\mathbf{k}_\perp, -k_{z\tau})$ , where  $k_z = ((\omega^2/c^2)\epsilon_0 - k_\perp^2)^{1/2}$ ,  $k_{z\tau} = ((\omega^2/c^2)\epsilon_0 - (\mathbf{k}_\perp + \boldsymbol{\tau})^2)^{1/2}$ .  $\mathbf{k}_n = (\mathbf{k}_\perp, k_{zn})$ ,  $\mathbf{k}_n^{(-)} = (\mathbf{k}_\perp, -k_{zn})$ ,  $k_{zn} = (\omega^2/c^2 - k_\perp^2)^{1/2}$  is the solution of the dispersion equation for electromagnetic radiation modes inside the particle beam moving in vacuum and in a magnetic field  $\mathbf{H}$  directed along the target surface. This field is needed because the spectrum of photon emission coincides with the spectrum of photon absorption by an electron beam in vacuum. The dispersion equation determining these modes is:

$$k^2 c^2 - \omega^2 - i(k_x^2 c^2 - \omega^2)\sigma = 0, \quad (2)$$

where

$$\sigma = -\frac{\omega_L^2}{i\gamma^3(\omega - k_x U)^2}$$

for the limit of “cold” beam and

$$\sigma = -\frac{\sqrt{\pi}}{\gamma^3} \frac{\omega_L^2}{\delta_0^2} x^t \exp(x^t)^2$$

for the limit of “hot” beam.

Here  $\omega_L$  is the Langmuir frequency of the electron beam,  $x^t = (\omega - k_x U)/(\sqrt{2}\delta_0)$ ;  $\delta_0^2 = (k_1^2 \Psi_1^2 + k_2^2 \Psi_2^2 + k_3^2 \Psi_3^2)u^2$ ;  $\Psi_i = \Delta u_i/u$  is the velocity spread of the electrons in the beam relative to the  $x, y, z$  axes, respectively.

$\mathbf{k}_i = (\mathbf{k}_\perp, k_{zi})$  where  $k_{zi}$  are the solutions of the diffraction dispersion equation (see Ref. [3]),  $i = 1, 2$  for the case of  $|\chi_0| \gg |\chi_\tau|$ .  $\mathbf{k}_{i\tau} = \mathbf{k}_i + \boldsymbol{\tau}$ ,  $a, b, c, d, f, g, c_i, s_i, c_\tau, d_\tau, c_l, d_l$  are the amplitudes of waves excited in the system under consideration. We assume that the synchronism condition is fulfilled only for the wave with  $\mathbf{k}$ . Consequently, we can consider that the particle beam does not affect the diffracted wave with  $\mathbf{k}_\tau^{(-)}$  and this wave is not refracted and not reflected by the particle beam. The reflection coefficient for the wave  $\mathbf{k}_0$  is included in the magnitude of  $f \neq 1$ . We will assume below for simplicity that  $k_y$  and  $\tau_y$  are equal to zero.

The boundary conditions for the electromagnetic field (1) are written as

$$z = -H,$$

$$b \exp(ik_{0z}H) = c \exp(-ik_{zn}H) + d \exp(ik_{zn}H),$$

$$-b \exp(ik_{0z}H) = (k_{0z}/k_{zn})(c \exp(-ik_{zn}H) - d \exp(ik_{zn}H));$$

$$z = -h_0,$$

$$c \exp(-ik_{zn}h) + d \exp(ik_{zn}h)$$

$$= f \exp(-ik_{0z}h) + g \exp(ik_{0z}h),$$

$$(k_{0z}/k_{zn})[c \exp(-ik_{zn}h) - d \exp(ik_{zn}h)]$$

$$= f \exp(-ik_{0z}h) - g \exp(ik_{0z}h);$$

$$z = 0,$$

$$f + g = c_1 + c_2 + c_\tau,$$

$$f - g = k_{zi}/\epsilon_0 k_{0z}[c_1 + c_2 - c_\tau],$$

$$a = s_1 c_1 + s_2 c_2 + d_\tau,$$

$$a = (k_{z\tau}/\epsilon_0 k_{0\tau})[s_1 c_1 + s_2 c_2 - d_\tau];$$

$$z = d_0,$$

$$c_1 l_1 + c_2 l_2 + c_\tau l_\tau = c_l \exp(ik_{0z}d),$$

$$(k_z/\epsilon_0 k_{0z})[c_1 l_1 + c_2 l_2 - c_\tau l_\tau] = c_l \exp(ik_{0z}d),$$

$$s_1 c_1 l_1 + s_2 c_2 l_2 + d_\tau l_\tau = d_l \exp(ik_{0z}d),$$

$$(k_{z\tau}/\epsilon_0 k_{0z\tau})[s_1 c_1 l_1 + s_2 c_2 l_2 - d_\tau l_{\tau\tau}]$$

$$= -d_l \exp(-ik_{0z\tau}d); \quad (3)$$

where  $l_i = \exp(ik_{zi}d)$ ,  $l_\tau = \exp(-ik_z d)$ ,  $l_{z\tau} = \exp(-ik_{z\tau}d)$ ; in the spirit of the present approximation we can assume  $k_{zi} \approx k_z$ , if a multiplier of the wave amplitude.

Solving the above linear system of equations we can derive the generation (dispersion) equation in the following form:

$$I_n = (1 + \alpha_D A)/(A + \alpha_D), \quad (4)$$

where

$$\alpha_D = \left(k_{0z} - \frac{k_z}{\epsilon_0}\right) \left(k_{0z} + \frac{k_z}{\epsilon_0}\right)^{-1},$$

$$\alpha_D^\tau = \left(k_{0z\tau} - \frac{k_{z\tau}}{\epsilon_0}\right) \left(k_{0z\tau} + \frac{k_{z\tau}}{\epsilon_0}\right)^{-1},$$

$$A = \alpha_D \exp(ik_z d) \frac{s_2(l_2 - \alpha_{D\tau}^2 l_\tau)l_1 - s_1(l_1 - \alpha_{D\tau}^2 l_\tau)l_2}{s_1(l_1 - \alpha_{D\tau} l_\tau) - s_2(l_2 - \alpha_{D\tau}^2 l_\tau)},$$

$$I_n = \kappa_0^2 \exp(-2\kappa_0 h) \frac{\omega_L^2}{\gamma^3(\omega - k_x U)^2} f(k, \delta)$$

for the limit of “cold” beam,

$$I_n = -\kappa_0^2 \exp(-2\kappa_0 h) \frac{i\sqrt{\pi} \omega_L^2}{\gamma^3 \delta_0^2} x^t$$

$$\times \exp(-(x^t)^2) f(k, \delta)$$

for the limit of “hot” beam,

$$f(k, \delta) = \frac{\sinh(\kappa_n \delta)}{(\kappa_0^2 + \kappa_n^2) \sinh(\kappa_n \delta) + 2\kappa_0 \kappa_n \cosh(\kappa_n \delta)},$$

$$\kappa_0 = k_{0z}/i, \quad \kappa_{zn} = k_{zn}/i.$$

The exact value of the frequency excited in the FEL is determined by the real part of the solution of Eq. (4)  $\omega = \omega(k_x)$ . Obviously, this frequency should satisfy both the synchronism condition and the diffraction condition for a given diffraction geometry characterized by the reciprocal lattice vector  $\tau$ . From Eq. (4) one can obtain for the magnitude characterizing the growth rate of the electromagnetic field over the threshold level:

$$\omega'' = \omega \left\{ 1 + \frac{kd}{2\gamma} \left[ 1 + \frac{1-\beta}{\beta^2\alpha^2 + 4\beta r} \right] \right\}^{-1} \times \left\{ \frac{I_n''}{\gamma^2} - \frac{k\chi_0''d}{2\gamma\epsilon_0} \left[ 1 + \frac{(1-\beta)r - \beta\alpha r''/(2\chi_0'')}{\beta^2\alpha^2 + 4\beta r} \right] \right\}. \quad (5)$$

The analysis shows that in the limit of a “hot” beam the process of generating coherent radiation is characterized by a threshold level while in the “cold” beam case the instability has no threshold behavior.

Using these results we consider as an example the possibility of constructing a surface, quasi-Cherenkov FEL in the visible spectral range ( $\lambda \approx 600$  nm) on the basis of the Los Alamos accelerator (parameters given in Ref. [4]). The analysis shows that the electron beam [4], with a transverse size less than 1 mm, should be considered “hot”. The surface electromagnetic wave interaction length can be estimated as  $\lambda\gamma \approx 12$   $\mu$ m for  $\gamma = 20$  and  $\lambda \approx 600$  nm. A transverse size of the beam larger than this leads to a reduction in the efficiency of the interaction. A beam size of  $\delta \approx 1$  mm corresponds to a velocity spread of  $\Delta\psi_z \approx 0.2$  mrad. This means that after passing a target with length  $L = 0.5$  cm, the transverse displacement of an

electron inside the beam is about 1  $\mu$ m, less than the radiation interaction length, and much less than the transverse beam size. Using the parameters from Eq. (4), we can estimate the growth rate for a solitary microbunch of the beam ( $\tau = 10$  s,  $l_b = 0.3$  cm). The estimate, made in the linear approximation according Eq. (5), shows that the growth rate is  $\approx 0.2$  at  $\omega'' \approx 2 \times 10^{10}$ /s. This means that the electromagnetic field enhancement is of the order of  $\exp(400)$  for a 10  $\mu$ s macrobunch containing  $2 \times 10^3$  microbunches. Obviously, in this case we need to use a system of mirrors to accumulate electromagnetic radiation emitted by different microbunches of the beam. The distance between the mirrors should be chosen in such a way that the time of electromagnetic wave passing between the mirrors is equal to the interval between the two neighboring microbunches (for  $\tau_{ij} \approx 4.8$  ns,  $L_{abc} \approx 144$  cm).

### 3. Conclusion

The scheme considered here is, at first sight, very similar to the Smith–Purcell FEL considered in Refs. [5–8]. However, there are differences. First, we do not need two gratings or mirrors to provide feedback. In our case distributed feedback is formed by the dynamical diffraction which determines the excited radiation modes. This means that oscillation is possible without any mirrors. The two mirrors shown in Fig. 1 are necessary only to accumulate radiated energy from different microbunches of the accelerator beam because of the small length of the microbunches. They do not influence the radiation modes. In addition, the generated frequency does not depend

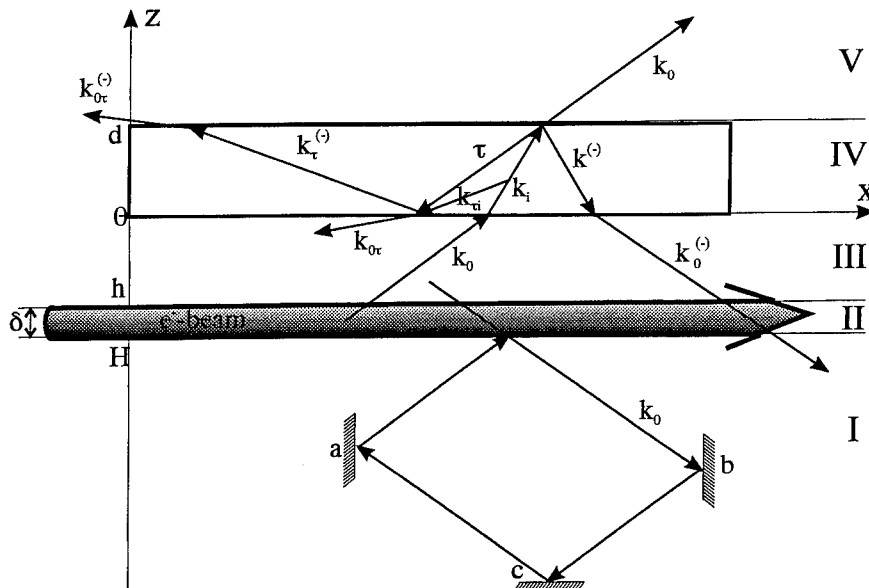


Fig. 1. Diagram of the quasi-Cherenkov surface FEL.



significantly on the particle energy in contrast with the Smith–Purcell FEL. A comparison between Cherenkov and diffraction (Smith–Purcell) radiation was made in Ref. [9]. The present study shows that the suggested scheme forms the basis for possible construction of a compact FEL in the visible spectral range.

## References

- [1] V.G. Baryshevsky, K.G. Batrakov and I.Ya. Dubovskaya, J. Phys. D 24 (1991) 1250.
- [2] V.G. Baryshevsky, K.G. Batrakov and I.Ya. Dubovskaya, Izv. Akad. Nauk Bel. SSR 3 (1992) 99.
- [3] V.G. Baryshevsky, K.G. Batrakov and I.Ya. Dubovskaya, Nucl. Instr. and Meth. A 341 (1994) 274.
- [4] D.S. Nguyen et al., Nucl. Instr. and Meth. A 341 (1994) 29.
- [5] L. Schachter and A. Kon, Phys. Rev. 40 (1989) 876.
- [6] E.J. Price and J.E. Walsh, Nucl. Instr. and Meth. A 304 (1991) 133.
- [7] J.E. Walsh, E. Fisch et al., Nucl. Instr. and Meth. A 296 (1990) 292.
- [8] G. Doucas, J.H. Mulvey et al., Phys. Rev. Lett. 69 (1992) 1761.
- [9] Generators of Diffraction Radiation (Naukova dumka, Kiev, 1991).



ELSEVIER

## Optimization of the free electron laser interaction via electron bunch trapping

A.A. Silivra<sup>a,\*</sup>, E.D. Belyavskiy<sup>b</sup>, I.A. Goncharov<sup>a</sup>

<sup>a</sup> Kiev University, Kiev, Ukraine

<sup>b</sup> Orion R & D Institute, Kiev, Ukraine

### Abstract

Electromagnetic wave amplification in free electron lasers with a reversed guide field and a right-hand polarized wiggler field is considered both analytically and numerically. Electron bunch trapping by the high frequency electromagnetic field is used for efficiency optimization. Based on motion stability criteria, the possibility of bunch trapping by tapering the FEL parameters is shown. For this purpose any of the FEL parameters, such as the spatial periodicity of the wiggler or the electromagnetic wave, or the strength of the wiggler or guide field may be tapered. The stability analysis of the electron motion is based on Lyapunov theory, permitting the determination of the optimum tapering rate.

A particle simulation was carried out for an FEL with a reversed guide field with only the wiggler field tapered. It was found that under the theoretically predicted tapering all electrons of the beam were trapped and it was possible to achieve as high an efficiency as allowed by the FEL mechanism. The interaction region lengthens in this case but is still experimentally realizable. In particular, for FEL parameters close to experimental ones (relativistic factor  $\gamma = 4.75$ , wiggler field strength  $B_w = 2.8$  kG, guide field strength  $B_0 = -1.4$  kG, operation wavelength  $\lambda = 6.2$  mm), it was found that the efficiency grew to over 50%, compared with about 20% efficiency in the homogeneous wiggler field case.

### 1. Introduction

The problem of efficiency enhancement and optimization is common to most electron devices (like TWTs). In the frame of a traditional approach one should provide conditions under which a compact electron bunch formed in the process of interaction with an electromagnetic wave remains in the decelerating phase as long as possible. Usually waveguide profiling is suggested to accomplish this goal. Similar results for an FEL can be achieved if the wiggler field or/and the focusing field are tapered. As the specific values of the transverse and the longitudinal velocities for a given total electron energy are determined by the magnetic field amplitudes, a longitudinal velocity decrease of the electron beam (due to energy transfer to the high frequency electromagnetic wave) can be compensated by varying the magnetic field amplitude along the interaction region. It is convenient to use the wiggler field for tapering since the transverse electron velocity is sensitive to it.

Among the experimental tests of such a method of FEL

efficiency enhancement, Ref. [1] should be noted first. In this experiment a microwave FEL amplifier operated with high gain (34 dB/m) and an efficiency of about 6%. When wiggler tapering down to 0.45 of the initial value was used, the efficiency increased to 34%. The point of power saturation was 1.3 m from the beginning of the interaction region. Wiggler tapering began after 1 m and lasted to 2.6 m. Optimization by computer showed good agreement between the calculated and experimentally determined laws of wiggler tapering.

A similar approach was used in Ref. [2]. Their FEL amplifier saturated at 1.2 m. The location of the beginning of the linear taper (0.8 m) and the rate of decrease of the wiggler field along the interaction region (down to 0.6 of nominal wiggler field value) were chosen experimentally. A rather high efficiency of 25–80% was achieved.

There are more investigations, both theoretical and experimental, of tapered FEL operation than can be referred to in one article. The principal importance of these investigations is that they have demonstrated the capability of such an approach and have shown that FELs are devices with technically reasonable efficiency. Unfortunately, they do not answer the question of how to determine an optimal law of magnetic field tapering to achieve optimal efficiency. That is the question to which this paper is devoted.

\* Corresponding author. Present address: 528 Walker Bldg., Penn State University, University Park, PA, 16802, USA, tel. +1 814 863 9400, e-mail: silivra@geosc.psu.edu.

## 2. Description of general approach

The main idea of our approach is that we propose to form relatively large electron bunches with a phase extent of order  $\pi$ . Then we taper the FEL parameters to displace the stable equilibrium position of the electron bunch toward a decelerating half-period of the combination electromagnetic wave. In this case an individual electron within the bunch is not in precise synchronism with the combination wave. The electron oscillates within the phase bunch limits and is unable to leave the bunch due to the potential barrier formed by the electromagnetic wave field. Thus, all of the electrons of the bunch are trapped [3] and energy transfer to the electromagnetic wave is achieved from the electron bunch as a whole. If the oscillating motion of the electrons is stable, the process of energy transfer is not restricted by typical effects such as an increase in the spread in the velocities of the electrons in the bunch, and in principle it is possible to achieve as high an efficiency as the FEL mechanism allows. It should be noted that the tapering of the FEL parameters must begin just after the bunch formation region, generally far before the saturation point.

Let us consider an electron beam propagating along the  $z$  axis in an FEL in the presence of the right-hand polarized electromagnetic wave. The static magnetic fields are given by:  $B_{st} = B_w(z)(e_x \cos(k_w z) + e_y \sin(k_w z)) + e_z B_0$ , where  $B_w(z)$ ,  $B_0$  are the wiggler and guide field amplitudes, and  $k_w = 2\pi/\lambda_w$  is the wiggler spatial periodicity.  $A$  is the amplitude of the electromagnetic wave vector potential described by  $A_{hf} = A e_x \cos(\omega t - kz) + e_y \sin(\omega t - kz)$ .

We restrict ourselves to the case when high-frequency space-charge forces in the electron beam are negligible in comparison with those of the static magnetic fields or the electromagnetic wave [4]. In the frame rotating with the wiggler field  $e_1 = e_x \cos(k_w z) + e_y \sin(k_w z)$ ,  $e_2 = e_x \sin(k_w z) - e_y \cos(k_w z)$ ,  $e_3 = e_z$  the equations for the electron motion and for the slowly varying electromagnetic wave amplitude are as follows:

$$\begin{aligned} \frac{dp_1}{dz} &= \left( \frac{\Omega_0}{k_w c p_3} - 1 \right) p_2 - \alpha_s \left( \frac{\gamma}{p_3} - \frac{ck}{\omega} \right) \sin \theta, \\ \frac{dp_2}{dz} &= - \left( \frac{\Omega_0}{k_w c p_3} - 1 \right) p_1 - \alpha_s \left( \frac{\gamma}{p_3} - \frac{ck}{\omega} \right) \cos \theta, \\ \frac{d\gamma}{dz} &= - \frac{\alpha_s}{p_3} (p_1 \sin \theta + p_2 \cos \theta), \\ \frac{d\theta}{dz} &= g \left( \frac{\gamma}{p_3} - \frac{ck}{\omega} \right) - 1, \\ \frac{d\alpha_s}{dz} &= \frac{j_0}{mc^3} \frac{\omega}{ck} \int_0^{2\pi} \frac{p_1 \sin \theta + p_2 \cos \theta}{p_3} d\theta_0, \end{aligned} \quad (1)$$

where  $z$  stands for  $k_w z$ ,  $\Omega_{0,w} = eB_{0,w}/(mc)$ ,  $\theta = \omega t - \int (k + k_w) dz$ ;  $\theta_0 \in [0-2\pi]$  are the initial phases of the electrons with respect to the electromagnetic wave;

$$\alpha_s = \frac{eA}{k_w mc^2} \frac{\omega}{c},$$

$p_{1,2,3} = \gamma v_{1,2,3}/c$  are normalized electron impulses satisfying the relation  $p_3 = (\gamma^2 - 1 - p_1^2 - p_2^2)^{-1/2}$ ;  $j_0 = en_0 v_0$  is the beam current density and  $g = \omega/(ck_w)$  is a frequency transformation factor.

Note that in the absence of an electromagnetic field ( $A = 0$ ), the first order solution of this system is easily obtained:

$$\begin{aligned} v_1 &= v_{\perp}(z), \\ v_2 &= -v'_{\perp}(z) \left/ \left( \frac{\Omega_0}{k_w v_{\parallel}(z)} - 1 \right) \right., \\ v_3 &= v_{\parallel}(z). \end{aligned} \quad (2)$$

## 3. Criteria of stability of electron bunch motion

Let us analyze the criteria of electron bunch motion stability under the assumption that high-frequency modulation of electron transverse velocities is negligible, i.e.

$$v_x = v_{\perp}(z) \cos k_w z, \quad v_y = v_{\perp}(z) \sin k_w z,$$

where  $v_{\perp}(z)$  is a slow function of the longitudinal coordinate  $z$  due to FEL parameter tapering. Under this assumption the third and forth equations of (1) can be written in the following form:

$$\begin{aligned} \frac{d\theta}{dt} &= h_0 (v_{ph} - v_z), \\ \frac{d\gamma}{dt} &= -\alpha_s k_w v_{\perp} \sin(\theta), \end{aligned} \quad (3)$$

where  $v_{ph} = \omega/h_0$  is the phase velocity of the combination wave,  $h_0 = k + k_w$ .

Choosing variables  $X_1 = \theta + \varphi_0$ ,  $X_2 = \gamma_1 - \gamma$ , where  $\gamma_1 = (\mu - v_{ph}^2/c^2)^{-1/2}$ ,  $\mu = 1 - v_{\perp}^2/c^2$ ,  $\sin(\varphi_0) = v_{ph}(d\gamma_1/dz)/\alpha_s k_w v_{\perp}$ , and assuming that  $\varphi_0$  is an adiabatic function of  $z$ , system (3) can be brought to the origin of the coordinates

$$\begin{aligned} \frac{dX_1}{dt} &= h_0 (v_{ph} - v_z(X_2)), \\ \frac{dX_2}{dt} &= \alpha_s v_{\perp} k_w \left[ \sin(X_1 - \varphi_0) + \sin(\varphi_0) \right. \\ &\quad \left. - \frac{\sin(\varphi_0)}{v_{ph}} (v_{ph} - v_z(X_2)) \right], \end{aligned} \quad (4)$$

where  $v_z(X_2) = c(\mu - (\gamma_1 - X_2)^{-2})^{1/2}$

Let us consider a new function

$$W_1 = \int_0^{X_2} (v_{ph} - v_z(X_2)) dx_2 - \alpha_s k_w v_{\perp} (\cos(\varphi_0) - \cos(X_1 - \varphi_0) + X_1 \sin(\varphi_0)) / h_0. \quad (5)$$

The derivative of this function with respect to time can be found using (4):

$$\frac{dW_1}{dt} = W_2 = -\alpha_s v_{\perp} k_w \frac{\sin(\varphi_0)}{v_{ph}} (v_{ph} - v_z(X_2))^2. \quad (6)$$

One can see that  $W_1 = W_2 = 0$  when  $X_1 = X_2 = 0$ . Function  $W_1$  will be a Lyapunov function [5] if within some vicinity of the origin it has a definite sign (in the present case  $W_1 > 0$ ). Thus, the equilibrium point will be stable if  $W_2 < 0$ . These conditions are satisfied if

$$\int_0^{X_2} (v_{ph} - v_z(X_2)) dx_2 > 0, \quad (7)$$

$$v_{\perp} \cos(\varphi_0) < 0, \quad (8)$$

$$v_{\perp} \sin(\varphi_0) > 0, \quad (9)$$

$$|\sin(\varphi_0)| < (1 - \cos(X_1)) \times ((1 - \cos(X_1))^2 + (X_1 - \sin(X_1))^2)^{-1/2}. \quad (10)$$

It follows from these conditions that electron trapping in an FEL can be achieved by appropriate tapering of any or all of the FEL parameters (wiggler fields, guide fields, wiggler or electromagnetic wave spatial periodicity). Analysis shows that condition (7) is almost always satisfied. Conditions (8) and (9) characterize the position of the equilibrium point with regard to the combination wave and point to the fact that bunch trapping can be achieved only when the equilibrium point is near the transition from an accelerating phase to a decelerating phase.

The most rigid condition for electron bunch motion stability is (10). It can be satisfied for all of the electrons in the bunch if it is satisfied for that electron in the bunch which has the maximum amplitude of oscillation (it is of order  $\pi$  in our case, see Fig. 2). We will therefore treat this inequality as

$$|\sin(\varphi_0)| = \xi, \quad (11)$$

where  $\xi < 1$  and must be determined by numerical calculations.

Using the previous definitions we can rewrite (11) as

$$\frac{d\Omega_w}{dz} = \xi \alpha_s \frac{k_w c}{2\pi} \times \int_0^{2\pi} \frac{\gamma_1}{P_{ph}} \frac{\frac{\Omega_0}{k_w c} - p_3 + \frac{p_1}{p_3} \left( p_1 + \frac{\Omega_w}{k_w c} \right)}{p_3} d\theta_0, \quad (12)$$

which is the actual rule of wiggler field tapering. As the tapering rule (12) has been obtained assuming that the electron bunches already exist, it is necessary to consider the problem of their formation from the initially homogeneous electron beam.

#### 4. Preliminary bunching of electrons

It is known that for a FEL to operate effectively electrons at the beginning of the interaction region have to get onto the stationary trajectories. Typically, the wiggler field amplitude is increased from 0 up to the nominal value (corresponding to synchronous longitudinal velocity) during the first 5–6 spatial periods of the wiggler. Our numerical simulation points out that in such a case it is impossible to put all of the electrons into a series of phase bunches. As this is one of the main conditions for further trapping, we have developed a special technique for the beginning wiggler fields to bring the region of electron bunching into coincidence with the region where the electrons are to get onto the stationary trajectories.

As is shown in Ref. [6], the FEL configuration with a reversed guide field is very stable with regard to a nonadiabatic wiggler field increase. Moreover this configuration has proven to be effective even under a sharp (step-like) increase of the wiggler field. Therefore, all further calculations will be carried out for an FEL with a reversed guide field.

The wiggler field is increased up to a value which is several percent larger than nominal (corresponding to the point of precise synchronism), then it drops to slightly less than the nominal value. The basis for this idea is the fact that it is necessary to slow electrons which enter in the accelerating electromagnetic wave half-period, providing that electrons which enter in the decelerating phase have no time to get out of synchronism with the electromagnetic wave.

Computer simulations based on Eqs. (2) have verified this idea. In Fig. 1 the dependence of the wiggler field

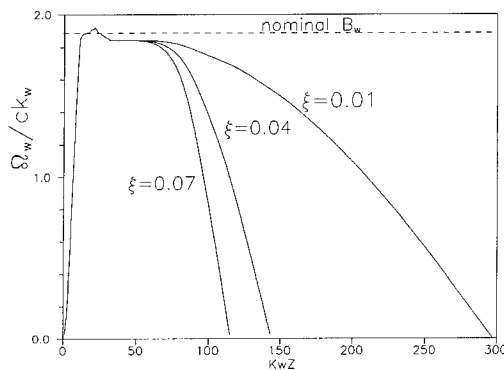


Fig. 1. Optimized wiggler field vs distance along the interaction region for different magnitudes of the parameter  $\xi$ .

versus the normalized longitudinal coordinate  $z$  is shown and in Fig. 2 the corresponding phase trajectories of the electrons are shown. As one can see, under such wiggler field tapering, a series of phase bunches with a width of order  $\pi$  and separated by  $2\pi$  has been created. Of special note is the fact that all electrons in the initially unmodulated beam are used, in contrast to the traditional bunching technique. The principal feature of this technique is that the electrons which initially were within  $0 \cdots 2\pi$  phase limits participate in bunch creation in the neighboring periods ( $+2\pi$  or  $-2\pi$ ), thus they all can contribute positively to the total FEL efficiency.

### 5. Results of computer simulation and conclusion

Let us apply the theory outlined above to the investigation of the nonlinear regime of an FEL with the following parameters: electron beam energy  $\varepsilon = 1.88$  MeV, which corresponds to  $\gamma = 4.75$ , guide magnetic field  $B_0 = -1.4$  kG, nominal value of wiggler field  $B_w = 2.8$  kG, spatial period of wiggler field  $\lambda_w = 7.2$  cm, and electromagnetic wave wavelength  $\lambda = 6.2$  mm. As above, we restrict ourselves to the case of wiggler field tapering. Particle simulation based on Eqs. (1) was used to model FEL operation. It should be noted that choosing the point for the beginning of the tapering is of great importance. In the present case it is started right after the region of bunching, since the electron bunch is not required to be compact.

To achieve an optimal tapering regime Eq. (12) was added to system (1). As  $\xi$  is not known in advance, for the optimal tapering rule it is searched selectively within the limits mentioned above. In Figs. 1 and 3 the dependences of the wiggler field and FEL efficiency versus  $z$  for different  $\xi$  are presented. One can see that an optimal tapering rule corresponding to  $\xi = 0.01$  appears to be nearly linear, giving an FEL efficiency of 55%. The interaction region increases but is still appropriate for

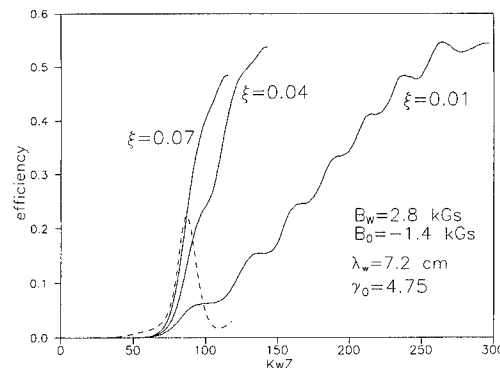


Fig. 3. FEL efficiency vs distance along the interaction region for different magnitudes of the parameter  $\xi$ , and for a non-tapered wiggler (dashed line),  $\alpha_s(0) = 0.02$ .

experimental realization. It can be seen from Fig. 2 that all of the electrons form phase bunches and participate in the energy exchange with the electromagnetic wave. The phase width of the bunch is about  $\pi$  along the entire interaction region.

In this paper an investigation of FEL efficiency optimization based on electron bunch trapping by the electromagnetic field is presented. To achieve 100% electron beam bunching, a special technique (specified by computer simulation) was proposed involving a wiggler field increase at the beginning of the interaction region. Using Lyapunov theory of motion stability, criteria for bunch trapping are obtained which result in an optimal wiggler field tapering rule. Computer simulation by the particle technique substantiates the assumption that for a derivation of electron bunch trapping criteria high-frequency modulation of electron transverse velocities can be ignored. The efficiency obtained for a millimeter wave FEL is 55%, reasonably close to the maximum value allowed in principle by the fundamental FEL mechanism in this particular case.

### References

- [1] T.J. Orzechowski, B.R. Anderson et al., Phys. Rev. Lett. 57 (1986) 2172.
- [2] A.A. Kaminsky, A.K. Kaminsky et al., Proc. 14th Int. Conf. on High Energy Accelerators, part 5, Tsukuba, Japan, 1989, p. 1879.
- [3] E.D. Belyavskiy, Radiotekhnika i elektronika 16 (1971) 208, in Russian.
- [4] N.S. Ginzburg and N.Yu. Peskov, J. Techn. Phys. 58 (1988) 859, in Russian.
- [5] E.A. Barbashin, Introduction to Stability Theory (Nauka, Moscow, 1967) 224 pp., in Russian.
- [6] A.A. Silivra and I.A. Goncharov, these Proceedings (16th Int. Free Electron Laser Conf., Stanford, CA, USA, 1994) Nucl. Instr. and Meth. A 358 (1995) 452.

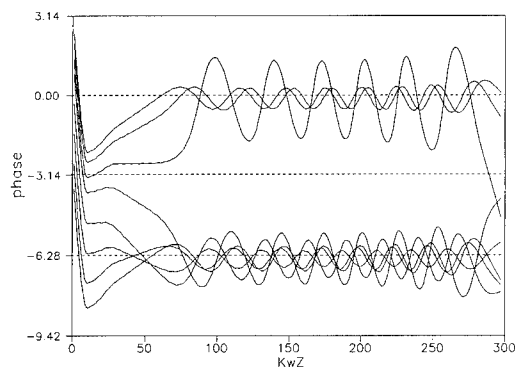


Fig. 2. Electron phase trajectories vs distance along the interaction region.



ELSEVIER

# 1-D free-electron laser model without the slowly-varying approximation

Chang-Bae Kim<sup>a,\*</sup>, Yong-Woong Uhm<sup>a</sup>, Jae-Koo Lee<sup>b</sup>

<sup>a</sup> Physics Department, Soong Sil University, Seoul, 156-743, South Korea

<sup>b</sup> Physics Department, POSTECH, Pohang 790-600, South Korea

## Abstract

A free-electron laser amplifier in the strong pump regime is studied without the slowly-varying envelope approximation (SVEA). A one-dimensional time-dependent code is used for numerical simulation of the evolution of the electron energy, the synchrotron phase of the electrons and the electric field of the laser. Electron-laser-facility-like parameters are used for the strong pump regime. Since the cooperation length is much smaller than the electron beam length, a steady-state solution is found to exist. Comparisons are made with the earlier results with the SVEA and the difference turns out to be negligible. It can be concluded that the SVEA can be applied to a wider class of problems than it sets out to be appropriate for.

## 1. Introduction

In this work, we study the temporal and spatial behavior of the free-electron laser (FEL) in the amplifier configuration without the so-called slowly-varying envelope approximation (SVEA).

An FEL is a device that generates coherent radiation out of incoherent radiation emitted by electrons wiggling under a periodically-varying external magnetic field (magnetic undulator) through the bunching of the electron beam by the radiation field [1]. A dimensional model of the FEL has been proven successful in reproducing many of the experimentally observed phenomena – for example, super-radiance [2–4] and super-radiant spikes [5–7]. It also predicts chaotic behaviors — transition from limit-cycle oscillations to chaos, quasi-periodicity and intermittency [8,9]. In previous works, the SVEA was applied to both analytical and the numerical studies [9,10]. The SVEA is valid when both the laser field amplitude and the laser phase change over length and time scales that are much longer than the laser wavelength and the laser frequency, respectively. As is pointed out in earlier works that used the SVEA, the results seem to indicate that the SVEA may not be an appropriate approximation since the laser amplitude and the phase change so rapidly as to violate the criterion for the SVEA. This observation motivates the work without the SVEA [11].

## 2. Model

The FEL model consists of a set of three equations: One, for the evolution of the electron energy through the interaction between the electron and the electric field of the laser; another, for the synchrotron (or ponderomotive) phase of the electron due to the changing axial velocity of the electron; the past, the electromagnetic wave equation with a current source arising from the electron motion. Space-charge effects are neglected because the plasma-oscillation frequency is much smaller than the laser frequency. The advantage of the SVEA is that it reduces the wave equation to a first-order differential equation instead of second order which is easier to handle. The equations are

$$\frac{d}{dt}\gamma = -\frac{a_w(z)E_y(z, t)}{\gamma c}, \quad (1)$$

$$\frac{d}{dt}\psi = c[(k_w + k)\beta_z - k], \quad (2)$$

$$\left(\frac{\partial}{\partial t} + c\frac{\partial}{\partial z}\right)f^+ = -F_b\left(\frac{\omega_p^2}{\gamma c}\right)a_w(z), \quad (3)$$

and

$$\left(\frac{\partial}{\partial t} - c\frac{\partial}{\partial z}\right)f^- = -F_b\left(\frac{\omega_p^2}{\gamma c}\right)a_w(z). \quad (4)$$

In Eqs. (1)–(4),  $\gamma$  is the relativistic factor,  $z$  is the coordinate along the wiggler axis,  $c$  is the speed of light,  $a_w(z) = a_{w0} \sin k_w z$  is the wiggler vector potential in the

\* Corresponding author. Tel. +82 2 820 0426, fax +82 2 824 4383, e-mail cbkim@plasma.soongsil.ac.kr.

y direction,  $E_y$  is the electric field of the radiation along the y direction,  $\psi \doteq (k_w + k)z - \omega t$  is the synchrotron phase,  $k_w$  and  $k$  are the wave numbers of the wiggler and the radiation  $k = \omega/c$ ,  $\beta_x$  is the ratio of the electron velocity to the speed of light,  $F_0$  is the filling factor simulating the three dimensional effect [10], and  $\omega_p$  the frequency of the plasma oscillation. In addition, we define

$$\frac{d}{dt} \doteq \frac{\partial}{\partial t} + v_z \frac{\partial}{\partial z}, \quad (5)$$

and

$$f^\pm \doteq B_x \mp E_y/c, \quad (6)$$

where  $B_x$  is the magnetic field of the radiation in the x direction. Here,  $a_w$ ,  $E_y$  and  $B_x$  are normalized by  $e/mc$ . In the SVEA,  $f^- \approx 0$  and  $f^+ \approx -(2/c)E_y$  and one ends up with three equations (1)–(3).

In order to obtain the amplitude and the phase of the electric field it is convenient to introduce the complex fields  $\tilde{f}^\pm$  such that  $f^\pm = \mathcal{T}\tilde{f}^\pm$ . By separating the complex field into two parts  $\tilde{f}^\pm \doteq \tilde{g}^\pm e^{i(kz - \omega t)}$  one can find the amplitude and the phase from  $\tilde{g}^\pm$  by averaging over the electrons. In numerically integrating Eqs. (1)–(4) we do the following [12]: As electrons advance by one step size  $\Delta z$  along the axis,  $g^+$  slips ahead while  $g^-$  slips behind, both by the length  $(\lambda/\lambda_w)\Delta z$  that is the same as the mesh size with which the electron beam is finite-differenced. At each mesh point a finite number of electrons is distributed. The input for the  $f^\pm$  is  $f^+ = -2ka_0 \cos(kz - \omega t + \phi)$  and  $f^- = 0$ . As Tsui points out [10], for strong pumping  $a_{w0}$  larger than 1 it is appropriate to use  $\gamma^2 = (1 + a_{w0}^2)/(1 - \beta_z^2)$  to express  $\beta_z$  in terms of  $\gamma$ .

The input parameters for the simulations are [10]: All the electrons have equal energy with  $\gamma = 6.8$  (3.1 MeV),  $a_{w0} = 3$  ( $B_w = 3.2$  kG),  $\lambda = 0.87$  cm,  $\lambda_w = 9.8$  cm, wiggler length  $L_w = 30\lambda_w$ , beam current 850 A, beam cross sectional area  $0.64$  cm<sup>2</sup>, the plasma frequency  $\omega_p = 3 \times 10^{10}$  rad/s, the filling factor  $F_b = 0.2$  and the input microwave power 50 kW (i.e.,  $a_0 = 1.47 \times 10^{-3}$ ). It is found that ten electrons at each mesh point is sufficient for our purpose.

### 3. Results

The electron energy  $\gamma$  and the gain  $G = 10 \log(E_{y0}^2/E_0^2)$  in two typical cases with and without the SVEA are plotted in Figs. 1 and 2. Here,  $E_{y0}$  is the amplitude of the electric field and  $E_0$  is the input amplitude. In Fig. 1, the beam size  $L_b = 6\lambda$  and, in Fig. 2,  $L_b = 30\lambda$ . In both cases, the results are taken at ten periods into the wiggler. Hence, one can conclude that although the SVEA does introduce detailed differences in the results

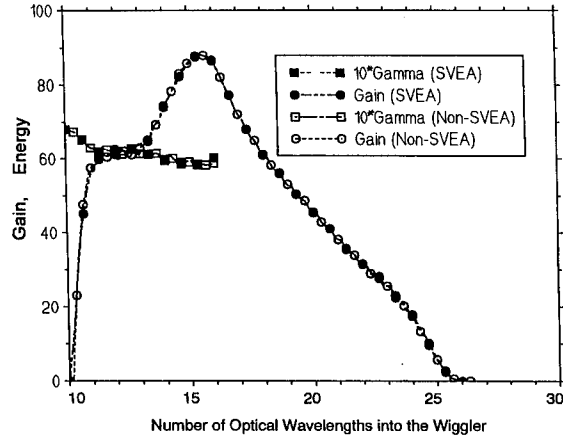


Fig. 1. Gain profile and electron energy at ten wiggler periods into the wiggler: Beam size  $L_b = 6\lambda$ ; open marks for the results without the SVEA and the filled marks for the case with the SVEA; circles for the gain and the squares for  $10\gamma$ ; the unit of the horizontal axis is the radiation wavelength  $\lambda$ .

obtained without the SVEA, the results with the SVEA do behave the same on the average as the non-SVEA results. It is, thus, expected that with the SVEA the global quantities such as the total power and the average efficiency are not far off from the values without the SVEA. It is yet to be worked out whether the same conclusion can be reached in the case of an oscillator configuration because the backward part of the field has more opportunities to interact with the electrons inside the resonator. Work in this direction is in progress and will be presented elsewhere.

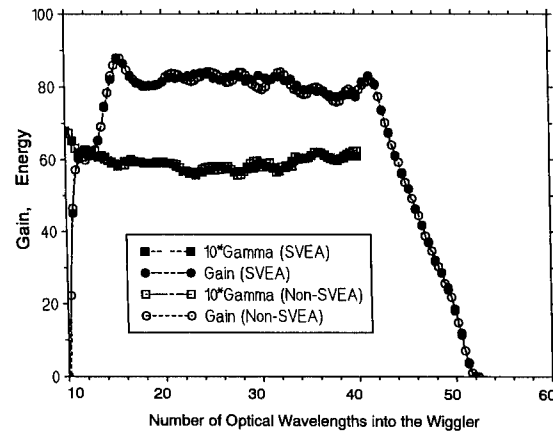


Fig. 2. The same caption as in Fig. 1 except that the beam size  $L_b = 30\lambda$ .

### Acknowledgement

The authors are grateful for Dr. Sang June Hahn for sharing his computer code that forms the basis of the present code.

### References

- [1] C.A. Brau, Free-Electron Lasers (Academic Press, Boston, USA, 1990).
- [2] R. Bonifacio and F. Casagrande, Nucl. Instr. and Meth. A 239 (1985) 36.
- [3] S.Y. Cai, J. Cao and A. Bhattacharjee, Phys. Rev. A 42 (1990) 4120.
- [4] R.M. Caloi, Phys. Rev. A 46 (1992) 7934.
- [5] S.Y. Cai and A. Bhattacharjee, Phys. Rev. A 43 (1991) 6934.
- [6] R.W. Warren, J.C. Goldstein and B.E. Newnam, Nucl. Instr. and Meth. A 250 (1986) 19.
- [7] B.A. Richman, J.M. Madey and E. Szarmes, Phys. Rev. Lett. 63 (1989) 1682.
- [8] T.M. Antonsen, in: Nonlinear Dynamics and Particle Acceleration, eds. Y.H. Ichikawa and T. Tajima (AIP Conf. Proc. No. 230, New York, 1991) p. 106.
- [9] S.H. Hahn, thesis, Pohang Institute of Science and Technology (1993).
- [10] K.H. Tsui, Phys. Fluids B 5 (1993) 3808.
- [11] E.H. Haselhoff, thesis (Aspects of a Compton Free-Electron Laser), Universiteit Twente (1993).
- [12] R. Bonifacio, B.W.J. McNeil and P. Pierini, Phys. Rev. A 40 (1989) 4467.



# A computer model of the energy–current loss instabilities in a recirculating accelerator system <sup>☆</sup>

J.A. Edighoffer, K.-J. Kim <sup>\*</sup>

*Center for Beam Physics, Lawrence Berkeley Laboratory, Berkeley, California, USA*

## Abstract

The computer program called ESRA (energy stability in a recirculating accelerator FELs) has been written to model bunches of particles in longitudinal phase space traversing a recirculating accelerator and the associated rf changes and aperture current losses. This code addresses stability issues and determines the transport, noise, feedback and other parameters for which these FEL systems are stable or unstable.

A representative system is modeled, the Novosibirsk high power FEL race-track microtron for photochemical research. The system is stable with prudent choice of parameters.

## 1. Introduction

The computer program called ESRA (energy stability in a recirculating accelerator FEL) has been written to address the energy-current loss instabilities in recirculating accelerators, in particular, when free electron lasers (FELs) are present. This energy-current loss instability was first seen by Los Alamos's FEL group [1,2] in their energy recovery experiments. The Novosibirsk high power FEL race-track microtron for photochemical research is a 100 kW class laser using recirculation and energy recovery [3,4]. NASA is interested in a upgraded version of the Novosibirsk FEL to provide 1–10 MW for satellite power beaming. The Japanese at Jaeri FEL laboratory are building a superconducting recirculating FEL. CEBAF is building a one loop IR FEL and is proposing to build a two loop UV FEL [5], both with energy recovery. All of these systems could be subject to this possible instability.

This instability arises from fluctuations in energy which cause current loss changes on apertures, which cause rf field changes which cause further energy changes and so on. As there are large average currents flowing around the system, these changes are very important. The FEL adds an additional complication in that it adds energy spread to the beam, equal to roughly twice its extraction efficiency.

At the dump, this fractional energy spread is multiplied by the ratio of the beam energy at the FEL to that at the dump, if no longitudinal phase space rotation takes place. A few percent energy spread at the FEL can then be a very large, relative energy spread at the dump, even with longitudinal phase space rotation. Avoiding very nearly all current loss is essential to be able to operate reliably.

This code addresses these stability issues and determines the transport, noise, feedback and other parameters for which these FEL systems are stable or unstable.

## 2. Methodology

Bunches are launched periodically from an injector, accelerated through multiple acceleration passes, interact with apertures and the FEL <sup>1</sup> and then decelerate <sup>2</sup> through the same path as the acceleration loops. Each bunch consists of a collections of beamlets, each of which is described by a point in energy and phase (time). Each beamlet has a charge, as well, which can be partially or totally clipped by the apertures. Each beamlet has the beta function and emittance of the whole beam. The beamlets thus are four dimensional transverse phase space objects represented by a point in longitudinal phase space, the sum of which is the six dimensional bunch.

The rf interaction consists of the beamlets each individually interacting with the field. The beamlets remove energy, change the rf phase and receive acceleration based

<sup>☆</sup> This work was supported by the Director, Office of Energy Research, Office of Basic Energy Sciences, Material Sciences Division, of the Department of Energy under Contract No. DE-AC03-76SF00098.

<sup>\*</sup> Corresponding author. Tel. +1 510 486 7224, fax +1 510 486 7981, e-mail kwangje@lbl.gov.

<sup>1</sup> The FEL can exist in any or all the loops, or none.

<sup>2</sup> The beam can be dumped without energy recovery if desired.

on their individual phases and charges. The code includes no HOM wakefields or space charge effects at this time. The calculation compresses the accelerator structure to its center; that is, the fields and particle energies are updated only when a bunch crosses this midplane position.

The rf feedback starts with the sampling of the accelerator amplitude and phase. These samples are then filtered with RC filters, followed by a propagation delay time. The feedback gain is multiplied in and the drive(klystron) power and phase is calculated at the input to the accelerator structures. The power changes are further filtered by the  $Q$  of the drive system (the klystron output cavity  $Q$ ). The in-phase and out-of-phase components are calculated and the cavity fields are updated based on the input coupling factor,  $\beta$ , and accelerator fields. The reflected power and phase are also calculated. This is updated once every rf cycle.

An accelerator tuneshift phase is also added each rf cycle. This is very important in the cases where the beam is accelerated and decelerated off the rf peak, as this leads to a large current driven phase shift unless there is a compensating accelerator tuneshift. This is because the stable phases for acceleration and deceleration are not  $180^\circ$  apart, but  $180^\circ$  minus twice the acceleration phase shift from the crest. For this reason, there is also a feedback loop that adjusts the tune of the accelerator in order to zero the average phase shift of the phase feedback loop. This loop takes the phase control signal, filters it with another longer time constant, correcting the average phase errors by tuning the accelerator frequency. This loop will take out long term current-loss phase loading effects.

The transport includes first and second order temporal dispersion, so beamlets can rotate in longitudinal phase space. The transverse beam properties at the apertures are modeled as though each beamlet of particles had the whole beam emittance, beta function and a Gaussian transverse distribution. This is used to calculate the number of standard deviations (sigmas) to the high and low energy aperture limits for each beamlet as they pass the apertures. Each beamlet position is calculated based on its energy relative to the set point energy for the center of the aperture. These aperture set point energies are based on the ideal trajectories, based on set point rf fields.

The scraping of beam off at the apertures is done in one of two ways. First, the beamlet can pass or not, in an all or nothing way. That is the beamlets charge get set to zero if its centroid hits an aperture. This is the zero emittance limit. This is useful for problems where the dispersion dominates the emittance at the apertures. Second, using a method which is more accurate and sensitive to emittance, but slower, that calculates the error functions associated with the tails of the Gaussian distribution chopped off by the apertures and removing these fractions of the charge from the beamlet. The beamlet centroid (energy) is changed to the new mean energy of the remaining distribution. The emittance and transverse distribution (Gaussian) remains

unchanged by the clipping on the apertures. If the beam loss is low, as must be the case for practical systems, the immutable transverse distribution should not be an important effect. Also the detailed trajectories are not followed, the beam size is simply calculated by the local beta function and the emittance and centroid position is calculated from its energy as each aperture is encountered.

### 3. Detailed description of code implementation

The code is written in Symantec C++ for the Apple Macintosh and Cray C++ for the Cray, with a single source with a single compiler directive to change between machines. The choice of using C++ was made to use object oriented programming (i.e. classes) and dynamic memory allocation. In this version, all of the inputs are in an include file, "init.h", thus requiring the code to be recompiled for each case run. As the compiler is fast this is not a large burden. It is intended when the code stabilizes that the program will be modified to read a separate input file, thus not requiring to be recompiled.

The bunches are generated at the injector position. The injector parameters include the number of beamlets, the bunch energy, the normalized emittance, the energy spread, the energy-spread-profile type, the bunch charge, the bunch repetition rate, the bunch-length, the bunch-length profile type, the gun voltage, and the injector acceleration phase. The profile types include uniform, triangular, parabolic and Gaussian distributions. The widths are 4 RMS for all distributions. In addition, there are injector noise parameters: bunch timing jitter amplitude, bunch energy jitter amplitude, bunch current jitter amplitude, and the primary jitter frequency. On top of the primary jitter frequency, there is added a white noise spectrum to excite all possible instability frequencies.

The accelerator is specified by its frequency, single pass voltage gain at peak phase, rf stored energy, the accelerator  $Q_0$ , the input coupler beta, and the maximum rf drive power at the input coupler. The feedback parameters include the RC time constants for amplitude, phase and tuning; the rf propagation delay; and the rf feedback gain in amplitude and phase. Also, the  $Q$  of the drive system is used to filter the output. The drive noise parameters include the drive amplitude and phase jitter amplitudes, and the primary jitter frequency.

At present, all the various jitter frequencies get reset to the inverse of the transit time from pass 1 to the last pass; that is the system transit time of a bunch. This is likely to be the most sensitive frequency for driving rf instabilities.

Each acceleration pass gets defined in a memory structure (class) which defines that pass and links it to the next pass. The pass parameters include the acceleration phase for the pass, the transit time from the previous pass through the end of this pass (loop transit time), a pointer to a linked list of apertures defined for this pass, the FEL

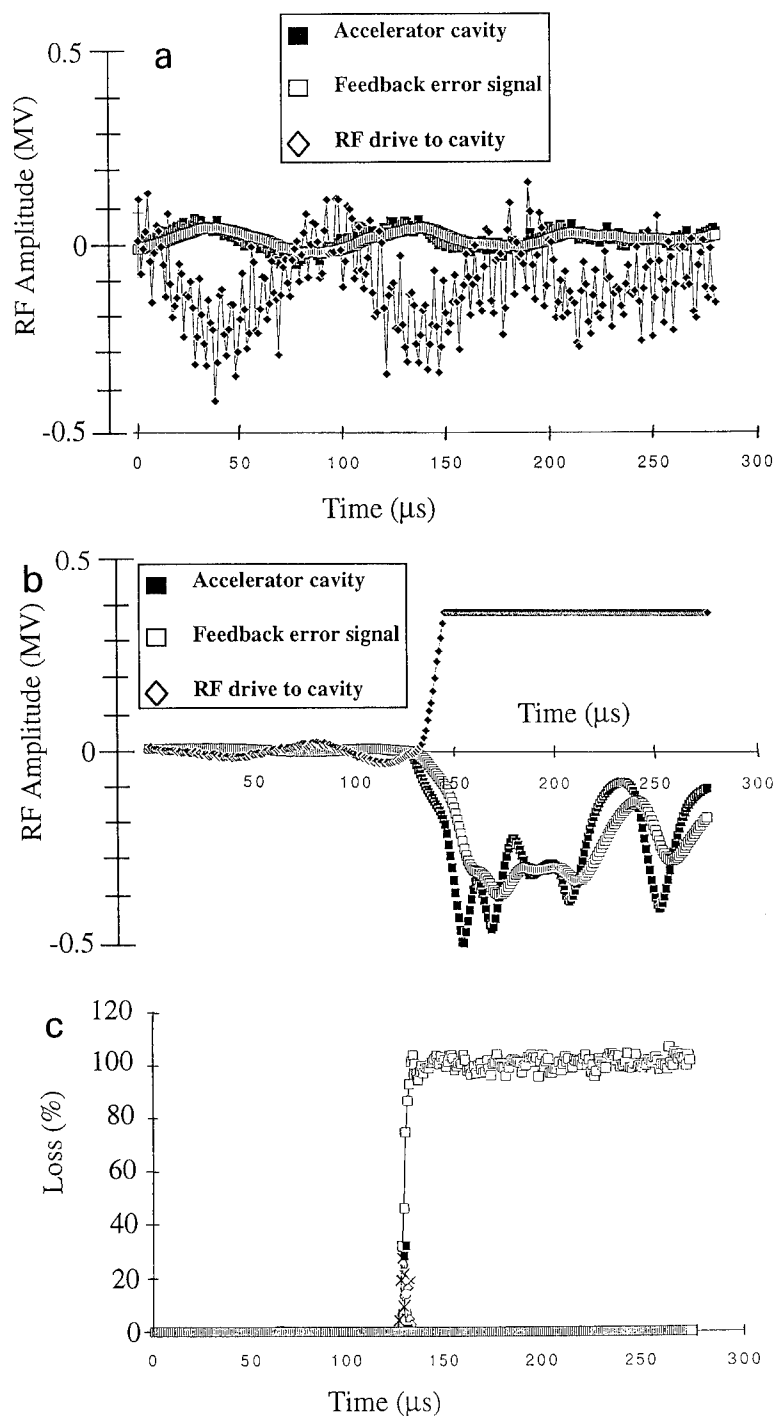


Fig. 1. ESRA results for the Novosibirsk microtron-FEL system. (a) RF amplitude at the accelerating cavity, the feedback error signal, and the RF drive to the cavity. The amplitude of the RF drive is spiky due to the noise. The system is stable. (b) The same as (a) except the current is 1.5 times higher than the design value. The system is unstable. (c) Aperture loss corresponding to the case (b). Various losses in the system cause an energy loss, which in turn causes beam loss at the first bend (shown as the open square) from which the system cannot recover.

efficiency if there is a FEL in this pass, the temporal dispersion around this loop and a pointer to the next pass. Up to four passes are currently enabled (easily expanded if needed). The deceleration loops are added automatically from the acceleration passes, if the deceleration flag is set.

Each aperture is defined in a structure (class) which includes the aperture size, the design (set) energy, the beta function at the aperture, the energy dispersion at the aperture, the position of the aperture from the beginning of the pass, and a pointer to the next aperture in the pass. The position parameter is currently not used. A physical aperture that intercepts more than one pass, would be defined separately for each pass.

The program main loop is over time in units of one rf period. The loop coding launches bunches from the injector at the injector bunch frequency (forced to be a subharmonically related to the accelerator frequency). It also moves all the bunches in the system forward one rf wavelength and does the rf feedback and accelerator field updates due to the drive power, phase and tunes shift.

If a bunch crosses a pass boundary, that bunch is updated by calculating its clipping on apertures within that pass, the FEL interaction if there is one in that pass, the rf interaction with the accelerator, updating both particles and accelerator fields, and finally updates the bunch pass pointer to the next pass. If the bunch exits the last pass, the bunch is deleted, having arrived at the dump. The bunch memory is dynamically allocated.

First and second order temporal dispersion is calculated for each beamlet once each pass.

There are two options for the FEL interaction. In the first, the FEL interaction consists of decelerating one-half of the beamlets. That is lowering the even numbered beamlet's energy by the full FEL-induced energy spread. A fractional noise component is added to this energy spread as specified in the input. This noise term is filtered by the optical cavity  $Q$ . Then all the particles are accelerated by half the noise-free FEL-induced energy spread in order to account for the reacceleration compensation rf cavity after the FEL, if it is present. At present, there is a cosine dependence on this acceleration, but no beam loading effects on the rf fields. There is second option for implementing the FEL induced energy spread. That is the beamlets are uniformly (randomly) distributed between the two positions just described. Depending on the FEL operation one or the other options may be a better approximation. Also, the induced energy spread and extraction efficiency can be specified separately.

The rf interaction is done by doing a vector sum of the beamlets charge and phase, and using this vector sum to do a vectorized fundamental mode beam loading of the accelerator. That is, the vector charge is multiplied by the accelerator impedance over two and vectorially subtracted from the accelerating field. This can be thought of as the superposition of the original accelerating field with the single pass field generated by the charge in an empty

structure. There is a factor of 2 reduction in the self fields because they involve fields from a single bunch acting on itself, or to satisfy energy conservation, if you prefer. The beamlets are accelerated individually based on their relative phases entering the accelerator. The bunch energy and energy spread are also updated.

To avoid a large startup transient, the beam loading effects on the accelerator fields are suppressed until the first bunch reaches the dump, so that the system is filled with bunches when the beam loading starts.

The rf feedback is done every rf cycle. First, a tunes shift phase change is added to the accelerator phase. The rf feedback then consists of taking the accelerator amplitude and phase errors, and generating updated RC-filtered error voltages. Previous RC filtered error voltages that have been delayed by the rf propagation delay are then used with the specified gains to calculate the drive power and phase. Finally, a drive  $Q$  is used to filter the rf output going to the accelerator input coupler. This power is broken into in-phase and out-of-phase components relative to the accelerator phase. The power dissipated by the accelerator walls is calculated. The net in-phase power into the cavity is calculated, as follows

$$P_{\text{net in phase into accelerator}} = -(1 + \beta)P_W + 2\sqrt{P_{\text{in phase}}\beta P_W},$$

where  $\beta$  is the standard rf input coupler coefficient which is the ratio of the power radiated out of the coupler ( $P_{\text{ext}}$ ) to the power loss in the walls ( $P_W$ ). Then the stored energy and the change in stored energy for one rf cycle are calculated.

$$U_{\text{updated}} = U + \frac{P_{\text{net in phase into accelerator}}}{\text{frequency}_{\text{accelerator}}}.$$

The in phase accelerator amplitude is calculated from the updated stored energy.

$$V_{\text{in phase}} = \sqrt{U_{\text{updated}} R / Q Q_0}.$$

The out phase component is calculated by taking the out of phase drive power and calculating the steady-state voltage limit this drive power would reach, and then using the rf filltime to calculate the fraction achieved in one rf cycle, that is

$$V_{\text{steady state}} = \sqrt{|P_{\text{out of phase}}| \frac{4\beta}{(1 + \beta)^2} R / Q Q_0},$$

$$V_{\text{out of phase}} = V_{\text{steady state}} (1.0 - e^{-(\text{rf period} / \text{RF fill time})}),$$

and the sign of this voltage is determined by the sign of the out of phase power. This is then vectorially added at  $90^\circ$  to the in-phase accelerator fields to get the final accelerator amplitude and phase at the end of this cycle. The tunes shift feedback loop is updated based on the delayed RC filtered phase error signal and the tunes shift's time constant.

Table 1  
Parameters of the Novosibirsk microtron recuperator FEL

|                                   |                  |
|-----------------------------------|------------------|
| <b>Injector</b>                   |                  |
| Energy                            | 2.1 MeV          |
| Emittance                         | $20 \pi$ mm mrad |
| Charge                            | 2.2 nC           |
| Gun voltage                       | 200 kV           |
| Bunch length                      | 9 ps             |
| Energy spread                     | 20%              |
| R56                               | 0.00012552 m/%   |
| Phase                             | $-50^\circ$      |
| <b>Accelerator</b>                |                  |
| Voltage                           | 14 MV            |
| Frequency                         | 181.3 MHz        |
| <b>FEL</b>                        |                  |
| Induced energy spread             | 3.4%             |
| <b>Temporal dispersion factor</b> |                  |
| Loop 1                            | 0.00092976 m/%   |
| Loop 2                            | 0.00139464 m/%   |
| Loop 3                            | 0.00185952 m/%   |
| Loop 4                            | 0.0023244 m/%    |

#### 4. Example: Novosibirsk's microtron recuperator FEL for photochemistry

Table 1 lists some of the key parameters of the FEL system. Assumptions were made about noise levels and the feedback parameters which will vary from actual values. Fig. 1a shows the rf amplitude, feedback signal, and drive at the design current, where the system is stable. Figs. 1b and 1c show data for the system at 1.5 times the design current, where it is unstable.

#### References

- [1] D. Feldman, et al., The Los Alamos free-electron laser energy-recovery experiment, Proc. 1987 Particle Accelerator Conf., Washington, DC, 1987.
- [2] H. Takeda, Transient analysis of coupled accelerator and decelerator system, Proc. 1987 Particle Accelerator Conf. Washington, DC, 1987.
- [3] N.G. Gavrilov et al., Nucl. Instr. and Meth. A 304 (1991) 228.
- [4] H. Bennet et al., Proc. 15th Int. Free Electron Laser Conf., The Hague, The Netherlands, Nucl. Instr. and Meth. A 341 (1994) 124.
- [5] G. Neil et al., NASA Review of the Laser Processing Consortium's Free Electron Laser Program, Mar 8–9, CEBAF, 1994.



ELSEVIER

## POP experiments of the photon–e-beam interaction in the supercavity

M. Fujita <sup>a,\*</sup>, T. Asakuma <sup>c</sup>, J. Chen <sup>a</sup>, K. Imasaki <sup>a</sup>, C. Yamanaka <sup>a</sup>, M. Asakawa <sup>b</sup>,  
N. Inoue <sup>b</sup>, K. Mima <sup>b</sup>, S. Nakai <sup>b</sup>, T. Agari <sup>c</sup>, N. Nakao <sup>c</sup>, A. Moon <sup>c</sup>, N. Ohigashi <sup>c</sup>,  
T. Minamiguchi <sup>d</sup>, Y. Tsunawaki <sup>d</sup>

<sup>a</sup> Institute for Laser Technology, 2-6 Yamada-oka, Suita, Osaka, Japan

<sup>b</sup> Institute of Laser Engineering, Osaka University, 2-6 Yamada-oka, Suita, Osaka, Japan

<sup>c</sup> Kansai University, 3-10-1 Senriyama-higashi, Suita, Osaka, Japan

<sup>d</sup> Osaka Sangyo University, 3-1-1 Daito, Osaka, Japan

### Abstract

Use of the supercavity for photon storage had been proposed to enhance the interaction between lasers and e-beams (Compton scattering). To demonstrate the feasibility of this technology, proof-of-principle (POP) experiments are in progress. A supercavity with  $\sim 99.99\%$  reflectivity mirrors has been constructed to confine the LD-pumped Nd:YAG laser light. The confined photons will be used to interact with 100 kV CW electron beams. It is expected that the interaction will be enhanced by  $10^4$  times, resulting in a scattered photon flux as much as  $2 \times 10^7$  photons  $s^{-1}$   $rad^{-1}$  at the wavelength  $\lambda \sim 0.4$   $\mu m$ .

### 1. Introduction

As a technological application of free electron lasers, we are developing compact high-brightness X-ray/ $\gamma$ -ray sources based on the interaction between photons and electrons. When photons are scattered by relativistic electrons the scattered photon energy is enhanced by a factor of  $2\gamma^2(1 - \cos \theta)$ , where  $\gamma$  is the relativistic factor of the electrons and  $\theta$  is the scattering angle. The scattered photon flux is confined within the angle  $1/\gamma$ . For 10 MeV electrons and 1  $\mu m$  laser light, the energy of the scattered photons is in the X-ray range ( $> 1$  keV) and the flux is confined within 50 mrad. More energetic electrons can be used to generate collimated  $\gamma$ -rays. For a few GeV electrons and 1  $\mu m$  laser light, the energy of the scattered photons exceeds 10 MeV and the  $\gamma$ -ray is confined within 0.5 mrad. Compared to synchrotron radiation from a storage ring, the required energy of the electrons is much lower for the same photon energy. Moreover, it is difficult to produce  $\gamma$ -rays of high brightness even in the large GeV storage rings.

Compton scattering has a great potential in the development of compact X-ray/ $\gamma$ -ray sources. There are, however, several technical issues to be solved, as the cross section of Compton scattering is very small. First, one has to increase the interaction density of photons and electrons.

For this purpose, we have proposed to use a supercavity to enhance the photon density [1]. The supercavity is a Fabry–Perot cavity with ultra high reflectivity mirrors ( $R > 99.99\%$ ) [2]. As the light inside the supercavity can go back and forth thousands times, photons can be accumulated. The intracavity power is roughly enhanced by a factor of  $(1 - R)^{-1}$ . Moreover, supercavities can be connected in series to multiply the interaction, as the transmission of the supercavity is nearly unity. Second, the photon and electron sources must be optimized to improve the duty factor of the interaction. For high average brightness radiation sources, a combination of CW laser system and CW electron accelerator or storage ring is preferable. On the contrary, a combination of pulsed laser and short electron bunches from an rf linac is suitable for high peak brightness sources.

To demonstrate the feasibility of enhanced Compton scattering, we started proof-of-principle (POP) experiments. A 100 kV CW electron gun and a supercavity with  $\sim 99.99\%$  reflectivity mirrors for 1.06  $\mu m$  laser light have been prepared. The photons are scattered by the 100 kV electrons at an angle of  $150^\circ$ . The scattered photon wavelength is in the visible range ( $\lambda \sim 0.4$   $\mu m$ ). With  $10^4$  enhancement by the supercavity, the photon flux will be as much as  $2 \times 10^7$  photons  $s^{-1}$   $rad^{-1}$ .

### 2. Laser heated 100 kV electron gun

To provide 100 kV electrons for the POP experiments, a Pierce-type electron gun was designed using the EGUN

\* Corresponding author. Tel. +81 6 879 8732, fax +81 6 877 4799.

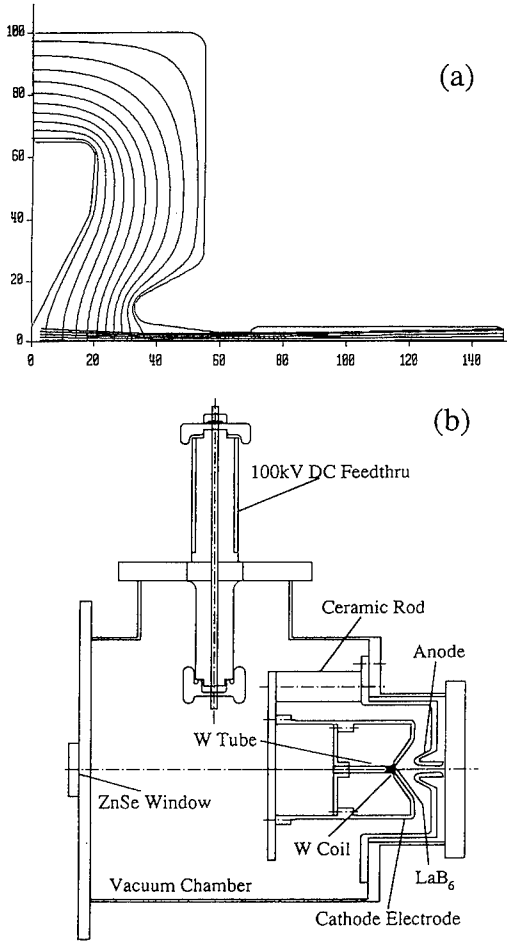


Fig. 1. (a) Numerical predictions of the EGUN code. Gun properties shown are shape of electrode, rays, and equipotential lines. (b) A schematic cross section of the 100 kV electron gun.

code [3]. Fig. 1a shows the gun geometry rays, and electrostatic equipotential lines. Fig. 1b shows an overall schematic view of the electron gun. The vacuum vessel is placed at ground potential for safe operation. The cathode and focusing electrode are placed at high potential and supported by three ceramic rods. There is no electrical heating system. Instead, the 3 mm-thick LaB<sub>6</sub> cathode is heated by a CW CO<sub>2</sub> laser beam to obtain thermionic emission. The back of the LaB<sub>6</sub> is covered by a carbon cap for efficient heating.

Fig. 2 shows the measured cathode temperature as a function of laser power on the cathode. The solid line shows the least square fitting of the data. We assumed that blackbody radiation loss is dominant and that absorbed laser power balances the radiation loss at equilibrium. Assuming all the laser power is absorbed at the cathode surface,

$$P + \alpha = A \varepsilon \sigma (T + \beta)^4, \quad (1)$$

where  $P$  is the laser power on the cathode in W,  $A$  is the effective surface area of the cathode in cm<sup>2</sup>,  $\varepsilon$  is the surface emissivity,  $\sigma$  is the Stefan–Boltzmann constant ( $= 5.6697 \times 10^{-12}$  W cm<sup>2</sup> K<sup>4</sup>),  $T$  is the cathode temperature in K, and  $\alpha$  and  $\beta$  represent systematic errors in the measurement. The least square fitting gave  $A \varepsilon \sigma \sim 7.0 \times 10^{-12}$ ,  $\alpha \sim 1.1$ , and  $\beta \sim 46$ . Assuming  $\varepsilon \sim 0.5$ , the effective surface area is 2.5 cm<sup>2</sup>, which is almost the same as the actual cathode surface area. The values of  $\alpha$  and  $\beta$  can be explained by detector calibration uncertainties. From the fitted curve, we obtain an operating temperature of 1200°C with a laser power of 40 W. The Richardson–Dushman law without the Schottky effect predicted a current density and total current of 0.1 A/cm<sup>2</sup> and 0.8 A for 1200°C (cathode surface area = 0.78 cm<sup>2</sup>).

### 3. Photon storage

For efficient photon storage, we optimized the parameters of the supercavity. Since the supercavity is an optical resonator, it has to satisfy the stability condition; [4]

$$0 < (1 - d/r_1)(1 - d/r_2) < 1, \quad (2)$$

where  $d$  is the cavity length and  $r_{1,2}$  is the curvature of the mirrors. To inject the laser light into the cavity, the curvature of the laser wave front has to match the curvature of the input mirror of the supercavity. Assuming the ideal Gaussian beam, the mode matching transformation by a thin lens is given by

$$(d_1 - f)(d_2 - f) = f^2 - f_0^2, \quad (3)$$

where  $f_0$  is  $\pi w_1 w_2 / \lambda$ ,  $\lambda$  is the laser wavelength,  $w_{1,2}$  are the beam radius at a distance  $d_{1,2}$  from the lens. Once the appropriate  $f$  ( $> f_0$ ) is chosen, the distance  $d_{1,2}$  has to be adjusted to satisfy the formula

$$d_1 = f \pm (w_1/w_2)(f^2 - f_0^2)^{1/2}, \quad (4a)$$

$$d_2 = f \pm (w_2/w_1)(f^2 - f_0^2)^{1/2}. \quad (4b)$$

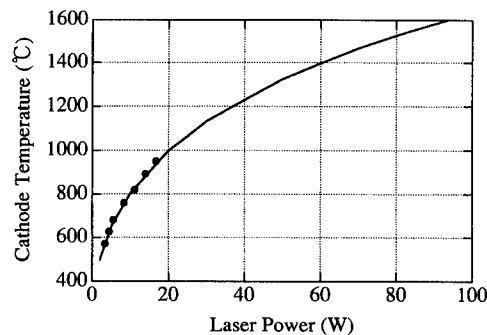


Fig. 2. The measured cathode temperature as a function of the laser power on the cathode. The solid line shows the least squares fitting of the experimental data.

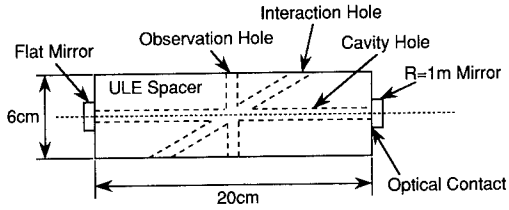


Fig. 3. A schematic of the supercavity.

The reflectivity of the mirrors ( $R_{1,2}$ ) and the cavity length  $d$  define the required spectral width of the laser light to be accumulated. Assuming  $R_1 = R_2 = R$ ,

$$\Delta f = (c/\pi d)(1 - R)2R^{1/2}, \quad (5)$$

where  $\Delta f$  is the acceptable spectral width of the supercavity, and  $c$  is the speed of light.

For photon storage in the supercavity, the loss  $A$  of the mirrors is also important. The internal cavity power  $P_i$  is given by

$$P_i = T/(1 - R)^2 P_0, \quad (6)$$

where  $T$  is the transmittance of the mirror,  $R + T + A = 1$ , and  $P_0$  is the input laser power. For fixed reflectivity, performance of the supercavity depends on the ratio  $T/A$ . The mirror reflectivity can be measured by the cavity decay time  $\tau$ ; [2]

$$\tau = (d/c)/(1 - R), \quad (7)$$

and the mirror transmittance  $T$  and loss  $A$  can be estimated by the cavity throughput ratio  $\eta_i$ ;

$$\eta_i = (1 + A/T)^{-2}. \quad (8)$$

Our supercavity, shown in Fig. 3, was assembled by Research Electro-Optics (Boulder, CO, USA). Mirror reflectivity and throughput of the supercavity is 0.99996 and 35% respectively for  $1.064 \mu\text{m}$ . The Finesse of the cavity is 75 000 and the acceptable spectral width is 10 kHz. The power enhancement factor is calculated to be  $1.5 \times 10^4$ .

There are strict requirements for the laser light stored in the supercavity. In the case of CW photon storage, the

laser must be narrow band single mode (transverse and longitudinal). Since the laser light is reflected back and forth thousands times in the cavity and must maintain coherence, the laser line should have a long coherent length (narrow spectral width). For these reasons, we chose a diode-pumped solid-state laser, Series 122 (Lightwave). This laser has the monolithic, non-planar, ring resonator (often called as MISER [5]) and the spectral width is less than 5 kHz. The laser frequency can be tuned by either heating the laser crystal for slow scanning, or by applying a stress (by a piezoelectric element) to the crystal for fast scanning. These features are also used to stabilize the laser frequency.

#### 4. Interaction experiments

The purposes of the experiments are 1) to study the effects of e-beam loading in the supercavity, 2) to verify the enhancement of the scattering process in the supercavity, and 3) to demonstrate CW interaction in the supercavity. Fig. 4 shows a schematic of the experimental setup. The narrow band laser light is injected into the supercavity via an optical isolator and an  $f = 1 \text{ m}$  mode matching lens. The reflected power of the laser is monitored by PD1 (photodiode 1). The transmitted light is monitored by PD2 and also by a CCD camera to check the transverse mode. The  $\text{CO}_2$  laser used to heat up the  $\text{LaB}_6$  cathode is focused by a 50 cm spherical mirror. The collision angle between laser and e-beam is  $150^\circ$ . The scattered photon flux is measured by an image intensifier or a photomultiplier, while the electron beam is dumped just after the interaction. The scattered light is dispersed by a prism and/or filtered by a couple of interference filters.

Fig. 5 shows the calculated scattering cross section in  $\text{m}^2/\text{rad}$  and the wavelength of the scattered light as a function of the scattering angle. The solid and dotted line show the case of 100 kV and 70 kV e-beam energy, respectively. Our setup allows observation angles of  $0^\circ$ ,

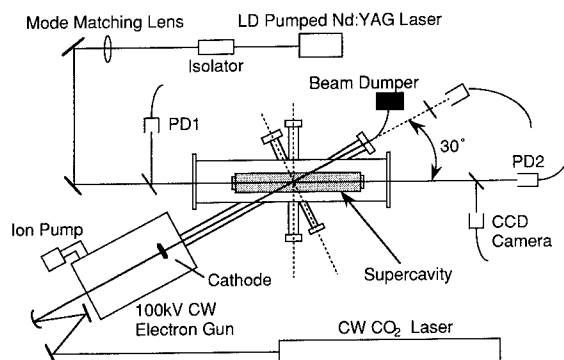


Fig. 4. Experimental setup of the POP experiments.

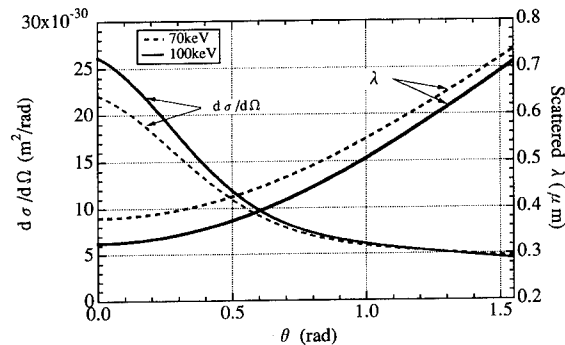


Fig. 5. Calculated scattering cross section and the wavelength of the scattered photons. The solid and dotted lines are the case of  $E_e = 100 \text{ kV}$  and  $70 \text{ kV}$ .



Table 1  
Future strategy of the enhanced Compton scattering radiation source.

| Phase | Mode     | Electron sources                   | Photon sources                                 | Scattered radiation |
|-------|----------|------------------------------------|--|---------------------|
| I     | CW       | 100 kV CW gun                      | 500 mW CW laser<br>+ supercavity               | visible             |
| II    | pulse    | 9 MeV RF linac                     | MW ~ TW modelocked<br>laser + multipass mirror | X-ray               |
| III   | CW       | 6 MeV electrostatic<br>accelerator | 10 W CW laser<br>+ supercavity                 | X-ray               |
| IV    | CW pulse | GeV SR                             | 100 W CW laser<br>+ supercavity                | $\gamma$ -ray       |

30°, and 60° at which the wavelengths of the scattered light are 0.34, 0.37, and 0.5  $\mu\text{m}$ . The photon flux to be observed is estimated by  $N_e (N_p/V)L(d\sigma/d\Omega)$ , where  $N_e$  is the number of electrons in the interaction region,  $(N_p/V)$  is the photon density,  $L$  is the interaction length,  $d\sigma/d\Omega$  is the differential cross section of the scattering. In our case, 1 A current corresponds to  $6.3 \times 10^{18}$  electrons/s, and 5 kW of 1.06  $\mu\text{m}$  laser power in a 20 cm cavity gives  $2.1 \times 10^{14}$  photons/cm<sup>3</sup>, assuming a 0.5 mm beam diameter. At the scattering angle of 0°,  $1.7 \times 10^7$  photons s<sup>-1</sup> rad<sup>-1</sup> can be observed.

## 5. Future strategy

The POP experiments are just the first phase of our future strategy as shown in Table 1. In the next phase, we will demonstrate X-ray generation by enhanced Compton scattering. Using the high-brightness rf linac with a photocathode and using a MW modelocked YAG laser or a TW Ti:Al<sub>2</sub>O<sub>3</sub> laser, pulsed X-ray sources of high brightness will be demonstrated. In this scheme, the multipass optical cavity will be used [6]. The third phase is demonstration of enhanced Compton scattering for industrial applications. For this purpose, a high energy CW electron accelerator and a CW laser with higher output power are necessary. The accelerator technology has been already developed (e.g. at UCSB) [7], while the high power CW laser is under development [8]. Finally, pulsed CW  $\gamma$ -ray sources will be realized using a GeV storage ring and a 100 W CW laser driven supercavity. The  $\gamma$ -ray source will open up a new frontier of high energy physics and industrial applications.

## 6. Conclusions

To demonstrate enhanced Compton scattering by the supercavity, POP experiments are in progress using a 100 kV CW electron gun and a 500 mW narrow band CW laser. The laser heated electron gun is expected to provide 1 A current. A supercavity with finesse of 75 000 is used to accumulate the 1.06  $\mu\text{m}$  CW laser. For an enhancement of  $10^4$ , the photon flux will be  $1.7 \times 10^7$  photons s<sup>-1</sup> rad<sup>-1</sup> at the wavelength of  $\sim 0.4 \mu\text{m}$ . The outcome of these experiments will be used to optimize future X-ray/ $\gamma$ -ray systems.

## Acknowledgement

The authors are grateful to Professor A. Murai for useful discussions.

## References

- [1] J. Chen, K. Imasaki, M. Fujita, C. Yamanaka, M. Asakawa, S. Nakai and T. Asakuma, Nucl. Instr. and Meth. A 341 (1994) 346.
- [2] G. Rempe, R.J. Thompson, H.J. Kimble and R. Lalezari, Opt. Lett. 17 (1992) 363.
- [3] S. Humphries, Jr., Charged Particle Beams (Wiley) p. 279.
- [4] H. Kogelnik and T. Li, Appl. Opt. 5 (1966) 1550.
- [5] T.J. Kane, A.C. Nilsson and R.L. Byer, Opt. Lett. 12 (1987) 175.
- [6] A. Bhowmik, Nucl. Instr. and Meth. A 318 (1992) 858.
- [7] G. Ramian, Nucl. Instr. and Meth. A 318 (1992) 225.
- [8] K. Ueda and N. Uehara, SPIE 1837 (1992) 336.



ELSEVIER

## Problems of autobunching and phase stability for the TBA-driver: calculations and design for a modeling experiment

G.G. Denisov <sup>a,\*</sup>, V.L. Bratman <sup>a</sup>, A.K. Krasnykh <sup>b</sup>, E.A. Perelstein <sup>b</sup>, A.V. Saviolov <sup>a</sup>,  
A.S. Sergeev <sup>a</sup>, A.P. Sumbaev <sup>b</sup>

<sup>a</sup> *Institute of Applied Physics, Russian Academy of Science, 603600, 46 Ulyanov Str., Nizhny Novgorod, Russian Federation*

<sup>b</sup> *Joint Institute for Nuclear Research, Dubna, 141980, Russian Federation*

### Abstract

Problems of stability and phase correlation of the TBA-driver radiation are studied on the basis of nonstationary spatio-temporal equations, applied to the model of discrete driver cells without RF connection between them. The design for the modeling experiment is described.

### 1. Introduction

The two-beam accelerator (TBA) of Sessler [1,2] is one of the most interesting and challenging physical ideas in high-frequency electronics suggested in recent years. According to this idea RF power can be provided for a low current electron linear accelerator with beam energy up to the TeV level by a distributed driver alongside the accelerator. In this driver an electron beam of modest energy (MeV or tens of MeV) and high-current (several kA) moves through an alternating set of generator (FELs, TWTs etc.) and re-accelerator (LIAs, RF-accelerators) sections. The high-current beam transforms the energy of the re-accelerator field into RF radiation with a high power per unit length and this is distributive to the low-current beam accelerator. In this system the state of the high-current beam is maintained constant on average.

Certainly, there are many principle and technological difficulties in realizing an effective TBA-driver. One of the main problems is maintaining the amplitude and especially the phase stability of the radiation. The radiation phase of each generator should be nearly independent of temporal variations of beam parameters, since the phase difference between neighboring generators is to be constant along the whole system. To stabilize the radiation phase and to increase the electronic efficiency it was suggested [1,2] to use the preliminarily bunched beam and generator sections in the form of oscillators with feedback. It is clear that to maintain radiation stability (both in time and along the driver) it is necessary to solve difficult problems of temporal stability of the electron beam and of its reproduction

from one cell to another. The most critical point of the TBA concept is the very short ( $\sim 10$  ns) duration of the high-current electron beam which is a consequences of the RF breakdown condition. It proves to be practically impossible to provide the RF connection between generators separated by a rather large length. Thus the “head” of the electron beam arrives in “empty” (without the RF field) generator sections. During the excitation of a generator the electron bunches belonging to the “head” have an energy loss smaller than subsequent bunches interacting with a saturated field. It means that the very short pulse of the re-accelerating electrical field must be profiled in time. However, even in this case the inevitable errors of the electron energy reproduction can, generally speaking, increase from one cell to another and propagate along the beam.

Developing the concept of the TBA-driver [2], we study the following cardinal problems: the electron-beam reproduction, the stability of electron bunches, the influence of temporal ripples of electron parameters, and the radiation stability along the driver. Our analysis is based on the code [3] which describes the excitation of an oscillator taking direct account of radiation losses (unlike that in Ref. [2]) and arbitrary cavity  $Q$ . From the beginning we study a system of discrete driver cells, each consisting of separated generator and re-accelerator sections. Then we describe the modeling experiment which is supposed to be carried out at the Joint Institute for Nuclear Research.

### 2. Nonstationary equations for a TBA-driver

In Refs. [1,2] it was suggested to use a preliminarily bunched high-current electron beam and oscillators (FELs

\* Corresponding author. Tel. +7 8312 384236, fax +7 8312 362061, e-mail den@appl.nnov.su.

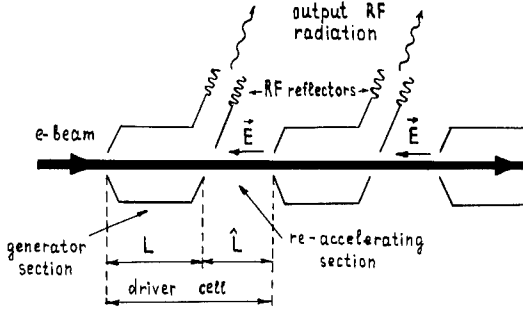


Fig. 1. Scheme of the TBA-driver.

or TWTs) with high- $Q$  cavities as generator parts of the driver cells. The electron-beam bunching makes it possible to get a rather high RF power per one short cell, to avoid the problem of longitudinal-mode competition by means of forcing the radiation frequency, and to improve the output radiation stability due to the decrease in amplitude of electron synchrotron oscillations. The relatively high  $Q$  of the generator cavities keeps constant the wave phase difference between the input and the output of each cell; it provides the definite distribution of the wave phase along the whole driver. Besides, the high- $Q$  systems provide the time stability of the radiation phase at the output of the cell in spite of a rather large temporal ripple of electron parameters (the input energy and the bunch phase) due to both the feedback and the relatively large RF-wave amplitude.

We use the model of discrete cells consisting of alternating generator and re-accelerator sections without RF connections between the cells (Fig. 1). Inside the generator section of each cell we use nonstationary spatio-temporal equations [3–5] for electrons

$$\frac{\partial u}{\partial \zeta} = \text{Im}(a_n e^{i\theta}), \quad \frac{\partial \theta}{\partial \zeta} = u - \Delta, \quad (1)$$

and for the RF field

$$\frac{\partial a_n}{\partial \zeta} + \frac{\partial a_n}{\partial \tau} = 2i\rho, \quad \rho = \langle e^{-i\theta} \rangle_\varphi \quad (2)$$

which can be used both for FEL and for TWT [4]. For an FEL  $u = \mu C^{-1}(1 - \mathcal{E}/\mathcal{E}_0)$  is the normalized energy loss of a particle ( $\mathcal{E} = mc^2\gamma$ ,  $\mathcal{E}_0 = mc^2\gamma_0$ ),  $a_n$  is the normalized amplitude of the RF field at its  $n$ th trip over the generation section space,  $\theta = \omega_s t - h_c z$  is the electron phase with respect to the synchronous combination wave,  $\zeta = h_c C z$  is the normalized coordinate,  $\tau = \omega_s C(t - z/v_{z0})(c/v_{gr} - c/v_{z0})^{-1}$ ,  $\Delta = (\omega_{\text{bunch}}/\omega_s - 1)C^{-1}$  is the mismatch between the frequency of the preliminary electron bunching  $\omega_{\text{bunch}}$  and the frequency of exact synchronism  $\omega_s = v_{z0} h_c(\omega_s)$ ,  $v_{z0}$  is the unperturbed longitudinal electron velocity,  $v_{gr}$  is the RF-wave group velocity at the frequency  $\omega_0$ ,  $c$  is the speed of light,  $C^3 = eI\mu\kappa^2/mc^3N\gamma_0$  is the Pierce amplification parameter,  $I$  is the average

electron current,  $N$  is the wave norm and  $\mu = \gamma_0^{-2}$  and  $\kappa = eA_u/mc^2\gamma_0$ .

The initial conditions for electrons at the input ( $\zeta = 0$ ) of the first cell are as follows:

$$u_{\text{inp}_1} = 0, \quad \theta_{\text{inp}_1} = \varphi, \quad (3)$$

where the phases of electrons  $\varphi$  are distributed uniformly along the bunch  $[0, \Delta\varphi]$  and  $\Delta\varphi$  is the bunch width. Electron energies and phases at the input ( $\zeta = 0$ ) of the  $j$ th generator section (after the re-accelerating field action) are related to the corresponding values at the output ( $\zeta = L$ ) of the  $(j-1)$ th generator by the following expression

$$u_{\text{inp}_j} = u_{\text{out}_{j-1}} - \varepsilon \hat{L}, \quad \theta_{\text{inp}_j} = \theta_{\text{out}_{j-1}} + u_{\text{out}_{j-1}} \hat{L} - \varepsilon \hat{L}^2/2. \quad (4)$$

Here  $L$  and  $\hat{L}$  are the normalized lengths of the generator and re-accelerator sections and  $\varepsilon$  is the normalized re-accelerating electrical field.

The boundary condition for the RF field inside the  $j$ th generator section relates the input field on its  $n$ th trip to the output field on the  $(n-1)$ th trip:

$$a_{n+1}(\zeta = 0, \tau) = R a_n(\zeta = L, \tau - T), \quad (5)$$

where  $R$  is the feedback coefficient and  $T$  is the feedback time (the index  $j$  is omitted for simplicity).

It is clear that to maintain radiation stability along the whole driver we must provide beam reproduction from cell to cell with some accuracy. In principle, like in a continuous system [6] where close RF-phase connection between cells takes place, simulations show that it can be provided using the regime of particle trapping by the RF wave. In a continuous system such a regime is obtained by providing the needed phase of the bunch centers with respect to the RF field  $\theta + \psi$ , where  $\psi = \arg(a)$ ; it has to be close to the field “zero”, where  $\theta + \psi = \pi$ . In this case the RF profile compresses the bunch over electron phases during the electron-wave interaction.

However, the discrete system differs significantly from the continuous one. Since RF connection between the cells is absent, the RF field is excited by the electron beam in each generator section and its phase is imposed by the beam. In this situation one has to provide a definite mismatch  $\Delta$  between the bunch frequency and the frequency of exact synchronism, which depends on the quality of the generator cavities.

### 3. Temporal beam ripple

In the real system the electron beam parameters (the electron energy and the phase difference between the bunches) can vary in time during the beam pulse. Despite this temporal ripple the amplitude and especially the phase of the output radiation of all the cells must be stable in time. Our simulations show that in accordance with the

suggestions [2] stability can be provided by the use of high- $Q$  generator sections.

As an example we have studied numerically the TBA-driver with the following parameters:  $L = 0.5$ ,  $\hat{L} = 0.1$ ,  $R = 0.8$ . The electron bunch size is assumed to be  $\Delta\varphi = 0.1\pi$ . In order to take into account the temporal ripple we use instead of Eq. (3) the following initial condition before the first cell:

$$u_{\text{inp}_i} = U \sin\left(2\pi \frac{\tau}{T_r}\right), \quad \theta_{\text{inp}_i} = \varphi + \Phi \sin\left(2\pi \frac{\tau}{T_r}\right),$$

simulating the ripple by means of a sinusoidal time dependence of both the electron energy and the bunch phase, where the ripple characteristic time  $T_r$  is several times smaller than the feedback time  $T$ . As seen from Fig. 2, where the amplitude and the phase of the output radiation of the first and second generator sections are shown, a rather large energy ripple of the electrons mainly induces ripple of the output amplitude (Fig. 2b). Naturally, the bunch phase ripple proves to have stronger influence on the stability of the output radiation phase than the energy ripple (Fig. 2c). However, even a large ripple of the bunch phase (four times larger than the bunch size) leads to rather small ripple of the output radiation phase (about 0.1 rad).

#### 4. Radiation correlation along the driver

Another problem of the TBA-driver is the radiation correlation along the whole system; the RF power has to be the same at the output of any cell, and the difference between RF phases of neighboring cells has to be constant. To satisfy these requirements it is necessary to keep the electron-beam properties constant. However, this is a difficult problem because different parts of the beam are under different conditions. The beam head arrives in “empty” (without RF field) generator sections, and its electrons lose less energy than other particles, arriving in the excited generator (Fig. 3a). Therefore, the re-accelerating electrical field of any cell must be defined by a temporal-profiled function corresponding to the energy losses of different particles of the beam [2]. However, it is difficult to provide the necessary temporal profile, and errors can result in perturbations of the energy of beam-head particles, both increasing with time and propagating along the electron-beam pulse from the head to the tail. We have investigated this effect neglecting the initial ripple of electron-beam parameters. Approximating the electric field re-accelerating the beam-head particles by means of the simplest linear dependence on time (Fig. 3a), we observe increasing perturbations of the electron energy in the beam head (Fig. 3b). They lead to appearance of the “bad” front of the output RF pulse, which is increased from one cell to another (Fig. 4). At the same time, far from this “bad”

front we obtain the independence of the saturated RF amplitude on the cell number (Fig. 4a) as well as the phase correlation of RF phases of different cells (Fig. 4b).

#### 5. Design for modeling experiment

Using the results of calculations, a driver consisting of an electron buncher and three TBA driver cells, has been designed based on the linear induction accelerator of the

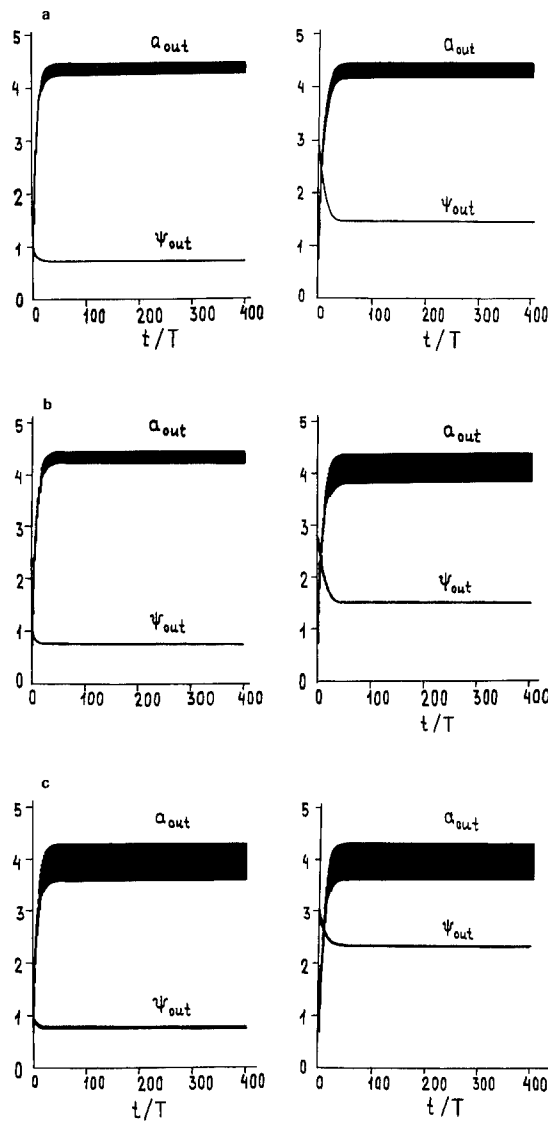


Fig. 2. Amplitude and phase of the RF output radiation after the first and second cells versus time in the presence of input temporal ripples of both the electron energy and the bunch phase. (a) Small ripples  $U = 0.05$ ,  $\Phi = 0.05\pi$ ; (b) large energy and small phase ripples  $U = 0.2$ ,  $\Phi = 0.05\pi$ ; (c) small energy and large phase ripples  $U = 0.05$ ,  $\Phi = 0.2\pi$ .

Joint Institute for Nuclear Research (Dubna). The accelerator provides an electron beam with energy 1.5 MeV, current 1 kA, and pulse duration 60 ns. Unlike the experiment [7], where beam bunching was provided using a choppertron, in the present experiment we are going to use the bunching scheme with a longitudinal electric field and the autophasing principle. The buncher is supposed to be a FEL amplifier capturing particles into “buckets” due to adiabatic change of the coupling coefficient of the traveling wave with electrons along the entire length. The preliminary estimations show that in an amplifier with a gain of about 30 dB, input RF power of about 100 kW and decrease of the coupling coefficient several ten times we could obtain the bunching on the available length of about 60 cm.

An FEL with output power about 150 MW and electronic efficiency about 10% is used as a generator section of each driver cell. The microwave system of each FEL consists of a rectilinear section of oversized rectangular waveguide, a splitter dividing electron and wave beams, wave reflectors, and an output waveguide with a radiator.

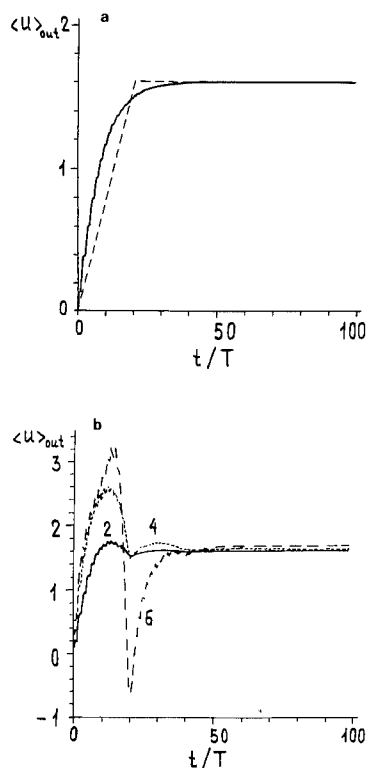


Fig. 3. (a) Averaged losses of the electron energy after the first generator section (solid) versus time and used temporal law of the re-accelerating electrical field (dashed). (b) Averaged losses of the electron energy after the second, fourth, and sixth generator sections versus time.

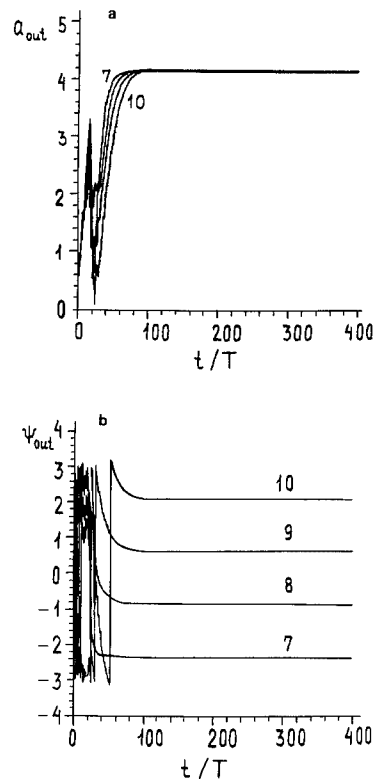


Fig. 4. Amplitude (a) and phase (b) of the RF output radiation after the seventh–tenth cells versus time (input ripples of electron parameters are absent).

$TE_{1,1}$ - or  $TE_{1,3}$ -mode of the rectangular waveguide are chosen as operating ones. Besides, in the present experimental scheme the driver cell includes the re-accelerator section.

## References

- [1] A.M. Sessler, Proc. Workshop on the Laser Acceleration of Particles, eds. C. Joshi and T. Katsouleas, AIP Conf. Proc. 91 (1982) 15.
- [2] A.M. Sessler et al., Nucl. Instr. and Meth. A 306 (1991) 592.
- [3] N.S. Ginzburg and A.S. Sergeev, Z. Tekhn. Fiz. 61 (1991) 133.
- [4] Ya. L. Bogomolov, V.L. Bratman, N.S. Ginzburg, M.I. Petelin and A.D. Yunakovsky, Opt. Commun. 36 (1981) 209.
- [5] T.M. Antonsen, Jr. and B. Levush, Phys. Fluids B 1 (1989) 1097.
- [6] N.S. Ginzburg et al., in: Relativistic High-Frequency Electronics, Issue 5, ed. A.V. Gaponov-Grekhov (IAP RAN, Gorky, 1988) p. 37.
- [7] G. Westenskow, Presented at the 4th Int. Workshop on Linear Colliders, July 1993, BINP, Protvino, Russia.



ELSEVIER

## Status of free electron lasers in 1994

W.B. Colson \*

*Physics Department, Naval Postgraduate School, Monterey, California 93943, USA*

### Abstract

Eighteen years after the first operation of the short wavelength free electron laser (FEL) at Stanford University, there have been many significant accomplishments. FEL research in the infrared, visible, ultraviolet, and X-ray wavelength regimes is discussed.

### 1. Historical perspective

The first sources of powerful coherent radiation were the radar and microwave electron tubes invented earlier this century. Even today, these tubes remain as the most successful and useful sources of coherent radiation, with wavelengths ranging from several meters down to about a millimeter. Electron tubes are known to be inexpensive, compact, reliable, efficient, and powerful. There is some justification for believing that this is the “right” way to generate coherent radiation. A particular microwave tube developed in 1960 by Phillips, called the Ubitron [1], was quite similar to the free electron laser in design and operation. The invention of the open resonator by Schawlow and Townes in 1958 [2] led to the development of the conventional atomic laser. The atomic laser has become successful in many scientific and commercial applications. Several limitations of the conventional laser, such as the lack of continuous tunability and breakdown at high power densities, are due to the use of excited electrons bound to atoms. The goal of the free electron laser (FEL), invented by Madey, is to extend the success of the microwave tube from millimeter to nanometer wavelengths [3–5].

### 2. FEL attributes in 1994

Most FEL attributes have been known for some time, but their status deserves a review in 1994. References and a table of experiments describing the topics found below can be found in these proceedings.

*Continuous tunability:* One of the most important and most often quoted FEL attributes is continuous tunability. The resonance condition depends on the electron velocity component along the undulator axis. At resonance, one wavelength of light passes over an electron as the electron passes through one undulator wavelength. The operating wavelength is typically varied on a slow time-scale by changing the undulator gap to control the undulator field strength and the electron  $z$  velocity, or on a fast time-scale by changing the electron beam energy. FEL facilities like CLIO (France), FOM (The Netherlands), Stanford, Vanderbilt, Duke, and UC Santa Barbara routinely provide tunable radiation to users. At many facilities today, the user can control the FEL wavelength from within his experimental laboratory space. The Stanford FEL controls the operating wavelength by varying the electron beam energy with a feedback system designed to hold the wavelength fixed at a wavelength of the user's choice.

*Reliable operation:* Microwave and RF electron tubes, medical linear accelerators, synchrotron light sources, storage rings and electrostatic accelerators all have proven to be reliable systems. The FEL is based on the same technology and could be expected to have similar reliability. The FEL facilities mentioned above have been providing over 2000 user hours of beam-time per year, limited largely by operating budgets.

*Flexible micropulse and macropulse structure:* The FEL optical pulse structure is determined by the longitudinal micropulse and macropulse structure of the electron beam. An FEL using a recirculating electrostatic accelerator can produce a CW or nearly CW beam for narrow band applications. An FEL driven by a RF linac can take advantage of the mature RF technology of linear accelerators used to manipulate and control the electron beam and thus the optical beam. The micropulses can be injected at frequencies up to the RF frequency. The micropulse length

\* Tel. +1 408 656 2896, fax +1 408 656 2834, e-mail colson@physics.nps.navy.mil.

can also be controlled by as much as a factor of ten over short time-scales. The FEL driven by a linac can produce micropulses which are locked to an external clock with sub-picosecond jitter. The FEL can also operate “simultaneously” at independently controlled wavelengths, providing for multiple color experiments. Similar tricks can be played with chirped micropulses, but on a picosecond time-scale. The longitudinal coherence is generally transform limited, except for FELs with extremely long pulses. In the infrared, the facilities at CLIO and Stanford can now produce micropulses that are less than a picosecond in length.

*Operation in higher harmonics:* If the undulator field is sufficiently strong, the FEL emits radiation in several higher frequency harmonics. Many FELs have a sufficiently strong undulator that there is significant power and gain in the higher harmonics. The gain and coherent emission into higher harmonics has been observed on several experiments. BNL and SLAC propose using higher harmonics to reach short UV or X-ray wavelengths. The APEX FEL at LANL has lased on the 3rd harmonic to produce ultraviolet light using a relatively low energy electron beam.

*Control of fundamental interaction:* The spontaneous emission bandwidth and the gain bandwidth can be as easily controlled in the FEL as in microwave tubes. A tapered undulator can significantly increase extraction efficiency and extend the saturation limit in the FEL by increasing gain in strong optical fields. In the klystron undulator, a dispersive magnet can be introduced in the middle of the undulator to increase gain in weak optical fields. The tapered or klystron undulator are examples of how the FEL undulator can be designed to alter the FEL interaction characteristics. Both have been demonstrated in experiments. About 10 years ago, research on the tapered undulator dominated, but now only the conventional and klystron undulators are being pursued.

*Ideal lasing medium:* The lasing medium of the FEL contains only relativistic electrons, the static undulator magnetic field, and the laser light in vacuum. Energy is “pumped” into the interaction volume at the speed of light, the gain medium cannot be damaged during high power operation, the amplifying medium is transparent to all wavelengths, and the waste heat is removed at the speed of light. The FEL has the potential for high peak power (GWs has been demonstrated), and high average power of several MWs should be possible. This is another advantage that is shared between the FEL and the high-power microwave tube.

*Single transverse mode:* A high density electron beam allows the formation of a single, diffraction limited, transverse optical mode. A fundamental optical mode in the visible with a Rayleigh length of one to a few meters yields an optical mode waist that is just a bit larger than a typical relativistic electric beam. Industrial applications at CEBAF require high beam quality as do long-range mili-

tary and power-beaming applications, such as the SELENE Project at the Naval Air Warfare Center, China Lake, CA.

*Flexible polarization:* The undulator polarization, linear or circular, determines the polarization of the laser light. Both types of FEL have been used successfully. Variable elliptical polarization can be achieved by using a specially designed undulator. This kind of undulator could be useful at a user facility where it may not be possible to use rotating optical components. At present, only the linear and helical undulators are in use.

*Theoretically predictable:* Theory continues to play an important role in the progress of FEL technology and concepts. Agreement between theory and experiment is excellent when the experimental parameters are correctly described. The design of proposed FELs is preceded with extensive analytical and numerical calculations. Since many new FELs proposed in new wavelength ranges would cost tens of millions of dollars, simulations are crucial to the design. The same theoretical formalism works from cm wavelengths to 0.1 nm wavelengths, and only depends on the FEL design, the electron mass  $m$ , the electron charge magnitude  $e$ , and the speed of light  $c$ . Nearly every major FEL laboratory has extensive simulation capability.

### 3. Exciting new directions in 1994

Some of the FEL's attributes have led to particularly exciting new directions. As these proposed directions develop, the next few years may become the most important in FEL history.

*Far-infrared (FIR) wavelength range operation:* Possibly the most significant FEL attribute is that it can be designed to operate in wavelength ranges not accessible by other sources. For wavelengths shorter than 500  $\mu\text{m}$ , there is little competition from microwave tubes, and for wavelengths longer than 10  $\mu\text{m}$ , there is little or no competition from conventional lasers. Several FEL facilities, CLIO, Stanford, Vanderbilt, Duke, UCSB and FOM, can operate in part of this range now, and are expanding their coverage. Most (except UCSB) also provide picosecond pulses for new scientific experiments in this wavelength range.

*Reducing FEL size and cost:* One of the most exciting aspects of the FIR FEL is that it is the lowest cost, smallest size, and lowest risk FEL to build. These critical issues have seriously impaired FEL development over the last 20 years. A FIR FEL is potentially a laboratory device costing under one million dollars and can be a facility that resides in individual departments of a major university, much like an electron microscope. Grumman and LANL are working on small laboratory scale FELs for a facility of this size now. Professor R. Pantell (Stanford) reports that he has just developed a FIR FEL for under 300K dollars that can be built and operated by graduate students. This will provide scientists with an FEL that fits in their own laboratory, and makes FEL research much less expensive.

*UV wavelength range operation:* The FEL in Novosibirsk has already reached a wavelength of 240 nm and other FELs are expected to soon operate below 100 nm. The FEL increases optical brightness and coherence by many orders of magnitude compared to a synchrotron source. The key technology required for the short-wavelength FEL is a high quality electron beam, and the necessary characteristics for UV operation have already been demonstrated. It is not a big stretch for the FEL to reach UV wavelengths. The FEL has a decided advantage at short wavelengths compared to the conventional laser. The FEL electron beam does not spontaneously emit in vacuum, so electrons remain in a given state until the beam enters the undulator. At present, a UV FEL appears to be a large laboratory machine costing tens of millions of dollars, with a reasonably high level of confidence for achieving expected goals. Further research should be used to explore reducing the cost, size, and residual risk of UV FELs. To reach the UV, BNL plans to explore higher harmonics, Duke University will use a high-energy storage ring, and LANL proposes to use a micro-undulator.

*X-ray wavelength range operation:* It has long been realized that the FEL may become the first true X-ray laser. In the 1 nm wavelength range, there are no available mirrors. With no mirrors, self-amplified spontaneous emission (SASE) would be used in a long undulator to develop coherent laser light from spontaneous emission in a single pass through the undulator. A proposal to use part of the SLAC accelerator would achieve about a GW of radiation power in a short pulse of about 200 fs with peak brightness and peak coherent power many orders of magnitude higher than third generation light sources. The electron beam energy would be about 10 GeV with peak beam current of 2500 A to 5000 A. The development of the RF photocathode electron gun, emittance preservation, electron pulse compression techniques, and a long, precise 50 m undulator are key factors in the development. Much of the required electron beam properties have been demonstrated at the Los Alamos National Laboratory and the Stanford Linear Collider. Harmonic emission may be used to reach even shorter wavelengths near 0.1 nm. The increased radiation brightness may result in sample damage that requires innovation by the experimenter. X-ray FEL development should be preceded by significant research in order to reduce risk, and cost.

It is worth mentioning that Vanderbilt plans to use backscattered X-rays from the infrared FEL to generate incoherent 20 keV photons for users. At NRL, a lower energy electron beam and a high peak power laser will be used to demonstrate the fundamental process.

*High-power, efficient operation:* The FEL has the potential for high power operation. The FEL has an advantage over the high power (MW) gyrotron at 1 mm and shorter wavelengths, because of the large interaction volume and the ability to dissipate heat. Since the FEL is based on the same principles as the microwave electron

tube, it has the potential of high efficiency. The FEL wall-plug efficiency is improved by recirculating the electron beam after each pass through the undulator. It has been estimated that the wall-plug efficiency in a superconducting RF FEL with electron beam recovery might reach several tens of percent.

There are several possible applications of a high-average power FEL. FOM (The Netherlands) is building a 1 MW, mm wave FEL for plasma heating and diagnostics. Industrial processing is being explored at CEBAF in collaboration with Dupont and other industrial partners. An FEL has been designed at CEBAF to produce 100 kW of UV power at 350 nm wavelength with a recirculating superconducting linac. A serious effort toward industrial applications is a new direction for FEL development that should prove extremely important.

The U.S. Navy needs to develop a better defense against sea-skimming missiles launched from a nearby shore. One possibility is a MW laser at about 3  $\mu\text{m}$  wavelength which would focus power onto a missile surface to reach, or exceed, 2 kW/cm<sup>2</sup> intensity for a 1 s duration. The engagement would only last about 10 s in order to defend the ship out to a range of about 10 km. This is far less ambitious than the SDIO scenario for missile defense. Boeing, Northrup, LANL, and Rocketdyne are pursuing research programs on high-power FELs for military applications.

The Naval Air Warfare Center (China Lake, CA), NASA, Duke University, the Naval Postgraduate School, and the FEL Group at Novosibirsk, Russia are studying the use of a high-power FEL for powering satellites and other space vehicles.

The Stanford FIREFLY FEL and the LANL Advanced FEL provide opportunities for achieving 1 kW average power demonstrations at relatively low cost. In each case, an existing FEL could be upgraded at a cost of about one million dollars, and would increase the FEL record for high average power from 10 W to 1 kW. This is an important and easily achievable goal for the FEL.

*National Research Council FEL Committee Report:* The National Research Council has been asked by the Department of Energy to study the scientific opportunities presented by FELs and other advanced coherent light sources. The report [6] results were described by the chairman of the committee, Dr. Don Levy, at this Free Electron Laser Conference. The committee's report recommends (i) building a user facility using a FIR FEL with picosecond pulses, (ii) supporting the development of technology for a vacuum ultraviolet FEL, and (iii) supporting the research and development necessary for an X-ray FEL. One of the important goals of this research and development should be to lower the cost of the FELs. In addition, the report states that a variety of communities potentially benefit from the type of research that will be necessary to produce scientifically useful FELs. It also states that the development of FELs is of interest for applications other



than scientific research, for example, industrial, defense, and medical applications. The committee recommendations may lead to a significant national program supporting the development of FELs for scientific applications.

#### Acknowledgements

The author is grateful for support of this work by the Naval Postgraduate School, Stanford University (N00014-91-C-0170), and SURA/CEBAF.

#### References

- [1] R.M. Phillips, IRE Trans. Electron Devices 7 (1960) 231.
- [2] A.L. Schawlow and C.H. Townes, Phys. Rev. 112 (1958) 1940.
- [3] J.M.J. Madey, J. Appl. Phys. 42 (1971) 1906.
- [4] L.R. Elias, W.M. Fairbank, J.M.J. Madey, H.A. Schwettman and T.I. Smith, Phys. Rev. Lett. 36 (1976) 717.
- [5] D.A.G. Deacon, L.R. Elias, J.M.J. Madey, G.J. Ramian, H.A. Schwettman and T.I. Smith, Phys. Rev. Lett. 38 (1977) 892.
- [6] Free Electron Lasers and Other Advanced Sources of Light (National Academy Press, Washington, DC, 1994).



ELSEVIER

## Materials science in the far-IR with electrostatic based FELs

S.J. Allen <sup>a,\*</sup>, K. Craig <sup>a</sup>, B. Galdrikian <sup>a</sup>, J.N. Heyman <sup>a</sup>, J.P. Kaminski <sup>a</sup>, J.S. Scott <sup>a</sup>,  
M.S. Sherwin <sup>a</sup>, K. Unterrainer <sup>a</sup>, M. Wanke <sup>a</sup>, K. Campman <sup>b</sup>, P.F. Hopkins <sup>b</sup>,  
A.C. Gossard <sup>b</sup>, D.H. Chow <sup>c</sup>, M. Lui <sup>c</sup>, T.K. Liu <sup>c</sup>

<sup>a</sup> Center for Free-electron Laser Studies and Physics Department, University of California, Santa Barbara, CA, USA

<sup>b</sup> Materials Department, University of California, Santa Barbara, CA, USA

<sup>c</sup> Hughes Research Laboratories, Malibu, CA, USA

### Abstract

A technology gap exists between  $\sim 100$  GHz and  $\sim 10$  THz. Free-electron lasers (FELs), driven by high quality, relatively low energy electron beams from electrostatic accelerators, and capable of generating kilowatts of coherent, tunable radiation, are ideally suited to explore the enabling science for future technology in this spectral range. We describe two experiments that use terahertz “optical rectification” to measure i) the intensity and temperature dependent energy relaxation in quantum wells and ii) the intrinsic relaxation of resonant tunneling diodes. Both benefit from the power and tunability of the UCSB FELs.

### 1. Introduction

A technology gap exists in the far-infrared, between approximately 100 GHz, the higher frequencies available from commercial electronic sources, and 10 THz or 30  $\mu\text{m}$ , marked by the lower frequency obtained from commercially available diode lasers. Fig. 1 graphically shows the awkward state of far-infrared or terahertz technology by depicting two terminal semiconductor electronics on one hand and laser diodes on the other. At the same time the far-infrared is scientifically rich. Semiconductor nanostructures have quantum and collective resonances in the far-infrared. Linear spectroscopy of these systems has proceeded apace with fixed frequency laser sources and black body sources, but the non-linear dynamics of nanostructured semiconductors has hardly been explored. Free-electron lasers (FELs), driven by high quality, relatively low energy electron beams from electrostatic accelerators, and capable of generating kilowatts of coherent tunable radiation, bridge the gap shown in Fig. 1 and are ideally suited to explore the non-linear dynamics in semiconductor nanostructures. If this scientific research is successful it should make possible new semiconductor technology to fill the gap between microwave electronics and infrared photonics, shown in Fig. 1.

In this review, we first briefly describe the operating

characteristics of the UCSB FELs, currently the only operational and user oriented electrostatic accelerator based FELs. We then focus on two recent experiments that have benefited from the power and tunability of the UCSB FELs. Both use terahertz “optical” rectification and measure i) the intensity and temperature dependent energy relaxation in quantum wells with subband transitions below the longitudinal optic, (LO), phonon [1] and ii) the intrinsic relaxation of resonant diodes [2]. While the UCSB FELs are indispensable to carrying out these experiments, we indicate areas of FEL improvement that could have an impact on these kinds of experiments.

### 2. The UCSB free-electron lasers

Currently there are two fully operational free-electron lasers that are driven by a recirculating electrostatic accelerator (maximum operating voltage of 6 MeV [3]). The millimeter wave FEL operates from 120 GHz to 1 THz while the far-infrared FEL operates from 1 THz to 4.8 THz. A third FEL coming on-line is designed to operate at the third harmonic and generate frequencies as high as 10 THz. The operating FELs produce kilowatts of power in a quasi-CW pulse that can be varied from 1  $\mu\text{s}$  to 10s of  $\mu\text{s}$  depending on the recirculation of the accelerator/electron beam line.

The three UCSB FELs are connected by an electron beam “switch yard” that delivers the beam to the desired FEL. The key to user friendly operation is a computer control system that controls the steering and focusing

\* Corresponding author. Tel. +1 805 893 7134, fax +1 805 893 4170, e-mail allen@sbfel2.physics.uscb.edu.

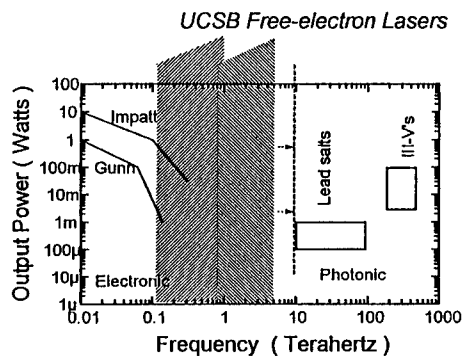


Fig. 1. Two terminal, state-of-the-art, semiconductor electronics reveal a technology gap from 100 GHz to 10 THz. The UCSB free-electron lasers are unique research tools to explore the enabling science for future technology in this spectral range.

magnets. An optical transport system directs the radiation to the user's laboratory by a series of mirrors and TPX lenses in an evacuated pipe and delivers the FEL radiation to any one of 13 different ports. These ports exit onto optical tables supporting a variety of experiments. In the following we describe the results of two experiments that provide a measure of the performance of these FELs "under fire".

### 3. Intersubband relaxation in semiconductor quantum wells

Semiconductor quantum wells are fabricated by growing semiconductor materials, layer by layer, in such a manner that a thin layer of relatively narrow band gap semiconductor is sandwiched between material with a substantially larger bandgap. In this way electrons can be confined to a narrow "quantum well" with quantized states called subbands, which have energy spacings controlled by the well width. These engineered materials are potentially important for sources, detectors and mixers.

While the intersubband relaxation for transition energies that exceed the LO phonon energy are well understood and proceed via LO phonon emission, the parameters that control relaxation when the transition energy is below the LO phonon energy is not well understood. Experimental values vary from nanoseconds to picoseconds [4–9].

To address this problem, Heyman and co-workers [1] fabricated a sample that consisted of a pair of quantum wells coupled by a thin barrier and having slightly different widths. This produced a system that had two states below the LO phonon and which lacked inversion symmetry. The latter introduces an important effect; when the carriers are excited from the ground state to the first excited state, it is accompanied by a finite change in polarization. The essential experiment measured the absorption between the two lowest states, as a function of

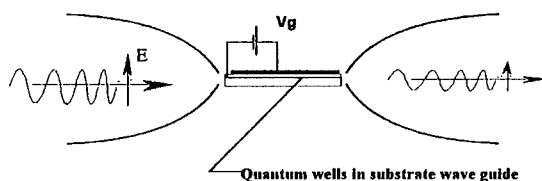


Fig. 2. Radiation from the free-electron lasers is absorbed by the quantum wells in a wave guide defined by the substrate.

FEL laser intensity and sample temperature, and simultaneously, the change in polarization induced by the carrier redistribution.

The experimental geometry is shown in Fig. 2. Radiation is guided in the substrate with the electric vector along the growth direction. A gate electrode on the top of the substrate makes it possible to charge and discharge the quantum wells by controlling the voltage on the gate with respect to the quantum wells. Equally important, changes in the polarization can be detected as a change in the voltage on the gate.

The results are shown in Fig. 3, where the absorption and polarization are shown as a function of gate voltage. The gate also serves to change the resonant frequency of the intersubband transition and is used to tune the resonance in Fig. 3.

By measuring the absorption and polarization as a function of intensity and temperature, they were able to extract both the intensity and temperature dependence of the intersubband relaxation time,  $T_1$ , shown in Figs. 4 and 5. These measurements have essentially resolved the wide disparity of measured intersubband relaxation rates. The measured relaxation time depends critically on the temperature and the intensity of the radiation field driving the system.

The features of the FELs that are critical for this experiment are the power (required to saturate the transition) and the tunability (required to bring the laser near resonance with the intersubband transition). It is important

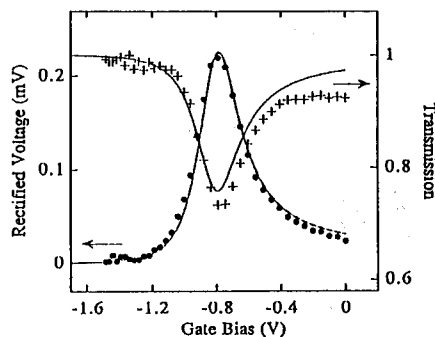


Fig. 3. Rectified voltage proportional to the induced polarization and transmission through the substrate wave guide at 10 K with  $0.5 \text{ W/cm}^2$  at 3.06 THz.

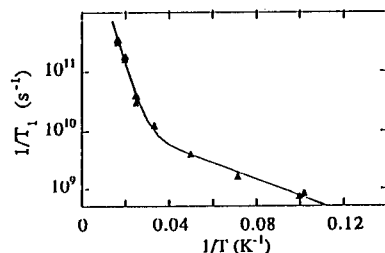


Fig. 4. Intersubband relaxation rate as a function of temperature.

to point out that we have recorded dynamical information over a time scale from picoseconds to nanoseconds. Although it is natural to imagine recovering relaxation rates with a picosecond pump probe experiment, it is doubtful that it could be carried out over three orders of magnitude in time delay without considerable effort. Further the pump and probe experiment would have to explore a wide range of pump powers as well, to properly expose the intensity dependence of the relaxation time. Although there are many situations where a picosecond pump and probe experiment are called for, here the quasi-steady-state saturation spectroscopy has proven most effective.

Although these experiments have been very effective, an experimental difficulty arises which is not apparent in any of the forgoing discussion. These lasers are not CW, have a repetition rate of 1 Hz and have a pulse-to-pulse frequency jitter of  $10^{-3}$ . In the overmoded, substrate waveguide shown in Fig. 2, this leads to amplitude fluctuations as the various modes interfere constructively and destructively depending on the pulse laser frequency. This frequency jitter is intrinsic to the lasers and must be dealt with by the user, by engineering the experiment to be insensitive to these fluctuations. Here Heyman and his collaborators expeditiously fine tuned the FEL to “quiet” spots.

#### 4. Intrinsic relaxation of resonant tunneling diodes

Resonant tunneling diodes, (RTDs), are quantum transport devices that exhibit strong differential negative resistance.

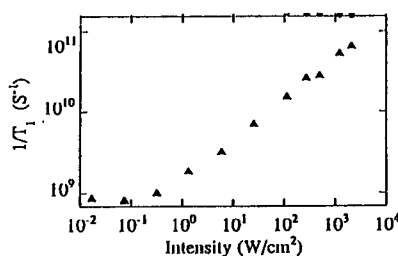


Fig. 5. Intersubband relaxation rate as a function of radiation intensity.

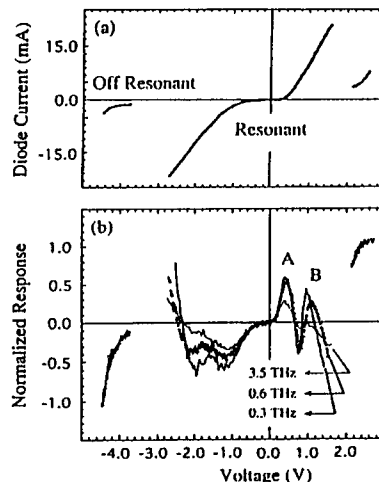


Fig. 6. Top: the DC  $I$ - $V$  characteristic of the RTD. Bottom: the normalized rectified response at 300 GHz, 600 GHz and 3.5 THz.

As a result, they are potentially important for high speed switching [10] and terahertz oscillators [11]. The resonant tunneling structure used here consisted of an InGaAs/AlAs/InGaAs/AlAs/InGaAs double barrier heterostructure grown on InP. Electrical transport only occurs if the device is biased such that the electron standing wave state supported by the AlAs barriers is resonant with electrons in the Fermi sea of the emitter. This results in the very non-linear  $I$ - $V$  shown in Fig. 6.

While we would ideally like to measure this  $I$ - $V$  at THz frequencies to determine the high frequency behavior of the resonant tunneling, this is not practical. Rather we measure the second derivative of the  $I$ - $V$  by treating the RTD as a detector. At low enough frequencies the “rectified response” will simply be proportional to the DC second derivative, while at frequencies where the device can no longer follow the high frequency fields, the response will “roll-off”. It is important to point out that the observation of a rectified response at some frequency does not provide much information. It is only the broad band frequency dependence of this response that conveys dynamical information.

The device is electrically probed in a conventional probe station while it is irradiated by the FEL. The probe tip acts as an antenna to couple the radiation into the device but the coupling is a very strong function of frequency, varying like  $\omega^{-4}$ . To remedy this defect, the response in the important part of the  $I$ - $V$  characteristic, the resonant tunneling regime, is normalized by the off resonant response at positive bias, beyond the negative resistance region.

In Fig. 6, the normalized response is shown for three different frequencies, 300 GHz, 600 GHz, and 3.5 THz. It is gratifying to find that the off-resonant response for negative bias, beyond the negative resistance region, shows

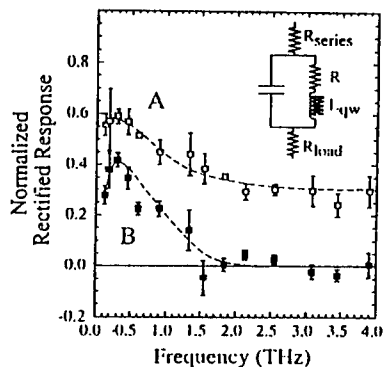


Fig. 7. The normalized rectified response at two different bias points in the resonant tunneling regime. Relaxation at 650 GHz implies a relaxation time of 240 fs.

little frequency dependence despite the strong relaxation in the resonant tunneling regime at high frequencies.

The normalized, rectified response is shown in Fig. 7 from 120 GHz to 3.8 THz for two different bias points. Both have a relaxation frequency of the order of 650 GHz but the behavior near threshold exhibits a plateau. This implies that there are contributions to resonant tunneling, and its rectified response, at threshold that are extremely fast and suffer no relaxation in our frequency range.

The roll-off at 650 GHz implies a relaxation time of 240 fs. It is tempting to ascribe this to the quasi-bound state lifetime, the time it takes an electron to tunnel through the double barrier/quantum well system. But, recent theory of quantum rectification in these devices by Wingreen [12] argues against this interpretation and we are forced to consider the relaxation time of the screening space charge in the structure. Although the relaxation behavior is not easily reconciled with existing theory, it does present a measure of the intrinsic relaxation of these quantum transport devices, at frequencies some two orders of magnitude higher than previously measured.

The free electron laser plays a critical role by delivering power over a wide frequency range, a necessity in order to recover dynamics in the frequency domain. This ability is graphically demonstrated in Fig. 7, where the frequency is swept by a factor of 30. On the one hand, power is not critical here since we wish to be in the low power limit at the RTD, to sense the true high frequency “rectified response”. But, on the other hand, the relatively high incident power enables us to use the very inefficient antenna, provided by the probe, to easily obtain detectable signals in the “square law” limit, at the highest frequencies available.

## 5. Summary

Electrostatic accelerator driven free-electron lasers, like those at UC Santa Barbara, are ideally suited to provide tunable high power radiation at THz frequencies. While there are many uses for high power radiation at these frequencies, an important science and technology arena is non-linear dynamics in semiconductor nanostructures and devices. In this arena, we wish to explore fundamental limits of materials and devices and explore new phenomena. The potential technology impact is to define the high frequency limits of conventional devices and invent new electronics at THz frequencies.

## Acknowledgements

We wish to thank the staff of the Center for Free-electron Laser Studies, J.R. Allen, G.R. Ramian, D. White and D. Enyeart without whom this work could not have taken place. The Center is supported by the Office of Naval Research. The research projects described here were also supported by the Air Force Office of Scientific Research, the Army Research Office and Hughes Research Lab and the University of California under the UC-Micro program.

## References

- [1] J.N. Heyman, K. Unterrainer, K. Craig, B. Galdrikian, M.S. Sherwin, K. Campman, P.F. Hopkins and A.C. Gossard, *Phys. Rev. Lett.*, to be published.
- [2] J.S. Scott, J.P. Kaminski, M. Wanke, S.J. Allen, D.H. Chow, M. Lui and T.Y. Liu, *Appl. Phys. Lett.* 64 (1994) 1995.
- [3] G.R. Ramian, *Nucl. Instr. and Meth. A* 318 (1992) 225.
- [4] W.J. Li, B.D. McCombe, J.P. Kaminski, S.J. Allen, M.J. Stockman, L.S. Muratov, L.N. Pandey, T.F. George and W.J. Schaff, *Semicond. Sci. Tech.* 9 (1994) 630.
- [5] K. Craig, C.L. Felix, J.N. Heyman, A.G. Markelz, M.S. Sherwin, K. Campman, P.F. Hopkins and A.C. Gossard, *Semicond. Sci. Tech.* 9 (1994) 627.
- [6] J. Faist, C. Sitori, F. Capasso, L. Pfeiffer and K. West, *Appl. Phys. Lett.* 64 (1994) 872.
- [7] J.A. Levinson, G. Dolique, J.L. Oudar and I. Abram, *Phys. Rev.* 41 (1990) 3688.
- [8] D.Y. Oberli, D.R. Wake, M.V. Klein, J. Klem, T. Henderson and H. Morkoc, *Phys. Rev. Lett.* 59 (1987) 696.
- [9] B.N. Murdin, G.M.H. Knippels, A.F.G. van der Meer, C.R. Pidgeon, C.J.G.M. Langerak, M. Helm, W. Heiss, K. Unterrainer, E. Gornik, K.K. Geerinck, N.J. Hovenier and W.T. Wenckebach, *Semicond. Sci. Tech.*, to be published.
- [10] E. Ozbay, D.M. Bloom, D.H. Chow and J.N. Shulman, *IEEE Electron Device Lett.* 14 (1993) 400.
- [11] E.R. Brown, J.R. Soderstrom, C.D. Parker, L.J. Mahoney, K.M. Molvar and T.C. McGill, *Appl. Phys. Lett.* 58 (1991) 2291.
- [12] N.S. Wingreen, *Appl. Phys. Lett.*, 56 (1990) 253.



ELSEVIER

## Vibrational dynamics in condensed matter probed with linac based FELs

A. Tokmakoff, Alfred Kowk, R. Urhdal, D.A. Zimdars, M.D. Fayer \*

*Department of Chemistry, Stanford University, Stanford, CA 94305, USA*

### Abstract

The super-conducting linac pumped free electron laser (FEL) at Stanford has been used to study the vibrational dynamics of molecules in liquids and glasses. A variety of experiments have been performed, including the world's first vibrational photon echo experiments in liquids and glasses and polarization selective pump-probe experiments. In this paper vibrational photon echo experiments are described and characteristics of the FEL important to these experiments are discussed. Vibrational photon echo experiments were performed on the asymmetric CO stretching mode of tungsten hexacarbonyl ( $1976\text{ cm}^{-1}$ ) in the organic glass dibutylphthalate as a function of temperature using sub-picosecond infrared pulses. The echo decays display pronounced beats and are bi-exponential. The beats and bi-exponential decays arise because the bandwidth of the transform limited FEL pulses exceeds the vibrational anharmonicity, leading to the excitation and dephasing of a multilevel coherence. From the beat frequency, the anharmonicity is determined to be  $14.7\text{ cm}^{-1}$ . From the bi-exponential decay components, the temperature-dependent homogeneous vibrational dephasing rates of both the  $\nu = 0 \rightarrow 1$  and  $\nu = 1 \rightarrow 2$  transitions are determined.

### 1. Introduction

In liquids and other condensed phase systems, vibrational spectra can have contributions from inhomogeneous broadening which mask the homogeneous vibrational line-shape [1,2]. Third-order coherent Raman experiments measure the free induction decay of the spontaneous Raman line, and cannot distinguish or eliminate contributions from inhomogeneous broadening [3]. For this reason, higher order Raman experiments, such as the Raman echo, are required to distinguish inhomogeneity in vibrational transitions [3–8].

As an alternative to these non-resonant techniques, resonant third order experiments, such as the vibrational photon echo, can be used to determine the homogeneous linewidth of a vibrational transition [1,2]. Unlike Raman experiments, resonant infrared experiments allow significant transfer of population to the excited vibrational state. Thus, when the bandwidth or Rabi frequency of the excitation source exceeds the anharmonicity of the vibrational transition, population can be further excited to higher vibrational levels [9–11]. Such experiments permit multilevel vibrational dynamics to be observed [10,11]. Resonant experiments have the additional distinct advantage of being able to separate pure dephasing and lifetime contri-

butions to the homogeneous vibrational linewidth [1], both of which can contribute significantly [1,12].

Here, we report the results of sub-picosecond infrared vibrational photon echo experiments, conducted with the Stanford super-conducting linac pumped free electron laser (FEL), in which the excitation bandwidth exceeds the vibrational anharmonicity. These experiments are the first to determine the homogeneous vibrational linewidth for both the  $\nu = 0 \rightarrow 1$  and  $\nu = 1 \rightarrow 2$  transitions. Furthermore, this measurement accurately determines the vibrational anharmonicity, which cannot be done by linear absorption spectroscopy.

Temperature dependent measurements were made on the asymmetric CO stretching mode of tungsten hexacarbonyl  $[\text{W}(\text{CO})_6]$  in the organic glass dibutylphthalate (DBP) from 10 K to 150 K. The results show vibrational dephasing dynamics with dramatically different temperature dependences, indicating different line broadening mechanisms. Furthermore, the echo decays show that the absorption line is massively inhomogeneously broadened over this temperature range.

In a vibrational photon echo experiment, two IR pulses tuned to the molecular vibration of interest, are crossed in the sample. The first pulse creates a coherent superposition state that begins to dephase due to inhomogeneous broadening. A second pulse, delayed by time  $\tau$ , initiates rephasing of the inhomogeneous contributions to the vibrational transition. This rephasing results in a macroscopic polar-

\* Corresponding author. Tel. +1 415 723 4446.

ization that is observed as an echo pulse at time  $2\tau$ . The echo emerges from the sample in a unique direction given by wave vector matching conditions. The integrated intensity of the echo pulse is measured as a function of  $\tau$ . For the case in which the laser bandwidth is narrow with respect to the vibrational anharmonicity, such that the vibrational coherence involves only the  $v=0 \rightarrow 1$  transition, the process is modeled well by a two level system, and the decay of the echo intensity measures the homogeneous vibrational dephasing time  $T_2$ . For a Lorentzian homogeneous lineshape with linewidth  $\Gamma=1/\pi T_2$ , the echo decays as

$$I(\tau) = I_0 \exp(-4\gamma_{10}\tau), \quad (1)$$

where  $\gamma_{10} = 1/T_2$  for the  $v=0 \rightarrow 1$  transition.

When the bandwidth of the excitation pulses exceeds the vibrational anharmonicity, population can be excited to higher vibrational levels. The extent of vibrational up-pumping is limited only by the magnitude of the vibrational anharmonic frequency splitting,  $\Delta$ , relative to the laser bandwidth,  $\Omega$ , or the Rabi frequency. For the case where  $\Delta \approx \Omega$ , short pulse excitation will create a three level coherence involving the  $v=0, 1$  and  $2$  vibrational levels. Extending a treatment of photon echoes in harmonic vibrational systems [13], Fourkas has derived an expression for the photon echo decay for a three level system with anharmonicity [14]. For a finite pulse bandwidth where the  $E$ -field differs at the frequencies of the two transitions, the Fourkas result can be extended, and the decay is given by

$$I(\tau) = \exp(-2\gamma_{10}\tau) \left[ E_{10}^2 \exp(-2\gamma_{10}\tau) + E_{21}^2 \exp(-2\gamma_{21}\tau) - 2E_{10}E_{21} \exp(-(\gamma_{10} + \gamma_{21})\tau) \cos(\Delta\tau) \right]. \quad (2)$$

This equation is based upon an on-resonance assumption with excitation  $E$ -field amplitudes  $E_{10}$  and  $E_{21}$  for the  $v=0 \rightarrow 1$  and  $v=1 \rightarrow 2$  transitions, respectively. Eq. (2) shows that the echo signal envelope decays in proportion to the dephasing rates of the  $v=0 \rightarrow 1$  and  $v=1 \rightarrow 2$  transitions, with exponentially damped beats observed at the frequency splitting,  $\Delta$ . For the narrow bandwidth case ( $E_{21} \approx 0$ ), Eq. (1) is recovered.

## 2. Experimental procedures

The infrared photon echo experiments reported here were performed with  $\sim 0.7$  ps ( $\sim 20$  cm $^{-1}$  bandwidth) IR pulses at  $5.06$   $\mu$ m ( $1976$  cm $^{-1}$ ) generated by the Stanford superconducting-accelerator-pumped free electron laser. FEL pulses are generated as transform-limited Gaussian pulses. The FEL emits a  $2$  ms macropulse at a  $10$  Hz repetition rate. Each macropulse consists of  $\sim 1$   $\mu$ J micropulses at a repetition rate of  $11.8$  MHz.

To avoid severe sample heating problems and to assure that the sample has returned to the initial condition prior to the application of the next pulse sequence, it is necessary to select single micropulses from the FEL macropulse. It cannot be emphasized enough the importance of being able to control the micropulse repetition rate to permit a wide variety of experiments to be performed properly. With the Stanford FEL, single pulse selection is made possible by the  $85$  ns separation between micropulses. A germanium acousto-optic single pulse selector was developed which permits pulses to be selected at any repetition rate. The experiments were conducted at  $50$  kHz during the macropulse, giving an overall repetition rate of  $1$  kHz. Also essential for these experiments is stabilization and continuous measurement, of the FEL wavelength and the duration and functional form of the optical pulse. In addition, methods for optical alignment, detection equipment, and specialized software are required to successfully perform photon echo and other experiments.

During one  $3$  ms macropulse, the RMS variation in power is only  $1.8\%$ . This is typical operation. Since the FEL must be tuned into a relatively narrow vibrational line, wavelength stability is essential. The variation is minimized by a feedback stabilization system. The RMS variation is only  $0.009\%$ . At  $2000$  cm $^{-1}$ , this is  $\sim 0.2$  cm $^{-1}$ . This variation should be compared to the transform limited bandwidth of the pulse, which is  $\sim 20$  cm $^{-1}$ . In addition, constant monitoring of the pulse duration using autocorrelation gives the pulse duration and pulse shape. All of the relevant information is provided directly to the user and this information is constantly updated.

To perform the echo experiments, the two pulses for the echo pulse sequence are obtained with a ZnSe beam splitter. The data was taken with pulse energies of  $15$  nJ for the first pulse and  $100$  nJ for the second pulse. The pulse energy of the second pulse gives a peak Rabi frequency, estimated from  $(\mu \cdot E)/\hbar$ , of approximately  $15$  cm $^{-1}$ . The more intense pulse was chopped at  $25$  kHz by a second AOM. The photon echo signal and an intensity reference signal were measured with two HgCdTe detectors sampled by two gated integrators. The reference detector was used for shot intensity windowing; all data with pulse intensities outside of a  $10\%$  window were discarded. Carefully performed power and repetition rate dependences demonstrated that the data is free of power and heating artifacts.

Vibrational photon echo data were taken on the triply degenerate  $T_{1u}$  asymmetric CO stretching mode of  $W(CO)_6$ . Data were taken on  $4 \times 10^{-3}$  M solutions of  $W(CO)_6$  in DBP (99.9%). The absorption bandwidth is  $26$  cm $^{-1}$  at all temperatures.

## 3. Results and discussion

Fig. 1 shows photon echo decays for several temperatures in the glass, as well as fits to Eq. (2). These decays

are consistent with the expected decay of a three level vibrational coherence. The decays are modulated at a 2.3 ps frequency, which is constant within error over all temperatures. Based on the average of several data sets, the vibrational anharmonic splitting is  $\Delta = 14.7 \pm 0.3 \text{ cm}^{-1}$ . This splitting is in accord with the value of  $15 \pm 1 \text{ cm}^{-1}$  recently obtained by Heilweil and co-workers from observation of the  $\nu = 1 \rightarrow 2$  and  $\nu = 2 \rightarrow 3$  transitions using transient infrared absorption [11]. The agreement between the anharmonicity obtained from the beat frequency and that obtained by transient absorption confirms the interpretation of the beats as arising from the multi-level coherence of an anharmonic oscillator.

Fits to the echo decay data also provide the rates of homogeneous dephasing for the two transitions involved in the multilevel coherence. Fig. 2 shows the homogeneous dephasing times for the  $\nu = 0 \rightarrow 1$  and  $\nu = 1 \rightarrow 2$  transitions at temperatures between 10 K and 150 K. These dephasing times, at all temperatures, are long compared to the inverse of the absorption linewidth and indicate a massively inhomogeneously broadened line.

At low temperatures, the dephasing rate, or homogeneous linewidth, of the  $\nu = 1 \rightarrow 2$  transition is more than

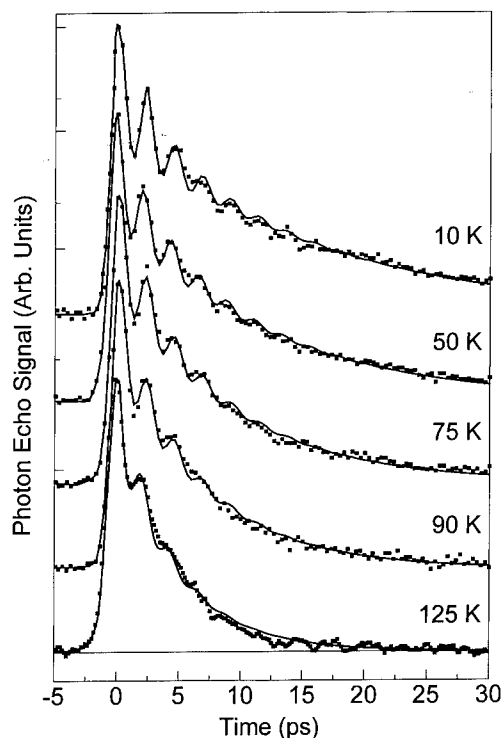


Fig. 1. Photon echo decays and fits for the asymmetric CO stretching mode of  $\text{W(CO)}_6$  in di-butylphthalate at several temperatures in the glass. Fits are to Eq. (2) and represent the homogeneous dephasing of the three level coherence with beating at the anharmonic vibrational frequency splitting.

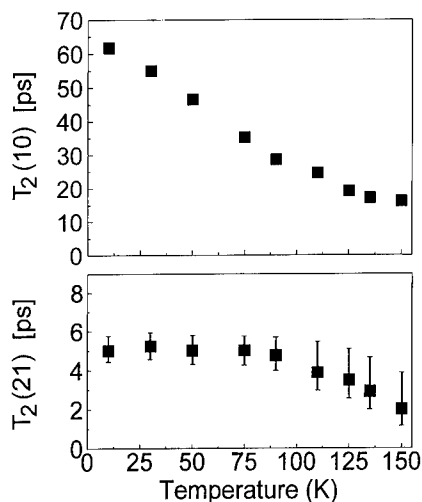


Fig. 2. Decay times  $T_2(10) = 1/\gamma_{10}$  and  $T_2(21) = 1/\gamma_{21}$  for temperatures between 10 K and 150 K obtained from fits to Eq. (2). Error bars for  $T_2(10)$  are on the order of the size of the squares. Error bars for  $T_2(21)$  show the influence of the small uncertainties in both  $T_2(10)$  and  $\Delta$  on the accuracy of the determination.

10 times that of the  $\nu = 0 \rightarrow 1$  transition. Temperature dependent photon echo studies of  $\text{W(CO)}_6$  in other glasses [1,2,12] indicate that the 10 K homogeneous line is dominated by lifetime broadening. The lack of temperature dependence of the homogeneous linewidth of the  $\nu = 1 \rightarrow 2$  transition between 10 K and  $\sim 100$  K suggests that the width arises from lifetime broadening since pure dephasing is temperature dependent. The  $\nu = 0 \rightarrow 1$  dephasing can display temperature dependent pure dephasing over this same temperature range because the  $\nu = 0 \rightarrow 1$  lifetime is much longer than the  $\nu = 1 \rightarrow 2$  lifetime.

The temperature dependence of the  $\nu = 0 \rightarrow 1$  dephasing is similar to that observed in other glasses [1,2] measured with photon echo experiments using the FEL. The rate of dephasing increases by a factor of  $\sim 6$  over the temperature range studied. If the 10 K point is assumed to be the temperature independent vibrational lifetime and is subtracted out of the homogeneous linewidth, the remaining linewidth, due to pure dephasing, has a power law temperature dependence,  $\Gamma \propto T^\alpha$  with  $\alpha = 1.8$ . This power law temperature dependence is representative of other measurements of the homogeneous linewidth in glasses, made with photon echoes [15] and infrared hole-burning [16,17]. A comparison of these results with those for two other glassy systems and the behavior in the three liquids will be presented in another publication [15]. As seen from the  $\nu = 0 \rightarrow 1$  data, the  $\nu = 1 \rightarrow 2$  dephasing rate begins to increase at higher temperatures as the pure dephasing rate approaches the upper level lifetime.

As evident from Eq. (2), at higher temperatures where  $\gamma_{10} + \gamma_{21} \geq \Delta$  and  $1/\gamma_{21}$  approaches the pulse width, an



accurate determination of  $\gamma_{21}$  cannot be made without proper convolution. When  $\gamma_{21} > \Delta$ , the decay of the  $v = 1 \rightarrow 2$  coherence appears as part of an oscillation of less than one cycle near  $t = 0$ . The discussion and interpretation of higher temperature data, including convolution with the proper echo response function [18] for the decay of a three-level coherence with the three field interactions of the photon echo, is the subject of continuing work. It was possible to determine  $\gamma_{10}$  all the way to room temperature. It was found that the vibrational line in the liquid even at room temperature is massively inhomogeneously broadened [15].

#### 4. Concluding remarks

This work presents the first measurements of homogeneous dephasing of a multilevel vibrational coherence in a condensed phase system. The infrared photon echo experiment, with excitation bandwidth wider than the vibrational anharmonicity, allows the determination of vibrational dephasing of both the  $v = 0 \rightarrow 1$  and  $v = 1 \rightarrow 2$  transitions, an accurate determination of the vibrational anharmonicity, and the removal of inhomogeneous contributions to the vibrational lineshape. These experiments suggest that performing this sort of Fourier transform spectroscopy with even shorter femtosecond pulses may make it possible to investigate more of the anharmonic potential of a vibrational mode by exciting many vibrational levels.

#### Acknowledgements

The authors thank Prof. John Fourkas for many helpful conversations on the theory of photon echoes in vibrational systems. The authors gratefully acknowledge Prof. Alan Schwettman and Prof. Todd Smith and their groups at the Stanford Free Electron Laser Center, whose efforts made these experiments possible. We thank Dr. Steve Arrivo and

Dr. Ted Heilweil for discussions and advance data on their transient absorption studies of up-pumping in metal carbonyl solutions. This work was supported by the Medical Free Electron Laser Program (N00014-91-C-0170), the National Science Foundation (DMR-9322504), and the Office of Naval Research (N00014-92-J-1227).

#### References

- [1] D. Zimdars, A. Tokmakoff, S. Chen, S.R. Greenfield and M.D. Fayer, *Phys. Rev. Lett.* 70 (1993) 2718.
- [2] A. Tokmakoff, D. Zimdars, B. Sauter, R.S. Francis, A.S. Kwok and M.D. Fayer, *J. Chem. Phys.* 101 (1994) 1741.
- [3] R.F. Loring and S. Mukamel, *J. Chem. Phys.* 83 (1985) 2116.
- [4] Y. Tanimura and S. Mukamel, *J. Chem. Phys.* 99 (1993) 9496.
- [5] D. Vanden Bout, L.J. Muller and M. Berg, *Phys. Rev. Lett.* 67 (1991) 3700.
- [6] L.J. Muller, D. Vanden Bout and M. Berg, *J. Chem. Phys.* 99 (1993) 810.
- [7] R. Inaba, K. Tominaga, M. Tasumi, K.A. Nelson and K. Yoshihara, *Chem. Phys. Lett.* 211 (1993) 183.
- [8] K. Tominaga, Y. Naitoh, T.J. Kang and K. Yoshihara, in: *Ultrafast Phenomena IX*, eds. G. Mourou, A.H. Zewail, P.F. Barbara and W.H. Knox (Springer, Berlin, 1994).
- [9] A. Tokmakoff, B. Sauter, A.S. Kwok and M.D. Fayer, *Chem. Phys. Lett.* 221 (1994) 412.
- [10] A. Tokmakoff, B. Sauter, A.S. Kwok and M.D. Fayer, in preparation.
- [11] S. Arrivo and E.J. Heilweil, personal communication.
- [12] A. Tokmakoff, R.S. Urdahl, D. Zimdars, A.S. Kwok, R.S. Francis and M.D. Fayer, submitted *J. Chem. Phys.*
- [13] J.T. Fourkas, H. Kawashima and K.A. Nelson, submitted *J. Chem. Phys.*
- [14] A. Tokmakoff, R.S. Urdahl, D. Zimdars, B. Sauter, A.S. Kwok, R.S. Francis and M.D. Fayer, in preparation.
- [15] H.-G. Cho and H.L. Strauss, *J. Chem. Phys.* 98 (1993) 2774.
- [16] S.P. Love and A.J. Seivers, *J. Lumin.* 45 (1990) 58.
- [17] S. Mukamel and R.F. Loring, *J. Opt. Soc. B* 3 (1986) 595.



ELSEVIER

## Scientific opportunities for FEL amplifier based VUV and X-ray research

Erik D. Johnson \*

*Brookhaven National Laboratory, National Synchrotron Light Source, Upton, NY 11973-5000, USA*

### Abstract

It has become increasingly clear to a wide cross section of the synchrotron radiation research community that FELs will be the cornerstone of fourth generation radiation sources. Through the coherent generation of radiation, they provide as much as 12 orders of magnitude increase in peak power over the third generation storage ring machines of today. Facilities have been proposed which will extend the operating wavelength of these devices well beyond the reach of existing solid state laser technology. In addition, it appears possible to generate pulses of unprecedented brevity, down to a few femtoseconds, with mJ pulse energies. The combination of these attributes has stimulated considerable interest in short wavelength FELs for experiments in chemical, surface and solid state physics, biology and materials science. This paper provides a brief overview of how the features of these FELs relate to the experimental opportunities.

### 1. Introduction

Although the subject of this paper has intentionally been limited to research applications utilizing short wavelength FEL amplifiers, the number of qualifying adjectives in the title is still insufficient to allow the comprehensive treatment of the subject in the available space. The discussion instead will highlight general features of these types of sources and how their attributes determine the choice of experiment and methodology for which they are appropriate. This selective treatment of short wavelength FEL science is not intended either to represent, or minimize, the potential of oscillator based sources, or the growing body of industrial and technological applications for which FEL sources may be appropriate. They are simply beyond the scope of the present work. I raise this point only to make it clear that these issues must also be considered by the interested reader, if the broad potential of FEL sources is to be fully appreciated.

The characteristics of single pass FELs have been the subject of several sessions of this conference [1], representing a wide range of technological issues and approaches. As a basis for the present discussion, the Brookhaven National Laboratory Deep Ultra-Violet (DUV) FEL [2], and the Stanford Linear Accelerator Center Linear Coherent Light Source (LCLS) [3] are taken as possible sources operating in the UV and X-ray regions of the spectrum. Both operate as single pass devices, providing very high

peak power and photon beam brightness. Since they are S-band linac driven machines requiring high peak currents for operation, the pulse repetition rates are unlikely to exceed 360 Hz. Further, the output pulse widths range from 10 ps to 10 fs, so these are comparatively low duty cycle sources. Although various options for multiple pulse formats with variable time delays and/or multi-color operation have been proposed, these are nominally single pulse sources, i.e., without inherent micropulse structure. Both machines should provide flexible wavelength tuning over their specified output range. Beyond these common parameters, the machines and the research they engender begin to diverge.

The DUV FEL is a seeded beam amplifier. It relies upon “conventional” laser technology for a “seed” photon beam to couple with the electron beam. Through various arrangements, the FEL acts either to amplify at the same wavelength as the seed laser or, through harmonic generation and subsequent amplification, to frequency multiply and amplify the original laser pulse. The advantage of this approach is that the output radiation has the frequency stability and relative bandwidth of the seed laser. Electron beam brightness and energy variations are expressed in the output radiation only as changes in intensity. The pulse width and shape are also to first order determined by the properties of the seed laser. The obvious disadvantage of this approach is the short wavelength limit imposed by the seed laser and practical considerations for the construction of the accelerator driver.

To cross this threshold, the LCLS FEL takes advantage of the high electron beam energies available from the

\* Tel. +1 516 282 4603, fax +1 516 282 3238.

SLAC linac to drive a Self Amplified Spontaneous Emission (SASE) FEL. Because of the high energy from the accelerator, the demands on the wiggler are somewhat relaxed (long period and moderate peak field). A wiggler of significant length (the order of 40–70 m) is, however, required to achieve saturation at wavelengths less than 1 nm. Since the LCLS is an SASE source, the output radiation wavelength stability depends upon the energy stabilization of the electron beam, and the intensity will be a strong function of the beam emittance and peak current. Clearly, for either source, the experiments must either be inherently insensitive to these inevitable variations, or suitable real-time, shot to shot diagnostics must be provided.

The foregoing discussion really contains all the essential information to determine what types of research are most suited to these machines. The operational wavelengths will determine the types of processes through which the source radiation will interact with the experiment. The tunability implies access to specific transitions, and opens a range of experimental opportunities as compared with line sources. The spectral properties (bandwidth, harmonic content, and source phase space) will be important in determining the requirements of the optical system for photon beam conditioning and transport. The high peak power is suggestive of studies of dilute systems, or non-linear optical studies where multi-photon excitations are important. The time structure of the radiation would provide a tool for the study of systems with picosecond dynamics, although the pulse separation would allow investigation of transient phenomena over much longer time scales. These sources also possess a high degree of coherence (both spatial and temporal), thus interference effects might be effectively employed for imaging and intensity correlation studies. This collection of general attributes clearly suggests that these sources could be powerful research tools. What follows are a few examples of possible research problems which would be well served by sources of the type described above, with some closing comments about important issues for mounting experimental programs with these devices.

## 2. Research in the ultra-violet

For a source operating in the vacuum ultraviolet, valence band electronic transitions are directly accessible by single photon excitation. This has important implications for the study of UV induced photochemistry, since the radiation is sufficiently energetic to break most chemical bonds. Molecules photoexcited by UV–VUV light frequently undergo fragmentation into atomic and/or smaller molecular species, most often radical species with open shells which readily undergo subsequent reactions with surrounding molecules and surfaces. To produce significant yields of these products the source must be extremely

intense, providing pulse energies the order of 1 mJ per shot, and in nearly every case of even moderate complexity, the excitation wavelength will have a profound effect on the product distribution and yield. Operation at wavelengths shorter than 200 nm (LiF window cutoff) allows the investigation of the electronic structure of many otherwise inaccessible species. This includes molecules such as  $\text{CH}_4$ ,  $\text{H}_2\text{O}$ ,  $\text{CO}_2$ , and most of the chloro-fluorohydrocarbons which are important in atmospheric photochemistry. The ability to perform the primary photochemistry by single photon excitation is a significant capability. One of the most powerful techniques for examining the state distribution of the reaction products involves so called vector correlation experiments, where the kinetic energy, momentum and identity of the photofragments are all determined. Much of the “memory” of the primary photoexcitation event can be lost when multi-photon probes are utilized, as is often done with longer wavelength lab based lasers. In addition, the requirement for a well known and conveniently arranged electronic manifold to apply these multi-photon techniques can significantly limit the range of species available for study.

The benefits of an FEL source for this type of work are clear; the high peak power implies access to dilute systems which include gas phase samples, surface adsorbates, and transient species such as excited states or radicals. The tunability allows the exploration of resonant processes including excited states and threshold phenomena. The flexible time structure adds the dimension of time dependent phenomena, such as relaxation and excitation processes, and the possibility of coherent control of quantum dynamics in the time domain. For FELs which are driven (and in this case seeded) by “conventional” lasers, synchronized multi-color pump-probe experiments become an obvious capability.

Many of the winning features of the FEL source are equally applicable to other fields, such as biology. For example, the tunability of the source is of great importance in the study of radiation damage in DNA and other molecular targets in living cells. For wavelengths longer than 200 nm, damage is induced by specific absorption and consequent photochemical changes in chromophores within the target molecule. At X-ray wavelengths, the absorption occurs primarily in water, so damage mechanisms occur through a large number of indirect processes. The advantage of utilizing VUV radiation to elucidate damage mechanisms in DNA, proteins, membranes, and other biological targets, is that the energy-per-photon is just adequate to produce a limited number of ionizations. The number of chemical reactions produced in a VUV exposure is much more limited than in the case of X-rays and other types of ionizing radiation, hence the complications resulting from a plethora of secondary reactions are avoided. Experiments of this type have been attempted utilizing synchrotron sources, but the comparatively low intensity available (in the requisite bandwidth) has, to date, restricted the range

of experiments. To harvest a meaningful quantities of photo-products, doses must be measured in moles of photons.

Time resolved phosphorescence and fluorescence studies of biological systems could also benefit from an FEL source. In studies performed thus far, the samples are often far more concentrated than would occur in the native biological system. The quenching rates observed with these techniques are known to be extremely sensitive to the proximity of ions, other amino acid residues, and dependent upon the conformation of the molecule. This in fact forms the basis of the structural information derived from these techniques. A high peak power source, like the FEL, should allow this work to be performed in environments that are far more representative of real biological systems, so ambiguities due to intermolecular coupling of the target species can be avoided. The tunability of the source allows high resolution probing of specific sites within the molecule, while the flexible time structure provides the opportunity to optimize the data collection rate for the decay time and damage threshold of the specific molecule under investigation.

Similar advantages can be envisaged for many fields where one is interested in science related to the photo-excitation of comparatively low lying electronic transitions. Many additional experiments have been explored in chemical dynamics and biology beyond those briefly described above. Applications have also been developed in solid state physics, materials science, and atomic physics. Many are predicated on extensions of existing research, where presently available sources have proved inadequate. While providing a semi-quantitative feel for the relative improvement made possible by an FEL, discussions of this type tend not to reach too far beyond existing science. This is much less the case for an X-ray FEL where the source is even further removed from existing technology.

### **3. Research in the X-ray region**

A source performing at the level of the proposed LCLS provides significant challenges to the imagination. It would produce a spectral brightness per shot which exceeds the brightness per second of third generation storage rings such as the ESRF, APS and Spring-8! With 150 fs pulses, the LCLS would possess a peak brightness 10 orders of magnitude higher than the new sources. The wavelength range of the source from roughly 0.1 to 4 nm, is suitable for examining core level electronic excitations, and perhaps more interestingly, is the appropriate length scale for a number of interesting imaging and scattering techniques. The tremendous coherence would be very useful for zone plate microscopy and holography in the water window (2 to 4 nm), where single shot images could be obtained. At somewhat shorter wavelengths, “normal” scattering techniques become viable although, given the pulse structure

of the source, dynamics could be explored at previously unavailable time scales.

Considerable discussion has in fact been given to the subject of X-ray time correlation spectroscopy (often known as speckle or intensity fluctuation spectroscopy) as a method to examine dynamics in condensed matter systems at time scales from  $10^{-3}$  to  $10^{-3}$  at length scales as small as 0.1 nm. The technique depends upon the introduction of phase shifts from different domains of a specimen which will be observable as intensity fluctuations in the scattering. This is true only when the sample is illuminated with a sufficiently coherent source. A short wavelength FEL satisfies these requirements, and provides access to a much shorter length scale than is available from any existing source.

A number of problems have been described where the understanding of microscopic dynamics could be enhanced through the use of time correlation spectroscopy. Among these are free standing smectic liquid crystal films, dipolar glasses, and thin film magnetic materials; all of potentially great technological importance. The source brightness would allow single shot speckle patterns to be obtained, and in principle, the time structure of the source would allow dynamics to be studied to the limit of the FEL repetition rate. Another side benefit of the source brightness is the possibility of examining small samples using a variety of otherwise “conventional” X-ray techniques. This is simply a result of the small source divergence.

Reaching a bit further beyond the present state of the art, interferometric techniques of various kinds have also been suggested, which again exploit the unique attributes of an X-ray FEL. For example, interference patterns on a sub-nanometer scale could be generated either to characterize or manipulate materials. Coherent lattice motions might be induced to drive specific structural rearrangements. By extension, the source tunability and polarization could be employed to resonantly enhance a particular process or induce a magnetic periodicity. The decay of these prepared states could be used as a characterization technique. Utilizing the FEL in this fashion could lead to a new suite of probes for studying the dynamics of both structural and magnetic order at short length scales. This could be especially valuable for the study of incommensurate systems.

The source brightness should also be sufficient to mount serious experiments on the non-linear optical properties of materials in the X-ray regime. Multi-color experiments could be envisioned where optically induced charge density modifications (say from a UV laser source) are probed with a pulse from an X-ray FEL. Alternatively, the FEL pulse could be split and time delayed to serve as the source for both the pump and probe beam. Multiple color experiments might also be possible using either harmonics from the FEL, or the continuum background, if they provide adequate intensity for the particular experiment being conducted.

Clearly, X-ray FELs provide a host of exciting at-

tributes, many of which are unavailable individually in any other source, and certainly not as a collective capability. Divining the new science that machines of this type engender is a tremendously challenging task, since the properties of the source are so far beyond current capabilities. Proposals for FELs of this type are sufficiently new to the research community, that I have no fear in asserting that the most exciting applications for this source are yet to be described.

#### 4. Closure

This brief look at potential research applications for short wavelength FEL amplifiers is perhaps less indicative of the research opportunities than it is of the sociology which will likely lead to their successful development and utilization. The UV FEL based science is close enough, in some respects, to existing laser derived technology that it borrows much from the communities that use conventional lasers for their research. Among these groups, the chemical and atomic physics communities are perhaps the most accustomed to being involved in the development of the photon sources for their research, the so-called “laser jocks” of the world. These communities were the first to seriously examine the potential of UV FELs on their science. Involvement from the biological sciences has been somewhat slower in developing, largely because photon sources are regarded as important tools for research; not the subject of research for this community. These machines could never-the-less become an important resource for work conducted in biology and other fields of research that are not, as yet, part of the “scientific case” for short wavelength FELs.

FELs are accelerator based sources, and much of the early application development for short wavelength FELs is now taking place at synchrotron sources. This is in part because the psychology of going to a remote location to perform experiments is familiar to synchrotron radiation researchers. A major component of this community is involved in condensed matter research, so it is not at all surprising that the problems which have been suggested for X-ray FELs are largely derived from that community. The difficulty is that even third generation source are, in many instances, inadequate to the task of providing a platform even for proof of principle experiments of the type which could be mounted at an FEL. They might be suggestive of interesting science, but the foibles of FELs

must be considered along with their potential experimental benefits.

For example, experiments performed at synchrotrons have a comparatively easy task in intensity normalization as contrasted with FELs. The experiments are usually only linear in nature (spectroscopies for example), and intensities at storage rings vary comparatively slowly. By contrast, at an FEL, many experiments may be inherently non-linear in nature (thus more sensitive to intensity variations), and the source variation shot-to-shot could be significant. A new problem for synchrotron people, old news to the laser folks. Similarly, refractive optics are clearly impractical at wavelengths shorter than 200 nm, which leaves laser people on unfamiliar ground, but practitioners of UV science at synchrotrons have long ago come to grips with this problem.

Clearly, what is required for the growth of short wavelength FEL research, is a fusion of approaches and ideas from practitioners of laser based research, and researchers who presently work at synchrotron sources. Further, source and science development need to advance together, so it is important to foster interaction between the machine “builders” and “users” at an early stage. This is one of many instances where I feel that the sum of the efforts of a coordinated, communicative community will vastly outstrip the performance of its individual members when left to their own devices.

#### Acknowledgements

This work was performed under the auspices of the United States Department of Energy, under contract DE-AC02-76CH00016.

#### References

- [1] These Proceedings (16th Int. Free Electron Laser Conf., Stanford, CA, USA, 1994) Nucl. Instr. and Meth. A 358 (1995). See for example papers from sessions on Single Pass UV/X-ray Free Electron Lasers, and Prebunched Beams and Coherence.
- [2] The Brookhaven National Laboratory Deep Ultra-Violet Free Electron Laser Conceptual Design Report, 2 Volumes, BNL Publication Number 49713 (1994).
- [3] Proc. Workshop on Scientific Applications of Coherent X-rays, February 12, 1994, SLAC Publication 437, SLAC/SSRL-0066.



ELSEVIER

## 1-D simulation model of an FEL with a plasma background

T.H. Chung <sup>a,\*</sup>, J.K. Lee <sup>b</sup>

<sup>a</sup> Dong-A University, Pusan 604-714, South Korea

<sup>b</sup> Pohang University of Science and Technology, Pohang, Kyungbuk 790-600, South Korea

In order to supply shorter wavelengths wigglers in the FEL configuration, there is a significant ongoing research effort. Among approaches to decreasing  $\lambda_w$  is the replacement of the magnetic undulator with an electrostatic plasma wave undulator [1]. This configuration is based on using a short wavelength, large amplitude relativistic plasma wave as undulator through which a moderately relativistic electron beam is injected.

The study of the interaction of a relativistic electron beam (REB) with a background plasma (or a gas) has been of interest in many areas of plasma and beam physics over the years. Relativistic electron beams have been injected into gas and plasma to develop high-power microwave and X-ray sources, and to study plasma accelerator concepts. The types of interaction depend on the experimental parameters such as the electron beam density, plasma density, and the geometry of the experiments. There can be several types of beam-plasma interactions. For example, electromagnetic waves can be produced by the scattering of electrostatic plasma waves off self-consistently produced ion-acoustic waves [2]. In this case, the plasma medium has a moderate density ( $n_p \approx 10^{12} \text{ cm}^{-3}$ ) and the electron beam density has the ratio of  $10^{-4} < n_b/n_p < 10^{-2}$  [2].

The plasma medium can function as the undulator itself [3], or the medium can be used to fill the FEL cavity in the wiggler magnets [4]. For the former case, the electrons propagate either parallel to or perpendicular to the wave fronts of the plasma waves, and emits radiation oscillating in the alternating wave's electrostatic field [1]. For the plasma wave undulator, electron trajectories are bent by the electric field of the travelling plasma wave which can be produced by laser beatwave excitation, laser wakefield excitation, or plasma wakefield excitation. In this scheme the medium plasma should be dense ( $n_p \approx 10^{17} \text{ cm}^{-3}$ ), and the electron beam should have a high density ( $n_b \approx 10^{15} \text{ cm}^{-3}$ ) [3].

Other plasma based undulators have been investigated

in recent years. The operation of plasma FELs are based on small transverse oscillations of relativistic electron beams in excited fields. In the ion ripple laser electrons oscillate in the transverse electric field of the ripple which is created by the excitation of an ion acoustic wave in a neutral plasma [5].

There can also be the mechanism of ion focusing, and this has been successfully employed in accelerator work. In the ion channel laser electron oscillations are due to electrostatic focusing in the channel [6,7,8].

In this synopsis we consider the so-called ion channel laser using the Maxwell Lorentz formulation. Then we investigate system characteristics using a many particle simulation.

The motion of an electron in the ion focused region with scattered EM fields is given as

$$\frac{d\gamma}{dz} = -\frac{ka_s a_p}{\gamma} \sin \psi, \quad (1)$$

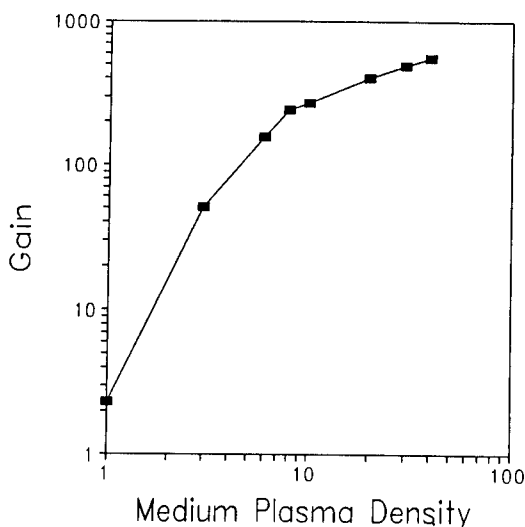


Fig. 1. Gain versus the medium plasma density (in units of  $10^{10} \text{ cm}^{-3}$ ).

\* Corresponding author. Tel. +82 51 200 7228, fax +82 51 200 7205, e-mail thchung@seunghak.donga.ac.kr.

$$\frac{d\psi}{dz} = k_s \beta_z - k_s + k_\beta \left( 1 - \frac{a_s}{2a_p} \cos \psi \right) + \frac{1}{2} \frac{k_s a_s a_p}{\gamma^2} \cos \psi + \frac{d\phi}{dz}, \quad (2)$$

where

$$\psi = (\omega_s - \omega_\beta)t - k_s z + \phi.$$

Note that  $\omega_\beta$  is the oscillation (betatron) frequency of the electron in the ion space charge field. Here  $\gamma$  is the relativistic factor of the electron beam,  $k_\beta$  and  $k_s$  are the wavenumbers of the pump field (that is, transverse betatron motion due to the ion space charge field) and scattered radiation,  $\phi$  is the phase of the scattered e.m. radiation, and  $a_s$  and  $a_p$  are the normalized amplitude of the scattered e.m. wave and pump wave, respectively.  $a_p$  is related to other variables as  $a_p = ak_s/2\gamma$ , where  $a$  is the electron beam radius.

Assuming a single frequency, the radiation field and pump field evolve according to

$$\frac{da_s}{dz} = \kappa \left\langle \frac{a_p \sin \psi}{\gamma} \right\rangle, \quad (3)$$

$$\frac{da_p}{dz} = -\frac{1}{2} a_s k_\beta \sin \psi, \quad (4)$$

$$\frac{d\phi}{dz} = \kappa \left\langle \frac{a_p}{a_s} \frac{\cos \psi}{\gamma} \right\rangle - \kappa \left\langle \frac{1}{\gamma} \right\rangle, \quad (5)$$

where  $\kappa = \omega_p^2 F / 2k_s c^2$  ( $F$  is the beam filling factor, and  $\langle \dots \rangle$  is the ensemble average. Similar formulations can be found in Refs. [7,8].

Using Eqs. (1)–(5), we calculate numerically the amplified wave amplitude throughout the interaction region and the nonlinear efficiency (or power gain) of the FEL system following the self-consistent evolution of the amplitude and phase of the wave. Radiation propagation is described by a paraxial difference method on a spatial grid on axis with 600 grid points. About 400 test particles loaded with uniformly distributed phases move in  $\gamma, \psi$  space according to Eqs. (1) and (2).

Fig. 1 shows the power gain as a function of the medium plasma density. The electron beam current density is  $10^7$  (A/m<sup>2</sup>), the beam energy  $\gamma = 4$ , and the initial pump strength is 0.8. The results show the exponential gain growth. Next, we investigate the effects of energy spread. For a low oscillation frequency case (i.e. moderate medium plasma density), the system does not exhibit severe gain decrease with increasing energy spread, but for a relatively high oscillation frequency case, the results

show a drastic degradation in gain. In addition, we note that there exists no significant gain for the UV and X-ray regions in contrast to previous studies [7,8], and for higher electron beam energy the gain decreases rapidly.

In an FEL with a plasma background, the electron beam passing through the undulator plasma might begin to thermalize due to various particle–particle and wave–particle interactions. Thus the effective interaction region becomes contracted, preventing coherence of the e.m. wave. To avoid such beam–plasma interaction the electron beam should be bunched and narrower than the skip depth.

In this study, we perform a particle simulation of beam transport along the interaction region for various pump conditions using the one-dimensional Maxwell–Lorentz formulation. The model operating parameters are chosen from on-going (or planned) experiments.

The main results can be summarized as follows:

(1) The ion channel laser may be a promising candidate for producing coherent e.m. radiation in the microwave and submillimeter region.

(2) The electron beam quality is crucial, especially for the high frequency region (high medium plasma density region).

(3) The overall performance depends on the undulator parameter  $a_p$  (pump strength) which is a function of beam radius, beam energy, and betatron frequency. Another important parameter is the medium plasma density.

## Acknowledgement

This work was supported in part by Korea Ministry of Education (Basic Science Research Institute), Korea Science and Engineering Foundation, and Research Division of Dong-A University.

## References

- [1] R.L. Williams, C.E. Clayton, C. Joshi and T.C. Katsouleas, IEEE Trans. Plasma Sci. PS-20 (1993) 156.
- [2] D.A. Whelan and R.L. Stenzel, Phys. Fluids 28 (1985) 958.
- [3] C. Joshi, T.C. Katsouleas, J.M. Dawson, Y.T. Yan and J.M. Slater, IEEE J. Quantum Electron. QE-23 (1987) 1572.
- [4] V.K. Tripathi and C.S. Liu, IEEE Trans. Plasma Sci. PS-18 (1990) 466.
- [5] K.R. Chen and J.M. Dawson, Phys. Rev. Lett. 68 (1992) 29.
- [6] K.R. Chen, T.C. Katsouleas and J.M. Dawson, IEEE Trans. Plasma Sci. PS-18 (1990) 837.
- [7] D.H. Whittum and A.M. Sessler, Phys. Rev. Lett. 64 (1990) 2511.
- [8] D.H. Whittum, Phys. Fluids B 4 (1992) 730.

## Status of the Grumman Compact Infrared FEL ☆

I.S. Lehrman<sup>\*</sup>, J. Krishnaswamy, R.A. Hartley, R. Bohanick, M.F. Reusch

*Grumman Aerospace Corporation, 4 Independence Way, Princeton, New Jersey 08540, USA*

### 1. Introduction

As part of Grumman's ongoing research in particle accelerators, we have designed and are building a Compact Infrared Free-Electron Laser (CIRFEL) for the study of high-brightness electron beams and free-electron lasers. Besides serving as a tool for FEL development, the CIRFEL laboratory, located at Princeton University, will be used in experiments ranging from basic FEL physics and biophysics to chemistry, materials science and medicine.

The CIRFEL is to lase initially in the 8–20  $\mu\text{m}$  range. The pulse format of this FEL is a train of micropulses, 5–10 ps is duration, at a repetition rate of 142.8 MHz. The micropulse energy is in excess of 100  $\mu\text{J}$ . The micropulses comprise a macropulse lasting approximately 10  $\mu\text{s}$ . The macropulse repetition rate is 10 Hz, thus the average power of the FEL is on the order of 1.5 W.

### 2. System description

The CIRFEL consists of the following system components: (1) a high-brightness photocathode electron gun, (2) a photocathode illumination laser, (3) a 30 MW S-band RF source, (4) the beam transport system, (5) the FEL wiggler, (6) the FEL optical cavity, and (7) the associated support hardware subsystems. Fig. 1 shows the layout of the CIRFEL beamline.

To allow for flexibility and possible future expansion, the beamline components are mounted on a pair of rails. The rails allow the axial positions of the beamline elements to be easily adjusted. The rails are mounted to non-magnetic optical tables which allows additional optics and diagnostics to be fixed to the tables with standard mounts.

The accelerator for the CIRFEL is a photocathode electron gun. The gun is only 20 cm long and produces electron beams with energies up to 9.3 MeV. The gun consists of  $3\frac{1}{2}$  cells operated in the  $\pi$ -mode phasing. The

gun is fed from a single waveguide which couples power directly to cells 2 and 3. Power is aperture coupled from cell 2 to cell 1 and from cell 3 to cell 4.

The gun has been modeled extensively with the MAGIC [1] particle-in-cell code. These results indicate that the beam emittance (RMS) will be between 2.7 and 5.2  $\pi$  mm-mrad depending upon the launch phase. The peak electric field at the cathode will be between 60 and 80 MV/m.

The photocathode, which is contained in the first cell, is a 6 mm diameter disc of Mg. Initial experiments were conducted with a  $\text{LaB}_6$  cathode which was externally heated to 1350°C to remove oxides from the surface. Experimentally, we found that the  $\text{LaB}_6$  had to be kept to about 800°C to maintain its quantum efficiency. This complicated the operation of the gun (outgassing and arcing) and it was decided to switch to a Mg cathode. Initial results with the Mg cathode indicate that it is far superior to the  $\text{LaB}_6$  and does not require conditioning. Approximately 7  $\mu\text{J}$  of UV (262 nm) is required to release 1 nC of charge [2].

Downstream of the photocathode gun, we are installing a two cell booster cavity to increase the beam energy to 14 MeV. This cavity is identical to the central two cells of the gun.

The photocathode laser for the CIRFEL gun consists of a ND:YLF mode-locked oscillator, a pulse slicer, two double-passed stages of amplification, and harmonic generation. The mode-locked oscillator is a Lightwave Electronics' diode-pumped unit operating at 142.8 MHz. The oscillator produces 7 ps IR pulses (1047 nm) at an average energy of 200 mW.

The oscillator was integrated into a macropulse amplifier by Continuum. A pulse slicer is used to slice out a 10  $\mu\text{s}$  portion of the beam. The beam is then double-passed through a 7 mm flash lamp-pumped ND:YLF amplifier. After spatially filtering the beam, the beam is passed through another 7 mm ND:YLF amplifier. Second and fourth harmonic generation crystals are used to produce 524 nm and 262 nm radiation. The laser is capable of producing in excess of 16  $\mu\text{J}$  per micropulse at 262 nm.

The RF system consists of a 700 W S-band amplifier which feeds a 30 MW ITT 2960 klystron. The modulator for the klystron has a 13 stage pulse forming network

<sup>\*</sup> This work is supported by Grumman Aerospace Corporation.

<sup>\*</sup> Corresponding author. Tel. +1 609 520 1808, fax +1 609 520 1810, e-mail lehrman@grump.com.



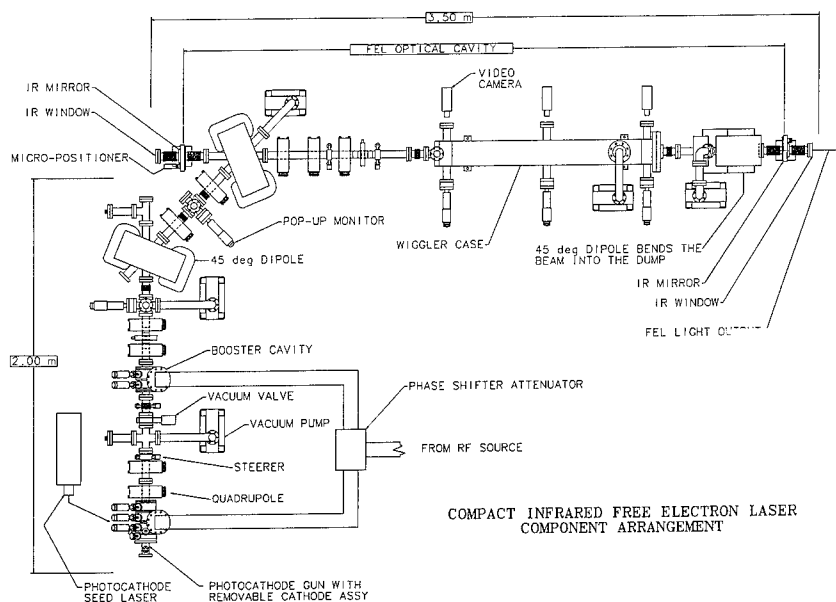


Fig. 1. Layout of the CIRFEL beamline.

(PFN) which produces a video pulse of 12  $\mu\text{s}$  (FWHM). The klystron has a flattop output of 10  $\mu\text{s}$ . In order to correct for the PFN ripple, we will be implementing feed-forward correction for both the RF amplitude and phase.

The TRACE3D [3] and PARMELA [4] beam optics/dynamics codes were used to model the CIRFEL beamline. A quadrupole doublet is used to focus the beam from the output of the gun. An achromatic bend was used to allow for mirror access for the FEL optical cavity. Depending upon the longitudinal phase space distribution of the beam, the achromat can act to compress the longitudinal length of the beam, thus increasing the peak current of the bunch.

A quadrupole triplet is used to focus the beam into the wiggler. In order to reduce horizontal defocusing effect of the 45° bending magnets, the poles were cut with 22.5° entrance angles. Once a TRACE3D solution was found for the beamline, the PARMELA code was used to determine the effect of space charge. PARMELA simulations indicate there is no significant space charge induced emittance growth for 1 nC bunches. Space charge will cause some slight changes in the effective focal lengths of some of the quadrupoles.

Initial experiments will be carried out with a 1.36 cm period, 73 period permanent magnet wiggler loaned from the Los Alamos National Laboratory. The wiggler gap is 7 mm and the RMS wiggler parameter,  $A_w = 0.164$ . Our calculations indicated that the single pass gain should be in excess of 100%.

The optical cavity is a near concentric, asymmetric stable cavity, with a Rayleigh range of  $\sim 0.5$  m. The cavity utilizes multilayer dielectric coated ZnSe mirrors

which have been designed to be used over a wide wavelength range, especially in the 8–12  $\mu\text{m}$  range. Since the mirrors are in vacuum, ZnSe output windows are used at the vacuum interface.

### 3. Status

As of August 1994, we installed all of the beamline components up to the first dipole and are awaiting delivery of the dipole beam boxes. The remaining beamline components and FEL optics will be installed in September. We have begun to characterize the photocurrent at the first phosphor monitor and expect to have an emittance measurement made by the end of September. Soon after that we will begin transporting the beam to the wiggler.

### References

- [1] G.D. Warren, L. Ludeking, J. McDonald, K. Nguyen and B. Goplen, Proc. Conf. on Computer Codes and the Linear Accelerator Community, Los Alamos National Laboratory, Jan. 22–25, 1990, ed. Richard Cooper, LA-11857-Z (1990), p. 57.
- [2] P.G. O'Shea, these Proceedings (16th Int. Free Electron Laser Conf., Stanford, CA, USA, 1994) Nucl. Instr. and Meth. A 358 (1995) 36.
- [3] K.R. Crandall, Los Alamos National Laboratory report LA-11054-MS (1987).
- [4] K.R. Crandall and L. Young, in: The Compendium of Computer Codes for Particle Accelerator Design and Analysis, Eds. H. Deaven and K.C. Chan, Los Alamos Nat. Lab report LA-UR-90-1766 (1990) p. 137.



ELSEVIER

## The Israeli tandem electrostatic accelerator FEL – status report

A. Arensburg<sup>a</sup>, M. Cohen<sup>a,\*</sup>, M. Draznin<sup>a</sup>, A. Eichenbaum<sup>a</sup>, A. Gover<sup>a</sup>, Y. Pinhasi<sup>a</sup>,  
V. Shternghartz<sup>a</sup>, I.M. Yakover<sup>a</sup>, J. Sokolovsky<sup>b</sup>, B. Mandelbaum<sup>c</sup>, A. Rosenberg<sup>c</sup>,  
J. Shiloh<sup>c</sup>, G. Hasak<sup>d</sup>, L.A. Levin<sup>d</sup>, O. Shahal<sup>d</sup>, M. Shapira<sup>e</sup>, V. Granatstein<sup>f</sup>

<sup>a</sup> Department of Physical Electronics, Tel-Aviv University, Tel-Aviv, Israel

<sup>b</sup> Weizmann Institute of Science, Rehovot, Israel

<sup>c</sup> Rafael, Haifa, Israel

<sup>d</sup> NRC, Beersheva, Israel

<sup>e</sup> Institute of Applied Physics, Nizhny Novgorod, Russian Federation

<sup>f</sup> University of Maryland, College Park, Maryland, USA

The development of the tandem Van de Graaff FEL was continued. The FEL is designed to operate at millimeter wavelength (100 GHz). The basic parameters of the FEL are given in Table 1.

During the last year most of the components, quadrupoles, power supplies, vacuum components etc. have been delivered and are being tested before installation in the accelerator. One of the two 3 MV acceleration (and deceleration) tubes was removed and replaced by a smaller 3 in. tube, on which the quadrupole lenses will be mounted [1]. This modification limits the acceleration voltage to a maximum of 3 MV but enables better focusing of the e-beam at the entrance to the wiggler. The voltage limit is of no concern since the FEL gain calculations show best gain near 1.5 MV at a frequency of 100 GHz.

We plan to perform beam diagnostics at several locations along the beam using fluorescent screens and CCD cameras. Two screens have been installed, one in the injection system and one at the HV terminal. The first screen can be readily observed with a CCD camera in order to determine the beam radius near the entrance to the accelerator tube. To observe the screen at the terminal, an optical fiber communication system will transmit the video signal from the high voltage terminal to a “frame grabber” as shown in Fig. 1. At least one more screen will be installed at the exit of the accelerator tube in order to measure the beam radius precisely at that point.

This data is important in obtaining good simulation of the beam transport through the quadrupoles; previous simulation results were based on estimates of the beam radius and of the divergence angle at the exit from the accelerator. The numerical simulations were made using TRANSPORT [2] and TRACE-3D [3] codes for several arrange-

ments of the quads. Mostly the equispaced and two doublets arrangements yielded satisfactory optimal transport conditions at 1.5 MV accelerating voltage, normalized emittance of 50 mm · mrad and currents up to 0.5 A. It was found that for radii between 6 and 8 mm and divergence angles from 0 to 6 mrad at the entrance to the free drift region (where the quadrupoles are mounted), with optimal excitation of the quads, the beam can be focused to a 1 mm radius (see Fig. 2). We expect to confirm these results with the fluorescent screens as soon as the CCD camera is installed at the terminal.

We expect to install the quadrupole magnets before the end of the summer. The next stage will be to reach optimal transport conditions. The shape of the waveguide requires a focusing of the e-beam to 1–3 mm radius. This will be determined using either scanning wires or fluorescent screens as mentioned earlier. Once this stage is accomplished we expect to have the FEL operational within a few months.

A mm-wave resonator using curved parallel plate waveguide and two wave splitters was built. The wave splitter is a segment of an overmoded rectangular waveguide, which

Table 1  
FEL Parameters

|                      |                           |
|----------------------|---------------------------|
| Accelerator          |                           |
| Electron beam energy | $E_k = 1\text{--}2.5$ MeV |
| Beam current         | $I_0 = 0.5\text{--}1$ A   |
| Wiggler              |                           |
| Magnetic induction   | $B_w = 2\text{--}3$ kG    |
| Period               | $\lambda_w = 4.4$ cm      |
| Number of periods    | $N_w = 20$                |
| Waveguide            |                           |
| Type                 | parallel curved plates    |
| Mode                 | TE <sub>01</sub>          |
| Operating frequency  | ~ 100 GHz                 |

\* Corresponding author. Tel. +972 3 640 8148, fax +972 3 642 3508, e-mail moshec@eng.tau.ac.il.

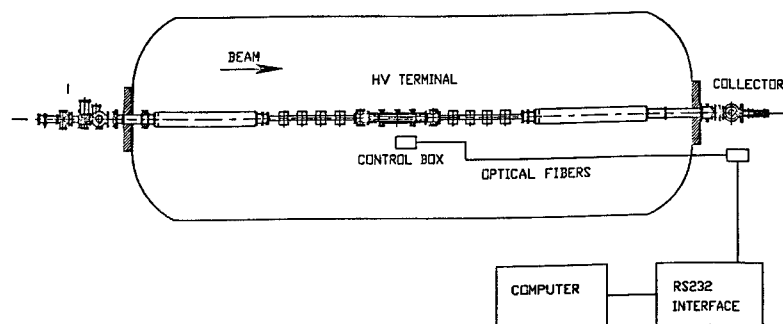


Fig. 1. Modified design of the tandem FEL including scheme of the communication system to the HV terminal.

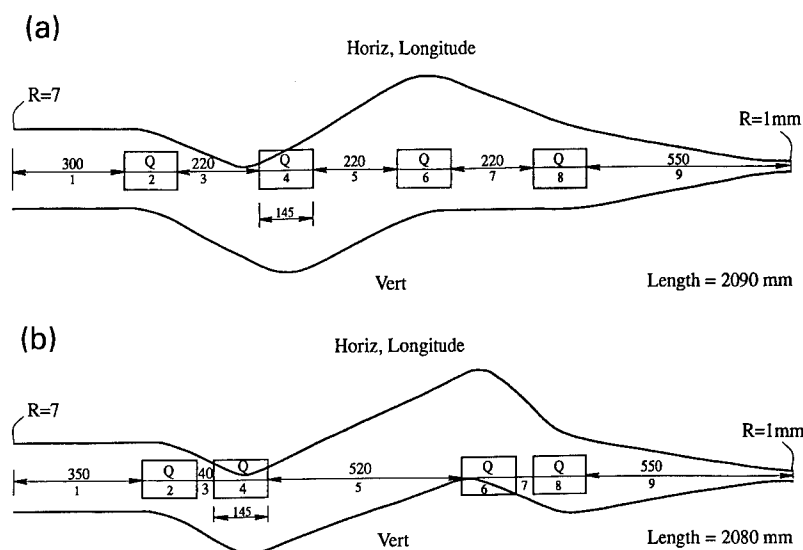


Fig. 2. TRACE-3D simulation results of e-beam transport using quadrupole lenses arranged in (a) equispaced and (b) two doublets configurations.

is connected at one end to the parallel plate waveguide, and is shorted at the other end by a metal plate with an aperture in the center for e-beam passage [1].

Measurements of waveguide losses were carried out in

the 98–102 GHz frequency band. Minimal attenuation, of the order of 0.1 dB, was observed at a frequency of 100.9 GHz. Measurements of the wave splitter's reflection coefficient were also made. The results of these measurements show that diffraction losses of the circular aperture are negligible as was predicted by theory [4].

We plan to couple out the mm-wave radiation generated at the HV terminal using a quasi-optical mirror transmission line as illustrated schematically in Fig. 3. Preliminary consideration, based on Gaussian beam optics theory show that it will be sufficient to use nine mirrors (three plane mirrors, two elliptical mirrors and two doublets of cylindrical mirrors).

## References

- [1] M. Cohen et al., Nucl. Instr. and Meth. A 341 (1994) ABS 58.
- [2] TRANSPORT, CERN-80-04.
- [3] K.R. Crandwall, TRACE-3D, revised by D.P. Rasthoi, Los-Alamos (1990).
- [4] I.M. Yakover, Y. Pinhasi and A. Gover, these Proceedings (16th Int. Free Electron Laser Conf., Stanford, CA, USA, 1994) Nucl. Instr. and Meth. A 358 (1995) 323.

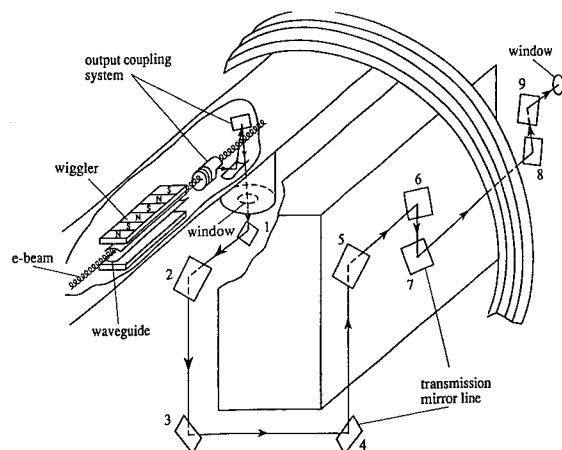


Fig. 3. Quasi-optical transmission line for radiation outcoupling.



ELSEVIER

## Application of a mm-wave free electron laser to the study of high- $T_c$ superconductors

E. Giovenale <sup>a,\*</sup>, V. Boffa <sup>b</sup>, P. Dore <sup>c</sup>, A. Doria <sup>a</sup>, G.P. Gallerano <sup>a</sup>, M.F. Kimmitt <sup>d</sup>,  
R. Trippetti <sup>c</sup>, I. Spassovsky <sup>a,1</sup>

<sup>a</sup> ENEA, INN-FIS, P.O. Box 65, 00044 Frascati, Italy

<sup>b</sup> ENEA, ERG-FUS, P.O. Box 65, 00044 Frascati, Italy

<sup>c</sup> Physics Department, Università di Roma "La Sapienza", 00185 Rome, Italy

<sup>d</sup> Physics Department, University of Essex, Colchester, CO4 3SQ, UK

The discovery of high- $T_c$  superconductors has led to much research on the optical properties of these materials [1]. Reflection and transmission measurements carried out below the critical temperature  $T_c$  in the mm-wave and far infrared region, in particular, can show evidence of the superconducting energy gap, as shown in the pioneering works of Glover and Tinkham [2] on conventional superconductors. In general, information on the frequency-dependent complex conductivity can be derived from spectroscopic measurements in the infrared region.

In studying the optical properties of high- $T_c$  superconductors, optical conductivity  $\sigma(\nu)$  (i.e. the real part of the complex conductivity) is usually obtained from Kramers–Kronig (K–K) transformations of reflectance spectra  $R(\nu)$ . In the case of thin films deposited on transparent substrates only reflectance measurements are possible. At low frequencies,  $\sigma(\nu)$  can thus be strongly affected [3] by the extrapolations employed to extend the measured spectra down to zero frequency. Therefore, an accurate determination of the optical conductivity  $\sigma(\nu)$  at low frequencies ( $\nu < 100 \text{ cm}^{-1}$ ) is still an open problem.

In studying the low frequency behaviour of  $\sigma(\nu)$ , we extended far infrared measurements down to frequencies as low as possible. Reflectance  $R(\nu)$  and transmittance  $T(\nu)$  spectra of thin  $\text{Y}_1\text{Ba}_2\text{Cu}_3\text{O}_{7-x}$  (YBCO) films deposited on MgO have been measured down to  $15 \text{ cm}^{-1}$  by using a conventional Michelson interferometer equipped with a silicon bolometer [4]. We remark that low-frequency transmittance measurements gave more reliable results than those obtained through reflectance measurements. However, accurate transmittance measurements require a transparent substrate and a powerful source; indeed, the trans-

mission of a high-quality film, even if of a thickness of the order of 50 nm, is very low.

We have in program mm-wave and far infrared transmission and reflection measurements on thin YBCO films deposited on  $\text{LaAlO}_3$ . This substrate allows epitaxial film growth and is transparent up to about  $100 \text{ cm}^{-1}$ , as shown by recent preliminary results (Fig. 1). High-quality films will be prepared by laser ablation at ENEA (ERG-FUS) [5]. Far infrared measurements will be made down to  $15 \text{ cm}^{-1}$  at the Physics Department of the Rome University, by using the above mentioned apparatus. For mm-wave measurements, the ENEA Compact FEL facility will be employed as radiation source, owing to its high peak power and continuous tunability features [6]. Preliminary measurements have been carried out on the substrate in order to choose the better experimental configuration and to confirm the data obtained with a conventional equipment.

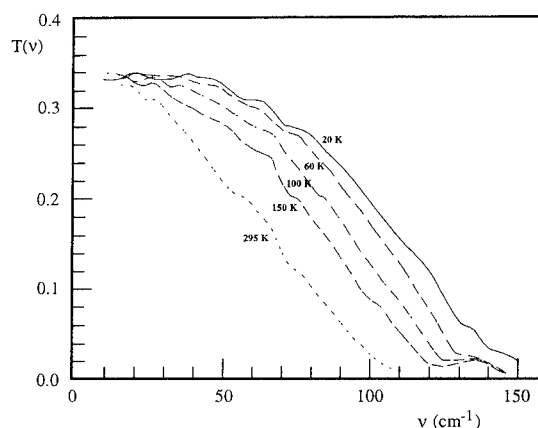


Fig. 1.  $\text{LaAlO}_3$  transmittance for  $T = 295, 150, 100, 60$  and  $20 \text{ K}$ . Sample thickness =  $0.5 \text{ mm}$ .

\* Corresponding author. Tel. +39 6 94001, fax +39 6 9400 5334, e-mail giovenale@efr419.enea.it.

<sup>1</sup> ENEA-ICTP Fellow.

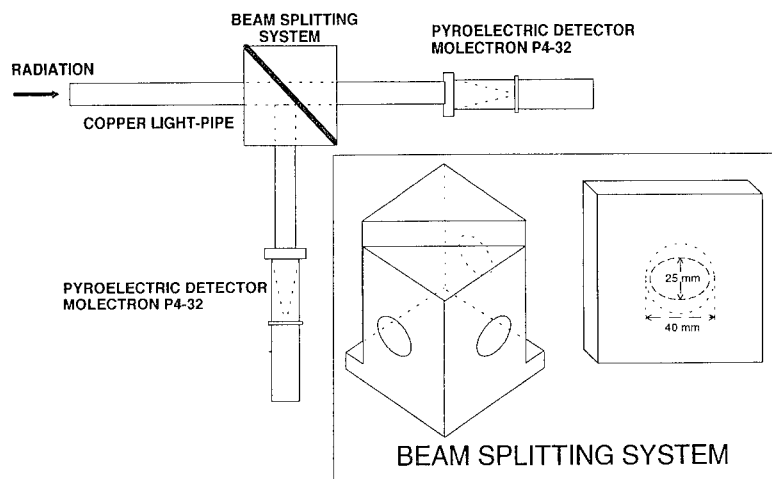


Fig. 2. Proposed experimental layout for mm-wave measurements.

The main difficulties of the measurement at low frequency arise from the fact that the sample size is comparable with the wavelength of the radiation. It is thus necessary to design an experimental apparatus in order to avoid diffraction and interference problems. Moreover the refraction index of the substrate has been measured to be about 4.5. This value, together with a sample thickness of 0.5 mm, can cause Fabry–Perot interference effects in the sample at wavelengths between 2 and 3 mm. Preliminary measurements have been carried out in this wavelength range ( $3\text{--}5\text{ cm}^{-1}$ ), and interference effects in the sample have been identified as the most annoying source of systematic errors. New measurements have been planned using coherent spontaneous emission radiation [6,7]. This broad band emission will be used, together with a Fabry–Perot spectrometer, to obtain a continuous spectrum for the sample transmission, and the interference fringes will be eliminated with a proper procedure. On the basis of the above results, the experimental setup shown in Fig. 2 has been designed. A waveguide system, using a directional coupler to measure simultaneously transmittance and reflectance, can also be considered for this experiment.

The use of the compact FEL facility, which will extend operation up to  $400\text{ }\mu\text{m}$  ( $25\text{ cm}^{-1}$ ) in 1995, together with a conventional far infrared apparatus, will allow the user to

cover the complete low-frequency range, thus obtaining reliable information on the low-frequency conductivity of high- $T_c$  materials.

## References

- [1] D.B. Tanner and T. Timusk, Optical properties of high- $T_c$  superconductors, in: *Physical Properties of High Temperature Superconductors*, ed. D.M. Ginsberg (World Scientific, Singapore, 1992).
- [2] R.E. Glover and M. Tinkham, *Phys. Rev.* 104 (1956) 844.
- [3] D. Miller and P.L. Richards, *Phys. Rev. B* 47 (1993) 12308.
- [4] S. Cunsolo, P. Dore, S. Lupi, R. Trippetti, C.P. Varsamis and A. Sherman, *Physica C* 211 (1993) 22; P. Dore, A. Paolone, S. Tatoni, C.P. Varsamis, V. Boffa, C. Romeo, S. Barbanera and F. Murtas, *Int. J. of IR&MM waves*, in press.
- [5] C. Romeo, V. Boffa, S. Bollanti, C. Alvani, M. Penna, S. Barbanera, P. Castrucci, R. Leoni and F. Murtas, *Physica C* 180 (1991) 77.
- [6] F. Ciocci, R. Bartolini, A. Doria, G.P. Gallerano, E. Giovenale, M.F. Kimmitt, G. Messina and A. Renieri, *Phys. Rev. Lett.* 70 (1993) 928.
- [7] A. Doria, R. Bartolini, J. Feinstein, G.P. Gallerano and R.H. Pantell, *IEEE J. Quantum Electron.* QE-29 (1993) 1428.



ELSEVIER

## Commissioning the FELI linac and IR-FEL facilities

T. Tomimasu <sup>a,\*</sup>, Y. Morii <sup>b</sup>, E. Ohshita <sup>a</sup>, S. Abe <sup>a</sup>, S. Nishihara <sup>a</sup>, A. Koga <sup>a</sup>,  
Y. Miyauchi <sup>a</sup>, A. Zakou <sup>a</sup>, E. Nishimura <sup>a</sup>, K. Saeki <sup>a</sup>, A. Kobayashi <sup>a</sup>, M. Yasumoto <sup>c</sup>,  
E. Tongu <sup>a</sup>, A. Nagai <sup>a</sup>

<sup>a</sup> Free Electron Laser Research Institute, Inc. (FELI), 4547-44, Tsuda, Hirakata, Osaka 573-01, Japan

<sup>b</sup> Toshiba Corp. Accelerator Group, 1-1-6 Uchisaiwai-cho, Chiyoda-ku, Tokyo 100, Japan

<sup>c</sup> Osaka National Research Institute, 8-31 Midorigaoka, Ikeda, Osaka 563, Japan

The FELI linac is operated in three pulse operation modes of 24  $\mu$ s, 12.5  $\mu$ s and 0.5  $\mu$ s [1]. At this stage, the linac consisting of a 6-MeV injector and three accelerating waveguides installed in April 1994 can withstand 26 MW rf pulses of 10  $\mu$ s duration from a klystron 3729. This klystron has been modified from a klystron E3712 (4  $\mu$ s, 80 MW) for long-pulse operation of 24  $\mu$ s, 25 MW and 12.5  $\mu$ s, 36 MW [2,3]. The operation of an FEL demands outstanding stability of the rf power. Therefore, the flatness of our klystron modulator pulses is improved to be 0.067% even at 24- $\mu$ s duration [4]. The first beam acceleration has been achieved on May 30. In the end of July the linac beam was sent to a 80-MeV beam transport (BT) line using S-type BT systems (22.5° bend  $\times$  2) [5] for the legal inspection of our radiation protection system. In August the beam has been sent to a 30-MeV BT line using S-type BT systems for a 5.4- $\mu$ m FEL experiment.

The layout of the 6-MeV electron injector is shown in Fig. 1. It is composed of a 150-kV thermionic triode gun, a 714-MHz prebuncher, and a 2856-MHz standing wave type buncher. The gun is a Pierce type gridded gun with a thermoelectronic dispenser cathode (EIMAC Y646B model). The gun emits 500 ps pulses of 2.3 A at frequencies of 22.3125 and 178.5 MHz. These pulses are compressed by the injector at 100 A  $\times$  7 ps. This target has not been achieved yet. The grid pulser (Kentech Instruments, Ltd., England) has two pulsers of 178.5 MHz and 22.3125 MHz. However, the 178.5 MHz pulser does not work well at this moment; the 22.3125 MHz pulses are sent to the 30-MeV BT line. The 714-MHz prebuncher made of stainless steel acts as a subharmonic buncher (SHB). The SHB will be powered by a modified klystron 1AV88R manufactured by Toshiba Corp.

The 2856-MHz buncher is of a standing wave type

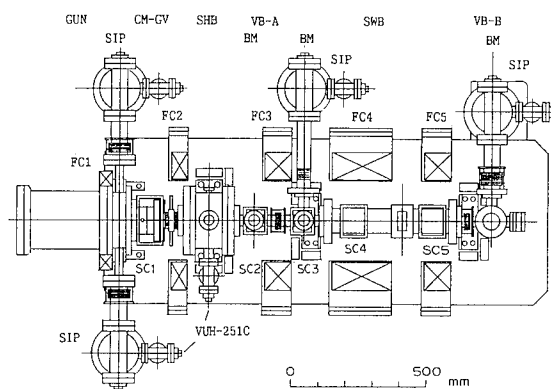


Fig. 1. The layout of the 6-MeV electron injector.

(SWB). The peak electric field will be around 14 MV/m for an rf input of 2 MW. From the Kapchinsky-Vladimirsky equation, an axial field  $B_s$  of a focusing solenoid

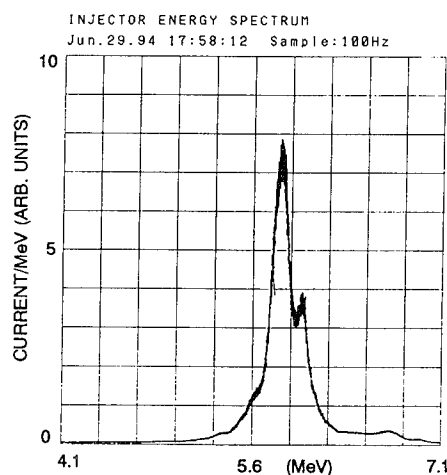


Fig. 2. Energy spectrum of the injector beam measured with the 2-mm slit.

\* Corresponding author. Tel: +81 720 96 0414, fax +81 720 96 0421.

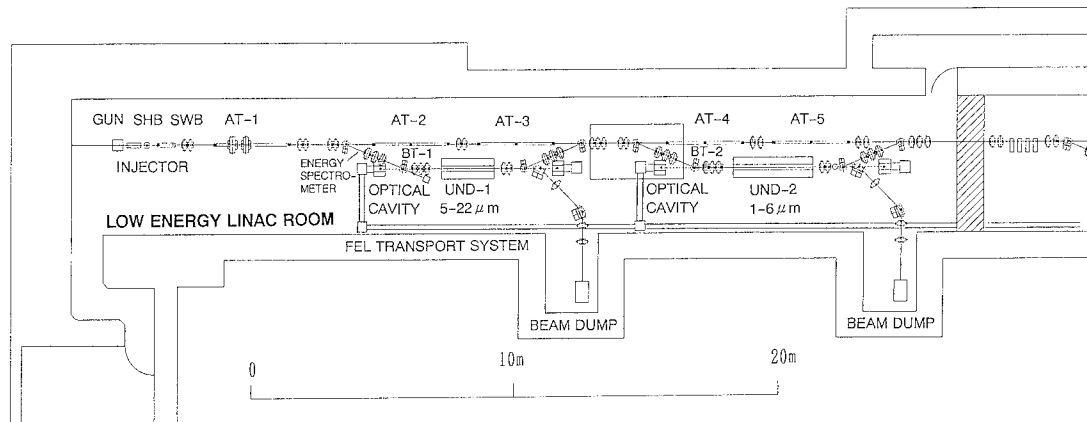


Fig. 3. The layout of the FELI 80-MeV linac and IR-FEL facilities.

keeping a beam radius  $r$  constant from the SHB to the SWB is given by

$$B_s = 3.69 \times 10^{-5} (I/\beta\gamma)^{1/2} / r, \quad (1)$$

where  $I$  is the peak current of bunched beam,  $\beta = v/c$  is the nominal particle velocity, and  $\gamma$  is the Lorentz factor. The maximum focusing field is designed to be about 0.19 T near the entrance of SWB. The diameter ( $2r_b$ ) of the injector beam was observed to be less than 2 mm with a 2-mm slit and a fluorescent screen at the outlet. The energy spectra of the injector beam were also measured with a 90°-bending magnet. Fig. 2 is a typical beam spectrum measured with the 2-mm slit. The main peak has passed through the slit, compared with the spectrum measured without the 2-mm slit. The energy spread (FWHM) is 150 keV (2.5%) for a 5.8-MeV electron beam as shown in Fig. 2. To monitor the beam size and the position in the FELI linac, screen monitors were installed at the outlet of the buncher and at the inlet and the outlet of each accelerating waveguide. The beam emittance ( $\varepsilon_n = \gamma r_o \theta$ ) is estimated to be  $12 \times 10^{-6}$  m · rad using two screen monitors installed between the injector and the first accelerating waveguide, where the two monitors are 0.96 m apart.

The layout of the FELI 80-MeV linac and IR-FEL facilities is shown in Fig. 3. Two S-type BT lines for 30-MeV and 80-MeV beams were installed in March and two undulators [6] were installed in May. However, the installation of an optical cavity ( $L_c = 6.718$  m) and transport system [7] for the 30-MeV BT line and the undulator-I ( $\lambda_w = 3.4$  cm,  $N = 58$ ,  $L_w = 2$  m,  $K_{\max} = 1$ , gap length  $\geq 20$  mm) was delayed from June to July. On August 2 a 32.2-MeV beam has been sent to the 30-MeV BT line where the 2-m long undulator is installed. Using five screen monitors installed in the undulator line, the beam size and position are adjusted along the axis so as to pass through a narrow vacuum chamber inserted to the 2-m long undulator-I. The beam passing through the undulator is focused and sent to a water dump using two 45°-bending

magnets. The water dump is used as a current monitor. Using variable slit systems installed in the 30-MeV BT line, the first 22.5°-bending magnet and a water absorber are used as an energy spectrometer. The energy spread (FWHM) is about 290 keV (0.9%) for a 32.2-MeV electron beam. The BT-1 system can transport the linac beam within an energy spread of 1.5% to the water dump. The present parameters set for a 5.4 μm FEL experiment are as follows: electron beam is 32.2 MeV, 22.3125 MHz micropulses in 10-Hz macropulses of 12.5-μs duration. The conditionings for the undulator-I beam line in beam current, size and position have just started. The rf ageing for the linac is also not enough, since the linac withstands only 25.6 MW rf pulses of 12.5 μs duration from the klystron 3729 that can supply 36 MW rf pulses of 12.5 μs duration. Therefore, it will need more than thirty days to achieve the full power operation. At the end of August another optical cavity ( $L_c = 8.4$  m) and transport system for 80-MeV BT line and undulator-II ( $\lambda_w = 3.8$  cm,  $N = 78$ ,  $L_w = 3$  m,  $K_{\max} = 1.4$ , gap length  $\geq 20$  mm) is installed. A 1.5-μm FEL experiment will be started in December with the undulator-II.

## References

- [1] T. Tomimasu et al., Nucl. Instr. and Meth. A 331 (1993) 175.
- [2] Y. Morii et al., Proc. 9th Symp. on Accelerator Science and Technology, KEK, Aug. 25–27, 1993, p. 175.
- [3] S. Abe et al., Proc. 19th Linear Accelerator Meeting, JAERI, Japan, July 20–22, 1994 p. 225.
- [4] E. Ohshita et al., *ibid.*, p. 242.
- [5] Y. Miyauchi et al., Proc. 9th Symp. on Accelerator Science and Technology, KEK, Aug. 25–27, 1993, p. 416.
- [6] A. Kobayashi et al., Proc. 6th Int. Symp. on Advanced Nuclear Energy Research, JAERI, March 23–25, 1994, to be published.
- [7] K. Saeeki et al., these Proceedings (16th Int. Free Electron Laser Conf., Stanford, CA, USA, 1994) Nucl. Instr. and Meth. A 358 (1995) ABS 56.



ELSEVIER

## Status of the Stuttgart Raman free-electron laser project

G. Renz \*, G. Spindler

*Institut für Technische Physik, German Aerospace Research Establishment (DLR), Pfaffenwaldring 38-40, 70503 Stuttgart, Germany*

Operation of a millimeter-wave free-electron laser was carried out by using a 600 kV voltage pulse of 100 ns duration. The accelerator consists of a Marx generator, a water filled Blümlein pulse line, and a cold cathode vacuum diode which is immersed in the guide field (Fig. 1). The electron beam current can be varied up to a couple of hundred amperes depending on the cathode-anode distance ( $\approx 1$  cm) and the guide field strength. The performance of the vacuum diode was simulated with the SLAC e-gun code [1]. It showed a radial increase of the electron density for the innermost electrons that were used for the FEL interaction. The calculation of the perveance of the vacuum diode resulted in approximately  $40 \mu\text{perv}$ . The helical wiggler has a total number of 40 periods ( $\lambda_w = 2$  cm) with an adiabatic entrance/exit of 7 periods. The maximum transverse magnetic field of the wiggler is 0.15 T, and the maximum guide field is 2.5 T. The FEL allows performance in the group-I orbit and group-II orbit regimes.

The energy and pulse length of the radiation is measured with a pyroelectric energy meter ("Molelectron", PD J50HP) and a Schottky diode ("Millimeter Products",

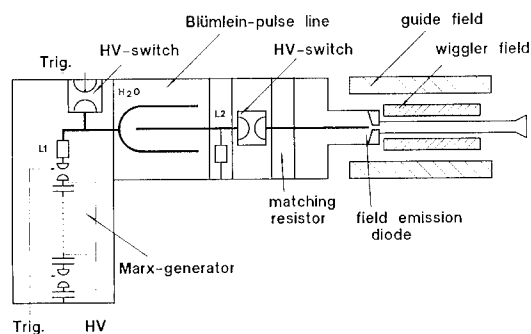


Fig. 1. Schematic of the experiment.

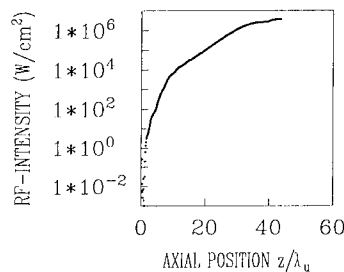


Fig. 2. Simulation of the output power versus axial position for the  $\text{TE}_{11}$  mode.

WM). The measured energy of the radiation pulses reached values up to 100 mJ. The determination of the energy of the electrons was accomplished in a way that the magnetic field parameters of the FEL were set to match the magnetoresonance condition, marked by a breakdown of the electron current at the beginning of the constant part of the wiggler. Simulating the electron dynamics for these parameters, the energy of the electrons could be determined.

In order to simulate the power of the radiation, a self-consistent description of the FEL using single-particle dynamics and radiation wave equation were used [2]. Fig. 2 shows the output power versus axial position. At the end of the wiggler the output power reaches a few  $\text{MW}/\text{cm}^2$  which is consistent with the experimental result.

In future experiments the determination of the output frequencies with an array of bandpass filters between 70 and 170 GHz should demonstrate the FEL and cyclotron lines (side-bands).

### References

- [1] W.B. Herrmannsfeldt, Electron Trajectory Program, Stanford Linear Accelerator Center (1979).
- [2] W.B. Colson and S.K. Ride, Phys. Lett. 76 (1980) 379.

\* Corresponding author.





ELSEVIER

# The optical resonator for the FELICITA I experiment <sup>☆</sup>

D. Nölle <sup>\*</sup>, A. Geisler, M. Ridder, C. Schellnock, T. Schmidt, S. Tammen, K. Wille

*Institute for Acceleratorphysics and Synchrotronradiation, University of Dortmund, 44221 Dortmund, Germany*

## 1. Introduction

FELICITA I (FEL In a Circular Test Accelerator) is the first FEL experiment at the 1.5 GeV storage ring DELTA at the University of Dortmund [DELTA Group, DELTA, a status report, University of Dortmund (1990)]. The facility DELTA will start operation at the end of this year. Using an electromagnetic undulator providing FEL and optical klystron operation modes, FELICITA I will cover the wavelengths from the visible down to the UV. This paper will discuss the design of the optical cavity and first tests for alignment and the feedback system.

## 2. Design of the optical cavity

The FELICITA I experiment is placed in one of the 20 m long straight sections of DELTA. In order to have a rather short optical cavity, 4 dipoles are used to form a kind of bypass [1]. The length of the optical cavity corresponds to 4 bunch operation of DELTA, yielding a distance from mirror to mirror of 14.4 m. Because of the small angle ( $3^\circ$ ) between electron and laser beam due to the form of the bypass, the complete optical cavity is placed inside the radiation shielding of DELTA. Therefore it has to be remote controlled. As the undulator is also used for synchrotron radiation experiments, at least the downstream mirror has to be removable. Therefore a compact mirror holder was developed [2] with both rough and fine alignment integrated on the holder inside the vacuum. Fine tuning is done by piezo actuators, rough alignment by Inchworm steppers. <sup>1</sup> To remove the mirror from the optical cavity it is pulled up using a bellow system. In the upper position an exchange of the mirrors is possible without breaking the vacuum. The design of the cavity is shown in Fig. 1 and the parameters are listed in Table 1.

## 3. Feedback system for mirror position control

As all components of the optical cavity have to be inside the radiation shielding, the cavity must be completely computer controlled. Therefore it is easy to combine the monitoring part of the cavity and the actuators to form a feedback system.

Each mirror of the optical cavity has its own system close to the design of Shewell [3]. It consists of a modified Michelson interferometer for length control and a position sensitive diode to detect angular movements. The feedback system is placed behind each mirror. The light from a red He–Ne laser hits the back of the mirror, reflected by a dielectric layer between the substrate of the mirror and the reflecting coating optimized for the FEL resonant wavelength. Such a system allows control of one of the mirrors without correlation to the other one. It has the advantage of being mounted on a single optical table. Therefore, it is more stable and reliable than a system with optical path lengths on the order of the length of the optical cavity, which cannot be placed on a single optical table.

## 4. Alignment of the optical cavity

The procedure consists of four steps: 1) localization of the axis of spontaneous undulator radiation; 2) directing an external laser to that axis; 3) adjusting the optical axis of the resonator with respect to the laser beam; 4) further optimization using the spontaneous undulator radiation.

This alignment procedure is tested using a test cavity. The experimental setup of the alignment system is shown in Fig. 2.

In the first step an optical axis of the optical cavity is fixed using two diaphragms  $D_1$ ,  $D_2$  adjusted to the axis of the spontaneous radiation (simply simulated by a laser beam up to now). Fixing the lateral position of the axis is possible with an accuracy of 0.3 mm utilizing the Airy fringes produced by the circular apertures. The angular accuracy is about  $\pm 30 \mu\text{rad}$ . This is done without the cavity mirrors.

In a second step a red 10 mW He–Ne laser with a waist of  $\omega_1 = 0.6 \text{ mm}$  is adjusted through the diaphragms and is

<sup>☆</sup> This work is supported by the Bundesministerium für Forschung und Technologie under contract 05 3PEAAI 0.

<sup>\*</sup> Corresponding author. Tel. +49 231 755 5382, fax +49 231 755 5383, e-mail dirk@marvin.physik.uni-dortmund.de.

<sup>1</sup> Trademark of Burleigh.

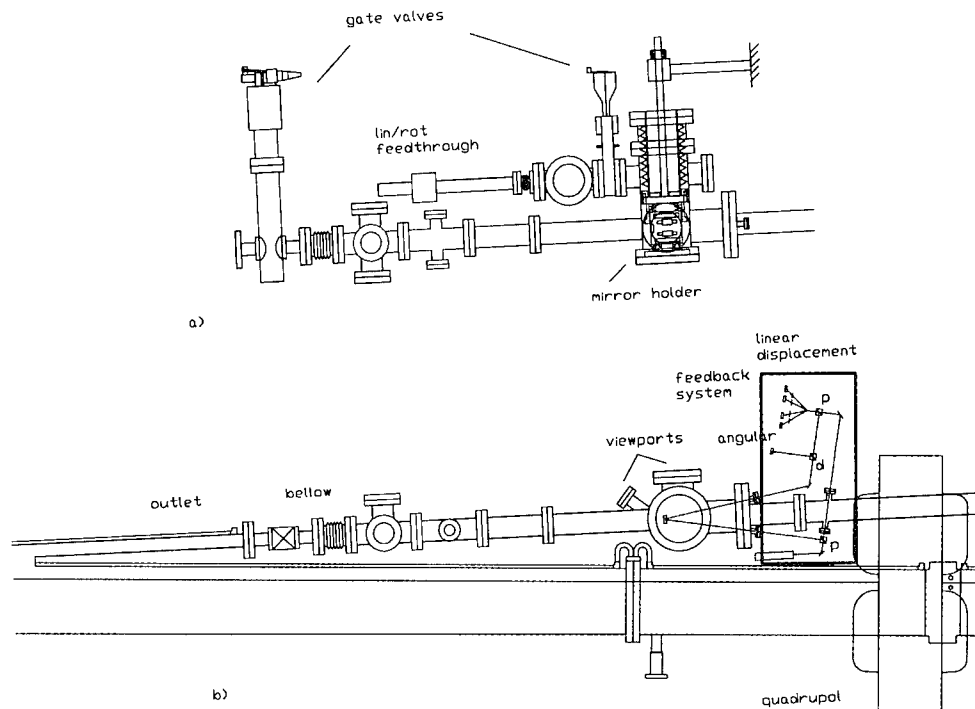


Fig. 1. Top (b) and sideview (a) of the downstream side of the optical cavity. The optical resonator is symmetric with respect to the center of the undulator. The mirror holder can be pulled up using the bellow system in order to pass undulator radiation to user experiments. In the upper position the mirror can be exchanged without breaking the vacuum.

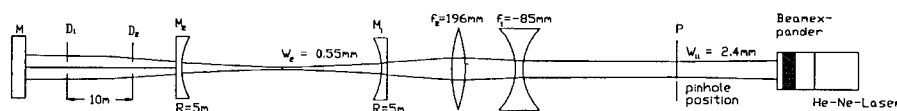


Fig. 2. Matching the optical axis of the FEL cavity to the laser beam by means of a beam expander and a Galilei telescope.

reflected back by a mirror M behind the second diaphragm. The laser is matched with a beam expander and a Galilei telescope to the optical cavity modes.

Now the cavity mirror  $M_2$  is put to its position. It is adjusted so that both contributions of the beam, the one reflected at the cavity mirror  $M_2$  and the part reflected at the adjustment mirror M behind the diaphragms, are reflected back to the pinhole. The same procedure is done for mirror  $M_1$ . By simply centering the reflected beams at the pinhole P, angular alignment accuracy of about  $150 \mu\text{rad}$  has been achieved.

Now further improvement of the adjustment should be possible using the undulator radiation.

As the feedback system of the optical cavity for FELICITA I uses red He–Ne lasers the adjustment will be

<sup>2</sup> The cavity mirror should have a reflectivity about 40% with respect to the alignment laser, which optimizes the reflected intensity from both mirrors.

Table 1

Parameter list of the optical resonator

|                          |         |                      |
|--------------------------|---------|----------------------|
| Cavity length            | 14.4 m  | $\pm 1 \mu\text{m}$  |
| Mirror curvature         | 7.7 m   | $\pm 4 \text{ cm}$   |
| Mirror diameter          | 2.54 cm |                      |
| Angular displacement     |         | $1 \mu\text{rad}$    |
| Transversal displacement |         | $\pm 0.1 \text{ mm}$ |

done with a green He–Ne laser ( $\lambda = 543 \text{ nm}$ ). This requires optical coatings of the mirrors providing high reflectivity at 633 nm, medium reflectivity at 543 nm and high reflectivity for the desired FEL wavelength.

## References

- [1] D. Nölle et al., Nucl. Instr. and Meth. A 296 (1990) 263.
- [2] C. Schellnock, Entwicklung und Aufbau eines optischen Resonators für das FEL-Experiment FELICITA I am Speicherring DELTA, diploma thesis (1994).
- [3] D.M. Shemwell et al., Nucl. Instr. and Meth. A 259 (1987) 56.

## Magnetic measurements of the electromagnetic undulator for the FELICITA I experiment ☆

M. Ridder \*, A. Geisler, D. Nölle, T. Schmidt, S. Suermann

*Institute for Acceleratorphysics and Synchrotronradiation, University of Dortmund, 44227 Dortmund, Germany*

The electromagnetic undulator for the FELICITA I experiment at the storage ring DELTA is currently under assembly. The undulator [1] has a period length of 250 mm and an overall length of 4875 mm. At the fixed gap of 50 mm we expect a peak magnetic field of 0.09 T at the nominal current of 83 A in the main coils.

Here we present the magnetic measurements of two of the five sections which make the undulator. We conducted conventional Hall-probe measurements as well as pulsed-wire experiments.

Since the upper part of the yoke is mounted on spacers, which rest on the lower part of the yoke, there is no continuous lateral access to the gap. Therefore an aluminum tube with a rectangular cross-section that fits into the gap is used. By means of a dc-motor and a belt drive the Hall probe mounted on a small wagon made of PVC is pulled through this tube. The belt itself is reinforced by Kevlar fibres to insure a very small stretchability. This is important since an angular encoder mounted on the axis of the motor is used to provide the trigger for the measurement of the Hall voltage, which is directly read by a fast DVM (Hewlett-Packard 3457 A). Since the Hall probe is not stopped during a measurement its speed is determined by the resolution of the DVM's analog-to-digital converter. A typical speed of the wagon is 5 mm/s. The Hall probe fabricated by Siemens is fed with a precision dc-current source made by Heinzinger (TNs 10-3). The data acquisition is controlled by a PC.

In a typical scan we take 100 readings per period. The accuracy of the longitudinal position of the Hall probe is 50  $\mu\text{m}$ . The on-axis magnetic field of the undulator measured with this device is shown in Fig. 1.

Additionally the pulsed-wire technique [2,3] was used to measure the field integrals. This method features the possibility to do very fast field integral measurements and to visualize on-line the effects of field tuning. These are very important features for matching the undulator at

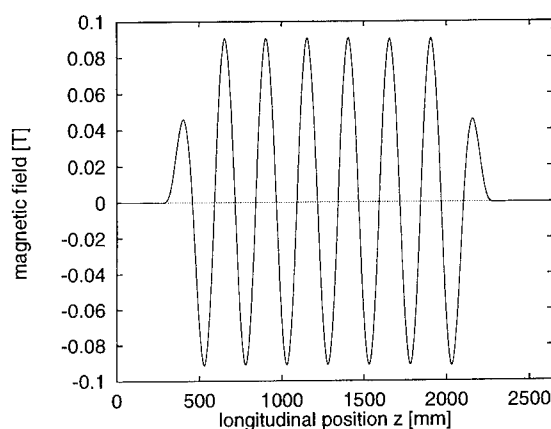


Fig. 1. The on-axis magnetic field of the two undulator sections measured with the Hall probe. The peak field of 0.0908 T is in good agreement with the design value. The peak field variation is 0.3% without the use of any correction coils.

different excitation levels. In our experiments a current pulse is sent through a 50  $\mu\text{m}$  diameter CuBe wire. The wire is mounted on two  $xy$ -translation stages fixed on two optical tables on either side of the undulator. Due to the

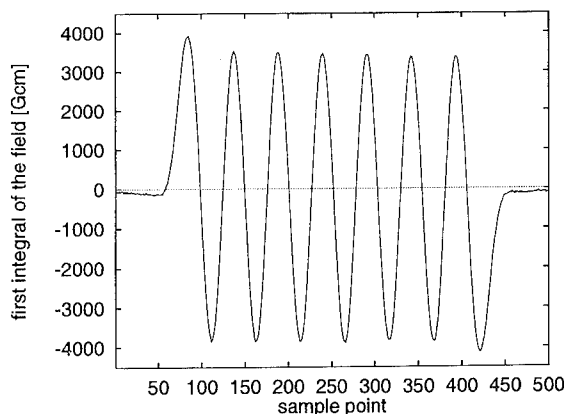


Fig. 2. The first integral of the field as measured with the pulsed wire technique. The residual field integral is less than 30 Gcm. The half period field integral error is 0.85%.

☆ This work has been supported by the Bundesministerium für Forschung und Technologie under contract 05 3PEAAI 0.

\* Corresponding author. Tel. +49 231 755 5382, fax +49 231 755 5383, e-mail markus@marvin.physik.uni-dortmund.de.

long wiggler period the magnetic field is very homogeneous even in the direction of the main field component, which eliminates any problems due the wire's sag and makes the wire positioning simple. The wire motion is detected by a laserdiode–photodiode arrangement (LD: PM670-5 by LaserGraphics; PD: BPX65). The signal of a photocurrent-to-voltage converter is viewed on an oscilloscope.

When measuring the first integral of the field the wire is tensioned to produce an acoustic wave velocity of  $c_a = 248$  m/s. In these measurements the length of the wire was 6 m. The 300 mA current pulse had a length of  $\tau_1 = 10$   $\mu$ s ( $c_a \tau_1 \ll \lambda_u$ ). For measuring the second field integral a current pulse of  $\tau_2 = 9$  ms length ( $c_a \tau_2 > L_{und}$ ) is produced and a 5 k $\Omega$  resistor is added in series to the wire to reduce the discharging of the pulser's capacitor. To reduce the noise level produced by air movements and electronics we typically average over 64 measurements. These parameters allowed the detection of a wire displacement of 0.1  $\mu$ m.

The first and second field integrals measured with the pulsed wire are shown in Figs. 2 and 3.

The measurements confirmed some of the design parameters of the undulator. Peak field: 0.0908 T (0.3% rms), half period field integral error: 0.85% rms.

For the measurements of the complete undulator ( $L_{wire} > 10$  m) we plan to use a coil at either side of the magnet, which produces a known field integral. This provides an

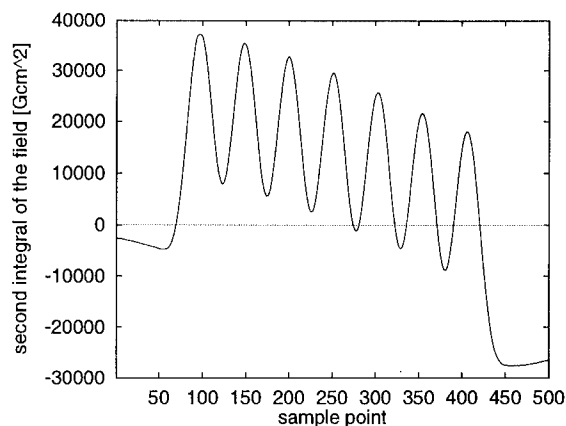


Fig. 3. The second integral of the field as obtained with the pulsed wire. The rather large displacement is due to the fact that we employed only two power supplies and therefore could not match the first and second integral at the same time.

on-line calibration of every measurement and gives an idea of the damping of the wire's motion.

## References

- [1] T. Schmidt et al., Nucl. Instr. and Meth. A 341 (1994) ABS 9.
- [2] R.W. Warren, Nucl. Instr. and Meth. A 272 (1988) 257.
- [3] A. Geisler, M. Ridder and T. Schmidt, DELTA Int. Rep. 94-08.



ELSEVIER

# Enhanced harmonic generation from a focussing two-period undulator

A.V. Tulupov \*

FOM-Institute for Plasma Physics, Postbus 1207, 3430 BE Nieuwegein, The Netherlands

The generation of harmonics in a FEL is a promising way to reach a shorter wavelength at a fixed energy of an electron beam. UV lasing has been recently demonstrated with a low energy electron beam [1]. In the usual case, the gain is the largest at the fundamental and decreases with the increase of the number of the harmonic. To enhance the generation of higher harmonics different modifications of the undulator field have been proposed [2–4]. Here we consider a simple two-period undulator field to enhance the gain of a chosen harmonic.

Consider the motion of electrons in the focussing field of a main undulator and a second periodic magnetic field:

$$a_x = a_w \sinh(k_f x) \sinh(k_f y) \cos(k_w z), \quad (1a)$$

$$a_y = -a_w \cosh(k_f x) \cosh(k_f y) \cos(k_w z)$$

$$-a_g \cos(k_g z). \quad (1b)$$

The amplitude of the second field is much lower than the main field,  $a_g \ll a_w$  (the relation between them will be specified below), the period of the second field is much larger,  $k_g \ll k_w$ ;  $k_f = k_w/\sqrt{2}$ . Following to the procedure of the separation of fast and slow transverse oscillations [5] one can get for the fast oscillations

$$\beta_{y1} = -a_w \gamma^{-1} \cosh(k_f x_0) \cosh(k_f y_0) \cos(k_w z) \quad (2)$$

( $\beta_{x1}$  gives a contribution of higher order than  $\beta_{y1}$ ) and for the slow oscillations

$$x_0 = x\beta \cos(k\beta z + \phi), \quad (3)$$

$$y_0 = a_g k_g \gamma^{-1} (k_\beta^2 - k_g^2)^{-1} \cos(k_g z), \quad (4)$$

where  $k_\beta$  is the betatron wavenumber,  $k_\beta = a_w k_w/2\gamma$ . The essential feature of the slow motion is that the oscillations in the  $y$ -direction are driven by the second undulator field. This allows adjustment of the bunching parameter [6].

In the presence of an electromagnetic wave with the amplitude  $a_s$ , frequency  $\omega_s$  and wavenumber  $k_s$  the equations of motion have the form

tions of motion have the form

$$\gamma' = -\frac{nk_s a_s a_w}{2\gamma} K_n \sin(n\theta), \quad \theta' = k_s + k_w - 1/\beta_{z0}, \quad (5a)$$

$$\beta_{z0} = 1 - \frac{1}{2\gamma^2} \left( 1 + \frac{a_w^2}{2} (1 + k_f^2 x_\beta^2) \right) - \frac{a_g^2 k_g^4}{2\gamma^2 (k_g^2 - k_\beta^2)^2}, \quad (5b)$$

where  $n$  is the number of the harmonic,  $\theta$  is the ponderomotive phase and  $\gamma$  is the relativistic factor. Only the resonant terms are kept in Eqs. (5). The term varying as  $2k_g z$  is neglected. This is valid if

$$\frac{k_s}{8\gamma^2 k_g} \frac{a_g^2 k_g^2}{k_\beta^2 - k_g^2} \ll 1. \quad (6)$$

Condition (6) defines the values of  $a_g$  and  $k_g$  for a given set of the basic parameters,  $\gamma$ ,  $k_s$  and  $k_\beta$ . It justifies also the perturbation analysis with  $\beta_{x,y} \ll \beta_z$ . Eqs. (5) are similar to the standard FEL equations [7], except that the longitudinal electron velocity has an extra term, modifying the bunching parameter [6]. In addition, the coupling factor,  $K_n$ , consists of two parts if  $n > 1$ :

$$K_n = J_0(n\nu_-)J_0(n\nu_+) \{J_{(n-1)/2}(n\nu) - J_{(n+1)/2}(n\nu)\} + J_0(n\nu)J_{(n-1)/2}(n\nu_+)J_{(n-1)/2}(n\nu_-). \quad (7)$$

The first part of Eq. (7) represents the slightly modified coupling parameter for the standard FEL. The second part is due to beating of the fast oscillations and the slow driven oscillations of the longitudinal electron velocity. The arguments of the Bessel functions are given by

$$\nu = \frac{k_s a_w^2}{8k_w \gamma^2}, \quad \nu_{\pm} = \frac{k_s a_w a_g k_g^2}{2k_{\pm} \gamma^2 (k_\beta^2 - k_g^2)}, \quad (8)$$

where  $k_+ = k_w + k_g$ ,  $k_- = k_w - k_g$ . In the small signal approximation the gain for the  $n$ th harmonic is given by the formula

$$G_n = G_{n0} B_n K_n^2 / K_{n0}^2, \quad (9)$$

\* Permanent address: Russian Research Centre “Kurchatov Institute”, Moscow 123182, Russia.

where  $G_{n0}$  is for the standard one period undulator [7],  $B_n$  is the modified bunching parameter,

$$B_n = 1 + \frac{a_g^2 k_g^4}{(k_g^2 - k_\beta^2)(1 + a_w^2/2)} + \frac{2a_g^2 k_g^4 k_\beta^2}{(k_g^2 - k_\beta^2)^3 (1 + a_w^2/2)}, \quad (10)$$

and  $K_n^2/K_{n0}^2$  is the modified coupling factor ( $n > 1$ ),

$$\frac{K_n^2}{K_{n0}^2} = \left\{ J_0(n\nu_+) J_0(n\nu_-) + \frac{J_0(n\nu) J_{(n-1)/2}(n\nu_+) J_{(n-1)/2}(n\nu_-)}{J_{(n-1)/2}(n\nu) - J_{(n+1)/2}(n\nu)} \right\}^2. \quad (11)$$

If  $n = 1$  the second term of Eq. (11) is absent. When  $a_g = 0$ ,  $B_n = 1$  and  $K_n^2/K_{n0}^2 = 1$ . The introduction of the second undulator field allows enhancement of the bunching parameter [6]. In the case of harmonic radiation the modification of the coupling factor (11) is more important. Generally, the radiation intensity at a given harmonic is the largest if the Bessel function  $J_{(n-1)/2}(n\nu)$  reaches its maximum value. Hence, for any harmonic the parameter  $\nu$  has to be about 0.6. For a conventional undulator  $\nu = a_w^2/4(1 + a_w^2)$ , that is  $\nu < 0.5$ , even if  $a_w \gg 1$ . In this sense an FEL generating harmonics is never optimized. Optimization can be achieved with a two-period undulator. The presence of the additional second term in the expression for the coupling factor (11) can enhance the gain of a given harmonic by an appropriate choice of the parameters

$\nu_{+,-}$  giving the maximum value of the Bessel functions. If the second undulator field is equal to  $a_g = (k_g/k_w)a_w$  then the parameters  $\nu_{+,-}$  can be expressed in the form

$$\nu_{+,-} = 4\nu \frac{k_g}{k_w} \frac{k_g^2}{k_\beta^2 - k_g^2}, \quad (12)$$

where  $\nu_+ = \nu_-$  is assumed because  $k_g \ll k_w$ . As follows from Eq. (12) the value of  $\nu_{+,-}$  can be easily varied at any value of  $\nu$  (the undulator parameter  $a_w$ ) in the range  $\nu_{+,-} \leq 0.6$  by the proper choice of the period of the second undulator field ( $k_g$ ). At the same time the condition (6) is satisfied ( $\beta_\perp \ll \beta_z$ ).

### Acknowledgements

The work was performed as part of the research program of the association agreement between the “Stichting voor Fundamenteel Onderzoek der Materie” (FOM) and Euratom, with financial support from the “Nederlandse Organisatie voor Wetenschappelijk Onderzoek” (NWO).

### References

- [1] P.G. O'Shea et al., Nucl. Instr. and Meth. A 341 (1994) 7.
- [2] Y.-P. Chou and T.C. Marshall, Nucl. Instr. and Meth. A 318 (1992) 528.
- [3] M. Asakawa et al., Nucl. Instr. and Meth. A 318 (1992) 538.
- [4] A.V. Tulupov, Nucl. Instr. and Meth. A 331 (1993) 554.
- [5] E.T. Scharlemann, J. Appl. Phys. 58 (1985) 2154.
- [6] B.A. Bazylev and A.V. Tulupov, Nucl. Instr. and Meth. A 331 (1993) 742.
- [7] W.B. Colson, IEEE J. Quantum Electron. QE-17 (1981) 1417.



ELSEVIER

## Improved electron beam transport and diagnosis system for the Darmstadt IR-FEL<sup>☆</sup>

H. Genz, H.-D. Gräf, R. Hahn<sup>\*</sup>, D.A. Jaroszynski, H. Loos, A. Richter, M. Reichenbach,  
V. Schlott, M. Thomas, J. Töpper, T. Wesp, M. Wiencken

*Institut für Kernphysik, Technische Hochschule Darmstadt, Schlossgartenstr. 9, D-64289 Darmstadt, Germany*

After having obtained an accumulation of intensity of up to twelve times compared to a single photon pulse, distinct amplification of spontaneous emission was found over a length region of about 200  $\mu\text{m}$  of the 15 m long optical cavity [1]. The reason for the observed broadening and shift to longer wavelengths of the spontaneous spectrum is either due to an incorrect matching of the undulator or to an energy shift of the electron beam during the macropulse. It became therefore apparent that several additional measures had to be taken in order to achieve lasing at the Darmstadt IR-FEL. As a consequence a new electron beam diagnosis system which consists of an electron spectrometer, an adjustable collimator and a movable view screen along the undulator has been incorporated into. These components are described in detail below. In order to achieve correct matching of the undulator and to avoid betatron motion of the electron beam as observed in the past, the beam transport system was improved by introducing two additional quadrupoles and powerful steering coils.

The FEL beamline is built as a bypass to the straight section of the first recirculation of the S-DALINAC [2]. In addition to several view screens and an rf position monitor in front of the undulator, we installed a wire chamber with a spatial resolution of 0.3 mm in front of the Faraday cup. The set-up for the QD2Q and the 3QD electron spectrometers shown in Fig. 1 allows the measurement of the energy distribution of the electron beam before and after passing the FEL bypass. With designed resolutions of at least  $\pm 15$  keV, it will be possible to optimize the accelerator and to meet the requirements for FEL operation. Furthermore two remote controlled, movable tantalum slits with an energy acceptance of  $\pm 0.5\%$  will be used as a collimator (see Fig. 1) in the dispersive region in front of the second dipole of the FEL bypass. By reading out the secondary

emission signal it will be possible to determine the energy spread of the electron beam during the macropulse and to tune, if necessary, the chopper–prebuncher system as well as the accelerator structures of the S-DALINAC on-line.

In order to improve the diagnosis of the electron beam inside the undulator we developed a movable screen, which can readily be placed anywhere inside the 3 m long vacuum tube of the undulator. This seemed to be necessary since different injection conditions of the electron beam led to the same positions of the beam on the two fixed undulator screens during the last beam time in December 1993. The movable screen consists of a chromium doped  $\text{Al}_2\text{O}_3$ -disc, 12 mm in diameter, which is mounted in a gold frame. It is moved through the beam tube by a 0.4 mm thin bronze wire which is driven by a dc motor. An externally aligned He–Ne laser defines the correct on axis position on the screen, so that it is possible to determine the actual electron beam position within  $\pm 0.25$  mm over the complete length of the undulator. The screen is observed by a TV camera via a mirror system in the upstream vacuum chamber of the optical resonator. Both the movable screen and the observation system are controlled remotely. After having tested the mechanical set-up and having improved the observation system, it will be possible to visualize and optimize the electron beam over the complete length of the undulator.

Operational experience of the last beam times and the fact that it was not possible to match the undulator correctly with the existing electron beam transport system led to the conclusion to recalculate the complete electron beam transport system for the Darmstadt IR-FEL. The calculations were based on the electron beam parameters measured in December 1993. They were performed using the interactive beam optics code XBEAM [3], developed at Darmstadt and verified by the established code MAD [4]. The calculations show that it is possible to match the undulator and to achieve less critical properties for the optics of the whole FEL beamline simultaneously by inserting two additional quadrupoles in the first recirculation of the S-DALINAC (1) in Fig. 1. It will be possible to

<sup>☆</sup> Supported by the BMFT contract number 05 345EA 1 and European Network contract number SC1-0471 C(A).

<sup>\*</sup> Corresponding author. Tel +49 6151 162 528, fax +49 6151 164 321, e-mail hahn@linac.ikp.physik.th-darmstadt.de.

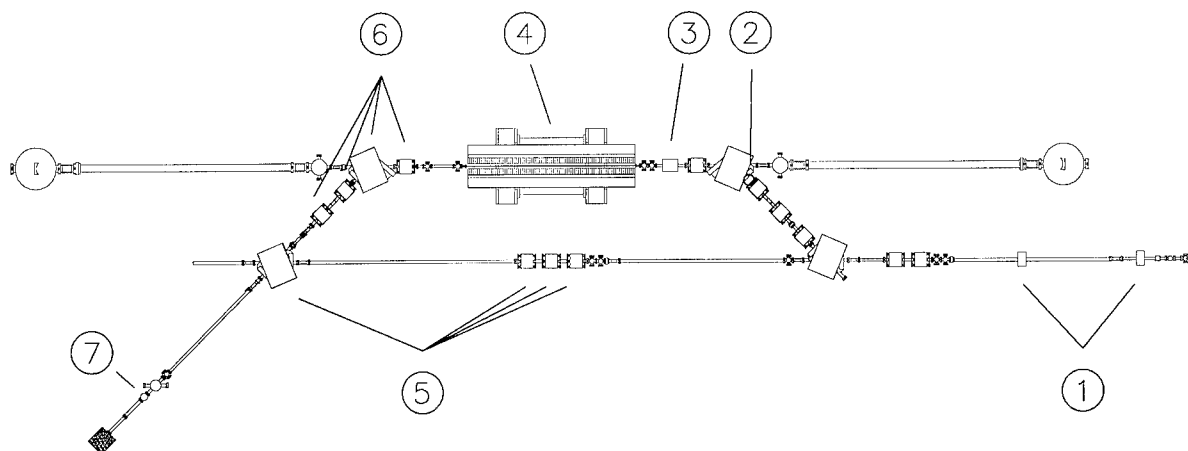


Fig. 1. FEL electron beam diagnostics. (1) Additional quadrupoles, (2) collimator, (3) rf position monitor, (4) undulator, (5) 3QD electron spectrometer, (6) QD2Q electron spectrometer and (7) wire chamber.

obtain a waist in the middle of the undulator with a beam envelope of 0.5 mm in the horizontal direction and 1.1 mm in the vertical direction. The new beamline and the calculated beam radii in both directions as well as the dispersion of the electron beam are shown in Fig. 2. In addition more powerful steerers have been installed along the FEL beamline in order to correct possible deviations of the electron beam in angle and position.

With the described improvements of the electron beam transport and diagnosis system, it should be possible to obtain the desired control over the electron beam in order to meet the requirements for FEL operation. During a

shut-down period in August/September 1994 several superconducting accelerator structures of the S-DALINAC have been chemically treated and two new structures have been installed, so that improved performance of the accelerator can be expected during the next beam time in October 1994. Since only twelve roundtrips of the optical beam in the resonator were observed so far, it was found to be necessary to determine the  $Q$ -value of the optical cavity. To accomplish this a  $\text{PbS}_{1-x}\text{Se}_x$  diode laser at a wavelength of  $6.7 \mu\text{m}$  has been set up on the downstream optical table of the FEL optical cavity. By determining the  $Q$ -value of the optical cavity it will be possible to separate the electron beam parameters from the optical parameters.

### Acknowledgements

We would like to thank R.J. Bakker, G.M.H. Knippels, W.J. Mastop, A.F.G. van der Meer, D. Oepts, H.A. Schwettman and A. Streun for many fruitful and stimulating discussions.

### References

- [1] J. Auerhammer, H. Genz, H.-D. Gräf, W. Grill, R. Hahn, A. Richter, V. Schlott, F. Thomas, J. Töpper, H. Weise, T. Wesp and M. Wiencken, Proc. 15th Int. Free Electron Laser Conf., Nucl. Instr. and Meth. A 341 (1993) p. 63.
- [2] H. Genz, H.-D. Gräf, J. Horn, V. Huck, D. Hummel, M. Knirsch, C. Lüttge, A. Richter, T. Rietdorf, K. Rühl, P. Schardt, E. Spamer, A. Stiller, F. Thomas, O. Titze, J. Töpper and H. Weise, 3rd Europ. Particle Accelerator Conf., EPAC 92, Berlin, ISBN 2-86332-114-5 (1992) p. 49.
- [3] T. Winkler, Diplomarbeit, TH-Darmstadt (1993) unpublished.
- [4] H. Grote and F.C. Iselin, The MAD Program, CERN (1994).

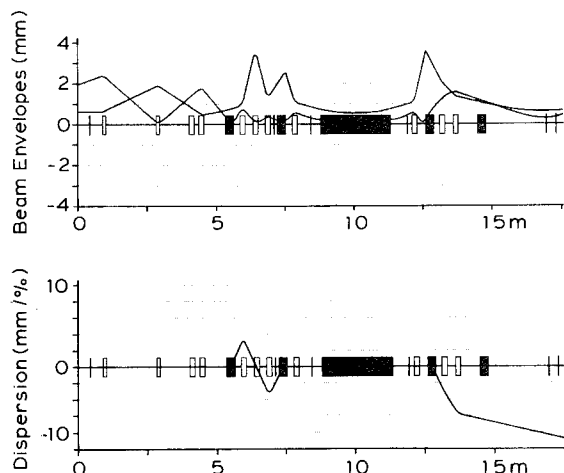


Fig. 2. Electron beam transport simulation performed with beam optics code XBEAM. Filled elements correspond to dipoles, unfilled elements are quadrupoles. Upper part: beam envelopes in horizontal and vertical plane. Lower part: dispersion of electron beam.





ELSEVIER

## Upgrade of the ENEA compact FEL in the sub-mm region

E. Giovenale <sup>a,\*</sup>, F. Ciocchi <sup>a</sup>, A. Doria <sup>a</sup>, G.P. Gallerano <sup>a</sup>, M.F. Kimmitt <sup>b</sup>, G. Messina <sup>a</sup>,  
P. Raimondi <sup>a</sup>, A. Renieri <sup>a</sup>, I. Spassovsky <sup>a,1</sup>

<sup>a</sup> ENEA, INN-FIS, P.O. Box 65, 00044 Frascati, Italy

<sup>b</sup> Department of Physics, University of Essex, Colchester CO4 3SQ, UK

In the last few years investigations have been carried out on the possible applications for a FEL source in the sub-mm/FIR region. A certain number of applications have been selected and preliminary measurements have been carried out on the present configuration of the ENEA Compact FEL, emitting in the spectral region between 2 and 3 mm [1–3]. Nevertheless, in order to fulfill users requirements, operation at shorter wavelength would be desirable.

In this paper we will describe the modifications that are being operated on the ENEA Compact FEL in order to increase its performance and to obtain laser emission down to 250  $\mu\text{m}$ . Moreover this operation range expansion will allow the ENEA Compact FEL to contribute at best to the multi-center Euro-FEL-Facility (EFF) proposal, the intent of which is to give users a series of FEL sources covering the spectrum between 2.5 and 3000  $\mu\text{m}$  (Fig. 1).

The first step in upgrading the ENEA Compact FEL was to build a new user area, adjacent to the FEL control

room, in order to allow the user to mount his experimental apparatus outside the FEL bunker, making it easier to perform the experiment. Radiation is extracted from the vacuum chamber that contains the undulator/resonator block and directed upwards over the ceiling of the bunker in a copper lightpipe (2.5 mm diameter). Subsequently, making use of three mirrors, radiation is sent to the user area, where an optical table, together with other facilities, is at the disposal of users.

The radiation attenuation along the lightpipe is negligible, while we have measured losses varying from 5 to 30% on the mirrors, with a total attenuation of about 50% from the output of the laser to the user area. At the moment efforts are aimed at optimizing the radiation transport, making use of elliptical mirrors, in order to reduce the losses on each mirror below 5%.

The second step consists in the installation of a new undulator, an upgrade of the presently installed one. The main parameters of the undulator are  $\lambda_u = 2.5$  cm and  $N = 16$ , in order to increase the gain without affecting the efficiency too much, and a variable gap that will allow fine tuning around a central frequency, determined by the waveguide gap;  $K$  will vary from 0.5 to 1.8. Changing the waveguide gap will allow tuning of the FEL wavelength from about 250  $\mu\text{m}$  to 700  $\mu\text{m}$ .

\* Corresponding author. Tel. +39 6 94001, fax +39 6 9400 5334, e-mail giovenale@efr419.enea.it.

<sup>1</sup> ENEA-ICTP Fellow.

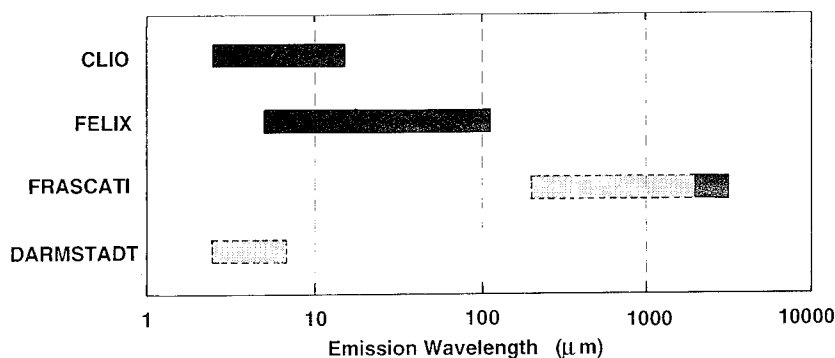


Fig. 1. European-FEL-Facility proposal; emission wavelength of the involved facilities. Black bars: actual operation; gray bars: planned upgrades.

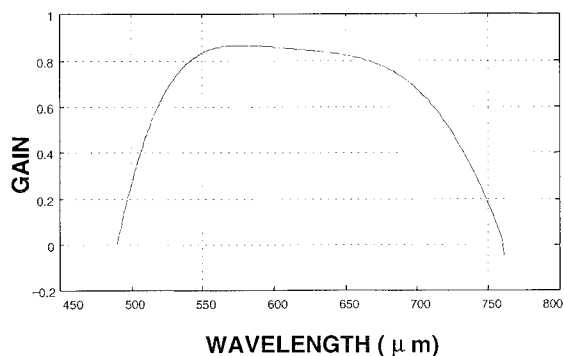


Fig. 2. Gain curve for a waveguide gap  $b = 0.199$  cm.

To operate with the new undulator in the required spectral range it is necessary to increase the microtron energy up to its maximum, i.e. 5.5 MeV. This is achieved moving the RF cavity inside the microtron in a way that the beam intercepts the extraction tube at the sixth orbit.

Moreover a new 15 MW klystron will be available as RF source. With this new source it will be possible to increase the stability of the current over a 2 to 12  $\mu$ s long macropulse. With this longer macropulse it will be possible to examine the exponential growth of the FEL pulse. Fig. 2 shows the gain curve for a waveguide gap equal to 0.199 cm, centered around 600  $\mu$ m.

Fig. 3 shows the distribution of the beam time between the different activities for the ENEA Compact FEL during the last 6 months. The main part was devoted to the study of FEL physics, namely of the optical stretching techniques, that will be used in an excited state spectroscopy of muonic atoms experiment (MUH Experiment) [2], and to

the study of the FEL pulse growth in the cavity. Another substantial part of the beam time was devoted to the FEL performance upgrade and optimization, and it comprises optimizing the optical beam line up to the user area and improving the FEL performance. The rest of the time was devoted to the applications that need a radiation source between 2 and 3 mm: studies on the response of solid state detectors, preliminary spectroscopic measurements on high- $T_c$  superconductors and spectroscopic tests of mm-wave materials. All these measurements will continue with the upgraded FEL at shorter wavelengths.

One special application, that is the realization of a peculiar laser source in the FIR region for the MUH experiment [2], will benefit from the new configuration of the FEL to test the limits of the spectral control of the radiation at the operating wavelengths, while, up to now, experiments have been carried out only at mm-wave wavelengths.

## References

- [1] A. Doria, G.P. Gallerano, E. Giovenale, M.F. Kimmitt and G. Messina, Nucl. Instr. and Meth. A 341 (1994) ABS 62.
- [2] F. Ciocci, F. Della Valle, A. Doria, G.P. Gallerano, L. Giannessi, E. Giovenale, P. Hauser, F. Kottmann, G. Messina, E. Milotti, C. Petitjean, L. Picardi, A. Renieri, C. Rizzo, C. Ronsivalle, L.M. Simons, D. Taqqu, A. Vacchi, A. Vignati and E. Zavattini, Nucl. Instr. and Meth. A 341 (1994) ABS 60.
- [3] E. Giovenale, G.P. Gallerano, V. Boffa, P. Dore, A. Doria, M.F. Kimmitt, R. Trippetti and I. Spassovsky, these Proceedings (16th Int. Free Electron Laser Conf., Stanford, CA, USA, 1994) Nucl. Instr. and Meth. A 358 (1995) ABS 9.

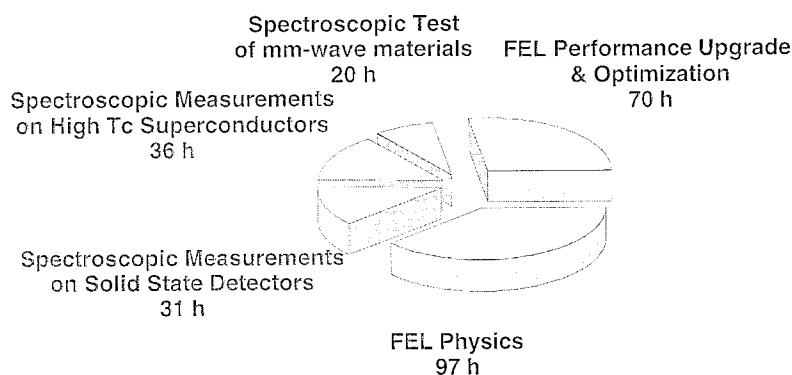


Fig. 3. Distribution of beam time during the first half of 1994 (beam time: 254 h).



ELSEVIER

## Design of a far infrared FEL with an electromagnetic wiggler

Victor L. Granatstein <sup>a,\*</sup>, Arne W. Fliflet <sup>b</sup>, Wallace M. Manheimer <sup>b</sup>, Avraham Gover <sup>c</sup>

<sup>a</sup> Institute for Plasma Research, University of Maryland, College Park, MD 20742, USA

<sup>b</sup> Plasma Physics Division, Naval Research Laboratory, Washington, DC 20375, USA

<sup>c</sup> Faculty of Engineering, Tel Aviv University, Tel Aviv 69978, Israel

A far infrared FEL for possible use in materials research is designed based on a state-of-the-art 350 kW average power modulator which recently became available at the University of Maryland [1]; this modulator and its associated electron gun will produce 600 keV, 870 A, 9.2 mm diameter, 10  $\mu$ s electron pulses. The electromagnetic wiggler for the FEL would be provided by a 94 GHz, 4 MW pulsed quasi-optical gyrotron which is currently under development at the Naval Research Laboratory; the suggestion of using a gyrotron to provide a wiggler wave was previously made by Danly et al. [2].

The experimental arrangement is sketched in Fig. 1. The wiggler wave is confined in HE<sub>11</sub> corrugated-wall waveguide where the FEL interaction length is 16 cm. A more detailed view of the corrugated-waveguide FEL interaction region is shown in Fig. 2. Note that the far infrared FEL radiation occupies only the central core portion of the electron beam. In our calculations, we have assumed that only the electrons in a core diameter of 3.1 mm (corresponding to a core current of 100 A) take part in the FEL interaction.

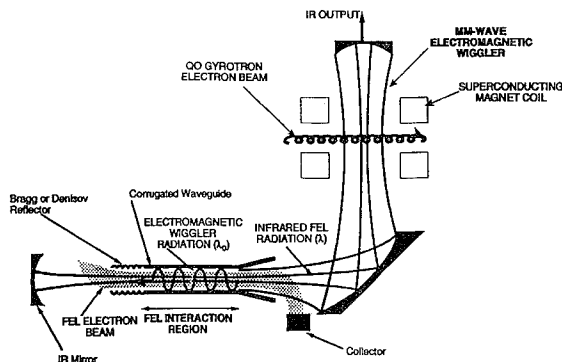


Fig. 1. Schematic of the far infrared FEL oscillator based on an electromagnetic wiggler supplied by a quasi-optical gyrotron.

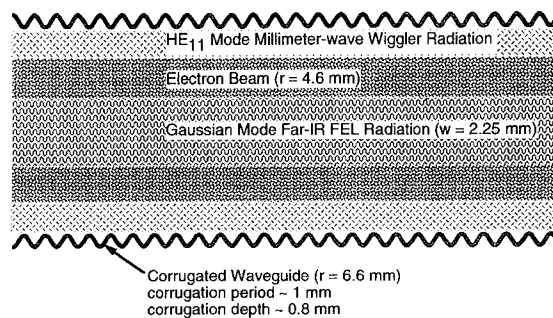


Fig. 2. Schematic of the FEL interaction region inside the HE<sub>11</sub> corrugated waveguide showing radiation and electron beam dimensions.

The FEL design parameters are displayed in Table 1. With a normalized beam emittance of 100 mm mrad, we calculate a single pass gain of 29% and an FEL output power of 115 kW at a wavelength of 195  $\mu$ m; this value of emittance should be easily achievable in the central core

Table 1  
Electromagnetic wiggler, far infrared FEL point design

|                                    |             |
|------------------------------------|-------------|
| Output wavelength ( $\lambda$ )    | 195 $\mu$ m |
| Wiggler wavelength ( $\lambda_0$ ) | 3.2 mm      |
| Electron beam energy               | 600 keV     |
| Effective beam current             | 100 A       |
| Effective electron beam diameter   | 3.1 mm      |
| Normalized emittance of beam core  | 100 mm mrad |
| Energy spread from modulator       | 3 keV       |
| FEL interaction length             | 16 cm       |
| Corrugated waveguide diameter      | 13.3 mm     |
| Wiggler circulating power          | 50 MW       |
| Wiggler resonator round-trip loss  | 8%          |
| Wiggler parameter ( $a_w$ )        | 0.022       |
| FEL radiation waist diameter       | 4.5 mm      |
| FEL gain per pass                  | 29%         |
| FEL interaction efficiency         | 0.5%        |
| FEL resonator saturation power     | 1.4 MW      |
| FEL resonator loss per pass        | 8%          |
| Output power                       | 115 kW      |

\* Corresponding author. Tel. +1 301 405 4956, fax +1 301 314 9437, e-mail vlg@plasma.umd.edu.

portion of the electron beam. The calculations of gain and output power took into account the effects of electron beam emittance, energy spread and electrostatic forces; the theoretical and numerical formalism has been described in previous publications [3,4].

#### Acknowledgement

This work was supported in part by the DoE, AFOSR, and the U.S.–Israel Binational Science Foundation.

#### References

- [1] R.M. Ness, B.L. Thomas and G. Schofield, 21st Int. Power Modulator Symp. Costa Mesa, CA, June 1994, to be published.
- [2] B.G. Danly, G. Bekefi, R.C. Davidson, R.J. Temkin, T.M. Tran and J.S. Wurtele, IEEE J. Quantum Electron. QE-23 (1987) 103.
- [3] A.W. Fliflet, W.M. Manheimer and R.P. Fischer, IEEE Trans. Plasma Sci. (special issue on high power microwave generation) to be published (1994).
- [4] A.W. Fliflet and W.M. Manheimer, IEEE J. Quantum Electron. QE-30 (1994) 185.



ELSEVIER

## Frequency response to an electron energy shift

R.K. Wong<sup>\*</sup>, W.B. Colson

Physics Department, Naval Postgraduate School, Monterey, California 93943, USA

In a free electron laser (FEL) oscillator, the optical pulse evolves through mode competition as a result of mirror losses, desynchronism, and amplification by the electron beam. The finite time for this evolution determines the optical response to an electron beam energy change. The ability of the FEL operating frequency to follow modulations in electron energy has been demonstrated experimentally [1–3] and theoretically [4]. Using a self-consistent FEL theory with dimensionless parameters [5], a longitudinal multimode simulation follows the evolution of the optical pulse over many passes of a FEL oscillator.

The optical frequency response to an electron energy shift is summarized in Fig. 1. The characteristic response time  $n_c$  measures the number of passes for the optical frequency centroid to reach  $1/e$  of its new steady-state position after an electron energy shift is imposed at steady-state saturation. The parameters in the simulation are chosen so that the optical pulse reaches steady-state saturation fields without the trapped-particle instability and the growth of optical sidebands. The current density  $j$  can be related to the weak-field, single-mode gain,  $G \approx 0.135j$ , and the energy loss at each pass is given by  $1/Q$ . The pulse length,  $\sigma_z$ , and desynchronism,  $d$ , are measured in terms of the slippage distance,  $\lambda\lambda$ .

For small  $Q$  and low desynchronism  $d$ , the optical pulse resides predominantly in the region of the electron pulse. Within the bulk of the optical pulse, strong-field saturation limits changes in the optical fields and the frequency remains unchanged. In the back of the optical pulse where the fields are weak and the interaction with the energy-shifted electron beam changes the optical frequency. Desynchronism  $d$  transfers these changes toward the front of the pulse at each pass. The centroid of the optical power spectrum shifts linearly with the number of passes during the middle of the response. In Fig. 1, for a given  $Q$  and  $\sigma_z = 2$  the response time  $n_c$  falls off as  $1/d$ .

For large  $Q$  and small  $\sigma_z$ , the bulk of the optical pulse resides in an exponentially decaying profile outside the interaction region. In the short interaction region, changes

in the optical frequency occur in a time less than the time for light of the initial frequency to decay as determined by  $Q$ . In the limit of high  $d$ , the characteristic response time  $n_c$  is approximately equal to  $Q$ .

For a given  $Q$ ,  $n_c$  is observed to increase linearly with  $\sigma_z$ . In Fig. 2, the characteristic response time is plotted for a longer  $\sigma_z = 4.0$  showing increasing response times in comparison to Fig. 1. In general the response time  $n_c$  changes as  $\sigma_z/d$  for pulses longer than the slippage distance. The response time does not vary significantly with  $j$ . Response to sinusoidal electron energy modulations follow the trends of the step energy change. As the modulation period becomes much less than the response time  $n_c$ , the optical frequency is unable to follow the electron energy modulation.

Experimentally, the response time is seen to increase with  $Q$  and  $\sigma_z/d$  [1]. Future work will further address the issues of short pulses and the trapped-particle instability. When the electron pulse length  $\sigma_z$  becomes smaller than the slippage distance the optical pulse length may not be on the order of  $\sigma_z$  and the response time may follow

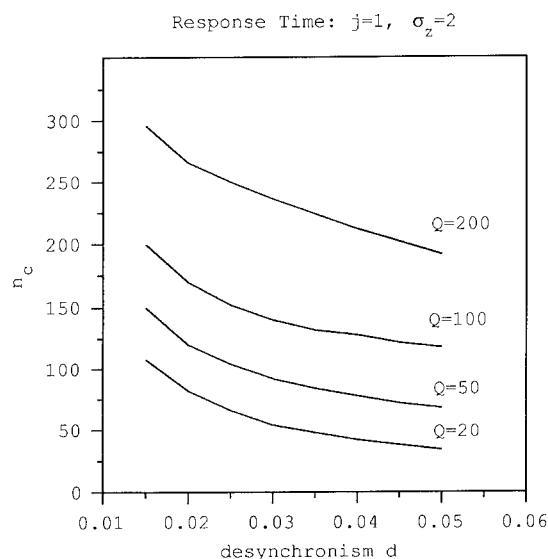


Fig. 1. Characteristic response time  $n_c$  as a function of desynchronism  $d$  and  $Q$ .

<sup>\*</sup> Corresponding author. Tel. +1 408 656 3114, fax +1 408 656 2834, e-mail wong@physics.nps.navy.mil.

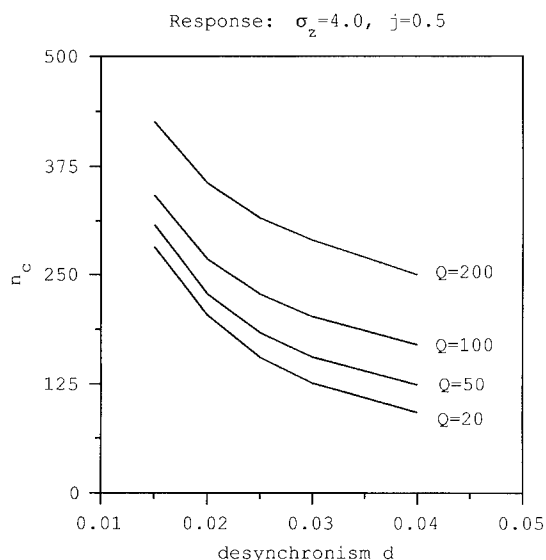


Fig. 2. Characteristic response with  $\sigma_z = 4.0$ .

different trends. Limit cycle behavior, which causes oscillations in the optical field, is also studied.

### Acknowledgements

The authors are grateful for support of this work by the Naval Postgraduate School, Stanford University (N00014-91-C-0170), and SURF/CEBAF.

### References

- [1] A. Marziani, T.I. Smith and H.A. Schwettman, these Proceedings (16th Int. Free Electron Laser Conf., Stanford, CA, USA, 1994) Nucl. Instr. and Meth. A 358 (1995) 252.
- [2] A. Marziani and T.I. Smith, Nucl. Instr. and Meth. A 331 (1993) 59.
- [3] R.W. Swent, K.W. Berryman, H.A. Schwettman and T.I. Smith, Nucl. Instr. and Meth. A 304 (1991) 228.
- [4] W. Wilkenson, Master's Thesis, Naval Postgraduate School (1993).
- [5] W.B. Colson, Free Electron Laser Handbook, eds. W.B. Col-

## Slicing single micropulses at FELIX

E.H. Haselhoff, G.M.H. Knippels, P.W. van Amersfoort \*

FOM Instituut voor Plasmafysica "Rijnhuizen", Postbus 1207, NL-3430 BE Rijnhuizen, The Netherlands

The user facility FELIX produces rapidly tuneable picosecond far-infrared radiation with macropulse powers exceeding 20 kW. This makes FELIX a unique tool for non-linear time-resolved studies on the interaction of radiation and matter in the wavelength range from 5 to 110  $\mu\text{m}$ . Nevertheless, the temporal characteristics of the macropulses (a 10  $\mu\text{s}$  train of picosecond micropulses at 1 ns separation) sometimes limit the FELIX users in their studies of relatively slow ( $> 1$  ns) interactions. Moreover, the high amount of energy in the macropulses may sometimes cause additional problems, in the form of unwanted thermal effects or even destruction of the samples under study. In order to avoid these problems, a "pulse slicer" has been constructed, which cuts a single micropulse out of the macropulse, by means of a synchronised semiconductor switch.

Semiconductor switching has been used successfully to generate pulsed radiation in the infrared by cavity-dumping [1–3] and slicing CW beams [4–7]. The principle of semiconductor switching consists of changing the optical properties of the semiconductor by generation of electron–hole pairs. This is done by illumination with photons that have an energy larger than the band gap of the semiconductor. When the photon flux is high enough, the induced free carriers in the semiconductor may exhibit the same reflective properties as a metallic mirror. In our experiment we have used high-purity silicon, which has a high transmission over the entire FELIX wavelength range and a bandgap of 1.1241 eV, corresponding to a threshold wavelength of 1.1  $\mu\text{m}$  for the switch laser.

Earlier experiments [4] combined both photon-induced increase of reflection and decrease of transmission in semiconductor slabs to slice short IR pulses out of a CW beam. One slab we used as a reflection switch, and a second slab as a transmission switch, while the IR beam travelled near-collinearly with the switch beam. Our set-up is a simplified form of this combined absorption/reflection switch, which however does the same thing. It uses both

the photon-induced reflection and absorption of a single semiconductor slab, illuminated by a frequency-doubled Nd:YAG laser (see Fig. 1). A slab of high-purity silicon is inserted under Brewster's angle in the IR beam. The YAG beam is projected on the silicon slab by means of an adjustable delay line, to control the timing. Single picosecond IR pulses are trapped between the silicon slab and a flat mirror, by firing the YAG pulse at the moment that the IR pulse travels between the silicon slab and the mirror. The long-lasting reflective state of the silicon (microseconds [3]) will still reflect only a single IR micropulse, because of the zero transmission of the silicon after the YAG has been fired. This effectively cuts off the entire "tail" of the IR-macropulse. Two requirements are crucial for the YAG laser: 1) The pulses should rise rapidly compared with the time between two IR micropulses (i.e. 1 ns), and 2) the YAG pulses need to be accurately synchronized with the IR-micropulses. Our YAG system consists of a Lightwave Electronics 131 YAG oscillator (CW modulated at 111.0474 MHz) which seeds a Continuum RGA 69 regenerative amplifier (RGA) running at 5–10 Hz. It produces a pulse energy up to 200 mJ in the IR, which is doubled to  $< 100$  mJ, 80 ps pulses at 532 nm. The timing jitter between the YAG pulses and the IR micropulses was specified by the manufacturer as less than a picosecond. This low jitter is obtained by controlling the Pockels cells in the RGA by digital counters, which are triggered by the same RF synthesiser that drives the FELIX RF system. Consequently, the YAG pulses are perfectly in phase with the electron pulses in the linac, and hence with the IR micropulses.

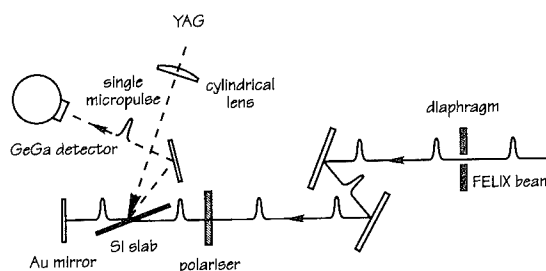


Fig. 1. Sketch of the experimental set-up.

\* Corresponding author. Tel. +31 34 02 31 224, fax +31 34 02 31 204, e-mail amersf@zeus.rijnh.nl.

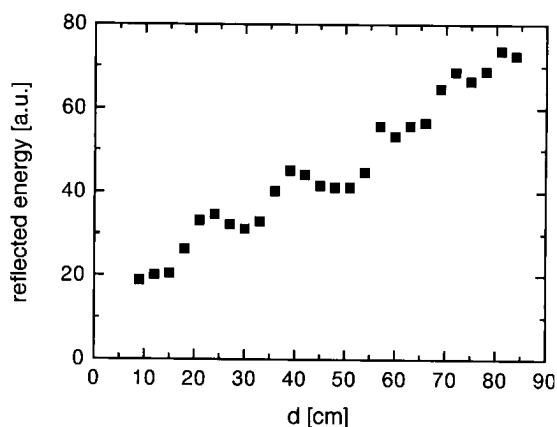


Fig. 2. Energy reflected by the optical switch, as a function of the distance  $d$  between the silicon wafer and the Au-mirror.

Pilot experiments showed, that low-purity silicon did not perform as well as high-purity versions. We therefore used a 2000  $\Omega$  cm p-type silicon slab as the optical switch. The single micropulse was detected by a sensitive, LHe cooled Ge(Ga) detector. In order to check if indeed single micropulses were sliced out of the macropulses, we measured the signal from the Ge(Ga)-detector as a function of the distance between the silicon slab and the flat mirror. When single micropulses are sliced, a step-like, linear increase should be measured, with a period of 15 cm, indicating the increasing number of “trapped” micropulses. This relatively simple measurement will work only however, when the energy of a single YAG-induced reflected micropulse is considerably higher than the total energy reflected by the rest of the macropulse, which will hit the Ge(Ga)-detector both by stray radiation scattering from optical mounts etc. and “non-Brewster’s angle reflections” from the silicon slab. The latter effect is caused by IR radiation hitting the silicon plate under angles different than Brewster’s angle, due to beam diffraction and misalignment. Careful alignment with the YAG laser switched off, and the use of a polariser sufficiently eliminated these reflections, while a diaphragm at the very beginning of the IR beamline was used to reduce stray light. Obviously, the diaphragm is only needed for this proof-of-principle experiment, and may be eliminated when the sliced micropulses are to be used for user experiments. Fig. 2 shows the signal from the Ge(Ga)-detector as a function of the distance between the silicon slab and the Au mirror (at a FELIX wavelength of 50  $\mu\text{m}$ ). Although the increase of the detector signal is not perfectly linear and slightly too low, the discontinuous increase in reflected energy is clearly observed, revealing the individual pulse character of the reflected signal. The contrast ratio of the switch was estimated to be in the order of  $1:10^6$ . We found that our set-up works satisfactorily over a large part of the FELIX wavelength range, which runs roughly from

5 to 110  $\mu\text{m}$ . For wavelengths shorter than 20  $\mu\text{m}$  however, the performance deteriorated significantly, which may be explained by the IR frequency exceeding the plasma frequency of the optically induced plasma, which is limited by the damage threshold of silicon [3,8]. Using other semiconductors (Ge, GaAs, CdTe) may be a solution to this problem [3,4,6,7].

By seeding an external cavity of 15 cm length, and coupling out the stored power by means of the silicon switch, successive micropulses can be “stacked” so as to increase the total power in a single micropulse [9,10]. At Stanford University a similar externally driven cavity is operated successfully [11,12], and the recent progress is described elsewhere in these proceedings [13,14]. At our laboratory two different ways of incoupling are under study: hole coupling [9,10] and incoupling through a partially transparent reflector (such as dielectric mirrors or metal-plated IR-transparent slabs). Hole coupling will allow large bandwidth operation, but since the incoupling mode cannot excite a cavity eigenmode while maintaining low cavity losses, the stored optical mode will presumably not have a significant power increase per unit solid angle. Partially transparent reflectors will not induce these problems, and may increase the single micropulse power by a factor of 10–20 [9]. However, this approach has the disadvantage of a small bandwidth so that the incoupling mirror will have to be replaced for operation at various FELIX wavelengths ranges.

## References

- [1] J. Burghoorn et al. Nucl. Instr. and Meth. A 318 (1992) 85.
- [2] J.P. Kaminski et al., Appl. Phys. Lett. 57 (1990) 2770.
- [3] R.E.M. Bekker, L.M. Claessen and P. Wyder, J. Appl. Phys. 68 (1990) 3729.
- [4] C. Rolland and P.B. Corkum, J. Opt. Soc. Am. B 3 (1986) 1625.
- [5] H. Salzmann, T. Vogel and G. Dodel, Opt. Commun. 47 (1983) 340.
- [6] S.A. Jamison and A.V. Nurmikko, Appl. Phys. Lett. 33 (1978) 598.
- [7] A.J. Alcock, P.B. Corkum and D.J. James, Appl. Phys. Lett. 27 (1975) 680.
- [8] F.E. Doany, D. Grischowsky and C.-C. Chi, Appl. Phys. Lett. 50 (1987) 460.
- [9] B. Faatz and G.P. Gallerano, Stacking of free-electron laser output pulses, submitted to J. Opt. Soc. Am. B.
- [10] B. Faatz, E.H. Haselhoff, V.I. Zhulin and P.W. van Amersfoort, Nucl. Instr. and Meth. A 341 (1994) ABS 136.
- [11] P. Haar, I.M. Fishman, T.I. Smith and H.A. Schwettman, Nucl. Instr. and Meth. A 318 (1992) 899.
- [12] P. Haar, H.A. Schwettman and T.I. Smith, Nucl. Instr. and Meth. A 331 (1993) 621.
- [13] P. Haar, H.A. Schwettman and T.I. Smith, these Proceedings (16th Int. Free Electron Laser Conf., Stanford, CA, USA, 1994) Nucl. Instr. and Meth. A. 358 (1995) ABS 40.
- [14] P. Haar, H.A. Schwettman and T.I. Smith, *ibid.*, p. 319.



## Status of the JAERI free electron laser facility driven by a superconducting rf linac

E.J. Minehara <sup>a,\*</sup>, R. Nagai <sup>a</sup>, M. Sawamura <sup>a</sup>, M. Takao <sup>a</sup>, M. Sugimoto <sup>a</sup>, S. Sasaki <sup>a</sup>,  
M. Ohkubo <sup>a</sup>, N. Kikuzawa <sup>a</sup>, J. Sasabe <sup>b</sup>, Y. Suzuki <sup>a</sup>, Y. Kawarasaki <sup>b</sup>, N. Shikazono <sup>a</sup>

<sup>a</sup> Free Electron Laser Laboratory, Department of Physics, Japan Atomic Energy Research Institute, 2-4 Shirakata-shirane, Tokai-mura,  
Naka-gun, Ibaraki-ken, 319-11 Japan

<sup>b</sup> Hamamatsu Photonics Co., Research Center, Hamakita-shi, Shizuoka-ken, 434 Japan

### 1. Introduction

As well known, a laser consists of three major parts, i.e., a laser driver, gain media, and an optical resonator. Since the invention of the laser in 1950s, the efficiency and average power of these devices have been limited by heat losses in the laser driver and gain media. If we use an FEL, we can neglect the heat loss in the gain media. Unfortunately, as long as the normal conducting accelerator was used as the laser driver, we could not realize the high efficiency and high average power level due to the heat losses in the accelerator. In order to make a highly-efficient, and high average power FEL, we must minimize the heat losses in the accelerator.

A developmental program [1,2] of a free electron laser (FEL) system for the far-infrared region (20–80  $\mu\text{m}$  or longer) has been undertaken at Japan Atomic Energy Research Institute (JAERI), Tokai. The purpose of the present JAERI FEL program lies in constructing a very long pulse or quasi-continuous wave (cw) superconducting rf electron linac, and demonstrating a high-average power FEL in the far-infrared wavelength region.

Because wall losses and required rf power become minimal in the superconducting accelerator cavity, we may realize a quasi-cw and high-current rf linac driver, and hence a high-average power laser. Each major part of the program has been reported in other papers [3–6] in the conference. Here, we present the program status including the future plan.

### 2. Injector

The injector of the JAERI FEL consists of a thermionic cathode electron gun with a pulsed grid, a sub-harmonic

buncher (SHB), and a buncher. The accelerating voltage in the single gap electron gun is typically around 243 kV, and the gun is usable from 200 to 250 kV.

The characteristics typically obtained are as follows: an electron beam of 130 mA and 2 ns bunch length was extracted from the gun. The beam was successfully compressed to 70 ps or less by the bunching system [1].

### 3. Superconducting rf linac

The JAERI superconducting rf linac consists of two pre-accelerator modules of the single-cell cavity type and two main modules of the 5-cell cavity type. The resonant frequency of the cavities is 499.8 MHz which is exactly the same as the buncher and the sixth harmonic of the SHB in the injector. Accelerating field strength of the pre-accelerators is 3.0–3.3 MV/m, and that of the main-accelerator is 5.5–6.0 MV/m. Lower field strengths in the pre-accelerators simply come from a limitation of the rf power source for them. Since receipt of the four superconducting accelerator modules in 1992 and 1993, we have never observed deterioration in the qualities of the modules except for the heater damage.

Design values of the strength and  $Q$ -value for the cavities are 5 MV/m and  $2 \times 10^9$ , respectively. In 1993 and 1994 Japanese fiscal years, we have successfully and routinely operated all JAERI superconducting accelerator modules with stand-by losses  $< 3.5$  W at 4.5 K and accelerating fields of  $E_{\text{acc}} \sim 7$  MV/m at  $Q \sim 2 \times 10^9$ .

### 4. Cryostat and refrigerators

We have developed a multi-refrigerator system [5] integrated into the superconducting accelerator module cryostat to realize a highly-efficient system without any liquid coolant. A heat exchanger of the 4 K closed-cycle He refrigerator, mounted just a few centimeter above the cavity module, was adopted to cool down and to recon-

\* Corresponding author. Tel. +81 292 82 5464, +81 292 82 5455, fax +81 292 82 5939, e-mail j3166@jpnjaeri.bitnet.

## Characterization of the mid-IR FEL at Stanford ☆

B.A. Richman \*, E.R. Crosson, R.L. Swent, H.A. Schwettman, T.I. Smith

Stanford Picosecond FEL Center, W.W. Hansen Experimental Physics Laboratory, Stanford University, Stanford, CA 94305, USA

### 1. Introduction

The new mid-IR FEL at the Stanford Picosecond FEL Center first lased in February and came on line for user experiments in July of 1994. In its first month of operation for users it produced more power (200 mW average), shorter pulses (0.6 ps), achieved a wider spectral range (3.3–10.3  $\mu\text{m}$  wavelength), and faster spectral tuning (20% change in 20 min) than its predecessor. In the future we expect to provide wavelengths as long as 15  $\mu\text{m}$ .

### 2. Design of the mid-IR FEL

Fig. 1 is a diagram of the new mid-IR FEL at Stanford. The resonator is in line with the linac, and complete electromagnetic chicanes shuttle the electron beam around the resonator mirrors. The chicanes are transversely achromatic, so that the beam does not need to be resteered if its energy (and the FEL wavelength) is changed. They have clearance for a 10% full range of energy or 20% of wavelength, which is the approximate width of the dielectric output coupler resonator mirrors. Then the entire mirror bandwidth may be covered without severe electron beam realignment.

The wiggler was constructed by STI in 1983 and has parameters listed in Table 1. Parameters of the SCA linac also appear in Table 1 and in Ref. [1]. Depending on the electron beam focussing in the wiggler, the gain was predicted to be as high as 15% at a wavelength of 5  $\mu\text{m}$ .

The resonator is 12.68 m long, and contains one micropulse, so that the micropulses are well separated and single pulses can be selected with acousto-optic modulators at the experimental stations. With resonator mirrors of 7 m curvature, the optical mode should clear the wiggler vacuum chamber (the limiting factor) up to a wavelength of 15  $\mu\text{m}$  with less than 2% loss per pass due to clipping.

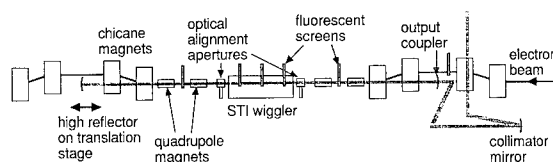


Fig. 1. Schematic of the mid-IR FEL at Stanford showing the wiggler, resonator, chicanes, and focussing magnets.

At wavelengths between 15  $\mu\text{m}$  and 18  $\mu\text{m}$ , anticipated losses increase to 4% per pass.

The optical transport from the output coupler end of the resonator to the diagnostics station [2] is entirely in vacuum to minimize atmospheric absorption. A few percent of the power is deflected near the output and monitored for the linac operator with a pyro-electric detector. A mirror then collimates the beam so that it remains less than 5 cm in diameter over the 40 m transport.

### 3. Characterization

Fig. 2 shows the relative power, small signal gain, optical spectral width, and optical pulse length as functions of the resonator cavity length detuning. These measurements were made with the optical diagnostics [2]. The laser was too unstable at detunings beyond maximum power to continue measurements. The optical wavelength for this

Table 1  
Physical parameters of the mid-IR FEL wiggler, resonator, and electron beam

|                         |                   |
|-------------------------|-------------------|
| $\lambda_w$             | 3.1 cm            |
| $N$ (periods)           | 72                |
| Length                  | 2.23 m            |
| Peak $B$ field          | 4.1 kG            |
| $K_{rms}$               | 0.83              |
| $\lambda$ at 37 MeV     | 5.0 $\mu\text{m}$ |
| Vacuum chamber diameter | 11 mm             |
| Maximum $\lambda$       | 15 $\mu\text{m}$  |
| Electron pulse length   | $\leq 2$ ps       |
| Peak current            | 4–6 A             |
| $\epsilon_n$            | 10 mm-mrad        |

☆ Work supported in part by the Office of Naval Research, Contract #N00014-91-C-0170.

\* Corresponding author. Tel. +1 415 723 0209, e-mail brich@leland.stanford.edu, fax +1 415 725 8311.

dense cold vapor in the liquid He container. Cooling capacity of the 4 K refrigerator is 11 W at 4.5 K.

Since the installation of the four superconducting accelerator modules at Tokai, the modules and refrigerator systems have been in service for about 10 000 hours. After several thousand hours of operation, air contamination in a return pipe to the Joule–Thomson valve was found at least 3 times in one of the refrigerator systems. To solve the problem, we finally replaced the contaminated rigid piping with a shortened flexible piping. Except for the contamination problem, the system has run very well and steadily without any maintenance and operation crew.

A 40 K/80 K two-stage closed-cycle He refrigerator, mounted in a vacuum vessel of the module, was adopted to cool down the 40 K and 80 K heat shields and other major components of the cryostat. The 40 K and 80 K heat shields are used to prevent heat transfer from outside into the liquid He container. The heat shields also work as a thermal anchor, the two cooling stages of the 40 K/80 K refrigerator in fact provided temperatures of 9 K and 50 K and estimated cooling capacities of < 10 W and < 50 W, respectively.

Vibrational problems in the superconducting accelerator module have been discussed as one of the most serious for the multi-refrigerators system. To minimize harmful effects from refrigerator vibration, both the 4 K and 40 K/80 K refrigerators are independently supported by a heavy and rigid steel frame. The frame is directly fixed on the floor, and has no direct connecting part with the accelerator module and module support. The measured amplitude of the module flange vibration is around 0.05  $\mu\text{m}$ . As the amplitude causes only a few tens of Hz error, we have not observed any harmful effect during beam operation.

## 5. Preliminary beam test

In 1994, a preliminary beam test of the JAERI superconducting rf linac FEL has been successfully performed

to get an electron beam of a few amperes of peak current after the main accelerator at around 15 MeV. Measured energy resolution of the pre-accelerated beam is about 3% (FWHM) and that of the fully-accelerated beam about 1% or less. Maximum transmission of the beam is now around 25% or less. As there are beam losses in the SHB, pre-accelerators and momentum filter, we plan to modify the elements and related parts including the gun and grid pulsing system.

## 6. Summary

In conclusion, we presented the status and purpose of the JAERI quasi-cw, high-average power FEL program using the superconducting rf linac driver, and other FEL elements. We reported the operational performances of the injector, superconducting rf linac, and liquid He refrigerators. We also reported the preliminary results of the transported electron beams in the superconducting rf linac.

## Acknowledgement

The authors would like to thank Dr. M. Ishii of JAERI for their continuous encouragement and interests in this work.

## References

- [1] M. Sawamura et al., Nucl. Instr. and Meth. A 318 (1992) 127.
- [2] M. Ohkubo et al., Nucl. Instr. and Meth. A 296 (1990) 270.
- [3] R. Kato et al., these Proceedings (16th Int. Free Electron Laser Conf., Stanford, CA, USA, 1994) Nucl. Instr. and Meth. A 358 (1995) ABS 77.
- [4] M. Sawamura et al., *ibid.*, p. ABS 73.
- [5] R. Nagai et al., *ibid.*, p. 403.
- [6] M. Sugimoto et al., *ibid.*, p. ABS 83.

# High gradient linac for compact FELs

P. Raimondi \*, G. Messina

CRE, ENEA, Via Enrico Fermi 27, 00044 Frascati (RM), Italy

## 1. Introduction

The necessity of high current sources for Compact FELs has brought us to develop a 2 MeV, 1 kA, 3 ns pulse duration, 1 kHz repetition rate, high gradient linac based on the magnetic pulse compression technique. In the following the accelerator characteristics are described. Preliminary results are also shown.

## 2. Accelerator description

The accelerator is composed of a cathode excited by a high voltage pulse generator (Fig. 1). The generator is capable of generating pulses up to 1 MV on a 300  $\Omega$  impedance and up to 2 MV on a bigger impedance, as when the load is the cathode itself. The pulse duration is 3 ns, while the repetition rate of the modulator could be as high as 1 kHz. The compactness required for the accelerator has brought us to develop a pulse generator based on magnetic compression by means of saturable inductors. The scheme of the pulser is shown in Fig. 2.

The first switch is a thyatron that generates a 20 kV, 1  $\mu$ s pulse. The following stages compress the pulse to 30 ns and raise the voltage to 350 kV with a transfer efficiency of about 70%. At the end of the compression system a 3 ns, 20  $\Omega$  blumline is charged, then a self-triggered spark-gap generates the final pulse. The 350 kV pulse is then transformed into a 1 MV pulse by means of a line transformer. Fig. 3 shows the pulses in the several stages.

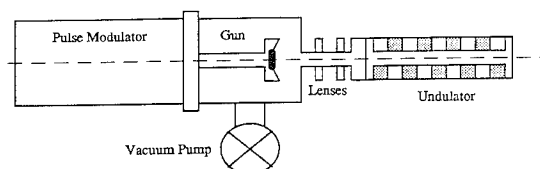


Fig. 1. Block scheme of the accelerator.

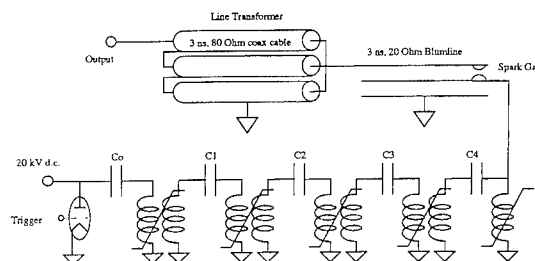


Fig. 2. Block scheme of pulse modulator.

Then the pulse, through a vacuum transition, excites the cathode. Fig. 4 shows the scheme of the cathode and the electron trajectories computed by the SLACGUN code [1].

Since the pulse is very short, it is possible to have a high electric field between cathode and anode. It has been shown [2] that for the expected pulse duration it is possible to hold a gradient up to 900 MV/m. To allow a safety margin, our cathode has been designed with a maximum gradient of 200 MV/m. With this gradient the electrons are emitted by a plasma effect, so the cathode is just a cold graphite pill of 4 mm diameter, with practically no limits for the current density.

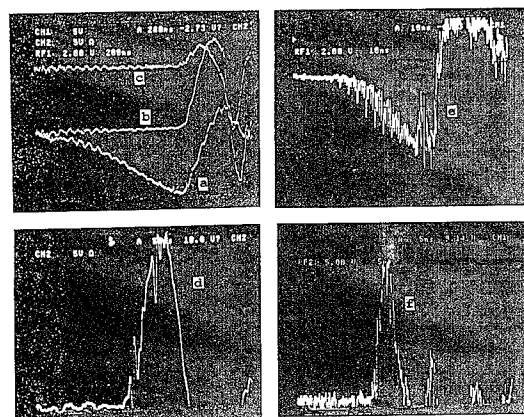


Fig. 3. (a) C1 charging voltage (20 kV/div); (b) C2 charging voltage (30 kV/div); (c) C3 charging voltage (30 kV/div); (d) C4 charging voltage (30 kV/div); (e) blumline charging voltage (100 kV/div); (f) output pulse (200 kV/div).

\* Corresponding author. E-mail 40355::raimondi.

data was  $4.5\ \mu\text{m}$ . Stable operation with a pulse length as short as  $0.6\ \text{ps}$  (at  $5\ \mu\text{m}$  wavelength) has been achieved. Note that the spectral width and pulse length vary inversely, indicating that the FWHM time–bandwidth product stays fixed at approximately  $0.8$ .

Fig. 3 shows the diagnostic spectrum and autocorrelation of a nearly-transform-limited optical pulse, taken simultaneously with “FROG” measurements discussed in Ref. [3]. The FWHM time–bandwidth product calculated using the diagnostics data is  $0.5$ . The pulse shape is nearly Gaussian and has very little aberration.

The wavelength was varied from  $3.3\ \mu\text{m}$  to  $7.3\ \mu\text{m}$  using dielectric output couplers, the combined bandwidths of which were limited to that span. User experiments were performed over that entire range of wavelengths. A silver-on-copper mirror with a  $\frac{1}{2}\ \text{mm}$  hole for output coupling

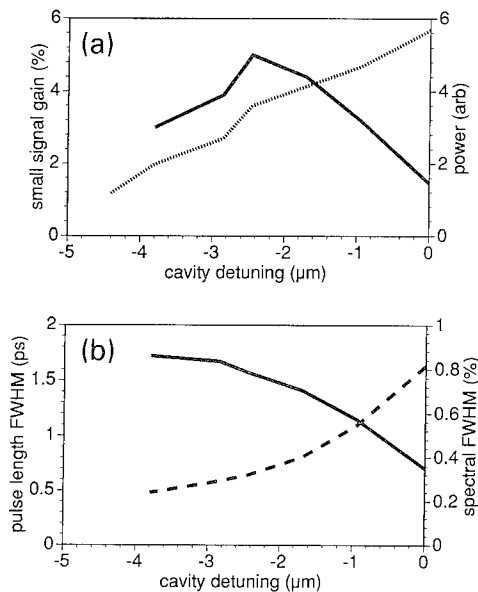


Fig. 2. (a) Relative optical power (dotted) and small signal gain (solid) and (b) optical pulse length (FWHM) and spectral width (FWHM) (dashed) versus resonator cavity length detuning. The laser was too unstable to obtain data beyond that shown.

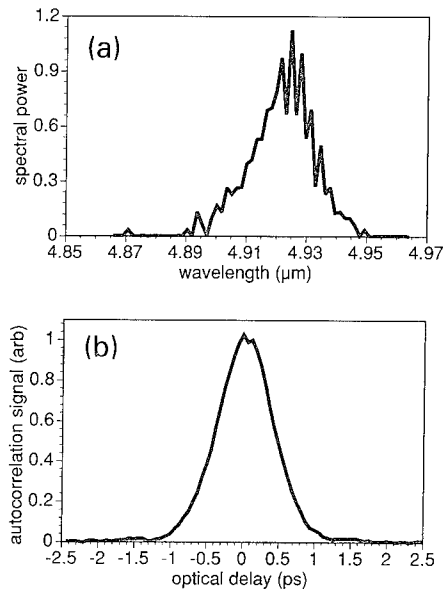


Fig. 3. (a) Typical spectrum and (b) autocorrelation for a near-transform-limit optical pulse. The FWHM time–bandwidth product is  $\approx 0.5$  (and the theoretical minimum is  $0.44$ ).

was used to lase from  $7.3\ \mu\text{m}$  to  $10.3\ \mu\text{m}$ , limited by time constraints.

#### 4. Conclusion

The new mid-IR FEL at Stanford has demonstrated lasing between  $3.3\ \mu\text{m}$  and  $10.3\ \mu\text{m}$  wavelength and should be capable of operation from  $3\ \mu\text{m}$  to  $15\ \mu\text{m}$ . Near-transform-limit optical pulses are attainable with pulse lengths ranging from  $0.6\ \text{ps}$  to  $2\ \text{ps}$ .

#### References

- [1] T.I. Smith et al., Proc. SPIE vol. 1854 (1993) 23.
- [2] K.W. Berryman et al., these Proceedings (16th Int. Free Electron Laser Conf., Stanford, CA, USA, 1994) Nucl. Instr. and Meth. A 358 (1995) 300.
- [3] B.A. Richman and K.W. DeLong, *ibid.*, p. 268.

Eq. (5) describes the excitation of a nonlinear plasma wave moving at a phase velocity  $v_0$ . Working from this equation, we can determine how the amplitude of the excited wave varies with the density  $N$  and length  $\tau$  of the electron beam. It turns out that the excitation of the plasma wave occurs in two stages. In the first stage, the electric field generated by the bunch accelerates plasma electrons in the direction opposite the direction in which the bunch itself is moving. After a time  $\tau$ , the electron bunch then moves off in the forward direction. The result is an abrupt change in the potential  $U(p)$  (see Eq. (6)), by an amount

$$U_0(p) = 4\pi e^2 n_0 \sqrt{p^2 + m^2}. \quad (7)$$

The plasma electrons then execute free oscillations, which are described by Eq. (5) with  $N=0$ , while the initial conditions are determined by the values which the variable  $p$  and  $dp/d\alpha$  have reached by the time  $\tau$ . It is easy to see that the amplitude of these wakefield oscillations is at a maximum if the “coordinate”  $p$  is at maximum at the time  $\tau$ , i.e., if  $dp/d\alpha = 0$ .

By virtue of the obvious conservation law

$$\begin{aligned} \frac{1}{2} \left( \frac{dp}{d\alpha} \right)^2 + 4\pi e^2 \left[ v_0 N p + (n_0 - N) \sqrt{p^2 + m^2} \right] \\ = 4\pi e^2 (n_0 - N) m \end{aligned} \quad (8)$$

the maximum amplitude which we are seeking,  $p_*$ , is determined by the equation

$$v_0 N p_* + (n_0 - N) \sqrt{p_*^2 + m^2} = (n_0 - N) m. \quad (9)$$

We find

$$p_* \approx \frac{-2(n_0 - N) m N}{n_0(n_0 - 2N)}. \quad (10)$$

It is easy to see that the  $N$  dependence of  $p_*$  has a pole  $|p_*| \rightarrow \infty$  as  $N \rightarrow n_0/2$ . The reason is that at  $N > n_0/2$  the potential  $U(p)$  loses its minimum, and the solution ceases to be oscillatory. Since only solutions with  $v < v_0$  are physically meaningful, this circumstance means that “traveling” solutions are generated only by relatively short pulses under condition

$$n_0 - 2N \leq (n_0/2) \sqrt{1 - v_0^2}.$$

Going back, we note that the electric field amplitude, thought of as a function of the plasma density, goes through a relatively sharp maximum at  $n_0 \sim 2N$ . Specifically, at  $n_0 > 2N$  we have

$$E_{\max} \approx 2\sqrt{4\pi N m} \sqrt{N/(n_0 - 2N)}. \quad (11)$$

The fraction in the second radical can reach the value  $\gamma_0 = (1 - v_0^2)^{-1/2}$  at the maximum. At  $n_0 < 2N$ , the electric field amplitude is determined by the breaking:

$$E_{\max} \approx 2\sqrt{4\pi N m} \sqrt{2\gamma_0 n_0/N}. \quad (12)$$

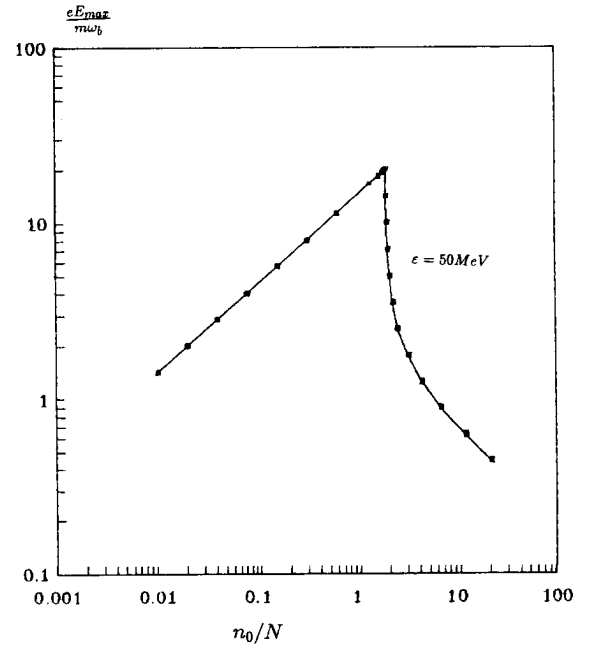


Fig. 1. Amplitude of the accelerating electric field in the wake of an electron bunch as a function of the plasma density. Here and in Fig. 2,  $\omega_b = (4\pi e^2 N/m)^{1/2}$ .

The corresponding length of the bunch is

$$\begin{aligned} \tau_0 = \int_{p_*}^0 dp \left[ v_0 - p / \sqrt{p^2 + m^2} \right] \\ / \sqrt{8ne^2 \left( (n_0 - N) \left[ m - \sqrt{p^2 + m^2} \right] - v_0 N p \right)}. \end{aligned} \quad (13)$$

This length also has a sharp maximum at  $n_0 \sim 2N$ .

Figs. 1 and 2 show curves plotted from Eqs. (11)–(13) for case  $\gamma_0 = 100$  (the energy of the accelerated electrons is 50 MeV.) We again note that reaching the maximum amplitude of the wakefield oscillations of a change at given beam density requires that the length of the bunch be strictly correlated with the plasma density. The amplitude of the wakefield oscillations falls off as the bunch becomes either shorter or longer.

In order to consider the influence of plasma waves upon the electron bunch, computer simulations were carried out. The equations of motion of a large number of electrons of the beam and plasma were solved together with Maxwell's equations.

The results are shown on Figs. 3–5 ( $j = 5$  kA/cm<sup>2</sup>,  $\gamma = 100$ ). The plasma electron density is shown in Fig. 3. The harmonic oscillations of plasma density (Fig. 3a:  $n_0 = 10^{13}$  cm<sup>-3</sup>) become nonlinear ones (Fig. 3b:  $n_0 = 3.3 \times 10^{12}$  cm<sup>-3</sup>; Fig. 3c:  $n_0 = 2.5 \times 10^{12}$  cm<sup>-3</sup>). The optimal dimensions of the bunch are equal to 0.6 cm, 1.7 cm, and 3.6 cm. respectively.

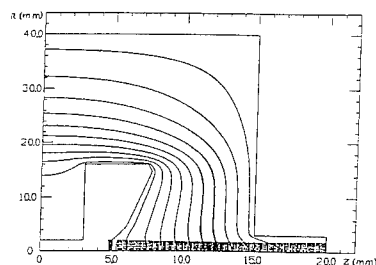


Fig. 4. Electron trajectories in the cathode region.

The design beam current is about 1 kA, the predicted unnormalized beam emittance is on the order of  $\pi$  mm mrad, while the energy spread is determined by the pulse shape on the cathode, and is expected to be on the order of 10%.

### 3. Results and conclusions

Up to now we have completed and tested the pulse generator up to 50 Hz repetition rate with no cooling

system. Moreover, we have already built the cathode and the vacuum chamber and we are assembling the pulser and the cathode. The first beam tests should start in September. We are also working on two more magnetic compression stages, using ferrites, to compress the pulse to 5 ns and avoid the use of the spark-gap. The overall cost of the accelerator is approximately 150 k\$.

Preliminary calculations show that an FEL operating in the submillimeter region should deliver up to 200 MW of peak power. Given these characteristics, this machine seems the ideal beam source for the future development of Compact FELs in the submillimeter region.

### References

- [1] W.B. Herrmannsfeldt, Electron Trajectory Program, SLAC-266, UC-28.
- [2] V. Baglin et al., High Gradient Experiments with Nanosecond Pulses, 1993 IEEE Proc.

# Numerical simulation studies of the design and performance of the AFEL for high average power operation <sup>☆</sup>

John C. Goldstein <sup>\*</sup>, Harunori Takeda, Dinh C. Nguyen

Group X-1, MS F645, Los Alamos National Laboratory, Los Alamos, NM 87544, USA

The AFEL (Advanced Free-Electron Laser) at Los Alamos [1–7] is compact free-electron laser oscillator which utilizes a very high-brightness electron beam generated by a high gradient linac whose source of electrons is a photocathode injector. This device has been operating, with 15–17 MeV electrons, at optical wavelengths in the 5.0–6.0  $\mu\text{m}$  range, since April of 1993 with a 1-cm-period, permanent-magnet wiggler which is 24 periods long. The linac produces about 12  $\mu\text{s}$  macropulses at a normal repetition rate of 1 Hz, while the micropulse repetition rate within a macropulse is 108.33 MHz, which is consistent with the optical cavity length of about 138.5 cm. A program is now under way to upgrade the subsystems of this laser in order to allow it to produce long-time-average optical output powers in the range of 0.1 to 1.0 kW. In this communication, we briefly indicate the details of the equipment upgrades, describe a new high-extraction-efficiency wiggler, and present the results of numerical simulation studies of the proposed design.

The accelerator has been designed from the onset for high average power operation, so no major changes are needed other than the addition of a new beam dump. The linac structure was designed to minimize dipole modes and, therefore, to increase the threshold current for cumulative beam-breakup instabilities. Also, the structure has good electrical efficiency despite having been designed primarily to preserve the brightness of the electron beam. The rf-system will be upgraded by installing a new modulator for the 30 MW peak-power klystron. This will allow longer macropulses and a higher macropulse repetition rate ( $\sim 100$  Hz). The rf-system will be capable of 50 kW average power operation. The Nd:YLF photocathode drive laser will be converted to a diode-pumped system which will allow operation at a micropulse repetition frequency

of 216 MHz, a macropulse duration of about 30  $\mu\text{s}$ , and a macropulse repetition rate of 100 Hz. As is true with the present laser, the upgraded laser will operate at the fourth harmonic,  $\lambda \sim 0.25 \mu\text{m}$ , and will illuminate a  $\text{Cs}_2\text{Te}$  photocathode. Increased drive laser energy per micropulse will allow for greater electron micropulse charge.

The proposed high-extraction-efficiency wiggler design is shown in the figures. Fig. 1 shows the variation of the wiggler wavelength ( $\lambda$ , solid line, left side scale) and wavenumber ( $k = 2\pi/\lambda$ , dashed line, right side scale) versus axial location. Fig. 2 shows the variation of the peak wiggler field amplitude  $b_0$  (solid line, left side scale) and associated dimensionless vector potential  $a_w (= eb_0\lambda/(2\pi mc^2)$ , dashed line, right side scale). The device consists of a short prebuncher wiggler, a drift distance (blank space in the figures), and a wiggler in which the wiggler wavenumber varies quadratically with axial location. The taper is 25%, which corresponds to a fractional deceleration of the bucket by almost 13%. The drift distance is filled by a dispersive magnetic field generated by four dipoles with a remotely-variable gap. The dispersive section is needed to reduce the overall

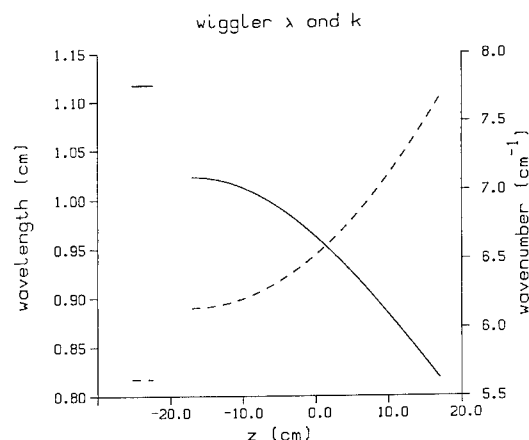


Fig. 1. Wiggler wavelength ( $\lambda$ , solid line, left side scale) and wavenumber ( $k = 2\pi/\lambda$ , dashed line, right side scale) versus axial location.

<sup>☆</sup> Work performed under the auspices of the U.S. Department of Energy and supported by Los Alamos National Laboratory Institutional Supporting Research funds.

<sup>\*</sup> Corresponding author. Tel. +1 505 667 7281, Fax +1 505 665 3389, e-mail jcg@lanl.gov.



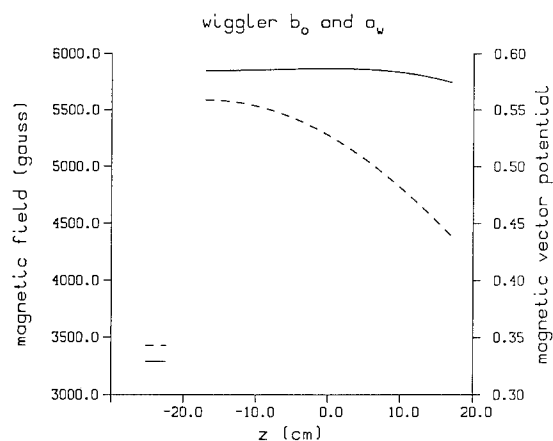


Fig. 2. Peak wiggler field amplitude  $b_0$  (solid line, left side scale) and associated dimensionless vector potential  $a_w$  (dashed line, right side scale) versus axial location.

length of the wiggler assembly, which otherwise would severely truncate the short Rayleigh range optical mode, while allowing for an optimum drift length for bunching to occur.

Simulations were performed with the following electron beam and optical resonator parameters: for the beam, kinetic energy 16.5 MeV ( $\gamma = 33.29$ ), peak current  $I = 200$  A (2 nC in a 10 ps FWHM Gaussian), “90%” normalized transverse emittance  $10 \pi$  mm-mrad, and fractional energy spread FWHM  $\Delta\gamma/\gamma = 0.5\%$ ; for the resonator, length 138.36 cm, Rayleigh range 8.587 cm, optical wavelength  $5.4 \mu\text{m}$ , empty cavity focal point 0.4 cm upstream of the center of the tapered wiggler, mirror radii 1 cm, and reflectance of copper 0.99.

The results of the simulations pointed up various features of the proposed design. 1-D, single-pass, single-wavefront calculations showed a reasonable small-signal gain of 53%. At an input to the prebuncher of 0.9 GW, the gain was 25.6% with an extraction efficiency  $\eta = 6.8\%$ , while at 2.5 GW input the gain dropped to 12.9% and  $\eta = 9.6\%$ . Hence, the wiggler operates at high efficiency only for internal power levels of several GW, and to reach those power levels requires cavity losses below 13%. The present resonator probably cannot tolerate more than about 1 GW before micropulse damage occurs on the downstream mirror on which the mode area is about  $1/7 \text{ cm}^2$ . Finite-pulse, multiple-pass 1-D results show that sidebands develop: at steady-state, an internal power of about 0.37

GW is reached, with  $\eta = 3.5\%$ , with 18.5% cavity loss, while reducing the loss to 12% increases the extraction to only  $\eta = 3.75\%$ . Hence, sidebands must be eliminated for efficient wiggler operation, but addition of such elements (a grating rhomb, or a Littrow grating on one of the mirrors) adds cavity loss and lowers the threshold for optical damage on those elements.

3-D single-wavefront, single-pass calculations show that, for 0.9 GW input, the gain (20.3%) and extraction efficiency ( $\eta = 5.4\%$ ) are reduced by 20% only if the transverse emittance is doubled, or the energy spread is quadrupled. 3-D single-wavefront, multiple-pass simulations show that a hole in the upstream mirror for outcoupling causes significant diffraction loss in the empty cavity: 13.5% for a 0.12 cm diameter hole (7% outcoupling), and 19.5% for a 0.1453 cm diameter hole (11% outcoupling). These losses increase for the loaded cavity: including a reflection loss of 1% for each mirror with the smaller outcoupling hole, a net small-signal gain of 17%, and a gross gain of 47%, was found, thus implying a total cavity loss of 20.4%. At large signal, a steady state was found with a net gain of 19.1% at 1.3 GW, implying a cavity loss of 16%.

These results show that the present resonator might be usable up to  $\sim 100$  W output, although the mirrors would have to be cooled to avoid thermal distortion. For greater power levels, sideband suppression is needed along with a longer resonator to reduce loading of the optical elements: either a ring resonator, or a “folded” resonator could be used. Further work is needed to complete the resonator design and evaluate the resulting FEL performance.

## References

- [1] D.C. Nguyen et al., these Proceedings (16th Int. Free Electron Laser Conf., Stanford, CA, USA, 1994) Nucl. Instr. and Meth. A 358 (1995) 27.
- [2] D.C. Nguyen et al., in: Gas, Metal Vapor, and Free Electron Lasers and Applications, eds. V. N. Smiley and F.K. Tittel, Proc. SPIE 2118 (1994) 260.
- [3] D.C. Nguyen et al., Nucl. Instr. and Meth. A 341 (1994) 29.
- [4] R.L. Sheffield et al., Nucl. Instr. and Meth. A 341 (1994) 371.
- [5] K.C.D. Chan et al., Nucl. Instr. and Meth. A 318 (1992) 149.
- [6] R.L. Sheffield, M.J. Browman, B.E. Carlsten and L.M. Young, Nucl. Instr. and Meth. A 318 (1992) 282.
- [7] J.C. Goldstein, T.-S.F. Wang and R.L. Sheffield, Nucl. Instr. and Meth. A 318 (1992) 617.

## Design of the pseudospark discharge for a Raman FEL<sup>☆</sup>

Ming Chang Wang<sup>a,\*</sup>, Junbiao Zhu<sup>a</sup>, Zhijiang Wang<sup>a</sup>, Jae Koo Lee<sup>b</sup>, T.H. Chung<sup>c</sup>

<sup>a</sup> Shanghai Institute of Optics and Fine Mechanics, Academia Sinica, P.O. Box 800211, Shanghai, China

<sup>b</sup> Pohang Institute of Science and Technology, P.O. Box 125, Pohang, 790-600, South Korea

<sup>c</sup> Dong-A University, Pusan, 604-714, South Korea

### 1. Introduction

During the last decade, the pseudospark discharge of the type first explored by Christiansen and Schultheiss [1] has gained considerable attention because of its capability of producing a high quality electron beam. In addition, its potential application to high power switch development, electron beam lithography and plasma processing are very attractive.

The pseudospark discharge is a new kind of gas discharge, based on the principles of a hollow cathode discharge and has of the property of a self-sustaining discharge. A high brightness electron beam of  $10^{11}$  A/m<sup>2</sup>rad<sup>2</sup> at 20 keV and 70 A peak current is produced by a pseudospark [2] an electron beam with intense current density ( $> 10^4$  A/cm<sup>2</sup>), narrow beam diameter ( $< 1$  mm) and very low emittance (tens of mm mrad) well qualified for use in free electron lasers. Several experiments have been reported in which high-brightness electron beams have been produced in pseudospark devices operating in the voltage range 20–50 keV [3].

The design of a pseudospark device operating at a voltage of 300–400 keV for a Raman FEL at SIOFM is presented. This study is to explore the scaling laws at high voltage. The preliminary results of the brightness diagnostics of pseudosparks produced electron beams are given.

### 2. Design consideration

It is well-known that electrical breakdown in gases is described by the Paschen law  $U = f(pd)$ , where  $p$  is the gas pressure (Torr) and  $d$  is the distance between anode and cathode (cm). A typical breakdown curve as a function of  $pd$  is numerically simulated as shown in Fig. 1. It is

characterized by a nearly linear rise at  $pd$ -values from 1.9 Torr cm to 10 Torr cm, a minimum around 0.53 to 1.0 Torr cm and a steep rise below the minimum. Above the minimum is a glow discharge. The region from 0.01 to 0.1 Torr cm is known as the pseudospark discharge. The breakdown below  $7.5 \times 10^{-4}$  Torr cm is called vacuum breakdown.

The breakdown voltage  $U$  of a multigap pseudospark device has been measured systematically for a wide range of ambient gas pressures  $p$  and anode–cathode gap distances  $d$  [2]. The breakdown voltage  $U$  (kV) is a function of  $(p^2d)^{2.2}$ . This is in contrast to Paschen's law, which is a function only of  $pd$ , i.e.  $(pd)U = \text{constant}$ . Now we use the experimental formula from Rhee's experiments [2],  $(p^2d)^k U = \text{constant}$ , where constant = 0.2,  $k = 2.2$ .

For our design of  $U = 400$  kV, we have  $(p^2d)^{2.2} = 5 \times 10^{-4}$ . The main discharge parameters can be considered as follows: if  $p = 0.1$  Torr,  $d = 3.2$  cm, the distance is too short; if  $p = 0.01$  Torr,  $d = 316$  cm, the distance is too long. If we take a compromise pressure  $p = 0.056$  Torr, then  $d = 10$  cm.

The distance  $d$  (cm) as a function of the pressure  $p$  at a given voltage was calculated as shown in Fig. 2. In the range of 100–500 kV, the curves at high pressure tend to

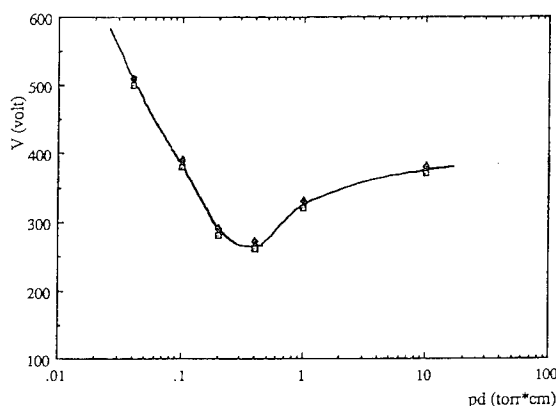


Fig. 1. A typical Paschen curve with numerical simulations.

<sup>☆</sup> This work was supported by the National Natural Science Foundation of China.

\* Corresponding author. Tel. +86 21 95 34 890, fax +86 21 95 28 812.

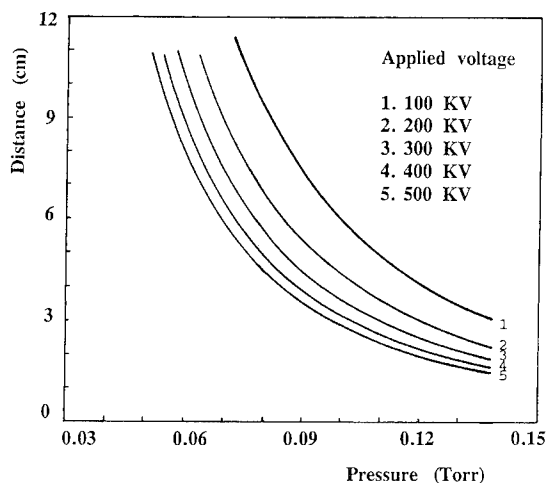


Fig. 2. The distance  $d$  (cm) is a function of the pressure  $p$  at a given voltage.

approximately 2 cm, while at the lower side of the pressure a reasonable distance should be 10 cm.

The experimental configuration of the pseudospark discharge is shown schematically in Fig. 3. The hollow cavity is a 3 cm diameter and 4.1 cm long cylindrical cavity. The discharge chamber consists of a planar cathode with a hollow cavity, sets of intermediate electrodes and insulators with a common channel, and a planar anode. The electrodes are made of brass and the insulators are of

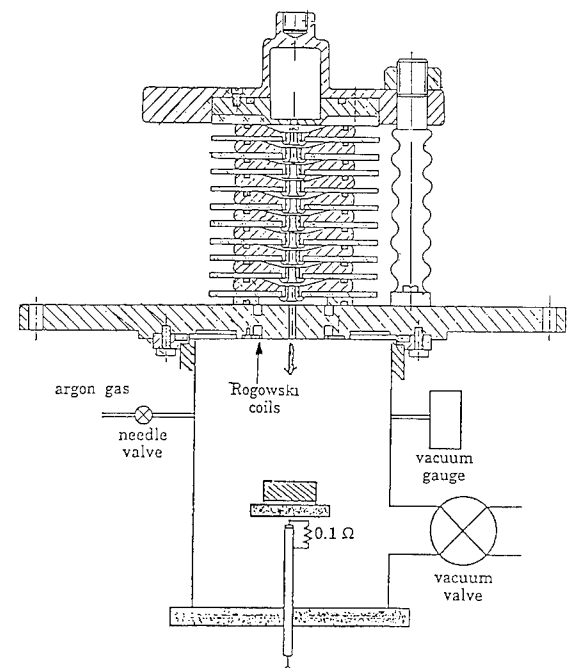


Fig. 3. The experimental configuration of the pseudospark discharge.

Plexiglas. The diameter of the channel is 3.2 mm and electrons generated in the hollow cathode region are accelerated through the channel to the extraction point on the anode side of the device. The anode–cathode gap distance is varied by employing a different number of intermediate electrode sets (each set is 10 mm thick).

The mechanism of electron beam generation has been considered. The field escalation model can be used to describe the physical processes in intense pulsed electron beams and the multiple kinds of ion beams produced in the multilateral discharge chamber. The condition for the hollow cathode effect is written approximately as follows:  $\phi p < 1$  Torr cm, where  $\phi$  is the internal diameter of the hollow cathode.

The chamber contains a low-pressure gas-filling of typical 0.056 Torr. The gas pressure of the chamber is controlled by a Vacuum Auto Controller, with measuring and control range from 0.15 to  $7.5 \times 10^{-7}$  Torr. The accuracy of the auto controller is  $\pm 1.5\%$  (full scale). The gas is filled by a piezo-electric needle valve, with maximum flow  $> 2.25 \times 10^{-3}$  Torr cm<sup>3</sup>/s.

When a high voltage pulse of 300–400 keV is applied between the anode and the cathode, a pseudospark discharge occurs (10–100 ns). A self-pinch electron beam is expected if the current exceeds some 10 A. Depending on the total current, the diameter of the electron beam at anode exit is expected to be between 0.1 and 0.5 mm.

A 63 cm long drift chamber was attached to the anode side to make room for diagnostics, including the emittance meter and the Faraday cup. A Rogowski coil was molded into the downstream side of the anode flange to monitor the electron beam current extracted through the anode hole. A Faraday cup was employed to measure the beam current at various axial positions. A pulse line accelerator which normally operates at 300–400 keV, 400–800 A, 40 ns was modified to produce a longer pulse duration of about 1  $\mu$ s. The configuration is used by eliminating the output pulse forming switch and connecting the load to the output of the pulse transformer via a water coax section.

The hollow cathode effect occurring in and near the hollow cathode hole is responsible for electron beam generation in the pseudospark chamber operating in the left branch of Paschen curve.

### Acknowledgements

The authors are grateful for valuable discussions with Professor M.J. Rhee, B.N. Ding and X.L. Jiang.

### References

- [1] L. Christiansen and C. Schultheiss, *Z. Phys. A* 290 (1979) 35.
- [2] M.J. Rhee and B.N. Ding, *Phys. Fluids B* 4 (1992) 764.
- [3] K.K. Jain, E. Boggasch et al. *Phys. Fluids B* 2 (1990) 2487.



ELSEVIER

## Demonstration of micropulse energy enhancement with the SCA/FEL external cavity system <sup>☆</sup>

P. Haar <sup>\*</sup>, H.A. Schwettman, T.I. Smith

Stanford Picosecond FEL Center, W.W. Hansen Experimental Physics Laboratory, Stanford University, Stanford, CA 94305-4085, USA

### 1. Introduction

We have recently demonstrated that FEL optical pulses can be stacked in our External Cavity System (ECS), increasing the micropulse energy by more than 70 times [1]. We can, in principle, make this increased micropulse energy available to experimenters by dumping the external cavity using an intracavity semiconductor switch; however, the repetition rate of such a system would be limited to 10–100 Hz by the external laser necessary to activate the switch. For modest enhancements, up to a factor of 9, it is possible to use enhanced outcoupling, as described below, and achieve repetition rates as high as 200 kHz. To reduce sample heating, many users at the Stanford Picosecond FEL Center reduce the micropulse rep rate to  $\leq 100$  kHz, so this approach allows us to deliver enhanced micropulses to experimenters at rep rates as high as they are presently using.

Under ideal conditions, energy will accumulate in the ECS on a time scale  $\tau = (2L/c)Q$ , where  $L$  is the length of the cavity and  $1 - \exp[-1/Q]$  is the round trip cavity loss. When it reaches steady state, the stored energy is

$$U = \frac{\delta_e U_{inc}}{(1 - e^{-1/Q})^2} \approx 4\delta_e Q^2 U_{inc}, \quad (1)$$

where  $\delta_e$  is the loss due to the coupling mirror and  $U_{inc}$  is the energy of the incident FEL micropulses. The latter expression is valid if all losses are small. In practice, the stored energy is limited by two important factors [1,2]. First, in our present unstabilized system, instability in the timing between the pulse circulating in the ECS and the incident FEL micropulses restricts significant stored energy to resonant peaks which occur at uneven intervals (at an average rate of a few Hz) and which last typically 100–500  $\mu$ s. The second effect, beam steering fluctua-

tions, causes variations in the stored energy from one resonant peak to the next, typically 5–10%.

The energy reflected from the cavity is a coherent superposition of the direct reflection of the incident FEL micropulses and the fraction of the circulating pulse which passes out of the cavity through the coupling mirror. If we denote the energy of this reflected pulse  $U_R$ , then at steady state conservation of energy requires

$$U_{inc} + \left( \frac{e^{-1/Q}}{1 - \delta_e} \right) U = U + U_R, \quad (2)$$

where the expression on the left in brackets is just the non-coupling losses.

### 2. Enhanced outcoupling (EOC)

If the incident FEL micropulses are interrupted, the reflected pulse will consist solely of the fraction of the circulating ECS pulse that passes out of the cavity through the coupling mirror. The total energy of the first pulse returning from the cavity after interruption is

$$U_{R4} = \delta_e \left( \frac{e^{-1/Q}}{1 - \delta_e} \right) U \approx 4\delta_e^2 Q^2 U_{inc}. \quad (3)$$

Each subsequent pulse leaving the cavity will be reduced from the previous one by the round trip losses; the stored energy will “ring down”. If the cavity is strongly overcoupled, so that  $Q \approx \delta_e^{-1}$ , then Eq. (3) reduces to  $4U_{inc}$ . We call this technique “fourfold enhanced outcoupling” or  $4 \times$  EOC.

Rather than interrupting the incident micropulses, we can abruptly phase shift them by  $\phi$  [3]. If  $\phi = \pi$ , it can be shown that the energy of the next pulse returning from the cavity is

$$U_{R\phi}(\pi) = 2[U_{R4} + (1 - \delta_e)U_{inc}] - U_R. \quad (4)$$

For a strongly overcoupled cavity with  $Q^{-1} \approx \delta_e \ll 1$ , this reduces to  $9U_{inc}$ . This technique is called “ninefold enhanced outcoupling” or  $9 \times$  EOC.

<sup>☆</sup> Work supported in part by the Office of Naval Research, contract # N00014-C-0170.

<sup>\*</sup> Corresponding author. Tel. +1 415 723 0291, fax +1 415 725 8311, e-mail paulhaar@leland.stanford.edu.

### 3. Experimental setup and results

A schematic layout of the external cavity system is shown in Fig. 1. The coupling mirror (C1) has a measured transmission  $\delta_e = 0.0259 \pm 0.0004$  at  $\lambda = 4.55 \mu\text{m}$ ; the other mirror is a high reflector ( $\ll 1\%$  loss). The stored energy ( $U$ ) is directly proportional to the energy transmitted through the cavity, which is measured on detector D1. The reflected energy ( $U_R$ ) is directed by the pickoff plate (P) onto detector D2. Both D1 and D2 are 1 MHz LN<sub>2</sub> cooled InSb detectors. We measured the cavity  $Q$  by using the non-resonant behavior of the cavity [1].

To measure the  $4 \times \text{EOC}$  signal we used the Electro-Optic Modulator (EOM) [4] and the Ge Brewster plate (B), which is oriented to pass vertically polarized light. When the EOM is triggered, the polarization of the incident FEL micropulses is rotated from vertical to horizontal. The portion of these pulses which reflect from C1 pass through the EOM a second time and are rotated back to vertical polarization and continue through B unattenuated. The pulse passing out of the cavity, however, only traverses the EOM once, and therefore hits B with horizontal polarization. At  $\lambda = 4.55 \mu\text{m}$ , 78% of this pulse is reflected from B onto D3, a 35 MHz LN<sub>2</sub> cooled InSb detector. Although this technique does not literally block the incident FEL micropulses, it has the same effect.

During the experiment we measured  $Q = 27.2 \pm 0.4$ . Due to equipment problems, direct measurement of  $U$  using D1 was not available; instead we calculated the stored energy using  $U_R$  and Eq. (2). The largest stored energy peaks had  $U_R = 0.16U_{\text{inc}}$  so that  $U = 80U_{\text{inc}} \pm 4U_{\text{inc}}$ . From these measurements we calculate  $U_{4R} = 2.05U_{\text{inc}} \pm 0.10$ . We observed the micropulses deflected onto D3 with an HP 54510A digital storage oscilloscope and stored calibration and  $4 \times \text{EOC}$  traces. Comparing the average energy of the calibration micropulses to the average of the  $4 \times \text{EOC}$  micropulses we find  $U_{4R} = 2.09U_{\text{inc}} \pm 0.11U_{\text{inc}}$ , in excellent agreement with our expectations.

To demonstrate  $9 \times \text{EOC}$ , we changed the role of our EOM from polarization rotation to phase modulation by inserting a polarizer between B and the EOM. The polarizer rotated the FEL polarization  $45^\circ$  so that it was parallel

to one of the induced birefringent axes [4]. Detector D2 was replaced by a 35 MHz LN<sub>2</sub> cooled InSb detector to measure the  $9 \times \text{EOC}$  signal. Although we did observe enhancement, these experiments are still in their preliminary stages, and as yet have not produced consistent results.

### 4. Conclusions

To implement  $4 \times \text{EOC}$  in a practical system, we will use a setup essentially identical to the one used for this experiment: an EOM and Ge Brewster plate will separate the two components of the reflected pulse. For  $9 \times \text{EOC}$  we will add a second EOM set up as a phase modulator. The two will be triggered so that the next FEL micropulse will be phase shifted by  $\pi$  as it heads toward the optical cavity and have its polarization rotated as it passes back through the EOMs, therefore being deflected by the Brewster plate.

There are three aspects of the current experiment which must be improved to make EOC viable. First, we must choose optimal coupling. The maxima of both EOC methods are very broad and overlap, so that one coupling value can be chosen to obtain high performance from both techniques. For the present experiment, the optimal  $4 \times \text{EOC}$  coupling is  $\delta_e = 0.186$ , whereas the optimal  $9 \times \text{EOC}$  coupling is  $\delta_e = 0.131$ . Choosing  $\delta_e = 0.15$  we would have  $U_{4R} = 3.24U_{\text{inc}}$  and  $U_{9R}(\pi) = 7.41U_{\text{inc}}$ .

Second, to find the net enhancement available to experimenters, we must factor in the losses in the ECS optics that precede the optical cavity and the 78% reflectivity of the Ge Brewster plate. A practical system must minimize these losses. It should be possible to achieve a net extraction efficiency of 60–70%, allowing a cavity with  $\delta_e = 0.15$  to provide optical pulses to experimenters with  $2.3U_{\text{inc}}$  using  $4 \times \text{EOC}$  and  $5.2U_{\text{inc}}$  using  $9 \times \text{EOC}$ .

The final major problem that must be addressed is that of stabilization. The current system produces significant stored energy only in limited duration peaks that occur at an uneven rate. To make EOC useful, we plan to stabilize the stored energy with a negative feedback loop, and produce enhanced micropulses at a rep rate up to 200 kHz.

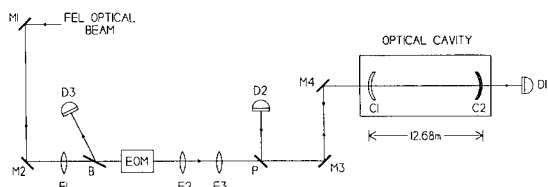


Fig. 1. Schematic of ECS setup as used for this experiment. Symbols: (M) steering mirror, (F) focussing element, (B) Ge Brewster plate, (P) 10% pick-off plate, (D) detector, (C1) cavity coupling mirror, and (C2) cavity high reflector mirror

### References

- [1] P. Haar, T.I. Smith and H.A. Schwettman, these Proceedings (16th Int. Free Electron Laser Conf., Stan CA, USA, 1994) Nucl. Instr. and Meth. A 358 (1995) 319.
- [2] P. Haar, HEPL Technical Note #92-3.
- [3] Z.D. Farkas, H.A. Hogg, G.A. Loew and P.B. Wilson, Proc. 9th Int. Conf. High Energy Accelerators, Stanford, May 1974, p. 576.
- [4] A. Yariv, Optical Electronics (Holt-Saunders, 1985) p. 288.



ELSEVIER

## A new inductive acceleration structure with multiple electrodes for an FEL

S. Kawasaki <sup>b,\*</sup>, H. Ishizuka <sup>c</sup>, A. Watanabe <sup>a</sup>, Y. Yamashita <sup>d</sup>, A. Tokuti <sup>e</sup>, S. Nakajima <sup>f</sup>,  
J. Kishiro <sup>g</sup>, K. Takayama <sup>g</sup>, M. Shiho <sup>a</sup>

<sup>a</sup> Japan Atomic Energy Research Institute, Fusion Research Establishment, Nakamachi, Ibaraki, 311-02 Japan

<sup>b</sup> Faculty of Science, Saitama University, Urawa, 338, Japan

<sup>c</sup> Department of Physics, Fukuoka Institute of Technology, Fukuoka, 811-02 Japan

<sup>d</sup> Hitachi Metals Ltd., Kumagaya, 360, Japan

<sup>e</sup> Niticon Co. Ltd., Kusatu, 525 Japan

<sup>f</sup> Hitachi Ltd., Hitachi, 316 Japan

<sup>g</sup> National Laboratory for High Energy Physics, Tsukuba, 305 Japan

At JAERI we have studied a long pulse Raman FEL with a mildly relativistic, intense electron beam of 1 MeV, 3 kA and 100 ns duration supplied by an induction accelerator module “LAX-1”. The FEL is operated in the Raman regime with a focusing planar wiggler and amplifies an input rf pulse of 100 W up to 6 MW in the frequency range of 30–45 GHz [1]. Upgrading of the JAERI accelerator to 2 MeV, 5 kA and 160 ns has been completed recently [2]. The accelerator has two independent sections. One is for beam generation and has a structure of an ordinary induction cavity fed with  $4 \times 250$  kV magnetic compression modules. The other is for post-acceleration and is equipped with a multi-electrode acceleration column, which could be isolated from the driving circuit. Details of the design for the accelerator and the power supply have been described elsewhere [3]. A schematic figure of the post acceleration module is shown in Fig. 1. It is driven with power supplies similar to those for the injector module. It has a radially double structure: an accelerating column made of ceramic with multiple electrodes located along the column with a nearly equal spacing is surrounded with the inductive driving circuits. The electrodes are connected with the driving circuit so as to get a distributed acceleration field. Stray capacitance between the driving circuit and the electrodes is estimated to be rather small and gives rise to a short rise time of the acceleration pulse. In this configuration we expect noise disturbance of the propagating beam caused by a pulse power line to be reduced to a small value since the driving

current does not flow along the wall of the beam pipe which should be kept at ground potential. The system was electrically tested in operation with a dummy load. The output accelerating voltage in the post-acceleration module shown in Fig. 2 has a rise time of 17 ns, compared with 24 ns in the injector module. Noise reduction to a fairly low level was also verified.

The equilibrium of the electron beam in the accelerating structure is calculated numerically for various arrangements of the electrodes. An example of the steady state flow is shown in Fig. 3. With a focusing longitudinal magnetic field of 3 kG superimposed, a beam of 5 kA can be transported without any serious loss. The quality of the beam accelerated inductively is one of the most important factors in the operation of Raman FELs. Degradation of the beam quality in the acceleration structure is caused by many effects. When the image current flowing along the wall of the beam pipe is interrupted by the gap it gives the beam a force of radial divergence. Another source of the beam divergence is the radiation in the gap area due to a sudden change of the wall impedance, or a wake field excitation. We wish here to simply point out that a more homogeneous distribution of accelerating fields would be preferred to provide adiabatic acceleration and to prevent growth of the beam emittance. A numerical simulation as well as an experimental demonstration of the emittance improvement are being prepared.

The most crucial instability in the course of the propagation of the intense relativistic electron beam inside a conductive boundary with a series of gaps should be BBU (beam break up) [4]. We (J.K. and K.T) developed a BBU code for the “diaphragmed” acceleration cell structure and applied it to the new configuration, to study the suppres-

\* Corresponding author. Tel. and fax +81 48 858 3371.

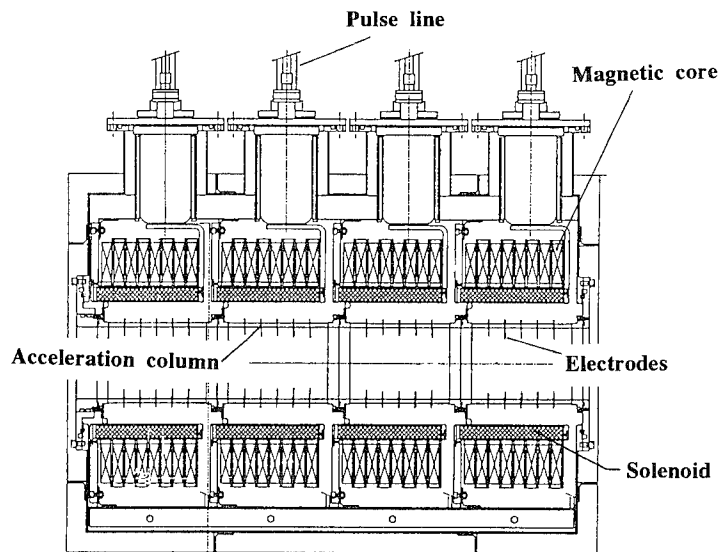


Fig. 1. A schematic figure of the post-acceleration module

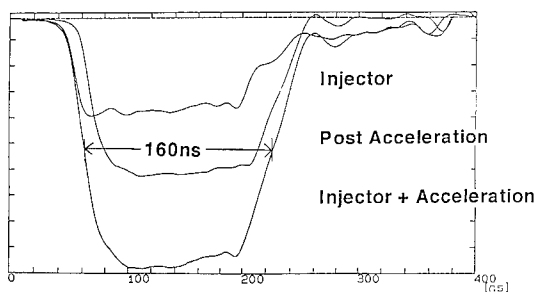


Fig. 2. The out-put accelerating voltage of the injector and post-acceleration modules.

sion of the instability by introducing a small randomness to the interspaces of the electrodes. Examples of the numerical calculation carried out for a beam of higher energy are shown in Figs. 4a and 4b. The instability was significantly reduced in case (b). In conclusion, we are optimistic that the new inductive acceleration cell will

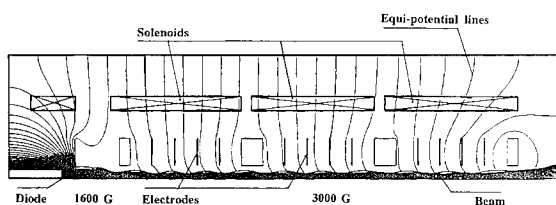


Fig. 3. A steady state electron beam accelerated in the structure.

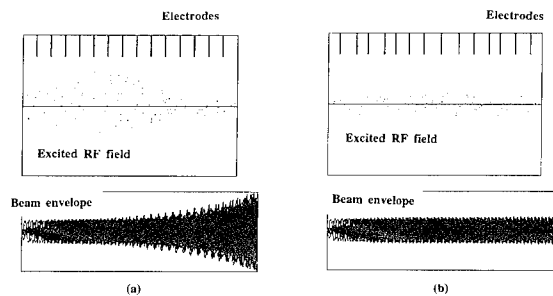


Fig. 4. Suppression of BBU mode. Beam current is 2.0 kA and particle energy is 20 MeV. The radius of the beam is a few mm. Resonant frequency of the cavity is near 1.4 GHz: (a) with regularly spaced electrodes; (b) with randomness introduced in the electrode spacing.

reduce the noise imposed on the beam and will provide a better quality.

## References

- [1] K. Sakamoto et al., J. Appl. Phys. 75 (1994) 36.
- [2] H. Ishizuka et al., Proc. 9th Int. Conf. on High-Power Particle Beams, San Diego, June 1994, to be published.
- [3] S. Kawasaki et al., Proc. 1993 Particle Accelerator Conf., Washington, DC, May 1993, p. 676.
- [4] Review papers on BBU and the references cited there are: G.J. Caporaso and A.G. Cole, AIP Conf. Proc. #249, The Physics of Particle Accelerators, Vol. II (1992) p. 1615, and D. Birk, *ibid.*, p. 1553.



ELSEVIER

## Simulations of the Stanford FIREFLY 1 kW free electron laser

D.W. Small \*, R.K. Wong, J. Blau, W.B. Colson

Physics Department, Naval Postgraduate School, Monterey, California, USA

A modification of Stanford's Superconducting Accelerator Free Electron Laser (SCAFEL) has been proposed to increase its average optical power to about 1 kW. The FIREFLY Free Electron Laser (FEL) would be a factor of 100 increase in output power over the most powerful FEL in operation now and would cost about 1 million dollars. Simulations show the evolution of longitudinal modes over many passes and the development of the trapped-particle instability. Power versus desynchronism is studied for different electron energies.

The simulations use the pendulum equation to describe the electron motion in the undulator and the wave equation to describe the optical field evolution. Dimensionless parameters are used for quantities such as  $j$ , the dimensionless electron beam current density, and  $|a|$ , the dimensionless optical field strength [1]. The electron pulse length  $\sigma_z = l_c/N\lambda$  and the desynchronism  $d = \Delta L/N\lambda$  are normalized to the slippage distance. Desynchronism is the adjustment of the optical cavity in order to overcome the effects of lethargy [1].

Simulations of the 1 kW FIREFLY FEL use an electron beam energy of 45 MeV to produce light at a wavelength of 7.6  $\mu\text{m}$ . Also simulated were beam energies of 25 MeV and 10 MeV with wavelengths of 24.1  $\mu\text{m}$  and 142  $\mu\text{m}$ , respectively. The peak current was 40 A with a micropulse length  $l_c/c = 2.1$  ps, and emittance of  $10\pi$  mm-mrad (FWHM). The undulator had  $N = 25$  periods, wavelength  $\lambda_0 = 6$  cm and an rms undulator parameter  $K = 1.1$ . The cavity length was 12.68 m with a resonator quality factor  $Q = 100$  [2].

Fig. 1 shows the results of a longitudinal multimode simulation using an electron beam energy of 45 MeV. The upper plots show the evolution of the optical field amplitude  $|a(z, n)|$  and phase  $\phi(z, n)$ , where  $z$  is the longitudinal position and  $n$  is the pass number. Also plotted is the

\* Corresponding author. Tel. +1 408 656 3114, fax +1 408 656 2834, e-mail small@physics.nps.navy.mil.

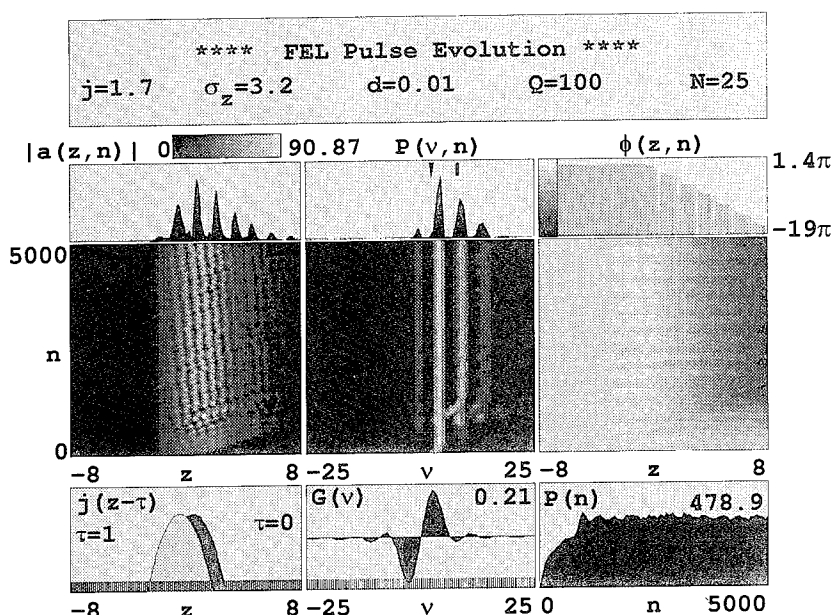


Fig. 1. Longitudinal multimode simulation of FIREFLY.



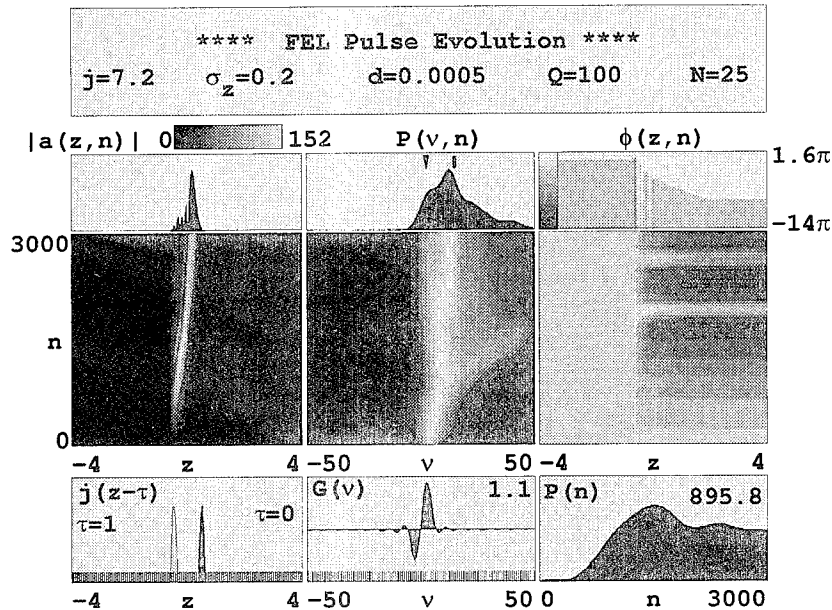


Fig. 2. Longitudinal multimode simulation of FIREFLY.

dimensionless power spectrum  $P(v, n)$ , where  $v$  is the phase velocity [1]. The three plots across the bottom of the figure are the electron pulse  $j(z)$  shown at the beginning ( $\tau=0$ ) and end ( $\tau=1$ ) of the undulator, the weak-field single-mode gain spectrum  $G(v)$ , and the dimensionless power evolution  $P(n)$ . At the wavelength 7.6  $\mu\text{m}$ , the electron pulse length is three times longer than the slippage distance. The trapped-particle instability results in a strong sideband in the power spectrum at steady-state. Note the limit-cycle behavior in the plot of  $P(n)$  at lower-right in the figure. The peak power was at a desynchronization of  $d=0.0005$ , where the average output power was calculated to be approximately 0.9 kW. Simulations using a 25 MeV electron beam resulted in a peak power at desynchronization  $d=0.003$  where the average output power was 140 W. The goal of 1 kW only applies to the FEL with an electron beam energy of 45 MeV.

Fig. 2 is the result of a simulation using an electron beam with energy 10 MeV and  $d=0.0005$ . Because of the long wavelength in this case, the electron pulse length is

much smaller than the slippage distance. Lower electron beam energy and pulse slippage effects reduce the output power to 20 W. The light pulse has reached steady-state and is shorter than the slippage distance resulting in a broad optical power spectrum  $P(v)$ .

#### Acknowledgements

The authors are grateful for support of this work by the Naval Postgraduate School, Stanford University (N00014-91-C-0170), and SURF/CEBAF.

#### References

- [1] W.B. Colson, Free Electron Laser Handbook, eds. W.B. Colson, C. Pellegrini and A. Renieri (North-Holland, Amsterdam, 1990) Chap. 5.
- [2] T.I. Smith and A. Marziani, Stanford University, private communication.



ELSEVIER

## Improved wire deflection method for magnetic field measurements in long undulators

A.A. Varfolomeev<sup>\*</sup>, A.S. Khlebnikov, N.S. Osmanov, S.V. Tolmachev

*CRL, Russian Research Center "Kurchatov Institute", Moscow 123182, Russian Federation*

### 1. Introduction

The method based on the deflection of a thin wire stretched through the investigated volume can be very useful for direct magnetic field measurements in undulators [1]. The first wire deflection systems did not provide high accuracy, for many reasons. To improve the method a new optical detector scheme [2] was introduced based on optical intensity measurement instead of direct wire position detection. With the above, an accuracy of magnetic field measurements comparable with that of high precision Hall probes was achieved [2].

The deviation of the wire from the ideal straight line leads to additional difficulties in the interpretation of the results. It becomes especially critical when the magnetic field changes significantly in distances comparable with the sag.

### 2. Wire device improvement

The sag value  $S$  for a wire stretched by the force  $P$  is given by the formula:  $S = g\rho\pi d^2 L^2 / 32P$ . Here  $S$  is the sag value,  $\rho$  is the density of the wire material,  $d$  is the wire diameter,  $g$  is the gravity acceleration constant and  $L$  is the wire length. Since the maximum of the ratio  $P/d^2$  is a material parameter, the sag value does not depend on the wire diameter if  $P$  is close to the break point [1]. Typically, the sag becomes comparable with the wire diameter if the wire length is about 1 m. The main parameter which defines the sag is its length. This means that the sag can be decreased with an appropriate decrease in the length. However, to avoid confusion by a superposition of the initial signal with a reflected noise signal, long wire exceeding 1.5 undulator length must be used. This leads to increased sag values, leading to contradictory demands on the wire length.

To solve the above sag and reflected noise problems we have introduced new elements into the wire deflection device. Two plates with sets of special oil bubbles played the role of dampers and eliminated reflected signals from the conventional wire supports. With these it was possible to decrease the distance between the supports to the length of the undulator and to decrease the sag significantly in comparison with conventional wire devices.

A schematic of the modified device is shown in Fig. 1. The basic parameters are similar to that given in Ref. [2]. The dampers (6) are placed near the supports (2). Damper oil drops are fixed on crest tips of a plate. The wire passes through the oil drops and does not touch the crest tips. The drops are larger in size for longer distances from the edge of the magnet system, so the resistance to the wire oscillations grows as the wave travels along the wire. The smallest has a 1 mm length along the  $Z$ -axis. The distances between drop edges were equal to one quarter of the undulator period, so that acoustic signals reflected from the drops interfered and suppressed each other.

Suppression of the reflected noise signals is demonstrated in Fig. 2 which shows the results as a function of oil drop number. The main acoustic signal and two reflected ones are clearly seen if no dampers are inserted (curve 1). Curves 2, 3 and 4 show a decrease in the reflected wave amplitudes with increasing number of drops

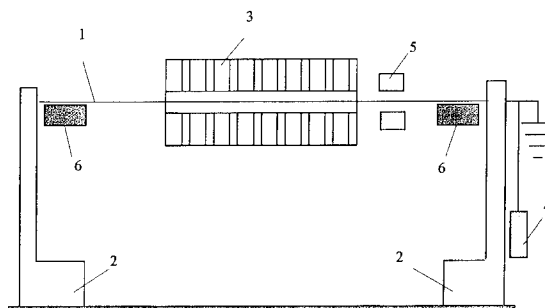


Fig. 1. Schematic of the wire deflection device. 1: wire; 2: supports; 3: undulator; 4: weight; 5: wire-position detector; 6: dampers.

<sup>\*</sup> Corresponding author. Tel. +7 095 196 7764, fax +7 095 196 7764, e-mail x1067@cuv1.net.kiac.su.

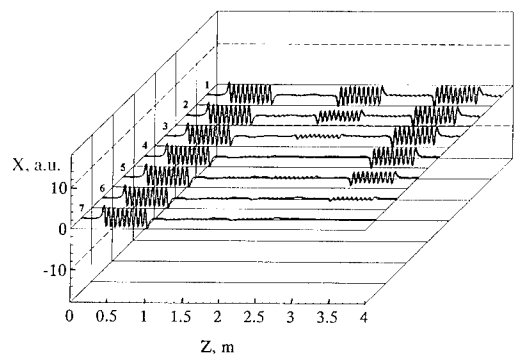


Fig. 2. Wire shapes showing acoustic wave signals for different damper structures. 1: no dampers; 2, 3, 4: one damper placed near one support; 5, 6, 7: two dampers near both supports.

in one of the two dampers. The curves 5, 6 and 7 correspond to the case when two dampers are located on both sides of the undulator. One can see that the dampers provide significant suppression of wave signals reflected from both wire supports.

We conclude that the wire deflection method with the described modification becomes more widely useful, as it provides smaller sag influence and lower noise signals.

## References

- [1] R.W. Warren, Nucl. Instr. and Meth. A 272 (1988) 257.
- [2] A.A. Varfolomeev, A.S. Khlebnikov, N.S. Osmanov and S.V. Tolmachev, Nucl. Instr. and Meth. A 341 (1994) 470.

# Conceptual design of a compact Compton backscatter X-ray source tunable from 3 to 33 keV <sup>☆</sup>

D.C. Nguyen <sup>a,\*</sup>, S.M. Gierman <sup>b</sup>, W. Vernon <sup>b</sup>, R.L. Sheffield <sup>a</sup>

<sup>a</sup> Los Alamos National Laboratory, Los Alamos, NM 87545, USA

<sup>b</sup> University of California, San Diego, 92093-0319, USA

## 1. Introduction

Tunable monochromatic X-ray sources are increasingly important in medical and biological research applications because they offer many advantages over conventional, broadband X-ray tubes. For example, using tunable monochromatic X-rays in mammography and digital-subtraction coronary angiography would reduce the patients' dosage and improve image definition [1]. Over the past few years, a number of novel schemes for producing tunable monochromatic X-rays have been proposed. These include a self-amplified spontaneous-emission FEL [2], nonlinear Thompson scattering with a terawatt laser [3], Compton backscattering (CB) of an electron beam with an FEL [4], and 90° CB with a femtosecond laser [5]. For the aforementioned applications, one needs a compact X-ray source that can produce a large X-ray flux. We present the conceptual design of a compact CB X-ray source based on a photoinjector and a diode-pumped solid-state laser.

## 2. Compact Compton backscatter design

Three key factors in our design of Compton backscattering contribute to the production of a large X-ray flux in a compact machine. First, we use a high-duty-cycle photoinjector to produce a low-emittance, high-brightness electron beam. Both the oscillator and the amplifiers of the photocathode drive laser are pumped by semiconductor laser diodes. Second, the drive laser with harmonic generation efficiently generates 527-nm (second harmonic) and 263-nm (fourth harmonic) light. Scattering the fundamental, second, and fourth harmonics of the drive laser off an

electron beam with energies of 12–21 MeV produces tunable X-rays in the energy range of 3–33 keV. Third, because the photoinjector electron pulses are produced by the same drive laser, the electron and the scattering laser pulses are perfectly synchronized.

We are performing a proof-of-principle experiment on the high-brightness Advanced FEL (AFEL) linac to demonstrate the feasibility of generating a large X-ray flux from a compact CB source. The 1-m-long AFEL photoinjector routinely produces a high-brightness electron beam at energies up to 18 MeV. We typically measure a “core” emittance of 3  $\pi$ -mm-mrad for 2 nC and 16 MeV. The AFEL currently uses a Cs<sub>2</sub>Te photocathode driven by the fourth harmonic of Nd:YLF [6].

In the first experiment, the second harmonic of Nd:YLF at 527 nm (2.3 eV) will be made to collide with a focused 16-MeV electron beam. The laser beam will enter the evacuated beam line through a quartz window and reflect off an aluminized beryllium mirror. We will use an optical transition radiation screen to overlap the laser beam with the electron beam. An Amptek X-ray detector with single photon sensitivity will detect the generated X-rays. The angle subtended by the detector area determines the detected X-ray flux and energy bandwidth.

For a small energy bandwidth, the forward scattered X-rays with energies within  $\Delta E$  of the maximum energy ( $E = 4\gamma^2 h\nu$  where  $\nu$  is the scattering laser frequency) will make up about 1.5 times  $\Delta E/E$  of the total scattered X-rays. For instance, if the angle between these selected X-rays and the electron beam is 3 mrad for the case described here, the number of X-rays within 1% of the maximum energy will be 1.5% of the total X-rays generated.

We estimate that scattering 5 nC of electron beam at 16 MeV focused to a 100- $\mu$ m-radius spot with 20  $\mu$ J of 527-nm light will produce 50 X-ray photons within a  $\pm 3$ -mrad angular cone in a single micropulse. The micropulse will be repeated every 9.23 ns (108 MHz) during a 30- $\mu$ s macropulse, so there will be  $1.7 \times 10^5$  X-ray photons in the range of 9.1–9.2 keV in a macropulse. The

<sup>☆</sup> Work supported by LANL Laboratory Directed Research and Development and performed under the auspices of the U.S. Department of Energy.

\* Corresponding author.

macropulses can be repeated at 60 times per second, yielding an X-ray production rate of  $1 \times 10^7$  photons per 1% bandwidth per second.

### 3. Conclusion

We design a compact high-flux monochromatic X-ray source based on CB between a picosecond laser and a high-brightness electron beam. The design is straightforward and has a number of key advantages, such as perfect synchronization and scalability to high-average X-ray flux. Further developments are required to increase the X-ray flux to beyond  $10^7$  photons per 1% bandwidth per second. One plausible strategy is to perform scattering in a photon storage “supercavity” [7] which increases the drive laser

intensity by a factor of  $10^4$ . A proof-of-principle experiment will be performed in the near future.

### References

- [1] F.E. Carroll et al., *Invest. Radiol.* 25 (1990) 465.
- [2] C. Pellegrini et al., *Nucl. Instr. and Meth. A* 331 (1993) 223.
- [3] E. Esarey, P. Sprangle and A. Ting, *Nucl. Instr. and Meth. A* 331 (1993) 545.
- [4] W.D. Andrews et al., *Nucl. Instr. and Meth. A* 318 (1992) 189.
- [5] K.-J. Kim et al., *Nucl. Instr. and Meth. A* 341 (1994) 351.
- [6] S. Kong et al., these Proceedings (6th Int. Free Electron Laser Conf., Stanford, CA, USA, 1994) *Nucl. Instr. and Meth. A* 358 (1995) 284.
- [7] J. Chen et al., *Nucl. Instr. and Meth. A* 341 (1994) 346.



ELSEVIER

## Three dimensional simulation of an FEL amplifier with an axial field

Anchal Srivastava, L.M. Bali<sup>\*</sup>, T.P. Pandya, Pallavi Jha, R.K. Shukla

Department of Physics, Lucknow University, Lucknow – 226007, India

Earlier investigations on free electron laser (FEL) configurations with realistic wigglers [1] report the existence of betatron oscillations in the wiggler magnetic field region. These oscillations play a significant role in electron beam confinement. Axial magnetic guide fields have also been used for this purpose. Since such guide fields give rise to interesting possibilities [2,3] their role in influencing the betatron oscillations appears worth investigating.

The equations of motion (averaged over a wiggler period) of an electron of energy  $\gamma m_e c^2$ , in the presence of a combined realistic magnetic wiggler, axial magnetic and electromagnetic field

$$A_x + iA_y = -A_w(x, y) \exp -ik_w z + \frac{ib(x + iy)}{2} + A_s \exp i(k_s z - \omega_s t + \phi_s) \quad (1)$$

may be written as

$$\begin{aligned} \frac{d}{dz}(P_x + iP_y) &= -\frac{1}{2\gamma\beta_z} \left( \frac{\partial}{\partial x} + i \frac{\partial}{\partial y} \right) a_w^2 + i \frac{B}{\gamma\beta_z} (P_x + iP_y) \\ &\quad - \frac{B^2}{\gamma\beta_z} (x + iy), \end{aligned} \quad (2)$$

$$\frac{d}{dz}(x + iy) = \frac{1}{\gamma\beta_z} [(P_x + iP_y) + iB(x + iy)], \quad (3)$$

$$d\gamma/dz = -(a_w a_s k_s / \gamma\beta_z) f_B \sin(\theta + \phi_s) - eE_z / m_e c^2, \quad (4)$$

$$d\theta/dz = k_w + k_s - k_s / \beta_z, \quad \text{and} \quad (5)$$

$$\begin{aligned} \beta_z &= \left[ 1 - \gamma^{-2} (1 + P_\perp^2 + a_s^2 + a_w^2 \right. \\ &\quad \left. - 2a_w a_s f_B \cos(\theta + \phi_s) \right. \\ &\quad \left. + B^2(x^2 + y^2) + 2B(xP_y - yP_x) \right]^{1/2}, \end{aligned} \quad (6)$$

where  $k_w$  and  $k_s$  are respectively the wiggler magnetic

and radiation wave numbers,  $A_w$  and  $A_s$  are respectively the amplitudes of the corresponding vector potentials,  $\theta = (k_w + k_s)z - \omega_s t$ ,  $b$  is the axial magnetic field ( $B = eb/2m_e c$ ),  $a_w = eA_w/m_e c$ ,  $a_s = eA_s/m_e c$ ,  $f_B = 1$  for a helical wiggler, and  $f_B = J_0[a_w^2/2(1 + a_w^2)] - J_1[a_w^2/2(1 + a_w^2)]$  for a planar wiggler,  $P$  is the canonical momentum and  $E_z$  [4] is the space-charge field.

For a planar wiggler with vector potential  $A_w(x, y)$  along the  $x$ -direction, Eq. (3) may be solved simultaneously with Eqs. (2) and (4)–(6) to get the transverse motion of the electron. This motion includes the transverse drift of the electron (due to combined uniform axial and realistic wiggler magnetic fields) and betatron oscillations. The wavenumber, of betatron oscillations in the  $y$ - $z$  plane as well as  $x$ - $z$  plane,  $k\beta_b = 2\pi/\lambda\beta_b = (1/\gamma\beta_z)((k_w^2 a_w^2 + 8B^2)/2)^{1/2}$  is seen to contain an additional term due to the guide field. This term increases the focussing of electron beam in the  $y$ - $z$  plane. Also the guide field introduces oscillations in the electron motion in the  $x$ - $z$  plane with the same wavelength  $\lambda\beta_b$  as those in the  $y$ - $z$  plane.

The evolution of the slowly varying amplitude and phase of the e.m. field in the presence of the electron beam current is obtained using the current densities and radiation vector potential in Maxwell's wave equation and assuming a single frequency. The numerical methodology used to solve the particle and wave equations is the same as given in Ref. [5]. Larmor precession of the electrons due to axial field is considered in its unaveraged form. Hence the step size is kept small compared to the Larmor wavelength.

Simulation results are presented for a microwiggler FEL amplifier operating at 40  $\mu\text{m}$  [4]. These are: (a) The refraction effect of the electron beam is found to shorten the Rayleigh range and to shift the waist of the input optical beam towards the entrance. These output beam parameters are then taken as the input parameters for the next reiterative run. Through this reiterative process, it is found that an input Gaussian beam (Fig. 1 curve b) which nearly maintains its shape during interaction with the electrons yields maximum FEL gain. These findings are valid for  $b = 0$ –3 kG for several values of current. However, when the axial field is increased beyond 3 kG, oscillations (of nearly the same magnitude as  $\lambda\beta_b$ ) in the optical beam cross section in the region where it becomes a minimum, set up (Fig. 1 curve d). Thus the output

<sup>\*</sup> Corresponding author. Tel. +91 522 70195, fax +91 522 384505.

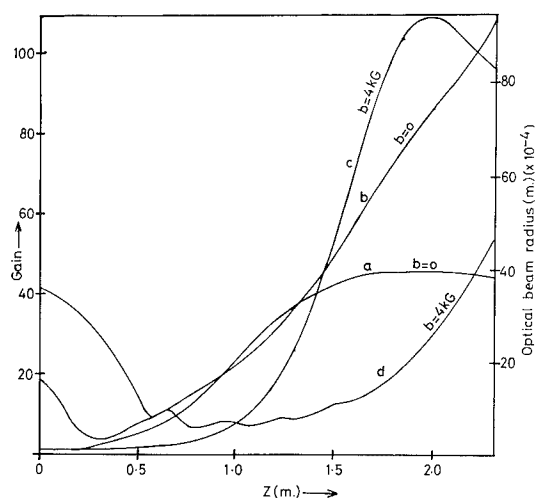


Fig. 1. Evolution of gains (a, c) and optical beam radii (b, d) along the FEL axis.

radiation beam undergoes appreciable deviation from the Gaussian form of the input beam, but the gain still increases. (b) Fig. 1 (curves a and c) shows that as  $b$

increases from 0 kG to 4 kG, the gain increases 2.7 folds. This increase is due to (i) the enhancement in focussing of the electron beam in both the transverse planes and (ii) the improved guiding of the radiation by the electron beam.

### Acknowledgement

Financial support of the Dept. of Electronics, Govt. of India is gratefully acknowledged.

### References

- [1] C.A. Brau, Free Electron Lasers (Academic Press, 1990).
- [2] L.M. Bali, T.P. Pandya, P. Jha, A. Srivastava and R.K. Shukla, Phys. Rev. A 43 (1991) 1633; J. Phys. Soc. Jpn. 62 (1993) 3432.
- [3] M.E. Conde and G. Bekefi, Phys. Rev. Lett. 67 (1991) 3082.
- [4] P. Jha and J.S. Wurtele, Nucl. Instr. and Meth. A 331 (1993) 477.
- [5] T.M. Tran and J.S. Wurtele, Phys. Rep. 195 (1990) 1.



ELSEVIER

## Wiggler-free FEL with an intense helical beam

K.H. Yeom<sup>a</sup>, Jae Koo Lee<sup>a,\*</sup>, T.H. Chung<sup>b</sup>

<sup>a</sup> Pohang University of Science and Technology, Pohang 790-784, South Korea

<sup>b</sup> Dong-A University, Pusan 604-714, South Korea

The cyclotron autoresonance maser (CARM) is a classical device that uses a beam of gyrating electrons passing through a magnetic field to amplify electromagnetic radiation by the cyclotron maser instability [1]. In the present work, we examine the nonlinear aspects of the CARM interaction with space charge effects. For space charge to be important, the electron beam should be gyrophase coherent (i.e., a helical beam). The random-gyrophased (i.e., gyrotropic) beam does not interact with the space charge wave. The helical (gyrotropic) beam consists of electrons which have the same (arbitrary) azimuthal angles in the plane perpendicular to the velocity space. A detailed description is found in Refs. [2–6].

We use the nonlinear differential equations [2]:

$$\left( \frac{d^2}{dz^2} + \frac{\omega^2}{c^2} - k_+^2 \right) \delta a = \frac{\omega_p^2}{c^2} \beta_{z0} \left\langle \frac{v_x \cos \psi - v_y \sin \psi}{|v_z|} \right\rangle, \quad (1)$$

$$2k_+^{1/2} \frac{d}{dz} (k_+^{1/2} \delta a) = -\frac{\omega_p^2}{c^2} \beta_{z0} \left\langle \frac{v_x \sin \psi - v_y \cos \psi}{|v_z|} \right\rangle, \quad (2)$$

$$\left( \frac{d^2}{dz^2} - k^2 \right) \delta \phi = 2 \frac{\omega_p^2}{c^2} v_{z0} \left\langle \frac{\cos \psi_{sc}}{|v_z|} \right\rangle, \quad (3)$$

$$2k^{1/2} \frac{d}{dz} (k^{1/2} \delta \phi) = -2 \frac{\omega_p^2}{c^2} v_{z0} \left\langle \frac{\sin \psi_{sc}}{|v_z|} \right\rangle, \quad (4)$$

$$u_z \frac{du_x}{d\xi} = -\Omega_0 u_y / \omega + \delta a (\gamma - n_s u_z) \sin \psi + \frac{d\delta a}{dz} u_z \cos \psi, \quad (5)$$

$$u_z \frac{du_y}{d\xi} = \Omega_0 u_x / \omega + \delta a (\gamma - n_s u_z) \cos \psi - \frac{d\delta a}{d\xi} u_z \sin \psi, \quad (6)$$

$$u_z \frac{du_z}{d\xi} = \delta a \left[ k_+ (u_x \sin \psi + u_y \cos \psi) - \frac{d\delta a}{d\xi} (u_x \cos \psi - u_y \sin \psi) \right] + \gamma \delta \phi \left[ \frac{d\delta \phi}{\delta \phi d\xi} \cos \psi_{sc} - n'_s \sin \psi_{sc} \right], \quad (7)$$

where the symbols are the same as in Ref. [2].

To validate the linear aspects of the nonlinear simulation results, we need a linear dispersion relation from an independent theory. We assume a single  $k$  mode and a cold electron distribution function, where

$$F = 2\pi u_\perp \delta(u_\perp - u'_\perp) \delta(u_z - u'_z) g(\zeta),$$

and  $\zeta = \alpha + (\Omega'/u_z)z$ ,  $g = 1[\delta(\zeta/2\pi)]$  for a gyrotropic (helical) beam.

Through linearization of the Vlasov equation, Maxwell's equations, and the continuity equation, the dispersion relation for a helical beam ECM (electron cyclotron maser) is given by

$$\left[ (\omega - Kv_z)^2 - \frac{\omega_p^2}{\gamma} (1 - \beta_z^2) \right] \times \left[ \omega^2 - k^2 c^2 - \frac{\omega_p^2}{\gamma} \frac{\omega - kv_z}{\omega - kv_z - \Omega} + \frac{1}{2} \frac{\omega_p^2}{\gamma} \beta_\perp^2 \frac{\omega^2 - k^2 c^2}{(\omega - kv_z - \Omega)^2} \right] = \frac{1}{2} \frac{\omega_p^4}{\gamma^2} \beta_\perp^2 \frac{\omega^2 \beta_z^2 - 2kv_z \omega + k^2 c^2}{(\omega - kv_z - \Omega)^2}, \quad (8)$$

where  $K = k + \Omega/v_z$ ,  $\beta_\perp = v_\perp/c$ , and  $\Omega = \Omega_0/\gamma$ .

\* Corresponding author. Tel. +82 562 279 2083, fax +82 562 279 3099, e-mail: jkl@vision.postech.ac.kr.



The initial conditions for the simulations are  $\gamma_0 = 1.8$  (corresponding to 400 keV), beam current of 500 A, beam density of  $3.32 \times 10^{12} \text{ cm}^{-3}$ , uniform axial magnetic field of 0.34 T, and beam perpendicular velocity of  $0.4c$  (pitch of 0.549). Figs. 1 and 2 summarize the nonlinear simulation runs with varying wave phase velocities (or varying values of  $k$  on the horizontal axis). Fig. 1 shows the comparison of the linear growth rates measured in our nonlinear simulations with those of the independent linear theory. The solid line is the helical beam case where the space charge effect and the dotted line is the gyrotropic beam case without the space charge effect; both are from the linear dispersion relation. The crosses (the circles) are the nonlinear simulation results with (without) the space charge effect. The normalized phase velocity varies from 0.98 to 1.4. For  $\beta_\phi = 1$ ,  $kv_z/\Omega$  is approximately 2.689 in the cyclotron mode. Fig. 2 shows the efficiency with the space charge effects in the autoresonance regime. In the slow wave region, the space charge effect reduces the efficiency and the gain.

Generally in the helical beam CARM the space charge effect enhances the growth rate for  $\beta_\phi > 1$ , but stabilizes it for  $\beta_\phi < 1$ . The gyrotropic beam CARM is stable at  $\beta_\phi = 1$ . In the random gyro-phased (gyrotropic) beam

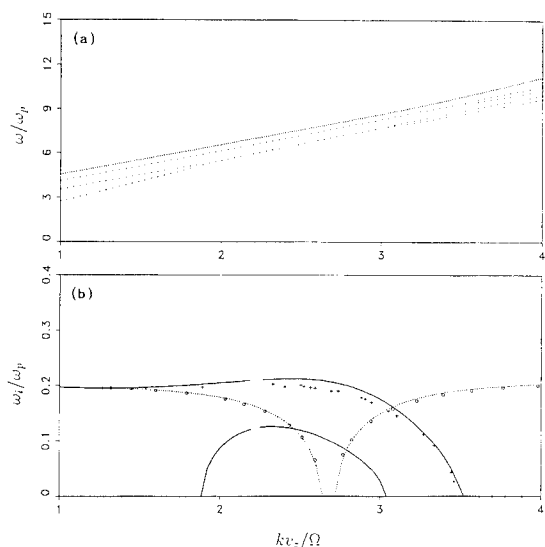


Fig. 1. The comparison of the linear frequencies and growth rates. (a) The real frequencies from the linear dispersion relation. (b) The growth rates of the unstable modes. The solid line is for the helical beam case and the dotted line for the gyrotropic beam case. The crosses and the circles are the simulation results with and without the space charge effects, respectively.

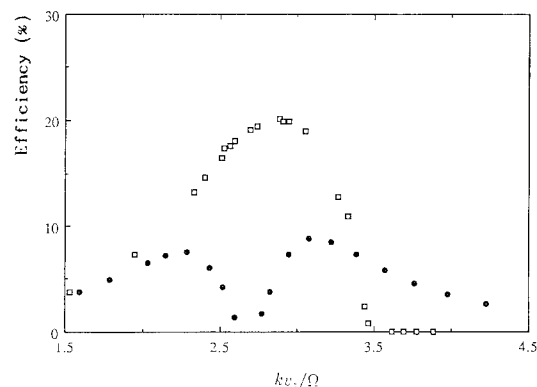


Fig. 2. The simulation efficiency in percent as a function of the normalized wave number. The nonlinear simulation results with (without) the space charge effects are indicated by squares (circles). The helical beam case with the space charge effects shows enhancement in the nonlinear efficiency especially in the regime where the autoresonance condition, i.e.,  $\omega/kc \sim 1$ , is satisfied near  $kv_z/\Omega \sim 2.7$ .

case, the space charge effect vanishes. The efficiency changes little with the space charge term for the gyrotropic beam CARM, which is in agreement with Ref. [7].

In summary, the space charge effect is pronounced in the autoresonance regime where  $\beta_\phi \sim 1$  and  $kv_z/\Omega_0 \sim 2.7$ . The nonlinear results from our simulation are consistent with the linear results from a kinetic theory.

### Acknowledgements

This work was supported by Korea Ministry of Education (Basic Science Research Institute) and by Korea Science and Engineering Foundation.

### References

- [1] V.L. Bratman, N.S. Ginzburg, G.S. Nusinovich, M.I. Pertelin and P.S. Strelkov, *Int. J. Electron.* 51 (1981) 541.
- [2] H.P. Freund and T.M. Antonsen, Jr., *Principles of Free-electron Lasers* (Chapman & Hall, London, 1992).
- [3] T.H. Kho, A.T. Lin and L. Chen, *Phys. Fluids* 31 (1988) 3120.
- [4] J.K. Lee, W.D. Bard, S.C. Chiu, R.C. Davidson and R.R. Goforth, *Phys. Fluids* 31 (1987) 1824.
- [5] A. Frutchman, *Phys. Fluids B* 4 (1992) 4101.
- [6] A. Frutchman and L. Friedland, *IEEE J. Quantum Electron* QE-19 (1983) 327.
- [7] C. Chen, B.G. Danly, G. Shvets and J.S. Wurtele, *IEEE Trans. Plasma Sci.* PS. 20 (3) (1992) 149.



ELSEVIER

## Carbon fiber electron injector for free-electron maser experiments

M. Korol, E. Jerby<sup>\*</sup>, S. Eckhouse, M. Bensal, A. Shahadi

*Faculty of Engineering, Tel-Aviv University, Ramat Aviv, Tel-Aviv 69978, Israel*

### 1. Introduction

The electron emission ability of carbon fibers was studied early in the 1970s [1,2]. Electron emission from single carbon fiber was obtained in a wide range of residual gas pressures. A long operation time of the fiber and good emittance stability are reported [1]. A current of 1 mA at a voltage of 3.5 kV was obtained. No breakdown was observed after 100 h of continuous operation [2]. The estimated current density from a single fiber is  $10^5$  A/cm<sup>2</sup>. The electron emission tends to be noisy in high pressures, above  $5 \times 10^{-7}$  Torr. The noise level can be reduced by heating the fiber, or by an appropriate resistor connected in series to the cathode.

Carbon-fiber emitters have been studied with commercial carbon yarns and with specially prepared fibers [3–7]

in a wide range of cathode voltage, from 250 V to 1 MV [3]. Electron currents were observed both in pulse [3] and in a continuous operation. A preliminary heating of the fibers up to 2900°C for a few hours leads to a better current stability [5]. A better current stability is received also by increasing the average current and the cathode operating time [6].

A carbon fiber emitter made of a bundle of  $\sim 300$  fibers is described in Ref. [4]. A current of 0.1 mA was measured at a voltage of 1–2.5 kV and a pressure of  $10^{-6}$  Torr, for  $\sim 10$  h of continuous operation.

Compared to other cathode types, the carbon-fiber emitter has the advantages of simplicity and low-voltage operation. Unlike the thermionic cathode, the carbon-fiber emitter does not require heating. Comparing it with the common carbon bulk field-emission cathode, it has the advantage of low-voltage operation, and it does not require special preparation and activation process.

Preliminary results of a carbon-fiber electron-gun experiment are described in this paper. The gun emits a

<sup>\*</sup> Corresponding author. Tel. +972 3 6 408 048, fax +972 3 6 423 508, e-mail jerby@tauniom.tau.ac.il.

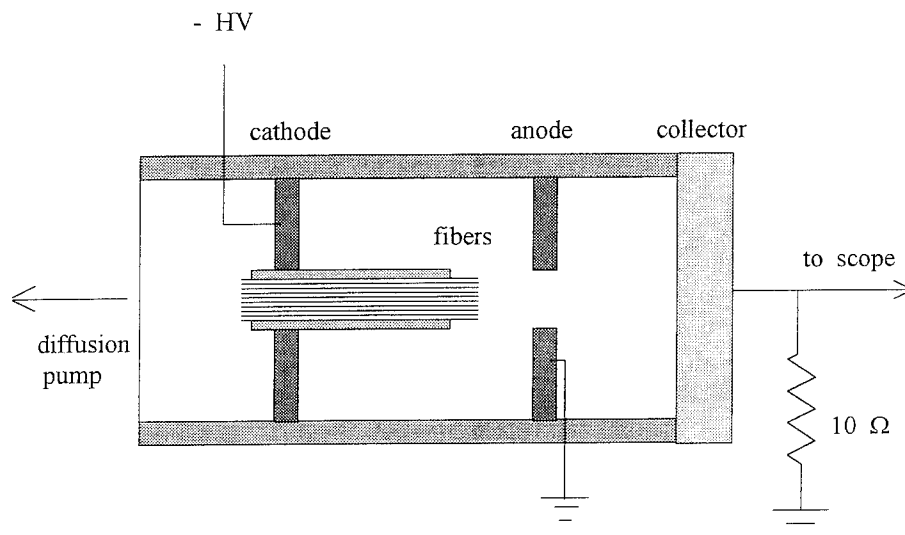


Fig. 1. Principal scheme of the carbon fiber gun.

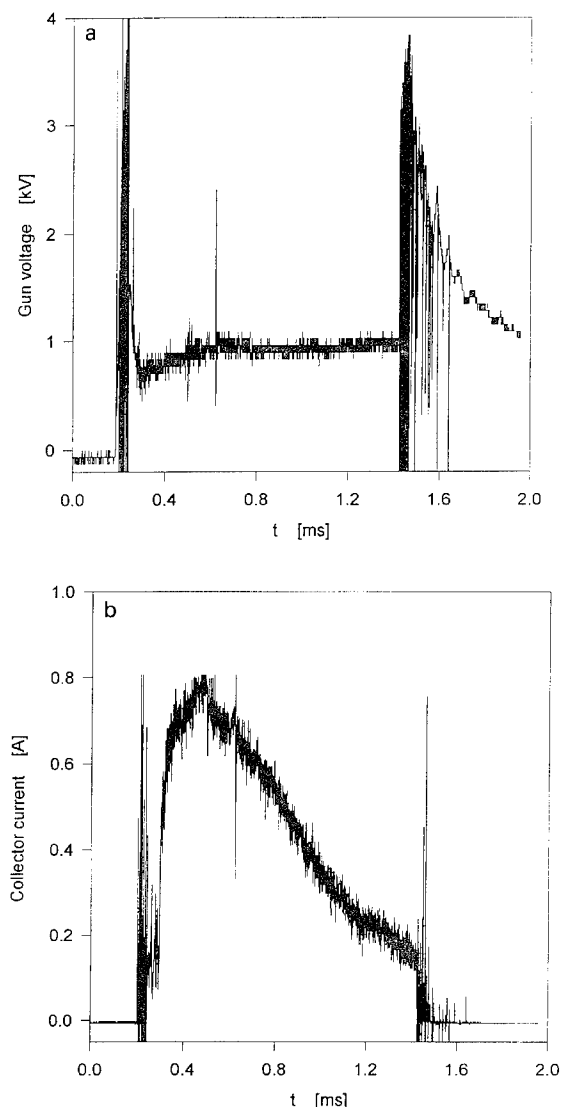


Fig. 2. Typical experimental results of the carbon fiber injector. (a) The carbon fiber gun voltage. (b) The electron beam current measured in the collector.

current of  $\sim 1$  A at  $\sim 1$  kV from a 5 mm diameter bundle of  $< 10$   $\mu\text{m}$  fibers. Possible applications of the carbon fiber gun in table-top cyclotron resonance maser and free-electron maser experiments are discussed.

## 2. Experiment

A scheme of the carbon fiber gun experiment is shown in the Fig. 1. The carbon-fiber electrode is placed inside the glass cylinder. Two tungsten electrodes, hermetically

melted into the glass, are connected to the brass disks which form the cathode and the anode. The diameter of the hole at the center of the anode disk is 3 mm. A bundle of over thousand carbon fibers is placed in a copper pipe (5 mm inner diameter). The pipe is mechanically pressed at the end in order to tighten the fiber bundle and to provide a proper electrical contact. The fibers are carefully cut in the cathode emitting surface (without any etching process). The distance between the emitting surface and the anode is 10 mm.

The anode is connected to ground potential. A negative 1–3 kV pulse (1 ms pulsewidth) is applied to the cathode. The blank vacuum flange which seals the glass tube acts also as an electron current collector. It is connected to ground by a 10  $\Omega$  resistor to measure the effective electron beam current. The other side of the glass cylinder is pumped by a diffusion pump.

The cathode voltage and the collector current signals are acquired by a Tektronix TDS 540 digital oscilloscope. Typical results are shown in Figs. 2a and 2b, respectively. The voltage trace in Fig. 2a shows high-voltage noise for short durations at the beginning and the end of the pulse. In between, a stable 1 kV voltage is observed for  $\sim 1$  ms. The current trace in Fig. 2b shows spikes at the pulse edges in accordance with the voltage noise durations. The current pulse reaches 0.8 A.

Further experiments are being conducted to study the electron emission characteristics from the carbon fiber cathode. The results presented in this paper motivate us to install carbon fiber guns in our nonrelativistic maser experiments at Tel-Aviv University. In particular, carbon fiber cathodes are designed to replace the existing thermionic cathodes in our traveling-wave FEM, the periodic and the non-dispersive waveguide cyclotron maser experiments, and in our recent masing TEM-mode FEM experiment [8].

## References

- [1] C. Lea, J. Phys. D 6 (1973) 1105.
- [2] F.S. Baker, A.R. Osborn and J. Williams, J. Phys. D 7 (1974) 2105.
- [3] R. Prohaska and A. Fisher, Rev. Sci. Instr. 53 (1982) 1092.
- [4] B.V. Bondarenko, V.I. Makukha and Ye. P. Sheshin, Radio Eng. Electr. Phys. 28 (1983) 147.
- [5] B.V. Bondarenko, V.A. Seliverstov and Ye. P. Sheshin, Sov. J. Commun. Tech. Electr. 30 (1985) 118.
- [6] B.V. Bondarenko, Yu. V. Pisarenko and Ye. P. Sheshin, Sov. J. Commun. Tech. Electr. 32 (1987) 118.
- [7] K. Evans, A. Fisher and E. Garate, IEEE Int. Conf. on Plasma Sci. Proc., New Jersey, 1993, p. 151.
- [8] R. Drori, E. Jerby and A. Shahadi, these Proceedings (16th Int. Free Electron Laser Conf., Stanford, CA, USA, 1994) Nucl. Instr. and Meth. A 358 (1995) 151, and references therein.



ELSEVIER

## Optical cavity and transport system for FELI

K. Saeki<sup>a,\*</sup>, E. Nishimura<sup>a</sup>, A. Kobayashi<sup>a</sup>, S. Abe<sup>a</sup>, A. Zako<sup>a</sup>, M. Yasumoto<sup>b</sup>,  
T. Tomimasu<sup>a</sup>

<sup>a</sup> Free Electron Laser Research Institute, Inc. (FELI), 4547-44, Tsuda, Hirakata, Osaka 573-01, Japan

<sup>b</sup> Osaka National Research Institute, 8-31, Midorigaoka, Ikeda, Osaka 563, Japan

### 1. Introduction

FELI (Free Electron Laser Research Institute, Inc.) is constructing four FEL facilities using a 165-MeV S-band linac. Each facility has an undulator and an optical cavity, and four facilities enable us to use broadband FELs 22.7–0.3  $\mu\text{m}$ . FELI has a pulse format (6-ps micropulse, 5.6-ns interpulse spacing, 24- $\mu\text{s}$  long macropulse duration, and 10-Hz repetition rate) which allows a maximum average power of up to 12 W and a maximum peak power over 50 MW [1,2].

Fig. 1 shows a bird's eye view of the FEL device at FELI. Each facility has an optical transport system, so one can use the broadband FELs in any users room, and the longest FEL path is about 80 m long.

In order to achieve optical beam stability we adopt a concept that the optical axis of mirrors and the FEL beam are adjusted to coincide with the electron beam position [3].

At first, the optical cavities and the optical pipes are constructed to coincide with a line which is extrapolated from the undulator magnet center. Next, the FEL beam which is outcoupled from the optical cavity is adjusted to coincide with the center line of the undulator magnet by installing the beam axis control units and the beam position monitors on the FEL path.

The optical and mechanical designs are reported in this paper.

### 2. Optical design

#### 2.1. Geometric constraints

The optical cavities are 6.72 m long for the undulator-1 (UND-1) and 8.40 m long for the undulator-2 (UND-2). The cavity mirrors are spherical and are gold coated on a

copper substrate. The outcoupling mirror has a hole of 1 mm diameter for UND-1 and 0.5 mm diameter for UND-2 in the center. The other optical characteristics are listed in Table 1.

The outcoupled FEL beam diffracts from the hole. A spherical mirror has been installed at a distance from the hole that is equal to its radius of curvature. The tilt angle with respect to the laser beam is kept small to avoid astigmatism.

#### 2.2. Alignment

Fig. 2 shows a schematic layout of an alignment system. First, the electron beam position in the beam duct of the undulator is detected using an OTR (Optical Transition Radiation) plate (aluminium) and images of OTR at the plate are observed by CCD cameras. Next, the reference laser beam position is detected as well as the electron beam position by means of a beam splitter, and the cavity mirrors are adjusted to the electron beam vertically using the reference laser. The resolution of position detection is 0.1 mm.

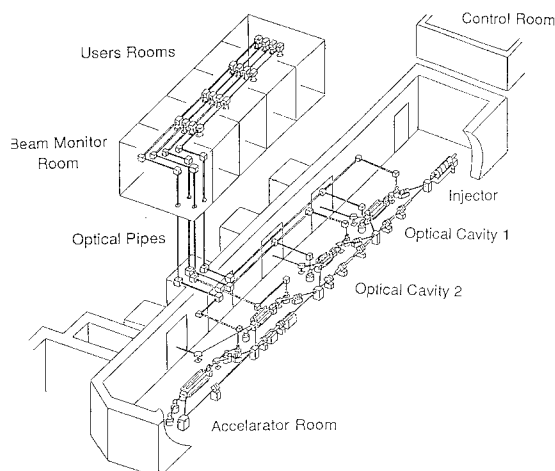


Fig. 1. Bird's eye view of the FEL device at FELI.

\* Corresponding author. Tel. +81 720 96 0417, fax +81 720 96 0421.

Table 1  
Characteristics of FELI optical cavities

| Optical cavity                                    | No. 1          | No. 2          |
|---|----------------|----------------|
| Type  | optical mode   | optical mode   |
| Length (m)  | 6.72           | 8.40           |
| Rayleigh length (m)                               | 1.0            | 1.5            |
| g-parameter                                       | −0.93<br>−0.76 | −0.77<br>−0.77 |
| Mirror curvature (m)                              | 3.490<br>3.827 | 4.735<br>4.735 |
| Mirror type                                       | Au on Cu       | Au on Cu       |
| Aperture diameter of<br>an extraction mirror (mm) | 1.0            | 0.5            |
| <i>Lasing</i>                                     |                |                |
| Wavelength (μm)                                   | 22.7–4.8       | 6.7–1.1        |
| Small signal gain (%)                             | 25.6–72.8      | 14.8–72.4      |
| Total cavity loss (%)                             | 2.1–4.6        | 2.1–4.6        |

Another concept is that the optical axis of the transport is adjusted to coincide with the line which is extrapolated from the center line of the undulator magnetic field. If the electron beam position is not on the center line, then the FEL beam line which is outcoupled from the optical cavity is adjusted to coincide with the center line by using beam axis control units.

### 3. Mechanical design

#### 3.1. Light axis control system

This system consists of the monitoring units and reference laser axis control units. The reference laser position

Table 2  
Characteristics of FELI FEL transport systems

| Transport                         | No. 1 | No. 2 |
|-----------------------------------|-------|-------|
| Overall length (m)                | 80    | 70    |
| Output beam diameter (mm)         | 4–32  | 13–34 |
| Transport pipe diameter (mm)      | 160   |       |
| Vacuum pressure (Torr)            | 0.1   |       |
| Overall transmission (%)          | > 50  |       |
| Short term drift precision (mm)   | < 5   |       |
| Short term angle precision (mrad) | < 0.2 |       |

in the beam duct of an undulator is detected by the beamsplitter target of the monitoring unit and this position is imaged on the CCD. The monitoring unit has three targets on a holder, a beam splitter for the reference laser, a Desmarquest plate with an aperture and OTR for the electron beam, and is driven by a stepping motor along a slide with a resolution of 50 μm. The axis control units have two bending mirror holders and the direction and tilt angle of each mirror is moved by stepping motors with a resolution of 5 μrad and a 30 mrad stroke. The reference laser beam position on the target (A) is moved close to the electron beam position by the bending mirror holder (A) and the target (B) is moved by the mirror bending mirror holder (B). We can coincide the reference laser beam position on the electron beam position by repeating these movements.

#### 3.2. Cavity length control units

We have prepared two methods to control the cavity length, one is an interferometer system and the other is a system that monitors the FEL power.

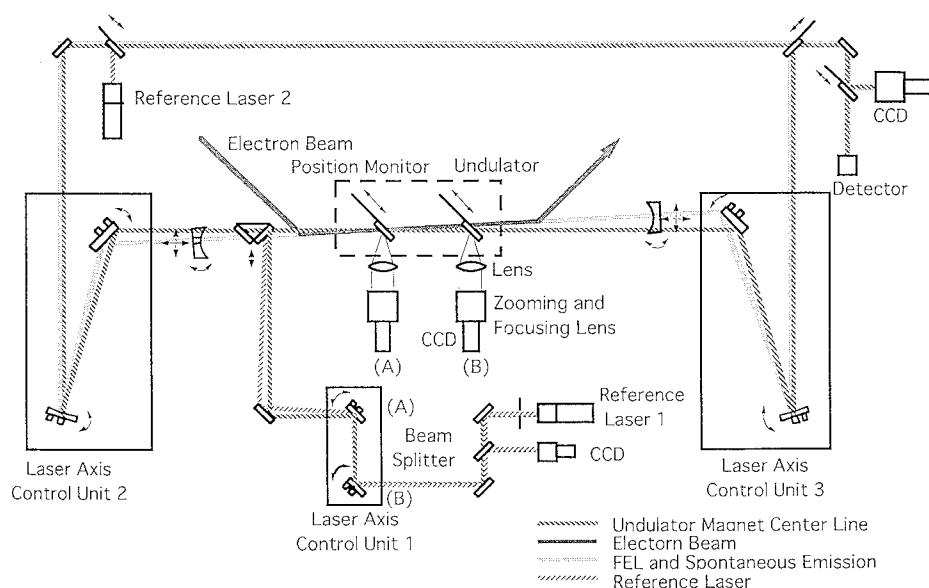


Fig. 2. Schematic layout of the alignment system.

A Hewlett-Packard interferometer system will be used to monitor the distance between the cavity mirrors. The interferometer beam is separated into two beams by a beam splitter and is applied to the reflector part of the cavity mirror through the plane mirror interferometer and goes back to the receiver. This system is used continuously without shutting down, and monitors the length's changes due to temperature. The resolution of this interferometer system is 0.5  $\mu\text{m}$ .

A HgCdTe detector will be used for detecting the spontaneous emission and FEL. The power intensity will be observed by an oscilloscope and the cavity length changed by moving the cavity mirrors while monitoring the power intensity. The cavity mirror is held in a solid gimbal mount carried by a precision translation stage and a piezo-electric actuator, and is moveable with a resolution of 0.1  $\mu\text{m}$ .

#### 4. Conclusion

The main results of optical and mechanical designs are summarized as follows.

(1) The  $g$ -parameters of the optical cavity are designed to be stable, and the FEL beam is outcoupled from the upstream mirror by hole output coupling.

(2) The axis of the optical mirrors is adjusted to coincide with the electron beam position by the monitoring units, the control units of the reference laser axis and cavity mirror movements.

(3) The interferometer system and the system monitoring FEL power are used to control the cavity length.

(4) In order to transport the FEL beam via a 80 m long path, the beam must be nearly parallel to that which is outcoupled from the optical cavity.

#### References

- [1] T. Tomimasu et al., Nucl. Instr. and Meth. A 331 (1993) 175.
- [2] Y. Morii et al., Proc. 9th Symp. on Accelerator Science and Technology, KEK, Aug. 25–27, 1993, p. 175.
- [3] E. Nishimura et al., Nucl. Instr. and Meth. A 341 (1994) 39.

## Wavelength and power stability measurements of the Stanford SCA/FEL

B. van der Geer, M.J. de Loos, M.E. Conde<sup>\*</sup>, W.P. Leemans

*Lawrence Berkeley Laboratory, Berkeley, CA 94720, USA*

### 1. Introduction

Characterization of Free Electron Laser (FEL) performance in terms of wavelength and power stability is often crucial for FEL users. At the Stanford SCA/FEL the time evolution of the spectrum during a macropulse has been measured using a high-resolution spectrometer with an image dissector [1] as readout system. The image dissector divides the (dispersed) output of the spectrometer into small intervals of wavelength (referred to as bins) and introduces a small time interval between these bins (in our case, 3.5 ns). These bins are then measured by a single element detector.

The measurements presented in this paper have studied the effect of two features incorporated in the SCA/FEL to improve stability: a wavelength feedback system which stabilizes the center wavelength by adjusting the beam energy via the amplitude of the RF power flowing into the accelerator [2]; and an acousto-optic modulator (AOM), referred to as the power clipper. The AOM is a feedforward system in which FEL output power during the macropulse is clipped through Bragg scattering above a user defined level, to obtain a more constant micropulse-to-micropulse power level.

### 2. Measurements and data analysis

The measurements were performed with the Super-Conducting Accelerator driven FEL at Stanford University. The FEL used a 3.6 cm period wiggler with 120 periods (referred to as TRW wiggler), and was set to run at a center wavelength of 4.08  $\mu\text{m}$  with a macropulse duration of 2 ms. We used a 1 m focal length spectrometer with a 300 grooves/mm grating, and its output light was divided by the image dissector into nineteen bins. Each wavelength

bin was measured to be 2.5 nm wide, yielding a total wavelength span of 47.5 nm, or  $\Delta\lambda/\lambda = 1.2\%$ .

A detailed description of the image dissector has been given previously [1]. The measured signal for two typical micropulses is shown in Fig. 1.

To reconstruct the spectra of the 23 000 micropulses within a macropulse of the FEL, a dedicated C program has been written to analyze the 4 MB of data recorded by the oscilloscope for each macropulse. A sophisticated algorithm, searching all the spectra, enables the program to detect pulses one or two counts above the noise level.

The program corrects for the different attenuations that each bin undergoes in the image dissector (caused by the multiple reflections in the image dissector cavity). It also corrects for the spill-over of light from one bin to the adjacent ones (caused by aberrations in the image dissector mirrors). We measured the square matrix **A**, where element  $A_{ij}$  is the intensity of bin number  $i$  when light corresponding to bin number  $j$  was sent into the image dissector. It was found that **A** is a diagonal dominated tridiagonal matrix where the largest off-diagonal element is about 25% of the nearest diagonal elements.

The total power and the center wavelength are calculated for the spectra of every micropulse within a macropulse. They are filtered with a Butterworth low-pass filter to reduce sampling noise. In order to eliminate the start-up and turn-off effects of the FEL, the first and last 5000 micropulses of each macropulse are not taken into account when calculating the wavelength and power stability.

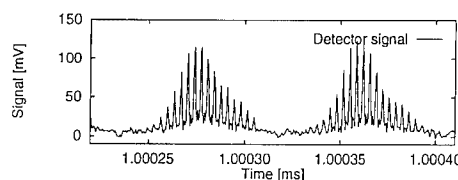


Fig. 1. Detector signal for two selected micropulses.

<sup>\*</sup> Corresponding author. Tel. +1 510 486 5076, e-mail conde@csa.lbl.gov.

### 3. Wavelength and power stability

Figs. 2 and 3 show typical temporal profiles of the center wavelength and output power during a macropulse,

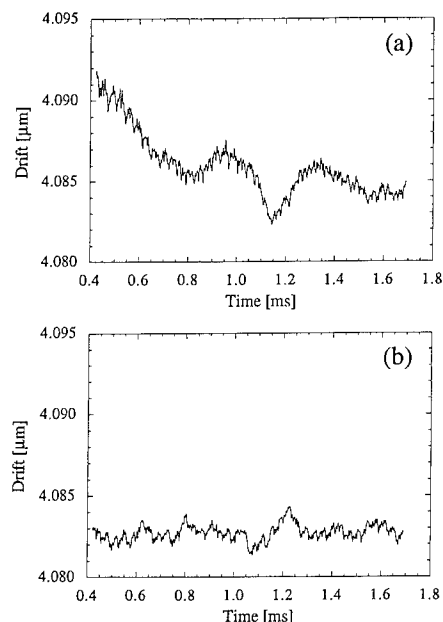


Fig. 2. Center wavelength for consecutive micropulses along a macropulse: (a) with both the wavelength feedback system and the power clipper off; (b) with both on.

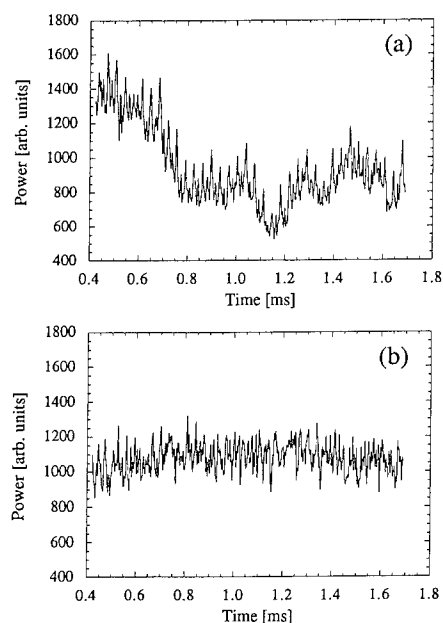


Fig. 3. Power for consecutive micropulses along a macropulse: (a) with both the wavelength feedback system and the power clipper off; (b) with both on.

with and without the presence of the two stabilizing features of the SCA/FEL, namely, the wavelength feedback control and the AOM. The graphs indicate a much greater stability of the FEL output, in terms of power and wavelength, when the feedback system and the AOM are used.

The wavelength feedback control system and AOM stabilize the FEL during a macropulse as follows. The wavelength stability ( $\delta\lambda/\lambda$ ) improves from  $3.5 (0.8) \times 10^{-4}$  to  $1.1 (0.1) \times 10^{-4}$ , and the power stability ( $\delta P/P$ ) improves from 18% to 7%. These numbers are obtained by calculating  $\delta\lambda/\lambda$  and  $\delta P/P$  for a macropulse and then averaging over five macropulses. The values inside the parentheses are the corresponding standard deviations. The results show that the feedback system and the AOM are very effective in stabilizing the output of the SCA/FEL. Not only do the wavelength and power become more stable throughout a macropulse, but variations from macropulse to macropulse decrease considerably.

The measurements have indicated that the spectral width of the emitted radiation is not affected by the operation of the wavelength feedback system and AOM. The FWHM of the pulses remain at approximately 23 nm, or  $(\Delta\lambda/\lambda)_{\text{FWHM}} = 0.55\%$ .

### 4. Conclusion

We have measured the spectrum and the output power of the Stanford SCA/FEL on a micropulse to micropulse basis. The measurements have verified the efficacy of an incorporated RF feedback system and an AOM in stabilizing the wavelength and output power of the FEL. These two features improve the typical wavelength and power stability throughout a given macropulse to the level of  $10^{-4}$  and 7% respectively.

### Acknowledgements

We would like to thank S. Chattopadhyay and A.M. Sessler for their encouragement and support, and the SCA/FEL team for their dedication and assistance.

### References

- [1] W.P. Leemans et al., Nucl. Instr. and Meth. A 331 (1993) 615 and Nucl. Instr. and Meth. A 341 (1994) 473.
- [2] A. Marziani and T.I. Smith, Nucl. Instr. and Meth. A 331 (1993) 59; A. Marziani, T.I. Smith and H.A. Schwettman, these Proceedings (16th Int. Free Electron Laser Conf., Stanford, CA, USA, 1994) Nucl. Instr. and Meth. A 358 (1995) 252.



## The effects of high gain in an FEL optical klystron

E. Kelsey, J. Blau<sup>\*</sup>, D.D. Quick, R.K. Wong, W.B. Colson

*Physics Department, Naval Postgraduate School, Monterey, CA 93943, USA*

Currently under construction in Novosibirsk, Russia, is a high-average-power FEL which will be used to test the theories and technologies required for the Space Laser Energy Project (SELENE) proposed for installation at the Naval Air Warfare Center, China Lake, California. This project uses a three-section klystron undulator in an FEL oscillator to bunch the electrons provided by a race-track microtron-recuperator [1]. The electrons are then injected into a separate undulator acting as a “radiator” to create a high-power source to be directed to satellites for electrical power transmission. The separate “oscillator” and “radiator” are required for high average power without damage to optical elements. The optical klystron improves gain with low electron beam currents and weak fields [2], and the high gain optical klystron can reduce the undulator length [3–5]. In this study, the use of the high gain klystron oscillator is intended to cause early saturation in relatively weak optical fields to prevent mirror damage.

Simulations using FEL theory based on a self-consistent solution of the coupled Maxwell–Lorentz equations to describe the evolution of the optical field and electron motion were used to investigate the effects of high gain in a standard two-section optical klystron. Dimensionless parameters [2] were used in the simulations, such as the dimensionless time  $\tau$ , the electron phase  $\zeta$ , the phase velocity  $v = d\zeta/d\tau$ , the dimensionless current density  $j$  and the optical field amplitude  $|a|$ . These simulations produce a gain spectrum at the end of a single pass through the undulator ( $\tau = 1$ ). Simulations are run at the resonance condition for maximum gain to determine the final optical power and bunching capability produced by a single pass of an electron beam passing through the klystron.

The FEL klystron is designed to improve electron bunching, or FEL gain, in weak optical fields and to shorten the total length of an undulator. The normal FEL klystron consists of two equal sections of undulator separated by a dispersive section. The optical fields of the first undulator, or “modulator”, prepare the electrons for bunching as they enter the dispersive section. The second

undulator, or “radiator” then allows the bunched electrons to radiate coherently. In the dispersive section, the electron phase  $\zeta$  is modulated by  $\Delta\zeta = vD$ , where  $D = N_D/N$  is the dimensionless time of the drift, and  $N_D$  is the number of equivalent undulator periods. A dispersive section is located at  $\tau = 0.5$  for the normal two-section klystron, and at  $\tau = \frac{1}{3}$ ,  $\tau = \frac{2}{3}$  for the three-section klystron [2].

The parameters used in the simulations of the two-section klystron were chosen to resemble the parameters for the Novosibirsk design with three sections [6]. The electron beam consists of micropulses of 20 to 100 ps in duration with a 2 to 45 MHz repetition frequency and a peak current of 20 to 100 A. The Novosibirsk oscillator uses three identical undulator sections with wavelength  $\lambda_0 = 9$  cm and  $N = 40$  periods. Each undulator is separated from the next by a dispersive section with  $D = 0.67$ . With a Lorentz factor of  $\gamma = 100$  and an undulator parameter of  $K = 1.4$  [2], the resulting optical wavelength is 13  $\mu\text{m}$ . The average filling factor is  $F = 0.023$  resulting in a dimensionless current density of  $j = 100$ .

Fig. 1 shows the gain spectrum for a standard two-section klystron with low gain,  $j = 1$ , and a weak initial optical field of  $a_0 = 0.01$ . A single dispersive section with  $D = 1.34$  is located at  $\tau = 0.5$ . The periodicity of the spectrum with respect to the initial phase velocity  $v_0$  can make the oscillator gain sensitive to electron beam quality. In the weak-field regime,  $a_0 < \pi$ , the optical field strength does not affect the gain spectrum. The ratio of maximum gain with the klystron to the maximum gain without the klystron is approximately 4.

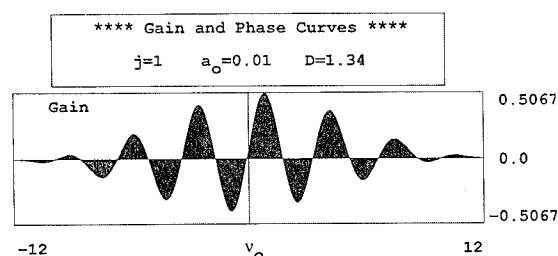


Fig. 1. Two-section FEL klystron gain spectrum. Low input current, low optical fields.

<sup>\*</sup> Corresponding author.

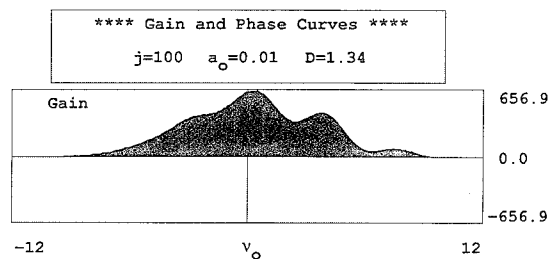


Fig. 2. Two-section FEL klystron gain spectrum. High input current, low optical fields.

Fig. 2 shows the gain spectrum for the same oscillator with  $j = 100$ . The maximum gain has increased drastically over the low-current case. As  $j$  increases, the shape of the klystron gain spectrum begins to approach that of a high-current non-klystron FEL. This provides for less sensitivity to changes in the electron beam energy. For  $j = 100$ , the klystron produces about 9 times more gain in weak fields than would be obtained without a klystron.

However, as the optical field is increased into strong field conditions, the klystron becomes less effective at improving the gain. As the optical field is reflected by the mirrors and used for subsequent electron pulses, the high gain of the optical klystron will produce strong field conditions. The gain spectrum of the same FEL with  $a_0 = 1.0$  and  $j = 100$  shows a decrease in maximum gain. The final dimensionless optical field strength for a single pass is  $a_t = 23$  and is well into the strong-field regime. The final gain is now only 7 times greater than it would be without a klystron, and continues to drop as stronger optical fields are reached.

In order to minimize the damage to the mirrors at Novosibirsk, the incident optical power on the mirrors must remain below about  $10 \text{ kW/cm}^2$ . Using a maximum

power density of  $5 \text{ kW/cm}^2$  results in a maximum dimensionless optical field strength of  $|a| = 8$ . With the high-current gain produced by the FEL klystron, this limit will be exceeded rapidly under continuous operation.

Comparison between the three-section klystron and the two-section klystron with similar parameters produced noticeably different gain spectrums.

The advantages of the FEL klystron for weak-field conditions are readily apparent. The high gain is a valuable boost for those FELs with low gain. However, for SELENE, the high gain appears to produce optical fields in excess of the damage limitations of the optical elements under continuous operation.

### Acknowledgement

The authors are grateful for the support of the Naval Postgraduate School, Stanford University (N00014-91-C-01710), and SURA/CEBAF.

### References

- [1] H.E. Bennett et al., Nucl. Instr. and Meth. A 341 (1994) 124.
- [2] W.B. Colson, Free Electron Laser Handbook, eds. W.B. Colson, C. Pellegrini and A. Renieri (North-Holland, Amsterdam, 1990) Chap. 5.
- [3] D. Nolle, Nucl. Instr. and Meth. A 304 (1991) 475.
- [4] C.M. Tang and W.P. Marable, Nucl. Instr. and Meth. A 318 (1992) 675.
- [5] R. Bonifacio, R. Corsini and P. Pierini, Phys. Rev. A 45 (1992) 4091.
- [6] D. Quick, Simulations of the High Average Power SELENE Free Electron Laser Prototype, MS Thesis, Naval Postgraduate School (1994).



ELSEVIER

## Formation and diagnostics of electron beams for micro-FELs

H. Ishizuka <sup>a,\*</sup>, S. Musyoki <sup>b</sup>, K. Sakamoto <sup>b</sup>, A. Watanabe <sup>b</sup>, M. Shiho <sup>b</sup>, S. Kawasaki <sup>c</sup>

<sup>a</sup> Fukuoka Institute of Technology, Higashi-ku, Fukuoka 811-02, Japan

<sup>b</sup> Japan Atomic Energy Research Institute, Naka Fusion Research Establishment, Naka, Ibaraki 311-02, Japan

<sup>c</sup> Faculty of Science, Saitama University, Shimo-ohkubo, Urawa, Saitama 336, Japan

Various schemes of compact FELs and micro-FELs operating at moderate energies (0.1–10 MeV) and currents (1  $\mu$ A to 10 A) have been proposed to generate short-wavelength electromagnetic radiation. There the requirement for beam quality, in particular the smallness of emittance, is stringent because it crucially limits the radiation wavelength. In previous papers we discussed a system that would produce ultrahigh-brightness electron beams for such FELs, assuming an array of microtriodes as the beam source [1,2]. An experiment on the beam formation and propagation has been carried out, tentatively using conventional arrays of gated microemitters. Emphasis is being laid on diagnosis of low emittance beamlets.

The schematic of the experimental setup is illustrated in Fig. 1. The vacuum chamber consists of a circular tank and a cylindrical drift tube. The whole system is made of stainless steel SUS304 and evacuated by two pumps: a turbomolecular pump (520 l/s) attached to the tank and an ion pump (60 l/s) attached to the drift tube. After baking the chamber at 200°C, the pressure is maintained below  $2 \times 10^{-7}$  Pa.

A field emitter array (FEA) is installed at one end of the drift tube. An electrostatic lens (einzellens) and deflecting electrodes (uniformly distributed 12 pole type with an inner radius of 10 mm) are arranged to form an electron gun together with the FEA. A short solenoid surrounding the drift tube serves as a magnetic lens. Inside the tank is placed, 1 m away from the FEA, a fluorescent screen for observing the beam profile and measuring the beam current. The beam profile is observed with a CCD camera through windows attached to the tank. An electrostatic quadrupole lens, utilized for emittance measurement, is inserted inside the drift tube as shown in Fig. 1. It has a bore radius of 1 cm and a length of 8 cm.

Two types of Spindt cathodes with the specifications given in Table 1 have been used as the beam source. A

response of a standard model Spindt cathode to a microsecond voltage pulse is shown in Fig. 2. The emission started when the gate voltage (upper trace) reached 100 V and the current (lower trace) rose up sharply with increasing gate voltage. In Fig. 2 the top of the voltage pulse looks flat but has a faint sag, which causes the significant droop of the emission current. The Fowler–Nordheim relation was found to hold even in the  $\mu$ s regime.

The beam was accelerated up to 5 keV and propagated down the drift tube to the fluorescent screen. The beam current detected there was 10–40% of the total emission, depending upon the aperture diameter of the electron gun. As the einzel lens is close to the emitter and far from the screen, a magnified image of the emitter was observed. Images of the standard model Spindt cathode showed many bright spots which were regularly distributed to form an array. The number of the spots was around nine for the high-current-density model Spindt cathode (Fig. 3a), indicating that the spots are real images of the emitter tips.

The emittance of the beam from the standard model Spindt cathode was  $6 \times 10^{-6}$   $\pi$  m rad. The emittance of each beamlet is estimated to be much smaller, because the images of the tips were observed separately on the fluorescent screen. The normalized emittance of beamlet we plan to reach is of the order of  $10^{-10}$   $\pi$  m rad. Conventional diagnostics such as the pepperpot method are inapplicable, and the beam cross section must be expanded for the emittance to be measured. A quadrupole lens elongates the image to a considerable size, and the emittance can be determined by the dependence of the image size on the

Table 1  
Specifications of the two types of Spindt cathodes

|                                  | Standard model    | High current density model       |
|----------------------------------|-------------------|----------------------------------|
| Array size                       | 1 mm diam.        | 7.5 $\mu$ m $\times$ 7.5 $\mu$ m |
| Tip density (#/cm <sup>2</sup> ) | $1.5 \times 10^6$ | $1.6 \times 10^7$                |
| Emission per tip ( $\mu$ A)      | $\approx 10$      | $\approx 10$                     |
| Operating voltage (V)            | $\approx 100$     | $\approx 100$                    |

\* Corresponding author. Tel. +81 92 606 3131, fax +81 92 608 3969, e-mail ishizuka@fit.ac.jp.

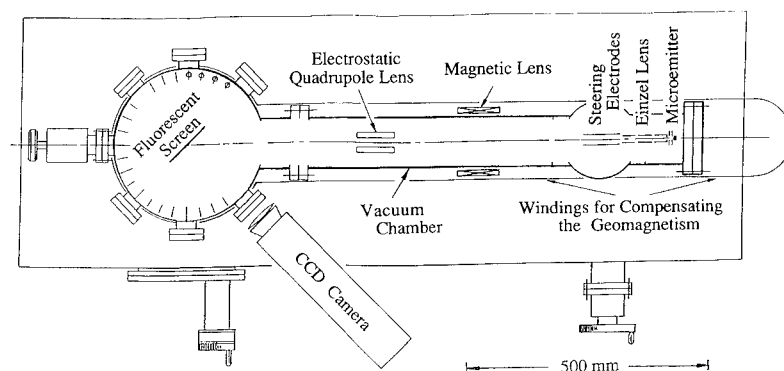


Fig. 1. Schematic of the experimental setup (top view).

lens strength. Details of the method are reported elsewhere [3]. The beam expansion was tested experimentally with the high-current-density model Spindt cathode. When the quadrupole lens was activated to expand the beamlet horizontally, the image was elongated as expected (Fig. 3b).

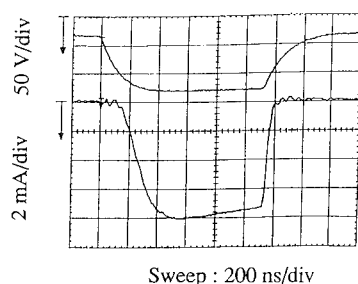


Fig. 2. Gate voltage (upper trace) and emission current (lower trace) in pulsed operation of a standard model Spindt cathode.

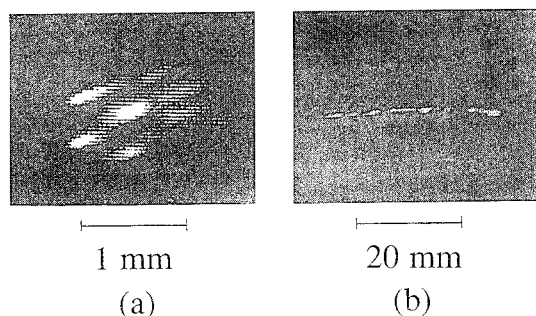


Fig. 3. CCD picture of images on the fluorescent screen. (a) Beam generated by a high-current-density model Spindt cathode. (b) The same beam elongated by the quadrupole lens.

Beams from FEAs are unique in that they are composed of many beamlets which are very bright at the source. Because of the large emission angle, the beamlets overlap each other within a short distance from the source. However, our experiment has shown that they can be separated again at a long distance. Conservation of emittance should be improved if parallel beamlets are released from the source. We started to try a microtriode array [4] to verify this, but unfortunately the first sample was accidentally damaged before taking data on the propagated beam. Our study will be continued mainly with this type of FEAs.

### Acknowledgement

Part of this work was supported by a Grand-in-Aid for Scientific Research from the Ministry of Education, Science and Culture, Japan.

### References

- [1] H. Ishizuka, Y. Nakahara, S. Kawasaki, N. Ogiwara, K. Sakamoto, A. Watanabe and M. Shiho, Nucl. Instr. and Meth. A 331 (1993) 577.
- [2] H. Ishizuka, Y. Nakahara, S. Kawasaki, K. Sakamoto, A. Watanabe, N. Ogiwara and M. Shiho, Proc. 1993 Particle Accelerator Conf., Vol. 2, 1566.
- [3] H. Ishizuka, Y. Nakahara, S. Kawasaki, S. Musyoki, H. Shimizu, A. Watanabe and M. Shiho, Jpn. J. Appl. Phys. 33 (1994) 5078.
- [4] J. Itoh, K. Morikawa, Y. Tohma and S. Kanemaru, Rev. Le Vide, les Couches Minces, Suppl. 271 (1994) 25.



ELSEVIER

# A comparison between two kinds of chromatic coherent light sources

Wu Ding<sup>\*</sup>, Xiaojian Shu, Xiangwan Du

*Institute of Applied Physics and Computational Mathematics, P.O. Box 8009, Beijing 100088, China*

## 1. Introduction

It is well known that there are two main mechanisms for generating coherent harmonics: an external source pre-bunching the electron beam in an optical klystron and the fundamental mode bunching the electron beam in a normal oscillator. In this paper, we will compare the coherent harmonics generated by these two mechanisms qualitatively.

## 2. External source prebunching

In Refs. [1,3], we have given an expression for the coherent harmonic power generated by external source prebunching in an optical klystron.

$$P_{nT}^{\text{OK}} = P_{nc}^{\text{OK}} \exp \left\{ - \left[ n 4 \pi (N_w + N_d) \frac{\Delta \gamma}{\gamma_0} \right]^2 \right\}, \quad (1)$$

$$P_{nc}^{\text{OK}} = \frac{\pi}{2} n_0^2 e^2 c \frac{a_w^2 L_b^2}{\gamma_0^2} F_{L, \theta n}^2 J_n^2(|A_{n1}|) \frac{\sin^2 \theta_n}{\theta_n^2}, \quad (2)$$

$$A_{n1} = -n 4 \pi N_d \frac{\Delta \gamma_{\text{mod}}}{\gamma_0}, \quad (3)$$

$$\theta_n = \frac{\Delta K_n L_b}{2}, \quad (4)$$

$$\Delta K_n = n \Delta K, \quad \Delta K = K_w - K(1/\beta_{\parallel}^{(0)} - 1). \quad (5)$$

## 3. Fundamental bunching

In Refs. [2,4], we have given an expression for the coherent harmonic power generated by the fundamental

bunching in a normal oscillator:

$$P_{nT}^{\text{os}} = P_{nc}^{\text{os}} \frac{\pi}{2} \frac{\alpha_n^2 - \Delta k_n^2}{\sigma_{\gamma n}^2} e^{-a_n^2/(2\sigma_{\gamma n}^2)} e^{-2\Delta k_n^2/(\sigma_{\gamma n}^2)} \times \left| \sum_{k=-\infty}^{\infty} (-1)^{k/2} I_{(n+k)/2} \left( \frac{\alpha_n^2}{4\sigma_{\gamma n}^2} \right) \right|^2 \times I_k(\alpha_n \Delta k_n / \sigma_{\gamma n}^2), \quad (6)$$

$$P_{nc}^{\text{os}} = \frac{\pi}{2} n_0^2 e^2 c \frac{a_w^2}{\gamma_0^2} F_{L, \theta n}^2 \frac{1}{\alpha_n^2 - \Delta k_n^2}, \quad (7)$$

$$\alpha_n = n \frac{4\pi}{\lambda_w} \frac{\Delta \gamma_{\text{mod}}}{\gamma_0}, \quad \sigma_{\gamma n} = n \frac{4\pi}{\lambda_w} \frac{\Delta \gamma}{\gamma_0}, \quad (8)$$

$$\frac{\Delta K_n}{\sigma_{\gamma n}} = \frac{\lambda_w \Delta K \gamma_0}{4\pi \Delta \gamma}, \quad \frac{\alpha_n}{\sigma_{\gamma n}} = \frac{\Delta \gamma_{\text{mod}}}{\Delta \gamma}. \quad (9)$$

$\Delta \gamma$  and  $\Delta \gamma_{\text{mod}}$  are the energy spread and the modulation depth of the electron beam;  $L_b$  and  $F_{L, \theta n}$  are the length of the prebunched electron beam and the interaction coupling factor between the optical beam and the electron beam;  $J_n$  and  $I_k$  are Bessel and modified Bessel functions of the first kind of order  $n$  and  $k$ . The meanings of other symbols used here are as the same as in the Refs. [1–4].

Comparing expressions (2) and (7), we see that there is a inequality.

$$P_{nc}^{\text{OK}} < P_{nc}^{\text{os}}, \quad (10)$$

because there are the following inequalities in the cold beam limit:

$$L_b \leq 1/\alpha_n \quad (\text{for } L_b \leq 1 \text{ cm, } 1/\alpha_n > 1 \text{ cm}),$$

$$|J_n| < 1, \quad (11)$$

$$\left| \frac{\sin \theta_n}{\theta_n} \right| < 1.$$

Comparing expressions (1) and (6) we see that for the external source prebunching the effect of the energy spread of the electron beam on the harmonic power is an exponentially decaying relation. The higher the harmonic order,

<sup>\*</sup> Corresponding author. Tel. +86 1 201 4411, fax +86 1 201 0108

the smaller the powers. For the fundamental mode bunching the harmonic power is not susceptible to the energy spread of the electron beam no matter how high the harmonic order.

Therefore, an optimal chromatic coherent light source is obtained from coherent harmonics generated by fundamental mode bunching in a normal oscillator. However, investigation of both the mirror reflectivity and power extraction for the different colors is required for the fundamental mode bunching in the normal oscillator.

## References

- [1] Wu Ding; Nucl. Instr. and Meth. A 318 (1992) 588.
- [2] Wu Ding, Phys. Rev. A 45(6) (1992) 4058.
- [3] Wu Ding, SPIE Laser and optoelectronics 1979 (1992) 107.
- [4] Wu Ding, Degradation of the power of the coherent harmonics generated by the fundamental mode bunching and electron beam quality, to be published.



ELSEVIER

# An FEL design code running on Mathcad<sup>TM</sup>☆

D.C. Nguyen<sup>a,\*</sup>, S.M. Gierman<sup>a</sup>, P.G. O'Shea<sup>b</sup>

<sup>a</sup> Los Alamos National Laboratory, Los Alamos, NM 87545, USA

<sup>b</sup> Duke University, Durham, NC 27708-0319, USA

## 1. Introduction

As free-electron lasers become increasingly a users' tool rather than an accelerator physicists' research facility, some users are getting involved in FEL physics for the first time. Many of them will understandably find the task of designing FEL experiments daunting. Some design decisions involve relatively straightforward issues such as the required wiggler period and electron beam energy for a given wavelength. Others such as the expected output energy and the macropulse length are a little more complicated. A few three-dimensional simulation codes already exist [1,2], but they are difficult to use effectively for designing FEL experiments. Furthermore, in comparing FEL performance, the ability to map out design parameters is highly desirable. It is thus important to obtain quick answers to basic FEL design questions without expensive numerical simulations. Toward this end, we wrote a program called FEL-CAD.

## 2. Description of FEL-CAD

FEL-CAD runs on both the IBM PC<sup>TM</sup> and the Apple Macintosh<sup>TM</sup> with the help of Mathcad<sup>TM</sup>. FEL-CAD is appropriate for Compton FELs that operate as low-gain oscillators driven by rf linac and permanent-magnet wigglers. We assume no sidebands and negligible slippage. We only treat linear resonators and cold-cavity optical mode. Parts of FEL-CAD were based on Dattoli's FEL saturation dynamics [3].

In FEL-CAD, the electron beam traveling in the  $z$  direction is wiggled in the  $x$  direction by the wiggler magnetic field in the  $y$  direction. The magnitudes of

different harmonic components of the wiggler magnetic field are calculated using the standard Halbach formula [4].

$$B_{\mu} = S^{\mu} 2 B_{\text{rem}} \left( \frac{\sin \left( \frac{\varepsilon n_{\mu} \pi}{M} \right)}{\frac{n_{\mu} \pi}{M}} \right) (1 - e^{-n_{\mu} k_w L}) \left( e^{-n_{\mu} k_w \frac{G}{2}} \right), \quad (1)$$

where  $B_{\text{rem}}$  is the remanent field;  $\varepsilon$  is the packing factor;  $n_{\mu}$  and  $\mu$  are the wiggler harmonic and harmonic index, respectively;  $M$  is the number of magnets per period;  $k_w$  is the wiggler wave number;  $L$  is the magnet height in the  $y$  direction; and  $G$  is the full gap. The factor  $S$  is  $-1$  for the case where  $M = 2$  and the magnetization is along the  $z$  direction.  $S$  is  $1$  for  $M = 4$ , or  $M = 2$  and the magnetization is along the  $y$  direction. The rms wiggler parameter  $a_w$  is calculated from the magnitude of the fundamental field,  $a_w = eB_0/(\sqrt{2} m c k_w)$ .

In rf-linac driven FELs, the first portion of the rf macropulse is used to fill the linac cavity to the steady-state accelerating field. The cavity fill time is defined as the time needed for the electron energy to be within  $1/2 N_w$  of the steady-state value. The difference between the rf macropulse and the cavity fill time is the usable macropulse length. Within the usable macropulse length, the electron micropulses have the right energy so that their emission will be amplified by subsequent electron micropulses.

The FEL output is assumed to occur at the wavelength of maximum small-signal gain. This wavelength is given by

$$\lambda = \frac{\lambda_w (1 + a_w^2)}{2 n \gamma^2 \left( 1 - \frac{1.303}{n N_w \pi} \right)}, \quad (2)$$

where  $\lambda_w$  is the wiggler period;  $n$  is the harmonic number;  $\gamma$  is the relativistic factor; and  $-1.303$  is the value of the detuning parameter at which the small-signal gain is maximum.

The electron beam is matched into the wiggler such that its  $y$  dimension is constant with respect to  $z$ . This constant dimension is given by  $\sigma_y = \sqrt{2 \varepsilon_y \lambda_{\beta} / (\pi^2 \gamma)}$

☆ Work supported by LANL Laboratory Directed Research and Development under the auspices of the US Department of Energy.

<sup>TM</sup> Trademarks of commercial hardware or software.

\* Corresponding author.

where  $\lambda_\beta$  is the betatron period; and  $\epsilon_y$  is the unnormalized emittance in the  $y$  direction. The  $x$  dimension of the beam follows the optical beam's contour,

$$\sigma_x = \sigma_y \sqrt{1 + \left( \frac{2\pi z \epsilon_x}{\lambda_\beta \epsilon_y} \right)^2}. \quad (3)$$

We calculate the number of spontaneous photons at fundamental frequency using Colson's formula  $N_{hv} = 2 N_e N_w \alpha_{fs} a_w^2$  [5]. The divergence angle of the TEM<sub>00</sub> cavity mode is used as the coherence angle. For  $a_w$  smaller than 1, the number of spontaneous photons emitted into the coherence angle  $\theta$  is approximated by

$$N_C \approx N_{hv} n JJ^2(n) \frac{\chi (3 + 3\chi + 2\chi^2)}{2 (1 + \chi)^3}, \quad (4)$$

where  $JJ(n)$  is the usual difference in Bessel functions; and  $\chi$  is  $(\gamma \theta)^2$ .

We use Dattoli's FEL gain saturation model to calculate the optimum outcoupling from the small-signal gain  $g_{ss}$  and total cavity loss  $\Gamma$  [4]. The total cavity loss is the sum of the outcoupling  $\Gamma_{OC}$  and dissipative loss  $\Gamma_{loss}$  which includes vignetting, absorption and other loss. In Dattoli's saturation model, the small signal gain is saturated according to

$$g(I) = \frac{g_{ss}}{1 + (1 - \alpha) \frac{I}{I_s} + \alpha \left( \frac{I}{I_s} \right)^2}, \quad (5)$$

where  $g(I)$  is the gain at a given intracavity intensity  $I$ ;  $g_{ss}$  is the small-signal gain;  $\alpha$  is the phenomenological fitting parameter which falls in the range 0.14–0.18;  $I_s$  is the saturation intensity defined as the intensity at which the small-signal gain is halved.

We perform a multi-pass calculation to predict the FEL output energy. The number of passes is equal to the number of usable micropulses divided by the number of optical pulses in the cavity. The intracavity intensity builds up from the spontaneous emission within the coherence angle. The FEL gain is modified by the optical intensity in the wiggler as given by Eq. (5). When the number of round-trips exceeds the number of usable micropulses, the FEL gain is reset to 0 and the cavity power is allowed to decay over a few  $1/e$  ringdowns of the resonator. The optical energy in a micropulse is calculated by multiplying the optical intensity with the average optical mode area in the wiggler and the micropulse length.

### 3. Conclusion

We have written a simple code to predict the performance of rf-linac driven FEL oscillators. The advantages of FEL-CAD over numerical simulations are its simplicity and speed. Although we welcome any changes the users may have, we believe that FEL-CAD should be kept at this level of complexity. More elaborate, 3-D simulations codes [1,2] should be used to make accurate prediction of FEL performance.

### References

- [1] J.C. Goldstein et al., Nucl. Instr. and Meth. A 285 (1989) 192.
- [2] T.M. Tran and J.S. Wurtele, Phys. Rep. 195 (1990) 1.
- [3] G. Dattoli et al., Nucl. Instr. and Meth. A 318 (1992) 495.
- [4] K. Halbach, Nucl. Instr. and Meth. 178 (1981) 109.
- [5] W.B. Colson, in: Free Electron Laser Handbook, eds. W.B. Colson, C. Pellegrini and A. Renieri (North-Holland, Amsterdam 1990) Chap. 5.





ELSEVIER

# The ultra-relativistic FEL near the threshold of stimulated emission

V.V. Ognivenko<sup>\*</sup>, V.I. Kurilko

*National Science Centre, Kharkov Institute of Physics & Technology, 310108 Kharkov, Ukraine*

An FEL operating in the self-amplification of spontaneous emission (SASE) mode does not differ externally from a classical incoherent spontaneous undulator radiation (SUR) source. In both nonequilibrium systems an electron beam and an undulator are used to produce magnetic bremsstrahlung. Physically, it is evident that for a system to make a transition from being an incoherent SUR source to operating in the SASE mode certain quantitative conditions must be satisfied. In this paper we present the results of a theoretical analysis of the simplest model of this class of nonequilibrium system.

We consider a monoenergetic electron beam with energy  $\mathcal{E} = m_0 c^2 \gamma_0$  moving along the OZ-axis of a helical undulator with period  $D$  and magnetic field  $\mathbf{H}_0 = H_u[\mathbf{e}_x \cos(k_u z) + \mathbf{e}_y \sin(k_u z)]$ , where  $k_u = 2\pi/D$ ,  $\mathbf{e}_x$ ,  $\mathbf{e}_y$  are unit vectors along the axes OX, OY, and  $\gamma_0 = (1 - \beta_0^2)^{-1/2}$ . We will determine the efficiency of emission of coherent radiation by beam electrons as a function of the number of radiators per SUR wavelength  $\lambda$  for a finite number of electrons. The solution will be sought by simulating the dynamics of the longitudinal motion of the beam electrons in the summed field of the undulator and the SUR in the dipole approximation ( $K = |e| H_u D / 2\pi m_0 c^2 \ll 1$ ) [1,2].

The dynamics of the longitudinal electron motion in the magnetic field  $\mathbf{H}_0$  and the SUR fields of neighbouring electrons is determined by the corresponding component of the Lorentz force [1,2]. In the dipole approximation the  $\mathbf{E}$  and  $\mathbf{H}$  fields of the electron in the undulator, derived from formulae for the fields of moving charges [3], take the form as given in Ref. [2]. To obtain the efficiency of coherent radiation generation in the self-amplification regime, we consider the simple case of a one-dimensional electron beam (linear chain of point electrons-radiators), where all the electrons enter the undulator rigorously along the OZ axis.

We define the efficiency as the ratio of the energy losses by electrons to their initial energy, this ratio being the ensemble average over all particles:

$$\eta_{\text{tot}} = \frac{1}{N} \sum_{s=1}^N \left[ 1 - \frac{\gamma(z, t_s)}{\gamma_0} \right].$$

The main parameter of the present study is the number of electrons per unit length  $n$ , i.e., their number per SUR wavelength. In the present analysis our interest lies in relatively small values of this number, for which the self-consistent solutions will be obtained numerically. We assume that the beam electrons at the undulator input are monoenergetic and are homogeneously distributed in the entry time  $t_s$  over the whole beam pulse length  $t_p$ . We will calculate the dependence of the kinetic energy loss by the beam along the longitudinal coordinate as a function of  $n$ .

Numerical simulations of the self-amplification process were carried out for a total beam pulse length equal to ten periods of the amplified wave and for  $\nu = 4r_0 k_u K^2 \gamma_0 \beta_0 / 3 = 10^{-9}$ . This value of the parameter  $\nu$  corresponds to the following undulator parameters:  $D = 1$  cm,  $H_u = 5$  kG ( $K = 0.5$ ), and to an electron energy  $\mathcal{E} = 850$  MeV. The amplified wavelength is approximately 2 nm.

Results of the simulations are presented in Figs. 1 and 2. Fig. 1 shows the efficiency versus the normalized distance along the undulator axis for different numbers of particles per wavelength:  $n = N/n_1$ ,  $n_1 = ct_p/\lambda = 10$ ;  $n = 7, 8$ . The spontaneous loss by an individual electron in the undulator:  $\eta_{\text{inc}} = \nu k_u z / 2$  is also shown.

The results of the particle simulations show that the total energy losses at small numbers of electrons per wavelength ( $n \leq 7$ ) approach the incoherent energy losses. Fig. 1 shows that even for seven particles per wavelength the total energy losses by the beam do not significantly exceed the losses due to incoherent bremsstrahlung of its particles. With an increased number of particles per wavelength ( $n > 8$ ) the peak of the total electron energy losses increases and the gain length decreases due to the coherence of individual electrons.

Fig. 2 gives the ratio  $\Delta\eta_{\text{coh}}/\eta_{\text{inc}}$  of the maximum excess of energy loss over incoherent radiation loss versus

<sup>\*</sup> Corresponding author.

the number of radiators per wavelength ( $\Delta\eta_{\text{coh}} = \eta_{\text{tot}} - \eta_{\text{inc}}$ ). This function represents the efficiency of self-amplification of coherent radiation by the beam particles. Fig. 2 shows that at  $n \geq 8$  the radiative interaction of the particles leads to an increase in beam energy losses as the parameter  $n$  grows. Saturation of this growth occurs at a level appreciably exceeding spontaneous incoherent losses. Fig. 2 also shows that the gain in the efficiency due to the coherent interaction of particles in the beam becomes appreciable only for the number of particles per wavelength greater than the threshold value  $n_*$ :  $n > n_* = 8$ .

In particular, it follows from Figs. 1 and 2 that in the model considered stimulated coherent radiation by the beam electrons occurs when their linear density is greater than 7 ( $n \geq n_* = 8$ ). In fact, for small  $n$  values ( $n \leq 7$ ) their collective radiative interaction in the undulator does not cause an excess of the total radiation intensity over that of incoherent SUR. Under these conditions the nonequilibrium system considered functions as a classical source of incoherent SUR. On the other hand, at  $n \geq 8$  this excess

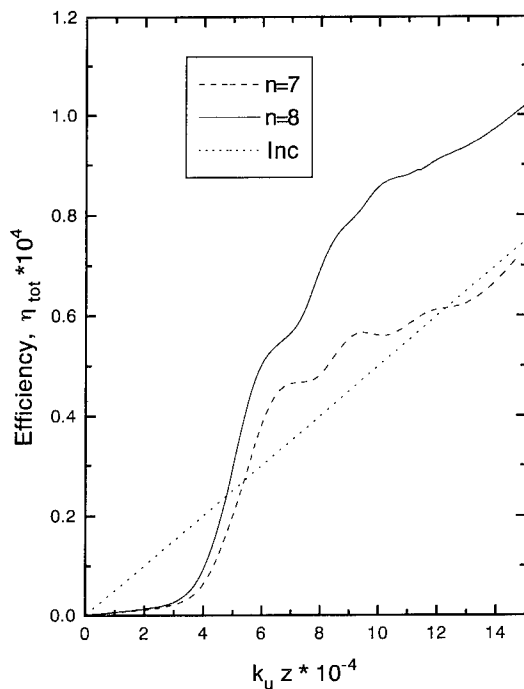


Fig. 1. The efficiency  $\eta_{\text{tot}}$  versus normalized distance along the undulator axis for the cases  $n=7$  (---), 8 (—) and incoherent energy losses  $\eta_{\text{inc}}$  (···).

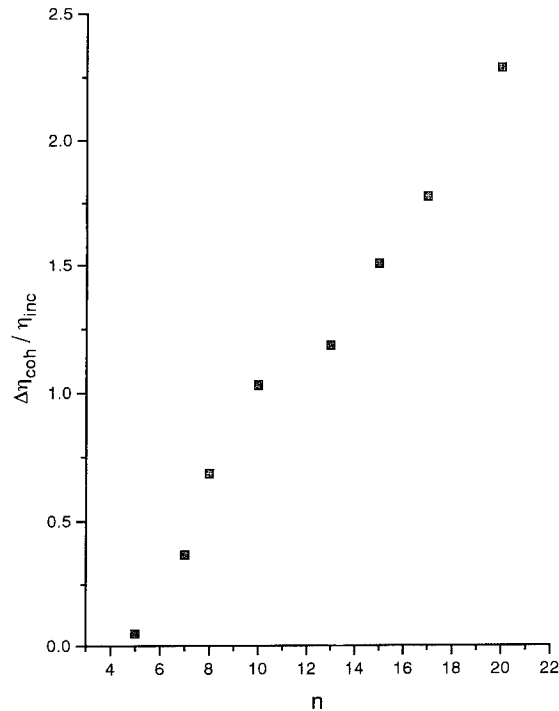


Fig. 2. The maximum excess of the efficiency over the spontaneous energy losses  $\Delta\eta_{\text{coh}}/\eta_{\text{inc}}$  versus the number of particles per wavelength  $n$ .

does take place. Its amplitude of the excess grows as the linear density  $n$  increases, and the position of the peak of the coherent radiation intensity approaches the undulator input. Physically, the only cause of the observed effect is the coherence of individual radiators (electrons). For this reason, we may suggest that for the present idealized model the threshold value of the number of radiators per wavelength corresponding to the transition of the beam + undulator system to the regime of stimulated coherent radiation is 8 ( $n_* = 8$ ).

## References

- [1] V.I. Kurilko and V.V. Ognivenko, DAN Rossii 335 (1994) 437, in Russian.
- [2] V.I. Kurilko and V.V. Ognivenko, Plasma Phys. Rep. 20 (1994) 634.
- [3] L.D. Landau, E.M. Lifshits, M: Fizmatgiz, Teoriya Polya (1960), in Russian.



ELSEVIER

# Simple theory of simultaneous harmonics operation of an FEL

B.A. Richman \*

Stanford Picosecond FEL Center, W.W. Hansen Experimental Physics Labs, Stanford University, Stanford, CA 94305, USA

## 1. Introduction

FELs have previously been suggested as the best possibility for obtaining high power coherent radiation at wavelengths shorter than what is attainable by conventional means [1,2]. Harmonic lasing methods have been proposed to overcome some of the problems that arise in this regime [2].

Earlier work has shown that lasing at the fundamental of the FEL wiggler produces “coherent spontaneous harmonics,” since both the wiggler and the electron bunching have harmonic Fourier content. This parametric process has been examined in the small signal, low gain limit by Elgin and Penman [3]. The spontaneous harmonic power is proportional to the square of the harmonic field produced by the coherently radiating bunches. If a harmonic field already exists, however, then the power is proportional to the square of the original plus radiated fields. The cross term is stimulated emission, which can be orders of magnitude larger than coherent spontaneous.

Although this method of obtaining harmonics may not be as efficient as that proposed by others [2], it can be accommodated in existing single wiggler FELs with relatively inexpensive modifications. I extend Colson’s one-dimensional classical gain calculation [1,4] in an analysis similar to that of Penman [3] to include an arbitrary number of simultaneous harmonics in order to examine the behavior of the harmonic stimulated emission as a function of radiation field powers.

## 2. Analytic theory

The derivation follows Colson’s theory based on single particle dynamics [1,4]. I assume a sinusoidal planar wiggler field, and a sum over odd harmonics of continuous wave planar radiation fields. I assume the harmonic fre-

quencies all to be exact multiples of the fundamental and the  $\phi$ ’s are constant. I define normalized time, electron phase  $\zeta$ , and resonance parameter  $\nu$  relative to the fundamental as in Ref. [1], Eqs. (15)–(18). The multiple pendulum equation derived is the same as that in [3] but ignoring the small cross terms, and the derivative is relative to normalized time,

$$\frac{d^2\zeta}{d\tau^2} = \sum_f |a_f| \cos(f\zeta + \phi_f). \quad (1)$$

The radiation fields  $a_f$  are defined as in Eq. (24) in Ref. [1]. To lowest order, the effects of each of the harmonics on the electrons are summed. The radiation equations of evolution are identical to Colson’s (Eq. (25) in Ref. [1]),

$$\frac{da_f}{d\tau} = -r_f \langle e^{-if\zeta} \rangle_{\zeta_0}. \quad (2)$$

We must solve Eq. (1) and perform the average in Eq. (2) to determine the power transfers among the radiation fields and the electron beam. Using the same perturbation expansion as in Ref. [4], but now with the sum of terms in Eq. (1), we find that,

$$\zeta^{(0)} = \nu\tau + \zeta_0, \text{ and}$$

$$\zeta^{(1)} = \sum_f \frac{|a_f|}{2f^2\nu^2} T_f \cos(\zeta_0 + \phi_f - \theta_f), \quad (3)$$

where

$$T_f^2/2 = 1 + \frac{f^2\nu^2\tau^2}{2} - \cos(f\nu\tau) - f\nu \sin(f\nu\tau), \quad (4)$$

and

$$\tan \theta_f = \frac{\sin(f\nu\tau) - f\nu\tau}{1 - \cos(f\nu\tau)}.$$

If we substitute Eqs. (3) and (4) into Eq. (2), the integral over  $\zeta_0$  (from 0 to  $2\pi$ ) cannot be evaluated directly. However, we can split the exponential into a product of factors, one of which has  $\zeta^{(0)}$ , and each of the rest of which contains one term from  $\zeta^{(1)}$ , and depends on

\* Tel. +1 415 723 0209, fax +1 415 715 8311, e-mail brich@lcland.stanford.edu.

only one harmonic field. This integral can be construed as the zero frequency component of the Fourier series in  $\zeta_0$  of the integral argument. Then the convolution theorem applies: the integral equals the 0th term of the discrete convolution of the Fourier transforms of all the factors. This is the sum over all products such that the sum of the indices of all the factors is zero. Using the integral form of Bessel functions,

$$\langle e^{-iF\zeta_0} \rangle_{\zeta_0} = e^{-iF\nu\tau} \sum_{-\infty < n_f < \infty} \left[ \prod_f e^{in_f(\phi_f - \theta_f - \pi/2)} \times J_{n_f} \left( \frac{|a_f|}{2f\nu^2} T_f \right) \right], \quad (5)$$

with condition  $\sum_f n_f = F$ .

Eq. (5) can be verified for the single frequency case by setting all  $a_f = 0$  except  $a_F$ , and comparing with Ref. [4]. The Bessel functions crudely describe saturation effects [4], but now saturation of one harmonic driving term can be caused by fields of other harmonics.

The small signal case corresponds to keeping the lowest order terms of each Bessel function. Because

$$J_n(X) \sim X^n \text{ for } X \ll 1, \quad (6)$$

the products in Eq. (5) are analogous to the basic form of nonlinear optical parametric interactions, where the nonlinear susceptibilities are the ratios of the terms to the products of field amplitudes. Eq. (5) has the same form and all the same terms as Ref. [3] Eq. (10), which shows the result of the fundamental ( $f=1$ ) on the 3rd harmonic ( $F=3$ ), but the coefficients are different. This difference is unresolved as of this writing. Eq. (5) defines the interactions among the radiation field amplitudes, not their intensities. The electron beam provides for energy conservation when Eqs. (2) for all harmonics are taken together. The phase matching is also analogous to typical nonlinear optics: the sum of the phases  $\phi_f$  determines the directions of energy transfers among the harmonics.

To find the total change in field amplitude in one pass through the wiggler, Eq. (5) must be integrated over  $\tau$ . I now consider the presence of only the fundamental and one harmonic  $F$ . I also assume that both wave amplitudes are in the small signal regime, so only the lowest order terms of the Bessel functions are retained. The change in the harmonic field amplitude over one pass is then,

$$\Delta a_F = r_F \frac{|a_F|}{4F\nu^2} e^{i\phi_F} G_{FF}(F\nu) + r_F \left( \frac{F|a_1|}{4\nu^2} \right)^F e^{iF\phi_1} G_{F1}(\nu), \quad (7)$$

where

$$G_{ff}(x) = \frac{2}{x} - i - \left( 1 + \frac{2}{x} \right) e^{-ix}, \quad (8)$$

and

$$G_{F1}(x) = \sum_{l=1}^F \frac{e^{-ilx} F!}{l(-l)^l (F-l)!} \sum_{q=0}^l \frac{(1+ix)^q l^q}{q!} - 1 - \sum_{l=1}^F \frac{1}{l(-l)^l} \frac{F!}{(F-l)!} \sum_{q=0}^l \frac{l^q}{q!}. \quad (9)$$

The stimulated emission is  $2\text{Re}(a_F^* \Delta a_F)$ . The first term of the stimulated emission (with  $G_{FF}$ ) divided by  $|a_F|^2$  is just the normal harmonic gain. The second term (with  $G_{F1}$ ) cannot be interpreted as simple gain. It corresponds to fundamental nonlinear conversion plus fundamental assisted electron beam energy extraction. Extraction by the harmonic may be significantly more than with no fundamental, provided the fundamental does not saturate the harmonic interaction.

### 3. Experimental proposal

I propose that an existing FEL system may be modified so that it can utilize enhanced harmonic lasing. First, the laser resonator mirrors must reflect all needed harmonics adequately. If the resonator contains dispersive optical elements, then the phase or group velocity dispersion must be eliminated, possibly with a Soleil-Babinet compensator.

Second, lower harmonics must be suppressed so as not to saturate the higher harmonics, with resonator mirrors with suitably different reflectivities for the different harmonics, or, if the FEL is mode-locked, using group velocity dispersion to walk off some harmonics temporally from the electron micropulses. Alternatively, a grating could be used to separate the harmonics and give each its own end mirror.

### 4. Conclusion

I have derived a simple theory which describes the operation of a single wiggler FEL at multiple simultaneous harmonics. The interaction among the harmonics is directly analogous to nonlinear optical wave mixing. One or many harmonics can be used to enhance the extraction by another. Existing FEL systems may be modified to accommodate the multiple lasing scheme.

### References

- [1] W.B. Colson, IEEE J. Quantum Electron. QE-17 (1981) 1417.
- [2] I. Ben-Zvi et al., Nucl. Instr. and Meth. A 318 (1992) 201 and 208, and references therein.
- [3] J.N. Elgin and C. Penman, Nucl. Instr. and Meth. A 304 (1991) 444.
- [4] W.B. Colson and S.K. Ride, Physics of Quantum Electronics, Vol. 7, Chap. 13, eds. S. Jacobs et al. (Addison-Wesley, 1978).

## RF systems for JAERI FEL linac

M. Sawamura<sup>\*</sup>, E.J. Minehara, R. Nagai, M. Sugimoto, M. Takao, R. Kato,  
N. Kikuzawa, M. Ohkubo

Free Electron Laser Laboratory, Japan Atomic Energy Research Institute (JAERI), Tokai-mura, Ibaraki-ken 319-11, Japan

### 1. Introduction

Construction of the superconducting linac-driven FEL system for far infrared oscillation has been continuing at JAERI. An outline of the JAERI FEL program has been reported elsewhere [1,2]. The JAERI FEL linac consists of a sub-harmonic buncher (SHB), a buncher, two single-cell superconducting modules (pre-accelerator), and two five-cell superconducting modules (main accelerator). All of the cavities have been installed. The superconducting modules are operated in a pulsed mode with 2 ms macropulses at a 10 Hz repetition rate. Two kinds of closed-loop helium gas refrigerators, 11 W at 4 K and 20 W at 20 K, have been installed on each module for cooling the superconducting accelerator cavities. Cooling tests [3] and RF tests of the superconducting cavities have been done [4], and beam accelerating tests have now begun. In this article, improvements of the RF system and the RF characteristics of the beam acceleration are reported and discussed briefly.

### 2. RF system using a frequency divider

When using harmonic frequencies in the operation of an accelerator there are two methods to generate the frequencies. One is multiplying the low frequency to produce the high frequency and the other is dividing the high frequency to produce the low one. When multiplying, the sine wave of the fundamental frequency is distorted into a waveform that has many harmonics and the desired frequency is selected from the various harmonics by a band-pass filter. The phase fluctuations of the multiplied frequency are estimated to depend on the time derivative of the distorted signal and are thus a multiple of the phase fluctuations of the fundamental frequency.

When using the method of dividing, on the other hand,

a pulsed signal with the period of the low frequency is generated by counting cycles of the higher frequency. The pulsed signal is turned into a sine wave by passing it through a low-pass filter. Although there is the merit of decreasing the phase fluctuation through the process of dividing, it might be difficult to choose a counter and divider which can work reliably at the high speeds required by the fundamental frequency.

The energy spread of the accelerated beam depends on the fluctuation of the phase and amplitude of the RF power in the accelerating cavities. The phase fluctuations generated by the methods of multiplying and dividing are shown in Fig. 1. The phase fluctuations of multiplying are larger than those of dividing. This shows the drawback of the multiplying approach, that the phase fluctuations are multiplied at the same time as the frequency.

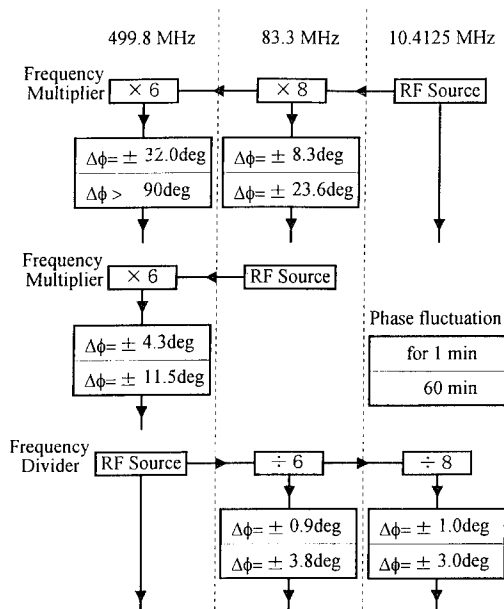


Fig. 1. Phase fluctuation caused by the frequency multipliers and dividers.

<sup>\*</sup> Corresponding author. Tel. +81 292 82 6752, fax +81 292 82 5939.

### 3. Improvement of the RF amplifiers

The five high power amplifiers of 499.8 MHz have similar construction. Each of them consists of a power divider, several or a few tens of low power amplifier modules, a power combiner and a directional coupler. The input power is divided by the power divider and fed into the low power amplifier modules, whose output power is combined to make the high power output. Each low power amplifier module has an isolator to protect itself from the reflected power. The directional coupler samples the power for monitoring and controlling.

The RF coupler of the superconducting accelerator is set to a position suitable for feeding the RF power into a beam-loaded cavity. The power absorbed by the beam is such a large percentage of the total absorbed power that the cavity is considerably over-coupled in the absence of a beam. Therefore, when the power is fed into the superconducting accelerator in pulsed mode, the reflected power from the accelerator to the RF amplifier varies drastically due to over-coupling.

The reflected power was thought to be divided by the power combiner and to be absorbed at the isolator of the low power module. Due to an impedance mismatch of the power combiner the reflected power was reflected again at the power combiner. This affected the feedback control signal and the output power became unstable. To solve this

a high power isolator was inserted between the power combiner and the directional coupler so that the reflected power could not affect the control signal from the directional coupler. RF field fluctuations in the cavity fed by an amplifier with a high power isolator are shown in Fig. 2.

### 4. Beam accelerating tests

The beam accelerating tests have started and the beam has been accelerated successfully to the end of the undulator. The voltage of the electron gun is about 250 kV. The bunch length at the exit of the gun was about 2 ns. The accelerating field of the superconducting accelerators is about 4.5 MV/m with the unloaded  $Q$ -value more than  $2 \times 10^9$ . The energy spread at the exit of the pre-accelerators was about 3%. The energy at the exit was about 15 MeV. The beam accelerating tests will be continued to improve the peak current of the beam and the energy spread, and the beam will be passed through the undulator to get FEL oscillation.

### 5. Conclusion

The stability of the RF system has been improved by adopting frequency dividers to generate the sub-harmonic frequencies, and by inserting isolators for the high power RF amplifiers. Improvement of the RF system makes the fluctuation of the phase and amplitude in the field less than several degrees and 1%, respectively and the beam acceleration more stable. The beam has been accelerated successfully up to 15 MeV to the end of undulator. The experiments on FEL oscillation will begin in the future.

### References

- [1] M. Sawamura et al., Proc. 13th Int. Free Electron Laser Conf., Santa Fe, NM, USA, 1991, Nucl. Instr. and Meth. A 318 (1992) 127.
- [2] E.J. Minchura et al., Proc. 14th Int. Free Electron Laser Conf., Kobe, Japan, 1992, Nucl. Instr. and Meth. A 331 (1993) 182.
- [3] N. Kikuzawa et al., *ibid.*, p. 276.
- [4] M. Sawamura et al., Proc. 15th Int. Free Electron Laser Conf., The Hague, The Netherlands, 1993, Nucl. Instr. and Meth. A 341 (1994) 391.

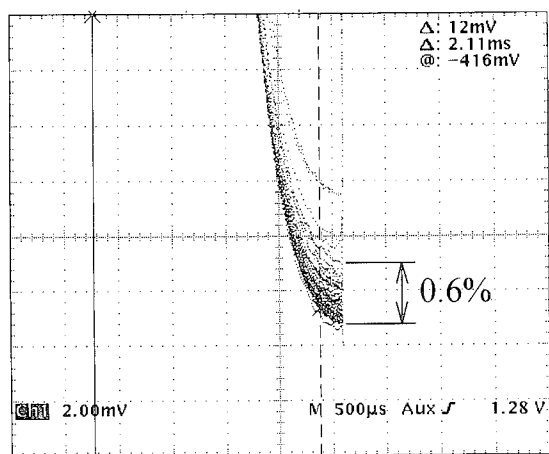


Fig. 2. Field fluctuations in the pre-accelerator cavity fed by the RF amplifier with a high power isolator.



ELSEVIER

## The UCLA high gain infrared FEL <sup>☆</sup>

G. Travish, M. Hogan <sup>\*</sup>, C. Pellegrini, J. Rosenzweig

*Department of Physics, UCLA, Los Angeles, CA 90024, USA*

### 1. Introduction and overview

The Particle Beam Physics Laboratory (PBPL) at UCLA is constructing a short period FEL which will operate in the high gain regime. The focus of the work has been the production of a high brightness electron beam suitable for short wavelength FELs. Once operational the FEL will be used to study phenomena of significance to short wavelength devices such as SASE and performance sensitivity to various beam parameters. Future studies may include the addition of a second undulator or amplification of an input source (CO<sub>2</sub> laser) to study saturation, superradiance, and optical guiding.

The electron beam is provided by a linac whose major components are a S-band copper photocathode gun and a Plane Wave Transformer (PWT) accelerator section. The UCLA photocathode gun is driven by a frequency quadrupled, pulse compressed Nd:YAG laser (UV) and has been characterized and described in detail elsewhere [1]. Solenoidal focusing controls the highly divergent beam as it exits the gun and provides for emittance compensation [2] into the PWT which accelerates the electrons to roughly 17 MeV [3]. During recent conditioning, the PWT has been operated at high power and the dark current measured at  $\sim 7.5$  MeV.

The UCLA experiment was designed to study issues important to future short wavelength devices. The short period undulator, combined with our moderate energy beam produces radiation in the infrared where a large number of diagnostics are available, without the added complexity of producing a higher energy beam that would be necessary for operation at shorter wavelengths. Further, working in the infrared (IR) does not suffer from the beam noise problems associated with past microwave FELs. The lack of suitable sources at short wavelengths makes the feasibility of start up from noise (SASE) important [4]. Lack of suitable mirrors makes an oscillator configuration

impractical for short wavelengths, so successful operation in the high gain regime is a necessary precursor to designing short wavelength devices. For these reasons the FEL studies will begin from SASE in the high gain regime.

### 2. The undulator

The hybrid planar undulator is 60 cm long with a 1.5 cm period, 5 mm fixed gap spacing and a greater than 7 kG peak field corresponding to an undulator parameter ( $K$ ) of 1. Measurements using both a Hall probe and pulsed wire technique show an rms field uniformity of better than 0.18% [9]. The second integral of the field along the beam axis shows that the rms electron beam deflection in the wiggle plane of  $\sim 105$   $\mu$ m satisfies the requirement that it be less than the rms beam waist of  $\sim 200$   $\mu$ m.

### 3. Measurements and simulations

Numerical simulations have been used to determine the expected FEL performance. Primarily, Tran and Wurtele's TDA3D code is used although it has been optimized for the Cray and modified to include rotated phase space for matching into the undulator [10].

Simulations of gain vs. current show that an increase (decrease) in current of 10% increases (decreases) the output power by  $\sim 40\%$  (25%). Of the various beam parameters, current can be controlled best and will be one of our primary tools for studying SASE. The spontaneous emission is broadband and scales linearly with the current, while the amplified radiation scales as the current raised to the four-thirds power. By using the current to control the effective length of the undulator and filtering out the broadband radiation, these scalings can be measured and compared to theory.

Wakefields (primarily from the linac) are expected to produce a correlated energy spread of a few percent. This gives rise to a subsequent broadening of the central line width, but most IR detectors are broadband and nearly linear over such linewidths. Our expected uncorrelated

<sup>☆</sup> Work supported by US DOE Grant DE-FG03-92ER-40493.

<sup>\*</sup> Corresponding author. Tel. +1 310 206 5584, fax +1 310 206 1091, e-mail: hogan@physics.ucla.edu.

energy spread of  $\sim 0.1\%$  does not substantially degrade FEL performance.

Fluctuations in the beam size are manifest as effective mismatching into the undulator, but simulations predict the FEL performance will be insensitive to achievable size fluctuations.

#### 4. Detection of SASE

The spectral and angular characteristics of the radiation emitted by an electron traversing an undulator are well known and may be numerically integrated over the bandwidth and solid angle of the FEL to give the total energy radiated (see Table 1). Results are similar to those obtained from simple 1-D theory [11]. The low level SASE signal ( $\sim \text{mW}$ ) requires the use of cryogenic detectors to obtain the necessary sensitivity. Detecting this weak SASE signal is hampered by background (blackbody) radiation which

peaks around  $10 \mu\text{m}$  at room temperature ( $25^\circ\text{C}$ ). Although the background signal constitutes a DC offset/pedestal that may be compensated for, the shot noise of the background will reduce the signal to noise ratio (SNR). This noise scales roughly as the square root of the number of blackbody photons. Additionally, available IR detectors have relatively long time constants ( $\sim \text{ns}$ ) with respect to the pulse ( $\sim \text{ps}$ ), so that the integrated background noise may be significant. Sample calculations for an available copper doped germanium detector yield a typical signal to noise ratio of  $\sim 10^3$ . This does not take into account signal loss in the optics, pre-amplifier noise, or reduction in detectivity due to operating far below the response time of the detector. By aperturing the field of view of the detector to limit the collected background, the SNR can be increased by several additional orders of magnitude. Other detectors such as mercury–cadmium–telluride photodiodes may offer the advantage of faster response times and/or higher quantum efficiencies while only needing to be cooled to liquid nitrogen temperature. Both the spontaneous emission and the amplified signal should be well within our sensitivity, and studies of SASE should be feasible.

Table 1  
Expected electron beam and FEL parameters for the UCLA IRFEL

|   |                         |
|---|-------------------------|
| Electron beam parameters (expected)       |                         |
| Energy                                    | 17 MeV                  |
| Energy spread (uncorrelated)              | 0.1%                    |
| Current (peak)                            | 200 A                   |
| Pulse length (rms)                        | $\sim 5 \text{ ps}$     |
| Normalized emittance (rms)                | 5 mm mrad               |
| Undulator parameters (measured)           |                         |
| Total length                              | 60 cm                   |
| Undulator period                          | 1.5 cm                  |
| Peak field on axis                        | 7.3 kG                  |
| Pole face gap (fixed)                     | 5 mm                    |
| Undulator parameter ( $K$ )               | $\sim 1$                |
| FEL parameter ( $\rho$ )                  | $\sim 1 \times 10^{-2}$ |
| FEL parameters (simulation)               |                         |
| Output radiation wavelength               | $10.6 \mu\text{m}$      |
| power gain (e-folding) length             | 7.2 cm                  |
| Spontaneous emission from one gain length | 3 mW                    |
| SASE peak power after 60 cm               | $\sim 1 \text{ W}$      |
| SASE saturation length                    | 1.6 m                   |
| Peak power at saturation                  | $\sim 20 \text{ MW}$    |

#### References

- [1] J. Rosenzweig et al., Nucl. Instr. and Meth. A 341 (1994) 379.
- [2] B.E. Carlsten, Nucl. Instr. and Meth. A 285 (1989) 313.
- [3] D. Swenson, Proc. Europ. Particle Accelerator Conf., ed. S. Tazzari (1988) p. 1418.
- [4] H. Winick et al., Proc. 8th SRI93, Gaithersburg, MD, August 23–26, 1993.
- [5] J. Rosenzweig and G. Travish, UCLA Dept. of Physics-CAA-TECH-NOTE #64 (1993).
- [6] E. Babenko et al., SLAC-PUB-6203 (1993).
- [7] G.H. Gillespie, Associates Inc., MacTrace Version 1.0 (1992).
- [8] K. Halbach, J. Physique, Coll. C1 (1983).
- [9] G. Travish, UCLA Dept. of Physics, CAA-TECH-NOTE #34.
- [10] T.M. Tran and J.S. Wurtele, Computer Phys. Commun. 54 (1989) 263 and T.M. Tran and J.S. Wurtele, Phys. Rep. 195 (1990).
- [11] K.J. Kim, Phys. Rev. Lett. 57 (1986) 1871.





ELSEVIER

## Performance of the optical cavity control system for the JAERI FEL project

R. Kato<sup>\*</sup>, M. Sugimoto, R. Nagai, M. Sawamura, M. Takao, N. Kikuzawa, M. Ohkubo,  
E.J. Minehara, Y. Suzuki

*Free Electron Laser Laboratory, Japan Atomic Energy Research Institute, Tokai, Ibaraki, 319-11, Japan*

### 1. Introduction

A prototype free electron laser driven by a 15 MeV, quasi-CW superconducting rf linac has been developed at Japan Atomic Energy Research Institute (JAERI), Tokai [1]. The JAERI-FEL consists of a 250 keV electron gun, 83.3 MHz subharmonic buncher (SHB), 499.8 MHz superconducting pre- and main-accelerator, beam transport system, undulator and optical cavity. Until now, all equipment except the undulator and optical cavity has been managed by a control system named the Free Electron Laser Operator Windows System (FELOWS) [2–4].

We have recently developed an optical cavity control system in the framework of FELOWS, the concept and design architecture of which are described in the following sections.

### 2. Hardware configuration and outline of FELOWS

Distributed personal computer (PC) units are connected on a local area network by Ethernet cable. There are PC units with and without a CAMAC crate system, but all PC units run the FELOWS system software.

FELOWS consists of an executive program, scheduler, virtual controller, individual interface programs named “panels” and individual device driver libraries. In FELOWS, there is no master nor slave computer and all PC’s exchange messages on equal terms. Therefore, we can control all devices from any PC. Fig. 1 shows the message flow from a panel program to a hardware device in the system. If we control a hardware device from a PC, a device driver called by the panel checks whether the unit number of the local PC equals that of the devices written in its device data file or not. For local control the device driver directly sends a message to the device (Fig. 1a). For

remote control the device driver sends one to a virtual controller, which forwards the message on the network. Virtual controllers on the PC with that device receives the message and calls the appropriate device driver. The device driver checks the unit numbers again and sends the message to the device hardware (Fig. 1b). In the system, panel programs only call functions provided by device drivers and are independent of configurations of the physical hardware device. The advantage of this approach is that for remote control the virtual controller receives the message instead of a hardware device, which means that we can develop device drivers without taking account of the network. If a new device is added to this system, we need only develop a new panel and device driver and rewrite the device data files. The optical cavity control system has been developed in this way.

### 3. Optical cavity design and control system

Main characteristics of the optical cavity are listed in Table 1. The mirror is set in a vacuum chamber that is mounted on a 5-axis stage with stepping motors and remotely adjusted by the optical cavity control system.

A “panel” window of the optical cavity control system is shown in Fig. 2. The user interface of the system is

Table 1  
Main characteristics of the optical cavity

| Item             | Specification                             |
|------------------|---|
| Length           | 14.4 m                                    |
| Mirrors          |   |
| Curvature radii  | 7.34 m (near concentric)                  |
| Aperture         | 60 mm (diameter)                          |
| Coating          | Au  |
| Substrate        | Cu  |
| Output coupling  | Hole (2 mm diameter)                      |
| Reflectance      | > 99% (without hole)<br>> 95% (with hole) |
| Undulator length | 1.8 m                                     |
| Rayleigh length  | 1 m                                       |

<sup>\*</sup> Corresponding author. Tel. +81 292 82 6752, fax +81 292 82 5939.

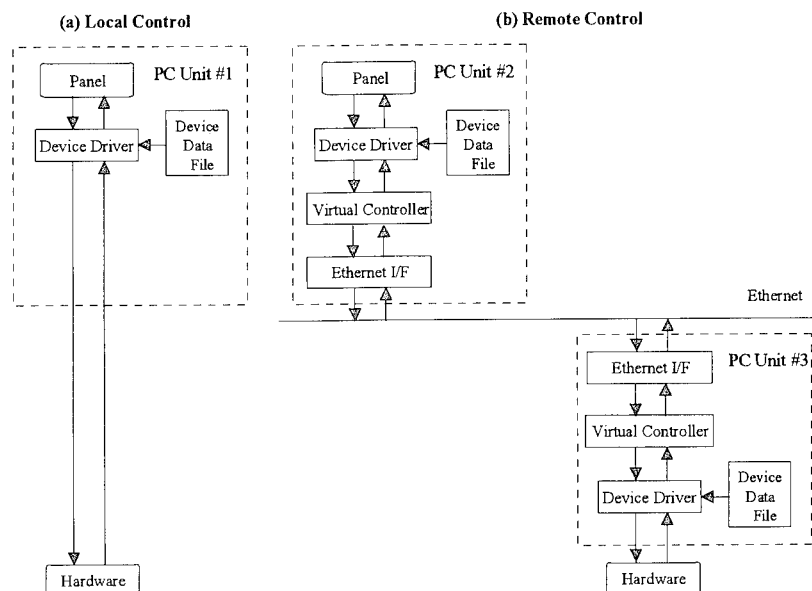


Fig. 1. A schematic diagram of the message flow from a panel program to a hardware device in the system. For local control (a), the device driver directly sends a message to the hardware device. For remote control (b), the device sends one to a virtual controller, which forwards the message on the network.

constructed using resources from the graphical user interface of Microsoft Windows, and graphically simulates the hardware controller, such as button switches, faders and meters. The panel program periodically checks the current data in a device driver and renews the indicators in the panel window. Also the device driver periodically checks the hardware devices and renews its internal data buffer. As mentioned above, panel programs are independent of the configurations of the physical hardware device. Only the device drivers check the device data files. The device data file of the optical cavity thus provides correspondence

between the logical control objects, such as mirror number and control axis, and the physical control objects, such as PC unit number, CAMAC slot number, GPIB address and subaddress.

#### 4. Conclusion

The FELOWS control system has the following advantages:

The software development and maintenance are very easy, because the user interface, the hardware device control and the network communication are independent of each other. A programmer of individual panels and device drivers is not required to know details of the accelerator control, but is only required to know Windows programming. Also simply by rewriting the device data files, we can rearrange control tasks between individual PCs. Hence, it is very easy to modify hardware configurations.

#### References

- [1] E. Minchura et al., Proc. 15th Free Electron Laser Conf., The Hague, The Netherlands, 1993, Nucl. Instr. and Meth. A 341 (1994).
- [2] M. Sugimoto, Proc. Int. Conf. on Accelerator and Large Experimental Physics Control Systems, 1991, Tsukuba, KEK Proc. 92-15 (1992) 198.
- [3] M. Sugimoto, Proc. 14th Int. Free Electron Laser Conf., Kobe, 1992, Nucl. Instr. and Meth. A 331 (1993) 340.
- [4] M. Sugimoto et al., *ibid.*

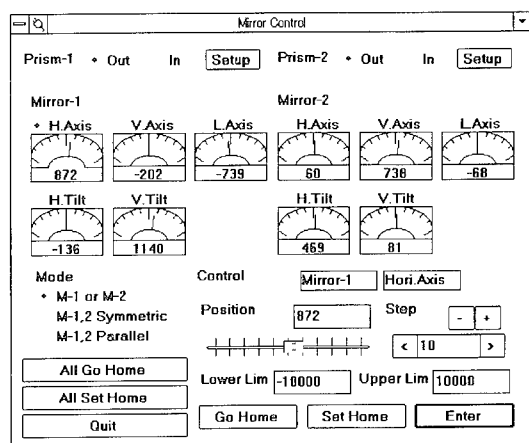


Fig. 2. A control panel for the optical cavity. The user interface graphically simulates the hardware controller, such as button switches, faders and meters.



ELSEVIER

# A new method of equalizing $\beta_{\parallel}$ (conditioning) in an electron beam propagating in a longitudinal magnetic field

V.A. Papadichev \*

*Lebedev Physical Institute, 53 Leninsky Prospect, 117924 Moscow, Russian Federation*

The transverse inhomogeneity of the undulator magnetic field and betatron oscillations of electrons moving off-axis cause electrons to acquire various transverse velocities, leading to a spread in longitudinal velocity in the beam and preventing some parts of the beam from taking part in the amplification of an electromagnetic wave along the entire FEL. A complex and expensive method was proposed recently by Sessler et al. [1] of accelerating the off-axis particles so that they acquire additional axial velocity correlated with betatron oscillation amplitude, resulting in all beam electrons moving through the undulator with the same longitudinal velocity (also correcting the effect of finite beam emittance).

Many FEL experiments are conducted with high-current electron beams at low and medium electron energies (0.5–15 MeV). Such beams are usually transported in a longitudinal magnetic field to prevent beam blow-up due to space-charge forces. Undulator field inhomogeneity prevents using large-diameter beams and fully exploiting the high-power possibilities of pulsed accelerators. A simple method is proposed to solve the problem in this case.

The equation of transverse electron motion for the simple model of a round cylindrical beam in a helical undulator and axial magnetic field  $B_{\parallel} \neq 0$ , using the method of [2], can be written as:

$$\frac{d^2\eta}{dz^2} - ik_c \frac{d\eta}{dz} + k_{bs}^2 \eta = -i \left( e / (m_0 c^2 \gamma \beta_{\parallel}) \right) (B_x + iB_y), \quad (1)$$

where  $\eta = x + iy$ ,  $i = (-1)^{1/2}$ ,  $v_z = v_{\parallel} = \text{const.}$ ,  $k_c = \omega / v_{\parallel}$  is the cyclotron-motion wave number,  $\omega = (eB_{\parallel}) / (m_0 c \gamma)$  is the cyclotron frequency in the longitudinal magnetic field  $B_{\parallel}$ ;  $B_x$  and  $B_y$  are undulator field components,  $k_{bs} = (k_{\beta}^2 - k_s^2)^{1/2}$  is the betatron wave number accounting for space-charge forces  $e(E_r - \beta_{\parallel} H_{\theta})$  when  $B_{\parallel} = 0$ ,  $k_{\beta} = k_0 \beta_{\perp 0} / (2^{1/2} \beta_{\parallel})$  is the betatron wave number without

space-charge influence when  $B_{\parallel} = 0$ ,  $k_s = (2I_b / I_0)^{1/2} / (\gamma^{1/2} \beta_{\parallel} \gamma_{\parallel} r_0)$  is the space-charge wave number accounting for electric and magnetic fields  $(E_r - \beta_{\parallel} H_{\theta})$  of the homogeneous cylindrical beam,  $I_b$  the beam current,  $I_0 = m_0 c^3 / e \approx 17$  kA,  $r_0$  beam outer radius, and  $\gamma_{\parallel} = (1 - \beta_{\parallel}^2)^{-1/2}$ .

The general solution is

$$\eta = A e^{ik_1 z} + B e^{ik_2 z} + C e^{ik_0 z}, \quad (2)$$

where  $k_{1,2} = k_c / 2 \pm ((k_c / 2)^2 + k_{bs}^2)^{1/2}$  are the wave numbers of the modified cyclotron gyration and azimuthal drift caused by the undulator focusing and beam space-charge forces. Usually  $k_{bs} \ll k_c$ ,  $k_1 \approx k_c$  and  $k_2 \approx -k_{bs}^2 / k_c$ ,

$$C = i \left( e B_{\perp 0} / (m_0 c^2 \gamma \beta_{\parallel}) \right) / (k_0^2 - k_c k_0 - k_{bs}^2) \\ = i \beta_{\perp 0} k_0 / (k_0^2 - k_c k_0 - k_{bs}^2) \approx i \beta_{\perp 0} / (k_0 - k_c). \quad (3)$$

$A$  and  $B$  depend on the initial coordinates and velocities  $R_0 = X_0 + iY_0$  and  $V_0 = V_{0x} + iV_{0y}$ :

$$A = -C(k_0 - k_2) / (k_1 - k_2) - k_2 R_0 / (k_1 - k_2) \\ - iV_0 / ((k_1 - k_2) v_{\parallel}); \\ B = C(k_0 - k_1) / (k_1 - k_2) + k_1 R_0 / (k_1 - k_2) \\ + iV_0 / ((k_1 - k_2) v_{\parallel}). \quad (4)$$

Thus, electrons experience three types of transverse motion: 1) undulator orbital motion  $\eta_1 = C e^{ik_0 z}$ , 2) cyclotron gyration  $A e^{ik_1 z}$  with slightly increased cyclotron frequency  $\Delta\omega / \omega = k_{bs}^2 / k_c^2$ , and 3) low-frequency circular drift  $B e^{ik_2 z}$  with  $k_d = k_2 \approx k_{bs}^2 / k_c$ .

Several methods are suitable to compensate transverse undulator field inhomogeneity. First, since electrons undergo cyclotron gyration with the amplitude proportional to the average value of the undulator magnetic field on the radius of injection if the undulator field starts abruptly ( $\Delta z \ll 2\pi / \max \{k_0, k_1, k_2\}$ , i.e., nonadiabatic injection) with all electrons oscillating in phase, it is necessary to subtract the same transverse velocity (equal to that of the outer electron) from all electrons to obtain the required  $v_c$  profile (Fig. 1). This can be done by exciting the homoge-

\* Tel. +7 095 132 6300, fax +7 095 938 2251, e-mail vityal@lpnu.flan.msk.su.

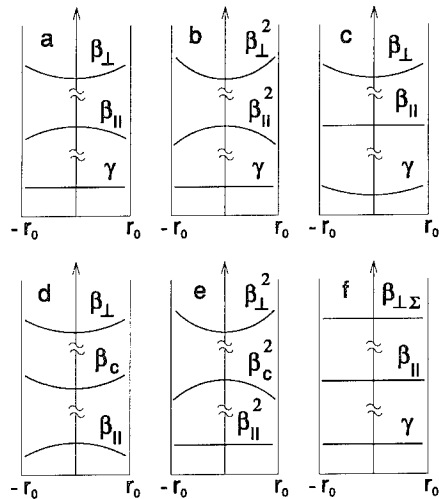


Fig. 1. Comparison of two methods of beam conditioning. Normalized transverse ( $\beta_{\perp}$ ) and longitudinal ( $\beta_{\parallel}$ ) velocities and electron energy ( $\gamma$ ) versus radius. (a), (b), and (c):  $B_{\parallel} = 0$ . (a) and (b): velocity and energy before conditioning. (c): velocity and energy after conditioning. (The outer electrons must be accelerated to achieve  $\beta_{\parallel} = \text{const.}$ ) (d), (e), and (f):  $B_{\parallel} \neq 0$ . (d): before conditioning, with orbital and cyclotron velocities uncorrelated. (e) and (f): after conditioning so that  $\beta_{\parallel} = \text{const.}$  ( $\beta_{\perp\Sigma}$  is the sum of  $\beta_{\perp}$  and  $\beta_c$ ).

neous transverse dipole magnetic field at the proper axial position at undulator entry.

The second method could be used when the undulator has an adiabatic entry, i.e., a slowly rising field, and injecting the beam into it results in negligible beam cyclotron velocities after passing the entry. One can employ in this case a combination of several half-periods of a helical undulator for exciting a parabolic velocity profile after passing it and a dipole magnet consisting of two windings for subtracting the maximum excited velocity.

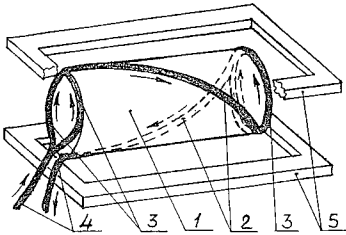


Fig. 2. Schematic drawing of one section of the conditioner: 1 – half-period-long helical undulator section, 2 – undulator winding, 3 – connecting wires, 4 – power feed, 5 – dipole magnetic field windings.

The transverse velocity acquired at coordinate  $z$  by the electrons after passing a region  $(0, z)$  of magnetic field if  $V(0) = 0$  at  $z = 0$ , is [2]:

$$V = v_x + i v_y$$

$$= -[ie/(m_0 c \gamma)] e^{i k_c z} \int_0^z (B_x + i B_y) e^{-i k_c z'} dz'. \quad (5)$$

Using formula (5) for averaged fields at the outer beam radius, one can calculate the necessary parameters of cyclotron velocity exciting means to get beam conditioning.

A simple method of electron beam conditioning for FEL is proposed for the case when the zero-emittance beam propagates in a longitudinal magnetic field. It consists of exciting cyclotron velocities in the beam with a radial profile that compensates for  $\beta_{\parallel}$  decrease of outer electrons in the beam due to undulator field inhomogeneity. The method could be employed for increasing the useful beam currents by an order of magnitude. It requires using an axial magnetic field and does not compensate in its simplest form the influence of a finite beam emittance effect. But if a finite emittance beam is acceptable for a FEL and using larger aperture is limited by undulator field inhomogeneity, it is possible by this method to employ beams of larger diameter and an order of magnitude larger currents. The required devices may be no longer than several tens of centimeters and a few centimeters in diameter. If axial magnetic field is used for transporting the electron beam, it can be used for beam conditioning with no substantial extra expenditures.

## Acknowledgements

The author would like to thank O.A. Smith, M.A. Mashkov and L.S. Kitaiskaya for their assistance in preparation of the paper.

It is a pleasure for the author to express his gratitude to the Physics Department, University of California, Irvine for the opportunity to finish this report during his stay there in July–August 1994.

## References

- [1] A.M. Sessler, D.H. Whittum and L.-H. Yu, Phys. Rev. Lett. 68 (1992) 309.
- [2] V.A. Papadichev, Proc. 12th Int. FEL Conf., Paris, France, 1990, Nucl. Instr. and Meth. A 304 (1991) 749.

## Power requirements for high-average power FELs

R.A. Lyon, W.B. Colson

*Physics Department, Naval Postgraduate School, Monterey, CA 93943, USA*

A compact, high-power FEL would have useful applications by industry [1] and the Department of Defense. Significant technological developments remain before a megawatt laser can be constructed. This paper outlines the power requirements for a general FEL design subject to a few specific constraints.

The design of this FEL will require it to be compact, power efficient, have a sufficiently low personnel radiation hazard, and produce a 1 MW optical beam at a wavelength of  $\lambda = 3 \mu\text{m}$ . The energy recovery system shown in Fig. 1 is suitable under these constraints. An undulator energy extraction efficiency of 2% and an energy recovery efficiency of 95% are assumed. To produce  $3 \mu\text{m}$  light, the resonance condition,  $\lambda = \lambda_0(1 + K^2)/2\gamma^2$ , implies an upper limit on the beam energy,  $W_b$ , of 100 MeV in order to prevent the total undulator length from becoming too large. Therefore, the beam power required at the undulator is based on an energy of 100 MeV with a 500 mA average current.

The components of the FEL architecture which dictate the prime power requirements are the accelerator and the electron injector. A superconducting RF (SRF) accelerator will consume power in liquid helium refrigeration systems and in transferring RF power to the electron beam. The RF losses into the accelerator structure,  $P_L$ , and the required refrigeration power,  $P_F$ , are given by [2,3]:

$$P_L = \frac{8W}{E\sqrt{f/500}} + \frac{EW}{380(f/500)9Q_T} + \frac{EW(f/500)^{1.1}(0.000028)^{-17.67/T}}{380(280)T}$$

and

$$P_F = \frac{1}{\eta_F} \left( \frac{300 - T}{T} \right) P_L,$$

where  $E$  is the average acceleration gradient (MV/m),  $W$  is the energy gain of the electrons (MeV),  $f$  is the frequency (MHz),  $T$  is the structure temperature (K),  $Q_r$  is the residual loss contribution to the quality factor, and  $\eta_F$  is the refrigeration compressor efficiency. SRF cavities can have acceleration gradients in excess of 10 MV/m [4]. For

$E = 10 \text{ MV/m}$  (chosen to minimize accelerator size),  $T = 4.2 \text{ K}$ ,  $W = 96 \text{ MeV}$ ,  $Q_r = 8 \times 10^9$ , and  $\eta_F = 30\%$ , an operating frequency of 400 MHz optimizes power efficiency with wall losses  $P_L = 1.2 \text{ kW}$ , and required refrigeration power of  $P_F = 275 \text{ kW}$ .

Room temperature (RT) cavities, normally fabricated from copper, have a shunt impedance,  $Z$ , which varies according to the square root of the frequency. Therefore, the RF loss into the accelerator structure is  $P_L = EW/kf^{1/2}$  [5] where  $k$  is a constant of proportionality that includes the material conductivity and permeability, and is heavily dependent on cavity geometry. Based on existing cavity designs [5,6], this constant varies over a wide range with  $0.9 < k < 4 \text{ (M}\Omega/\text{m MHz}^{1/2})$  inclusive. The geometry considerations affecting these values also affects beam quality in a non-correlated quantitative way. Practical predictions on the suitability of a design with  $k = 4$  for a high power laser is possible only with numerical simulations. For a value of  $k = 3.5$ ,  $E = 1.5 \text{ MV/m}$ , and  $W = 96 \text{ MeV}$ , the power losses are  $P_L = 41.1 f^{-1/2} \text{ MW}$ . For a high-power laser, cavity energy storage will limit the allowed operating frequencies to below 1 GHz [5]. For an operating frequency of 200 MHz, the power loss is 2.9 MW.

The power absorbed by the beam in accelerating it from 4 MeV to 100 MeV is 48 MW. 1 MW of power is removed by the undulator. Only a small fraction of this energy will be lost in optical components so we essentially have a 1 MW optical output. 46.6 MW of RF power is recovered within the accelerator. Therefore, only 1.4 MW of RF power is needed from the RF power source to

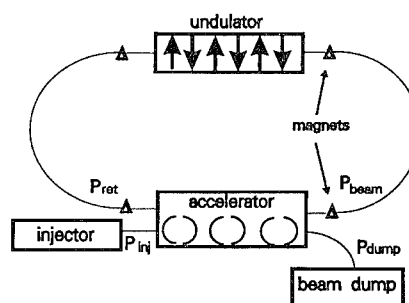


Fig. 1.

Table 1  
FEL power requirements

| Parameter  | SRF             | RT              |
|--|-----------------|-----------------|
| $f$ (MHz)  | 400             | 200             |
| $W_b$ (MeV)  | 100             | 100             |
| $I_{\text{avg}}$ (mA)                              | 500             | 500             |
| $E$ (MV/m)   | 10              | 1.5             |
| $Z$ ( $\Omega/\text{m}$ )                          | 311             | 990             |
| $O_r$  | $8 \times 10^9$ | –               |
| $O_o$  | $3 \times 10^9$ | $5 \times 10^4$ |
| $P_{\text{beam}}$ (MW)                             | 50              | 50              |
| $P_{\text{ret}}$ (MW)                              | 49              | 49              |
| $P_{\text{inj}}$ (MW)                              | 2               | 2               |
| $P_{\text{dump}}$ (MW)                             | 2.45            | 2.45            |
| $P_{\text{HVdc}}$ (kW)                             | 250             | 250             |
| $P_{\text{Linj}}$ (kW)                             | 150             | 150             |
| $P_L$ (kW)   | 1.2             | 2900            |
| $P_{\text{rf}}$ (MW) ( $\eta_{\text{rf}} = 0.65$ ) | 6.6             | 9.2             |
| $P_F$ (kW)   | 275             | –               |
| $P_{\text{ss}}$ (kW)                               | 100             | 100             |
| $P_{\text{out}}$ (MW)                              | 1               | 1               |
| Wall plug efficiency (%)                           | 17.4            | 10.4            |

accelerate the injected beam to 100 MeV. Neglecting wall losses and assuming a typical RF power conversion efficiency,  $\eta_{\text{rf}}$ , of 65%, 2.2 MW would be needed from the prime power source to accelerate the beam.

The electron injector will have an electron beam output of 4 MeV with a current of 500 mA produced from a dc photocathode gun. The low voltage power requirements for the electron gun to produce a 500 mA current is a fraction of a kilowatt, so essentially all of the power used goes into electron acceleration. A 500 kV potential ( $P_{\text{HVdc}} = 250$

kW) provides an initial electron acceleration. RT RF cavities and magnetic lens are used to bunch the beam at the expense of the acceleration gradient and inject them into the accelerator. In this example, 3 MeV (1.5 MW) must be added to the electron beam in this bunching process. Using the same model as for the RT accelerator cavity, approximately 150 kW ( $P_{\text{Linj}}$ ) is lost to the buncher cavity walls.

A brief summary of the power requirements for both the SRF and RT cases is presented in Table 1. A support systems power allocation,  $P_{\text{ss}}$ , of only 100 kW is made. This value is highly application specific.

### Acknowledgements

The authors would like to thank G. Neil of the Continuous Electron Beam Accelerator Facility for his efforts in assisting this project, the Naval Postgraduate School and Stanford University (N00014-91-C-0170).

### References

- [1] The Laser Processing Consortium, Continuous Electron Beam Accelerator Facility, May 1994.
- [2] C. Rode et al., Continuous Electron Beam Accelerator Facility, Newport News, VA.
- [3] H. Padamsee et al., Annu. Rev. Nucl. Part. Sci. 43 (1993) 635.
- [4] J. Kirchgessner et al., Laboratory of Nuclear Studies, Cornell University, Ithaca, NY.
- [5] J. Watson, Los Alamos National Laboratory, 6 Dec. 82.
- [6] G. Neil, private communication.



ELSEVIER

## Operator supports for the JAERI FEL

M. Sugimoto<sup>\*</sup>, R. Nagai, R. Kato, M. Sawamura, M. Takao, N. Kikuzawa, M. Ohkubo,  
E.J. Minehara

*Free Electron Laser Laboratory, Japan Atomic Energy Research Institute (JAERI), Tokai, Ibaraki, 319-11, Japan*

### 1. Introduction

We have developed a superconducting linac to study the quasi-CW oscillation of a FEL in the far infrared region [1]. The control system has the capability of helping operators to acquire knowledge about the properties of the equipment and the integrated system [2]. Such experiences are important for true-CW operation to obtain a stable and high power radiation source in the future. Sections 2 and 3 describe the outline of the control system and contents of the operator supports, respectively.

### 2. Control system

The characteristics of the control system are as follows. (1) It consists of DOS machines operated under Microsoft Windows. (2) We use a proprietary protocol for a local area network of such PCs. (3) An abstraction of the real hardware simplifies the maintenance and modification of the control software. (4) The devices are controlled by CAMAC systems connected to each PC. (5) All PC nodes run the same control software and a configuration file defines the actual hardware specific to each node. The commands are checked by the configuration data and delivered to the appropriate node through the network. (6) The software consists of three layers: the drivers, the libraries, and the applications. The application programs consist of operator console panels using the Windows graphical user interface. (7) The operator supports can help with routine operation and in understanding present performance of the FEL.

### 3. Operator supports

The objective of the operations of the facility is to collect the results of the control and monitored data and

use these to determine a method appropriate to get the optimal conditions for laser oscillation. This is a knowledge management problem which can be dealt with using knowledge-based applications. First, we must gather the facts of the system. For this purpose, a dynamic data logging system has been developed. Second, the collected data must be categorized as 1) shallow knowledge such as symptoms vs. defects pairs in the diagnostic system, or 2) deep knowledge based on the physical models and the simulation methods. The shallow expertise is smarter and faster than deep expertise when the rules are known well. However, our objective is to discover such rules from operating experience. So, at the primary stage, we must choose simulation models which can be improved after analyzing the gathered data. We must choose a simple model to simulate the current status of beam handling [3] and the properties laser oscillation to save processing time, since this analysis step is an on-line process.

*Dynamic data logger.* To analyze the current state it is necessary to know the past state. Drop down strip charts are attached to major items and show short term trends. Three forms of data logging are available: (1) trend log data equivalent to the chart recorder, (2) log sheet which is a snap shot of the current status, and (3) log note which briefly describes the operating condition.

*Interpretation of the beam status.* Good indicators are desirable to confirm the level of achievement during the beam study. Usually, these are provided by the beam diagnostic elements. Sometimes, we need to characterize the beam when no diagnostics are present. A beam dynamics code is helpful to obtain such information and so a beam matrix code developed before [3] has been updated for Windows. It can acquire the current parameters of the beam line elements and display beam in the requested section of the beam line.

*Prediction of laser oscillation property.* The study of the FEL oscillation will be completed by observing the generated light, which gives the most important information about the beam in the resonator. For this purpose, we have developed a simulation code for laser oscillation [4]. These results and a more simple calculation method based on analytical formulae can be employed as the primary

<sup>\*</sup> Corresponding author. Tel. +81 292 82 5455, +81 292 82 5462, fax +81 292 82 5939.

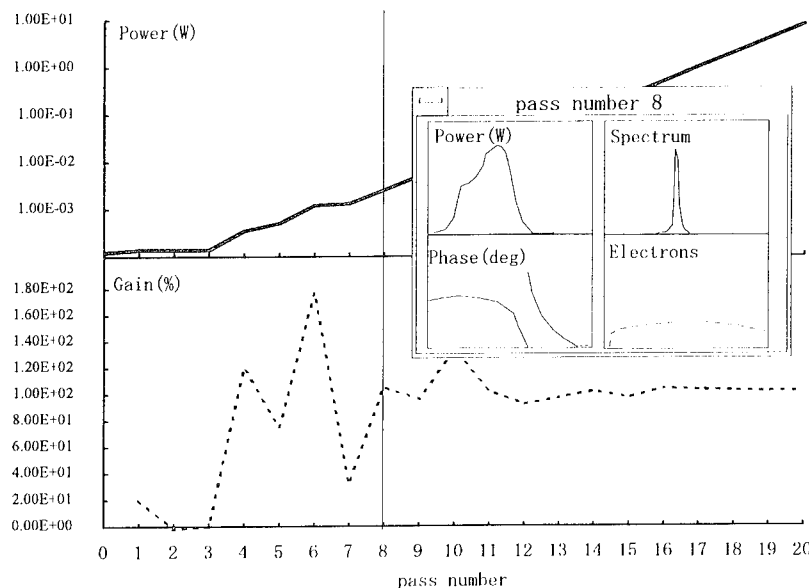


Fig. 1. A schematic output of the evaluation of the laser performance for the current beam status. The database for the estimation are prepared externally by using other simulation codes, and a reasonable result is retrieved from them.

sources of this knowledge. The characteristics of the generated light are displayed by selecting a menu item in the beam simulation code described above. Fig. 1 shows the schematic output for the typical beam condition: energy of 12.5 MeV with 1% resolution, 1 A peak current, 20 ps bunch and a 67.6  $\mu\text{m}$  wavelength. In the next step, the input parameters necessary for the evaluation are automatically estimated from the beam dynamics simulation results.

**Diagnostics of the malfunctions.** Some complex components have behaviors which are difficult to understand immediately. Our refrigerator system consists of several He compressors, He gas transfer lines, 4K- and shield-refrigerators, and cryostats. It is also closely coupled with the vacuum system. When malfunctions occur, the symptoms may not appear directly so operators need assistance with understanding and predicting unwanted failures. The control system monitors the pressures for each cryostat periodically. These are kept to be 0 using the heater system. If an abnormal trend is found in the logged data, the control system asks the operators about the facts (symptoms) and deduces the present status of the refrigerator systems.

#### 4. Conclusion

The control system for JAERI FEL employs the PCs and the network with a simplified protocol. The software is built under a windowing system with a graphical user

interface. It also provides operator support capabilities such as: automatic logging, on-line beam simulation, evaluation of laser properties, and assistance with the diagnostics. These are helpful to accumulate experience about beam operation and measurements for future steps.

#### Acknowledgements

The authors would like to thank to Dr. N. Shikazono, Dr. Y. Kawarasaki, and Dr. Y. Suzuki for their continuous encouragement and strong interests on the project.

#### References

- [1] M. Sawamura et al., Proc. 13th Int. Free Electron Laser Conf. Santa Fe 1991, Nucl. Instr. and Meth. A 318 (1992) 127; E. Minchura et al., Proc. 14th Int. Free Electron Laser Conf., Kobe, 1992, Nucl. Instr. and Meth. A 331 (1993) 182; M. Sugimoto et al., Proc. 15th Int. Free Electron Laser Conf., The Hague, 1993, Nucl. Instr. and Meth. A 341 (1994) ABS 41.
- [2] M. Sugimoto, Proc. 14 Int. Free Electron Laser Conf., Kobe, 1992, Nucl. Instr. and Meth. A 331 (1993) 340.
- [3] M. Sugimoto and M. Takao, Proc. 13th Int. Free Electron Laser Conf., Sante Fe, 1991, Nucl. Instr. and Meth. A 318 (1992) 335.
- [4] K. Sasaki et al., Proc. 14th Int. Free Electron Laser Conf., Kobe, 1992, Nucl. Instr. and Meth. A 331 (1993) 450.



## The “TEUFEL” undulator

J.W.J. Verschuur<sup>\*</sup>, G.J. Ernst, W.J. Witteman

*University of Twente, P.O. Box 217, 7500 AE Enschede, The Netherlands*

The construction of the undulator for the TEUFEL-project is almost completed [1]. This is a hybrid (permanent magnets with poles) undulator with a wavelength of 25 mm and 50 periods [2]. The peak magnetic field is 0.69 T. In short the construction is done in the following way: the  $\text{Sm}_2\text{CO}_5$  permanent magnets were measured in a

Helmholtz coil pair. The magnets are sorted in such a way that the magnetization spread in a “sixblock” is minimized. A sixblock and a pole are glued in a holder. This is done in a way as reproducible as possible in a special holder. This holder contains spacers like those used in the undulator and a piece with the shape of the gap. The holders with the magnets can be clamped to a beam to form the top (or bottom) part of the undulator. After assembling the two halves are put together.

The assembling of the holders on the backing beam is

<sup>\*</sup> Corresponding author. Fax +31 53 338 065.

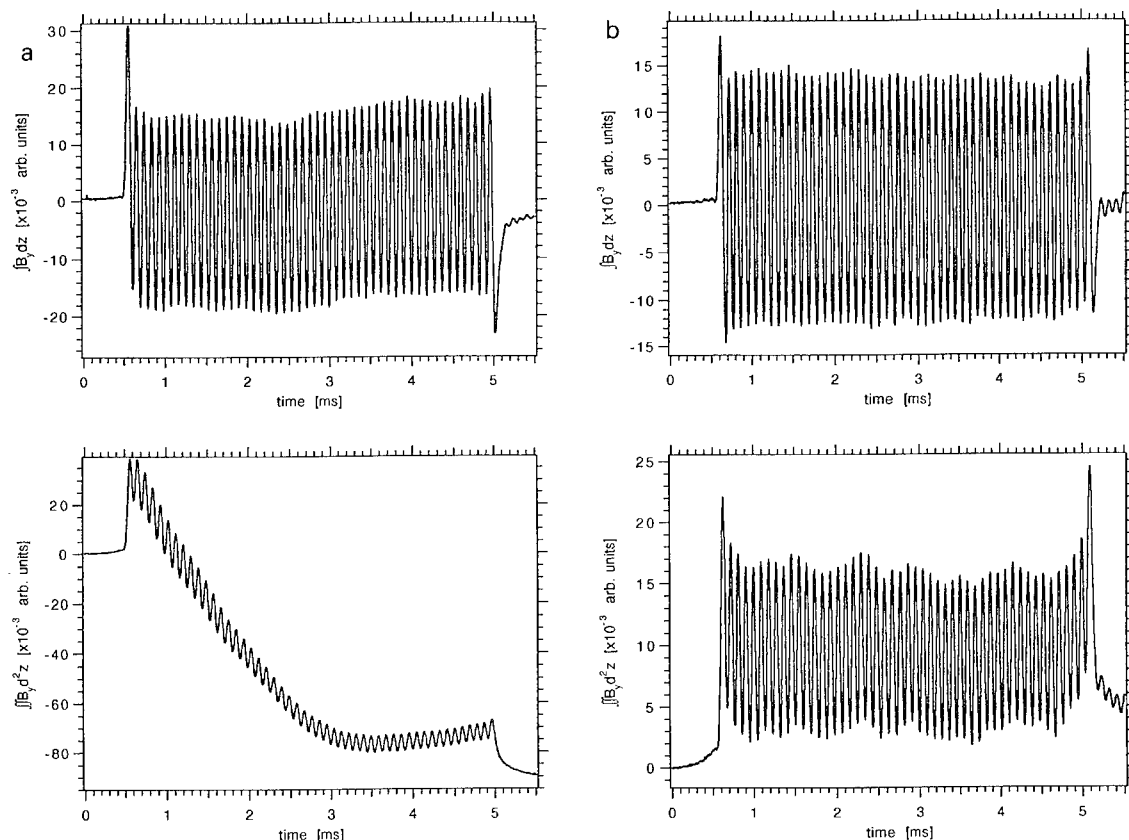


Fig. 1. (a) Top trace: first integral of the magnetic field of the complete undulator before shimming. Bottom trace: second integral of the magnetic field of the complete undulator before shimming. (b) Top trace: first integral of the magnetic field of the complete undulator after shimming. Bottom trace: second integral of the magnetic field of the complete undulator after shimming.

done while continuously measuring the second integral of the magnetic field to have full control over the assembly. This is done with the pulsed wire method [3]. Above the beam, approximately at the place the electron beam will be, a tungsten wire is positioned. This wire has a diameter of 50  $\mu\text{m}$  and the weight on the wire is between 250 and 350 g. Since the magnetic field in the center of the undulator is dominated by nearby poles, this method can be used during assembly of the undulator. At the entrance and exit of the undulator the method is less accurate due to flux leakage. However the entrance and exit are tuned separately when the two halves are put together. Although the difference in strength of the individual holders can in principle be measured we used a trial and error method for the assembly. Part of the bottom part was built and measured. Except for the temporary edge holders a good impression of the relative fields could be obtained. By changing holders even steering errors could be minimized. It is obvious that no absolute value for the field can be obtained, since the configuration of the field is different from the complete undulator. Due to the clamped construction of the undulator it is quite easy to interchange holders. A measurement of the first integral of the magnetic field gives already a quite reasonable result for both parts. The measurement of the second integral showed two major steering errors in the top part, whereas the bottom part already looked reasonable and has only some minor displacement errors.

After finishing the two halves of the undulator they were put together. The two halves are kept apart with 12 spacers that stand on the holders. In this way the tolerances on the gap could be kept as tight as possible. The magnetic field of the complete undulator was quite reasonable (see Fig. 1a). As expected, the error in the top part is most clearly present in the completed undulator. However the effect is smeared out a bit. These steering errors had to be corrected. The correction was performed with shims while again continuously monitoring the progress with the pulsed wire measurements. This method has proved to be successful as demonstrated by Warren et al. [4] in the construction and correction of a pure permanent magnet undulator. In this way dipole (steering) and quadrupole (displacement) errors were minimized. The shims used are small metal plates of a few tenths of a millimeter thickness and a few millimeters square. These shims were placed at the pole face at the edge of the pole. In this way they short circuit part of the field at the outer side of the undulator without affecting the shape of the field in the electron beam region. The fine-shimming was done with the vacuum tube in position in order to correct for possible effects of the tube too (although not expected). The result after an almost complete shimming is presented in Fig. 1b. Only the end part of the undulator is not completely shimmed in this figure. The shimming resulted in a maximum displacement of the electron beam of about 30% of the wiggle amplitude, and a negligible steering.

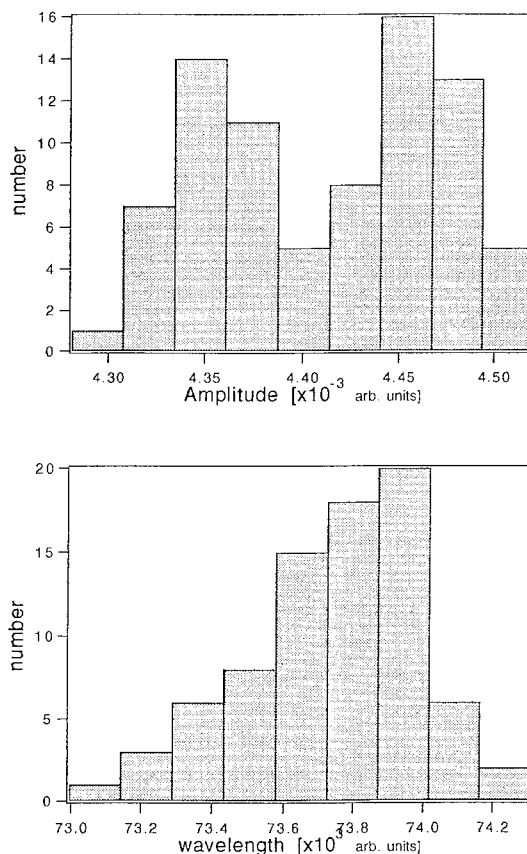


Fig. 2. Amplitude variation (top) and wavelength variation (bottom) of the complete shimmed undulator.

Finally the whole undulator is measured accurately to check the amplitude and wavelength variation over the whole undulator. The amplitude variation is found to be  $\delta A/A = 2.8\%$ ; the wavelength stability is found to be  $\delta \lambda/\lambda = 0.72\%$ . The amplitude and wavelength stability is determined from the first integral of the field. Sections of the measured signal with a length of one wavelength were fitted to a sine function. See Figs. 2a and 2b for the statistics on the amplitude and wavelength respectively.

The focusing properties of the undulator could also be measured with the pulsed wire technique. At the moment measurements are being made and further improvements are being achieved on the focusing properties of the undulator.

## References

- [1] G.J. Ernst et al., Nucl. Instr. and Meth A 318 (1992) 173.
- [2] J.W.J. Verschuur et al., Nucl. Instr. and Meth A 318 (1992) 847.
- [3] R.W. Warren, Nucl. Instr. and Meth A 272 (1988) 257.
- [4] R.W. Warren et al., Nucl. Instr. and Meth A 341 (1994) 444.



ELSEVIER

## Low-level RF control for the AFEL <sup>☆</sup>

C.D. Ziomek <sup>\*</sup>, J.M. Kinross-Wright, J.G. Plato

*Los Alamos National Laboratory, Los Alamos, NM 87545, USA*

### 1. Low-level RF system description

The stability of the RF field in the electron accelerator is a dominant factor affecting the performance of the advanced free electron laser (AFEL). The RF field must be maintained at precise amplitude and phase levels in order for the FEL to lase reliably, throughout the entire RF pulse, during every RF pulse, and with a constant light output level. Any phase or amplitude fluctuations in the RF accelerating field will affect the electron beam and degrade the FEL performance. A low-level RF control system performs the amplitude and phase regulation through electronic signal processing.

Fig. 1 shows a block diagram of the RF system, detailing the low-level RF components. This low-level RF system controls the amplitude and phase of the RF accelerating field by processing the RF signals in their Cartesian coordinates: in-phase and quadrature ( $I/Q$ ). The detected  $I/Q$  components of the RF accelerating field are compared to desired setpoints, and any deviations are processed in a feedback/feedforward compensator. The feedback loop is based upon a proportional, integral, derivative (PID) controller and provides the regulation and noise rejection for low-frequency disturbances (DC to 100 kHz). The adaptive feedforward provides the high-frequency disturbance-rejection (100 kHz to 2 MHz) for repetitive errors using digital signal processing techniques. The resulting compensated signal is used to derive a low-level RF output signal that drives the high power klystron amplifier. The klystron amplifies the low-level RF signal to the approximately 12 MW level needed for electron acceleration. Automation has been designed into the low-level RF system to allow optimization through computer algorithms. This allows advanced control techniques to be accomplished in a hands-off manner. Also, significant diagnostic capabilities

are incorporated into the system to allow remote diagnosis and archival of the accelerator performance.

### 2. Results, modeling, and analysis

Over many months of FEL operation, the low-level RF control system has achieved long-term amplitude and phase stabilities of  $\pm 0.25\%$  and  $\pm 0.33^\circ$  respectively. The field is maintained at this level of stability for 15  $\mu$ s during an RF pulse. The error levels indicate noise reduction factors of more than 20 over the entire frequency range of interest. The noise sources include PFN ripple, beam noise, cathode voltage fluctuations, and resonance shifts in the RF accelerating cavity.

In order to improve the RF field stability further, detailed system analysis and modeling were used. Physical measurements were performed on all subsystems, including the low-level RF control electronics, the two RF driver amplifiers, the klystron amplifier, the waveguide isolator, the RF accelerating cavity, and the interconnecting transmission lines. Time-domain reflectometer measurements were performed upon all cabling to determine their lengths and match properties. A pulsed s-parameter test set was used to measure the gain, bandwidth, and phase characteristics of each component in the system. The measured quantities were used to model the system, predict the performance-limiting components, and determine possible improvements.

Time-domain modeling of the RF system was accomplished using the Matrix<sub>x</sub> multivariable simulation software. The dynamic properties, including non-linearities, of the entire accelerator RF system were entered into the model. A baseline performance with the nominal operating conditions was determined. This baseline performance provided a best-case response by excluding known noisy or time-varying effects. Each suspect error source was added individually to determine its adverse effects upon the system. The suspect error sources include an off-resonance accelerator cavity, beam current fluctuations, klystron cathode voltage fluctuations, klystron saturation, low-level RF noise, and a limited low-level RF bandwidth. Of these possibilities, the dominant performance-limiting factor was

<sup>☆</sup> Work performed under the auspices of the United States Department of Energy and supported by Los Alamos National Laboratory Institutional Supporting Research funds.

<sup>\*</sup> Corresponding author. Tel. +1 505 667 1200, fax +1 505 665 2818, e-mail cziomek@lanl.gov.

determined to be beam current fluctuations. A secondary factor was the limited low-level RF bandwidth.

### 3. Upgrades

Fluctuations in beam current is the dominant factor limiting the performance of the RF field control system. The photo-cathode system that produces the electron beam for the FEL has demonstrated around 10% fluctuations in the beam-current magnitude. Also, the non-linear properties of the photo-cathode system create an exponential shape to the beam current pulse. A feedback/feedforward system similar to the existing low-level RF control system could be applied to the laser-light source that drives the photo-cathode. This system, as depicted in Fig. 2, processes the detected light output in a feedback/feedforward loop that adjusts the drive to the Pockel's cell to shape the light pulse. Any deviations from the nominal square pulse

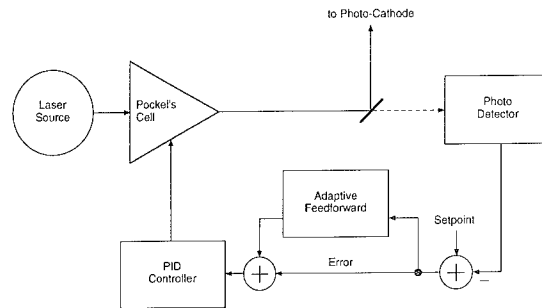


Fig. 2. Feedback/feedforward controller for photo-cathode pulse shaping.

at the desired level would be adjusted by the control system. The end result would be a more stable electron beam source and a more stable RF field.

The second performance-limiting factor for the RF field control system is the limited bandwidth of the low-level RF electronics. The inherent bandwidth of the low-level RF system must be much greater than the desired control bandwidth. The PID compensator, which was designed for a lower-bandwidth accelerator, needs to be adjusted for the AFEL application. Also, the main bandwidth-limiting component in the system, the upconverter, is being modified to provide broader bandwidth. This redesign is in progress and should provide noticeable improvement in the low-level RF control capability.

These two improvements to the low-level RF system will further expand the stability of the RF accelerating field which will improve the quality of the electron beam. The improved electron beam will enhance the overall performance of the AFEL by improving its reliability and reproducibility.

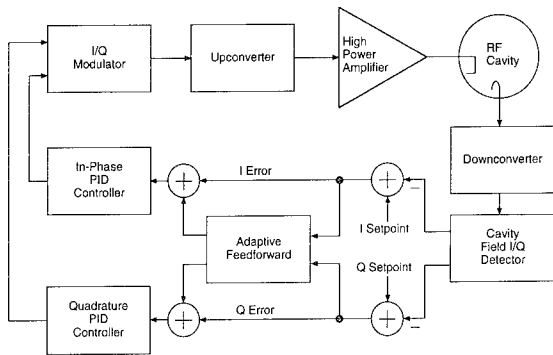


Fig. 1. Block diagram of RF system.

## Electron beam diagnostics for an FEL using optical transition radiation

E. Nishimura <sup>a,\*</sup>, K. Saeki <sup>a</sup>, T. Tomimasu <sup>a</sup>, T. Sakai <sup>b</sup>, S. Okuda <sup>b</sup>, J. Ohkuma <sup>b</sup>

<sup>a</sup> Free Electron Laser Research Institute, Inc., 44547-44 Tsuda, Hirakata, Osaka, 537-01, Japan

<sup>b</sup> Radiation Laboratory, The Institute of Scientific and Industrial Research, Osaka University, Osaka, Japan

Electron beam diagnostics for an FEL has been studied in detail [1]. It is very important to detect the direction of the electron beam near the entrance of the undulator because it determines the trajectory of the electron beam in the undulator such as “betatron oscillation”. In a beam line full of magnets, steering coils and so on, it is impractical to detect the direction of the electron beam by measuring positions of the electron beam at two points. So we need a new method which can measure the direction of the electron beam at a single point in the beam line. The use of

optical transition radiation (OTR), studied since Ginzburg predicted it theoretically [2], has been suggested for the beam diagnostics [3–5].

In this paper, we describe a new diagnostic method using OTR which can measure the position and the direction of the electron beam simultaneously, that is, the position in phase space (we call this method POPS) at a single point in a beam line.

Fig. 1 shows a schematic diagram of the diagnostic system. An aluminum (0.2  $\mu\text{m}$  thick) coated quartz (0.2 mm thick) plate was used as the OTR plate. The OTR plate was set at  $45^\circ$  to the fiducial line marked by an alignment laser. An SIT camera (Hamamatsu C2741-08)

\* Corresponding author.

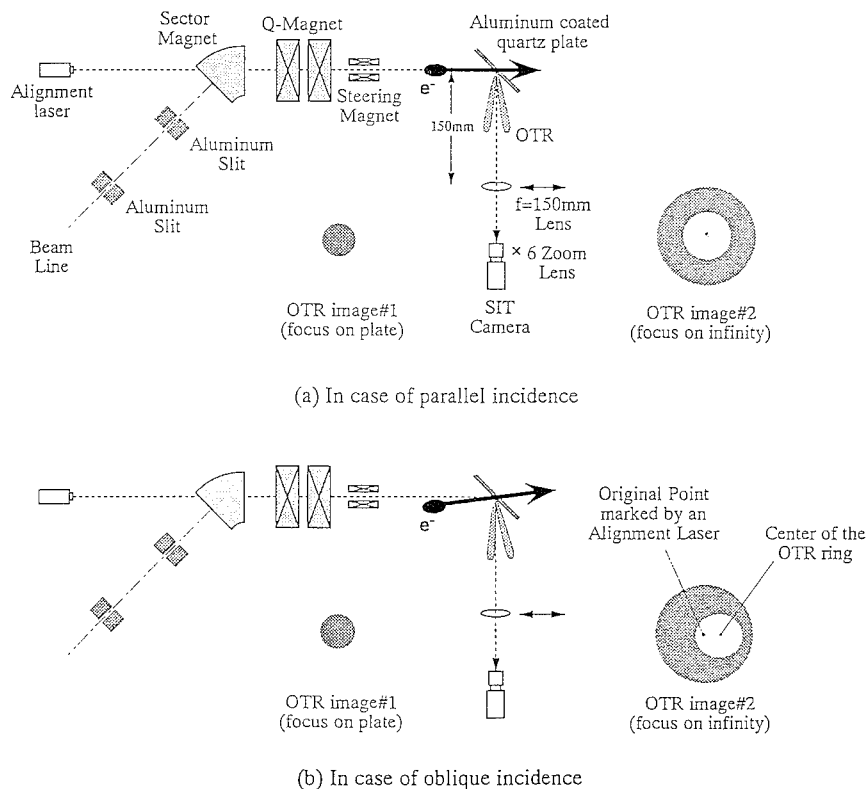
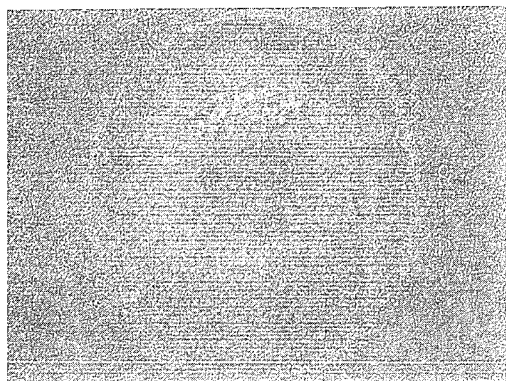
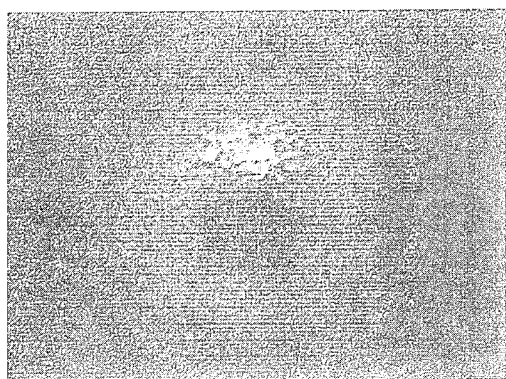


Fig. 1. Schematic diagram of the diagnostic system of the position of the electron beam in the phase space.

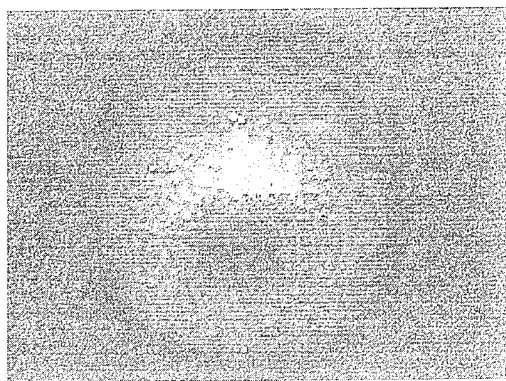
with a zoom lens (Canon j6x11R-II) was set below the OTR plate. The position and profile of the electron beam can be obtained with the SIT camera by focusing at the image plane. The OTR angular distribution (the OTR ring) can be also obtained by focusing at the focal plane.



(a) 0 mrad



(b) 8 mrad



(c) 16 mrad

Fig. 2. The dependence of the position of the center of the OTR ring on the incident angle of the electron beam.

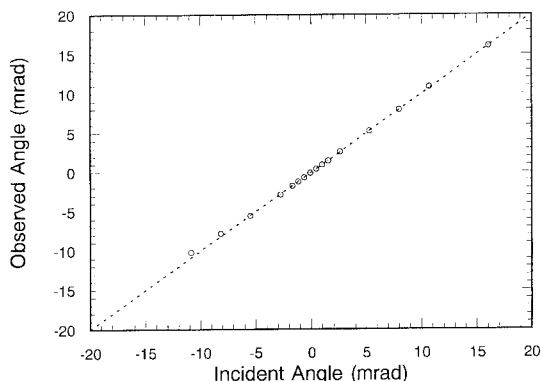


Fig. 3. Correlation of the observed angle to the incident angle of the electron beam.

When the electron beam direction is parallel to the fiducial line, the center of the OTR ring coincides with the alignment laser spot as shown in Fig. 1a.

In case of oblique incidence, as shown in Fig. 1b, the center line of the OTR lobe tilts by the same angle as the electron beam makes with the fiducial line. Thus the tilt angle of the electron beam (that is, the beam direction) can be determined by measuring the distance between the center of the OTR ring and the original point.

The experiments were performed using the L-band linac of the ISIR, Osaka University. The accelerator was operated at 20 MeV with 20 mA of average current in a 1.5  $\mu$ s long macropulse with 2 pps repetition. Fig. 2 shows the dependence of the position of the center of the OTR ring on the tilt angle, where tilt angles are 0, 8, and 16 mrad in Fig. 2(a), Fig. 2(b) and Fig. 2(c) respectively. Fig. 3 shows the correlation of the observed angle with the incident angle of the electron beam. There is a good linearity between them.

This method may enable feedback control of the beam optics in order to get an optimized beam at the entrance of the undulator for FEL oscillation experiments.

#### Acknowledgements

The authors would like to thank S. Suemine and T. Yamamoto for operating the accelerator and Dr. T. Yamamoto for his useful discussions.

#### References

- [1] R.W. Warren, SPIE Vol. 738, Free Electron Lasers (1987) p. 146.
- [2] V.L. Ginzburg and I.M. Frank, J. Phys. (Moscow) 9 (1945) 353.
- [3] A.H. Lumpkin et al., Nucl. Instr. and Meth. A 285 (1989) 343.
- [4] S.G. Iversen et al., Proc. 1987 IEEE Particle Accelerator Conf., Washington, DC, 1987 (1987) p. 573.
- [5] L. Wartski et al., J. Appl. Phys. 46 (1975) 3644.

## Development of the quasi non-destructive electron beam diagnostic method and the measurement of beam emittance

T. Sakai <sup>a,\*</sup>, T. Yamamoto <sup>a</sup>, S. Okuda <sup>a</sup>, J. Ohkuma <sup>a</sup>, E. Nishimura <sup>b</sup>, K. Saeki <sup>b</sup>,  
A. Kobayashi <sup>b</sup>, T. Tomimasu <sup>b</sup>

<sup>a</sup> The Institute of Scientific and Industrial Research, Osaka University, 8-1 Mihogaoka, Ibaraki, Osaka 567, Japan

<sup>b</sup> Free Electron Laser Research Institute, Inc. (FELI), 44547-44 Tsuda, Hirakata, Osaka 537-01, Japan

Diagnostic for the electron beam are necessary to get an optimized electron beam for FELs. Non-destructive methods are more favorable, since they do not disturb the actual operation of FEL systems. Optical Transition Radiation (OTR) is very useful for characterizing the electron beam, because it reflects the characteristics of the beam, such as direction, energy, divergence, current, and spatial distribution [1,2]. Since OTR is emitted from the interface between media, the OTR foil can be made very thin, which reduces the beam divergence caused by multiple scattering. This technique has the additional advantage, that the beam can be observed at different points and thus the beam emittance of a single pulse can be measured.

We adopted an aluminum coated thin Mylar film as the OTR emitter. The thickness of the Mylar foil was 1.5  $\mu\text{m}$  and the thickness of the aluminum was 0.2  $\mu\text{m}$ . The energy loss and beam divergence caused by multiple scattering in this Mylar foil were estimated [3,4]. The results showed that the energy loss was negligible and the beam divergence was small compared to the initial values at an electron beam energy of 20 MeV. Moreover, the emittance growth due to multiple scattering can be minimized by setting the foil at the optimized position.

In the experiments, we have measured the electron beam divergence caused by multiple scattering in this foil and the beam emittance. The experiments were performed with the ISIR L-band electron linac of Osaka University. The experimental set up is shown in Fig. 1. The electron beam was collimated by two pairs of aluminum slits and its emittance was ascertained by the quadrupole magnet scan method [5]. The amplitude of multiple scattering in this foil was measured by comparing the radii of the beam before and after penetrating the film. We used a well-col-

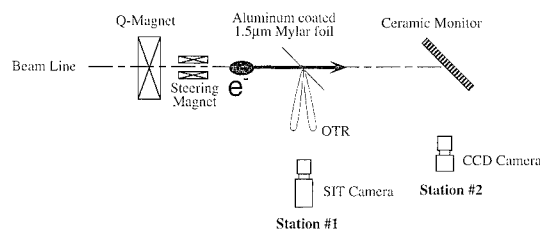


Fig. 1. Schematic of the experimental set-up.

limated electron beam ( $0.04 \pi \text{ mm mrad}$ , rms) for this measurement. The measured divergence for this film was 1.5 mrad (rms).

The emittance growth was determined by measuring two beam profiles. We set the slit acceptance to  $2.5 \pi \text{ mm mrad}$  to measure the beam emittance growth. The results are presented in Fig. 2. The measured emittances were 2.3 to  $2.6 \pi \text{ mm mrad}$  with no foil, and  $2.7 \pi \text{ mm mrad}$  with the Mylar film under the condition that the beam had its

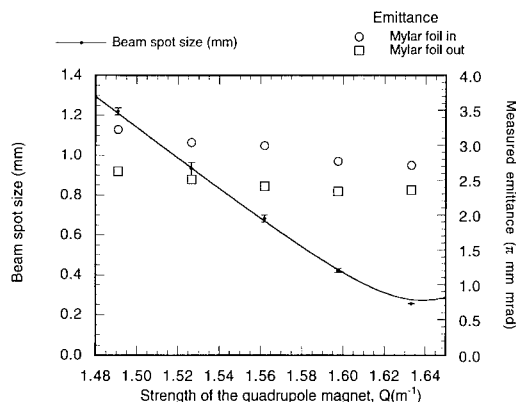


Fig. 2. The relation of obtained emittance and the quadrupole strength measured by two-profiles method.

\* Corresponding author. Tel. +81 6 879 8486, fax +81 6 879 8489.

waist at the foil. This condition was achieved for a quadrupole magnet strength of  $Q = 1.63 \text{ m}^{-1}$ . To our knowledge, this is the first measurement of the beam emittance of a single electron pulse. The emittance growth was 9% of the original one. This result shows that the thin foil method does not affect the beam emittance too much. We have also investigated the change in reflectivity of this thin Mylar foil as a result of irradiation by the electron beam. The experimental results show that this foil has the sufficient durability.

In conclusion, the present results have shown the effec-

tiveness of this method as a quasi non-destructive technique for diagnosing the electron beams used for FELs.

### References

- [1] L. Wartski et al., J. Appl. Phys. 46 (1975) 3644.
- [2] A.H. Lumpkin et al., Nucl. Instr. and Meth. A 285 (1989) 343.
- [3] H.A. Bethe, Handbuch der Phys., vol. 24 (1933).
- [4] H.A. Bethe and W. Heitler, Proc. Roy. Soc. A 146 (1934) 83.
- [5] J.E. Clendenin et al., IEEE Trans. Nucl. Sci. NS-28 (3) (1983) 2452.





ELSEVIER

## A flexible far-infrared FEL user facility ☆

K.W. Berryman<sup>\*</sup>, T.I. Smith

*Stanford Picosecond FEL Center, W.W. Hansen Experimental Physics Laboratory, Stanford University, Stanford, CA 94305-4085, USA*

### 1. Introduction

The Stanford Picosecond FEL Center is dedicated to performing experiments with FELs. As a User Center, we must place an emphasis on flexibility and range of operation, in order to accommodate as many experiments as possible [1,2]. FIREFLY was conceived in order to extend the available wavelength range at the Center into the far infrared, complementing our existing mid-infrared FEL systems. FIREFLY uses the existing Stanford Superconducting Accelerator (SCA) and an electromagnetic undulator to allow operation between 20 and 100  $\mu\text{m}$ , with picosecond optical pulses and pulse energies on the order of a microjoule.

FIREFLY had its first scheduled operation during the June/July 1994 experimental run at the Stanford FEL Center. The electron optics and undulator were evaluated, as was the optical resonator. Length enhancement of spontaneous radiation was observed, although lasing was not achieved. Nonetheless, we have confidence that FIREFLY will begin operation during our next experimental run, and will be providing high quality beam for experiments in the far infrared in the near future.

### 2. FIREFLY design

All FELs require an energetic electron beam as a source of power. For FIREFLY, the SCA serves this purpose. It provides micropulses of about a ps duration which repeat at 12 MHz within a macropulse of a few ms duration. The micropulse peak current is on the order of a few amperes, while the macropulse repeats at 10 Hz for a total duty factor of a few percent. The available energy for FIREFLY can be tuned between 10 and 30 MeV. Furthermore, the FIREFLY system resides between two of the SCA accelerating sections, which allows energy variations

to be controlled separately from the existing mid-infrared FEL. Thus, the FIREFLY wavelength and the mid-infrared FEL wavelength can be adjusted independently in real time.

After the electron beam, all FELs must have an undulator. For FIREFLY this is an electromagnetic device consisting of twenty-five 6-cm periods. The undulator, built by GMW enterprises, consists of two 1.5-m long steel pieces milled into square poles, with an appropriate support structure to provide a uniform 2-cm gap. Fifty coils wired in series produce a field of 0.28 T when excited at 280 A. This field corresponds to an rms undulator parameter ( $K$ ) of 1.

An electromagnetic undulator provides flexibility in both field strength and shape. Changing the field strength allows for rapid tuning of wavelength. Field shaping can be accomplished with multiple power supplies, by adjusting the pole excitation to match a desired sinusoid. Operation with arbitrarily long undulator period can be achieved in this manner. Even with only a single power supply, the undulator can be converted into an optical klystron simply by reversing a small number of the coils. With our system, changing from klystron to undulator can be accomplished in less than an hour. The measured magnetic field in the

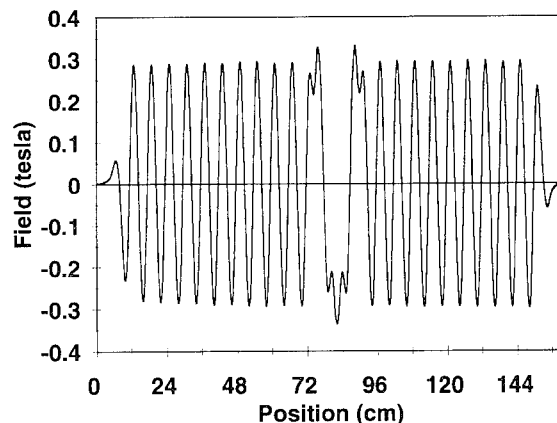


Fig. 1. The magnetic field in the undulator when operated in optical klystron configuration. The field was measured with a conventional gaussmeter and Hall probe.

<sup>\*</sup> Work supported in part by the Office of Naval Research, Contract #N00014-91-C-0170.

<sup>\*</sup> Corresponding author. Tel +1 415 723 9556, fax +1 415 725 8311, e-mail: berryman@leland.stanford.edu.

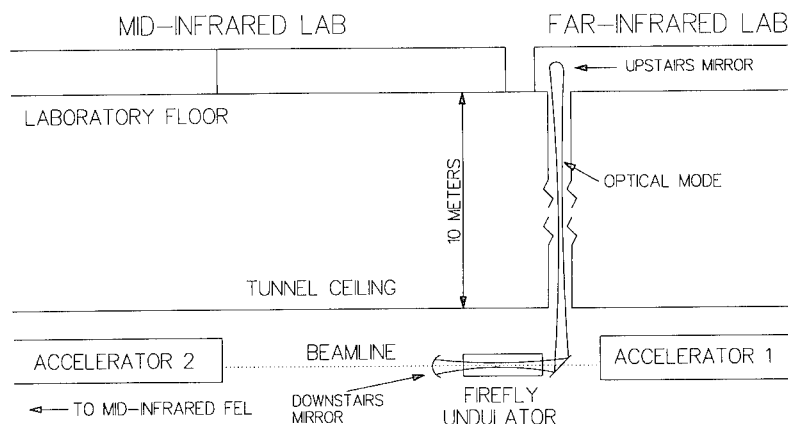


Fig. 2. A schematic layout of the FIREFLY system and the existing mid-infrared FEL at the Stanford Picosecond FEL Center.

klystron configuration is presented in Fig. 1. The observed electron beam trajectory was quite good; the total beam deflection between the undulator on and off states was less than 1 mm at the exit of the undulator.

In addition to an electron beam and an undulator, with most FELs an optical resonator is necessary to allow the optical field to grow to saturation after many passes. Since our FELs have a typical single pass gain of only a few percent, many hundreds of round trips are necessary before saturation is achieved. The length of the optical resonator is set by the repetition rate of the linac – in our case, this requires a 12.7-m resonator. For FIREFLY, the limitations of existing space and a desire to increase flexibility led us to adopt a folded resonator. This layout is pictured in Fig. 2. The cavity has three mirrors; two curved mirrors and a flat fold mirror.

For any FEL to be of actual use, some method of outcoupling power must be used. With FIREFLY we have the option of either hole or pickoff outcoupling. The upstairs mirror has a small centered hole which passes a small fraction, less than 1%, of the optical power. There is also a mirror which may be inserted a variable distance into the optical mode, to provide continuously variable outcoupling. When this mirror is placed at the center of the optical mode, it will outcouple approximately 10% of the total power.

### 3. First operation

FIREFLY was first operated during the Stanford Center's June/July experimental run. During this run the electron transport through the undulator was evaluated, and preliminary attempts to lase were made. Experiments were conducted with both the klystron and undulator configurations. The spontaneous radiation was monitored with a helium cooled Ga:Ge detector, while a 0.34-m monochromator was used to measure spontaneous spectra.

Electron beam transport through the chicane and undulator was achieved immediately. A spontaneous radiation signal was also acquired quickly. The spontaneous radiation was seen to be partially coherent, as length enhancement occurred at many cavity lengths, in increments of one-half the optical wavelength. Large length enhancements, over thirty times the quiescent signal, were observed. The optical cavity ringdown was also measured, indicating losses of approximately 3%, for a cavity  $Q$  of 30.

### 4. Conclusion

FIREFLY has been designed to be the workhorse for far-infrared studies at the Stanford FEL Center. It is hoped that simultaneous operation with the mid-infrared FEL at the Center will be possible, simply by inserting a shutter in the optical resonator which will prevent lasing in FIREFLY on alternate macropulses. In this way, multiple experiments can be supported simultaneously.

Several experiments have already been proposed for FIREFLY. Its wavelength range is ideal for studying vibrations in large molecules, the superconducting gap in high- $T_c$  materials, and transitions in quantum well structures, just to mention a few possibilities. Rapid tunability and high peak power in the far-infrared make these experiments possible. We therefore believe that FIREFLY will become an extremely valuable scientific tool.

### References

- [1] T.I. Smith, H.A. Schwettman, K.W. Berryman and R.L. Swent, SPIE 1854 (1993) 23.
- [2] H.A. Schwettman, T.I. Smith and R.L. Swent, Nucl. Instr. and Meth. A 341 (1994) ABS 19.

Part III  
Tables of operating and proposed FELs

## Long wavelength free electron lasers in 1994

H.P. Freund<sup>a,\*</sup>, V.L. Granatstein<sup>b</sup>

<sup>a</sup> Naval Research Laboratory, Washington, DC 20375, USA

<sup>b</sup> University of Maryland, College Park, MD 20742, USA

### Abstract

A short summary of the current status and most important future directions for long wavelength free-electron lasers is presented. For the purposes of the discussion, long wavelength refers to wavelengths longer than 0.5 mm. The distinction between long and short wavelengths is not entirely arbitrary since different physical processes may be important. For example, higher current beams are typically employed at long wavelengths and space-charge effects may be important. Indeed, the dominant interaction mechanism is often coherent Raman rather than coherent Compton scattering. In addition, dispersion due to the beam dielectric effects and finite transverse dimensions in the drift tubes and cavities are important effects at longer wavelengths. The ultimate goals of long wavelength FEL research are to achieve much higher average powers with good overall efficiency in a compact design, and the highest average power produced in an FEL to date (36 W) has been recorded in the Ku-band. At the present time, electrostatic accelerators and long pulse modulators appear to be the prime candidates for drivers for these systems; however, advances in induction linac technology which lead to higher repetition rates and improved beam quality could alter this conclusion.

Our purpose in this paper is to provide a summary of long wavelength ( $\geq 0.5$  mm) free-electron lasers (FELs) which are currently either in operation or under construction that can be used as a guide to the current state of this branch of the field. Note that a companion paper appears in this volume dealing with “short wavelength” FELs [1]. Our basic criterion for inclusion in the table is that the FEL must either be in operation or under construction. Projects which are still in the proposal stage, therefore, fall outside of the scope of this table and have been excluded. In compiling this list, we conducted a search which relies upon (1) contributions to general literature and the proceedings of the annual Free-Electron Laser Conferences, and (2) personal contacts. Personal contacts have proven to be an important source of information concerning FEL programs which are either in the early operational stages or still under construction and have not as yet been described in archival literature. As a consequence, the best reference for many of the entries to the table are personal communications. In addition, despite our best efforts to compile an exhaustive list, it is possible that several long

wavelength FELs have been inadvertently omitted. Our intention is for this compilation to become an annual process associated with the FEL Conference, and we hope that each group will keep us abreast of their experimental results and that any groups we might have missed will contact us with the relevant data on their experiments.

The distinction between long and short wavelength FELs is not entirely arbitrary since different physical processes may be important at longer wavelengths. For example, higher current beams are typically employed in this regime and space-charge effects are more important. In particular, the dominant interaction mechanism is often coherent Raman rather than coherent Compton scattering. In addition, while short wavelength FELs excite optical modes, dispersion due to the beam dielectric effects and finite transverse dimensions in the drift tubes and cavities are important effects at longer wavelengths.

At the present time, we have identified 28 long wavelength FEL experiments which are either in operation or under construction around the world. The table lists the most relevant parameters describing the experiments including: wavelength/frequency, peak power, pulse time, repetition rate, beam voltage and current, wiggler period and field strength, and the type of device and accelerator employed. We have chosen to denote the wiggler parameter by  $K$  ( $= 0.0934 B_w \lambda_w$ , where  $B_w$  is the wiggler amplitude in kG and  $\lambda_w$  is the wiggler period in cm); however,

\* Corresponding author. Tel. +1 703 734 5840, fax +1 703 821 1134, e-mail freund@mmacc.nrl.navy.mil. Permanent address: Science Applications International Corp., McLean, VA 22102, USA.

this parameter is often called  $a_w$  in the literature. Since it is impossible to give all the relevant information concerning each device in this format, some compromises have been made. For example, most of these FELs operate over a fairly broad spectral range, and the wavelength and frequency listed have been chosen to correspond to the

shortest accessible wavelength. We have also chosen to list the peak powers since the average powers can be obtained from the specified pulse times and repetition rates. The wiggler type shown refers to helical (H), planar (P), circular (C), and coaxial hybrid iron (CH) [2] wigglers. It is important to note that an axial guide field is often used in

Table 1

| FEL<br>[Ref.] | $\lambda$ (mm)/<br>$f$ (GHz) | $P_{\text{peak}}$<br>(MW) | $\tau_p$<br>( $\mu$ s) | $\nu_{\text{rep}}$<br>(Hz) | $V_b/I_b$<br>(MV/A) | $\lambda_w$ (cm)/<br>$K$ (type) | Type/<br>acc. |
|---------------|------------------------------|---------------------------|------------------------|----------------------------|---------------------|---------------------------------|---------------|
| TAU [11]      | 370/0.8                      | $10^{-5}$                 | 100                    | SS                         | 0.001/0.2           | 2/0.04 (P)                      | A/IC          |
| TAU [12]      | 76/4.9                       | UC                        | 10                     | 100                        | 0.07/1              | 4.4/0.12 (P)                    | SASE/ES       |
| UL [13]       | 35/8                         | $5 \times 10^{-10}$       | CW                     |                            | 0.055/0.001         | 1.9/0.05 (P)                    | A & O/M       |
| KEK [7]       | 32/9.4                       | 100                       | 0.015                  | 0.07                       | 1.5/450             | 16/1.5 (P)                      | A/IL          |
| ISAS [14]     | 26/12                        | 0.6                       | 0.4                    | SS                         | 0.44/150            | 3.25/0.27 (C)                   | O/PL          |
| NRL [10]      | 20/15                        | 4.2                       | 1                      | 6                          | 0.25/100            | 2.5/0.07 (H)                    | A/M           |
| MIT [15]      | 8/33                         | 60                        | 0.025                  | SS                         | 0.75/300            | 3.1/0.4 (H)                     | A/PL          |
| CESTA [16]    | 8/35                         | 50                        | 0.03                   | SS                         | 1.8/400             | 8/2.24 (H)                      | A/PL          |
| NRL [17]      | 8/35                         | UC                        | 1                      | 6                          | 150/10              | 0.75/0.2 (CH)                   | A/M           |
| UT [18]       | 8/35                         | 0.04                      | 100                    | SS                         | 0.5/200             | 3/0.53 (H)                      | SASE/PL       |
| IEE [19]      | 8/35                         | 140                       | 0.05                   |                            | 3.4/800             | 11/3.5 (P)                      | A/IL          |
| JINR [20]     | 8/35                         | 4                         | 0.2                    | SS                         | 1.5/200             | 7.2/1.3 (H)                     | O/IL          |
| JINR [20]     | 8/35                         | 30                        | 0.2                    | SS                         | 1.5/200             | 7.2/1.3 (H)                     | A/IL          |
| SIOFM [21]    | 8/35                         | UC                        | 0.02                   | SS                         | 0.4/800             | 2.2/1 (H)                       | SASE/PL       |
| ISAS [14]     | 7/40                         | 1                         | 0.5                    | SS                         | 0.5/150             | 3.27/0.27 (C)                   | O/PL          |
| IAP [20]      | 6/47                         | 6                         | 0.02                   | SS                         | 0.5/100             | 2/0.2 (H)                       | O/PL          |
| ENEA [22]     | 2/150                        | 0.001                     | 4                      | 40                         | 2.3/0.27            | 2.5/1.42 (P)                    | O/MI          |
| JAERI [23]    | 5/60                         | UC                        | 0.12                   | 1                          | 1/1000              | 4.5/0.76 (P)                    | O/IL          |
| IAP/INP [24]  | 4/70                         | 1500                      | 2                      | SS                         | 1/15000             | 4/0.3 (H)                       | O/PL          |
| INP [20]      | 4/70                         | 30                        | 2                      | SS                         | 1/1500              | 4/0.3 (H)                       | O/PL          |
| UM [25]       | 3.5/85                       | 0.2                       | 0.02                   | SS                         | 0.45/17             | 0.96/0.36 (P)                   | PL/A          |
| NSWC/MRC [26] | 3/95                         | 10                        | 0.25                   | SS                         | 2.5/100             | 10/1.9 (H)                      | O/PL          |
| DLR [27]      | 3/100                        | 1–2                       | 0.1                    | SS                         | 0.5/150             | 2/0.19 (H)                      | SASE/PL       |
| KAERI [28]    | 3/100                        | UC                        | CW                     |                            | 0.43/2              | 3.6/0.4 (H)                     | O/ES          |
| TAU/WI [29]   | 3/100                        | UC                        | 1000/CW                |                            | 2.5/1               | 4.4/1.8 (P)                     | O/ES          |
| CU [30]       | 2/150                        | 5                         | 0.15                   | SS                         | 0.8/150             | 1.85/0.25 (H)                   | A/PL          |
| FOM [9]       | 1/260                        | UC                        | $1 \times 10^{-5}$     | 1                          | 2/12                | 2/0.67 (P)                      | O/ES          |
| UCLA [31]     | 0.5/560                      | UC                        | $2 \times 10^{-6}$     |                            | 15/150              | 10/2.8 (P)                      | O/RFL         |

A – amplifier

C – circular

CESTA – Centre d'Etudes Scientifique e  
Techniques d'Aquitaine

CH – CHI wiggler

CU – Columbia University, USA

CW – continuous wave

DLR – German Aerospace Research  
Establishment

ES – electrostatic accelerator

H – helical wiggler

IAP – Institute of Applied Physics, Russia

INP – Institute of Nuclear Physics, Russia

IC – Ignition Coil

IEE – Institute of Electron Engineering, China

IL – Induction Linac

ISAS – Institute of Space and Astronautical  
Science, Japan

JAERI – Japan Atomic Energy Research Institute

JINR – Joint Institute for Nuclear Research, Russia

KAERI – Korean Atomic Energy Research Institute

KEK – National Laboratory for High Energy  
Physics, Japan

NRL – Naval Research Laboratory

NSWC – Naval Surface Weapons Center, USA

M – modulator

MI – microtron

MRC – Mission Research Corp.

O – oscillator

P – planar wiggler

PL – pulse line accelerator

RFL – radio frequency linac

SASE – self amplified spontaneous emission

SIOFM – Shanghai Institute of Optics and

Fine Mechanics

SS – single shot

TAU – Tel Aviv University

UC – under construction

UL – University of Liverpool, UK

UM – University of Maryland, USA

UT – University of Twente, The Netherlands

WI – Weizmann Institute, Israel

conjunction with helical wigglers in intense beam FELs, but that the brevity of this format did not permit inclusion of this information in the table.

As the table illustrates, long wavelength FELs employ many types of accelerator (modulators, pulse line accelerators, electrostatic accelerators, microtrons, induction and radio frequency accelerators, and even an automobile ignition coil). As a result, the group exhibits a wide variety of pulse formats and peak and average powers. However, the bulk of the experiments employ pulse line accelerators which operate in a single-shot (SS) mode with high peak powers. Historically, the pioneering work on long wavelength FELs was performed by R.M. Phillips [3] prior to 1964 using modulator technology developed in the microwave tube community (note that Phillips referred to his devices as ubitrons and that the term free-electron laser first came into usage in the early 1970s when it was coined by J.M.J. Madey). Long wavelength FEL research began again at various laboratories in the early 1970s with the intention of extending Phillips' work using intense relativistic electron beams. Much of this work was directed at exploring the basic physics of the Raman regime [4], and high average power was not an essential goal. As a result, single-shot pulse line accelerators are often used since they are capable of producing beams with energies of several MeV and currents of many kiloamperes.

In order to achieve the necessary beam quality from pulse line accelerators, careful design of the diode is essential. The fundamental diode design used in most of the pulse line accelerator-based FELs [5] employ a shaped cathode/anode which is immersed in a converging axial guide field. The anode is designed to "scrape" a large fraction of the beam so that only a central core with a low velocity spread is injected into the wiggler. Typically, the diodes are designed in these configurations to scrape off approximately 90% of the beam but, since pulse line accelerators often produce beam currents in the tens of kiloamperes, this still leaves an appreciable current. As a result, collective FELs built using pulse line accelerators have produced high peak powers, although they suffer from the disadvantages of a low wall-plug efficiency and a low average power.

The principal thrusts of current long wavelength FEL research include the achievements of high average powers, broad bandwidths, and compact systems. In this sense, pulse line accelerator FELs must be considered as proof-of-principle experiments, and the development of practical long wavelength FELs depends upon other accelerator technologies.

Induction linacs have the advantage over pulse line accelerators in that they can be repetitively pulsed. Hence, it is possible, at least in principle, to produce high average powers and high efficiencies. However, there are two practical difficulties with induction linacs for FEL applications. The first is that it is difficult to operate at high repetition rates. The ELF experiment [6] which produced a

peak power of approximately 1 GW at 35 GHz operated with a pulse time of 10–20 ns and a repetition rate of 0.5 Hz which represents an average power of only about 7 W. The second is emittance growth which often results in unacceptably high thermal spreads, and the necessity of beam scraping. For example, approximately 80% of the beam was scraped off in the ELF experiment. Thus, while the extraction efficiency was about 34% from the beam that passed through the wiggler, the overall efficiency (using the total beam power prior to scraping) was closer to 7%. In view of this, the recent results from the induction linac-based FEL at KEK [7] which produced a peak power of 100 MW using some beam scraping and ion channel guiding represents a possibly significant advance.

Other approaches which may hold more promise for achieving high average powers and efficiencies involve long pulse modulators and electrostatic accelerators. In the case of electrostatic accelerators, full CW operation is possible if nearly total beam recycling can be achieved. This has been accomplished at infrared wavelengths at the University of California at Santa Barbara [8]. However, the level of beam recovery which can be achieved decreases with increasing extraction efficiency from the FEL, and this may prove to be a limiting factor in the technology. A significant experiment using electrostatic accelerators is currently under construction at FOM in The Netherlands [9]. The ultimate goal of this experiment is to build a CW FEL designed to produce 1 MW at 260 GHz for the heating of plasmas in magnetic fusion reactors. Based upon a beam current of 12 A and a kinetic energy of 2 MeV, this yields an extraction efficiency of the order of 4%. However, the overall system efficiency can be much larger due to the beam recovery system. It will be interesting to see how effective beam recovery can be in a system with this level of extracted power.

One disadvantage associated with electrostatic accelerators is that they are low current devices which often implies low gains as well. For this reason, the FOM configuration is that of an oscillator. A related disadvantage arises since high output power requires high beam power; hence, a high power electrostatic accelerator-based FEL also requires high energies which implies a large physical size. This would be inconsistent with applications requiring compact devices.

For applications which require more compact devices, long pulse modulators may have advantages. A research program at the Naval Research Laboratory has been devoted to the development of this concept with goals of high average power. The present experiment [10] employs a 250 kV/100 A modulator with a pulse time of 1  $\mu$ s and a repetition rate of 6 Hz to produce approximately 4.2 MW in Ku-band. This represents an average power of about 36 W which is the highest average power produced in an FEL to date. The direction of this program is to achieve still higher powers at higher frequencies using lower voltage electron beams. To this end, a follow-on experiment is in

the design stages now which will employ some form of dispersion control (i.e., a rippled-wall waveguide) to permit lower voltage operation.

In summary, the highest average power produced in an FEL has now been recorded in a Ku-band FEL; however, the ultimate goals of long wavelength FEL research are to achieve much higher average powers with good overall efficiency. In addition, many applications require more compact designs than have yet been achieved. At the present time, electrostatic accelerators and long pulse modulators appear to be the prime candidates for drivers for these systems; however, advances in induction linac technology which lead to higher repetition rates and improved beam quality could change this conclusion.

## References

- [1] W.B. Colson, these Proceedings (16th Int. Free Electron Laser Conf., Stanford, CA, USA, 1994) Nucl. Instr. and Meth. A 358 (1995) 555.
- [2] R.H. Jackson, H.P. Freund, D.E. Pershing and J.M. Taccetti, Nucl. Instr. and Meth. A 341 (1994) 454.
- [3] R.M. Phillips, IRE Trans. Electron Devices ED-7 (1960) 231.
- [4] H.P. Freund and T.M. Antonsen, Jr., Principles of Free-electron Lasers (Chapman & Hall, London, 1992).
- [5] R.H. Jackson, S.H. Gold, R.K. Parker, H.P. Freund, P.C. Efthimion, V.L. Granatstein, M. Herndon, A.K. Kinkad, J.E. Kosakowski and T.J.T. Kwan, IEEE J. Quantum Electron. QE-19 (1983) 346.
- [6] T.J. Orzechowski, B.R. Anderson, J.C. Clark, W.M. Fawley, A.C. Paul, D. Prosnitz, E.T. Scharlemann, S.M. Yarema, D.B. Hopkins, A.M. Sessler and J.S. Wurtele, Phys. Rev. Lett. 57 (1986) 2172.
- [7] K. Takayama, J. Kishiro, K. Ebihara, T. Ozaki, S. Hiramatsu and H. Katoh, these Proceedings (16th Int. Free Electron Laser Conf. Stanford, CA, USA, 1994) Nucl. Instr. and Meth. A 358 (1995) 122.
- [8] G. Ramian, Nucl. Instr. and Meth. A 318 (1992) 225.
- [9] W.G. Urbanus, W.A. Bongers, G. van Dijk, C.A.J. van der Geer, J.P. van Ieperen, A. van der Linden, P. Manintveld, A.B. Stuk, A.V. Tulupov, A.G.A. Verhoeven and M.J. van der Wiel, these Proceedings (16th Int. Free Electron Laser Conf., Stanford, CA, USA, 1994) Nucl. Instr. and Meth. A 358 (1995) 155.
- [10] D.E. Pershing, R.D. Seeley, R.H. Jackson and H.P. Freund, *ibid.*, p. 104.
- [11] R. Drori, E. Jerby and A. Shahadi, *ibid.*, p. 151.
- [12] M. Cohen, A. Kugel, D. Chairman, M. Arbel, H. Kleinman, D. Ben-Haim, A. Eichenbaum, M. Drainin, Y. Pinhasi, Y. Yakover and A. Gover, *ibid.*, p. 82.
- [13] G. Dearden, E.G. Quirk, A.I. Al-Shamma'a, R.A. Stuart and J. Lucas, Nucl. Instr. and Meth. A 341 (1994) 80.
- [14] T. Mizuno, T. Ootuki and H. Saito, these Proceedings (16th Int. Free Electron Laser Conf., Stanford, CA, USA, 1994) Nucl. Instr. and Meth. A 358 (1995) 131.
- [15] M.E. Conde and G. Bekefi, Phys. Rev. Lett. 67 (1991) 3082.
- [16] J.L. Rullier, A. Devin, J. Gardelle, J. Labrousse and P. Le Taillandier, Phys. Rev. E, submitted for publication.
- [17] R.H. Jackson, J.M. Taccetti, M. Blank, H.P. Freund, D.E. Pershing and V.L. Granatstein, these Proceedings (16th Int. Free Electron Laser Conf., Stanford, CA, USA, 1994) Nucl. Instr. and Meth. A 358 (1995) 193.
- [18] P. Zambon, W.J. Witteman and P.J.M. van der Slot, these Proceedings (16th Int. Free Electron Laser Conf., Stanford, CA, USA, 1994) Nucl. Instr. and Meth. A 358 (1995) 126.
- [19] M. Fanbao, personal communication.
- [20] N.S. Ginzburg, personal communication.
- [21] M.C. Wang, J.B. Zhu, Z.J. Wang, J.K. Lee and T.H. Chung, these Proceedings (16th Int. Free Electron Laser Conf., Stanford, CA, USA, 1994) Nucl. Instr. and Meth. A 358 (1995) ABS 38.
- [22] F. Ciocci, R. Bartolini, A. Doria, G.P. Gallerano, E. Giovannale, M.F. Kimmitt, G. Messina and A. Renieri, Phys. Rev. Lett. 70 (1993) 928.
- [23] S. Kawasaki, H. Ishizuka, S. Musyoki, A. Watanabe and M. Shiho, these Proceedings (16th Int. Free Electron Laser Conf., Stanford, CA, USA, 1994) Nucl. Instr. and Meth. A 358 (1995) 114.
- [24] A.V. Arzhannikov, V.B. Bobylev, S.L. Sinitsky, A.V. Tarasov, N.S. Ginzburg and N.Yu. Peskov, *ibid.*, p. 112.
- [25] S. Cheng and W.W. Destler, *ibid.*, p. 200.
- [26] J. Pasour, personal communication.
- [27] G. Renz and G. Spindler, these Proceedings (16th Int. Free Electron Laser Conf., Stanford, CA, USA, 1994) Nucl. Instr. and Meth. A 358 (1995) ABS 13.
- [28] Lee Byung-Cheol, Kim Sun-Kook, Jeong Young-Ug, Cho Sung-Oh and Lee Jongmin, Experiments on millimeter-wave free electron laser, presented at this Conference (16th Free Electron Laser Conf., Stanford, CA, 1994).
- [29] A. Arensburg, M. Cohen, M. Draiznin, A. Goldring, A. Gover, Y. Pinhasi, S. Witman, I.M. Yakover, J. Sokolowski, B. Mandelbaum, A. Rosenberg, J. Shiloh, G. Hazak, L.A. Levin, O. Shahal, M. Shapira and V.L. Granatstein, these Proceedings (16th Free Electron Laser Conf., Stanford, CA, 1994) Nucl. Instr. and Meth. A 358 (1995) ABS 7.
- [30] L.-Y. Lin and T.C. Marshall, Phys. Rev. Lett. 70 (1993) 2403.
- [31] F. Hartemann, personal communication.



ELSEVIER

## Short wavelength free electron lasers in 1994

W.B. Colson

*Physics Department, Naval Postgraduate School, Monterey CA 93943, USA*

The following table lists the existing and proposed relativistic free electron lasers (FELs) in 1994. The top part of the table lists existing FELs. These are substantially complete experiments that may not be operating at the present time. The bottom part of the table lists proposed FELs. Each FEL, existing or proposed, is identified by a location, or institution, followed by the FEL's name in parentheses. There are 46 experiments listed from 7 countries representing all continents in the northern hemisphere and indicating the international character of this field.

The first column of the table lists the operating wavelength  $\lambda$ , or wavelength range, in micrometers ( $\mu\text{m}$ ). The large range of operating wavelengths, six orders of magnitude, indicates the flexible design characteristics of the FEL mechanism. The second column describes the electron pulse length divided by the speed of light  $c$ , and ranges from CW to short picosecond pulse time scales. The expected optical pulse length can be 5 to 10 times shorter or longer than the electron pulse depending the optical cavity  $Q$ , the FEL desynchronization, and the FEL gain. Most FEL oscillators produce an optical spectrum that is Fourier transform limited by the optical pulse length.

The electron beam energy  $E$  and peak current  $I$  provided by the accelerator are listed in the third and fourth columns in units of MeV and Amperes. The accelerator type is listed as the first entry in the last column with a code such as RF for the radio-frequency linac. While there are a variety of accelerators used, about 75% are RF and about 15% are electron storage rings. Storage rings tend to be used for the short wavelength applications, while the electrostatic accelerators provide longer wavelengths.

The next three columns list the number of undulator periods  $N$ , the undulator wavelength  $\lambda_0$  in centimeters, and the undulator parameter  $K = e\bar{B}\lambda_0/2\pi mc^2$  where  $e$  is the electron charge magnitude,  $\bar{B}$  is the rms undulator field strength, and  $m$  is the electron mass. For an FEL klystron undulator, there are multiple undulator sections as listed in the  $N$ -column. Note that the range of values for  $N$ ,  $\lambda_0$ , and  $K$  are much smaller than for the other parameters indicating that most undulators are similar. Only about 15% of the FELs use the klystron undulator, none use the

tapered undulator at present, and the rest use the conventional periodic undulator. The FEL resonance condition,

$$\lambda = \frac{\lambda_0(1 + K^2)}{2\gamma^2},$$

where  $\gamma$  is the relativistic Lorentz factor  $\gamma = E/mc^2$ , provides a relationship that can be used to derive  $K$  from  $\lambda$ ,  $E$ , and  $\lambda_0$ . The middle entry of the last column lists the FEL type: "O" for oscillator, "A" for amplifier, etc. Less than 10% of the FELs are amplifiers, while the rest are FEL oscillators. A reference describing the FEL is provided at the end of each line entry.

For the conventional undulator, the peak optical power can be estimated by the fraction of the electron beam peak power that spans the undulator spectral bandwidth,  $1/4N$ , or  $P \approx EI/4eN$ . For the FEL using a storage ring, the optical power causing saturation is substantially less than this estimate and depends on ring properties. For the high-gain FEL amplifier, the optical power at saturation can be substantially more. The average FEL power is determined by the duty cycle, or spacing between electron pulses, and is generally many orders of magnitude lower than the peak power.

In the FEL oscillator, the optical mode that best couples to the electron beam in an undulator of length  $L = N\lambda_0$  has Rayleigh length  $z_0 \approx L/\sqrt{12}$  and has a mode waist radius of  $w_0 \approx \sqrt{N}\gamma\lambda/\pi$ . The FEL optical mode typically has more than 90% of the power in the fundamental mode described by these parameters.

### Acknowledgements

The author is grateful for support of this work by the Naval Postgraduate School, Stanford University (N00014-91-C-0170), and SURF/CEBAF.



## Relativistic short wavelength free electron lasers (1994)

| FEL                  | $\lambda$<br>( $\mu\text{m}$ ) | $\sigma_z$       | $E$<br>(MeV) | $I$<br>(A) | $N$           | $\lambda_0$<br>(cm) | $K$  | Accelerator, type <sup>a</sup> [Ref.] |
|----------------------|--------------------------------|------------------|--------------|------------|---------------|---------------------|------|---------------------------------------|
| Existing FELs        |                                |                  |              |            |               |                     |      |                                       |
| UCSB (mm FEL)        | 340                            | 25 $\mu\text{s}$ | 6            | 2          | 42            | 7.1                 | 0.7  | EA, O [1]                             |
| Stanford (FIRFEL)    | 80–200                         | 15 ps            | 4            | 8          | 50            | 1                   | 0.7  | RF, O [39]                            |
| UCSB (FIR FEL)       | 60                             | 25 $\mu\text{s}$ | 6            | 2          | 150           | 2                   | 0.1  | EA, O [1]                             |
| Tokyo (UT-FEL)       | 43                             | 10 ps            | 13           | 20         | 40            | 4                   | 0.7  | RF, O [2]                             |
| Netherlands (FELIX)  | 40                             | 5 ps             | 25           | 50         | 38            | 6.5                 | 1.5  | RF, O [3]                             |
| Osaka (ISIR)         | 40                             | 30 ps            | 17           | 50         | 32            | 6                   | 1    | RF, O [24]                            |
| Bruyeres (ELSA)      | 20                             | 30 ps            | 18           | 100        | 30            | 3                   | 0.8  | RF, O [4]                             |
| Stanford (FIREFLY)   | 20–100                         | 2 ps             | 20           | 6          | 25            | 6                   | 1    | RF, O [29]                            |
| Frascati (LISA)      | 15                             | 7 ps             | 25           | 5          | 50            | 4.4                 | 1    | RF, O [5]                             |
| Grumman (CIRFEL)     | 14                             | 5 ps             | 14           | 150        | 73            | 1.4                 | 0.2  | RF, O [23]                            |
| Beijing (IHEP)       | 10                             | 4 ps             | 30           | 14         | 50            | 3                   | 1    | RF, O [6]                             |
| Orsay (CLIO)         | 8                              | 0.3 ps           | 50           | 80         | 48            | 4                   | 1    | RF, O [7]                             |
| LANL (AFEL)          | 4–6                            | 10 ps            | 15           | 200        | 24            | 1                   | 0.3  | RF, O [8]                             |
| Darmstadt (IR-FEL)   | 5                              | 2 ps             | 40           | 2.7        | 80            | 3.2                 | 1    | RF, O [9]                             |
| Stanford (SCAFEL)    | 3–10                           | 0.7 ps           | 37           | 10         | 72            | 3.1                 | 0.8  | RF, O [10]                            |
| Vanderbilt (FELI)    | 3                              | 1 ps             | 43           | 50         | 47            | 2.3                 | 1    | RF, O [11]                            |
| Duke (Mark III)      | 3                              | 3 ps             | 44           | 20         | 47            | 2.3                 | 1    | RF, O [12]                            |
| BNL (ATF)            | 0.5                            | 6 ps             | 50           | 100        | 70            | 0.88                | 0.4  | RF, O [36]                            |
| LANL (APEX)          | 0.37                           | 10 ps            | 46           | 140        | 73            | 1.4                 | 0.6  | RF, O [13]                            |
| Tsukuba (NIJI-IV)    | 0.35                           | 160 ps           | 300          | 5          | $2 \times 42$ | 7.2                 | 2    | SR, O [14]                            |
| Orsay (Super-ACO)    | 0.35                           | 250 ps           | 800          | 0.1        | $2 \times 10$ | 13                  | 4    | SR, O [15]                            |
| Okazaki (UVSOR)      | 0.3                            | 6 ps             | 500          | 5          | $2 \times 8$  | 11                  | 2    | SR, O [16]                            |
| BNL (ATF-UV)         | 0.25                           | 6 ps             | 70           | 100        | 70            | 0.88                | 0.4  | RF, O [36]                            |
| Novosibirsk (VEPP)   | 0.24                           | 35 ps            | 350          | 6          | $2 \times 33$ | 10                  | 1.6  | SR, O [17]                            |
| Proposed FELs        |                                |                  |              |            |               |                     |      |                                       |
| Florida (CREOL)      | 200–600                        | CW               | 1.7          | 0.2        | 185           | 0.8                 | 0.15 | EA, O [18]                            |
| Netherlands (TEUFEL) | 180                            | 20 ps            | 6            | 350        | 50            | 2.5                 | 1    | RF, O [38]                            |
| Rutgers (IRFEL)      | 140                            | 25 ps            | 38           | 1.4        | 50            | 20                  | 1    | MA, O [19]                            |
| Moscow (Lebedev)     | 100                            | 20 ps            | 30           | 0.25       | 35            | 3.2                 | 0.8  | MA, O [21]                            |
| Tokai (SCARLET)      | 40                             | 40 ps            | 15           | 10         | 62            | 3.3                 | 1    | RF, O [20]                            |
| LBL (IRFEL)          | 3–50                           | 30 ps            | 55           | 60         | 40            | 5                   | 1    | RF, O [22]                            |
| CEBAF (IRFEL)        | 2–24                           | 2 ps             | 50           | 100        | 25            | 6                   | 2    | RF, O [25]                            |
| Boeing (APLE)        | 10                             | 60 ps            | 17           | 140        | 100           | 2.4                 | 0.2  | RF, O [27]                            |
| Boeing (APLE)        | 10                             | 20 ps            | 34           | 450        | 257           | 3.9                 | 1.2  | RF, A [27]                            |
| Stanford (FEL)       | 10                             | 4 ps             | 24           | 25         | 52            | 2.6                 | 0.9  | RF, O [28]                            |
| Osaka (ILT)          | 10                             | 2 ps             | 9            | 100        | 30            | 0.66                | 0.3  | RF, O [20]                            |
| UCLA (IRFEL)         | 10                             | 2 ps             | 20           | 200        | 40            | 1.5                 | 1    | RF, A [35]                            |
| Novosibirsk (RTM)    | 7                              | 50 ps            | 51           | 100        | $4 \times 40$ | 9                   | 1    | RF, O [26]                            |
| BNL (HGHG)           | 3.4                            | 10 ps            | 30           | 110        | 83            | 1.8                 | 1.4  | RF, A [37]                            |
| CEBAF (UVFEL)        | 0.15–2                         | 0.4 ps           | 200          | 200        | 48            | 3                   | 1.5  | RF, O [31]                            |
| Osaka (FELI)         | 1                              | 2 ps             | 170          | 100        | 50            | 6                   | 1.3  | RF, O [20]                            |
| Rocketdyne (FEL)     | 0.84                           | 3 ps             | 90           | 500        | 160           | 2.4                 | 1.4  | RF, MOPA [40]                         |
| Dortmund (DELTA)     | 0.4                            | 50 ps            | 500          | 90         | 17            | 25                  | 2    | SR, O [30]                            |
| Harima (HIT)         | 0.28                           | 100 ps           | 500          | 3          | 170           | 1.8                 | 4.2  | SR, O [20]                            |
| BNL (DUVFEL)         | 0.075                          | 6 ps             | 310          | 300        | 682           | 2.2                 | 1.5  | RF, A [32]                            |
| Duke (Ring)          | 0.05                           | 10 ps            | 1000         | 350        | $2 \times 33$ | 10                  | 1.7  | SR, O [33]                            |
| SLAC (LCLS)          | 0.0004                         | 0.1 ps           | 7000         | 2500       | 723           | 8.3                 | 4.4  | RF, A [34]                            |

<sup>a</sup> RF: RF linac accelerator; MA: microtron accelerator; SR: electron storage ring; EA: electrostatic accelerator; A: FEL amplifier; O: FEL oscillator; MOPA: master-oscillator power-amplifier.

## References

- [1] G. Ramian, Nucl. Instr. and Meth. A 318 (1992) 225.
- [2] E. Nishimura et al., Nucl. Instr. and Meth. A 341 (1994) 39.
- [3] D.A. Jaroszynski et al., Nucl. Instr. and Meth. A 331 (1993) 52.
- [4] P. Guimbal et al., Nucl. Instr. and Meth. A 341 (1994) 43.
- [5] M. Castellano et al., Nucl. Instr. and Meth. A 304 (1991) 204.
- [6] J. Xie et al., Nucl. Instr. and Meth. A 331 (1993) 204; Nucl. Instr. and Meth. A 341 (1994) 34.
- [7] J.M. Ortega et al., Nucl. Instr. and Meth. A 341 (1994) 138; R. Prazeres et al., Nucl. Instr. and Meth. A 341 (1994) 54.
- [8] D.C. Nguyen et al., Nucl. Instr. and Meth. A 341 (1994) 29.
- [9] J. Auerhammer et al., Nucl. Instr. and Meth. A 341 (1994) 63.
- [10] T. Smith and A. Marzali, Nucl. Instr. and Meth. A 331 (1993) 59; T.I. Smith et al., Proc. SPIE 1854 (1993) 23.
- [11] C. Brau, Nucl. Instr. and Meth. A 318 (1992) 38.
- [12] S.V. Benson et al., Nucl. Instr. and Meth. A 250 (1986) 39.
- [13] P.G. O'Shea et al., Nucl. Instr. and Meth. A 341 (1994) 7.
- [14] T. Yamazaki et al., Nucl. Instr. and Meth. A 331 (1993) 27; T. Yamazaki et al., Nucl. Instr. and Meth. A 341 (1994) ABS 3.
- [15] T. Hara et al., Nucl. Instr. and Meth. A 341 (1994) 21.
- [16] S. Takano et al., Nucl. Instr. and Meth. A 331 (1993) 20; H. Hama et al., Nucl. Instr. and Meth. A 341 (1994) 12.
- [17] I.B. Drobyasko et al., Nucl. Instr. and Meth. A 282 (1989) 424.
- [18] L.R. Elias et al., Nucl. Instr. and Meth. A 304 (1991) 2919; M. Tecimen, Nucl. Instr. and Meth. A 341 (1994) 219.
- [19] E.D. Shaw et al., Nucl. Instr. and Meth. A 318 (1992) 47.
- [20] N. Ohigashi et al., presented at this Conference (16th Int. Free Electron Laser Conf. Stanford, CA, USA, 1994).
- [21] K.A. Belovintsey et al., Nucl. Instr. and Meth. A 341 (1994) ABS 45; A. Agafonov et al., Nucl. Instr. and Meth. A 331 (1993) 186.
- [22] K.J. Kim et al., Nucl. Instr. and Meth. A 341 (1994) 280.
- [23] I.S. Lehrman et al., Nucl. Instr. and Meth. A 341 (1994) ABS 31.
- [24] S. Okuda et al., Nucl. Instr. and Meth. A 341 (1994) 59.
- [25] G. Neil, Nucl. Instr. and Meth. A 318 (1992) 212; G. Neil et al., Nucl. Instr. and Meth. A 341 (1994) ABS 39.
- [26] N.A. Vinokurov et al., Nucl. Instr. and Meth. A 331 (1993) 3.
- [27] D. Quimby et al., Nucl. Instr. and Meth. A 318 (1992) 696.
- [28] J.F. Schmerge and R. Pantell, Nucl. Instr. and Meth. A 341 (1994) 335.
- [29] T.I. Smith et al., Proc. SPIE 1854 (1993) 23; A. Schwettman et al., Nucl. Instr. and Meth. A 341 (1994) ABS 19.
- [30] D. Nolle et al., Nucl. Instr. and Meth. A 341 (1994) ABS 7; Schmidt et al., Nucl. Instr. and Meth. A 341 (1994) ABS 9.
- [31] G. Neil, High-Power UV FEL For Industrial Processing, The Laser Processing Consortium Proposal (1994).
- [32] S. Krinsky (Ed.), The BNL DUV FEL Report (1994).
- [33] J.M.J. Madey et al., Nucl. Instr. and Meth. A 341 (1994) 363.
- [34] C. Pellegrini et al., Nucl. Instr. and Meth. A 341 (1994) 326.
- [35] G. Baranov et al., Nucl. Instr. and Meth. A 331 (1993) 228.
- [36] K. Batchelor et al., Nucl. Instr. and Meth. A 318 (1992) 159.
- [37] I. Ben-Zvi et al., Nucl. Instr. and Meth. A 318 (1992) 208.
- [38] J.I.M. Botman et al., Nucl. Instr. and Meth. A 341 (1994) 402.
- [39] R.H. Pantell et al., presented at this Conference (16th Int. Free Electron Laser Conf. Stanford, CA, USA, 1994).
- [40] R.J. Burke et al., Proc. SPIE: Laser Power Beaming, Los Angeles, Jan. 27–28, 1994, Vol. 2121.



ELSEVIER

## Author index

- Abe, S., see Tomimasu, T. . . . . 358 (1995) ABS 11  
Abe, S., see Saeki, K. . . . . 358 (1995) ABS 56  
Agafonov, A.V., see van der Slot, P.J.M. . . . . 358 (1995) 100  
Agari, T., see Asakawa, M. . . . . 358 (1995) 399  
Agari, T., see Fujita, M. . . . . 358 (1995) 524  
Allen, S.J., K. Craig, B. Galdrikian, J.N. Heyman, J.P. Kaminski, J.S. Scott, M.S. Sherwin, K. Unterrainer, M. Wanke, K. Campman, P.F. Hopkins, A.C. Gossard, D.H. Chow, M. Lui and T.K. Liu, Materials science in the far-IR with electrostatic based FELs. . . . . 358 (1995) 536  
Antonsen, T., see Caplan, M. . . . . 358 (1995) 174  
Arbel, M., see Cohen, M. . . . . 358 (1995) 82  
Arcioni, P., M. Bressan, F. Broggi, G. Conciauro, L. Perregrini and P. Pierini, The groove guide as an interaction structure for a microwave FEL. . . . . 358 (1995) 108  
Arensburg, A., M. Cohen, M. Draznin, A. Eichenbaum, A. Gover, Y. Pinhasi, V. Shternghartz, I.M. Yakover, J. Sokolovsky, B. Mandelbaum, A. Rosenberg, J. Shiloh, G. Hasak, L.A. Levin, O. Shahal, M. Shapira and V. Granatstein, The Israeli tandem electrostatic accelerator FEL – status report . . . . . 358 (1995) ABS 7  
Arzhannikov, A.V., V.B. Bobylev, S.L. Sinitzky, A.V. Tarasov, N.S. Ginzburg and N.Yu. Peskov, Ribbon-FEL experiments at one-dimension distributed feedback . . . . . 358 (1995) 112  
Arzhannikov, A.V., see Ginzburg, N.S. . . . . 358 (1995) 189  
Asakawa, M., see Chen, J. . . . . 358 (1995) 14  
Asakawa, M., N. Inoue, K. Mima, S. Nakai, K. Imasaki, M. Fujita, J. Chen, C. Yamanaka, N. Nakao, T. Agari, T. Asakuma, A. Moon, N. Ohigashi, T. Minamiguchi and Y. Tsunawaki, Development of a modified wiggler for higher harmonic lasing of a free-electron laser . . . . . 358 (1995) 399  
Asakawa, M., see Fujita, M. . . . . 358 (1995) 524  
Asakuma, T., see Chen, J. . . . . 358 (1995) 14  
Asakuma, T., see Asakawa, M. . . . . 358 (1995) 399  
Asakuma, T., see Fujita, M. . . . . 358 (1995) 524  
Bakker, R.J., R. Maas, G. Luijckx, V.N. Litvinenko, B. Faatz and P.W. van Amersfoort, Expected performance of FELINA, the Dutch VUV-FEL in Amsterdam . . . . . 358 (1995) 358  
Bali, L.M., see Srivastava, A. . . . . 358 (1995) ABS 50  
Balleyguier, P., see Guimbal, Ph. . . . . 358 (1995) 240  
Barnett, G., see Litvinenko, V.N. . . . . 358 (1995) 345  
Barnett, G.A., S.V. Benson, J.M.J. Madey and E.B. Szarmes, Hole coupling experiments on the Mark III FEL . . . . 358 (1995) 311  
Baron, Y., see Shahadi, A. . . . . 358 (1995) 143  
Baryshevsky, V.G., K.G. Batrakov and I.Ya. Dubovskaya, Formation of distributed feedback in an FEL under multi-wave diffraction . . . . . 358 (1995) 493  
Baryshevsky, V.G., K.G. Batrakov, I.Ya. Dubovskaya and S. Sytova, Visible surface quasi-Cherenkov FEL . . . . 358 (1995) 508  
Batrakov, K.G., see Baryshevsky, V.G. . . . . 358 (1995) 493  
Batrakov, K.G., see Baryshevsky, V.G. . . . . 358 (1995) 508  
Bazylev, V., V. Goloviznin, M.M. Pitatelev, A. Tulupov and T. Schep, On the possibility of the construction of plasma undulators . . . . . 358 (1995) 433  
Bazylev, V.A. and M.M. Pitatelev, Multisectional FELs with dispersion and undulator sections . . . . . 358 (1995) 64  
Bekefi, G., see Shahadi, A. . . . . 358 (1995) 143  
Belyavskiy, E.D., see Silivra, A.A. . . . . 358 (1995) 512  
Ben-Haim, D., see Cohen, M. . . . . 358 (1995) 82  
Ben-Zvi, I., Milestone experiments for single pass UV/X-ray FELs. . . . . 358 (1995) 52  
Benesch, J., see Liu, H. . . . . 358 (1995) 475  
Bensal, M., see Korol, M. . . . . 358 (1995) ABS 54  
Bensal, M., see Shahadi, A. . . . . 358 (1995) 143  
Benson, S., see Liu, H. . . . . 358 (1995) 475  
Benson, S.V., see Neil, G.R. . . . . 358 (1995) 159  
Benson, S.V., see Barnett, G.A. . . . . 358 (1995) 311

- Berryman, K.W. and T.I. Smith, A flexible far-infrared FEL user facility . . . . . 358 (1995) ABS 93
- Berryman, K.W., see Crosson, E.R. . . . . 358 (1995) 216
- Berryman, K.W., P. Haar and B.A. Richman, FEL cavity length measurement with an external laser . . . . . 358 (1995) 260
- Berryman, K.W., B.A. Richman, H.A. Schwettman, T.I. Smith and R.L. Swent, FEL center user diagnostics and control . . . . . 358 (1995) 300
- Berryman, K.W., see Swent, R.L. . . . . 358 (1995) 482
- Berset, J.M., see Prazeres, R. . . . . 358 (1995) 212
- Bessonov, E.G., Free-ion lasers with radiative ion cooling . . . . . 358 (1995) 204
- Billardon, M., see Hara, T. . . . . 358 (1995) 341
- Billardon, M., see Couprie, M.E. . . . . 358 (1995) 374
- Billardon, M., see Couprie, M.E. . . . . 358 (1995) 382
- Billardon, M., see Garzella, D. . . . . 358 (1995) 387
- Binet, A., see Guimbal, Ph. . . . . 358 (1995) 240
- Bisognano, J., see Liu, H. . . . . 358 (1995) 475
- Blank, M., see Taccetti, J.M. . . . . 358 (1995) 193
- Blau, J., see Small, D.W. . . . . 358 (1995) ABS 44
- Blau, J., see Kelsey, E. . . . . 358 (1995) ABS 61
- Blau, J., R.K. Wong and W.B. Colson, Ultra-short pulse free electron laser oscillators . . . . . 358 (1995) 441
- Blésès, J.P., see Guimbal, Ph. . . . . 358 (1995) 240
- Bobylev, V.B., see Arzhannikov, A.V. . . . . 358 (1995) 112
- Boffa, V., see Giovenale, E. . . . . 358 (1995) ABS 9
- Bogomolov, Ya.L., N.S. Ginzburg and E.R. Golubyatnikova, Chaotic particle deceleration and FEL efficiency enhancement with an incoherent pump wave or a stochastic undulator. . . . . 358 (1995) 171
- Bohanick, R., see Lehrman, I.S. . . . . 358 (1995) ABS 5
- Bongers, W.A., see Urbanus, W.H. . . . . 358 (1995) 155
- Bouzouloukov, Yu.P., see Varfolomeev, A.A. . . . . 358 (1995) 396
- Bratman, V.L., G.G. Denisov, M.M. Ofitserov, M.I. Petelin and S.V. Samsonov, Concept of a submillimeter wavelength CARM. . . . . 358 (1995) 135
- Bratman, V.L., see Urbanus, W.H. . . . . 358 (1995) 155
- Bratman, V.L. and A.V. Saviolov, Competition of longitudinal modes and the scenario of single-mode regime build-up for the FOM-Fusion-FEM project . . . . . 358 (1995) 182
- Bratman, V.L., see Denisov, G.G. . . . . 358 (1995) 528
- Brazuna, M., see Garzella, D. . . . . 358 (1995) 387
- Bressan, M., see Arcioni, P. . . . . 358 (1995) 108
- Broggi, F., see Arcioni, P. . . . . 358 (1995) 108
- Burnham, B., see Litvinenko, V.N. . . . . 358 (1995) 334
- Burnham, B., see Litvinenko, V.N. . . . . 358 (1995) 345
- Burnham, B., see Litvinenko, V.N. . . . . 358 (1995) 349
- Burnham, B., see Litvinenko, V.N. . . . . 358 (1995) 369
- Campman, K., see Allen, S.J. . . . . 358 (1995) 536
- Caplan, M., see Urbanus, W.H. . . . . 358 (1995) 155
- Caplan, M., T. Antonsen, B. Levush, A. Tulupov and W. Urbanus, Predicted operating conditions for maintaining mode purity in the 1 MW 200 GHz FOM free electron maser . . . . . 358 (1995) 174
- Castellano, M., M. Ferrario, M. Minestrini, P. Patteri, F. Tazzioli, F. Cevenini and L. Catani, First operation and perspectives of the superconducting linac LISA. . . . . 358 (1995) 331
- Catani, L., see Castellano, M. . . . . 358 (1995) 331
- Catellino, M., see Urbanus, W.H. . . . . 358 (1995) 155
- Cevenini, F., see Castellano, M. . . . . 358 (1995) 331
- Chairman, D., see Cohen, M. . . . . 358 (1995) 82
- Chaix, P. and P. Guimbal, Turbulent FEL theory and experiment on ELSA at Bruyeres-le-Chatel . . . . . 358 (1995) 96
- Chao, C., see Xie, J. . . . . 358 (1995) 256
- Chattopadhyay, S., see Edighoffer, J. . . . . 358 (1995) 18
- Chen, J., K. Imasaki, M. Fujita, M. Asakawa, T. Asakuma, S. Nakai and C. Yamanaka, Compact high-brightness radiation sources . . . . . 358 (1995) 14
- Chen, J., see Asakawa, M. . . . . 358 (1995) 399
- Chen, J., see Fujita, M. . . . . 358 (1995) 524
- Cheng, J.-b., see Qian, M.-q. . . . . 358 (1995) 280
- Cheng, S. and W.W. Destler, High power operation of a wiggler-focused sheet beam free electron laser amplifier . . . . . 358 (1995) 200
- Chiwaki, M., see Yamazaki, T. . . . . 358 (1995) 353
- Chiwaki, M., see Yokoyama, M. . . . . 358 (1995) 378

- Chiwaki, M., see Yamada, K. . . . . 358 (1995) 392
- Chow, D.H., see Allen, S.J. . . . . 358 (1995) 536
- Chung, T.H. and J.K. Lee, 1-D simulation model of an FEL with a plasma background . . . . . 358 (1995) ABS 3
- Chung, T.H., see Wang, M.C. . . . . 358 (1995) ABS 38
- Chung, T.H., see Yeom, K.H. . . . . 358 (1995) ABS 52
- Chung, T.H., see Park, E.H. . . . . 358 (1995) 448
- Ciocchi, F., see Giovenale, E. . . . . 358 (1995) ABS 22
- Codarbox, J.H., see Couprie, M.E. . . . . 358 (1995) 374
- Cohen, M., see Arensburg, A. . . . . 358 (1995) ABS 7
- Cohen, M., A. Kugel, D. Chairman, M. Arbel, H. Kleinman, D. Ben-Haim, A. Eichenbaum, M. Draznin, Y. Pinhasi,  
I. Yakover and A. Gover, Free electron maser experiment with a prebunched beam . . . . . 358 (1995) 82
- Colson, W.B., see Wong, R.K. . . . . 358 (1995) ABS 26
- Colson, W.B., see Small, D.W. . . . . 358 (1995) ABS 44
- Colson, W.B., see Kelsey, E. . . . . 358 (1995) ABS 61
- Colson, W.B., see Lyon, R.A. . . . . 358 (1995) ABS 81
- Colson, W.B., see Winter, G.H. . . . . 358 (1995) 68
- Colson, W.B., see Blau, J. . . . . 358 (1995) 441
- Colson, W.B., Status of free electron lasers in 1994 . . . . . 358 (1995) 532
- Colson, W.B., Short wavelength free electron lasers in 1994 . . . . . 358 (1995) 555
- Conciauro, G., see Arcioni, P. . . . . 358 (1995) 108
- Conde, M.E., see van der Geer, B. . . . . 358 (1995) ABS 59
- Conde, M.E., see Leemans, W.P. . . . . 358 (1995) 208
- Couperus, J., see van der Slot, P.J.M. . . . . 358 (1995) 100
- Couprie, M.E., see Hara, T. . . . . 358 (1995) 341
- Couprie, M.E., D. Garzella, T. Hara, J.H. Codarbox and M. Billardon, A longitudinal feedback for the Super-ACO  
free electron laser stability in the UV . . . . . 358 (1995) 374
- Couprie, M.E., D. Garzella and M. Billardon, Optical cavities for UV free electron lasers . . . . . 358 (1995) 382
- Couprie, M.E., see Garzella, D. . . . . 358 (1995) 387
- Craig, K., see Allen, S.J. . . . . 358 (1995) 536
- Crosson, E.R., see Richman, B.A. . . . . 358 (1995) ABS 32
- Crosson, E.R., K.W. Berryman, T.I. Smith, R.L. Swent, H.C. Lihn and H. Wiedemann, Sub-picosecond FEL  
micropulse length and electron bunch measurements . . . . . 358 (1995) 216
- Dattoli, G., L. Giannessi and A. Renieri, Theory of the longitudinal dynamics of a storage ring FEL . . . . . 358 (1995) 338
- Delboulbé, A., see Hara, T. . . . . 358 (1995) 341
- Delboulbé, A., see Garzella, D. . . . . 358 (1995) 387
- DeLong, K.W., see Richman, B.A. . . . . 358 (1995) 268
- de Loos, M., see Leemans, W.P. . . . . 358 (1995) 208
- de Loos, M.J., see van der Geer, B. . . . . 358 (1995) ABS 59
- Deng, R.-p., see Qian, M.-q. . . . . 358 (1995) 280
- Denisov, G.G., see Bratman, V.L. . . . . 358 (1995) 135
- Denisov, G.G., see Urbanus, W.H. . . . . 358 (1995) 155
- Denisov, G.G., V.L. Bratman, A.K. Krasnykh, E.A. Perelstein, A.V. Savilov, A.S. Sergeev and A.P. Sumbaev,  
Problems of autobunching and phase stability for the TBA-driver: calculations and design for a modeling  
experiment . . . . . 358 (1995) 528
- Destler, W.W., see Cheng, S. . . . . 358 (1995) 200
- DiCrescenzo, J., see Guimbal, Ph. . . . . 358 (1995) 240
- Dikhtiar, V., see Shahadi, A. . . . . 358 (1995) 143
- Ding, W., X. Shu and X. Du, A comparison between two kinds of chromatic coherent light sources . . . . . 358 (1995) ABS 65
- Donohue, J.T., Ph. Gouard and J.L. Rullier, Electron trajectories in a helical wiggler with a uniform axial guide field:  
a comparison of numerical results with results obtained using an approximate but analytical method . . . . . 358 (1995) 422
- Dore, P., see Giovenale, E. . . . . 358 (1995) ABS 9
- Doria, A., see Giovenale, E. . . . . 358 (1995) ABS 9
- Doria, A., see Giovenale, E. . . . . 358 (1995) ABS 22
- Doria, A., see Gallerano, G.P. . . . . 358 (1995) 78
- Douglas, D., see Liu, H. . . . . 358 (1995) 475
- Draznin, M., see Arensburg, A. . . . . 358 (1995) ABS 7
- Draznin, M., see Cohen, M. . . . . 358 (1995) 82
- Drori, R., see Shahadi, A. . . . . 358 (1995) 143
- Drori, R., E. Jerby and A. Shahadi, Free-electron maser oscillator experiment in the UHF regime . . . . . 358 (1995) 151
- Du, X., see Ding, W. . . . . 358 (1995) ABS 65

- Dubovskaya, I.Ya., see Baryshevsky, V.G. . . . . 358 (1995) 493  
 Dubovskaya, I.Ya., see Baryshevsky, V.G. . . . . 358 (1995) 508  
 Dylla, F., see Edighoffer, J. . . . . 358 (1995) 18  
 Dylla, H.F., see Neil, G.R. . . . . 358 (1995) 159
- Ebihara, K., see Takayama, K. . . . . 358 (1995) 122  
 Eckhouse, S., see Korol, M. . . . . 358 (1995) ABS 54  
 Edighoffer, J., K.-J. Kim, M. Xie, F. Dylla, R. Sheffield and S. Chattopadhyay, A path towards a compact, CW FEL using superconducting rf accelerator technology . . . . . 358 (1995) 18  
 Edighoffer, J.A., see Hahn, S.J. . . . . 358 (1995) 167  
 Edighoffer, J.A. and K.-J. Kim, A computer model of the energy-current loss instabilities in a recirculating accelerator system . . . . . 358 (1995) 519  
 Eecen, P.J., A.V. Tulupov and T.J. Schep, Spectral dynamics of the FEM . . . . . 358 (1995) 178  
 Eichenbaum, A., see Arensburg, A. . . . . 358 (1995) ABS 7  
 Eichenbaum, A., see Cohen, M. . . . . 358 (1995) 82  
 Elias, L.R., see Kimel, I. . . . . 358 (1995) 20  
 Elias, L.R., see Kimel, I. . . . . 358 (1995) 186  
 Ernst, G.J., see Verschuur, J.W.J. . . . . 358 (1995) ABS 85  
 Ernst, G.J., see van Oerle, B.M. . . . . 358 (1995) 287
- Faatz, B., see van Werkhoven, G.H.C. . . . . 358 (1995) 304  
 Faatz, B., see Knippels, G.M.H. . . . . 358 (1995) 308  
 Faatz, B., see Bakker, R.J. . . . . 358 (1995) 358  
 Fawley, W.M., see Travish, G. . . . . 358 (1995) 60  
 Fawley, W.M., see Hahn, S.J. . . . . 358 (1995) 167  
 Fayer, M.D., see Tokmakoff, A. . . . . 358 (1995) 540  
 Feinstein, J., see Lewellen, J.W. . . . . 358 (1995) 24  
 Feinstein, J., see Huang, Y.C. . . . . 358 (1995) 315  
 Ferrario, M., see Castellano, M. . . . . 358 (1995) 331  
 Fliflet, A.W., see Granatstein, V.L. . . . . 358 (1995) ABS 24  
 Fontenay, V., see Guimbal, Ph. . . . . 358 (1995) 240  
 Fourdin, P., see Guimbal, Ph. . . . . 358 (1995) 240  
 Freund, H.P., see Pershing, D.E. . . . . 358 (1995) 104  
 Freund, H.P., R.H. Jackson, D.E. Pershing and J.M. Taccetti, Theory of the free-electron laser based upon a coaxial hybrid wiggler . . . . . 358 (1995) 139  
 Freund, H.P., M.E. Read, R.H. Jackson, D.E. Pershing and J.M. Taccetti, Design study of a G-band FEL amplifier for application to cyclotron resonant heating in magnetic fusion reactors . . . . . 358 (1995) 163  
 Freund, H.P., see Taccetti, J.M. . . . . 358 (1995) 193  
 Freund, H.P., A re-examination of scaling laws in the traveling wave interaction . . . . . 358 (1995) 497  
 Freund, H.P. and V.L. Granatstein, Long wavelength free electron lasers in 1994. . . . . 358 (1995) 551  
 Fruchtmann, A., see Shahadi, A. . . . . 358 (1995) 143  
 Fu, E., see Xie, J. . . . . 358 (1995) 256  
 Fujita, M., see Chen, J. . . . . 358 (1995) 14  
 Fujita, M., see Asakawa, M. . . . . 358 (1995) 399  
 Fujita, M., T. Asakuma, J. Chen, K. Imasaki, C. Yamanaka, M. Asakawa, N. Inoue, K. Mima, S. Nakai, T. Agari, N. Nakao, A. Moon, N. Ohigashi, T. Minamiguchi and Y. Tsunawaki, POP experiments of the photon-e-beam interaction in the supercavity . . . . . 358 (1995) 524  
 Furukawa, H., see Sentoku, Y. . . . . 358 (1995) 463
- Galdrikian, B., see Allen, S.J. . . . . 358 (1995) 536  
 Gallerano, G.P., see Giovenale, E. . . . . 358 (1995) ABS 9  
 Gallerano, G.P., see Giovenale, E. . . . . 358 (1995) ABS 22  
 Gallerano, G.P., A. Doria, E. Giovenale and G. Messina, Coherence effects in FEL radiation generated by short electron bunches . . . . . 358 (1995) 78  
 Ganguly, A.K., see Hirshfield, J.L. . . . . 358 (1995) 129  
 Gardelle, J., see Rullier, J.L. . . . . 358 (1995) 118  
 Garzella, D., see Hara, T. . . . . 358 (1995) 341  
 Garzella, D., see Couprie, M.E. . . . . 358 (1995) 374  
 Garzella, D., see Couprie, M.E. . . . . 358 (1995) 382  
 Garzella, D., M.E. Couprie, T. Hara, L. Nahon, M. Brazuna, A. Delboulbé and M. Billardon, Mirror degradation and heating in storage ring FELs . . . . . 358 (1995) 387

- Geisler, A., see Nölle, D. . . . . 358 (1995) ABS 14
- Geisler, A., see Ridder, M. . . . . 358 (1995) ABS 16
- Genz, H., H.-D. Gräf, R. Hahn, D.A. Jaroszynski, H. Loos, A. Richter, M. Reichenbach, V. Schlott, M. Thomas, J. Töpper, T. Wesp and M. Wiencken, Improved electron beam transport and diagnosis system for the Darmstadt IR-FEL . . . . . 358 (1995) ABS 20
- Giannessi, L., see Dattoli, G. . . . . 358 (1995) 338
- Gierman, S.M., see Nguyen, D.C. . . . . 358 (1995) ABS 48
- Gierman, S.M., see Nguyen, D.C. . . . . 358 (1995) ABS 67
- Gierman, S.M., see Nguyen, D.C. . . . . 358 (1995) 27
- Gillespie, W.A., A.M. MacLeod, P.F. Martin, G.M.H. Knippels, A.F.G. van der Meer, E.H. Haselhoff and P.W. van Amersfoort, Electron energy spectral measurements in the large-slippage regime . . . . . 358 (1995) 232
- Gillespie, W.A., see Yu, J. . . . . 358 (1995) 471
- Ginzburg, N.S., see Arzhannikov, A.V. . . . . 358 (1995) 112
- Ginzburg, N.S., see Bogomolov, Ya.L. . . . . 358 (1995) 171
- Ginzburg, N.S., N.Yu. Peskov, A.S. Sergeev, A.V. Arzhannikov and S.L. Sinitsky, Super-power free electron lasers with two-dimensional distributed feedback . . . . . 358 (1995) 189
- Giovenale, E., V. Boffa, P. Dore, A. Doria, G.P. Gallerano, M.F. Kimmitt, R. Trippetti and I. Spassovsky, Application of a mm-wave free electron laser to the study of high- $T_c$  superconductors . . . . . 358 (1995) ABS 9
- Giovenale, E., F. Ciocchi, A. Doria, G.P. Gallerano, M.F. Kimmitt, G. Messina, P. Raimondi, A. Renieri and I. Spassovsky, Upgrade of the ENEA compact FEL in the sub-mm region . . . . . 358 (1995) ABS 22
- Giovenale, E., see Gallerano, G.P. . . . . 358 (1995) 78
- Glotin, F., see Prazeres, R. . . . . 358 (1995) 212
- Glotin, F., see Jaroszynski, D.A. . . . . 358 (1995) 224
- Glotin, F., see Jaroszynski, D.A. . . . . 358 (1995) 228
- Goldstein, J.C., H. Takeda and D.C. Nguyen, Numerical simulation studies of the design and performance of the AFEL for high average power operation . . . . . 358 (1995) ABS 36
- Goldstein, J.C., see Nguyen, D.C. . . . . 358 (1995) 27
- Goldstein, M., see Tang, C.M. . . . . 358 (1995) 7
- Golightly, W.J. and S.K. Ride, The interaction between low- and high-frequency waves in a waveguide free-electron laser amplifier . . . . . 358 (1995) 504
- Goloviznin, V., see Bazylev, V. . . . . 358 (1995) 433
- Golub, Yu.Ya. and N.E. Rozanov, Nonlinear wave processes during the propagation of a high-current electron beam in an ion-beam undulator. . . . . 358 (1995) 479
- Golubyatnikova, E.R., see Bogomolov, Ya.L. . . . . 358 (1995) 171
- Goncharov, I.A., see Silivra, A.A. . . . . 358 (1995) 452
- Goncharov, I.A., see Silivra, A.A. . . . . 358 (1995) 512
- Gossard, A.C., see Allen, S.J. . . . . 358 (1995) 536
- Gouard, Ph., see Donohue, J.T. . . . . 358 (1995) 422
- Gover, A., see Arensburg, A. . . . . 358 (1995) ABS 7
- Gover, A., see Granatstein, V.L. . . . . 358 (1995) ABS 24
- Gover, A., see Cohen, M. . . . . 358 (1995) 82
- Gover, A., see Pinhasi, Y. . . . . 358 (1995) 86
- Gover, A., see Yakover, I.M. . . . . 358 (1995) 323
- Govil, R., see Leemans, W.P. . . . . 358 (1995) 208
- Gräf, H.-D., see Genz, H. . . . . 358 (1995) ABS 20
- Granatstein, V., see Arensburg, A. . . . . 358 (1995) ABS 7
- Granatstein, V.L., A.W. Fliflet, W.M. Manheimer and A. Gover, Design of a far infrared FEL with an electromagnetic wiggler . . . . . 358 (1995) ABS 24
- Granatstein, V.L., see Shahadi, A. . . . . 358 (1995) 143
- Granatstein, V.L., see Taccetti, J.M. . . . . 358 (1995) 193
- Granatstein, V.L., see Freund, H.P. . . . . 358 (1995) 551
- Graves, W.S., see Solomon, L. . . . . 358 (1995) 411
- Graves, W.S., L. Solomon and I. Lehrman, End fields in the harmonic generation superconducting FEL at BNL-NSLS . . . . . 358 (1995) 414
- Grinberg, V., see Shahadi, A. . . . . 358 (1995) 143
- Grinberg, V., E. Jerby and A. Shahadi, Low-cost electron-gun pulser for table-top maser experiments. . . . . 358 (1995) 327
- Gubankov, V.V., see Varfolomeev, A.A. . . . . 358 (1995) 70
- Guimbal, Ph., see Chaix, P. . . . . 358 (1995) 96
- Guimbal, Ph., D. Iracane, S. Joly, P. Balleyguier, A. Binet, J.P. Blésès, J. DiCrescenzo, V. Fontenay, P. Fourdin, G. Haouat, J.G. Marmouget, Y. Pranal, F. Sabary, S. Striby and D. Touati, High efficiency results at 23  $\mu$ m on the ELSA FEL and operation with the MONA wiggler . . . . . 358 (1995) 240

- Haar, P., H.A. Schwettman and T.I. Smith, Demonstration of micropulse energy enhancement with the SCA/FEL external cavity system . . . . . 358 (1995) ABS 40
- Haar, P., see Berryman, K.W. . . . . 358 (1995) 260
- Haar, P., H.A. Schwettman and T.I. Smith, Pulse stacking in the SCA/FEL external cavity . . . . . 358 (1995) 319
- Hahn, R., see Genz, H. . . . . 358 (1995) ABS 20
- Hahn, S.J., see Kim, K.-J. . . . . 358 (1995) 93
- Hahn, S.J., W.M. Fawley, K.-J. Kim and J.A. Edighoffer, Time-dependent multi-dimensional simulation studies of the electron output scheme for high power FELs . . . . . 358 (1995) 167
- Hairetdinov, A.H., see Varfolomeev, A.A. . . . . 358 (1995) 70
- Hairetdinov, A.H., see Varfolomeev, A.A. . . . . 358 (1995) 426
- Hall, J., see Winter, G.H. . . . . 358 (1995) 68
- Hama, H., J. Yamazaki, T. Kinoshita, K. Kimura and G. Isoyama, Observation of micro-macro temporal structure and saturation mechanism on the UVSOR free electron laser. . . . . 358 (1995) 365
- Hamada, S., see Yamazaki, T. . . . . 358 (1995) 353
- Hamada, S., see Yokoyama, M. . . . . 358 (1995) 378
- Hamada, S., see Yamada, K. . . . . 358 (1995) 392
- Haouat, G., see Guimbal, Ph. . . . . 358 (1995) 240
- Hara, T., M.E. Couprie, A. Delboulbé, D. Garzella, L. Nahon and M. Billardon, Dynamic behavior of the Super-ACO FEL micropulse . . . . . 358 (1995) 341
- Hara, T., see Couprie, M.E. . . . . 358 (1995) 374
- Hara, T., see Garzella, D. . . . . 358 (1995) 387
- Harhel, T., see Shahadi, A. . . . . 358 (1995) 143
- Hartley, R.A., see Lehrman, I.S. . . . . 358 (1995) ABS 5
- Hasak, G., see Arensburg, A. . . . . 358 (1995) ABS 7
- Haselhoff, E.H., G.M.H. Knippels and P.W. van Amersfoort, Slicing single micropulses at FELIX . . . . . 358 (1995) ABS 28
- Haselhoff, E.H., see Gillespie, W.A. . . . . 358 (1995) 232
- Haselhoff, E.H., see Knippels, G.M.H. . . . . 358 (1995) 308
- Heyman, J.N., see Allen, S.J. . . . . 358 (1995) 536
- Hiramatsu, S., see Takayama, K. . . . . 358 (1995) 122
- Hirshfield, J.L., T.C. Marshall, T.B. Zhang, A.K. Ganguly and P.A. Sprangle, A microwave inverse free-electron-laser accelerator (MIFELA) . . . . . 358 (1995) 129
- Hogan, M., see Travish, G. . . . . 358 (1995) ABS 75
- Honda, Y., see Okuda, S. . . . . 358 (1995) 244
- Honda, Y., see Okuda, S. . . . . 358 (1995) 248
- Hopkins, P.F., see Allen, S.J. . . . . 358 (1995) 536
- Hori, T., see Okuda, S. . . . . 358 (1995) 244
- Hori, T., see Okuda, S. . . . . 358 (1995) 248
- Hu, K.-s., see Qian, M.-q. . . . . 358 (1995) 280
- Huang, Y., see Xie, J. . . . . 358 (1995) 256
- Huang, Y.C., see Lewellen, J.W. . . . . 358 (1995) 24
- Huang, Y.C., R.H. Pantell, J.F. Schmerge and J. Feinstein, Maximization of FEL gain for a hole-coupled resonator . . . . . 358 (1995) 315
- Ikeda, N., see Inoue, F. . . . . 358 (1995) 407
- Ikehata, T., see Nagai, R. . . . . 358 (1995) 403
- Imasaki, K., see Chen, J. . . . . 358 (1995) 14
- Imasaki, K., see Kuruma, S. . . . . 358 (1995) 90
- Imasaki, K., see Asakawa, M. . . . . 358 (1995) 399
- Imasaki, K., see Fujita, M. . . . . 358 (1995) 524
- Inoue, F., N. Ikeda, K. Okubo, M. Takahashi and T. Yamanaka, Development of a short-period hybrid wiggler . . . . . 358 (1995) 407
- Inoue, N., see Asakawa, M. . . . . 358 (1995) 399
- Inoue, N., see Fujita, M. . . . . 358 (1995) 524
- Iracane, D., see Guimbal, Ph. . . . . 358 (1995) 240
- Ishida, S., see Okuda, S. . . . . 358 (1995) 244
- Ishii, S., G. Shvets and J.S. Wurtele, Computationally efficient spectral analysis of an FEL oscillator using a Green function analysis . . . . . 358 (1995) 489
- Ishizuka, H., see Kawasaki, S. . . . . 358 (1995) ABS 42
- Ishizuka, H., S. Musyoki, K. Sakamoto, A. Watanabe, M. Shiho and S. Kawasaki, Formation and diagnostics of electron beams for micro-FELs . . . . . 358 (1995) ABS 63
- Ishizuka, H., see Kawasaki, S. . . . . 358 (1995) 114
- Isoyama, G., see Hama, H. . . . . 358 (1995) 365



|  |                   |
|--|-------------------|
| Ivanchenkov, S.N., see Varfolomeev, A.A. . . . .   | 358 (1995) 70     |
| Ivanchenkov, S.N., see Urbanus, W.H. . . . .   | 358 (1995) 155    |
| Ivanchenkov, S.N., see Varfolomeev, A.A. . . . .   | 358 (1995) 396    |
| Iwata, A., see Yamazaki, T. . . . .  | 358 (1995) 353    |
| Jackson, R.H., see Pershing, D.E. . . . .  | 358 (1995) 104    |
| Jackson, R.H., see Freund, H.P. . . . .  | 358 (1995) 139    |
| Jackson, R.H., see Freund, H.P. . . . .  | 358 (1995) 163    |
| Jackson, R.H., see Taccetti, J.M. . . . .  | 358 (1995) 193    |
| Jaroszynski, D., see Prazeres, R. . . . .  | 358 (1995) 212    |
| Jaroszynski, D.A., see Genz, H. . . . .  | 358 (1995) ABS 20 |
| Jaroszynski, D.A., see Oepts, D. . . . .   | 358 (1995) 72     |
| Jaroszynski, D.A., R. Prazeres, F. Glotin and J.M. Ortega, Two-colour operation of the free-electron laser using a step-tapered undulator . . . . .  | 358 (1995) 224    |
| Jaroszynski, D.A., R. Prazeres, F. Glotin, J.M. Ortega, D. Oepts, A.F.G. van der Meer, G. Knippels and P.W. van Amersfoort, Free-electron laser operation and self-amplified spontaneous emission using a step-tapered undulator . . . . . | 358 (1995) 228    |
| Jerby, E., see Korol, M. . . . .   | 358 (1995) ABS 54 |
| Jerby, E., see Shahadi, A. . . . .   | 358 (1995) 143    |
| Jerby, E., see Drori, R. . . . .   | 358 (1995) 151    |
| Jerby, E., see Grinberg, V. . . . .  | 358 (1995) 327    |
| Jha, P., see Srivastava, A. . . . .  | 358 (1995) ABS 50 |
| Johnson, E.D., Scientific opportunities for FEL amplifier based VUV and X-ray research . . . . .   | 358 (1995) 544    |
| Joly, S., see Guimbal, Ph. . . . .   | 358 (1995) 240    |
| Kaminski, J.P., see Allen, S.J. . . . .  | 358 (1995) 536    |
| Karbushev, N.I., Free electron lasers with static and dynamic plasma wigglers . . . . .  | 358 (1995) 437    |
| Karbushev, N.I., V.D. Sazhin and P.V. Mironov, Higher harmonic generation in a FEL with an axisymmetric undulator of the induction type . . . . .  | 358 (1995) 467    |
| Kato, R., see Sawamura, M. . . . .   | 358 (1995) ABS 73 |
| Kato, R., M. Sugimoto, R. Nagai, M. Sawamura, M. Takao, N. Kikuzawa, M. Ohkubo, E.J. Minehara and Y. Suzuki, Performance of the optical cavity control system for the JAERI FEL project . . . . .  | 358 (1995) ABS 77 |
| Kato, R., see Sugimoto, M. . . . .   | 358 (1995) ABS 83 |
| Kato, R., see Nagai, R. . . . .  | 358 (1995) 403    |
| Katoh, H., see Takayama, K. . . . .  | 358 (1995) 122    |
| Kawai, M., see Yamazaki, T. . . . .  | 358 (1995) 353    |
| Kawai, M., see Yokoyama, M. . . . .  | 358 (1995) 378    |
| Kawai, M., see Yamada, K. . . . .  | 358 (1995) 392    |
| Kawarasaki, Y., see Minehara, E.J. . . . .   | 358 (1995) ABS 30 |
| Kawasaki, S., H. Ishizuka, A. Watanabe, Y. Yamashita, A. Tokuti, S. Nakajima, J. Kishiro, K. Takayama and M. Shiho, A new inductive acceleration structure with multiple electrodes for an FEL . . . . .                                   | 358 (1995) ABS 42 |
| Kawasaki, S., see Ishizuka, H. . . . .   | 358 (1995) ABS 63 |
| Kawasaki, S., H. Ishizuka, T. Koarai, A. Watanabe and M. Shiho, Analysis of chaotic behaviour in a Raman FEL . . . . .   | 358 (1995) 114    |
| Kelsey, E., J. Blau, D.D. Quick, R.K. Wong and W.B. Colson, The effects of high gain in an FEL optical klystron . . . . .  | 358 (1995) ABS 61 |
| Khlebnikov, A.S., see Varfolomeev, A.A. . . . .  | 358 (1995) ABS 46 |
| Khlebnikov, A.S., see Varfolomeev, A.A. . . . .  | 358 (1995) 70     |
| Khlebnikov, A.S., see Urbanus, W.H. . . . .  | 358 (1995) 155    |
| Khlebnikov, A.S., see Varfolomeev, A.A. . . . .  | 358 (1995) 396    |
| Kikuzawa, N., see Minehara, E.J. . . . .   | 358 (1995) ABS 30 |
| Kikuzawa, N., see Sawamura, M. . . . .   | 358 (1995) ABS 73 |
| Kikuzawa, N., see Kato, R. . . . .   | 358 (1995) ABS 77 |
| Kikuzawa, N., see Sugimoto, M. . . . .   | 358 (1995) ABS 83 |
| Kikuzawa, N., see Nagai, R. . . . .  | 358 (1995) 403    |
| Kim, C.-B., Y.-W. Uhm and J.-K. Lee, 1-D free-electron laser model without the slowly-varying approximation . . . . .  | 358 (1995) 516    |
| Kim, K.-J., see Edighoffer, J. . . . .   | 358 (1995) 18     |
| Kim, K.-J., UV/X-ray free electron lasers through high-gain single pass amplifiers: basic principles and key issues . . . . .  | 358 (1995) 31     |
| Kim, K.-J., see Travish, G. . . . .  | 358 (1995) 60     |
| Kim, K.-J. and S.J. Hahn, Finite pulse effects in self-amplified-spontaneous-emission . . . . .  | 358 (1995) 93     |
| Kim, K.-J., see Hahn, S.J. . . . .   | 358 (1995) 167    |
| Kim, K.-J., see Edighoffer, J.A. . . . .   | 358 (1995) 519    |
| Kimel, I. and L.R. Elias, A compact, bright and tunable CW source of soft X-rays . . . . .   | 358 (1995) 20     |

- Kimel, I. and L.R. Elias, Electrostatic-accelerator FELs for power beaming . . . . . 358 (1995) 186
- Kimmitt, M.F., see Giovenale, E. . . . . 358 (1995) ABS 9
- Kimmitt, M.F., see Giovenale, E. . . . . 358 (1995) ABS 22
- Kimura, K., see Hama, H. . . . . 358 (1995) 365
- Kimura, N., see Okuda, S. . . . . 358 (1995) 244
- Kimura, N., see Okuda, S. . . . . 358 (1995) 248
- Kinoshita, T., see Hama, H. . . . . 358 (1995) 365
- Kinross-Wright, J., see Kong, S.H. . . . . 358 (1995) 272
- Kinross-Wright, J., see Kong, S.H. . . . . 358 (1995) 284
- Kinross-Wright, J.M., see Ziomek, C.D. . . . . 358 (1995) ABS 87
- Kinross-Wright, J.M., see Nguyen, D.C. . . . . 358 (1995) 27
- Kishiro, J., see Kawasaki, S. . . . . 358 (1995) ABS 42
- Kishiro, J., see Takayama, K. . . . . 358 (1995) 122
- Kleev, A.I., A.B. Manenkov and H. Yamada, The barrel shaped resonator for the photon storage ring . . . . . 358 (1995) 362
- Kleinman, H., see Cohen, M. . . . . 358 (1995) 82
- Knippels, G., see Jaroszynski, D.A. . . . . 358 (1995) 228
- Knippels, G.M.H., see Haselhoff, E.H. . . . . 358 (1995) ABS 28
- Knippels, G.M.H., see Gillespie, W.A. . . . . 358 (1995) 232
- Knippels, G.M.H., G.H.C. van Werkhoven, E.H. Haselhoff, B. Faatz, D. Oepts and P.W. van Amersfoort, Influence of the radial mode structure on the losses in the FELIX hole-coupled resonators . . . . . 358 (1995) 308
- Koarai, T., see Kawasaki, S. . . . . 358 (1995) 114
- Kobayashi, A., see Tomimasu, T. . . . . 358 (1995) ABS 11
- Kobayashi, A., see Saeki, K. . . . . 358 (1995) ABS 56
- Kobayashi, A., see Sakai, T. . . . . 358 (1995) ABS 91
- Kobayashi, H., see Nagai, R. . . . . 358 (1995) 403
- Koga, A., see Tomimasu, T. . . . . 358 (1995) ABS 11
- Koltsov, A.V. and A.V. Serov, Stimulated radiation from an electron beam traversing an inhomogeneous electromagnetic wave . . . . . 358 (1995) 444
- Kong, S.H., see Nguyen, D.C. . . . . 358 (1995) 27
- Kong, S.H., J. Kinross-Wright, D.C. Nguyen and R.L. Sheffield, Photocathodes for free electron lasers . . . . . 358 (1995) 272
- Kong, S.H., D.C. Nguyen, R.L. Sheffield and B.A. Sherwood, Fabrication and characterization of cesium telluride photocathodes: A promising electron source for the Los Alamos Advanced FEL . . . . . 358 (1995) 276
- Kong, S.H., J. Kinross-Wright, D.C. Nguyen, R.L. Sheffield and M.E. Weber, Performance of cesium telluride photocathodes as an electron source for the Los Alamos Advanced FEL . . . . . 358 (1995) 284
- Korol, M., E. Jerby, S. Eckhouse, M. Bensal and A. Shahadi, Carbon fiber electron injector for free-electron maser experiments . . . . . 358 (1995) ABS 54
- Korol, M., see Shahadi, A. . . . . 358 (1995) 143
- Kowk, A., see Tokmakoff, A. . . . . 358 (1995) 540
- Krasnopolsky, V.A., see van der Slot, P.J.M. . . . . 358 (1995) 100
- Krasnykh, A.K., see Denisov, G.G. . . . . 358 (1995) 528
- Krastelev, E.G., see van der Slot, P.J.M. . . . . 358 (1995) 100
- Krishnaswamy, J., see Lehrman, I.S. . . . . 358 (1995) ABS 5
- Kugel, A., see Cohen, M. . . . . 358 (1995) 82
- Kurilko, V.I., see Ognivenko, V.V. . . . . 358 (1995) ABS 69
- Kuruma, S., K. Mima, K. Imasaki, S. Nakai and C. Yamanaka, Simulation of radiation build-up in an FEL oscillator: the effect of the electron beam micropulse shape . . . . . 358 (1995) 90
- Kuruma, S., see Sentoku, Y. . . . . 358 (1995) 463
- Labrousche, J., see Rullier, J.L. . . . . 358 (1995) 118
- Lc Taillandier, P., see Rullier, J.L. . . . . 358 (1995) 118
- Lebedev, A.N., see van der Slot, P.J.M. . . . . 358 (1995) 100
- Lee, J.-K., see Kim, C.-B. . . . . 358 (1995) 516
- Lee, J.K., see Chung, T.H. . . . . 358 (1995) ABS 3
- Lee, J.K., see Wang, M.C. . . . . 358 (1995) ABS 38
- Lee, J.K., see Yeom, K.H. . . . . 358 (1995) ABS 52
- Lee, J.K., see Park, E.H. . . . . 358 (1995) 448
- Leemans, W.P., see van der Geer, B. . . . . 358 (1995) ABS 59
- Leemans, W.P., M.E. Conde, R. Govil, B. van der Geer, M. de Loos, H.A. Schwettman, T.I. Smith and R.L. Swent, Time-resolved study of sideband generation and transition to chaos on an infrared FEL . . . . . 358 (1995) 208
- Lehrman, I., see Solomon, L. . . . . 358 (1995) 411
- Lehrman, I., see Graves, W.S. . . . . 358 (1995) 414

- Lehrman, I.S., J. Krishnaswamy, R.A. Hartley, R. Bohanick and M.F. Reusch, Status of the Grumman Compact Infrared FEL . . . . . 358 (1995) ABS 5
- Levin, L.A., see Arensburg, A. . . . . 358 (1995) ABS 7
- Levush, B., see Caplan, M. . . . . 358 (1995) 174
- Lewellen, J.W., J.F. Schmerge, Y.C. Huang, J. Feinstein and R.H. Pantell, Preliminary emission characteristic measurements for a \$300k FIR FEL . . . . . 358 (1995) 24
- Li, L., see Xie, J. . . . . 358 (1995) 256
- Li, Y., see Xie, J. . . . . 358 (1995) 256
- Lihn, H.C., see Crosson, E.R. . . . . 358 (1995) 216
- Lin, S., see Xie, J. . . . . 358 (1995) 256
- Lin, Z.-l., see Qian, M.-q. . . . . 358 (1995) 280
- Litvinenko, V.N., B. Burnham, J.M.J. Madey and Y. Wu, Giant laser pulses in the Duke storage ring UV FEL . . . . 358 (1995) 334
- Litvinenko, V.N., Y. Wu, B. Burnham, G. Barnett and J.M.J. Madey, mm-wave isochronous FEL and hard X-ray inverse Compton source at the Duke storage ring . . . . . 358 (1995) 345
- Litvinenko, V.N., Y. Wu, B. Burnham and J.M.J. Madey, Expected performance of the mm-wave isochronous FEL at the Duke storage ring . . . . . 358 (1995) 349
- Litvinenko, V.N., see Bakker, R.J. . . . . 358 (1995) 358
- Litvinenko, V.N., B. Burnham, J.M.J. Madey and Y. Wu, Dynamics of the Duke storage ring UV FEL . . . . . 358 (1995) 369
- Liu, H., see Neil, G.R. . . . . 358 (1995) 159
- Liu, H., J. Benesch, S. Benson, J. Bisognano, D. Douglas, G. Neil, D. Neuffer, C. Sinclair and B. Yunn, Modeling of space charge dominated performance of the CEBAF FEL injector . . . . . 358 (1995) 475
- Liu, T.K., see Allen, S.J. . . . . 358 (1995) 536
- Loos, H., see Genz, H. . . . . 358 (1995) ABS 20
- Lui, M., see Allen, S.J. . . . . 358 (1995) 536
- Luijckx, G., see Bakker, R.J. . . . . 358 (1995) 358
- Lyon, R.A. and W.B. Colson, Power requirements for high-average power FELs . . . . . 358 (1995) ABS 81
- Maas, R., see Bakker, R.J. . . . . 358 (1995) 358
- MacLeod, A.M., see Gillespie, W.A. . . . . 358 (1995) 232
- Madden, A.D., see Szarmes, E.B. . . . . 358 (1995) 220
- Madey, J.M.J., see Szarmes, E.B. . . . . 358 (1995) 220
- Madey, J.M.J., see Richman, B.A. . . . . 358 (1995) 236
- Madey, J.M.J., see McKee, C.B. . . . . 358 (1995) 264
- Madey, J.M.J., see Barnett, G.A. . . . . 358 (1995) 311
- Madey, J.M.J., see Litvinenko, V.N. . . . . 358 (1995) 334
- Madey, J.M.J., see Litvinenko, V.N. . . . . 358 (1995) 345
- Madey, J.M.J., see Litvinenko, V.N. . . . . 358 (1995) 349
- Madey, J.M.J., see Litvinenko, V.N. . . . . 358 (1995) 369
- Malov, Yu.A. and D.F. Zaretsky, A superlattice as an undulator . . . . . 358 (1995) 11
- Mandelbaum, B., see Arensburg, A. . . . . 358 (1995) ABS 7
- Manenkov, A.B., see Kleev, A.I. . . . . 358 (1995) 362
- Manheimer, W.M., see Granatstein, V.L. . . . . 358 (1995) ABS 24
- Manintveld, P., see Urbanus, W.H. . . . . 358 (1995) 155
- Marmouget, J.G., see Guimbal, Ph. . . . . 358 (1995) 240
- Marshall, T.C., see Hirshfield, J.L. . . . . 358 (1995) 129
- Marshall, T.C., see Zhang, T.B. . . . . 358 (1995) 459
- Martin, P.F., see Gillespie, W.A. . . . . 358 (1995) 232
- Marziali, A., T.I. Smith and H.A. Schwettman, Wavelength shifting in the Stanford FEL . . . . . 358 (1995) 252
- Mase, H., see Nagai, R. . . . . 358 (1995) 403
- McKee, C.B., P.G. O'Shea and J.M.J. Madey, Phase space tomography of relativistic electron beams . . . . . 358 (1995) 264
- McVey, B., see Richman, B.A. . . . . 358 (1995) 236
- Messina, G., see Giovenale, E. . . . . 358 (1995) ABS 22
- Messina, G., see Raimondi, P. . . . . 358 (1995) ABS 34
- Messina, G., see Gallerano, G.P. . . . . 358 (1995) 78
- Mikado, T., see Yamazaki, T. . . . . 358 (1995) 353
- Mikado, T., see Yokoyama, M. . . . . 358 (1995) 378
- Mikado, T., see Yamada, K. . . . . 358 (1995) 392
- Mima, K., see Kuruma, S. . . . . 358 (1995) 90
- Mima, K., see Taguchi, T. . . . . 358 (1995) 291
- Mima, K., see Asakawa, M. . . . . 358 (1995) 399
- Mima, K., see Sentoku, Y. . . . . 358 (1995) 463

- Mima, K., see Fujita, M. . . . . 358 (1995) 524
- Minamiguchi, T., see Asakawa, M. . . . . 358 (1995) 399
- Minamiguchi, T., see Fujita, M. . . . . 358 (1995) 524
- Minehara, E., see Nagai, R. . . . . 358 (1995) 403
- Minehara, E.J., R. Nagai, M. Sawamura, M. Takao, M. Sugimoto, S. Sasaki, M. Ohkubo, N. Kikuzawa, J. Sasabe, Y. Suzuki, Y. Kawarasaki and N. Shikazono, Status of the JAERI free electron laser facility driven by a superconducting rf linac . . . . . 358 (1995) ABS 30
- Minehara, E.J., see Sawamura, M. . . . . 358 (1995) ABS 73
- Minehara, E.J., see Kato, R. . . . . 358 (1995) ABS 77
- Minehara, E.J., see Sugimoto, M. . . . . 358 (1995) ABS 83
- Minestrini, M., see Castellano, M. . . . . 358 (1995) 331
- Mironov, P.V., see Karbushev, N.I. . . . . 358 (1995) 467
- Miyauchi, Y., see Tomimasu, T. . . . . 358 (1995) ABS 11
- Mizuno, T., T. Ootuki, T. Ohshima and H. Saito, Experimental mode analysis of the circular free electron laser . . . . 358 (1995) 131
- Moon, A., see Asakawa, M. . . . . 358 (1995) 399
- Moon, A., see Fujita, M. . . . . 358 (1995) 524
- Morii, Y., see Tomimasu, T. . . . . 358 (1995) ABS 11
- Musyoki, S., see Ishizuka, H. . . . . 358 (1995) ABS 63
- 
- Nagai, A., see Tomimasu, T. . . . . 358 (1995) ABS 11
- Nagai, R., H. Kobayashi, S. Sasaki, M. Sawamura, M. Sugimoto, R. Kato, N. Kikuzawa, M. Ohkubo, E. Minehara, T. Ikehata and H. Mase, Performance of the undulator for JAERI FEL project . . . . . 358 (1995) 403
- Nagai, R., see Minehara, E.J. . . . . 358 (1995) ABS 30
- Nagai, R., see Sawamura, M. . . . . 358 (1995) ABS 73
- Nagai, R., see Kato, R. . . . . 358 (1995) ABS 77
- Nagai, R., see Sugimoto, M. . . . . 358 (1995) ABS 83
- Nahon, L., see Hara, T. . . . . 358 (1995) 341
- Nahon, L., see Garzella, D. . . . . 358 (1995) 387
- Nakai, S., see Chen, J. . . . . 358 (1995) 14
- Nakai, S., see Kuruma, S. . . . . 358 (1995) 90
- Nakai, S., see Asakawa, M. . . . . 358 (1995) 399
- Nakai, S., see Sentoku, Y. . . . . 358 (1995) 463
- Nakai, S., see Fujita, M. . . . . 358 (1995) 524
- Nakajima, S., see Kawasaki, S. . . . . 358 (1995) ABS 42
- Nakao, N., see Asakawa, M. . . . . 358 (1995) 399
- Nakao, N., see Fujita, M. . . . . 358 (1995) 524
- Neil, G., see Liu, H. . . . . 358 (1995) 475
- Neil, G.R., S.V. Benson, H.F. Dylla and H. Liu, CEBAF UV/IR FEL subsystem testing and validation program . . . 358 (1995) 159
- Neuffer, D., see Liu, H. . . . . 358 (1995) 475
- Nguyen, D.C., see Goldstein, J.C. . . . . 358 (1995) ABS 36
- Nguyen, D.C., S.M. Gierman, W. Vernon and R.L. Sheffield, Conceptual design of a compact Compton backscatter X-ray source tunable from 3 to 33 keV . . . . . 358 (1995) ABS 48
- Nguyen, D.C., S.M. Gierman and P.G. O'Shea, An FEL design code running on Mathcad<sup>TM</sup> . . . . . 358 (1995) ABS 67
- Nguyen, D.C., S.M. Gierman, J.C. Goldstein, J.M. Kinross-Wright, S.H. Kong, J.G. Plato, S.J. Russell, R.L. Sheffield, F.E. Sigler, B.A. Sherwood, M.E. Weber and C. Ziomek, Recent progress of the compact AFEL at Los Alamos . . . . . 358 (1995) 27
- Nguyen, D.C., see Kong, S.H. . . . . 358 (1995) 272
- Nguyen, D.C., see Kong, S.H. . . . . 358 (1995) 276
- Nguyen, D.C., see Kong, S.H. . . . . 358 (1995) 284
- Nishihara, S., see Tomimasu, T. . . . . 358 (1995) ABS 11
- Nishimura, E., see Tomimasu, T. . . . . 358 (1995) ABS 11
- Nishimura, E., see Sacki, K. . . . . 358 (1995) ABS 56
- Nishimura, E., K. Sacki, T. Tomimasu, T. Sakai, S. Okuda and J. Ohkuma, Electron beam diagnostics for an FEL using optical transition radiation . . . . . 358 (1995) ABS 89
- Nishimura, E., see Sakai, T. . . . . 358 (1995) ABS 91
- Nishimura, E., see Yamada, K. . . . . 358 (1995) 392
- Noguchi, T., see Yamazaki, T. . . . . 358 (1995) 353
- Noguchi, T., see Yokoyama, M. . . . . 358 (1995) 378
- Noguchi, T., see Yamada, K. . . . . 358 (1995) 392

- Nölle, D., A. Geisler, M. Ridder, C. Schellnock, T. Schmidt, S. Tammen and K. Wille, The optical resonator for the FELICITA I experiment . . . . . 358 (1995) ABS 14
- Nölle, D., see Ridder, M. . . . . 358 (1995) ABS 16
- Nuhn, H.-D., see Travish, G. . . . . 358 (1995) 60
- 
- Oepts, D., D.A. Jaroszynski, H.H. Weits and P.W. van Amersfoort, Coherent spontaneous emission in FELIX . . . . . 358 (1995) 72
- Oepts, D., see Jaroszynski, D.A. . . . . 358 (1995) 228
- Oepts, D., see Knippels, G.M.H. . . . . 358 (1995) 308
- Ofitserov, M.M., see Bratman, V.L. . . . . 358 (1995) 135
- Ognivenko, V.V. and V.I. Kurilko, The ultra-relativistic FEL near the threshold of stimulated emission . . . . . 358 (1995) ABS 69
- Ohdaira, T., see Yamazaki, T. . . . . 358 (1995) 353
- Ohdaira, T., see Yamada, K. . . . . 358 (1995) 392
- Ohgaki, H., see Yamazaki, T. . . . . 358 (1995) 353
- Ohgaki, H., see Yokoyama, M. . . . . 358 (1995) 378
- Ohgaki, H., see Yamada, K. . . . . 358 (1995) 392
- Ohigashi, N., see Asakawa, M. . . . . 358 (1995) 399
- Ohigashi, N., see Fujita, M. . . . . 358 (1995) 524
- Ohkubo, M., see Minehara, E.J. . . . . 358 (1995) ABS 30
- Ohkubo, M., see Sawamura, M. . . . . 358 (1995) ABS 73
- Ohkubo, M., see Kato, R. . . . . 358 (1995) ABS 77
- Ohkubo, M., see Sugimoto, M. . . . . 358 (1995) ABS 83
- Ohkubo, M., see Nagai, R. . . . . 358 (1995) 403
- Ohkuma, J., see Nishimura, E. . . . . 358 (1995) ABS 89
- Ohkuma, J., see Sakai, T. . . . . 358 (1995) ABS 91
- Ohkuma, J., see Okuda, S. . . . . 358 (1995) 244
- Ohkuma, J., see Okuda, S. . . . . 358 (1995) 248
- Ohnishi, M., see Yoshikawa, K. . . . . 358 (1995) 295
- Ohshima, T., see Mizuno, T. . . . . 358 (1995) 131
- Ohshita, E., see Tomimasu, T. . . . . 358 (1995) ABS 11
- Okada, T., see Okuda, S. . . . . 358 (1995) 244
- Okada, T., see Okuda, S. . . . . 358 (1995) 248
- Okubo, K., see Inoue, F. . . . . 358 (1995) 407
- Okuda, S., see Nishimura, E. . . . . 358 (1995) ABS 89
- Okuda, S., see Sakai, T. . . . . 358 (1995) ABS 91
- Okuda, S., Y. Honda, N. Kimura, J. Ohkuma, T. Yamamoto, S. Suemine, T. Okada, S. Ishida, T. Yamamoto, S. Takeda, K. Tsumori and T. Hori, Free-electron laser oscillation with a multibunch electron beam of the 38 MeV L-band linear accelerator at ISIR . . . . . 358 (1995) 244
- Okuda, S., Y. Honda, N. Kimura, J. Ohkuma, T. Yamamoto, S. Suemine, T. Okada, S. Takeda, K. Tsumori and T. Hori, Single-bunch and multibunch electron beam generation for FEL experiments with the 38 MeV L-band linear accelerator at ISIR . . . . . 358 (1995) 248
- Ootuki, T., see Mizuno, T. . . . . 358 (1995) 131
- Ortega, J.M., see Prazeres, R. . . . . 358 (1995) 212
- Ortega, J.M., see Jaroszynski, D.A. . . . . 358 (1995) 224
- Ortega, J.M., see Jaroszynski, D.A. . . . . 358 (1995) 228
- O'Shea, P.G., see Nguyen, D.C. . . . . 358 (1995) ABS 67
- O'Shea, P.G., High-brightness rf photocathode guns for single pass X-ray free-electron lasers . . . . . 358 (1995) 36
- O'Shea, P.G., see McKee, C.B. . . . . 358 (1995) 264
- Osmanov, N.S., see Varfolomeev, A.A. . . . . 358 (1995) ABS 46
- Osmanov, N.S., see Varfolomeev, A.A. . . . . 358 (1995) 70
- Osmanov, N.S., see Varfolomeev, A.A. . . . . 358 (1995) 396
- Ozaki, T., see Takayama, K. . . . . 358 (1995) 122
- 
- Pan, Q., see Qian, M.-q. . . . . 358 (1995) 280
- Pandya, T.P., see Srivastava, A. . . . . 358 (1995) ABS 50
- Pantell, R.H., see Lewellen, J.W. . . . . 358 (1995) 24
- Pantell, R.H., see Huang, Y.C. . . . . 358 (1995) 315
- Papadichev, V.A., A new method of equalizing  $\beta_{||}$  (conditioning) in an electron beam propagating in a longitudinal magnetic field . . . . . 358 (1995) ABS 79
- Papadichev, V.A., Betatron oscillations, undulator acceptance and beam conditioning ( $\beta_{||}(r) = \text{const.}$ ) taking space charge effects into account . . . . . 358 (1995) 418

- Papadichev, V.A., Fourier analysis for the rapid calculation of distorted undulator orbits and their correction . . . . . 358 (1995) 429
- Park, E.H., J.K. Lee and T.H. Chung, Self-oscillations and chaos of free-electron laser oscillators with space charge effects. . . . . 358 (1995) 448
- Patteri, P., see Castellano, M. . . . . 358 (1995) 331
- Pellegrini, C., see Travish, G. . . . . 358 (1995) ABS 75
- Pellegrini, C., see Travish, G. . . . . 358 (1995) 60
- Perelstein, E.A., see Denisov, G.G. . . . . 358 (1995) 528
- Perregrini, L., see Arcioni, P. . . . . 358 (1995) 108
- Pershing, D.E., R.D. Seeley, R.H. Jackson and H.P. Freund, Amplifier performance of the NRL ubitron . . . . . 358 (1995) 104
- Pershing, D.E., see Freund, H.P. . . . . 358 (1995) 139
- Pershing, D.E., see Freund, H.P. . . . . 358 (1995) 163
- Pershing, D.E., see Taccetti, J.M. . . . . 358 (1995) 193
- Peskov, N.Yu., see Arzhannikov, A.V. . . . . 358 (1995) 112
- Peskov, N.Yu., see Ginzburg, N.S. . . . . 358 (1995) 189
- Petelin, M.I., see Bratman, V.L. . . . . 358 (1995) 135
- Pierini, P., see Arcioni, P. . . . . 358 (1995) 108
- Pinhasi, Y., see Arensburg, A. . . . . 358 (1995) ABS 7
- Pinhasi, Y., see Cohen, M. . . . . 358 (1995) 82
- Pinhasi, Y. and A. Gover, Mode-locked super-radiant free-electron laser oscillator . . . . . 358 (1995) 86
- Pinhasi, Y., see Yakover, I.M. . . . . 358 (1995) 323
- Pitatelev, M.M., see Bazylev, V.A. . . . . 358 (1995) 64
- Pitatelev, M.M., see Bazylev, V. . . . . 358 (1995) 433
- Plato, J.G., see Ziomek, C.D. . . . . 358 (1995) ABS 87
- Plato, J.G., see Nguyen, D.C. . . . . 358 (1995) 27
- Pranal, Y., see Guimbal, Ph. . . . . 358 (1995) 240
- Prazeres, R., J.M. Berset, F. Glotin, D. Jaroszynski and J.M. Ortega, Sub-picosecond laser pulse generation on the CLIO FEL . . . . . 358 (1995) 212
- Prazeres, R., see Jaroszynski, D.A. . . . . 358 (1995) 224
- Prazeres, R., see Jaroszynski, D.A. . . . . 358 (1995) 228
- Qian, M.-q., M.-r. Yang, Q. Pan, K.-s. Hu, R.-p. Deng, J.-j. Shi, Z.-c. Tao, J.-b. Cheng, Q.-j. Ran and Z.-l. Lin, Photoemission studies on LaB<sub>6</sub> and pure metals using a nanosecond KrF excimer laser . . . . . 358 (1995) 280
- Quick, D.D., see Kelsey, E. . . . . 358 (1995) ABS 61
- Raimondi, P., see Giovenale, E. . . . . 358 (1995) ABS 22
- Raimondi, P. and G. Messina, High gradient linac for compact FELs . . . . . 358 (1995) ABS 34
- Ran, Q.-j., see Qian, M.-q. . . . . 358 (1995) 280
- Raubenheimer, T.O., Electron beam acceleration and compression for short wavelength FELs . . . . . 358 (1995) 40
- Read, M.E., see Freund, H.P. . . . . 358 (1995) 163
- Reichenbach, M., see Genz, H. . . . . 358 (1995) ABS 20
- Renieri, A., see Giovenale, E. . . . . 358 (1995) ABS 22
- Renieri, A., see Dattoli, G. . . . . 358 (1995) 338
- Renz, G. and G. Spindler, Status of the Stuttgart Raman free-electron laser project . . . . . 358 (1995) ABS 13
- Reusch, M.F., see Lehrman, I.S. . . . . 358 (1995) ABS 5
- Richman, B.A., E.R. Crosson, R.L. Swent, H.A. Schwettman and T.I. Smith, Characterization of the mid-IR FEL at Stanford. . . . . 358 (1995) ABS 32
- Richman, B.A., Simple theory of simultaneous harmonics operation of an FEL. . . . . 358 (1995) ABS 71
- Richman, B.A., B. McVey and J.M.J. Madey, Experimental measurement of short pulse guiding effects in a free-electron laser . . . . . 358 (1995) 236
- Richman, B.A., see Berryman, K.W. . . . . 358 (1995) 260
- Richman, B.A., K.W. DeLong and R. Trebino, Temporal characterization of the Stanford mid-IR FEL micropulses by "FROG". . . . . 358 (1995) 268
- Richman, B.A., see Berryman, K.W. . . . . 358 (1995) 300
- Richter, A., see Genz, H. . . . . 358 (1995) ABS 20
- Ridder, M., see Nölle, D. . . . . 358 (1995) ABS 14
- Ridder, M., A. Geisler, D. Nölle, T. Schmidt and S. Suermann, Magnetic measurements of the electromagnetic undulator for the FELICITA I experiment. . . . . 358 (1995) ABS 16
- Ride, S.K., see Golightly, W.J. . . . . 358 (1995) 504
- Rosenberg, A., see Arensburg, A. . . . . 358 (1995) ABS 7
- Rosenzweig, J., see Travish, G. . . . . 358 (1995) ABS 75
- Rozanov, N.E., see Golub, Yu.Ya. . . . . 358 (1995) 479

- Rullier, J.L., J. Gardelle, J. Labrousche and P. Le Taillandier, Strong coupling operation of a FEL amplifier with an axial magnetic field . . . . . 358 (1995) 118
- Rullier, J.L., see Donohue, J.T. . . . . 358 (1995) 422
- Russell, S.J., see Nguyen, D.C. . . . . 358 (1995) 27
- Ruvinsky, I., see Shahadi, A. . . . . 358 (1995) 143
- Sabary, F., see Guimbal, Ph. . . . . 358 (1995) 240
- Saeki, K., see Tomimasu, T. . . . . 358 (1995) ABS 11
- Saeki, K., E. Nishimura, A. Kobayashi, S. Abe, A. Zako, M. Yasumoto and T. Tomimasu, Optical cavity and transport system for FELI . . . . . 358 (1995) ABS 56
- Saeki, K., see Nishimura, E. . . . . 358 (1995) ABS 89
- Saeki, K., see Sakai, T. . . . . 358 (1995) ABS 91
- Saeki, K., see Yamada, K. . . . . 358 (1995) 392
- Saito, H., see Mizuno, T. . . . . 358 (1995) 131
- Sakai, T., see Nishimura, E. . . . . 358 (1995) ABS 89
- Sakai, T., T. Yamamoto, S. Okuda, J. Ohkuma, E. Nishimura, K. Saeki, A. Kobayashi and T. Tomimasu, Development of the quasi non-destructive electron beam diagnostic method and the measurement of beam emittance . . . . . 358 (1995) ABS 91
- Sakamoto, K., see Ishizuka, H. . . . . 358 (1995) ABS 63
- Salop, A., see Urbanus, W.H. . . . . 358 (1995) 155
- Samsonov, S.V., see Bratman, V.L. . . . . 358 (1995) 135
- Sasabe, J., see Minehara, E.J. . . . . 358 (1995) ABS 30
- Sasaki, S., see Minehara, E.J. . . . . 358 (1995) ABS 30
- Sasaki, S., see Nagai, R. . . . . 358 (1995) 403
- Savilov, A.V., see Bratman, V.L. . . . . 358 (1995) 182
- Savilov, A.V., see Denisov, G.G. . . . . 358 (1995) 528
- Sawamura, M., see Minehara, E.J. . . . . 358 (1995) ABS 30
- Sawamura, M., E.J. Minehara, R. Nagai, M. Sugimoto, M. Takao, R. Kato, N. Kikuzawa and M. Ohkubo, RF systems for JAERI FEL linac . . . . . 358 (1995) ABS 73
- Sawamura, M., see Kato, R. . . . . 358 (1995) ABS 77
- Sawamura, M., see Sugimoto, M. . . . . 358 (1995) ABS 83
- Sawamura, M., see Nagai, R. . . . . 358 (1995) 403
- Sazhin, V.D., see Karbushev, N.I. . . . . 358 (1995) 467
- Schellnock, C., see Nölle, D. . . . . 358 (1995) ABS 14
- Schep, T., see Bazylev, V. . . . . 358 (1995) 433
- Schep, T.J., see Eecen, P.J. . . . . 358 (1995) 178
- Schep, T.J., see van Werkhoven, G.H.C. . . . . 358 (1995) 304
- Schep, T.J., see van Werkhoven, G.H.C. . . . . 358 (1995) 485
- Schlott, V., see Genz, H. . . . . 358 (1995) ABS 20
- Schlueter, R.D., Undulators for short wavelength FEL amplifiers . . . . . 358 (1995) 44
- Schmerge, J.F., see Lewellen, J.W. . . . . 358 (1995) 24
- Schmerge, J.F., see Huang, Y.C. . . . . 358 (1995) 315
- Schmidt, T., see Nölle, D. . . . . 358 (1995) ABS 14
- Schmidt, T., see Ridder, M. . . . . 358 (1995) ABS 16
- Schwettman, H.A., see Richman, B.A. . . . . 358 (1995) ABS 32
- Schwettman, H.A., see Haar, P. . . . . 358 (1995) ABS 40
- Schwettman, H.A., see Leemans, W.P. . . . . 358 (1995) 208
- Schwettman, H.A., see Marziani, A. . . . . 358 (1995) 252
- Schwettman, H.A., see Berryman, K.W. . . . . 358 (1995) 300
- Schwettman, H.A., see Haar, P. . . . . 358 (1995) 319
- Scott, J.S., see Allen, S.J. . . . . 358 (1995) 536
- Seeley, R.D., see Pershing, D.E. . . . . 358 (1995) 104
- Sei, N., see Yamazaki, T. . . . . 358 (1995) 353
- Sei, N., see Yokoyama, M. . . . . 358 (1995) 378
- Sei, N., see Yamada, K. . . . . 358 (1995) 392
- Sentoku, Y., H. Furukawa, K. Mima, T. Taguchi, S. Kuruma, H. Yasuda, C. Yamanaka and S. Nakai, 3D simulations on output power fluctuation in a short bunch rf-linac FEL . . . . . 358 (1995) 463
- Sergeev, A.S., see Ginzburg, N.S. . . . . 358 (1995) 189
- Sergeev, A.S., see Denisov, G.G. . . . . 358 (1995) 528
- Serov, A.V., see Koltsov, A.V. . . . . 358 (1995) 444
- Shahadi, A., see Korol, M. . . . . 358 (1995) ABS 54

- Shahadi, A., E. Jerby, M. Korol, R. Drori, M. Sheinin, V. Dikhtiar, V. Grinberg, I. Ruvinsky, M. Bensal, T. Harhel, Y. Baron, A. Fruchtman, V.L. Granatstein and G. Bekefi, Cyclotron resonance maser experiment in a non-dispersive waveguide . . . . . 358 (1995) 143
- Shahadi, A., see Drori, R. . . . . 358 (1995) 151
- Shahadi, A., see Grinberg, V. . . . . 358 (1995) 327
- Shahal, O., see Arensburg, A. . . . . 358 (1995) ABS 7
- Shapira, M., see Arensburg, A. . . . . 358 (1995) ABS 7
- Sheffield, R., see Edighoffer, J. . . . . 358 (1995) 18
- Sheffield, R.L., see Nguyen, D.C. . . . . 358 (1995) ABS 48
- Sheffield, R.L., see Nguyen, D.C. . . . . 358 (1995) 27
- Sheffield, R.L., see Kong, S.H. . . . . 358 (1995) 272
- Sheffield, R.L., see Kong, S.H. . . . . 358 (1995) 276
- Sheffield, R.L., see Kong, S.H. . . . . 358 (1995) 284
- Sheinin, M., see Shahadi, A. . . . . 358 (1995) 143
- Sherwin, M.S., see Allen, S.J. . . . . 358 (1995) 536
- Sherwood, B.A., see Nguyen, D.C. . . . . 358 (1995) 27
- Sherwood, B.A., see Kong, S.H. . . . . 358 (1995) 276
- Shi, J.-j., see Qian, M.-q. . . . . 358 (1995) 280
- Shiho, M., see Kawasaki, S. . . . . 358 (1995) ABS 42
- Shiho, M., see Ishizuka, H. . . . . 358 (1995) ABS 63
- Shiho, M., see Kawasaki, S. . . . . 358 (1995) 114
- Shikazono, N., see Minchira, E.J. . . . . 358 (1995) ABS 30
- Shiloh, J., see Arensburg, A. . . . . 358 (1995) ABS 7
- Shimizu, T., see Yamada, K. . . . . 358 (1995) 392
- Shinzato, T., see Yoshikawa, K. . . . . 358 (1995) 295
- Shternghartz, V., see Arensburg, A. . . . . 358 (1995) ABS 7
- Shu, X., see Ding, W. . . . . 358 (1995) ABS 65
- Shukla, R.K., see Srivastava, A. . . . . 358 (1995) ABS 50
- Shvets, G. and J.S. Wurtele, Green function analysis of a Raman FEL . . . . . 358 (1995) 147
- Shvets, G., see Ishii, S. . . . . 358 (1995) 489
- Sigler, F.E., see Nguyen, D.C. . . . . 358 (1995) 27
- Silivra, A.A. and I.A. Goncharov, Features of operation of a FEL with reversed guide field . . . . . 358 (1995) 452
- Silivra, A.A., E.D. Belyavskiy and I.A. Goncharov, Optimization of the free electron laser interaction via electron bunch trapping . . . . . 358 (1995) 512
- Sinclair, C., see Liu, H. . . . . 358 (1995) 475
- Sinitsky, S.L., see Arzhannikov, A.V. . . . . 358 (1995) 112
- Sinitsky, S.L., see Ginzburg, N.S. . . . . 358 (1995) 189
- Small, D.W., R.K. Wong, J. Blau and W.B. Colson, Simulations of the Stanford FIREFLY 1 kW free electron laser . . . . . 358 (1995) ABS 44
- Smirnov, A.V., see Varfolomeev, A.A. . . . . 358 (1995) 197
- Smith, T.I., see Richman, B.A. . . . . 358 (1995) ABS 32
- Smith, T.I., see Haar, P. . . . . 358 (1995) ABS 40
- Smith, T.I., see Berryman, K.W. . . . . 358 (1995) ABS 93
- Smith, T.I., see Leemans, W.P. . . . . 358 (1995) 208
- Smith, T.I., see Crosson, E.R. . . . . 358 (1995) 216
- Smith, T.I., see Marziali, A. . . . . 358 (1995) 252
- Smith, T.I., see Berryman, K.W. . . . . 358 (1995) 300
- Smith, T.I., see Haar, P. . . . . 358 (1995) 319
- Sokolovsky, J., see Arensburg, A. . . . . 358 (1995) ABS 7
- Solomon, L., W.S. Graves and I. Lehrman, Magnetic field measurements of the harmonic generation FEL superconducting undulator at BNL-NSLS . . . . . 358 (1995) 411
- Solomon, L., see Graves, W.S. . . . . 358 (1995) 414
- Spassovsky, I., see Giovenale, E. . . . . 358 (1995) ABS 9
- Spassovsky, I., see Giovenale, E. . . . . 358 (1995) ABS 22
- Spindler, G., see Renz, G. . . . . 358 (1995) ABS 13
- Sprangle, P.A., see Hirshfield, J.L. . . . . 358 (1995) 129
- Srivastava, A., L.M. Bali, T.P. Pandya, P. Jha and R.K. Shukla, Three dimensional simulation of an FEL amplifier with an axial field . . . . . 358 (1995) ABS 50
- Sterk, A.B., see Urbanus, W.H. . . . . 358 (1995) 155
- Striby, S., see Guimbal, Ph. . . . . 358 (1995) 240
- Su, J., see Xie, J. . . . . 358 (1995) 256
- Suemine, S., see Okuda, S. . . . . 358 (1995) 244



- Suemine, S., see Okuda, S. . . . . 358 (1995) 248  
 Suermann, S., see Ridder, M. . . . . 358 (1995) ABS 16  
 Sugimoto, M., see Minehara, E.J. . . . . 358 (1995) ABS 30  
 Sugimoto, M., see Sawamura, M. . . . . 358 (1995) ABS 73  
 Sugimoto, M., see Kato, R. . . . . 358 (1995) ABS 77  
 Sugimoto, M., R. Nagai, R. Kato, M. Sawamura, M. Takao, N. Kikuzawa, M. Ohkubo and E.J. Minehara, Operator supports for the JAERI FEL . . . . . 358 (1995) ABS 83  
 Sugimoto, M., see Nagai, R. . . . . 358 (1995) 403  
 Sugiyama, S., see Yamazaki, T. . . . . 358 (1995) 353  
 Sugiyama, S., see Yokoyama, M. . . . . 358 (1995) 378  
 Sugiyama, S., see Yamada, K. . . . . 358 (1995) 392  
 Sumbaev, A.P., see Denisov, G.G. . . . . 358 (1995) 528  
 Suzuki, R., see Yamazaki, T. . . . . 358 (1995) 353  
 Suzuki, R., see Yokoyama, M. . . . . 358 (1995) 378  
 Suzuki, R., see Yamada, K. . . . . 358 (1995) 392  
 Suzuki, Y., see Minehara, E.J. . . . . 358 (1995) ABS 30  
 Suzuki, Y., see Kato, R. . . . . 358 (1995) ABS 77  
 Swent, R.L., see Richman, B.A. . . . . 358 (1995) ABS 32  
 Swent, R.L., see Leemans, W.P. . . . . 358 (1995) 208  
 Swent, R.L., see Crosson, E.R. . . . . 358 (1995) 216  
 Swent, R.L., see Berryman, K.W. . . . . 358 (1995) 300  
 Swent, R.L. and K.W. Berryman, FEL gain calculation for imperfectly matched electron beams . . . . . 358 (1995) 482  
 Swyden, T.A., see Tang, C.M. . . . . 358 (1995) 7  
 Sytova, S., see Baryshevsky, V.G. . . . . 358 (1995) 508  
 Szarmes, E.B., A.D. Madden and J.M.J. Madey, Observation and characterization of frequency-chirped optical pulses on the Mark III free-electron laser . . . . . 358 (1995) 220  
 Szarmes, E.B., see Barnett, G.A. . . . . 358 (1995) 311
- Taccetti, J.M., see Freund, H.P. . . . . 358 (1995) 139  
 Taccetti, J.M., see Freund, H.P. . . . . 358 (1995) 163  
 Taccetti, J.M., R.H. Jackson, H.P. Freund, D.E. Pershing, M. Blank and V.L. Granatstein, Design and performance calculations for a  $K_{\alpha}$ -band CHI wiggler ubitron amplifier . . . . . 358 (1995) 193  
 Taguchi, T. and K. Mima, Laser cooling of an electron beam by the coherent scattering of a strong laser beam . . . . . 358 (1995) 291  
 Taguchi, T., see Sentoku, Y. . . . . 358 (1995) 463  
 Takahashi, M., see Inoue, F. . . . . 358 (1995) 407  
 Takao, M., see Minehara, E.J. . . . . 358 (1995) ABS 30  
 Takao, M., see Sawamura, M. . . . . 358 (1995) ABS 73  
 Takao, M., see Kato, R. . . . . 358 (1995) ABS 77  
 Takao, M., see Sugimoto, M. . . . . 358 (1995) ABS 83  
 Takayama, K., see Kawasaki, S. . . . . 358 (1995) ABS 42  
 Takayama, K., J. Kishiro, K. Ebihara, T. Ozaki, S. Hiramatsu and H. Katoh, Experimental results on the 1.5 MeV ion-channel guided X-band free-electron laser . . . . . 358 (1995) 122  
 Takeda, H., see Goldstein, J.C. . . . . 358 (1995) ABS 36  
 Takeda, S., see Okuda, S. . . . . 358 (1995) 244  
 Takeda, S., see Okuda, S. . . . . 358 (1995) 248  
 Tammen, S., see Nölle, D. . . . . 358 (1995) ABS 14  
 Tang, C.M., M. Goldstein, T.A. Swyden and J.E. Walsh, Free electron micro-lasers . . . . . 358 (1995) 7  
 Tao, Z.-c., see Qian, M.-q. . . . . 358 (1995) 280  
 Tarasov, A.V., see Arzhannikov, A.V. . . . . 358 (1995) 112  
 Tatchyn, R., Particle beam modulation techniques for the generation of subfemtosecond photon pulses in the VUV/soft X-ray range. . . . . 358 (1995) 56  
 Tazzioli, F., see Castellano, M. . . . . 358 (1995) 331  
 Thomas, M., see Genz, H. . . . . 358 (1995) ABS 20  
 Tokmakoff, A., A. Kowk, R. Urhda, D.A. Zimdars and M.D. Fayer, Vibrational dynamics in condensed matter probed with linac based FELs . . . . . 358 (1995) 540  
 Tokuti, A., see Kawasaki, S. . . . . 358 (1995) ABS 42  
 Tolmachev, S.V., see Varfolomeev, A.A. . . . . 358 (1995) ABS 46  
 Tolmachev, S.V., see Varfolomeev, A.A. . . . . 358 (1995) 70  
 Tolmachev, S.V., see Varfolomeev, A.A. . . . . 358 (1995) 396  
 Tomimasu, T., Y. Morii, E. Ohshita, S. Abe, S. Nishihara, A. Koga, Y. Miyauchi, A. Zakou, E. Nishimura, K. Saeki, A. Kobayashi, M. Yasumoto, E. Tongu and A. Nagai, Commissioning the FELI linac and IR-FEL facilities . . . . . 358 (1995) ABS 11

- Tomimasu, T., see Saeki, K. . . . . 358 (1995) ABS 56
- Tomimasu, T., see Nishimura, E. . . . . 358 (1995) ABS 89
- Tomimasu, T., see Sakai, T. . . . . 358 (1995) ABS 91
- Tomimasu, T., see Yamada, K. . . . . 358 (1995) 392
- Tongu, E., see Tomimasu, T. . . . . 358 (1995) ABS 11
- Töpper, J., see Genz, H. . . . . 358 (1995) ABS 20
- Touati, D., see Guimbal, Ph. . . . . 358 (1995) 240
- Travish, G., M. Hogan, C. Pellegrini and J. Rosenzweig, The UCLA high gain infrared FEL . . . . . 358 (1995) ABS 75
- Travish, G., Performance simulation and parameter optimization for high gain short wavelength FEL amplifiers . . . . . 358 (1995) 48
- Travish, G., W.M. Fawley, K.-J. Kim, H.-D. Nuhn, C. Pellegrini, H. Winick and M. Xie, Parametric study of an X-ray FEL . . . . . 358 (1995) 60
- Trebino, R., see Richman, B.A. . . . . 358 (1995) 268
- Trippetti, R., see Giovenale, E. . . . . 358 (1995) ABS 9
- Tsumori, K., see Okuda, S. . . . . 358 (1995) 244
- Tsumori, K., see Okuda, S. . . . . 358 (1995) 248
- Tsunawaki, Y., see Asakawa, M. . . . . 358 (1995) 399
- Tsunawaki, Y., see Fujita, M. . . . . 358 (1995) 524
- Tulupov, A., see Caplan, M. . . . . 358 (1995) 174
- Tulupov, A., see Bazylev, V. . . . . 358 (1995) 433
- Tulupov, A.V., Enhanced harmonic generation from a focussing two-period undulator . . . . . 358 (1995) ABS 18
- Tulupov, A.V., see Urbanus, W.H. . . . . 358 (1995) 155
- Tulupov, A.V., see Eecen, P.J. . . . . 358 (1995) 178
- Uhm, Y.-W., see Kim, C.-B. . . . . 358 (1995) 516
- Unterrainer, K., see Allen, S.J. . . . . 358 (1995) 536
- Urbanus, W., see Caplan, M. . . . . 358 (1995) 174
- Urbanus, W.H., W.A. Bongers, G. van Dijk, C.A.J. van der Geer, J.P. van Ieperen, A. van der Linden, P. Man-  
intveld, A.B. Sterk, A.V. Tulupov, A.G.A. Verhoeven, M.J. van der Wiel, V.L. Bratman, G.G. Denisov, A.A.  
Varfolomeev, S.N. Ivanchenkov, A.S. Khlebnikov, M. Catellino, A. Salop and M. Caplan, A 130–260 GHz, 1  
MW free electron maser for fusion . . . . . 358 (1995) 155
- Urbanus, W.H., see Varfolomeev, A.A. . . . . 358 (1995) 396
- Urhdal, R., see Tokmakoff, A. . . . . 358 (1995) 540
- Van Amersfoort, P.W., see Haselhoff, E.H. . . . . 358 (1995) ABS 28
- Van Amersfoort, P.W., see Oepts, D. . . . . 358 (1995) 72
- Van Amersfoort, P.W., see Jaroszynski, D.A. . . . . 358 (1995) 228
- Van Amersfoort, P.W., see Gillespie, W.A. . . . . 358 (1995) 232
- Van Amersfoort, P.W., see Knippels, G.M.H. . . . . 358 (1995) 308
- Van Amersfoort, P.W., see Bakker, R.J. . . . . 358 (1995) 358
- Van der Geer, B., M.J. de Loos, M.E. Conde and W.P. Leemans, Wavelength and power stability measurements of  
the Stanford SCA/FEL . . . . . 358 (1995) ABS 59
- Van der Geer, B., see Leemans, W.P. . . . . 358 (1995) 208
- Van der Geer, C.A.J., see Urbanus, W.H. . . . . 358 (1995) 155
- Van der Linden, A., see Urbanus, W.H. . . . . 358 (1995) 155
- Van der Meer, A.F.G., see Jaroszynski, D.A. . . . . 358 (1995) 228
- Van der Meer, A.F.G., see Gillespie, W.A. . . . . 358 (1995) 232
- Van der Slot, P.J.M., J. Couperus, W.J. Witteman, A.N. Lebedev, E.G. Krastelev, A.V. Agafonov, V.S. Voronin and  
V.A. Krasnopolsky, A Cherenkov free electron laser with high peak power . . . . . 358 (1995) 100
- Van der Slot, P.J.M., see Zambon, P. . . . . 358 (1995) 126
- Van der Wiel, M.J., see Urbanus, W.H. . . . . 358 (1995) 155
- Van der Wiel, M.J., see Varfolomeev, A.A. . . . . 358 (1995) 396
- Van Dijk, G., see Urbanus, W.H. . . . . 358 (1995) 155
- Van Ieperen, J.P., see Urbanus, W.H. . . . . 358 (1995) 155
- Van Oerle, B.M. and G.J. Ernst, On the use of CsK<sub>2</sub>Sb photocathodes in RF linacs . . . . . 358 (1995) 287
- Van Werkhoven, G.H.C., B. Faatz and T.J. Schep, The influence of hole-coupling on the transverse structure of  
intra-cavity light pulses . . . . . 358 (1995) 304
- Van Werkhoven, G.H.C., see Knippels, G.M.H. . . . . 358 (1995) 308
- Van Werkhoven, G.H.C. and T.J. Schep, Non-linear macroscopic equations for pulse evolution in a high-gain  
Compton FEL . . . . . 358 (1995) 485
- Varfolomeev, A.A., A.S. Khlebnikov, N.S. Osmanov and S.V. Tolmachev, Improved wire deflection method for  
magnetic field measurements in long undulators . . . . . 358 (1995) ABS 46

- Varfolomeev, A.A., V.V. Gubankov, A.H. Hairetdinov, S.N. Ivanchenkov, A.S. Khlebnikov, N.S. Osmanov and S.V. Tolmachev, Mock-up of the focusing undulator for the SLAC X-ray FEL project. . . . . 358 (1995) 70
- Varfolomeev, A.A., see Urbanus, W.H. . . . . 358 (1995) 155
- Varfolomeev, A.A. and A.V. Smirnov, Beam transport through undulators designed for high power FEMs . . . . . 358 (1995) 197
- Varfolomeev, A.A., Yu.P. Bouzouloukov, S.N. Ivanchenkov, A.S. Khlebnikov, N.S. Osmanov, S.V. Tolmachev, W.H. Urbanus and M.J. van der Wiel, Magnetic field full test of two-section KIAE-4 undulator. . . . . 358 (1995) 396
- Varfolomeev, A.A. and A.H. Hairetdinov, Focusing properties of an undulator with anharmonic magnetic fields . . . . . 358 (1995) 426
- Verhoeven, A.G.A., see Urbanus, W.H. . . . . 358 (1995) 155
- Vernon, W., see Nguyen, D.C. . . . . 358 (1995) ABS 48
- Verschuur, J.W.J., G.J. Ernst and W.J. Witteman, The "TEUFEL" undulator . . . . . 358 (1995) ABS 85
- Voronin, V.S., see van der Slot, P.J.M. . . . . 358 (1995) 100
- Walsh, J.E., see Tang, C.M. . . . . 358 (1995) 7
- Wang, G., see Xie, J. . . . . 358 (1995) 256
- Wang, M.C., J. Zhu, Z. Wang, J.K. Lee and T.H. Chung, Design of the pseudospark discharge for a Raman FEL . . . . . 358 (1995) ABS 38
- Wang, Y., see Xie, J. . . . . 358 (1995) 256
- Wang, Z., see Wang, M.C. . . . . 358 (1995) ABS 38
- Wanke, M., see Allen, S.J. . . . . 358 (1995) 536
- Watanabe, A., see Kawasaki, S. . . . . 358 (1995) ABS 42
- Watanabe, A., see Ishizuka, H. . . . . 358 (1995) ABS 63
- Watanabe, A., see Kawasaki, S. . . . . 358 (1995) 114
- Weber, M.E., see Nguyen, D.C. . . . . 358 (1995) 27
- Weber, M.E., see Kong, S.H. . . . . 358 (1995) 284
- Weits, H.H., see Oepts, D. . . . . 358 (1995) 72
- Wesp, T., see Genz, H. . . . . 358 (1995) ABS 20
- Wiedemann, H., see Crosson, E.R. . . . . 358 (1995) 216
- Wiencken, M., see Genz, H. . . . . 358 (1995) ABS 20
- Wille, K., see Nölle, D. . . . . 358 (1995) ABS 14
- Winick, H., see Travish, G. . . . . 358 (1995) 60
- Winter, G.H., J. Hall, R.K. Wong and W.B. Colson, Simulations of a klystron undulator for the SLAC X-ray FEL. . . . . 358 (1995) 68
- Witteman, W.J., see Verschuur, J.W.J. . . . . 358 (1995) ABS 85
- Witteman, W.J., see van der Slot, P.J.M. . . . . 358 (1995) 100
- Witteman, W.J., see Zambon, P. . . . . 358 (1995) 126
- Wong, R.K. and W.B. Colson, Frequency response to an electron energy shift . . . . . 358 (1995) ABS 26
- Wong, R.K., see Small, D.W. . . . . 358 (1995) ABS 44
- Wong, R.K., see Kelsey, E. . . . . 358 (1995) ABS 61
- Wong, R.K., see Winter, G.H. . . . . 358 (1995) 68
- Wong, R.K., see Blau, J. . . . . 358 (1995) 441
- Wu, G., see Xie, J. . . . . 358 (1995) 256
- Wu, Y., see Litvinenko, V.N. . . . . 358 (1995) 334
- Wu, Y., see Litvinenko, V.N. . . . . 358 (1995) 345
- Wu, Y., see Litvinenko, V.N. . . . . 358 (1995) 349
- Wu, Y., see Litvinenko, V.N. . . . . 358 (1995) 369
- Wurtele, J.S., see Shvets, G. . . . . 358 (1995) 147
- Wurtele, J.S., see Ishii, S. . . . . 358 (1995) 489
- Xie, J., J. Zhuang, Y. Huang, Y. Li, S. Lin, R. Ying, Y. Zhong, L. Zhang, G. Wu, Y. Zhang, C. Chao, L. Li, E. Fu, J. Su, Y. Wang and G. Wang, The saturation of the Beijing FEL. . . . . 358 (1995) 256
- Xie, M., see Edighoffer, J. . . . . 358 (1995) 18
- Xie, M., see Travish, G. . . . . 358 (1995) 60
- Yakover, I., see Cohen, M. . . . . 358 (1995) 82
- Yakover, I.M., see Arensburg, A. . . . . 358 (1995) ABS 7
- Yakover, I.M., Y. Pinhasi and A. Gover, Resonator design and characterization for the Israeli tandem electrostatic FEL project . . . . . 358 (1995) 323
- Yamada, H., see Kleev, A.I. . . . . 358 (1995) 362
- Yamada, K., see Yamazaki, T. . . . . 358 (1995) 353
- Yamada, K., see Yokoyama, M. . . . . 358 (1995) 378
- Yamada, K., T. Yamazaki, N. Sci, T. Shimizu, R. Suzuki, T. Ohdaira, M. Kawai, M. Yokoyama, S. Hamada, K. Saeki, E. Nishimura, T. Mikado, T. Noguchi, S. Sugiyama, M. Chiwaki, H. Ohgaki and T. Tomimasu, Degradation and restoration of dielectric-coated cavity mirrors in the NIJI-IV FEL. . . . . 358 (1995) 392

- Yamamoto, T., see Sakai, T. . . . . 358 (1995) ABS 91
- Yamamoto, T., see Okuda, S. . . . . 358 (1995) 244
- Yamamoto, T., see Okuda, S. . . . . 358 (1995) 244
- Yamamoto, T., see Okuda, S. . . . . 358 (1995) 248
- Yamamoto, Y., see Yoshikawa, K. . . . . 358 (1995) 295
- Yamanaka, C., see Chen, J. . . . . 358 (1995) 14
- Yamanaka, C., see Kuruma, S. . . . . 358 (1995) 90
- Yamanaka, C., see Asakawa, M. . . . . 358 (1995) 399
- Yamanaka, C., see Sentoku, Y. . . . . 358 (1995) 463
- Yamanaka, C., see Fujita, M. . . . . 358 (1995) 524
- Yamanaka, T., see Inoue, F. . . . . 358 (1995) 407
- Yamashita, Y., see Kawasaki, S. . . . . 358 (1995) ABS 42
- Yamazaki, J., see Hama, H. . . . . 358 (1995) 365
- Yamazaki, T., see Yoshikawa, K. . . . . 358 (1995) 295
- Yamazaki, T., K. Yamada, N. Sei, H. Ohgaki, S. Sugiyama, T. Mikado, R. Suzuki, T. Noguchi, M. Chiwaki, T. Ohdaira, M. Kawai, M. Yokoyama, S. Hamada and A. Iwata, Lasing in the ultraviolet region with the NIJI-IV storage-ring free-electron laser. . . . . 358 (1995) 353
- Yamazaki, T., see Yokoyama, M. . . . . 358 (1995) 378
- Yamazaki, T., see Yamada, K. . . . . 358 (1995) 392
- Yang, M.-r., see Qian, M.-q. . . . . 358 (1995) 280
- Yasuda, H., see Sentoku, Y. . . . . 358 (1995) 463
- Yasumoto, M., see Tomimasu, T. . . . . 358 (1995) ABS 11
- Yasumoto, M., see Saeki, K. . . . . 358 (1995) ABS 56
- Yeom, K.H., J.K. Lee and T.H. Chung, Wiggler-free FEL with an intense helical beam . . . . . 358 (1995) ABS 52
- Ying, R., see Xie, J. . . . . 358 (1995) 256
- Yokoyama, M., see Yamazaki, T. . . . . 358 (1995) 353
- Yokoyama, M., N. Sei, M. Kawai, K. Yamada, S. Hamada, S. Sugiyama, H. Ohgaki, T. Mikado, T. Noguchi, R. Suzuki, M. Chiwaki and T. Yamazaki, Effects of an optical klystron on the electron beam of the storage ring NIJI-IV for free-electron lasers . . . . . 358 (1995) 378
- Yokoyama, M., see Yamada, K. . . . . 358 (1995) 392
- Yoshikawa, K., T. Shinzato, Y. Yamamoto, M. Ohnishi and T. Yamazaki, Visualization of spatial profiles of spectra and intensities in FEL simulations . . . . . 358 (1995) 295
- Yu, J. and W.A. Gillespie, Nonlinear evolution of the equilibrium electron orbits in a helical wiggler with a positive axial guide magnetic field at magnetoresonance . . . . . 358 (1995) 471
- Yu, L.H., Femtosecond deep UV pulse by high gain harmonic generation from a chirped seed. . . . . 358 (1995) 74
- Yunn, B., see Liu, H. . . . . 358 (1995) 475
- Zako, A., see Saeki, K. . . . . 358 (1995) ABS 56
- Zakou, A., see Tomimasu, T. . . . . 358 (1995) ABS 11
- Zambon, P., W.J. Witteman and P.J.M. van der Slot, Experimental study of the spatial evolution of the spectrum of a Raman FEL. . . . . 358 (1995) 126
- Zaretsky, D.F., see Malov, Yu.A. . . . . 358 (1995) 11
- Zavtrak, S.T., Free gas bubbles acoustic laser. . . . . 358 (1995) 473
- Zhang, L., see Xie, J. . . . . 358 (1995) 256
- Zhang, T.B., see Hirshfield, J.L. . . . . 358 (1995) 129
- Zhang, T.B. and T.C. Marshall, High power self-similar radiation pulse in a free electron laser . . . . . 358 (1995) 459
- Zhang, Y., see Xie, J. . . . . 358 (1995) 256
- Zholents, A.A. and M.S. Zolotarev, A proposal for the generation of ultra-short X-ray pulses . . . . . 358 (1995) 455
- Zhong, Y., see Xie, J. . . . . 358 (1995) 256
- Zhu, J., see Wang, M.C. . . . . 358 (1995) ABS 38
- Zhuang, J., see Xie, J. . . . . 358 (1995) 256
- Zhulin, V.I., Theoretical investigation of a waveguide application in a FEL with large  $\mu_c$  . . . . . 358 (1995) 501
- Zimdars, D.A., see Tokmakoff, A. . . . . 358 (1995) 540
- Ziomek, C., see Nguyen, D.C. . . . . 358 (1995) 27
- Ziomek, C.D., J.M. Kinross-Wright and J.G. Plato, Low-level RF control for the AFEL . . . . . 358 (1995) ABS 87
- Zolotarev, M.S., see Zholents, A.A. . . . . 358 (1995) 455